Mesoscale Meteorological Modeling

ROGER A. PIELKE SR.
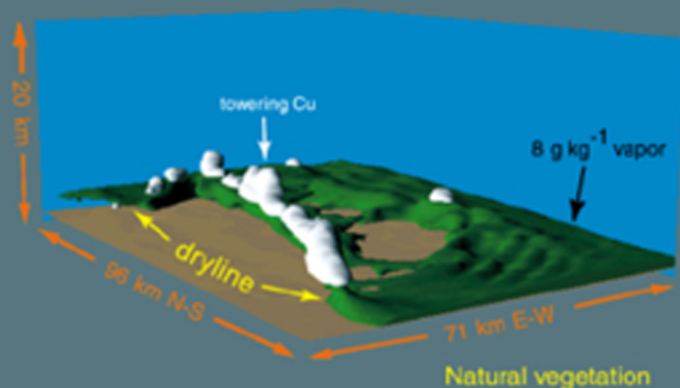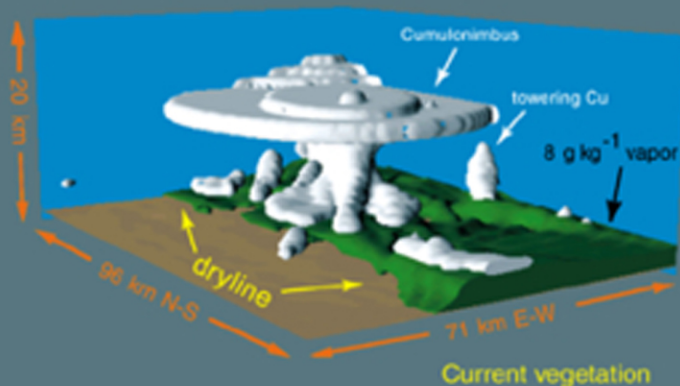
Cumulonimbus

towering Cu

8 g kg^{-1} vapor

20 km

96 km N-S

dryline

71 km E-W

Current vegetation

towering Cu

8 g kg^{-1} vapor

20 km

96 km N-S

dryline

71 km E-W

Natural vegetation

Mesoscale Meteorological Modeling

Second Edition

Mesoscale Meteorological Modeling

Second Edition

Roger A. Pielke, Sr.

Department of Atmospheric Science
Colorado State University
Fort Collins, Colorado

Contents

This Page Intentionally Left Blank

Preface

The purpose of this monograph is to provide an overview of mesoscale numerical modeling, beginning with the fundamental physical conservation relations. An overview of the individual chapters is given in the introduction. This book is an outgrowth of my article entitled "Mesoscale Numerical Modeling" which appeared in Volume 23 of *Advances in Geophysics*.

The philosophy of the book is to start from basic principles as much as possible when explaining specific subtopics in mesoscale modeling. Where too much preliminary work is needed, however, references to other published sources are given so that a reader can obtain the complete derivation (including assumptions). Often only an investigator's recent work is listed; however, once that source is found it is straightforward to refer to his or her earlier work, if necessary, by using the published reference list appearing in that paper. An understanding of the assumptions upon which the mathematical relations used in mesoscale modeling are developed is essential for fluency in this subject. To address as wide an audience as possible, basic material is provided for the beginner as well as a more in-depth treatment for the specialist.

The author wishes to acknowledge the contributions of a widely proficient group of people who provided suggestions and comments during the preparation of this book. The reading of all or part of the draft material for this text was required for a course in mesoscale meteorological modeling taught at the University of Virginia and at Colorado State University. Among the students in that course who provided significant suggestions and corrections are Raymond Arritt, David Bader, Charles Cohen, Omar Lucero, Jeffrey McQueen, Charles Martin, Jenn-Luen Song, Craig Tremback, James Toth, and George Young. P. Flatau is acknowledged for acquainting me with several Soviet works of relevance to mesoscale meteorology. Suggestions and aid were also provided by faculty members in the Atmospheric Science Department at Colorado State University, including Duane E. Stevens, Richard H. Johnson, Wayne H. Schubert, and Richard Pearson, Jr.

Several chapters were also sent to a number of acknowledged experts in certain aspects of mesoscale meteorology. These scientists included Andrè Doneaud (Chapters 1-5, 7, and 8), George Young (Chapter 5), Tzvi Gal-Chen (Chapter 6), Raymond Arritt (Chapter 7), Richard McNider (Chapter 7), Steven Ackerman (Chapter 8), Andrew Goorch (Chapter 8), Larry Freeman (Chapter 8), Michael Fritsch (Chapter 9), William Frank (Chapter 9), Jenn-Luen Song (Chapter 9), R.D. Farley (Chapter 9), Harold Orville (Chapter 9), Robert Lee (Chapter 10), Mike McCumber (Chapter 11), Joseph Klemp (Chapter 12), Mordecay Segal (Chapters 2, 3, 10, 11, and 12), and Robert Kessler (Chapter 12). For their help in reviewing the material I am deeply grateful.

I would also like to thank the individuals who contributed to the summary tabulation of models in Appendix B. Although undoubtedly not a comprehensive list (since not every modeling group responded or could be contacted), it should provide a perspective of current mesoscale modeling capabilities.

I would also like to acknowledge the inspiration of William R. Cotton and Joanne Simpson, who facilitated my entry into the field of mesoscale meteorology. In teaching the material in this text and in supervising graduate research. I have sought to adopt their philosophy of providing students with the maximum opportunity to perform independent, innovative investigations. I would also like to give special thanks to Andrè Doneaud and Mordecay Segal, whose patient, conscientious reading of portions of the manuscript has significantly strengthened the text. In addition, I would like to express my sincere appreciation to Thomas H. Vonder Haar who provided me with an effective research environment in which to complete the preparation of this book.

In writing the monograph, I have speculated in topic areas in which there has been no extensive work in mesoscale meteorology. These speculative discussions, most frequent in the sections on radiative effects, particularly in polluted air masses, also occur in a number of places in the chapters on parameterization, methods of solution, boundary and initial conditions, and model evaluation. Such speculation is risky, of course, because the extensive scientific investigation required to validate a particular approach has not yet been accomplished. Nevertheless, I believe such discussions are required to complete the framework of the text and perhaps may be useful in providing some direction to future work. The introduction of this material is successful if it leads to new insight into the field of mesoscale modeling.

Finally, the writing of a monograph or textbook inevitably results in errors, for which I must assume final responsibility. It is hoped that they will not significantly detract from the usefulness of the book and that the reader will benefit positively from ferreting out mistakes. In any case, I would appreciate comments from users about errors of any sort, including the neglect of relevant current work.

Finally and most importantly, I would like to acknowledge the support of my family—Gloria, Tara, and Roger Jr.—in completing this time-consuming and difficult task.

This Page Intentionally Left Blank

Preface to the Second Edition

Mesoscale meteorological modeling has matured greatly since the first edition was published. From a research tool, mesoscale models are routinely used in operational numerical weather prediction. These models have also been extended into longer-term weather studies, such as seasonal weather prediction and even in climate change studies.

As a result of the proliferation of this atmospheric science modeling tool, the number of published papers has greatly expanded. While I attempted to be reasonably comprehensive in listing this work in the first edition, it is now virtually impossible to be comprehensive today. In fact, with the introduction of the Internet and electronic library searches, the best way to obtain relevant research papers is to access through the World Wide Web!

This edition has new material but also deletes sections. The section on the finite element solution technique in Chapter 10, for example, has been removed since despite its promise, it remains an approach that is used by only a very small subset of mesoscale modelers. Problems have been added to the new addition, based on work in the course Mesoscale Meteorological Modeling (AT 730) which I have taught almost every two years, both at the Department of Environmental Science at the University of Virginia, and in the Department of Atmospheric Science at Colorado State University.

One perspective in this text is the introduction of a new perspective in dissecting meteorological modeling capabilities. There are two emphases to this perspective. First, once the models are stripped to their most basic level, what is their accuracy as a function of wavelength? For the fundamental terms in the equations, this involves the numerical approximation of the local temporal derivative, the advection, the pressure gradient force, and the Coriolis term. For derived terms, this involves the numerical approximations of the vertical and horizontal subgrid-scale fluxes, and the source/sink terms in the conservation equations. Secondly, by defining the individual terms in separate levels of detail,

it is straightforward to dissect the expressions (parameterizations) and ascertain how uncertainty (error) propagates throughout the parameterizations to the level at which their effects are introduced into the conservation equations.

There are quite a few colleagues who provided me comments, corrections, and suggestions with respect to the First and Second Editions. This includes the extensive and thorough cross-checking of the First Edition by Xingzhen Zhang, Changxin Yang, Linsheng Chen, and Jifan Chou in their translation into Chinese. Fredi Boston of the Colorado State University library is thanked for helping find references for the Second Edition.

These colleagues also include Pinhas Alpert, Ray Arritt, Louis Berkofsky, Bob Bornstein, Chris Castro, Guy Cautenet, Tom Chase, Linsheng Cheng, Liu Feng, Mike Flannigan, Zhu Fu-Cheng, Piotr Flatau, Louie Grasso, Mark Hadfield, Bert Holtslag, Hartmut Kapitza, Richard Krasner, Rene Laprise, Alan Lipton, Glen Liston, Guta Mihailovic, Chuck Mollenkamp, Mike Moran, Joseph Mukabana, Peter Olsson, Bill Physick, Andy Pitman, Jim Purdom, Feng Zhi Qiang, Nelson Seaman, Moti Segal, Qingqiu Shao, Graeme Stephens, Lou Steyaert, Roger Stocker, John Strack, Gene Takle, Craig Tremback, Sue Van Den Heever, Glenn Van Knowe, Pier Luigi Vidale, Tomi Vukićević, Roger Wakimoto, Bob Walko, Doug Wesley, Xubin Zeng, and Conrad Ziegler.

I particularly thank Ytzhaq Mahrer, Roni Avissar, Bill Cotton, and Joanne Simpson who have always provided encouragement in the field of mesoscale meteorology and whose counsel and advice I value so much.

I want to acknowledge Dallas Staley who performed an exceptional, outstanding job in typing and editing the text. Her very significant contribution was essential to the completion of the book, and I am very fortunate to have her work with me on this.

Finally, as with the First Edition, my family has been very supportive. I want to dedicate this book to them—Gloria, Roger Jr., Tara, Julie, Richard, Harrison, Megan, and Jacob!

Foreword

While synoptic meteorology and micrometeorology have enjoyed steady progress over the past decades, mesoscale meteorology started to blossom only since the 1970's. Easier access to supercomputers and the subsequent revolution in computing resource availability created by the introduction of workstations and, more recently, PC clusters, has allowed the simulation of nonhydrostatic, three-dimensional atmospheric numerical models over scales of thousands of kilometers which has greatly contributed to the rapid evolution of this field.

Roger A. Pielke, Sr. is closely associated with the field of mesoscale meteorology, and he has been a key figure in its development. During his career, Professor Pielke worked as a Research Meteorologist for the NOAA's Experimental Meteorology Lab in Miami, and as faculty member in the Department of Environmental Sciences at the University of Virginia and the Department of Atmospheric Science at Colorado State University. The three-dimensional mesoscale numerical model that he developed during his graduate studies was truly pioneering and an inspiration in the field. This model has subsequently evolved into one of the state-of-the-art mesoscale numerical models. This was recognized by the American Meteorological Society, which awarded him the Leroy Mesinger Award in 1977 for "fundamental contributions to mesoscale meteorology through numerical modeling of the sea breeze and interaction among the mountains, oceans, boundary layer, and the free atmosphere." His association with ecologists and hydrologists, which started at the University of Virginia, has matured into a solid cooperation at Colorado State University. This collaboration has given him the broad knowledge needed to propel the discipline forward. Indeed, it is now quite obvious the atmosphere is significantly affected by many hydrological and ecological processes occurring near the ground surface. Professor Pielke has pioneered the introduction of these processes in atmospheric models.

Having been at the forefront of the research in mesoscale numerical modeling for the past thirty years, and having served as Chief Editors for the *Monthly*

Weather Review and the *Journal of the Atmospheric Sciences*, Professor Pielke
was in a unique position to write a thorough text on this topic. This is clearly
demonstrated by the more than 2000 references included in this book.

   This book will prove beneficial for teaching purposes and reflects the expe-
rience and knowledge gained by Professor Pielke in teaching the course of
Mesoscale Meteorological Modeling at the University of Virginia and Colorado
State University. Students with a solid background in fluid dynamics and numer-
ical methods can cover the material in one semester. The list of additional
reading material provided at the end of each chapter provides students with
background material on the topics covered in the chapter, while the problems
will help students retain the key points made in the text. I trust that meteorol-
ogy teachers and students alike will find this book very useful, enjoyable, and
a "must have" reference manual for their personal shelves.

<div align="right">

Roni Avissar
Gardner Professor and Chair
Department of Civil and
    Environmental Engineering
Duke University

</div>

Chapter 1

Introduction

To utilize mesoscale dynamical simulations of the atmosphere effectively, it is necessary to understand the basic physical and mathematical foundations of the models and to have an appreciation of how the particular atmospheric system of interest works. This text provides such an overview of the field and should be of use to the practitioner as well as to the researcher of mesoscale phenomena. Because the book starts from fundamental concepts, it should be possible to use the text to evaluate the scientific basis of any simulation model that has been or will be developed.

Mesoscale can be descriptively defined as having a temporal and a horizontal spatial scale smaller than the conventional rawinsonde network, but significantly larger than individual cumulus clouds. This implies that the horizontal scale is on the order of a few kilometers to several hundred kilometers or so. For the purposes of this book, the focus is on mesoscale atmospheric modeling for simulated time scales of a few hours to 24 hours or so. The vertical scale extends from tens of meters to the depth of the troposphere. Clearly, this is a somewhat arbitrary limit; however, the smaller spatial scale corresponds to atmospheric features that for weather forecasting purposes can be described only statistically, whereas the longer limit corresponds to the smallest features that we can generally distinguish on a synoptic weather map. Mesoscale can also be defined as those atmospheric systems that have a horizontal extent large enough for the hydrostatic approximation to the vertical pressure distribution to be valid, yet small enough for the geostrophic and gradient winds to be inappropriate as approximations to the actual wind circulation above the planetary boundary layer. This scale of interest, then, along with computer and cost limitations, defines the domain and grid sizes of mesoscale models. In this text, examples of specific circulations will be presented, illustrating scales of mesoscale circulations.

In this text, the outline of material is as follows. In Chapters 2 and 3 the fundamental conservation relations are introduced and appropriate simplifica-

tions given. In Chapter 4 the equations are averaged to conform to a mesoscale model grid mesh. In Chapter 5 types of models are discussed and their advantages and disadvantages to properly simulate mesoscale phenomena presented. The transformation of the equations to a generalized coordinate representation is given in Chapter 6, and the parameterizations in a mesoscale model of the planetary boundary layer, electromagnetic radiation, and moist thermodynamics are introduced in Chapters 7–9. Methods of solution are illustrated in Chapter 10, and boundary and initial conditions and grid structure are discussed in Chapter 11. The procedure for evaluating models is given in Chapter 12. Examples of mesoscale simulations of particular mesoscale phenomena are provided in Chapter 13. Finally, a summary of several current state-of-the-art mesoscale models is given in Appendix B.

Chapter 2

Basic Set of Equations

The foundation for any model is a set of conservation principles. For mesoscale atmospheric models, these principles are

1. conservation of mass,
2. conservation of heat,
3. conservation of motion,
4. conservation of water, and
5. conservation of other gaseous and aerosol materials.

These principles form a coupled set of relations that must be satisfied simultaneously and that include sources and sinks in the individual expressions.

The corresponding mathematical representations of these principles for atmospheric applications are developed as follows.

2.1   Conservation of Mass

In the earth's atmosphere, mass is assumed to have neither sinks nor sources.[1] Stated another way, this concept requires that the mass into and out of an infinitesimal box must be equal to the change of mass in the box. Such a volume is sketched in Figure 2-1, where $\rho u|_1 \, \delta y \, \delta z$ is the mass flux into the left side and $\rho u|_2 \, \delta y \, \delta z$ the mass flux out of the right side. The symbols δx, δy, and δz represent the perpendicular sides of the box, ρ represents the density, and u represents the velocity component normal to the $\delta z \, \delta y$ plane.

If the size of the box is sufficiently small, then the change in mass flux across the box can be written as

$$[\rho u|_1 - \rho u|_2]\delta y \, \delta z = \left[\rho u|_1 - \rho u|_1 - \left.\frac{\partial \rho u}{\partial x}\right|_1 \delta x - \frac{1}{2}\left.\frac{\partial^2 \rho u}{\partial x^2}\right|_1 (\delta x)^2 - \cdots \right]\delta y \, \delta z$$

$$= \frac{\delta M}{\delta t},$$
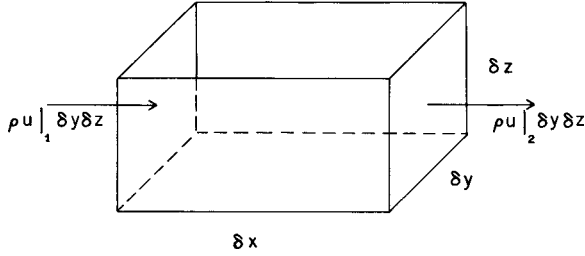
Fig. 2-1. A schematic of the volume used to derive the conservation of mass relation.

where $\rho u|_2$ has been written in terms of a one-dimensional Taylor series expansion and $\delta M/\delta t$ is the rate of increase or decrease of mass in the box. Neglecting terms in the series of order $(\delta x)^2$ and higher, this expression can be rewritten as

$$-\frac{\partial \rho u}{\partial x}\bigg|_1 \delta x\,\delta y\,\delta z \simeq \frac{\delta M}{\delta t},$$

and since the mass M is equal to ρV (where $V = \delta x\,\delta y\,\delta z$ is the volume of the box), this expression can be rewritten as

$$-\frac{\partial \rho u}{\partial x}\bigg|_1 \delta x\,\delta y\,\delta z \simeq V\frac{\delta \rho}{\delta t},$$

assuming the volume is constant with time.

If the mass flux through the sides $\delta x\,\delta y$ and $\delta x\,\delta z$ is considered in a similar fashion, then the complete equation for mass flux in the box can be written as

$$-\frac{\partial}{\partial x}\rho u\bigg|_1 \delta x\,\delta y\,\delta z - \frac{\partial}{\partial y}\rho v\bigg|_1 \delta x\,\delta y\,\delta z - \frac{\partial}{\partial z}\rho w\bigg|_1 \delta x\,\delta y\,\delta z \simeq V\frac{\delta \rho}{\delta t},$$

and, dividing by volume, the resulting equation is

$$-\frac{\partial \rho u}{\partial x}\bigg|_1 - \frac{\partial \rho v}{\partial y}\bigg|_1 - \frac{\partial \rho w}{\partial z}\bigg|_1 \simeq \frac{\delta \rho}{\delta t}.$$

If the time and spatial increments are taken to zero in the limit, then

$$\lim_{\substack{\delta x\to 0,\delta y\to 0\\ \delta z\to 0,\delta t\to 0}}\left(-\frac{\partial \rho u}{\partial x}\bigg|_1 - \frac{\partial \rho v}{\partial y}\bigg|_1 - \frac{\partial \rho w}{\partial z}\bigg|_1\right) = \lim_{\substack{\delta x\to 0,\delta y\to 0\\ \delta z\to 0,\delta t\to 0}}\frac{\delta \rho}{\delta t},$$

since the remainder of the terms in the Taylor series expansion contain δx, δy, or δz. Written in an equivalent fashion,

$$-\left[\frac{\partial}{\partial x}\rho u + \frac{\partial}{\partial y}\rho v + \frac{\partial}{\partial z}\rho w\right] = \frac{\partial \rho}{\partial t}, \tag{2-1}$$

where the subscript 1 has been dropped because the volume of the box has gone to 0 in the limit. Equation (2-1) is the mathematical statement of the

conservation of mass. It is also called the *continuity equation*. In vector notation, it is written as

$$-(\nabla \cdot \rho \vec{V}) = \partial \rho / \partial t. \tag{2-2}$$

2.2   Conservation of Heat

   The atmosphere on the mesoscale behaves very much like an ideal gas and is considered to be in local *thermodynamic equilibrium*.[2] The first law of thermodynamics for the atmosphere states that differential changes in heat content, dQ, are equal to the sum of differential work performed by an object, dW, and differential increases in internal energy, dI. Expressed more formally, the first law of thermodynamics states that

$$dQ = dW + dI. \tag{2-3}$$

   If we represent the region over which Eq. (2-3) applies as a box (Figure 2-2), with volume $\delta x \, \delta y \, \delta z$, then an incremental increase in the x direction, caused by a force F, can be expressed as

$$dW = F \, dx,$$

and since force can be expressed as a pressure P exerted over an area $\delta y \, \delta z$,

$$dW = p \, \delta y \, \delta z \, \delta x. \tag{2-4}$$

The term $\delta y \, \delta z \, \delta x$ represents a change in volume dV, so that Eq. (2-4) can be rewritten as

$$dW = p \, dV,$$
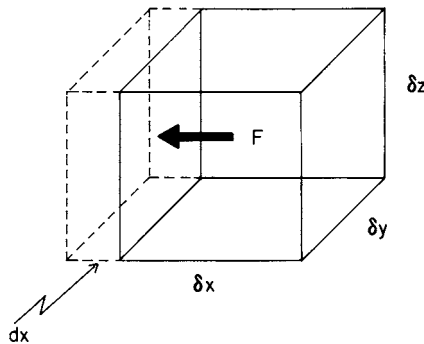
Fig. 2-2.   A schematic of the change in size of a volume of gas resulting from a force F exerted over the surface $\delta z \, \delta y$.

For a unit mass of material, it is convenient to rewrite the expression as

$$dw = p \, d\alpha, \tag{2-5}$$

where α is the specific volume (i.e., volume per unit mass). In an ideal gas, which the atmosphere closely approximates, as discussed later, the pressure in Eq. (2-5) is exerted uniformly on all sides of the gas volume.

The expression for work in Eq. (2-3) could also have included external work performed by such processes as chemical reactions, phase changes, or electromagnetism; however, these effects are not included in this derivation of work.

The ideal gas law, referred to previously, was derived from observations of the behavior of gases at different pressures, temperatures, and volumes. Investigators in the seventeenth and eighteenth centuries found that for a given gas, pressure times volume equals a constant at any fixed temperature (Boyle's law) and that pressure divided by temperature equals a constant at any fixed volume (Charles's law). These two relations can be stated more precisely as

$$p\alpha = F_1(T) \tag{2-6}$$

and

$$p/T = F_2(\alpha), \tag{2-7}$$

where a unit mass of gas is assumed. If Eq. (2-6) is divided by T and Eq. (2-7) is multiplied by α, then

$$p\alpha/T = (1/T)F_1(T) = \alpha F_2(\alpha). \tag{2-8}$$

Since the two right-side expressions are functions of two different variables, the entire expression must be equal to a constant, conventionally denoted as R. Thus Eq. (2-8) is written as

$$p\alpha/T = R, \tag{2-9}$$

where R has been found to be a function of the chemical composition of the gas. The extent to which actual gases obey Eq. (2-9) specifies how closely they approximate an ideal gas.

The value of the gas constant R for different gases is determined using Avogadro's hypothesis that at a given temperature and pressure, gases containing the same number of molecules occupy the same volume. From experimental work, for example, it has been shown that at a pressure of 1 atm ($P_0 = 1014$ mb) and a temperature of $T_0 = 273$ K, 22.4 kL of a gas (V_0) will have a mass in kilograms equal to the molecular weight of the gas μ. This quantity of gas is defined as 1 kmol.

Using this information, the ideal gas law [Eq. (2-9)], and the definition $\alpha_0 = V_0/\mu$, we have

$$P_0 V_0/\mu T_0 = R,$$

or, by definition,

$$P_0 V_0/\mu T_0 = R = R^*/\mu \text{ [so that } P_0 V_0/T_0 = R^*], \tag{2-10}$$

where R^* is called the universal gas constant and μ has units of kg/kmole. From experiments, $R^* = 8.314472 \times 10^3$ J K^{-1} kmol^{-1} (Mohr and Taylor 2000). Since Eq. (2-10) is valid for any combination of pressure, temperature, and volume,

$$p\alpha/T = R = R^*/\mu. \tag{2-11}$$

In the atmosphere, the apparent molecular weight of air, μ_{atm}, is determined by the fractional contribution by mass of each component gas (Table 2-1) from the equation

$$\mu_{atm} = \sum_{i=1}^{N} m_i \bigg/ \sum_{i=1}^{N} (m_i/\mu_i),$$

where m_i is the fractional contribution by mass of the N individual gases in the atmosphere ($\sum_{i=1}^{N} m_i = 1$) and μ_i represents their respective molecular weights.[3] For the gaseous components in Table 2-1, excluding water vapor,

$$\mu_{dry\ atm} = \frac{0.7551 + 0.2314 + 0.0128}{(0.7551/28.016) + (0.2314/32.00) + (0.0128/39.94)} = 28.98,$$

so that the dry gas constant of the atmosphere, R_d, is

$$R_d = R^*/28.98 = 287 \,\text{J}\,\text{K}^{-1}\,\text{kg}^{-1}.$$

When water vapor is included, the apparent molecular weight can be written as

$$\mu_{atm} = 1 \bigg/ \left(\frac{1-q}{28.98} + \frac{q}{18.02} \right),$$

TABLE 2-1

Molecular Weight and Fractional Contribution by Mass of Major Gaseous
Components of the Atmosphere

Gas	Molecular weight	Fractional contribution by mass
N_2	28.016	0.7551
O_2	32.00	0.2314
Ar	39.94	0.0128
H_2O	18.02	Variable

From Wallace and Hobbs 1977.

where q is the specific humidity or ratio of the mass of water vapor M to the mass of dry air M_d. Expanding this relation,

$$
\begin{aligned}
\mu_{atm} &= \frac{1}{(1/28.98)(1 - q + (28.98/18.02)q)} \\
&= \frac{28.98}{1 - q + (28.98/18.02)q} \\
&= \frac{28.98}{1 + q[(28.98/18.02) - 1]} \\
&= \frac{28.98}{1 + 0.61q},
\end{aligned}
$$

and inserting μ_{atm} into Eq. (2-11) gives

$$
p\alpha = R_d(1 + 0.61q)T. \tag{2-12}
$$

This form of the ideal gas law includes the contribution of water vapor and is often written as

$$
p\alpha = R_d T_V, \tag{2-13}
$$

where T_V is called the *virtual temperature*, or the temperature required in a dry atmosphere to have the same value of $p\alpha$ as in an atmosphere with a specific humidity q of water vapor. For typical atmospheric conditions (e.g., $q = 0.006$ kg/kg), the difference between the virtual and actual temperatures is about 1°C. Since $T_V \leq T$, air at the same pressure and temperature is less dense when water vapor is present than when it is not. The virtual temperature is generally used by convention in preference to recomputing the gas constant $R = R_d(1 + 0.61q)$.

To complete the derivation of the first law of thermodynamics for an ideal gas, it is useful to introduce the concept of exact differentials. If a function F exists such that

$$
F = F(x, y),
$$

where x and y are two independent variables,[4] then

$$
dF = (\partial F/\partial x)dx + (\partial F/\partial y)dy = M\,dx + N\,dy
$$

by the chain rule of calculus. If

$$
\partial M/\partial y = \partial N/\partial x,
$$

then

$$
\partial^2 F/\partial x\,\partial y = \partial^2 F/\partial y\,\partial x, \tag{2-14}
$$

and F is an exact differential. Stated more physically, if Eq. (2-14) is valid, then the path over which the function is evaluated (e.g., $\partial/\partial x$ first, then $\partial/\partial y$, as contrasted with $\partial/\partial y$ first, then $\partial/\partial x$) is unimportant. If the left and right sides of Eq. (2-14) are not equal however, then dF is an inexact differential, and different paths of computing it will give different answers.

To ascertain whether the change in work given by Eq. (2-5) is an exact differential or not, it is useful to rewrite the expression as

$$dw = d(p\alpha) - \alpha\,dp,$$

using the product rule of differentiation $[d(p\alpha) = p\,d\alpha + \alpha\,dp]$. Thus by the gas law [Eq. (2-13)],

$$dw = R_d dT_V - \alpha\,dp.$$

To check for exactness, let $M = R_d$ and $N = -\alpha$; then

$$\partial M/\partial p = \partial R_d/\partial p = 0 \qquad \text{and} \qquad \partial N/\partial T_V = \partial(-\alpha)/\partial T_V = -R_d/p.$$

Therefore, dw is not an exact differential. The path in which work is performed is important in determining its value.

The internal energy I in Eq. (2-3), expressed for a unit mass of material, can be written as

$$e = e(T_V, \alpha), \tag{2-15}$$

where, as a result of the ideal gas law, the virtual temperature T_V and the specific volume α can be used to determine the internal energy of the material. From the chain rule of calculus,

$$de = (\partial e/\partial T_V)dT_V + (\partial e/\partial \alpha)d\alpha,$$

but from experiments with gases that closely follow the ideal gas law [Eq. (2-13)], internal energy changes only when temperature changes (i.e., $\partial e/\partial \alpha = 0$). And if we define heat per unit mass from Eq. (2-3) as h, then

$$dh = dw + de = p\,d\alpha + (\partial e/\partial T_V)dT_V$$

and

$$\partial h/\partial T_V = \partial e/\partial T_V = C_\alpha,$$

where C_α is defined as the specific heat at constant volume.

Experiments have shown C_α to be only a slowly varying function of temperature. Thus the internal energy relationship for an ideal gas is expressed as

$$de = C_\alpha dT_V.$$

Since $M = \partial e/\partial T_V = C_\alpha$ and $N = \partial e/\partial \alpha = 0$, it is obvious that $\partial M/\partial \alpha = \partial N/\partial T = 0$, so that internal energy for an ideal gas is an exact differential.

Our first law of thermodynamics [Eq. (2-3)] can now be written as

$$dh = de + dw = C_\alpha dT_V + p\,d\alpha, \tag{2-16}$$

where the diagonal slash through the two terms indicates that they are inexact differentials (dh is inexact because the sum of an exact and an inexact differential must be inexact). It is not convenient to work with this form of the first law, however, because the path taken to go from one set of temperature and pressure, for example, to a different set will affect the amount of heat lost or gained and the amount of work performed.

To eliminate this dependency on path, Eq. (2-16) can be made an exact differential by dividing by temperature T_V and using the ideal gas law [Eq. (2-13)] so that

$$dh/T_V = C_\alpha(dT_V/T_V) + (R_d/\alpha)d\alpha. \tag{2-17}$$

Since $M = C_\alpha/T_V$ and $N = R_d/\alpha$, we have $\partial M/\partial \alpha = 0$ and $\partial N/\partial T_V = 0$, so that

$$dh/T_V = ds$$

is an exact differential, where s is defined as *entropy*.

Unfortunately, Eq. (2-17) is not in a convenient form for use by meteorologists because temperature and pressure are measured and specific volume is not. To generate a more useful form of Eq. (2-17), we differentiate the ideal gas law [Eq. (2-13)] logarithmically so that

$$(1/\alpha)d\alpha = (1/T_V)dT_V - (1/p)dp,$$

and substituting into Eq. (2-17) yields

$$ds = dh/T_V = (C_\alpha dT_V/T_V) + (R_d dT_V/T_V) - (R_d/p)dp$$

or

$$ds = dh/T_V = (C_\alpha + R_d)(dT_V/T_V) - (R_d/p)dp. \tag{2-18}$$

Since

$$dh = (C_\alpha + R_d)dT_V - \alpha\,dp,$$

we have

$$\partial h/\partial T_V = C_\alpha + R_d = C_p,$$

where C_p is defined as the specific heat at constant pressure. Therefore, Eq. (2-18) is written as

$$ds = C_p(dT_V/T_V) - (R_d/p)dp. \tag{2-19}$$

For an ideal monotomic gas, the ratio of $C_p : C_\alpha : R_d$ is $5 : 3 : 2$, whereas for a diatomic gas (such as the atmosphere closely approximates) the ratio of $C_p : C_\alpha : R_d$ is $7 : 5 : 2$.

  For the situation when no heat is gained or lost (e.g., $ds = 0$),

$$dT_V/T_V = (R_d/C_p)dp/p,$$

which can be rewritten as

$$d \ln T_V = (R_d/C_p)d \ln p. \tag{2-20}$$

If a parcel of air moves between two points with temperatures and pressures given by (T_{V_1}, P_1) and (T_{V_2}, P_2), then integrating Eq. (2-20) gives

$$\int_{T_{V_1}}^{T_{V_2}} d \ln T_V = (R_d/C_p) \int_{P_1}^{P_2} d \ln P = \ln(T_{V_2}/T_{V_1}) = (R_d/C_p) \ln(P_2/P_1).$$

Taking antilogs yields

$$T_{V_2}/T_{V_1} = (P_2/P_1)^{R_d/C_p},$$

which is customarily called *Poisson's equation*. If we set $P_2 = 1000$ mb and T_{V_2} is defined as the *potential temperature* θ, then

$$\theta = T_V(1000/p)^{R_d/C_p}, \tag{2-21}$$

where p is in millibars.

  To determine the relationship between the potential temperature θ and the entropy s, logarithmically differentiate Eq. (2-21) and multiply by C_p, which yields

$$(C_p/\theta)d\theta = (C_p/T_V)dT_V - (R_d/p)dp,$$

which is identical to Eq. (2-19), so that

$$(C_p/\theta)d\theta = ds = dh/T_V. \tag{2-22}$$

Thus a change in potential temperature is equivalent to a change in entropy.

  If the change in potential temperature is observed following a parcel, then Eq. (2-22) can be written as

$$\frac{C_p}{\theta} \frac{d\theta}{dt} = \frac{ds}{dt} = \frac{1}{T_V} \frac{dh}{dt} = S_\theta \frac{C_p}{\theta}, \tag{2-23}$$

where S_θ represents the sources and sinks of heat as expressed by changes in potential temperature. The contributors to S_θ include the sum of the following processes:

$$S_\theta = \begin{bmatrix} + \text{ freezing} \\ - \text{ melting} \end{bmatrix} + \begin{bmatrix} + \text{ condensation} \\ - \text{ evaporation} \end{bmatrix} + \begin{bmatrix} + \text{ deposition} & \text{(vapor to solid)} \\ - \text{ sublimation} & \text{(solid to vapor)} \end{bmatrix}$$

$$+ \begin{bmatrix} + \text{ exothermic chemical reactions} \\ - \text{ endothermic chemical reactions} \end{bmatrix}$$

$$+ \begin{bmatrix} + \text{ net radiative flux convergence} \\ - \text{ net radiative flux divergence} \end{bmatrix}$$

$$+ \begin{bmatrix} \text{dissipation of kinetic energy} \\ \text{by molecular motions} \end{bmatrix}. \tag{2-24}$$

The precise evaluation of these terms can be complicated, and further discussion of them is deferred to later chapters. In Eq. (2-23), the transfer of heat by molecular processes is not included. The neglect of molecular transfers of heat, or other properties of the air, on the mesoscale is justified by the relative contributions to such exchanges through the motion of the fluid, as contrasted with molecular diffusion. This neglect is discussed further in Section 2.3.2 of this chapter, as well as in Section 3.3.2 of Chapter 3 and Section 5.1 of Chapter 5.

The term $d\theta/dt$ denotes changes of potential temperature following a parcel, with the operator d/dt often called the *Lagrangian derivative*. Since θ is a function of the three coordinate directions x, y, and z of a parcel at a given time t [i.e., $\theta = \theta(x(t), y(t), z(t), t)$], then, by the chain rule of calculus,

$$\frac{d\theta}{dt} = \frac{\partial\theta}{\partial t} + \frac{\partial\theta}{\partial x}\frac{dx}{dt} + \frac{\partial\theta}{\partial y}\frac{dy}{dt} + \frac{\partial\theta}{\partial z}\frac{dz}{dt} = S_\theta$$

or

$$\frac{\partial\theta}{\partial t} = -u\frac{\partial\theta}{\partial x} - v\frac{\partial\theta}{\partial y} - w\frac{\partial\theta}{\partial z} + S_\theta = -\vec{V}\cdot\nabla\theta + S_\theta, \tag{2-25}$$

where $\partial\theta/\partial t$ represents local changes in potential temperature and the operation $\partial/\partial t$ is called the *Eulerian derivative*. This equation is a standard form of the conservation of heat relation (often called the potential temperature equation) used in mesoscale models.

It should be noted, however, that since $dh/dt = (C_p T_V/\theta)d\theta/dt$, the potential temperature equation is proportional to, but not equal to, changes in heat content. The proportionality term is given by $C_p T_V/\theta$. The conservation of heat relation is represented by a potential temperature equation rather than by dh/dt, because, as pointed out earlier, the latter form is an inexact differential and thus depends on the path taken to accomplish a change. However, $d\theta/dt$ is independent of path.

2.3   Conservation of Motion

The conservation of motion is expressed by Newton's second law, which states that a force exerted on an object causes an acceleration, as given by

$$\vec{F} = M\vec{a},$$

where $\vec{F}$ and $\vec{a}$ are the force and acceleration vectors, respectively, and M is the mass of the object. In atmospheric science it is conventional to work with force normalized by mass, so this expression can be written as

$$\vec{F}/M = \vec{f} = \vec{a}. \qquad (2\text{-}26)$$

Since acceleration represents the change of velocity with time following an object, $\vec{a}$ can be written as

$$\vec{a} = d_{\mathrm{n}}\vec{V}_{\mathrm{n}}/dt, \qquad (2\text{-}27)$$

where the subscript n refers to a nonaccelerating coordinate system. However, because atmospheric motions are referenced to a rotating earth, the acceleration must be expressed in a different form.

If the earth is rotating with constant angular velocity $\vec{\Omega}$, then the velocity $\vec{V}_{\mathrm{n}}$ of an object or parcel of air may be written as the sum of the velocity relative to the earth and the velocity resulting from rotation. Expressed mathematically,[5]

$$\vec{V}_{\mathrm{n}} = \vec{V} + \vec{\Omega} \times \vec{R}, \qquad (2\text{-}28)$$

where $\vec{R}$ represents the position vector of the parcel as measured from the origin of the earth's center, as shown in Figure 2-3. The time differential operator can be similarly described by the sum of a derivative relative to the earth's surface and changes resulting from the rotation rate of the planet, as given by

$$\frac{d_{\mathrm{n}}}{dt} = \frac{d}{dt} + \vec{\Omega} \times . \qquad (2\text{-}29)$$

Substituting Eqs. (2-29) and (2-28) into Eq. (2-27) yields

$$\vec{a} = \left(\frac{d}{dt} + \vec{\Omega}\times\right)\vec{V}_{\mathrm{n}} = \frac{d\vec{V}_{\mathrm{n}}}{dt} + \vec{\Omega} \times \vec{V}_{\mathrm{n}} = \frac{d}{dt}(\vec{V} + \vec{\Omega} \times \vec{R}) + \vec{\Omega} \times (\vec{V} + \vec{\Omega} \times \vec{R}).$$

Simplifying and rearranging results in

$$\vec{a} = (d\vec{V}/dt) + 2(\vec{\Omega} \times \vec{V}) + \vec{\Omega} \times (\vec{\Omega} \times \vec{R}), \qquad (2\text{-}30)$$

where the relation $\vec{V} = d\vec{R}/dt$ has been used.

The first term on the right side of Eq. (2-30) is the acceleration as viewed from the rotating earth. The second term, the *Coriolis acceleration*, operates
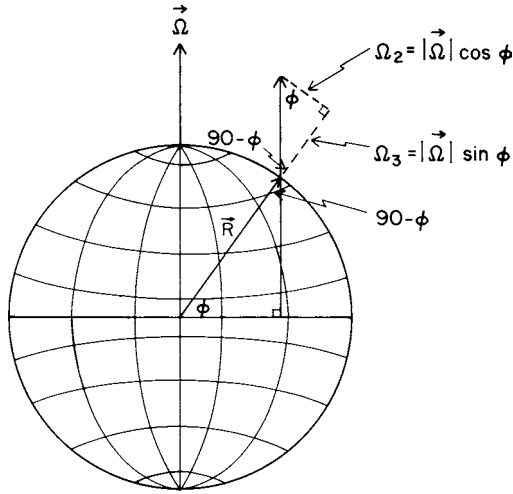
Fig. 2-3. The components of the angular velocity of the earth $\vec{\Omega}$ as a function of latitude ϕ. For the earth, $|\vec{\Omega}| = \Omega = 2\pi/24\ h$.

only when there is motion, and the last term, the *centripetal acceleration*, acts on a parcel at all times.

   After describing acceleration relative to the earth, we need to specify the forces that cause changes in motion. In performing this analysis, it is convenient to consider forces as acting *externally* and *internally* to a parcel. External forces include those resulting from pressure gradients, gravity, and so on, and are independent of motion; internal forces are caused by fluid interactions with itself involving frictional dissipation by molecules. This concept of external and internal forces is related to our idea of a parcel that, although assumed to be "infinitesimally" small so that we can apply the concepts of differential calculus, is still presumed to be large relative to individual molecules. In other words, this parcel must be sufficiently large so that only the statistical properties of molecules are important (and are expressed in terms of such so-called macroscopic quantities as pressure and temperature).

2.3.1 External Forces

   The pressure gradient force can be derived in a similar fashion to that used for the continuity-of-mass equation (Section 2.1). The pressure difference across a box, depicted in Figure 2-4, can be expanded in a one-dimensional series and expressed as

$$P_2 - P_1 = \frac{\partial p}{\partial x}\bigg|_1 \delta x + \frac{1}{2}\frac{\partial^2 p}{\partial x^2}\bigg|_1 (\delta x)^2 + \cdots + \mathrm{O}((\delta x)^3).$$
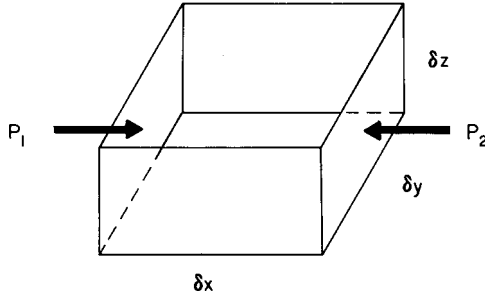
Fig. 2-4. A schematic of a volume with pressure (P_1 and P_2) on two opposing sides.

Since pressure is force per unit area and is directed toward lower pressure, the force per unit mass in the x direction f_{PGF_x} required in Eq. (2-26) can be written as

$$f_{\mathrm{PGF}_x} = -\frac{(P_2 - P_1)A}{M} = -\frac{\partial p}{\partial x}\bigg|_1 \frac{\delta x A}{M} - \frac{1}{2}\frac{\partial^2 p}{\partial x^2}\bigg|_1 \frac{(\delta x)^2 A}{M} + \cdots, \qquad (2\text{-}31)$$

where

$$A = \delta y\,\delta z \qquad \text{and} \qquad M = \rho V = \rho\,\delta x\,\delta y\,\delta z.$$

Substituting A and M into Eq. (2-31) yields

$$f_{\mathrm{PGF}_x} = -\frac{1}{\rho}\frac{\partial p}{\partial x}\bigg|_1 - \frac{1}{2\rho}\frac{\partial^2 p}{\partial x^2}\bigg|_1 \partial x - \cdots,$$

and if we require δx to become very small,

$$f_{\mathrm{PGF}_x} = \lim_{\delta x \to 0}\left[-\frac{1}{\rho}\frac{\partial p}{\partial x}\bigg|_1 - \frac{1}{2\rho}\frac{\partial^2 p}{\partial x^2}\bigg|_1 \partial x - \cdots\right] = -\frac{1}{\rho}\frac{\partial p}{\partial x}.$$

An equivalent derivation in the y and z directions[6] results in a pressure gradient force given by

$$\vec{f}_{\mathrm{PGF}} = -\frac{1}{\rho}\left[\frac{\partial p}{\partial x}\vec{i} + \frac{\partial p}{\partial y}\vec{j} + \frac{\partial p}{\partial z}\vec{k}\right] = -\frac{1}{\rho}\nabla p,$$

where $\vec{i}$, $\vec{j}$, and $\vec{k}$ are the unit vectors in the three spatial directions.

Gravity is another external force. If the gravitational force between the earth and an air parcel is defined as $\vec{G}$, it is customary to include the centripetal acceleration, given in Eq. (2-30), in the definition of a *modified gravitational force*. The force $\vec{G}$ is directed toward the center of the earth with a magnitude proportional to the mass of the earth and inversely proportional to the square of the distance of a parcel from the center of the earth. Subtracting the centripetal acceleration from $\vec{G}$ produces the modified gravity, given as

$$-g\vec{k} = \vec{G} - \vec{\Omega} \times (\vec{\Omega} \times \vec{R}).$$

In its application to atmospheric flows, variations of g because of height above the ground or location on the earth's surface are sometimes considered; however, for mesoscale circulations these small variations in the troposphere are customarily ignored, and the modified gravity is treated as a constant ($g = 9.80665$ m s^{-2}; Mohr and Taylor 2000).

Other external forces, such as electromagnetism, could be included, but for mesoscale circulations within the troposphere only gravity and the pressure gradient are typically included as external forces.

2.3.2 Internal Forces

Internal forces are required to account for the dissipation of momentum by molecular motions. Defined in terms of postulates, the effects of these forces on the momentum are expressed in terms of the viscosity of the gas (or liquid) and the deformation of the momentum field. In the atmosphere, on the mesoscale, the viscosity is sufficiently small and the velocities are sufficiently great that the influence of the internal forces is ignored. We demonstrate the reasons for the neglect of these forces more quantitatively in Sections 3.3.2 and 5.1.

The conservation-of-motion relation, Eq. (2-26), can now be written as

$$d\vec{V}/dt = -(1/\rho)\nabla p - g\vec{k} - 2\vec{\Omega} \times \vec{V}, \tag{2-32}$$

where the last term on the right side, although only an apparent force arising because of the coordinate frame of reference, is referred to as the *Coriolis force*.

Since

$$\vec{V} = \vec{V}(x(t), y(t), z(t), t)$$

(i.e., the velocity is a function of time and the spatial location at a given time), by the chain rule of calculus,

$$\frac{d\vec{V}}{dt} = \frac{\partial\vec{V}}{\partial x}\frac{dx}{dt} + \frac{\partial\vec{V}}{\partial y}\frac{dy}{dt} + \frac{\partial\vec{V}}{\partial z}\frac{dz}{dt} + \frac{\partial\vec{V}}{\partial t}$$

or

$$\frac{d\vec{V}}{dt} = \vec{V}\cdot\nabla\vec{V} + \frac{\partial\vec{V}}{\partial t}.$$

Therefore, Eq. (2-32) can be rewritten as

$$\frac{\partial\vec{V}}{\partial t} = -\vec{V}\cdot\nabla\vec{V} - \frac{1}{\rho}\nabla p - g\vec{k} - 2\vec{\Omega} \times \vec{V}, \tag{2-33}$$

which is a standard form of the conservation of momentum, often called the *equation of motion*.

2.4   Conservation of Water

Water can occur in three forms: solid, liquid, and vapor. To write a conserva-
tion law for this substance, we thus need to keep track of the changes of phase
of water and to follow its movement through the atmosphere.

The conservation law for water can be written as

$$dq_n/dt = S_{q_n}, \quad n = 1, 2, 3, \tag{2-34}$$

where q_1, q_2, and q_3 are defined as the ratio of the mass of the solid, liquid,
and vapor forms of water, respectively, to the mass of air in the same volume.
The source-sink term S_{q_n} refers to the processes whereby water undergoes phase
changes, as well as to water generated or lost in chemical reactions. For most
mesoscale applications, chemical changes in water mass can be neglected and
the terms can be expressed as contributions owing to the following processes:

$$S_{q1} = \begin{bmatrix} + \text{ freezing} \\ - \text{ melting} \end{bmatrix} + \begin{bmatrix} + \text{ deposition} & \text{(vapor to solid)} \\ - \text{ sublimation} & \text{(solid to vapor)} \end{bmatrix}$$

$$+ \begin{bmatrix} + \text{ fallout from above} \\ - \text{ fallout to below} \end{bmatrix}$$

$$S_{q2} = \begin{bmatrix} + \text{ melting} \\ - \text{ freezing} \end{bmatrix} + \begin{bmatrix} + \text{ condensation} \\ - \text{ evaporation} \end{bmatrix} + \begin{bmatrix} + \text{ fallout from above} \\ - \text{ fallout to below} \end{bmatrix}$$

$$S_{q3} = \begin{bmatrix} + \text{ evaporation} \\ - \text{ condensation} \end{bmatrix} + \begin{bmatrix} + \text{ sublimation} & \text{(solid to vapor)} \\ - \text{ deposition} & \text{(vapor to solid)} \end{bmatrix}.$$

The manner in which these terms are expressed mathematically can be very
involved. In cumulus cloud models, for example, the condensation of water
onto aerosols and their subsequent development into hydrometeors that fall to
the ground are accounted for by categorizing cloud droplets into a spectrum
of interacting size classes. Incorporation of the ice phase creates an even more
complex set of interactions.

By contrast, the simplest representation of these sources and sinks of water
is to prohibit relative humidities above 100%[7] and liquid or solid water below
100%. Excess water vapor over 100% is immediately condensed (or deposited)
and falls out as rain or snow. As it falls through an unsaturated environment,
water evaporates (or sublimates) to the water vapor phase, thereby elevating the
relative humidity.

Using the chain rule, Eq. (2-34) can be written in terms of the local time rate
of change as

$$\partial q_n/\partial t = -\vec{V} \cdot \nabla q_n + S_{q_n}, \quad n = 1, 2, 3. \tag{2-35}$$

Further discussion regarding the source-sink term S_{q_n} is given in Chapter 9.

2.5 Conservation of Other Gaseous and Aerosol Materials

Conservation relations of the form given by Eq. (2-34) can be written for any gaseous or aerosol material in the atmosphere, expressed mathematically as

$$d\chi_m/dt = S_{\chi_m}, \qquad m = 1, 2, 3, \ldots, M, \tag{2-36}$$

where χ_m refers to any chemical species except water [which is explained by Eq. (2-35)] and is expressed as the mass of the substance to the mass of air in the same volume. Examples of important occasional constituents in the atmosphere include carbon dioxide, methane, sulfur dioxide, (SO_2) sulfates, nitrates, ozone, and the herbicide 2-4-5-T. The source-sink term S_{χ_m} can be written to include changes of state (analogous to that performed for water) as well as chemical transformations, precipitation, and sedimentation.[8] In the atmosphere, for instance, it is well known that SO_2 will convert to sulfate within several days after release. In general, the mathematical representation of this source-sink term can be very complex.

Using the chain rule, Eq. (2-36) can be written as

$$\partial\chi_m/\partial t = -\vec{V} \cdot \nabla\chi_m + S_{\chi_m}, \qquad m = 1, 2, \ldots, M. \tag{2-37}$$

As more researchers begin to realize the serious impact of air pollution on our health and economic well-being and of trace gases and aerosols within the Earth's climate system, they are including this conservation relation in their mesoscale models.

2.6 Summary

Equations (2-2), (2-25), (2-33), (2-35), and (2-37) are listed together as

$$\partial\rho/\partial t = -(\nabla \cdot \rho\vec{V}), \tag{2-38}$$

$$\partial\theta/\partial t = -\vec{V} \cdot \nabla\theta + S_\theta, \tag{2-39}$$

$$\partial\vec{V}/\partial t = -\vec{V} \cdot \nabla\vec{V} - 1/\rho\nabla p - g\vec{k} - 2\vec{\Omega} \times \vec{V}. \tag{2-40}$$

$$\partial q_n/\partial t = -\vec{V} \cdot \nabla q_n + S_{q_n}, \qquad n = 1, 2, 3, \tag{2-41}$$

and

$$\partial\chi_m/\partial t = -\vec{V} \cdot \nabla\chi_m + S_{\chi_m}, \qquad m = 1, 2, \ldots, M. \tag{2-42}$$

When we use these equations in the remainder of the text, it is convenient to adopt the formalism of tensor notation. This makes the equations much easier

to handle, providing that the following simple rules are used:

1. Repeated indices are summed (e.g., in a three-dimensional space, $a_{ii} = a_{11} + a_{22} + a_{33}$).

2. Single indices in a term are called free indexes and refer to the order of a tensor, e.g., a_i is a tensor of order one (a vector), a_{ij} is a tensor of order two (a matrix), and a is a tensor of order zero (a scalar). The maximum value that a free index can attain depends on the spatial dimensions of the system ($i = 3$ for the atmosphere).

3. Only tensors of the same order can be added.

4. Multiplication of tensors can be performed as for scalars (because they are commutative with respect to addition and multiplication, a definite advantage as compared to vectors).

5. Parameters are defined to simplify the writing of the gravitational and Coriolis accelerations; i.e.,

$$\delta_{ij} = \begin{bmatrix} 1 & 0 & 0 \\ 0 & 1 & 0 \\ 0 & 0 & 1 \end{bmatrix} = \begin{cases} 1 \text{ for } i = j \\ 0 \text{ for } i \neq j, \end{cases}$$

where i refers to the row and j refers to the column, and

$$\epsilon_{i,j,k} = \left. \begin{matrix} \overbrace{\begin{bmatrix} 0 & 0 & 0 \\ 0 & 0 & 1 \\ 0 & -1 & 0 \end{bmatrix}}^{j} \begin{bmatrix} 0 & 0 & -1 \\ 0 & 0 & 0 \\ 1 & 0 & 0 \end{bmatrix} \underbrace{\begin{bmatrix} 0 & 1 & 0 \\ -1 & 0 & 0 \\ 0 & 0 & 0 \end{bmatrix}}_{k} \end{matrix} \right\} i,$$

where the following device has been used: for 0, $i = j$, $i = k$, or $j = k$; for 1, even permutations of i, j, and k; and for -1, odd permutations of i, j, and k.

Using this notational device, along with the requirement that the independent spatial variables $x_1 = (x, y, z)$ are perpendicular to each other at all locations. Equations (2-38)–(2-42) can be rewritten as

$$\frac{\partial \rho}{\partial t} = -\frac{\partial \rho u_j}{\partial x_j}, \tag{2-43}$$

$$\frac{\partial \theta}{\partial t} = -u_j \frac{\partial \theta}{\partial x_j} + S_\theta, \tag{2-44}$$

$$\frac{\partial u_i}{\partial t} = -u_j \frac{\partial u_i}{\partial x_j} - \frac{1}{\rho}\frac{\partial p}{\partial x_i} - g\delta_{i3} - 2\epsilon_{ijk}\Omega_j u_k, \tag{2-45}$$

$$\frac{\partial q_n}{\partial t} = -u_j \frac{\partial q_n}{\partial x_j} + S_{q_n}, \qquad n = 1, 2, 3 \tag{2-46}$$

and

$$\frac{\partial \chi_m}{\partial t} = u_j \frac{\partial \chi_m}{\partial x_j} + S_{\chi_m}, \qquad m = 1, 2, \ldots, M. \tag{2-47}$$

The definition of potential temperature, given by Eq. (2-21), is

$$\theta = T_{\text{V}}(1000/p(\text{in mb}))^{R_{\text{d}}/C_{\text{P}}}, \tag{2-48}$$

and the ideal gas law [Eq. (2-13)] can be written as

$$p = \rho R_{\text{d}} T_{\text{V}}, \tag{2-49}$$

where density ρ is the inverse of specific volume. The virtual temperature is given by

$$T_{\text{V}} = T(1 + 0.61 q_3), \tag{2-50}$$

from Eqs. (2-12) and (2-13).

Equations (2-43)–(2-50) represent a simultaneous set of $11 + M$ non-linear partial differential equations in the $11 + M$ dependent variables $(\rho, \theta, T, T_{\text{V}}, p, u_i, q_n,$ and $\chi_m)$ that must be solved if mesoscale circulations are to be studied quantitatively, The independent variables are time t and the three-space coordinates $x_1 = x$, $x_2 = y$, and $x_3 = z$. The remainder of the text discusses methods of simplification and solution for these fundamental physical relations. In working with mesoscale models and their results, investigators must *always determine the extent to which the equations used in specific simulations correspond to these fundamental basic principles.*

Notes to Chapter 2

1. Gases and aerosols that move into or out of the earth's land and water bodies and those that are lost to space are presumed to have an inconsequential effect on the mass present.

2. Coulson (1975:10) and Kondratyev (1969:23, 24) discuss thermodynamic equilibrium. To be in equilibrium, the intensity of radiation cannot be dependent on direction (i.e., radiation must be *isotropic*), and temperature cannot depend on the frequency and direction of electromagnetic radiation, i.e., the Stefan–Boltzman law (8.8) must apply. In other words, temperature must be controlled by molecular collisions rather than by interaction of the molecules with the radiation field. At levels below 50 km or so in the earth's atmosphere, the density of air is sufficiently great so that over short distances, molecular collisions dominate and a state of local equilibrium occurs.

3. The form of μ_{atm} is derived using Dalton's law of partial pressures; Dalton's law is $p = \sum_{i=1}^{N} p_i$, when p_i represents the pressure contribution of the individual gases that make up the gas mixture (see, e.g., Haltiner and Martin 1957:10).

4. For an ideal gas, the independent variables are any two of temperature, pressure, and specific volume. Given two of these variables, the gas law determines the third. These variables are also referred to as *state variables*.

5. The symbol $\times$ is used to indicate a vector cross-product.

6. More appropriately, a three-dimensional Taylor series expansion should be applied for each component of the pressure difference (and also in deriving the conservation-of-mass equation in Section 2.1) which results in cross-derivative terms. However, in the limit, as the horizontal distance approaches zero, the result is the same differential relationship.

7. Relative humidity is defined with respect to water or ice, depending on the temperature and the availability of ice nuclei.

8. *Sedimentation* refers to the fallout of material that has undergone no phase change and has not been produced as the result of a chemical reaction; precipitation, in contrast, is a fallout of material that has been produced as the result of a phase change or chemical reaction.

Additional Readings

Several useful texts are available to provide additional in-depth information on the material in this chapter, including the following:

Bohren, C. F., and B. A. Albrecht. 1998. "Atmospheric Thermodynamics." Oxford University Press, New York, 402 pp.

Dutton, J. A. 1976. "The Ceaseless Wind: An Introduction to the Theory of Atmospheric Motion." McGraw-Hill, New York, 579 pp. (New editions, corrected in large, were published in 1986 and 1995.)

    An excellent book that examines the equations of motion in considerable detail. Dutton's book is a necessity for those who wish to probe deeper into the fundamental set of meteorological equations.

Iribarne, J. V. and W. L. Godson. 1973. "Atmospheric Thermodynamics." D. Reidel Publishing, Boston, 222 pp.

    This text provides a comprehensive review of the principles of thermodynamics and their applications to atmospheric problems.

Gutman, L. N. 1972. "Introduction to the Nonlinear Theory of Mesoscale Meteorological Processes," Keter Press, Jerusalem, Israel, 224 pp.

    This book discusses aspects of meteorological processes on the mesoscale, including a presentation of the basic equations. As such, it represents the first attempt to provide a text on mesoscale meteorology.

Chapter 3

Simplification of the Basic Equations

Equations (2-43)–(2-47) can be simplified for specific mesoscale meteorological simulations. By mathematical operations, some of these relations can also be changed in form. In this chapter, commonly made assumptions are reviewed and the resultant equations presented. In all cases, Eqs. (2-43)–(2-47) are altered in form or simplified, or both, to permit their solution in an easier, more economical fashion.

The method of *scale analysis*[1] is often used to determine the relative importance of the individual terms in the conservation relations. This technique involves estimation of their order of magnitude using representative values of the dependent variables and constants that make up these terms. Scale analysis can be applied either to individual terms in the fundamental conservation equations, as applied in this chapter, or to analytic solutions of a coupled set of the conservation equations, as discussed in Section 5.2.2 in Chapter 5. The most rigorous analysis procedure is, of course, to evaluate specific solutions of the conservation equations with and without particular terms to establish their importance. An example of such an analysis, for the hydrostatic assumption in sea breeze simulations, is described in Section 5.2.3.

In this chapter, the use of scale analysis is illustrated. Discussions by investigators such as Thunis and Bornstein (1996) provide additional descriptions of using scale analysis to investigate scales of motion on the mesoscale.

3.1 Conservation of Mass

In Chapter 2, the mass-conservation relation was given by Eq. (2-43). To determine appropriate and consistent approximate forms of this equation, portions of the scale analysis of this equation by Dutton and Fichtl (1969) are used in the following discussion.

Using the relationship between density and specific volume given by

$$\rho = 1/\alpha,$$

Eq. (2-43) can be rewritten as

$$\frac{\partial \alpha}{\partial t} = -u_j \frac{\partial \alpha}{\partial x_j} + \alpha \frac{\partial u_j}{\partial x_j}. \tag{3-1}$$

If it is assumed that

$$\alpha = \alpha_0 + \alpha',$$

where α_0 is defined as a synoptic-scale reference specific volume and α' is the mesoscale perturbation from this value,[2] then Eq. (3-1) can be rewritten as

$$\frac{\partial(\alpha_0 + \alpha')}{\partial t} = -u_j \frac{\partial}{\partial x_j}(\alpha_0 + \alpha') + (\alpha_0 + \alpha')\frac{\partial u_j}{\partial x_j}. \tag{3-2}$$

To simplify the scale analysis of this equation, it is assumed that

$$\left|\frac{\partial \alpha_0}{\partial t}\right| \ll \left|\frac{\partial \alpha'}{\partial t}\right|; \quad \left|\frac{\partial \alpha_0}{\partial x}\right| \ll \left|\frac{\partial \alpha'}{\partial x}\right|; \quad \left|\frac{\partial \alpha_0}{\partial y}\right| \ll \left|\frac{\partial \alpha'}{\partial y}\right|, \tag{3-3}$$

so that Eq. (3-2) becomes

$$\frac{\partial \alpha'}{\partial t} = -u \frac{\partial \alpha'}{\partial x} - v \frac{\partial \alpha'}{\partial y} - w \frac{\partial \alpha'}{\partial z} - w \frac{\partial \alpha_0}{\partial z}$$
$$+ \alpha_0 \left(1 + \frac{\alpha'}{\alpha_0}\right)\left(\frac{\partial u}{\partial x} + \frac{\partial v}{\partial y} + \frac{\partial w}{\partial z}\right). \tag{3-4}$$

For mesoscale atmospheric circulations, adoption of the assumptions given in Eq. (3-3) requires that the synoptic state change much more slowly than the mesoscale system and that the horizontal synoptic gradients be much lower than the mesoscale gradients.

It is also assumed that

$$|\alpha'/\alpha_0| \ll 1,$$

so that Eq. (3-4) reduces to

$$\frac{\partial \alpha'}{\partial t} = -u \frac{\partial \alpha'}{\partial x} - v \frac{\partial \alpha'}{\partial y} - w \frac{\partial \alpha'}{\partial z} - w \frac{\partial \alpha_0}{\partial z} + \alpha_0 \left(\frac{\partial u}{\partial x} + \frac{\partial v}{\partial y} + \frac{\partial w}{\partial z}\right). \tag{3-5}$$

This requirement for the ratio of the mesoscale perturbation specific volume to the synoptic-scale reference value is reasonable when realistic values of temperature and pressure are inserted into the ideal gas law [Eq. (2-13)].

For example, a representative climatological value of α_0 at sea level is $0.80 \text{ m}^3 \text{ kg}^{-1}$. Since $\alpha = R_d T_V/p$, upper and lower bounds on specific volume

can be estimated for realistic mesoscale situations using the highest temperature and lowest pressure and the lowest temperature and highest pressure likely to occur at a given location over a reasonably short time period (say 12–24 hours). If

$$T_V = 40°C, \qquad p = 990 \text{ mb}$$

and

$$T_V = 20°C, \qquad p = 1030 \text{ mb},$$

then $\alpha = 0.91$ m³ kg⁻¹ and $\alpha = 0.82$ m³ kg⁻¹ for the two cases, so that $|\alpha'|/\alpha_0$ is at most around ±5%.

The method of scale analysis is used to estimate the magnitude of the remaining terms in Eq. (3-5), so that

$$\left| \frac{\partial \alpha'}{\partial t} \right| \sim \frac{\alpha'}{t_\alpha}, \qquad \left| u \frac{\partial \alpha'}{\partial x} \right| \sim U \frac{\alpha'}{L_x}, \qquad \left| v \frac{\partial \alpha'}{\partial y} \right| \sim V \frac{\alpha'}{L_y},$$

$$\left| w \frac{\partial \alpha'}{\partial z} \right| \sim W \frac{\alpha'}{L_z}, \quad \left| w \frac{\partial \alpha_0}{\partial z} \right| \sim W \frac{\alpha_0}{H_\alpha}, \quad \left| \alpha_0 \frac{\partial u}{\partial x} \right| \sim \alpha_0 \frac{U}{L_x}, \qquad (3\text{-}6)$$

$$\left| \alpha_0 \frac{\partial v}{\partial y} \right| \sim \alpha_0 \frac{V}{L_y}, \quad \text{and} \quad \left| \alpha_0 \frac{\partial w}{\partial z} \right| \sim \alpha_0 \frac{W}{L_z},$$

where t_α^{-1} represents the characteristic frequency of variations in specific volume on the mesoscale; U, V, and W are representative values of the components of velocity; L_x, L_y, and L_z are the spatial scales of the mesoscale disturbance; and H_α, the *density-scaled height* of the atmosphere, is defined as

$$H_\alpha^{-1} = \frac{1}{\alpha_0} \frac{\partial \alpha_0}{\partial z}.$$

In the earth's troposphere, H_α is approximately 8 km, as illustrated schematically in Figure 3-1.

3.1.1 Deep Continuity Equation

To examine the necessity for retaining individual terms in Eq. (3-5), it is customary to examine their ratio relative to one of the terms that is expected to remain. In the first case that we examine, the terms are divided by the order
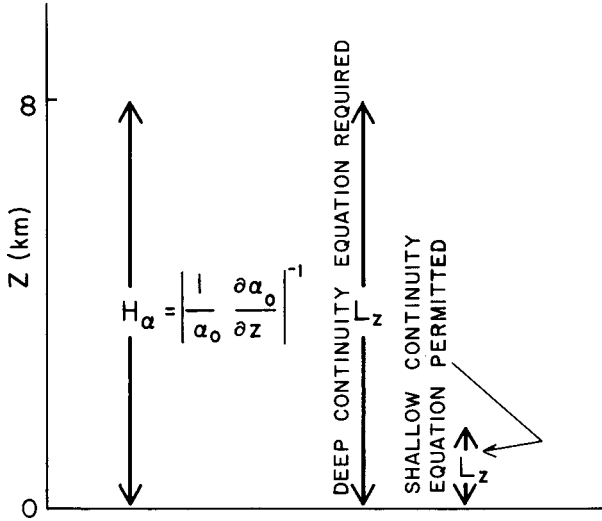
Fig. 3-1. Schematic illustration contrasting deep and shallow atmospheric circulations. The depth L_z corresponds to the vertical extent of the circulation. In the earth's atmosphere, $H_\alpha = 8$ km.

of magnitude estimate for $w\,\partial\alpha_0/\partial z$, resulting in

$$\left|\frac{\partial\alpha'}{\partial t}\right|\bigg/\left|w\frac{\partial\alpha_0}{\partial z}\right| \sim \frac{\alpha'}{\alpha_0}\frac{H_\alpha}{t_\alpha W}, \qquad \left|u\frac{\partial\alpha'}{\partial x}\right|\bigg/\left|w\frac{\partial\alpha_0}{\partial z}\right| \sim \frac{\alpha'}{\alpha_0}\frac{U}{W}\frac{H_\alpha}{L_x},$$

$$\left|v\frac{\partial\alpha'}{\partial y}\right|\bigg/\left|w\frac{\partial\alpha_0}{\partial z}\right| \sim \frac{\alpha'}{\alpha_0}\frac{V}{W}\frac{H_\alpha}{L_y}, \qquad \left|w\frac{\partial\alpha'}{\partial z}\right|\bigg/\left|w\frac{\partial\alpha_0}{\partial z}\right| \sim \frac{\alpha'}{\alpha_0}\frac{H_\alpha}{L_z},$$

$$\left|\alpha_0\frac{\partial u}{\partial x}\right|\bigg/\left|w\frac{\partial\alpha_0}{\partial z}\right| \sim \frac{U}{W}\frac{H_\alpha}{L_x}, \qquad \left|\alpha_0\frac{\partial v}{\partial y}\right|\bigg/\left|w\frac{\partial\alpha_0}{\partial z}\right| \sim \frac{V}{W}\frac{H_\alpha}{L_y},$$

and

$$\left|\alpha_0\frac{\partial w}{\partial z}\right|\bigg/\left|w\frac{\partial\alpha_0}{\partial z}\right| \sim \frac{H_\alpha}{L_z}.$$

Since $|\alpha'/\alpha_0| \ll 1$, the terms $u\,\partial\alpha'/\partial x$, $v\,\partial\alpha'/\partial y$, and $w\,\partial\alpha'/\partial z$ are much less than $\alpha_0\,\partial u/\partial x$, $\alpha_0\,\partial v/\partial y$, and $\alpha_0\,\partial w/\partial z$ and can be neglected in Eq. (3-5), provided that

$$\text{(i) } L_z \sim H_\alpha, \qquad \text{(ii) } \frac{U}{W}\frac{H_\alpha}{L_x} \sim 1, \qquad \text{(iii) } \frac{V}{W}\frac{H_\alpha}{L_y} \sim 1,$$

$$\text{and} \qquad \text{(iv) } \frac{H_\alpha}{t_\alpha W} \sim 1. \tag{3-7}$$

Then Eq. (3-5) can be written as

$$w \frac{\partial \alpha_0}{\partial z} - \alpha_0 \left(\frac{\partial u}{\partial x} + \frac{\partial v}{\partial y} + \frac{\partial w}{\partial z} \right) = 0. \tag{3-8}$$

Since L_z is approximately equal to H_α, conditions (ii) and (iii) in Eq. (3-7) require that

$$U/L_x \sim W/L_z \qquad \text{and} \qquad V/L_y \sim W/L_z. \tag{3-9}$$

If, therefore, L_x is one or two orders of magnitude larger than L_z, then the vertical velocity W is expected to be one or two orders of magnitude less than U and V (e.g., for $L_x \sim 80$ km and $L_z \sim 8$ km, $W \sim 0.1U$). This relation between velocities and the horizontal and vertical scales of atmospheric circulations results from the condition that $|\alpha'/\alpha_0| \ll 1$. Because of this constraint, velocities in a longer, horizontal leg of an atmospheric circulation must be proportionately stronger to preserve mass continuity without creating large fluctuations in specific volume.

The last requirement remaining to be justified in Eq. (3-7) is condition (iv). The scaled variable t_α represents a time period in which significant variations in specific volume occur on the mesoscale and can be approximated by

$$t_\alpha \sim L/C, \tag{3-10}$$

where L is the wavelength over which variations occur and C is the rate of movement of these variations. If the changes are caused by advection, then U, V, or W is used to represent C, whereas if wave propagation is dominant, then a characteristic group velocity C_g is used. The wavelength L is estimated as L_x and L_y for horizontal motion and L_z for vertical motion. When changes in specific volume are assumed to be primarily caused by advection or when the wave group velocity has approximately the same speed as the wind velocity,[3] we have

$$t_\alpha W \sim LW/C \sim \begin{cases} L_x W/U \sim L_y W/V \sim H_\alpha \\ L_z W/W \sim L_z \sim H_\alpha \end{cases},$$

where conditions (i)–(iii) in Eq. (3-7) have been used. Therefore,

$$\left| \frac{\partial \alpha'}{\partial t} \right| \Big/ \left| w \frac{\partial \alpha_0}{\partial z} \right| \sim \left| \frac{\alpha'}{\alpha_0} \right|,$$

so that local variations in density can be neglected in the conservation-of-mass relation if $|\alpha'/\alpha_0| \ll 1$.

Finally, if $L_y \ll L_x$, then mesoscale variations in the x direction are expected to be dominant and the y derivatives in Eq. (3-8) can be ignored. In this case

the equation reduces to the two-dimensional form given by

$$w \frac{\partial \alpha_0}{\partial z} - \alpha_0 \left(\frac{\partial u}{\partial x} + \frac{\partial w}{\partial z} \right) = 0.$$

Equation (3-8) is customarily written to include the terms $u \, \partial \alpha_0 / \partial x$ and $v \, \partial \alpha_0 / \partial y$ and is given by

$$\frac{\partial}{\partial x_j} (\alpha_0^{-1} u_j) = 0$$

or, returning to the use of density instead of specific volume, by

$$\frac{\partial}{\partial x_j} (\rho_0 u_j) = 0, \tag{3-11}$$

where $\rho_0 = 1/\alpha_0$.

Dutton and Fichtl (1969) call this relation the *deep convection continuity equation,* because the vertical depth of the circulation is on the same order as the density scale depth. As originally shown by Ogura and Phillips (1962), and discussed by Lipps and Hemler (1982), and as will be shown in Section 5.2.2, the use of this form of the conservation-of-mass relation eliminates sound waves as a possible solution, which led Ogura and Phillips to refer to Eq. (3-11) as the *anelastic*, or *soundproof, assumption*. Because such waves are of no direct interest in most applications of mesoscale meteorology, this equation is often used to represent mass conservation in mesoscale models in lieu of the more complete prognostic conservation-of-mass equation given by Eq. (3-1). Moreover, as discussed in Section 10.4 in Chapter 10, the elimination of sound waves permits more economical use of certain numerical solution techniques, because their computational stability is dependent on having a time step less than or equal to the time that it takes for a wave to travel between grid points. Sound waves are the fastest nonelectromagnetic waveform in the atmosphere.

3.1.2 Shallow Continuity Equation

A more restrictive mass-conservation relation is derived by dividing the scaled terms in Eq. (3-6) by the scaled form of $\alpha_0 \, \partial w / \partial z$, resulting in

$$\left| \frac{\partial \alpha'}{\partial t} \right| \bigg/ \left| \alpha_0 \frac{\partial w}{\partial z} \right| \sim \frac{\alpha'}{\alpha_0} \frac{L_z}{Wt_\alpha}, \qquad \left| u \frac{\partial \alpha'}{\partial x} \right| \bigg/ \left| \alpha_0 \frac{\partial w}{\partial z} \right| \sim \frac{\alpha'}{\alpha_0} \frac{U}{W} \frac{L_z}{L_x},$$

$$\left| v \frac{\partial \alpha'}{\partial y} \right| \bigg/ \left| \alpha_0 \frac{\partial w}{\partial z} \right| \sim \frac{\alpha'}{\alpha_0} \frac{V}{W} \frac{L_z}{L_y}, \qquad \left| w \frac{\partial \alpha'}{\partial z} \right| \bigg/ \left| \alpha_0 \frac{\partial w}{\partial z} \right| \sim \frac{\alpha'}{\alpha_0},$$

$$\left| w \frac{\partial \alpha_0}{\partial z} \right| \bigg/ \left| \alpha_0 \frac{\partial w}{\partial z} \right| \sim \frac{L_z}{H_\alpha}, \qquad \left| \alpha_0 \frac{\partial u}{\partial x} \right| \bigg/ \left| \alpha_0 \frac{\partial w}{\partial z} \right| \sim \frac{U}{W} \frac{L_z}{L_x},$$

and

$$\left| \alpha_0 \, \frac{\partial v}{\partial y} \right| \Big/ \left| \alpha_0 \, \frac{\partial w}{\partial z} \right| \sim \frac{V}{W} \frac{L_z}{L_y}.$$

As in the previous analysis, since $|\alpha'/\alpha_0| \ll 1$, $u \, \partial \alpha'/\partial x$, $v \, \partial \alpha'/\partial y$, and $w \, \partial \alpha'/\partial z$ can be neglected in Eq. (3-5), provided that

$$L_z/Wt_\alpha \sim 1 \qquad \text{and} \qquad L_z/H_\alpha \ll 1. \tag{3-12}$$

Then Eq. (3-5) can be written as

$$\alpha_0 \left(\frac{\partial u}{\partial x} + \frac{\partial v}{\partial y} + \frac{\partial w}{\partial z} \right) = 0. \tag{3-13}$$

The first condition in Eq. (3-12) is easier to satisfy than the equivalent requirement in Eq. (3-7), because $L_z \ll H_\alpha$. This requirement implies that the neglect of specific volume variations in Eq. (3-13) is even less important than it is in Eq. (3-11). The second condition in Eq. (3-12) requires that the depth of the circulation be much less than the scale depth of the atmosphere. For this reason, Dutton and Fichtl (1969) refer to Eq. (3-13) as the *shallow convection continuity equation*. Written in tensor form, Eq. (3-13) is given by

$$\partial u_j/\partial x_j = 0, \tag{3-14}$$

and this relation is often referred to as the *incompressibility assumption*. This expression not only removes soundwaves, but also ignores spatial variations in density. For the case of a *homogeneous* (constant density) fluid, this would be the exact form of the conservation-of-mass equation.

Many mesoscale models use this expression to represent the conservation of mass. There is a certain irony in its use, of course, because although air closely follows the ideal gas law, it is also accurately approximated by the incompressible form of the conservation-of-mass equation when the atmospheric circulations have a limited vertical extent. This apparent discrepancy is explained by realizing that air movement generally is not physically constrained. For example, when air moves into one side of a parcel, either the density can increase by compression or an equivalent mass of air can move out of the other side of the parcel. As long as the atmospheric parcel is not restricted to a fixed volume, the creation of a pressure gradient between the two sides of the parcel as a result of the different velocities will force the air out of one side so that mass conservation is closely approximated by the incompressible relation [Eq. (3-14)].

In mesoscale models, either the *prognostic equation* (time-dependent equation) for density [Eq. (2-43)] or the *diagnostic equation* (no time-tendency term) [Eq. (3-11) or (3-14)] can be used to represent mass conservation.

3.2   Conservation of Heat

In mesoscale meteorology, an equivalent, rather exhaustive scale analysis of the conservation-of-heat relation [Eq. (2-44)] is not generally made. This is because of the complex mathematical form of the source-sink term S_θ. In contrast, the conservation-of-mass relation has no such source-sink term, so the analysis is relatively simple.

Equation (2-44) is modified by making simplifying assumptions regarding the form of S_θ. The development of simplified mathematical representations for any of the source-sink terms is one type of *parameterization*. The most stringent assumption for the conservation of potential temperature relation is to require that all motions be adiabatic, so $S_\theta = 0$ and Eq. (2-44) reduces to

$$\partial\theta/\partial t = -u_j\,\partial\theta/\partial x_j, \qquad (3\text{-}15)$$

or, equivalently,

$$d\theta/dt = 0.$$

It is valid to use this assumption in representing mesoscale atmospheric systems provided that

$$|S_\theta| \ll \left|\frac{\partial\theta}{\partial t}\right|; \quad \left|u\,\frac{\partial\theta}{\partial x}\right|; \quad \left|v\,\frac{\partial\theta}{\partial y}\right|; \quad \left|w\,\frac{\partial\theta}{\partial z}\right|.$$

This condition is most closely fulfilled when the following are met:

1.   the atmosphere is dry, with no phase changes of water occurring,
2.   comparatively short time periods are involved, so that radiational heating or cooling of the air is relatively small,
3.   heating or cooling of the lowest levels of the atmosphere by the bottom surface is of comparatively small magnitude.

More specific examples of when S_θ must be retained in Eq. (2-44) and how this term can be parameterized are discussed in Chapters 8 and 9.

3.3   Conservation of Motion

A wide range of assumptions have been used to either simplify or alter the form of the conservation-of-motion equation [Eq. (2-45)]. In performing scale analysis on this equation, it is convenient to decompose the equation into its vertical and horizontal components, since the gravitational acceleration is included only in the equation for vertical acceleration.

3.3.1   Vertical Equation of Motion

The vertical component of Eq. (2-45) can be written as

$$\frac{\partial w}{\partial t} + u\frac{\partial w}{\partial x} + v\frac{\partial w}{\partial y} + w\frac{\partial w}{\partial z} = -\frac{1}{\rho}\frac{\partial p}{\partial z} - g + 2\Omega u\cos\phi \qquad (3\text{-}16)$$

or, equivalently,

$$\frac{dw}{dt} = -\alpha\frac{\partial p}{\partial z} - g + 2\Omega u\cos\phi. \qquad (3\text{-}17)$$

As in Section 3.1, these terms can be estimated by the *method-of-scale analysis*. The terms on the left side of Eq. (3-16) can be estimated as

$$\left|\frac{\partial w}{\partial t}\right| \sim \frac{W}{t_w}; \quad \left|u\frac{\partial w}{\partial x}\right|; \quad \left|v\frac{\partial w}{\partial y}\right|; \quad \left|w\frac{\partial w}{\partial z}\right| \sim \frac{U}{L_x}W,$$

where t_w is a time scale related to the period required for significant changes in vertical velocity to occur. A similar definition was given in Section 3.1 for t_α. As before, W and U are the characteristic vertical and horizontal velocities that, if $|\alpha'/\alpha_0| \ll 1$, permit the use of Eq. (3-9) to relate the magnitudes of the two velocities. (Here V and L_y are assumed to have the same magnitudes as U and L_x.) Using the same justification for the vertical velocity time scale t_w as was used for t_α, we have

$$t_w \sim L_x/U,$$

so that the four terms on the left side of Eq. (3-16) and, therefore, the total vertical acceleration given on the left side of [Eq. (3-17)] have the scale of

$$\left|\frac{\partial w}{\partial t}\right|; \quad \left|u\frac{\partial w}{\partial x}\right|; \quad \left|v\frac{\partial w}{\partial y}\right|; \quad \left|w\frac{\partial w}{\partial z}\right|; \quad \left|\frac{dw}{dt}\right| \sim \frac{UW}{L_x} = \frac{U^2 L_z}{L_x^2}.$$

To estimate the vertical pressure gradient term in Eq. (3-17), it is convenient to use the ideal gas law [Eq. (2-13)], yielding

$$\alpha\frac{\partial p}{\partial z} = R_\mathrm{d}\frac{\partial T}{\partial z} - \frac{RT}{\alpha}\frac{\partial\alpha}{\partial z},$$

where, for convenience, the subscripts d and V have been deleted from R and T. To simplify the scale analysis, we assume that the atmosphere is isothermal $(\partial T/\partial z = 0)$ and that

$$\frac{1}{\alpha}\frac{\partial\alpha}{\partial z} \simeq \frac{1}{\alpha_0}\frac{\partial\alpha_0}{\partial z} = H_\alpha^{-1},$$

so that

$$\left|\alpha\frac{\partial p}{\partial z}\right| \sim R_\mathrm{d}T/H_\alpha.$$

The two remaining terms are given as $|g|$ and $|2\Omega u\cos\phi| \sim 2\Omega U$.

The significance of the individual terms in Eq. (3-17) in relation to, for example, the vertical pressure gradient term can then be estimated using these scale estimates. The ratio of the orders of magnitude of the vertical acceleration to the vertical pressure gradient is given by

$$\left|\frac{dw}{dt}\right| \bigg/ \left|\alpha\,\frac{\partial p}{\partial z}\right| \sim \frac{H_\alpha L_z}{L_x^2}\,\frac{U^2}{RT} = R_w. \tag{3-18}$$

For the case where Eq. (3-8) is used as the continuity equation, $L_z \sim H_\alpha$, so that

$$\left|\frac{dw}{dt}\right| \bigg/ \left|\alpha\,\frac{\partial p}{\partial z}\right| \sim \frac{H_\alpha^2}{L_x^2}\,\frac{U^2}{RT} = R_w. \tag{3-19}$$

The scale analysis ratio given by Eq. (3-19) implies that the vertical accelerations become more important as the horizontal velocity increases and less important with higher temperatures and longer horizontal wavelengths.

Thus, according to this scale analysis, for us to neglect the vertical acceleration term in Eq. (3-17), R_w must be much less than unity. Unfortunately, however, this analysis is not complete, because we have shown only that the magnitude of the gravitational and pressure gradient accelerations are separately much larger than the vertical acceleration. Of more significance is the magnitude of the difference between these two terms. To better examine this relationship, we can conveniently define a large-scale averaged atmosphere that has an exact balance between the gravitational and pressure gradient terms. This can be defined as

$$\partial p_0/\partial z = -\rho_0 g,$$

where the 0 subscript is used to indicate a large-scale average. [Such an average could be defined as given by Eq. (4-12).] If any dependent variable is defined to be equal to such an average value plus a deviation from that average (i.e., $\phi = \phi_0 + \hat{\phi}$, where ϕ is any one of the dependent variables), then Eq. (3-17) can also be written as

$$\frac{dw}{dt} = -\alpha_0\,\frac{\partial \hat{p}}{\partial z} + g\,\frac{\hat{\alpha}}{\alpha_0} + 2\Omega u \cos\phi, \tag{3-20}$$

where $|\hat{\alpha}|/\alpha_0 \ll 1$ has been assumed. In Eq. (3-20), the first two terms on the right side are of much less magnitude than the first two terms on the right side of Eq. (3-17).

The magnitude of the perturbation vertical pressure gradient can be estimated from

$$\left| \frac{1}{\rho_0} \frac{\partial \hat{p}}{\partial z} \right| \simeq \frac{1}{\rho_0} \left| T_0 R \frac{\partial \hat{\rho}}{\partial z} + R\widehat{T} \frac{\partial \rho_0}{\partial z} + R\rho_0 \frac{\partial \widehat{T}}{\partial z} \right|$$

$$\sim \left| -R \frac{\delta T}{L_z} \right| + \left| R \frac{\delta T}{H_\alpha} \right| + \left| R \frac{\delta T}{L_z} \right| \sim R \frac{|\delta T|}{L_z},$$

where for the purposes of this scale analysis, the large-scale atmosphere is assumed to be isothermal and the linearized ideal gas law of the form $\delta\rho/\rho \simeq -(\delta T/T) + (\delta p/p) \simeq -\delta T/T$ is used. For this analysis, the term with the vertical gradient of the large-scale density ρ_0 can be neglected if $L_z \ll H_\alpha$.

The ratio of the vertical acceleration to this perturbation pressure gradient term is thus given as

$$\widehat{R}_w = \frac{L_z^2}{L_x^2} \frac{UC_x}{R\delta T} = \frac{H_\alpha^2}{L_x^2} \frac{UC_x}{R\delta T} \text{ (when } L_z \sim H_\alpha). \tag{3-21}$$

This relationship is more restrictive than R_w, since δT rather than T is in the denominator. [Note that $\widehat{R}_w$ does not increase without bound, because UC_x results from horizontal gradients in temperature (see, e.g., Section 3.3.2), so as δT goes to 0 in Eq. (3-21), so must UC_x.[4]] If $\widehat{R}_w \ll 1$, $g\widehat{\alpha}/\alpha_0$ must be of the same order of magnitude as the perturbation vertical pressure gradient [since $2\Omega u \cos\phi$ is small relative to the first two terms in Eq. (3-20) under all expected atmospheric conditions, as is discussed shortly].

To illustrate the magnitude of $\widehat{R}_w$ for representative values on the mesoscale, δT and U are set equal to 10°C and 10 m s^{-1} (based on observed values), C_x is set equal to U, and R is equal to 287 J K^{-1} kg^{-1}. This yields

$$\widehat{R}_w = 0.03 H_\alpha^2 / L_x^2,$$

where $H_\alpha \simeq 8$ km (Wallace and Hobbs 1977). If the depth of the circulation is less than the scale height ($L_z < H_\alpha$), then $\widehat{R}_w$ is proportionately smaller (e.g., if $L_z = 0.1H_\alpha$, then $\widehat{R}_w = 0.0003 H_\alpha^2 / L_x^2$). Thus from this analysis, a conservative estimate for neglecting vertical accelerations relative to the vertical pressure gradient term in Eq. (3-17) is

$$H_\alpha / L_x \gtrsim 1. \tag{3-22}$$

The remaining two terms are evaluated by

$$g / |\alpha \, \partial p / \partial z| \sim g H_\alpha / RT$$

and

$$|2\Omega u \cos\phi| / |\alpha \, \partial p / \partial z| \sim 2\Omega U H_\alpha / RT,$$

and if, for example, $g \sim 10$ m s^{-2}, $T = 270$ K, $\Omega \sim 7 \times 10^{-5}$ s$^{-1} = 2\pi$/day, $U \sim 20$ m s^{-1}, $H_\alpha \sim 8$ km, and $R = 287$ J K^{-1} kg^{-1}, then

$$g/|\alpha\ \partial p/\partial z| \sim 1$$

and

$$|2\Omega \cos \phi|/|\alpha\ \partial p/\partial z| \sim 3 \times 10^{-4}.$$

Thus the influence of the rotation of the earth on the vertical acceleration is inconsequential for any reasonable velocity and can be neglected in Eq. (3-17). However, the gravitational acceleration cannot be neglected relative to the vertical pressure gradient.

If Eq. (3-22) is valid, then Eq. (3-17) reduces to

$$\partial p/\partial z = -g/\alpha = -\rho g \qquad (3\text{-}23)$$

and is called the *hydrostatic equation*.[5] In this relationship, it must be emphasized that the results of the scale analysis imply only that the magnitude of the vertical acceleration is much less than the magnitude of the pressure gradient force, *not* that the magnitude of the vertical acceleration is identically 0 (e.g., $|dw/dt| \ll |\alpha\ \partial p/\partial z|$, *not* $|dw/dt| = 0$).

3.3.2 Horizontal Equation of Motion

The horizontal component of Eq. (2-45) can be written as

$$\frac{\partial u}{\partial t} = -u \frac{\partial u}{\partial x} - v \frac{\partial u}{\partial y} - w \frac{\partial u}{\partial z} - \frac{1}{\rho} \frac{\partial p}{\partial x} + 2v\Omega \sin \phi - 2w\Omega \cos \phi \qquad (3\text{-}24)$$

and

$$\frac{\partial v}{\partial t} = -u \frac{\partial v}{\partial x} - v \frac{\partial v}{\partial y} - w \frac{\partial v}{\partial z} - \frac{1}{\rho} \frac{\partial p}{\partial y} - 2u\Omega \sin \phi. \qquad (3\text{-}25)$$

To estimate the approximate magnitude of the pressure gradient term in Eqs. (3-24) and (3-25), we use two methods. First, it is useful to apply the vertically integrated form of Eq. (3-23), assuming that the density ρ is a constant ρ^* so that

$$p_{z=0} = \int_{z=0}^{z=D} \rho^* g\, dz = \rho^* g \int_{z=0}^{z=D} dz = \rho^* gD,$$

where the pressure at height D is assumed to equal 0. Thus if the magnitude of the pressure gradient at $z = 0$ is representative of the pressure gradient at any level in the troposphere, then

$$\left| \frac{1}{\rho} \frac{\partial p}{\partial x} \right| \sim g \frac{\delta D}{L_x}, \quad \text{and} \quad \left| \frac{1}{\rho} \frac{\partial p}{\partial y} \right| \sim g \frac{\delta D}{L_y},$$

where L_x and L_y are the representative horizontal scales of the mesoscale system and δD is the representative change of D over L_x and L_y. The parameter δD represents the relation between horizontal pressure gradient and horizontal gradients in the depth of a homogeneous atmosphere (i.e., $\delta p/L_x \sim \rho^* g\, \delta D/L_x$).

The second technique involves replacing pressure in Eq. (3-24) with the ideal gas law [Eq. (2-13)], yielding for the x derivative (for convenience subscripts d and V have been dropped)

$$\frac{\partial p}{\partial x} = \rho R\, \frac{\partial T}{\partial x} + TR\, \frac{\partial \rho}{\partial x} \simeq \rho_0 R\, \frac{\partial T}{\partial x}, \tag{3-26}$$

where to estimate the magnitude of the pressure gradient, the term $T\, \partial \rho/\partial x$ is neglected and ρ_0 is used to approximate ρ.

Thus, using these two analyses, we have

$$\left| \frac{1}{\rho}\, \frac{\partial p}{\partial x} \right| \sim \frac{R\, \delta T}{L_x} \sim g\, \frac{\delta D}{L_x} \qquad \text{and} \qquad \left| \frac{1}{\rho}\, \frac{\partial p}{\partial y} \right| \sim \frac{R\, \delta T}{L_y} \sim \frac{g\, \delta D}{L_y},$$

where δT is the representative magnitude of the horizontal temperature variations across the mesoscale system. From these relations, $\delta D \sim (R/g)\delta T$.

The advection terms are given by

$$|u\, \partial u/\partial x| \sim U^2/L_x, \qquad |v\, \partial u/\partial y| \sim UV/L_y,$$
$$|w\, \partial u/\partial z| \sim WU/L_z, \qquad |u\, \partial v/\partial x| \sim UV/L_x,$$
$$|v\, \partial v/\partial y| \sim V^2/L_y, \qquad |w\, \partial v/\partial z| \sim WV/L_z. \tag{3-27}$$

If $U \sim V$ and $L_x \sim L_y$ (as would be expected in general), and since $W/L_z \sim U/L_x$ from relation 3.9, these terms are of the same order. If $L_y \gg L_x$, the y derivative terms in Eq. (3-27) can be neglected, and Eqs. (3-24) and (3-25) reduce to their two-dimensional forms. Henceforth, in this section U^2/L_x represent the advective terms and V and L_y are replaced by U and L_x whenever they appear.

The local tendency terms in Eqs. (3-24) and (3-25) are estimated by

$$|\partial u/\partial t| \sim U/t_u \sim UC/L_x \quad \text{and} \qquad |\partial v/\partial t| \sim V/t_v \sim VC/L_y \sim UC/L_x,$$

where, as for the vertical component of the conservation-of-motion equation, $C \simeq U$ for both advective and internal gravity wave changes in mesoscale systems often can be assumed.

The remaining three terms in Eqs. (3-24) and (3-25) can be represented as

$$|2u\Omega \sin \phi| \sim |fu| \sim |f|U, \qquad |2v\Omega \sin \phi| \sim |fv| \sim |f|V \sim |f|U,$$
$$\text{and} \qquad |2w\Omega \cos \phi| \sim |\hat{f}w| \sim |\hat{f}|W \sim |\hat{f}|(L_z/L_x)U,$$

where $f = 2\Omega \sin \phi$ and is called the *Coriolis parameter* and $\hat{f} = 2\Omega \cos \phi$.

TABLE 3-1

The Ratio of the Orders of Magnitude of the Individual Terms in Eqs. (3-24) and (3-25)[a]

	$\left\|\dfrac{\partial u}{\partial t}\right\|; \left\|\dfrac{\partial v}{\partial t}\right\|$	Advective terms, e.g., $\left\|u\dfrac{\partial u}{\partial x}\right\|$	$\left\|\dfrac{1}{\rho}\dfrac{\partial p}{\partial x}\right\|; \left\|\dfrac{1}{\rho}\dfrac{\partial p}{\partial y}\right\|$	$\|fu\|; \|fv\|$	$\|\hat{f}w\|$
$\left\|\dfrac{\partial u}{\partial t}\right\|; \left\|\dfrac{\partial v}{\partial t}\right\|$	1	C/U	$\dfrac{UC}{R\delta T} \sim \dfrac{UC}{g\delta D}$	$\dfrac{C}{\|f\|L_x} = \dfrac{C}{U}R_0$	$\dfrac{C}{\|\hat{f}\|L_x} = \dfrac{C}{U}\dfrac{L_x}{L_z}R_0$
Advective terms, e.g., $\left\|u\dfrac{\partial u}{\partial x}\right\|$	U/C	1	$\dfrac{U^2}{R\delta T} \sim \dfrac{U^2}{g\delta D}$	$\dfrac{U}{\|f\|L_x} = R_0$	$\dfrac{U}{\|\hat{f}\|L_z} = \dfrac{L_x}{L_z}R_0$
$\left\|\dfrac{1}{\rho}\dfrac{\partial p}{\partial x}\right\|; \left\|\dfrac{1}{\rho}\dfrac{\partial p}{\partial y}\right\|$	$\dfrac{R\delta T}{UC} \sim \dfrac{g\delta D}{UC}$	$\dfrac{R\delta T}{U^2} \sim \dfrac{g\delta D}{U^2}$	1	$\dfrac{R\delta T}{\|f\|UL_x} \sim \dfrac{g\delta D}{\|f\|UL_x}$	$\dfrac{R\delta T}{\|\hat{f}\|UL_z} \sim \dfrac{g\delta D}{\|\hat{f}UL_z\|}$
$\|fu\|; \|fv\|$	$\dfrac{\|f\|L_x}{C} = \dfrac{U}{CR_0}$	$\dfrac{\|f\|L_x}{U} = \dfrac{1}{R_0}$	$\dfrac{\|f\|UL_x}{R\delta T} \sim \dfrac{\|f\|UL_x}{g\delta D}$	1	$\dfrac{L_x}{L_z}$
$\|\hat{f}w\|$	$\dfrac{\|\hat{f}\|L_z}{C} = \dfrac{U}{C}\dfrac{L_z}{L_xR_0}$	$\dfrac{\|\hat{f}\|L_x}{U} = \dfrac{L_z}{L_xR_0}$	$\dfrac{\|\hat{f}\|UL_z}{R\delta T} \sim \dfrac{\|\hat{f}\|UL_z}{g\delta D}$	$\dfrac{L_z}{L_x}$	1

[a]The elements in the columns are divided by the elements in the rows.

The ratios of the scales of the individual terms are given in Table 3-1 where the elements in the columns are divided by those in the rows. In this table, $R_0 = U/|f|L_x$ is the *Rossby number*.

Interpretations that can be made from this analysis include the following:

1. The local time tendency terms $\partial u/\partial t$ and $\partial v/\partial t$ can be neglected if the movement of the mesoscale system is much less than the advecting wind speed (e.g., $C \sim C_g \ll U$). Such a system is said to be *steady state* if $C_g = 0$ or *quasi-steady* if $C_g \neq 0$ but $C_g \ll U$.

2. The terms associated with the rotation of the earth (fu, fv, and $\hat{f}w$) can be neglected if $R_0 \gg 1$. Since R_0 is inversely proportional to L_x, the larger the horizontal scale of the mesoscale system, the more inappropriate it becomes to neglect those terms. The magnitude of the $\hat{f}w$ term is dependent on the ratio of L_z/L_x (e.g., if $L_z = 0.1L_x$, then it is expected to be about 10% of fu and fv).

3. The ratio of the pressure gradient force and advective terms is inversely proportional to the square of the wind speed and proportional to the horizontal temperature gradient. Since the horizontal pressure gradient is approximately a linear term,

$$\left(\text{e.g.,}\quad \frac{1}{\rho}\frac{\partial p}{\partial x} \simeq \frac{1}{\rho_0}\frac{\partial p}{\partial x}, \quad \text{since} \quad \left|\frac{\rho'}{\rho_0}\right| \sim \left|\frac{\alpha'}{\alpha_0}\right| \ll 1\right),$$

whereas the advective terms are nonlinear, solutions to the conservation relations are greatly simplified if the ratio is large and the nonlinear contribution of advection to the equations can be ignored. Equations (3-24) and (3-25) are linearized if $\rho = \rho_0$ is used in the pressure gradient term, and the advective terms are deleted.

Representative values of R_0, D, and δD can be estimated for mesoscale systems in the earth's troposphere. With $|f| \sim 10^{-4}$ s^{-1}, $U \sim 20$ m s^{-1}, $p_{z=0} \sim 1000$ mb, $g = 10$ m s^{-2}, $\rho_0 = 1.25$ kg m^{-3}, $\delta T \sim 5°C$, $L_x = 100$ km, and $L_z = D$, for example,

$$D = 8 \text{ km} \sim H_\alpha, \quad R_0 = 2.0, \quad \delta D = 143 \text{ m}, \quad \text{and} \quad L_z/L_x = 0.08.$$

Thus for this case it would be appropriate to neglect the term $\hat{f}w$ but not fu and fv. Moreover, because the ratio of the magnitudes of the pressure gradient force term to the advective terms is on the order of four, neither of these terms can be neglected in Eqs. (3-24) and (3-25). The local tendency terms $\partial u/\partial t$ and $\partial v/\partial t$ also cannot be ignored if $C \sim U$, since for this case their ratio to the pressure gradient force term is approximately 0.3.

These scaled terms need to be reevaluated for each study of different mesoscale systems to determine the appropriate form of Eqs. (3-24) and (3-25) to use. If one is in doubt as to whether or not to exclude a term, it is, of course, consistent to include it.[6] In the limiting case of $R_0 \ll 1$, $L_z \ll L_x$, $U \sim C$,

and $R\delta T \gg U^2$ with $\delta D \sim |f|UL_x/g$ (which is the same as $\delta T \sim |f|UL_x/R$), Eqs. (3-24) and (3-25) reduce to

$$v_g = \frac{1}{\rho f}\frac{\partial p}{\partial x} \qquad \text{and} \qquad u_g = -\frac{1}{\rho f}\frac{\partial p}{\partial y}, \qquad (3\text{-}28)$$

where v_g and u_g are called the *geostrophic wind components*.[7] At the other extreme, if $R_0 \gg 1$, the Coriolis terms can be neglected relative to the advective terms. This is the assumption used in cumulus and other smaller-scale models.

A final analysis of the vertical and horizontal equations of motion is to examine the magnitude of the molecular viscous forces to the terms in Eq. (2-45). As stated in the discussion of internal forces in Section 2.3.2 in Chapter 2, molecular forces are assumed to be insignificant on the mesoscale and are ignored in Eq. (2-45). To justify this assumption, the method-of-scale analysis is used, in which the molecular dissipation of motion D is approximated by

$$D_i = v\partial^2 u_i/\partial x_j\partial x_j, \qquad |D| \sim vS/L^2, \qquad (3\text{-}29)$$

where L represents L_x, L_y, or L_z (for $j = 1, 2$, or 3) and S represents U, V, or W (for $i = 1, 2$, or 3). The kinematic viscosity v is about 1.5×10^{-5} m^2 s^{-1} for air. To examine the significance of the viscous force, it is customary to compare it to the advective terms, which have a magnitude of U^2/L_x in the horizontal equation and a magnitude of W^2/L_z in the vertical equation of motion. For this analysis, if it is assumed that $L_x \sim L_z \sim L$, so that $W \sim U \sim S$, then the ratio of the magnitude of the advective terms to the viscous force is given by

$$\frac{S^2/L}{vS/L^2} = \frac{SL}{v} = Re,$$

where Re is called the *Reynolds number*. When $Re \gg 1$, changes in motion by advection are much more important than the dissipation of velocity by molecular interactions. Under this condition, the flow is said to be *turbulent*, and transfers of all properties of the air (e.g., heat, water vapor) are performed through the movement of air from one point to another. In contrast, when $Re \ll 1$, the molecular dissipation of velocity dominates, and the flow is said to be *laminar*. Under this condition, properties of the air are transferred on the molecular scale. When $Re \sim 1$, both effects are important, and initial and boundary conditions imposed on the flow will determine whether laminar or turbulent mixing predominates.[8]

On the mesoscale, the Reynolds number is very large, and the flow is highly turbulent. With $S = W = 1.5$ cm s^{-1} and $L = L_z = 1$ km, for example, $Re = 10^6$. Only near the ground do molecular transfers become important. In this situation, air flow with $L_z \sim 0.1$ mm and $W \sim 1.5$ cm s^{-1}, for example, result in a Reynolds number of 0.1, so that the movement of air is laminar. However, since atmospheric flow above a centimeter or so off the ground has a Reynolds number much greater than unity, the viscous dissipation term is neglected in Eq. (2-45).

Using the scale analysis in this section, a more formal definition of mesoscale than presented in Chapter 1 can be given. The criteria are as follows:

1.   The horizontal scale must be sufficiently large so that the hydrostatic equation can be applied,

2.   The horizontal scale must be sufficiently small so that the Coriolis term is small (although it can still be significant) relative to the advective and pressure gradient forces, resulting in a flow field that is substantially different from the gradient wind relation even in the absence of friction effects.

This definition of mesoscale is similar to that proposed by Emanuel (1982a). He defined this scale to occur when both ageostrophic advection and Coriolis accelerations are important, which is essentially the same as given in criterion 2. In addition, since in this text criterion 2 forms the upper bound in terms of horizontal scale of mesoscale circulations, this meteorological definition is a function of latitude. At the equator, for example, much larger atmospheric features would be expected to be mesoscale, since the winds are not constrained by the gradient wind relation. In contrast, at high latitudes, the upper bound on mesoscale is more limited, since the Coriolis term is larger and the wind closely approximates gradient balance above the boundary layer even for relatively small horizontal scales. Thus at low latitudes, mesoscale mass adjustment dominates, even for relatively large circulation features (e.g., several thousand kilometers), whereas at higher latitudes for the same-sized features, this restructuring of the mass field is performed by near-gradient wind synoptic motions.[9] On other planets with their different rotation rates and diameters, the maximum horizontal scale as function of latitude at which the systems are mesoscale will differ from that of the earth's.

Scales of motion in which vertical accelerations become important can be termed the microscale and correspond to the meso-γ scale as defined by Orlanski (1975). This scale of motion, somewhat smaller than the mesoscale, has also been called the cumulus scale, with the smallest sizes referenced as the turbulence scale. Scales larger than the mesoscale where the Coriolis effect becomes of the same magnitude as the pressure gradient are termed the regional (synoptic) scale and correspond to Orlanski's meso-α and larger. Therefore, mesoscale as defined in this text corresponds closely to Orlanski's meso-β scale.

If the atmospheric feature is on the mesoscale, as defined here, Eq. (3-23) could replace the vertical equation of motion ($i = 3$) from Eq. (2-45), and Eqs. (3-14) or (3-11) could be used in lieu of Eq. (2-43) to represent the conservation of mass. The vertical equation of motion can be retained, of course, even though the atmospheric feature being modeled is on the mesoscale. Indeed, this practice has been generally adopted, as discussed in Sections 10.4 and 10.5 of Chapter 10. However, knowledge that a system is mesoscale or larger permits us

to directly obtain the pressure field from knowledge of the vertical temperature profile, as shown in Chapter 4. As a result of these simplifications, mesoscale circulations are defined to be *anelastic, hydrostatic*, and *significantly nongradient wind* meteorological systems. In Sections 5.2.2 and 5.2.3 in Chapter 5, the scales of motion in which the hydrostatic assumption applies are examined more quantitatively, since scale analysis provides only very qualitative guidance.

3.4   Conservation of Water and Other Gaseous and Aerosol Contaminants

As with the conservation relation for heat, the source-sink expressions for the conservation of water and other gaseous and aerosol contaminants, S_{q_n} and S_{χ_m}, are complex. The most restrictive relation is to assume that q_n and χ_m are conserved so that

$$\partial q_n/\partial t = -u_j \partial q_n/\partial x_j, \quad n = 1, 2, 3$$

and

$$\partial \chi_m/\partial t = -u_j \partial \chi_m/\partial x_j, \quad m = 1, 2, \ldots, M$$

or, equivalently,

$$dq_n/dt = 0 \quad \text{and} \quad d\chi_m/dt = 0.$$

It is valid to use these equations to represent atmospheric circulation if

$$|S_{q_n}| \ll \left|\frac{\partial q_n}{\partial t}\right|; \quad \left|u\frac{\partial q_n}{\partial x}\right|; \quad \left|v\frac{\partial q_n}{\partial y}\right|; \quad \left|w\frac{\partial q_n}{\partial z}\right|$$

and

$$|S_{\chi_m}| \ll \left|\frac{\partial \chi_m}{\partial t}\right|; \quad \left|u\frac{\partial \chi_m}{\partial x}\right|; \quad \left|v\frac{\partial \chi_m}{\partial y}\right|; \quad \left|w\frac{\partial \chi_m}{\partial z}\right|.$$

The first of these conditions is most closely fulfilled when the amount of water undergoing phase changes between solid, liquid, and gas, and when that created by chemical reactions is much less than changes caused by the advection of water. Similarly, the second condition is satisfactory if the aerosol and gaseous constituents undergo phase and chemical changes that are much smaller in magnitude than the advective changes. Scale analysis of S_{q_n} and S_{χ_m} could be performed; however, the complexity and high degree of parameterization of these terms would make such a qualitative evaluation of dubious value. Therefore, a discussion of the scale analysis of these source-sink terms is not presented here. S_{q_n} is discussed in more detail in Chapter 9.

Notes to Chapter 3

1. Scale analysis is specifically a procedure for using the dimensions of a set of variables to interrelate them. Buckingham (1914) originally developed this method of dimensional analysis. Recent overviews have been reported in Schmidt and Housen (1995) and Vogel (1998). Hicks (1978) and Meroney (1998) discuss misinterpretation of dimensional analyses if the nondimensional variables are not properly selected.

2. In Section 4.1, α_0 and α' are defined more formally.

3. As discussed in Chapter 5, one of the significant types of wave motions on the mesoscale is an internal gravity wave. Speeds as high as 30 m s^{-1} or so are typical of such features (see, e.g., Gedzelman and Donn 1979). Also, as illustrated by Dutton (1976, Figure 12-5) the relationship between the group velocity for internal gravity waves and their wavelength is given by an expression similar to Eq. (3-9), i.e., $C_{gx}/L_x \sim C_{gz}/L_z$, where C_{gx} and C_{gz} are the group velocities in the x and z directions.

4. In addition, if the horizontal pressure gradient force and the horizontal acceleration are assumed to be of equal magnitude, then using the analysis discussed in Section 3.3.2, Eq. (3-21) can also be written as $\hat{R}_w = (L_z^2 \delta_x T)/(L_x^2 \delta T)$, where the subscript x on δ in the numerator is used to indicate that the difference in T is in the horizontal direction. (In contrast to past analyses by other investigators, δT and $\delta_x T$ need not be of the same magnitude.) Thus for this situation, a greater difference in temperature over the same horizontal scale L_x results in a greater vertical acceleration, whereas a greater change in the perturbation temperature for a specific vertical scale L_z reduces the importance of the vertical acceleration relative to the vertical pressure gradient. This latter result implies that the more rapidly a temperature disturbance decreases with height (perhaps because of a more stable large-scale atmosphere), the greater the reduction in the importance of the vertical acceleration.

5. This form of the hydrostatic equation is actually valid only for a flat world, since the $x - y - z$ Cartesian system was used in its derivation. However, as discussed by Bannon et al. (1997), since the earth is a sphere, the actual pressure change with altitude is slightly modified from that in Eq. (3-23). The actual surface pressure, for example, would be about 0.25% less than that calculated using Eq. (3-23).

6. In addition, quantitative linear (see, e.g., Section 5.2.3) and nonlinear (see, e.g., Section 12.4) models should be integrated with and without selected terms in the conservation equations to determine their importance for specific atmospheric circulations.

7. When curvature of the synoptic horizontal pressure field is included, the resultant wind is called the *gradient wind*.

8. Tennekes and Lumley (1972) reported that boundary-layer flows in a zero pressure gradient become turbulent at $Re \sim 600$, whereas a fluid far from a boundary attains this condition at values of the Reynolds number much closer to unity.

9. The *omega equation* (Carlson 1991; Bluestein 1992, 1993; Pielke 1995) is an effective mathematical framework for assessing the resulting synoptic-scale vertical motion.

Additional Readings

Lilly, D.K. 1996. A comparison of incompressible, anelastic and Boussinesq dynamics. *Atmos. Res.* **40**, 143–151.

>   This article discusses different formulations for the conservation equations. Among its conclusions is that the incompressible form of the conservation of mass equation is not nondivergent, and that when the Boussinesq assumption is made, mass is not conserved.

Thunis, P. and R. Bornstein. 1996. Hierarchy of mesoscale flow assumptions and equations. *J. Atmos. Sci.* **53**, 380–397.

Chapter 4

Averaging the Conservation Relations

4.1   Definition of Averages

Equations (2-43)–(2-47) and their simplified forms introduced in Chapter 3 are defined in terms of the differential operators $(\partial/\partial t, \partial/\partial x_i)$, and thus in terms of mathematical formalism are valid only in the limit when δt, δx, δy, and δz approach 0. In terms of practical application, however, they are valid only when the spatial increments δx, δy, and δz are much larger than the spacing between molecules (so that only the statistical characteristics of molecular motion, rather than the movement of individual molecules themselves, are important), but are small enough so that the differential terms over these distances and over the time interval δt can be represented accurately by a constant. If these terms vary significantly within the intervals, however, then Eqs. (2-43)–(2-47) must be integrated over the distance and time intervals over which they are being applied.

Stated more formally, if

$$l_{\mathrm{m}} \ll \delta x, \delta y, \text{ and } \delta z, \tag{4-1}$$

where l_{m} is the representative spacing between molecules, and if

$$\frac{\partial}{\partial x} \rho u \gg \frac{(\delta x)}{2} \frac{\partial^2 \rho u}{\partial x^2}, \quad \frac{\partial}{\partial y} \rho v \gg \frac{(\delta y)}{2} \frac{\partial^2 \rho v}{\partial y^2},$$

$$\frac{\partial \rho}{\partial t} \gg \frac{(\delta t)}{2} \frac{\partial^2 \rho}{\partial t^2}, \ldots, \text{ etc.,} \tag{4-2}$$

then using Eqs. (2-43)–(2-47) (or a simplified form of this system of equations) is justified.

In the atmosphere, the criteria given by Eqs. (4-1) and (4-2) limit the direct application of Eqs. (2-43)–(2-47) to space scales on the order of about 1 cm and to time scales of 1 second or so. Therefore, to use Eqs. (2-43)–(2-47) to

represent the atmosphere accurately, they must be evaluated over those space
and time intervals. Because mesoscale circulations have horizontal scales on the
order of 10 to 100 km or more and a vertical size of up to approximately 10
km, these equations would have to be solved at 10^{18}–10^{20} locations. Unfortu-
nately, this amount of information far exceeds the capacity of any existing or
foreseeable computer system.

Therefore, to circumvent this problem, it is necessary to integrate the con-
servation equations over specified spatial and temporal scales, whose sizes are
determined by the available computer capacity, including its speed of opera-
tion. For a specific mesoscale system, the smaller these scales, the better the
resolution of the circulation.

In performing this integration, it is convenient to perform the following
decomposition:

$$\phi = \bar{\phi} + \phi'',$$

where ϕ represents any one of the dependent variables and

$$\bar{\phi} = \int_t^{t+\Delta t} \int_x^{x+\Delta x} \int_y^{y+\Delta y} \int_z^{z+\Delta z} \phi \, dz \, dy \, dx \, dt / (\Delta t)(\Delta x)(\Delta y)(\Delta z). \qquad (4\text{-}3)$$

Thus $\bar{\phi}$ represents the average of ϕ over the finite time increment Δt and space
intervals Δx, Δy, and Δz. The variable ϕ'' is the deviation of ϕ from this average
and is often called the *subgrid-scale perturbation*. In a numerical model, Δt is
called the *time step* and Δx, Δy, and Δz represent the model *grid intervals*, as
illustrated schematically in Figure 4-1.

One convenient decomposition is to define the averaging volume such that
the subgrid-scale perturbation includes the nonhydrostatic part of the solution
and the resolvable scale is accurately represented by the hydrostatic assump-
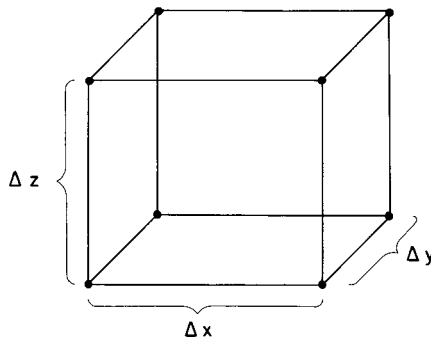

Fig. 4-1. A schematic of a grid volume. Dependent variables are defined at the cor-
ners of the rectangular solid.

tion. Thus the influence of the nonhydrostatic component of a model would be parameterized and the hydrostatic portion explicitly resolved.

Using this definition, Eq. (2-45) can be rewritten as

$$\frac{\partial\left(\bar{u}_i + u_i''\right)}{\partial t} = -\left(\bar{u}_j + u_j''\right)\frac{\partial}{\partial x_j}\left(\bar{u}_i + u_i''\right) - \left(\bar{\alpha} + \alpha''\right)\frac{\partial\left(\bar{p} + p''\right)}{\partial x_i}$$

$$- g\delta_{i3} - 2\epsilon_{ijk}\Omega_j\left(\bar{u}_k + u_k''\right). \tag{4-4}$$

Performing the integration of Eq. (4-4) over the intervals Δx, Δy, Δz, and Δt yields

$$\overline{\frac{\partial}{\partial t}\left(\bar{u}_i + u_i''\right)} = \overline{-\left(\bar{u}_j + u_j''\right)\frac{\partial}{\partial x_j}\left(\bar{u}_i + u_i''\right)} - \overline{\left(\bar{\alpha} + \alpha''\right)\frac{\partial\left(\bar{p} + p''\right)}{\partial x_i}}$$

$$- g\delta_{i3} - 2\epsilon_{ijk}\overline{\Omega_j\left(\bar{u}_k + u_k''\right)}, \tag{4-5}$$

where the overbar represents the integral operation

$$\overline{(\ )} = \int_t^{t+\Delta t}\int_x^{x+\Delta x}\int_y^{y+\Delta y}\int_z^{z+\Delta z}(\ )\,dz\,dy\,dx\,dt\,(\Delta t)(\Delta x)(\Delta y)(\Delta z), \tag{4-6}$$

as performed on ϕ in Eq. (4-3). This operation is often called *grid-volume averaging*, since it is performed over the spatial increments Δx, Δy, and Δz.[1]

To simplify this equation, it is convenient to assume that the averaged dependent variables change much more slowly in time and space than do the deviations from the average. This *scale separation* between the average and the perturbation implies that $\bar{\phi}$ is approximately constant and ϕ'' significantly fluctuates across the distance Δx, Δy, and Δz and time interval Δt. Examples illustrating when this scale separation is valid and when it is not are given in Figure 4-2. In addition, the grid intervals and time increments are also presumed to not be functions of location or time, so that the derivatives (i.e., $\partial/\partial t$, $\partial/\partial x_j$) can be straightforwardly removed from inside the integrals. Equation (4-5) then reduces to

$$\frac{\partial\bar{u}_i}{\partial t} = -\bar{u}_j\frac{\partial\bar{u}_i}{\partial x_j} - \overline{u_j''\frac{\partial u_i''}{\partial x_j}} - \bar{\alpha}\frac{\partial\bar{p}}{\partial x_i} - \overline{\alpha''\frac{\partial p''}{\partial x_i}} - g\delta_{i3} - 2\epsilon_{ijk}\Omega_j\bar{u}_k, \tag{4-7}$$

where the conditions prescribed previously permit the following type of simplifications:[2]

$$\bar{\bar{u}}_i = \bar{u}_i, \ \overline{u_i''} = 0, \ \overline{\frac{\partial \bar{u}_i}{\partial t}} = \frac{\partial\bar{u}_i}{\partial t}, \ \overline{\frac{\partial\bar{u}_i}{\partial x_j}} = \frac{\partial\bar{u}_i}{\partial x_j}, \ \text{etc.} \tag{4-8}$$

The stipulation that the average of the deviations is 0 $(\overline{\phi''} = 0)$ is commonly called the *Reynolds assumption*.
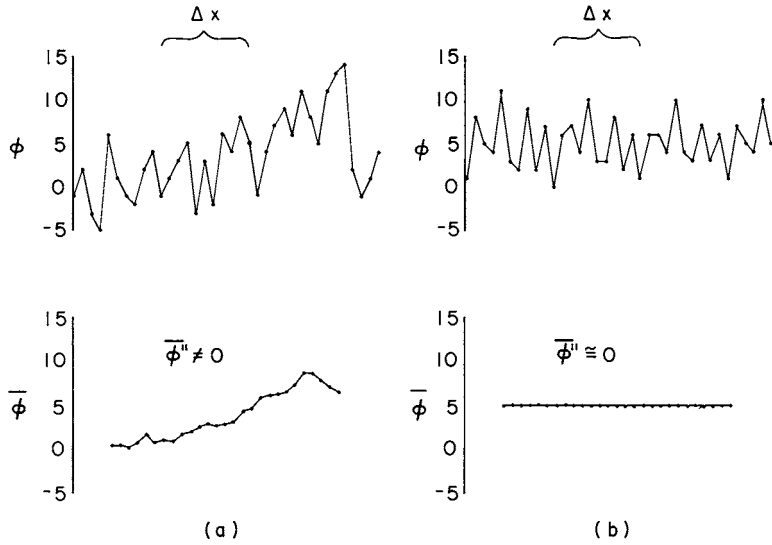
Fig. 4-2. A one-dimensional schematic illustration of a situation where (a) $\overline{\phi''} \neq 0$ and (b) $\overline{\phi''} \simeq 0$. The averaging length is illustrated by the interval Δx drawn on the figure ($\bar{\phi} = \frac{1}{10} \int_{x_i}^{x_i+10} \phi \, dx$). Since $\phi = \bar{\phi} + \phi''$, $\overline{\phi''} = 0$ only if $\bar{\phi} = \bar{\bar{\phi}}$.

Even with the simplifications, Eq. (4-7) contains two additional terms not found in Eq. (2-45) that involve the correlation between the subgrid-scale variables. The second of these terms, $\overline{\alpha'' \partial p''/\partial x_i}$, could be eliminated if the assumption is made in Eq. (4-4) that $|\alpha''|/\bar{\alpha} \simeq |\alpha''|/\alpha_0 \ll 1$ [In Section 3.1, α_0 was defined as a synoptic-scale specific volume in the derivation of the approximate forms of the conservation-of-mass relation. The mathematical definition of this synoptic scale is given by Eq. (4-12).]

With this requirement on specific volume and the assumption that Eq. (3-11) can be written as

$$\frac{\partial}{\partial x_j} \rho_0 u_j \simeq \frac{\partial}{\partial x_j} \bar{\rho} u_j \quad \left(\text{since } \frac{|\alpha''|}{\bar{\alpha}} \simeq \frac{|\alpha''|}{\alpha_0} \ll 1 \right), \tag{4-9}$$

using the simplifying assumptions given by Eq. (4-8), Eq. (4-5) can be written as

$$\bar{\rho} \frac{\partial \bar{u}_i}{\partial t} = -\frac{\partial}{\partial x_j} \bar{\rho} \, \bar{u}_j \, \bar{u}_i - \frac{\partial}{\partial x_j} \bar{\rho} \overline{u_j'' u_i''} - \frac{\partial \bar{p}}{\partial x_i} - \bar{\rho} g \delta_{i3} - 2\epsilon_{ijk} \Omega_j \bar{u}_k \bar{\rho}, \tag{4-10}$$

where, since $|\alpha''|/\bar{\alpha} \ll 1$, the pressure gradient term is represented by $\bar{\alpha} \, \partial \bar{p}/\partial x$. The remaining *subgrid-scale correlation term*, $\bar{\rho} \overline{u_j'' u_i''}$, represents the contributions of the smaller scales on the resolvable grid scale resulting from fluctuating velocity components and is in general very important in all aspects of dynamic

meteorology. This term, also called the *turbulent velocity flux*, must be *param-eterized* in terms of averaged quantities to ensure that the number of unknowns is equal to the number of equations. Terms of this sort, which arise in the averaged conservation relations, are often of the same order or even larger than the terms that involve only resolved dependent variables. The proper specification of this and similar subgrid-scale correlation terms as functions of resolvable averaged quantities, is referred to as the *closure* problem and is discussed further in Chapter 7.

Equation (4-10) can be written in a second way by assuming that

$$\bar{\phi} = \phi_0 + \phi', \tag{4-11}$$

where (as before, ϕ represents any one of the dependent variables)

$$\phi_0 = \int_x^{x+D_x} \int_y^{y+D_y} \bar{\phi} \, dx \, dy / D_x D_y \tag{4-12}$$

and is called the *layer domain-averaged variable*. Here D_x and D_y represent distances that are large compared to the mesoscale system of interest [perhaps the horizontal size (*domain*) of the mesoscale model representation], so that ϕ_0 is assumed to represent the synoptic-scale atmospheric conditions, as referred to previously. Thus the variable ϕ' represents the mesoscale deviations from this larger scale.

Substituting Eq. (4-11) into Eq. (4-10) and rearranging results in

$$\frac{\partial(u_{i_0}+u_i')}{\partial t} = -(u_{j_0}+u_j')\frac{\partial}{\partial x_j}(u_{i_0}+u_i') - \frac{1}{\rho_0[1+(\rho'/\rho_0)]}\frac{\partial}{\partial x_j}\rho_0\left(1+\frac{\rho'}{\rho_0}\right)\overline{u_j''u_i''}$$

$$- \alpha_0\left(1+\frac{\alpha'}{\alpha_0}\right)\frac{\partial(p_0+p')}{\partial x_i} - g\delta_{i3} - 2\epsilon_{ijk}\Omega_j(u_{k_0}+u_k'). \tag{4-13}$$

If $|\alpha'|/\alpha_0 \ll 1$ is required, then the horizontal and vertical components of Eq. (4-13) can be rewritten as

$$\frac{\partial \bar{u}_i}{\partial t} = -\bar{u}_j\frac{\partial \bar{u}_i}{\partial x_j} - \frac{1}{\rho_0}\frac{\partial}{\partial x_j}\rho_0\overline{u_j''u_o''} - \alpha_0\frac{\partial \bar{p}}{\partial x_i} - 2\epsilon_{ijk}\Omega_j\bar{u}_k, \quad i=1,2 \tag{4-14}$$

and

$$\frac{\partial \bar{w}}{\partial t} = -\bar{u}_j\frac{\partial \bar{w}}{\partial x_j} - \frac{1}{\rho_0}\frac{\partial}{\partial x_j}\rho_0\overline{u_j''w''} - \alpha_0\frac{\partial p'}{\partial z} + \frac{\alpha'}{\alpha_0}g + 2\bar{u}\Omega\cos\phi, \quad i=3 \tag{4-15}$$

where it is assumed that the synoptic-scale pressure field is hydrostatic ($\partial p_0/\partial z = -g/\alpha_0$), so that

$$(\alpha_0 + \alpha')\frac{\partial}{\partial z}(p_0 + p') + g = \alpha_0\left(1 + \frac{\alpha'}{\alpha_0}\right)\frac{\partial p'}{\partial z} - g + g - \frac{\alpha'}{\alpha_0}g$$

$$\simeq \alpha_0\frac{\partial p'}{\partial z} - \frac{\alpha'}{\alpha_0}g.$$

The term $(\alpha'/\alpha_0)g$ is the only expression retained in Eqs. (4-14) and (4-15) that contains temporal variations in specific volume when $|\alpha'|/\alpha_0 \ll 1$. Neglecting temporal variations of density (as given by α') except for $(\alpha'/\alpha_0)g$ is called the *Boussinesq approximation*. This term can also be rewritten by logarithmically differentiating the ideal gas law so that

$$\frac{d\alpha}{\alpha} = \frac{dT}{T} - \frac{dp}{p}. \tag{4-16}$$

When the changes of α, T, and p are assumed to be much less than their absolute magnitudes (e.g., $|d\alpha| \ll \alpha$, $|dT| \ll T$, and $|dp| \ll p$), and if $\alpha \simeq \alpha_0$, $T \simeq T_0$, and $p \simeq p_0$, then Eq. (4-16) can be approximated by

$$\frac{\alpha'}{\alpha_0} \simeq \frac{T'}{T_0} - \frac{p'}{p_0}. \tag{4-17}$$

Since $|\alpha'|/\alpha_0$ has already been assumed much less than unity, the requirement that $|T'|/T_0 \ll 1$ and $|p'|p_0 \ll 1$ is implied from Eq. (4-17). Thus the vertical component of acceleration can also be written as

$$\frac{\partial \bar{w}}{\partial t} = -\bar{u}_j\frac{\partial \bar{w}}{\partial x_j} - \frac{1}{\rho_0}\frac{\partial}{\partial x_j}\rho_0\overline{u_j''w''}$$

$$- \alpha_0\frac{\partial p'}{\partial z} + \left(\frac{T'}{T_0} - \frac{p'}{p_0}\right)g + 2\bar{u}\Omega\cos\phi. \tag{4-18}$$

Finally, since $\theta = T(1000/p)^{R_d/C_p}$, α'/α_0 can also be approximated by

$$\frac{\alpha'}{\alpha_0} = \frac{\theta'}{\theta_0} - \frac{C_v}{C_p}\frac{p'}{p_0}, \tag{4-19}$$

which represents another form of the ideal gas law when $|\alpha'|/\alpha_0 \ll 1$. Here the relation $C_p = C_v + R_d$ has been used to obtain the given form. This approximate form for α'/α_0 can be simplified when the vertical scale of the circulation, L_z,

is much smaller than the scale depth of the atmosphere, H_α. Using the scale analysis procedure introduced in Chapter 3, we have

$$|\alpha_0\, \partial p'/\partial z| \sim \alpha_0 |p'|/L_z,$$

and assuming that the vertical mesoscale pressure perturbation and the density perturbation terms are of the same order of magnitude, we have

$$|\alpha_0\, \partial p'/\partial z| \sim |\alpha'/\alpha_0| g,$$

so that

$$\frac{R\, T_0 |p'|}{L_z p_0} \sim \frac{|\alpha'|}{\alpha_0}\, g$$

or

$$\frac{|p'|}{p_0} \sim \frac{L_z g}{R\, T_0} \frac{|\alpha'|}{\alpha_0} = \frac{L_z g}{p_0 \alpha_0} \frac{|\alpha'|}{\alpha_0} = \frac{L_z}{D} \frac{|\alpha'|}{\alpha_0} \sim \frac{L_z}{H_\alpha} \frac{|\alpha'|}{\alpha_0},$$

where the results from Chapter 3 that $p_0 \sim \rho_0 g D$ and $D \sim H_\alpha$ have been used. Thus if $L_z \ll H_\alpha$, then

$$|p'|/p_0 \ll |\alpha'|/\alpha_0 \qquad \text{and} \qquad |\alpha'|/\alpha_0 \sim |\theta'|/\theta_0,$$

so that for this situation, Eq. (4-18) can be written as

$$\frac{\partial \bar{w}}{\partial t} = -u_j \frac{\partial \bar{w}}{\partial x_j} - \frac{1}{\rho_0} \frac{\partial}{\partial x_j} \rho_0 \overline{u_j'' w''} - \alpha_0 \frac{\partial p'}{\partial z} + \frac{\theta'}{\theta_0} g + 2\bar{u}\Omega \cos \phi. \qquad (4\text{-}20)$$

Thus when the shallow form of the conservation-of-mass equation [Eq. (3-14)] can be used, it is appropriate to use Eq. (4-20) as the vertical equation of motion.

Equations (4-14) and (4-15) can, therefore, be written in tensor form as

$$\frac{\partial \bar{u}_i}{\partial t} = -\bar{u}_j \frac{\partial \bar{u}_i}{\partial x_j} - \frac{1}{\rho_0} \frac{\partial}{\partial x_j} \rho_0 \overline{u_j'' u_i''} - \alpha_0 \frac{\partial p'}{\partial x_i} - \alpha_0 \left(\frac{\partial p_0}{\partial x} \delta_{i1} + \frac{\partial p_0}{\partial y} \delta_{i2} \right)$$

$$+ \frac{\alpha'}{\alpha_0} g\delta_{i3} - 2\epsilon_{ijk}\Omega_j \bar{u}_k, \qquad (4\text{-}21)$$

where

$$\alpha'/\alpha_0 = (\theta'/\theta_0) - (C_v p'/C_p p_0)$$

for deep atmospheric circulations and

$$\alpha'/\alpha_0 = \theta'/\theta_0$$

for shallow systems. Either Eq. (4-21) or Eq. (4-10) can be used to predict velocity fluctuations.

The remainder of the prognostic equations [Eqs. (2-43), (2-44), (2-46), and (2-47)] can be averaged in the same manner as performed for the conservation-of-motion relations.

The complete conservation-of-mass equation (2-43), after using the averaging operation given by Eqs. (4-3) and (4-6) along with the assumptions listed in Eq. (4-8), is given as

$$\frac{\partial \bar{\rho}}{\partial t} = -\frac{\partial}{\partial x_j} \bar{\rho}\, \bar{u}_j - \frac{\partial}{\partial x_j} \overline{\rho'' u_j''}, \tag{4-22}$$

whereas averaging the approximate forms of this relation given by Eqs. (3-11) and (3-14) yields

$$\frac{\partial}{\partial x_j} \rho_0 \bar{u}_j \simeq \frac{\partial}{\partial x_j} \bar{\rho}\, \bar{u}_j = 0 \qquad \text{and} \qquad \frac{\partial \bar{u}_j}{\partial x_j} = 0. \tag{4-23}$$

The remainder of the prognostic equations [Eqs. (2-44), (2-46), and (2-47)], are similar in form, and the equivalent averaged forms can be written as

$$\frac{\partial \bar{\theta}}{\partial t} = -\bar{u}_j \frac{\partial \bar{\theta}}{\partial x_j} - \frac{1}{\rho_0} \frac{\partial}{\partial x_j} \rho_0 \overline{u_j'' \theta''} + \overline{S}_\theta, \tag{4-24}$$

$$\frac{\partial \bar{q}_n}{\partial t} = -\bar{u}_j \frac{\partial \bar{q}_n}{\partial x_j} - \frac{1}{\rho_0} \frac{\partial}{\partial x_j} \rho_0 \overline{u_j'' q_n''} + \overline{S}_{q_n}, \quad n = 1, 2, 3, \tag{4-25}$$

and

$$\frac{\partial \overline{X}_m}{\partial t} = -\bar{u}_j \frac{\partial \overline{X}_m}{\partial x_j} \rho_0 \overline{u_j'' X_m''} + \overline{S}_{X_m}, \quad m = 1, 2, \ldots, M, \tag{4-26}$$

where $\overline{S}_\theta$, $\overline{S}_{q_n}$ and $\overline{S}_{X_m}$, represent the integrated contributions of the source-sink terms over the intervals defined by Eq. (4-6).

Using the conservation-of-mass relation, given by Eq. (4-23), the advection terms in Eqs. (4-24)–(4-26) can be given as

$$-\bar{u}_j \frac{\partial \bar{\theta}}{\partial x_j} = -\frac{1}{\rho_0} \frac{\partial}{\partial x_j} \rho_0 \bar{u}_j \bar{\theta}, \tag{4-27}$$

$$-\bar{u}_j \frac{\partial \bar{q}_n}{\partial x_j} = -\frac{1}{\rho_0} \frac{\partial}{\partial x_j} \rho_0 \bar{u}_j \bar{q}_n, \tag{4-28}$$

and

$$-\bar{u}_j \frac{\partial \overline{X}_m}{\partial x_j} = -\frac{1}{\rho_0} \frac{\partial}{\partial x_j} \rho_0 \bar{u}_j \overline{X}_m, \tag{4-29}$$

where the right side is often referred to as the *flux form* of the advection terms.

The averaged conservation-of-motion equations given by (4-21) [or by (4-10)] along with Eqs. (4-23)–(4-26) are often called the *primitive equations*, because

they are derived straightforwardly from the original conservation principles presented in Chapter 2. As evident from the assumptions required to obtain them, however, they are not the most fundamental form of the conservation laws, as implied by the word "primitive."

4.2 Vorticity Equation

The conservation-of-motion equation has not always been used in the primitive equation form. Equation (4-21) can be rewritten as

$$\frac{\partial \rho_0 \bar{u}_i}{\partial t} = -\frac{\partial}{\partial x_j}\, \rho_0 \bar{u}_j \bar{u}_i - \frac{\partial}{\partial x_j}\, \rho_0 \overline{u_j'' u_i''} - \frac{\partial p'}{\partial x_i} - \left(\frac{\partial p_0}{\partial x}\, \delta_{i1} + \frac{\partial p_0}{\partial y}\, \delta_{i2}\right)$$

$$+ \frac{\alpha'}{\alpha_0^2}\, g\delta_{i3} - 2\epsilon_{ijk}\Omega_j \bar{u}_k \rho_0,$$

where the conservation-of-mass relation given on the left side of Eq. (4-23) has been used, along with the assumption that $|\bar{u}_i \partial \rho_0/\partial t| \ll |\rho_0\, \partial \bar{u}_i/\partial t|$.

A vorticity equation[3] can be derived from this relation by applying the operator $\epsilon_{pqi}\, \partial/\partial x_q$ (e.g., the vector curl operation $\nabla\times$). The parameter ϵ_{pqi} has the same definition as given in Chapter 2, where it is equal to 0 if any of the indices are the same, to $+1$ for even permutations, and to -1 for odd permutations of the indices p, q, and i. This results in the equation

$$\frac{\partial}{\partial t}\left[\epsilon_{pqi}\, \frac{\partial}{\partial x_q}\, \rho_0 \bar{u}_i\right] = -\frac{\partial}{\partial x_j}\left[\bar{u}_j\, \epsilon_{pqi}\, \frac{\partial \bar{u}_i \rho_0}{\partial x_q}\right] - \frac{\partial}{\partial x_j}\left[\rho_0 \bar{u}_i\, \epsilon_{pqi}\, \frac{\partial \bar{u}_j}{\partial x_q}\right]$$

$$- \epsilon_{pqi}\, \frac{\partial}{\partial x_q}\, \frac{\partial}{\partial x_j}\, \rho_0 \overline{u_j'' u_i''} - \epsilon_{pqi}\, \frac{\partial}{\partial x_q}\, \frac{\partial p'}{\partial x_i}$$

$$- \epsilon_{pqi}\, \frac{\partial}{\partial x_q}\left[\frac{\partial p_0}{\partial x}\, \delta_{i1} + \frac{\partial p_0}{\partial y}\, \delta_{i2}\right]$$

$$+ \epsilon_{pqi}\, \frac{\partial}{\partial x_q}\, \frac{\alpha'}{\alpha_0^2}\, g\delta_{i3} - 2\epsilon_{pqi}\epsilon_{ijk}\Omega_j\, \frac{\partial \rho_0 \bar{u}_k}{\partial x_q}, \qquad (4\text{-}30)$$

where $\epsilon_{pqi}(\partial/\partial x_q)(\partial p'/\partial x_i) = 0$. This latter identity can be shown by expanding the term into its nine components. In vector terminology, this identity is written as $\nabla\times\nabla p' = 0$; that is, the curl of a gradient is always 0. The large-scale pressure term ($\epsilon_{pqi}(\partial/\partial x_q)\,[(\partial p_0/\partial x)\delta_{i1} + (\partial p_0/\partial y)\delta_{i2}]$) is identically 0 when $\partial p_0/\partial z$ is included in the calculation of curl of the synoptic pressure gradient, so it will be deleted henceforth.

Defining a density-weighted mesoscale vorticity (hereafter referred to as vorticity) by

$$\omega_p = \epsilon_{pqi} \frac{\partial}{\partial x_q} \rho_0 \bar{u}_i$$

(this is equivalent to $\omega_p = \nabla \times \rho_0 \vec{V}'$), Eq. (4-30) can be written as

$$\frac{\partial \omega_p}{\partial t} = -\frac{\partial}{\partial x_j}(\bar{u}_j \omega_p) - \epsilon_{pqi}\frac{\partial}{\partial x_j}\left(\rho_0 \bar{u}_i \frac{\partial \bar{u}_j}{\partial x_q}\right) - \epsilon_{pqi}\frac{\partial}{\partial x_q}\frac{\partial}{\partial x_j}\left(\rho_0 \overline{u_j'' u_i''}\right)$$

$$+ \delta_{i3} g \epsilon_{pqi} \frac{\partial}{\partial x_q} \frac{\alpha'}{\alpha_0^2} - 2\epsilon_{pqi}\epsilon_{ijk}\Omega_j \frac{\partial \rho_0 \bar{u}_k}{\partial x_q}. \qquad (4\text{-}31)$$

The individual terms in Eq. (4-31) correspond to the following:

1. The local tendency of vorticity ($\partial \omega_p / \partial t$).
2. The gradient of the resolvable flux of vorticity ($-(\partial/\partial x_j)\bar{u}_j \omega_p$).
3. The *tilting term*[4] ($\epsilon_{pqi}(\partial/\partial x_j)\rho_0 \bar{u}_i \partial \bar{u}_j/\partial x_q = \epsilon_{pqi}[\rho_0 \bar{u}_i(\partial^2 \bar{u}_j/\partial x_j \partial x_q) + (\partial \bar{u}_j/\partial x_q)(\partial \rho_0 \bar{u}_i/\partial x_j)]$), whereby vorticity is transferred between the three spatial components as a result of velocity shear and as a result of planar convergence/divergence of vorticity.
4. The subgrid-scale term ($-\epsilon_{pqi}(\partial/\partial x_q)(\partial/\partial x_j)\rho_0 \overline{u_j'' u_i''}$), in which vorticity is created or destroyed by small-scale motions.
5. The *solenoidal term* $[\delta_{i3} g \epsilon_{pqi}(\partial/\partial x_q)(\alpha'/\alpha_0^2)]$, in which vorticity is created or removed as a result of gradients in density. For shallow atmospheric circulations, this term becomes $\delta_{i3} g \epsilon_{pqi}(\partial/\partial x_q)(\rho_0 \theta'/\theta_0)$, so that differential heating is one mechanism to change the vorticity.
6. The solid-body rotation term $[2\epsilon_{pqi}\epsilon_{ijk}\Omega_j(\partial \rho_0 \bar{u}_k/\partial x_q)]$, in which vorticity is created or destroyed as a result of the rotation of the earth.

The advantages of replacing Eq. (4-21) with Eq. (4-31) to study mesoscale phenomena include the following:

1. When $\alpha'/\alpha_0 \simeq \theta'/\theta_0$, the mesoscale pressure perturbation term p' does not appear in the equation; hence it is not necessary to compute pressure.
2. Since the integral of vorticity over a volume equals circulation, results obtained using Eq. (4-31) are straightforward to interpret physically.

The disadvantages of using Eq. (4-31) include the following:

1. There is a computational difficulty in applying this equation to represent three-dimensional mesoscale flows, since the velocity $\bar{u}_j$ must be mathematically recovered from ω_p.
2. Boundary conditions required to initialize and solve the vorticity equation are more difficult to apply than those required for Eq. (4-21). This is partially

a result of the definition of vorticity, since the differentiation operation (e.g., $\partial/\partial x_q$) magnifies errors in initial, imposed velocity fields.

Most uses of the vorticity equation to represent the conservation of motion in meteorological flows have been limited to one of its components. Early synoptic models, such as the equivalent barotropic model (Haltiner 1971), used a simplified form of the vertical component of vorticity to simulate the movement of large-scale troughs and ridges in the middle troposphere. In mesoscale and cumulus cloud models, one of the horizontal components of vorticity has been used to simulate a vertical cross-section of the circulation. Examples of the latter usage include Orville (1965, 1968), Murray (1970), Orville and Sloan (1970), and Pearson (1973).

Meteorological investigators have increasingly declined to use a vorticity equation of the form of Eq. (4-31) to represent the conservation of motion and instead have relied on Eq. (4-21) or its equivalent, because of its computational and conceptual simplicity. The only three-dimensional mesoscale model that uses the vorticity form of which the author is aware is described most recently in Thunis and Clappier (2000). For this reason, the remainder of the text focuses on the primitive equation format.

4.3 Diagnostic Equation for Nonhydrostatic Pressure

The use of Eq. (4-21) or (4-10), however, requires an evaluation of pressure. If $H_\alpha/L_x \lesssim 1$ such that the motion can be assumed to be hydrostatic, then it is straightforward to integrate Eq. (3-23) to obtain pressure at any level. Using the averaging procedures discussed in this chapter, the vertical equation of motion in Eq. (4-10), in its hydrostatic form can be represented by

$$\partial\bar{p}/\partial z = -\bar{\rho}g, \tag{4-32}$$

and the equivalent expression for use in the third component of Eq. (4-21) is

$$\partial p'/\partial z = g\alpha'/\alpha_0^2, \tag{4-33}$$

which can be replaced by

$$\partial p'/\partial z = g\rho_0\theta'/\theta_0 \tag{4-34}$$

if $L_z \ll H_\alpha$.

If $|\alpha''|/\alpha_0$ is not assumed to be much less than unity and if the hydrostatic assumption is not expected to be valid or is otherwise not used, then pressure $\bar{p}$ can be computed from the ideal gas law and from Eq. (4-22), assuming that $\overline{\rho''u_j''}$ can be parameterized in terms of known quantities or ignored. If either of the approximate forms of the conservation-of-mass relation given by Eq. (4-23)

is used, however, then pressure cannot be computed in this fashion. In this case, the divergence $\partial/\partial x_i$ (equivalent to $\nabla\cdot$ in vector notation) of Eq. (4-21) yields

$$\frac{\partial}{\partial t}\frac{\partial}{\partial x_i}\rho_0\bar{u}_i = -\frac{\partial^2}{\partial x_i\partial x_j}(\rho_0\bar{u}_j\bar{u}_i) - \frac{\partial^2}{\partial x_i\partial x_j}\rho_0\overline{u_j''u_i''} - \frac{\partial^2 p'}{\partial x_i^2}$$

$$- \frac{\partial}{\partial x_i}\left[\frac{\partial p_0}{\partial x}\delta_{i1} + \frac{\partial p_0}{\partial y}\delta_{i2}\right] + \delta_{i3}g\frac{\partial}{\partial x_i}\frac{\alpha'}{\alpha_0^2} - 2\epsilon_{ijk}\Omega_j\frac{\partial}{\partial x_i}\rho_0\bar{u}_k.$$

Using the left side of Eq. (4-23) along with the approximation for α'/α_0 given by Eq. (4-19) gives the *diagnostic* second-order differential equation for the mesoscale pressure perturbation,

$$\frac{\partial^2 p'}{\partial x_i^2} + \frac{gC_v}{C_p}\frac{\partial}{\partial z}\left(\frac{\rho_0 p'}{p_0}\right) = -\frac{\partial^2}{\partial x_i\partial x_j}(\rho_0\bar{u}_j\bar{u}_i) - \frac{\partial^2}{\partial x_i\partial x_j}\rho_0\overline{u_j''u_i''}$$

$$- \frac{\partial}{\partial x_i}\left[\frac{\partial p_0}{\partial x}\delta_{i1} + \frac{\partial p_0}{\partial y}\delta_{i2}\right] + g\frac{\partial}{\partial z}\left(\frac{\rho_0\theta'}{\theta_0}\right)$$

$$- 2\epsilon_{ijk}\Omega_j\frac{\partial}{\partial x_i}\rho_0\bar{u}_k. \tag{4-35}$$

When $L_z \ll H_\alpha$, the second term on the left side of Eq. (4-35) does not appear, in which case Eq. (4-35) is referred to as a *Poisson partial differential equation* (see, e.g., Hildebrand 1962).

When Eq. (4-35) is used to diagnose pressure, the vertical component of Eq. (4-21) must be dropped, otherwise the system of equations that includes (4-19), (4-21), (4-23)–(4-26), and (4-35) would be *overspecified* (i.e., one more equation than the number of unknowns). Vertical velocity can be diagnosed directly from the appropriate form of Eq. (4-23); the right side of (4-23) can be used if $L_z \ll H_\alpha$.

The advantages of using Eq. (4-35) to compute pressure include the following:

1. The horizontal wavelength of the mesoscale system L_x can be of any size without concern for when the hydrostatic assumption is valid.

2. By using Eq. (4-23), sound waves, which in general are not expected to be meteorologically important on the mesoscale, are excluded. (This is demonstrated in Section 5.2.2.)

The disadvantages include the following:

1. The required computation time is increased, since pressure must be evaluated from the involved formulation given by Eq. (4-35).

2. As with the vorticity equation [Eq. (4-31)], the mathematical operation of differentiation magnifies errors in the evaluation of Eq. (4-35).

Models that use Eq. (4-35) to determine pressure, or the more general method of using the complete conservation-of-mass equation [i.e., Eq. (4-22)], along with the ideal gas law and definition of potential temperature to obtain pressure, are referred to as *nonhydrostatic models*. Of course, it actually is not appropriate to refer to such models as nonhydrostatic since, as shown in Song *et al.* (1985) and discussed in detail in Section 5.2.3.2, the pressure perturbation typically remains close to hydrostatic balance even when nonhydrostatic pressure effects become important. The nonhydrostatic pressure is also referred to as the *dynamic pressure*. The relative importance of hydrostatic and dynamic pressures is discussed in Chapter 5.

Investigators who have used an equation of the form given by Eq. (4-35) include Ogura and Charney (1961) and Neumann and Mahrer (1971). Models such as those reported by Tapp and White (1976), Cotton and Tripoli (1978), and Pielke *et al.* (1992) preferred to retain the more complete conservation-of-mass relation of the form given by Eq. (4-22). This is being done in recent models since, as shown in Section 10.4, the computational problems associated with retaining sound waves as a solution to the model equations have been eliminated.

4.4   Scaled Pressure Form

Finally, in mesoscale modeling, it has often been convenient to replace the pressure gradient term in Eq. (2-45) with

$$\frac{1}{\rho}\frac{\partial p}{\partial x_i} = \theta\frac{\partial \pi}{\partial x_i}, \tag{4-36}$$

where the ideal gas law [Eq. (2-49)] and the definition of potential temperature [Eq. (2-48)] have been used, so that

$$\pi = C_p(p/p_{00})^{R_d/C_p} = C_p T_v/\theta.$$

The variable π is often referred to as the *Exner function*.[5] Using the definitions of averaging presented in this chapter, we have

$$\overline{\theta\frac{\partial \pi}{\partial x_i}} = \bar{\theta}\frac{\partial \bar{\pi}}{\partial x_i} + \overline{\theta''\frac{\partial \pi''}{\partial x_i}}.$$

The subgrid-scale correlation term on the right side of this expression is of the same form as the $\overline{\alpha''\partial p''/\partial x_i}$ term in Eq. (4-7); however, it cannot be eliminated by using the approximate form of the conservation-of-mass relation [Eq. (4-9)], as was done in creating Eq. (4-10). To remove this term, it is necessary to use results from measurements (e.g., Lumley and Panofsky 1964) that show that

$$\overline{u_j''\,\partial u_i''/\partial x_j} \gg \overline{\theta''\,\partial \pi''/\partial x_i}.$$

In mesoscale systems, this inequality is reasonable since u_j'' often has variations in magnitude over short distances equal to or greater than $\bar{u}_j$ (e.g., if $\bar{u} = 5$ m s^{-1}, then it is common to have wind gusts to 10 m s^{-1} ($u'' = +5$ m s^{-1}), whereas if $\bar{\theta}$ and $\bar{\pi}$ have magnitudes around 300 K and 10^3 J kg^{-1}K^{-1}, respectively, then θ'' and π'' are observed to vary at most 10 K and 3 J kg^{-1} K^{-1}, respectively, (assuming a p'' of 10 mb over the same distances).

Therefore,

$$\overline{\theta \frac{\partial \pi}{\partial x_i}} \simeq \bar{\theta} \frac{\partial \bar{\pi}}{\partial x_i} \tag{4-37}$$

is a reasonable approximation for the averaged pressure gradient term.

Decomposing $\bar{\theta}$ and $\bar{\pi}$ into synoptic and mesoscale components yields

$$\theta_0 \left(1 + \frac{\theta'}{\theta_0} \right) \frac{\partial \bar{\pi}}{\partial x_i} \simeq \theta_0 \frac{\partial \bar{\pi}}{\partial x_i}, \quad i = 1, 2,$$

and

$$(\theta_0 + \theta') \frac{\partial}{\partial z} (\pi_0 + \pi') + g = \theta_0 \left(1 + \frac{\theta'}{\theta_0} \right) \frac{\partial \pi'}{\partial z} - g + g - \frac{\theta'}{\theta_0} g$$

$$\simeq \theta_0 \frac{\partial \pi'}{\partial z} - \frac{\theta'}{\theta_0} g. \tag{4-38}$$

where the synoptic scale is presumed to be hydrostatic; i.e., $(1/\rho_0)(\partial p_0/\partial z) = \theta_0 \, \partial \pi_0/\partial z = -g$.

The total resolvable form of the conservation-of-motion relation, equivalent to Eq. (4-10) and using $\bar{\pi}$ as the scale pressure, can then be written as

$$\frac{\partial \bar{u}_i}{\partial t} = -\bar{u}_j \frac{\partial \bar{u}_i}{\partial x_j} - \frac{1}{\rho_0} \frac{\partial}{\partial x_j} \rho_0 \overline{u_j'' u_i''} - \bar{\theta} \frac{\partial \bar{\pi}}{\partial x_i} - g\delta_{i3} - 2\epsilon_{ijk}\Omega_j \bar{u}_k, \tag{4-39}$$

and the form equivalent to Eq. (4-21) is given by

$$\frac{\partial \bar{u}_i}{\partial t} = -\bar{u}_j \frac{\partial \bar{u}_i}{\partial x_j} - \frac{1}{\rho_0} \frac{\partial}{\partial x_j} \rho_0 \overline{u_j'' u_i''} - \theta_0 \frac{\partial \pi'}{\partial x_i}$$

$$+ \theta_0 \left[\frac{\partial \pi_0}{\partial x} \delta_{i1} + \frac{\partial \pi_0}{\partial y} \delta_{i2} \right] + \frac{\theta'}{\theta_0} g\delta_{i3} - 2\epsilon_{ijk}\Omega_j \bar{u}_k. \tag{4-40}$$

If the hydrostatic assumption is used, then the vertical equation of motion ($i = 3$) from Eq. (4-39) is replaced with

$$\partial \bar{\pi}/\partial z = -g/\bar{\theta}, \tag{4-41}$$

and Eq. (4-40) yields

$$\partial \pi'/\partial z = g\theta'/\theta_0^2 \tag{4-42}$$

for the same situation.

The major advantages of writing the equations in this form are as follows:

1. The pressure perturbation term p', or its equivalent π', does not occur in the gravity term even if the depth of the circulation is on the same order as the scale depth of the atmosphere ($L_z \sim H_\alpha$).

2. The need to compute the density perturbation ($\rho' = 1/\alpha'$) is removed; thus one less equation needs to be evaluated.

3. The vertical gradient of π is much less than that of p, hence approximating that term using finite difference techniques introduces less error (i.e., $[\partial\bar{\pi}/\partial z/(\partial\bar{p}/\partial z)] = 1/(\bar{\rho}\bar{\theta}) \ll 1$).

The disadvantages include that in deriving a nonelastic equation for π', equivalent to Eq. (4-35), a first-derivative term in π' arises in all three spatial directions,

$$
\rho_0\theta_0 \frac{\partial^2\pi'}{\partial x_i^2} + \frac{\partial\pi'}{\partial x_i}\frac{\partial\rho_0\theta_0}{\partial x_i} = -\frac{\partial}{\partial x_i}\rho_0\bar{u}_j\frac{\partial\bar{u}_i}{\partial x_j} - \frac{\partial^2}{\partial x_i\partial x_j}\rho_0\overline{u''_j u''_i}
$$

$$
- \frac{\partial}{\partial x_i}\rho_0\theta_0\left[\frac{\partial\pi_0}{\partial x}\delta_{i1} - \frac{\partial\pi_0}{\partial y}\delta_{i2}\right] + \frac{\partial}{\partial x_i}\rho_0\frac{\theta'}{\theta_0}g\delta_{i3}
$$

$$
- 2\epsilon_{ijk}\Omega_j\frac{\partial}{\partial x_i}\bar{u}_k\rho_0
$$

(assuming $|\bar{u}_i\partial\rho_0/\partial t| \ll |\rho_0\partial\bar{u}_i/\partial t|$).

The inequality given by Eq. (3-22) suggests when either of the hydrostatic equations given by Eqs. (4-41) and (4-42) can be used in lieu of the third equation of motion. Since, as shown in Chapter 10, the smallest-sized horizontal feature that can be resolved with reasonable accuracy in a mesoscale model has a size corresponding to $4\Delta x$, then

$$
H_\alpha/L_x = H_\alpha/4\,\Delta x \gtrsim 1 \tag{4-43}
$$

defines a restriction for the use of the hydrostatic equation. If $\Delta x = 2$ km, for example, then the adequacy of the hydrostatic approximation seems assured, at least, based on the analysis given in Chapter 3. Additional and more quantitative evaluation of the accuracy of the hydrostatic assumption are given in Chapter 5, Sections 5.2.2 and 5.2.3.

4.5   Summary

Using the averaging technique presented in this chapter, consistent sets of the conservation relations can be derived. To develop a consistent set of equations,

the number of equations must be the same as the number of dependent variables. These averaged equations can be presented in several forms.

In determining the specific grid-volume-averaged equations, it is essential to identify the form used for:

- the conservation-of-mass equation (a scalar equation)
- the conservation-of-heat equation (a scalar equation)
- the conservation-of-motion equation (a vector equation)
- the conservation-of-water equation (three scalar equations)
- the conservation-of-other gaseous and aerosol materials equations (M scalar equations)
- the equation of state.

If simplified forms of any of these equations are used, the assumptions need to be stated.

The terms that constitute these equations also need to be identified. These terms are in one of the following forms:

- externally prescribed variables (e.g., u_{i_0}, θ_0)
- dependent variables (e.g., u_i', θ', $\overline{u_j'' u_i''}$, $\overline{u_j'' \theta''}$, $\overline{S_\theta}$)
- prescribed constants or functions (e.g., g, f).

The dependent variables can be further categorized into two types:

- those that are predicted from the conservation equations (e.g., u_i', θ')
- those for which parameterizations are often introduced (e.g., $\overline{u_j'' u_i''}$, $\overline{u_j'' \theta''}$, $\overline{S_\theta}$). Parameterizations are based on the variables that are predicted. As shown in Chapter 7, terms such as $\overline{u_j'' u_i''}$ can be predicted or parameterized. For each model, the approach adopted needs to be identified.

In Chapters 7–9, examples of methods to parameterize grid-volume-average values variables are described. Chapter 10 describes how the predicted variables are represented in the conservation equations.

Notes to Chapter 4

1. Equation (4-6) can be generalized to an *ensemble average*, as discussed in Cotton and Anthes (1989:Chapter 3). In that approach, an ensemble average can be defined as $\langle (\ ) \rangle = \lim_{N \to \infty} \sum_{i=1}^{N} \overline{(\ )}$, where Eq. (4-6) is an average for a particular case (e.g., a model *realization*). The number of realizations is N. When the results are sensitive to, for example, initial conditions, there will be a spread of realization results, which is called the ensemble. The grid-volume average has been stochastically chosen for some applications from an ensemble, as shown in, for example, Pielke (1984:Section 7.5) and Uliasz *et al.* (1996) for estimating atmospheric dispersion. More generally, however, as shown in Chapters 7–9 and 11, parameterizations exclusively use ensemble-average representations.

2. Raupach and Shaw (1982:80–82) discuss the situation in which these assumptions fail at interfaces with rigid objects. Galmarini and Thunis (1999) and Galmarini *et al.* (2000) discuss the errors introduced when the Reynold's assumption is invalid.

3. Vorticity and circulation are directly proportional to one another, i.e., $\oint_C u_T ds = \int \int_s (\nabla \times \vec{u}) \cdot \vec{n}\, dS$ using the theorem of Stokes (see, e.g., Kaplan 1952:275), where u_T is the tangential velocity along the perimeter of the surface S (i.e., the circulation). The variable $\vec{n}$ is a unit vector normal to S.

4. Referred to as the tilting term, it should more appropriately be referred to as simultaneous tilting and vortex line convergence. Convergence occurs when the cross-sectional area normal to the axis of the vortex tube changes (Pielke *et al.* 1995a).

5. The term "Exner function" is also often used for $\pi = (p/p_{00})^{R_d/C_p}$. Such a definition yields a nondimensional pressure variable. However, C_p is the specific heat of air and thus can be treated as nearly a constant. Consequently, it is reasonable to incorporate C_p into the definition of π.

Additional Readings

Cotton, W. R., and R. A. Anthes. 1989. *Storm and Cloud Dynamics*. Academic Press, San Diego.
  Cotton and Anthes provide an extensive discussion of types of averaging as applied to the conservation equations, as well as the use of scale analysis to derive consistent forms for these equations. Their text provides a useful complement to the material in Chapters 3 and 4 in this text.
Green, S. (Ed.) 1994. *Fluid Vortices*. Kluwer Academic Publishers, Amsterdam.
  Sheldon Green provides a thorough review of the use of vorticity to investigate fluid flow as well as many other aspects of the circulation of fluids.

Problems

Select an atmospheric model.

1. List the specific form of the following grid-volume conservation equations used. Assume flat terrain so that the equations appear in a simpler form. State each of the assumptions used to obtain the equations.
    (a) Mass
    (b) Heat
    (c) Motion
    (d) Water
    (e) Other gases and aerosols

2. List the following. Of the dependent variables used in the selected model, which are predicted from the conservation equations and which are parameterized? Does the number of conservation equations agree with the number of dependent variables which are predicted? To be a consistent model, they must be the same number!
    (a) Externally prescribed variables
    (b) The dependent variables
    (c) The prescribed constants

3. To select a model to investigate, refer to Appendix B for examples and references.

Chapter 5

Physical and Analytic Modeling

There are two fundamental methods of simulating mesoscale atmospheric flows: *physical models* and *mathematical models*. With the first technique, scale model replicas of observed ground surface characteristics (e.g., topographic relief, buildings) are constructed and inserted into a chamber such as a wind tunnel (water tanks are also used). The flow of air or other gases or liquids in this chamber is adjusted so as to best represent the larger-scale observed atmospheric conditions. Mathematical modeling, in contrast, utilizes such basic analysis techniques as algebra and calculus to solve directly all or a subset of Eqs. (2-43)–(2-50). As discussed later in this chapter, certain subsets of Eqs. (2-43)–(2-50) can be solved exactly, whereas other subsets, including the complete system of equations, requires the approximate solution technique called *numerical modeling*. Numerical modeling methods are described in Chapters 7–12.

Models are used for three purposes: diagnostic evaluations, process studies, and predictions. Diagnostic models, for example, use the conservation equations combined with whatever observations are available to interpolate data throughout a region. Process models utilize the conservation equations to improve physical understanding of atmospheric dynamics and thermodynamics. Predictive models are designed to provide forecasts. Predictive models that use the conservation equations need to improve on the forecast skill of statistical prediction models to demonstrate that they have forecast skill (Landsea and Knaff 2000). A series of papers on the topic of prediction as a link between science and decision making, have been published in Sarewitz *et al.* (2000).

Bankes (1993) separates models into consolidative and exploratory models. Consolidative models are intended to be a surrogate for an actual system. Exploratory models are used to explore the implications of various assumptions and hypotheses, but recognizing that there is incomplete knowledge to actually represent the real system. In the context of mesoscale models, if, for example,

the parameterizations of the physical system are not universally applicable, then the model is an exploratory model.

5.1 Physical Models

As shown in Chapter 3, the ratio of the individual terms in Eqs. (2-43)–(2-47) have representative orders of magnitudes that are dependent on the time and space scales of the phenomena being studied. In that chapter, nondimensional parameters such as the Rossby number and Reynolds number were introduced to examine the relative importance of the individual terms.

When constructing a physical-scale model of a real tropospheric circulation, it is desirable that these dimensionless parameters have the same order of magnitude in the model as in the actual atmosphere. Indeed, neglecting to observe proper scaling in such endeavors as the filming of scale models for motion pictures is easily evident to viewers, such as when explosions destroy replica buildings much too easily or a fire flickers too quickly.

Using the order of magnitude estimates for the dependent variables introduced in Chapter 3, and assuming that L and S are the representative length and velocity scale of the circulation of interest (i.e., no distinction is made here between U, V, and W or between L_x, L_y, and L_z), the scaled version of Eq. (4-39) can be written as

$$\left[\frac{S^2}{L}\right]\frac{\partial \hat{\bar{u}}_i}{\partial \hat{t}} = -\left[\frac{S^2}{L}\right]\hat{\bar{u}}_j \frac{\partial \hat{\bar{u}}_i}{\partial \hat{x}_j} - \left[\frac{e_{u_i}^2}{L}\right]\frac{\partial}{\partial \hat{x}_j}\widehat{\overline{u_j'' u_i''}} - \left[\frac{R\,\delta\theta}{L}\right]\hat{\theta}_0 \frac{\partial \hat{\pi}'}{\partial \hat{x}_i}$$

$$-\left[\frac{R\,\delta\theta}{L}\right]\hat{\theta}_0\left\{\frac{\partial \hat{\pi}_0}{\partial \hat{x}}\delta_{i1} + \frac{\partial \hat{\pi}_0}{\partial \hat{y}}\delta_{i2}\right\}$$

$$+\left[\frac{\delta\theta}{\theta_0}\right]g\,\hat{\theta}'\delta_{i3} - [\Omega S]2\epsilon_{ijk}\widehat{\Omega}_j\hat{\bar{u}}_k, \tag{5-1}$$

where a circumflex (ˆ) over a dependent variable or an independent variable indicates that it is nondimensional. The scaled parameter e_{u_i} is a measure of the subgrid-scale velocity correlations that can be estimated from the mean subgrid-scale kinetic energy given by

$$e_{u_i} = \left[\left(\overline{u_i''^2}/2\right)\right]^{1/2}.$$

Including the estimate for the molecular viscous dissipation given by Eq. (3-29), and multiplying Eq. (5-1) by L/S^2 (to obtain a nondimensional

equation for the local acceleration) results in

$$\frac{\partial \hat{\bar{u}}_i}{\partial \hat{t}} = -\hat{\bar{u}}_j \frac{\partial \hat{\bar{u}}}{\partial \hat{x}_j} - \left[\frac{e^2_{u_i}}{S^2}\right] \frac{\partial}{\partial \hat{x}_j} \widehat{\overline{u''_j u''_i}} - \left[\frac{R\,\delta\theta}{S^2}\right]\hat{\theta}_0 \frac{\partial \hat{\pi}}{\partial \hat{x}_i}$$

$$- \left[\frac{R\,\delta\theta}{S^2}\right]\hat{\theta}_0 \left\{\frac{\partial \hat{\pi}_0}{\partial \hat{x}}\,\delta_{i1} + \frac{\partial \hat{\pi}_0}{\partial \hat{y}}\,\delta_{i2}\right\}$$

$$+ \left[\frac{gL\delta\theta}{\theta_o S^2}\right]\hat{\theta}\delta_{i3} - \left[\frac{\Omega L}{S}\right]2\epsilon_{ijk}\widehat{\Omega}_j\hat{\bar{u}}_k - \left[\frac{v}{LS}\right]\frac{\partial^2 \hat{\bar{u}}_i}{\partial \hat{x}_j \partial \hat{x}_j}. \qquad (5\text{-}2)$$

To use a scaled physical model to accurately represent the conservation-of-motion relation in the atmosphere, one of the following conditions must hold:

1. the individual bracketed terms be equal in the model and in the atmosphere,
2. the bracketed terms that are not equal must be much less in magnitude than the other bracketed terms in Eq. (5-2).

When these conditions are met, the actual and modeled atmospheres are said to have *dynamical similarity*.

Two of these bracketed terms are of the same form as defined in Chapter 3, Section 3.3.2, and are given as

$$\Omega L / S = 1/R_0$$

and

$$v/LS = 1/\text{Re},$$

where R_0 is the Rossby number and Re is the Reynolds number, and

$$gL(\delta\theta/\theta_0)/S^2 = \text{Ri}_{\text{bulk}}$$

is called the *bulk Richardson number*. (Here $\delta\theta$ represents the potential temperature perturbation and is the same order as δT used in Section 3.3.)

From Eq. (5-2), to maintain dynamic similarity, it is implied that to represent all of the terms in the equation properly, the following criteria must be met:

1. The ratio of the subgrid-scale kinetic energy to the grid-volume average kinetic energy must be kept constant.
2. Reducing the length scale L in the physical model requires:
    (a) an increase in the magnitude of the horizontal temperature perturbation $\delta\theta$ or a reduction in the simulated wind flow speed S, or both
    (b) an increase in the rotation rate Ω or a reduction in S, or both
    (c) a decrease in the viscosity v or an increase in S, or both.

   3.   An increase in $\delta\theta$ in the pressure gradient term necessitates that S also
increase.

   Unfortunately, it is impossible to satisfy all of these requirements simultane-
ously in existing physical models of mesoscale atmospheric circulations. Such
physical models are constructed inside of buildings, which limits the dimensions
of the simulated circulations to the size of meters, whereas actual mesoscale
circulations extend over kilometers.
   To illustrate the difficulty of obtaining dynamic similarity in a mesoscale
physical model for all terms in Eq. (5-2), let the horizontal scale of a moun-
tain ridge be 10 km, whereas the physical model of this geographic feature
utilizes a 1-m representation. The scale reduction is, therefore, 10^4. Thus if $S =$
10 m s^{-1} in the real situation and air is used in the scaled model atmosphere,
then the simulated wind speed would have to be 10^5 m s^{-1} to maintain identical
Reynolds number similarity! In addition, to have the same Rossby number for
this example, the physical model must rotate 10,000 times more rapidly than
the earth, or the wind speed must be reduced by 10,000. Of course, reducing the
speed is contradictory to what is required to obtain Reynolds number similarity!
Only if the results are relatively insensitive to changes in these nondimensional
quantities—as suggested by, for example, Cermak (1975) for large values of the
Reynolds number in simulations of the atmospheric boundary layer—can one
ignore large differences in the nondimensional parameters.
   From the example just given, however, it should be clear that it is impossible
to obtain *exact* dynamic similarity between mesoscale atmospheric features and
the physical model when all of the terms in Eq. (5-2) are included. Nonethe-
less, investigators who use physical models have proposed a type of similarity
between actual mesoscale atmospheric circulations in which $e_{u_i}^2/S^2 \gg v/LS$
and physical model representations in which $e_{u_i}^2/S^2 \ll v/LS$. With this type of
simulation, it is assumed that the mixing by molecular motions, as expressed by
Eq. (3-29), acts in the same manner as the mixing by air motions as given by
the turbulence flux divergence term $(\partial/\partial\hat{x}_j)\widehat{u''_j u''_i}$. In its dimensional form, this
latter term can be approximated by

$$\frac{\partial}{\partial x_j}\overline{u''_j u''_i} \simeq \frac{\partial}{\partial x_j}\left(-K\frac{\partial\bar{u}_i}{\partial x_j}\right) \qquad (5\text{-}3)$$

(an approximation discussed in detail in Chapter 7), where K is called the
turbulent exchange coefficient and is analogous to the kinematic viscosity v.
If a *turbulent Reynolds number*, Re_{turb}, is defined as the ratio of the advective
terms to the subgrid-scale correlation terms, then, by scale analysis,

$$\text{Re}_{\text{turb}} = L_{\text{meso}}\, S_{\text{meso}}/K,$$

where the subscript "meso" refers to the mesoscale. Similarity of flow between the real atmosphere and the physical model are then assumed to occur when

$$\mathrm{Re}_{\mathrm{turb}} = L_{\mathrm{meso}}\, S_{\mathrm{meso}}/K = \mathrm{Re} = L_{\mathrm{model}}\, S_{\mathrm{model}}/\upsilon,$$

where the subscript "model" refers to the scaled physical representation.

If both the actual and simulated wind speeds are equal, $S_{\mathrm{meso}} = S_{\mathrm{model}}$, then if $L_{\mathrm{meso}} = 10^4 L_{\mathrm{model}}$, for example, $K = 10^4 \upsilon$ is used to justify similarity between the mesoscale and the physical model, *when subgrid-scale mixing is the dominant forcing term* in Eq. (5-2). If air is used in the physical model, then $\upsilon = 1.5 \times 10^{-5}$ m^2 s^{-1}, so that K must be equal to 1.5×10^{-1} m^2 s^{-1}—a condition that may be fulfilled near the ground when the air is very stably stratified.

Using this analysis, physical modelers assume that turbulent mesoscale atmospheric circulations are accurately simulated by laminar laboratory models, provided that the appropriate ratio between the eddy exchange coefficient and kinematic viscosity is obtained.

Using the same assumptions applied to produce Eq. (5-1), the conservation-of-heat relation, represented by the potential temperature equation (4-24), can be written as

$$\left[\frac{\delta\theta\,S}{L}\right]\frac{\partial\hat{\bar{\theta}}}{\partial\hat{t}} = -\left[\frac{\delta\theta\,S}{L}\right]\hat{\bar{u}}_j\,\frac{\partial\hat{\bar{\theta}}}{\partial\hat{x}_j} - \left[\frac{e_\theta e_{u_i}}{L}\right]\frac{\partial}{\partial\hat{x}_j}\widehat{\overline{u_j''\theta''}} + \left[\frac{\delta\theta\,S}{L}\right]\hat{\bar{S}}_\theta, \qquad (5\text{-}4)$$

where $e_\theta e_{u_i}$ is a measure of the subgrid-scale correlation between the fluctuating velocities and temperatures, with e_θ perhaps represented by

$$e_\theta = [(\overline{\theta''^2}/2)]^{1/2}.$$

If the molecular conduction of potential temperature C_θ is included in Eq. (5-4) and represented in analogy with the viscous dissipation term as

$$C_\theta = \frac{k_\theta}{\rho C_{\mathrm{p}}}\,\frac{\partial^2\bar{\theta}}{\partial x_j \partial x_j}; \qquad |C_\theta| \sim \frac{k_\theta}{\rho_0 C_{\mathrm{p}}}\,\frac{\delta\theta}{L^2},$$

where k_θ is the potential temperature molecular conduction coefficient, then multiplying Eq. (5-4) by $L/\delta\theta\,S$ and including the order-of-magnitude estimate of C_θ yields

$$\frac{\partial\hat{\bar{\theta}}}{\partial\hat{t}} = -\hat{\bar{u}}_j\,\frac{\partial\hat{\bar{\theta}}}{\partial\hat{x}_j} - \left[\frac{e_\theta e_{u_j}}{\delta\theta\,S}\right]\frac{\partial}{\partial\hat{x}_j}\widehat{\overline{u_j''\theta''}} + \left[\frac{k_\theta}{\rho_0 C_{\mathrm{p}}\upsilon}\right]\left[\frac{\upsilon}{LS}\right]\frac{\partial^2\hat{\bar{\theta}}}{\partial\hat{x}_j^2} + \hat{\bar{S}}_\theta. \qquad (5\text{-}5)$$

The ratio

$$k_\theta/\rho_0\,C_{\mathrm{p}}\,\upsilon = \mathrm{Pr}^{-1}$$

where Pr represents the *Prandtl number* and is of order unity for air.

Thus, to obtain *thermal similarity* between the mesoscale circulation and its laboratory representation, the Reynolds number must also be very large and the partitioning of heat transport between the subgrid-scale and resolvable fluxes must be the same. If in Eq. (5-2), for example, the temperature perturbation $\delta\theta$ must be increased in the bulk Richardson number, $\mathrm{Ri}_{\mathrm{bulk}}$, to compensate for a decrease of L in the laboratory model, then in Eq. (5-5) the turbulent fluctuations in the simulated atmosphere also must be increased.

The nondimensional source-sink term for potential temperature $\widehat{S}_\theta$ is included in the analysis. However, the mathematical procedure of representing it as a single variable masks its physical complexity. As discussed in Chapters 8 and 9, this term includes such effects as radiative flux divergence, phase changes of water, etc. and is an involved function of the dependent variables. Thus it is extremely difficult to evaluate this term using scale analysis, and in practice physical modelers exclude it in their representation of mesoscale atmospheric flows. An equivalent similarity analysis can be performed for water substance and other aerosol and gaseous contaminants. Because of the inability to accurately represent the sources and sinks of these variables (i.e., $\widehat{\bar{S}}_{q_n}$ and $\widehat{\bar{S}}_{\chi_m}$), however, physical modelers have studied the movement of nonreactive, conservative pollutants only around terrain and building obstacles.

When utilizing physical models, the conservation-of-mass relation given by Eq. (2-43) must also be satisfied, and as long as the ratio of the variations of specific volume to the average specific volume in the physical model is much less than unity, Eqs. (3-11) and (3-14) are satisfactory approximations. The scaled version of the incompressible conservation-of-mass equation (3-14) shows that

$$W \sim L_z U / L_x \qquad \text{and} \qquad W \sim L_z V / L_y,$$

so that if the ratio of the vertical scale to the horizontal scale of the circulation is kept constant between the physical model and the atmosphere, then *kinematic similarity* is obtained. This requirement could be satisfied provided that the horizontal to vertical representation of the terrain and other physical features of the ground surface in the physical model are not exaggerated. This latter condition is called *geometric similarity*.

The final similarity conditions needed in physical models include the requirement that air flowing into the simulated mesoscale region have velocity and temperature profiles scaled according to the nondimensional relations given by Eqs. (5-2) and (5-5) and that the flow be close to equilibrium; i.e., $\partial \widehat{\bar{u}}_i / \partial \widehat{t}$ and $\partial \widehat{\bar{\theta}} / \partial \widehat{t}$ are small relative to the remaining terms in Eqs. (5-2) and (5-5). In addition, such bottom conditions as surface temperature and aerodynamic roughness must be scaled so as to produce kinematic, dynamic, and thermal similarity in the lowest levels of the physical model. These requirements are referred to as *boundary similarity*, and their creation necessitates a comparatively long fetch

from the input region of the laboratory apparatus to the region of simulation, as well as obstacles such as a lattice placed upwind in the flow to generate specific velocity profiles and turbulence characteristics.

With all of these requirements, physical modeling of the mesoscale has been primarily limited to stably stratified flows over irregular terrain. Even for this case, however, such observed features of the real atmosphere as the veering of the winds with height, radiational cooling, and condensation cannot be reproduced.

The main advantage of physical models of the mesoscale, therefore, has been to provide qualitative estimates of airflow over terrain obstacles during dense, overcast, or nighttime situations. Figure 5-1, reproduced from Cermak (1971), illustrates such a simulation for a scale model of Port Arguello, California, where helium is released as a tracer to represent pollution dispersal. The influence of the model topography on the flow was very marked and corresponded well with the observed trajectories and concentrations. A number of other physical model simulations of relevance to the mesoscale have been performed, including those of Cermak (1970), Chaudhry and Cermak (1971), Yamada and Meroney (1971), SethuRaman and Cermak (1973), Hunt *et al.* (1978), Meroney *et al.* (1978), Baines (1979), Baines and Davis (1980), Lee *et al.* (1981), Mitsumoto *et al.* (1983), Noto (1996), Poreh (1996), and Chen *et al.* (1999a). Egan (1975) also discusses physical modeling over complex terrain. Avissar *et al.* (1990) provide a review of the ability of meteorological wind tunnels
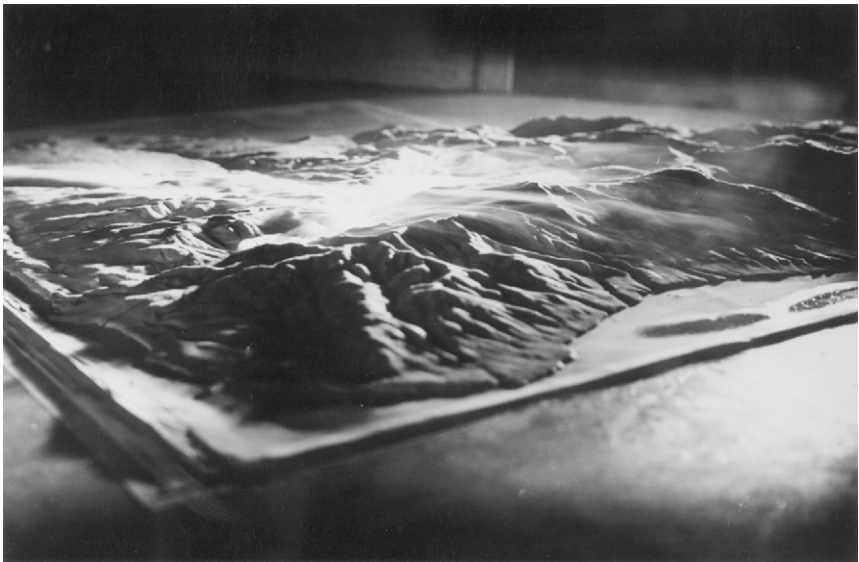

Fig. 5-1. Visualization of advective dispersion over Port Arguello, California in a stably stratified laminar flow in a wind tunnel. (From Cermak 1971.)

to simulate sea and land breezes. Cermak (1996) provides a recent review of physical modeling.

Because physical models are severely limited in their applicability to the mesoscale, however, it is necessary to utilize the techniques of mathematical modeling. The remainder of the text is devoted to this methodology.

5.2   Linear Models

As discussed previously, the system of equations given by Eqs. (2-43)–(2-50), represents a *simultaneous set of nonlinear partial differential equations*. The set is termed "simultaneous" because each conservation relation must be satisfied at any given time, and they involve *partial derivatives* because four independent variables, x, y, z, and t, are involved. The *nonlinear* character of the equations occurs because products of the dependent variables (e.g., $\bar{u}\,\partial\bar{u}/\partial x$, $\bar{w}\,\partial\bar{\theta}/\partial z$) are included in the relationships.

Mathematical techniques have evolved over the last several hundred years that permit exact solutions of a range of algebraic and differential equations. However, except for a few highly simplified and idealized situations, no method exists to solve exactly general sets of nonlinear equations. To solve these non-linear equations, the differential operators must be *approximated* for use in a *numerical model*, as discussed in Chapter 10, so that the results obtained are *not exact*.

To obtain exact[1] solutions to the conservation relationships, it is necessary to remove the nonlinearities in the equations. Results from such simplified, linear equations are useful for the following reasons:

1.   The exact solutions of simplified linear differential equations gives some idea as to the physical mechanisms involved in specific atmospheric circulations. Because precise solutions are obtained, an investigator can be certain that the results are not caused by computational errors, as can be true with numerical models.

2.   Results from these linear equations can be contrasted with those obtained from a numerical model in which the magnitude of the nonlinear terms are determined to be small relative to the linear terms. An accurate nonlinear numerical model must be able to reproduce the linear results closely when the products of the dependent variables are small.

Linear representations of the conservation relations have been used to investigate wave motions in the atmosphere, as well as to represent actual mesoscale circulations. Kurihara (1976), for example, applied a linear analysis to investigate spiral bands in a tropical storm. Klemp and Lilly (1975) used such an

approach to study wave dynamics in downslope wind storms to the lee of large mountain barriers. Other linear models of airflow over mountain barriers include the model of Wang and Lin (1999).

Simultaneous sets of linear partial differential equations relevant to atmospheric circulations are derived from Eqs. (2-43)–(2-50), or from their approximate forms. For example, with shallow adiabatic atmospheric circulations, Eqs. (4-21), (4-23), and (4-24) can be written in linear form as

$$\frac{\partial \bar{u}_i}{\partial t} = -u_{j_0} \frac{\partial \bar{u}_i}{\partial x_j} + K \frac{\partial^2 \bar{u}_i}{\partial x_j^2} - \alpha_0 \frac{\partial p'}{\partial x_i} - \alpha_0 \left[\frac{\partial p_0}{\partial x} \delta_{i1} + \frac{\partial p_0}{\partial y} \delta_{i2} \right]$$

$$+ \frac{\theta'}{\theta_0} g\delta_{i3} - 2\epsilon_{ijk}\Omega_j \bar{u}_k, \tag{5-6}$$

$$\frac{\partial \bar{u}_j}{\partial x_j} = 0 \tag{5-7}$$

and

$$\frac{\partial \bar{\theta}}{\partial t} = -u_{j_0} \frac{\partial \bar{\theta}}{\partial x_j} + K \frac{\partial^2 \bar{\theta}}{\partial x_j^2}, \tag{5-8}$$

where the subgrid-scale correlation terms have been replaced by

$$\frac{1}{\rho_0} \frac{\partial}{\partial x_j} \rho_0 \overline{u_j'' u_i''} \simeq -K \frac{\partial^2 \bar{u}_i}{\partial x_j^2} \tag{5-9}$$

and

$$\frac{1}{\rho_0} \frac{\partial}{\partial x_j} \rho_0 \overline{u_j'' \theta''} \simeq -K \frac{\partial^2 \bar{\theta}}{\partial x_j^2}, \tag{5-10}$$

with K equal to either a constant or a function of the independent variables. Besides these subgrid-scale terms, only the advective terms $\overline{u}_j \partial \bar{u}_i \partial x_j$ and $\bar{u}_j \partial \bar{\theta}/\partial x_j$ are directly affected by the linearization for this particular atmospheric system. Since $|\alpha'|/\alpha_0 \ll 1$, the pressure gradient force and the conservation-of-mass relation were already assumed to be linear in Chapter 4, and the term involving the rotation of the earth, $2\epsilon_{ijk}\Omega_j \bar{u}_k$, was a linear contribution in the original derivation of the conservation-of-motion equation given in Chapter 2.

The linearizing assumptions made to obtain Eqs. (5-6) and (5-8) from Eqs. (4-21) and (4-24) are major oversimplifications of the atmosphere and are made only so that exact solutions can be obtained. Observations, nonlinear numerical model results (see, e.g., Chapter 13), and even linear solutions (as is shown in this chapter) demonstrate that the mesoscale velocity perturbations u_j' are not in general much less than the synoptic components u_{j_0}. In addition, as discussed in Chapter 7, subgrid-scale mixing is not represented accurately

for most situations using such a simple form of the exchange coefficient as assumed in Eqs. (5-9) and (5-10).

In the remainder of this chapter, examples of simplified linear models are discussed.

5.2.1 Tank Model

5.2.1.1 *Single Homogeneous Fluid*

Among the simplest of these models is a model that represents a homogeneous fluid ($\bar{\rho} = \rho_0 =$ a constant) situated in a two-dimensional rectangular tank. This model is frequently used to test numerical computational schemes, since the physical response of this system is straightforward and easily understood.

Figure 5-2 illustrates this tank, where P_h is the pressure at the free surface h, ρ_0 is the density of the fluid, and P_B is the pressure at the bottom. A set of equations to describe the flow in this tank can be obtained from Eqs. (4-10), (4-32), and (4-23) and written in component form to yield

$$\frac{\partial u'}{\partial t} = -\frac{\partial}{\partial x} u'^2 - \frac{\partial}{\partial z} w'u' - \frac{1}{\rho_0} \frac{\partial \bar{p}}{\partial x}, \tag{5-11}$$

$$\frac{\partial \bar{p}}{\partial z} = -\rho_0 g, \tag{5-12}$$

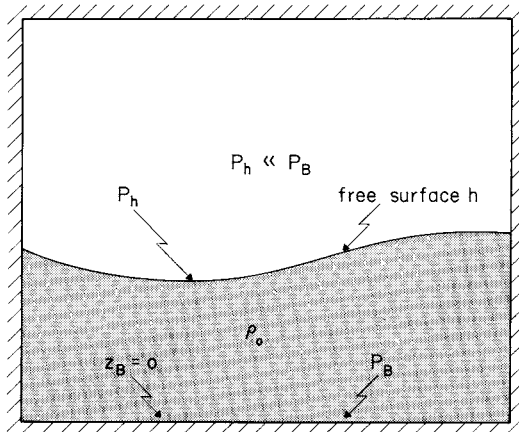$$\frac{\partial u'}{\partial x} + \frac{\partial w'}{\partial z} = 0, \tag{5-13}$$

Fig. 5-2. A two-dimensional tank containing one fluid with constant density ρ_0. The pressure at the free surface h is P_h. On the flat bottom, pressure is indicated by P_B.

where the hydrostatic relation has been presumed valid, the thermodynamic equation is not required since α' is identically 0, the subgrid-scale mixing and the rotation of the earth are ignored, and the large-scale velocities (u_0, w_0) and their gradients are set identically to 0. Further, the flow is assumed to be two-dimensional. Since the fluid is homogeneous, Eq. (5-13) is the exact form of the conservation of mass relation. In this system of equations, only the advective terms in Eq. (5-11) are nonlinear.

Using the homogeneous nature of the fluid in the tank, Eqs. (5-11)–(5-13) can be further simplified. The vertical derivative of the horizontal pressure gradient force can be given as

$$\frac{\partial}{\partial z} \frac{1}{\rho_0} \frac{\partial \bar{p}}{\partial x} = \frac{1}{\rho_0} \frac{\partial}{\partial x} \frac{\partial \bar{p}}{\partial z} = \frac{1}{\rho_0} \frac{\partial}{\partial x}(-\rho_0 g) = 0,$$

since ρ_0 and g are constants. Thus the horizontal pressure gradient does not change with height.

Integrating Eq. (5-12) between the bottom $z = 0$ and the surface of the fluid h yields

$$\int_0^h \frac{\partial \bar{p}}{\partial z} \, dz = P_h - P_B = -\rho_0 gh, \tag{5-14}$$

and if $P_h \ll P_B$ (if a vacuum exists above h, then P_h is identically equal to 0), then

$$P_B = \rho_0 gh. \tag{5-15}$$

Differentiating Eq. (5-15) with respect to x and rearranging results in

$$\frac{1}{\rho_0} \frac{\partial P_B}{\partial x} = g \frac{\partial h}{\partial x}, \tag{5-16}$$

which, since the horizontal pressure gradient is invariant with height [i.e., $(1\rho_0)(\partial P_B/\partial x) = 1(1/\rho_0)(\partial \bar{p}/\partial x)$], permits the horizontal pressure gradient in Eq. (5-11) to be replaced by the right side of Eq. (5-16).

Next, differentiating Eq. (5-11) with respect to height and rearranging yields

$$\frac{\partial}{\partial t}\left(\frac{\partial u'}{\partial z}\right) + u'\frac{\partial}{\partial x}\left(\frac{\partial u'}{\partial z}\right) + w'\frac{\partial}{\partial z}\left(\frac{\partial u'}{\partial z}\right) = 0.$$

where $(\partial u'/\partial x + \partial w'/\partial z) = 0$ was applied. Thus if $\partial u'/\partial z = 0$ initially, then it can never be generated, since the terms in this expression require existing velocity shear to be nonzero. With this result, Eq. (5-11) can now be written as

$$\frac{\partial u'}{\partial t} = -u'\frac{\partial u'}{\partial x} - g\frac{\partial h}{\partial x}. \tag{5-17}$$

Equation (5-13) can also be given in a different form by integrating between $z = 0$ and $z = h$, so that

$$\int_0^h \frac{\partial w'}{\partial z}\, dz = w'_h - w'_0 = w'_h = -\int_0^h \frac{\partial u'}{\partial x}\, dz, \qquad (5\text{-}18)$$

where $w_0 = 0$ since the bottom is flat. Since

$$\frac{\partial}{\partial z}\frac{\partial u'}{\partial x} = \frac{\partial}{\partial x}\frac{\partial u'}{\partial z} = 0,$$

because $\partial u'/\partial z$ is identically equal to 0, then the horizontal gradient of u' is not a function of height and Eq. (5-18) can be written as

$$w'_h = -\frac{\partial u'}{\partial x}\, h. \qquad (5\text{-}19)$$

If h is defined to be a *material surface*, which moves up and down with the vertical velocity, then

$$w'_h = \frac{dh}{dt} = \frac{\partial h}{\partial t} + u'\frac{\partial h}{\partial x},$$

using the chain rule of calculus, where it is assumed that $h = h(t, x(t))$ and $u_0 = 0$.

Thus Eq. (5-19) can be written as

$$\frac{\partial h}{\partial t} = -u'\frac{\partial h}{\partial x} - h\frac{\partial u'}{\partial x}. \qquad (5\text{-}20)$$

Along with Eq. (5-17), these two relations are in the form most commonly applied to the single-fluid tank model. Even though this situation of a homogeneous fluid in a tank is conceptually simple, Eqs. (5-17) and (5-20) are, of course, still nonlinear, and no general analytic solution is obtainable.

One way to linearize this system of equations is to set $h = h_0 + h'$, where h_0 is a constant defined to be equal to the average depth of the fluid, so that Eq. (5-20) is written as

$$\frac{\partial h}{\partial t} = -u'\frac{\partial h'}{\partial x} - h_0\frac{\partial u'}{\partial x} - h'\frac{\partial u'}{\partial x}. \qquad (5\text{-}21)$$

Then, by neglecting products of the dependent variables in Eqs. (5-17) and (5-21), a set of two simultaneous linear partial differential equations is given by

$$\frac{\partial u'}{\partial t} = -g\frac{\partial h'}{\partial x} \qquad (5\text{-}22)$$

$$\frac{\partial h'}{\partial t} = -h_0\frac{\partial u'}{\partial x}. \qquad (5\text{-}23)$$

This system of equations is rigorously fulfilled when $h' \ll h_0$, so that, for example, in a tank 1 m deep, a perturbation height of 1 cm (a 1% deviation) might be said to satisfy this inequality.

The method of solving Eqs. (5-22) and (5-23) involves representing h' and u' as functions of wavenumber k and frequency ω (i.e., a Fourier transform). This relationship can be expressed mathematically as

$$u'(x, t) = \int_{-\infty}^{\infty} \int_{-\infty}^{\infty} \tilde{u}(k, \omega) e^{i(\omega t + kx)} \, dk \, d\omega \qquad (5\text{-}24)$$

$$h'(x, t) = \int_{-\infty}^{\infty} \int_{-\infty}^{\infty} \tilde{h}(k, \omega) e^{i(\omega t + kx)} \, dk \, d\omega, \qquad (5\text{-}25)$$

where $\tilde{u}(k, \omega)$, $\tilde{h}(k, \omega)$, and $e^{i(\omega t + kx)}$ are complex variables. The advantage of performing this transformation is that the *linear partial differential* equations given by Eqs. (5-22) and (5-23) are replaced by two *algebraic* equations. The exponential term can also be written as

$$e^{i(\omega t + kx)} = \cos(\omega t + kx) + i \sin(\omega t + kx),$$

which corresponds to a unit vector of components $\cos(\omega t + kx)$ on the real axis and $\sin(\omega t + kx)$ on the imaginary axis. The frequency ω and wavenumber k can also be expressed as a complex number. As an example, if

$$\omega = \omega_r + i\omega_i,$$

then

$$e^{i\omega t} = e^{i(\omega_r + i\omega_i)t} = e^{-\omega_i t} e^{i\omega_r t} = e^{-\omega_i t} \left(\cos \omega_r t + i \sin \omega_r t \right), \qquad (5\text{-}26)$$

so that $e^{-\omega_i t}$ can indicate whether $u'(x, t)$ and $h'(x, t)$ damps ($\omega_i > 0$) or amplifies ($\omega_i < 0$) with time, and the term $\cos \omega_r t + i \sin \omega_r t$ is used to determine changes in $u'(x, t)$ and $h(x, t)$ owing to propagation. A similar decomposition can be applied to the wavenumber k, where $e^{-k_i x}$ denotes the damping or amplification of the dependent variables in the x direction as a function of wavelength and $\cos k_r x + i \sin k_r x$ refers to the periodic portion of the spatial distribution of the dependent variables.

When the complex form is used to solve a system of differential equations, only the real part of the solution gives information on the magnitude of the dependent variables. Complex variables are valuable tools in the solutions of equations expected to have periodic solutions.

One crucial advantage of linearizing a system of differential equations is that any single term inside of the integral of Eqs. (5-24) and (5-25) is separately a solution to Eqs. (5-22) and (5-23). In a nonlinear system, products of integrals arise (e.g., from the multiplication of the Fourier representation of u' by that for $\partial h'/\partial x$), reflecting the interactions between different scales of motion. No such interaction is possible with a linear system, however.

Since Eqs. (5-22) and (5-23) are linear equations,

$$u'(x, t) = \tilde{u}(k, \omega) e^{i(\omega t + kx)} \qquad (5\text{-}27)$$

and

$$h'(x, t) = \tilde{h}(k, \omega)e^{i(\omega t + kx)} \tag{5-28}$$

can be used to represent the two dependent variables in those equations. The complete solution can be obtained by adding together the solutions for all possible wavenumbers in a particular problem. Since no sources or sinks of velocity are permitted in Eqs. (5-22) and (5-23), we also assume that $\tilde{u}$, $\tilde{h}$, ω, and k are all real, so that no terms of the form given by $e^{-w_i t}$, for example, are produced. We also assume that the fluid extends indefinitely in the horizontal direction (i.e., there are no lateral walls). Substituting Eqs. (5-27) and (5-28) into the two differential equations (5-22) and (5-23) yields the two algebraic equations

$$\omega\tilde{u}e^{i(kx+\omega t)} + gk\tilde{h}e^{i(kx+\omega t)} = 0$$

$$\omega\tilde{h}e^{i(kx+\omega t)} + h_0 k\tilde{u}e^{i(kx+\omega t)} = 0.$$

Since $e^{i(k, x\omega t)}$ cannot equal 0, these equations can be reduced to

$$\omega\tilde{u} + gk\tilde{h} = 0,$$

$$h_0 k\tilde{u} + \omega\tilde{h} = 0, \tag{5-29}$$

which is given in matrix form as

$$\begin{bmatrix} w & gk \\ h_0 k & \omega \end{bmatrix} \begin{bmatrix} \tilde{u} \\ \tilde{h} \end{bmatrix} = \begin{bmatrix} 0 \\ 0 \end{bmatrix}. \tag{5-30}$$

The solution to this set of algebraic equations can be determined either by performing algebraic rearrangement of Eq. (5-29) or by applying concepts of linear algebra to Eq. (5-30). In the first case, solving the top equation for $\tilde{u}$ and substituting it into the bottom relation yields

$$\tilde{h}\left[-\frac{h_0 k^2 g}{\omega} + \omega\right] = 0.$$

Since $\tilde{h}$ does not equal 0 in general, the bracketed quantity must equal 0 so that the equation

$$\omega/k = \pm\sqrt{gh_0}$$

expresses the relationship between ω and k in Eqs. (5-22) and (5-23).

The determination of the solution using the matrix form is not as straightforward but is introduced here because it plays an important role in the evaluation of the computational stability of numerical solution techniques (Chapter 10) and in the solution of Eq. (5-44). Matrix equation (5-30) represents a system of two *linear homogeneous algebraic* equations in two unknowns. It is linear because the coefficients of the 2×2 matrix on the left side of Eq. (5-30) are not functions of $\tilde{u}$ and $\tilde{h}$, and it is homogeneous since there is no nonzero function in

the equation that is not a function of $\tilde{u}$ and $\tilde{h}$. [This is the reason that the right side of Eq. (5-30) is 0.]

As shown by, for example, Murdoch (1957), a system of homogeneous algebraic equations has a *nontrivial solution* (a solution other than when the dependent variables are identically equal to 0) only if the determinant of the coefficients is 0. Therefore,[2]

$$\begin{vmatrix} \omega & gk \\ h_0 k & \omega \end{vmatrix} = 0 = \omega^2 - gh_o k^2$$

or

$$\omega/k = \mp\sqrt{gh_0}. \tag{5-31}$$

Finally, since $\omega = 2\pi/P$ and $k = 2\pi/L$, where P is the period and L is a wavelength, setting the exponents of Eqs. (5-27) and (5-28) equal to 0 (i.e., $\omega t + kx = 0$ and $\omega/k = -x/t$), yields $\omega/k = -c$, where c is the phase velocity. Therefore,

$$c = \pm\sqrt{gh_o}, \tag{5-32}$$

and the movement in the tank model corresponds to two waves that can propagate in two opposite directions with a speed given by Eq. (5-32). This wave is called an *external gravity wave*, since it is found only at the top of the fluid and requires gravitational acceleration to occur. For $g = 9.8$ m s^{-2} and $h_0 = 10$ km, for example, $c \simeq \pm 313$ m s^{-1}.

5.2.1.2 Two-Layered Fluids

A somewhat more complicated tank model can be derived if it is assumed that P_h is not much less than P_B in Eq. (5-14).[3] Such a situation is depicted in Figure 5-3, where a fluid of one uniform density ρ_1 overlies a second homogeneous fluid with a greater density ρ_0. The pressure at the rigid top of the second fluid is assumed to be much less than the pressure at the interface P_h. In the lower fluid, pressure is determined by Eq. (5-12), whereas in the upper fluid, the hydrostatic relation

$$\partial\bar{p}/\partial z = -\rho_1 g$$

is presumed to be valid.

Integrating Eq. (5-12) between the bottom and the initial interface height h_0 yields

$$\int_0^{h_0} \frac{\partial\bar{p}}{\partial z} dz = P_{h_0} - P_B = -\rho_0 g h_0. \tag{5-33}$$

The pressure variation at h_0 is given by
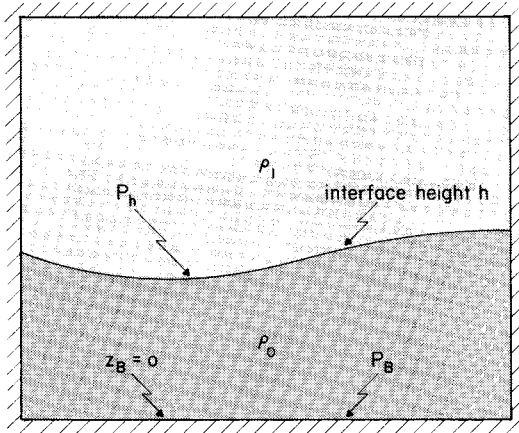
$$\delta P_{h_0} = \rho_0 g\delta h - \rho_1 g\delta h,$$

Fig. 5-3. A two-dimensional tank containing two fluids with densities ρ_0 and ρ_1 ($\rho_0 > \rho_1$). The pressure at the interface h is P_h. On the flat bottom, pressure is indicated by P_B. The depth of the upper fluid is assumed to be much greater than the displacement height, δh, of the interface.

since when $\delta h > 0$, fluid with density ρ_0 moves above h_0, displacing fluid of density ρ_1, whereas when $\delta h < 0$ the reverse is true. Therefore,

$$\frac{\delta P_{h_0}}{\delta x} = (\rho_0 - \rho_1)g\frac{\delta h}{\delta x}$$

or

$$\lim_{\delta x \to 0} \frac{\delta P_{h_0}}{\delta x} = \frac{\partial P_{h0}}{\partial x} = \frac{\partial \bar{p}}{\partial x} = (\rho_0 - \rho_1)g\frac{\partial h}{\partial x}, \tag{5-34}$$

where the invariance of the pressure gradient with height has been applied in both fluids. Thus the horizontal pressure gradient for this case can be written as

$$-\frac{1}{\rho_0}\frac{\partial \bar{p}}{\partial x} = -\frac{(\rho_0 - \rho_1)}{\rho_0}g\frac{\partial h}{\partial x},$$

so that the equation equivalent to Eq. (5-17) for two fluids becomes

$$\frac{\partial u'}{\partial t} = -u'\frac{\partial u'}{\partial x} - \frac{(\rho_0 - \rho_1)}{\rho_0}g\frac{\partial h}{\partial x}. \tag{5-35}$$

Equation (5-20) has the same form for this situation, except that h now refers to the interface between the two fluids.

   The linear forms of Eqs. (5-35) and (5-20) are written as

$$\frac{\partial u'}{\partial t} = -\frac{\rho_0 - \rho_1}{\rho_0}g\frac{\partial h}{\partial x}$$

$$\frac{\partial h}{\partial t} = -h_0\frac{\partial u'}{\partial x}.$$

Applying the same solution technique to this model and assuming that the fluid extends indefinitely in the horizontal direction (as in the single fluid tank) results in the phase velocity equation

$$c = \pm\sqrt{\Delta\rho g h_0/\rho_0}, \tag{5-36}$$

where $\Delta\rho = \rho_0 - \rho_1$.

Waves that form on such discontinuous interfaces between fluids are one type of *internal gravity wave*. In Section 5.2.2, it is shown that internal waves can occur even without a density discontinuity. Equation (5-36) reduces to the external gravity wave when the overlying layer has a much smaller density than the bottom fluid (i.e., $\rho_0 \gg \rho_1$), such as is the case for air ($\rho_1 \sim 1.25$ kg m^{-3}) and water ($\rho_0 \sim 1000$ kg m^{-3}). From Eq. (5-36), it is evident that internal gravity waves of this type always travel more slowly than external waves. For $g = 9.8$ m s^{-2}, $h_0 = 1$ km, and $\Delta\rho/\rho_0 = 0.1$, for example, $c \simeq 31$ m s^{-1}. This speed of motion is close to that observed on frontal interfaces in the atmosphere when cold, dense air is being overrun by warmer, less dense air aloft (e.g., Gedzelman and Donn 1979).

These tank models are, of course, gross oversimplifications to any type of mesoscale circulation. But even in terms of real tanks with one or two fluids, these models have serious shortcomings, including the following:

1. Although propagation speeds of waves are specified once motion is initiated, there are no mechanisms in these models to generate waves.

2. As is well known, waves generated in tanks can attain a sufficient size such that breaking and overturning occurs. These models are unable to represent such an event.

3. The influence of bottom and lateral friction and of side walls have been excluded. Thus waves in these models will persist indefinitely in space and time.

Although some of these shortcomings can be minimized by adding linear terms to the original tank model equations (5-11)–(5-13), the basic problem with such models is the neglect of nonlinear effects. For example, breaking of waves can occur when h' is a significant fraction of h_0, so that $h' \ll h_0$ is no longer fulfilled. Nevertheless, because exact analytic solutions can be obtained, these simple models are often used to evaluate computational schemes as well as to demonstrate procedures used in numerical models. The tank model is used in this context in Section 10.1.4.

5.2.2   Generalized Linear Equations

The tank models discussed in the previous section represent a situation in which the conservation laws are greatly reduced in form, thereby permitting a

straightforward, comparatively simple solution to the possible forms of motion. Unfortunately, by simplifying, only one wave solution was obtained.

To obtain a more complete representation of the types of wave motion in the mesoscale atmosphere, it is desirable to retain as many terms as possible in the conservation relations, yet still linearize the equations so that exact solutions are possible. These solutions not only will aid in the evaluation of the more complete nonlinear numerical models, but also should provide insight into the physical mechanisms involved in atmospheric circulations.

In the following derivation, the main goal is to obtain the characteristic phase velocity of different classes of atmospheric wave motion. This information is essential for successfully applying computational techniques to numerical mesoscale models. To illustrate how the more general equations can be linearized, Eqs. (4-19), (4-21), (4-22), and 4.24 can be reduced to the linear form as follows:

$$\rho_0 \frac{\partial u'}{\partial t} = -\frac{\partial p'}{\partial x} + \rho_0 f v', \tag{5-37}$$

$$\frac{\partial v'}{\partial t} = -f u', \tag{5-38}$$

$$\lambda_1 \rho_0 \frac{\partial w'}{\partial t} = -\frac{\partial p'}{\partial z} - \rho' g, \tag{5-39}$$

$$\frac{\partial \theta'}{\partial t} = -w' \frac{\partial \theta_0}{\partial z}, \tag{5-40}$$

$$\lambda_2 \frac{\partial \rho'}{\partial t} = -\rho_0 \left[\frac{\partial u'}{\partial x} + \frac{\partial w'}{\partial z} \right] - w' \frac{\partial \rho_0}{\partial z}, \tag{5-41}$$

$$\rho' = \rho_0 \frac{C_v}{C_p} \frac{p'}{p_0} - \rho_0 \frac{\theta'}{\theta_0}, \tag{5-42}$$

where the following conditions hold:

1.   The layer-domain averaged fields ($u_0, v_0, w_0, \theta_0, p_0, \rho_0$) are hydrostatic, horizontally homogeneous, and unchanging in time.
2.   All subgrid-scale correlation terms are ignored.
3.   Gradients in the y direction ($i = 2$) are neglected.
4.   The Coriolis term is neglected in the vertical equation of motion, as is the term involving w' and the Coriolis term $\hat{f}$.
5.   All motion is adiabatic ($\overline{S}_\theta = 0$).
6. u_0, v_0, and w_0 are assumed to be identically equal to 0.
7.   The vertical gradients of θ_0 and ρ_0 are constant throughout the atmosphere.
8.   Variations of ρ', p', and θ' are assumed to be much less than the magnitudes of ρ_0, p_0, and θ_0, so that $\rho_0 \simeq \bar{\rho}$.

9. Products of the mesoscale dependent variables are removed (e.g., $u'_j \partial u'_i / \partial x_j$ and $u'_j \, \partial \theta' / \partial x_j$).

10. Moisture and effects of other gaseous and aerosol atmospheric materials are ignored.

The parameters λ_1 and λ_2 are defined as

$$\lambda_1 = \begin{cases} 1 & \text{for the nonhydrostatic representation} \\ 0 & \text{for the hydrostatic representation} \end{cases}$$

$$\lambda_2 = \begin{cases} 1 & \text{for the compressible representation} \\ 0 & \text{for the anelastic representation.} \end{cases}$$

These are used to keep track of the terms that are neglected when either the hydrostatic or the anelastic assumptions are made.

This simplified set of six linear algebraic and differential equations in the six unknowns, u', v', w', p', θ', and ρ', can be solved using the Fourier representation method, such as that applied to the linear tank model equations. In the application of this method to Eqs. (5-37)–(5-42), the following forms are used where the dependent variables are assumed to have a periodic wave form in each of the independent variables:

$$
\begin{aligned}
u'(x, z, t) &= \tilde{u}(k_x, k_z, \omega)e^{i(k_x x + k_z z + \omega t)}, \\
v'(x, z, t) &= \tilde{v}(k_x, k_z, \omega)e^{i(k_x x + k_z z + \omega t)}, \\
w'(x, z, t) &= \tilde{w}(k_x, k_z, \omega)e^{i(k_x x + k_z z + \omega t)}, \\
\theta'(x, z, t) &= \tilde{\theta}(k_x, k_z, \omega)e^{i(k_x x + k_z z + \omega t)}, \\
p'(x, z, t) &= \tilde{p}(k_x, k_z, \omega)e^{i(k_x x + k_z z + \omega t)}, \\
\rho'(x, z, t) &= \tilde{\rho}(k_x, k_z, \omega)e^{i(k_x x + k_z z + \omega t)}.
\end{aligned}
\tag{5-43}
$$

As discussed in the solution of the linearized tank model equations, any individual term in a Fourier representation (also called a *harmonic*) is a solution. Any linear combination is also a solution, with the complete representation given by adding together all of the harmonics. Thus Eq. (5-43) is used to represent the dependent variables in Eqs. (5-37)–(5-42).

Rearranging and substituting Eq. (5-43) into these equations yields the simultaneous set of six linear homogeneous algebraic equations in six unknowns:

$$\rho_0 i \omega \tilde{u} + i k_x \tilde{p} - \rho_0 f \tilde{v} = 0,$$

$$i \omega \tilde{v} + f \tilde{u} = 0,$$

$$\lambda_1 \rho_0 i \omega \tilde{w} + i k_z \tilde{p} + g \tilde{\rho} = 0,$$

$$i \omega \tilde{\theta} + \tilde{w} \frac{\partial \theta_0}{\partial z} = 0,$$

$$\lambda_2 i\omega\tilde{\rho} + \rho_0 ik_x\tilde{u} + \rho_0 ik_z\tilde{w} + \tilde{w}\frac{\partial\rho_0}{\partial z} = 0,$$

$$\tilde{\rho} + \frac{\rho_0}{\theta_0}\tilde{\theta} - \frac{\rho_0}{p_0}\frac{C_v}{C_p} = 0.$$

Rewriting this system of equations in matrix form gives

$$
\begin{bmatrix}
\rho_0 i\omega & -f\rho_0 & 0 & 0 & 0 & ik_x \\
f & i\omega & 0 & 0 & 0 & 0 \\
0 & 0 & \lambda_1\rho_0 i\omega & 0 & g & ik_z \\
0 & 0 & \dfrac{\partial\theta_0}{\partial z} & i\omega & 0 & 0 \\
\rho_0 ik_x & 0 & \left[\rho_0 ik_z + \dfrac{\partial\rho_0}{\partial z}\right] & 0 & \lambda_2 i\omega & 0 \\
0 & 0 & 0 & \dfrac{\rho_0}{\theta_0} & 1 & -\dfrac{\rho_0 C_v}{p_0 C_p}
\end{bmatrix}
\begin{bmatrix}
\tilde{u} \\ \tilde{v} \\ \tilde{w} \\ \tilde{\theta} \\ \tilde{\rho} \\ \tilde{p}
\end{bmatrix}
=
\begin{bmatrix}
0 \\ 0 \\ 0 \\ 0 \\ 0 \\ 0
\end{bmatrix}. \tag{5-44}
$$

As briefly discussed for the tank model, a nontrivial solution exists for a homogeneous system of equations, only if the determinant of the coefficients of the matrix equation is 0. Large determinants, such as obtained from Eq. (5-44), are unfortunately not as simple to interpret as the 2×2 determinant of the tank model, nor as simple to evaluate. Fortunately, programs such as Mathematica (Wolfram 1988) provide a computationally efficient procedure to solve Eq. (5-44).[4]

Expanding the determinants of Eq. (5-44) and rearranging yields the fifth-order equation for ω

$$
\begin{aligned}
|A| = \left(\omega^2 - f^2\right)&\left\{\frac{\rho_0}{\theta_0}\frac{\partial\theta_0}{\partial z}\lambda_2\omega k_z - \frac{\rho_0^2}{p_0}i\omega^3\frac{C_v}{C_p}\lambda_2\lambda_1\right. \\
&\left. + \omega k_z\left[\rho_0 ik_z + \frac{\partial\rho_0}{\partial z}\right] - \frac{\rho_0}{p_0}i\omega\frac{C_v}{C_p}g\left[\rho_0 ik_z + \frac{\partial\rho_0}{\partial z}\right]\right\} \\
&+ \omega^3 k_x^2\lambda_1\rho_0 i - g\omega k_x^2\frac{\rho_0}{\theta_0}i\frac{\partial\theta_0}{\partial z} = 0, \tag{5-45}
\end{aligned}
$$

which can also be written as

$$|A| = \left[\frac{\rho_0^2}{p_0}i\frac{C_v}{C_p}\lambda_2\lambda_1\right]\omega^4 + \left[-k_x^2\lambda_1\rho_0 i + \frac{\rho_0}{p_0}i\frac{C_v}{C_p}g\left(\rho_0 ik_z + \frac{\partial\rho_0}{\partial z}\right)\right.$$

$$\left. - k_z\left(\rho_0 ik_z + \frac{\partial\rho_0}{\partial z}\right) - f^2\frac{\rho_0^2}{p_0}i\frac{C_v}{C_p}\lambda_2\lambda_1 - \frac{\rho_0}{\theta_0}\frac{\partial\theta_0}{\partial z}\lambda_2 k_z\right]\omega^2$$

$$+ f^2\frac{\rho_0}{\theta_0}\frac{\partial\theta_0}{\partial z}\lambda_2 k_z + f^2 k_z\left(\rho_0 ik_z + \frac{\partial\rho_0}{\partial z}\right)$$

$$- f^2\frac{\rho_0}{p_0}i\frac{C_v}{C_p}g\left(\rho_0 ik_z + \frac{\partial\rho_0}{\partial z}\right) + gk_x^2\frac{\rho_0}{\theta_0}i\frac{\partial\theta_0}{\partial z} = 0, \qquad (5\text{-}46)$$

where the trivial solution $\omega = 0$ has been removed. Ogura and Charney (1961) obtained a similar fourth-order algebraic equation in frequency in the analysis of a similar set of the conservation relations.

Despite our linearization of the conservation equations, along with our simplifying assumptions (e.g., $\overline{S}_\theta = 0$, $\bar{u}_0 = 0$), evaluation of Eqs. (5-45) and (5-46) is not simple. The tedious effort to get to this point is not in vain, however, since it is possible to make further simplifying assumptions to aid interpretation of these relations.

If it is assumed that $k_x = 0$ (i.e., no variations of the dependent variables are permitted in the x directions), $f = 0$ (i.e., the earth's rotation is neglected), and k_z and ω are real (so that there is no amplification or decay of waves in the vertical direction or in time), then, after rearranging, Eq. (5-46) reduces to

$$- \lambda_1\lambda_2\omega^2 - igk_z - \frac{g}{\rho_0}\frac{\partial\rho_0}{\partial z} + \frac{p_0}{\rho_0}\frac{C_p}{C_v}k_z^2$$

$$- \frac{p_0}{\rho_0^2}\frac{C_p}{C_v}k_z i\frac{\partial\rho_0}{\partial z} - \frac{C_p}{C_v}i\frac{p_0}{\rho_0\theta_0}\frac{\partial\theta_0}{\partial z}\lambda_2 k_z = 0. \qquad (5\text{-}47)$$

Using the ideal gas law and definition of potential temperature for the synoptic scale ($p_0 = \rho_0 R T_0$ and $\theta_0 = T_0(1000/p_0 \text{ (in mb)})^{R_d/C_p}$), we have

$$\frac{1}{\theta_0}\frac{\partial\theta_0}{\partial z} = \left(1 - \frac{R}{C_p}\right)\frac{1}{p_0}\frac{\partial p_0}{\partial z} - \frac{1}{\rho_0}\frac{\partial\rho_0}{\partial z} = \frac{C_v}{C_p}\frac{1}{p_0}\frac{\partial p_0}{\partial z} - \frac{1}{\rho_0}\frac{\partial\rho_0}{\partial z}$$

$$= -\frac{g\rho_0}{p_0}\frac{C_v}{C_p} - \frac{1}{\rho_0}\frac{\partial\rho_0}{\partial z},$$

where the synoptic scale is assumed to be hydrostatic ($\partial p_0/\partial z = -\rho_0 g$).

Substituting this expression into Eq. (5-47) results in

$$-\lambda_2\lambda_1\omega^2 + (\lambda_2 - 1)(igk_z) + (\lambda_2 - 1)i\frac{C_p p_0}{C_v \rho_0^2}k_z\frac{\partial\rho_0}{\partial z}$$

$$-\frac{g}{\rho_0}\frac{\partial\rho_0}{\partial z} + \frac{p_0}{\rho_0}\frac{C_p}{C_v}k_z^2 = 0.$$

If the compressible continuity of mass relation ($\lambda_2 = 1$) is used, then

$$\lambda_2\lambda_1\omega^2 = \frac{p_0}{\rho_0}\frac{C_p}{C_v}k_z^2 - \frac{g}{\rho_0}\frac{\partial\rho_0}{\partial z}. \tag{5-48}$$

The ratio of the two terms on the right side is

$$\left|\frac{g}{\rho_0}\frac{\partial\rho_0}{\partial z}\right| \Big/ \left|\frac{p_0}{\rho_0}\frac{C_p}{C_v}k_z^2\right| \simeq \frac{1}{H_\alpha D k_z^2} = \frac{L_z^2}{(2\pi)^2 H_\alpha^2},$$

since $(1/\rho_0)\partial\rho_0/\partial z = H_\alpha^{-1}$, $p_0/\rho_0 g = D \sim H_\alpha$, and $k_z = 2\pi/L_z$. Even if $L_z \sim H_\alpha$, this ratio is still less than unity ($(1/2\pi)^2 = 0.03$), so that the solution to Eq. (5-48) can be reasonably estimated by dropping the second term on the right in Eq. (5-48). Therefore, when $\lambda_2 = \lambda_1 = 1$,

$$\frac{\omega^2}{k_z^2} \simeq \frac{p_0}{\rho_0}\frac{C_p}{C_v} = RT_0\frac{C_p}{C_v} \simeq c^2.$$

The wave propagation speed (*phase speed*), c, for this situation,

$$c \simeq \pm\left(RT_0\frac{C_p}{C_v}\right)^{1/2}, \tag{5-49}$$

is that of a *vertically propagating sound (acoustic) wave*, which moves upward and downward at the same speed. When either $\lambda_1 = 0$ (i.e., the hydrostatic assumption is applied) or $\lambda_2 = 0$ (i.e., the local time tendency of density is neglected) a wave solution to Eq. (5-48) *does not exist*. This is the reason that the conservation-of-mass relation given by Eq. (3-11) is termed the *anelastic assumption*, since vertically propagating sound waves (and, as is shown shortly, sound waves with horizontal components) are eliminated as a possible solution. For reasonable values of temperature (e.g., $T_0 = 300$ K), $c \simeq 350$ m s^{-1} in the earth's lower troposphere.

Another type of wave motion can be isolated from Eq. (5-46) by prescribing $\lambda_2 = 0$ and neglecting the terms associated with the rotation rate of the earth (e.g., terms multiplied by f). Equation 5-46 then reduces to

$$\left[-k_x^2\lambda_1\rho_0 i + \frac{\rho_0}{p_0}i\frac{C_v}{C_p}g\left(\rho_0 ik_z + \frac{\partial\rho_0}{\partial z}\right) - k_z\left(\rho_0 ik_z + \frac{\partial\rho_0}{\partial z}\right)\right]\omega^2$$

$$+ gk_x^2\frac{\rho_0}{\theta_0}i\frac{\partial\theta_0}{\partial z} = 0,$$

which can be rewritten as

$$\left[-\rho_0 i\left(\lambda_1 k_x^2 + k_z^2\right) + \frac{\rho_0}{p_0} i\frac{C_v}{C_p} g\frac{\partial\rho_0}{\partial z} - \frac{\rho_0^2}{p_0}\frac{C_v}{C_p} gk_z - k_z\frac{\partial\rho_0}{\partial z}\right]\omega^2$$

$$+ gk_x^2\frac{\rho_0}{\theta_0} i\frac{\partial\theta_0}{\partial z} = 0. \tag{5-50}$$

In this equation it is specified that k_x and ω are real. (Waves are assumed to not amplify or decay in the horizontal direction or in time.) The vertical wave number k_z is prescribed as complex, however, to account for the imaginary terms that appear in this relation.

Rewriting Eq. (5-50) and rearranging with $k_z = k_{z_r} + ik_{z_i}$ yields

$$\left[\rho_0\left[\lambda_1 k_x^2 + k_{z_r}^2 - k_{z_i}^2\right] - g\frac{\rho_0}{p_0}\frac{C_v}{C_p}\frac{\partial\rho_0}{\partial z} + \frac{\rho_0^2}{p_0}\frac{C_v}{C_p} gk_{z_i} + k_{z_i}\frac{\partial\rho_0}{\partial z}\right]\omega^2$$

$$- gk_x^2\frac{\rho_0}{\theta_0}\frac{\partial\theta_0}{\partial z} + i\left[2\rho_0 k_{z_i}k_{z_r} - \frac{\rho_0^2}{p_0}\frac{C_v}{C_p} gk_{z_r} - k_{z_r}\frac{\partial\rho_0}{\partial z}\right]\omega^2 = 0. \tag{5-51}$$

Thus, to ensure that Eq. (5-51) is a real equation,

$$k_{z_i} = \frac{\rho_0 C_v}{2p_0 C_p} g + \frac{1}{2\rho_0}\frac{\partial\rho_0}{\partial z}$$

is required, so that Eq. (5-51) reduces to

$$\left\{\rho_0\left(\lambda_1 k_x^2 + k_z^2\right) + \frac{1}{4}\frac{\rho_0^3}{p_0^2}\left(\frac{C_v}{C_p}\right)^2 g^2 + \frac{1}{4\rho_0}\left(\frac{\partial\rho_0}{\partial z}\right)^2 - \frac{1}{2}\frac{\rho_0}{p_0}\frac{C_v}{C_p} g\frac{\partial\rho_0}{\partial z}\right\}\omega^2$$

$$- gk_x^2\frac{\rho_0}{\theta_0}\frac{\partial\theta_0}{\partial z} = 0, \tag{5-52}$$

where k_{z_r} is written as k_z to simplify the notation. In permitting the vertical wave number to be complex, the assumed solutions given by Eq. (5-43) include the exponential term $e^{-\beta z}$, where

$$\beta = \frac{\rho_0}{2p_0}\frac{C_v}{C_p} + \frac{1}{2\rho_0}\frac{\partial\rho_0}{\partial z}.$$

Thus, for example,

$$\phi'(x, z, t) = \tilde{\phi}\left(k_x, k_z, \omega\right)e^{-\beta z}e^{1\left(k_x x + k_{z_r} z + \omega t\right)},$$

where ϕ represents any one of the dependent variables in Eq. (5-43).

Using scale analysis, the ratios of the magnitudes of the three right-side terms within the braces of the first term can be examined:

$$\left|\frac{1}{4}\frac{\rho_0^3}{p_0^2}\left(\frac{C_v}{C_p}\right)^2 g^2\right| \bigg/ \left|\rho_0(\lambda_1 k_x^2 + k_z^2)\right| \sim \frac{1}{4}\left(\frac{C_v}{C_p}\right)^2 \frac{g^2}{R^2 T_0^2 \bar{k}^2}$$

$$\approx 4.2 \times 10^{-11} L^2 \text{ (in meters)},$$

$$\left|\frac{1}{4\rho_0}\left(\frac{\partial\rho_0}{\partial z}\right)^2\right| \bigg/ \left|\rho_0(\lambda_1 k_x^2 + k_z^2)\right| \sim \frac{1}{4 H_\alpha^2 \bar{k}^2}$$

$$\approx 9.9 \times 10^{-11} L^2 \text{ (in meters)},$$

$$\left|\frac{1}{2}\frac{\rho_0}{p_0}\frac{C_v}{C_p} g \frac{\partial\rho_0}{\partial z}\right| \bigg/ \left|\rho_0(\lambda_1 k_x^2 + k_z^2)\right| \sim \frac{1}{2}\frac{C_v}{C_p}\frac{g}{RT_0 H_\alpha \bar{k}^2}$$

$$\approx 13.1 \times 10^{-11} L^2 \text{ (in meters)}$$

where $\bar{k}$ is used to represent the wavenumber $[\bar{k} \sim (k_z^2 + k_x^2)^{1/2}]$ and $\bar{k} = 2\pi/L$, where L is the representative wavelength of the atmospheric circulation. A temperature of 300 K and $H_\alpha = 8$ km were used in this scale estimate along with the values of R, C_p, and C_v for dry air (287, 1004, and 717 J deg^{-1} kg^{-1}, respectively). Thus if we assume that a ratio of 0.01 is sufficient justification for neglecting the largest of these three terms, then

$$L \gtrsim 10 \text{ km}$$

is required. For longer wavelengths, and for quantitative analyses, these terms must be retained. The terms are about equal for wavelengths on the order of 100 km.

If it is appropriate to neglect the three terms, then Eq. (5-52) reduces to[5]

$$\omega^2 \simeq \frac{k_x^2}{\lambda_1 k_x^2 + k_z^2}\frac{g}{\theta_0}\frac{\partial\theta_0}{\partial z}. \tag{5-53}$$

As shown for the tank model, the negative of the phase speed is equal to the frequency ω divided by the wavenumber in the direction of wave propagation k. The phase speeds in component form are given by

$$c_x = \frac{-\omega k_x}{k_x^2 + k_z^2} \quad \text{and} \quad c_z = \frac{-\omega k_z}{k_x^2 + k_z^2}.$$

Equation (5-53) can be written as

$$c^2 \simeq \frac{k_x^2}{(k_x^2 + k_z^2)(\lambda_1 k_x^2 + k_z^2)}\frac{g}{\theta_0}\frac{\partial\theta_0}{\partial z} \tag{5-54}$$

or, when $\lambda_1 = 1$,

$$c \simeq \pm \frac{k_x}{k_x^2 + k_z^2} \left(\frac{g}{\theta_0} \frac{\partial \theta_0}{\partial z} \right)^{1/2}. \tag{5-55}$$

On the one hand, if the wave motion is primarily in the horizontal, then $c_z \ll c_x$ and thus $k_z \ll k_x$, so Eq. (5-55) is written as

$$c \simeq \pm \frac{1}{k_x} \left(\frac{g}{\theta_0} \frac{\partial \theta_0}{\partial z} \right)^{1/2}. \tag{5-56}$$

On the other hand, if the wave motion is predominantly in the vertical, so that $c_z \gg c_x$ and thus $k_z \gg k_x$, we have

$$c \sim \pm \frac{k_x}{k_z^2} \left(\frac{g}{\theta_0} \frac{\partial \theta_0}{\partial z} \right)^{1/2}. \tag{5-57}$$

This wave motion is a type of internal gravity wave that can occur in a *continuously and uniformly stratified* fluid. In the two-layer tank model discussed earlier, an internal gravity wave that can occur at a *density discontinuity* was presented. Gravitational acceleration is required for both of these types of waves to occur.

If Eq. (3-22) (i.e., $H_\alpha / L_x \lesssim 1$) is applicable, then the hydrostatic assumption can be applied ($\lambda_1 = 0$), and Eq. (5-53) reduces to

$$\omega^2 = \frac{k_x^2}{k_z^2} \frac{g}{\theta_0} \frac{\partial \theta_0}{\partial z}. \tag{5-58}$$

Comparing Eqs. (5-53) and (5-58), an alternate justification for applying the hydrostatic assumption is valid if the atmospheric circulation of interest is primarily influenced by this kind of internal gravity wave. In this case, if

$$k_x^2 \ll k_z^2$$

or, equivalently,

$$L_x^2 \gg L_z^2, \tag{5-59}$$

then using the hydrostatic assumption is valid.

Using Eq. (5-55), speeds of propagation of internal gravity waves can be estimated. As discussed in Section 10.1.4, this information is essential for successfully utilizing numerical simulation methods. For example, using representative values of the parameters in Eqs. (5-56) and (5-57) (i.e., $\theta_0 = 300$ K, $\partial \theta_0 / \partial z = 1°/100$ m, and $g = 9.8$ m s^{-2}), we have $c \simeq 15$ m s^{-1} for $L_x = 5$ km and $L_z = 25$ km and $c \simeq 3$ m s^{-1} for $L_x = 25$ km and $L_z = 5$ km. Thus in a hydrostatic system with a constant temperature lapse rate, the phase speed of the internal gravity wave is primarily upward with a relatively slow propagation speed. When the hydrostatic assumption is not valid, wave propagation

tends to be more horizontal and somewhat faster, but still more than an order of magnitude slower than the phase speed of vertically propagating sound waves.

From Eq. (5-55), it is seen that a nonzero value of $\partial \theta_0 / \partial z$ is needed to produce an internal gravity wave. Thus if we require that the vertical gradient of potential temperature be 0 and neglect terms that include the gravitational acceleration, then it is possible to determine wave solutions from Eq. (5-46) that are not gravity waves. To simplify the analysis, we also assume that $\partial \rho_0 / \partial z$ is 0[6] and that the rotation of the earth is negligible. With these conditions, Eq. (5-46) reduces to

$$\lambda_2 \lambda_1 \omega^2 = \frac{p_0}{\rho_0} \frac{C_p}{C_v} (\lambda_1 k_x^2 + k_z^2) = RT_0 \frac{C_p}{C_v} (\lambda_1 k_x^2 + k_z^2) \qquad (5\text{-}60)$$

and, since $\omega^2 / (k_x^2 + k_z^2) = c^2$,

$$c = \pm (RT_0 C_p / C_v)^{1/2} \qquad (5\text{-}61)$$

when $\lambda_1 = \lambda_2 = 1$. The phase speed given by Eq. (5-61) is the same as that given by Eq. (5-49) and corresponds to the speed of sound propagation. From Eq. (5-60), it is evident that either the hydrostatic or the anelastic assumptions eliminate this form of wave propagation.[7] In numerical models (as shown in Chapter 10), the ability to correctly resolve a wave form in a model (and often to produce stable results) requires that the time step used be less than or equal to the time it takes for a wave to travel between grid points. With sound waves removed by applying the hydrostatic or the anelastic assumption, the fastest waves are gravity waves.

A final wave form that we examine includes the influence of the earth's rotation. We can illustrate this relation most easily by assuming that the lapse rate is adiabatic ($\partial \theta_0 / \partial z = 0$) and that either the hydrostatic assumption is used ($\lambda_1 = 0$) or no variations are permitted in the x-direction. In this case, Eq. (5-45) reduces to the simple frequency equation for an *inertial wave*,[8]

$$\omega = \pm f. \qquad (5\text{-}62)$$

Our final discussion regarding the types of wave motions concerns the effect of two or more waves traveling at different propagation speeds. As is evident from Eq. (5-54), for example, phase speed is dependent on the wavenumber. Thus the complete solution to the system of linear equations (5-37)–(5-42) is a linear superposition of the solutions given by all of the harmonics of the form given by Eq. (5-43). When the speeds of the different waves are in phase, *constructive reinforcement* occurs, and the amplitude of the solution is a maximum. If the waves are out of phase, *destructive reinforcement* results, and the amplitudes of the individual waves can sum to 0. The propagation speed of the locations of constructive and destructive reinforcement is called the *group velocity*.

To illustrate this more mathematically, let two waves of the same amplitude but different wavelengths coexist such that

$$\phi_1(x, t) = \tilde{\phi} \cos(k_1 x + \omega_1 t) = \tilde{\phi} \cos(2\pi/l_1)(x - c_1 t) \qquad (5\text{-}63)$$

$$\phi_2(x, t) = \tilde{\phi} \cos(k_2 x + \omega_2 t) = \tilde{\phi} \cos(2\pi/l_2)(x - c_2 t), \qquad (5\text{-}64)$$

where $\tilde{\phi} = \tilde{\phi}(k_1, \omega_1) = \tilde{\phi}(k_2, \omega_2)$, $\omega_1/k_1 = -c_1$, and $\omega_2/k_2 = -c_2$. Defining $c_1 = c - \delta c$, $c_2 = c + \delta c$, $l_1 = l - \delta l$, and $l_2 = l + \delta l$, where δc and δl are small incremental changes in phase speed and wavelength, for ϕ_1 we have

$$\frac{2\pi}{l_1}(x - c_1 t) = \frac{2\pi}{l - \delta l}(x - ct + t\delta c) \simeq \frac{2\pi}{l}\left(1 + \frac{\delta l}{l}\right)(x - ct + t\delta c)$$

$$+ \frac{2\pi}{l}(x - ct) + \frac{2\pi}{l}\left(t\,\delta c + \frac{\delta l}{l}x - \frac{\delta l}{l}ct + \frac{t\delta l\delta c}{l}\right)$$

$$\simeq \frac{2\pi}{l}(x - ct) + \frac{2\pi}{l}\left(t\delta c + \frac{\delta l}{l}x - \frac{\delta l}{l}ct\right)$$

$$= \frac{2\pi}{l}(x - ct) + \frac{2\pi}{l^2}\delta l\left[x - \left(c - l\frac{\delta c}{\delta l}\right)t\right],$$

where the binomial expansion [i.e., $(1 - \epsilon)^{-n} \simeq 1 + \epsilon$ for $\epsilon \ll 1$] has been used and δc and δl are assumed to be much less than c and l. A similar expression can be derived for the second wave,

$$\frac{2\pi}{l_2}(x + c_2 t) \simeq \frac{2\pi}{l}(x + ct) + \frac{2\pi}{l^2}\delta l\left[-x + \left(c - l\frac{\delta c}{\delta l}\right)t\right].$$

Defining $\alpha = (2\pi/l)(x - ct)$ and $\beta = (2\pi/l^2)\delta l\{x - [c - l(\delta c/\delta l)]t\}$, to simplify the notation, the linear superposition of the two waves of similar but not equal phase speeds and wavelengths given by Eqs. (5-63) and (5-64) yields

$$\phi_1(x, t) + \phi_2(x, t) = \tilde{\phi}\left[\cos(\alpha + \beta) + \cos(\alpha - \beta)\right]$$

$$= \tilde{\phi}\left[\cos\alpha\cos\beta - \sin\alpha\sin\beta + \cos\alpha\cos\beta + \sin\alpha\sin\beta\right]$$

$$= 2\tilde{\phi}\left[\cos\alpha\cos\beta\right]0.$$

$$= 2\tilde{\phi}\left[\cos\frac{2\pi}{l}(x - ct)\cos\frac{2\pi\,\delta l}{l^2}\left(x - \left(c - l\frac{\delta c}{\delta l}\right)t\right)\right].$$

The second term in the brackets represents the linear interaction between the two waves leading to constructive reinforcement if $x = (c - l(\delta c/\delta l))t$. The

quantity $c - l(\delta c/\delta l)$ is the *group velocity*, which in the limit when δc and δl approach 0 can be written as

$$c_g = c - l\frac{dc}{dl} = \frac{d}{dk}(kc(k)) = -\frac{d\omega}{dk},$$

since $c = -\omega/k$.

The group velocity c_g in the coordinate directions can be written as

$$c_{gi} = -\partial\omega/\partial k_i \tag{5-65}$$

by the change rule, because in general ω is a function of the three components of the wavenumber; e.g., $\omega = \omega(k_x, k_y, k_z) = \omega(k_i)$; $i = 1, 2, 3$.

Thus using Eq. (5-65), one can determine the group velocity for any of the wave forms that we have derived. For example, the components of the internal gravity wave group velocity when $L_x^2 \gg L_z^2$ can be calculated from Eq. (5-58) as

$$c_{g_x} = \pm\left(\frac{g}{\theta_0}\frac{\partial\theta_0}{\partial z}\right)^{1/2}\frac{L_z}{2\pi}$$

and

$$c_{g_z} = \pm\left(\frac{g}{\theta_0}\frac{\partial\theta_0}{\partial z}\right)^{1/2}\frac{L_z}{2\pi}\left(\frac{L_z}{L_x}\right),$$

so that when the hydrostatic assumption is valid, the group velocity is predominantly in the horizontal direction (in contrast with the phase velocity, which is primarily vertical).

With a definition of group velocity, we conclude discussion of specialized wave forms in the atmosphere. On the mesoscale, the internal gravity and inertial waves are the most important classes of oscillatory motion generated. Both internal waves in a continuously stratified atmosphere and on density inversions are important. Sound waves, in contrast, are considered insignificant on the mesoscale, and it is desirable to eliminate them from the solutions if computational problems arise because of their presence. All of these wave forms were derived after linearizing the conservation relations, as well as making additional simplifying assumptions that allowed us to remove certain terms from the equations. Of course, in the atmosphere such limitations on the modes of interaction are not present. Hence it is seldom possible to observe the idealized wave forms that have been derived here. Such features as velocity shear and multiple temperature inversions, for example, even if the response of the atmosphere were linear, would produce phase and group velocities of internal gravity waves different than those we have derived. Nonetheless, an understanding of these idealized wave forms is essential if one is to effectively apply numerical solution techniques. Numerical models are the preferred tool, however, since they

can include nonlinear interactions and thus provide a more physically complete representation.

From the analysis of internal waves, the ratio of the vertical scale to the horizontal scale of the atmospheric circulation [Eq. (5-59)] suggests whether or not the hydrostatic assumption should be used in the simulation. If the smallest horizontal feature that can be resolved with reasonable accuracy in a numerical model is $4\Delta x$, as used to obtain Eq. (4-43), and $H_\alpha \simeq 8$ km is used to estimate the largest expected vertical wavelength, then $\Delta x \geq 6$ km appears to be needed to ensure that the hydrostatic assumption is valid within about a 10% error for all internal waves formed in a continuously stratified medium in that model representation. If the predominant horizontal wavelength of such waves is assumed to be determined by bottom surface variations (e.g., a mountain), then such forcings must have a horizontal scale of 25 km or more. This criterion for using the hydrostatic assumption is more restrictive than that given by Eq. (4-43), but it must be emphasized that it applies only in mesoscale models in which internal gravity waves propagating in a continuously stratified medium are an important part of the physical solution.

5.2.3 Mesoscale Linearized Equations

5.2.3.1 Defant Model

Although the linear analysis presented in Section 5.2.2 illustrates characteristic wave motions expected in the atmosphere, it does not represent any actual mesoscale atmospheric system. This inability to represent such features results from the assumed periodic solution in time and space given by Eq. (5-43). To relax this constraint, at least part of the solution to the linearized equations must include nonperiodic spatial structure.

Linear models have been developed from the basic conservation relations for a number of different mesoscale features (e.g., Walsh 1974, sea breeze; Klemp and Lilly 1975, forced airflow over a mountain) to improve the fundamental understanding of mesoscale systems. During the years before computers, linear models provided the only means for representing atmospheric circulations mathematically.

To illustrate a method of solving a linear mesoscale model, a modified version of Defant's (1950) sea- and land-breeze formulation is used in this section. The analysis presented here was extracted and slightly modified from that presented in Martin (1981) and Martin and Pielke (1983).

Equations (5-37)–(5-42) can be written as

$$\frac{\partial u'}{\partial t} = -\alpha_0 \frac{\partial p'}{\partial x} + fv' - \sigma_x u', \qquad (5\text{-}66)$$

$$\frac{\partial v'}{\partial t} = -fu' - \sigma_y v', \tag{5-67}$$

$$\lambda_1 \frac{\partial w'}{\partial t} = \gamma\theta' - \alpha_0 \frac{\partial p'}{\partial z} - \lambda_1 \sigma_z w', \tag{5-68}$$

$$\frac{\partial u'}{\partial x} + \frac{\partial w'}{\partial z} = 0, \tag{5-69}$$

$$\frac{\partial \theta'}{\partial t} + w'\beta = K\left\{\frac{\partial^2 \theta'}{\partial x^2} + \frac{\partial^2 \theta'}{\partial z^2}\right\}, \tag{5-70}$$

where $\beta = \partial\theta_0/\partial z$ and $\gamma = g/\theta_0$. The assumptions used here are the same as given following Eq. (5-42), except that the incompressible form of Eq. (5-41) is used and several of the subgrid flux terms are retained from Eqs. (4-21) and (4-24). These flux terms are represented by

$$\frac{1}{\bar{\rho}} \frac{\partial}{\partial x} \bar{\rho} \overline{u''^2} + \frac{1}{\bar{\rho}} \frac{\partial}{\partial z} \bar{\rho} \overline{u'' w''} = \sigma_x u',$$

$$\frac{1}{\bar{\rho}} \frac{\partial}{\partial x} \bar{\rho} \overline{v'' u''} + \frac{1}{\bar{\rho}} \frac{\partial}{\partial z} \bar{\rho} \overline{v'' w''} = \sigma_y v',$$

$$\frac{1}{\bar{\rho}} \frac{\partial}{\partial x} \bar{\rho} \overline{u'' w''} + \frac{1}{\bar{\rho}} \frac{\partial}{\partial z} \bar{\rho} \overline{w''^2} = \sigma_z w',$$

$$\frac{1}{\bar{\rho}}\left\{\frac{\partial}{\partial z} \bar{\rho} \overline{w'' \theta''} + \frac{\partial}{\partial x} \bar{\rho} \overline{u'' \theta''}\right\} = -K\left\{\frac{\partial^2 \theta'}{\partial x^2} + \frac{\partial^2 \theta'}{\partial z^2}\right\},$$

where we assume that $\sigma_x = \sigma_y$. The terms that involve $(\partial/\partial y)\,\bar{\rho}\overline{v''^2}$, $(\partial/\partial y)\bar{\rho}\overline{u''v''}$, and $(\partial/\partial y)\,\bar{\rho}\overline{w''v''}$ are neglected (or they could be considered included in the parameterizations involving σ_x and σ_z). When $\lambda_1 = 0$, the equations are hydrostatic.

To solve Eqs. (5-66)–(5-70) in five unknowns (i.e., u', v', w', p', and θ'), Defant recognized that u' and v' must be 90° out of phase with w', p', and θ' since the first two dependent variables are expressed in terms of derivatives of the others. Moreover, the solutions should be a function of height above the ground surface rather than simply a periodic function, since the sea and land breeze does not extend upward indefinitely. Defant, therefore, assumed solutions of the form

$$w'(x, z, t) = \tilde{w}(z)e^{i\omega t} \sin k_x x, \quad u'(x, z, t) = \tilde{u}(z)e^{i\omega t} \cos k_x x,$$

$$p'(x, z, t) = \tilde{p}(z)e^{i\omega t} \sin k_x x, \quad v'(x, z, t) = \tilde{v}(z)e^{i\omega t} \cos k_x x, \tag{5-71}$$

$$\theta'(x, z, t) = \tilde{\theta}(z)e^{i\omega t} \sin k_x x,$$

with the boundary conditions

$$w'(z = 0) = w'(z \to \infty) = \theta'(z \to \infty) = 0 \quad \text{and} \quad \theta'(z = 0) = M\,e^{i\omega t} \sin k_x x,$$

where M is the amplitude of the maximum mesoscale perturbation surface potential temperature. In general, $\tilde{w}$, $\tilde{p}$, $\tilde{\theta}$, $\tilde{u}$, and $\tilde{v}$ are complex valued variables. The wave number k_x is equal to 2π divided by the wavelength L_x of the assumed periodic function. In this model, $0.5L_x$ corresponds to the size of land in which the maximum heating occurs $0.25L_x$ inland from the coast. The frequency ω represents the temporal periodic variation in the system, which for a sea- and land-breeze simulation corresponds to the diurnal period.

The assumed solutions given by Eq. (5-71) are substituted into Eqs. (5-66)–(5-70), which after simplification yields

$$i\omega\tilde{u} = -k_x\alpha_0\tilde{p} + f\tilde{v} - \sigma_x\tilde{u}, \tag{5-72}$$

$$i\omega\tilde{v} = -f\tilde{u} - \sigma_x\tilde{v}, \tag{5-73}$$

$$i\omega\lambda_1\tilde{w} = -\lambda_1\sigma_z\tilde{w} - \alpha_0\frac{d\tilde{p}}{dz} + \gamma\tilde{\theta}, \tag{5-74}$$

$$-k_x\tilde{u} + \frac{d\tilde{w}}{dz} = 0, \tag{5-75}$$

$$i\omega\tilde{\theta} = -\tilde{w}\beta - K\tilde{\theta}k_x^2 + K\frac{d^2\tilde{\theta}}{dz^2}. \tag{5-76}$$

These equations, with boundary conditions, are solved simultaneously for the dependent variables $\tilde{u}$, $\tilde{v}$, $\tilde{w}$, $\tilde{\theta}$, and $\tilde{p}$, which are now only functions of z.

Rearranging Eqs. (5-72)–(5-76) yields

$$\tilde{u} = \frac{1}{k_x}\frac{d\tilde{w}}{dz}, \tag{5-77}$$

$$\tilde{v} = \frac{-f}{i\omega + \sigma_x}\tilde{u}, \tag{5-78}$$

$$\tilde{p} = -\frac{1}{\alpha_0 k_x}\left[\frac{(i\omega + \sigma_x)^2 + f^2}{(i\omega + \sigma_x)}\right]\tilde{u}, \tag{5-79}$$

$$\frac{d^2\tilde{w}}{dz^2} = \eta^2\tilde{w} + r\tilde{\theta}, \tag{5-80}$$

$$\frac{d^2\tilde{\theta}}{dz^2} = \epsilon\tilde{w} + s\tilde{\theta}, \tag{5-81}$$

where

$$\eta^2 = k_x^2\frac{(i\omega + \sigma_x)\lambda_1(i\omega + \sigma_z)}{(i\omega + \sigma_x)^2 + f^2}; \quad r = -\frac{\gamma k_x^2(i\omega + \sigma_x)}{(i\omega + \sigma_x)^2 + f^2};$$

$$\epsilon = \frac{\beta}{K}; \quad \text{and} \quad s = \frac{i\omega}{K} + k_x^2.$$

   The complex-valued variables $\tilde{w}$ and $\tilde{\theta}$ are assumed to have a solution of the form

$$\tilde{w}(z) = Ae^{az} + Be^{-bz} \tag{5-82}$$

and

$$\tilde{\theta}(z) = Ce^{az} + De^{-bz}. \tag{5-83}$$

Applying the lower boundary condition $\tilde{w}(z = 0) = 0$ to Eq. (5-82) results in

$$A = -B,$$

so that

$$\tilde{w}(z) = A(e^{az} - e^{-bz}). \tag{5-84}$$

Substituting this expression for $\tilde{w}$ into Eq. (5-80) gives

$$A(a^2 e^{az} - b^2 e^{-bz}) = \eta^2 A(e^{az} - e^{-bz}) + r\tilde{\theta}. \tag{5-85}$$

The lower boundary condition on θ' requires that

$$M e^{i\omega t} \sin k_x x = [C + D]e^{i\omega t} \sin k_x x, \tag{5-86}$$

which reduces to $D = M - C$, as long as $e^{i\omega t}$ or $\sin k_x x$ does not equal 0. Equation (5-83) then becomes

$$\tilde{\theta} = M e^{-bz} + C(e^{az} - e^{-bz}). \tag{5-87}$$

Substituting this expression for $\tilde{\theta}$ into Eq. (5-85) and setting z to 0 yields

$$A = -rM(b^2 - a^2)^{-1}. \tag{5-88}$$

To obtain C, Eqs. (5-81), (5-87), and (5-88) are combined with z set equal to 0, resulting in

$$b^2 M e^{-bz} + C(a^2 e^{az} - b^2 e^{-bz}) = \epsilon\left(\frac{-rM}{b^2 - a^2}\right)(e^{az} - e^{-bz})$$
$$+ s[M e^{-bz} + C(e^{az} - e^{-bz})],$$

which reduces to

$$C = \frac{b^2 - s}{b^2 - a^2}M. \tag{5-89}$$

   All of the coefficients in the assumed solutions, with the exception of a and b, are now expressed in terms of the physical parameters. Using the equations for

A, B, C, and D and Eqs. (5-87), (5-84), and (5-77)–(5-80), the analytic forms for $\tilde{\theta}$, $\tilde{w}$, $\tilde{u}$, $\tilde{v}$, and $\tilde{p}$ are given by

$$\tilde{\theta}(z) = Me^{-bz} + \frac{b^2 - s}{b^2 - a^2} M\{e^{az} - e^{-bz}\}, \tag{5-90}$$

$$\tilde{w}(z) = \frac{-rM}{b^2 - a^2}(e^{az} - e^{-bz}), \tag{5-91}$$

$$\tilde{u}(z) = -\frac{1}{k_x}\frac{rM}{b^2 - a^2}(ae^{az} + be^{-bz}), \tag{5-92}$$

$$\tilde{v}(z) = \frac{f}{i\omega + \sigma_x}\frac{1}{k_x}\frac{rM}{b^2 - a^2}(ae^{az} + be^{-bz}), \tag{5-93}$$

$$\tilde{p}(z) = \frac{1}{\alpha_0 k_x^2}\frac{(i\omega + \sigma_x)^2 + f^2}{(i\omega + \sigma_x)}\frac{rM}{b^2 - a^2}(ae^{az} + be^{-bz}). \tag{5-94}$$

To solve for the parameters a and b, Eq. (5-83) is substituted into Eq. (5-85) (using $D = M - C$, as derived previously), yielding, after rearranging and simplifying,

$$(Aa^2 - A\eta^2 - rC)e^{az} - (Ab^2 - A\eta^2 + rM - rC)e^{-bz} = 0. \tag{5-95}$$

A similar relation is found by differentiating Eq. (5-83) twice with respect to z, resulting in

$$d^2\tilde{\theta}/dz^2 = Ca^2 e^{az} + (M - C)b^2 e^{-bz},$$

and then combining this with Eqs. (5-81), (5-84), and (5-87) to give

$$(Ca^2 - \epsilon A - sC)e^{az} + (Mb^2 - Cb^2 + \epsilon A - sM + sC)e^{-bz} = 0. \tag{5-96}$$

The quantities e^{az} and e^{-bz} are independent functions, and $e^{az} - e^{-bz} \neq 0$ in general if $a \neq b$. If this is true, then each of the exponential coefficients in Eqs. (5-95) and (5-96) are equal to 0, leading to the following two systems of equations:

$$A(a^2 - \eta^2) - rC = 0,$$
$$-A\epsilon + C(a^2 - s) = 0$$

and

$$A(b^2 - \eta^2) + r(M - C) = 0,$$
$$A\epsilon + (M - C)(b^2 - s) = 0.$$

Since the determinant of the coefficients of these two systems of algebraic equations must equal 0, the quadratic equations in a^2 and b^2 given by

$$(a^2 - \eta^2)(a^2 - s) - \epsilon r = 0 \text{ or } a^4 - (\eta^2 + s)a^2 + (\eta^2 s - \epsilon r) = 0,$$

and

$$(b^2 - \eta^2)(b^2 - s) - \epsilon r = 0 \text{ or } b^4 - (\eta^2 + s)b^2 + (\eta^2 s - \epsilon r) = 0,$$

are produced.

The quadratic formula is used to compute the complex valued parameters a^2 and b^2, yielding

$$a^2; b^2 \left\{ = \frac{\eta^2 + s}{2} \pm \frac{1}{2}\sqrt{(\eta^2 + s)^2 - 4(\eta^2 s - \epsilon r)}. \right. \tag{5-97}$$

It follows that a and b can have the values

$$a = \pm\sqrt{a^2} \quad \text{and} \quad b = \pm\sqrt{b^2}. \tag{5-98}$$

The question remains of which roots to choose in Eqs. (5-97) and (5-98). To avoid division by 0, a^2 and b^2 must be opposite roots of Eq. (5-97). Solutions of the model equations, however, showed that identical results were obtained whether a^2 was the first root and b^2 the second root of Eq. (5-97), or vice versa. Furthermore, to satisfy the boundary condition $w(z \to \infty) = 0$, in conjunction with Eq. (5-91), b must have a positive real part and a must have a negative real part. This is no restriction, since the square roots of a complex number will yield one with a positive real part and one with a negative real part.

With this information, the analytic solution to Defant's linear model is obtained. Values of the dependent variables w', p', θ', u', and v' as functions of x, z, and t are determined by calculating the real parts of Eqs. (5-71) and (5-90)–(5-94), using Eqs. (5-97), (5-98), and the formulas following Eq. (5-81) to determine the values of η^2, γ, s, ϵ, a^2, b^2, a, and b.

Figure 5-4 illustrates the $\tilde{u}$, $\tilde{w}$, $\tilde{\theta}$, and $\tilde{p}$ fields at 6 hours after simulated sunrise obtained using this linear model. The values of the parameters used in the model were

$$\left. \begin{array}{l} \partial\theta_0/\partial z = \beta = 1°\text{C/1 km}, \ K = 10\,\text{m}^2\,\text{s}^{-1}, \ \alpha_0 = 0.758\,\text{m}^3\,\text{kg}^{-1}, \\[4pt] \sigma_x = \sigma_z = 10^{-3}\,\text{s}^{-1}, \ f = 1.031 \times 10^{-4}\,\text{s}^{-1}, \ g = 9.8\,\text{m s}^{-2}, \\[4pt] \theta_0 = 273\,\text{K}, \ M = 10°\text{C}, \ \text{and } k_x = 2\pi/100\,\text{km}. \end{array} \right\} \tag{5-99}$$

The symmetric circulation evident in Figure 5-4 is a result of the horizontal periodicity assumed in the solutions. Land and water are differentiated in the model only by the magnitude of k_x. [The same dependent variables over water and land are always of opposite sign because of the form of the assumed solution, Eq. (5-71).]

This solution illustrates the interrelation between the dependent variables. Because of the prescribed heating–cooling pattern in the model, pressure falls develop in the region of heating, whereas rises occur where cooling is specified. This pressure pattern causes horizontal accelerations toward regions of lower
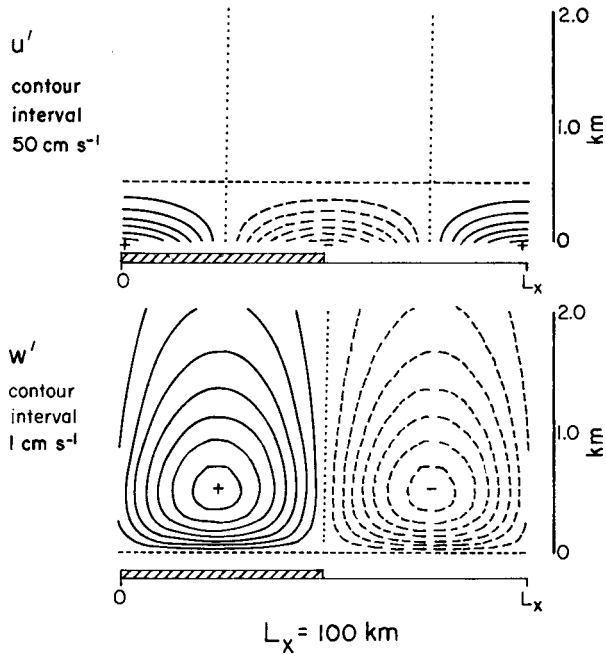
Fig. 5-4. The horizontal and vertical velocity fields predicted from Defant's (1950) model 6 hours after sunrise using the input parameters given by Eq. (5-99). (From Martin 1981.)

pressure, as evident from Eq. (5-66). Since mass conservation is required from Eq. (5-69), upward motion necessarily results in the region of heating, whereas subsidence occurs in the region of cooling.

Varying the parameters in the model, as was done by Martin (1981), also provides insight into the physics of this specific mesoscale circulation. To examine the importance of the hydrostatic assumption, for example, it is possible to calculate nonhydrostatic and hydrostatic results from this model by letting $\lambda_1 = 1$ and $\lambda_1 = 0$. Since the scale analysis presented previously in this book [i.e., Eqs. (3-22) and (5-59)] suggest that the horizontal-scale length of a mesoscale circulation L_x is the most important indicator of whether or not the hydrostatic assumption is valid, it is desirable to determine, as a function of L_x, the influence of several of the parameters in Eq. (5-99) on the hydrostatic assumption.

To perform this analysis, following Martin (1981), the relative error between the nonhydrostatic and hydrostatic amplitudes of a given dependent variable is given by

$$E = 2\frac{|\phi_h| - |\phi_{nh}|}{|\phi_h| + |\phi_{nh}|},$$

where $|\phi_n|$ and $|\phi_{nh}|$ are the maximum absolute amplitudes over time and space for a given set of parameters such as listed in Eq. (5-99). The subscripts "h" and "nh" correspond to hydrostatic and nonhydrostatic versions, respectively.

Figure 5-5 illustrates one such comparison, where E is evaluated as a function of the domain-averaged lapse rate, β, and L_x. As the atmosphere becomes more stably stratified, according to Defant's model, the hydrostatic relation becomes a more accurate assumption for a given horizontal scale of the circulation.

With a value of $\beta = 1°C/100$ m, for instance, the maximum error is less than 2% even with $L_x = 1$ km, whereas an equivalent level of accuracy is not attained for $\beta = 0.01°C/100$ m until L_x is about 10 km. Figure 5-6 shows a similar analysis for the magnitude of the exchange coefficient for heat K, which is assumed to be a constant in a given solution of Defant's model. In the model, as the rate in which heat is mixed up increases, the hydrostatic relation becomes a poorer assumption for the pressure distribution in the model. With values of
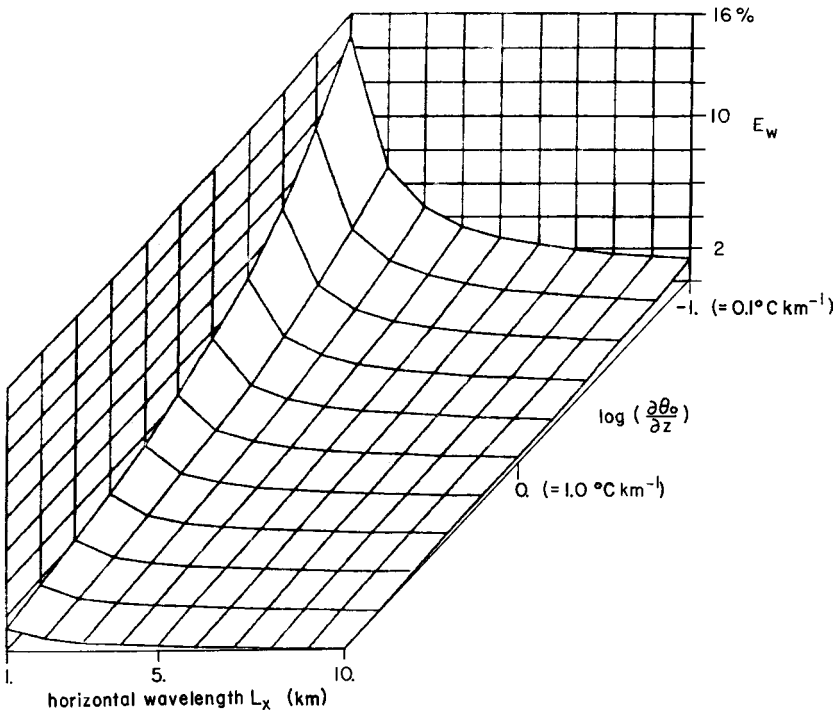

Fig. 5-5. Relative error in vertical velocity E_w between nonhydrostatic and hydrostatic models. The units for $\partial\theta_0/\partial z = \beta$ are in °C/km. (From Martin 1981.)
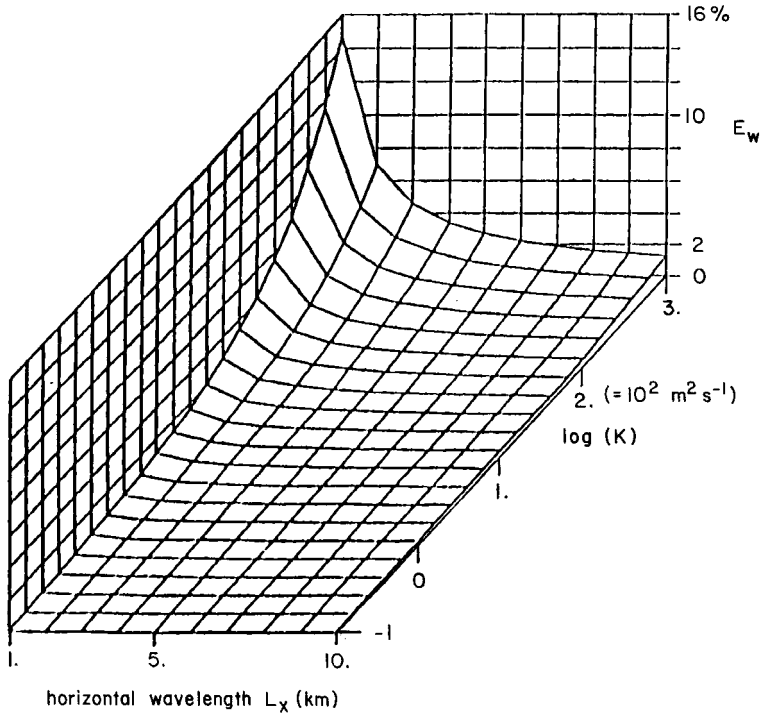
Fig. 5-6. Relative error in vertical velocity E_w between nonhydrostatic and hydrostatic models. The units for K are in $m^2 s^{-1}$. (From Martin 1981).

$K = 10^2$ m^2 s^{-1} and $L_x = 1$ km, for example, the maximum error is about 4%, whereas it increases to more than 14% for $K = 10^3$ m^2 s^{-1}.

These results are at variance with the conclusion reached by Wipperman (1981) and Orlanski (1981). Wipperman suggested that the hydrostatic assumption is valid only for horizontal scales larger than 10 km or so, whereas Orlanski claimed that $H_\alpha/\Delta x \ll 1$ is needed before the hydrostatic assumption can be accurately applied. However, both of these studies examined only frequency equations of the form given in Section 5.2.2, where no boundary conditions were applied. Thus their conclusion regarding the hydrostatic assumption, which is consistent with that given by Eq. (5-59), is valid only for meteorological systems where internal gravity wave propagation in the free atmosphere is the dominant disturbance. Consistent with Martin's (1981) result, Wipperman found the hydrostatic assumption to be valid for smaller scales when the atmosphere is more stable. He also stated that increased wind speed has the same effect as decreased thermal stability.

As illustrated here, such solutions provide insight into the physical mechanisms that generate and influence the strength of sea and land breezes. Unfortunately, in Defant's model, physical interactions such as the following are inappropriately represented, or not even included:

1.   The subgrid-scale parameterizations for σ and K are assumed to be independent of time and space, so that the intensity of the land breeze is equal to that of the sea breeze. Because vertical mixing is known to be reduced at night over land, however, the land breeze is usually observed to be more shallow and weaker than the sea breeze (e.g., Mahrer and Pielke 1977a; see also Section 13.1.1). Moreover, realistic parameterizations of the subgrid-scale mixing are nonlinear functions of the dependent variables, as discussed in Chapter 7.

2.   Advection of temperature and velocity are ignored. Even if the large-scale prevailing flow is zero, the marine air is known to move the region of maximum upward motion inland when a sea breeze occurs (e.g., Estoque 1961).

3.   The vertical profile of the large-scale potential temperature is assumed to be linear. In general, such a condition does not exist, and subgrid-scale mixing causes changes in potential temperature owing to curvature in the large scale as well as in the perturbation field.

4.   The surface temperature perturbation is prescribed, whereas in reality it is a function of the mesoscale circulation (e.g., Physick 1976; see also Figure 11-26).

5.   No interactions are permitted among the dependent variables. Although a necessary condition for obtaining analytic results, if $u'\,\partial' u'/\partial x$, for example, attains a magnitude on the order of $(1/\rho_0)(\partial p'/\partial x)$, nonlinear effects need to be considered.

Although some of these shortcomings were eliminated in later linear models (e.g., Smith 1957 included a linear advection term), it is still impossible to solve the conservation equations analytically when one or more of the terms involve products of dependent variables. Such nonlinear terms arise in the representation of the subgrid-scale processes, the source–sink terms, and the expression for advection. The effect of the nonlinear advection (e.g., $u'\partial u'/\partial x$, $u'\partial \theta'/\partial x$) on numerical model results for two values of surface heating in a sea-breeze model, as described by Martin (1981), is discussed in Chapter 11, Section 11.1.1.1, and illustrated by Figure (11-3). Those calculations show that the sea-breeze circulation becomes asymmetric owing to nonlinear advection for larger values of surface heating, which results in intensified low-level convergence and weakened low-level divergence. Such asymmetry develops because the advection enhances the convergence in the region of heating, thereby causing a larger horizontal pressure gradient. This increased pressure gradient generates additional convergence because of horizontal advection, and this *positive feedback* contin-

ues until surface frictional retardation, horizontal turbulent mixing, or cooling of the surface limits the horizontal velocity acceleration.

With regard to the hydrostatic assumption, however, the reduction in horizontal scale caused by nonlinear advection dictates that a complete nonlinear model must be used to more completely examine the importance of nonhydrostatic pressure forces when such advection is present. This question is examined in Chapter 12, Section 12.4.

5.2.3.2 *Further Exploration of the Nonhydrostatic Pressure Perturbations Using the Defant Model*

The Defant model can be used to investigate additional aspects of the nonhydrostatic and hydrostatic pressure components (Song *et al.* 1985). As shown in Section 5.2.3.1, when the hydrostatic assumption is made, $\lambda_1 = 0$; thus $\eta^2 = 0$, and a and b are obtained from

$$a_H^2 = b_H^2 = \frac{s}{2} \pm \frac{1}{2}(s^2 + 4\epsilon r)^{1/2} \tag{5-100}$$

$$a_H = \pm\sqrt{a_H^2}, \qquad b_H = \pm\sqrt{b_H^2} \tag{5-101}$$

where the subscript "H" of any quantity denotes hydrostatic and a_H and b_H are obtained in the same manner as a and b.

Since all of the prognostic variables are functions of a and b, we know that they will have different solutions if a_H and b_H replace a and b. Thus, to obtain the exact solution for the differences between the hydrostatic and nonhydrostatic quantities, we need to consider this difference in all of the prognostic variables in the governing equations.

The residual (i.e., nonhydrostatic) pressure perturbation (denoted by R, where $R \equiv p - p_H$) is obtained as follows:

$$\text{Take } \frac{\partial}{\partial x} \quad (1): \quad \frac{\partial^2 p}{\partial x^2} = -\frac{1}{\alpha_0}\frac{\partial}{\partial x}\frac{\partial u}{\partial t} + \frac{f}{\alpha_0}\frac{\partial v}{\partial x} - \frac{\sigma_x}{\alpha_0}\frac{\partial u}{\partial x} \tag{5-102}$$

$$\text{Take } \frac{\partial}{\partial z} \quad (3): \quad \frac{\partial^2 p}{\partial z^2} = -\frac{1}{\alpha_0}\frac{\partial}{\partial z}\frac{\partial w}{\partial t} + \frac{g}{\theta_0\alpha_0}\frac{\partial \theta}{\partial z} - \frac{\sigma_z\partial w}{\alpha_0\partial z}. \tag{5-103}$$

Similarly, for the hydrostatic system, we obtain

$$\frac{\partial^2 p_H}{\partial x^2} = -\frac{1}{\alpha_0}\frac{\partial}{\partial x}\frac{\partial u_H}{\partial t} + \frac{f}{\alpha_0}\frac{\partial v_H}{\partial x} - \frac{\sigma_x}{\sigma_0}\frac{\partial u_H}{\partial x} \tag{5-104}$$

$$\frac{\partial^2 p_H}{\partial z^2} = \frac{g}{\theta_0\alpha_0}\frac{\partial \theta_H}{\partial z}. \tag{5-105}$$

Subtracting Eq. (5-104) from (5-102), and (5-105) from (5-103) and adding the results yields the Poisson equation for the pressure residual term:

$$\nabla^2 R = -\frac{1}{\alpha_0}\frac{\partial}{\partial x}\frac{\partial}{\partial t}(u - u_H) + \frac{f}{\alpha_0}\frac{\partial}{\partial x}(v - v_H)$$

$$-\frac{\sigma_x}{\alpha_0}\frac{\partial}{\partial x}(u - u_H) + \frac{g}{\theta_o\alpha_0}\frac{\partial}{\partial z}(\theta - \theta_H)$$

$$-\frac{1}{\alpha_0}\frac{\partial}{\partial z}\frac{\partial w}{\partial t} - \frac{\sigma_z}{\alpha_0}\frac{\partial w}{\partial z}. \tag{5-106}$$

Using Defant's analytic solutions, listed in Eqs. (5-90)–(5-94), we have, for example, the first term on the right side of Eq. (5-106):

$$-\frac{1}{\alpha_0}\frac{\partial}{\partial x}\frac{\partial}{\partial t}(u - u_H) = \frac{i\omega r M}{\alpha_0}e^{i\omega t} \times \sin k_x x\left[\frac{a_H e^{a_H z} + b_H e^{-b_H z}}{b_H^2 - a_H^2} - \frac{ae^{az} + be^{-bz}}{b^2 - a^2}\right].$$

Similar expressions can be obtained for the other terms on the right side of Eq. (5-106). After rearrangement, the Poisson equation for the pressure residual can be rewritten as

$$\nabla^2 R = \frac{M}{\alpha_0}e^{i\omega t}\sin k_x x[Ae^{az} + Be^{-bz} + Ce^{a_H z} + De^{-b_H z}], \tag{5-107}$$

where

$$\left.\begin{array}{l} A = \dfrac{a}{b^2 - a^2}\left[\dfrac{-rf^2}{i\omega + \sigma_x} - r\sigma_x + r\sigma_z + \dfrac{g}{\theta_0}(b^2 - s)\right] \\[12pt] B = \dfrac{b}{b^2 - a^2}\left[\dfrac{rf^2}{i\omega + \sigma_x} - r\sigma_x + r\sigma_z + \dfrac{g}{\theta_0}(a^2 - s)\right] \\[12pt] C = \dfrac{a_H}{b_H^2 - a_H^2} \times \left[i\omega r + \dfrac{rf^2}{i\omega + \sigma_x} + r\sigma_x - \dfrac{g}{\theta_0}b_H^2 - s)\right] \\[12pt] D = \dfrac{b_H}{b_H^2 - a_H^2} \times \left[i\omega r + \dfrac{rf^2}{i\omega + \sigma_x} + r\sigma_x - \dfrac{g}{\theta_0}(a_H^2 - s)\right] \end{array}\right\} \tag{5-108}$$

Equations (5-107) and (5-108) provide the exact solution for the pressure residual term, which represents the analytic difference of pressure perturbation between hydrostatic and nonhydrostatic states in Defant's model. However, the formulation has quantities belonging to both states (the a, b and a_H, b_H) that need to be evaluated simultaneously. This means that the complete residual can be used for diagnostic purposes only if applied in a nonlinear numerical model, since it would be just as easy to use the complete anelastic equation for p.

To obtain a practical method that calculates nonhydrostatic effects using only information available from a hydrostatic model, following Pielke (1972), the equation for the quasi-nonhydrostatic residual (denoted by R_H) is obtained in the same manner as in Eqs. (5-102)–(5-106), except that the difference between hydrostatic and nonhydrostatic appears in only the time derivative term and the vertical friction term. Thus we have

$$\nabla^2 R_H = -\frac{1}{\alpha_0}\frac{\partial}{\partial x}\frac{\partial u}{\partial t} + \frac{1}{\alpha_0}\frac{\partial}{\partial x}\frac{\partial u_H}{\partial t} - \frac{1}{\alpha_0}\frac{\partial}{\partial z}\frac{\partial w}{\partial t} - \frac{\sigma_z}{\alpha_0}\frac{\partial w}{\partial z}.$$

Using the incompressible continuity, this equation is reduced to

$$\nabla^2 R_H = \frac{1}{\alpha_0}\frac{\partial}{\partial x}\frac{\partial u_H}{\partial t} - \frac{\sigma_z}{\alpha_0}\frac{\partial w}{\partial z}. \tag{5-109}$$

This is analogous to the form as applied in Pielke (1972) and Martin and Pielke (1983) in their numerical model evaluations.

Comparing Eq. (5-109) with Eq. (5-106), we see that Eq. (5-109) can be obtained directly from Eq. (5-106) by neglecting the differences between u, v, θ and u_H, v_H, θ_H and assuming incompressibility. Using the assumption of incompressibility, Eq. (5-109) becomes

$$\nabla^2 R_H = \frac{1}{\alpha_0}\frac{\partial}{\partial x}\frac{\partial u_H}{\partial t} + \frac{\sigma_z}{\alpha_0}\frac{\partial u_H}{\partial x}. \tag{5-110}$$

It is then clear that Eq. (5-110) is of practical value because only hydrostatic quantities are involved in the estimation of the nonhydrostatic effects, all of which can be obtained in a hydrostatic model. Also, comparing Eq. (5-110) with Eq. (5-106), we see that the neglected terms in the derivation of Eq. (5-110) are the first four terms in Eq. (5-106), which involve the immediate feedback associated with the buoyancy, horizontal friction, and the Coriolis terms.

In terms of Defant's analytic solutions, Eq. (5-110) is written as

$$\nabla^2 R_H = \frac{M}{\alpha_0} e^{i\omega t} \sin kx [C' e^{a_H z} + D' e^{-b_H z}], \tag{5-111}$$

where

$$C' = \frac{a_H}{b_H^2 - a_H^2}(i\omega r + r\sigma_z)$$

$$D' = \frac{b_H}{b_H^2 - a_H^2}(i\omega r + r\sigma_z).$$

The solutions for Eqs. (5-107) and (5-111) are obtained using the method of separation of variables. However, it is straightforward to show that the solution

for R_H is exactly the solution for R, except with a_H and b_H replacing a and b. Written formally, the solution for R is

$$R = \frac{M}{\alpha_0} e^{i\omega t} \sin k_x x \left[\frac{A}{a^2 - k_x^2} e^{az} + \frac{B}{b^2 - k_x^2} e^{-bz} \right.$$

$$\left. + \frac{C}{a_H^2 - k_x^2} e^{a_H z} + \frac{D}{b_H^2 - k_x^2} e^{-b_H z} \right], \qquad (5\text{-}112)$$

with A, B, C, and D defined in Eq. (5-108).

The pressure terms (p, p_H) and the residual terms (R, R_H) can be analyzed as functions of the horizontal length scale, large-scale stability, subgrid-scale heat diffusion, heating amplitude, and surface friction. The purpose of these analyses is to determine how the nonhydrostatic pressure residual varies with changing physical conditions within the framework of Defant's model. Furthermore, as stated before, since the nonhydrostatic effects are evaluated using Eqs. (5-107) and (5-108) instead of using $\lambda = 1$ in Defant's model, it seems necessary to show the consistency of the results obtained from the two independent procedures. Unless otherwise mentioned, the values of the parameters used for the examples are those listed in Table 5-1.

Figure 5-7 shows the maximum amplitude for the pressure terms (p, p_H) and the residual terms (R, R_H) as functions of horizontal length scale (L) plotted on a logarithmic scale. (All of the dependent variables in the following section and figures are presented at their maximum.) The range of scales is chosen from 200 m to 50 km, which should cover most of the spatial scales for which there is concern about the adequacy of the hydrostatic assumption in a model. Since the pressure perturbations are caused by surface heating in this study, and since all perturbation quantities decrease exponentially with height, the perturbations are evaluated near the surface $(z = 15$ m$)$. All of the pressure and the residual terms are given in units of millibars.

TABLE 5-1

Control Values for the Parameters

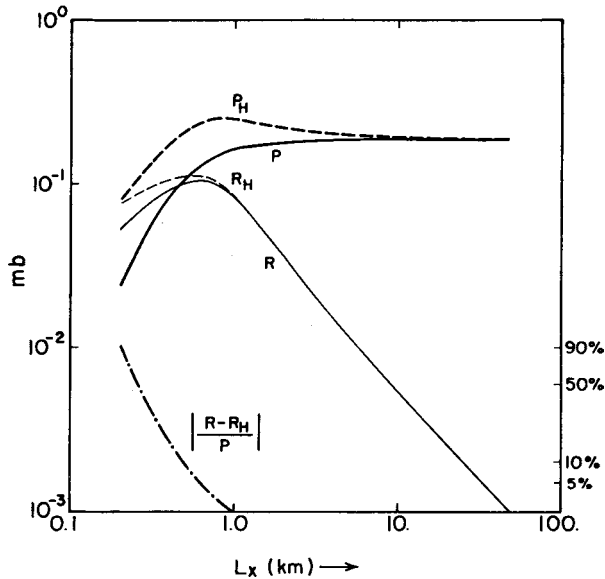|	
$\beta\left(= \frac{d\theta_0}{dz}\right)$	$0.01°C$ km^{-1}
K	10 m^2 s^{-1}
α_0	0.758 m^3 kg^{-1}
σ_x, σ_z	10^{-3}s^{-1}
P	1 h
θ_0	273 K
M	$10°C$
L	1 km
z	15 m
f	10^{-4}s^{-1}

Fig. 5-7. Variations of the pressure perturbation and the residual terms (p, p_H and R, R_H; mb) and the absolute error term ($|R - R_H|/|P|$, %) as a function of the horizontal length scale (L_x). Other physical parameters are given in Table 5-1. (From Song *et al.* 1985.)

As can be seen, when the length scale becomes large, p becomes nearly constant. The difference between p and p_H (i.e., R) becomes negligible for larger scales. This feature can be explained using the definitions of the parameters following Eq. (5-81): as $L \to \infty$, $k_x \to 0$, and $\eta^2 \to 0$, $r \to 0$; also, $s = s(\omega, k)$. Thus there is a decreasing dependence on the length scale as it becomes large, resulting in a nearly constant p. Also, it can be seen that there are virtually no differences between a, b and a_H, b_H when the scale is large.

For smaller scales, k^2 becomes large, and the situation is more complicated. From Figure 5-7, we see that for scales less than about 1 km, the residuals are of the same order of magnitude as the pressure terms. This indicates that for such small scales, the nonhydrostatic effect is significant and that p_H is significantly overestimating the true pressure perturbation. Pielke (1972, Figure 19) schematically illustrated how the hydrostatic pressure overestimates the real pressure.

What is also of interest here is how R_H behaves as compared to R. From Figure 5-7, we see that for length scales larger than about 1 km, there is essentially no difference between R and R_H, while for the smaller scales, this difference becomes significant. The quantity $|(R - R_H)/P|$, hereafter called the absolute error and expressed as a percentage, is also plotted. This measure illus-

trates how much error is introduced as a fraction of the true pressure perturbation, when R_H is used instead of the complete nonhydrostatic pressure residual R. Figure 5-7 shows that this absolute error drops to essentially 0 for $L > 1$ km, but increases sharply when $L < 1$ km. It is clear that under this near-neutral condition ($\beta = 0.01°C$ km^{-1}) with a surface heating of 10°C effective for 1 hour, the quasi-nonhydrostatic residual method gives an accurate measure of the nonhydrostatic effect for horizontal length scales as small as about 1 km.

The dependence of p, p_H, R, and R_H on the large-scale stability is illustrated for $L = 10$ km (Figure 5-8) and $L = 1$ km (Figure 5-9). The strength of the surface heating, the heating period, and the strength of the eddy heat diffusion are all the same as used to create Figure 5-7. In Figure 5-8, we see that for $L = 10$ km, the difference between p and p_H is negligible for all of the chosen stabilities (β; from 0.01 to 20°C km^{-1}). R_H and R, although they differ somewhat relative to each other, are both negligibly small compared to the pressure terms. Thus the absolute error term is very small for all of the chosen stabilities (with the largest error 1.5%, occurring at $\beta = 0.4°C$ km^{-1}). The result shown here indicates that for the scales normally considered in mesoscale analyses ($L = 10$ km or larger), in which the driving mechanism is surface heating and the upward transport of this heating occurs primarily through the associated turbulent eddy processes, the situation is approximately hydrostatic, and the residual method can be used to accurately calculate the small nonhydrostatic effects.
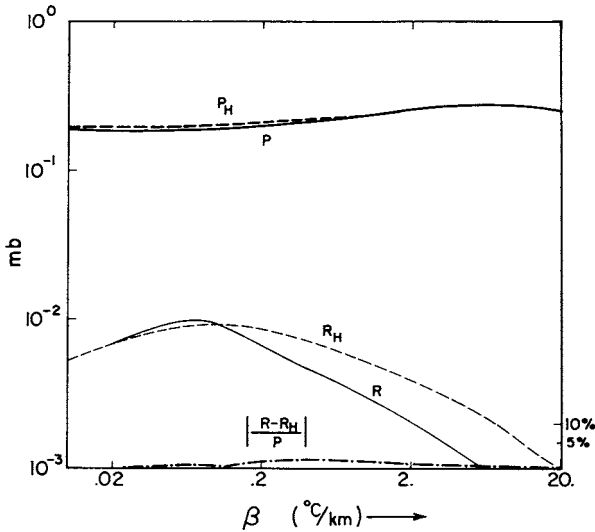

Fig. 5-8. As in Figure 5-7, except as a function of the stability parameter (β); $L_x = 10$ km. (From Song *et al.* 1985.)
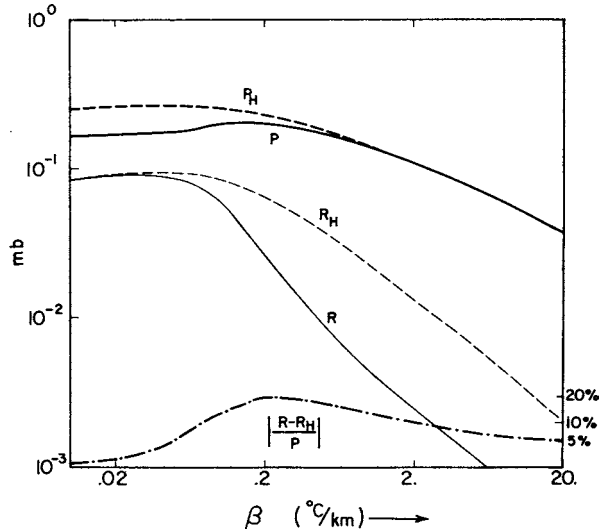
Fig. 5-9. As in Figure 5-8 with $L_x = 1$ km. (From Song *et al.* 1985.)

When the length scale is reduced to 1 km, however, the residuals become relatively larger than for the previous case, and, as seen in Figure 5-9, R_H departs significantly from R for a wide range of stabilities. Figure 5-9, shows that for the less stable situations ($\beta \leq 0.1°C$ km^{-1}), R_H differs more significantly from R.

The dependence of the pressure and the residual terms upon the strength of the eddy heat diffusion is shown in Figure 5-10. The horizontal length scale is 1 km, and the other parameters are the same as in the aforementioned cases. The range of the (constant) diffusion coefficient K is from 0.5 to 50 m^2 s^{-1}. Figure 5-10 shows that as the strength of eddy heat diffusion increases, the pressure perturbations increase. The hydrostatic pressure perturbation consistently exceeds the real pressure perturbation. For this small horizontal scale (1 km), the residual is the same order of magnitude as the pressure terms. Here R_H gives a very accurate measure of the nonhydrostatic effect associated with the vertical turbulent mixing of heat, except when the diffusion coefficient becomes very large.

Figures 5-11 and 5-12 illustrate the dependence of P, P_H, R, and R_H on the horizontal scale of heating for small K ($K = 1$ m^2 s^{-1}) and large K ($K = 50$ m^2 s^{-1}), respectively. Figure 5-11 shows that when the eddy heat diffusion is sufficiently small, R_H gives an accurate measure of the nonhydrostatic effects for scales as small as about 300 m. For very large diffusion (Figure 5-12), the residual is the same order of magnitude as the pressure for scales of a few kilometers or less. The absolute error is rather large for the small scales and drops to essentially 0 at scales greater than about 3 km. The
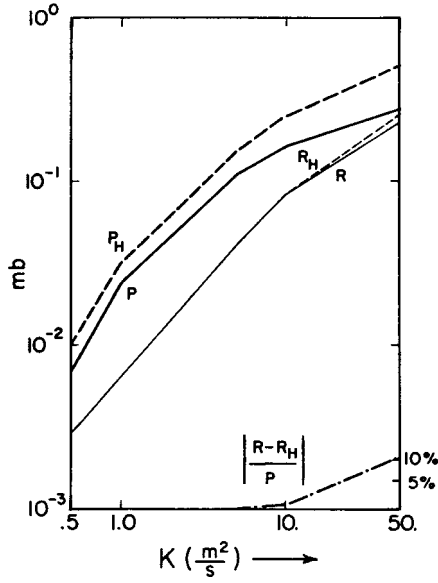
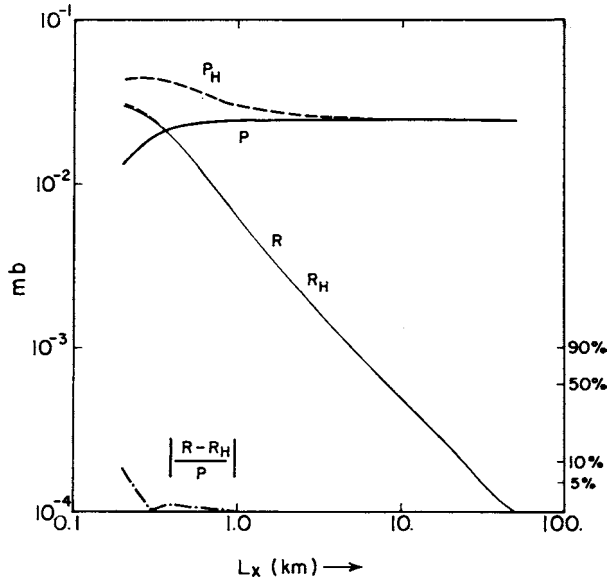**Fig. 5-10.** As in Figure 5-7, except as a function of the heat diffusion coefficient (K). (From Song *et al.* 1985.)

Fig. 5-11. As in Figure 5-7, except $K = 1.0$ m^2 s^{-1}. (From Song *et al.* 1985.)
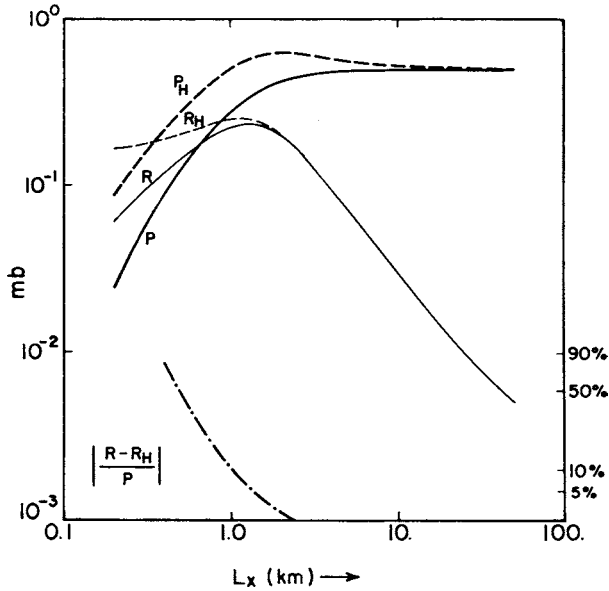
Fig. 5-12. As in Figure 5-7, except $K = 50 \text{ m}^2\text{s}^{-1}$. (From Song *et al.* 1985.)

increase of the nonhydrostatic effect with increasing strength of the eddy heat diffusion was also illustrated in Martin and Pielke (1983).

The discrepancy between R and R_H for very large K (Figure 5-10) is found only for small horizontal scales. Figure 5-12 shows that the same strength of heat diffusion ($K = 50 \text{ m}^2\text{s}^{-1}$), the difference between R and R_H is essentially zero at scales larger than about 3 km. This implies that when a strong energy input is coupled with a small horizontal scale, there may be buoyancy oscillations excited which cause departures of R_H from R. From Figures 5-11 and 5-12, we see that either increasing the horizontal scale or decreasing the strength of heat diffusion will minimize the discrepancy between R_H and R.

The strength of the surface heating is obviously important in producing non-hydrostatic effects. However, this forcing appears only as a constant in Defant's linear model [see Eq. (5-90) for $\tilde{\theta}(z)$], thus preventing the interactions between surface heating and mesoscale circulation from occurring.

Finally, the effect of the frictional term on pressure and the residual terms is shown in Figure 5-13. The physical parameters are the same as in Figure 5-7 except that the (constant) frictional coefficient is reduced by one order of magnitude. Comparing Figure 5-13 with Figure 5-7, we see that reducing the friction produces negligible effects on the pressure perturbations. The absolute error is within 2% for scales larger than about 2 km.
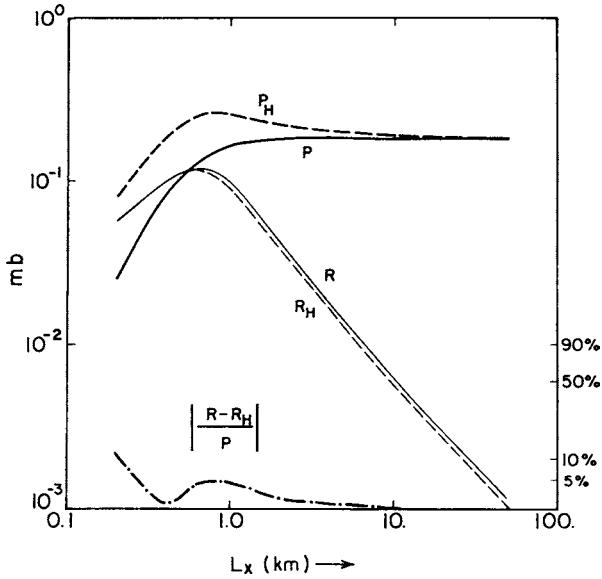
Fig. 5-13. As in Figure 5.7, except with a smaller Rayleigh friction coefficient (10^{-4}s^{-1}). (From Song *et al.* 1985.)

Two other different approximate residual formations (based on the Defant model) can be derived. Using Defant's linear model, the Orlanski (1981) pressure correction term is derived from a vertical integration of the local time derivative of the hydrostatically obtained vertical velocity. Written in an appropriate form for the comparisons here, the equation for the Orlanski residual (hereafter denoted by R_Q) is

$$\frac{\partial^2}{\partial z^2} R_Q = -\frac{1}{\alpha_0} \frac{\partial}{\partial z} \frac{\partial w_H}{\partial t}. \tag{5-113}$$

It is seen from Eqs. (5-106), (5-109), and (5-113) that R_Q can be derived from Eq. (5-106) by making, in addition to the simplifications made for obtaining R_H, two simplifications concerning the horizontal second derivative of the residual and the vertical friction term. This can be clearly seen if we compare the formal solutions for R_H and R_Q:

$$R_H = \frac{1}{\alpha_0} e^{i\omega t} \sin k_x x \left(\frac{rM}{b_H^2 - a_H^2} \right) \left[(i\omega) \left(\frac{a_H}{a_H^2 - k_x^2} e^{a_H z} + \frac{b_H}{b_H^2 - k_x^2} e^{-b_H z} \right) \right.$$
$$\left. + \sigma_z \left(\frac{a_H}{a_H^2 - k_x^2} e^{a_H z} + \frac{b_H}{b_H^2 - k_x^2} e^{-b_H z} \right) \right] \tag{5-114}$$

$$R_Q = \frac{1}{\alpha_0} e^{i\omega t} \sin k_x x \left(\frac{1}{rM} b_H^2 - a_H^2 \right) \times \left[(i\omega) \left(\frac{1}{a_H} e^{a_H z} + \frac{1}{b_H} e^{-b_H z} \right) \right]. \tag{5-115}$$

Neglecting the friction term, we see that R_Q can be obtained directly from R_H by setting k_x to 0. Thus when the horizontal scale of heating becomes large, in the absence of friction (which, as discussed previously, is a relatively small term), R_Q and R_H are asymptotic to the same value.

Mathematically, the quantity k_x^2 is associated with the x-direction second derivative of the residual, which is derived from the horizontal equation-of-motion in which the nonhydrostatic effect is explicitly included. That is, from Eq. (5-66), we have

$$\frac{\partial^2}{\partial x^2}(p - p_H) = -\frac{1}{\alpha_0}\frac{\partial}{\partial t}\frac{\partial}{\partial x}(u - u_H) + \frac{f}{\alpha_0}\frac{\partial}{\partial x}(u - u_H)$$

$$- \frac{\sigma_x}{\alpha_0}\frac{\partial}{\partial x}(u - u_H). \tag{5-116}$$

Therefore, setting k_x^2 to 0 is also equivalent to neglecting the nonhydrostatic horizontal momentum residual (i.e., the horizontal velocity residual).

Since in an incompressible system the horizontal velocity gradient is directly related to the generation of vertical acceleration [Eq. (5-69)], it is thought necessary to further examine the effect of neglecting k_x^2 (but retaining other important terms). For this purpose, a new residual (hereafter denoted by R_z) is considered which is obtained from the complete vertical equation of motion; that is

$$\frac{\partial^2}{\partial z^2}R_z = -\frac{1}{\alpha_0}\frac{\partial}{\partial z}\left(\frac{\partial w_H}{\partial t}\right) - \frac{\sigma_z}{\alpha_0}\frac{\partial w}{\partial z} + \frac{g}{\theta_0\alpha_0}\frac{\partial}{\partial z}(\theta - \theta_H). \tag{5-117}$$

Thus there are four different residuals to be compared: R, R_H, R_Q, and R_z, obtained from Eqs. (5-106), (5-109), (5-113), and (5-117), respectively. Aside from the friction and the Coriolis terms (which are not essential to the main conclusion), R_H and R_Q differ from R and R_z in that the former do not include the nonhydrostatic buoyancy residual [i.e., the potential temperature residual term, as in Eqs. (5-106) and (5-117)]. On the other hand, R_z and R_Q differ from R and R_H in that the former neglect the nonhydrostatic horizontal momentum residual or, equivalently, *they are based on the assumption of an infinite horizontal length scale.*

To have consistent numerical experiments with those in the previous section, the following computations are performed using, unless otherwise mentioned, the physical parameters listed in Table 5-1. Another set of experiments was also performed using the heating period of 12 hours. Since the general patterns of the residuals are similar using either 1 hour or 12 hours as the heating period, only the 1-hour results are analyzed here.

In Figure 5-14, the four residuals are plotted as functions of the horizontal length scale for three selected stabilities. For the scale range between about 1 and 10 km, the magnitude of the total pressure perturbations are on the order of 10^{-1} mb. We first see that for a given length scale, the nonhydrostatic residuals
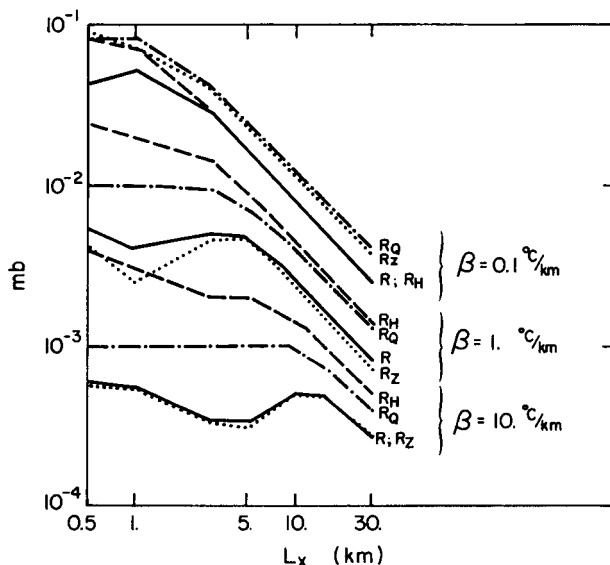
Fig. 5-14. The magnitudes (in mb) of the four residuals at $z = 15$ m: R (solid line), R_H (dashed line), R_z (dotted line), and R_Q (dashed-dotted line), as functions of the length scale and of three selected stabilities ($\beta = 0.1, 1, 10°C$ km^{-1}, as shown). (From Song *et al.* 1985.)

increase with decreasing stability. For the stable situation ($\beta = 10°C$ km^{-1}), all of the residuals are about two orders of magnitude smaller than the total pressure perturbation, while for the near-neutral situation ($\beta = 0.1°C$ km^{-1}), the residuals are comparable to the total pressure perturbation for the smaller length scales. For a given stability, the residuals are generally decreasing with increasing length scale. The closer to the neutral state, the greater the rate of decrease of the residuals with increasing length scale. An exception to this is the nonmonotonic variation of R and R_z in the more stable categories, which indicates that an optimal horizontal scale exists in which vertical acceleration is maximized as a result of contributions to convergence from opposite coasts (e.g., Abe and Yoshida 1982). This relative maximum is not as significant in the 12-hour period experiments.

With regard to the comparison among the residuals, Figure 5-14 shows that in the stable situation, R_z matches with R, while R_H and R_Q deviate from R. On the other hand, in the near-neutral situation, R_H matches with R, while R_Q and R_z deviate from R. To more clearly analyze the relative magnitudes of the residuals, vertical profiles of the residuals are plotted for a selected length scale (1 km) and for two stabilities: $\beta = 0.001°C$ km^{-1} (Figure 5-15), and $\beta = 10°C$ km^{-1} (Figure 5-16). The magnitudes of the corresponding total pressure perturbations
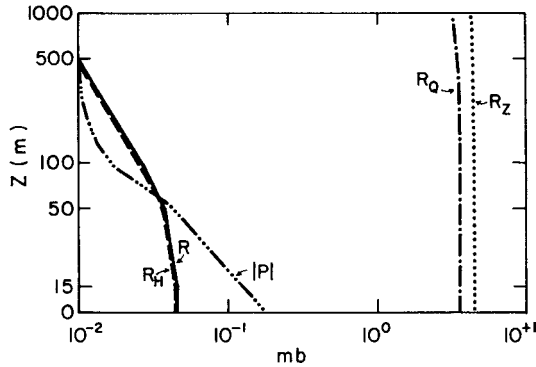
Fig. 5-15. Vertical profiles of the four residuals (with the same notations as in Figure 5-14) and $|p|$ for the near-neutral stability case ($\beta = 0.001°$C km^{-1}). The vertical levels are at $z = 0$, 15, 50, 100, 500, and 1000 m. (From Song *et al.* 1985.)

are also shown to indicate the possible absolute errors which are introduced when a certain residual is used.

Figure 5-15 shows that in the near-neutral situation, R_H matches with R everywhere, while R_z and R_Q are both about two orders of magnitude larger than R. Furthermore, both R_z and R_Q are around more than one order of magnitude larger than the total pressure perturbation. It seems clear that the R_Q approach should not be considered for the situations where the environmental stability is near neutral. On the other hand, R_H provides an accurate measure of the nonhydrostatic effect under the near-neutral condition.

Figure 5-16, shows that in the stable situation, R_z matches with R while R_Q and R_H deviate somewhat from R, with R_Q slightly better than R_H. In this case, however, all the residuals are almost more than two orders of magnitude smaller than the total pressure perturbation. Clearly, this result indicates that
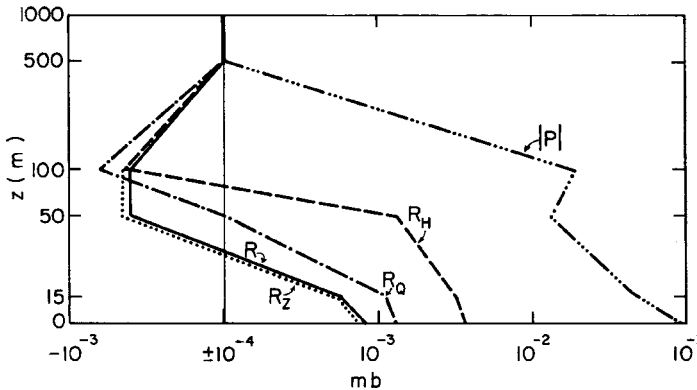

Fig. 5-16. As in Figure 5-15, except for $\beta = 10°$C km^{-1}. (From Song *et al.* 1985.)

nonhydrostatic effects are negligible in the stable situation, and thus the discrepancies are of little practical importance. As discussed previously, the difference between the exact residual and other residuals is related to the nonhydrostatic buoyancy and horizontal momentum residuals. That is, the horizontal momentum change and the buoyancy associated with the surface heating are the two most important physical mechanisms that contribute to the generation of nonhydrostatic effects for the situations considered in this study. The vertical profiles of θ and θ_H (Figure 5-17), and u and u_H (Figure 5-18), are plotted for the same length scale (1 km) and the same stabilities ($\beta = 0.001$; 10°C km^{-1}).

Figure 5-17 shows that θ is slightly larger than $\theta_H (\theta - \theta_H \leq 0.1°C)$ for the stable situation, while matching with each other everywhere in the near-neutral situation. This explains why R_Q and R_H [in which the $(\theta - \theta_H)$ term is neglected] deviate from R for the stable situation. Physically, this implies that for a system being heated from below, the more thermodynamically stable the system, the larger the fractional contribution of the nonhydrostatic buoyancy to the residual generated within the system. In the absolute sense, however, the nonhydrostatic effect is negligible in this case, as computed with the total pressure perturbation.
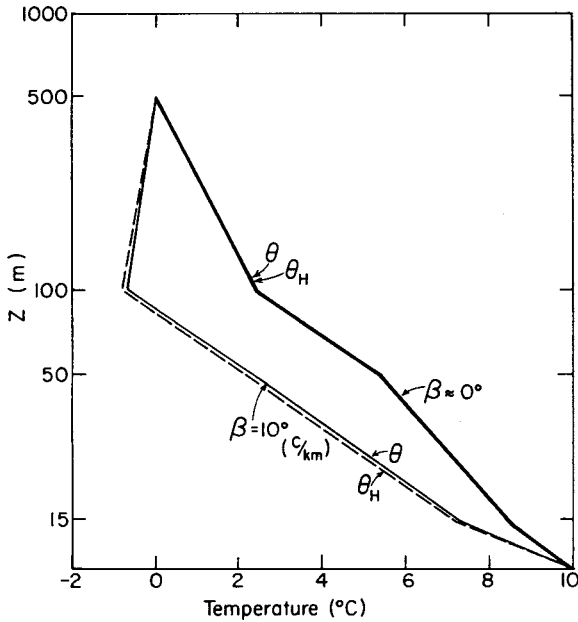

Fig. 5-17. Vertical profiles of θ (solid line) and θ_H (dashed line) for the near-neutral case (thick line) and the stable case (thin line.) (From Song *et al.* 1985.)
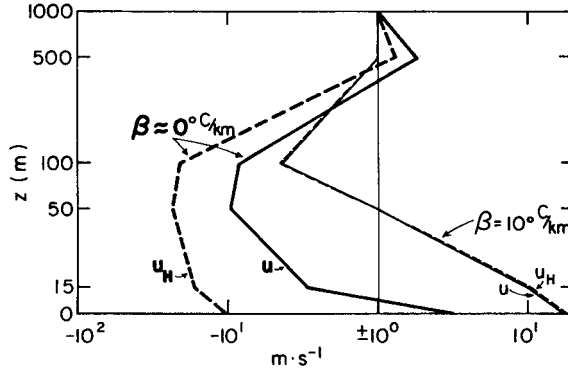
Fig. 5-18. Vertical profiles of u (solid line) and u_H (dashed line) for the neutral case (thick line) and the stable case (thin line.) (From Song *et al.* 1985.)

Figure 5-18 shows that for the stable situation u and u_H are almost equal, while for the near-neutral situation they differ significantly from each other. Again, this explains why R_Q and R_z [in which the $(u - u_H)$ term is neglected] deviate significantly from R in the near-neutral case, and R_H [which contains the $(u - u_H)$ term] matches with R. Physically, this implies that for an incompressible system, the closer the system's stability toward neutral stratification, the stronger the wind velocity generated within the system. Thus the horizontal momentum change plays a more important role in generating nonhydrostatic effects (i.e., vertical acceleration) compared to the situation with only weak horizontal velocity perturbations.

Finally, computations presented in Figures 5-14–5-18 were repeated for various β values between those of the very stable case ($\beta = 10°C$ km^{-1}) and the near-neutral case ($\beta = 0.001°C$ km^{-1}). These results, which are not shown, reflected intermediate features to those presented in these figures.

Defant's linear model is used to derive a mathematically exact solution for the nonhydrostatic pressure residual (total pressure perturbation minus hydrostatic pressure perturbation). From the complete form of this exact residual, we can see that the thermally induced nonhydrostatic effects are caused, within the linear framework, by physical processes such as horizontal momentum variations, buoyancy effects, frictional effects, and Coriolis effects. Since the complete residual requires simultaneous evaluation of hydrostatic and nonhydrostatic quantities, this residual can be used only in a diagnostic analysis for numerical modeling purposes. For the purpose of deriving a prognostic approach to incorporate nonhydrostatic effects into one or more subdomains of a mesoscale model, the complete residual must be simplified so as to neglect those terms that cannot be evaluated without a complete nonhydrostatic model.

One type of simplification made to the exact residual for the purpose of deriving a prognostic approach is to neglect the nonhydrostatic buoyancy residual term. Together with the incompressible continuity, this results in the residual approach introduced in Pielke (1972). Aside from the horizontal friction and the Coriolis terms (which are found to be not critical to the discussions of this study), the Pielke (1972) method differs from the exact residual only in the buoyancy residual term, which in the experiments performed in this study is relatively important only in the very thermally stable environments. For such stable situations, the nonhydrostatic pressure perturbations are generally about two orders of magnitude smaller than the total pressure perturbation. Thus the discrepancy between the approximate residual and the exact residual is of little practical importance.

For near-neutral stabilities, the Pielke (1972) residual approach has been found to be capable of providing accurate approximations to the true pressure perturbation, indicating that it is of practical value for evaluating nonhydrostatic effects within a subdomain of a mesoscale model when the environment is in a near-neutral state.

Another type of simplification is to neglect the nonhydrostatic horizontal momentum residual term. Within Defant's linear framework, this simplification results in the residual approach introduced in Orlanski (1981). It is found that this residual can be obtained from the exact residual by merely making an assumption that the involved horizontal length scale is very large (i.e., a wavenumber approaching 0). This simplification is equivalent to neglecting the nonhydrostatic velocity perturbation. The nonhydrostatic velocity (momentum) residual is relatively much more important in a near-neutral environment than in a stable environment. Neglecting this velocity residual causes the Orlanski residual to overestimate the nonhydrostatic pressure perturbation by about two orders of magnitude.

Physically, the previous results imply that for an incompressible system being heated from below, the actual pressure perturbation tends to depart from the hydrostatic pressure perturbation by an amount depending primarily on the system's environmental thermal stability and horizontal scale of heating. A sufficiently stable system has negligible nonhydrostatic effects. On the other hand, when the stability is near neutral, relatively stronger perturbations will develop that tend to more closely connect the vertical acceleration with the horizontal momentum variations. In such situations, a residual approach must include the nonhydrostatic momentum residual term, such as the approach of Pielke (1972), to accurately evaluate the nonhydrostatic effects. The residual approach presented here can be applied for subregions within a mesoscale model where vertical accelerations are large, while the hydrostatic assumption can be applied in the remainder of the model. At the boundaries of the model subdomain, the

boundary condition $R_H = 0$ would be applied in the solution of the nonlinear form of Eq. (5-109).

Other studies that have explored the differences in results when hydrostatic and nonhydrostatic versions of a model are used include Sun (1984a), Rõõm and Männik (1999), Cassano and Parish (2000), and Crook and Klemp (2000).

5.3 Long's Analytic Solution to Nonlinear Momentum Flow

There are special cases of exact solutions to nonlinear atmospheric flow. The Long (1953, 1955) model is one of these cases. Long's solutions are valid only for the special case when the flow is steady state and the density multiplied by the domain-averaged horizontal velocity squared is independent of height. The limitations of Long's solution to actual stratified flows over an obstacle is discussed by Baines (1977). Durran (1981) has referenced studies by other investigators who obtained exact solutions for specialized sets of the nonlinear conservation equations.

The derivation of Long's (1953) exact solution is straightforward. Assuming incompressibility[9] [see Eq. (4-23), right-side expression], Eq. (4-10) for $i = 1$ and 3 can be written as

$$\bar{\rho}\frac{\partial}{\partial x}\left(\frac{\bar{u}^2 + \bar{w}^2}{2}\right) - \left(\frac{\partial \bar{w}}{\partial x} - \frac{\partial \bar{u}}{\partial z}\right)\bar{\rho}\bar{w} = -\frac{\partial \bar{p}}{\partial x} \tag{5-118}$$

$$\bar{\rho}\frac{\partial}{\partial z}\left(\frac{\bar{u}^2 + \bar{w}^2}{2}\right) + \left(\frac{\partial \bar{w}}{\partial x} - \frac{\partial \bar{u}}{\partial z}\right)\bar{\rho}\bar{u} = -\frac{\partial \bar{p}}{\partial z} - \bar{\rho}g, \tag{5-119}$$

where steady-state conditions have been assumed and the Coriolis and subgrid mixing effects have been neglected. Differentiating Eq. (5-118) with respect to z and Eq. (5-119) with respect to x and subtracting the first equation from the second yields

$$\bar{u}\frac{\partial}{\partial x}\left(\frac{\partial \bar{w}}{\partial x} - \frac{\partial \bar{u}}{\partial z}\right) + \bar{w}\frac{\partial}{\partial z}\left(\frac{\partial \bar{w}}{\partial x} - \frac{\partial \bar{u}}{\partial z}\right) + \frac{1}{\bar{\rho}}\frac{\partial \bar{\rho}}{\partial x}\frac{\partial}{\partial z}\left(\frac{\bar{u}^2 + \bar{w}^2}{2}\right)$$
$$-\frac{1}{\bar{\rho}}\frac{\partial \bar{\rho}}{\partial z}\frac{\partial}{\partial x}\left(\frac{\bar{u}^2 + \bar{w}^2}{2}\right) + \frac{1}{\bar{\rho}}\frac{\partial \bar{\rho}}{\partial x}g + \left(\frac{\partial \bar{w}}{\partial x} - \frac{\partial \bar{u}}{\partial z}\right)\left(\bar{u}\frac{\partial \bar{\rho}}{\partial x} + \bar{w}\frac{\partial \bar{\rho}}{\partial z}\right) = 0. \tag{5-120}$$

Using the definition of vorticity[10] given by $\bar{\xi}_2 = \epsilon_{2qi}\partial \bar{u}_i/\partial x_q$, requiring that density surfaces form a material surface [i.e., $d\bar{\rho}/dt = \bar{u}(\partial \bar{\rho}/\partial x) + \bar{w}(\partial \bar{\rho}/\partial z) = 0$ with $\partial \bar{\rho}/\partial t = 0$, since a steady-state assumption has been applied][11], and writing $\bar{u}^2 + \bar{w}^2 = \bar{q}^2$, Eq (5-120) can be written as

$$\frac{d\xi_2}{dt} + \frac{1}{\bar{\rho}}\frac{\partial \bar{\rho}}{\partial x}\frac{\partial \bar{q}^2/2}{\partial z} - \frac{1}{\bar{\rho}}\frac{\partial \bar{\rho}}{\partial z}\frac{\partial \bar{q}^2/2}{\partial x} + \frac{1}{\bar{\rho}}\frac{\partial \bar{\rho}}{\partial x}g = 0. \tag{5-121}$$

Defining the streamlines using the stream function $\psi(x, z)$ so that

$$\bar{u} = -\frac{\partial \psi}{\partial z} \qquad \text{and} \qquad \bar{w} = \frac{\partial \psi}{\partial x} \qquad (5\text{-}122)$$

[i.e., $(\partial \bar{u}/\partial x) + (\partial \bar{w}/\partial z) = (\partial^2 \psi/\partial z \partial x) - (\partial^2 \psi/\partial x \partial z) = 0$]; then Eq. (5-121) can be rewritten as

$$\frac{d\xi_2}{dt} + \frac{1}{\bar{\rho}} \frac{d\bar{\rho}}{d\psi} \left(-\frac{\partial \psi}{\partial z} \frac{\partial \bar{q}^2/2}{\partial x} + \frac{\partial \psi}{\partial x} \frac{\partial \bar{q}^2/2}{\partial z} \right) + \frac{g}{\bar{\rho}} \frac{d\bar{\rho}}{d\psi} \frac{\partial \psi}{\partial x} = 0 \qquad (5\text{-}123)$$

In Eq. (5-123), density is defined in the form $\bar{\rho} = \bar{\rho}(\psi)$, and the chain rule of calculus with $\psi = \psi(x, z)$ is used. Using the definitions of $\bar{u}$ and $\bar{w}$ given by Eq. (5-122), Eq. (5-123) can be rewritten as

$$\frac{d}{dt} \left[\xi_2 + \frac{1}{\bar{\rho}} \frac{d\bar{\rho}}{d\psi} \left(\frac{\bar{q}^2}{2} + gz \right) \right] = 0, \qquad (5\text{-}124)$$

where the definition of $\bar{w} = dz/dt$ and the requirement $d\bar{\rho}/dt = (d/dt) \times (\partial \bar{\rho}/\partial \psi) = 0$ have been used. Using the definition of the stream function given by Eq. (5-122), Eq. (5-124) can be rewritten as

$$\frac{d}{dt} \left[\nabla^2 \psi + \frac{1}{\bar{\rho}} \frac{d\bar{\rho}}{d\psi} \left(\frac{\bar{q}^2}{2} + gz \right) \right] = 0,$$

which can be integrated to yield

$$\nabla^2 \psi + \frac{1}{\bar{\rho}} \frac{d\bar{\rho}}{d\psi} \left(\frac{\bar{q}^2}{2} + gz \right) = \beta \psi, \qquad (5\text{-}125)$$

where the integration constant β is a function of ψ since the definition of a stream function requires that $d\psi/dt = 0$.

Far upstream from an obstacle, Eq. (5-125) dictates that

$$\beta(\psi) = \xi_{2_0}(\psi) + \frac{1}{\bar{\rho}} \frac{d\bar{\rho}}{d\psi} \left(\frac{u_0^2}{2} + gh_0 \right),$$

where $\xi_{2_0}(\psi)$ is the upstream vorticity; u_0 is the synoptic wind flow, which can be a function of height (with w_0 assumed to equal 0); and $h_0(\psi)$ represents the upwind streamline heights, where $\partial \psi/\partial x = 0$. With this definition of the integration constant, Eq. (5-125) can be written as

$$\nabla^2 \psi + \frac{1}{\bar{\rho}} \frac{d\bar{\rho}}{d\psi} \frac{\bar{q}^2}{2} = \xi_{2_0}(\psi) + \frac{1}{\bar{\rho}} \frac{d\bar{\rho}}{d\psi} \left[\frac{u_0^2}{2} + g(h_0 - z) \right]. \qquad (5\text{-}126)$$

Using the definition of the stream function given by Eq. (5-122) evaluated far upstream and the chain rule of calculus,

$$\frac{d}{d\psi} = -\frac{1}{u_0} \frac{d}{dh_0} \qquad \text{and} \qquad -u_0 \frac{\partial^2 h_0}{\partial z^2} = -u_0 \nabla^2 h_0 = \nabla^2 \psi.$$

Thus Eq. (5-126) can be rewritten, after rearranging, as

$$\frac{\partial^2 h_0}{\partial z^2} + \frac{1}{2}\frac{d\ln\bar{\rho}u_0^2}{dh_0}\left[\frac{\bar{q}^2}{u_0^2} - 1\right] = \frac{g}{\bar{\rho}u_0^2}\frac{d\bar{\rho}}{dh_0}(h_0 - z). \qquad (5\text{-}127)$$

In obtaining Eq. (5-127), the condition that u_0 is a constant has been used. Defining $\delta = z - h_0$, Eq. (5-127) can be written as

$$\frac{\partial^2 \delta}{\partial z^2} + \frac{1}{2}\left[\frac{d}{dh_0}\ln\bar{\rho}u_0^2\right]\left[\frac{\bar{q}^2}{u_0^2} - 1\right] = \frac{g}{\bar{\rho}u_0^2}\frac{d\bar{\rho}}{dh_0}\delta. \qquad (5\text{-}128)$$

As evident from Eq. (5-128), a linear solution is possible if $\bar{\rho}u_0^2$ is a constant, so that Eq. (5-128) reduces to

$$\frac{\partial^2 \delta}{\partial z^2} + \sigma^2\delta = 0, \qquad (5\text{-}129)$$

where

$$\sigma^2 = -\frac{g}{\bar{\rho}u_0^2}\frac{d\bar{\rho}}{dh_0},$$

with $\bar{\rho}$ linear[12] in h_0.

Lilly and Klemp (1979) provide solutions to Eq. (5-129) for a wide range of terrain shapes, $z_G(x)$, where the bottom boundary condition needed to solve Eq. (5-129) is given by

$$\delta(x, z_G) = z_G(x), \qquad (5\text{-}130)$$

and the upper boundary is defined such that upward propagating energy exits the model domain without reflection (i.e., a *radiative boundary condition*; see Section 11.3.2). As adapted from the analysis of Lilly and Klemp, and as can be verified by substitution, the solution to Eq. (5-129) can be written as

$$\delta(x, z) = a_1(x)e^{-i\sigma(z-z_G)} + a_2(x)e^{+i\sigma(z-z_G)}, \qquad (5\text{-}131)$$

where $a_1(x)$ and $a_2(x)$ are integration constants and are in general complex functions of x. Since by Eq. (5-130), $\delta(x, z_G)$ is a real quantity, a_2 must be equal to the complex conjugate of a_1. Hence Eq. (5-131) can be written as

$$\delta(x, z) = \text{Re}\{Z_G e^{-i\sigma(z-z_G)}\} = \frac{1}{2}\{Z_G e^{-i\sigma(z-z_G)} + Z_G^* e^{i\sigma(z-z_G)}\}, \qquad (5\text{-}132)$$

where $2a_1(x) = Z_G = z_G + iz_{G_i}$ and $2a_2(x) = Z_G^* = z_G - iz_{G_i}$. Here Re indicates that only the real portion of the expression in the braces is used. The complex conjugate of Z_G is Z_G^*.

Evaluating Eq. (5-132) at $z = 0$ yields

$$\delta(x, 0) = \frac{1}{2}\{Z_G e^{i\sigma z_G} + Z_G^* e^{-i\sigma z_G}\} = \int_{-\infty}^{\infty} \tilde{\delta}(k_x, 0)e^{ik_x x}dk_x, \qquad (5\text{-}133)$$

where the right side of Eq. (5-133) is the Fourier transform[13] of the displacement height at $z = 0$. The inverse transform of Eq. (5-133) is defined as

$$\tilde{\delta}(k_x, 0) = \frac{1}{2\pi}\int_{-\infty}^{\infty} \delta(x, 0)e^{-ik_x x}dx. \qquad (5\text{-}134)$$

The vertical group velocity of internal gravity waves generated by terrain is upward in the troposphere if there is no reflection or dissipation of wave energy in the troposphere. For this situation, the wave disturbance is dissipated at higher levels. However, below the region of dissipation, some of this energy can be reflected back downward as a result of such effects as large changes in the height of the vertical gradients of velocity and thermodynamic stability. Dissipation of the vertically propagating wave energy can occur because of turbulence within the troposphere or stratosphere, or through the excitation of horizontally propagating waves.

The vertical group velocity can be computed from Eq. (5-58) for the forced hydrostatic airflow over terrain situation where ω^2 is replaced with $(\omega - u_0 k_x)^2$. The frequency $u_0 k_x$ is subtracted from ω since a nonzero base current (i.e., $u_0 \neq 0$) acts to change the time period of a parcel within a wave. In a linear representation, the frequency depends directly on the large-scale wind speed and inversely on the horizontal wavelength. In the derivation of Eq. (5-58), $u_0 = 0$ was assumed.

The modified form of Eq. (5-58) (applicable to hydrostatic flow) is then written as

$$(\omega - u_0 k_x)^2 = \frac{k_x^2}{k_z^2}\frac{g}{\theta_0}\frac{\partial\theta_0}{\partial z}. \qquad (5\text{-}135)$$

Using the ideal gas law [Eq. (2-49)] and definition of potential temperature [Eq. (2-48)] evaluated for the domain-averaged [i.e., Eq. (4-12)] values, differentiating logarithmically with respect to height and substituting for the hydrostatic relation $\partial p_0/\partial z = -\rho_0 g$ and for the speed of sound c_a [see Eq. (5-49)] yields the alternative expression for Eq. (5-135), given as

$$(\omega - u_0 k_x)^2 = \frac{-k_x^2}{k_z^2}\left[\frac{g}{\rho_0}\frac{\partial\rho_0}{\partial z} - \frac{g^2}{c_a^2}\right]. \qquad (5\text{-}136)$$

For realistic values in Eq. (5-136), $|(1/\rho_0)\partial\rho_0/\partial z| \simeq 1/(8 \text{ km})$ (see Figure 3-1) and $g/c_a^2 \simeq 1/(12 \text{ km})$, so the two terms are of the same order. To evaluate the direction of wave energy propagation, however, the second term in the brackets in Eq. (5-136) is dropped. (No loss of generality results, because both terms

are of the same sign.) Thus with $\rho_0 \simeq \bar{\rho}$ [see Eq. (4-9)], Eq. (5-136) can be represented as

$$(\omega - u_0 k_x)^2 \simeq \frac{-k_x^2}{k_z^2} \frac{g}{\bar{\rho}} \frac{\partial \bar{\rho}}{\partial z}. \tag{5-137}$$

From Eq. (5-65), the vertical group velocity is given by $c_{g_z} = -\partial \omega / \partial k_z$. Therefore, differentiating Eq. (5-137) with respect to k_z and rearranging yields

$$c_{g_z} = -(\omega - u_0 k_x)/k_z, \tag{5-138}$$

so that the group velocity is upward as long as k_x and k_z are of the same sign, $\omega = 0$ and $u_0 > 0$.

Rearranging Eq. (5-137) and solving for k_z gives

$$k_z = \pm \frac{k_x}{(\omega - u_0 k_x)} \left(\frac{-g}{\bar{\rho}} \frac{\partial \bar{\rho}}{\partial z} \right)^{1/2} = \pm \frac{k_x}{(\omega - u_0 k_x)} \left(\frac{-g}{\bar{\rho}} \frac{d\bar{\rho}}{dh_0} \right)^{1/2}, \tag{5-139}$$

where $\partial \bar{\rho} / \partial z = d\bar{\rho}/dh_0$ is used to define the vertical density gradient. Equation (5-138) is then written as

$$c_{g_z} = \mp (\omega - u_0 k_x)^2 \Big/ k_x \left(\frac{-g}{\bar{\rho}} \frac{d\bar{\rho}}{dh_0} \right)^{1/2}. \tag{5-140}$$

For the steady-state situation represented by Long's equation [Eq. (5-129)], $\omega = 0$, so Eq. (5-140) reduces to

$$c_{g_z} = \pm |u_0| k_x \Big/ \left(-\frac{g}{\bar{\rho} u_0^2} \frac{d\bar{\rho}}{dh_0} \right)^{1/2} = \pm \frac{|u_0| k_x}{\sigma}. \tag{5-141}$$

From Eq. (5-141), the group velocity of these internal gravity waves is directly proportional to the prevailing wind speed and inversely proportional to the vertical thermodynamic stability. The quantity σ is often called the *Scorer parameter* (also discussed in Section 13.1.4).

Since from Eq. (5-138), only upward group velocities occur when the flow is assumed to be constant with time and no dissipation or reflection of wave energy is permitted, Eq. (5-133) can be partitioned into

$$Z_G e^{i\sigma z_G} = \frac{1}{\pi} \int_{-\infty}^{\infty} \delta(\hat{x}, 0) \int_0^{\infty} e^{ik_x(x-\hat{x})} dk_x d\hat{x}$$

$$Z_G^* e^{-i\sigma z_G} = \frac{1}{\pi} \int_{-\infty}^{\infty} \delta(\hat{x}, 0) \int_{-\infty}^0 e^{ik_x(x-\hat{x})} dk_x d\hat{x}, \tag{5-142}$$

where Eq. (5-134) has been used to substitute for $\tilde{\delta}(k_x, 0)$ and the order of integration has been reversed. The partitioning is permitted to ensure an upward

group velocity $-\sigma = k_z$ when $k_x < 0$ and $\sigma = k_z$ when $k_x > 0$, thereby requiring the removal of $Z_G^* e^{i\sigma z_G}$ with $k_x > 0$ and $Z_G e^{i\sigma z_G}$ with $k_x < 0$.

The right-side integrals of Eq. (5-142) are evaluated using the relation

$$\int_{\infty}^{\infty} e^{ik_x(x-\hat{x})} dk_x = 2\pi \Delta(x - \hat{x}), \tag{5-143}$$

where the term on the right side arises from the definition of the delta function.[14] Equation (5-143) can be rewritten as

$$\int_{-\infty}^{0} e^{ik_x(x-\hat{x})} dk_x = 2\pi \Delta(x - \hat{x}) - \int_{0}^{\infty} e^{ik_x(x-\hat{x})} dk_x$$

$$\int_{0}^{\infty} e^{ik_x(x-\hat{x})} dk_x = 2\pi \Delta(x - \hat{x}) - \int_{-\infty}^{0} e^{ik_x(x-\hat{x})} dk_x, \tag{5-144}$$

where the integrals needed in Eq. (5-142) are on the left side.

The integrals on the right side of Eq. (5-144) can be written as

$$\int_{0}^{\infty} e^{ik_x(x-\hat{x})} dk_x = \int_{-\infty}^{0} e^{ik_x(\hat{x}-x)} dk_x = \pi \Delta(x - \hat{x}) + \frac{i}{\hat{x} - x},$$

where, since the real part of the left side of Eq. (5-143) is symmetric around $k_x = 0$, the term with the Dirac delta function is also symmetric. Substituting the relations given by Eq. (5-144) into Eq. (5-142), and using the evaluation for the right-side integrals in Eq. (5-144), yields

$$Z_G e^{i\sigma z_G} = \frac{1}{\pi} \int_{\infty}^{\infty} \left[\pi \Delta(x - \hat{x}) - \frac{i}{\hat{x} - x} \right] \delta(\hat{x}, 0) d\hat{x}$$

$$Z_G^* e^{-i\sigma z_G} = \frac{1}{\pi} \int_{\infty}^{\infty} \left[\pi \Delta(x - \hat{x}) - \frac{i}{\hat{x} - x} \right] \delta(\hat{x}, 0) d\hat{x}. \tag{5-145}$$

Multiplying through by i and expanding the left side of Eq. (5-145) gives

$$i(z_G \cos \sigma z_G - z_{G_i} \sin \sigma z_G) - z_{G_i} \cos \sigma z_G - z_G \sin \sigma z_G$$

$$= \frac{1}{\pi} \int_{-\infty}^{\infty} \left[\pi i \, \Delta(x - \hat{x}) + \frac{1}{\hat{x} - x} \right] \delta(\hat{x}, 0) d\hat{x}$$

$$i(z_G \cos \sigma z_G - z_{G_i} \sin \sigma z_G) + z_{G_i} \cos \sigma z_G + z_G \sin \sigma z_G$$

$$= \frac{1}{\pi} \int_{-\infty}^{\infty} \left[\pi i \, \Delta(x - \hat{x}) - \frac{1}{\hat{x} - x} \right] \delta(\hat{x}, 0) d\hat{x}. \tag{5-146}$$

Subtracting the top equation in Eq. (5-146) from the bottom one yields

$$z_{G_i} \cos \sigma z_G + z_G \sin \sigma z_G = -\frac{1}{\pi} \int_{-\infty}^{\infty} \frac{(z_G \cos \sigma z_G - z_{G_i} \sin \sigma z_G)}{\hat{x} - x} d\hat{x}, \tag{5-147}$$

where $\delta(x, 0)$ from the middle formulation of Eq. (5-133) has been used.

The evaluation of Eq. (5-147) must include the influence of the singularity when $\hat{x} = x$. Mathematical techniques have been developed to handle this type of integral; the right side of this expression is a Hilbert transform[15] of $z_G \cos \sigma z_G - z_{G_i} \sin \sigma z_G$. The inverse Hilbert transform is skew-symmetric (i.e., of the same form except with a minus sign), so that the inverse transform of Eq. (5-147) is

$$z_G \cos \sigma z_G - z_{G_i} \sin \sigma z_G = -\frac{1}{\pi} \int_{-\infty}^{\infty} \frac{(z_{G_i} \cos \sigma z_G + z_G \sin \sigma z_G)}{x - \hat{x}} d\hat{x}. \quad (5\text{-}148)$$

Multiplying Eq. (5-147) by $\cos \sigma z_G$ and Eq. (5-148) by $\sin \sigma z_G$ and subtracting the second equation from the first yields

$$z_{G_i}(x) = -\frac{1}{\pi} \int_{-\infty}^{\infty} \left\{ \frac{z_G(\hat{x}) \cos \sigma[z_G(\hat{x}) - z_G(x)] - z_{G_i}(\hat{x}) \sin \sigma[z_G(\hat{x}) - z_G(x)]}{x - \hat{x}} \right\} d\hat{x}. \quad (5\text{-}149)$$

Multiplying Eq. (5-147) by $\sin \sigma z_G$ and Eq. (5-148) by $\cos \sigma z_G$ and adding the two resulting equations gives

$$z_G(x) = \frac{1}{\pi} \int_{-\infty}^{\infty} \left\{ \frac{z_G(\hat{x}) \sin \sigma[z_G(\hat{x}) - z_G(x)] + z_{G_i}(\hat{x}) \cos \sigma[z_G(\hat{x}) - z_G(x)]}{x - \hat{x}} \right\} d\hat{x}. \quad (5\text{-}150)$$

Equation (5-149) can be rewritten as

$$z_{G_i}(x) = (-1/\pi) \int_{-\infty}^{\infty} \{z_G(\hat{x})(\cos \sigma[z_G(\hat{x}) - z_G(x)] - 1).$$
$$- z_{G_i}(\hat{x}) \sin \sigma[z_G(\hat{x}) - z_G(x)]\}/(x - \hat{x}) d\hat{x}$$
$$- \frac{1}{\pi} \int_{-\infty}^{\infty} \frac{z_G(\hat{x})}{x - \hat{x}} d\hat{x} \quad (5\text{-}151)$$

to avoid the singularity at $x = \hat{x}$. When $z_G(x)$ is a known analytic function, the first term in the first integral in Eq. (5-151) and the last term in Eq. (5-151) generally can be evaluated exactly. However, because z_{G_i} is in the middle term of Eq. (5-151), an iterative evaluation for z_{G_i} is required, where the first guess can be obtained by neglecting the middle term. Satisfactory convergence can be defined by substituting z_{G_i} into Eq. (5-150) and determining whether the calculated value of z_G agrees within certain limits of the known value of z_G used in Eq. (5-151).

Lilly and Klemp (1979) presented several results using this solution technique. Among their major conclusions, they found that the wave amplitude caused by forced airflow over rough terrain is enhanced for mountains with gentle windward and steep leeward slopes. Their solutions of Long's equation [Eq. (5-129)] provides an effective mechanism for examining the fidelity of numerical model results. Carruthers and Choularton (1982), for example, con-

trasted their results with those of Lilly and Klemp to investigate the influence of boundary conditions on a solution of airflow over rough terrain. However, Laprise and Peltier (1989a) used a linear stability analysis to show that Long's steady-state solution is unstable when the terrain is high enough to cause local overturning of the streamlines. In a related paper (Laprise and Peltier 1989b), used the Long steady-state solution as a tendency-free initial state for their time-dependent numerical model. Another example of the application of the Long model is presented in Hu *et al.* (1988).

Notes to Chapter 5

1. Exact solutions are also referred to as *analytic* solutions.

2. A two-by-two determinant, $\begin{vmatrix} a_{11} & a_{12} \\ a_{21} & a_{22} \end{vmatrix}$ is equal to $a_{11}a_{22} - a_{21}a_{12}$.

3. The following material is based on the analysis given in Holton (1972:169–171).

4. The introduction of symbolic algebra (e.g., Hearn 1973) onto computers has removed much of the drudgery associated with expanding such large determinants. Derickson and Pielke (2000) have used this technique to investigate the influence of nonlinear interactions associated with advection.

5. The quantity $[(g/\theta_0)\partial\theta_0/\partial z]^{1/2}$ is called the *Brunt–Väisälä frequency*. Durran and Klemp (1982a) discuss the proper form of the Brunt–Väisälä frequency in a saturated atmosphere.

6. In the atmosphere, if $\partial\theta_0/\partial z = 0$, then, using the ideal gas law and definition of potential temperature, it can be shown that ρ_0 will decrease with height. In the analysis used to obtain Eq. (5-61), this change of density with height is ignored.

7. If only the hydrostatic assumption is made, then a periodic motion called the *Lamb wave* can occur that has a speed on the same order as sound waves (see, e.g., Haltiner and Williams 1980:35). Pielke *et al.* (1993a) and Nicholls and Pielke (1994a,b; 2000) show how the magnitude of the Lamb wave can be directly associated with the magnitude of diabatic heating in cumulus convection. Bannon (1995) discusses how the Lamb wave is related to hydrostatic adjustment. Tijm and Van Delden (1998) discuss the role of sound waves in sea breezes. Rõõm and Männik (1999) conclude that a linear nonhydrostatic compressible model provides the most realistic simulation at all spatial scales, but that the hydrostatic version is equally as accurate at space scales from 10 km to 500–700 km.

8. Egger (1999) provides the solution for inertial motion when more complete versions of the equations are retained.

9. As discussed in Raymond (1972), it is appropriate to represent the atmosphere as an incompressible fluid as long as the depth of displacement as air is forced over a topographic barrier is much less than the density-scale height of the atmosphere. His conclusion is consistent with the scale analysis argument used to derive Eq. (3-14). When this requirement of air motion is fulfilled, then as reported by Raymond, the fractional density variation along a streamline is equal to the negative fractional variation in potential temperature [i.e., see following Eq. (4-21)].

10. See Section 4.2 for a brief discussion of the representation of the conservation-of-motion equation using a vorticity formulation.

11. The condition that $d\bar{\rho}/dt = 0$ and $\partial\bar{\rho}/\partial t = 0$ dictates that lines of constant density coincide with streamlines. This requirement is in addition to the incompressibility assumption [Eq. (4-23) right-side expression]. That equation only states that velocity gradients are much larger than local changes of density, but *not* that such local changes are identically zero.

12. As long as the streamline displacement is small relative to the density scale height of the atmosphere, the requirement that both $\bar{\rho}u_0^2$ and $d\bar{\rho}/dh_0$ equal constant values is a reasonable assumption.

13. Fourier transforms are briefly discussed in Section 5.2.1.1. For a more detailed discussion of Fourier transforms, the reader should consult such specialty texts as Churchill (1963).

14. That is, $\int_{-\infty}^{\infty} f(x)\Delta(x - \hat{x})dx = f(\hat{x})$ and $\int_{-\infty}^{\infty} \Delta(x - \hat{x})dx = 1$. Thus the Fourier transform of a delta function can be written as $e^{-ik_x\hat{x}} = \int_{-\infty}^{\infty} e^{-ik_x x}\Delta(x - \hat{x})dx$ with its inverse transform given by $\Delta(x - \hat{x}) = (1/2\pi)\int_{-\infty}^{\infty} e^{ik_x x}e^{-ik_x\hat{x}} \, dk_x = (1/2\pi)\int_{-\infty}^{\infty} e^{ik_x(x-\hat{x})}dk_x$; see Carrier *et al.* (1966:318) for a detailed discussion of the Dirac delta function.

15. A Hilbert transform is formally defined as

$$g(y) = \frac{1}{\pi}\fint_{-\infty}^{\infty} \frac{f(x)}{(x - y)} \, dx,$$

where x and y are real and

$$\fint_{-\infty}^{\infty} = \lim_{\epsilon \to 0}\left(\int_{-\infty}^{y-\epsilon} + \int_{y+\epsilon}^{\infty}\right), \epsilon > 0.$$

This is the formal procedure used to avoid the singularity at $x = y$. Erdélyi *et al.* (1954: Chapter 14) provided an overview of Hilbert transforms.

Additional Readings

Among the numerous books and texts that can be used to provide additional quantitative understanding of the material presented in this chapter are the following.

Dutton, J. A. 1976. "The Ceaseless Wind, An Introduction to the Theory of Atmospheric Motion." McGraw-Hill, New York.
  As already mentioned in Chapter 2, this is a valuable source text. The discussion on wave motions provides considerable, clearly written material on wave dynamics.
Hildebrand, F. B. 1962. "Advanced Calculus for Applications." Prentice-Hall, Englewood Cliffs, NJ.
  Chapter 10 provides a useful discussion of functions of complex variables.
Lilly, D. K., 1982. Gravity waves and mountain waves. Lecture notes prepared for the NATO Advanced Study Institute on Mesoscale Meteorology—Theory, Observation, and Models, July 13–21, 1982, Gascogne, France.
  These notes succinctly describe the derivation of linearized wave equations for gravity wave motion with x and t periodicity assumed. The solutions for linear airflow over idealized terrain are discussed.
Dalu, G. A., and R. A. Pielke. 1989. An analytical study of the sea breeze. *J. Atmos. Sci.* **46**, 1815–1825.
Dalu, G. A. and R. A. Pielke. 1993. Vertical heat fluxes generated by mesoscale atmospheric flow induced by thermal inhomogeneities in the PBL. *J. Atmos. Sci.* **50**, 919–926.
Dalu, G. A., R. A. Pielke, M. Baldi, and X. Zeng. 1996. Heat and momentum fluxes induced by thermal inhomogeneities with and without large-scale flow. *J. Atmos. Sci.* **53**, 3286–3302.
  Using a linear model, these three *Journal of Atmospheric Science* research articles describe how spatial variation in land-surface heating influence the magnitude and structure of mesoscale flow. In the most recent article, the influence of linear advective effects are included. Among the major conclusions is that horizontal turbulent diffusion and horizontal advection both work to horizontally homogenize the atmosphere above small-scale patches.

Thunis, P., and A. Clappier. 2000. Formulation and evaluation of a nonhydrostatic Mesoscale Vor-
    ticity Model (TVM). *Mon. Wea. Rev.* **128**, 3236–3251.
        This article assesses the adequacy of the hydrostatic and anelastic assumptions in simulating
        thermally induced circulations as well as describes their vorticity-based model.
Wolfram, S. 1988. "Mathematica: A System for Doing Mathematics by Computer." Addison-Wesley,
    Reading, MA.

Problems

1.   Program the Defant model using the analytic solutions given by Eqs. (5-90)–(5-94). Calculate
the solution given for the parameters specified by Eq. (5-99). Then assess the changes of the results
as each parameter is altered by 10% of its value. (In Chapter 10 you are asked to write a finite
difference version of the Defant model, to ascertain whether you can recreate the analytic solutions
calculated here.)

2.   Program the Long model defined by Eq. (5-132). Calculate the solution for $z_G = z_{G_{max}} b^2/(x^2 + b^2)$, where b is the half-width of the mountain and $z_{G_{max}}$ is the maximum height
of the terrain. Calculate the solution to the Long model for $b = 10$ km and $b = 100$ km, and for
$z_{G_{max}} = 1$ m, 1 km, and 3 km.

3.   Using Eq. (5-46), calculate phase speed in two different ways. First, set $f = 0$, $\lambda_1 = 0$, and
$\lambda_2 = 0$. For the second approach, let $\partial \rho_o/\partial z = 0$ and assume that the horizontal length scale is
less than 10 km (so that you can use scale analysis to remove terms). Show that both approaches
converge to Eq. (5-57).

Chapter 6

Coordinate Transformations

6.1 Tensor Analysis

Thus far in this text we have used the independent spatial variables x, y, and z in the derivation of the conservation relationships. These spatial coordinates have been defined to be perpendicular to each other at all locations.

In the application of the conservation relations, however, it is not always desirable to use this coordinate representation. In synoptic meteorology, for example, since pressure, p, is the quantity measured by the radiosonde, it is usually used to replace height, z, as the vertical coordinate. When a different coordinate form is used, however, the conservation relations that are developed from fundamental physical principles must be unchanged despite the different mathematical representation. Thus, in transforming the conservation relations from one coordinate system to another, the equations must be written so that the physical representation is *invariant* in either system. The mathematical operation developed to preserve this invariance requires some knowledge of the methods of *tensor analysis*.[1]

If, for example, in the rectangular coordinate system x^i, which has been used in this text up to now ($x^i = x^1, x^2, x^3 = x, y, z$),

$$r_i = f_i, \tag{6-1}$$

where r_i and f_i represent functions and derivatives of functions [e.g., the left and right sides of Eq. (2-45)], then in another coordinate system $\tilde{x}^i$ that is related to the x^i coordinate system by a functional transformation, the same physical relation must be

$$\tilde{r}_i = \tilde{f}_i$$

to preserve physical invariance. The components of $\tilde{x}^i$ are $\tilde{x}^1$, $\tilde{x}^2$, and $\tilde{x}^3$. The transformation between coordinate representations is defined in terms of the

functional relation between the independent variables in the two coordinate systems. Transformations between coordinate systems are of two types.

The first-order tensor $\tilde{f}_i$ is defined to be *covariant* if the transformation between the x^i and $\tilde{x}^i$ coordinate systems is given by

$$\tilde{f}_i = \frac{\partial x^j}{\partial \tilde{x}^i} f_j, \tag{6-2}$$

where $\partial x^j / \partial \tilde{x}^i$ is the operation that transforms f_j into its proper representation in the $\tilde{x}^i$ coordinate system. The *Jacobian* of the transformation is $\partial x^j / \partial \tilde{x}^i$. The use of a subscript denotes that $\tilde{f}_i$ is a *covariant vector (a tensor of order 1)*, since it transforms according to Eq. (6-2). By convention, a superscript in the *denominator* of a derivative quantity (e.g., $\partial / \partial x^j$) is defined as a covariant quantity.

The relation given by Eq. (6-1) can also be written as

$$r^i = f^i,$$

so that in the transformed coordinate system $\tilde{x}^i$, this physical relation must be written as

$$\tilde{r}^i = \tilde{f}^i,$$

where

$$\tilde{f}^i = \frac{\partial \tilde{x}^i}{\partial x^j} f^j. \tag{6-3}$$

When the transformation operation is given by $\partial \tilde{x}^i / \partial x^j$, $\tilde{f}^i$ is called a *contravariant vector (or tensor of order 1)* and is indicated using a superscript.

Higher-order tensors are defined in the same way, so that

$$\widetilde{B}_{mn} = \frac{\partial x^r}{\partial \tilde{x}^m} \frac{\partial x^s}{\partial \tilde{x}^n} B_{rs}, \quad \widetilde{B}^{mn} = \frac{\partial \tilde{x}^m}{\partial x^r} \frac{\partial \tilde{x}^n}{\partial x^s} B^{rs}, \quad \text{and} \quad B^m_n = \frac{\partial \tilde{x}^m}{\partial x^r} \frac{\partial x^s}{\partial \tilde{x}^n} B^r_s$$

refer to, respectively, the covariant, contravariant, and mixed tensors of order 2.

In the rectangular coordinate system that we have used up to now, the covariant and contravariant forms are identical, so that, for example, $u_i = u^i$. However, in nonorthogonal coordinate systems, $\tilde{u}_i \neq \tilde{u}^i$ in general, because $\tilde{u}_i$ is defined in terms of base vectors $\vec{\eta}^i$ that are *perpendicular to the surface* $\tilde{x}^i = constant$, whereas $\tilde{u}^i$ is defined in terms of base vectors $\vec{\tau}_i$ that are *tangent to the curve along which each coordinate except* $\tilde{x}^i$ *is a constant*, as illustrated in Figure 6-1. In the coordinate system that we have used up to this point, the two sets of basis vectors are coincident, and there is no need to differentiate between the covariant and contravariant forms.

In terms of the original rectangular coordinate system, these basis vectors in the transformed coordinate system are defined as

$$\vec{\tau}_j = \frac{\partial}{\partial \tilde{x}^j} (x^1 \vec{i} + x^2 \vec{j} + x^3 \vec{k}) = \frac{\partial \vec{x}}{\partial \tilde{x}^j}, \tag{6-4}$$

$$\vec{\eta}^i = \vec{i} \frac{\partial}{\partial x^1} \tilde{x}^i + \vec{j} \frac{\partial}{\partial x^2} \tilde{x}^i + \vec{k} \frac{\partial}{\partial x^3} \tilde{x}^i + \vec{\nabla} \tilde{x}^i, \tag{6-5}$$
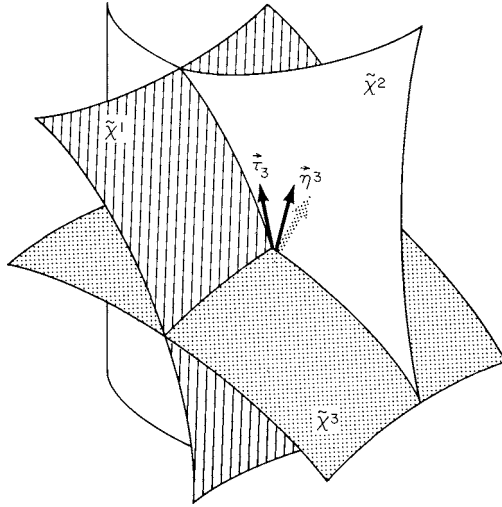
Fig. 6-1. Illustration of the two types of basis vectors in a nonorthogonal coordinate representation. The vector $\vec{\eta}^3$ is perpendicular to the plane $\tilde{x}^3 =$ constant, whereas $\vec{\tau}_3$ is tangent to the curve along which each coordinate, except $\tilde{x}^3$ is a constant. (From Dutton 1976.)

where $\vec{i}, \vec{j}$, and $\vec{k}$ are the orthogonal unit basis vectors in the rectangular coordinate representation. A coordinate system is *orthogonal* when the vector dot product of the basis vectors $\vec{\tau}_j \cdot \vec{\tau}_i$ and $\vec{\eta}^i \cdot \vec{\eta}^j$ is 0 at all points except when $i = j$ and *nonorthogonal* when they are not 0. Also, in an orthogonal system, $\vec{\tau}_i = \vec{\eta}^i$.

Scalar products[2] involving dependent and independent variables require that a covariant component be multiplied by a contravariant component. This is evident from the scalar product of the basis functions, since

$$\vec{\tau}_j \cdot \vec{\eta}^i = \frac{\partial \vec{x}}{\partial \tilde{x}^j} \cdot \vec{\nabla} \tilde{x}^i = \frac{\partial x^l}{\partial \tilde{x}^j} \frac{\partial \tilde{x}^i}{\partial x^l} = \frac{\partial \tilde{x}^i}{\partial \tilde{x}^j} = \delta^i_j,$$

where the chain rule,

$$\frac{\partial \tilde{x}^i}{\partial \tilde{x}^j} = \frac{\partial x^l}{\partial \tilde{x}^j} \frac{\partial \tilde{x}^i}{\partial x^l},$$

has been used along with the definition of the Kronecker delta given in Chapter 2, except that δ^i_j is now represented as a mixed tensor with one covariant component and one contravariant component. Since a vector in the transformed coordinate system can be given in terms of either set of basis vectors, then vectors $\vec{f}$ and $\vec{h}$, which represent physical quantities and are thus invariant between coordinate systems, can be represented by

$$\vec{f} = \tilde{f}_i \vec{\eta}^i = \tilde{f}^j \vec{\tau}_j,$$

and

$$\vec{h} = \tilde{h}_i \vec{\eta}^i = \tilde{h}^j \vec{\tau}_j,$$

so that the scalar products $\vec{f} \cdot \vec{f}$ and $\vec{f} \cdot \vec{h}$, for example, are given by

$$\vec{f} \cdot \vec{f} = \vec{\eta}^i \cdot \vec{\tau}_j \tilde{f}_i \tilde{f}^j = \delta^i_j \tilde{f}_i \tilde{f}^j = \tilde{f}_i \tilde{f}^i$$

and

$$\vec{f} \cdot \vec{h} = \vec{\eta}^i \cdot \vec{\tau}_j \tilde{f}_i \tilde{h}^j = \vec{\eta}^i \cdot \vec{\tau}_j \tilde{f}^j \tilde{h}_i = \tilde{f}^i \tilde{h}_i = \tilde{f}_i \tilde{h}^i.$$

Thus scalar products require multiplication of the covariant and contravariant components of the same index.

The contravariant and covariant components of a vector are thus found by taking the scalar product of the contravariant and covariant basis functions, yielding

$$f^i = \vec{\eta}^i \cdot \vec{f} \quad \text{and} \quad f_i = \vec{\tau}_i \cdot \vec{f}.$$

In our original orthogonal coordinate system, x^i, the square of the length of a differential line segment, is expressed by

$$(ds)^2 = dx^i \, dx^i.$$

To express $(ds)^2$ in the transformed coordinates, note that $dx^i = (\partial x^i / \partial \tilde{x}^j) d\tilde{x}^j$, and hence

$$(ds)^2 = \left(\frac{\partial x^i}{\partial \tilde{x}^j} d\tilde{x}^j \right) \left(\frac{\partial x^i}{\partial \tilde{x}^m} d\tilde{x}^m \right) \equiv \tilde{G}_{jm} d\tilde{x}^j \, d\tilde{x}^m, \tag{6-6}$$

where $\tilde{G}_{jm}$ is the *metric tensor*, defined by $(\partial x^i / \partial \tilde{x}^j)(\partial x^i / \partial \tilde{x}^m)$. This metric tensor is fundamental in the requirement that the conservation laws are invariant regardless of the functional form of the coordinate transformation. In the rectangular coordinate system used up to now, $G_{jm} = \delta_{jm}$; thus the individual coordinate axis (x^1, x^2, and x^3) is independent of and orthogonal to one another at all points.

The inverse of the metric tensor is defined by the relation

$$\tilde{G}^{jl} = \frac{\partial \tilde{x}^j}{\partial x^n} \frac{\partial \tilde{x}^l}{\partial x^n}. \tag{6-7}$$

To verify Eq. (6-7), note that

$$\tilde{G}_{jm} \tilde{G}^{jl} = \frac{\partial x^r}{\partial \tilde{x}^j} \frac{\partial x^r}{\partial \tilde{x}^m} \frac{\partial \tilde{x}^j}{\partial x^n} \frac{\partial \tilde{x}^l}{\partial x^n} = \frac{\partial x^r}{\partial \tilde{x}^j} \frac{\partial \tilde{x}^j}{\partial x^n} \frac{\partial x^r}{\partial \tilde{x}^m} \frac{\partial \tilde{x}^l}{\partial x^n}$$

$$= \delta^r_n \frac{\partial x^r}{\partial \tilde{x}^m} \frac{\partial \tilde{x}^l}{\partial x^n} = \frac{\partial x^r}{\partial \tilde{x}^m} \frac{\partial \tilde{x}^l}{\partial x^r} = \delta^l_m.$$

These forms of the metric tensor can also be expressed as

$$\widetilde{G}_{jm} = \vec{\tau}_j \cdot \vec{\tau}_m \quad \text{and} \quad \widetilde{G}^{jl} = \vec{\eta}^j \cdot \vec{\eta}^l.$$

One advantage of the metric tensor and its inverse is their ability to change a covariant tensor to a contravariant tensor and vice versa. This ability is needed because *only tensors of the same type* (e.g., covariant or contravariant) can be added. The reason for this is that covariant tensors are defined in terms of different basis vectors than contravariant tensors, and thus adding them together would be somewhat similar to adding the $\vec{i}$ unit vector to the $\vec{k}$ unit vector in our original x^i coordinate system.

To illustrate this capability of the metric tensor, let

$$\tilde{f}_l = \frac{\partial x^i}{\partial \tilde{x}^l} f_i;$$

then

$$\widetilde{G}^{lj}\tilde{f}_l = \left(\frac{\partial \tilde{x}^l}{\partial x^m}\frac{\partial \tilde{x}^j}{\partial x^m}\right)\frac{\partial x^i}{\partial \tilde{x}^l}f_i = \frac{\partial \tilde{x}^l}{\partial x^m}\frac{\partial x^i}{\partial \tilde{x}^l}\frac{\partial \tilde{x}^j}{\partial x^m}f_i = \delta^i_m\frac{\partial \tilde{x}^j}{\partial x^m}f_i = \frac{\partial \tilde{x}^j}{\partial x^i}f_i = \tilde{f}^j. \quad (6\text{-}8)$$

Similarly, the covariant component $\tilde{f}_l$ can be created by multiplying $\tilde{f}^j$ by $\widetilde{G}_{lj}$.

To determine whether or not a quantity is a tensor [i.e., transforms according to Eq. (6-2) or (6-3) for *all coordinate systems*], it is necessary to define a third coordinate representation given by, for example, $\bar{x}^i$, which is related to the $\tilde{x}^i$ coordinate system by a functional transformation.

If ϕ is defined here to be a scalar, then, using the chain rule,

$$\frac{\partial \phi}{\partial \bar{x}^i} = \frac{\partial \tilde{x}^j}{\partial \bar{x}^i}\frac{\partial \phi}{\partial \tilde{x}^j} = \frac{\partial \tilde{x}^j}{\partial \bar{x}^i}\frac{\partial x^l}{\partial \tilde{x}^j}\frac{\partial \phi}{\partial x^l}.$$

Hence derivatives of scalar quantities transform according to Eq. (6-2), and ϕ is a covariant tensor of order 0.

However, if $\bar{\phi}_m$ is defined to be a vector representation in the $\bar{x}^i$ coordinate system, then

$$\frac{\partial \bar{\phi}_m}{\partial \bar{x}^i} = \frac{\partial}{\partial \bar{x}^i}\left(\frac{\partial \tilde{x}^l}{\partial \bar{x}^m}\tilde{\phi}_l\right) = \frac{\partial \tilde{x}^l}{\partial \bar{x}^m}\frac{\partial \tilde{\phi}_l}{\partial \bar{x}^i} + \tilde{\phi}_l\frac{\partial^2 \tilde{x}^l}{\partial \bar{x}^i \partial \bar{x}^m},$$

so that derivatives of a vector are *not* tensors, since they do not transform between coordinate systems according to Eq. (6-2) or (6-3). To circumvent this problem, let

$$\tilde{\phi}_l = \frac{\partial x^j}{\partial \tilde{x}^l}\phi_j,$$

so that $\tilde{\phi}_l$ is a covariant tensor. But

$$\frac{\partial \tilde{\phi}_l}{\partial \tilde{x}^m} = \frac{\partial^2 x^j}{\partial \tilde{x}^m \partial \tilde{x}^l}\phi_j + \frac{\partial \phi_j}{\partial \tilde{x}^m}\frac{\partial x^j}{\partial \tilde{x}^l} \qquad\qquad\qquad (6\text{-}9)$$

is not a tensor, as has already been shown. Since

$$\frac{\partial \phi_j}{\partial \tilde{x}^m} = \frac{\partial x^r}{\partial \tilde{x}^m} \frac{\partial \phi_j}{\partial x^r}$$

by the chain rule, and since

$$\phi_j = \frac{\partial \tilde{x}^s}{\partial x^j} \tilde{\phi}_s,$$

substituting these two relations into Eq. (6-9) and rearranging yields

$$\frac{\partial \tilde{\phi}_l}{\partial \tilde{x}^m} = \frac{\partial^2 x^j}{\partial \tilde{x}^m \partial \tilde{x}^l} \frac{\partial \tilde{x}^s}{\partial x^j} \tilde{\phi}_s = \frac{\partial x^r}{\partial \tilde{x}^m} \frac{\partial x^j}{\partial \tilde{x}^l} \frac{\partial \phi_j}{\partial x^r}. \tag{6-10}$$

Thus a quantity has been created that transforms as a covariant tensor. By convention, Eq. (6-10) is written as

$$\tilde{\phi}_{l;m} = \frac{\partial \tilde{\phi}_l}{\partial \tilde{x}^m} - \tilde{\Gamma}^s_{ml} \tilde{\phi}_s = \frac{\partial x^r}{\partial \tilde{x}^m} \frac{\partial x^j}{\partial \tilde{x}^l} \frac{\partial \phi_j}{\partial x^r} \tag{6-11}$$

and is called the *covariant derivative*, where

$$\tilde{\Gamma}^s_{ml} = \frac{\partial^2 x^j}{\partial \tilde{x}^m \partial \tilde{x}^l} \frac{\partial \tilde{x}^s}{\partial x^j} \tag{6-12}$$

and is called the *Christoffel symbol*. In the $\bar{x}^i$ coordinate system,

$$\bar{\phi}_{t;u} = \frac{\partial \bar{\phi}_t}{\partial \bar{x}^u} - \bar{\Gamma}^i_{ut} \bar{\phi}_i = \frac{\partial \tilde{x}^v}{\partial \bar{x}^u} \frac{\partial \tilde{x}^w}{\partial \bar{x}^t} \frac{\partial \tilde{\phi}_w}{\partial x^v},$$

so that the proper tensorial transformation properties are maintained between coordinate systems. Using an analogous derivation, it is also true that the covariant derivative of a contravariant vector is given by

$$\tilde{\phi}^t_{;u} = \frac{\partial \tilde{\phi}^t}{\partial \tilde{x}^u} + \tilde{\Gamma}^t_{us} \tilde{\phi}^s. \tag{6-13}$$

Other important tensor relations are listed as follows. The Christoffel symbol and the metric tensor are related by

$$\tilde{\Gamma}^s_{ml} = \frac{1}{2} \tilde{G}^{sj} \left(\frac{\partial \tilde{G}_{ij}}{\partial \tilde{x}^m} + \frac{\partial \tilde{G}_{mj}}{\partial \tilde{x}^l} - \frac{\partial \tilde{G}_{lm}}{\partial \tilde{x}^j} \right), \tag{6-14}$$

as can be shown by substituting for the metric tensor on the right side. In addition, since in the original Cartesian coordinate system $\delta^{ij} = G_{ij} = G^{ij}$, it must also be true that in any coordinate system, the covariant derivative of the metric tensor is

$$\tilde{G}_{ij;k} = \tilde{G}^{ij}_{;k} = 0. \tag{6-15}$$

The covariant derivative of a second-order tensor can also be shown to have a form similar to that given by Eqs. (6-11) and (6-13), except that two Christoffel

symbols appear. If, for example, $\tilde{\phi}_k^j$ is a mixed tensor of order 2 in the $\tilde{x}_i$ coordinate system, then the covariant derivative is given by

$$\tilde{\phi}_{k;i}^j = \frac{\partial \tilde{\phi}_k^j}{\partial x^i} - \tilde{\Gamma}_{ki}^s \, \tilde{\phi}_s^j + \tilde{\Gamma}_{iu}^j \, \tilde{\phi}_k^u.$$

Using this relation, the product rule of differentiation can be shown to be valid since if $\tilde{\phi}_k^j = \tilde{a}_k \tilde{b}^j$, then

$$\left(\tilde{a}_k \tilde{b}^j\right)_{;i} = \frac{\partial \tilde{a}_k \tilde{b}^j}{\partial x^i} - \tilde{\Gamma}_{ki}^s a_s b^j + \tilde{\Gamma}_{iu}^j a_k b^u$$

$$= \tilde{b}^j \frac{\partial \tilde{a}_k}{\partial x^i} - \tilde{\Gamma}_{ki}^s a_s b^j + \tilde{a}_k \frac{\partial \tilde{b}^j}{\partial x^i} + \tilde{\Gamma}_{iu}^j a_k b^u = \tilde{b}^j \tilde{a}_{k;i} + \tilde{a}_k \tilde{b}_{;i}^j.$$

Moreover, using this rule along with Eq. (6-15),

$$\tilde{\phi}_{j;i} = \left(\tilde{G}_{jl} \tilde{\phi}^l\right)_{;i} = \tilde{G}_{jl} \tilde{\phi}_{;i}^l,$$

so that the covariant derivative of contravariant and covariant components can be interchanged using the metric tensor.

The determinant of the metric tensor is another important quantity that can be used in specifying the conservation relations in any coordinate system. The determinant is related to the Jacobian of the transformation and its inverse by

$$\tilde{G}^{1/2} = \left| \frac{\partial x^i}{\partial \tilde{x}^m} \right| = \left| \frac{\partial \tilde{x}^m}{\partial x^i} \right|^{-1}, \tag{6-16}$$

where $\tilde{G}$ is the determinant of the metric tensor $\tilde{G}_{jm}$. This quantity is very valuable in representing the Christoffel symbol when its contravariant and one of its covariant components are the same, such as when u is set equal to t in Eq. (6-13), so that

$$\tilde{\phi}_{;t}^t = \frac{\partial \tilde{\phi}^t}{\partial \tilde{x}^t} + \tilde{\Gamma}_{ts}^t \tilde{\phi}^s = \frac{1}{\sqrt{\tilde{G}}} \frac{\partial}{\partial \tilde{x}^s} \left(\sqrt{\tilde{G}} \tilde{\phi}^s\right). \tag{6-17}$$

In obtaining the right side of the expression, the relation

$$\tilde{\Gamma}_{ts}^t = \frac{1}{\sqrt{\tilde{G}}} \frac{\partial}{\partial \tilde{x}^s} \sqrt{\tilde{G}} \tag{6-18}$$

has been used, where Eq. (6-18) is obtained from Eq. (6-14) using the definition of matrix inverses and derivatives of matrices in terms of cofactors and determinants (see, e.g., Dutton 1976:142).

To transform the conservation relations into a separate coordinate system, it is also necessary to require the proper tensorial transformation of the term ϵ_{ijk},

which is used to represent the curl operation in vector notation. This is achieved by the operation

$$\tilde{\epsilon}_{ijk} = \sqrt{\overline{G}}\epsilon_{ijk}, \tag{6-19}$$

since the determinant of the Jacobian of a three-dimensional transformation can be expanded into

$$\sqrt{\overline{G}} = \frac{\partial x^r}{\partial \tilde{x}^1}\frac{\partial x^s}{\partial \tilde{x}^2}\frac{\partial x^t}{\partial \tilde{x}^3}\,\epsilon_{rst} \tag{6-20}$$

and, therefore,

$$\frac{\partial x^r}{\partial \tilde{x}^i}\frac{\partial x^s}{\partial \tilde{x}^j}\frac{\partial x^t}{\partial \tilde{x}^k}\,\epsilon_{rst} = \sqrt{\overline{G}}\,\epsilon_{ijk}. \tag{6-21}$$

The left side of Eq. (6-21) is equal to Eq. (6-20) since the term is 0 if any of the indices are equal. The expression given by Eq. (6-20) is valid only when transforming from our original rectangular coordinate system, where $\sqrt{G} = 1$. In the general case,

$$\frac{\partial \tilde{x}^r}{\partial \bar{x}^i}\frac{\partial \tilde{x}^s}{\partial \bar{x}^j}\frac{\partial \tilde{x}^t}{\partial \bar{x}^k}\sqrt{\overline{G}}\epsilon_{rst} = \bar{\epsilon}_{ijk} \tag{6-22}$$

is used to transform this term properly.

The contravariant transformation form of the term ϵ_{ijk} is obtained by multiplying the covariant form by the inverse of the metric tensor, using the method given in Eq. (6-8), so that

$$\sqrt{\overline{G}}\widetilde{G}^{ir}\widetilde{G}^{js}\widetilde{G}^{kt}\epsilon_{ijk} = \epsilon_{rst}/\sqrt{\overline{G}} = \tilde{\epsilon}^{rst}, \tag{6-23}$$

where $\widetilde{G}^{ir}\widetilde{G}^{js}\widetilde{G}^{kt}$ is equal to the determinant of the inverse of the metric tensor using the same procedures as followed in obtaining Eq. (6-21). This determinant is then equal to $1/\widetilde{G}$ using Eq. (6-16).

Using these properties of tensor transformations, it is possible to rewrite the conservation equations in any coordinate system of our choosing with the certainty that the physical representations, which are represented by these conservation relations, remain unchanged. By convention, the equations are written in the contravariant form, using the covariant differentiation operation given by Eq. (6-13).

Therefore, the original prognostic conservation relations given by Eqs. (2-43)–(2-47) in Chapter 2 can be written as

$$\frac{\partial \rho}{\partial t} = -\left(\rho \tilde{u}^i\right)_{;i} = -\frac{1}{\sqrt{\tilde{G}}}\frac{\partial}{\partial \tilde{x}^i}\left(\rho\sqrt{\tilde{G}}\tilde{u}^i\right), \tag{6-24}$$

$$\frac{\partial \theta}{\partial t} = \tilde{u}^j \frac{\partial \theta}{\partial \tilde{x}^j} + \tilde{S}_\theta, \tag{6-25}$$

$$\frac{\partial \tilde{u}^i}{\partial t} = -\tilde{u}^j\,\tilde{u}^i_{\ ;j} - \tilde{G}^{ij}\,\theta\,\frac{\partial \pi}{\partial \tilde{x}^j} - \frac{\partial \tilde{x}^i}{\partial x^3}\,g - 2\tilde{\epsilon}^{ijl}\tilde{\Omega}_j\tilde{u}_l, \tag{6-26}$$

$$\frac{\partial q_n}{\partial t} = -\tilde{u}^j\,\frac{\partial q_n}{\partial \tilde{x}^j} + \tilde{S}_{q_n}, \quad n = 1, 2, 3, \tag{6-27}$$

$$\frac{\partial \chi_m}{\partial t} = -\tilde{u}^j\,\frac{\partial \chi_m}{\partial \tilde{x}^j} + \tilde{S}_{\chi_m}, \quad m = 1, 2, \ldots, M, \tag{6-28}$$

where the pressure gradient term is represented in terms of the scaled pressure π defined by Eq. (4-36). The definitions of the tensor transformation parameters needed to preserve the physical invariance of these operations (e.g., $\sqrt{\tilde{G}}$, $\tilde{G}^{ij}$, $\tilde{\epsilon}^{ijl}$, and $\tilde{u}^i_{\ ;j}$) are given by Eqs. (6-20), (6-7), (6-23), and (6-13). These equations are then valid for *any* functional coordinate representation.

The major rules for obtaining a consistent representation of the conservation laws in the generalized coordinate system are as follows:

1.   Require that the individual terms have the same number of contravariant and covariant indices. If they do not, then use the metric tensor to change between covariant and contravariant forms. (Remember that a superscript on independent variables in the denominator of a derivative indicates, by convention, that it is a covariant form.)

2.   Use the definition of covariant differentiation to ensure that the derivatives retain physical invariance.

3.   Use the Jacobian to transform dependent variables in a covariant representation from one coordinate to the next. Use the inverse of the Jacobian when a contravariant representation is desired.

4.   The square root of the determinant of the metric tensor must be used to transfer the parameter ϵ_{ijk} between coordinate systems properly.

6.2   Generalized Vertical Coordinate

In the application of these equations to simulate mesoscale atmospheric flows, only the vertical coordinate in the rectangular system is customarily transformed. This procedure is adopted in the discussion that follows. In addition, it is necessary to average the transformed equations since, of course, Eqs. (6-24)–(6-28)

are valid only over spatial and temporal intervals that are much smaller than the mesoscale space and time scales.

The functional form of this generalized vertical coordinate transformation, in terms of the original Cartesian system, can be written as

$$\tilde{x}^1 = x, \qquad\qquad x = \tilde{x}^1,$$

$$\tilde{x}^2 = y, \qquad\qquad y = \tilde{x}^2,$$

$$\tilde{x}^3 = \sigma(x, y, z, t), \qquad z = h(\tilde{x}^1, \tilde{x}^2, \tilde{x}^3), t.$$

The functional form of σ has been specified in a number of forms, including

$$\sigma = \theta, \qquad\qquad\qquad \sigma = s(z - z_G)/(s - z_G),$$

$$\sigma = p, \qquad\qquad\qquad \sigma = (p_G - p)/(p_G - p_T),$$

$$\sigma = p/p_G \qquad\qquad\qquad \sigma = (\theta - \theta_T)/(\theta_G - \theta_T).$$

$$\sigma = \left[\frac{p - p_T}{p_G - p_T}\right]\left[\frac{p_{\text{ref}}(0) - p_T}{p_{\text{ref}}(z_G) - p_T}\right].$$

In these expressions, p_G, θ_G, p_T, and θ_T refer to the pressures and potential temperatures at the bottom and top of the coordinate representation; z_G and s specify the terrain height and height of the top; and $p_{\text{ref}}(0)$ and $p_{\text{ref}}(z_G)$ are the pressure at sea level and at z_G using a standard reference atmosphere that is the same across the model (Black 1994). The first two forms of σ on the left are referred to as *isentropic* and *isobaric* representations, and the remaining six are *terrain-following* coordinate systems, usually called *sigma* representations. The bottom formulation in the right column for σ is a normalized isentropic representation introduced by Branković (1981).

The innovative form of σ at the bottom of the lefthand column is called the "Eta coordinate system" (Janjić *et al.* 1988, Janjić 1990; Mesinger and Black 1992; Black 1994; Mesinger 1996, 1997, 1998; Mesinger *et al.* 1997) and is the system used by the U.S. National Centers for Environmental Prediction (NCEP) for one of their regional models. The Eta system has the advantage of a form of sigma system that is nearly horizontal, while meeting the requirement that the system not intersect the terrain. Gallus and Klemp (2000) provide a recent comparison of model simulations of airflow over mountains using the Eta coordinate and another form of a terrain-following coordinate system. In ocean models, a coordinate system that uses density as a vertical coordinate is often used (see, e.g., Bleck and Boudra 1981). Adcroft *et al.* (1997) and Marshall *et al.* (1997) use a partial grid volume coordinate system (called "shaved cells") at their ocean bottom–ocean interface. Laprise (1992a) suggests using hydrostatic pressure as the vertical coordinate.

Phillips (1957) originated the concept of the lowest coordinate surface being coincident with the ground. Deaven (1974, 1976), Friend *et al.* (1977), Bleck (1978), Uccellini *et al.* (1979), and Johnson and Uccellini (1983), have used an isentropic system well above the ground and a type of sigma representation near the ground. Kasahara (1974) and Sundquist (1979) have discussed various types of vertical coordinates, including the sigma system.

In the expressions for σ, p_T and s are generally prescribed as constant in time and space, although several investigators (e.g., Mahrer and Pielke 1975, 1978a) permitted temporal and spatial variations of their top coordinate. Examples of two-dimensional cross-sections in several of these representations are given in Figure 6-2, where a mountain is situated in the center of the region.

This concept of defining a coordinate surface coincident with the bottom topography permits more efficient use of computer resources, and it simplifies the application of lower boundary conditions. In Phillips's original form, adopted by many models (e.g., the U.S. Weather Service forecast models; Rieck 1979), pressure is used to define the independent vertical coordinate σ, where surface pressure is used as the lower boundary. Haltiner (1971), for example, defines $\sigma = p/p_G$, where p_G is the surface pressure whereas p is the pressure at any level. For this example, $\sigma = 1$ corresponds to the ground surface. In mesoscale models, however, σ is often defined using one of its forms that is a function of height rather than pressure. This is advantageous because p_G is a function of time, whereas terrain height is not.
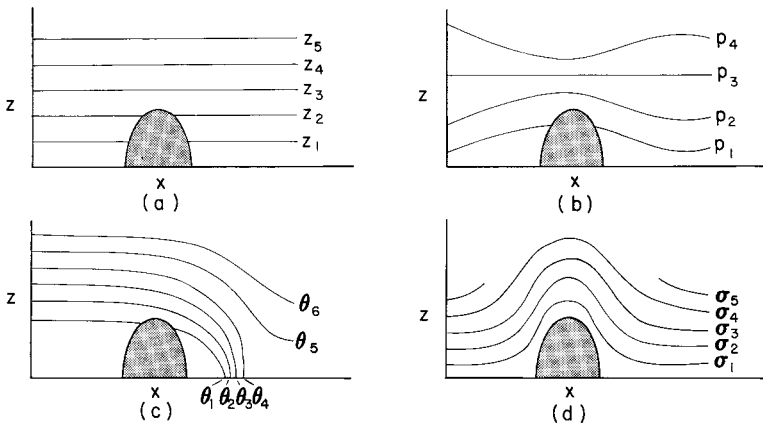

Fig. 6-2. Schematic illustrations of (a) rectangular, (b) isobaric, (c) isentropic, and (d) sigma coordinate representations as viewed in a rectangular coordinate framework.

The contravariant and covariant forms of the metric tensor $\widetilde{G}^{ij}$ and $\widetilde{G}_{ij}$ for the generalized vertical coordinate are given as

$$
\widetilde{G}^{ij} = \frac{\partial \tilde{x}^i}{\partial x^l}\frac{\partial \tilde{x}^j}{\partial x^l} =
\begin{bmatrix}
1 & 0 & \dfrac{\partial \sigma}{\partial x} \\[2ex]
0 & 1 & \dfrac{\partial \sigma}{\partial y} \\[2ex]
\dfrac{\partial \sigma}{\partial x} & \dfrac{\partial \sigma}{\partial y} & \left\{ \left(\dfrac{\partial \sigma}{\partial x}\right)^2 + \left(\dfrac{\partial \sigma}{\partial y}\right)^2 + \left(\dfrac{\partial \sigma}{\partial z}\right)^2 \right\}
\end{bmatrix}
$$

$$(6\text{-}29)$$

$$
\widetilde{G}_{ij} = \frac{\partial x^l}{\partial \tilde{x}^i}\frac{\partial x^l}{\partial \tilde{x}^j} =
\begin{bmatrix}
1 + \left(\dfrac{\partial h}{\partial \tilde{x}^1}\right)^2 & \dfrac{\partial h}{\partial \tilde{x}^1}\dfrac{\partial h}{\partial \tilde{x}^2} & \dfrac{\partial h}{\partial \tilde{x}^1}\dfrac{\partial h}{\partial \tilde{x}^3} \\[2ex]
\dfrac{\partial h}{\partial \tilde{x}^1}\dfrac{\partial h}{\partial \tilde{x}^2} & 1 + \left(\dfrac{\partial h}{\partial \tilde{x}^2}\right)^2 & \dfrac{\partial h}{\partial \tilde{x}^2}\dfrac{\partial h}{\partial \tilde{x}^3} \\[2ex]
\dfrac{\partial h}{\partial \tilde{x}^1}\dfrac{\partial h}{\partial \tilde{x}^3} & \dfrac{\partial h}{\partial \tilde{x}^2}\dfrac{\partial h}{\partial \tilde{x}^3} & \left(\dfrac{\partial h}{\partial \tilde{x}^3}\right)^2
\end{bmatrix},
$$

using Eqs. (6-6) and (6-7), and the only nonzero Christoffel symbol is

$$
\widetilde{\Gamma}^3_{jl} = \frac{\partial \sigma}{\partial z}\frac{\partial^2 h}{\partial \tilde{x}^j \partial \tilde{x}^l} \tag{6-30}
$$

[from Eq. (6-12)], so that the covariant derivative of velocity is given by

$$
u^i_{;j} =
\begin{cases}
\dfrac{\partial \tilde{u}^i}{\partial \tilde{x}^j}, & i = 1, 2 \\[3ex]
\dfrac{\partial \tilde{u}^3}{\partial \tilde{x}^j} + \widetilde{\Gamma}^3_{jl}\tilde{u}^l, & i = 3
\end{cases}
\tag{6-31}
$$

[from Eq. (6-13)]. The determinant of the Jacobian of the transformation,

$$
\left(\left| \frac{\partial x^i}{\partial \tilde{x}^j} \right| = \sqrt{\widetilde{G}} \right)
$$

[(from Eq. (6-16)], is given by

$$
\left| \frac{\partial x^i}{\partial \tilde{x}^j} \right| =
\begin{vmatrix}
1 & 0 & 0 \\[1ex]
0 & 1 & 0 \\[1ex]
\dfrac{\partial h}{\partial \tilde{x}^1} & \dfrac{\partial h}{\partial \tilde{x}^2} & \dfrac{\partial h}{\partial \tilde{x}^3}
\end{vmatrix}
= \sqrt{\widetilde{G}} = \frac{\partial h}{\partial \tilde{x}^3} \equiv \frac{\partial h}{\partial \sigma}.
\tag{6-32}
$$

The tangent and normal basis vectors for the generalized vertical coordinate system in terms of the rectangular representation are given by

$$\vec{\tau}_1 = \vec{i} + \vec{k}\frac{\partial h}{\partial \tilde{x}^1}, \quad \vec{\eta}^1 = \vec{i},$$

$$\vec{\tau}_2 = \vec{j} + \vec{k}\frac{\partial h}{\partial \tilde{x}^2}, \quad \vec{\eta}^2 = \vec{j}, \qquad (6\text{-}33)$$

$$\vec{\tau}_3 = \vec{k}\frac{\partial h}{\partial \tilde{x}^3}, \quad \vec{\eta}^3 = \vec{i}\frac{\partial \sigma}{\partial x} + \vec{j}\frac{\partial \sigma}{\partial y} + \vec{k}\frac{\partial \sigma}{\partial z}$$

[using Eqs. (6-4) and (6-5)], where, since $\vec{\tau}_i \cdot \vec{\tau}_j$ does not equal 0 when $i \neq j$, this coordinate system in general is *nonorthogonal*. In the original rectangular coordinate system, the normal and tangent basis functions are the same (i.e., $\vec{i}, \vec{j},$ and $\vec{k}$) and are orthogonal to one another. Since $\vec{\tau}_3$ is tangent to the curve in which only $\tilde{x}^3$ varies, the σ coordinate is vertical at all points, that is, $\vec{\tau}_3$ is in the direction of $\vec{k}$, from Eq. (6-33).

The individual contravariant and covariant velocity components are found from $\tilde{u}^i = \vec{\eta}^i \cdot \vec{u}$ and $\tilde{u}_i = \vec{\tau}_i \cdot \vec{u}$, respectively, where $\vec{u} = u\vec{i} + v\vec{j} + w\vec{k}$, so that

$$\tilde{u}^1 = u, \qquad\qquad \tilde{u}_1 = u + \frac{\partial h}{\partial \tilde{x}^1}w,$$

$$\tilde{u}^2 = v, \qquad\qquad \tilde{u}_2 = v + \frac{\partial h}{\partial \tilde{x}^2}w, \qquad (6\text{-}34)$$

$$\tilde{u}^3 = u\frac{\partial \sigma}{\partial x} + v\frac{\partial \sigma}{\partial y} + w\frac{\partial \sigma}{\partial z}, \quad \tilde{u}_3 = w\frac{\partial h}{\partial \tilde{x}^3}.$$

Kinetic energy is computed from these expressions by

$$e^2 = \frac{1}{2}\left(\tilde{u}^1\tilde{u}_1 + \tilde{u}^2\tilde{u}_2 + \tilde{u}^3\tilde{u}_3\right). \qquad (6\text{-}35)$$

The Coriolis term in the transformed coordinate system is expressed in terms of the rectangular representation as

$$2\tilde{\epsilon}^{ijl}\widetilde{\Omega}_j\tilde{u}_l = 2\epsilon_{ijl}\frac{\partial \sigma}{\partial z}\widetilde{\Omega}_j\tilde{u}_l \qquad (6\text{-}36)$$

[using Eq. (6-23)], where

$$2\widetilde{\Omega}_1 = 2\left(\Omega_1 + \frac{\partial h}{\partial \tilde{x}^1}\Omega_3\right) = 2\frac{\partial h}{\partial \tilde{x}^1}\Omega_3 = 2\frac{\partial h}{\partial \tilde{x}^1}\Omega \sin \phi = \frac{\partial h}{\partial \tilde{x}^1}f(\Omega_1 = 0),$$

$$2\widetilde{\Omega}_2 = 2\left(\Omega_2 + \frac{\partial h}{\partial \tilde{x}^2}\Omega_3\right) = 2\Omega \cos \phi + 2\frac{\partial h}{\partial \tilde{x}^2}\Omega \sin \phi = \hat{f} + \frac{\partial h}{\partial \tilde{x}^2}f,$$

$$2\widetilde{\Omega}_3 = 2\Omega_3\frac{\partial h}{\partial \tilde{x}^3} = 2\frac{\partial h}{\partial \tilde{x}^3}\Omega \sin \phi = \frac{\partial h}{\partial \tilde{x}^3}f$$

with $f = 2\Omega \sin \phi$ and $\hat{f} = 2\Omega \cos \phi$. (Here Ω is the rotation rate of the earth and ϕ is the latitude.)

Averaging of Eqs. (6-24)–(6-28) is of course required if these equations are to be used in meteorological numerical models with finite grid and time intervals. The averaging operator given by Eq. (4-6) in Chapter 4 is not the correct one, however, because $\Delta x \Delta y \Delta z \Delta t$ is no longer the appropriate averaging volume. In the transformed coordinate system, the appropriate grid-volume–averaging operator is defined as[3]

$$(\overline{\quad\quad}) = \frac{\int_t^{t+\Delta t} \int_{\tilde{x}^1}^{\tilde{x}^1+\Delta \tilde{x}^1} \int_{\tilde{x}^2}^{\tilde{x}^2+\Delta \tilde{x}^2} \int_\sigma^{\sigma+\Delta\sigma} (\ ) d\sigma\, d\tilde{x}^2\, d\tilde{x}^1 dt}{(\Delta \tilde{x}^1)(\Delta \tilde{x}^2)(\Delta\sigma)(\Delta t)}. \tag{6-37}$$

The dependent variables can be decomposed into an average and a subgrid-scale perturbation expressed as

$$\phi = \bar{\phi} + \phi'',$$

where ϕ'' is a deviation from the grid-volume average given by Eq. (6-37). The symbol ϕ represents any one of the dependent variables.

For example, Eq. (6-26) can be rewritten using Eq. (6-37) as

$$\frac{\partial \bar{\tilde{u}}^i}{\partial t} = -\bar{\tilde{u}}^j \bar{\tilde{u}}^i_{;j} - \overline{\tilde{u}^{j''} \tilde{u}^{i''}_{;j}} - \widetilde{G}^{ij} \bar{\theta} \frac{\partial \bar{\pi}}{\partial \tilde{x}^j} - \frac{\partial \tilde{x}^i}{\partial z} g - 2\bar{\tilde{\epsilon}}^{ijl} \bar{\tilde{\Omega}}_j \bar{\tilde{u}}_l. \tag{6-38}$$

In deriving this form, we have assumed that $\theta = \bar{\theta}[1 + (\theta''/\bar{\theta})] \cong \bar{\theta}$ and that

$$\bar{\bar{\tilde{u}}}^i = \bar{\tilde{u}}^i, \quad \overline{\partial \bar{u}_i / \partial t} = \partial \bar{u}_i / \partial t, \text{ etc. (and, therefore, } \overline{\tilde{u}^{i''}} = 0, \text{ etc.),} \tag{6-39}$$

as was required in Section 4.1. To make this assumption in the transformed coordinate system, however, it is necessary *to require that changes of the metric tensor over the four-dimensional grid-volume* $\Delta \tilde{x}^1 \Delta \tilde{x}^2 \Delta\sigma \Delta t$ *are small*, since this tensor appears in Eq. (6-38). Expressed mathematically, this requirement can be written as

$$\overline{\widetilde{G}^{ij}} = \frac{\int_t^{t+\Delta t} \int_{\tilde{x}^1}^{\tilde{x}+\Delta \tilde{x}^1} \int_{\tilde{x}^2}^{\tilde{x}^2+\Delta \tilde{x}^2} \int_\sigma^{\sigma+\Delta\sigma} \widetilde{G}^{ij} d\sigma\, d\tilde{x}^2\, d\tilde{x}^1\, dt}{(\Delta t)(\Delta \tilde{x}^1)(\Delta \tilde{x}^2)(\Delta\sigma)} \simeq \widetilde{G}^{ij}.$$

This requirement has significant implications for the choice of the vertical generalized coordinate, since *it must be selected such that variations of the gradient of the transformed coordinate within the grid volume are small* compared to the grid-volume–averaged gradient.

The advection term in Eq. (6-38) is derived from

$$\overline{\tilde{u}^j \tilde{u}^i_{;j}} = \overline{\tilde{u}^j \frac{\partial \tilde{u}^i}{\partial \tilde{x}^j}} + \overline{\widetilde{\Gamma}^i_{jl} \tilde{u}^j \tilde{u}^l} \simeq \overline{\tilde{u}^j \frac{\partial \tilde{u}^i}{\partial \tilde{x}^j}} + \widetilde{\Gamma}^i_{jl} \overline{\tilde{u}^j \tilde{u}^l}$$

$$\simeq \bar{\tilde{u}}^j \frac{\partial \bar{\tilde{u}}^i}{\partial \tilde{x}^j} + \overline{\tilde{u}^{j''} \frac{\partial \tilde{u}^{i''}}{\partial \tilde{x}^j}} + \widetilde{\Gamma}^i_{jl}[\bar{\tilde{u}}^j \bar{\tilde{u}}^l + \overline{\tilde{u}^{j''} \tilde{u}^{l''}}] = \bar{\tilde{u}}^j \bar{\tilde{u}}^i_{;j} + \overline{\tilde{u}^{j''} \tilde{u}^{i''}_{;j}},$$

where the assumption that changes of the metric tensor and its derivatives are small permits removal of the Christoffel symbol from the integrand. This assumption can also be written as

$$\widetilde{\Gamma}^i_{jl} = \overline{\widetilde{\Gamma}}^i_{jl} + \widetilde{\Gamma}''^i_{jl} = \overline{\widetilde{\Gamma}}^3_{jl} + \widetilde{\Gamma}''^3_{jl} \cong \overline{\widetilde{\Gamma}}^3_{jl}, \ \text{ where } \left|\widetilde{\Gamma}''^3_{jl}\right| \ll \left|\overline{\widetilde{\Gamma}}^3_{jl}\right|.$$

The Coriolis term can be expanded as

$$2\tilde{\epsilon}^{ijl}\widetilde{\Omega}_j\bar{\tilde{u}}_l = \frac{2\widetilde{\Omega}_j\widetilde{G}_{lm}\bar{\tilde{u}}^m\epsilon_{ijl}}{\sqrt{\widetilde{G}}} = 2\epsilon_{ijl}\frac{\partial x^r}{\partial \tilde{x}^j}\Omega_r\widetilde{G}_{lm}\bar{\tilde{u}}^m\frac{\partial\sigma}{\partial z},$$

with $\Omega_r = (0, \Omega\cos\phi, \Omega\sin\phi) = (0, \hat{f}/2, f/2)$.

In addition,

$$\frac{\partial h}{\partial \tilde{x}^3}\frac{\partial\sigma}{\partial x^3} = 1$$

and

$$\frac{\partial \tilde{x}^1}{\partial z} = \frac{\partial \tilde{x}^2}{\partial z} = 0.$$

Thus, with the decomposition of the variables into resolvable and subgrid-scale terms, Eq. (6-38) can be written for the generalized vertical coordinate representation in its component form as

$$\frac{\partial\bar{\tilde{u}}^1}{\partial t} = -\bar{\tilde{u}}^j\frac{\partial\bar{\tilde{u}}^1}{\partial\tilde{x}^j} - \overline{\tilde{u}^{j''}\frac{\partial\tilde{u}^{1''}}{\partial\tilde{x}^j}} - \bar{\theta}\frac{\partial\bar{\pi}}{\partial\tilde{x}^1} - \bar{\theta}\frac{\partial\sigma}{\partial x}\frac{\partial\bar{\pi}}{\partial\tilde{x}^3}$$

$$- \hat{f}\left(\frac{\partial h}{\partial\tilde{x}^1}\bar{\tilde{u}}^1 + \frac{\partial h}{\partial\tilde{x}^2}\bar{\tilde{u}}^2 + \frac{\partial h}{\partial\tilde{x}^3}\bar{\tilde{u}}^3\right) + f\bar{\tilde{u}}^2, \tag{6-40}$$

$$\frac{\partial\bar{\tilde{u}}^2}{\partial t} = -\bar{\tilde{u}}^j\frac{\partial\bar{\tilde{u}}^2}{\partial\tilde{x}^j} - \overline{\tilde{u}^{j''}\frac{\partial\tilde{u}^{2''}}{\partial\tilde{x}^j}} - \bar{\theta}\frac{\partial\bar{\pi}}{\partial\tilde{x}^2} - \bar{\theta}\frac{\partial\sigma}{\partial y}\frac{\partial\bar{\pi}}{\partial\tilde{x}^3} - f\bar{\tilde{u}}^1, \tag{6-41}$$

and

$$\frac{\partial\bar{\tilde{u}}^3}{\partial t} = -\bar{\tilde{u}}^j\frac{\partial\bar{\tilde{u}}^3}{\partial\tilde{x}^j} - \overline{\tilde{u}^{j''}\frac{\partial\tilde{u}^{3''}}{\partial\tilde{x}^j}} - \bar{\widetilde{\Gamma}}^3_{jl}\bar{\tilde{u}}^j\bar{\tilde{u}}^l - \bar{\widetilde{\Gamma}}^3_{jl}\overline{\tilde{u}^{j''}\tilde{u}^{l''}}$$

$$- \bar{\theta}\left\{\frac{\partial\sigma}{\partial x}\frac{\partial\bar{\pi}}{\partial\tilde{x}^1} + \frac{\partial\sigma}{\partial y}\frac{\partial\bar{\pi}}{\partial\tilde{x}^2} + \left[\left(\frac{\partial\sigma}{\partial x}\right)^2 + \left(\frac{\partial\sigma}{\partial y}\right)^2 + \left(\frac{\partial\sigma}{\partial z}\right)^2\right]\frac{\partial\bar{\pi}}{\partial\tilde{x}^3}\right\}$$

$$+ \left(\hat{f} + \frac{\partial h}{\partial\tilde{x}^2}f\right)\frac{\partial\sigma}{\partial z}\left[\left(1 + \left(\frac{\partial h}{\partial\tilde{x}^1}\right)^2\right)\bar{\tilde{u}}^1 + \frac{\partial h}{\partial\tilde{x}^1}\frac{\partial h}{\partial\tilde{x}^2}\bar{\tilde{u}}^2 + \frac{\partial h}{\partial\tilde{x}^1}\frac{\partial h}{\partial\tilde{x}^3}\bar{\tilde{u}}^3\right]$$

$$- \frac{\partial h}{\partial\tilde{x}^1}f\frac{\partial\sigma}{\partial z}\left[\frac{\partial h}{\partial\tilde{x}^2}\frac{\partial h}{\partial\tilde{x}^1}\bar{\tilde{u}}^1 + \left(1 + \left(\frac{\partial h}{\partial\tilde{x}^2}\right)^2\right)\bar{\tilde{u}}^2 + \frac{\partial h}{\partial\tilde{x}^2}\frac{\partial h}{\partial\tilde{x}^3}\bar{\tilde{u}}^3\right] - \frac{\partial\sigma}{\partial z}g. \tag{6-42}$$

Since from Section 6.1, the vector velocity $\vec{v} = \bar{\bar{u}}^j \vec{\tau}_j$, $\bar{\bar{u}}^3$ is in the same direction as the Cartesian velocity $\bar{w}$, whereas $\bar{\bar{u}}^1$ and $\bar{\bar{u}}^2$ are in general at some angle to $\bar{u}$ and $\bar{v}$ in the original rectangular coordinate system, as shown by Eqs. (6-33) and (6-34).

The transformed grid-volume–averaged conservation-of-mass relation [from Eq. (6-24)], can be written as

$$\frac{\partial \bar{\rho}}{\partial t} = -\frac{\partial \sigma}{\partial z} \frac{\partial}{\partial \tilde{x}^j}\left(\frac{\partial h}{\partial \tilde{x}^3}\overline{\rho \tilde{u}^j}\right), \tag{6-43}$$

which, since $\partial \rho / \partial t = -(\partial / \partial x_j)\rho u_j$ in the rectangular coordinate system [i.e., Eq. (2-43)] can be approximated by

$$0 = -\frac{\partial \sigma}{\partial z} \frac{\partial}{\partial \tilde{x}^j}\left(\rho_0 \frac{\partial h}{\partial \tilde{x}^3}\overline{\tilde{u}^j}\right) = -\frac{\partial}{\partial \tilde{x}^j}\left(\rho_0 \frac{\partial h}{\partial \tilde{x}^3}\overline{\tilde{u}^j}\right) \simeq -\frac{\partial}{\partial \tilde{x}^j}\left(\bar{\rho} \frac{\partial h}{\partial \tilde{x}^3}\overline{\tilde{u}^j}\right) \tag{6-44}$$

if it is assumed that $|\alpha''|/\bar{\alpha} \sim |\alpha''|/\alpha_0 \ll 1$, as was done in obtaining Eqs. (3-11) and (4-9). In invoking the assumption that $|\alpha''|$ is much less than $\bar{\alpha}$ and α_0, so that Eq. (6-44) can be written in its existing form, one must remember that the averaging volume is in the transformed coordinate system.

The conservation of heat as represented by potential temperature and the conservation-of-water substance and other gaseous and aerosol atmospheric material given by Eqs. (6-25), (6-27), and (6-28) can be written in grid-volume–averaged form as

$$\frac{\partial \bar{\theta}}{\partial t} = -\bar{\bar{u}}^j \frac{\partial \bar{\theta}}{\partial \tilde{x}^j} - \overline{\tilde{u}^j \frac{\partial \theta''}{\partial \tilde{x}^j}} + \overline{\bar{S}}_\theta, \tag{6-45}$$

$$\frac{\partial \bar{q}_n}{\partial t} = -\bar{\bar{u}}^j \frac{\partial \bar{q}_n}{\partial \tilde{x}^j} - \overline{\tilde{u}^{j''} \frac{\partial q_n''}{\partial \tilde{x}^j}} + \overline{\bar{S}}_{q_n}, \quad n = 1, 2, 3 \tag{6-46}$$

$$\frac{\partial \bar{\chi}_m}{\partial t} = -\bar{\bar{u}}^j \frac{\partial \bar{\chi}_m}{\partial \tilde{x}^j} - \overline{\tilde{u}^{j''} \frac{\partial \chi_m''}{\partial \tilde{x}^j}} + \overline{\bar{S}}_{\chi_m}, \quad m = 1, 2, \ldots, M \tag{6-47}$$

In summary, the $8 + M$ prognostic equations [(6-40)–(6-42), (6-44), (6-46), and (6-47)] in the $8 + M$ unknowns $\bar{\bar{u}}$, $\bar{\theta}$, $\bar{\pi}$, $\bar{q}_n$, and $\bar{\chi}_m$ can be used to represent the conservation relations in any generalized vertical coordinate system, as long as the assumptions such as given by Eq. (6-39) are valid. Because tensor transformation rules were used, one can be certain that the physical representation of the conservation relations is unaffected.

These equations can also be manipulated to obtain equivalent expressions for other forms of the conservation equations. The diagnostic equation for pressure in the transformed system, for example, can be obtained by taking the divergence of Eqs. (6-40)–(6-42). This operation can be performed by applying the covariant differentiation operation with respect to the free index i [i.e., $(\ )_{;i}$ is applied] to the grid-volume–averaged form of Eq. (6-26).

6.3   The Sigma-z Coordinate System

Terrain-following coordinate systems that are a function of z have been used extensively in regional and mesoscale models (e.g., Mahrer and Pielke 1975; Colton 1976; Blondin 1978; Yamada 1978a) in which the hydrostatic assumption has been applied and in mesoscale models in which the hydrostatic assumption has not been made (e.g., Gal-Chen and Somerville 1975a, b; Clark 1977; Pielke *et al.* 1992; Shi *et al.* 2000).

6.3.1   The Hydrostatic Assumption Derivation

In developing hydrostatic model equations, investigators have generally applied the chain rule *separately* in the vertical and horizontal dimensions (using the hydrostatic relation). Using the terrain-following coordinate system defined by

$$\sigma = s\frac{z - z_{\mathrm{G}}}{s - z_{\mathrm{G}}}, \tag{6-48}$$

for example, where s is a constant and z_{G} is a function of x and y, application of the chain rule to the hydrostatic relation given by Eq. (4-40) yields

$$\frac{\partial \bar{\pi}}{\partial \sigma} = -\frac{s - z_{\mathrm{G}}}{s}\frac{g}{\bar{\bar{\theta}}}. \tag{6-49}$$

Applying the chain rule separately to Eq. (4-41) is appropriate if the hydrostatic assumption is *exactly* satisfied. However, the invariance of the physical representation is lost if the assumption is not exact, as discussed by Dutton (1976:242), since a correct tensor transformation is required. When the horizontal scales are much larger than the vertical scales of motion, the hydrostatic relation is very closely satisfied, and such a separation of the vertical and horizontal equation may be justified. By making the hydrostatic assumption before the coordinate transformation, however, significant insight into the effect of the change of coordinates on the form of the physical invariance of the conservation relations in the transformed system cannot be evaluated. To provide such insight, it is necessary to use the methods of tensor analysis to transform coordinate systems, and then to invoke a more general form of the hydrostatic assumption. A more in-depth understanding of the coordinate transformation is then obtained.

To examine the effect of using the hydrostatic assumption in Eqs. (6-40), (6-41), and (6-42), Eq. (6-48) is defined as the generalized vertical coordinate.
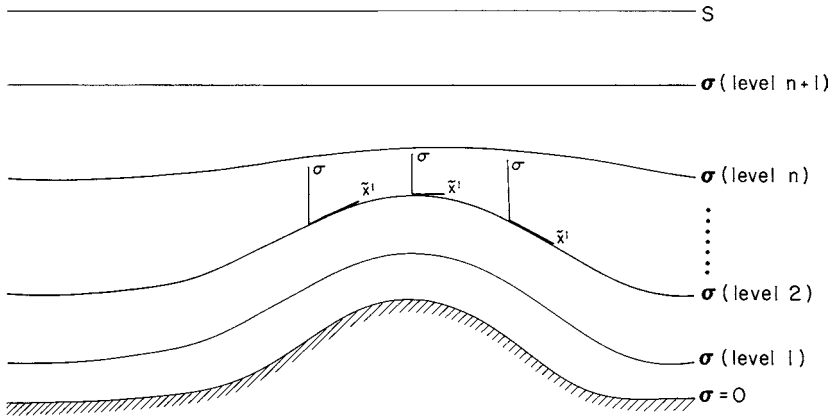
Fig. 6-3. Schematic representation of σ-coordinate surfaces as they would appear in a rectangular representation, as defined by Eq. (6-48).

The relation between the spatial coordinates in the two representations is given by

$$
\begin{aligned}
\tilde{x}^1 &= x, & x &= \tilde{x}^1, \\
\tilde{x}^2 &= y, & y &= \tilde{x}^2, \\
\tilde{x}^3 &= \sigma = s[z - z_G(x, y)] & z &= h = (\sigma/s)[s - z_G(\tilde{x}^1, \tilde{x}^2)] \\
& \quad /[s - z_G(x, y)], & & \quad + z_G(\tilde{x}^1, \tilde{x}^2),
\end{aligned}
\tag{6-50}
$$

so that the nonzero quantities needed to evaluate the Jacobian and its determinant [Eq. (6-32)], metric tensor [Eq. (6-29)], and Christoffel symbol [Eq. (6-30)] are given as

$$
\frac{\partial \sigma}{\partial x} = \frac{\partial z_G}{\partial x}\left(\frac{\sigma - s}{s - z_G}\right), \ \frac{\partial h}{\partial \tilde{x}^1} = \frac{\partial z_G}{\partial \tilde{x}^1}\left(\frac{s - \sigma}{s}\right), \ \frac{\partial \sigma}{\partial y} = \frac{\partial z_G}{\partial y}\left(\frac{\sigma - s}{s - z_G}\right),
$$

$$
\frac{\partial h}{\partial \tilde{x}^2} = \frac{\partial z_G}{\partial \tilde{x}^2}\left(\frac{s - \sigma}{s}\right), \ \frac{\partial \sigma}{\partial z} = \frac{s}{s - z_G}, \quad \frac{\partial h}{\partial \sigma} = \frac{s - z_G}{s} = \sqrt{G}
\tag{6-51}
$$

and

$$
\tilde{\Gamma}^3_{11} = \frac{s - \sigma}{s - z_G}\frac{\partial^2 z_G}{\partial \tilde{x}^{1^2}}, \tilde{\Gamma}^3_{22} = \frac{s - \sigma}{s - z_G}\frac{\partial^2 z_G}{\partial \tilde{x}^{2^2}}, \tilde{\Gamma}^3_{21} = \frac{s - \sigma}{s - z_G}\frac{\partial^2 z_G}{\partial \tilde{x}^1 \partial \tilde{x}^2},
$$

$$
\tilde{\Gamma}^3_{23} = -\frac{1}{s - z_G}\frac{\partial z_G}{\partial \tilde{x}^2}, \quad \text{and} \quad \tilde{\Gamma}^3_{13} = -\frac{1}{s - z_G}\frac{\partial z_G}{\partial \tilde{x}^1},
\tag{6-52}
$$

with $\tilde{\Gamma}^3_{21} = \tilde{\Gamma}^3_{12}$, $\tilde{\Gamma}^3_{23} = \tilde{\Gamma}^3_{32}$, and $\tilde{\Gamma}^3_{13} = \tilde{\Gamma}^3_{31}$.

Figure 6-3 schematically illustrates this coordinate transformation as viewed in the Cartesian coordinate framework.

The velocity vector $\vec{V}$, can be expressed as (Pielke and Cram 1989)

$$\vec{V} = \tilde{u}_i \vec{\eta}^i = \tilde{u}^i \vec{\tau}_j = u\vec{i} + v\vec{j} + w\vec{k},$$

$$\vec{V} = \tilde{u}_1 \vec{i} + \tilde{u}_2 \vec{j} + \tilde{u}_3 \left[\vec{i}\left(\frac{\sigma - s}{s - z_G}\right)\frac{\partial z_G}{\partial x} + \vec{j}\left(\frac{\sigma - s}{s - z_G}\right)\frac{\partial z_G}{\partial y} + \vec{k}\left(\frac{s}{s - z_G}\right) \right],$$

$$\vec{V} = \tilde{u}^1 \left[\vec{i} + \vec{k}\left(\frac{s - \sigma}{s}\right)\frac{\partial z_G}{\partial \tilde{x}^1} \right] + \tilde{u}^2 \left[\vec{j} + \vec{k}\left(\frac{s - \sigma}{s}\right)\frac{\partial z_G}{\partial \tilde{x}^2} \right]$$

$$+ \tilde{u}^3 \vec{k}\left(\frac{s - z_G}{s}\right).$$

(6-53)

The velocities $\tilde{u}_i$ and $\tilde{u}^i$ are the covariant and contravariant components, respectively, and are given by

$$\tilde{u}^1 = u,$$

$$\tilde{u}^2 = v,$$

$$\tilde{u}^3 = u\left(\frac{\sigma - s}{s - z_G}\right)\frac{\partial z_G}{\partial x} + v\left(\frac{\sigma - s}{s - z_G}\right)\frac{\partial z_G}{\partial y} + w\left(\frac{s}{s - z_G}\right),$$

$$\tilde{u}_1 = u + \left(\frac{s - \sigma}{s}\right)\frac{\partial z_G}{\partial \tilde{x}^1}w,$$

$$\tilde{u}_2 = v + \left(\frac{s - \sigma}{s}\right)\frac{\partial z_G}{\partial \tilde{x}^2}w,$$

$$\tilde{u}_3 = \left(\frac{s - z_G}{s}\right).$$

(6-54)

Therefore, the vectors in Eq. (6-53) can be rewritten in terms of the Cartesian quantities as

$$\vec{V} = \left[u + \left(\frac{s - \sigma}{s}\right)\frac{\partial z_G}{\partial \tilde{x}^1}w \right]\vec{i} + \left[v + \left(\frac{s - \sigma}{s}\right)\frac{\partial z_G}{\partial \tilde{x}^2}w \right]\vec{j}$$

$$+ w\left(\frac{1}{s}\right)\left[\vec{i}(\sigma - s)\frac{\partial z_G}{\partial x} + \vec{j}(\sigma - s)\frac{\partial z_G}{\partial y} + \vec{k} \right]$$

$$\vec{V} = u\left[\vec{i} + \vec{k}\left(\frac{s - \sigma}{s}\right)\frac{\partial z_G}{\partial \tilde{x}^1} \right] + v\left[\vec{j} + \vec{k}\left(\frac{s - \sigma}{s}\right)\frac{\partial z_G}{\partial \tilde{x}^2} \right]$$

$$+ \left[u(\sigma - s)\frac{\partial z_G}{\partial x} + v(\sigma - s)\frac{\partial z_G}{\partial y} + w(s) \right]\vec{k}\left(\frac{1}{s}\right).$$

(6-55)

Figure 6-4 shows the vector $\vec{V}$ presented in the Cartesian, covariant, and contravariant forms for a two-dimensional case.

Cartesian   Contravariant   Covariant
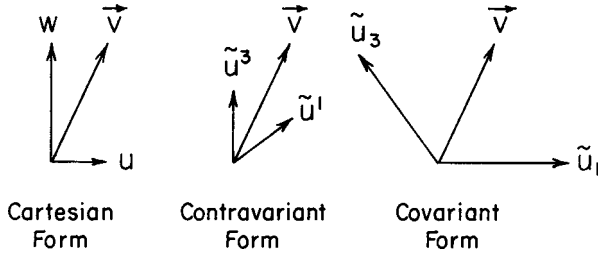Form   Form   Form

Fig. 6-4.   Vector $\vec{V}$ as expressed in Cartesian, covariant, and contravariant components in a terrain-following coordinate system. The σ surface is parallel to $\tilde{u}^1$ and perpendicular to $\tilde{u}_3$. (From Pielke and Cram 1989.)

Note that the contravariant form has a component in the vertical direction and a component parallel to the σ surface, which at $\sigma = 0$ is the ground. The covariant form, in contrast, has a component perpendicular to the σ surface and a horizontal component. The consistent form of kinetic energy is $\frac{1}{2}\vec{V} \cdot \vec{V}$ and can be calculated from

$$\vec{V} \cdot \vec{V} = \tilde{u}_i \vec{\eta}^i \tilde{u}^j \vec{\tau}_j = \delta^i_j \tilde{u}_i \tilde{u}^j = \tilde{u}_i \tilde{u}^i.$$

The covariant components must be multiplied by the corresponding contravariant components, that is,

$$\tilde{u}_i \tilde{u}^i = \tilde{u}_1 \tilde{u}^1 + \tilde{u}_2 \tilde{u}^2 + \tilde{u}_3 \tilde{u}^3$$

or

$$\tilde{u}_i \tilde{u}^i = u\left[u + \left(\frac{s-\sigma}{s}\right)\frac{\partial z_G}{\partial \tilde{x}^1} w\right] + v\left[v + \left(\frac{s-\sigma}{s}\right)\frac{\partial z_G}{\partial \tilde{x}^2} w\right]$$

$$+ w\left[u\left(\frac{\sigma-s}{s}\right)\frac{\partial z_G}{\partial x} + v\left(\frac{\sigma-s}{s}\right)\frac{\partial z_G}{\partial y} + w\right]$$

$$= u^2 + v^2 + w^2. \tag{6-56}$$

The complete conservation-of-motion equation in the contravariant form can be written in general form for the coordinate transformation as

$$\frac{\partial \tilde{u}^1}{\partial t} = -\tilde{u}^j \frac{\partial \tilde{u}^1}{\partial \tilde{x}^j} - \theta \frac{\partial \pi}{\partial \tilde{x}^1} + \theta \frac{\sigma-s}{s-z_G}\frac{\partial z_G}{\partial x}\frac{\partial \pi}{\partial \tilde{x}^3} - \hat{f}\tilde{u}^3 + f\tilde{u}^2, \tag{6-57}$$

$$\frac{\partial \tilde{u}^2}{\partial t} = -\tilde{u}^j \frac{\partial \tilde{u}^2}{\partial \tilde{x}^j} - \theta \frac{\partial \pi}{\partial \tilde{x}^2} + \theta \frac{\sigma-s}{s-z_G}\frac{\partial z_G}{\partial y}\frac{\partial \pi}{\partial \tilde{x}^3} - f\tilde{u}^1, \tag{6-58}$$

and

$$\frac{\partial \tilde{u}^3}{\partial t} = -\tilde{u}^j \frac{\partial \tilde{u}^3}{\partial \tilde{x}^j} - \frac{1}{(s - z_G)} \left[(s - \sigma) \frac{\partial^2 z_G}{\partial \tilde{x}^{1^2}} (\tilde{u}^1)^2 + (s - \sigma) \frac{\partial^2 z_G}{\partial \tilde{x}^{2^2}} (\tilde{u}^2)^2 \right.$$

$$+ 2(s - \sigma) \frac{\partial^2 z_G}{\partial \tilde{x}^1 \partial \tilde{x}^2} \tilde{u}^1 \tilde{u}^2 - 2 \frac{\partial z_G}{\partial \tilde{x}^1} \tilde{u}^1 \tilde{u}^3 - 2 \frac{\partial z_G}{\partial \tilde{x}^2} \tilde{u}^2 \tilde{u}^3 \right]$$

$$- \theta \left\{ \frac{\partial z_G}{\partial x} \left(\frac{\sigma - s}{s - z_G} \right) \frac{\partial \pi}{\partial \tilde{x}^1} + \frac{\partial z_G}{\partial y} \left(\frac{\sigma - s}{s - z_G} \right) \frac{\partial \pi}{\partial \tilde{x}^2} \right.$$

$$+ \left[\left(\left(\frac{\partial z_G}{\partial x} \right) \left(\frac{\sigma - s}{s - z_G} \right) \right)^2 + \left(\left(\frac{\partial z_G}{\partial y} \right) \left(\frac{\sigma - s}{s - z_G} \right) \right)^2 \right.$$

$$\left. \left. + \left(\frac{s}{s - z_G} \right)^2 \right] \frac{\partial \pi}{\partial \tilde{x}^3} \right\} - \frac{s}{s - z_G} g, \tag{6-59}$$

where, to reduce notational complexity, the Coriolis term was left out of the $\tilde{u}^3$ equation.[4] Equations (6-57) and (6-58) are applied parallel to σ surfaces, while Eq. (6-59) is applied in the vertical axis along a σ coordinate [see Eq. (6-53)].

6.3.2   Generalized Hydrostatic Equation

A generalized hydrostatic form of Eq. (6-59) can be derived if it is assumed that vertical accelerations are small compared to the remaining terms, which yields

$$0 = -\theta \left\{ \frac{\partial z_G}{\partial x} \left(\frac{\sigma - s}{s - z_G} \right) \frac{\partial \pi}{\partial \tilde{x}^1} + \frac{\partial z_G}{\partial y} \left(\frac{\sigma - s}{s - z_G} \right) \frac{\partial \pi}{\partial \tilde{x}^2} \right.$$

$$+ \left[\left(\left(\frac{\partial z_G}{\partial x} \right) \left(\frac{\sigma - s}{s - z_G} \right) \right)^2 + \left(\left(\frac{\partial z_G}{\partial y} \right) \left(\frac{\sigma - s}{s - z_G} \right) \right)^2 \right.$$

$$\left. \left. + \left(\frac{s}{s - z_G} \right)^2 \right] \frac{\partial \pi}{\partial \tilde{x}^3} \right\} - \frac{s}{s - z_G} g. \tag{6-60}$$

Rearranging Eq. (6-60) to solve for $\partial \pi / \partial \tilde{x}^3$ produces

$$\frac{\partial \pi}{\partial \tilde{x}^3} = - \left(\frac{s}{s - z_G} \frac{g}{\theta} + \frac{\partial z_G}{\partial x} \left(\frac{\sigma - s}{s - z_G} \right) \frac{\partial \pi}{\partial \tilde{x}^1} + \frac{\partial z_G}{\partial y} \left(\frac{\sigma - s}{s - z_G} \right) \frac{\partial \pi}{\partial \tilde{x}^2} \right)$$

$$\left/ \left[\left(\frac{\partial z_G}{\partial x} \left(\frac{\sigma - s}{s - z_G} \right) \right)^2 + \left(\frac{\partial z_G}{\partial y} \left(\frac{\sigma - s}{s - z_G} \right) \right)^2 + \left(\frac{s}{s - z_G} \right)^2 \right] \right. . \tag{6-61}$$

Equation (6-61) is a generalized hydrostatic equation because accelerations are neglected in the σ direction but permitted in the σ-parallel orientation, thereby retaining some nonhydrostatic motion when referred back to the Cartesian hydrostatic equation.[5]

When slope angles are small, Eq. (6-61) reduces to

$$\frac{\partial \pi}{\partial \tilde{x}^3} = -\left(\frac{s - z_G}{s}\right)\frac{g}{\theta},\tag{6-62}$$

which is the form generally applied to represent the hydrostatic assumption in atmospheric models with a terrain-following coordinate system [Eq. (6-48)]. Equation (6-62) is, therefore, the shallow-slope generalized hydrostatic approximation. Physick (1986) did apply the complete form given by Eq. (6-61) in his simulation of the flow in the Grand Canyon, however.

The main result of this analysis is that a generalized hydrostatic equation can be derived that retains some nonhydrostatic motions when referred back to the Cartesian coordinate system. Section 6.4 discusses this approach applied to drainage flow models.

6.3.3 Generalized Geostrophic Wind

A generalized geostrophic wind can be derived from Eqs. (6-57) and (6-58), where a balance between the pressure gradient force and the Coriolis term is assumed, and Eq. (6-62), used to represent $\partial \pi / \partial \tilde{x}^3$ (Pielke and Cram 1987; Cram and Pielke 1989), that is,

$$\tilde{u}_g^2 = \frac{1}{f}\left[\theta\frac{\partial \pi}{\partial \tilde{x}^1} - g\frac{\sigma - s}{s}\frac{\partial z_G}{\partial x}\right]$$
$$\tilde{u}_g^1 = -\frac{1}{f}\left[\theta\frac{\partial \pi}{\partial \tilde{x}^2} - g\frac{\sigma - s}{s}\frac{\partial z_G}{\partial y}\right]\tag{6-63}$$

(where, for simplicity, the $\hat{f}\tilde{u}^3$ term was ignored).[6]

Since $\tilde{u}_g^1\vec{\tau}_1$ and $\tilde{u}_g^2\vec{\tau}_2$ are the components on σ surfaces, a horizontal component of the generalized geostrophic wind can be derived from

$$u_g = \tilde{u}_g^1\vec{\tau}_1 \cdot \vec{i} \qquad \text{and} \qquad v_g = \tilde{u}_g^2\vec{\tau}_2 \cdot \vec{j},$$

which, using the form of $\vec{\tau}_j$ and $\tilde{u}^j$ in Eqs. (6-53) and (6-54), yields

$$u_g = u \qquad \text{and} \qquad v_g = v,$$

so that the horizontal geostrophic wind derived from the terrain-following coordinate system is the same as would be derived in a Cartesian framework.

At the surface, $z = z_G(\sigma = 0)$, so that Eq. (6-63) reduces to

$$v_g = \frac{\theta}{f}\frac{\partial \pi}{\partial \tilde{x}^1} + \frac{g}{f}\frac{\partial z_G}{\partial x} = \frac{\theta}{f}\frac{\partial \tilde{\pi}}{\partial x}$$
$$u_g = -\frac{\theta}{f}\frac{\partial \pi}{\partial \tilde{x}^2} - \frac{g}{f}\frac{\partial z_G}{\partial y} = \frac{-\theta}{f}\frac{\partial \tilde{\pi}}{\partial y}\tag{6-64}$$

Equation (6-64) is an equation for the surface geostrophic wind that can be used to obtain a corresponding horizontal pressure gradient over flat terrain

$(\partial \tilde{\pi}/\partial x, \partial \tilde{\pi}/\partial y)$, which defines the surface geostrophic wind components u_g and v_g. The values of $\tilde{\pi}$ are obtained from the equation

$$\frac{\partial^2 \tilde{\pi}}{\partial x^2} + \frac{\partial^2 \tilde{\pi}}{\partial y^2} = \frac{\partial}{\partial x}\left(\frac{v_g f}{\theta}\right) - \frac{\partial}{\partial y}\left(\frac{u_g f}{\theta}\right), \tag{6-65}$$

where u_g and v_g are evaluated from Eq. (6-64). The geostrophic wind defined by Eq. (6-63) is parallel to the σ surfaces and thus includes a nonzero vertical component. The component of the σ-system pressure gradient that we want to display for analysis purposes, however, is the one on a flat surface. Since in a flat, mean-sea-level z system, the geostrophic wind is nondivergent except for the effect of north–south f variations, v_g is differentiated by $\partial/\partial x$ and u_g by $\partial/\partial y$; then subtraction yields the elliptic equation for $\tilde{\pi}$.

Potential temperature must be known and the horizontal boundary values of $\tilde{\pi}$ specified to permit the solution of Eq. (6-65) to obtain $\tilde{\pi}$ (and thus pressure) everywhere within the domain. The boundary values of $\tilde{\pi}$ can be specified using the standard lapse rate reduction, and the interior values of $\tilde{\pi}$ can be obtained using a relaxation procedure such as that discussed in Chapter 10.

Surface values of θ were used for θ, although the procedure was found to be relatively insensitive to the θ field. The most consistent specification of the lateral boundary conditions needed in Eq. (6-65) would be from a domain in which the perimeter is at sea level.

Sangster (1960) developed the idea that the streamline and potential fields of the surface geostrophic winds can provide a better intuitive estimate of the horizontal pressure gradients than can reduce pressure. The analysis of horizontal pressure gradients using Eq. (6-65) is less arbitrary than the conventional reduced mean sea level (MSL) pressure analyses routinely shown on synoptic weather maps and easily and directly interpreted by a weather forecaster.

To demonstrate the technique, Figure 6-5 illustrates the smoothed topography of the western United States and northern Mexico. The U.S. Air Force 30-minute average elevation data were splined to a 1° latitude–by–1° longitude grid (40 × 30 grid points, from 25° to 49°N and 130° to 91°W) and then operated on with five passes of a two-dimensional, five-point smoother. The data for the two cases discussed were obtained from the National Meteorological Center (NMC) 2.5° global analyses of heights and temperatures on the standard pressure surfaces. These were splined horizontally and interpolated vertically to the 40 × 30 grid and surface elevations.

The conventional MSL-reduced pressure analyses were calculated by using the assumption of a standard lapse rate of temperature $\partial T/\partial Z = -6.5 \times 10^{-3}$ K m^{-1} below the ground surface to permit a comparison of the two procedures of surface weather map analysis. More sophisticated procedures to estimate what would be the temperature lapse rate below elevated terrain are
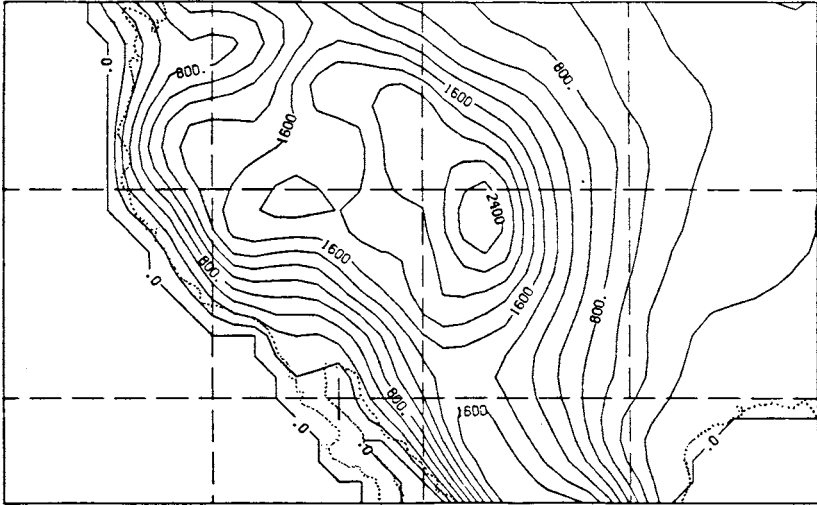
Fig. 6-5.   Surface elevation in meters. (From Pielke and Cram 1987.)

used by the national weather services; however, the need to arbitrarily extrapo-
late below the surface of the ground remains. These analyses are compared to
those obtained using Eq. (6-65). The boundary conditions for that solution are
obtained using the conventional pressure reduction.

The conventionally reduced MSL pressure analysis for 1200 UTC,
February 5, 1980 is shown in Figure 6-6. The geostrophic wind vectors and
wind magnitude computed from this analysis, that is,

$$u_{g_s} = -\frac{\theta}{f}\frac{\partial \pi}{\partial y} \qquad \text{and} \qquad v_{g_s} = \frac{\partial}{f}\frac{\partial \pi}{\partial x},$$

are given as Figures 6-7 and 6-8. A large pressure gradient and correspond-
ing large geostrophic wind speeds are evident along the base of the high-
pressure ridge. In contrast, using Eq. (6-64) along with the terrain gradients
from Figure 6-5 and the surface pressure distribution in Figure 6-9 produces
the much smoother and somewhat reduced geostrophic wind speed pattern illus-
trated in Figures 6-10 and 6-11. The much more chaotic distribution of wind
speeds in Figure 6-8 as compared to the distribution in Figure 6-11 is a result
of the arbitrary reduction of pressure to sea level used to obtain Figure 6-8.
The corresponding pressure analysis derived using Eq. (6-65) is shown in Fig-
ure 6-12. The conventional MSL reduction analysis has a much stronger high-
pressure area (stronger by as much as 6 mb) over the Great Basin, and associ-
ated stronger horizontal pressure gradients. The conventionally reduced pressure
analysis results in overly strong pressure gradients and has overly strong surface
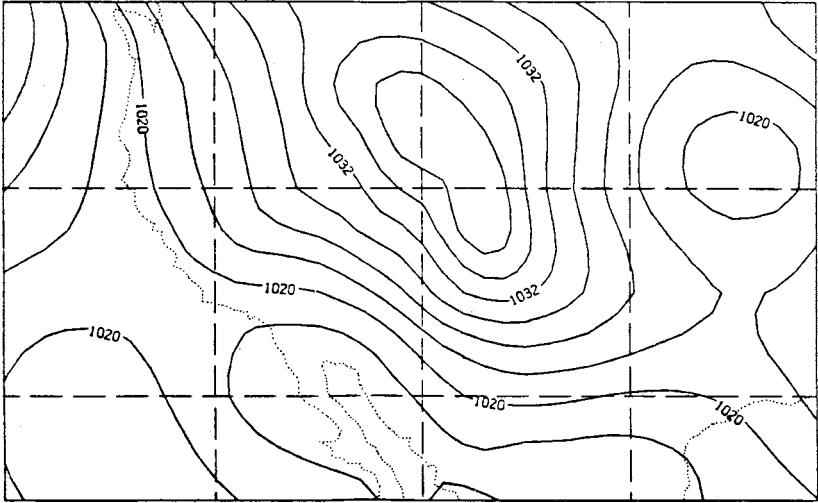geostrophic winds.

Fig. 6-6. MSL pressure (mb), p_{MSL}, obtained by using a standard lapse rate reduction for February 5, 1980. (From Pielke and Cram 1987.)
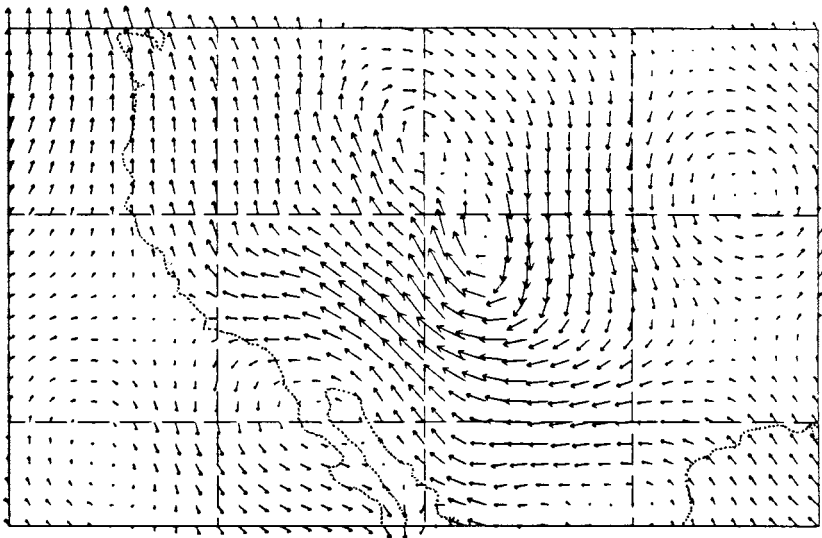

Fig. 6-7. Geostrophic wind vectors for February 5, 1980 from p_{MSL} in Figure 6-6. (From Pielke and Cram 1987.)
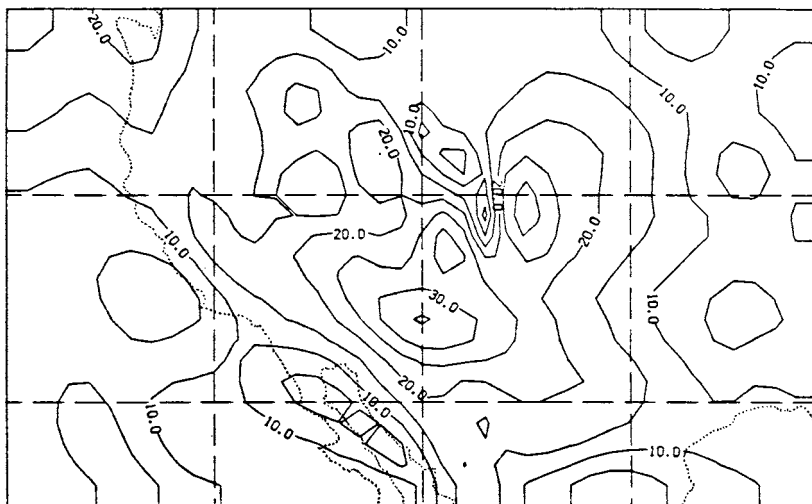
Fig. 6-8.   Geostrophic wind magnitudes (m s^{-1}) for February 5, 1980 from p_{MSL} in Figure 6-6. (From Pielke and Cram 1987.)
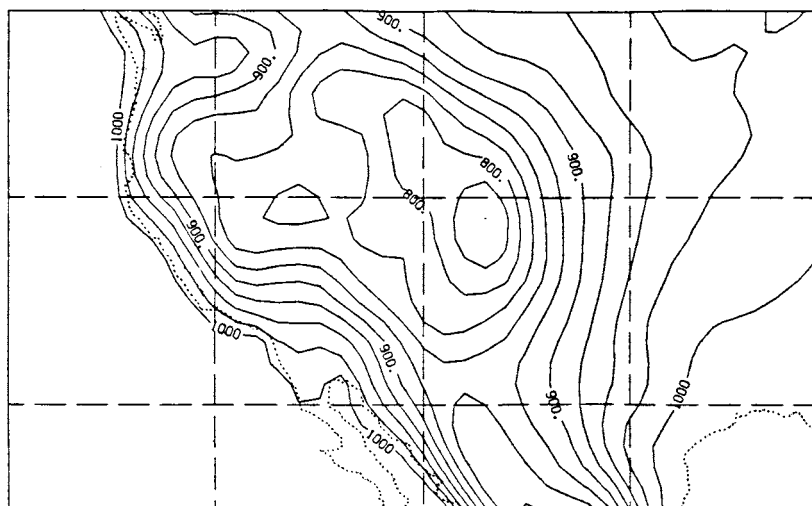

Fig. 6-9.   Surface pressure (mb) for February 5, 1980. (From Pielke and Cram 1987.)
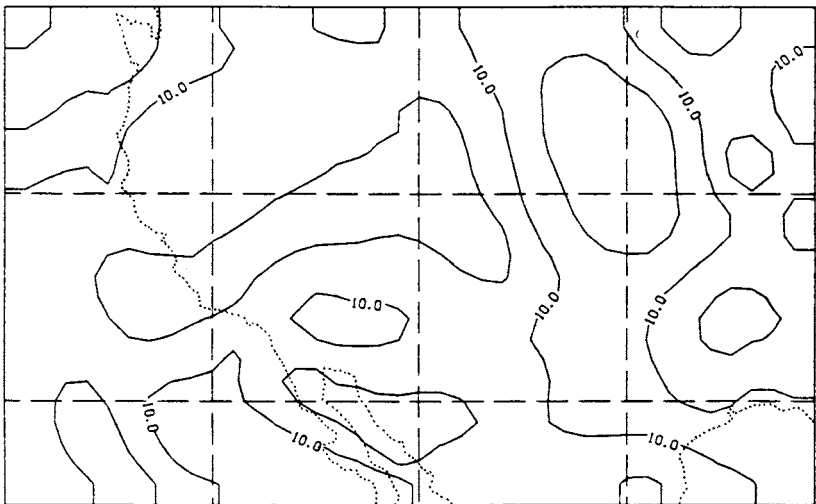
50.0
MAXIMUM VECTOR
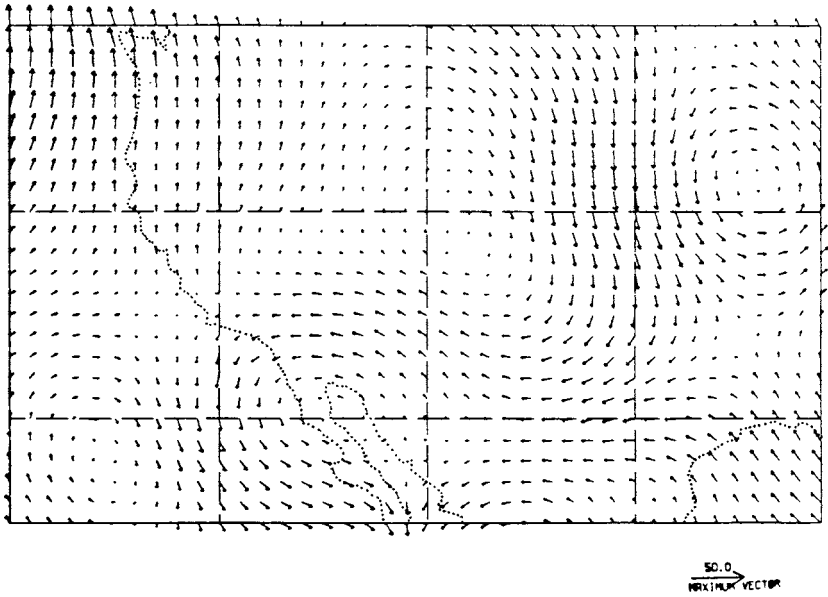
Fig. 6-10. Geostrophic wind vectors for February 5, 1980 calculated using Eq. (6-64). (From Pielke and Cram 1987.)

Fig. 6-11. Geostrophic wind magnitudes (m s^{-1}) for February 5, 1980 calculated using Eq. (6-64). (From Pielke and Cram 1987.)
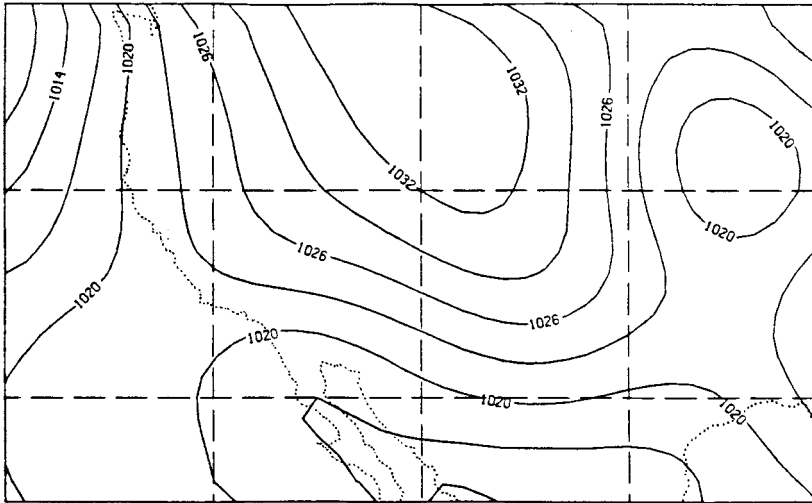
Fig. 6-12.   Geostrophic pressure analysis obtained from Eq. (6-65) for February 5, 1980. (From Pielke and Cram 1987.)

A summertime situation (1200 UTC, July 20, 1981) is presented in Figures 6-13–6-19. As with the February 5, 1980 example, a comparison between Figure 6-15 (geostrophic wind evaluated from reduced MSL pressure) and Figure 6-18 (geostrophic wind evaluated at the ground surface) shows that the large geostrophic wind speed and somewhat chaotic pattern is eliminated when the ad hoc, arbitrary reduction of pressure to sea level is not performed. Figure 6-19 is the derived pressure analysis [from Eq. (6-65)] for the summer case. The strength of the analyzed high-pressure area over the western United States is again reduced by approximately 6 mb, and the surrounding pressure gradients are correspondingly decreased. The surface pressure analysis in Figure 6-19 is less misleading than that in Figure 6-13.

The main result of this analysis is a simple methodology for analyzing surface geostrophic wind and pressure that eliminates the arbitrariness of reducing pressure to MSL in areas of elevated terrain. The method reduces the apparently excessive pressure gradients that result from conventional MSL pressure reduction analyses. The procedure uses a geostrophic wind defined in terms of a terrain-following coordinate system to derive a flat ground surface pressure field that is consistent in concept (i.e., nondivergent except for the f variation with latitude) with the currently applied MSL analyses. This approach is easy to implement and would be useful to both operational meteorologists in interpreting real-time synoptic data and researchers in their analysis of model output and observational data.
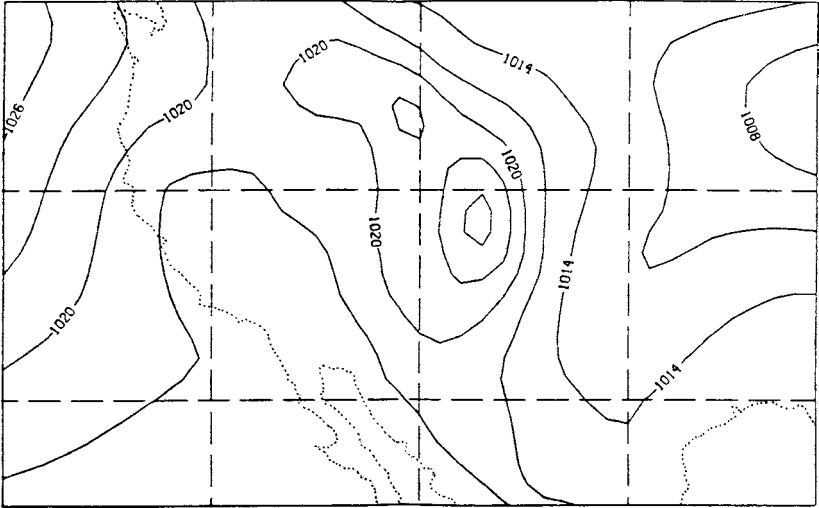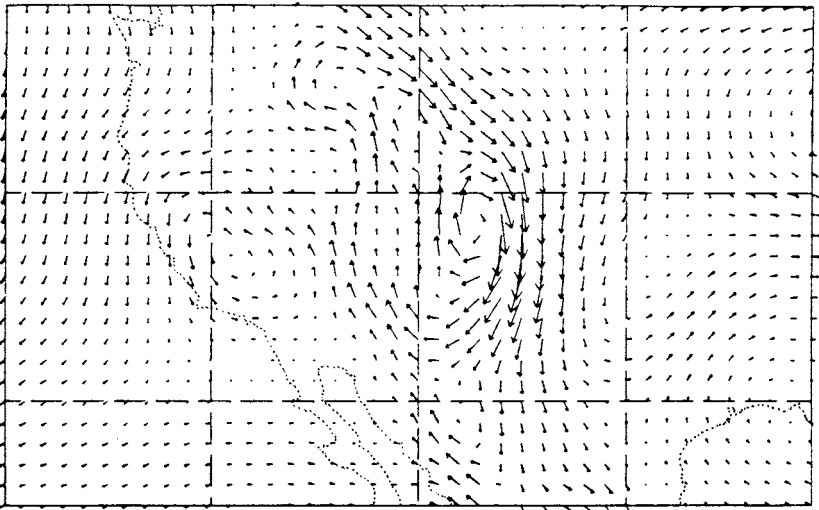
Fig. 6-13. MSL pressure (mb), p_{MSL}, obtained by using a standard lapse rate reduction for July 20, 1981. (From Pielke and Cram 1987.)

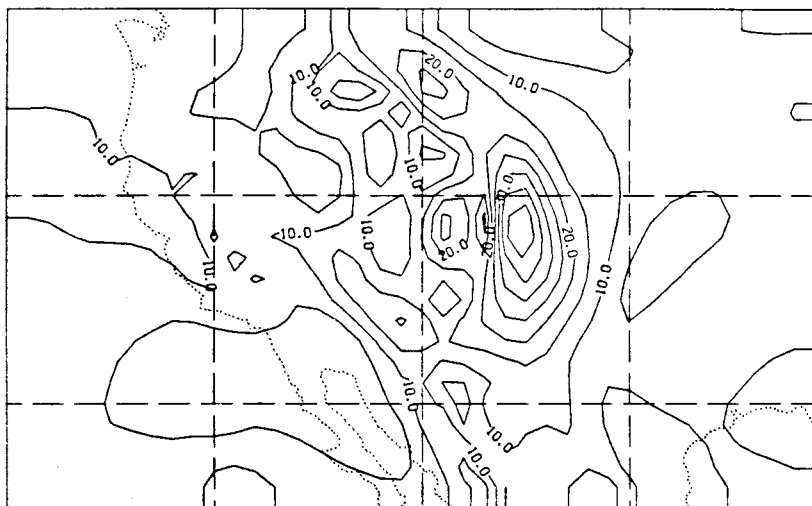**Fig. 6-14.** Geostrophic wind vectors for July 20, 1980 from p_{MSL} in Figure 6-13. (From Pielke and Cram 1987.)

Fig. 6-15.   Geostrophic wind magnitudes (m s^{-1}) for July 20, 1981 from p_{MSL} in Figure 6-13. (From Pielke and Cram 1987.)
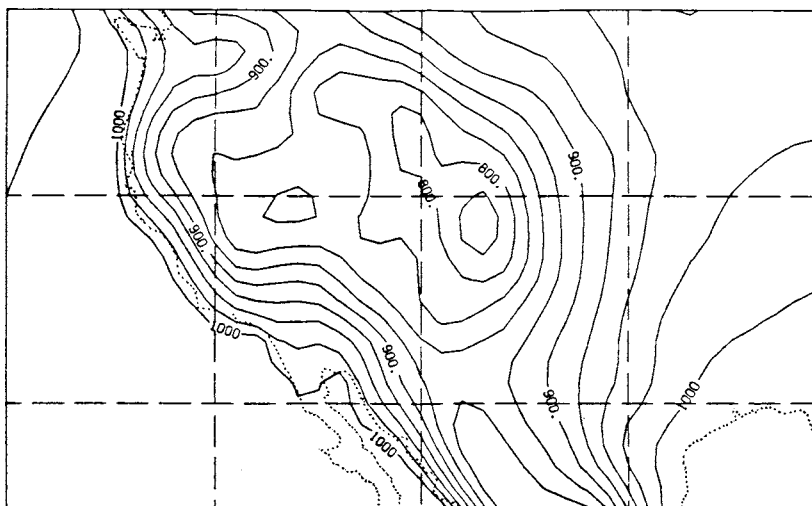

Fig. 6-16.   Surface pressure (mb) for July 20, 1981. (From Pielke and Cram 1987.)
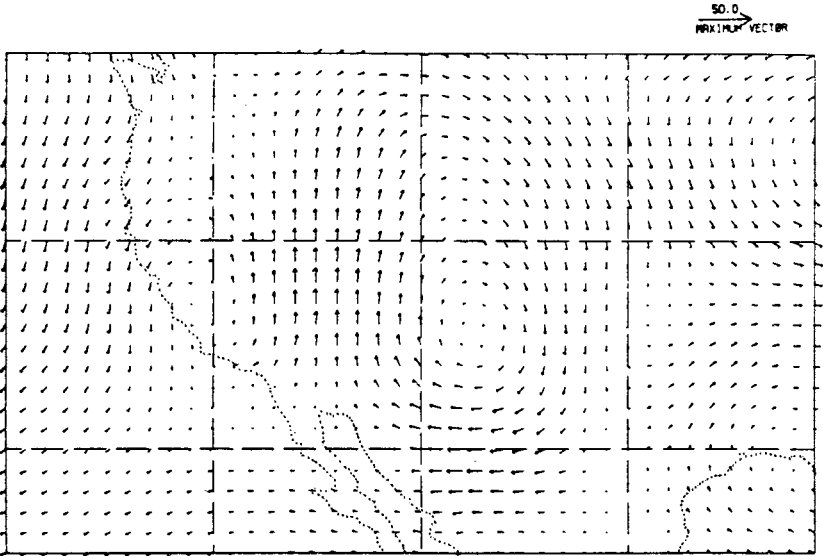
Fig. 6-17.   Geostrophic wind vectors for July 20, 1981 calculated using Eq. (6-64). (From Pielke and Cram 1987.)
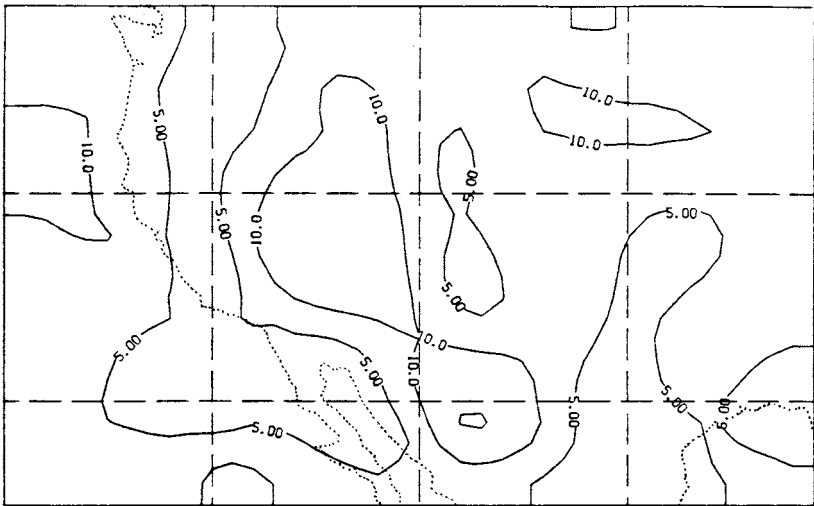

Fig. 6-18.   Geostrophic wind magnitudes (m s^{-1}) for July 20, 1981 calculated using Eq. (6-64). (From Pielke and Cram 1987.)
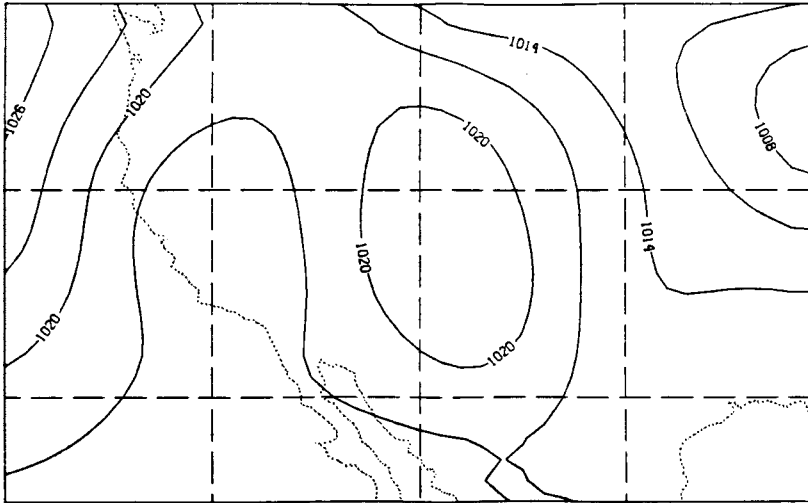
Fig. 6-19. Geostrophic pressure analysis obtained from Eq. (6-65) for July 20, 1981. (From Pielke and Cram 1987.)

6.4   Derivation of Drainage Flow Equations Using Two Different Coordinate Representations

In this section two transformations for drainage flow modeling are examined and, for simplicity, illustrated for two-dimensional formulations originally described in Berkofsky (1993) and Pielke *et al.* (1985, 1993b). The extension to three dimensions is straightforward. The formulations are as follows:

Transformation I.

$$\tilde{x}^1 = x$$
$$\tilde{x}^3 = z - z_G(x)$$
$$x = \tilde{x}^1$$
$$z = \tilde{x}^3 + z_G(\tilde{x}^1)$$

Transformation II.

$$\tilde{x}^1 = x \cos \gamma + z \sin \gamma$$
$$\tilde{x}^3 = z \cos \gamma - x \sin \gamma$$
$$x = \tilde{x}^1 \cos \gamma - \tilde{x}^3 \sin \gamma$$
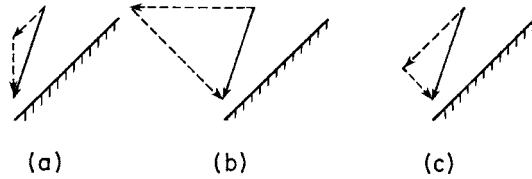$$z = \tilde{x}^1 \sin \gamma + \tilde{x}^3 \cos \gamma$$

Fig. 6-20. Representations of a drainage flow wind using (a) the contravariant and (b) covariant forms of the velocity components derived from transformation I, and (c) the velocity components obtained by the orthogonal rotation transformation II. The magnitude and direction of the components of the vector in the different representations have been given in terms of the Cartesian velocity components u and w and basis vectors $\bar{i}$ and $\bar{k}$. The slope $\partial z_{\mathrm{G}}/\partial x = \alpha$ and γ is the slope angle. (From Pielke *et al.* 1985.)

Here z_{G} is terrain height and $\gamma = \tan^{-1}[\partial z_{\mathrm{G}}/\partial x]$ is the slope angle of the terrain.

Transformation I represents one form of the nonorthogonal generalized vertical coordinate transformations given at the beginning of Section 6.2. As shown in Figure 6-4, the $\tilde{x}^3$ coordinate is parallel to the gravity vector and $\tilde{x}^1$ lies along the terrain slope. Transformation II represents an orthogonal rotation in which $\tilde{x}^1$ is parallel and $\tilde{x}^3$ perpendicular to the terrain. Both transformations are illustrated in Figure 6-20.

The orthogonal rotation is of the form commonly used to develop idealized analytic models of slope flow as summarized by for example, Mahrt (1982) and applied by McNider (1982). Mahrt suggests that one advantage of such a coordinate transformation is that the

> . . . gravitational force perpendicular to the ground is approximately balanced by the pressure gradient force, while the component of the gravitational force parallel to the slope is not balanced and leads to downslope acceleration.

This type of separation into a hydrostatic part and a nonhydrostatic component is of substantial usefulness in developing analytic (and numerical) slope flow models. Its application and generalization are explored using Transformations I and II.

6.4.1   Transformation I

Using the definition of $\widetilde{G}^{ik}$ and $\partial \tilde{x}^i/\partial z$ and covariant differentiation and Transformation I, we obtain

$$\widetilde{G}^{ik} = \begin{bmatrix} 1 & -\dfrac{\partial z_{\mathrm{G}}}{\partial x} \\[2ex] -\dfrac{\partial z_{\mathrm{G}}}{\partial t} & \left(\dfrac{\partial z_{\mathrm{G}}}{\partial x}\right)^2 + 1 \end{bmatrix} \; ; \dfrac{\partial \tilde{x}^i}{\partial z} = (0, 1).$$

For two dimensions, when subgrid-scale flux[7] terms with $\hat{f}$ and f are ignored and the pressure gradient force is represented by p' instead of $\bar{\pi}$, Eqs. (6-40) and (6-42) can be written as

$$\frac{\partial \tilde{u}^1}{\partial t} + \tilde{u}^j \frac{\partial \tilde{u}^1}{\partial \tilde{x}^j} = -\frac{1}{\rho_0} \frac{\partial p'}{\partial \tilde{x}^1} + \frac{1}{\rho_0} \frac{\partial z_{\mathrm{G}}}{\partial x} \frac{\partial p'}{\partial \tilde{x}^3} \tag{6-66}$$

$$\frac{\partial \tilde{u}^3}{\partial t} + \tilde{u}^j \frac{\partial \tilde{u}^3}{\partial \tilde{x}^j} = +\frac{1}{\rho_0} \left\{ \frac{\partial z_{\mathrm{G}}}{\partial x} \frac{\partial p'}{\partial \tilde{x}^1} - \left[\left(\frac{\partial z_{\mathrm{G}}}{\partial x} \right)^2 + 1 \right] \frac{\partial p'}{\partial \tilde{x}^3} \right\} + g \frac{\theta'}{\theta_0}. \tag{6-67}$$

This type of coordinate transformation has considerable utility, because a type of hydrostatic assumption can be assumed to be valid in the $\tilde{x}^3$ direction but with accelerations still explicitly resolved in the terrain-parallel direction, which for nonzero slope has a component in the vertical direction. This form of hydrostatic representation is different from that suggested by Mahrt (1982).

If the assumption is made that in the $\tilde{x}^3$ direction, $d\tilde{u}^3/dt$ is small relative to the other terms (i.e., a generalized hydrostatic assumption, as discussed in Section 6.3.2), then Eqs. (6-66) and (6-67) reduce to

$$\frac{\partial \tilde{u}^1}{\partial t} + \tilde{u}^1 \frac{\partial \tilde{u}^1}{\partial \tilde{x}^1} + \tilde{u}^3 \frac{\partial \tilde{u}^1}{\partial \tilde{x}^3} = -\frac{1}{\rho_0} \frac{\partial p'}{\partial \tilde{x}^1} + \frac{1}{\rho_0} \frac{\partial z_{\mathrm{G}}}{\partial x} \frac{\partial p'}{\partial \tilde{x}^3} \tag{6-68}$$

and

$$\frac{\partial p'}{\partial \tilde{x}^3} = \frac{1}{\left[(\partial z_{\mathrm{G}}/\partial x)^2 + 1 \right]} \left(\frac{g \theta'}{\theta_0} \rho_0 + \frac{\partial z_{\mathrm{G}}}{\partial x} \frac{\partial p'}{\partial \tilde{x}^1} \right). \tag{6-69}$$

Inserting Eq. (6-69) into Eq. (6-66) and rearranging yields

$$\frac{\partial \tilde{u}^1}{\partial t} + \tilde{u}^1 \frac{\partial \tilde{u}^1}{\partial \tilde{x}^1} + \tilde{u}^3 \frac{\partial \tilde{u}^1}{\partial \tilde{x}^3} = -\frac{1}{\rho_0} \frac{\partial p'}{\partial \tilde{x}^1} \times \left[1 - \frac{(\partial z_{\mathrm{G}}/\partial x)^2}{\left[(\partial z_{\mathrm{G}}/\partial x)^2 + 1 \right]} \right]$$
$$+ \frac{\partial z_{\mathrm{G}}/\partial x}{\left[(\partial z_{\mathrm{G}}/\partial x)^2 + 1 \right]} g \frac{\theta'}{\theta_0},$$

or

$$\frac{\partial \tilde{u}^1}{\partial t} = -\frac{1}{\rho_0} \frac{\partial p'}{\partial \tilde{x}^1} \left(1 - \frac{\alpha^2}{1 + \alpha^2} \right) + g \frac{\alpha}{(\alpha^2 + 1)} \frac{\theta'}{\theta_0} - \tilde{u}^1, \frac{\partial \tilde{u}^1}{\partial \tilde{x}^1} - \tilde{u}^3 \frac{\partial \tilde{u}^1}{\partial \tilde{x}^3}, \tag{6-70}$$

where $\alpha = \partial z_{\mathrm{G}}/\partial x$ has been defined for convenience. For flat terrain, this relation reduces to the original Cartesian horizontal equation of motion.

6.4.2   Transformation II

Using the definition of $\widetilde{G}^{ik}$ and $\partial \tilde{x}^i / \partial z$ and covariant differentiation and Transformation II, we obtain

$$
G^{ik} = \begin{bmatrix} 1 & 0 \\ 0 & 1 \end{bmatrix}; \; \frac{\partial \tilde{x}^i}{\partial z} = (\sin \gamma, \cos \gamma).
$$

Using Eq. (6-38), in which the same assumptions used to derive Eqs. (6-66) and (6-67) are applied, the simplified equations can be written as

$$
\frac{\partial \tilde{u}^1}{\partial t} + \tilde{u}^k \frac{\partial \tilde{u}^1}{\partial \tilde{x}^k} = -\frac{1}{\rho_0} \frac{\partial p'}{\partial \tilde{x}^1} + g \frac{\theta'}{\theta_0} \sin \gamma \qquad (6\text{-}71)
$$

$$
\frac{\partial \tilde{u}^3}{\partial t} + \tilde{u}^k \frac{\partial \tilde{u}^3}{\partial \tilde{x}^k} = -\frac{1}{\rho_0} \frac{\partial p'}{\partial \tilde{x}^3} + g \frac{\theta'}{\theta_0} \cos \gamma. \qquad (6\text{-}72)
$$

If a hydrostatic-type assumption is made in the $\tilde{x}^3$ direction, as suggested by Mahrt (1982) for sufficiently small slopes, then Eqs. (6-71) and (6-72) reduce to

$$
\frac{\partial \tilde{u}^1}{\partial t} + \tilde{u}^k \frac{\partial \tilde{u}^1}{\partial \tilde{x}^k} = -\frac{1}{\rho_0} \frac{\partial p'}{\partial \tilde{x}^1} + g \frac{\theta'}{\theta_0} \sin \gamma \qquad (6\text{-}73)
$$

$$
\frac{\partial p'}{\partial \tilde{x}^3} = \rho_0 g \frac{\theta'}{\theta_0} \cos \gamma. \qquad (6\text{-}74)
$$

To compare quantitatively the result of differences in the two transformations, we can develop a layer-integrated momentum and thermodynamic system for a uniform slope configuration and solve it analytically. The layer-integrated thermodynamic equation can be expressed in the general system by

$$
\frac{\partial \bar{\theta}}{\partial t} + \tilde{u}^k \frac{\partial \bar{\theta}}{\partial \tilde{x}^k} = \overline{L}_c, \qquad (6\text{-}75)
$$

where $\overline{L}_c$ is the local warming rate for the integrated layer including both radiative and turbulent processes. Using $\bar{\theta} = \theta_0 + \theta'$, where θ_0 is a function of z only, and assuming $\partial \theta_0 / \partial t = 0$, we have

$$
\frac{\partial \theta'}{\partial t} = -\left(\tilde{u}^1 \frac{\partial \theta_0}{\partial \tilde{x}^1} + \tilde{u}^1 \frac{\partial \theta'}{\partial \tilde{x}^1} + \tilde{u}^3 \frac{\partial \theta'}{\partial \tilde{x}^3} \right) + \overline{L}_c. \qquad (6\text{-}76)
$$

For an infinite uniform slope, $\partial \theta' / \partial \tilde{x}^1 = 0$, and mass continuity requires that $\tilde{u}^3 = 0$. Thus, using the chain rule,

$$
\frac{\partial \theta_0}{\partial \tilde{x}^1} = \frac{\partial \theta_0}{\partial z} \frac{\partial x^3}{\partial \tilde{x}^1}, \qquad (6\text{-}77)
$$

so that Eq. (6-76) can be written as

$$
\frac{\partial \theta'}{\partial t} = -\tilde{u}^1 \frac{\partial \theta_0}{\partial x^3} \frac{\partial x^3}{\partial \tilde{x}^1} + \overline{L}_c. \qquad (6\text{-}78)
$$

For Transformation I, the generalized hydrostatic system for the uniform slope is

$$\frac{\partial \tilde{u}^1}{\partial t} = g \frac{\tan \gamma}{(\tan^2 \gamma + 1)} \frac{\theta'}{\theta_0} \tag{6-79}$$

$$\frac{\partial \theta'}{\partial t} = -\tilde{u}^1 \beta \tan \gamma + \overline{L}_c, \tag{6-80}$$

where $\tilde{u}^1$ and θ' represent layer quantities, $\tan \gamma = \partial z_G / \partial x$, $\tan \gamma = \partial x^3 / \partial \tilde{x}^1 = \partial z / \partial \tilde{x}^1$, and $\beta = \partial \theta_0 / \partial z$. Since the slope is uniform, $\partial p' / \partial \tilde{x}^1 = 0$ is assumed. Following McNider (1982), take $\partial / \partial t$ of Eq. (6-79) and substitute for $\partial \theta' / \partial t$, giving

$$\frac{\partial^2 \tilde{u}^1}{\partial t^2} = \frac{g}{\theta_0} \frac{\tan \gamma}{(\tan^2 \gamma + 1)} (-\tilde{u}^1 \beta \tan \gamma + \overline{L}_c) \tag{6-81}$$

or

$$\frac{\partial^2 \tilde{u}^1}{\partial t^2} + \frac{g}{\theta_0} \beta \sin^2 \gamma \tilde{u}^1 - \frac{g}{\theta_0} \cos \gamma \sin \gamma \overline{L}_c = 0. \tag{6-82}$$

Since the slope is uniform and represents a single layer, the equation is an ordinary differential equation that becomes

$$\frac{d^2 \tilde{u}^1}{dt^2} + \frac{g}{\theta_0} \beta \sin^2 \gamma \tilde{u}^1 - \frac{g}{\theta_0} \cos \gamma \sin \gamma \overline{L}_c = 0. \tag{6-83}$$

In a similar manner, the differential equation for Transformation II is

$$\frac{d^2 \hat{u}^1}{dt^2} + \frac{g}{\theta_0} \beta \sin^2 \gamma \hat{u}^1 - \frac{g}{\theta_0} \sin \gamma \overline{L}_c = 0, \tag{6-84}$$

where a caret ($^\wedge$) rather than a tilde ($\sim$) is placed over u^1 to indicate that $\tilde{u}^1$ and $\hat{u}^1$ are different velocities. Note that the difference in Eqs. (6-83) and (6-84) is a $\cos \gamma$ coefficient in the last term in Eq. (6-83), so that the variation in the two formulations increases for increasing slope angles. For initial conditions

$$\hat{u}^1 = \tilde{u}^1 = 0 \qquad \text{and} \qquad \frac{d\hat{u}^1}{dt} = \frac{d\tilde{u}^1}{dt} = 0,$$

the solution for Eq. (6-83) (Transformation I) becomes

$$\tilde{u}^1 = \frac{\overline{L}_c}{\beta \tan \gamma} (1 - \cos \tau t), \tag{6-85}$$

where

$$\tau^2 = \frac{g\beta}{\theta_0} \sin^2 \gamma.$$

TABLE 6-1

Values of $\tan \gamma$ and $\sin \gamma$ for Several
Different Slope Angles, γ.

γ	$\sin \gamma$	$\tan \gamma$
5°	0.09	0.09
10°	0.17	0.18
15°	0.26	0.27
20°	0.34	0.36
25°	0.42	0.47
30°	0.50	0.58
35°	0.57	0.70
40°	0.64	0.84
45°	0.71	1.00

Likewise, the solution for Eq. (6-84) (Transformation II) is

$$\hat{u}^1 = \frac{\overline{L}_c}{\beta \sin \gamma} (1 - \cos \hat{\tau} t), \tag{6-86}$$

with

$$\hat{\tau}^2 = \frac{g \beta}{\theta_0} \sin^2 \gamma,$$

where τ and $\hat{\tau}$ are the periods of oscillation in the frictionless results.

Relative values of $\hat{u}^1$ and $\tilde{u}^1$, for both transformations, are tabulated for several slope angles in Table 6-1. The terrain-following formulation (Transformation I) should be more realistic, since nonhydrostatic accelerations along the terrain slope can be represented. Nonetheless, slopes greater than about 20° would be required before the difference in the two velocities would exceed 6%. The oscillation periods, τ and $\hat{\tau}$, are identical in the two coordinate transformations, however.

6.5 Summary

Based on the derivations in this chapter, the conservation equations can be written for any vertical coordinate system, σ, as

$$\frac{\partial \bar{\tilde{u}}^1}{\partial t} = -\bar{\tilde{u}}^j \frac{\partial \bar{\tilde{u}}^1}{\partial \tilde{x}^j} - \overline{\tilde{u}^{j''} \frac{\partial \tilde{u}^{1''}}{\partial \tilde{x}^j}} - \bar{\theta} \frac{\partial \bar{\pi}}{\partial \tilde{x}^1} - \bar{\theta} \frac{\partial \sigma}{\partial x} \frac{\partial \bar{\pi}}{\partial \tilde{x}^3}$$

$$- \hat{f} \left(\frac{\partial h}{\partial \tilde{x}^1} \bar{\tilde{u}}^1 + \frac{\partial h}{\partial \tilde{x}^2} \bar{\tilde{u}}^2 + \frac{\partial h}{\partial \tilde{x}^3} \bar{\tilde{u}}^3 \right) + f \bar{\tilde{u}}^2, \tag{6-87}$$

$$\frac{\partial \bar{\tilde{u}}^2}{\partial t} = -\bar{\tilde{u}}^j \frac{\partial \tilde{u}^2}{\partial \tilde{x}^j} - \overline{\tilde{u}^{j''} \frac{\partial \tilde{u}^{2''}}{\partial \tilde{x}^j}} - \bar{\theta} \frac{\partial \bar{\pi}}{\partial \tilde{x}^2} - \bar{\theta} \frac{\partial \sigma}{\partial y} \frac{\partial \bar{\pi}}{\partial \tilde{x}^3} - f \bar{\tilde{u}}^1, \tag{6-88}$$

$$\frac{\partial \bar{\tilde{u}}^3}{\partial t} = -\bar{\tilde{u}}^j \frac{\partial \tilde{u}^3}{\partial \tilde{x}^j} - \overline{\tilde{u}^{j''} \frac{\partial \tilde{u}^{3''}}{\partial \tilde{x}^j}} - \overline{\tilde{\Gamma}}^3_{jl} \bar{\tilde{u}}^j \bar{\tilde{u}}^l - \overline{\tilde{\Gamma}}^3_{jl} \overline{\tilde{u}^{j''} \tilde{u}^{l''}}$$

$$- -\bar{\theta} \left\{ \frac{\partial \sigma}{\partial x} \frac{\partial \bar{\pi}}{\partial \tilde{x}^1} + \frac{\partial \sigma}{\partial y} \frac{\partial \bar{\pi}}{\partial \tilde{x}^2} + \left[\left(\frac{\partial \sigma}{\partial x}\right)^2 + \left(\frac{\partial \sigma}{\partial y}\right)^2 + \left(\frac{\partial \sigma}{\partial z}\right)^2 \right] \frac{\partial \bar{\pi}}{\partial \tilde{x}^3} \right\}$$

$$+ \left(\hat{f} + \frac{\partial h}{\partial \tilde{x}^2} f \right) \frac{\partial \sigma}{\partial z} \left[\left(1 + \left(\frac{\partial h}{\partial \tilde{x}^1}\right)^2 \right) \bar{\tilde{u}}^1 + \frac{\partial h}{\partial \tilde{x}^1} \frac{\partial h}{\partial \tilde{x}^2} \bar{\tilde{u}}^2 + \frac{\partial h}{\partial \tilde{x}^1} \frac{\partial h}{\partial \tilde{x}^3} \bar{\tilde{u}}^3 \right]$$

$$- \frac{\partial h}{\partial \tilde{x}^1} f \frac{\partial \sigma}{\partial z} \left[\frac{\partial h}{\partial \tilde{x}^2} \frac{\partial h}{\partial \tilde{x}^1} \bar{\tilde{u}}^1 + \left(1 + \left(\frac{\partial h}{\partial \tilde{x}^2}\right)^2 \right) \bar{\tilde{u}}^2 + \frac{\partial h}{\partial \tilde{x}^2} \frac{\partial h}{\partial \tilde{x}^3} \bar{\tilde{u}}^3 \right] - \frac{\partial \sigma}{\partial z} g, \tag{6-89}$$

$$\frac{\partial \bar{\theta}}{\partial t} = -\bar{\tilde{u}}^j \frac{\partial \bar{\theta}}{\partial \tilde{x}^j} - \overline{\tilde{u}^{j''} \frac{\partial \theta''}{\partial \tilde{x}^j}} + \overline{\tilde{S}}_\theta, \tag{6-90}$$

$$\frac{\partial \bar{q}_n}{\partial t} = -\bar{\tilde{u}}^j \frac{\partial \bar{q}_n}{\partial \tilde{x}^j} - \overline{\tilde{u}^{j''} \frac{\partial q_n''}{\partial \tilde{x}^j}} + \overline{\tilde{S}}_{q_n}, \quad n = 1, 2, 3, \tag{6-91}$$

$$\frac{\partial \bar{\chi}_m}{\partial t} = -\bar{\tilde{u}}^j \frac{\partial \bar{\chi}_m}{\partial \tilde{x}^j} - \overline{\tilde{u}^{j''} \frac{\partial \chi_m''}{\partial \tilde{x}^j}} + \overline{\tilde{S}}_{\chi_m}, \quad m = 1, 2, \ldots, M, \tag{6-92}$$

$$\frac{\partial \bar{\rho}}{\partial t} = -\frac{\partial \sigma}{\partial z} \frac{\partial}{\partial \tilde{x}^j} \left(\frac{\partial h}{\partial \tilde{x}^3} \overline{\rho \tilde{u}^j} \right), \tag{6-93}$$

$$\bar{p} = \bar{\rho} R_d \bar{T}_v, \tag{6-94}$$

$$\bar{\theta} = \bar{T}_v (1000 \text{ mb}/p)^{R_d/C_p} \tag{6-95}$$

Equations (6-87)–(6-89) are the conservation-of-velocity equations. Equation (6-90) is the conservation-of-heat equation, Eq. (6-91) is the conservation-of-water substance equation, Eq. (6-92) is the conservation-of-other atmospheric gases and aerosols equation, and Eq. (6-93) is the conservation-of-mass of the air equation. Equation (6-94) is the ideal gas law, which is the equation of state for the air, and Eq. (6-95) is the definition of potential temperature. The overbar in these equations is of course the generalized form of the grid-volume average, as defined by Eq. (6-37). In the derivation of these equations, it is assumed that $(|\theta''|/\bar{\theta}) \ll 1$, $|\overline{\tilde{u}^{i''}}| = 0$, and $\overline{\tilde{G}^{ij}} = \tilde{G}^{ij}$. These equations can be manipulated in various ways in a model; however, it must always be possible to work backward to these fundamental conservation relationships.

Among the standard approximations used in these equations is the replacement of Eq. (6-89) with

$$\frac{\partial \bar{\pi}}{\partial \tilde{x}^3} = -\frac{g}{\bar{\theta}}\left(\frac{\partial \sigma}{\partial z}\right)^{-1},\tag{6-96}$$

where all vertical acceleration terms and terms involving f and $\hat{f}$ are ignored and $|\partial \sigma / \partial z| \gg |\partial \sigma / \partial x| \sim |\partial \sigma / \partial y|$ is assumed. This makes Eqs. (6-87)–(6-88), (6-90)–(6-95), and (6-96) a hydrostatic set of nonlinear partial differential equations. Another common assumption (the "anelastic approximation," introduced in Section 3.1.1) is to replace Eq. (6-93) with Eq. (6-44).

6.6   Application of Terrain-Following Coordinate Systems

Unfortunately, the use of terrain-following coordinate systems introduces several new computational problems to accurate numerical modeling. These can be summarized as follows.

1.   The two terms that represent the pressure gradient force along a σ surface, for example, [see, e.g., Eqs. (6-87) and (6-88)] represent differences between large terms. Slight errors in their definition (Mahrer and Pielke 1977a; Fortunato and Baptista 1996) can introduce significant errors in the model. Sun (1995) suggests using a reference local vertical pressure gradient from which a perturbation pressure gradient in the σ system is computed; however, two terms (albeit smaller) still appear.

2.   When the vertical grid increments ($\Delta \sigma$) are much smaller than the grid increments Δx and Δy, the interpolation needed to define gradients in the x and y directions introduce significant errors, as shown by Mahrer (1984). There is no known solution for this problem, except to limit how small the ratio of $\Delta \sigma / \Delta x$ and $\Delta \sigma / \Delta y$ can be. Mahrer 1984 concludes that $\Delta \sigma \leq [(s - \sigma)/(s - z_{\mathrm{G}})]\Delta z_{\mathrm{G}}$ is needed, where Δz_{G} is the change in terrain height across one horizontal grid interval.

3.   The subgrid-scale flux terms along a σ surface produce fluxes in the vertical ($\vec{k}$) direction. This is not desirable since turbulence fluxes (Chapter 7) are represented separately in the vertical and horizontal directions.

Mesoscale models have been developed that successfully use terrain-following coordinate systems as summarized in Appendix B. To take advantage of the terrain-following coordinate representation and still retain some of the benefits of a Cartesian coordinate system, models such as RAMS (Pielke *et al.* 1992) interpolate the dependent variables to a Cartesian gradient so that horizontal

gradients, rather than σ-parallel gradients, are calculated for use in the numerical form of the conservation equations. However, problems such as 2 and 3 above still appear as a result of the interpolation.

As a new approach, the developers of RAMS are testing a Cartesian coordinate system for use in complex terrain, where the eta-coordinate system or the shaved-coordinate system[8] are retained for the dynamics of the model (i.e., the pressure gradient force, advection, the Coriolis term), while the model parameterizations (Chapters 7–9) are evaluated on a Cartesian grid. Since all of the parameterizations are expressed in a one-dimensional framework, there is no need to use a terrain-following coordinate system. There is only the need to define the bottom of the parameterization as the earth's surface (i.e., $z_{\text{surface}} = z_{\text{G}}$, with $\tilde{z} = z - z_{\text{G}}$ the Cartesian height above the surface).

The insertion of at least some subgrid-scale topographic effects into the models [i.e., $z_{\text{G}}''(x)$] has, as reported by Marty Bell (2000, ASTeR—Mission Research Corporation, personal communication) and based in part on the ideas of Roger Ridley, used averaging, silhouette topography, envelope topography (Wallace *et al.* 1983), or reflected envelope topography to represent these smaller-scale effects. With the averaging approach, the average grid area terrain height is used. The silhouette method fills in the valleys [i.e., $z_{\text{G}}''(x) \leq 0$ within the grid] in computing the grid-area–averaged $\bar{z}_{\text{G}}$. The envelope terrain representation uses the grid-area–averaged terrain height plus a user-defined variation (such as $\sigma_{z_{\text{G}}}$) within the grid area to compute the z_{G} value applied for that grid point. The reflected envelope topography, which is currently applied in RAMS, is the envelope scheme mirrored about the local mean topography heights. If it is a local maximum or minimum, then the user-defined variation is inserted. None of these approaches is a completely adequate form for representing the appropriate grid-volume–averaging effect [Eq. (6-37)], but each is an improvement over not considering subgrid-scale terrain effects at all.

Notes to Chapter 6

1. The following discussion of tensor analysis uses Dutton's (1976) excellent in-depth description of this mathematical tool. Readers who require a more in-depth discussion of tensor analysis should refer to that source.

2. In vector terminology, this operation is also called the dot product.

3. It must be stressed that Eq. (6-37) does *not* represent the same volume as does Eq. (4-6). To do that, the integrand must include the determinant of the Jacobian of the transformation. It is not desirable to do this here, because $\tilde{x}^3$, $\tilde{x}^2$, $\tilde{x}^1$, and t are the coordinates of a grid that will be used in a numerical model and are thus the appropriate averaging volume.

4. One can manipulate Eqs. (6-57)–(6-59) as performed by Clark (1977) and Clark (1988, personal communication), such that explicit prognostic equations for $\tilde{u}^1$, $\tilde{u}^2$, and w (the Cartesian vertical velocity) are obtained. This rearrangement makes use of the contravariant velocity component

definitions in Eq. (6-54). These equations can be written in a flux form, which is advantageous for computational accuracy, as pointed out by Clark. The mathematical equivalence of the Christoffel symbols still occur in his equations, however, appearing in his diagnostic pressure equation derived using Eqs. (6-57)–(6-59).

5. It is important to recognize that while the Cartesian hydrostatic equation represents a balance of forces between the vertical pressure gradient and gravitational forces, the generalized hydrostatic equation as defined here retains those vertical accelerations that are parallel to σ surfaces.

6. Sangster (1987) also introduced an improved procedure to compute the geostrophic wind at the ground surface. Cram and Pielke (1989) demonstrate that the flat pressure field derived in this section is essentially equivalent to the streamfunction of Sangster, although the two methods have different lateral boundary conditions, formulations, and resulting sensitivities to these boundary conditions.

7. A straightforward assumption for the subgrid-scale fluxes in the vertical direction in Eq. (6-68) for use in an analytic model could be written as $-\tilde{u}^{3''}\frac{\partial \tilde{u}^{1''}}{\partial \tilde{x}^3} = \frac{\partial}{\partial \tilde{x}^3}\left(K\frac{\partial \tilde{u}^1}{\partial \tilde{x}^3}\right)$. Integrating this expression vertically between the surface and the top of a drainage flow, h, yields $\int_{\tilde{x}^3=0}^{\tilde{x}^3=h} \overline{\tilde{u}^{3''}\frac{\partial \tilde{u}^{1''}}{\partial \tilde{x}^3}}\,d\tilde{x}^3 = K\frac{\partial \tilde{u}^1}{\partial \tilde{x}^3}\Big|_{\text{at }\tilde{x}^3=0}^{\text{at }\tilde{x}^3=h}$, which could be used in a layered model of drainage flow; $K[\partial \tilde{u}^1/\partial \tilde{x}^3]$ at $\tilde{x}^3 = 0$ could be approximated as $C_D(\tilde{u}^1)^2$, for example, while $K[\partial \tilde{u}^1/\partial \tilde{x}^3]$ at h could be used to represent entrainment at the top of the drainage flow. An additional advantage of using Transformation I is that the integration is in the vertical direction rather than in the direction perpendicular to the $\tilde{x}^3$ surface.

8. Adcroft *et al.* (1997), and Marshall *et al.* (1997) use partial grid volumes at the bottom of their model (called "shaved cells") in an ocean model. Shaved models permit sloping terrain, yet retain a Cartesian framework.

Additional Readings

Byun, D. W. 1999a. Dynamically consistent formulations in meteorological and air quality models for multiscale atmospheric studies. Part I: Governing equations in a generalized coordinate system. *J. Atmos. Sci.* **56**, 3789–3807.

Byun, D. W. 1999b. Dynamically consistent formulations in meteorological and air quality models for multiscale atmospheric studies. Part II: Mass conservation issues. *J. Atmos. Sci.* **56**, 3808–3820.

> These articles provide an effective overview of terrain-following coordinate transformations, including excellent figures that illustrate different forms of the transformations.

Dutton, J. A. 1976. "The Ceaseless Wind." McGraw-Hill, New York.

> Dutton provides an outstanding review of tensor analysis and generalized vertical coordinate representations. Pages 129–144 and 248–251 were particularly useful in preparing this chapter.

Gal-Chen, T., and R. C. J. Somerville. 1975a. On the use of a coordinate transformation for the solution of the Navier–Stokes equations. *J. Comput. Phys.* **17**, 209–228.

> This article provides an excellent overview of the application of a specific terrain-following coordinate system for use in a nonhydrostatic meteorological model. The material on pages 215–219 was referred to frequently during the writing of this chapter.

Other references that provide supplemental information on the material presented in this chapter are as follows.

Clark, T. L. 1977. A small-scale dynamic model using a terrain-following coordinate transformation. *J. Comput. Phys.* **24**, 186–215.

Kasahara, A. 1974. Various vertical coordinate systems used for numerical weather prediction. *Mon. Wea. Rev.* **102**, 509–522.

Lapidus, A. 1967. A detached shock calculation by second-order finite difference. *J. Comput. Phys.* **2**, 154–177.

Phillips, N. A. 1957. A coordinate system having some special advantages for numerical forecasting. *J. Meteor.* **14**, 184–185.

Problems

1. Show that for flat terrain, the equations listed in Section 6.5 reduce to the grid-volume–averaged form of the conservation equations presented in Chapter 4.

2. Substitute one of the specific terrain-following coordinate systems listed at the beginning of Section 6.2 and write the form of each of the conservation equations listed in Chapter 4.

3. Select an atmospheric model that uses a generalized vertical coordinate system (e.g., MM5, ARPS, Eta) and use their form of σ to derive their specific form of the equations in Section 6.5.

4. For the model in problem 3, write the conservation equations used for flat terrain. Identify (a) the advective terms, (b) the vertical subgrid-scale flux terms, (c) the horizontal subgrid-scale flux terms, (d) the pressure gradient force term, and (e) the Coriolis terms.

Chapter 7

Parameterization-Averaged
Subgrid-Scale Fluxes

The grid-volume averaging of the conservation relations as described in Chapters 4 and 6 results in averaged subgrid-scale correlation terms [e.g., $\rho_0 \overline{u_j'' u_i''}$ from Eq. (4-21)] and averaged source–sink terms [e.g., $\overline{S_\theta}$ from Eq. (4-24)]. In the following three chapters, the representation in mesoscale models of three types of physical processes are introduced. This specification of subgrid-scale and source–sink processes using experimental data and simplified fundamental concepts is called *parameterization*. Usually the parameterizations are not defined in terms of basic conservation principles. A parameterization does not necessarily have to actually simulate the physical processes that it is representing to be a realistic representation of these terms.

Indeed, if the quantitative accuracy of a parameterization is not sacrificed, then it is desirable to make the parameterization as computationally simple as possible. The three processes to be parameterized are

- averaged subgrid-scale fluxes [i.e., $\rho_0 \overline{u_j'' u_i''}$, $\rho_0 \overline{u_j'' \theta}$, etc., in Eqs. (4-21) and (4-24)–(4-26)]
- averaged radiation flux divergence [i.e., part of $\overline{S_\theta}$ in Eq. (4-24)]
- averaged effects of the change of phase of water, including precipitation [i.e., $\overline{S_{q_n}}$ in Eq. (4-25), part of $\overline{S_\theta}$ in Eq. (4-24)].

The averaged effects of change of phase, precipitation, and/or change into other chemical species of atmospheric gases and aerosols other than water [i.e., S_{χ_m} in Eq. (4-26)] is not covered in this text. The reader is referred to Seinfeld (1975) and Seinfeld and Pandis (1997) for reports on the status of parameterizing these complex effects.

This chapter describes the parameterization of the averaged vertical subgrid fluxes. As discussed in Section 10.5 in Chapter 10, horizontal subgrid-scale fluxes are used only for computational reasons, since little is known of

horizontal subgrid-scale mixing on the mesoscale (or in other models whenever $\Delta x; \Delta y \gg \Delta z$), although work for ocean mixing, such as that of Young *et al.* (1982), offers an avenue for future research. As discussed in Chapter 4, the magnitude of the subgrid-scale variables and fluxes often can be the same or even larger than the resolvable dependent variables. A wind gust of 5 m s^{-1} (representing u''), for example, is not uncommon with an average wind speed of 5 m s^{-1} (representing $\bar{u}$). Figure 7-1 schematically illustrates a subgrid-scale correlation between vertical velocity and potential temperature. In this example, assumed to be close to flat ground so the grid-volume–averaged vertical velocity is approximately 0 (i.e., $\bar{w} \simeq 0$), the ground surface is assumed to be warmer than the air above, so that an upward perturbation vertical velocity tends to transport warm air upward, whereas descending motion tends to advect cooler air downward.[1] Averaging over the grid interval in this example yields an upward flux of heat ($\overline{w''\theta''} > 0$ with a magnitude of 6.9 cm K s^{-1}). Thus, despite the insignificant vertical flux of heat associated with the resolvable dependent variables (i.e., $\bar{w}\bar{\theta} \simeq 0$, since $\bar{w} \simeq 0$), a substantial transport of heat will occur because of the positive correlation between the subgrid-scale vertical velocity and potential temperature perturbation.

In developing subgrid-scale averaged quantities, however, one must recognize that the preferred representation is an ensemble average over the grid volume, rather than simply the grid-volume average as defined by Eq. (4-6). The ensemble average represents the most likely value of the subgrid-scale quantity, whereas the grid-volume average represents just one realization. Unless the subgrid-scale quantity is completely deterministic (i.e., without a statistical component), the two averages will not in general be the same. Thus in the parameterizations discussed in this chapter, it is assumed that they are the most
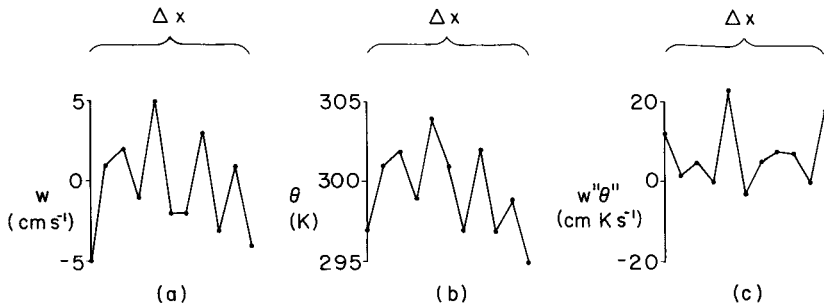

Fig. 7-1. Schematic illustration of subgrid-scale values of vertical velocity, w, potential temperature, θ, and the subgrid-scale correlation, $w''\theta''$. In this example, the grid-averaged value of vertical motion is required to be approximately 0 (i.e., $\bar{w} \simeq 0$), and $\bar{\theta} = 299.5$ K is used. Both grid value averages are assumed to be constant over Δx. The grid-averaged subgrid-scale correlation $\overline{w''\theta''}$ is equal to 6.9 cm K s^{-1}.

likely (i.e., ensemble) estimates. Wyngaard (1982, 1983) and Cotton and Anthes (1989) discuss ensemble averaging in more depth. Defining a parameterization in terms of a realization from a probability distribution is an area meriting future research. Preliminary work in this area has been completed, as reported in Garratt and Pielke (1989), Garratt *et al.* (1990), and Avissar (1991, 1992).

7.1   Basic Terms

To develop parameterization for these subgrid-scale correlations, it is necessary to introduce several basic definitions. To simplify the interpretation, a Cartesian coordinate framework is applied in this analysis. Modifications for when a generalized vertical coordinate system is used were discussed in Chapter 6.

Neglecting the Coriolis effect, Eq. (4-4) can be rewritten as

$$
\frac{\partial}{\partial t}(\bar{u}_i + u_i'') = -(\bar{u}_j + u_j'')\frac{\partial}{\partial x_j}(\bar{u}_i + u_i'')
$$

$$
- (\theta_0 + \theta' + \theta'')\frac{\partial(\bar{\pi} + \pi'')}{\partial x_i} - g\delta_{i3}, \tag{7-1}
$$

where Eq. (4-36) is used to represent the pressure gradient force, with θ and π decomposed using the definitions given by Eqs. (4-3) and (4-12). Assuming that the synoptic-scale variables are in hydrostatic equilibrium, and that fluctuations in potential temperature (i.e., θ' and θ'') are neglected relative to θ_0 except when multiplied by gravity,[2] Eq. (7-1) can be rewritten as

$$
\frac{\partial}{\partial t}(\bar{u}_i + u_i'') = -(\bar{u}_j + u_j'')\frac{\partial}{\partial x_j}(\bar{u}_i + u_i'') - \theta_0 \frac{\partial(\pi' + \pi'')}{\partial x_i}
$$

$$
- \theta_0\left[\frac{\partial \pi_0}{\partial x}\delta_{i1} + \frac{\partial \pi_0}{\partial y}\delta_{i2}\right] + \frac{g\theta'}{\theta_0}\delta_{i3} + \frac{g\theta''}{\theta_0}\delta_{i3}. \tag{7-2}
$$

Averaging this equation over a grid volume using Eq. (4-6) and applying the assumptions given by Eq. (4-8) yields

$$
\frac{\partial \bar{u}_i}{\partial t} = -\bar{u}_j\frac{\partial}{\partial x_j}\bar{u}_i - \overline{u_j''\frac{\partial}{\partial x_j}u_i''} - \theta_0\frac{\partial \pi'}{\partial x_i}
$$

$$
- \theta_0\left[\frac{\partial \pi_0}{\partial x}\delta_{i1} + \frac{\partial \pi_0}{\partial y}\delta_{i2}\right] + g\frac{\theta'}{\theta_0}\delta_{i3}. \tag{7-3}
$$

Subtracting Eq. (7-3) from (7-2) gives

$$\frac{\partial u_i''}{\partial t} = -\bar{u}_j \frac{\partial}{\partial x_j} u_i'' - u_j'' \frac{\partial u_i''}{\partial x_j} - u_j'' \frac{\partial \bar{u}_i}{\partial x_j} + \overline{u_j'' \frac{\partial u_i''}{\partial x_j}} - \theta_0 \frac{\partial \pi''}{\partial x_i} + g \frac{\theta''}{\theta_0} \delta_{i3}, \quad (7\text{-}4)$$

which is a prognostic equation for the subgrid-scale velocity perturbation.

Multiplying Eq. (7-4) by u_i'', averaging using Eq. (4-6), and applying the assumption[3] $\overline{u_i''} = 0$ results in

$$\frac{\partial \bar{e}}{\partial t} = -\bar{u}_j \frac{\partial \bar{e}}{\partial x_j} - \overline{u_j'' \frac{\partial e}{\partial x_j}} - \overline{u_j'' u_i''} \frac{\partial \bar{u}_i}{\partial x_j} - \theta_0 \overline{u_i'' \frac{\partial \pi''}{\partial x_i}} + g \frac{\overline{u_i'' \theta''}}{\theta_0} \delta_{i3}, \quad (7\text{-}5)$$

where $\bar{e} = \frac{1}{2}\overline{u_i''^2}$ and $e = \frac{1}{2}u_i''^2$. In the context of a numerical model, Eq. (7-5) is the grid-volume–averaged, subgrid-scale perturbation kinetic energy equation. This equation is usually called the *turbulent kinetic energy equation*,[4] with $\bar{e}$ the average turbulent kinetic energy.[5] The individual terms in Eq. (7-5) have the interpretation given in Table 7-1.

TABLE 7-1.
An Interpretation of the Individual Terms in Eq. (7-5)[a]

Term	Interpretation
$\dfrac{\partial \bar{e}}{\partial t}$	Local grid-volume change of averaged subgrid-scale perturbation kinetic energy $\bar{e}$
$\bar{u}_j \dfrac{\partial \bar{e}}{\partial x_j}$	Advection of $\bar{e}$ by the grid-volume–averaged velocity
$\overline{u_j'' \dfrac{\partial e}{\partial x_j}}$	Grid-volume–averaged advection of e by the subgrid-scale perturbation velocity
$\overline{u_j'' u_i''} \dfrac{\partial \bar{u}_i}{\partial x_j}$	Extraction from or input to $\bar{e}$ from the existence of both an average velocity shear and subgrid-scale velocity fluxes; also referred to as the *shear production* of turbulent kinetic energy
$\theta_0 \overline{u_i'' \dfrac{\partial \pi''}{\partial x_i}}$	Multiplying this term by ρ_0 and assuming that the anelastic conservation-of-mass equation is valid for the subgrid scale (i.e., $(\partial/\partial x_i)\rho_0 u_i'' = 0$) yields $\theta_0 (\partial/\partial x_i) \rho_0 \overline{u_i'' \pi''}$. Therefore, when the anelastic assumption is valid, this term causes changes in $\bar{e}$ only by advection through the boundaries of the grid volume. As discussed by Lumley and Panofsky (1964), the influence of the correlation between the turbulent velocity and pressure variables is to transfer kinetic energy between the three velocity components.
$g \dfrac{\overline{u_i'' \theta''}}{\theta_0} \delta_{i3} = g \dfrac{\overline{w'' \theta''}}{\theta_0}$	Extraction or production of $\bar{e}$ by buoyancy; referred to as the *buoyant production* of turbulent kinetic energy

[a]Lumley and Panofsky (1964), from which the derivation of Eq. (7-5) was based, discuss the turbulent kinetic energy equation and its derivation in detail.

If Eq. (7-5) were used to simulate the details of turbulence in a model, then the molecular dissipation of average turbulent kinetic energy would be included to guarantee a sink for this energy. In a mesoscale model, however, as discussed in Section 10.6, computational devices such as horizontal filters are applied to prevent the artificial accumulation of kinetic energy at short wavelengths. Such mechanisms are necessitated by the inability to resolve both the mesoscale and the small spatial scales in which the molecular dissipation of kinetic energy becomes significant.[6]

To contrast the relative contribution of the two source–sink terms of $\bar{e}$ in Eq. (7-5), it is useful to define the ratio

$$R_f = \frac{g}{\theta_0} \overline{w''\theta''} \Bigg/ \left[\overline{w''u''} \frac{\partial \bar{u}}{\partial z} + \overline{w''v''} \frac{\partial \bar{v}}{\partial z} \right], \tag{7-6}$$

where R_f is called the *flux Richardson number*. In this expression, horizontal contributions to the shear production of $\bar{e}$ are neglected and $|\partial \bar{u}/\partial z| \simeq |\partial \bar{v}/\partial z| \gg |\partial \bar{w}/\partial z|$. The flux Richardson number is a measure of the relative contribution of the buoyant production or dissipation of averaged, subgrid-scale kinetic energy relative to its generation or extraction by the vertical shear of the averaged horizontal wind.

In analogy with the molecular fluxes of heat and momentum [e.g., Eq. (3-29)], the vertical subgrid-scale flux terms $\overline{w''\theta''}$, $\overline{w''u''}$, and $\overline{w''v''}$ are often represented by

$$\overline{w''\theta''} = -K_\theta \frac{\partial \bar{\theta}}{\partial z}, \qquad \overline{w''q_k''} = -K_\theta \frac{\partial \bar{q}_k}{\partial z}, \qquad \overline{w''\chi_m''} - K_\theta \frac{\partial \overline{X}_m}{\partial z},$$

$$\overline{w''u''} = -K_m \frac{\partial \bar{u}}{\partial z}, \qquad \text{and} \qquad \overline{w''v''} = -K_m \frac{\partial \bar{v}}{\partial z}, \tag{7-7}$$

as assumed, for example, by Eq. (5-3), where K_θ and K_m are referred to as *exchange coefficients*. This form of representing the grid-volume subgrid-scale fluxes is called *first-order closure*. As discussed later in this section, however, it is important to note that although molecular mixing is a function of the type of fluid involved, turbulent mixing, such as represented by Eq. (7-7), is a function of the flow. Therefore, the turbulent exchange coefficients K_θ and K_m given in Eq. (7-7) are not constant in time or in space. Moreover, the expressions given by Eq. (7-7) require that the subgrid-scale fluxes be *downgradient* as long as the exchange coefficients are positive. In the atmosphere, *countergradient* turbulent fluxes are often observed (e.g., Deardorff 1966), as discussed just before Section 7.3.3.3. Nonetheless, Eq. (7-7) has been shown to be a useful representation of subgrid-scale fluxes.

Substituting Eq. (7-7) into Eq. (7-6) yields

$$R_f = K_\theta \frac{g}{\theta_0} \frac{\partial \bar{\theta}}{\partial z} \Big/ K_m \left[\left(\frac{\partial \bar{u}}{\partial z} \right)^2 + \left(\frac{\partial \bar{v}}{\partial z} \right)^2 \right]$$

$$= \frac{K_\theta}{K_m} \frac{g}{\theta_0} \frac{\partial \bar{\theta}}{\partial z} \Big/ \left[\left(\frac{\partial \bar{u}}{\partial z} \right)^2 + \left(\frac{\partial \bar{v}}{\partial z} \right)^2 \right] = \frac{K_\theta}{K_m} \, Ri, \qquad (7\text{-}8)$$

where Ri is called the *gradient Richardson number*. The sign of Ri is determined by the sign of the lapse rate of potential temperature. Thus the following conditions apply:

- Ri > 0 corresponds to $\partial \bar{\theta}/\partial z > 0$, which indicates a stably-stratified layer.
- Ri = 0 corresponds to $\partial \bar{\theta}/\partial z = 0$, which corresponds to neutral stratification.
- Ri < 0 corresponds to $\partial \bar{\theta}/\partial z < 0$, which indicates an unstably stratified layer.

Theory (e.g., Dutton 1976:79) indicates that when Ri is greater than 0.25, the stable stratification sufficiently suppresses turbulence so that the flow becomes laminar, even in the presence of mean wind shear. This value of Ri is called the *critical Richardson number*.

The unstable-stratified layer itself is broken down into two regimes:

- $|Ri| \leq 1$, where the shear production of subgrid-scale kinetic energy is important (a regime referred to as *forced convection*).
- $|Ri| > 1$, where the shear production becomes unimportant relative to the buoyant product of subgrid-scale kinetic energy (a regime called *free convection*).

The characteristic size of turbulent eddies in the atmosphere are larger during free convection than under forced convection. Brutsaert (1999) provides a recent review of boundary-layer turbulence during free convection.

As reported in Turner (1969), the intensity of turbulence near the ground can be estimated straightforwardly using a wind speed of 10 m, incoming solar radiation, cloud cover, and time of day. The stability classification scheme discussed by Turner forms the foundation of most air quality assessments on the mesoscale in the United States today. Unfortunately, although the dispersion estimates were developed from observations of diffusion over flat, horizontally homogeneous terrain, Gaussian plume models using these estimates are being applied for a wide range of mesoscale systems that are neither flat nor homogeneous. As reported by the American Meteorological Society in a position paper (AMS 1978), over flat, horizontally homogeneous terrain, Gaussian plume models probably give estimates of downwind plume concentrations within a

factor of 2. However, much more serious errors can result when this idealized topography is not achieved (e.g., Pielke *et al.* 1983).

Equation (7-4) can be used to obtain prognostic conservation equations for the subgrid-scale fluxes. Multiplying Eq. (7-4) by u_k'' yields

$$
u_k'' \frac{\partial u_i''}{\partial t} = -u_k'' \bar{u}_j \frac{\partial}{\partial x_j} u_i'' - u_k'' u_j'' \frac{\partial u_i''}{\partial x_j} - u_k'' u_j'' \frac{\partial \bar{u}_i}{\partial x_j}
$$
$$
+ u_k'' u_j'' \overline{\frac{\partial u_i''}{\partial x_j}} - u_k'' \theta_0 \frac{\partial \pi''}{\partial x_i} + g\, u_k'' \frac{\theta''}{\theta_0} \delta_{i3}. \tag{7-9}
$$

Writing Eq. (7-4) with k as the free index and then multiplying by u_i'' yields an equation for $u_i'' \partial u_k'' / \partial t$. Adding that equation to Eq. (7-9) results in

$$
\frac{\partial}{\partial t} (u_k'' u_i'') = -\bar{u}_j \frac{\partial}{\partial x_j} u_k'' u_i'' - u_j'' \frac{\partial}{\partial x_j} u_k'' u_i'' - u_i'' u_j'' \frac{\partial \bar{u}_k}{\partial x_j} - u_k'' u_j'' \frac{\partial \bar{u}_i}{\partial x_j}
$$
$$
+ u_i'' u_j'' \overline{\frac{\partial}{\partial x_j} u_k''} + u_k'' u_j'' \overline{\frac{\partial u_i''}{\partial x_j}} - u_i'' \theta_0 \frac{\partial \pi''}{\partial x_k}
$$
$$
- u_k'' \theta_0 \frac{\partial \pi''}{\partial x_i} + g u_i'' \frac{\theta''}{\theta_0} \delta_{k3} + g\, u_k'' \frac{\theta''}{\theta_0} \delta_{i3}. \tag{7-10}
$$

Grid-volume averaging Eq. (7-10) using the assumptions given by Eq. (4-8) yields

$$
\frac{\partial}{\partial t} \overline{u_k'' u_i''} = -\bar{u}_j \frac{\partial}{\partial x_j} \overline{u_k'' u_i''} - \overline{u_j'' \frac{\partial}{\partial x_j} u_k'' u_i''} - \overline{u_i'' u_j''} \frac{\partial \bar{u}_k}{\partial x_j} - \overline{u_k'' u_j''} \frac{\partial \bar{u}_i}{\partial x_j}
$$
$$
- \theta_0 \overline{u_i'' \frac{\partial \pi''}{\partial x_k}} - \theta_0 \overline{u_k'' \frac{\partial \pi''}{\partial x_i}} + \frac{g}{\theta_0} \delta_{k3} \overline{u_i'' \theta''} + \frac{g}{\theta_0} \delta_{i3} \overline{u_k'' \theta''}. \tag{7-11}
$$

Prognostic subgrid-scale equations can also be obtained for $\overline{u_i'' \theta''}$, $\overline{u_i'' q_k''}$, and $\overline{u_i'' \chi_m''}$. To illustrate how these equations are derived, multiply Eq. (7-4) by θ'', which results in

$$
\theta'' \frac{\partial u_i''}{\partial t} = -\theta'' \bar{u}_j \frac{\partial}{\partial x_j} u_i'' - \theta'' u_j'' \frac{\partial u_i''}{\partial x_j} - \theta'' u_j'' \frac{\partial \bar{u}_i}{\partial x_j}
$$
$$
+ \theta'' u_j'' \overline{\frac{\partial u_i''}{\partial x_j}} - \theta'' \theta_0 \frac{\partial \pi''}{\partial x_i} + g \frac{\theta''^2}{\theta_0} \delta_{i3}. \tag{7-12}
$$

A prognostic equation for θ'' can be obtained in a manner analogous to that used to obtain Eq. (7-4). Equation (2-44) for θ can be written as

$$
\frac{\partial}{\partial t} (\bar{\theta} + \theta'') = -(\bar{u}_j + u_j'') \frac{\partial}{\partial x_j} (\bar{\theta} + \theta'') + S_\theta.
$$

The source–sink term, S_θ, can be decomposed into a portion that is dependent only on grid-resolved quantities, which are defined here as $\bar{S}_\theta$, and a remainder that is also a function of subgrid-scale effects, S_θ''. Averaging this relation over a grid volume using Eq. (4-6) and applying the assumptions given by Eq. (4-8) yields

$$\frac{\partial \bar{\theta}}{\partial t} = -\bar{u}_j \frac{\partial}{\partial x_j} \bar{\theta} - \overline{u_j'' \frac{\partial \theta''}{\partial x_j}} + \bar{S}_\theta.$$

Note that requiring $\overline{S_\theta''} \equiv 0$ assumes that the source–sink term has subgrid-scale effects that average to 0 across the grid volume. This assumption is likely to be often unrealistic, but nonetheless is used here in the derivation of θ''.

Subtracting the equation for $\frac{\partial \bar{\theta}}{\partial t}$ from $\frac{\partial (\bar{\theta} + \theta'')}{\partial t}$ yields

$$\frac{\partial \theta''}{\partial t} = -\bar{u}_j \frac{\partial \theta''}{\partial x_j} - u_j'' \frac{\partial}{\partial x_j} (\bar{\theta} + \theta'') + \overline{u_j'' \frac{\partial \theta''}{\partial x_j}} + S_\theta - S_\theta''. \tag{7-13}$$

Equation (7-13) can be multiplied by u_i'' and added to Eq. (7-12). Performing the grid-volume average to this equation, using the assumptions given by Eq. (4-8) results in

$$\frac{\partial}{\partial t} \overline{u_i'' \theta''} = -\bar{u}_j \frac{\partial}{\partial x_j} \overline{u_i'' \theta''} - \overline{u_j'' u_i''} \frac{\partial \bar{\theta}}{\partial x_j} - \overline{\theta'' u_j''} \frac{\partial \bar{u}_i}{\partial x_j} - \overline{u_j'' u_i'' \frac{\partial \theta''}{\partial x_j}}$$

$$- \overline{\theta'' u_j'' \frac{\partial u_i''}{\partial x_j}} - \theta_0 \overline{\theta'' \frac{\partial \pi''}{\partial x_i}} + \frac{g}{\theta_0} \delta_{i3} \overline{\theta''^2} + \overline{u_i'' S_\theta''}. \tag{7-14}$$

The prognostic equation for $\overline{\theta''^2}$ can be determined from Eq. (7-13) by multiplying that expression by θ'' and applying the assumption given by Eq. (4-8), which results in

$$\frac{\partial \overline{\theta''^2}}{\partial t} = -\bar{u}_j \frac{\partial}{\partial x_j} \overline{\theta''^2} - \overline{u_j'' \theta''} \frac{\partial}{\partial x_j} \bar{\theta} - \overline{u_j'' \frac{\partial}{\partial x_j} \theta''^2} - \overline{\theta'' S_\theta''}.$$

These prognostic equations for the subgrid-scale fluxes are referred to as *second-order closure equations*, since they provide explicit conservation equations that are part of

- the conservation-of-velocity equation, $\partial (\overline{u_k'' u_i''})/\partial t$,

- the conservation-of-heat equation, $\partial (\overline{u_i'' \theta''})/\partial t$,

- the conservation-of-water equation, $\partial (\overline{u_i'' q''})/\partial t$,

- the conservation-of-other atmospheric gases and
  aerosols equation, $\partial (\overline{u_i'' \chi_m''})/\partial t$, and

- the conservation-of-mass of air equation, $\partial (\overline{\rho'' u_i''})/\partial t$. $\tag{7-15}$

Of these equations, when the assumption that $|\rho''|/\rho_0 \ll 1$ is made, an equation for $\overline{\rho'' u_i''}$ is ignored.

The full equations represented by Eq. (7-15) are computationally expensive to solve, and in all cases either prognostic equations must be developed for the third-order correlation terms (i.e., $\overline{u_j'' \frac{\partial}{\partial x_j} \theta''^2}$, $\overline{u_j'' \frac{\partial}{\partial x_j} u_k'' u_i''}$, etc.) or an assumption made regarding their functional form. The development of prognostic equations will introduce fourth-order correlation terms with an even higher computational cost. The necessity of truncating the derivation of successively higher-order subgrid-scale prognostic equations is called *closure*. Second-order closure, for example, means that functional forms are assumed for the third-order correlation terms. Third-order closure means that functional terms are specified for the fourth-order closure terms that appear in the prognostic equations for the third-order terms.

Mellor and Yamada (1974) present a classic overview of subgrid-scale flux closure schemes. They start with the complete subgrid flux equations such as those shown by, for example, Eqs. (7-11) and (7-14). They then define different levels of complexity in which they discriminate into four levels of detail in the parameterizations. Their level 4, for example, retains the complete subgrid flux equations in their prognostic form, while level 1 is of the form given by Eq. (7-7). Shafran *et al.* (2000) discuss level-1.5 parameterizations in which the only prognostic subgrid flux equation used is the equation for subgrid-scale kinetic energy. In the words of Mellor and Yamada (1974), the goal of developing a hierarchical representation is to obtain a parameterization that is "intuitively attractive and which optimizes computational speed and convenience without unduly sacrificing accuracy." Petersen and Holtslag (1999) discuss, for example, a first-order closure for the fluxes and covariances of χ. Sharan *et al.* (1999) use a level-2 Mellor–Yamada framework to represent σ_w in a stable boundary layer. Glendening (2000) discusses the turbulent kinetic energy budgets for strong shear conditions.

7.2 Surface Layer Parameterization

A parameterization of the vertical subgrid-scale fluxes near the ground can be obtained using relations such as those given by Eq. (7-7), along with the requirement of dimensional consistency.[7] This parameterization plays a major role in the parameterization of the planetary boundary layer as discussed later in this chapter.

From Eq. (7-7),

$$\overline{w''u''} = -K_m \frac{\partial \bar{u}}{\partial z} = -u_*^2 \cos \mu$$

$$\overline{w''v''} = -K_m \frac{\partial \bar{v}}{\partial z} = -u_*^2 \sin \mu,$$

(7-16)

with

$$\arctan(\bar{v}/\bar{u}) = \mu \qquad \text{and} \qquad \bar{\rho} u_*^2 = \tau.$$

Equation (7-16) is a level-1 representation. The parameter u_* is called the *friction velocity*,[8] which, when squared and multiplied by the fractional contribution of the mean wind to each component direction, is equal to the subgrid-scale fluxes on the left side of Eq. (7-16). The variable τ is the *shearing stress* caused by the horizontal wind. If $\bar{V}$ is the magnitude of the grid-volume–averaged flow $[\bar{V} = (\bar{u}^2 + \bar{v}^2)^{1/2}]$, then Eq. (7-16) can also be written as

$$K_m \, \partial \bar{V}/\partial z = u_*^2.$$

(7-17)

Since K_m has dimensions of a length multiplied by a velocity, it is reasonable to assume that

$$K_m = kz u_*.$$

(7-18)

In Eq. (7-16), the friction velocity is the characteristic velocity and kz is used as a length scale of turbulent eddies near the ground. The constant of proportionality, k, is called *von Karman's constant*, which from observations in the atmosphere (e.g., Högström 1996) is estimated to have a value of $k = 0.40 \pm 0.01$ (although Bergmann 1998 reports on a value of $k = 0.3678$; discussions of this value of the von Karman constant are given in Andreas and Treviño 2000 and Bergmann 2000). The relation given by Eq. (7-18), however, only applies when buoyancy production of turbulent kinetic energy is negligible (i.e., Ri $\simeq 0$), with the shear of the mean wind providing the source for the turbulent energy.

Substituting Eq. (7-18) into (7-17) yields

$$\partial \bar{V}/\partial z = u_*/kz,$$

(7-19)

which, integrating between the level $\bar{V} = 0$ (defined as z_0) and an arbitrary level above the ground z, gives

$$\int_{z_0}^z \frac{\partial \bar{V}}{\partial z} \, dz = \bar{V}(z) = \int_{z_0}^z \frac{u_*}{kz} \, dz = \frac{u_{*0}}{k} \int_{z_0}^z \frac{dz}{z} = \frac{u_{*0}}{k} \ln \frac{z}{z_0}.$$

(7-20)

This relation is called the *logarithmic wind profile*, and z_0 is called the *aerodynamic roughness*. With relatively homogeneous upwind fetch, Carl *et al.* (1973) found no significant deviation of the wind profile from Eq. (7-20) up to 150 m when |Ri|, as computed from data at 18 and 30 m on a tower, was

less than 0.05. In performing the integration in Eq. (7-20), u_* was assumed to be invariant with height; thus the layer over which Eq. (7-20) is an accurate approximation is often called the *constant flux layer*. This term is inaccurate, however, since the flux usually decreases exponentially near the surface. If the surface layer were associated with a constant flux, then the wind speeds could not decrease near the surface, since $\frac{\partial}{\partial z} u_*^2 = \frac{\partial}{\partial z} \overline{V''w''}$ would be 0! It is more appropriate to define u_* as the layer-averaged value using the mean-value theorem of calculus to factor u_* through the integral in Eq. (7-20). This is the reason why the subscript "0" was included in u_* in Eq. (7-20). In addition, the wind is assumed to not change direction with height; otherwise, Eq. (7-20) could not be written as a scalar equation.

The value of z_0 depends on the characteristics of the surface, ranging from a value of 0.001 cm over smooth ice to 10 m over large buildings (Oke 1978). Driese and Reiners (1997) provide values of z_0 for semi-arid natural shrubland. Over some surfaces, such as long grasses and water, z_0 can be a function of the friction velocity. Over sand, for example, as reported by Bagnold (1973), and Vugts and Cannemeijer (1981), z_0 increases substantially when $u_* \geq 0.1(\rho_s \bar{\rho}^{-1} g d)^{1/2}$, because of the aeolian transport of sand at stronger wind speeds. In this expression, ρ_s is the density of sand and d is the diameter of the sand grains, assuming that all are of the same size.

Over water, Garratt (1992) suggested the form

$$z_0 = (0.01625 \pm 0.00225)u_*^2/g, \qquad (7\text{-}21)$$

while Sheih *et al.* (1979) suggested the form

$$z_0 = \left(0.016u_*^2/g\right) + v/(9.1u_*),$$

where v is the kinematic viscosity of air ($\sim 1.5 \times 10^{-5}$ s^{-1}). Additional discussion of values of z_0 to use over water, including the effect of waves, is given in Powers and Stoelinga (2000). The modification of surface drag by ocean waves is discussed in Donelan *et al.* (1997). Zeng *et al.* (1998) also summarize forms of z_0 to use over water. Chamberlain (1983) suggested that Eq. (7-21) may also apply over other mobile surfaces, such as sand and snow.

Representative values of z_0 are presented in Table 7-2. A useful illustration of characteristic values of roughness is given in McRae *et al.* (1982a, Figure 3). The paper by van Dop (1983) provides a map of estimated average values of z_0 for areas on the order of 20×20 km^2 in the Netherlands based on several land-type categories.

For specific locations, z_0 is calculated by taking wind observations at several heights within the surface layer when the mean wind speed is strong, so that Ri = 0 and $\overline{V} \simeq (u_*/k) \ln(z/z_0)$ from Eq. (7-20) can be used. The winds are then plotted as a function of the natural logarithm of height, as illustrated in Figure 7-2 and extrapolated to the value $\overline{V} = 0$. The intersection of the ln z-axis

TABLE 7-2.

Representative Values of Aerodynamic Roughness for a Uniform Distribution
of These Types of Ground Cover.

	Aerodynamic roughness, z_0	Height of of ground cover	Displacement height, D
Ice[a]	0.001 cm		
Smooth mud flats[f]	0.001 cm		
Snow[a]	0.005–0.01 cm		
Sand[a]	0.03 cm		
Smooth desert[f]	0.03 cm		
Smooth snow on short grass [c]	0.005 cm		
Snow surface, natural prairie[c]	0.1 cm		
Soils[a]	0.1–1 cm		
Short grass[a]	0.3–1 cm	2–10 cm	
Mown grass[c]	0.2 cm	1.5 cm	
	0.7 cm	3 cm	
	2.4 cm with $\overline{V}$ at 2 m = 2 m s^{-1}	4.5 cm	
	1.7 cm with $\overline{V}$ at 2 m = 6.8 m s^{-1}		
Long grass[a]	4–10 cm	25 cm–1 m	
Long grass (60–70 cm)	15 cm[f], 9 cm[c] with $\overline{V}$ at 2 m = 1.5 m s^{-1}		
	11 cm[f], 6.1 cm[c] with $\overline{V}$ at 2 m = 3.5 m s^{-1}		
	8 cm[f], 3.7 cm[c] with $\overline{V}$ at 2 m = 6.2 m s^{-1}		
Agricultural crops[a]	4–20 cm[d]	~40 cm–2 m[d]	~27–~1.3 m[e]
Orchards[a]	50–1 m[d]	~5 m–10 m[d]	~3.3–~6.7 m[e]
Deciduous forests[a]	1–6 m[d]	~10 m–60 m[d]	~6.7–~40 m[e]
Coniferous forests[a]	1–6 m[d]	~10 m–60 m[d]	~6.7–~40 m[e]
Rural Delmarva peninsula[b]	33 cm (for NW flow)		
Pakistan desert[c]	0.03 cm		

[a] From Oke (1978).
[b] From Snow (1981).
[c] From Priestly (1959).
[d] Using Eq. (7-36).
[e] Using Eq. (7-35).
[f] From Sellers (1965).

defines z_0. For particularly complex locations, such as city centers, Davenport
et al. (2000) recommends determining effective roughness using scale models
in wind tunnels.

When the atmosphere near the ground is not neutrally stratified, Eq. (7-19)
must be generalized to include buoyancy effects. The flux Richardson number
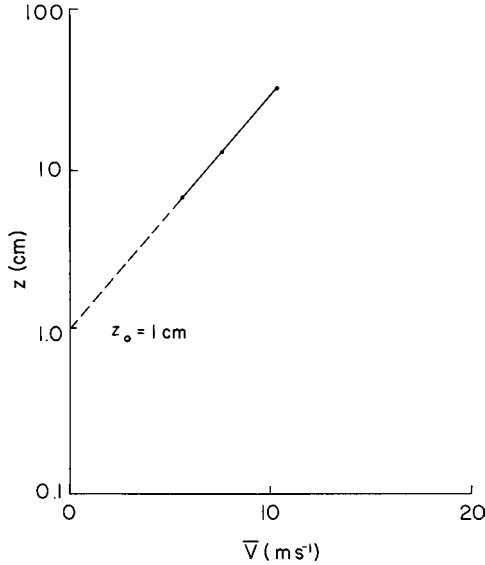
Fig. 7-2. Schematic illustration of the procedure used to compute z_0 from observations of mean wind speed at three levels near the ground in a neutrally stratified atmosphere. The slope of the line gives k/u_*.

given by Eq. (7-6) can be written as

$$R_f = \frac{-g}{\theta_0} \overline{w''\theta''} \Big/ u_*^2 \frac{\partial \overline{V}}{\partial z}, \tag{7-22}$$

using Eq. (7-16) and the definition of $\overline{V}$.[9] The flux Richardson number is then multiplied by

$$\phi_M = \frac{kz}{u_*} \frac{\partial \overline{V}}{\partial z}, \tag{7-23}$$

where ϕ_M is called the *nondimensional wind shear*, yielding

$$R_f \, \phi_M = -g \, \overline{w''\theta''} \, kz/\theta_0 \, u_*^3 = z/L. \tag{7-24}$$

The value of ϕ_M is defined as unity under neutral stratification [so that Eq. (7-19) is satisfied] and as a function of the flux Richardson number otherwise. The parameter $L = -\theta_0 \, u_*^3/g\overline{w''\theta''} \, k$ has the dimensions of a length and is called the *Monin length*. Since ϕ_M is assumed to be a function of R_f, ϕ_M can be written as

$$\phi_M = \phi_M(R_f) = \phi_M(\phi_M R_f/\phi_M) = \phi_M\big((z/L)\phi_M\big) = \phi_M(z/L)$$

using Eq. (7-24), so that ϕ_M is a function of z/L only. Values of ϕ_M determined from observations are given in Figure 7-3. When $z/L < 0$ (the atmosphere
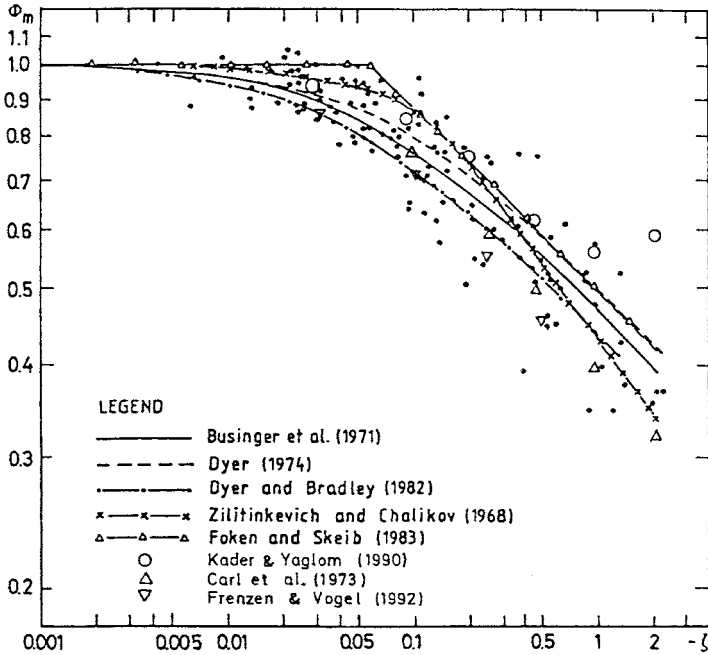
Fig. 7-3. Plot of ϕ_M against $(z-d)/L$ in log-log representation for unstable stratification. The small dots are data from Högström (1988). The other symbols have been derived from modified expressions from the sources listed in the key. (From Högström 1996 with kind permission from Kluwer Academic Publishers.)

is unstably stratified), $\phi_M < 1$, while under a stable stratification, $\phi_M > 1$. The modification to the wind profile can be determined using Eq. (7-23) and Figure 7-3. The definition given by Eq. (7-23) can be rewritten as

$$\frac{kz}{u_*}\frac{\partial \overline{V}}{\partial z} = 1 - (1 - \phi_M),$$

or

$$\frac{\partial \overline{V}}{\partial z} = \frac{u_*}{kz} - \frac{(1 - \phi_M)}{kz}u_*. \tag{7-25}$$

Integrating Eq. (7-25) with height, as was performed to achieve Eq. (7-20), gives

$$\overline{V} = \frac{u_{*0}}{k}\ln\frac{z}{z_0} - \frac{u_{*0}}{k}\int_{z_0/L}^{z/L}(1 - \phi_M)d\ln\frac{z}{L}, \tag{7-26}$$

where a change of variable was made in the integrand and limits. In writing the right side of Eq. (7-26), L_0 and u_{*0} are assumed to be constant with height

(L_0 is the layer-averaged value of the Monin length, L). Equation (7-26) is often written in the form

$$\overline{V}(z) = \frac{u_*}{k} \left[\ln \frac{z}{z_0} - \psi_\mathrm{M}\left(\frac{z}{L} \right) \right], \tag{7-27}$$

where $z/L \gg z_0/L$ is assumed; that is,

$$\psi_\mathrm{M} = \int_0^{z/L} \frac{(1 - \phi_\mathrm{M})}{z/L} \, d\left(\frac{z}{L} \right). \tag{7-28}$$

The function $\psi_\mathrm{M}(z/L)$ is the correction to the logarithmic wind profile resulting from the deviation from neutral stratification. For a neutral stratification, $\psi_\mathrm{M} = 0$. Figure 7-4 schematically illustrates the form of $\overline{V}$ when plotted as a function of $\ln z$ for stable, unstable, and neutral stratification. Note that z_0 is presumed to be independent of stability, so that each profile is extrapolated to the same value. This is required since ϕ_M approaches unity as z decreases (i.e., $z/L = z_0/L \simeq 0$ if $z_0 \ll L$). Specific observational estimates of ϕ_M are discussed in Högström (1996), with one suggested formula presented in Eq. (7-42).

Expressions analogous to ϕ_M and ψ_M can also be derived for the vertical subgrid-scale fluxes of potential temperature, water, and other gaseous and
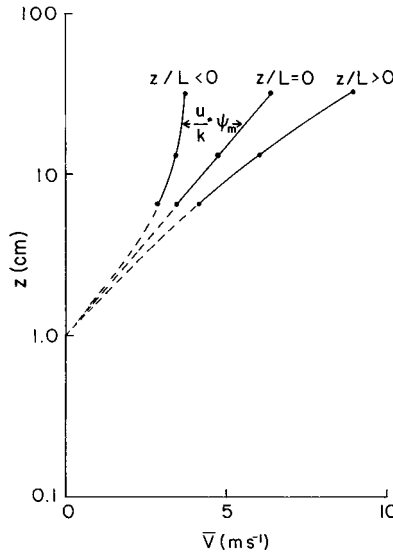
Fig. 7-4. Schematic illustration of the procedure used to compute the wind profile near the ground from observations of mean wind speed at three levels, along with the knowledge of the stability as measured by z/L. The difference between the logarithmic wind profile and the actual wind profile at any level is given by $(u_*/k)\,\psi_\mathrm{M}$ [from Eq. (7-27); $\psi_\mathrm{M} < 0$ when $z/L > 0$, $\psi_\mathrm{M} > 0$ when $z/L < 0$].
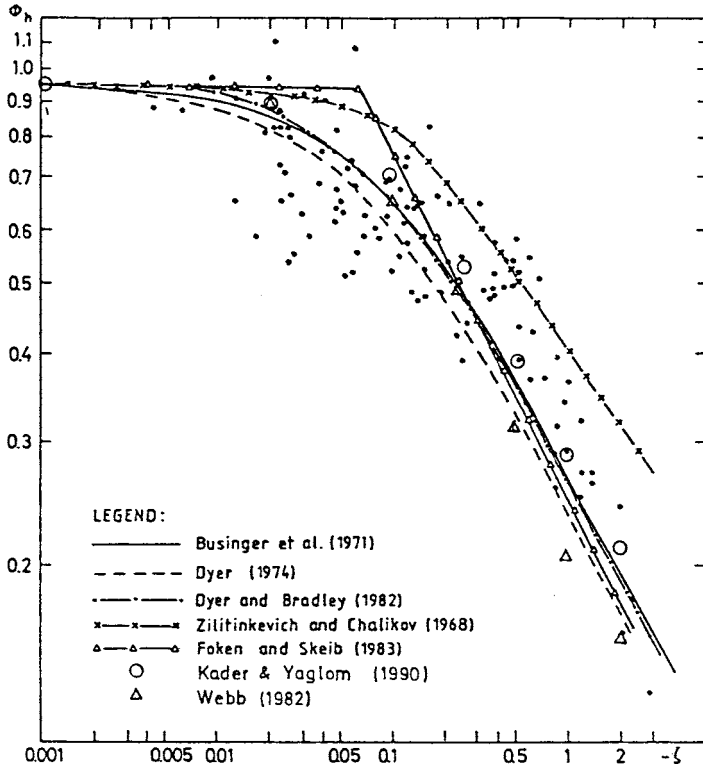
Fig. 7-5. As in Figure 7-3 except for ϕ_H. (From Högström 1996 with kind permission from Kluwer Academic Publishers.)

aerosol atmospheric materials. Figure 7-5 illustrates a function form for ϕ_H. From Eq. (7-7), and using the same form to represent $\overline{w''q_n''}$ and $\overline{w''\chi_m''}$,

$$\overline{w''\theta''} = -K_\theta \frac{\partial \bar{\theta}}{\partial z} = -u_* \theta_*,$$

$$\overline{w''q_n''} = -K_q \frac{\partial \bar{q}_n}{\partial z} = -u_* q_{n_*}, \qquad (7\text{-}29)$$

$$\overline{w''\chi_m''} = -K_\chi \frac{\partial \overline{\chi}_m}{\partial z} = -u_* \chi_{m_*}.$$

The parameter θ_* could be called the *flux temperature*, and q_{n_*} and χ_{m_*} are similar variables that have not been assigned labels. Generally, K_q and K_χ are assumed to be equal to K_θ (Yamada 1977), since within the surface layer, θ, q_n, and χ_m are presumed to mix solely by subgrid-scale advection. The value of K_m, in contrast, also includes the effect of the subgrid-scale pressure on the subgrid-scale velocity [as is evident from, for example, Eq. (7-4)], so that in

general, K_m is not assumed to be equal to the other three exchange coefficients. Warhaft (1976) also shows that there should be differences between K_θ and K_{q_3} when the correlation $\overline{\theta'' q_3''}$ is small or when $\partial \bar{\theta}/\partial z$ and $\partial \bar{q}/\partial z$ have opposite signs. However, these effects are expected to have a relatively small effect on the magnitude of the exchange coefficients (Wyngaard 1981, personal communication), although Lang *et al.* (1983) presented evidence that K_θ and K_{q_3} can be significantly different when substantial horizontal advection of heat and moisture occur over a cool surface. Nevertheless, in the analysis presented below, an equality between K_θ and K_{q_3} is assumed, which should be valid except over wet areas surrounded by warmer, dry land. This topic requires additional study.

By analogy with Eq. (7-23),

$$\frac{\beta k z}{\theta_*} \frac{\partial \bar{\theta}}{\partial z} = \frac{\beta k z}{q_{n_*}} \frac{\partial \bar{q}_n}{\partial z} = \frac{\beta k z}{\chi_{m_*}} \frac{\partial \overline{\chi_m}}{\partial z} = \beta \phi_{\mathrm{H}} = \hat{\phi}_{\mathrm{H}}, \qquad (7\text{-}30)$$

where the scale and intensity of turbulent mixing of $\bar{\theta}$, $\bar{q}_n$, and $\overline{\chi_m}$ are assumed to be the same, with β used to indicate that the characteristic vertical mixing length for $\bar{\theta}$, $\bar{q}$, and $\overline{\chi_m}$ can be different than that for $\overline{V}$. It has also been shown that radiative cooling can significantly affect the magnitude of ϕ_{H} (Garratt and Brost 1981; Gopalakrishnan *et al.* 1998). In Eq. (7-30), $\hat{\phi}_{\mathrm{H}}$ equal to unity at $z/L = 0$ is required.

Following the same procedure as that used to derive Eq. (7-25) yields

$$\bar{\theta}(z) = \bar{\theta}(z_0) + \frac{\theta_*}{\beta k} \left[\ln \frac{z}{z_0} - \psi_{\mathrm{H}} \left(\frac{z}{L} \right) \right],$$

$$\bar{q}_n(z) = \bar{q}_n(z_0) + \frac{q_{n_*}}{\beta k} \left[\ln \frac{z}{z_0} - \psi_{\mathrm{H}} \left(\frac{z}{L} \right) \right], \qquad (7\text{-}31)$$

$$\overline{\chi}(z) = \overline{\chi_m}(z_0) + \frac{\chi_{m_*}}{\beta k} \left[\ln \frac{z}{z_0} - \psi_{\mathrm{H}} \left(\frac{z}{L} \right) \right],$$

where

$$\psi_{\mathrm{H}} = \int_0^{z/L} \frac{1 - \hat{\phi}_{\mathrm{H}}}{z/L} \, d(z/L), \qquad (7\text{-}32)$$

with a plot of ϕ_{H} as a function of z/L from Högström (1996) given in Figure 7-5. In the derivation of ψ_{H}, $z_0 \ll z$ has been assumed. The first terms on the right side of each equation in Eq. (7-31) are the values of $\bar{\theta}$, $\bar{q}_n$, and $\overline{\chi_m}$ evaluated at the level where $\overline{V}$ becomes 0 (i.e., z_0), although some conclude that a different roughness length should be used (see Mahrt 1996:95–96 for a discussion; also Bosveld *et al.* 1999, Junfang *et al.* 1999, and Ren *et al.* 1999). Ma and Daggupaty (1998) discuss effective roughness lengths of momentum and heat exchange associated with roughness changes. Sun (1999) concluded

that it is more accurate to define $\theta(z_0)$ in terms of the surface irradiance temperature rather than using the surface radiation temperature and adjusting a z_0 specifically for θ. She also found that a roughness length defined for θ varies in space and time much more than z_0 as obtained from Eq. (7-20). Hence in this chapter we use the same z_0 for Eq. (7-31).

Substituting from Eqs. (7-30) and (7-23) for the vertical gradient terms in Eqs. (7-29) and (7-17) gives

$$K_m = \frac{k u_* z}{\phi_{\mathrm{M}}} \qquad \text{and} \qquad K_\theta = \frac{\beta k u_* z}{\hat{\phi}_{\mathrm{H}}}, \qquad (7\text{-}33)$$

which provides estimates of the exchange coefficients near the ground.

The relation between K_θ and K_m can be derived for certain circumstances. Pandolfo (1966) has shown from observations that $z/L = \mathrm{Ri}$ near the ground under neutral and unstably stratified lapse rates. When this is true,

$$\mathrm{Ri} = z/L = \phi_{\mathrm{M}} R_{\mathrm{f}} = \phi_{\mathrm{M}}(K_\theta/K_m)\mathrm{Ri},$$

from Eqs. (7-24) and (7-8), so that $K_m/K_\theta = \phi_{\mathrm{M}}$. Therefore, from Eq. (7-33),

$$K_\theta = k u_* z/\phi_{\mathrm{M}}^2.$$

Thus, since $\phi_{\mathrm{M}} < 1$ when $z/L < 0$ (see, e.g., Figure 7-3), the turbulent mixing of $\bar{\theta}$, $\bar{q}_n$, and $\overline{\chi}_m$ is greater than that for velocity in unstable air near the ground. Unfortunately, this result is not consistent with a value of β different than 1. From this analysis, $K_m = K_\theta$ when $z/L = 0$, since ϕ_{M} for that value is unity. However, from Eq. (7-33) and Figs. 7-3 and 7-5, $K_\theta \simeq 1.05 K_m$ at $z/L = 0$. Reexamination of the data is needed to clear up this discrepancy near $z/L = 0$. However, the values of K_m and K_{H} are closer to each other at $z/L = 0$ using the Högström (1996) paper than in the earlier Businger et al. (1971) formulation summarized in Pielke (1982).

When the ground cover is sufficiently high so that significant turbulent flow can occur below the top (e.g., within a pine forest, cornfield, etc.), Eqs. (7-27) and (7-31) must be rewritten as

$$\left.\begin{aligned}
\overline{V}(\bar{z}) &= \frac{u_*}{k}\left[\ln\frac{z-D}{z_0} - \psi_{\mathrm{M}}\left(\frac{z-D}{L}\right)\right] \\
\bar{\theta}(z) &= \bar{\theta}_0(D+z_0) + \frac{\theta_*}{\beta k}\left[\ln\frac{z-D}{z_0} - \psi_{\mathrm{H}}\left(\frac{z-D}{L}\right)\right] \\
\bar{q}_n(z) &= \bar{q}_{n_0}(D+z_0) + \frac{q_{n_*}}{\beta k}\left[\ln\frac{z-D}{z_0} - \psi_{\mathrm{H}}\left(\frac{z-D}{L}\right)\right] \\
\overline{\chi}_m(z) &= \overline{\chi}_{m_0}(D+z_0) + \frac{\chi_{m_*}}{\beta k}\left[\ln\frac{z-D}{z_0} - \psi_{\mathrm{H}}\left(\frac{z-D}{L}\right)\right]
\end{aligned}\right\} \; z \geq D+z_0, \qquad (7\text{-}34)$$

where D is called the *zero-plane displacement*.[10] Values of z_0 used in these relations are displaced a distance D from the actual ground surface. In other words, because of the significant height of ground cover, $\overline{V}$, $\bar{\theta}$, $\bar{q}_n$, and χ_m respond to the aerodynamic roughness of the top of the ground cover (e.g., the canopy) rather than the ground surface or the morphology within the high ground cover. To be a realistic representation of the ground cover, however, the cover must be uniformly distributed, such as in a forest or large agricultural area. The values of $\bar{\theta}(D + z_0)$, $\bar{q}_{n_0}(D + z_0)$, and $\overline{\chi}_{m_0}(D + z_0)$ are the values that would occur if the height $z = D$ actually corresponded to $z \simeq 0$. Similarly, $\overline{V}(D + z_0)$ would equal 0 if $z = D$ actually were $z \simeq 0$, as shown schematically by the dashed line in Figure 7-6.

Values of D are determined experimentally by plotting wind speed as a function of $\ln(z - D)$ for strong winds. Different D values are substituted into the expression for $\overline{V}$ given in Eq. (7-34) until the logarithmic wind profile is achieved (i.e., a straight line, as illustrated schematically in Figure 7-7).

A useful formula to estimate D for closely spaced stands of crops and trees (from Oke 1978:98) is given by

$$D = \frac{2}{3}h, \tag{7-35}$$
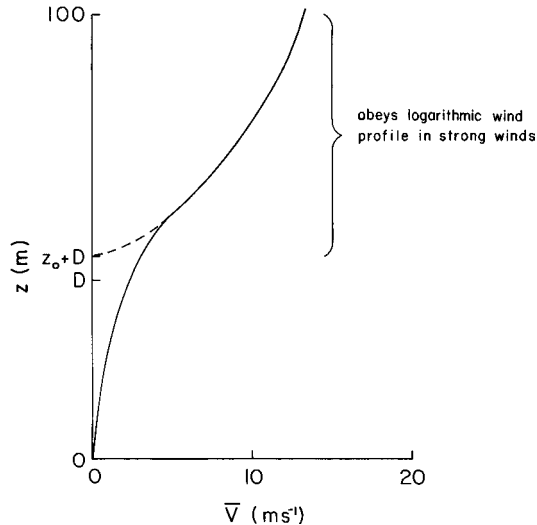
Fig. 7-6. Schematic illustration of a wind profile (solid line) above and within a dense, horizontally and vertically uniform ground cover. The dashed line represents the expected wind profile if $D = 0$. Below $z_0 + D$, the profile obeys Eq. (7-37) with a constant value of a.
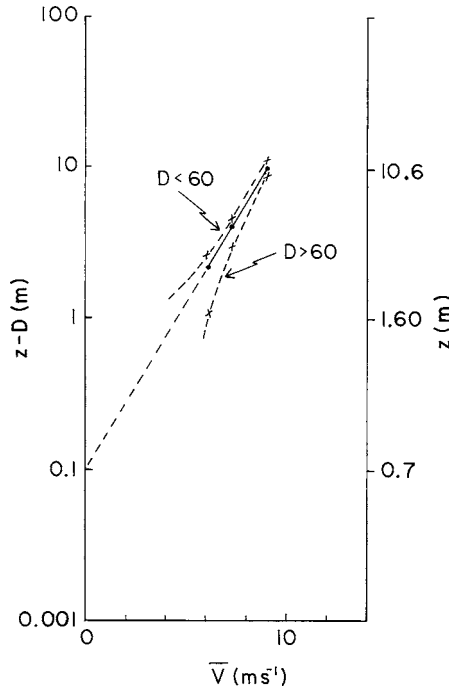
Fig. 7-7. Schematic illustration of the procedure used to compute the wind profile over tall, dense ground cover given three wind observations over the cover and Ri $\simeq$ 0. In this example, $D = 60$ cm is assumed to give the best fit to the logarithmic wind profile; z_0 is then determined to equal 10 cm.

where h is the height of the vegetation. Oke (1978:119) also reports on a suggested relationship between roughness and vegetation height for tall, dense vegetation, which is given by

$$\log_{10} z_0 = \log_{10} h - 0.98, \tag{7-36}$$

so that $z_0 \simeq h/10$. Rosenberg (1974) reports on a formulation for D, based on observations over different types of agricultural crops given by

$$\log_{10} D = 0.979 \log_{10} h - 0.154.$$

Within the ground cover, a wind profile of

$$\overline{V} = \overline{V}_D \exp a \left(\frac{\ln z}{\ln D} - 1 \right) \qquad (a > 0) \tag{7-37}$$

can be assumed, with $\overline{V} = \overline{V}_D$ at the zero-plane displacement height and $\lim_{z \to 0} \overline{V} \to 0$.[11] However, this expression is accurate only when the density of

the ground cover is uniform with height. In a non-uniformly distributed ground cover, such as a deciduous forest, a local wind maximum can occur below the leaf canopy in the trunk region. Monteith (1975b) provides details on wind profiles (and vertical distributions of other variables) in a variety of vegetation types. When Eq. (7-37) is used within a vegetative cover, a is assumed to be directly proportional to the *leaf area index* L_A, where

$$L_A = A_S/A_G, \tag{7-38}$$

with A_S the total leaf area per area of ground surface A_G.

The value of a in Eq. (7-37) is experimentally determined by plotting observed wind speeds in the form of $\ln\left(\overline{V}/\overline{V}_D\right)$ within the ground cover as a function of $(\ln z/ln\, D) - 1$. Fitting the data with a straight line, and recognizing that $\overline{V} = 0$ at $z = 0$, yields a. Within corn, for example, Blackadar (1969, personal communication) estimates a value of $a \simeq 2.0$ using the relationship $\overline{V} = \overline{V}_D \exp a[(z/D) - 1]$.

In his simulation of drainage flow, Garrett (1983a) also found that wind speeds are substantially influenced by the presence of forest. With a 50% coverage of forest, his model predicts a 50% decrease in maximum velocity and depth of the nocturnal drainage flow. Yamada's (1982) model of the boundary layer structure over flat terrain simulates nearly constant low wind speeds within a forest canopy with large wind shears near the treetops. Oke (1978:131) concluded that for a given wind speed, the atmosphere is more turbulent over a forest than over any other natural surface (excluding topographic effects). Wilson and Shaw (1977) have presented results using a second-order–closure, one-dimensional model of the flow within a corn crop. Lord *et al.* (1972) used a one-dimensional model to investigate the effect of tundra vegetation on the land-air interface and concluded that a three-dimensional representation is necessary to account for the horizontal heterogeneity caused by the presence of thaw lakes atop the permafrost.

Figure 7-6 illustrates how a wind profile would appear during neutral stratification above and within a dense, horizontally and vertically uniform ground cover when Eqs. (7-34) and (7-37) apply. The profiles of $\bar{\theta}(z)$, $\bar{q}_n(z)$, and $\overline{\chi_m}(z)$ within such ground cover are generally more complex, however, since $\bar{\theta}(z)$ is significantly influenced by radiative flux divergence, whereas water and other gaseous and aerosol atmospheric materials flow into and out of the soil and vegetation. The radiation and moisture budgets within and above vegetation are discussed in Section 11.3.3.2.

Enough basic material has been introduced to permit the discussion of the parameterization of the planetary boundary layer within mesoscale models. Additional discussion of similarity theory can be found in such sources as Jensen and Busch (1982), Arya (1988), Stull (1988), Sorbjan (1989), and Garratt (1992).

7.3 Planetary Boundary-Layer Parameterization

Representation of the planetary boundary layer in mesoscale models is handled primarily through the subgrid-scale correlation terms, since the model grid resolution is too large to resolve explicitly the small-scale fluxes found in this layer. Treatment of the influence of the planetary boundary layer in numerical models can be grouped into two classes:

- those that treat it as a single layer (e.g., Deardorff 1972; Mahrt 1974; Smith and Mahrt 1981)
- those that resolve it into a number of discrete levels.

In mesoscale models, the second approach is the most common. As shown by Anthes *et al.* (1980), for example, detailed boundary-layer resolution is essential for accurate solutions when differential heating along complex terrain and across land–water boundaries is being represented, since significant vertical gradients of the meteorological variables occur within the planetary boundary layer.

With the discrete level approach, the planetary boundary layer can be divided into three sections: viscous sublayer, surface layer, and transition layer.

7.3.1 Viscous Sublayer

The viscous sublayer[12] is defined as the level near the ground ($z < z_0$; with $D \simeq 0$), where the transfer of the dependent variables by molecular motions become important. Zilitinkevich (1970) and Deardorff (1974a) suggest relating temperature and specific humidity at the top of the layer $\bar{\theta}_{z_0}$ and $\bar{q}_{z_0}$ to the surface values of the variables $\bar{\theta}_G$ and $\bar{q}_G$ using expressions of the form

$$\bar{\theta}_{z_0} = \theta_G + 0.0962(\theta_*/k)(u_* z_0/v)^{0.45}$$

and

$$\bar{q}_{z_0} = q_G + 0.0962(q_*/k)(u_* z_0/v)^{0.45}. \tag{7-39}$$

By analogy,

$$\overline{\chi}_{z_0} = \chi_G + 0.0962(\chi_*/k)(u_* z_0/v)^{0.45}.$$

In these expressions, v is the kinematic viscosity of air ($\sim 1.5 \times 10^{-5}\ \text{m}^2\ \text{s}^{-1}$) and k is von Karman's constant with θ_*, u_*, q_*, and χ_* defined by Eqs. (7-27) and (7-31). Between $z = z_0$ and $z = z_G$, $\bar{u} = \bar{v} = \bar{w} = 0$, whereas variations of $\bar{p}$ and $\bar{\pi}$ across this depth are ignored.

As discussed by Businger (1973), $u_* z_0/v$ may be considered the Reynolds number of the smallest turbulent eddy in the flow. Businger also reports on a study by Nikuradse (1933) in which laminar flow occurs with $u_* z_0/v < 0.13$,

whereas turbulent motion dominates with $u_* z_0/v > 2.5$. In between these two limits, a transition regime exists. The laminar situation is said to be *aerodynamically smooth*, whereas the fully turbulent flow is *aerodynamically rough*.

7.3.2   Surface Layer

The surface layer extends from z_0 to h_s, with h_s (the top of the surface layer) usually varying from about 10 m to about 100 m. In this layer, the subgrid-scale fluxes are represented by mean-layer values that are assumed to be independent of height and where the veering of the wind with height owing to the Coriolis effect is neglected, as used to derive Eqs. (7-27) and (7-32). With the assumption that the conditions in this layer are steady and horizontally homogeneous, investigators (e.g., Yamamoto 1959; Yamamoto and Shimanuki 1966; Shimanuki 1969) have developed empirical formulations for Eqs. (7-23), (7-28), (7-30), and (7-32), to specify the relationship between the dependent variables and the subgrid-scale fluxes. Högström (1996) provides a recent summary of these formulations. Only a limited number of studies with nonhomogeneous terrain have been done (e.g., Peterson 1969; Taylor 1977a, b; Taylor and Gent 1981) or sloping terrain (e.g., Gutman and Melgarejo 1981), and this work has yet to be applied to mesoscale models.

One of the most common formulations for Eqs. (7-27) and (7-31) used in mesoscale models is that reported by Högström (1996) and Högström (2000, personal communication), in which[13]

$$
\begin{aligned}
u_{*_0} &= k\overline{V}/\big[\ln(z/z_0) - \psi_{\mathrm{M}}(z/L)\big], \\
\theta_{*_0} &= k\big(\bar{\theta}(z) - \bar{\theta}_{z_0}\big)/0.95\big[\ln(z/z_0) - \psi_{\mathrm{H}}(z/L)\big], \\
q_{*_0} &= k\big(\bar{q}_3(z) - \bar{q}_{z_0}\big)/0.95\big[\ln(z/z_0) - \psi_{\mathrm{H}}(z/L)\big], \\
\chi_{*_{m0}} &= k\big(\overline{\chi}_m(z) - \overline{\chi}_{z_{0_m}}\big)/0.95\big[\ln(z/z_0) - \psi_{\mathrm{H}}(z/L)\big],
\end{aligned}
\tag{7-40}
$$

where

$$
\begin{aligned}
\psi_{\mathrm{M}} &= \begin{cases} 2\ln\big[(1+\zeta)/2\big] + \ln\big[1+(\zeta^2/2)\big] - 2\tan^{-1}\zeta + \pi/2, & z/L \leq 0 \\ -5.3\zeta, & 0 < z/L \leq 0.5, \\ \quad\quad \text{where } \zeta = (1 - 19z/L)^{1/4}, \end{cases} \\[2mm]
\psi_{\mathrm{H}} &= \begin{cases} 2\ln\big[(1+\zeta_{\mathrm{H}}^2)/2\big], & z/L \leq 0 \\ -8.0\zeta, & 0 < z/L \leq 0.5, \\ \quad\quad \text{where } \zeta_{\mathrm{H}} = (1 - 11.6z/L)^{1/4}. \end{cases}
\end{aligned}
\tag{7-41}
$$

Högström (2000, personal communication) found that his experimental data for $z/L > 0.5$ show that ϕ_H and ϕ_M tend to level off, but the data are very scattered:

$$\phi_M = \frac{kz}{u_{*_0}}\frac{\partial \overline{V}}{\partial z} \simeq \begin{cases} (1-19z/L)^{-1/4}, & z/L \leq 0 \\ 1+5.3z/L, & 0.5 > z/L > 0 \end{cases}$$

$$\phi_H = \frac{kz}{\theta_{*_0}}\frac{\partial \bar{\theta}}{\partial z} = \frac{kz}{q_{*_0}}\frac{\partial \bar{q}_3}{\partial z} = \frac{kz}{\chi_{*_{m_0}}}\frac{\partial \overline{X}_m}{\partial z} \simeq \begin{cases} (1-11.6z/L)^{-1/2}, & z/L \leq 0 \\ 1+8.0z/L, & 0 \leq z/L \leq 0.5, \end{cases}$$

(7-42)

with the definition of L given in Eq. (7-24), written as $L = \bar{\theta}u_{*_0}^2/kg\theta_{*_0}$. The value of β in Eq. (7-31) was determined to be 1.05. The accuracy of ϕ_M is estimated as 10–20% for unstably stratified surface layers with z/L greater than −0.5. The same accuracy is assumed for ϕ_H for unstably stratified surface layers with z/L greater than −2.0 (Högström 1988). Alternative formulas for these parameters have been suggested by, for example, Viswanadham and Nogueira (1982), who provided estimates of ϕ_M for very stable, unstable, and near-neutral surface-layer stability conditions. Carl et al. (1973), using tower data over homogeneous terrain, concluded that ϕ_M approaches a $(-z/L)^{-1/2}$ relationship in an unstably stratified surface layer with $|z/L|$ large, rather than $(-z/L)^{-1/4}$, as given in Eq. (7-42). DeBruin (1999) proposes a formulation for ϕ_M which is a function of $(-z/L)^{-1/3}$ as $(-z/L)$ becomes large and approaches the free convection limit. Hsu et al. (1999) propose $\psi_M(z/L) = a(-z/L)^b$, with $a = 1.0496$ and $b = 0.4591$ for $z/L < 0$. However, these refinements to ϕ_M and ϕ_H as applied to mesoscale modeling are relatively minor and should have only a small effect on the resultant mean profiles of the dependent variables.

The subgrid-scale flux of other gaseous and atmospheric materials can also be written as

$$\overline{w''\chi_m''} = -v_s\overline{X}_{m_z},$$

where v_s is called the *deposition velocity*[14] and $\overline{X}_{m_z}$ is the mixing ratio of the gas or aerosol at level z. In the absence of scavenging by rain or snow (called *wet deposition*), this deposition velocity is used to estimate the *dry deposition* of materials with a negligible fall velocity onto the ground and vegetation surfaces. The value of v_s also depends on the chemical species involved. For SO_2, the deposition velocity is estimated to be on the order of 1 cm s^{-1}, whereas sulfates of size 0.1–1 μm are reported to have values of around 0.01–1 cm s^{-1} (Eliassen 1980). Everett et al. (1979) found a value of $v_s = 1.4$ cm s^{-1} for particulate sulfur, whereas Wesely et al. (1978) reports values of v_s for ozone during the daytime ranging from 0.2 to 0.8 cm s^{-1} with its peak in midmorning. Lenschow et al. (1981) gave a value of v_s of about 0.5 cm s^{-1} for ozone over a portion of eastern Colorado during the day. These values of v_s are for specific measurement heights (since $\overline{X}_{m_z}$ is a function of z).

Sheih *et al.* (1979) report on a formulation for the deposition velocity of SO_2 over land given by

$$v_{SO_2} = ku_* \left[\ln(z/z_0) + 2.6 + ku_* r_{SO_2} - \psi_H \right]^{-1}, \quad (7\text{-}43)$$

where r_{SO_2} represents the surface resistance to SO_2 uptake. For a vegetative surface, r_{SO_2} is the integrated effect of the stomatal resistance of the plants (called the *effective bulk canopy stomatal resistance*). Over water, Sheih *et al.* (1979) suggest the formulation

$$v_{SO_2} = ku_* \left[\ln(ku_* z/v_s) - \psi_H \right]^{-1}, \quad (7\text{-}44)$$

where v_s is the molecular kinematic diffusivity of SO_2 in air ($v_s \simeq 0.2$ cm^2 s$^{-1}\pm$ 50%)[15] with $r_{SO_2} = 0$, since SO_2 is highly soluble in water. Values of r_{SO_2} as a function of stability class are given in Sheih et al. (1979). The deposition velocity of sulfate aerosols over land and water is given in Sheih *et al.* (1979) as

$$v_{SO_4} = ku_* \left[\ln(z/z_0) + kr_{SO_4} u_* - \psi_H \right]^{-1}, \quad (7\text{-}45)$$

where r_{SO_4}, the surface resistance to particle deposition, is assumed to be 1 s cm^{-1}.

Additional discussions of deposition are given by Wesely and Hicks (1977), Galloway *et al.* (1980), Brook *et al.* (1999), Jackson and Lyford (1999), and Ma and Daggupaty (2000). Slinn (1982) discusses particle dry deposition to vegetation.

7.3.3 Transition Layer

The transition layer extends from h_s to z_i, which ranges from 100 m or so to several kilometers or more. Above the surface layer, the mean wind changes direction with height and approaches the *free-stream velocity* at the height z_i as the subgrid-scale fluxes $\overline{u''w''}$ and $\overline{u''v''}$ decrease in magnitude. The definition of z_i, the top of the boundary layer, is *the lowest level in the atmosphere at which the ground surface no longer influences the dependent variables through the turbulent transfer of mass.*[16] Tennekes (1974) gives a useful qualitative discussion of the atmospheric boundary layer, and Krishnamurti *et al.* (1983) discuss different types of boundary layers resulting from different sets of balance of forces: (a) a balance among Coriolis, pressure gradient, and frictional forces (an *Ekman* boundary layer); (b) a balance between the pressure gradient and frictional forces and the advective accelerations (an *advective boundary layer*); and (c) a balance between the pressure gradient and frictional forces (a *Stokes boundary layer*). When thunderstorms occur, the boundary layer can extend into

the stratosphere. However, for most applications in mesoscale models, the planetary boundary layer is between a few hundred meters and several kilometers or so above the ground.

When the bottom surface is heated, the planetary boundary layer tends to be well mixed, particularly in potential temperature. Specific humidity is somewhat less well mixed because the entrainment of dry air into a growing boundary layer permits a gradient in $\bar{q}_3$ to exist between the top of the planetary boundary layer and the (usually) more moist surface (Mahrt 1976). Because of horizontal pressure gradients, winds are the least well mixed. When the surface is cool, relative to the overlying air, vertical gradients in all of the dependent variables exist within the planetary boundary layer.

The depth of the planetary boundary layer, z_i, is usually associated with an inversion. As discussed by Oke (1978), there are three types of inversions:

- *inversions caused by cooling*: radiational cooling at night, or above stratiform clouds and smog layers, and evaporative cooling over moist ground
- *inversions caused by warming*: synoptic subsidence and cumulus-induced subsidence
- *inversions caused by advection*: frontal inversions; warm air over cold land, water, or snow; and vertical differences in the horizontal advection of temperature.

Busch *et al.* (1982) discussed the formation of inversions over huge areas in the polar region caused by several of these mechanisms. Diurnal variations in the height of the inversion and stability within the boundary layer can contribute to a large wind maximum just above z_i, as discussed by Blackadar (1957), Hoxit (1975), Zeman (1979), McNider and Pielke (1981), Arritt (1985), Arritt and Pielke (1986), and others. Large wind shears can also develop at that level, caused by increased surface-layer thermodynamic stability over land during a hurricane landfall (Powell 1982). Internal gravity waves can occur on such inversions (see Section 5.2.1.2), and can influence boundary-layer structure below that level (see, e.g., Finnegan and Finnegan 1981). Horizontal roll vortices are often observed within inversion-capped boundary layers that are heated from below.[17]

In the absence of an inversion, when the air is neutrally stratified, Blackadar and Tennekes (1968) suggested that z_i is proportional to u_*/f. In contrast, Deardorff (1972) and Mahrt (1972), as reported by Moss (1978), suggested that the lifting condensation level is the appropriate height.

Formulations for the depth of the nocturnal boundary layer have been suggested by Yu (1978), Nieuwstadt and Driedonks (1979), Yamada (1979a), Zeman (1979), Mahrt (1981a), Nieuwstadt and Tennekes (1981), Wetzel (1982), Stull (1983), and others. Tomasi (1983) has evaluated the use of several of these

schemes to predict the height of the nocturnal inversion in Italy's Po Valley
during stagnate, clear synoptic conditions. In Yamada's formulation, nocturnal
longwave radiational cooling is included. Gopalakrishnan (1996) concluded that
with light winds on clear nights, radiational cooling dominates the creation of
the nocturnal boundary-layer depth. Sharan and Gopalakrishnan (1997) evaluate
several parameterizations of turbulence in strongly and weakly stable boundary
layers.

Mahrt (1981b) has studied the transition of a daytime mixed layer to a
nocturnal boundary layer. He found that the ageostrophic wind increases during
the transition because the surface shearing stress decreases more slowly than
does the downward transport of momentum associated with the decreased depth
of turbulence; therefore, the winds turn more toward lower pressure. André and
Mahrt (1982) conclude that for the observational datasets in clear sky conditions
which they investigated, the lower part of the nocturnal inversion is turbulent,
although strongly stratified, while the upper portion, despite its weaker strat-
ification, is created almost completely by longwave radiative flux divergence.
Arya (1981) provides a brief summary of proposed diagnostic and prognostic
relations for parameterizing the height of the nocturnal boundary layer. Mahrt
(1983) gives a brief survey of studies on stably stratified boundary layers. Dayan
and Rodnizki (1999) provide a summary of the behavior of a boundary layer
over Israel for a 3-year period.

Variations of the planetary boundary-layer depth caused by subgrid-scale
fluxes need not be parameterized when a local representation to the exchange
coefficients are used, but will appear through changes in the vertical profile of
the dependent variables. However, when a well-defined inversion is present, it
is useful to include an equation that represents its change over time.

When the surface layer is superadiabatic (i.e., $\partial \bar{\theta}/\partial z < 0$), a simplified
boundary-layer formulation, called a *jump model*, has been proposed (e.g.,
Ball 1960; Lilly 1968; Tennekes 1973; Deardorff 1974a; Driedonks 1982a).
Illustrated in Figure 7-8, this model has a potential temperature discontinuity
at z_i of a magnitude of $\Delta \theta_i$. Below z_i, the turbulent flux of heat, $\overline{w''\theta''}$ is
assumed to decrease linearly with height and to become negative in the upper
boundary layer, with its minimum value of $\overline{w''_{z_i}\theta''_{z_i}}$ at the inversion. Above z_i,
the lapse rate, defined as $\partial \bar{\theta}^+/\partial z$, is stably stratified. Such a boundary layer
is called a *mixed layer*, because the dependent variables, particularly $\bar{\theta}$, tend to
be uniformly distributed with height.

In this representation, following the discussions of Lilly (1968) and Tennekes
(1973), the growth of z_i is given by

$$(dz_i/dt) - \bar{w}_{z_i} = -\overline{w''_{z_i}\theta''_{z_i}}/\Delta \bar{\theta}_i, \qquad (7\text{-}46)$$

where $\bar{w}_{z_i}$ represents mesoscale or synoptic vertical motion, or both, at z_i. When
$\bar{w}_i = 0$, the change in height of z_i with time depends on the rate of entrainment
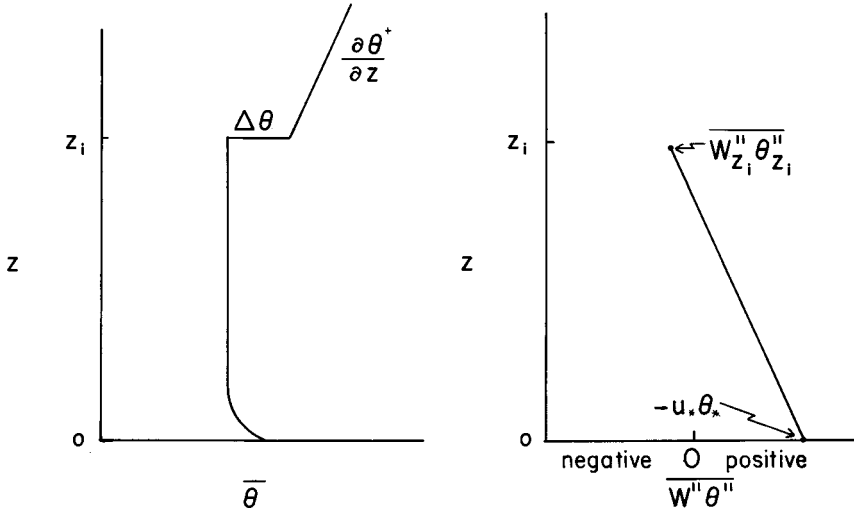
Fig. 7-8. The potential temperature and heat flux profiles assumed in the "jump" model.

of mass into the boundary layer.[18] The prognostic expression for $\Delta\bar{\theta}_i$ is

$$\frac{d\Delta\bar{\theta}_i}{dt} = \left(\frac{dz_i}{dt} - \bar{w}_{z_i}\right)\frac{\partial\bar{\theta}^+}{\partial z} + \frac{\overline{w''_{z_i}\theta''_{z_i}} - \overline{w''_s\theta''_s}}{z_i}, \tag{7-47}$$

where $\overline{w''_s\theta''_s}$ is the surface heat flux equal to $-u_*\theta_*$ from Eq. (7-29). The first term on the right side of Eq. (7-47) represents the tendency to increase $\Delta\bar{\theta}_i$ as the boundary layer rises, whereas the second term tends to decrease $\Delta\bar{\theta}_i$ as the layer warms from the surface. To specify the heat flux at z_i in terms of the surface heat flux, the assumption is made that

$$\overline{w''_{z_i}\theta''_{z_i}} = -\alpha\overline{w''_s\theta''_s} = +\alpha u_*\theta_*, \tag{7-48}$$

where $\alpha = 0.2$ is usually used (e.g., Yamada and Berman 1979; Driedonks 1982b). Stull (1976) summarized published values of α obtained from observations, while Betts *et al.* (1992), and Hägeli *et al.* (2000) reported on values of α that are quite different than 0.2. Sun (1993a) concluded that representing entrainment in such a simple form does not work very well when clouds are present such that evaporation and radiative cooling can produce negative buoyancy at the inversion height. If $d\Delta\theta_i/dt$ is assumed to be small relative to the other two terms in Eq. (7-47), then Eq. (7-47) can be written as

$$\frac{dz_i}{dt} = \bar{w}_{z_i} = -\frac{1.2u_*\theta_*}{z_i\partial\bar{\theta}^+/\partial z} \tag{7-49}$$

Deardorff (1974a) has improved on the formulation given by Eq. (7-49) using his three-dimensional numerical planetary boundary-layer simulation of Day 33 of the Wangara Experiment (Clarke *et al.* 1971). Deardorff's (1974a) parameterization has subsequently been adopted by Pielke and Mahrer (1975) and others and shown to be very realistic when the variation of z_i with time is strongly influenced by surface heating. This prognostic representation for the planetary boundary-layer height can be written as

$$
\frac{\partial z_i}{\partial t} = -\bar{u}_{z_i}\frac{\partial z_i}{\partial x} - \bar{v}_{z_i}\frac{\partial z_i}{\partial y} + \bar{w}_{z_i} + \left[1.8(w_*^3 + 1.1u_*^3\right.
$$
$$
\left. - 3.3u_*^2 f z_i)\right] \Big/ \left(g\frac{z_i^2}{\bar{\theta}_{h_s}}\frac{\partial \bar{\theta}^+}{\partial z} + 9w_*^2 + 7.2u_*^2\right), \qquad (7\text{-}50)
$$

where

$$
w_* = \begin{cases} \left(-\frac{g}{\bar{\theta}_{h_s}}u_*\theta_* z_i\right)^{1/3}, & \theta_* \leq 0 \\ 0, & \theta_* > 0 \end{cases}
$$

and $\bar{\theta}_{h_s}$ is the potential temperature at the top of the surface layer. The scaling velocity, w_*, has been called the convective velocity scale, or the Deardorff velocity (Stull 2000). As in Eq. (7-49), in Eq. (7-50) the growth of z_i is directly proportional to the surface heat flux and mesoscale vertical velocity and inversely proportional to the overlying stability.

Equation (7-50) can also be used to estimate $\bar{w}_{z_i}$ if it is assumed the boundary-layer height is unchanging over time and horizontally homogeneous, $\theta_* = 0$, and the net radiational flux divergence is 0. For this case, Eq. (7-50) reduces to

$$
\bar{w}_{z_i} = -\left(1.98u_*^3 - 5.94u_*^2 f z_i\right) \Big/ \left(g\frac{z_i^2}{\bar{\theta}_{h_s}}\frac{\partial \bar{\theta}^+}{\partial z} + 7.2u_*^2\right),
$$

where z_i is obtained from a radiosonde or other observational platform. For example, with typical values of $u_* = 50$ cm s^{-1}, $f = 10^{-4}$s^{-1}, $\theta_{h_s} = 300$ K, $\partial\bar{\theta}^+/\partial z = 1°/100$ m, and $z_i = 1$ km, we have $\bar{w}_{z_i} = 0.03$ cm s^{-1}.

When $\theta_* = 0$, $\bar{w}_{z_i} = 0$, $\partial\bar{\theta}^+/\partial z = 0$, and $dz_i/dt = 0$, Eq. (7-50) reduces to $z_i = 0.33u_*/f$, which is the expected depth of the planetary boundary layer in a steady-state, horizontally homogeneous, neutrally stratified boundary layer. Obviously, this latter representation for a neutral boundary layer must be modified in the tropics, where f approaches 0.

The height of the surface layer, h_s, can be estimated from z_i as

$$
h_s = 0.04z_i. \qquad (7\text{-}51)
$$

For example, with $z_i = 1$ km, $h = 40$ m. This formulation was based on the results of Blackadar (1972, personal communication) and Blackadar and Tennekes (1968), who found the best agreement between their predictions and

observations in a neutrally stratified boundary layer when Eq. (7-51) was adopted.

When clouds are present at the top of the mixed layer, the effect of cumulus-induced subsidence must be included in the $\bar{w}_{z_i}$ term in Eq. (7-50). Brost *et al.* (1982a, b) discussed the mean and turbulent budgets in a marine stratocumulus-topped mixed layer off the California coast, and Augstein and Wendel (1980) presented a one-dimensional tradewind boundary-layer model with nonprecipitating cumulus clouds. Chen and Cotton (1983b) discussed a one-dimensional simulation of a stratocumulus-capped mixed layer in which the relative importance of turbulence, radiation, and subgrid-scale cloud condensation are contrasted.

In Augstein and Wendel's study, the authors concluded that radiation was as important in boundary-layer development as large-scale subsidence and the horizontal advection of heat and water vapor. According to their model calculations, solar heating reduces the effect of both condensational heating within the active cloud layer and evaporative cooling at the top of the cloud layer, as compared to that occurring at night. This response, resulting from the dependence of saturation specific humidity on temperature, results in deeper clouds at night because the cumulus convection is more vigorous in the absence of this solar heating.

7.3.3.1   Idealized Theory

An idealized representation of the winds in the transition layer can be derived from a simplified form of Eq. (4-21) given in component form by

$$
\begin{aligned}
0 &= K\frac{\partial^2 \bar{u}}{\partial z^2} + f(\bar{v}-v_g) \\
0 &= K\frac{\partial^2 \bar{v}}{\partial z^2} + f(u_g-\bar{u}),
\end{aligned}
\tag{7-52}
$$

where only the large-scale horizontal pressure gradient term (as represented by the geostrophic wind components u_g and v_g [see, e.g., Eq. (3-28)], the Coriolis terms $f\bar{u}$ and $f\bar{v}$, and the vertical subgrid flux terms are retained. The geostrophic wind is assumed to be constant with height, whereas the subgrid-scale flux terms are approximated with a constant exchange coefficient K. The horizontal wind components $\bar{u}$ and $\bar{v}$ do not vary with time or in the x and y directions. An atmosphere represented by these two equations is in steady-state equilibrium and horizontally homogeneous.

Following Dutton (1976:449), these equations can be written using complex notation as

$$
0 = \frac{\partial^2 V_{\mathrm{H}}}{\partial z^2} + i\frac{f}{K}(V_{\mathrm{G}}-V_{\mathrm{H}}),
\tag{7-53}
$$

where $V_H = \bar{u} + i\bar{v}$ and $V_G = u_g + iv_g$. Substituting V_H into Eq. (7-53), it is straightforward to show that

$$V_H - V_G = a_1 \exp\left[(1+i)l_E^{-1}z\right] + a_2 \exp\left[-(1+i)l_E^{-1}z\right],$$

where $l_E = \sqrt{2K/f}$.

The boundary conditions needed to solve this equation are

$$V_H = 0 \quad \text{at} \quad z = 0 \qquad \text{and} \qquad \lim_{z \to \infty} V_H = V_G.$$

Therefore, a_1 must equal 0 and $a_2 = -V_G$, so that

$$
\begin{aligned}
V_H - V_G &= -V_G \exp\left[-1(1+i)l_E^{-1}z\right] \\
&= -V_G e^{-z/l_E}\left[\cos(z/l_E) - i\sin(z/l_E)\right], \tag{7-54}
\end{aligned}
$$

where $z = \pi l_E \simeq z_i$ is a representative depth for the boundary layer (i.e., the first level above the ground where $V_H = V_G$), assuming that Eq. (7-52) is applicable. The solution to Eq. (7-54) for particular values of f and K is plotted in Figure 7-9. In the northern hemisphere, where $f > 0$, the winds near the surface, according to Eq. (7-54), are to the left of the geostrophic wind (i.e., toward low pressure). The wind *veers* (i.e., turns clockwise) with height and slightly overshoots the geostrophic value. This spiral wind profile, called the *Ekman profile*, is useful in the initialization of mesoscale models, as illustrated by Eq. (11-13) in Chapter 11. The transition layer is also called the *Ekman layer*, because this is that section of the planetary boundary layer in which the average wind direction changes with height. Kahl and Samson (1988) and Moran and Pielke (1996a, b) have shown how such wind shear influences the transport and dispersion of pollution.
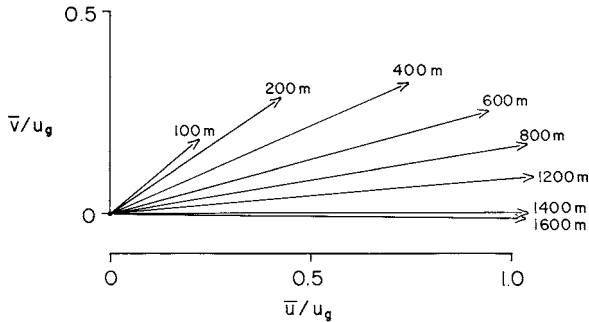
Fig. 7-9. A plot of the Ekman wind using Eq. (7-54), with $f = 10^{-4}$ and $K = 10 \text{ m}^2 \text{ s}^{-1}$; $l_E = 450$ m and $z_i \simeq 1400$ m. Without loss of generality, the components of Eq. (7-54) can be written as $\bar{u} = u_g(1 - e^{-z/E}\cos z/l_E)$ and $\bar{v} = u_g e^{-z/l_E}\sin z/l_E$ by setting $v_g = 0$, which is how they are displayed in this figure. Rotating the figure through the angle given by the arctangent of v_g/u_g gives the solution of Eq. (7-54) for any direction of the geostrophic wind.

7.3.3.2   *Parameterization of the Transition Layer*

The parameterization of the subgrid-scale correlation terms in the planetary boundary layer can be grouped into four categories:

- drag coefficient representations
- local exchange coefficients
- exchange coefficients derived from profile functions
- explicit equations for the subgrid-scale fluxes.

The first three classes above are often called *first-order closure representations*, because the subgrid-scale correlations are specified as functions of one or more of the grid-volume–averaged dependent variables $(\bar{u}_i, \bar{\theta}, \bar{q}_n, \bar{\chi}_m)$. The fourth category is called *second-order closure*, because prognostic equations are developed for the fluxes,[19] which include triple-correlation terms involving subgrid-scale variables [e.g., $\overline{u_j'' \, \partial e / \partial x_j}$ in Eq. (7-5)] that must be represented in terms of the double-correlation terms or the averaged dependent variables or both. The procedure to obtain the prognostic equations for the subgrid-scale fluxes $(\overline{u_j'' u_i''}, \overline{u_j'' \theta''}, \overline{u_j'' q_n''}$, and $\overline{u_j'' \chi_m''})$ was presented in Section 7.1.

Lewellen (1981), Zeman (1981), Mellor and Yamada (1982), and Wyngaard (1982) provide derivations and discussion of second-order equations, and Mellor and Yamada (1974) discuss the different levels of complexity using various simplifications of these explicit representations of the subgrid-scale fluxes. Yamada (1979b) performed a planetary boundary-layer analysis using one level of the Mellor–Yamada formulation. Libersky (1980, Table 2) provides an effective summary of approximations to the terms in second-order closure models, and Burk (1981) and Lewellen *et al.* (1983) provide other examples of simulations using second-order models. As illustrated in Section 7.3.3.4; accurate parameterizations of the planetary boundary layer in mesoscale models can be obtained without using second-order closure, despite arguments to the contrary suggested by such investigators as Zeman (1981).

The drag coefficient form (also called the *bulk aerodynamic* formulation) is given by, for example,

$$\overline{w''u''} = -C_D \overline{V}^2 \cos \mu, \quad \overline{w''v''} = -C_D \overline{V}^2 \sin \mu, \quad \text{and}$$
$$\overline{w''\theta''} = C_D' \overline{V} \big(\bar{\theta}(z_0) - \bar{\theta} \big), \tag{7-55}$$

where $\overline{V}$ and $\bar{\theta}$ are evaluated at some height within the surface layer (often 10 m) with μ equal to the arctan $(\overline{V}/\bar{u})$. The parameters C_D and C_D' are called *drag coefficients*. Above this level, a local exchange coefficient form is sometimes used if there is vertical resolution within the boundary layer. Rosenthal (1970), Lavoie (1972), and others have obtained realistic simulations using this form. Rosenthal used a value of $C_D = 3 \times 10^{-3}$ for velocity and $C_D' = 0$ for heat and moisture. Lavoie used $C_D = 7 \times 10^{-3}$ over land and $C_D = 1.5 \times 10^{-3}$ over water

for velocity, and used $C'_D = 1.5 \times 10^{-3}$ for heat if the surface layer was defined to be superadiabatic and $C'_D = 0$ otherwise. Fujitani (1981) presents observational estimates of the drag coefficient as measured over the East China Sea with mean values of $C_D = 1.3 \times 10^{-3}$ and $C'_D = 1.2 \times 10^{-3}$, although both values were lower for stable surface conditions. In that study, C_D had a larger value of about 2.1×10^{-3}, with high variability, for light winds ($\overline{V}$ less than 4 m s^{-1}).

Because using Eq. (7-16), $u_*^2 = C_D \overline{V}^2$ from Eq. (7-55), and by Eq. (7-29), $u_* \theta_* = C'_D \overline{V} (\overline{\theta} - \overline{\theta}(z_0))$ from Eq. (7-55), substituting for $\overline{V}$ from Eq. (7-27) and $\overline{\theta} - \overline{\theta}(z_0)$ from Eq. (7-31), and rearranging yields the expressions for C_D and C'_D given by[20]

$$
\begin{aligned}
C_D &= k^2 \Big/ \left[\ln \frac{z}{z_0} - \psi_{\mathrm{M}} \left(\frac{z}{L} \right) \right]^2 \\
C'_D &= \beta k^2 \Big/ \left[\ln \frac{z}{z_0} - \psi_{\mathrm{M}} \left(\frac{z}{L} \right) \right] \left[\ln \frac{z}{z_0} - \psi_{\mathrm{H}} \left(\frac{z}{L} \right) \right].
\end{aligned}
\tag{7-56}
$$

Thus, except for special cases such as when the winds are strong [so that $\psi_{\mathrm{M}}(z/L) = \psi_{\mathrm{H}}(z/L) \simeq 0$] and the aerodynamic roughness of the surface is unchanging, it is inappropriate to treat the drag coefficient as a constant. Using drag coefficients, fluxes in the boundary layer can be represented by requiring $C_D = C'_D = 0$ at z_i with a specified functional form between the surface and z_i.

The use of exchange coefficients is of the form given by Eq. (7-7), for example, where K_θ and K_m are exchange coefficients. If these coefficients are defined only in terms of local gradients, then they are called *local exchange coefficients*, but if they are derived from a vertical interpolation formula that is independent of local gradients, then they are called *profile coefficients*. Blackadar (1979) suggested one form of local exchange coefficient when the layer being simulated is stably stratified air ($\partial \overline{\theta}/\partial z > 0$), which is expressed as[21]

$$
K_m = K_\theta = \begin{cases} 1.1 (\mathrm{Ri_C} - \mathrm{Ri}) l^2 |\partial \vec{V}/\partial z|/\mathrm{Ri_C}, & \mathrm{Ri} \leq \mathrm{Ri_C} \\ 0, & \mathrm{Ri} > \mathrm{Ri_C}, \end{cases}
\tag{7-57}
$$

where l is a mixing length and $\vec{V} = \bar{u}\vec{i} + \bar{v}\vec{j}$. In the form used by McNider (1981) and McNider and Pielke (1981), l is given as

$$
l = \begin{cases} kz, & z < 200 \text{ m} \\ 70 \text{ m}, & z \geq 200 \text{ m}. \end{cases}
$$

The parameter $\mathrm{Ri_C}$ is the critical Richardson number, described following Eq. (7-8), which should equal 0.25 in the limit as the vertical grid spacing approaches 0. The finite difference value of $\mathrm{Ri_C}$ increases as the vertical grid increment increases, as discussed by, for example, Shir and Bornstein (1977).

Another example of a local exchange coefficient representation is that of Orlanski *et al.* (1974), where K_m and K_θ vary from a background value of these coefficients only when $\partial \bar{\theta}/\partial z < 0$. Klemp and Lilly (1978) use a form of mixing equivalent to a local exchange coefficient, which requires that the Richardson number in their model always equal or exceed the critical Richardson number, 0.25. A local exchange coefficient is appropriate when the vertical grid resolution is high (so that the gradients can be accurately approximated), when horizontal advection of turbulence is small, and when the characteristic length scales of the subgrid-scale mixing are approximately the same size or less than twice the vertical grid spacing.[22]

With such a representation, fluxes are always *downgradient*, since $K_m = K_\theta \geq 0$ (i.e., toward smaller values of $\bar{u}$, $\bar{v}$, $\bar{\theta}$, $\bar{q}_n$, and $\overline{\chi}_m$). As shown by Deardorff (1966), however, *countergradient* fluxes are known to occur when the surface layer is superadiabatic (i.e., $z/L < 0$). Deardorff suggested that the vertical gradient of potential temperature used in the representation $\overline{w''\theta''} = -K_\theta \partial \bar{\theta}/\partial z$ be modified to $\overline{w''\theta''} = -K_\theta \partial \bar{\theta}_C/\partial z$ with

$$\frac{\partial \bar{\theta}_C}{\partial z} = \frac{\partial \bar{\theta}}{\partial z} - \gamma_C, \tag{7-58}$$

where $\gamma_C = 0.65 \times 10^{-3}$ K m^{-1} to permit fluxes of heat upgradient. Tijm et al. (1999a), based on Holtslag and Boville (1993) and Holtslag *et al.* (1995), expressed the countergradient flux effect for $z/L \ll 0$ in the following form:

$$\overline{w''\theta''} = -K_\theta \left(\frac{\partial \bar{\theta}}{\partial z} - \gamma_C \right), \tag{7-59}$$

where

$$K_\theta = 1.4 k w_* z \left(1 - \frac{z}{z_i} \right)^2, \tag{7-60}$$

with w_* defined as

$$w_* = \left(\frac{-g}{\theta_{h_s}} u_* \theta_* z_i \right)^{1/3}. \tag{7-61}$$

The countergradient term in Eq. (7-59), expressed using the variables defined in this chapter, is

$$\gamma_C = -10 \frac{u_* \theta_*}{w_* z_*}. \tag{7-62}$$

K_θ is an example of an exchange coefficient derived from a profile function.

7.3.3.3 *Parameterization Complexity*

It is useful to dissect a parameterization algorithm to determine the number of dependent variables and adjustable and universal parameters that are introduced. This dissection can be illustrated through the following simple example. Holtslag and Boville (1993) and Tijm et al. (1999a) propose the following form for K_θ above the boundary layer:

$$K_\theta = l_\theta^2 S F_\theta(\text{Ri}), \tag{7-63}$$

where

$$\frac{1}{l_\theta} = \frac{1}{kz} + \frac{1}{\lambda_\theta}, \tag{7-64}$$

$$S = \left| \frac{\partial \vec{V}}{\partial z} \right|, \tag{7-65}$$

and

$$F_\theta(\text{Ri}) = \begin{cases} (1 - 18 \, \text{Ri})^{1/2}, & \text{Ri} \leq 0 \\ 1/(1 + 10 \, \text{Ri} + 80 \, \text{Ri}^2), & \text{Ri} > 0, \end{cases} \tag{7-66}$$

with

$$\lambda_\theta = \begin{cases} 300 \text{ m}, & z \leq 1 \, \text{km} \\ 30 \text{ m} + 270 \exp(1 - (z/1000 \text{ m})). \end{cases} \tag{7-67}$$

This formulation for K_θ includes the following dependent variables, parameters, and prescribed constants:

- In Eq. (7-63), the dependent variables l_θ, S, and F_θ define K_θ.
- In Eq. (7-64), l_θ is defined with the independent variable z, the dependent variable λ_θ, and the parameter k.
- In Eq. (7-65), S is defined by the vertical gradient of $\vec{V}$.
- In Eq. (7-66), F_θ (Ri) is defined by the dependent variable Ri [which is defined by Eq. (7-8)] and the constants 18, 10, and 80 and the exponent 1/2.
- In Eq. (7-67), λ_θ is defined by the independent variable z and the constants 300, 30, 270, and 1000.

Therefore, to represent the term K_θ, in addition to the fundamental variables $\bar{u}_i$ and $\bar{\theta}$, one parameter (k) and eight constants (18, 10, 80, 1/2, 300, 30, 270, 1000) must be provided.

A sensitivity analysis can be applied to show how K_θ responds to slight changes in the dependent variables and constants. For example, in Eq. (7-67), if 100 m were used instead of 300 m when λ_θ dominates in Eq. (7-64), then K_θ would be 1/9 as large, since K_θ is proportional to l_θ^2. Clearly, the form of

Eq. (7-67) will exert a major effect on the parameterized turbulent mixing in a model.

Niyogi *et al.* (1999) discuss such a sensitivity analysis (in their case for surface fluxes) in terms of the question "What scenarios make a particular parameter significant?" They also appropriately conclude that parameter uncertainty is not only related to its deviation, but is also dependent on the values of the other parameters used in a parameterization.

7.3.3.4 *Parameterization Comparisons*

Various forms of the explicit representation of the subgrid-scale fluxes [e.g., $(\partial/\partial t)\overline{u''_j u''_i}$, $(\partial/\partial t)\overline{u''_j \ \theta''}$] have been used by Donaldson (1973), Deardorff (1974a, b), Lumley and Khajeh-Nouri (1974), Wyngaard and Coté (1974), Burk (1977), André *et al.* (1978), Brost and Wyngaard (1978), Gambo (1978), Lee and Kao (1979), Abdella and McFarlane (1997, 1999), Mironov et al. (1999), and others. As mentioned earlier in this chapter, Mellor and Yamada (1974) categorized the level of complexity of those second-order representations. Although theoretically more satisfying, this more expensive approach, with its greater degrees of freedom, has not improved simulations of the evolution for the resolvable dependent variables in the planetary boundary layer over those obtained using the best first-order representations.

For example, Days 33 and 34 of the Wangara Experiment (Clarke *et al.* 1971) has been used extensively to examine the accuracy of various parameterizations of the planetary boundary layer. Deardorff (1974a), Wyngaard and Coté (1974), Pielke and Mahrer (1975), Yamada and Mellor (1975), Dobosy (1979), Sun and Ogura (1980), Blondin and Therry (1981), Mailhot and Benoit (1982), Chen and Cotton (1983a), Therry and Lacarrere (1983), Sun (1993a), and Finkele (1998), among others, have attempted to simulate boundary layer structure for all or a portion of these days. Figure 7-10(a), reproduced from the sophisticated higher-order model of André *et al.* (1978), illustrates the evolution of the averaged vertical potential temperature in the boundary layer using a model that has an explicit representation of the subgrid-scale fluxes. Figure 7-10(b) shows the results for the same period using first-order closure, as described in McNider and Pielke (1981), to represent the vertical exchange coefficient.

Both results closely correspond to the observed profile [Figure 7-10(c)]. The profiles of the other dependent variables produced by the two models also closely agree. Yu's (1977) results support part of this conclusion in that he found that using the McNider and Pielke (1981) parameterization produced accurate simulations of the growth of the mixed layer when compared to a range of other schemes, including a simplified second-order representation.

Sharan and Gopalakrishnan (1997) provide another comparison study of the accuracy of several turbulent closure schemes in terms of their ability
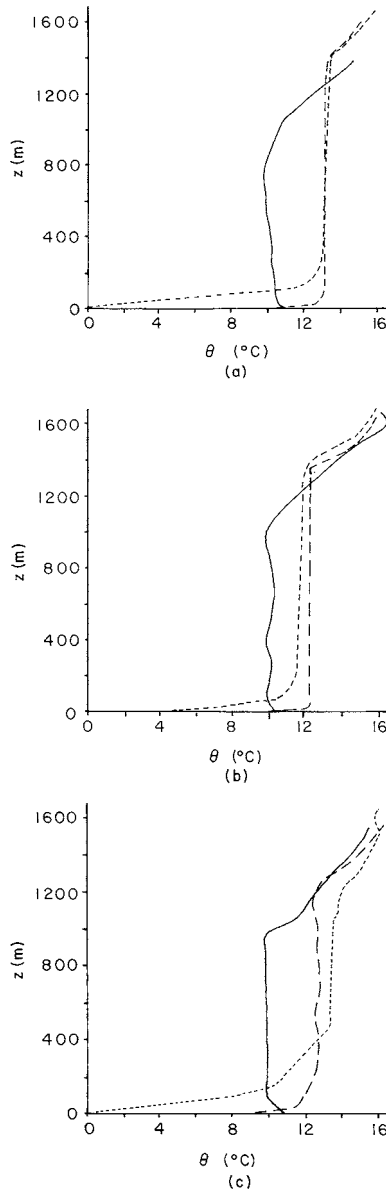
Fig. 7-10. Comparison of predictions using (a) higher-order closure (André *et al.* 1978) for Day 33–34 of the Wangara Experiment, (b) first-order closure (McNider and Pielke 1981), and (c) observational data presented by André *et al.* (1978). The solid and dashed lines correspond to 1200 LST and 1800 LST on Day 33; the dotted line corresponds to 0300 LST on Day 34.

to represent the stable boundary layer. Another modeling study of several boundary-layer parameterizations is discussed in Alapaty and Mathur (1998).

Zeman (1979) claims that his economical one-layer model compares favorably against second-order closure models in simulating the evolution of a nocturnal boundary layer. Klöppel *et al.* (1978) showed that the development and decay of ground-based inversions can be satisfactorily simulated by simple models. Chang (1979) produced accurate results using a Richardson number adjustment scheme for heat and momentum exchanges and concluded that this method provides an economical and realistic alternative to higher-order closure schemes.

Finally, investigators such as Mailhot and Benoit (1982) have suggested that an exchange coefficient must depend on the past history of the flow, so they use a coefficient that is dependent on the second-order property $\frac{1}{2}\bar{u}_i''^2$ and a length scale. However, the first-order exchange coefficients (which are dependent only on resolvable quantities, such as, $\bar{u}_i$ and $\bar{\theta}$) also depend on the history of the flow, since the resolvable variables themselves were determined in part from the response to turbulent mixing at previous times. Therefore, contrary to the conclusion of Mailhot and Benoit, unless significant turbulent (i.e., subgrid-scale) energy created at one grid point is *advected or diffused* to another grid cell, it appears unnecessary to include any prognostic equations for the second-order terms to parameterize the influence of subgrid-scale mixing on the grid-volume–averaged flow in mesoscale models.

Second-order closure boundary-layer models, of course, remain valuable tools to use in developing the most accurate first-order closure schemes and in developing effective parameterizations of the diffusion of pollutants, as described in Zannetti (1990), Uliasz *et al.* (1996), and Sharan *et al.* (1999). Of even more value, however, may be the use of large-eddy simulation (LES) models (e.g., such as reported in Bader and McKee 1983) to determine small-scale responses over nonhomogeneous terrain to specific sets of mesoscale forcing. Deardorff (1974a) has used this approach very effectively to develop parameterizations of mixed layer height for use in mesoscale models. A model is an LES when the model-resolved fluxes are much larger than the subgrid-scale fluxes (e.g., $|\overline{w''\theta''}| \ll |\bar{w}\bar{\theta}|$).

Examples of studies of using LES modeling to improve our understanding of homogeneous and nonhomogeneous landscapes on the convective boundary layer include Avissar and Schmidt (1998), Avissar *et al.* (1998), Stevens *et al.* (1998, 1999), Gopalakrishnan and Avissar (2000), and Gopalakrishnan *et al.* (2000). Mason and Brown (1999) used high-resolution LES modeling to conclude that length scales of turbulence should be buoyancy dependent, and to increase with unstable buoyant transfer.

7.4   Heterogenous Boundary Layers

When the surface is unevenly heated, or of different aerodynamic roughness, even though it is flat, the resultant surface and boundary-layer fluxes will be different (see, e.g., Vickers and Mahrt 1999). As air blows across this landscape, air near the surface will be directly responding to the turbulent fluxes which result from that surface, while air higher up will be still responding to the fluxes that resulted from the passage of the air over the original surface. The interface between these two sources of turbulent fluxes is called the *internal boundary layer*. Figures 7-11 and 7-12 illustrate schematically the behavior of the internal boundary layer for several different spatial distributions of surface heterogeneity. Examples of recent papers that discuss the internal boundary layer include Batchvarova *et al.* (1999) and Jegede and Foken (1999).

An internal boundary layer resulting from spatially varying surface turbulent sensible heat fluxes is called a *thermal internal boundary layer*. Turbulence that remains above the internal boundary layer will leave an altered vertical and horizontal structure of the temperature, winds, and other variables once it decays. This remnant of the turbulence is called *fossil turbulence* (Gibson 1999). Nieuwstadt and Brost (1986) estimate that it can take up to an hour or so for surface-forced convective eddies to decay once surface heating is removed. Mahrt (2000) concludes that internal boundary layers have more a diffuse vertical structure than textbook examples—a result, perhaps, of the heterogenous character of real world landscapes.

As discussed by Kerman (1982) and others, the growth of such a boundary layer can substantially influence the occurrence and location of fumigation in coastal regions. It can also influence the propagation of electromagnetic radiation (e.g., Gossard 1978) and the diffusion of pollutants (e.g., Gryning and
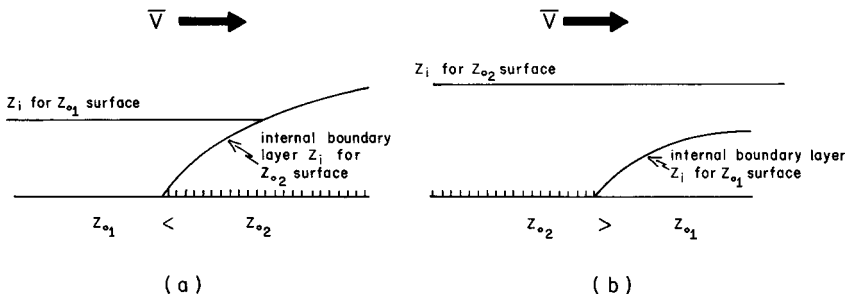
Fig. 7-11. Schematic illustration of the growth of an internal boundary layer with a neutrally stratified surface layer as airflow advects (a) from a smooth (small z_0) to a rough surface (large z_0); and (b) from a rough (large z_0) to a smoother (small z_0) surface. Note that for (a), eventually only one planetary boundary layer remains, whereas for (b), two levels of z_i remain, with separate and distinct regions of turbulence that last until the turbulent kinetic energy in the upper layer decays by dissipation.
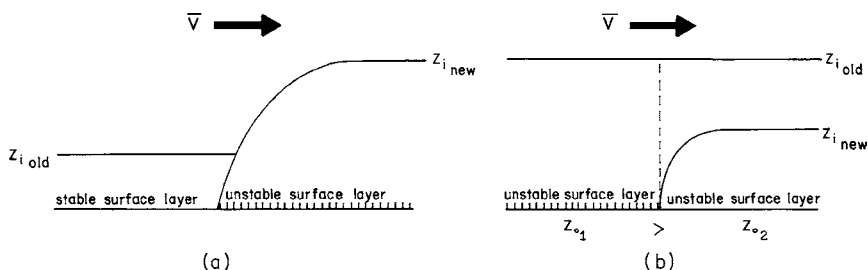
Fig. 7-12. Schematic illustration of the growth of an internal boundary layer as air advects (a) from a stably stratified surface to a region with an unstably stratified surface layer, and (b) from one unstably stratified region to another in which the equilibrium height of z_i over the new surface is lower.

Larsen 1981). Olsson and Harrington (2000) simulated the growth of an internal cloudy boundary layer as air flowed off of sea ice to over a relatively warm ocean surface. Physick *et al.* (1989) investigated how well a mesoscale model could simulate an internal boundary layer.

Onishi (1968), Peterson (1969), and others have numerically simulated changes in surface-layer structure caused by inhomogeneous terrain using two-dimensional, steady-state models. Peterson showed that in neutrally stratified air, the internal boundary layer grows about 1 unit upward for its first 10 units downstream of a change in surface characteristics. He further claims that the horizontal fetch must be 100 times its height for the new boundary layer to be equilibrium.

In an unstably stratified lower boundary layer, the growth of the internal boundary layer should be more rapid, as shown by Venkatram (1977), Højstrup (1981), Gamo *et al.* (1983), and others, since the rate of growth is coupled with the surface heat fluxes [see, e.g., Eq. (7-50)]. Højstrup reported that the growth of the internal boundary layer in the direction of the mean wind n can be written as

$$\partial z_{\mathrm{IBL}}/\partial n = D\sigma_w/\overline{V},$$

where D is a constant of order 1 and σ_w is the standard deviation of the vertical velocity as a function of height after z_{IBL} has reached its equilibrium value. With a highly unstable surface layer, $\overline{V}$ is almost constant with height (except very close to the ground). Since σ_w reaches a maximum in the midlevels of the boundary layer (see, e.g., McNider 1981), z_{IBL} will have its largest increases for a given downwind distance at those levels. Higher up, as σ_w approaches 0, the growth rate diminishes. From Højstrup's results, the ratio of the rate of growth of z_{IBL} to the distance traveled downstream during its early development was about 1–7 for the most unstable case examined and approximately 1–10 for the most neutral situation. Venkatram (1977) concluded that the growth of such internal mixed layers is enhanced by an increase of roughness, z_0, an increase of the

temperature difference between the new and original surfaces, and a decrease in the prevailing wind speed, $\overline{V}$. Venkatram's results agree closely with the observational results of Raynor *et al.* (1974). However, slower growth, occurs when the surface layer is stably stratified (e.g., Mulhearn 1981). For example, Lyons (1975) reported growth of a boundary layer to only 375 m even after several days of transit over cold ocean waters.

If the development of the internal mixed layer of 1 unit upward for 10 units downstream is used as the slowest growth rate (i.e., for $\theta_* = 0$), then a 10-km horizontal distance should be sufficient to generate a 1-km–deep planetary boundary layer. (The degree and the heights to which this mixed layer is in equilibrium with its new surface needs to be investigated further, however.)

When $\theta_* < 0$, the growth rate would be greater, as previously discussed. Hsu's (1973) observations support the rapid growth of a heated boundary layer after a change in surface characteristic from relatively cool ocean to land during the daytime over Florida. Using two towers, one of 10-m elevation over a beach and one of 100-m elevation 10 km inland, he found that the observations agreed closely with surface-layer theory developed for horizontally homogeneous steady conditions. Similarly, Kerman *et al.* (1982) found a rapid adjustment toward equilibrium ($\sim$10 km inland) as cold air over Lake Erie advected onshore over warm land. Additional detailed observations, such as those performed by Vugts (1980) and Gamo *et al.* (1982), provide further insight into the growth of the heated internal boundary layer.

These studies indicate that the larger the horizontal grid increment, the more appropriate it is to represent the boundary-layer structure as being in local equilibrium after a change of surface temperature and roughness, with the most rapid adjustment occurring when the surface layer is very unstable. Unfortunately, larger grid increments reduce the horizontal resolution so that the gains in consistency using boundary-layer theory, which is strictly valid only for horizontally homogeneous conditions, must be weighed against the need for greater spatial resolution of the forcing.

If the original surface is unstably stratified near the ground, then two layers of different turbulent characteristics can still result if the equilibrium z_i value of the downwind surface is less than that of upwind surface [e.g., caused by a smaller z_0, as illustrated in Figure 7-12(b)]. For this situation, turbulence formulations that are parameterized in terms of z_i will fail to provide proper estimates of mixing within the upper layer, although the lower region should be represented satisfactorily. In the upper region, a formulation such as that applied by McNider (1981), based on the work of Panofsky *et al.* (1960) and Blackadar (1979) and given by

$$K_m = K_\theta = (1 - 18 R_i)^{+1/2} l^2 |\partial \vec{V}/\partial z|,$$

could be used. [Here l can be defined using formulas such as Eq. (7-64) or the definition of l following Eq. (7-57).] This relation can also be used when air

with $\partial\bar{\theta}/\partial z < 0$ advects over a region that has a stably stratified ($\theta_* > 0$) surface layer.

Studies that evaluate the effect of spatially varying heat fluxes include Hadfield *et al.* (1991, 1992), Serreze *et al.* (1992), Walko *et al.* (1992), Avissar and Schmidt (1998), Banta *et al.* (1998), Liston and Sturm (1998), Burba *et al.* (1999), Cai (1999), Hasager and Jensen (1999), Laubach and Teichmann (1999), Liston (1999), Panin and Tetzlaff (1999), and Van Breugel *et al.* (1999). Rodriguez-Camino and Avissar (1999) discuss the use of *effective parameters* to describe surface heat fluxes in heterogenous terrain. They conclude that nonlinear relations provide more accurate representations of the surface fluxes than does linear averaging.

The concept of an effective parameter assumes that an interpolation variable can be used to accurately represent area-averaged fluxes over a heterogenous landscape. This interpolation variable itself has no explicit physical realism (i.e., it cannot be directly measured or even diagnosed from point measurements). As shown by Rodriguez-Camino and Avissar (1999) and Ronda and De Bruin (1999), the relationship between most land-surface characteristics and surface heat fluxes are nonlinear. This makes the computation of effective parameters more difficult. Other papers that discuss the effective parameter approach include Hu *et al.* (1999).

Analytic and numerical modeling studies indicate that surface fluxes over heterogeneous flat terrain can be linearly weighted to compute area-averaged surface fluxes as long as the spatial scale of the landscape variations are smaller than about 5–10 km on a side (Dalu *et al.* 1991; Avissar and Schmidt 1998). This linear averaging of the surface fluxes is called the *mosaic approach*. These surface fluxes can be calculated using the theoretical basis for subgrid-scale parameterizations, as introduced in this chapter. On these spatial scales, it is assumed (as based on the model) that the surface fluxes *blend* into a homogeneous boundary layer above the surface layer. The heights at which this occurs is called the *blending height* (see, e.g., Goode and Belcher 1999). When the blending height is within or at the top of the surface layer, this necessarily means that the internal boundary layer is contained within the surface layer.

However, when the internal boundary layer is above the surface layer, the mosaic approach is necessarily inadequate. Variations in the boundary-layer depth can create mesoscale wind circulations (Dalu and Pielke 1993; Zeng and Pielke 1995a, b). Moreover, when internal boundary layers above the surface layer are important, parameterizations for subgrid-scale fluxes as used in all mesoscale and larger-scale models will have errors. *There is no parameterization of subgrid-scale fluxes that include the effects of such internal boundary layers.*

The presence of terrain elevation variability introduces an additional type of landscape variability (Gopalakrishnan and Avissar 2000). This elevation varia-

tion will accelerate and decelerate the wind flow, even in the absence of surface frictional effects, as represented by z_0. The effect of terrain variability on the flow is referred to as *form drag*. This topic was introduced in Section 5.3 and is discussed further in Section 12.5.3. With respect to large-scale models, form drag is discussed in Palmer *et al.* (1986), and McFarlane (1987).

The results of Panofsky *et al.* (1981, 1982) suggest that the turbulence spectra of airflow over complex terrain rapidly reaches an equilibrium with the new topography for wavelengths that are short compared to the fetch over the new terrain. Since the vertical velocity spectra generally contain less long-wavelength energy than the horizontal velocity spectra, it tends to reach equilibrium faster. Over hilly terrain, the long-wavelength portion of the horizontal velocity spectra, which is normal to the topography, loses energy to the horizontal terrain-parallel flow and to vertical motion. This change in the energy within the individual components results from the distortion of the mean flow by the terrain. Højstrup (1981) reached the conclusion that the adjustment of the low frequencies to changing terrain may require hours, so that in reality an equilibrium for these long wavelengths is never achieved.

Other studies of the influence of terrain on boundary-layer airflow include the wind tunnel studies by Britter *et al.* (1981), Pearse *et al.* (1981), and Neal *et al.* (1982); the numerical modeling simulations of a two-dimensional ridge by Taylor (1981) and of a three-dimensional isolated hill in Alberta by Walmsley *et al.* (1982); the analytic study of Jackson and Hunt (1975); and the observational studies of Camuffo (1982). Hunt and Simpson (1982) summarize the understanding of the change in boundary-layer structure as air advects over irregular terrain and other differential surface characteristics. Roth (2000) discusses how the boundary layer within about three times the height of buildings in cities is not adequately represented by standard boundary-layer parameterizations (such as discussed in this chapter and used by all existing mesoscale models). Clearly, this is an aspect of the models that needs improvement.

In any case, the current lack of alternative parameterizations for the boundary layer in heterogeneous nonsteady conditions requires that *only theory developed for horizontally homogeneous steady-state boundary layers are available for use in mesoscale models to represent subgrid-scale fluxes.*

Notes to Chapter 7

1. In this example, and in actual measurements, upward motion does not always transport warmer air aloft even if the ground is warmer, because cooler air mixed downward at an earlier time or different location may be entrained in an upward-moving region.

2. This is essentially the Boussinesq approximation. See Chapter 4 following Eq. (4-15) for a description of this assumption.

3. The Reynolds assumption; see following Eq. (4-8).

4. Although the reference to Eq. (7-5) as a turbulent kinetic energy equation is relatively standard, it is imprecise to do so, since molecular viscosity [e.g., Eq. (3-29)] was ignored in the original equations [e.g., Eq. (2-45)]. Therefore, molecular dissipation of turbulent energy is excluded in Eq. (7-5).

5. It is important to note that the averaging operation given by Eq. (4-6) is not the same as that used in turbulence theory. Standard turbulence observations involve measurements at specific points on a tower or along an aircraft track. In the first case, averaging is in time, whereas in the second case a one-dimensional space average is used. The parameterization of subgrid-scale fluxes, however, uses the results from these observational studies, as discussed in this chapter. Such an equivalence is justified only if the measured turbulence characteristics are essentially the same as those occurring throughout the averaging grid volume. Porch (1982) presented an example of a comparison of volume averaging (using an optical anemometer) and a point measurement (a cup anemometer) for a drainage flow observational study in a California valley. He concluded for that study that point measurements should be averaged for a relatively long time (around 2 hours) to represent more accurately the volume-averaged values. Unfortunately, of course, if the spatial variations are too large across the volume, then no amount of time averaging at a point can provide the appropriate average.

6. A discussion of the number of grid points required to resolve such a range of scales is given at the beginning of Chapter 4.

7. Schmidt and Housen (1995) provide a useful summary of the use of dimensional analysis in geophysical problems.

8. Weber (1999) discusses alternative definitions of the friction velocity.

9. $[\overline{w''u''}\frac{\partial \bar{u}}{\partial z} + \overline{w''v''}\frac{\partial \bar{v}}{\partial z}] = -u_*^2[\cos \mu \frac{\partial \bar{u}}{\partial z} + \sin \mu \frac{\partial \bar{v}}{\partial z}] = -u_*^2[\cos^2 \mu \frac{\partial \overline{V}}{\partial z} + \sin^2 \mu \frac{\partial \overline{V}}{\partial z}] = -u_*^2 \frac{\partial \overline{V}}{\partial z}$.

10. Hicks and Everett (1979) commented that the displacement height could be different for each of the dependent variables in Eq. (7-34). However, since additional research is needed to ascertain whether this is true, in this section D is treated the same for all variables.

11. A somewhat different formation given by $\overline{V} = \overline{V}_D \exp a[(z/D) - 1]$ is often used. However, with this expression, $\overline{V}_D$ does not equal 0 at $z = 0$, as it should. Pinker and Moses (1982) have given an example of the estimation of the flow within an evergreen tropical forest using this formulation.

12. Traditionally, this layer was called a "laminar sublayer," although, as evident in Eq. (7-39), turbulent fluxes still occur within $z < z_0$ since u_*, q_*, and χ_* still appear.

13. When a zero-plane displacement D is required, the formulation given by Eq. (7-34) must be used. Also, in this section, only the flux of water vapor (i.e., $n = 3$) is discussed.

14. The deposition velocity, as reported by, for example, Galloway *et al.* (1980), is dependent on the rate of uptake of the gas or aerosol by vegetation, the speed of transfer through the laminar layer just above the leaf surfaces of the vegetation, and the intensity of turbulent mixing at the top of the vegetation.

15. This was estimated by R. Pearson, Jr., CSU (1982, personal communication).

16. In the context of a model, the height of the planetary boundary layer is the grid-area (i.e., $\Delta \tilde{x}^1$ by $\Delta \tilde{x}^2$)–averaged depth z_i, to which the grid-volume–averaged fluxes of heat, momentum, moisture, and pollutants extend *through the transfer of mass*.

17. Roll vortices also can occur in neutrally stratified boundary layers. In a neutral boundary layer, roll vortices obtain their kinetic energy from vertical shear of the horizontal wind, whereas in inversion-capped heated boundary layers, the energy is derived primarily from buoyancy (see, e.g., Mason and Sykes 1980, 1982).

18. $\overline{w''_{z_i} \theta''_{z_i}}/\Delta \bar{\theta}_i = \overline{w''_{z_i}(\theta''_{z_i}/\Delta \bar{\theta}_i)} = \overline{w''_{z_i}(\rho''_{z_i}/\Delta \bar{\rho}_i)}$ as long as $|\theta''_{z_i}| \ll \Delta \bar{\theta}_i \ll \bar{\theta}_0$.

19. Some investigators (e.g., Mailhot and Benoit 1982) define first-order closure as meaning that an exchange coefficient is used to represent the subgrid-scale fluxes [see, e.g., Eq. (7-7)]. In this text, however, first-order closure means that the exchange coefficients must be defined *only* in terms

of the grid-volume–averaged dependent variables and *not* by averages of the higher moments of the subgrid-scale fluctuations, such as the grid-volume–averaged subgrid-scale kinetic energy $\frac{1}{2}\overline{u_i''^2}$.

20. The 0.01 uncertainty in the value of k [see the text before Eq. (7-19)], results in an uncertainty in C_D and, therefore, the fluxes that can be as large as 10% $(\overline{u''w''} = -u_*^2 \sim -k^2)$.

21. In the surface layer, when Ri = 0, Eq. (7-57) should reduce to $K_m = ku_*z$ [Eq. (7-18)]. Substituting Eq. (7-19) for $|\partial V/\partial z| = \partial\overline{V}/\partial z$ in Eq. (7-57), yields $K_m = 1.1\, ku_*z$ however. Thus the reason for the coefficient 1.1 in Eq. (7-57) is not clear. In addition, from Eq. (7-33), K_m and K_θ are not equal at Ri $= 0$ in the surface layer. Finally, as discussed by Gutman *et al.* (1973), the vertical derivative of the horizontal wind vector, rather than the vertical derivative of the wind speed, should be used in Eq. (7-57) unless the wind direction is invariant with height.

22. A minimum of two grid lengths are needed to represent even a portion of a feature in a model, and at least four grid lengths are required for somewhat accurate resolution in the conservation equations, as discussed in Chapter 10.

Additional Readings

To understand the parameterization techniques for representing the subgrid-scale fluxes used in mesoscale models, it is necessary to understand atmospheric turbulence. Among the valuable texts in this area are the following:

Lumley, J. L., and H. A. Panofsky. 1964. "The Structure of Atmospheric Turbulence." Interscience Monographs and Texts in Physics and Astronomy, Vol. 12, Interscience, New York.

> John Lumley wrote the first half of this classic book, and Hans Panofsky wrote the second. Lumley's sections provide the mathematical basis for turbulence theory, and Panofsky's portion emphasizes specific applications of this theory to an improved understanding of mixing in the atmosphere.

Tennekes, H., and J. L. Lumley. 1972. "A First Course in Turbulence." MIT Press, Cambridge, MA.

> The authors introduce turbulence theory using effective physical examples of such mixing. This text is a valuable reference source for nomenclature and clear explanations of turbulence theory.

The following contributions provide excellent in-depth discussions on how to parameterize the atmospheric boundary layer.

Bélair, S., J. Mailhot, J. W. Strapp, and J. I. MacPherson. 1999. An examination of local versus nonlocal aspects of a TKE-based boundary layer scheme in clear convective conditions. *J. Appl. Meteor.* **38**, 1499–1518.

Beljaars, A. C. M., and P. Viterbo. 1998. Role of the boundary layer in a numerical weather prediction model. In "Clear and Cloudy Boundary Layers," A. M. Holstlag and P. G. Duynkerke, Eds., Royal Netherlands Academy of Arts and Sciences, Amsterdam., 287–304.

Blackadar, A. K. 1979. High-resolution models of the planetary boundary layer. "Adv. Environ. Sci. Eng." **I**, J. R. Pfafflin and E. N. Ziegler, Eds., Gordon and Breach Science Publishers, 50–85.

Cuijpers, J. W. M., and A. A. M. Holtslag. 1998. Impact of skewness and nonlocal effects on scalar and buoyancy fluxes in convective boundary layers. *J. Atmos. Sci.* **55**, 151–162.

Eugster, W., W. R. Rouse, R. A. Pielke Sr., J. P. McFadden, D. D. Baldocchi, T. G. F. Kittel, F. S. Chapin III, G. E. Liston, P. L. Vidale, E. Vaganov, and S. Chambers. 2000. Land-atmosphere energy exchange in Arctic tundra and boreal forest: Available data and feedbacks to climate. *Global Change Biology*, **6**, 84-115.

Garratt, J. R. and G. D. Hess. 2001. The idealized neutrally stratified planetary boundary layer. In "Encyclopedia of Atmospheric Sciences," J. Holton and P. Taylor, Eds., Academic Press, London.

Holtslag, A. A. M. 1998. Fluxes and gradients in atmospheric boundary layers. In "Clear and Cloudy Boundary Layers," A. A. M. Holtslag and P. G. Duynkerke, Eds., Royal Netherlands Academy of Arts and Sciences, Amsterdam.

Moran, M. D. 2001. Basic aspects of mesoscale atmospheric dispersion. In "Mesoscale Atmospheric Dispersion," edited by Z. Boybeyi, Vol. 9, Advances in Air Pollution Series. Wit Press, Ashurst, Southampton, United Kingdom.

Uliasz, M. 1994. Subgrid scale parameterizations. In "Mesoscale Modeling of the Atmosphere," R. Pearce and R. A. Pielke, Eds., 13–19, American Meteorological Society, Boston, MA.

Velho, H. F. C., R. R. Rosa, F. M. Ramos, R. A. Pielke Sr., G. A. Degrazia, C. Rodrigues Neto, and A. Zanandrea. 2001. Multifractal model for eddy diffusivity and counter-gradient term in atmospheric turbulence. *Physica A*, **295**, 219–223.

Vermeulen, J. P. L. 2001. The atmospheric boundary layer over a heterogeneous vegetated landscape. Ph.D. Thesis, Vrije University, Amsterdam, 164 pp.

There are a series of excellent books on boundary-layer theory. The following texts are among the best.

Arya, S. P. 1988. "Introduction to Micrometeorology." Academic Press, San Diego.

Garratt, J. R. 1992. "The Atmospheric Boundary Layer." Cambridge University Press, Cambridge, U.K.

Garstang, M., and D. Fitzjarrald. 1999. "Observations of Surface to Atmospheric Interactions in the Tropics." Oxford University Press, New York.

Holtslag, A. A. M., and P. G. Duynkerke. 1998. "Clear and Cloudy Boundary Layers." Royal Netherlands Academy of Arts and Sciences, Amsterdam.

Sorbjan, Z. 1989. "Structure of the Atmospheric Boundary Layer." Prentice-Hall, Englewood Cliffs, NJ.

Stull, R. B. 1988. "An Introduction to Boundary Layer Meteorology." Kluwer Academic Publishers, The Netherlands.

Stull, R. B. 2000. "Meteorology for Scientists and Engineers." 2nd ed., Brooks/Cole Thomson Learning.

A very useful summary of field campaigns and long-term observational facilities to monitor the boundary layer is reviewed in Tunick (1999). Recent valuable review papers include Avissar (1995) and Brutsaert (1998).

Problems

1. Select a parameterization for the subgrid-scale heat fluxes from an atmospheric model of your choice. Dissect the parameterization using the technique outlined in Section 7.3.3.3. List the additional new dependent variables, and adjustable and universal parameters. Assess the sensitivity in the calculated value of the flux for uncertainties of $\pm 10\%$ as a function of one or more of the adjustable constants and universal parameters.

2. Perform problem. 1, except for the subgrid-scale parameterization used for the velocity fluxes. What are the differences between the two parameterizations?

3. Derive an equation in which $\overline{S_\theta''} = 0$ is not assumed.

Chapter 8

Averaged Radiation Flux Divergence

8.1   Introduction

The radiative flux divergence source–sink term $\bar{S}_\theta$ in Eq. (4-24) can be written in part as

$$\bar{S}_\theta = \left.\frac{\partial \overline{T}}{\partial t}\right|_{\text{rad}} = -\frac{1}{\bar{\rho} C_\text{p}} \frac{\partial \overline{R}}{\partial z}, \qquad (8\text{-}1)$$

where $\partial \overline{R}/\partial z$ is the grid-volume–averaged vertical gradient of absorbed *irradiance* (i.e., radiative energy per area per time) from all wavelengths of electromagnetic energy. In writing Eq. (8-1), the divergence of $\overline{R}$ in the horizontal direction is neglected, since on the mesoscale, variations of $\overline{R}$ are much larger in the vertical.[1] In addition, changes in pressure resulting from the divergence of $\overline{R}$ are also neglected in Eq. (8-1). It is important to note that $\overline{R}$ contains subgrid-scale effects as well as resolvable effects. This chapter discusses methodologies for parameterizing the divergence of irradiance.

8.2   Basic Concepts[2]

The unit of differential area on the surface of a hemisphere can be written as

$$dS = \cos Z \sin Z \, dA \, dZ \, d\psi, \qquad (8\text{-}2)$$

where as shown in Figure 8-1, dA is a differential area on a plane through the equator of the hemisphere, Z is the angle between the axis of the hemisphere and a line to dS (i.e., the *zenith angle*)[3], and ψ is the longitude of dS on the hemisphere (i.e., the *azimuth angle*). The quantity $\sin Z \, dZ \, d\psi$ is called a *differential solid angle* and has units called steradians.
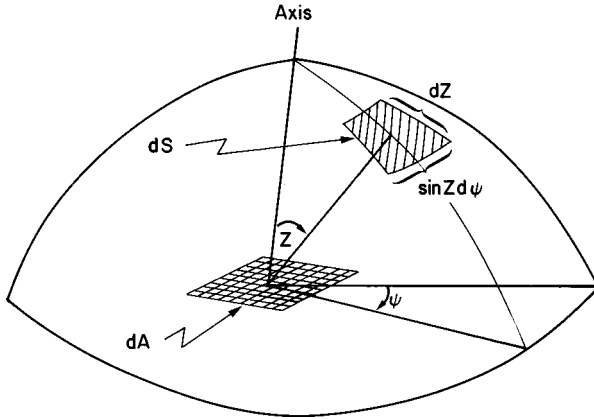
Fig. 8-1. An illustration of the relation between a differential area, *dA*, on a flat surface and the projection of this area, *dS*, onto the surface of a hemisphere with a radius of unity. The angles ψ, and Z are the longitude and zenith. (Adapted from Liou 1980, Figure 1.3.)

Using Eq. (8-2) and following Liou (1980), the monochromatic[4] intensity (radiance) of electromagnetic radiation through *dS* per time per wavelength can be written as

$$I_\lambda(Z, \psi) = de_\lambda / (\cos Z \sin Z \, dA \, dZ \, d\psi \, d\lambda \, dt), \qquad (8\text{-}3)$$

where de_λ is the differential amount of radiant energy at a given frequency passing through *dS* in the time interval *dt*.

Integrating Eq. (8-3) over the entire hemisphere yields the monochromatic *irradiance* on *dA* from all points above that differential surface,

$$R_\lambda = \int_0^{2\pi} \int_0^{\pi/2} I_\lambda(Z, \psi) \cos Z \sin Z \, dZ \, d\psi, \qquad (8\text{-}4)$$

which can be written as

$$R_\lambda = \pi I_\lambda \qquad (8\text{-}5)$$

when $I_\lambda(z, \psi)$ is independent of direction.[5] The total isotropic irradiance is obtained by integrating Eq. (8-5) over all wavelengths,

$$R = \pi \int_0^\infty I_\lambda \, d\lambda. \qquad (8\text{-}6)$$

The concept of a *blackbody* is essential in the economical parameterization of Eq. (8-1). A blackbody is defined as an object that absorbs all radiation that

impinges on it. As shown, by, for example, Coulson (1975), the intensity of electromagnetic radiation emitted by such a blackbody as a function of wavelength λ is given by

$$B_\lambda(T) = C_1 \left/ \left[\lambda^5 \left(e^{C_2/\lambda T} - 1 \right) \right] \right. . \tag{8-7}$$

The monochromatic radiance given by Eq. (8-7), called the *Planck function*, represents the maximum intensity of emitted radiative energy that can occur for particular values of temperature and wavelength.

The derivation of Eq. (8-7) using the concepts of quantum mechanics is described by Liou (1980:9–11 and App. C) and Kondratyev (1969:30–32). In Eq. (8-3), $B_\lambda(T)$ has the same units as $I_\lambda(z, \psi)$. The values $C_1 = 1.191 \times 10^{-16}$ W m^2 st^{-1} and $C_2 = 1.4388 \times 10^{-2}$ m K (NBS 1974) are fundamental physical constants derived from the speed of light and the Planck and Boltzmann constants (see Liou 1980:10–11); values of fundamental (universal) physical constants are given in Mohr and Taylor (2000).

Integrating Eq. (8-7) over all wavelengths and all directions within the hemisphere depicted in Figure 8-1 (see Kondratyev 1969:33–34; Liou 1980:11), where the emitted radiation is assumed to be isotropic, yields

$$R^* = \pi \int_0^\infty B_\lambda(T) d\lambda = \sigma T^4 \left[\sigma = 5.67400 \times 10^{-8} \text{ W m}^{-2} K^{-4} \right] \tag{8-8}$$

(Mohr and Taylor 2000), which is called the *Stefan-Boltzmann law*; σ is the Stefan-Boltzmann constant. The quantity R^* is the blackbody irradiance over all wavelengths and is equal to the maximum amount of radiative energy per unit area that an object can emit at a given temperature.

Figure 8-2, obtained from the work of List (1971:412), illustrates the blackbody irradiance computed as a function of wavelength using Eq. (8-7) with $T = 6000$ K (e.g., corresponding to the surface of the sun) at the distance of the earth from the sun, and with $T = 290$ K (e.g., corresponding to the surface of the earth). As this figure shows, the two distributions (also called *spectra*) of electromagnetic radiation have almost no overlap. For this reason, irradiance from the sun is often referred to as *shortwave radiation*[6], whereas radiation emitted from the earth is called *longwave (infrared) radiation*. The wavelength separation of these two electromagnetic spectra simplifies the parameterization of Eq. (8-1), as is shown shortly. Using Eq. (8-7), the peak emission from the sun's surface has a wavelength of 0.475 μm (blue light), whereas the earth, using $T = 290$ K, has a peak of around 10 μm.

As electromagnetic radiation traverses a layer in the atmosphere, it can be absorbed, reflected, or transmitted. This relation can be written quantitatively as

$$\frac{I_\lambda(\text{absorbed})}{B_\lambda} + \frac{I_\lambda(\text{reflected})}{B_\lambda} + \frac{I_\lambda(\text{transmitted})}{B_\lambda} = 1,$$
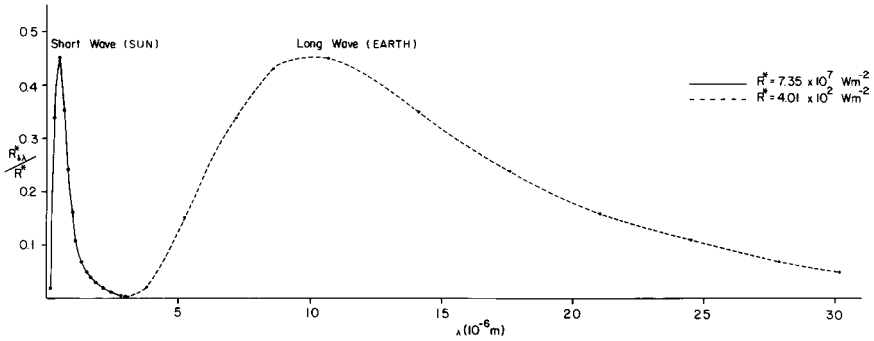
Fig. 8-2. Radiative flux, defined by $R^*_{\delta\lambda} = \int_\lambda^{\lambda+\delta\lambda} E^*_\lambda(T)d\lambda$, divided by the total black-body radiation R^* [from Eq. (8-8)] as a function of wavelength λ. Note that the values of R^* are different for $T = 6000$ K and $T = 290$ K. However, at the distance of the earth from the sun, the two values of R^* must be almost the same, since the earth's total irradiance is always essentially equal to the annual irradiance received from the sun at the earth's orbital distance.

or

$$a_\lambda + r_\lambda + t_\lambda = 1, \qquad (8\text{-}9)$$

where a_λ, r_λ, and t_λ are called *monochromatic absorptivity, reflectivity*, and *transmissivity*, respectively. In addition, the reflectivity can be decomposed into that which through multiple reflections (*scattering*) is transmitted in the forward direction, and that which through scattering propagates at a different angle than that of the incoming electromagnetic energy. The sum of the absorption and scattering out of the incident direction is called *attenuation* or *extinction* of the electromagnetic radiation (Paltridge and Platt 1976:38). As shown by Kondratyev (1969:22), when an element of volume is in local thermodynamic equilibrium[7], $a_\lambda = \epsilon_\lambda$ for that volume, where ϵ_λ is the *monochromatic emissivity*. This relationship between absorptivity and emissivity is called *Kirchhoff's law*. Levels in the earth's atmosphere below about 50 km or so are in local thermodynamic equilibrium. With a blackbody, $a_\lambda = 1$, so that $\epsilon_\lambda = 1$ as well. When a_λ is independent of wavelength but $\epsilon_\lambda = a_\lambda < 1$, the object is called a *graybody*.

Following Liou (1980), the change of radiance as the electromagnetic energy travels a distance in the atmosphere, ds, can be written as

$$dI_\lambda/(k_\lambda\rho\,ds) = -I_\lambda + B_\lambda(T) + J_\lambda, \qquad (8\text{-}10)$$

where ρ is the density of air and k_λ is the mass extinction cross-section (in S.I. units of meters squared per kilogram of radiatively active material). The first term on the right side of Eq. (8-10) is the loss of radiance from attenuation, and $B_\lambda(T)$ is the emission and J_λ the source of radiance from scattering into the line segment ds.

Because of the separation of wavelength in the spectra plotted in Figure 8-2, it is convenient to develop separate parameterizations for long and short wavelengths.

8.3   Longwave Radiative Flux

8.3.1   Clear Atmosphere

In a clear atmosphere, scattering of longwave radiation is neglected relative to the absorption and emission of electromagnetic energy (Liou 1980). Thus Eq. (8-10) can be written as

$$dl_\lambda/(k_\lambda \rho \, ds) = -I_\lambda + B_\lambda(T). \qquad (8\text{-}11)$$

To apply the solution of Eq. (8-11) to Eq. (8-1), it is necessary to define dI_λ with respect to the vertical direction. Since $\cos Z = dz/ds$ (see Figure 8-3), and attenuation results only from absorption, Eq. (8-11) can be written as

$$\cos Z \frac{dI_\lambda}{k_{a\lambda}\rho \, dz} = -\cos Z \frac{dI_\lambda}{d\tau_\lambda} = -I_\lambda + B_\lambda(T), \qquad (8\text{-}12)$$

where

$$\tau_\lambda = \int_z^\infty k_{a\lambda}\rho \, dz \qquad (8\text{-}13)$$

is called the *normal optical thickness*.[8]

When solving Eq. (8-12), it is useful to evaluate this differential equation separately for upward and downward radiances. The procedure for obtaining the solution is to multiply Eq. (8-12) by the integrating factor[9] $e^{\tau_\lambda/\cos Z}$, integrate from τ_λ to τ_{G_λ}, and multiply the result by $e^{\tau_\lambda/\cos Z}$. The optical thickness τ_{G_λ} is
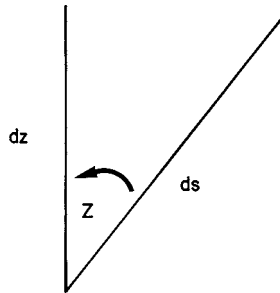
Fig. 8-3.   Schematic illustration of the relation between the zenith angle Z and ds and dz.

defined by Eq. (8-13) with z equal to the ground elevation (i.e., $z = z_G$). The result of this evaluation is

$$I_\lambda\uparrow = I_\lambda\uparrow|_G e^{-(\tau_{G_\lambda} - \tau_\lambda)/\cos Z} + \int_{\tau_\lambda}^{\tau_{G_\lambda}} B_\lambda(T)\Big|_{\hat{\tau}_\lambda} e^{-[(\hat{\tau}_\lambda - \tau_\lambda)/\cos Z]} \frac{d\hat{\tau}_\lambda}{\cos Z}$$

$$(1 \geq \cos Z > 0), \quad (8\text{-}14)$$

where $I_\lambda\uparrow|_G$ is the upward radiance from the ground. The downward radiance is obtained in a similar fashion (see, e.g., Liou 1980:24), where Eq. (8-12) is integrated downward from the top τ_{T_λ} to τ_λ,[10]

$$I_\lambda\downarrow = I_\lambda\downarrow|_T e^{-(\tau_\lambda - \tau_{T_\lambda})/\cos Z} + \int_{\tau_{T_\lambda}}^{\tau_\lambda} B_\lambda(T)\Big|_{\hat{\tau}_\lambda} e^{-[(\tau_\lambda - \hat{\tau}_\lambda)/\cos Z]} \frac{d\hat{\tau}_\lambda}{\cos Z}$$

$$(1 \geq \cos Z > 0), \quad (8\text{-}15)$$

where $I_\lambda\downarrow|_T$ represents downward radiance from the top of the model. Using the definition of irradiance given by Eq. (8-4) and assuming that the radiative transfer is independent of azimuth and that $I_\lambda\uparrow|_G$ and $I_\lambda\downarrow|_T$ emit as blackbodies,[11] Eqs. (8-14) and (8-15) can be written as

$$R_\lambda\uparrow = 2\pi B_\lambda(T_G)E_3(\tau_{G_\lambda} - \tau_\lambda) + 2\pi \int_{\tau_\lambda}^{\tau_{G_\lambda}} B_\lambda(T)|_{\hat{\tau}_\lambda} E_2(\hat{\tau}_\lambda - \tau_\lambda)d\hat{\tau}_\lambda \quad (8\text{-}16)$$

$$R_\lambda\downarrow = 2\pi\widetilde{B}_\lambda(T_T^*)E_3(\tau_\lambda - \tau_{T_\lambda}) + 2\pi \int_{\tau_{T_\lambda}}^{\tau_\lambda} B_\lambda(T)|_{\hat{\tau}_\lambda} E_2(\tau_\lambda - \hat{\tau}_\lambda)d\hat{\tau}_\lambda, \quad (8\text{-}17)$$

where

$$E_3(y) = \int_0^1 e^{-y/\cos Z} \cos Z\, d(\cos Z)$$

$$E_2(y) = \int_0^1 e^{-y/\cos Z} d(\cos Z) = -dE_3(y)/dy$$

$$(8\text{-}18)$$

and $\widetilde{B}_\lambda(T_T^*)$ is evaluated including any attenuation above level z_T for wavelength λ. The temperatures T_G and T_T^* correspond to the ground surface temperature and the effective temperature at the model top (if $z, \to \infty$, then $T_T^* \to 0$). In Eq. (8-18), y of course can correspond to $\tau_{G_\lambda} - \tau_\lambda$, $\tau_\lambda - \tau_{T_\lambda}$, $\hat{\tau}_\lambda - \tau_\lambda$, or $\tau_\lambda - \hat{\tau}_\lambda$.

The total upward and downward radiative flux at level z is obtained by integrating Eqs. (8-16) and (8-17) over all wavelengths, giving

$$R\uparrow = \int_0^\infty R_\lambda\uparrow d\lambda \quad \text{and} \quad R\downarrow = \int_0^\infty R_\lambda\downarrow d\lambda. \quad (8\text{-}19)$$

In principle, as pointed out by Liou (1980), Eq. (8-19) can be used to determine the total irradiance from the integrated longwave spectrum. However, the optical thickness, τ_λ, is a complicated and rapidly varying function of wavelength, as illustrated in Figure 8-4. In the clear atmosphere, this complex distribution
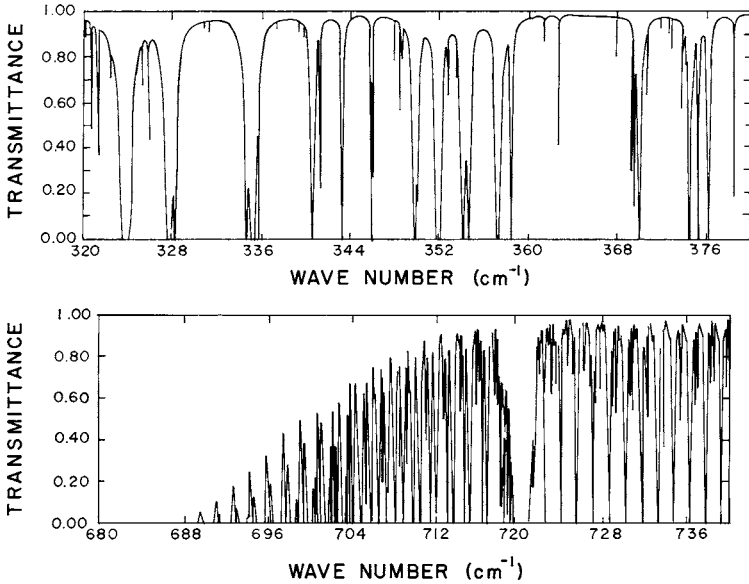
Fig. 8-4. (a) Monochromatic transmissivity t_λ of water vapor between wavelengths 31 (corresponding to 320 cm^{-1}) and 26 μm (corresponding to 376 cm^{-1}), and (b) CO$_2$ between wavelengths 14.7 (corresponding to 680 cm^{-1}) and 13.6 μm (corresponding to 736 cm^{-1}). (From Liou 1980, as adapted from McClatckey and Selby 1972.)

of τ_λ is caused by the absorption spectra of certain gases in the air. The triatomic molecules, particularly carbon dioxide (CO$_2$), water vapor, and ozone, have numerous significant absorption lines in this portion of the electromagnetic spectrum. Thus, as pointed out by Liou (1980:95), evaluation of Eq. (8-19) would require the double integration using very small increments of λ and τ_λ to properly represent the thousands of absorption lines within the infrared region.

To circumvent this problem, *a transmission function*, defined as

$$\Gamma_{\bar\lambda}(\tau) = \frac{1}{\Delta\lambda} \int_{\lambda_1}^{\lambda_2} e^{-\tau} d\lambda, \quad \Delta\lambda = \lambda_2 - \lambda_1, \tag{8-20}$$

is used, where the interval is large enough so that several absorption lines are included but small enough so that $B_\lambda(T)$ is approximately constant across the interval [i.e., $B_{\bar\lambda}(T) \simeq B_\lambda(T)$]. Equations (8-16) and (8-17) are then integrated over $\Delta\lambda$, yielding

$$R_{\bar\lambda}\uparrow = \int_{\lambda_1}^{\lambda_2} R_\lambda\uparrow \frac{d\lambda}{\Delta\lambda} = 2\pi B_{\bar\lambda}(T_G) \int_{\lambda_1}^{\lambda_2} E_2(\tau_{G_\lambda} - \tau_\lambda) \frac{d\lambda}{\Delta\lambda}$$

$$+ 2\pi \int_{\tau_{\bar\lambda}}^{\tau_{G_{\bar\lambda}}} B_{\bar\lambda}(T)\Big|_{\hat\tau_{\bar\lambda}} \int_{\lambda_1}^{\lambda_2} E_3(\hat\tau_\lambda - \tau_\lambda) \frac{d\hat\tau_\lambda}{\Delta\lambda} d\lambda \tag{8-21}$$

and

$$R_{\bar{\lambda}} \downarrow = \int_{\lambda_1}^{\lambda_2} R_{\lambda} \downarrow \frac{d\lambda}{\Delta\lambda} = 2\pi \, \widetilde{B}_{\bar{\lambda}}(T_T^*) \int_{\lambda_1}^{\lambda_2} E_3(\tau_{\lambda} - \tau_{T_{\lambda}}) \frac{d\lambda}{\Delta\lambda}$$

$$+ 2\pi \int_{\tau_{\bar{\lambda}T}}^{\tau_{\bar{\lambda}}} B_{\bar{\lambda}}(T) \Big|_{\hat{\tau}_{\bar{\lambda}}} \int_{\gamma_1}^{\gamma_2} E_2(\tau_{\lambda} - \hat{\tau}_{\lambda}) \frac{d\hat{\tau}_{\lambda}}{\Delta\lambda} \, d\lambda. \tag{8-22}$$

The *slab transmission function* is then defined by

$$\Gamma_{\bar{\lambda}}^s(y) = 2 \int_{\lambda_1}^{\lambda_2} E_3(y) \frac{d\lambda}{\Delta\lambda}, \tag{8-23}$$

so that from Eq. (8-18), we have

$$\frac{d\Gamma_{\bar{\lambda}}^s(y)}{dy} = -2 \int_{\lambda_1}^{\lambda_2} E_2(y) \frac{d\lambda}{\Delta\lambda}. \tag{8-24}$$

Therefore, Eqs. (8-21) and (8-22) can be written as

$$R_{\bar{\lambda}} \uparrow = \pi B_{\bar{\lambda}}(T_G) \Gamma_{\bar{\lambda}}^s(\tau_{G_{\bar{\lambda}}} - \tau_{\bar{\lambda}}) - \int_{\tau_{\bar{\lambda}}}^{\tau_{G_{\bar{\lambda}}}} \pi B_{\bar{\lambda}}(T) \Big|_{\hat{\tau}_{\bar{\lambda}}} \frac{d\Gamma_{\bar{\lambda}}^s}{d\hat{\tau}_{\bar{\lambda}}} (\hat{\tau}_{\bar{\lambda}} - \tau_{\bar{\lambda}}) d\hat{\tau}_{\bar{\lambda}} \tag{8-25}$$

$$R_{\bar{\lambda}} \downarrow = \pi \widetilde{B}_{\bar{\lambda}}(T_T^*) \Gamma_{\bar{\lambda}}^s(\tau_{\bar{\lambda}} - \tau_{T_{\bar{\lambda}}}) + \int_{\tau_{\bar{\lambda}T}}^{\tau_{\bar{\lambda}}} \pi B_{\bar{\lambda}}(T) \Big|_{\hat{\tau}_{\bar{\lambda}}} \frac{d\Gamma_{\bar{\lambda}}^s}{d\hat{\tau}_{\bar{\lambda}}} (\tau_{\bar{\lambda}} - \hat{\tau}_{\bar{\lambda}}) d\hat{\tau}_{\bar{\lambda}}. \tag{8-26}$$

(Note that by averaging over λ, $d\hat{\tau}_{\lambda}$ becomes $d\hat{\tau}_{\bar{\lambda}}$.)

If a *normal path length*[12] is defined as

$$u = \int_0^z \rho \, dz \qquad u_{\infty} = \int_0^{\infty} \rho \, dz, \tag{8-27}$$

then Eq. (8-13) can be written as $\tau_{\lambda} = \int_u^{u_{\infty}} k_{a\lambda} \, du$, by the change of variable given by Eq. (8-27). In making this coordinate transformation, changes of k_{λ} with u (e.g., because of temperature changes with height) are neglected.

Using this change of variable, Eqs. (8-25) and (8-26) can be written as

$$R_{\bar{\lambda}} \uparrow = \pi B_{\bar{\lambda}}(T_G) \Gamma_{\bar{\lambda}}^s(u) + \int_0^u \pi B_{\bar{\lambda}}(T) \Big|_{\hat{u}} \frac{d\Gamma_{\bar{\lambda}}^s}{d\hat{u}} (u - \hat{u}) d\hat{u} \tag{8-28}$$

and

$$R_{\bar{\lambda}} \downarrow = \pi \widetilde{B}_{\bar{\lambda}}(T_T^*) \Gamma_{\bar{\lambda}}^s(u_T - u) + \int_{u_T}^u \pi B_{\bar{\lambda}}(T) \Big|_{\hat{u}} \frac{d\Gamma_{\bar{\lambda}}^s}{d\hat{u}} (\hat{u} - u) \, d\hat{u}. \tag{8-29}$$

Integrating over all wavelengths and using Eq. (8-8) yields

$$R \uparrow = \sigma T_G^4 t^s(u, T_G) = \int_0^u \sigma T^4 \Big|_{\hat{u}} \frac{dt^s(u - \hat{u}, T)}{d\hat{u}} d\hat{u} \tag{8-30}$$

and

$$R\downarrow = \widetilde{B} + \int_{u_T}^{u} \sigma T^4 \left.\frac{dt^s(\hat{u} - u, T)}{d\hat{u}}\right|_{\hat{u}} d\hat{u}, \tag{8-31}$$

where

$$t^s(u, T) = \int_0^\infty \pi B_\lambda(T)\Gamma_\lambda^s(u)d\lambda/\sigma T^4 \tag{8-32}$$

is called the *broadband flux transmissivity*, defined in terms of the transmission function Eq. (8-23) when $\lambda_2 = \lambda_1$. $\widetilde{B}$ is the longwave radiative flux reaching the model top which has energy in the radiatively active wavelengths. In deriving Eqs. (8-30) and (8-31), T is assumed to be constant within each differential path length du so that $B_\lambda(T)$ can be incorporated within the derivative term in the integrals of Eqs. (8-30) and (8-31).

The *broadband emissivity* is then defined as

$$\epsilon^s(u, T) = 1 - t^s(u, T), \tag{8-33}$$

from Eq. (8-9), since $a_\lambda = \epsilon_\lambda$ for all wavelengths and $r_\lambda = 0$, as assumed by Eq. (8-11).

To apply Eqs. (8-30) and (8-31) to a model, the integral given by Eq. (8-32) is represented by one or more intervals, so that using Eq. (8-8), Eq. (8-33) can be written as

$$\epsilon^s(u, T) = \sum_{i=1}^{I} \pi B_{\bar{\lambda}_i}(T) \left[1 - \Gamma_{\bar{\lambda}_i}^s(u)\right] \Delta_i \lambda/\sigma T^4, \tag{8-34}$$

where $\bar{\lambda}_i$ is the average wavelength within the interval $\lambda_{i+1} - \lambda_i = \Delta_i\lambda$.

The emissivities given by Eq. (8-34) are also often written separately for the major absorbers of infrared radiation in the atmosphere. Atwater (1974), using data from Kuhn (1963), for example, suggests values of broadband emissivity for water vapor, which can be written as

$$\epsilon_{q3}(u, T) \simeq \epsilon_{q3}(\delta P) = \begin{cases} 0.104\log_{10}\delta P + 0.440, & -4 < \log_{10}\delta P \leq -3 \\ 0.121\log_{10}\delta P + 0.491, & -3 < \log_{10}\delta P \leq -1.5 \\ 0.146\log_{10}\delta P + 0.527, & -1.5 < \log_{10}\delta P \leq -1.0 \\ 0.161\log_{10}\delta P + 0.542, & -1.0 < \log_{10}\delta P \leq 0 \\ 0.136\log_{10}\delta P + 0.542, & \log_{10}\delta P > 0, \end{cases} \tag{8-35}$$

where δP is in grams per centimeter squared and

$$\delta P = \int_z^{z+\delta z} \rho q_3 \, dz$$

is the optical path length for water vapor between z and $z + \delta z$. When $\delta z \to \infty$ and $z \to z_G$, $\delta P \to P$, where P is called *precipitable water*. To use Eq. (8-35), δP must be expressed in units of grams per centimeters squared. Since 1 g of water is 1 cm deep (i.e., $\rho_{q_2} = 1$ g cm^{-3}), δP is also equal to the precipitable water in centimeters within the path length. For the application of ϵ_{q_3} in the parameterization of the heating associated with longwave radiation in models, the dependence of ϵ_{q_3} on temperature is inconsequential compared to that of water vapor. Figure 8-5(a) illustrates this relation between ϵ_{q_3} and δP as reported by Liou (1980, Figure 4.8), along with the algorithm given by Eq. (8-35).

For the broadband emission for CO_2, Kondratyev (1969) proposed the formulation

$$\epsilon_{\chi_{CO_2}}(u, T) \simeq \epsilon_{\chi_{CO_2}}(\delta H_c) = 0.185[1 - \exp(-0.39\,\delta H_c^{0.4})],$$

$$(\delta H_c \text{ is in centimeters}) \qquad (8\text{-}36)$$

where δH_c in centimeters is given by

$$\delta H_c = 0.252\,(p_0 - p) \qquad (8\text{-}37)$$

with pressure p in millibars at height z and $p_0 = p$ (at $z = 0$) = 1014 mb (i.e., sea-level pressure) used to obtain Eq. (8-37). Since CO_2 is well mixed vertically and horizontally above the planetary boundary layer in the troposphere and in the stratosphere, the density of CO_2 in the air [prescribed as 320 parts of CO_2 to 1 million parts of air to obtain Eq. (8-37)] is assumed to depend only on pressure in Eq. (8-36). This assumption permits an empirical formulation for δH_c in terms of pressure below sea-level pressure.

Figure 8-5(b) illustrates $\epsilon_{\chi_{CO_2}}$ as a function of δH_c. In contrast to the broadband emissivity for water vapor, the emissivity of CO_2 depends on temperature for larger values of δH_c. The empirical representation given Eq. (8-37), does not consider this effect however.

Finally, before using ϵ_{q_3} and $\epsilon_{\chi_{CO_2}}$ to represent $\epsilon^s(u, T)$ in Eq. (8-34), it is necessary to ensure that the emissivities are not double-counted in those portions of the infrared spectrum where absorption by water vapor and CO_2 overlaps. To ensure that this does not occur, Eq. (8-34) can be written as

$$\epsilon^s(u, T) = \epsilon^s(u_{q_3}, T) + \epsilon^s(u_{CO_2}, T) - \Delta\epsilon^f(u_{q_3}, u_{CO_2}, T)$$

$$\simeq \epsilon_{q_3}(\delta P) + \epsilon_{\chi_{CO_2}}(\delta H_c) - \Delta\epsilon^f(u_{q_3}, u_{CO_2}, T). \qquad (8\text{-}38)$$

However, work by Staley and Jurica (1970) shows that $\Delta\epsilon^f$ is a small correction, on the order of 0.05–0.10 for a pathlength through an entire typical mid-latitude atmosphere. Shorter pathlengths and lower temperatures have smaller values of the overlap term. Tables 3–6 in Staley and Jurica (1970) provide
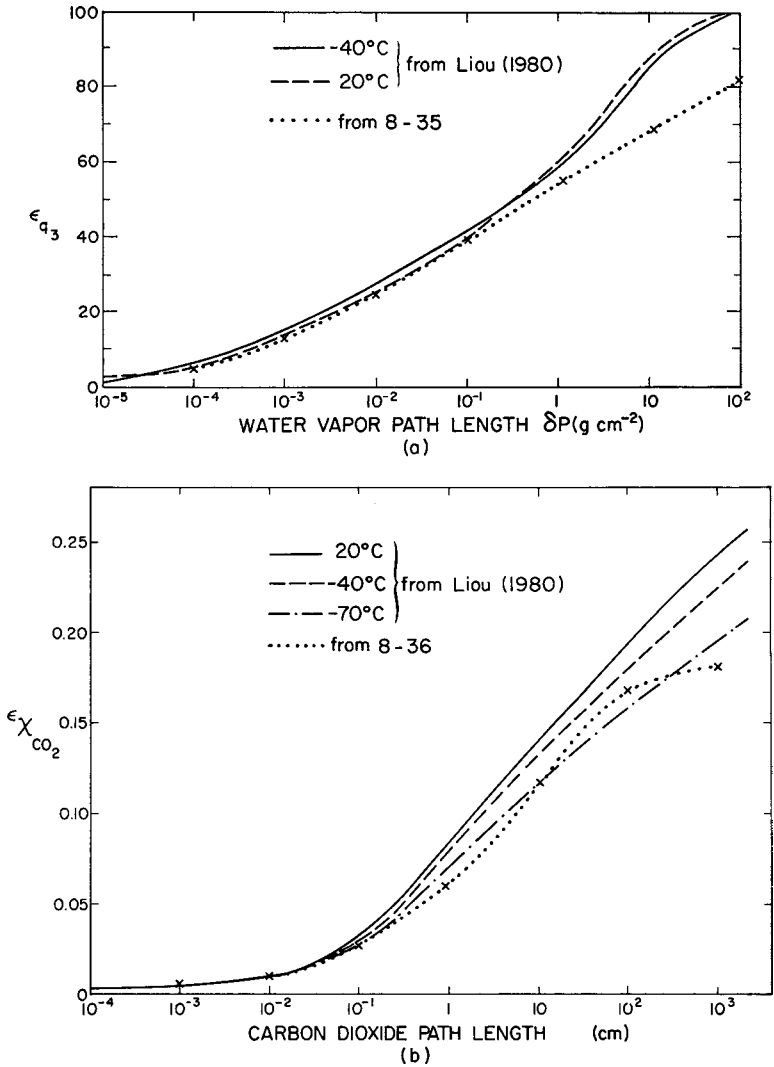
Fig. 8-5. Broadband emissivity for (a) water vapor, $\epsilon_{q_3}(\delta P)$, as a function of δP, and (b) CO_2 $\epsilon_{\chi_{CO_2}}(\delta H_c)$, as a function of δH_c. (Adapted from Liou 1980.)

values of $\Delta\epsilon^f$ as a function of pathlength and temperature, although for most mesoscale model applications it seems appropriate to neglect this term. Ozone, methane, and other trace gases could also be included in Eq. (8-34), using an empirical representation for its broadband emissivity, such as that performed by Sasamori (1968).

For use in a model, Eqs. (8-30) and (8-31) are often written in a different form. Integrating the integrals in these two equations by parts yields

$$R\uparrow = \sigma T_G^4 + \int_0^u \epsilon\,(u - \hat{u}, T)\,\frac{d}{d\hat{u}}\sigma T^4 d\hat{u}$$

$$R\downarrow = \sigma T_T^4 + \int_{u_T}^u \epsilon\,(\hat{u} - u, T)\,\frac{d}{d\hat{u}}\sigma T^4 d\hat{u},$$

(8-39)

where $T(u = 0)$ corresponds to T_G and Eq. (8-33) was used to replace the broadband transmissivity, t^s, with the broadband emissivity, ϵ^s.

Up to this point in the representation of longwave radiative fluxes, grid-volume averaging, as described in Chapter 4, has not been introduced. As indicated by Eq. (8-1), such averaged quantities are needed to represent the source-sink term S_θ. Therefore, to use Eq. (8-39), the net upward irradiance over all longwave wavelengths must be written as

$$\overline{R\uparrow} - \overline{R\downarrow} = \overline{\sigma\left(\overline{T}_G + T_G''\right)^4} - \overline{\sigma\left(\overline{T}_T + T_T''\right)^4}$$

$$+ \int_0^u \overline{\epsilon\left(u - \hat{u}, \overline{T} + T''\right)\frac{d}{d\hat{u}}\sigma\left(\overline{T} + T''\right)^4}\,d\hat{u}$$

$$- \int_T^u \overline{\epsilon\left(\hat{u} - u, \overline{T} + T''\right)\frac{d}{d\hat{u}}\sigma\left(\overline{T} + T''\right)^4}\,d\hat{u},$$

where the assumption is made that $\rho \simeq \bar{\rho}$ can be used [see, e.g., Eq. (4-9)]. Subgrid-scale correlations of temperature with itself and with the broadband emissivity are usually neglected in the parameterization of $R\uparrow$ and $R\downarrow$. Since $|T''| \ll \overline{T}$, in general, such an approximation seems reasonable, although under what circumstances the correlation terms can be neglected must be quantitatively assessed. Thus T and ϵ in Eq. (8-39) are replaced by the grid-volume–resolvable quantities $\overline{T}$ and $\bar{\epsilon}$.[13]

The vertical gradients of $R\uparrow$ and $R\downarrow$ from Eq. (8-39), needed in Eq. (8-1), thus can be written as

$$\frac{\partial R\uparrow}{\partial u} = \int_0^u \frac{d\epsilon\left(u - \hat{u}, \overline{T}\right)}{du}\frac{d}{d\hat{u}}\sigma\overline{T}^4 d\hat{u}$$

$$\frac{\partial R\downarrow}{\partial u} = \int_{u_T}^u \frac{d\epsilon\left(\hat{u} - u, \overline{T}\right)}{du}\frac{d}{d\hat{u}}\sigma\overline{T}^4 d\hat{u},$$

(8-40)

where Leibnitz's rule [see Note 8 for Eq. (8-13)] and the requirement that $\epsilon(0, T) = 0$ have been used.

Sasamori (1972) suggested a simpler (and thus more economical) form for Eq. (8-40). If the atmosphere between the top and the ground is assumed to be isothermal at the height of interest, then the integrals in Eq. (8-40) reduce to

$$\lim_{u\to 0} \int_0^u \frac{d\epsilon\left(u - \hat{u}, \overline{T}\right)}{du} \frac{d}{d\hat{u}}\, \sigma\, \overline{T}^4\, d\hat{u} \to \sigma \frac{d\epsilon\left(u, \overline{T}\right)}{du}\left[\overline{T}^4(u) - \overline{T}_G^4\right]$$

and

$$\lim_{u\to u_T} \int_{u_T}^u \frac{d\epsilon\left(\hat{u} - u, \overline{T}\right)}{du} \frac{d}{d\hat{u}}\, \sigma\, \overline{T}^4\, d\hat{u} \to \sigma \frac{d\epsilon\left(u_T - u, \overline{T}\right)}{du}\left[\overline{T}_T^4 - \overline{T}^4(u)\right]$$

using Riemann-Stieltzes integration (see, e.g., Lumley and Panofsky 1964:220), where $(d/du)\sigma\,\overline{T}^4$ is 0 everywhere except infinitesimally close to the top and ground, where its value is infinite (i.e., a discontinuous function). Thus Eq. (8-40), using Sasamori's (1972) isothermal approximation, neglecting subgrid-scale quantities, and assuming that $\bar{\rho}$ is constant over the interval du (so that u can be replaced with z), can be written as

$$\frac{\partial \overline{R}\!\uparrow}{\partial z} \simeq \sigma \frac{d\epsilon\left(u, \overline{T}\right)}{dz}\left[\overline{T}^4(z) - \overline{T}_G^4\right]$$

$$\frac{\partial \overline{R}\!\downarrow}{\partial z} \simeq \sigma \frac{d\epsilon\left(u_T - u, \overline{T}\right)}{dz}\left[\overline{T}_T^4 - \overline{T}^4(z)\right]. \tag{8-41}$$

The vertical derivatives of ϵ are evaluated for $\partial\overline{R}\!\uparrow/\partial z$ and $\partial\overline{R}\!\downarrow/\partial z$ at a distance z above the ground. To use Eqs. (8-35) and (8-36) in Eq. (8-41), $\delta P = \int_z^{z_T} \rho q_3\, dz$ and $\delta H_c = 0.252(p - p_T)$ cm must be used when the argument of ϵ is $u_T - u$.

Equation (8-1) can also be written as

$$\bar{S}_\theta = \left.\frac{\partial \overline{T}}{\partial t}\right|_{rad} = -\frac{1}{\bar{\rho}C_p}\left[\left.\frac{\partial \overline{R}}{\partial z}\right|_{lw} + \left.\frac{\partial \overline{R}}{\partial z}\right|_{sw}\right], \tag{8-42}$$

where the subscripts "lw" and "sw" refer to the absorption of longwave and shortwave irradiance, respectively. Equation (8-41), or the more complete form in Eq. (8-40), can be used to represent $\partial \overline{R}/\partial z\,|_{lw}$, where

$$\left.\frac{\partial \overline{R}}{\partial z}\right|_{lw} = \frac{\partial \overline{R}\!\uparrow}{\partial z} - \frac{\partial \overline{R}\!\downarrow}{\partial z}.$$

Figure 8-6, calculated by R. T. McNider (1981, personal communication), illustrates the accuracy of using Eq. (8-41) in lieu of Eq. (8-40) to calculate temperature change in Eq. (8-42) for the night of Day 33 of the Wangara Experiment (see Figure 7-10 in Chapter 7 and associated discussion for a description of the Wangara simulation). As evident from Figure 8-6, at least for this particular simulation, Sasamori's simplified form [Eq. (8-41)] yields very realistic results,
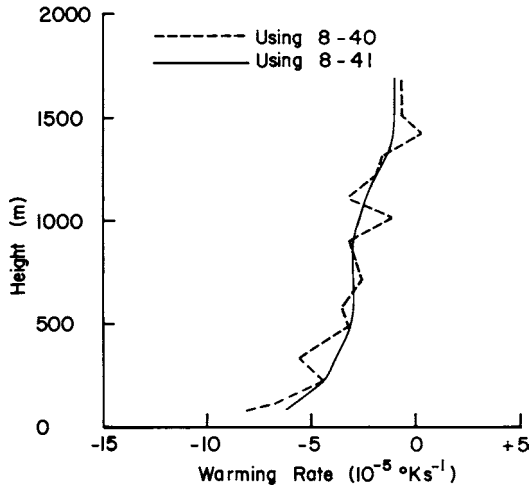
Fig. 8-6. A comparison of a longwave radiational heating-cooling computation obtained for the night of Day 33 during the Wangara Experiment using Sasamori's simplified parameterization [Eq. (8-41)] and a more complete parameterized form [(Eq. 8.40)]. (Computed by R. T. McNider 1981, personal communication.)

although detailed small-scale variations of temperature changes from longwave flux divergence are not reproduced.

In a clear atmosphere without pronounced temperature and water vapor discontinuities, Paltridge and Platt (1976:187) suggested a particularly simple formulation for estimating longwave radiational cooling,

$$-\frac{1}{\bar{\rho}C_{\mathrm{p}}}\left.\frac{\partial \overline{R}}{\partial z}\right|_{\mathrm{lw}} = -\left[0.017\overline{T} + 1.8\right] \tag{8-43}$$

(in units of degrees Celsius per day, $\overline{T}$ in degrees Celsius, and $-90°C \leq \overline{T} \leq 30°C$), with a standard deviation of 0.33°C. With this relation, a temperature of 0°C yields a cooling rate of 1.8°C day^{-1}.

Kuo (1979), using a more complete parameterization of longwave radiation, reported that for clear air with a temperature and moisture profile approximating that of the U.S. standard atmosphere, the infrared cooling rate is about 1.2°C day^{-1}, with a maximum at the surface and at 7.5 km and a minimum at 2 km and the tropopause. However, as emphasized by Paltridge and Platt (1976), representations such as that given by Eq. (8-43) are inappropriate when significant vertical gradients of temperature or water vapor occur or when clouds exist. In general, for clear air, a longwave radiation parameterization given by Eqs. (8-40) or (8-41) appears to be appropriate for use in a mesoscale model.

The importance of longwave radiative fluxes relative to turbulent fluxes in stable nocturnal boundary layers has been investigated by Gopalakrishnan

et al. (1998). With weak winds, radiative flux divergence can dominate turbulent fluxes for this situation. Jiang *et al.* (2000) use large-eddy simulations of shallow cumulus convection to assess the relative importance of microphysics and radiative fluxes.

8.3.2 Cloudy Air

When clouds are present, their water content strongly influences the optical path length for infrared radiation. As reported by Stephens (1978a), a cumulonimbus cloud with a liquid water content of 2.5 g m^{-3} has such a small path length that it radiates as a blackbody beyond a depth of 12 m into the cloud. In contrast, a thin stratus cloud with a liquid water content of 0.05 g m^{-3} requires a depth of at least 600 m before it radiates as a blackbody. Liou and Wittman (1979) have reported that cirrus, because of its relatively low amount of water content (in the ice phase), is too shallow to be treated as a blackbody at any depth. Charlock (1982) has suggested that changes of the liquid water content of the thinnest clouds have the most significant effect on climate. Wyser *et al.* (1999) discussed the importance of the size of cloud droplets and ice crystals.

The radiational cooling at the top of such cloud layers can be very substantial. Roach and Slingo (1979), for example, found a cooling rate of 8.7°C h^{-1} from the 1-mb layer at the top of nocturnal stratocumulus over England. Such cooling can have a substantial impact on the entrainment rate of higher-level air into the stratocumulus layer (see, e.g., Deardorff 1981) and on cold downward-moving plumes within the cloud (see, e.g., Caughey *et al.* 1982).

Stephens and Webster (1981) have shown that vertical temperature structure (and, therefore, mesoscale dynamics) is highly sensitive to cloud height, although it is sensitive only to water path for clouds that are shallow relative to the infrared optical path length. They contend that high, thin clouds at low and middle latitudes and all clouds at high latitudes tend to warm the surface compared with a clear sky, whereas all other clouds cool. Platt's (1981) results suggest that cirrus clouds with an optical depth greater than 12 in the tropics and about 5 in the midlatitudes will result in a cooling tendency below the clouds. Mesoscale models (e.g., McCumber 1980; Thompson 1993) have often treated clouds as blackbodies in the longwave portion of the spectrum, where no infrared radiation is transmitted through the cloud.

Clouds consist of liquid and/or ice crystals in a range of distribution sizes, and the details of their radiative properties are very complex, particularly for ice crystals. Therefore, in the parameterization of infrared fluxes within clouds, ice crystals are normally considered in terms of a particle with a radius defined in terms of the surface area of the crystal (Paltridge and Platt 1976), since

no analytic theory exists to describe the absorption and scattering of irregular particles such as ice crystals. Moreover, scattering by both ice and water droplets is generally ignored, because infrared scattering occurs predominantly in the forward direction, so that the direction of the incoming radiation is essentially unaffected (Paltridge and Platt 1976).

Stephens (1978a) suggested a useful parameterization for longwave radiation within a water cloud given by

$$\overline{R}\uparrow = \overline{R}_{CB}\uparrow[1 - \epsilon\uparrow] + \epsilon\uparrow\sigma\overline{T}^4$$
$$\overline{R}\downarrow = \overline{R}_{CT}\downarrow[1 - \epsilon\downarrow] + \epsilon\downarrow\sigma\overline{T}^4,$$
(8-44)

where $\overline{R}_{CT}\downarrow$ and $\overline{R}_{CB}\uparrow$ are the clear-air irradiance at the cloud top z_{CT} and cloud base z_{CB}, respectively, determined from a formulation such as Eq. (8-39).[14] The temperature, $\overline{T}$, and the effective emissivity, $\epsilon\downarrow$ and $\epsilon\uparrow$, are evaluated at desired levels within a cloud.

As reported by Stephens (1978b), these effective emissivities were obtained by solving Eq. (8-44) for $\epsilon\downarrow$ and $\epsilon\uparrow$, using a detailed radiational model with eight cloud types in a U.S. standard atmosphere to obtain $\overline{R}\downarrow$, $\overline{R}\uparrow$, and $\overline{T}$. The values of $\epsilon\downarrow$ and $\epsilon\uparrow$ were then determined as a function of integrated liquid water content (see Figure 8-7). The resultant empirical formulation is given by[15]

$$\epsilon\uparrow = 1 - e^{-a\uparrow W\uparrow} \qquad \text{and} \qquad \epsilon\downarrow = 1 - e^{-a\downarrow W\downarrow}, \tag{8-45}$$

where $a\uparrow = 0.130$ m^2 g^{-1} and $a\downarrow = 0.158$ m^2 g^{-1} were found to give the best fit to the data derived from Stephens' (1978b) detailed theoretical model. The integrated water content in the cloud above and below the level of interest ($W\downarrow$ and $W\uparrow$) was found to have the most pronounced influence on the effective emissivity, a conclusion further substantiated from the observational study of nocturnal stratocumulus in Great Britain by Slingo *et al.* (1982). A validation and extension of Stephens' (1978a) parameterized model is given by Chýlek and Ramaswamy (1982), who conclude that emissivity is only a function of integrated liquid water for wavelengths of 8–11.5 μm, but maintain that it is also a function of the droplet size distribution for wavelengths greater than 11.5 μm. For typical drop size distributions for stratus, altocumulus, and cumulus clouds, they stated that the effect on the flux emissivity in the 8- to 14-μm band is about $\pm 35\%$. Liou and Ou (1981) also present a parameterization of infrared radiative transfer in the presence of a semitransparent cloud layer and compare their results to observations and a more detailed theoretical model. Liou and Ou used a model with five broadband emissivity values to represent the five major absorption regions in the infrared spectrum.

Stephens (1978a), however, concluded that cloud drop distribution, ambient temperature, and water vapor distributions within the cloud are not important
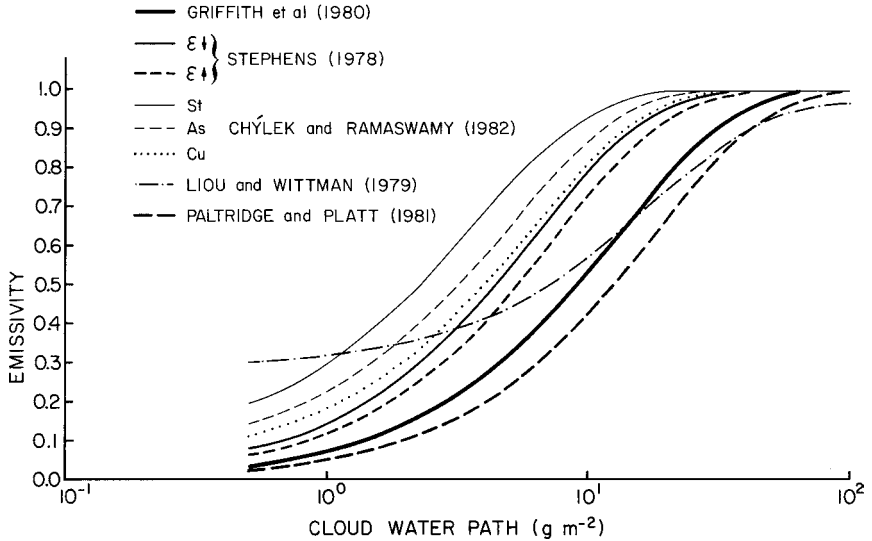
Fig. 8-7. Cloud emittance as a function of cloud water path for various parameterizations. The parameterization of Liou and Wittman (1979), Griffith *et al.* (1980), and Paltridge and Platt (1981) included only ice, and the others were for liquid water clouds. (From S. Ackerman, CSU, 1983, personal communication.)

in estimating this emissivity for water clouds. We use this result in the following discussion. It is implied from Paltridge and Platt (1976) that ice clouds can be similarly represented by expressions such as Eqs. (8-45) and (8-44), using the definition of integrated water content given in Note 15 to Eq. (8-45). Figure 8-7 illustrates the emissivity as a function of cloud water path for several parameterization schemes, demonstrating the uncertainty remaining in the representation of emissivity in clouds. Those of Liou and Wittman (1979), Griffith *et al.* (1980), and Paltridge and Platt (1981) are for ice clouds, and the rest are for liquid water clouds.

For application to a mesoscale model, Eq. (8-44) can be used when a grid volume is saturated with cloud material, and formulations such as Eq. (8-39) can be used in a clear atmosphere. The vertical gradient of Eq. (8-44), needed in Eq. (8-1), can be written as

$$
\begin{aligned}
\frac{\partial \overline{R}\uparrow}{\partial z} &= a\uparrow \frac{\partial W\uparrow}{\partial z} e^{-a\uparrow W\uparrow} \left[\sigma \overline{T}^4 - \overline{R}_{CB}^\uparrow \right] + \epsilon\uparrow \frac{\partial}{\partial z} \sigma \overline{T}^4 \\
\frac{\partial \overline{R}\downarrow}{\partial z} &= a\downarrow \frac{\partial W\downarrow}{\partial z} e^{-a\downarrow W\downarrow} \left[\sigma \overline{T}^4 - \overline{R}_{CT}^\downarrow \right] + \epsilon\downarrow \frac{\partial}{\partial z} \sigma \overline{T}^4.
\end{aligned}
\tag{8-46}
$$

If the cloud layer is assumed to be isothermal at the height of interest [analogous to the assumption used by Sasamori 1972 to derive Eq. (8-41)], then the right-side terms in Eq. (8-46) can be neglected.

When a grid volume is only partially saturated by clouds (usually denoted as a fractional coverage σ_c), $\partial \overline{R}/\partial z|_{lw}$ in Eq. 8.42 can be written using

$$\left. \frac{\partial \overline{R}}{\partial z} \right|_{lw} = \sigma_c \left[\frac{\partial \overline{R}\uparrow}{\partial z} - \frac{\partial \overline{R}\downarrow}{\partial z} \right] + (1 - \sigma_c) \left[\frac{\partial \overline{R}\uparrow}{\partial z} - \frac{\partial \overline{R}\downarrow}{\partial z} \right], \qquad (8\text{-}47)$$

where, for example, the first term on the right side could be from Eq. (8-46) and the second from Eq. (8-41).

If multiple cloud layers are present, then each clear and each cloudy region can be treated separately using the adjacent regions as the vertical boundary conditions, as illustrated schematically in Figure 8-8. For this example, the layer-averaged upward and downward irradiances needed to calculate the longwave heating-cooling in Eq. (8-42) are computed as follows:

$$\text{G--1: } \overline{R}_{lw} = \left[1 - \left(\sigma_{c_1} + \sigma_{c_2} + \sigma_{c_3}\right)\right] R_A + \sigma_{c_2} \left(1 - \sigma_{c_1}\right) R_J$$
$$+ \sigma_{c_1} R_H + \left(1 - \sigma_{c_1}\right) \left(1 - \sigma_{c_2}\right) \sigma_{c_3} R_F;$$

$$\text{1--2: } \overline{R}_{lw} = \left[1 - \left(\sigma_{c_1} + \sigma_{c_2} + \sigma_{c_3}\right)\right] R_A + \left(1 - \sigma_{c_1}\right) \sigma_{c_2} R_J$$
$$+ \sigma_{c_1} R_{\sigma_{c_1}} + \left(1 - \sigma_{c_1}\right) \left(1 - \sigma_{c_2}\right) \sigma_{c_3} R_F;$$

$$\text{2--3: } \overline{R}_{lw} = \left[1 - \left(\sigma_{c_1} + \sigma_{c_2} + \sigma_{c_3}\right)\right] R_A + \left(1 - \sigma_{c_1}\right) \sigma_{c_2} R_J$$
$$+ \sigma_{c_2} \sigma_{c_1} R_I + \left(1 - \sigma_{c_2}\right) \left(1 - \sigma_{c_3}\right) \sigma_{c_1} R_K;$$
$$+ \left(1 - \sigma_{c_2}\right) \sigma_{c_1} \sigma_{c_3} R_E + \left(1 - \sigma_{c_1}\right) \left(1 - \sigma_{c_2}\right) \sigma_{c_3} R_F$$

$$\text{3--4: } \overline{R}_{lw} = \left[1 - \left(\sigma_{c_1} + \sigma_{c_2} + \sigma_{c_3}\right)\right] R_A + \sigma_{c_2} R_{\sigma_{c_2}}$$
$$+ \left(1 - \sigma_{c_2}\right) \left(1 - \sigma_{c_3}\right) \sigma_{c_1} R_K + \left(1 - \sigma_{c_2}\right) \sigma_{c_1} \sigma_{c_3} R_E$$
$$+ \left(1 - \sigma_{c_1}\right) \left(1 - \sigma_{c_2}\right) \sigma_{c_3} R_F;$$

$$\text{4--5: } \overline{R}_{lw} = \left[1 - \left(\sigma_{c_1} + \sigma_{c_2} + \sigma_{c_3}\right)\right] R_A + \sigma_{c_2} \left(1 - \sigma_{c_3}\right) R_B + \sigma_{c_2} \sigma_{c_3} R_D$$
$$+ \sigma_{c_1} \left(1 - \sigma_{c_2}\right) \left(1 - \sigma_{c_3}\right) R_K + \sigma_{c_1} \left(1 - \sigma_{c_2}\right) \sigma_{c_3} R_E$$
$$+ \left(1 - \sigma_{c_1}\right) \left(1 - \sigma_{c_2}\right) \sigma_{c_3} R_F;$$

$$\text{5--6: } \overline{R}_{lw} = \left[1 - \left(\sigma_{c_1} + \sigma_{c_2} + \sigma_{c_3}\right)\right] R_A + \sigma_{c_2} \left(1 - \sigma_{c_3}\right) R_B$$
$$+ \sigma_{c_1} \left(1 - \sigma_{c_2}\right) \left(1 - \sigma_{c_3}\right) R_K + \sigma_{c_3} R_{\sigma_{c_3}};$$

$$\text{above 6: } \overline{R}_{lw} = \left[1 - \left(\sigma_{c_1} + \sigma_{c_2} + \sigma_{c_3}\right)\right] R_A + \sigma_{c_2} \left(1 - \sigma_{c_3}\right) R_B$$
$$+ \sigma_{c_1} \left(1 - \sigma_{c_2}\right) \left(1 - \sigma_{c_3}\right) R_K + \sigma_{c_3} R_C,$$
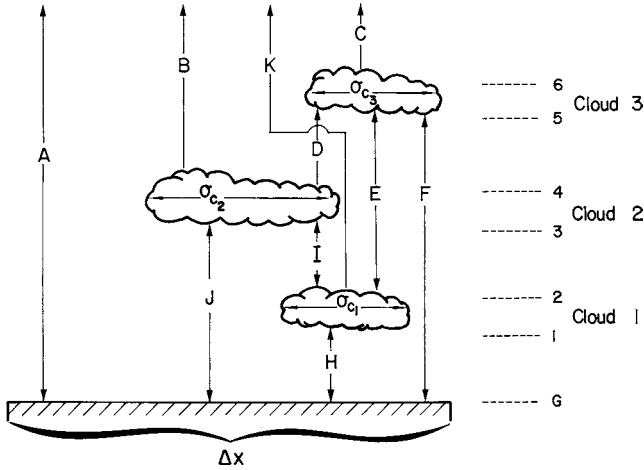
Fig. 8-8. A schematic representation of a procedure for computing longwave irradiance in a model grid mesh when multiple cloud levels covering various fractions of the grid increment exist. The letters indicate the subregions outside of the clouds where a formulation such as Eq. (8-39) is used to compute irradiance, with the temperature at the ground replaced with $\overline{T}$ at the cloud top height in B, D, C, I, K, and E and the temperature at the model top replaced with T at the cloud base height in J, D, E, F, I, and H. Inside the clouds, irradiance is computed using a form such as given by Eq. (8-44).

where the subscripts indicate over which layer the irradiances are evaluated and σ_{c_1}, σ_{c_2}, and σ_{c_3} refer to the three clouds in Figure 8-8. Atwater (1974) used a similar form to proportionally weight the upward and downward longwave irradiances by the fractional coverage of a grid increment by clouds.

8.3.3 Polluted Air

Observations have shown that even naturally occurring aerosols significantly affect the net radiation balance in the atmosphere (Alpert *et al.* 1998; Cautenet *et al.* 2000). For example, Carlson and Benjamin (1980) found typical heating rates from the combined shortwave and longwave spectrum to exceed 1°C for most of the atmosphere below 500 mb in a region of suspended Sahara Desert dust. Ackerman and Cox (1982) determined that aerosols in the desert air over Saudi Arabia approximately doubled the clear sky shortwave absorption and may play an important role in the maintenance of the heat low over the peninsula.

Human activities such as manufacturing, agriculture, and transportation input large quantities of aerosols and gases into the atmosphere. For example, Wallace and Hobbs (1977) note that a typical urban air mass may have 10^5 or more aerosols per cm^3, whereas an air mass over land far from developed areas

typically has a concentration of aerosols on the order of 10^4 per cm³. Such changes of concentration can have a significant effect on the infrared irradiance. Saito (1981), for instance, has found that as visibility over central Tokyo decreases from 20 to 10 to 2 km, the downward longwave radiation increases by 1.3, 2.8, and 6.0%, respectively.

As with cloud droplets and ice crystals (as reported in Section 8.3.2), scattering of infrared radiation by suspended pollution particles is generally neglected, since scattering occurs predominantly in the forward direction (Paltridge and Platt 1976:227). Moreover, since aerosols are usually smaller than water droplets, they are less effective at absorbing and scattering electromagnetic radiation than an equal number of cloud water particles. Ackerman *et al.* (1976) include scattering in their treatment of longwave irradiance in a polluted atmosphere, although Viskanta *et al.* (1977a) conclude that scattering increases the importance of absorption only slightly by increasing the path length of the electromagnetic radiation.

Performing detailed calculations of the infrared extinction (i.e., absorption plus backscatter) requires knowledge of the size distribution, composition, and refractive indices of the aerosols. The refractive index $\eta = \eta_r + i\eta_i$ (discussed in detail by Liou 1980:78) is a complex number in which the real and imaginary components correspond to the scattering and absorption properties, respectively, of a particle. When no absorption occurs, the refractive index has no imaginary component.

The representation of the scattering and absorption of radiation by aerosols is expected to be more complicated than that by water droplets and ice crystals. This results from the diversity of chemical species in an aerosol layer, as contrasted with one chemical substance in a clean water cloud.

In parameterizing the influence of aerosols on the infrared irradiance, Paltridge and Platt (1976:227) suggested that only a rough estimate of the absorption by these particles is required. To determine this simple representation, a *volume absorption coefficient* (in the S.I. system, the units are m⁻¹),

$$\beta_{a\lambda} = k_{a\lambda}\rho_\chi, \tag{8-48}$$

is defined, where $k_{a\lambda}$ is the mass absorption coefficient specified by Eq. (8-13) with ρ_χ as the density of the contaminant. Of course, this definition of an absorption coefficient can also be applied to a gaseous contaminant in the atmosphere. For aerosol materials (or for water), Eq. (8-48) is also written as

$$\beta_{a\lambda} = \pi \int_0^\infty \frac{dn(r)}{dr}\, r^2\, E_{a\lambda}\, dr, \tag{8-49}$$

where $dn(r)/dr$ is the number of particles per radius interval per unit volume at radius r and $E_{a\lambda}$ is defined as the ratio of the absorption cross-section to the geometric cross-section of a single spherical particle.[16] As discussed by

Paltridge and Platt (1976:78), when using a spherical representation for the aerosols, one assumes that in a population of aerosols, their orientation is random, so a spherical shape can be used to represent their integrated influence on the flux of radiation. (Of course, such an assumption is invalid when irregular-shaped aerosols have a preferential orientation; e.g., thin disks will tend to fall with their long axis more or less parallel to the ground.)

From observations (e.g., Paltridge and Platt 1976, Figure A.4; Wallace and Hobbs 1977), the distribution of aerosols are well approximated by the relation

$$dn(r)/dr = (b_1/2.3)\, r^{-(1+b_2)} \qquad (8\text{-}50)$$

in a size range of greater than 0.1 μm or so, where b_1 and b_2 are constants (b_1 has dimensions, whereas b_2 is dimensionless). This function, called the *Junge distribution*, is recommended by Paltridge and Platt (1976:281) as being particularly useful in radiation problems, at least in moderately polluted continental atmospheres. (However, in clean maritime air masses, Paltridge and Platt state that the Junge distribution is invalid, although for infrared radiation calculations, the low numbers of aerosols in that environment imply that $\beta_{a\lambda}$ will be very small relative to the absorption from water vapor and CO_2.) Modified gamma, standard gamma, and lognormal distributions of aerosols, as summarized by Paltridge and Platt (1976, Table A.1), have also been used in lieu of Eq. (8-50). In addition, Abele and Clement (1980) discuss several functional forms, including Chebyshev polynomials, to use in representing these distributions.

Equation (8-49) can also be written as

$$\beta_{a\lambda}(r_1, r_2) = \pi \int_{r_1}^{r_2} r^2\, E_{a\lambda}(r) \frac{dn(r)}{dr}\, dr$$

$$= \frac{\pi b_1}{2.3} \int_{r_1}^{r_2} E_{a\lambda}(r) r^{1-b_2}\, dr, \qquad (8\text{-}51)$$

where $\beta_{a\lambda}(r_1, r_2)$ is the volume absorption coefficient resulting from aerosols between radius r_1 and r_2, and Eq. (8-50) is used to represent $dn(r)/dr$. As suggested by Paltridge and Platt (1976:227), based on observations, the absorption efficiency $E_{a\lambda}$ can be decomposed into two parts,

$$E_{a\lambda} = \begin{cases} b_3 r, & r_{\min} < r < r_m \\ 1.0, & r_m \le r < r_{\max}, \end{cases}$$

so that

$$\beta_{a\lambda} = \frac{\pi b_1 b_3}{2.3} \left[\int_{r_{\min}}^{r_m} r^{2-b_2}\, dr \right] + \frac{\pi b_1}{2.3} \int_{r_m}^{r_{\max}} r^{1-b_2}\, dr. \qquad (8\text{-}52)$$

For a Junge distribution with $\eta = 1.55 - 0.1i$, Paltridge and Platt give values of $r_{\min} = 0.01$ μm, $r_m = 7$ μm, and $r_{\max} = 70$ μm. The constant b_1 is proportional

to the total number of aerosols in the distribution, whereas b_3 is a function of wavelength λ and the refractive index of the aerosol particle. Obviously, the greater the number of the same type of aerosols, the greater the absorption. The exponent b_2 has been found observationally in polluted air masses to have values between 2 to 4 (Liou 1980:238), with $b_2 = 3$ the most common (Paltridge and Platt 1976:280). The value for b_3 is determined from[17]

$$b_3 = \frac{dE_{a\lambda}}{dr} = \left(\frac{2\pi}{\lambda}\right) \frac{24\eta_i\eta_r}{\left[\left(\eta_r^2 - \eta_i^2 + 2\right)\right]^2 + \left(2\eta_i\eta_r\right)^2} \qquad (8\text{-}53)$$

(from Paltridge and Platt 1976:227), where the right side of this relation is derived using the concepts of refraction discussed by Paltridge and Platt (1976:222, 227) and Liou (1980, App. D). Using representative values for polluted air of $b_2 = 3$ and $b_1 = 2.3 \times 10^{-11}$ [since $b_2 = 3$, b_1 is dimensionless for this form of Eq. (8-51)] and a value of b_3 of 1.34×10^3 cm^{-1}, as given by Paltridge and Platt (1976:228), yields a value for Eq. (8-52) of

$$\beta_{q\lambda} = 3.24 \times 10^{-2} \text{ km}^{-1}. \qquad (8\text{-}54)$$

Of course, other values of the complex index of refraction yield different values of $\beta_{a\lambda}$. For example, Paltridge and Platt give a value of $\beta_{a\lambda} = 1.9 \times 10^{-1}$ km^{-1} for a carbonaceous aerosol with a value of $\eta_i = 0.6$.

When condensation occurs on dry hydroscopic aerosols, the refractive index is assumed to approach a pure water droplet as it grows larger. Hänel (1971) proposed the following empirical formulation for shortwave irradiance, which is also equally applicable in the infrared region:

$$\begin{aligned}
\eta_r &= \eta_{r_{q_2}} + \left(\eta_r - \eta_{r_{q_2}}\right)/\left(r_{q_2}/r_0\right)^3 \\
\eta_i &= \eta_{i_{q_2}} + \left(\eta_i - \eta_{i_{q_2}}\right)/\left(r_{q_2}/r_0\right)^3,
\end{aligned} \qquad (8\text{-}55)$$

where $\eta_{r_{q_2}}$ and $\eta_{i_{q_2}}$ refer to the real and imaginary components of the refractive index of liquid water and r_{q_2}/r_0 is the ratio of the radius of the liquid droplet to that of the dry aerosol [see Eq. (8-80)]. Equation (8-55) is also given by Nilsson (1979) for aerosol extinction of longwave radiation.

In applying Eq. (8-52) or other analogous formulations to the atmosphere, it is generally recognized that the absorption of infrared radiation by aerosols will be important only within the wavelength band from 8 to 14 μm. Elsewhere in the longwave region, the absorption by CO_2 and water vapor is assumed to be dominant[18] (see, e.g., Ackerman *et al.* 1976:33; Zdunkowski *et al.* 1976:2403; Welch *et al.* 1978:140).

It is therefore necessary to integrate Eq. (8-52) over the wavelengths 8 to 14 μm. As shown by Paltridge and Platt (1976, App. A), however, η_r and η_i can vary substantially as a function of wavelength within even this small interval.

Therefore, one procedure is to evaluate $\beta_{a\lambda}$ over smaller intervals of wavelength in which η_r and η_i can be assumed to be constant.

In a polluted atmosphere without clouds, the emissivities could then be computed from[19]

$$\epsilon_{\chi_m}(\Delta z_a) = \sum_{m=1}^{M} \alpha \sum_{\Delta\lambda} \left[1 - b_{s_m} \exp\left(-\beta_{a\bar{\lambda}}^{\chi_m} \Delta z_a\right) \right] \quad (8\ \mu m \leq \lambda \leq 14\ \mu m), \quad (8\text{-}56)$$

where the sum $\sum_{\Delta\lambda}$ (using a constant $\Delta\lambda$) is over as many wavelength intervals as needed to represent η_r and η_i as constants within that interval. The coefficient α is inserted to represent the average value of $\frac{\pi \beta_{\bar{\lambda}}(T)}{\sigma T^4}$ within the wavelength interval. Within each interval, $\Delta\lambda$ for each chemical species, $\beta_{a\bar{\lambda}}^{\chi_m}$ is the average volume absorption coefficient. The parameter b_{s_m} is used ($b_{s_m} \leq 1$; $\sum_{m=1}^{M} b_{s_m} = 1$) to account for overlap in the wavelength of absorption of different pollutants. The use of b_{s_m} permits the parameterization of the cumulative effect of absorption by each type of aerosol or gaseous contaminant for each wavelength interval [see Note 19 to Eq. (8-56)]. The quantity Δz_a is a depth within an aerosol layer. It may also be necessary to define two separate emissivities, $\epsilon_{\chi_m}\downarrow$ and $\epsilon_{\chi_m}\uparrow$, using the form given by Eq. (8-56), analogous to that required for a water cloud [i.e., Eq. (8-45)], since the spectral composition of the irradiance at the top and bottom of the aerosol clouds could be different.

To estimate the divergence of infrared irradiance caused by pollution needed in Eq. (8-42), Eq. (8-56) can be used in an expression such as

$$\frac{\partial R\uparrow}{\partial z} = \int_{z_{A_B}}^{z} \frac{d\epsilon_{\chi_m}(z - \hat{z})}{dz} \frac{d}{d\hat{z}} \sigma \overline{T}^4 \, d\hat{z}$$

$$\frac{\partial R\downarrow}{\partial z} = \int_{z_{A_T}}^{z} \frac{d\epsilon_{\chi_m}(\hat{z} - z)}{dz} \frac{d}{d\hat{z}} \sigma \overline{T}^4 \, d\hat{z}, \tag{8-57}$$

where z_{A_B} and z_{A_T} are the bottom and the top of the aerosol layer, respectively. This formulation is analogous to Eq. (8-40). A simplified representation such as Eq. (8-41) could also possibly be used with T_G and T_T replaced by the temperatures at the base and top of the aerosols and u defined in terms of distance from the base of the aerosols.

In actual parameterizations of polluted air masses, several methods have been used to represent the absorption of infrared radiation by pollutants. For example, Viskanta *et al.* (1977a, b) used ethylene, which has a strong absorption in the 8- to 12-μm interval to represent the net effect of all pollutants. Atwater (1971a) assumed a modified gamma distribution given by

$$n(r) = 5.7 \times 10^{19} \, r^3 \exp\left(-45 r^{0.25}\right)$$

to represent the size distribution of aerosols, and an imaginary part of the refractive index of 0.25 for infrared radiation. His distribution of aerosols assumed

a concentration of 10^6 cm^{-3} with a modal radius of 0.005 μm. The value of the volume absorption coefficient that he used to represent the entire infrared spectrum varied from 0 to 0.8 km^{-1} for his summer simulations and from 0 to 0.5 km^{-1} for his winter simulations over an urban area. The higher values of the absorption coefficient were adopted to represent severe pollution conditions. Atwater (1971b) stated that volume absorption coefficients greater than 0.1 km^{-1} cause changes in temperature that exceed those caused by water vapor. Andreyev and Ivlev (1980) found that large aerosols (i.e., ≥ 0.5 μm) tend to be minerals and to absorb primarily between the 2- to 15-μm wavelengths.

Welch and Zdunkowski (1976), Zdunkowski *et al.* (1976), and Welch *et al.* (1978) used a parameterization developed by Korb *et al.* (1975) to represent both the scattering and absorption of infrared radiation by aerosols (and water vapor) in the atmospheric window. They used measured values for dry aerosol parameters from the industrialized area of Mainz, Germany and determined that, in general, η_i increases with wavelength. For $\lambda = 10$ μm, they found $\eta_r = 1.7$ and $\eta_i = 0.34$ for the dry aerosols with $\beta_{a\lambda} = 4.04 \times 10^{-3}$ km^{-1} when the total particle concentration was 2262 cm^{-3}. These investigators also included the effect of relative humidity on $\beta_{a\lambda}$. They estimated the ratio of $\beta_{a\lambda}$ for a hydroscopic particle in a moist atmosphere to $\beta_{a\lambda}$ of a completely dry aerosol as 1.01, 1.54, 3.12, and 11.03 for relative humidities of 20, 75, 95, and 99%, respectively, with $\lambda = 10$ μm.

Ackerman *et al.* (1976) also included scattering, as well as absorption, in their simulation of infrared irradiance within a polluted atmosphere, although they neglected the dependence of aerosol properties on relative humidity. Using aerosol data from 342 distributions measured in Los Angeles, for an observed average concentration of 10^5 cm^{-3}, they found excess cooling caused by aerosols in the lowest 1 km of almost 1°C day^{-1}. They also concluded that increasing the concentration of aerosols tends to produce more isotropic scattering and to increase the fraction of infrared energy absorbed. Additional discussion of the effect of pollution on radiation is presented in Section 8.4.3 and Section 13.1.5 in Chapter 13.

8.4   Shortwave Radiative Flux

Shortwave irradiance is composed of two components: direct irradiance and diffuse irradiance. Direct shortwave irradiance reaches a point without being absorbed or scattered from its line of propagation by the intervening atmosphere. The image of the sun's disk as a sharp and distinct object represents that portion of the shortwave radiation that reaches the viewer directly. In contrast, diffuse irradiance reaches the observer after first being scattered from its line of propagation. On an overcast day, for example, the sun's disk is not visible, and all

of the shortwave irradiance is diffuse. On such days, this diffuse solar radiation may be nearly isotropic (Zdunkowski *et al.* 1980).

The direct downward solar irradiance reaching a horizontal surface of unit area at the top of the atmosphere $R^{\downarrow}_{sw_0}$, can be written as

$$R^{\downarrow}_{sw_0} = \overline{R}^{\downarrow}_{sw_0} = \begin{cases} S_0 \left(a^2/r^2\right) \cos Z, & |Z < 90°| \\ 0, & |Z \geq 90°| . \end{cases} \tag{8-58}$$

The ratio of the average distance of the earth from the sun to its location at any time of the year can be calculated, from Paltridge and Platt (1976:57, 63), as

$$\frac{a^2}{r^2} = 1.000110 + 0.034221 \cos d_0 + 0.001280 \sin d_0 + 0.000719 \cos 2d_0 + 0.000077 \sin 2d_0, \tag{8-59}$$

with

$$d_0 = 2\pi m/365. \tag{8-60}$$

The variable m is the day number, starting with 0 on 1 January and ending on 31 December. The quantity $S_0 = 1376$ W m^{-2} (Hickey *et al.* 1980) is the irradiance from the sun on a surface of unit area perpendicular to the direction of propagation of the sun's electromagnetic energy at the semimajor axis distance of the earth's elliptical orbit from the sun a; S_0 is called the *solar constant*. The distance of the earth from the sun at any given time varies from $r = 0.98324a$ in early January to $r = 1.01671a$ in early July [List 1971, Table 170 and from Eq. (8-59)]. The variable Z is the zenith angle (see, e.g., Figure 8-1), defined as 90° when the sun's disk bisects the horizon and as 0° when it is overhead.

The zenith angle is defined by

$$\cos Z = \cos \phi \cos \delta_{sun} \cos h_r + \sin \delta_{sun} \sin \phi, \tag{8-61}$$

where ϕ is latitude, δ_{sun} is the declination of the sun (which ranges between +23.5° on 21 June to −23.5° on 22 December),[20] and h_r is the hour angle (0° ≡ noon). Using Eq. (8-61), sunrise and sunset occur when $Z = \pm 90°$ and can be obtained from

$$h_r = \arccos \left\{ -\tan \delta_{sun} \tan \phi \right\}.$$

(When $\tan \delta_{sun} \tan \phi < -1$, night occurs for the entire time, whereas for $\tan \delta_{sun} \tan \phi > 1$, the sun is up for the entire 24-hour period.)

8.4.1 Clear Air

8.4.1.1 *Direct Irradiance*

In a clear, clean atmosphere, ozone, water vapor, and the gases given in Table 2.1 (particularly diatomic oxygen; see Kondratyev 1969:261) are the principal absorbers of shortwave irradiance. Of these atmospheric constituents, water vapor is the major source of heating by shortwave absorption within the troposphere (e.g., List 1971:420; Paltridge and Platt 1976:94). Within the boundary layer, heating as a result of shortwave absorption has been shown to be substantial (e.g., Moores 1982). This water vapor absorption occurs at the near-infrared portion of the solar spectrum.

Paltridge and Platt (1976:95) have suggested a formulation for fractional absorption over the entire solar spectrum, based on Yamamoto's (1962) study, which is given by

$$a_{q3} = 2.9\, \delta P / \left[(1 + 141.5\, \delta P)^{0.635} + 5.925\, \delta P \right],$$

where δP in units of grams per centimeter squared is defined following Eq. (8-35) using $\delta z \to \infty$. The slight effect of CO_2 and O_2 absorption is also included in this empirical formulation, which is accurate to within 1% over values of δP ranging from 10^{-2} to 10 g cm^{-2}. With $\delta P = 10$ g cm^{-2}, for instance, $a_{q3} = 0.18$. Note that the δP terms that appear in this expression would need to be multiplied by $(\cos Z)^{-1}$ to account for slanted path lengths of sunlight through the atmosphere.

Atwater (1974) also uses a similar representation to represent the absorption of shortwave irradiance. Obtained from McDonald (1960), this empirical relation has been expressed by McCumber (1980) as[21]

$$a_{q3} = 0.077 (\delta P / \cos Z)^{0.3}.$$

With $\delta P = 10$ g cm^{-2}, a_{q3} in this relation with $Z = 0$ is equal to 0.15. These formulations for absorption are given in Eq. (8-42) as

$$\frac{\partial \overline{R} \downarrow_{sw}}{\partial z} = \; \simeq \; -\frac{a^2}{r^2} \frac{\partial S_0 \cos Z a_{q3}}{\partial z} = -S_0 \frac{a^2}{r^2} \cos Z \frac{\partial a_{q3}}{\partial z}. \qquad (8\text{-}62)$$

Upward shortwave reflections from such surfaces as clouds, ground, and water bodies can also influence radiative heating. Unfortunately, because of the small-scale irregularities of these surfaces, the impinging solar radiation is generally not reflected as in a mirror,[22] but rather is reoriented to a wide range of vertical directions. Such reorientation explains why, for example, except over water, ground reflections when looking away from the sun are about as bright as those when looking in the direction of the sun. Heating from these reflections has not been included in mesoscale models, although its incorporation would be straightforward, assuming isotropic reflection from the surface.

The shortwave irradiance absorbed by the ground can be written as

$$\overline{R}_{sw_G} = \left(\overline{R}^{\downarrow}_{sw_G} + \overline{R}^{D}_{sw_G}\right)(1 - A),\qquad(8\text{-}63)$$

where $\overline{R}^{D}_{sw_G}$ is the diffuse irradiance at the ground (see Section 8.4.1.2), A is the *albedo*[23] (reflectance) of the ground, and $\overline{R}^{\downarrow}_{sw_G}$ is determined from a formulation such as Eq. (8-62) by integrating through the depth of the atmosphere. Thus the upward reflected irradiance from the ground is given by

$$\overline{R}^{up}_{sw_G} = A\left(\overline{R}^{\downarrow}_{sw_G} + \overline{R}^{D}_{sw_G}\right).$$

The albedo is discussed in more detail in Section 11.3.3.2 in Chapter 11. For use in Eq. (8-42), the divergence of upward irradiance could be written as

$$\partial\overline{R}^{up}_{sw}/\partial z = -\overline{R}^{up}_{sw_G}\,\partial a_{q_3}/\partial z.\qquad(8\text{-}64)$$

8.4.1.2   Diffuse Irradiance

In a clear, clean atmosphere, scattering of shortwave irradiance occurs as this electromagnetic energy propagates through the gases in the atmosphere. Discussed in detail in a number of texts (e.g., Liou, 1980, Section 3.7), this type of multiple reflection is called *Rayleigh scattering* and is roughly inversely proportional to the fourth power of wavelength. Rayleigh scattering, which accounts for the blue color of the sky, occurs when the wavelength of the radiation is much larger than the objects causing the scatter (e.g., visible light has a wavelength much greater than the size of the molecules of gas in the air). The scattering of shortwave irradiance increases its path length and thereby enhances the heating of the atmosphere.

Atwater and Brown (1974) used an expression for fractional transmissivity of shortwave irradiance at the ground that accounted for downward Rayleigh scattering caused by O_3, O_2, and CO_2, as well as the absorption from these gases. Originally presented by Kondratyev (1969), this relation is given by

$$t = 1.03 - 0.08\sqrt{[9.49 \times 10^{-4}p\text{ (in mb) } + 0.051]/\cos Z}.$$

Atwater and Ball (1981) present a similar formulation for t. For $p = 1000$ mb and $Z = 0$, this gives a value of $t = 0.95$; $Z = 45°$ yields $t = 0.93$. Equation (8-63) can then be written as[24]

$$\overline{R}_{sw_G} = \left(t - a_{q3}\right)(1 - A)\,R^{\downarrow}_{sw_0},\qquad(8\text{-}65)$$

where the absorption loss from water vapor is included. Above the surface,

$$\overline{R}_{sw} = \overline{R}^{\downarrow}_{sw} + \overline{R}^{D}_{sw} = \left(t - a_{q3}\right)R^{\downarrow}_{sw_0}$$

can be used, with t and a_{q3} evaluated at the pressure height p. The middle expression in $\overline{R}_{sw}$ is the direct plus diffuse radiation, and the righthand side includes the astronomical effect [in $R^{\downarrow}_{sw_0}$; see Eq. (8-58)], the extinction from water vapor absorption (in a_{q3}), and the Rayleigh scattering effect (in t) as the shortwave radiation is transmitted through the atmosphere. The derivative of $\overline{R}_{sw}$ with height yields the heating from direct plus diffuse solar radiation.

As reported by List (1971:420), as long as the scattering particles are small in comparison with the wavelength of the incident light (i.e., Rayleigh scattering), half of the scattering is downward and half is upward. This simplifies the incorporation of diffuse irradiance into t, such as described by List.

8.4.2   Cloudy Air

The influence of clouds on solar irradiance is significant. Gannon (1978), for example, found that the sea-breeze circulation over south Florida was terminated as the shading from cirrus clouds over land markedly reduced the solar flux reaching the ground. Using a numerical model, Carpenter (1982b) demonstrated that differential ground heating as a result of cloud shadowing by a bank of altocumulus clouds can generate significant mesoscale ascent. This region of upward motion apparently resulted in substantial thunderstorm activity over England as the cloud bank moved eastward on the case study day that he examined. In a regional model (i.e., $\Delta x = \Delta y \simeq 58$ km), Wong *et al.* (1983a) illustrated that large errors in precipitation and pressure fields can occur if cloud influences on both longwave and shortwave radiative flux divergence are not included. Sasamori (1972) concluded that when clouds are present, their effect in the solar wavelengths is primarily to reduce shortwave radiation transmission below clouds rather than cause heating within them. Transmission is reduced as the radiation is reflected into space because of the relatively high albedo of the top surfaces of water and ice clouds. Gu *et al.* (2001) found that a cumulus cloud field can focus solar reflection from clouds to a sufficient degree so that the surface insolation can occasionally exceed the solar input at the top of the atmosphere. Using a model, Harrington *et al.* (2000) investigated the radiative impacts on the growth of cloud droplets within Arctic stratus clouds.

In cloudy air (and in layers of aerosols), the radiative transfer of shortwave electromagnetic energy is more complicated than in clear air, because scattering becomes much more important and involves a complex pattern of multiple reflections when the wavelength of the radiant energy and particle size is about the same. For longwave irradiance, scattering is generally of less importance, as discussed in Sections 8.3.2 and 8.3.3.

The mathematical procedure used to represent this scatter is often referred to as *Mie scattering*, after the first individual who solved the equations for radia-

tive transfer when the wavelength and particle size are about equal. Described in detail by Kondratyev (1969, Section 4.4) and Liou (1980, Chapter 5), the formulation for this type of scattering (even for spherical particles) is much more involved than for Rayleigh scattering. The term "Mie scattering" is used when the incident wavelength is equal to or smaller than the particles that cause the scatter. Qualitatively, as discussed by Liou (1980:7), particles tend to scatter radiative energy preferentially in the forward direction but with complicated side lobes[25] when the particle size and wavelength of radiation are of the same order. As particles become larger, their forward scatter becomes greater for the same wavelength of irradiance.

As discussed by Paltridge and Platt (1976:103), multiple scattering of short-wave irradiance within a cloud increases its absorption, since its path length has increased. Although the imaginary component of the refractive index of ice and water (which is proportional to the absorption) is very small at wavelengths less than 2 μm, and the wavelengths of absorption of water vapor and of ice and liquid water are similar, Paltridge and Platt (1976:105) have suggested that cloud absorption by droplets and ice crystals may be a subtle but important component in cloud dynamics. However, such an effect has not yet been included in mesoscale models, although Stephens (1978a) presents one such parameterization.

Stephens divides the solar spectrum into two intervals: 0.3–0.75 μm, where absorption is neglected, and 0.75–4.0 μm, where absorption is included. Using the definition of optical thickness given by Eq. (8-13), the volume absorption coefficient given by Eqs. (8-48) and (8-49), with $n(r)$ corresponding to a cloud of liquid droplets, yields

$$\tau_\lambda = \pi \int_z^{z+\Delta z_c} \int_0^\infty n(r) r^2 E_{a\lambda} \, dr \, dz. \tag{8-66}$$

In this expression for optical thickness, Δz_c is a portion or all of the cloud thickness. [In contrast to Eq. (8-13), this expressions for τ_λ is not integrated to the top of the atmosphere.] Since cloud droplets are large relative to shortwave irradiance, Eq. (8-66) can be written as

$$\tau \simeq 2\pi \int_z^{z+\Delta z_c} \int_0^\infty n(r) r^2 \, dr \, dz, \tag{8-67}$$

where the ratio of the scattering cross-section to the geometric cross-section (i.e., $E_{a\lambda}$) is 2, as determined from Mie theory. (The condition that $E_{a\lambda} = 2$ is called the *large-drop assumption*, since the wavelength of the electromagnetic energy is presumed to be much smaller than the size of the cloud droplets.) In addition, because $E_{a\lambda}$ is identically equal to 2, the wavelength dependence

in τ is removed. Stephens then defined an effective radius of the cloud droplet distribution as

$$r_e = \int_0^\infty n(r)r^3 \, dr \bigg/ \int_0^\infty n(r)r^2 \, dr, \tag{8-68}$$

so that, because volume $= \frac{4}{3}\pi r^3$, Eq. (8-67) can be written as

$$\tau \simeq \frac{3}{2} \, \delta p_{q2} \big/ \left(r_e \rho_{q2}\right). \tag{8-69}$$

The importance of the effective radius in mesoscale models has been explored by Wyser *et al.* (1999). They found, for example, that cloud droplet size information has its largest effect on the shortwave radiative fluxes of thin clouds.

The quantity δp_{q_2}, analogous to δP_{q_3} defined following Eq. (8-35), is given by

$$\delta p_{q_2} = \frac{4}{3}\pi \int_z^{z+\Delta z_c} \int_0^\infty \rho_{q_2} n(r)r^3 \, dr \, dz.$$

The integral $\int_0^\infty \frac{4}{3}\pi \rho_{q_2} n(r)r^3 \, dr$ is the *liquid water content* of the cloud at a given level; δp_{q_2} is in units of mass per unit area.

Grid-volume averages of Eq. (8-69) [see Eq. (4-6) in Chapter 4] or a more general form for τ or τ_λ should be made, of course. However, essentially no information is known regarding subgrid-scale fluctuations on the mesoscale within clouds.

Using Mie theory, Stephens developed empirical formulations for τ as a function of integrated liquid water content, given as

$$\log_{10} \tau = \begin{cases} 0.2633 + 1.7095 \ln\left[\log_{10} W\right], & 0.30\,\mu m \le \lambda \le 0.75\,\mu m \\ 0.3492 + 1.6518 \ln\left[\log_{10} W\right], & 0.75\,\mu m \le \lambda \le 4.0\,\mu m, \end{cases} \tag{8-70}$$

where $W = \delta p_{q_2}$ is in units of grams per meter squared. For a value of $W = 100$ g m^{-2} (typical of an altostratus cloud), $\tau = 28$ for the shorter wavelengths and $\tau = 31$ for the longer wavelengths. Twomey (1978) noted that when $\tau \ge 10$, all solar irradiance exiting from the bottom of the cloud is diffuse.

Assuming that the ground surface is nonreflective (i.e., $A = 0$) and any underlying cloud layer is nonreflective, Stephens writes

$$r_c = \frac{\beta_1 \tau / \cos Z}{1 + \beta_1 \tau / \cos Z}, \quad t_c = 1 - r_c \quad (0.3\,\mu m \le \lambda \le 0.75\,\mu m)$$

$$\left. \begin{aligned} r_c &= \left(u^2 - 1\right)\left[\exp\left(\tau_{\text{eff}}\right) - \exp\left(-\tau_{\text{eff}}\right)\right]/R_c \\ t_c &= 4u/R_c, \quad a_c = 1 - r_c - t_c \end{aligned} \right\} \quad (0.75\,\mu m < \lambda \le 4.0\,\mu m), \tag{8-71}$$

where

$$u^2 = (1 - \omega + 2\beta_2\omega)/(1 - \omega),$$

$$\tau_{\text{eff}} = \{(1 - \omega)[1 - \omega + 2\beta_2\omega]\}^{1/2} \, \tau/\cos Z,$$

$$R_{\text{c}} = (u + 1)^2 \exp(\tau_{\text{eff}}) - (u - 1)^2 \exp(-\tau_{\text{eff}}).$$

The β terms represent the fraction of incident radiation backscattered. Using his theoretical model, Stephens (1978b) estimated values of β_1, β_2, and ω, as given in Table 8-1.

With these two spectral region parameterizations, radiative heating in model layers within and transmission of radiation through a cloud can be determined using Eq. (8-71), Table 8-1, and Eq. (8-70). Shortwave heating within the cloud, for use in Eq. (8-42), is obtained from

$$\partial \overline{R}_{\text{sw}_{\text{c}}}/\partial z = -\left(\overline{R}_{\text{sw}}^{\downarrow} + \overline{R}_{\text{sw}}^{\text{D}}\right)_{\text{CT}} \partial a_{\text{c}}/\partial z, \tag{8-72}$$

where $\left(\overline{R}_{\text{sw}}^{\downarrow} + \overline{R}_{\text{sw}}^{\text{D}}\right)_{\text{CT}}$ is the incident direct and diffuse shortwave irradiance at the top of the cloud. The amount of irradiance transmitted through the cloud is given by Eq. (8-71). For a single cloud layer, the shortwave radiation at the ground given by Eq. (8-65) is modified to

$$\overline{R}_{\text{sw}_{\text{G}}} = t_{\text{c}} (1 - A) \left(\overline{R}_{\text{sw}}^{\downarrow} + \overline{R}_{\text{SW}}^{\text{D}}\right)_{\text{CT}}, \tag{8-73}$$

where the scattering and absorption below the cloud has been neglected.[26]

For multiple cloud layers, the irradiance reaching each cloud top can be estimated using a value corresponding to the irradiance that exited downward from the next highest cloud base minus the extinction in the free atmosphere below that cloud base. Since each cloud will absorb and backscatter shortwave radiative energy, the free atmosphere irradiance reaching lower clouds will be progressively smaller. When clouds are assumed to cover only a portion of a grid mesh (such as sketched in Figure 8-8), a fractional weighting of the clouds' contribution to absorption and scattering can be performed, although cloud shape (Welch *et al.* 1980; Welch and Zdunkowski 1981a) and shading of adjacent clouds will influence the flux of shortwave radiation. The second effect will be particularly important when the clouds are in close proximity to one another (Gube *et al.* 1980). However, if backscatter is neglected from the ground and overlying clouds and if shading and variations in cloud shape are ignored, then the shortwave irradiance at the ground can be parameterized for use in mesoscale models as

$$\overline{R}_{\text{sw}_{\text{G}}} = \prod_{i=1}^{d} \left[1 - \sigma_{\text{c}_i} \left(1 - t_{\text{c}_i}\right)\right] (1 - A) \left(\overline{R}_{\text{sw}}^{\downarrow} + \overline{R}_{\text{sw}}^{\text{D}}\right)_{\text{CT}} \tag{8-74}$$

TABLE 8-1

The Broadband Values of ω, β_1, and β_2 Used to Determine Eq. (8-71)

τ	$\cos Z$
	1.0	0.8	0.7	0.6	0.5	0.4	0.3	0.2	0.1
Average values of $1 - \omega$									
1	0.0225	0.0222	0.0218	0.0208	0.0199	0.0155	0.0109	0.0059	0.0017
2	0.0213	0.0200	0.0179	0.0176	0.0156	0.0118	0.0078	0.0038	0.0010
5	0.0195	0.0166	0.0146	0.0125	0.0096	0.0069	0.0043	0.0021	0.0005
10	0.0173	0.0138	0.0114	0.0093	0.0070	0.0049	0.0026	0.0013	0.0003
16	0.0156	0.0111	0.0090	0.0073	0.0052	0.0035	0.0019	0.0009	0.0002
25	0.0115	0.0088	0.0069	0.0052	0.0038	0.0026	0.0014	0.0007	0.0001
40	0.0104	0.0055	0.0042	0.0032	0.0023	0.0014	0.0008	0.0003	0.0001
60	0.0083	0.0050	0.0038	0.0028	0.0020	0.0013	0.0007	0.0003	0.0001
80	0.0069	0.0043	0.0035	0.0022	0.0018	0.0011	0.0006	0.0003	0.0000
100	0.0060	0.0043	0.0035	0.0022	0.0018	0.0011	0.0006	0.0003	0.0000
200	0.0044	0.0031	0.0025	0.0016	0.0011	0.0007	0.0004	0.0002	0.0000
500	0.0026	0.0018	0.0014	0.0010	0.0007	0.0005	0.0003	0.0001	0.0000
Average values of β_1									
1	0.0421	0.0557	0.0657	0.0769	0.0932	0.1111	0.1295	0.1407	0.1196
2	0.0472	0.0615	0.0708	0.0803	0.0924	0.1017	0.1077	0.1034	0.0794
5	0.0582	0.0692	0.0744	0.0782	0.0815	0.0812	0.0776	0.0680	0.0483
10	0.0682	0.0726	0.0737	0.0733	0.0723	0.0685	0.0626	0.0527	0.0359
16	0.0734	0.0738	0.0728	0.0707	0.0680	0.0631	0.0564	0.0465	0.0310
25	0.0768	0.0744	0.0723	0.0691	0.0653	0.0598	0.0526	0.0427	0.0281
40	0.0791	0.0749	0.0719	0.0680	0.0636	0.0575	0.0501	0.0402	0.0261
60	0.0805	0.0752	0.0717	0.0674	0.0627	0.0563	0.0488	0.0389	0.0251
80	0.0812	0.0754	0.0717	0.0672	0.0622	0.0558	0.0481	0.0382	0.0246
100	0.0820	0.0757	0.0717	0.0670	0.0619	0.0553	0.0475	0.0376	0.0241
200	0.0831	0.0763	0.0721	0.0672	0.0619	0.0552	0.0473	0.0374	0.0241
500	0.0874	0.0800	0.0755	0.0703	0.0647	0.0576	0.0494	0.0392	0.0262
Average values of β_2									
1	0.0477	0.0627	0.0734	0.0855	0.1022	0.1200	0.1379	0.1465	0.1207
2	0.0537	0.0690	0.0788	0.0886	0.1003	0.1090	0.1133	0.1065	0.0794
5	0.0660	0.0769	0.0817	0.0850	0.0871	0.0864	0.0801	0.0688	0.0474
10	0.0759	0.0793	0.0795	0.0781	0.0757	0.0705	0.0629	0.0516	0.0339
16	0.0801	0.0787	0.0766	0.0732	0.0689	0.0626	0.0543	0.0434	0.0277
25	0.0807	0.0759	0.0724	0.0678	0.0625	0.0555	0.0471	0.0368	0.0229
40	0.0770	0.0700	0.0656	0.0603	0.0545	0.0476	0.0396	0.0302	0.0184
60	0.0699	0.0621	0.0575	0.0522	0.0466	0.0401	0.0329	0.0248	0.0148
80	0.0634	0.0556	0.0510	0.0460	0.0408	0.0348	0.0283	0.0211	0.0125
100	0.0534	0.0461	0.0420	0.0376	0.0330	0.0279	0.0225	0.0166	0.0097
200	0.0415	0.0353	0.0319	0.0283	0.0246	0.0206	0.0165	0.0120	0.0068
500	0.0251	0.0208	0.0186	0.0163	0.0140	0.0115	0.0090	0.0064	0.0032

From Stephens (1982, personal communication).

(Atwater and Ball 1981), where, as in Eq. (8-73), the contributions to a_{q3} from within the cloud layers should be excluded.

Newiger and Bähnke (1981) reported that aerosol particles incorporated into clouds may be the main absorber of solar radiation in clouds in the visible wavelengths, rather than the pure water in the cloud droplets. Knowledge of the liquid water content alone is not sufficient for determining the absorption of solar radiation within a cloud—the aerosol content (and type) within the cloud must also be known. Feingold and Kreidenweis (2000), for example, discuss whether the heterogeneous processing of aerosols increases the number of cloud droplets.

8.4.3 Polluted Air

In contrast with infrared radiation, scattering of shortwave electromagnetic radiation by aerosols is recognized by all investigators as an important component in the transfer of this energy. This scattering is what causes the white or yellow sky color usually associated with a polluted atmosphere. As discussed by Cerni (1982) and Weber and Baker (1982), unless the air is exceptionally clean, the ratio of diffuse to direct solar radiation is significantly affected by the quantity of pollution and also is a strong function of zenith angle, particularly when that angle is greater than 70° or so and the optical depth is large.

The absorption of shortwave energy by aerosols is also recognized as important, although its magnitude, as represented by the imaginary index of refraction, is not known except for a few specific substances. Hänel *et al.* (1982), for example, have reported heating rates from absorption of solar radiation by aerosols as large as about 0.5°C h^{-1} during the middle of the day under clear sky conditions over Frankfurt, Germany. They concluded that such absorption "is of high climatological importance, especially in industrial areas."

The extinction (absorption plus net backscattering) of solar energy by aerosols can be evaluated using an equation similar to that applied to estimate the absorption of longwave energy by aerosols (Section 8.3.3). In general, the optical path length for aerosols in the visible wavelengths is about 10 times that in the infrared (Paltridge and Platt 1976:215). An analogous equation to Eq. (8-52), except for extinction, is given by

$$\beta_{e\lambda}(r_1, r_2) = \frac{\pi b_1}{2.3} \int_{r_1}^{r_2} E_{e\lambda}(r) r^{1-b_2} \, dr, \tag{8-75}$$

where $\beta_{e\lambda}$ is a *volume extinction coefficient* and $E_{e\lambda}$ defined as the ratio of the extinction cross-section to the geometric cross-section of a single spherical particle. As in Section 8.3.3, the Junge distribution of aerosols [Eq. (8-50)] is

used over the size range r_1 to r_2. If the change of variable, given as $\xi = 2\pi r/\lambda$, is used in Eq. (8-75). Then

$$\beta_{e\lambda}(r_1, r_2) = \frac{\pi b_1}{2\pi} \left(\frac{\lambda}{2\pi}\right)^{2-b_2} \int_{\xi_1}^{\xi_2} E_{e\lambda}(\xi)\, \xi^{1-b_2}\, d\xi$$

or

$$\beta_{e\lambda}(r_1, r_2) \simeq \beta_{e\lambda}(0, \infty) \simeq \frac{\pi b_1}{2\pi} \left(\frac{\lambda}{2\pi}\right)^{2-b_2} \int_{0}^{\infty} E_{e\lambda}(\xi)\, \xi^{1-b_2}\, d\xi \qquad (8\text{-}76)$$

if, as assumed by Junge (1963), particles smaller than r_1 are too small and particles larger than r_2 are too few to contribute significantly to extinction. As discussed after Eq. (8-50), the Junge distribution is a realistic representation of the distribution of aerosols in polluted air masses. As discussed by Paltridge and Platt (1976:217, 222), the refractive index of aerosols is essentially independent of wavelength in the shortwave intervals, and since $E_{e\lambda}(\xi)$ is a function only of the refractive index, the integral in Eq. (8-76) is a function only of refractive index. Therefore, Eq. (8-76) can be written as[27]

$$\beta_{e\lambda} = b_4 \lambda^{2-b_2}, \qquad (8\text{-}77)$$

where b_4 is a function of particle refractive index, which itself is a function of radius and chemical characteristic of the aerosol. Thus, using $b_2 = 3$ [see after Eq. (8-53)], shortwave irradiance reaching the ground, as given by an expression such as Eq. (8-65), is given by

$$\overline{R}_{\text{sw}_G} = (t - a_{q3})\, t_a (1 - A) R_{\text{sw}_0}^{\downarrow}, \qquad (8\text{-}78)$$

where

$$t_a = \sum_{m=1}^{M} \sum_{\Delta\lambda} \left[b_{5_m} \exp\left(-b_{4_m} \lambda^{-1} \Delta z_a\right) \right], \qquad (8\text{-}79)$$

with b_{4_m} defined for each aerosol and gaseous contaminant. The quantity Δz_a is the depth of a layer within the aerosol cloud. The parameter b_{5_m} is included to account for the overlap in attenuation when two or more contaminants are present [see after Eq. (8-56)]. When using Eq. (8-79) in this form, however, changes of the distribution of aerosol sizes and composition with height are ignored.

The effect of humidity on the radius size (which will also, in general, change b_{4_m}) for a moderately polluted air mass can be estimated for relative humidities below 90% or so, following Kasten (1969), as

$$r = r_0 \left[1 - (q_3/q_{3_s}) \right]^{-0.23}, \qquad (8\text{-}80)$$

where q_{3_s} is the saturation-specific humidity ($100 q_3 / q_{3_s}$ is the relative humidity). According to Eq. (8-80), for a relative humidity of 50%, $r \simeq 1.17\, r_0$, whereas at a relative humidity of 90%, $r \simeq 1.7\, r_0$. Zdunkowski and Liou (1976) examined the effects of pollution on the absorption of shortwave irradiance and found it inconsequential for relative humidities of 30–70%, although, as implied by Eq. (8-80), a significant effect might be expected only for relative humidities closer to 100%, where r and r_0 become significantly different.

Although Eq. (8-79) provides the information to evaluate the extinction of solar radiation caused by atmospheric pollutants, it does not permit determination of the effect of these materials on the flux divergence term in Eq. (8-42). Performing this evaluation requires the amount of absorption of solar irradiance by the aerosols. Absorption occurs when the imaginary component of the particle refractive index is nonzero. A volume absorption coefficient, analogous to Eq. (8-77), can be written as

$$\beta_{a\lambda} = b_6 \lambda^{2-b_2} = b_6 \lambda^{-1}, \qquad (8\text{-}81)$$

where b_6 is a function of particle refractive index and the number of aerosols but in general is different than b_4. The shortwave heating within the aerosol layer, for use in Eq. (8-42), can then be obtained from

$$\frac{\partial \overline{R}_{\mathrm{sw}_a}}{\partial z} = -\left(\overline{R}_{\mathrm{sw}}^{\downarrow} + \overline{R}_{\mathrm{sw}}^{\mathrm{D}}\right) \frac{\partial a_a}{\partial z}, \qquad (8\text{-}82)$$

where $\overline{R}_{\mathrm{sw}}^{\downarrow} + \overline{R}_{\mathrm{sw}}^{\mathrm{D}}$ in Eq. (8-82) is evaluated at the top of the aerosol layer and

$$a_a = \sum_{m=1}^{M} \sum_{\Delta\lambda} \left[1 - b_{7_m} \exp\left(-b_{6_m} \lambda^{-1} \Delta z_a \right) \right]. \qquad (8\text{-}83)$$

The absorptivity, a_a, is defined analogously to Eq. (8-79), with b_{7_m} included to account for the overlap in absorptivities by different aerosols within the same spectral interval ($\sum_{m=1}^{M} b_{7_m} = 1$) and b_{6_m}, a function of the refractive index for each type of aerosol.

However, Paltridge and Platt (1976:222) question the use of Eq. (8-81) to represent the absorption of solar irradiance by very small aerosol particles ($r < 0.1\,\mu$m—called *Aitken particles*). From Mie theory, they present a value of single-particle absorption efficiency given by

$$E_{a\lambda} = -4 \left(\frac{2\pi r}{\lambda} \right) \mathrm{Im}\left[\left(n_c^2 - 1 \right) / \left(\eta_c^2 + 2 \right) \right], \qquad (8\text{-}84)$$

where η_c is the refractive index ($\eta_c = \eta_r - i\eta_i$). Thus

$$\beta_{a\lambda}\left(r_* \right) = (3/4 r_*)\, E_{a\lambda}. \qquad (8\text{-}85)$$

Values of η_c in the visible range are estimated as $1.8-0.5i$ for graphites, soots, and coals (Twitty and Weinman 1971); $1.55-0.044i$ for fly ash (Grams et al. 1972), and about $1.5-0.005i$ for dry atmospheric aerosol (Paltridge and Platt 1976:287). Liquid water ranges from a value of $1.34-1.86 \times 10^{-9}i$ at $\lambda = 0.4\,\mu\text{m}$ to $1.33-1.25 \times 10^{-7}i$ at $\lambda = 0.8\,\mu\text{m}$ (Paltridge and Platt 1976, Table 1.4). In obtaining Eq. (8-85) for $\beta_{a\lambda}$, the aerosol cloud is assumed to have only one radius size r_* with the same value of $E_{a\lambda}$. To use this expression, one could define r_* as the effective radius [see Eq. (8-68)] for aerosol particles smaller than $0.1\,\mu\text{m}$. The radiative heating from these Aitken aerosols could then be estimated by Eq. (8-82), where

$$a_a = \sum_{m=1}^{M} \sum_{\Delta\lambda} \left[1 - b_{\gamma_m} \exp\left(-\frac{3}{4r_{*_m}} E_{a\lambda}^m \Delta z_a \right) \right] \quad r_* < 0.1\,\mu\text{m}, \qquad (8\text{-}86)$$

which is analogous to Eq. (8-83). The quantities $E_{a\lambda}^m$ and r_{*_m} could be defined for each absorbing Aitken aerosol component (with b_{γ_m} suitably defined) or a representative value of r_* and $E_{a\lambda}$, with $b_{\gamma_m} = 1$, used to represent the averaged absorption characteristics.[28] Since $E_{a\lambda}$ is proportional to radius, $E_{a\lambda}^m/r_{*_m}$ is independent of radius in Eq. (8-86) as long as the refractive index is a constant for all sizes of each Aitken aerosol type.

   As discussed by Paltridge and Platt (1976:224), radiative heating by aerosols, as given by Eq. (8-86), is most important for highly absorbent materials such as carbonaceous aerosols ($\eta_i = 0.66$). As η_i decreases, the heating by sizes larger than $0.1\,\mu\text{m}$ becomes dominant (although because of their large numbers in polluted air, Aitken aerosols can still exert a significant effect on radiative heating).

   Parameterized versions of solar irradiance in a polluted atmosphere include those reported by Welch and Zdunkowski (1976), Zdunkowski et al. (1976), and Welch et al. (1978). Using a spherical harmonic representation for the Mie equations of radiative transfer, as described by Zdunkowski and Korb (1974), they represent multiple scattering and absorption separately for three intervals in the solar spectrum: the water vapor region, where all absorption bands of water vapor are included; the nitrous oxide (NO_2) region, where absorption and scattering by this gas can occur; and the remainder of the solar spectrum. All three intervals include absorption and scattering by aerosols and the constant gases. Their method, too detailed to present here, is discussed in Welch and Zdunkowski (1976). Among their results, they found that solar irradiance can cause heating in a polluted boundary layer in excess of $4°\text{C h}^{-1}$ with a zenith angle of $45°$. Welch et al. (1978), in their two-dimensional simulation of the effects of polluted air on an urban-rural area, found temperatures at the ground in the urban area during stagnant synoptic conditions to be reduced by $2°\text{C}$ because

of low-level pollution sources and by up to 7°C when upper-level sources occur, a result partially caused by the enhanced reflection and absorption of solar radiation by suspended aerosols. (Changes in albedo and roughness over the urban area also influenced these temperature changes.)

Viskanta *et al.* (1977a, b) and Viskanta and Daniel (1980) also used the method of spherical harmonics (Bergstrom and Viskanta 1973a) to solve the equations of radiative transfer. Using complex indices of refraction, as reported by Bergstrom (1972), they divided the solar spectrum into 12 intervals. They also concluded that the absorption of shortwave irradiance was an important component of the heat budget in polluted air masses, of a magnitude on the same order as for water vapor.

Atwater (1971a, b) used a simpler form to represent shortwave absorption and scattering. To represent $\beta_{a\lambda}$, he used a modified gamma distribution and values of $E_{a\lambda}$ for $\lambda = 0.485\,\mu\text{m}$, ignoring height dependence. In Atwater (1971b), he found heating rates of 30°C day^{-1} for 1 ppm of NO_2; 0.1–0.2°C day^{-1} for 1 ppm of SO_2, 0.1 ppm ethyl nitrate, 0.1 ppm biacetyl, 0.1 ppm ozone, and 0.1 ppm methyl propenyl ketone; and less than 0.005°C day^{-1} for 1 ppm nitric acid vapor, 0.1 ppm hydrogen peroxide, and 0.1 ppm ethyl nitrate.

Reck and Hummel (1981), using a model with both shortwave and longwave radiative effects, concluded that aerosols can lead to heating or cooling at the surface, depending on the surface albedo and on the imaginary part of the index of refraction η_i. For surface albedos above about 0.38, they found that the presence of absorbing aerosols ($\eta_i \neq 0$) always resulted in heating at the surface. They also concluded that the surface temperature is insensitive to its size distribution, although the chemical composition (and hence η_i) depend on the size spectra. Similarly, Porch and MacCracken (1982) determined that the aerosol size distribution was relatively unimportant in determining the radiative heating and cooling resulting from shortwave radiation in the Arctic. From an observational study over a specific region (St. Louis), Method and Carlson (1982) concluded that the total radiative effects of aerosols over the city was negligible, apparently because the aerosols had low absorptance (i.e., η_i small).

It remains to be determined whether detailed treatments of radiative transfer, such as those proposed by Welch and Zdunkowski (1976) and Viskanta *et al.* (1977a, b), are required for accurate simulations of radiative heating and cooling resulting from aerosols in a mesoscale model. Although a complete treatment is of course desirable, *the accuracy of any one parameterization in a model need not be any more precise than the least accurate parameterization of significant physical processes for the atmospheric system of interest.* Additional work is needed to test detailed, as opposed to simplified, parameterizations of radiative transfer in mesoscale models.

8.5   Examples of Parameterizations and Level of Complexity

In three-dimensional mesoscale models, radiation physics has not yet received the attention that has been given to planetary boundary-layer dynamics. However, the importance of longwave radiative flux divergence to such atmospheric features as nocturnal mesoscale drainage flows and of both shortwave and longwave fluxes in polluted atmospheres over urban areas during the day suggests that the accurate parameterization of radiation in mesoscale models is a fertile area for future research.

8.5.1   Equation 8.43

This algorithm is a particularly simple representation of longwave radiative flux divergence. It requires only $\overline{T}$, which is one of the variables in the conservation-of-heat equation. There are two adjustable (i.e., tunable) coefficients. This formula ignores CO_2 and water vapor effects, so the coefficients need to be altered for different humidities and other trace gas concentrations.

8.5.2   Equation 8.41

A more sophisticated algorithm for longwave radiative flux divergence is given by Eq. (8-41). In this representation, the dependent variables are $\overline{T}$, $\bar{\rho}$, $\bar{q}_3$, and $\bar{p}$. The coefficient, σ, is the Stefan-Boltzmann constant, which is assumed to be a fundamental quantity based on quantum mechanics. The emissivities, ϵ_{q_3} and $\epsilon_{\chi_{CO_2}}$, involve a set of observationally determined coefficients [Eqs. (8-35), (8-36), and (8-37)]. The independent variable is z.

8.5.3   Equation 8.58

Equation 8.58 for direct solar radiation requires the specification of the solar constant, S_0, the day of the year [using Eq. (8-60)], and the latitude, declination of the sun, and time of day from Eq. (8-61). This equation is based on astronomical measurements to determine the coefficients in Eq. (8-59). Spherical geometry is used to obtain Eq. (8-61).

Notes to Chapter 8

1. This variation occurs because the vertical gradients of such atmospheric properties as density, carbon dioxide, and water vapor are generally much larger than their horizontal gradients. The only major exception to this characteristic of the atmosphere occurs when clouds are present. In this situation, however, horizontal gradients of irradiance have been neglected in mesoscale models, with

the justification that the horizontal resolution on the mesoscale generally is significantly less than the vertical resolution. However, heterogeneities on the subgrid scale of clouds have been shown to be important in radiative flux calculations (Tiedtke 1996; O'Hirok and Gautier 1998a, b). Over tropical ocean regions (30°S–30°N), Tiedtke found that in a global weather forecast model, the net downward shortwave radiative fluxes are increased about 10 W m^{-2} when subgrid-scale effects are included.

2. The discussion of basic concepts presented in this section makes extensive use of Liou's (1980) excellent treatise on atmospheric radiation.

3. The zenith angle is also equal to $90° - E$, where E is called the *elevation angle*.

4. Single wavelength.

5. Radiation that is not dependent on direction is called *isotropic* radiation.

6. Shortwave radiation consists of ultraviolet, visible, and near-infrared wavelengths.

7. Local thermodynamic equilibrium is defined in Note 2 in Chapter 2.

8. Using Leibnitz's rule (see, e.g., Hildebrand 1962:360), $d\tau_\lambda = -k_{a\lambda}\rho\,dz$. Note that since k_λ has units of area per mass, $\tau_{a\lambda}$ is called the *mass absorption coefficient*.

9. See Spiegel (1967) or another introductory text on ordinary differential equations for discussions of integrating factors.

10. In the real atmosphere, τ_{T_λ} would be set equal to 0 using Eq. (8-13) with $z \to \infty$. Here, however, the optical thickness τ_{T_λ} is not set equal to 0, since numerical model tops are generally within the atmosphere.

11. The earth's surface radiates in the infrared close to its blackbody value (see Tables 11-2 and 11-8 in Chapter 11). To make the same assumption for $I_\lambda\downarrow|_{z_T}$, one can specify an effective temperature at the model top to represent the infrared emission from above z_T as if it were a blackbody. More appropriately, of course, the actual values of $I_\lambda\downarrow|_{z_T}$ should be used.

12. Note that despite being referred to as a length, u has dimensions of mass per area. The value of u increases monotonically with height z since $\rho > 0$, until $z \to \infty$.

13. André *et al.* (1978) did include such fluctuations in their higher-order closure planetary boundary-layer model, although such sophistication is prohibitively expensive for mesoscale applications. Moreover, as illustrated in Figure 7-10, accurate mean structure within daytime and nocturnal nonpolluted boundary layers apparently do not require such a detailed representation. For notational convenience, $\bar{\epsilon}$ is replaced by ϵ in the subsequent text.

14. In the absence of other cloud layers, the top part of Eq. (8-39) is used to determine $\overline{R}_{CB}\uparrow$, and the bottom of Eq. (8-39) is applied to calculate $\overline{R}_{CT}\downarrow$.

15. $W\uparrow = \int_{z_{CB}}^{z}\rho_i\bar{q}_1\,dz + \int_{z_{CB}}^{z}\rho_l\bar{q}_2\,dz$ and $W\downarrow = \int_z^{z_{CT}}\rho_i\bar{q}_1\,dz + \int_z^{z_{CT}}\rho_l\bar{q}_2\,dz$, where the contribution from the presence of ice has been added to the Stephens representation and ρ_i and ρ_l are the densities of ice and water. The appropriateness of including ice in this fashion needs to be determined.

16. An absorption efficiency for the electromagnetic radiation of wavelength λ is represented by $E_{a\lambda}$. In addition, the function $n(r)$, for mathematical clarity could also be written as $n(r, \delta r)$ to indicate that the magnitude of n is also a function of the chosen radius interval, δr. In this chapter, however, as is standard in publications on atmospheric radiation, this relation to δr is assumed when the function form $n(r)$ is used.

17. In deriving this expression, any variation of η_i and η_r with r is neglected.

18. The region of the electromagnetic spectrum between 8 and 14 μm is called the *atmospheric window*, since radiation is transmitted through the air relatively unattenuated at these wavelengths. CO_2 and water vapor do not have substantial absorption lines in this portion of the spectrum.

19. Equation (8-56) can be used with $b_{s_m} = 1$ only if the absorption of each different chemical species is over different intervals. If not, the regions of overlap in absorption for these materials must be corrected for (see, e.g., Eq. (8-38) for CO_2 and H_2O) to not include erroneous excessive absorption. To the author's knowledge, there has not been any work using a simple parameteri-

zation such as Eq. (8-56) for use in a mesoscale model, although it appears to be a reasonable representation.

20. $\delta_{sun} = 0.006918 - 0.399912 \cos d_0 + 0.070257 \sin d_0 - 0.006758 \cos 2d_0 + 0.000907 \sin 2d_0 - 0.002697 \cos 3d_0 + 0.001480 \sin 3d_0$; δ_{sun} is in radians (Paltridge and Platt 1976:63).

21. For large zenith angles, the influence of the earth's curvature should also be considered. For values of $Z \gtrsim 80°$, this expression for a_{q3} is very accurate. For larger values of Z, the ratio $1/\cos Z = \sec Z$ gives a result that is too large because of the curvature of the earth and refraction effects (see List 1971, Table 137).

22. The exception to this observation is over calm water bodies. Visible satellite imagery often reveals the disk image of the sun over ocean areas in which the winds are very light.

23. Representative values of A are given in Table 11-4.

24. Note that a_{q3} can be subtracted from t in this fashion, because there is little spectral overlap between absorption and scattering by the standard atmospheric gases and by water vapor. The standard gases scatter predominantly in the shorter visible wavelength, whereas water vapor absorbs mostly in the near-infrared spectrum.

25. Side lobes refer to local maxima in scattered radiation at various angles off of the original line of propagation of the electromagnetic energy.

26. For thick, low clouds, neglecting the extinction of shortwave radiation by water vapor and the other gases below clouds is reasonable. When the clouds are optically thin or at high levels, however, the reduction of solar radiation as it propagates through the air below the clouds should be included.

27. The total aerosol optical depth because of extinction $\tau_a = \int_0^\infty \int_{z_G}^\infty \beta_{e\lambda}\, dz\, d\lambda$ is called the *turbidity* (Liou 1980:238).

28. Paltridge and Platt (1976:225), however, caution against using mean absorption characteristics of a range of different aerosol types to compute absorption.

Additional Readings

Several texts were particularly useful in preparing this chapter.

Kondratyev, K. 1969. "Radiation in the Atmosphere." Academic Press, New York.
> Although its format and notation are somewhat difficult to follow in places, this classic text is a valuable source for a wide range of radiative transfer subjects. Particularly valuable is the treatment of fundamental principles in radiation.

Liou, K.-N. 1980. "An Introduction to Atmospheric Radiation." Academic Press, New York.
> The discussion of fundamentals in radiative transfer and of representations of infrared irradiance were well written and clearly documented. A comprehensive mathematical treatment of the Mie equations is included. A new version of Professor Liou's book was published in 1992 entitled "Radiation and Cloud Processes in the Atmosphere: Theory, Observation and Modeling" by Oxford University Press.

Paltridge, G. W., and C. M. R. Platt. 1976. "Radiative Processes in Meteorology and Climatology." Elsevier, Amsterdam.
> These authors emphasize the physical explanation of radiative transfer. Their discussions of shortwave and longwave irradiance in clouds and through aerosols was extensively used in this chapter.

Stephens, G. L. 1984. Parameterization of radiation for numerical weather prediction models. *Mon. Wea. Rev.* **112**, 826–867.

Other valuable review references include Rockel and Raschke (1994) and Stephens (1994).

Problems

1. Obtain a clear-sky longwave radiative flux divergence parameterization that is used in a model of your choice. Write the dependent variables, universal constants, and tunable coefficients that are used. Assess the differences that result with ±10% and ±25% changes in the values of the tunable coefficients and the dependent variables.

2. Do the same as in problem 1, but for direct and diffuse solar radiation.

3. Repeat problems 1 and 2 for a cloudy atmosphere.

4. Repeat problems 1 and 2 for a polluted atmosphere.

5. Obtain a copy of the NCAR Community Climate Radiation Model (CRM) and decompose the specific algorithms that are used for the radiative fluxes, using the same techniques as in problems 1–4. The model version 2.0 is available at http://www.cgd/ucar.edu/cms/crm.

Chapter 9

Parameterization of Moist Thermodynamic Processes

9.1 Introduction

   In many mesoscale systems such as the sea breeze and squall line, phase changes of water occur as mesoscale and/or subgrid-scale circulations lift air above its condensation level and as water falls back out of or detrains from clouds and begins to evaporate. The presence of water as solid, liquid, and gas necessitates that the complete form of the conservation equations for water substance [e.g., Eq. (4-25)] be included in a mesoscale model. In addition, the proper representation of the source–sink term for diabatic heating [i.e., S_θ in Eq. (4-24)] is required. This chapter discusses procedures to allow the effects of the phase change of water to be included in grid-volume–averaged conservation equations, such as given by Eqs. (4-24) and (4-25).

   To parameterize the effects of phase changes in a mesoscale model, it is helpful to catalog the grid-volume–averaged atmosphere in a vertical column as *convectively stable* if $\partial \bar{\theta}_E / \partial z > 0$ everywhere above the condensation-sublimation level of z_{cl}, or *convectively unstable* if for at least one level above z_{cl}, $\partial \bar{\theta}_E / \partial z \leq 0$. When a layer is convectively stable, forced lifting of the layer must continue to sustain the conversion of water vapor to liquid or solid once the specific humidity equals the saturation-specific humidity. If the layer is convectively unstable, however, clouds continue to grow without further forced lifting of the layer once saturation is reached. Convective instability is also called *potential instability*, or *layer instability*.

   The variable $\bar{\theta}_E$, the grid-volume–averaged *equivalent potential temperature*, is used to determine grid-volume–averaged convective instability. This temperature is derived as follows from the conservation-of-heat relation expressed by Eq. (2-23). Let the contribution resulting from the first three terms in

Eq. (2-24) for the source–sink term S_θ be written as

$$\frac{C_\mathrm{p}}{\theta} S_\theta^* = -\left(\delta_\mathrm{f} L_\mathrm{f} + \delta_\mathrm{c} L_\mathrm{c}\right) T_\mathrm{v}^{-1} \frac{dq_\mathrm{s}}{dt} = \frac{C_\mathrm{p}}{\theta} \frac{d\theta}{dt}, \tag{9-1}$$

where q_s is the saturation-specific humidity[1] and L_c and L_f are the latent heats of condensation and freezing, respectively ($L_\mathrm{c} = 2.5 \times 10^6$ J kg^{-1} and $L_\mathrm{f} = 0.33 \times 10^6$ J kg^{-1} at 0°C).[2] The parameters $\delta_\mathrm{f} = 1$ if freezing or melting occurs, $\delta_\mathrm{c} = 1$ if condensation or evaporation occurs, $\delta_\mathrm{c} = \delta_\mathrm{f} = 1$ if deposition or sublimation occurs, and 0 otherwise. Using Eq. (2-22), Eq. (9-1) can also be written as

$$C_\mathrm{p} \frac{d\theta}{\theta} = -L T_\mathrm{v}^{-1} dq_\mathrm{s} \simeq -L d\left(q_\mathrm{s}/T_\mathrm{v}\right), \tag{9-2}$$

where the approximation $T_\mathrm{v}^{-1} \left| dq_\mathrm{s} \right| \gg q_\mathrm{s} T_\mathrm{v}^{-2} \left| dT_\mathrm{v} \right|$ has been used[3] and L is equal to either L_c or $L_\mathrm{f} + L_\mathrm{c}$.

If at low temperatures, $q_\mathrm{s}/T_\mathrm{v} \to 0$ (i.e., the saturation-specific humidity goes to 0 faster than temperature approaches absolute 0 [see, e.g., Eq. (9-8)], then Eq. (9-2) can be integrated to yield

$$C_\mathrm{p} \int_\theta^{\theta_\mathrm{ES}} d\ln\hat\theta = -L \int_{q_\mathrm{s}/T_\mathrm{v}}^0 d\left(\hat q_\mathrm{s}/\widehat{T}_\mathrm{v}\right),$$

where C_p and L are treated as constants. The upper limit of integration θ_ES is called the *saturation equivalent potential temperature*, since specific humidity is given by its saturated value q_s. The integrated form of this relation can then be written as

$$\theta_\mathrm{ES} = \theta \exp\left(\frac{L}{C_\mathrm{p}} \frac{q_\mathrm{s}}{T_\mathrm{v}}\right) = \theta \exp\left(\frac{L q_\mathrm{s}}{\pi \theta}\right), \tag{9-3}$$

where the definition of π given after Eq. (4-36) is used. With $L = L_\mathrm{c}$, θ_ES represents the saturation equivalent potential temperature with respect to liquid water, and with $L = L_\mathrm{c} + L_\mathrm{f}$, the temperature is defined with respect to ice. This formulation for θ_ES is a measure of the change in potential temperature if all of the moisture is condensed ($L = L_\mathrm{c}$), or deposited, or condensed and frozen ($L = L_\mathrm{c} + L_\mathrm{f}$), with the heat released used to warm a parcel of air. Because of the approximations made [e.g., Eq. (9-2)], the expression is not exact (see Simpson 1978 and Bolton 1980 for a precise derivation of θ_ES); however, it is in a suitable form for use in most mesoscale model calculations.[4]

The grid-volume–averaged form of Eq. (9-3) is defined by replacing the instantaneous values of the dependent variables in Eq. (9-3) with their grid-volume–averaged counterparts. Expressed formally,

$$\bar\theta_\mathrm{ES} = \bar\theta \exp\left(L \bar q_\mathrm{s}/C_\mathrm{p} \overline{T}_\mathrm{v}\right) = \bar\theta \exp\left(L \bar q_\mathrm{s}/\bar\pi \bar\theta\right). \tag{9-4}$$

When an air panel is not saturated, $\bar{q}_s$ in Eq. (9-4) is replaced by the specific humidity of the parcel $\bar{q}$, yielding

$$\bar{\theta}_E = \bar{\theta}\exp\left(L\bar{q}/\bar{\pi}\bar{\theta}\right), \tag{9-5}$$

where $\bar{\theta}_E$ is the *equivalent potential temperature*. A layer with $\partial\bar{\theta}_E/\partial z \leq 0$ will become less stable as it is lifted (as shown graphically by, e.g., Byers 1959:191), whereas a layer with $\partial\bar{\theta}_E/\partial z > 0$ will become more stable. It is the vertical distribution of $\bar{\theta}_E$ that is used to assess convective stability.

Betts (1974) has demonstrated that vertical profiles of the difference $\bar{\theta}_{ES} - \bar{\theta}_E$ is a measure of convective regimes. Over Venezuela, he found that in the lowest levels (i.e., the 10-mb layer nearest the ground) $\bar{\theta}_{ES} - \bar{\theta}_E = 40°C$ or so on dry days, and this difference was reduced by about half on disturbed days with extensive cumulus connection.

9.2   Parameterization of the Influences of Phase Changes of Water in a Convectively Stable Atmosphere ($\partial\bar{\theta}_E/\partial z > 0$)

If the atmosphere is convectively stable on the resolvable scale (i.e., $\partial\bar{\theta}_E/\partial z > 0$) everywhere in a column above the lowest saturation level,[5] and if a layer is lifted until saturation occurs, then one of the following will apply:

1.   Only stratiform clouds will develop if $\partial\theta_E/\partial z$ is also greater than 0 everywhere within all of the grid volumes that are saturated.[6]

2.   Some cumuliform clouds can develop if $\partial\theta_E/\partial z \leq 0$ locally within one or more grid volumes that are saturated. The number, height, and vigor of these clouds is expected to depend on the magnitude and distribution of these regions of subgrid-scale convective instability.

Figure 9-1 illustrates examples, as seen from below the cloud base, of a situation when only stratiform clouds develop and of a situation when some cumulus convection develops in an otherwise layered stratiform cloud layer. Sommeria and Deardorff (1977) discuss the use of a statistical model when only a portion of a grid volume becomes saturated in a planetary boundary-layer model. Vali *et al.* (1998) illustrate the observed variable spatial structure of stratus clouds.

The mechanics of precipitation formation within these two categories of equivalent potential temperature stratification are very different. As summarized by Houze (1981), stratiform precipitation occurs with weak ascending motion with precipitation particles forming near the top of the clouds and growing as they fall. Convective precipitation is associated with strong updrafts, where

Fig. 9-1.   (a) A stratus cloud over northern Illinois, December 1, 1974, and (b) a stratocumulus cloud over Gogebic, in the upper peninsula of Michigan, June 1972. (Photographed by Ron Holle.)

cloud droplets are initiated near the cloud base and grow as they are transported upward. Precipitation from convective systems falls to the ground when gravitational sedimentation exceeds the upward velocity within the cloud or when the precipitation is advected to regions within or outside of the cloud where the ascent is weak or negative.

9.2.1 Convectively Stable Everywhere Within a Column Above the Saturation Level

9.2.1.1 Detailed Representation of the Microphysics

In an atmosphere that is convectively stable at all points within a grid volume, the conversion of water between its phases can be represented straightforwardly using formulations such as those developed for cloud models. The degree of sophistication can involve a detailed simulation of the microphysics, including nuclei activation and the growth to precipitation-sized liquid and ice particles. Taylor and Ackerman (1999), for example, found that the microphysical structure and cloud top of stratus clouds were significantly affected by aerosol emissions from a ship into otherwise clean maritime clouds. To study these types of effects, Clark (1973) incorporated a detailed representation of *warm cloud* (i.e., $T > 0°C$ everywhere in the cloud) *microphysics* in his cumulus model. As pointed out by Orville (1980), the conservation-of-water equation [e.g., Eq. (4-25)] can be broken into as many as 50–100 equations to represent the growth of cloud droplets to precipitation-sized particles. One equation for each size category of liquid or ice particles is used. However, with present computer limitations, such sophistication is not practical in a mesoscale model. Interested readers who desire a thorough discussion of the procedure used to represent the microphysics in detail are referred to Orville (1980, Section 3.1), Pruppacher (1982), and Pruppacher and Klett (1978) for an extensive review of this subject.

9.2.1.2 Bulk Representation of the Microphysics

An alternative to the detailed microphysical representation is called the *parameterized microphysical* or *bulk* representation. With this procedure, liquid water and ice can be categorized into the four classes:

- cloud liquid water
- cloud ice
- rain
- snow.

Thus the equations for $\partial \bar{q}_1/\partial t$ and $\partial \bar{q}_2/\partial t$ in Eq. (4-25) need to be composed into only two equations each. The reason for this particular form of categorization is that rain and snow are assumed to have a size such that gravitational sedimentation is appreciable (i.e., they have a significant *fall velocity*),[7] whereas cloud liquid water and cloud ice do not.

9.2.1.2.1   The Conservation Equations for Water and Potential Temperature. With these decompositions and following Orville (1980), Eq. (4-25) can be written as

$$\frac{\partial \bar{q}_1^{\text{ci}}}{\partial t} = -\bar{u}_j \frac{\partial}{\partial x_j} \bar{q}_1^{\text{ci}} - \frac{1}{\rho_0} \frac{\partial}{\partial x_j} \rho_0 \overline{u_j'' q_1''^{\text{ci}}} + S_{\text{freezing}} + S_{\text{deposition}} - P_{\text{S1}} - P_{\text{S2}},$$

$$\frac{\partial \bar{q}_1^{\text{s}}}{\partial t} = -\bar{u}_j \frac{\partial}{\partial x_j} \bar{q}_1^{\text{s}} - \frac{1}{\rho_0} \frac{\partial}{\partial x_j} \rho_0 \overline{u_j'' q_1''^{\text{s}}} - V_T^{\text{s}} \frac{\partial}{\partial z} \bar{q}_1^{\text{s}}$$
$$+ P_{\text{S1}} + P_{\text{S2}} + P_{\text{S3}} + P_{\text{S4}} - P_{\text{S5}},$$

$$\frac{\partial \bar{q}_2^{\text{cw}}}{\partial t} = -\bar{u}_j \frac{\partial}{\partial x_j} \bar{q}_2^{\text{cw}} - \frac{1}{\rho_0} \frac{\partial}{\partial x_j} \rho_0 \overline{u_j'' q_2''^{\text{cw}}} + S_{\text{condensation}} + S_{\text{freezing}} \qquad (9\text{-}6)$$
$$- P_{\text{R1}} - P_{\text{R2}} - P_{\text{S3}},$$

$$\frac{\partial \bar{q}_2^{\text{R}}}{\partial t} = -\bar{u}_j \frac{\partial}{\partial x_j} \bar{q}_2^{\text{R}} - \frac{1}{\rho_0} \frac{\partial}{\partial x_j} \rho_0 \overline{u_j'' q_2''^{\text{R}}} - V_T^{\text{R}} \frac{\partial}{\partial z} \bar{q}_2^{\text{R}} + P_{\text{R1}} + P_{\text{R2}} + P_{\text{S5}} - P_{\text{R3}},$$

$$\frac{\partial \bar{q}_3}{\partial t} = -\bar{u}_j \frac{\partial}{\partial x_j} \bar{q}_3 - \frac{1}{\rho_0} \frac{\partial}{\partial x_j} \rho_0 \overline{u_j'' q_3''} - S_{\text{condensation}} - S_{\text{deposition}} - P_{\text{S4}} + P_{\text{R3}},$$

where $\bar{q}_1^{\text{ci}}$, $\bar{q}_1^{\text{s}}$, $\bar{q}_2^{\text{cw}}$, and $\bar{q}_2^{\text{R}}$ are the grid-volume–averaged values of specific humidity for cloud ice, snow, cloud water, and rain, respectively. The notations S_{freezing}, $S_{\text{deposition}}$, and $S_{\text{condensation}}$ represent changes in $\bar{q}_1^{\text{ci}}$, $\bar{q}_2^{\text{cw}}$, and $\bar{q}_3$ resulting from freezing, deposition, and condensation [see after Eq. (2-34)], respectively, and P_{R1}, P_{R2}, P_{R3}, P_{S1}, P_{S2}, P_{S3}, P_{S4}, and P_{S5} represent different mechanisms for the conversion of cloud ice and cloud water to snow and rain that are defined in, for example, Section 9.4.1. The fall velocities of snow and ice are V_T^{s} and V_T^{R}, respectively.

The vertical subgrid-scale flux terms in Eq. (9-6) (e.g., $\overline{u_j'' q_1''^{\text{ci}}}$) can be represented by

$$\overline{w'' q_1''^{\text{ci}}} = -K_\theta \frac{\partial \bar{q}_1^{\text{ci}}}{\partial z}, \qquad \overline{w'' q_1''^{\text{s}}} = -K_\theta \frac{\partial \bar{q}_1^{\text{s}}}{\partial z},$$

$$\overline{w'' q_2''^{\text{cw}}} = -K_\theta \frac{\partial \bar{q}_2^{\text{cw}}}{\partial z}, \qquad \overline{w'' q_2''^{\text{R}}} = -K_\theta \frac{\partial \bar{q}_2^{\text{R}}}{\partial z}, \qquad \text{and} \qquad \overline{w'' q_3''} = -K_\theta \frac{\partial \bar{q}_3}{\partial z},$$

where K_θ could be evaluated using Eq. (7-57), except that with saturated air, the gradient Richardson number should be redefined as

$$R_i = \frac{g}{\theta_0} \frac{\partial \bar{\theta}_{ES}}{\partial z} \bigg/ \left[\left(\frac{\partial \bar{u}}{\partial z} \right)^2 + \left(\frac{\partial \bar{v}}{\partial z} \right)^2 \right].$$

The source–sink terms in Eq. (9-6) can be written as

$$S_{\text{deposition}} = -\delta_s \, \bar{w} \, \frac{\partial \bar{q}_{si}}{\partial z}, \qquad \overline{T}_V \leq T_0^s; \quad \bar{q}_3 = \bar{q}_{si}, \quad \text{then } \delta_s = 1;$$

$$S_{\text{condensation}} = -\delta_c \, \bar{w} \, \frac{\partial \bar{q}_{sw}}{\partial z}, \qquad \overline{T}_V > T_0^s; \quad \bar{q}_3 = \bar{q}_{sw}, \quad \text{then } \delta_c = 1; \qquad (9\text{-}7)$$

$$S_{\text{freezing}} = \delta_f \, \frac{\delta \bar{q}^{ci}}{\delta t}, \qquad\qquad \overline{T}_V \leq T_0^f; \quad \bar{q}_2^{cw} > 0, \quad \text{then } \delta_f = 1,$$

where $\bar{q}_{si}$ and $\bar{q}_{sw}$ are the saturation-specific humidities with respect to ice and water, respectively, and $\delta_s = 1$ when deposition or sublimation occurs[8] but 0 otherwise. The threshold temperatures[9] in Eq. (9-7) are defined as occurring when the air is cold enough such that direct vapor to ice conversion occurs (T_0^s) and such that the liquid water freezes (T_0^f). Equation (9-7) considers only vertical gradients, because they are usually much larger, in general, than the horizontal gradients of saturation-specific humidity. A similar assumption was made in defining radiative flux divergence for use in mesoscale models [i.e., Eq. (8-1)]. The quantity $\delta \bar{q}_1^{ci}/\delta t$, which represents the freezing of cloud water, could be defined such that complete glaciation from cloud water occurs within one time step once $\overline{T}$ becomes less than or equal to T_0^f.

The saturation-specific humidity of water vapor with respect to liquid water and to ice is determined using the Clausius-Clapeyron equation (see, e.g., Wallace and Hobbs 1977:95). This equation for liquid water and ice can be written as

$$de_{sw}/e_{sw} = L_c \, dT/(R_v T_v^2); \qquad de_{si}/e_{si} = L_s \, dT/(R_v T_v^2),$$

where e_{sw} and e_{si} are the saturation vapor pressures of water vapor with respect to liquid water and ice, respectively. (See List 1971:351–364 for specific values of e_{sw} and e_{si}.) The gas constant for water vapor is R_v ($R_v = 461$ J K kg^{-1}; Wallace and Hobbs 1977), with T_v the virtual temperature.

Since saturation-specific humidity and vapor pressure are related by

$$q_s = 0.622 e_s/(p - 0.378 e_s) \simeq 0.622 e_s/p, \qquad e_s \ll p,$$

we have

$$\frac{dq_{si}}{q_{si}} = \frac{L_s}{R_v} \frac{dT}{T_v^2} \qquad \text{and} \qquad \frac{dq_{sw}}{q_{sw}} = \frac{L_c dT}{R_v T_v^2}$$

if the change in saturation vapor pressure is assumed to occur isobarically (i.e., $dp \equiv 0$). As T approaches 0 K, q_{sw} and q_{si} approach 0, since e_{sw} and e_{si} approach 0 at that temperature.

The saturation-specific humidities of water vapor with respect to liquid water and ice for reasonable values of temperature and pressure within the troposphere are then given by

$$q_{si} \simeq \frac{3.8}{\bar{p}} \exp\left[\frac{21.9(\overline{T}_v - 273.2)}{\overline{T}_v - 7.7}\right]$$

$$q_{sw} \simeq \frac{3.8}{\bar{p}} \exp\left[\frac{17.3(\overline{T}_v - 273.2)}{\overline{T}_v - 35.9}\right] \tag{9-8}$$

(where T_v is in degrees Kelvin), using the empirical formulas for e_{sw} and e_{si} given by Murray (1967). A similar formulation for q_{sw} can be derived from Bolton's (1980) representation of e_{sw}. At $\bar{p} = 1000$ mb, the maximum difference between q_{sw} and q_{si} occurs at $\overline{T} \simeq 12°C$ and is equal to approximately 0.2 g kg^{-1}. At all temperatures below 0°C, $q_{sw} > q_{si}$.

The influence of these phase changes on the potential temperature in Eq. (4-24) can be written as

$$\frac{\partial \theta}{\partial t} = -\bar{u}_j \frac{\partial \bar{\theta}}{\partial x_j} - \frac{1}{\rho_0} \frac{\partial}{\partial x_j} \rho_0 \overline{u_j'' \theta''} - \frac{\bar{\theta}}{\overline{T}_v C_p}\left[\delta_s L_s\left(\bar{w} \frac{\partial \bar{q}_{si}}{\partial z} - P_{S4}\right)\right.$$

$$\left. + \delta_c L_c\left(\bar{w} \frac{\partial \bar{q}_{sw}}{\partial z} + P_{R3}\right) - \delta_f L_f\left(\frac{\delta \bar{q}_1^{ci}}{\delta t} - P_{S5} + P_{S3}\right)\right] \tag{9-9}$$

using Eq. (9-1) with $L_f + L_c = L_s$. In Eq. (9-9), $\bar{\theta}/(\overline{T}_v C_p)$ can be replaced with $1/\bar{\pi}$, using the definition of π given after Eq. (4-36).

However, using Eqs. (9-6) and (9-7) requires that changes of heat content caused by the phase changes of water be considered, since from Eq. (9-8), $\bar{q}_{si}$ and $\bar{q}_{sw}$ are functions of temperature. One procedure to account for this effect in the absence of precipitation-sized particles is to use an algorithm given by

$$\left.\frac{\partial \bar{\theta}}{\partial t}\right|_{pc}^n = \frac{1}{\bar{\pi}}\left[-\delta_s L_s \bar{w} \left.\frac{\partial \bar{q}_{si}}{\partial z}\right|^n - \delta_c L_c \bar{w} \left.\frac{\partial \bar{q}_{sw}}{\partial z}\right|^n + \delta_f L_f \left.\frac{\delta \bar{q}_1^{ci}}{\delta t}\right|^n\right],$$

$$\left.\frac{\partial \bar{q}_1^{ci}}{\partial t}\right|_{pc}^n = -\delta_s \bar{w} \left.\frac{\partial \bar{q}_{si}}{\partial z}\right|^n + \delta_f \left.\frac{\delta \bar{q}_1^{ci}}{\delta t}\right|^n,$$

$$\left.\frac{\partial \bar{q}_2^{cw}}{\partial t}\right|_{pc}^n = -\delta_c \bar{w} \left.\frac{\partial \bar{q}_{sw}}{\partial z}\right|^n - \delta_f \left.\frac{\delta \bar{q}_1^{ci}}{\delta t}\right|^n, \tag{9-10}$$

$$\left.\frac{\partial \bar{q}_3}{\partial t}\right|_{pc}^n = +\delta_c \bar{w} \left.\frac{\partial \bar{q}_{sw}}{\partial z}\right|^n + \delta_s \bar{w} \left.\frac{\partial \bar{q}_{si}}{\partial z}\right|^n,$$

where $n = 1, 2, 3, \ldots, N$ represents the number of iterations required before the local changes in $\bar{\theta}$, $\bar{q}_1^{\text{ci}}$, $\bar{q}_2^{\text{cw}}$, and $\bar{q}_3$ resulting from phase changes approach 0.[10] [Conversions to and from precipitation-sized particles are ignored in Eq. (9-10), although it would be straightforward to add these effects if equations for $\bar{q}_1^{\text{S}}$ and $\bar{q}_2^{\text{R}}$ from Eq. (9-6) were also included.]

During each iteration, Eq. (9-8) is used to determine a new saturation-specific humidity and to evaluate the relation of the actual temperature to the threshold temperatures in Eq. (9-7). The initial values of $\bar{\theta}$, $\bar{q}_1^{\text{ci}}$, $\bar{q}_2^{\text{cw}}$, and $\bar{q}_3$ in the iteration are evaluated from the first two terms on the right side of Eqs. (9-6) and (9-9). The vertical velocity $\bar{w}$ remains constant during the iteration. McCumber (1980), in his determination of the appropriate values for potential temperature and specific humidity for water vapor in a water cloud, used convergence criteria for $\partial\bar{\theta}/\partial t|_{pc}^n$ and $\partial\bar{q}_3/\partial t|_{pc}^n$ of 0.05 K/120 s and 0.005 g kg^{-1}/120 s. No more than 17 iterations were ever required in his three-dimensional mesoscale simulation of rainfall over south Florida.

9.2.1.2.2   Simplified Forms for the Conservation of Water.   In the past, most mesoscale models have used a simpler form than Eq. (9-6) to represent phase changes. For example McCumber (1980), using a procedure introduced by Asai (1965), determines whether a grid volume has been supersaturated with respect to liquid water. If it has, then temperature is adjusted using a formulation similar to Eq. (9-10), with condensate formed so as to reduce the supersaturation to 0.[11] All of the remaining condensate, which is assumed to be of precipitation size, falls to the next grid level. If this layer is subsaturated, then some or all of the precipitation will evaporate, causing cooling and moistening. If condensate remains and the layer becomes saturated, then the precipitation falls to the next level. This process continues until all of the precipitation either evaporates or reaches the ground.

Nickerson (1979), in contrast, permitted only cloud water and excluded precipitation. Although not detailed in his paper, cloud water appears to be created using a formulation such as given by $S_{\text{condensation}}$ in Eq. (9-7) and advected with an equation similar to $\partial\bar{q}_2^{\text{cw}}/\partial t$ in Eq. (9-6) but ignoring the last three terms.

Colton (1976) used a somewhat more sophisticated parameterization for clouds and precipitation. Although he only had one equation for liquid water [i.e., he combined $\partial\bar{q}_2^{\text{cw}}/\partial t$ and $\partial\bar{q}_2^{\text{R}}\partial t$ in Eq. (9-6), with none for ice], he included terminal velocities, developed by Ogura and Takahashi (1971), which are representative of rain and snow. When the temperature was at or below 0, he used a terminal velocity representative of snow, and above freezing he used a rainwater value. The expressions that he used are given as

$$V_{\text{T}}^{\text{R}} = \begin{cases} 31.2\left(\bar{\rho}\bar{q}_2^{\text{cw}}\right)^{0.125}, & \overline{T} > 0°\text{C} \\ 5.9\left(\bar{\rho}\bar{q}_2^{\text{cw}}\right)^{0.11}, & \overline{T} \leq 0°\text{C}, \end{cases}$$

where to use these formulas as given, $\bar{\rho}$ must be in grams per centimeters cubed. V_T^R then is in meters per second.

Colton permitted no supersaturation and used a direct method to compute the amount of condensate given by

$$\overline{T}_v = \overline{T}_v^* + L_c \delta M_1/C_p,$$
$$\bar{q}_2 = \bar{q}_2^* + \delta M_1 \quad (\bar{q}_2 = \bar{q}_2^R + \bar{q}_2^{cw}), \qquad (9\text{-}11)$$
$$\bar{q}_3 = \bar{q}_3^* - \delta M_1,$$

where $\bar{q}_2^*$ and $\bar{q}_3^*$ are changes in specific humidity for liquid water and water vapor resulting from advection and subgrid-scale fluxes; (that is, the first two terms in each of the last three equations in Eq. (9-6). If $\delta M = \bar{q}_3^* - \bar{q}_{sw}$, then

$$\delta M_1 = \delta M \left[1 + L_c^2 \bar{q}_{sw}/\left(C_p R_v \overline{T}_v^{*2} \right) \right]^{-1}.$$

The temperature $\overline{T}_v^*$ is computed from $\bar{\theta}^*$, which is calculated from the first two terms on the right of Eq. (9-9). Using the definition of θ given by Eq. (2-48) and the definition of π given after Eq. (4-36), $\overline{T}^* = \theta^* \bar{\pi}/C_p$. As shown by Asai (1965) and used by Ogura and Takahashi (1973), this expression for δM_1 provides an exact evaluation for the changes in temperature and water content caused by moistening and warming caused by condensation. Evaporation can also be determined using Eq. (9-11), since $\delta M_1 < 0$ when $\bar{q}_3^* < \bar{q}_{sw}$ (i.e., the air is subsaturated). Colton apparently calculated precipitation rates at the surface from the term $V_T^R \bar{q}_2$, which is evaluated from values of these terms at the first model level above the ground. As illustrated in Figure 9-2, Colton successfully in predicted precipitation rates using his scheme.
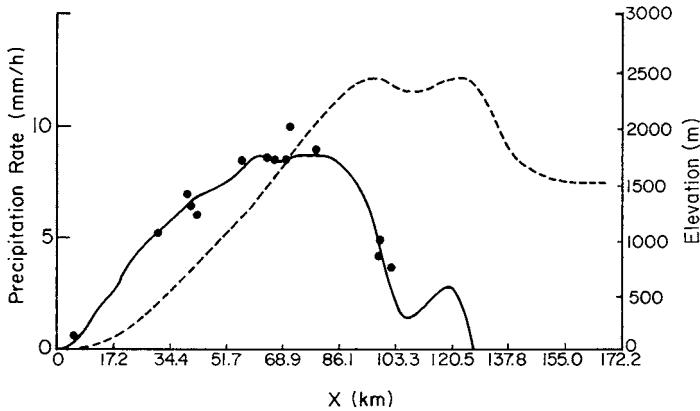
Fig. 9-2. Model-predicted precipitation rates (solid line) and observed precipitation rates (black dots) along a cross-section of the Sierra Nevada (dashed line) for December 21-22, 1964. (Adapted from Colton 1976.)

9.2.2   Subgrid-Scale Regions of Convective Instability Above the Saturation Level but with $\partial \bar{\theta}_{\mathrm{E}} / \partial z > 0$

Up to this point in Section 9.2, only the situation $\partial \theta_{\mathrm{E}} / \partial z > 0$ everywhere has been considered in the parameterization. When the atmosphere has subgrid regions that are convectively unstable *and* in which condensation or sublimation occur, the representations for phase change previously mentioned may be unsatisfactory. This is particularly true if these regions of $\partial \theta_{\mathrm{E}} / \partial z < 0$ extend through a significant depth of the atmosphere and cover a substantial portion of the grid domain. To represent these regions in a mesoscale model, when the grid-volume–averaged vertical gradient of equivalent potential temperature is stable (i.e., $\partial \bar{\theta}_{\mathrm{E}} / \partial z > 0$), will require innovative parameterization techniques. Indeed, to accurately represent moist thermodynamics for such a situation, it may be necessary to reduce the grid volume.

9.3   Parameterization of the Influences of Phase Changes of Water in a Convectively Unstable Atmosphere ($\partial \bar{\theta}_{\mathrm{E}} / \partial z \leq 0$)

If the atmosphere is convectively unstable on the resolvable scale (i.e., $\partial \bar{\theta}_{\mathrm{E}} / \partial z \leq 0$) somewhere in a column above the lowest saturation level and saturation occurs where $\partial \bar{\theta}_{\mathrm{E}} / \partial z$ is less than or equal to 0, then (1) only cumuliform clouds will form if $\partial \theta_{\mathrm{E}} / \partial z \leq 0$ everywhere within saturated grid volumes in that column, or (2) some layer-form clouds can form if $\partial \bar{\theta}_{\mathrm{E}} / \partial z > 0$ locally within a grid volume, which is saturated. The extent and levels of such clouds depend on the distribution of regions that are convectively stable.

Figure 9-3 illustrates examples, as seen from below the base, when only cumuliform clouds develop and when some layered clouds form in a predominantly cumuliform cloud mass. Johnson *et al.* (1999) suggests that there are three distinct types of tropical convective clouds: shallow cumulus, cumulus congestus, and cumulonimbus. Nair *et al.* (1998) used satellite imagery to determine the spatial patterning of cumulus cloud fields.

Cumuliform clouds also form when the top of the planetary boundary exceeds the saturation level and the surface layer is superadiabatic. For this situation, cumulus clouds are the visible manifestation of the turbulent eddies within the planetary boundary layer. When such clouds occur with $\partial \theta_{\mathrm{E}} / \partial z > 0$ everywhere above the boundary layer, their growth into deeper cumulus clouds (e.g., cumulus congestus) will not occur. Sommeria (1976) investigated turbulent processes in a tradewind boundary layer over water when such shallow cumulus

Fig. 9-3.   (a) A group of cumulus clouds over southern Florida at 0930 LST, August 15, 1978, and (b) a cumulus congestus complex with layered clouds on its periphery located in southern Arizona at 1615 LST, October 23, 1974. (Photographed by Ron Holle.)

clouds formed, using an extension of Deardorff's (1973) sophisticated planetary boundary-layer model.

In contrast with stratiform cloud systems, cumulus clouds generally have smaller spatial dimensions and more irregular patterns of updrafts and downdrafts. Except for cumulonimbus-size systems, individual cumulus clouds have smaller horizontal dimensions than can be resolved by a mesoscale model grid. Moreover, the depth that a cumulus cloud attains depends more on the magnitude and vertical distribution of convective instability than on the intensity of the mesoscale ascent, once saturation is attained. Along with such effects as precipitation, downdrafts, ground shadowing, and cumulus-induced subsidence, the accurate representation of the influence of cumulus clouds on the mesoscale has been and will remain one of the more difficult problems in mesoscale meteorology.

The ability to represent cumulus clouds accurately in a mesoscale model requires that the mesoscale dynamic and thermodynamic structure control the regions of initiation and development of this moist convective activity. There is evidence that this situation occurs. As illustrated in Figure 9-4(b), for example, Ulanski and Garstang (1978) found significant correlation between boundary-layer convergence patterns and subsequent cumulus-produced rainfall over land. This low-level convergence was found to precede cumulus rainfall by as much as 90 minutes. They also found that the amount of rainfall was significantly correlated with the duration of the precedent boundary-layer convergence, as shown in Figure 9-4(a). Holle and Watson (1983) found from their dataset that (defining an event period as the time between initial surface convergence and complete dissipation) that the first visible cloud occurs at an average of about 1/6 into this period, with the most rapid cloud growth at around 1/3 of the event lifetime. Doneaud *et al.* (1983) confirmed the relationship between antecedent low-level convergence and subsequent cumulus convective activity over southeastern Montana, although Achtemeir (1983) found the relationship between convergence and rainfall to be more complex over St. Louis based on summer METROMEX 1975 data.

On a larger spatial scale, Pielke (1974a) also found qualitative agreement between predicted sea-breeze convergence and the subsequent actual development of cumulonimbus activity, and Simpson *et al.* (1980) obtained a large positive correlation between merged thunderstorm complexes and sea-breeze convergence for three case study days over south Florida. For a particular summer day over south Florida, Pielke and Mahrer (1978) obtained a 4-hour lag between this predicted mesoscale convergence and thunderstorm activity. Pielke *et al.* (1991) and Pielke (2001) summarized how mesoscale convergence preconditions the environment for thunderstorm development. Most of the rainfall in these sea-breeze events occurs in large cumulonimbus complexes (Simpson *et al.* 1980).
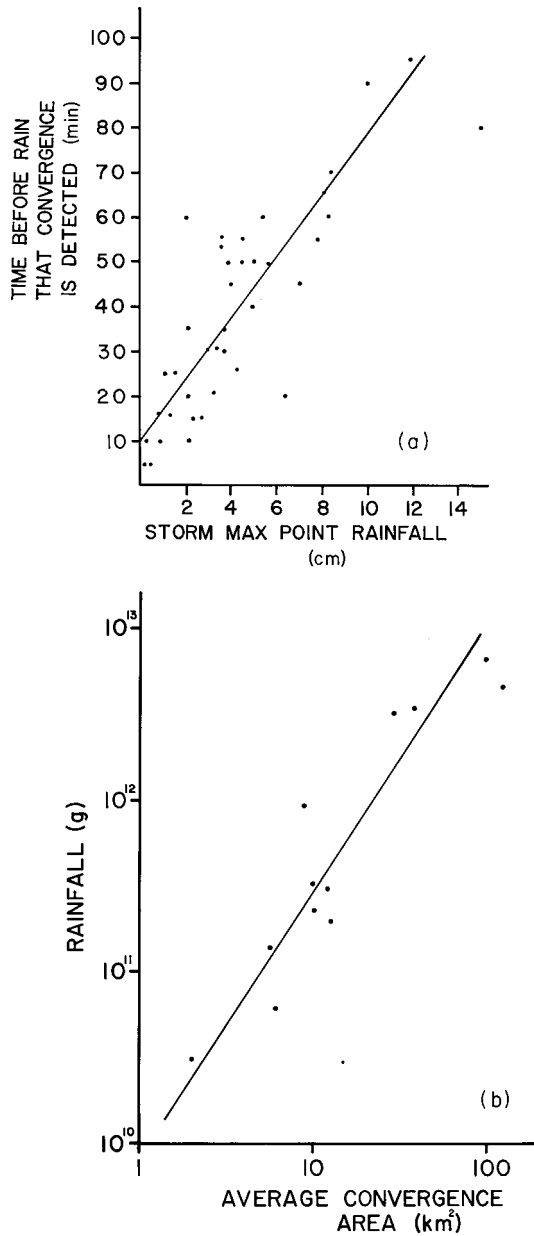
Fig. 9-4. (a) The relationship between the duration of boundary-layer convergence and subsequent rainfall during a summer season over south Florida, and (b) the relation between convergence area and rainfall amount. (From Ulanski and Garstang 1978.)

In the 1974 GARP Atlantic Tropical Experiment (GATE), Ogura *et al.* (1979) found low-level convergence to be present or enhanced before the development of organized convective systems in all cases considered. Krishnamurti *et al.* (1983) concluded from the GATE data that incorporating the influence of mesoscale convergence is essential for successful cumulus parameterization. Over Oklahoma, Sun and Ogura (1979) observed a well-defined band of low-level convergence, apparently generated by a horizontal temperature gradient, to precede the development of showers and thunderstorms for a particular day.

In considering methodologies to represent cumulus clouds in a mesoscale model, it is useful to group them into the four classes:

- convective adjustment
- use of one-dimensional cloud models
- use of a cumulus field model, or set of equivalent observations
- explicit representation of moist thermodynamics.

9.3.1 Convective Adjustment

With the first method, as discussed by Kurihara (1973), Krishnamurti *et al.* (1980), and others, the lapse rate is forced to be moist adiabatic over all or part of the model grid when saturation occurs. This is the simplest and cheapest form of cumulus parameterization, although unfortunately with this approach, regions of potential instability are removed too quickly on the mesoscale. In addition, this scheme provides poor vertical profiles of the averaged subgrid-scale heating and moistening. For these reasons, more sophisticated parameterization schemes have been developed (Hong and Pan 1998). Haltiner and Williams (1980) review convective adjustment schemes for use in larger-scale models.

9.3.2 Use of One-Dimensional Cloud Models

In the second group, Kuo (1965, 1974), Krishnamurti and Moxim (1971), Ooyama (1971), Arakawa and Schubert (1974), Yenai (1975), Kreitzberg and Perkey (1976, 1977), Anthes (1977), Johnson (1977), Fritsch and Chappell (1980a,b), Yamazaki and Ninomiya (1981), Molinari (1982), Hong and Pan (1998), Gallus (1999) and others discuss or use one-dimensional cloud models to represent the feedback of cumulus scales to the larger scale. In using one-dimensional models, it has often been assumed that in deep cumulonimbus systems, the vertical distribution of heating on the cloud scale is essentially the same as the vertical distribution of heating on the model grid scale (see, e.g., Anthes 1977), although such an assumption is certainly not true for shallow

cumulus or when substantial downdrafts exist. Using this approach, Kuo and Raymond (1980) concluded that the main heating from cumulus activity was from latent heat release, although subsidence warming is also important, particularly close to cloud top. Yenai (1975) presented a review of these types of cumulus representations, as did Hsu (1979), who also used an extension of Kuo's (1974) parameterization. An early but useful summary of cumulus parameterization is given by Ogura (1972). Cotton (1975) and Simpson (1976, 1983) provide reviews of one-dimensional cumulus models. One-dimensional models of clouds are also referred to as *single-column models* (see, e.g., Das *et al.* 1999; Wu *et al.* 2000b).

The previous types of schemes achieve closure by assuming either that moisture convergence in the lower troposphere supplied by the mesoscale or a larger scale is necessary for cumulus development or that cumulus clouds develop when sufficient thermodynamic instability is achieved on the mesoscale or a larger scale. The effects of wind shear on precipitation efficiency are included using data such as that shown in Figure 9-5. The relation of cumulus-caused downdrafts to previous cumulus-caused updrafts has been developed using observational data, such as that shown in Figure 9-6.

One of the most commonly used cumulus convection schemes is the Kuo scheme, originally developed by Kuo (1974). A form of this scheme, as modified by Molinari (1985), is as follows, as reported in Tremback (1990). The source terms in the conservation-of-heat and conservation-of-water equations from deep cumulus convection are written as

$$\overline{S}_\theta\big|_{cu} = L(1 - b)\pi^{-1} I Q_1 \big/ \int Q_1 dz$$

and

$$\overline{S}_{q_3}\big|_{cu} = b I Q_2 \big/ \int Q_2 \, dz,$$

where I is the rate at which the resolvable scale supplies moisture to a model grid column. Molinari and Corsetti (1985) suggest representing I as the resolvable vertical water vapor flux (i.e., $\bar{w}\bar{q}_3$) through the lifting condensation level. Kuo (1974) defined b as the fraction of I that increases the moisture of the column, while $1 - b$ precipitates. The quantity $1 - b$ is the precipitation efficiency, which can be evaluated using Figure 9-5.

The quantities Q_1 and Q_2 represent the vertical profiles of heating and moistening from the deep cumulus convection. Q_1 is the difference between the potential temperature outside the cloud, $\bar{\theta}_e$, and the potential temperature within the cloud $\bar{\theta}_c$. This latter temperature is computed as a weighted average between updraft and downdraft profiles. The updraft potential temperature corresponds to the moist adiabat through the lifting condensation level. The downdraft potential temperature is evaluated to begin at the altitude in the outside air where $\bar{\theta}_E$ is a
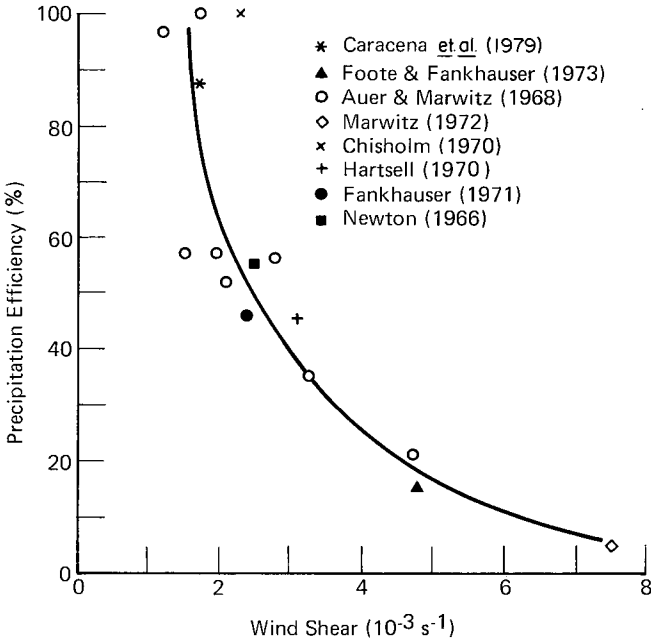
Fig. 9-5. Precipitation efficiency ϵ_p, defined as the ratio of rainout to water vapor inflow as a function of the vertical shear of the horizontal wind in the layer between cloud base and cloud top. (Reproduced from Fritsch and Chappell 1980a.) The data sources are indicated.

Fig. 9-6. Average cumulus convective transports over a portion of south Florida on days with substantial convective activity, where the dotted line indicates upward transport and the solid line indicates downward transport. (Adapted from Cooper *et al.* 1982.)

minimum, with the downdraft air temperature equal to the temperature outside the cloud at that height. At the lifting condensation level, the downdraft air is assumed to be 2°C cooler than the outside air. At the surface, the downdraft air is assumed to be 5°C cooler. Other levels are linearly interpolated.

The fractional area covered by downdraft is assumed to be 1% where it is initiated, 10% at the lifting condensation level, 20% at the height of maximum downdraft mass flux, and 100% at the surface. The outside cloud temperature is used instead of the updraft below the lifting condensation level. Knupp (1987) discusses the observed kinematic structure of downdrafts in more detail.

For Q_2, the layer below the lifting condensation level is dried at the rate I (since this is the flux of water vapor through the lifting condensation level). The anvil region of the cloud is defined as 2/3 of the height between the level with the highest value of $\bar{\theta}_E$ within 3 km of the ground and the cloud top, where moistening is uniform at the rate bI.

The scheme is implemented so that the moist adiabat is never exceeded. If it is exceeded, then I is arbitrarily reduced in magnitude. The Kuo scheme is activated only if the lapse rate is convectively unstable and $\bar{w} > w_{\text{threshold}}$ at the lifting condensation level, where $w_{\text{threshold}}$ is arbitrarily selected. Cloud top is defined as the height at which the moist adiabat through the lifting condensation level intersects the temperature outside the cloud (the *equilibrium level*). Pielke (1995) summarizes the concepts of lifting condensation level and equilibrium level and shows how they are computed.

The downdraft mass flux over land on days with extensive cumulus activity tends to lag the equivalent updraft values by about 1/2 hour or so, at least until midafternoon. Cooper *et al.* (1982) concluded that downdraft-induced convergence sustains cumulus convection until the available buoyant energy is used up. This available buoyant energy accumulates because of mesoscale horizontal wind convergence (see, e.g., Pielke *et al.* 1991) during the earlier, pre-cumulus portion of the day. This conclusion is consistent with the observation of Fritsch *et al.* (1976) that the large scale typically requires many hours to generate potential buoyant energy, but once cumulus convection develops, this energy is much more quickly removed.

9.3.3   Use of a Cumulus Field Model or Set of Equivalent Observations

With this approach, as described in Golden and Sartor (1978), two- or three-dimensional cumulus field model simulations or sets of observations are evaluated to determine the temporal and spatial response of cumulus clouds to a particular set of mesoscale dependent variables, as well as their subsequent feedback to the mesoscale. Examples of possible models for such use include Hill (1974), Miller and Pearce (1974), Pastushkov (1975), Cotton and

Tripoli (1978), Klemp and Wilhelmson (1978a,b), Clark (1979), Schlesinger (1980), and Simpson *et al.* (1982). Yau and Michaud (1982) have simulated the evolution of a cumulus cloud field in three-dimensions using Hill's method of random surface heating as an initiation mechanism for convection. Schlesinger (1982a) gives a summary of three-dimensional cumulus convection models. Cumulus field models are also referred to as *cloud resolving models* or *cloud ensemble models* (Tao *et al.* 1999, 2001). McNider and Kopp (1990) have introduced an imaginative procedure to initiate cumulus convection in such models where the boundary-layer parameterization in the model is used to specify the spatial scale and intensity of the initial thermal perturbation that produces the cumulus cloud. Cloud-resolving models have been used in both two and three dimensions (Tompkins 2000). Other examples of cloud-resolving simulations include Grabowski (2000) and Jiang *et al.* (2000).

Chang and Orville (1973), Cotton *et al.* (1976), Chen and Orville (1980), Soong and Tao (1980), Tripoli and Cotton (1980), and Schlesinger (1982b), for instance, have examined the response of cloud models to mesoscale convergence and changes in the thermodynamic and wind structure by mesoscale circulations. Fritsch and Chappell (1980a) justified their form for small-scale temperature perturbations by using the result of Chen and Orville (1980) that thermals are stronger and larger when low-level convergence is present, a result that has been replicated by Soong and Tao (1980).

Beniston and Sommeria (1981) have used Deardorff's (1973) fine-mesh (50-m horizontal grid increment) planetary boundary-layer model, as modified by Sommeria (1976), to test two cumulus parameterization schemes (e.g., those of Betts 1975, 1976 and Fraedrich 1976) using model-generated data, as well as to develop specific empirical relations for the response of shallow, nonprecipitating tradewind cumulus to larger-scale forcing. Among their results are that these shallow clouds (less than 1 km in depth) have a cloud depth to radius ratio of 0.4 ± 0.1 and that cloud base mass flux is related to cloud volume with a correlation coefficient on the order of 0.8 by

$$M_u(z_{LCL}) = 3.204 \times 10^{-9} \text{s}^{-1} \text{ kg m}^{-5} \ V_c + 2.18 \text{ kg m}^{-2}\text{s}^{-1},$$

as illustrated in Figure 9-7(a). The variable $M_u(z_{LCL})$ is the mass flux at cloud base and V_c is the cloud volume, where $V_c = 10^8 \text{m}^3$ would correspond to a spherical cloud with a radius of 288 m. Beniston and Sommeria also found that the growth and decay times for individual modeled clouds were about equal and positively related to the maximum area a_c of the cloud at its peak of activity. They estimated the lifetime of shallow tradewind cumulus as

$$\tau_c = 3.17 \times 10^{-2} \text{ s m}^{-2} \ a_c + 173 \text{ s},$$
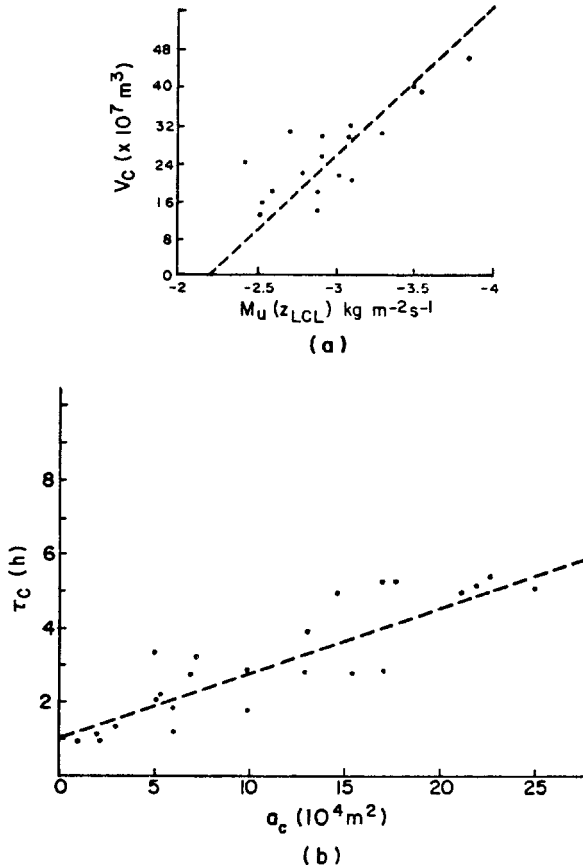
Fig. 9-7. (a) Cloud volume V_c as a function of the mass flux at cloud base $M_u(z_{LCL})$, and (b) cloud lifetime τ_c as a function of its maximum areal coverage a_c. (From Beniston and Sommeria 1981.)

as illustrated in Figure 9-7(b). Such a formulation for cloud lifetime, if extended to larger cumulus clouds, could provide an improved value of cloud lifetime used in cumulus parameterization schemes. Beniston and Sommeria also found that thermodynamic fluxes in tradewind cumulus could be represented by a single cloud mass-flux profile rather than by a complex cloud distribution (e.g., that of Arakawa and Schubert 1974). French *et al.* (1999) observed the actual evolution and pulsation of small cumulus clouds in Florida.

The use of such cumulus models to parameterize the response of cumulus clouds to the larger-scale environment is innovative and offers great hope for improved parameterization schemes.

9.3.4   Explicit Representation of Moist Thermodynamics

Rosenthal (1979a) has suggested that in tropical mesoscale models, cumulus clouds should be represented explicitly in the same fashion as stratiform clouds. He maintains that the successful implementation of cumulus parameterization schemes requires a strong coupling between the cloud and a larger scale. Thus, although tropical cyclogenesis may be well represented with such an approach, squall lines, such as reported by Zipser (1971), cannot. As discussed by Rosenthal (1978), these squall lines have a distribution of moist and dry downdrafts such that convection is diminished near the center of the larger-scale system with subsequent deep cumulus clouds forced to develop away from the region of larger-scale vertical ascent. Zipser (1977) gave an example of such destructive interference between the cumulus scale and the larger scale. Weisman *et al.* (1997) examined the degradation of the simulation of squall lines as the horizontal grid interval was changed from 1 km to 12 km.

Because of this limitation, Rosenthal (1978, 1979a) replaced one-dimensional cumulus parameterizations with an explicit treatment of moist thermodynamics on a grid with a 20-km horizontal grid mesh interval. With this approach, he was able to simulate tropical storms that represent the constructive reinforcement between the cumulus and mesoscales, as well as tropical squall lines in which the larger-scale fields of dependent variables have little effect after the initiation of the system. Studies by Yamasaki (1977) and Jones (1980) also show that realistic hurricane simulations can be obtained when latent heat is released on the resolvable grid scale in such convectively unstable atmospheres. The type of system that develops (i.e., the tropical storm or squall line) depends on the magnitude of the vertical shear of the horizontal wind and the dryness of the middle atmosphere. Rosenthal (1979b) concludes that the further use of cumulus parameterization schemes in hurricane simulations "seems to be of dubious value." He contends that an "experienced numerical experimenter can pick and choose closures that will provide almost any desired result."

Rosenthal (1978, 1980) included an explicit representation for moist thermodynamics using equations for water vapor, rain, and cloud water similar to those given by Eq. (9-6). Ice processes were neglected. His representation closely followed the work of Kessler (1969), although a similar formulation, such as that proposed by Orville (1980), presumably could also be used. Bhumralkar (1972, 1973) also obtained realistic results using an explicit representation of moist thermodynamics in his two-dimensional model simulation of the airflow over Grand Bahama Island during the day.

Justification for the neglect of cumulus parameterization may occur when, above the lifting condensation level,

$$\left| \bar{w} \frac{\partial \bar{\theta}}{\partial z} \right| \gg \left| w'' \frac{\partial \theta''}{\partial z} \right| \qquad \text{and} \qquad \left| \bar{w} \frac{\partial \bar{q}_n}{\partial z} \right| \gg \left| w'' \frac{\partial q_n''}{\partial z} \right|,$$

so that the vertical transport of heat and water is predominantly on the resolvable scale rather than on the subgrid scale. Such a condition may be true in the saturated hurricane environment even for relatively coarse horizontal resolution.

For instance, Black and Holland (1995), examining Hurricane Kerry off the Australian coast, documented a peak in the spectrum of $w\theta$ around a wavelength of 20 km with values dropping by a factor of about 7 for wavelengths of 10 km. The use of a 20-km horizontal grid with a bulk parameterization of the microphysics, as applied by Rosenthal (1978), although perhaps somewhat too large (at least for a simulation of a storm such as Kerry), nevertheless may be a reasonable approach to the realistic simulation of tropical storms. In contrast, for mesoscale convective cluster development over land, Fritsch and Chappell (1980a, b) introduced a subgrid-scale fluctuation temperature term to account for the significant contributions by such subgrid-scale flux terms. Fritsch and Chappell (1980b) also used a 20-km horizontal grid. Weisman *et al.* (1997) investigated the effect of model resolution on the simulation of cumulus convective systems. Warner and Hsu (2000) provide a valuable analysis of the effects of applying parameterized cumulus convection on the outer coarse grid of a model and applying grid-volume–resolved cumulus convection on the inner fine grid of a nested model.

The need to satisfy this inequality may determine the appropriate grid sizes needed in a mesoscale model when the atmosphere is convectively unstable in regions of saturation. Since at least four grid intervals or more in each spatial direction are required to represent variables in a numerical model properly (as discussed in Chapter 10), *moist processes such as condensation and sublimation should be predominantly realized on spatial scales at least this large.*

9.3.5 Subgrid-Scale Regions of Convective Stability Above the Saturation Level Within Saturated Grid Volumes Where $\partial \bar{\theta}_{\mathrm{E}} / \partial z \leq 0$

When regions of convective stability ($\partial \theta_{\mathrm{E}} / \partial z > 0$) occur within the grid volume, layered clouds can form when saturation occurs. If the percentage areal extent of such clouds is sufficiently large, then shortwave and longwave radiative fluxes will be affected (see Figure 8-8), thereby altering subsequent cumulus cloud activity and the mesoscale response. The influence of such layered clouds

on the subgrid-scale fluxes and source–sink terms in mesoscale models has not yet been investigated.

9.4 Examples of Parameterizations and Level of Complexity

9.4.1 Conversion Terms for Use in Eq. (9-6)

There are a number of parameterizations for the conversion terms in Eq. (9-6) (e.g., Rutledge and Hobbs 1983, 1984). In this section, the suggested forms proposed by Orville (1980) and Lin *et al.* (1983) are used to illustrate one possible technique for parameterization. A schematic of such conversion terms is reported in Rotstayn (1999, Figure 1). Following the work of these investigators, the conversion terms in Eq. (9-6) can be evaluated from

P_S = conversion from cloud ice to snowflakes + accretion of cloud ice crystals by snow + accretion of cloud droplets by snow + depositional growth of snow (or − sublimational loss of snow) − melting of snow to form rain = $P_{S1} + P_{S2} + P_{S3} + P_{S4} - P_{S5}$

and

P_R = conversion of cloud droplets to rain + accretion of cloud droplets by raindrops − evaporation of raindrops + melting of snow to form rain = $P_{R1} + P_{R2} - P_{R3} + P_{S5}$.

The dimensional unit of P_S and P_R is s^{-1}. The formulations for the components of P_S and P_R are defined by Orville (1980) and Lin *et al.* (1983) as follows for rain and for graupel-like snow of hexagonal type. Other types of snow require somewhat different values of the constants in these expressions.

1. $P_{S1} = \alpha_1(\bar{q}_1^{ci} - \bar{q}_*^{ci})$, $\alpha_1 = 10^{-3} s^{-1} \exp(0.025(\overline{T} - 273\,\text{K}))$, $\overline{T} < 0°\text{C}$,

where $\bar{q}_*^{ci}$ is a threshold value of specific humidity for cloud ice. In Lin *et al.* 1983, this value is set as $\bar{q}_*^{ci} = 0.001$. This formulation for P_{S1}, based on Kessler's (1969) original work as modified by Chang (1977), is called *autoconversion*, since no physical mechanism is included to explain why precipitation-sized ice crystals form only after cloud ice concentrations exceed a certain amount.

This algorithm requires the dependent variables $\bar{q}_1^{ci}$ and $\overline{T}$, and tunable coefficients α_1, and $\bar{q}_*^{ci}$.[12]

2. $$P_{S2} = \frac{0.79 E_s^{ci} n_{0s} c \bar{q}_1^{ci} \Gamma(3+d)}{b_s^{3+d}} \left(\frac{\bar{\rho}_{z_G}}{\bar{\rho}}\right)^{1/2},$$

when $\overline{T} < 0°C$, which represents the accretion of cloud ice by snow. In this expression,

$$E_s^{ci} = \exp\left[0.025\left(\overline{T} - 273 \text{ K}\right)\right]$$

is the collection efficiency of snow for cloud ice. The term $(\bar{\rho}_{z_G}/\bar{\rho})^{1/2}$ was included to account for changes of terminal velocity with height, where $\bar{\rho}_{z_G}$ is the density at ground level. The constants d and c were set at $d = 0.25$ and $c = 152.93 \text{ cm}^{1-d} \text{ s}^{-1} = 152.93 \text{ cm}^{0.75} \text{ s}^{-1}$, which were suggested as being representative for the graupel-like snow of hexagonal type.[12]

The values of n_{0s} and b_s are determined from

$$n_s = n_{0s} \exp\left(-b_s D_s\right),$$

where D_s is the diameter of the snow particles and n_s is their number per unit volume per increment of diameter size. As listed by Orville, $n_{0s} = 3 \times 10^{-2} \text{ cm}^{-4} = 3 \times 10^6 \text{ m}^{-4}$ from measurements by Gunn and Marshall (1958), and

$$b_s = \left(3.14 \rho_s n_{0s}/\bar{\rho}\bar{q}_1^s\right)^{1/4},$$

with ρ_s the density of the snow crystal, given as 0.1 g cm^{-3} for graupel-like snow of hexagonal type. Other investigators use different values. Scott (1982), for example, uses a value of $n_{0s} = 5 \times 10^7 \text{ m}^{-4}$, although he reports on observational values ranging from $n_{0s} = 10^8 \text{ m}^{-4}$ at the top of tropical cumulus (Simpson and Wiggert 1969) to $n_{0s} = 3 \times 10^6 \text{ m}^{-4}$ for precipitation water concentrations below 1.4 g m^{-3} and temperatures between -2 and $-32°C$ (Houze et al. 1979).

The equation for n_s is called the *Marshall-Palmer* distribution, since these investigators originated the concept for rain (Marshall and Palmer 1948).

3. $$P_{S3} = \frac{0.79 \, E_s^{cw} n_{0s} c \bar{q}_2^{cw} \Gamma(3+d)}{b_s^{3+d}} \left(\frac{\bar{\rho}_{z_G}}{\bar{\rho}}\right)^{1/2},$$

which represents the accretion of cloud water by snow. The collection efficiency of snow for cloud water, E_s^{cw}, is assumed to be unity. When the air temperature is below 0°C, these cloud droplets will freeze and increase the amount of snow.

4. $$P_{S4} = \frac{6.28(S_i - 1)}{\bar{\rho}(a_1 + a_2)} n_{0s} \left[0.78 b_s^{-2} + 0.31 s_c^{1/3} \Gamma\left(\frac{d+5}{2}\right) c^{0.5}\right.$$
$$\left. \times \left(\frac{\bar{\rho}_{z_G}}{\bar{\rho}}\right)^{1/4} v^{-0.5} \, b^{-(d+5)/2}\right],$$

when $\overline{T} < 0°C$, $\bar{q}_2^{cw} + \bar{q}_1^{ci} + \bar{q}_1^s > 0$, and $\bar{q}_1^{ci} + \bar{q}_1^s \neq 0$. This expression represents the depositional growth or sublimation loss of snow. In this equation, S_i is the supersaturation of water vapor over ice, defined as $\bar{q}_3/\bar{q}_{si}$ using Eq. (9-8).

$\Gamma\{d+5)/2\} \simeq 1.79$ for $d = 0.25$. The variables v and s_c are the kinematic viscosity of air ($v \simeq 1.5 \times 10^{-5}$ m^2 s^{-1}) and the Schmidt number[14] ($s_c \simeq 0.8$). Also,

$$a_1 = L_s^2/(k_a R_v \overline{T}^2) \quad \text{and} \quad a_2 = 1/\bar{\rho}q_{si}\psi,$$

where ψ is the molecular diffusivity of water vapor in air and k_a is the thermal conductivity of air. The formulation for P_{S4} is based on the work of Byers (1965), with a modification for wind ventilation given by Beard and Pruppacher (1971). Depending on the sign of S_i, P_{S4} is positive or negative.

5.
$$P_{S5} = -\frac{6.28}{\bar{\rho}L_f}[k_a\overline{T}(°C) - L_c\psi\bar{\rho}(q_{si} - \bar{q}_3)]n_{0s}$$
$$\times \left[0.78\, b_s^{-2} + 0.31 s_c^{1/3}\Gamma\left(\frac{d+5}{2}\right)c^{0.5} \right.$$
$$\left. \times \left(\frac{\rho_{z_G}}{\bar{\rho}}\right)^{1/4} v^{-0.5}\, b_s^{-(d+5)/2_s} \right] - \frac{C_w T(°C)}{L_f}P_{S3}$$

when $\overline{T} > 0°C$. This expression, based on Mason (1956), represents the melting of snow to form rain. The specific heat of liquid water, C_w, is 4.187×10^3 J kg^{-1} K^{-1}.

6.
$$P_{R1} = \bar{\rho}(\bar{q}_2^{cw} - \bar{q}_*^{cw})^2$$
$$\times \left[1.2 \times 10^{-4} + \{1.569 \times 10^{-12}\, n_R/(d_0[\bar{q}_2^{cw} - \bar{q}_*^{cw}])\} \right]^{-1},$$

which represents the conversion of cloud droplets by collision and collection (i.e., *coalescence*) to form raindrops. Based on Berry (1967) and modified by Orville (1980) and Lin *et al.* (1983), n_R is the number concentration of droplets, d_0 is the dispersion of the droplets (i.e., their standard deviation around their mean size), and $\bar{q}_*^{cw}$ is a threshold value of specific humidity for cloud water required before there is a significant probability for the formation of raindrops. Orville and Lin *et al.* reported a value of $\bar{q}_*^{cw} = 0.002$.

7.
$$P_{R2} = \frac{0.79\, E_R^{cw} n_{0R}\bar{q}_2^{cw}\Gamma(3+f)}{b_R^{3+f}}$$

This expression represents the accretion of cloud water by raindrops, with the collection efficiency given by $E_R^{cw} = 1$. The values of n_{0R} and b_R are determined from

$$n_R = n_{0R}\exp(-b_R D_R),$$

where D_R is the diameter of the raindrops and n_R the number per unit volume per increment of diameter size. As given by Marshall and Palmer (1948), $n_{0R} =$

8×10^{-2} cm^{-4}. Scott (1982), using Merceret (1975), suggests a value of $n_{0R} = 10^7$ m^{-4}. The value of b_R is given by

$$b_R = \left(3.14\,\rho_2 n_{0R}/\bar{\rho}\bar{q}_2^R\right)^{1/4},$$

where ρ_2 is the density of liquid water ($\rho_2 = 1$ g cm$^{-3} = 10^3$ kg m^{-3}). Condensational growth of raindrops is insignificant compared to growth by collision–collection (see, e.g., Wallace and Hobbs 1977) and is neglected in P_{R2}.

8. $P_{R3} = -6.28(s_w - 1)n_{0R}\left[0.78b_R^{-2} + 0.31s_c^{1/3}\Gamma\left[\dfrac{f+5}{2}\right]a_3^{0.5}v^{-0.5}\right.$

$$\times \left(\frac{\bar{\rho}_{z_G}}{\bar{\rho}}\right)^{1/4} b_R - \left[\frac{f+5}{2}\right]\right]\frac{1}{\bar{\rho}}\left(\frac{L_c^2}{k_a R_v \bar{T}^2} + \frac{1}{\bar{\rho}q_{sw}\psi}\right)^{-1}, \quad s_w < 1,$$

where $s_w = \bar{q}_3/q_{sw}$. This term represented the evaporation of rainwater in a subsaturated environment. The values of f and a_3 are 0.8 and 2115 cm^{1-f} s$^{-1} = 2115$ cm$^{0.2}$ s^{-1}, respectively. With this value of f, $\Gamma(3+f) \simeq 5.59$ and $\Gamma[(f+5)/2] \simeq 1.92$.

Orville (1980) and Lin *et al.* (1983) also present conversion terms for such effects as the accretion of rain by cloud ice, the accretion of cloud ice by rain, the accretion of snow by rain, raindrop freezing, and hail generation and growth. Except for raindrop freezing (i.e., the creation of sleet), these other processes are expected to be significant only when the atmosphere is convectively unstable.

Finally, the terminal velocities of snow and rain required in Eq. (9-6), given by Orville and Lin *et al.* are[15]

$$V_T^R = \frac{a_3\Gamma(4+f)}{6(b_R)^f}\left(\frac{\bar{\rho}_{z_G}}{\bar{\rho}}\right)^{1/2}$$

and

$$V_T^s = \frac{c\Gamma(4+d)}{6(b_s)^d}\left(\frac{\bar{\rho}_{z_G}}{\bar{\rho}}\right)^{1/2}.$$

These velocities are the mass-weighted mean velocities, defined originally by Srivastava (1971) as

$$V_T^R = \frac{1}{\bar{q}_2^R}\int_0^\infty V_T^R(D)\bar{q}_2^R(D)dD \quad\text{and}\quad V_T^s = \frac{1}{\bar{q}_1^s}\int_0^\infty V_T^s(D)\bar{q}_1^s(D)dD,$$

where $V_T^R(D)$ and $V_T^s(D)$ are terminal velocities or rain and snow for particular diameter particles. The quantities $\bar{q}_2^R(D)$ and $\bar{q}_1^s(D)$ represent the specific humidity of raindrops and snow per unit increment of diameter sizes. Figure 9-8 illustrates the relationship between mass-weighted mean velocities and total rain or snow content for several different values of atmospheric density. Values of
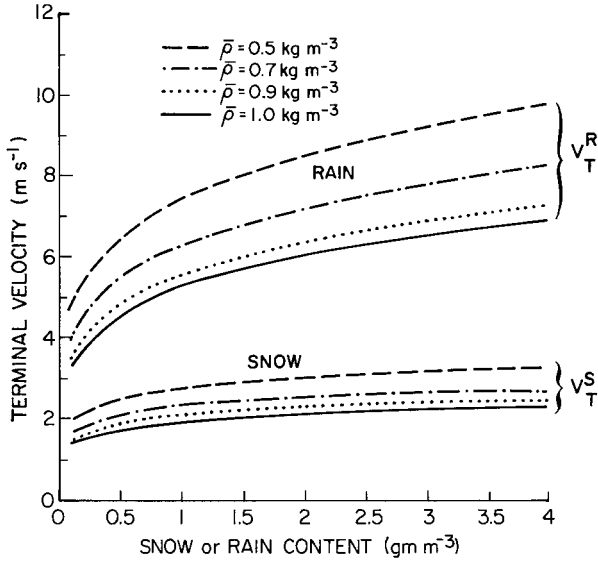
Fig. 9-8. Mass-weighted mean terminal velocities for rain and snow as a function of rain and snow water content. (Adapted from Orville 1980.)

the terminal fall velocity in meters per second for specific diameters in meters can be estimated by

$$V_T^R(D) = 130D^{0.5} \text{ (from Kessler 1969)}$$

and

$$V_T^s(D) = \begin{cases} 2.71D^{0.206} \text{ aggregates of dendrites and plates} \\ \quad \text{(from Jiusto and Bosworth 1971)} \\ 3.95D^{0.206} \text{ aggregates of columns} \\ \quad \text{(from Jiusto and Bosworth 1971),} \end{cases}$$

as summarized by Scott (1982). The values of $\bar{q}_2^R(D)$ and $\bar{q}_1^s(D)$ can be estimated from $\bar{q}_2^R(D) = 0.52n_{0R}(\rho_2/\bar{\rho})D^3 e^{-b_R D}$ and $\bar{q}_1^s(D) = 0.52n_{0s}(\rho_1/\bar{\rho})D^3 e^{-b_s D}$ using the Marshall-Palmer distribution for rain and snow and assuming that the volume of a raindrop and snow crystal can be represented as $0.52D^3$.

Other forms of these conversion terms can be found in, for example, Meyers *et al.* (1997), Zhao *et al.* (1997), Grabowski (1998), and Rotstayn *et al.* (2000).

9.4.2 The Kuo Scheme

The Kuo deep cumulus parameterization scheme requires the resolved variables, $\bar{\theta}$ and $\bar{q}_3$, and several adjustable coefficients including b, the temperatures

associated with the downdrafts, the height of initiation of the downdrafts, the mixing (or lack thereof) of the updrafts, the fractional coverage of the cloud area by downdrafts and its change with altitude, and the height of the anvil and the manner in which moisture is distributed through this layer. As clearly evident from this summary, several terms in the parameterization are tunable, with several of them discontinuous (e.g., $\bar{w}_{\text{threshold}}$).

There are numerous comparison studies of cumulus convection parameterizations including Molinari and Dudek (1992), Sun and Haines (1996), Wang and Seaman (1997), Sud and Walker (1999a,b), Bélair *et al.* (2000), Ferretti *et al.* (2000), and Vaidya and Singh (2000). Park and Droegemeier (1999) have assessed the sensitivity of a one-dimensional representation of a cumulus cloud to several model parameters. Seaman (1999, 2000) provides a very effective summary, including an historical review, of cumulus cloud parameterizations. He critiques several parameterizations, as listed in Appendix C.

Notes to Chapter 9

1. Specific humidity is defined as the ratio of the density of the gas or aerosol to the density of the air including this gas or aerosol. *Mixing ratio* is defined as the ratio of the gas or aerosol to the rest of the air excluding this gas or aerosol. At low concentrations (e.g., less than 5 parts per 100) the two are almost equal, so that the two terms can be used interchangeably for that situation.

2. From Wallace and Hobbs (1977).

3. $q_s T_v^{-2} |dT_v|/T_v^{-1}|dq_s| = (q_s/T_v)|dT_v/dq_s|$ is much less than unity for most reasonable atmospheric conditions. For example, the ratio is about 0.07 at warm temperatures (i.e., $T_v = 300$ K, $q_s = 0.02$) and approximately 0.06 at cold temperatures (i.e., $T_v = 250$ K, $q_s = 0.0002$), where $dT_v|/|dq_s|$ is evaluated over a $5°$ interval; q_{si} and q_{sw} as a function of T_v are given by Eq. (9-8).

4. Betts (1982) introduced a concept called *saturation point* to represent the thermodynamic properties of clear and nonprecipitation-sized cloudy air.

5. The *saturation level* is the height at which lifting of a parcel of air causes sufficient cooling to generate condensation or deposition. The saturation level can of course vary spatially within a grid volume. This level is also called the *lifting condensation level*. The height of this level will vary depending on the height of origin of the air parcel.

6. θ_E is defined using the decomposition given before Eq. (4-3); that is, $\theta_E = \bar{\theta}_E + \theta_E''$, where θ_E'' is the subgrid-scale equivalent potential temperature.

7. Fall velocity is also referred to as terminal velocity.

8. In other words, $\delta_s = 1$ when $\delta_c = \delta_f = 1$, as defined following Eq. (9-1).

9. The specific values of T_0^s and T_0^f depend on the activation temperature of the ice nuclei that are assumed to be present.

10. Since $S_{\text{deposition}}$ and $S_{\text{condensation}}$ are discontinuous functions at T_0^s, and S_{freezing} is discontinuous at T_0^f, there may be difficulty obtaining convergence when $\overline{T}$ is near these values. The practical solution to this problem is to not permit the threshold criteria in Eq. (9-7) to occur more than once during an iteration.

11. In some mesoscale applications, supersaturation has been arbitrarily defined to occur at less than 100% relative humidity. McCumber (1980) used a value of 90%. Such a reduction in the

saturation value, used in synoptic models, has been justified by assuming that although the grid-volume–averaged specific humidity is unsaturated, a significant number of subgrid-scale values will become saturated once the relative humidity exceeds a certain value. In a nonturbulent, stably stratified atmosphere, such an approximation would be inappropriate, but is reasonable with q_3'' is not identically equal to 0.

12. The determination of the dependent variables, tunable coefficients, and universal constants (if any) for each of these conversion terms is left as an exercise in the problem section.

13. The gamma function $\Gamma(3 + d)$ can be evaluated using standard mathematical tables (e.g., Selby 1967:461). Using those tables, $\Gamma(3.25) \simeq 5.44$.

14. The Schmidt number is defined as v/ψ. At 0°C and $\bar{p} = 1000$ mb, $\psi \simeq 1.875 \times 10^{-5}$ m^2 s^{-1} (Beard and Prupaccher 1971).

15. For $d = 0.25$ and $f = 0.8$, $\Gamma(4 + d) \simeq 21.8$ and $\Gamma(4 + f) \simeq 22.4$.

Additional Readings

Orville, H. D. 1980. Numerical modeling of clouds. In "Lecture Notes, IFAORS Short Course 450 on Clouds: Their Formation, Properties, and Effects," Williamsburg, VA, December 1–5, 1980. Perhaps the best reference material for the explicit representation of moist processes, this material, compiled for a workshop from theses and articles produced by the modeling group of the Institute of Atmosphere Sciences at the South Dakota School of Mines and Technology, provides an effective summary of parameterized microphysics, as well as the more detailed representation of the growth of different sizes of water and ice hydrometeors. Much of the information in that workshop report also appears in Lin *et al.* (1983).

For the incorporation of moist processes using cumulus parameterization the following excellent sources are available.

Cotton, W. R., and R. A. Anthes. 1989. "Storm and Cloud Dynamics." Academic Press, San Diego. This book provides in-depth reviews of a wide range of aspects of cloud physics and dynamics.

Droegemeier, K. K. 1997. The numerical prediction of thunderstorms: Challenges, potential benefits, and results from realtime operational tests. *WMO Bull.* **46**, 324–336. The article reviews the level of skill involved in the explicit prediction of thunderstorms. The ability to predict thunderstorms using a model with an explicit representation of microphysics represents the best that could potentially be achieved with cumulus parameterization schemes.

Frank, W. M. 1983. The cumulus parameterization problem. *Mon. Wea. Rev.* **111**, 1859–1871. A valuable summary of the difficulties of cumulus parameterization is given in this short review article. Also included are references to more in-depth reports on the current status of this difficult parameterization problem.

Haltiner, G. J., and R. T. Williams. 1980. "Numerical Prediction and Dynamic Meteorology." 2nd ed., John Wiley and Sons, New York. Although written with respect to synoptic- and hemispheric-scale models, about 20 pages are devoted to cumulus parameterization. Haltiner and Williams also provide a section on convective adjustment (which is most relevant for scales larger than the mesoscale), as well as a short but useful section (5 pages) dealing with the bulk parameterization of microphysics.

Ludlam, F. H. 1980. "Clouds and Storms." Pennsylvania State University Press, University Park, PA.

This book surveys cloud physics and cloud dynamics. Included are discussions of shallow and deep cumulus convection, although cumulus parameterization is not discussed. An appendix provides a series of excellent black and white photographs of different types of clouds as viewed from the ground, aircraft, and satellites.

Other valuable reference resources include the following:

Foufoula-Georgiou, E., and W. Krajewski. 1995. Recent advances in rainfall modeling estimation, and forecasting. U.S. National Report to the IUGG 1991–1994. *Rev. Geophys.*, (Supp.) **33**, 1125–1137.

Meyers, M. P., R. L. Walko, J. Y. Harrington, and W. R. Cotton. 1997. New RAMS cloud microphysics parameterization. Part II: The two-moment scheme. *Atmos. Res.* **45**, 3–39.

Mocko, D. M., and W. R. Cotton. 1995. Evaluation of fractional cloudiness parameterizations for use in a mesoscale model. *J. Atmos. Sci.* **52**, 2884–2901.

Straka, J. M. 1994. Representing moisture processes in mesoscale numerical models. In "Mesoscale Modeling of the Atmosphere," R. A. Pielke Sr. and R. P. Pearce, Eds., pp. 29–38. American Meteorological Society, Boston, MA.

Tripoli, G. J., and W. R. Cotton. 1981. The use of ice-liquid water potential temperature as a thermodynamic variable in deep atmospheric models. *Mon. Wea. Rev.* **109**, 1094–1102.

Walko, R. L., W. R. Cotton, M. P. Meyers, and J. Y. Harrington. 1995a. New RAMS cloud microphysics parameterization. Part I: The single-moment scheme. *Atmos. Res.* **38**, 29–62.

Weissbluth, M. J., and W. R. Cotton. 1993. The representation of convection in mesoscale models. Part I: Scheme fabrication and calibration. *J. Atmos. Sci.* **50**, 3852–3872.

Problems

1.   Using conversion relations for P_S and P_R in Section 9.4.1, determine the dependent variables, turnable coefficients, and universal constants (if any). Calculate how the individual conversion terms change with a $\pm 10\%$ and $\pm 25\%$ change in the tunable coefficients and the dependent variables.

2.   Complete the exercise in #1, but use conversion equations from another model.

3.   Program the Kuo model, and determine the sensitivity of the parameterization to $\pm 10\%$ and $\pm 25\%$ changes in the tunable coefficients and relationships.

Chapter 10

Methods of Solution

As was explained in Chapter 5, sets of simultaneous, nonlinear, partial differential equations cannot be solved using known analytic methods. Rather, their solution requires numerical methods of computation where the equations are discretized and solved on a lattice. This lattice corresponds to the grid volume defined by Eq. (4-6) in Chapter 4.

Several broad classes of solution techniques are available to represent terms involving the derivatives in the spatial coordinates of these differential equations, including:

- *finite difference* schemes,[1] which use a form of truncated Taylor series expansion
- *spectral* techniques, in which dependent variables are transformed to wavenumber space using a global basis function (e.g., a Fourier transform)
- the *pseudospectral* method, which uses a truncated spectral series to approximate derivatives
- *finite element* schemes, which seek to minimize the error between the actual and approximate solutions using a local basis function
- *interpolation* schemes, in which polynomials are used to approximate the dependent variables in one or more spatial directions.

In mesoscale models, only the finite difference and interpolation schemes have generally been used. The finite element techniques have been applied in mesoscale models by only a few authors. Interested readers can refer to the first edition of this book for the derivation of finite element algorithms. This chapter gives an introduction to finite difference and interpolation schemes.

The spectral technique is highly accurate (e.g., Fox and Deardorff 1972; Machenhauer 1979; Orszag 1971) and eliminates the fictitious feedback of energy to the larger scale called aliasing (discussed in Section 10.5). However, the mathematical expressions that result from the Fourier transformation are

cumbersome and require periodic boundary conditions to make it work effectively. Thus this scheme has not found acceptance among mesoscale models.

The pseudospectral technique was introduced by Fox and Orszag (1973) and was contrasted with the spectral technique and conventional finite difference methods by Christensen and Prahm (1976). A brief review of the pseudospectral method was given in Merilees and Orszag (1979). Eliassen (1980) summarized the uses of these and other representations in air pollution transport modeling. Although the pseudospectral technique appears to be a viable tool for use in mesoscale models, it has not been adopted [although several researchers, (e.g., Lee 1981; Patrinos and Leach 1982) have investigated its utility]. The major reason why these spectral schemes have been neglected up to now may be the interest in the interpolation approach, as well as the difficulty in handling nonperiodic boundary conditions using either of the spectral techniques.

10.1   Finite Difference Schemes—An Introduction

10.1.1   Advection

Most mesoscale models use the finite difference method, because of its comparative ease of coding onto a computer and its conceptual simplicity. This technique simply involves approximating the differential terms, including time, by one or more terms in a Taylor series expansion. For example, the local tendency and advective terms in the prognostic Eqs. (4-21) and (4-24)–(4-26) can be approximated by

$$\frac{\partial \bar{\phi}}{\partial t} = -\bar{u}\,\frac{\partial \bar{\phi}}{\partial x} \simeq \frac{\phi_i^{\tau+1} - \phi_i^{\tau}}{\Delta t} = -u_i^{\tau}\,\frac{\phi_{i+1}^{\tau} - \phi_{i-1}^{\tau}}{2\Delta x}, \qquad (10\text{-}1)$$

where the overbar has been dropped to simplify the notation, τ is used to indicate the number of time steps taken, i indicates the grid point location in the x direction (as illustrated in Figure 10-1), $\Delta t = t(\tau + 1) - t(\tau)$, and $\Delta x = x(i + 1) - x(i)$. The dependent variable ($\bar{\phi}$) refers to any one of the dependent variables. Note that the tensor subscript notation is not used here, rather, a new mathematical shorthand is introduced to represent the time and space locations of the dependent variables. The equation on the right side of Eq. (10-1) is called a *difference equation*.

In making such an approximation to a differential equation, several questions are asked concerning its ability to represent the actual differential equation accurately, including:

- When Δt and Δx approach 0, does the approximate form converge to the differential equation?
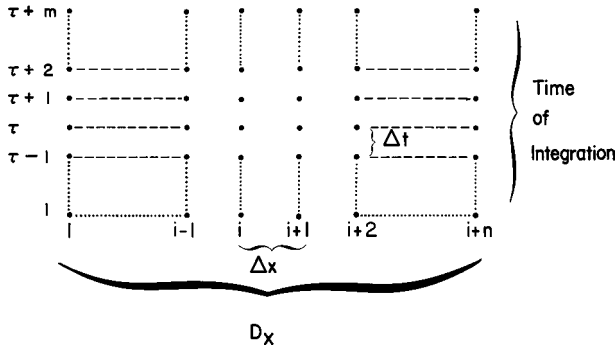
Fig. 10-1. A schematic illustration of an $x - t$ grid representation where $\Delta x = x(i) - x(i-1) = x(i+1) - x(i)$, etc., and $\Delta t = t(\tau) - t(\tau - 1) = t(\tau + 1) - t(\tau)$, etc. (Here n and m are integers greater than 2.)

- Is the numerical representation linearly stable to small perturbations?
- If the scheme is linearly stable, how well are the amplitudes and phases represented for waves of different wavelengths relative to the exact solution?

These three questions must be considered for all computational approximation techniques.

The difference equation given by Eq. (10-1) appears to be a straightforward and reasonable form for representing the corresponding differential equation. However, as will be shown shortly, although the approximation does converge to the correct representation when Δt and Δx approach 0 in the limit, the scheme is *linearly unstable* to small perturbations and thus cannot be used.

To illustrate the first criterion, let the dependent variable ϕ have the form

$$\phi = \hat{\phi} \cos kx$$

(where $\hat{\phi}$ has constant amplitude), so that

$$\partial\phi/\partial x = -\hat{\phi}k \sin kx.$$

One finite difference approximation to this term [as used in Eq. (10-1)] is

$$\frac{\phi_{i+1} - \phi_{i-1}}{2\Delta x} = \frac{\hat{\phi}}{2\Delta x}\left[\cos k(x + \Delta x) - \cos k(x - \Delta x)\right], \qquad (10\text{-}2)$$

which, by expanding $\cos k(x + \Delta x)$ and $\cos k(x - \Delta x)$, can be written as

$$\frac{\phi_{i+1} - \phi_{i-1}}{2\Delta x} = -\frac{\hat{\phi}}{\Delta x}\sin kx \sin k\Delta x. \qquad (10\text{-}3)$$

The ratio of the approximate to actual forms of this differential quantity is thus given by

$$\frac{\phi_{i+1} - \phi_{i-1}}{2\Delta x} \bigg/ \frac{\partial\phi}{\partial x} = \frac{\sin k\Delta x}{k\Delta x}. \qquad (10\text{-}4)$$

By a Taylor series expansion,

$$\sin k\Delta x = k\Delta x - \frac{(k\Delta x)^3}{3!} + \frac{(k\Delta x)^5}{5!} - \cdots.$$

Thus, when $k\Delta x \ll 1$,[2] Eq. (10-4) can be written as

$$\frac{\phi_{i+1} - \phi_{i-1}}{2\Delta x} \bigg/ \frac{\partial \phi}{\partial x} \sim \frac{k\Delta x}{k\Delta x} = 1.$$

Since $k = 2\pi/L$, writing L in terms of the grid spacing $L = n\Delta x$, where n is the number of grid points in one cycle of the cosine function, $k\Delta x \ll 1$ requires that $2\pi/n \ll 1$ or $n \gg 1$. In other words, the cosine wave must have a very long wavelength for its derivative to be represented accurately by Eq. (10-2).

In contrast, if $L = 2\Delta x$, then

$$\frac{\phi_{i+1} - \phi_{i-1}}{2\Delta x} \bigg/ \frac{\partial \phi}{\partial x} = \frac{\sin \pi}{\pi} = 0,$$

so that the representation given by Eq. (10-2) fails to resolve a feature that has a wavelength of two grid increments. Examples of a longwave and a shortwave are given in Figure 10-2.

Thus the representation of the derivative of a function using values at neighboring grid points provides very poor representations of short waves relative to the grid mesh Δx, whereas longer waves are reasonably well resolved. The ability, or lack thereof, of a numerical scheme to resolve features of different wavelengths properly is a crucial consideration in the use of a numerical approximation scheme.

The linear stability of Eq. (10-1) can be evaluated using the techniques for representing waves in terms of complex variables introduced in Chapter 5.[3] As discussed there, a dependent variable ϕ, for example, can be represented as

$$\phi(x, t) = \hat{\phi}(k, \omega)e^{i(kx+\omega t)}, \tag{10-5}$$

where $\hat{\phi}$, k, and ω can be complex. In a numerical model, the spatial and temporal independent variables can be written as

$$x = n\Delta z \qquad \text{and} \qquad t = \tau \Delta t,$$

so that Eq. (10-5) can also be written as

$$\phi(x, t) = \phi(n\Delta x, \tau \Delta t) = \hat{\phi}(k, \omega)e^{i(kn\Delta x + \omega \tau \Delta t)}. \tag{10-6}$$

As discussed in Chapter 5, to use the formulation given by Eq. (10-5) in a differential equation, it is necessary to linearize the equation. As written, Eq. (10-1)
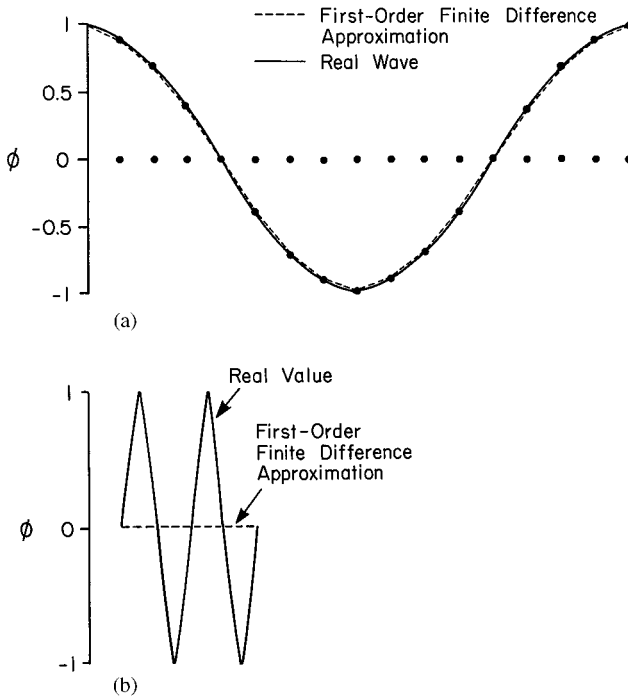
Fig. 10-2. Centered finite difference representation using Eq. (10-2) for (a) a 16 Δx wave and (b) a $2\Delta x$ wave.

is not in a linear form, since the right side involves products of dependent variables. The procedure, therefore, is to replace the advecting velocity u_i^τ with a constant value U, so that the finite difference approximation becomes

$$\frac{\phi_i^{\tau+1} - \phi_i^{\tau}}{\Delta t} = -U \frac{\phi_{i+1}^{\tau} - \phi_{i-1}^{\tau}}{2\Delta x}. \tag{10-7}$$

This difference equation has one unknown, $\phi_i^{\tau+1}$, since it is assumed that values of ϕ at time τ are known; therefore, the equation is well posed and solvable. The finite difference representation given by Eq. (10-7) is called *forward in time, centered in space*.

At this point, it is useful to comment on the standard procedure for examining the computational linear stability of numerical schemes. As shown in Chapter 5, even the linearized form of the conservation relations can produce complicated solutions. Therefore, investigators generally examine subsets of the linearized relations. Simple numerical approximations to advection, for example, such as given by Eq. (10-7), are examined separately from the remaining terms in the conservation relations. Numerical approximations to the subgrid-scale fluxes and

the Coriolis terms are other portions of the conservation relations that we investigate later in this chapter. The basic assumption is that if the computational approximation to the individual linearized subsets of the equations are accurate, then they will also be accurate representations when used in the nonlinear framework. However, as is discussed in Section 10.5, accuracy of the linear differential equations is a *necessary but not a sufficient condition* to guarantee satisfactory nonlinear solutions.

Using Eq. (10-6), Eq. (10-7) can be rewritten as

$$\hat{\phi}(k, \omega)e^{i(kn\,\Delta x + \omega\tau\Delta t)}\big[e^{i\omega\,\Delta t} - 1\big] = -\frac{U\,\Delta t}{2\Delta x}\,\hat{\phi}(k, \omega)e^{i(kn\,\Delta x + \omega\tau\,\Delta t)}\big[e^{ik\,\Delta x} - e^{-ik\,\Delta x}\big]$$

or

$$\big[e^{i\omega\,\Delta t} - 1\big] = -\frac{U\,\Delta t}{2\Delta x}\big[e^{ik\,\Delta x} - e^{-ik\Delta x}\big]. \tag{10-8}$$

At this point, it is convenient to introduce a notational representation suggested by Arthur Mizzi (1979, personal communication) in which

$$\psi^1 = e^{i\omega\,\Delta t}, \qquad \psi_1 = e^{ik\,\Delta x}, \qquad \text{and} \qquad \psi_{-1} = e^{-ik\,\Delta x},$$

so that $\psi_1 - \psi_{-1} = 2i \sin k\Delta x$. This is shown by expanding $e^{ik\,\Delta x}$ and $e^{-ik\,\Delta x}$ in terms of $\cos a + i \sin a$, where $a = k\Delta x$ in the first exponential and $a = -k\Delta x$ in the second.

With these definitions, Eq. (10-8) can be written as

$$(\psi^1 - 1) = -\frac{U\,\Delta t}{\Delta x}\,i \sin k\Delta x. \tag{10-9}$$

This mathematical shorthand is a versatile tool to examine linear computational stability and is used throughout this chapter.

Equation (10-9) can then be rearranged, yielding

$$\psi^1 = 1 - \frac{U\,\Delta t}{\Delta x}\,i \sin k\Delta x = 1 - Ci \sin k\Delta x, \tag{10-10}$$

where C is called the *Courant number*. If C is greater than unity, then the distance traveled in one time step because of advection is greater than the grid separation, whereas the opposite is true if C is less than 1.

In the original differential [Eq. (10-1)], no sources or sinks of velocity appear; however, in the difference representation, Eq. (10-7), damping or amplifying in time of the result is possible because of the imprecise approximation for the derivatives. To evaluate this effect, the frequency ω is decomposed into real and imaginary parts, given by

$$\omega = \omega_r + i\omega_i.$$

Using this definition for ω, Eq. (10-10) can be rewritten as

$$\lambda e^{i\omega_r\Delta t} = 1 - Ci \sin k\Delta x, \tag{10-11}$$

where $\lambda = \pm e^{-\omega_i \Delta t}$ and is called the amplitude change of the solution per time step (λ^τ is then the change in amplitude after τ time steps). Since Eq. (10-1) has no sources or sinks of velocity, λ should be identically equal to $+1$.

To solve for λ, $e^{i\omega_r \Delta t}$ is expanded into $\cos \omega_r \Delta t + i \sin \omega_r \Delta t$. The real and imaginary parts of Eq. (10-11) must separately be equal[4] so that Eq. (10-11) can be written as

$$\lambda \cos \omega_r \Delta t = 1$$

$$\lambda \sin \omega_r \Delta t = -C \sin k\Delta x.$$

Squaring both sides of these two expressions and adding yields

$$\lambda^2 \left(\cos^2 \omega_r \, \Delta t + \sin^2 \omega_r \Delta t \right) = \lambda^2 = 1 + C^2 \sin^2 k\Delta x,$$

or

$$\lambda = \pm \sqrt{1 + C^2 \sin k\Delta x}. \tag{10-12}$$

Except when the wavenumber becomes very small (e.g., $L \to \infty$), or as the grid increment Δx approaches 0, or for a $2\Delta x$ wave, $C^2 \sin^2 k\Delta x$ is greater than 0 and $|\lambda|$ is greater than 1.

The numerical representation given by Eq. (10-7) is thus *linearly unstable*, since the solution amplifies each time step. No such amplification will occur in the linear form of the differential equation given by the left side of Eq. (10-1) (i.e., $\partial \bar{\phi}/\partial t = -U \, \partial \bar{\phi}/\partial x$). If a numerical scheme is linearly unstable, then its use in approximating the nonlinear differential equation is rejected, since small perturbations with such a representation will grow fictitiously.

The failure of the right-side equation in Eq. (10-1) to accurately approximate the corresponding differential equation is surprising, because it appeared to be the most natural choice. In examining solution techniques, therefore, intuition is not sufficient, and stability analyses must be undertaken to determine the accuracy of numerical approximations. The methodology for examining linear computational stability introduced here will be used in the remainder of the chapter to examine the fidelity of different numerical representation techniques.

10.1.1.1   Forward-Upstream Differencing

Another approximation to the advection equation, given on the left side of Eq. (10-1), is

$$\frac{\partial \bar{\phi}}{\partial t} = -\bar{u}\frac{\partial \bar{\phi}}{\partial x} \simeq \frac{\phi_i^{\tau+1} - \phi_i^\tau}{\Delta t} = \begin{cases} -u_i^\tau \frac{\phi_{i+1}^\tau - \phi_i^\tau}{\Delta x}, & u_i \leq 0 \\ -u_i^\tau \frac{\phi_i^\tau - \phi_{i-1}^\tau}{\Delta x}, & u_i > 0, \end{cases} \tag{10-13}$$

which is referred to as the *forward-upstream* scheme since the space derivative is evaluated upwind from the grid point. Linearizing this approximation by setting

u_i^τ equal to a constant advecting velocity U, then for $U > 0$, the representation of this relation in terms of wave number and frequency is[5]

$$\psi^1 = 1 - C(1 - \psi_{-1})$$

or, equivalently,

$$\lambda e^{i\omega_r \Delta t} = 1 - C(1 - \cos k\Delta x + i \sin k\Delta x).$$

Equating real and imaginary components,

$$\lambda \cos \omega_r \Delta t = 1 - C(1 - \cos k\Delta x)$$
$$\lambda \sin \omega_r \Delta t = -C \sin k\Delta x, \tag{10-14}$$

squaring and adding yields

$$\lambda^2 = [1 - C(1 - \cos k\Delta x)]^2 + C^2 \sin^2 k\Delta x.$$

After expanding and rearranging, this expression can be written as

$$\lambda = \pm\sqrt{1 + 2C(\cos k\Delta x - 1)(1 - C)}.$$

In contrast to the forward-in-time, centered-in-space scheme, the upstream representation is linearly stable ($|\lambda| \leq 1$) as long as

$$-1 \leq 2C(\cos k\,\Delta x - 1)(1 - C) \leq 0.$$

Since $\cos k\Delta x \leq 1$, the quantity inside the left parentheses is always less than or equal to 0, and the inequality holds as long as $C \leq 1$. Numerical approximation techniques that must satisfy certain criteria to have linearly stable results are called *conditionally stable schemes*. When $C = 1$ or $k \simeq 0$ (i.e., $L \to \infty$), $\lambda = 1$ and the solutions neither damp nor amplify. Other values of λ, displayed in Table 10-1 as functions of wavelength $L = n\Delta x$ and C, the Courant number, show that except for the longest waves and $C = 0$ or 1, the scheme damps the solution with the most error at $C = 0.5$. With this latter value of C, wavelengths of $2\Delta x$ are completely eliminated—a result that can be seen most easily by rewriting the linear form of Eq. (10-13) as

$$\phi_i^{\tau+1} = (1 - C)\phi_i^\tau + C\phi_{i-1}^\tau \quad \text{(for } U > 0\text{)}.$$

Since a $2\Delta x$ wave can be represented as $\phi_i^\tau = (-1)^i a_1 + a_0$, where a_1 and a_0 are constants and i is the spatial index counter, then for $C = 0.5$, $\phi_i^{\tau+1} = 0$.

   The predicted phase speed as a function of wavenumber can also be obtained from Eq. (10-14) by dividing the imaginary components by the real components, yielding

$$\sin \omega_r \Delta t / \cos \omega_r \Delta t = \tan \omega_r \Delta t = -C \sin k\Delta x / [1 + C(\cos k\Delta x - 1)],$$

or since the phase speed c is equal to the negative of the frequency divided by the wavenumber [see, e.g., the text preceding Eq. (5-32)],

$$\tilde{c}_\phi = \frac{-1}{k\Delta t} \tan^{-1}\left[\frac{-C\sin k\Delta x}{1 + C(\cos k\Delta x - 1)}\right].$$

Since the actual solution[6] to the differential equation

$$\frac{\partial\bar{\phi}}{\partial t} = -\frac{U}{\partial x}\frac{\partial\bar{\phi}}{\partial x}$$

is

$$\frac{\omega}{k} = -\tilde{c}_\phi = -U,$$

the ratio of the computational solution to the true solution of the phase speeds is

$$\frac{\tilde{c}_\phi}{U} = \frac{1}{kU\Delta t} \tan^{-1}\left[\frac{C\sin k\Delta x}{1 + C(\cos k\Delta x - 1)}\right].$$

The accuracy of a linear numerical solution depends on how well the calculated values of λ and $\tilde{c}_\phi$ approximate the exact solutions of the differential equation: λ_{exact} and $c_{\phi\text{exact}}$, where in this case, $\lambda_{\text{exact}} = 1$ and $\tilde{c}_{\phi\text{exact}} = U$. If $|\lambda| > 1$ for any possible wavelength, then the solution technique is *linearly unstable*. If it is not linearly unstable but the absolute value of $\lambda/\lambda_{\text{exact}}$ is less than unity for any wavelength, then the scheme is *damping*, and if λ is identically equal to λ_{exact}, then the technique yields the correct amplitude. (Note that λ_{exact} can be less than 1, such as for the diffusion equation; see Section 10.1.2.) When $\tilde{c}_\phi \neq c_{\phi\text{exact}}$, the approximation representation is *erroneously dispersive*. (The exact solution, of course, is *dispersive* if $c_{\phi\text{exact}}$ is a function of k.)

It is also important to determine the damping over a specified time period, such as the time it takes the wave to travel one grid increment. This means that a scheme could be only slightly damping for each time step, but if the time step were small, the accumulated damping over time could be quite large. For example, from Table 10-1, in Scheme I for $4\Delta x$ and $C = 0.1$, after 10 time steps (the time required for the exact solution to travel Δx), the wave would be 37% of its correct amplitude (i.e., $\lambda^{10} = 0.34$). With $C = 0.5$, while the amplitude change per time step is greater than with $C = 0.1$, the amplitude change after the wave travels one $\Delta x (\lambda^2)$ is 0.5.

Values of $\tilde{c}_\phi/U$ are given in Table 10-1 for various combinations of C and k. As with the amplitude, a wavelength of $2\Delta x$ generally has the poorest representation of the proper phase speed. Only at $C = 1$ and at $C = 0.5$ (where the amplitude of a $2\Delta x$ wave is eliminated in one time step) is the phase accurately represented for all wavelengths. When $0.5 < C < 1.0$, waves travel faster in the finite difference representation than the true solution, whereas they travel more slowly when $0 < C < 0.5$.

TABLE 10-1

Values of the Amplitude λ^1 and Phase Error $\tilde{c}_\phi/U$ per Time Step as a Function of Wavelength for Different Computational Approximations to the Advection Equation $\partial\phi/\partial t = -U\,\partial\phi/\partial x$

Scheme		Wavelength	0.001	0.01	0.1	0.2	0.3	0.4	0.5	0.6	0.7	0.8	0.9	1.0	1.1
I. Forward-in-time linear interpolation upstream	λ	$2\Delta x$	0.998	0.980	0.800	0.600	0.400	0.200	0.000	0.200	0.400	0.600	0.800	1.000	$\lvert\lambda\rvert > 1$
		$4\Delta x$	0.999	0.990	0.906	0.825	0.762	0.721	0.707	0.721	0.762	0.825	0.906	1.000	
		$10\Delta x$	1.000	0.998	0.983	0.969	0.959	0.953	0.951	0.953	0.959	0.969	0.983	1.000	
		$20\Delta x$	1.000	1.000	0.996	0.992	0.990	0.988	0.988	0.988	0.990	0.992	0.996	1.000	
	$\tilde{c}_\phi/U$	$2\Delta x$	0.000	0.000	0.000	0.000	0.000	0.000	1.000	1.667	1.429	1.250	1.111	1.000	
		$4\Delta x$	0.637	0.643	0.704	0.780	0.859	0.936	1.000	1.043	1.060	1.055	1.033	1.000	
		$10\Delta x$	0.936	0.937	0.953	0.968	0.981	0.992	1.000	1.005	1.008	1.008	1.005	1.000	
		$20\Delta x$	0.984	0.984	0.988	0.992	0.995	0.998	1.000	1.001	1.002	1.002	1.001	1.000	
II. Centered-in-time centered-in-space (leapfrog)	λ	$2\Delta x$	1.000	1.000	1.000	1.000	1.000	1.000	1.000	1.000	1.000	1.000	1.000	1.000	$\lvert\lambda\rvert > 1$
		$4\Delta x$	1.000	1.000	1.000	1.000	1.000	1.000	1.000	1.000	1.000	1.000	1.000	1.000	
		$10\Delta x$	1.000	1.000	1.000	1.000	1.000	1.000	1.000	1.000	1.000	1.000	1.000	1.000	
		$20\Delta x$	1.000	1.000	1.000	1.000	1.000	1.000	1.000	1.000	1.000	1.000	1.000	1.000	
	$\tilde{c}_\phi/U_{\text{physical mode}}$	$2\Delta x$	0.000	0.000	0.000	0.000	0.000	0.000	0.000	0.000	0.000	0.000	0.000	0.000	
		$4\Delta x$	0.637	0.637	0.638	0.641	0.647	0.655	0.667	0.683	0.705	0.738	0.792	1.000	
		$10\Delta x$	0.935	0.935	0.936	0.938	0.940	0.944	0.950	0.956	0.964	0.974	0.986	1.000	
		$20\Delta x$	0.984	0.984	0.984	0.984	0.985	0.986	0.988	0.989	0.991	0.994	0.997	1.000	

III. Forward-in-time upstream spline interpolation	λ	$2\Delta x$	1.000	0.999	0.944	0.792	0.568	0.296	0.000	0.296	0.568	0.792	0.944	1.000	1.000
		$4\Delta x$	1.000	1.000	0.997	0.989	0.981	0.975	0.972	0.975	0.981	0.989	0.997	1.000	0.888
		$10\Delta x$	1.000	1.000	1.000	1.000	1.000	1.000	1.000	1.000	1.000	1.000	1.000	1.000	0.996
		$20\Delta x$	1.000	1.000	1.000	1.000	1.000	1.000	1.000	1.000	1.000	1.000	1.000	1.000	1.000
	$\bar{c}_\phi/U$	$2\Delta x$	0.000	0.000	0.000	0.000	0.000	0.000	0.000	0.000	0.000	0.000	0.000	0.000	0.000
		$4\Delta x$	0.955	0.955	0.958	0.967	0.979	0.980	1.000	1.007	1.009	1.008	1.005	1.000	1.042
		$10\Delta x$	0.999	0.999	0.999	0.999	1.000	1.000	1.000	1.000	1.000	1.000	1.000	1.000	1.001
		$20\Delta x$	1.000	1.000	1.000	1.000	1.000	1.000	1.000	1.000	1.000	1.000	1.000	1.000	1.000
IV. Adam-Bashford centered-in-space[2]	λ	$2\Delta x$	1.000	1.000	1.000	1.000	1.000	1.000	1.000	1.000	1.000	Computational mode is			
		$4\Delta x$	1.000	1.000	1.000	0.999	0.997	0.991	0.977	0.950	0.893	unstable for at least			
		$10\Delta x$	1.000	1.000	1.000	1.000	1.000	0.999	0.997	0.994	0.990	one of the wavelengths			
		$20\Delta x$	1.000	1.000	1.000	1.000	1.000	1.000	1.000	1.000	0.999				
	$\bar{c}_\phi/U_{\text{physical mode}}$	$2\Delta x$	0.000	0.000	0.000	0.000	0.000	0.000	0.000	0.000	0.000	Computational mode is			
		$4\Delta x$	0.637	0.637	0.637	0.637	0.638	0.642	0.642	0.661	0.674	unstable for at least			
		$10\Delta x$	0.935	0.935	0.935	0.936	0.936	0.937	0.938	0.941	0.945	one of the wavelengths			
		$20\Delta x$	0.984	0.984	0.984	0.984	0.984	0.984	0.984	0.984	0.984				

[1]It should be noted that in an approximate scheme which is damping (i.e., $|\lambda| < 1$), reducing Δt for the same Δx does not necessarily result in less total damping after a period of time. This results because the solution technique is used more frequently during that time because of the smaller Δt. Therefore, for improved accuracy and computational efficiency, as large a Δt as permitted by the linear stability criteria, should be chosen when an approximation scheme has computational damping (computed by Charlie Martin and Jeff McQueen).

[2]The values for the Adams–Bashford scheme were computed by Alex Costa and Sue van den Heever.

The damping characteristics of upstream differencing can be examined in a different fashion using a truncated Taylor series approximation to Eq. (10-13), where

$$\phi_i^{\tau+1} \simeq \phi_i^{\tau} + \frac{\partial \phi}{\partial t} \Delta t + \frac{1}{2} \frac{\partial^2 \phi}{\partial t^2} (\Delta t)^2$$

$$\phi_{i-1}^{\tau} \simeq \phi_i^{\tau} - \frac{\partial \phi}{\partial t} \Delta x + \frac{1}{2} \frac{\partial^2 \phi}{\partial x^2} (\Delta x)^2,$$

where it is understood that the derivative terms are evaluated at τ and i. These two forms are substituted into the right-side equation in Eq. (10-13) (with the advecting velocity u_i^{τ} set equal to the constant velocity U; $U > 0$), yielding

$$\phi_i^{\tau} + \frac{\partial \phi}{\partial t} \Delta t + \frac{1}{2} \frac{\partial^2 \phi}{\partial t^2} (\Delta t)^2 - \phi_i^{\tau} = -C \left[\phi_i^{\tau} - \phi_i^{\tau} + \frac{\partial \phi}{\partial x} \Delta x - \frac{1}{2} \frac{\partial^2 \phi}{\partial x^2} (\Delta x)^2 \right]$$

or, after subtracting identical terms and rearranging,

$$\frac{\partial \phi}{\partial t} + U \frac{\partial \phi}{\partial x} + \frac{1}{2} \frac{\partial^2 \phi}{\partial t^2} \Delta t - \frac{1}{2} U \frac{\partial^2 \phi}{\partial x^2} \Delta x = 0. \qquad (10\text{-}15)$$

The first two terms on the left side are in the same form as the original linear differential equation [i.e., the left side of Eq. (10-13), with $\bar{u} = U$], and the right side represents the *computational diffusion*, which results from using forward, upstream differencing. As Δt and Δx approach 0 in the limit, Eq. (10-15) reduces to the proper differential equation.

This diffusion can be written in another form by differentiating in time the left-side equation in Eq. (10-13) with $\bar{u} = U$, resulting in

$$\frac{\partial^2 \phi}{\partial t^2} = -U \frac{\partial}{\partial t} \frac{\partial \phi}{\partial x} = -U \frac{\partial}{\partial x} \frac{\partial \phi}{\partial t} = -U \frac{\partial}{\partial x} \left(-U \frac{\partial \phi}{\partial x} \right) = U^2 \frac{\partial^2 \phi}{\partial x^2},$$

so that the two terms on the right side of Eq. (10-15) can also be written as

$$\frac{1}{2} \frac{\partial^2 \phi}{\partial t^2} \Delta t - \frac{1}{2} U \frac{\partial^2 \phi}{\partial x^2} \Delta x = \frac{1}{2} U \Delta x \left(U \frac{\Delta t}{\Delta x} - 1 \right) \frac{\partial^2 \phi}{\partial x^2} = v_c \frac{\partial^2 \phi}{\partial x^2},$$

where v_c is called the *computational diffusion coefficient*. This coefficient has no physical significance and is simply an artifact of the computational scheme.

Forward-in-time, upstream differencing has been used extensively in mesoscale numerical modeling. Its characteristic damping and failure to preserve the proper phase have generated serious criticisms of this technique, however. It is now generally believed that this method is appropriate only if advection and wave propagation are not dominant in the conservation relations for a particular mesoscale feature. Furthermore, if subgrid-scale mixing is important, then v_c must be less than the corresponding physically relevant turbulent exchange coefficient. However, it may be possible to modify this numerical approach to improve its accuracy. Smolarkiewicz (1983), for instance,

presents a scheme to reduce the implicit diffusion of upstream differencing by adding a corrective step to the calculation. Brown and Pandolfo (1980) provide a discussion of upstream differencing. Wang (1996) describes an extension of forward-in-time, upstream differencing for nonuniform and time-dependent advection that achieves better accuracy.

10.1.1.2   Leapfrog Centered-in-Space Differencing Scheme

A third finite difference representation to the advection equation is

$$\frac{\phi^{\tau+1} - \phi^{\tau-1}}{2\Delta t} = -u_i^\tau \frac{\phi_{i+1}^\tau - \phi_{i-1}^\tau}{2\Delta x}, \tag{10-16}$$

where the right side is in the same form as the difference representation given in Eq. (10-1) and the left side is *centered in time*. This scheme is often called *leapfrog*, because ϕ_i^τ does not appear in Eq. (10-16). As will be shown shortly, using a centered-in-time representation permits Eq. (10-16) to be linearly stable under certain conditions.

Assuming that $u_j = U$, Eq. (10-16) can be rewritten as a function of wavenumber and frequency as

$$\psi^1 = \psi^{-1} - i\alpha, \tag{10-17}$$

where $\alpha = 2C \sin k\Delta x$. From the definitions of ψ^1 and ψ^{-1} (i.e., $\psi^1 = \lambda e^{i\omega_r \Delta t}$ and $\psi^{-1} = \lambda^{-1} e^{-i\omega_r \Delta t}$) Eq. (10-17) can be rewritten as

$$\psi^2 + i\alpha\psi^1 - 1 = 0, \tag{10-18}$$

where the identity $\psi^2 = (\psi^1)(\psi^1) = (\psi^1)^2$ has been used. Since the solution of a quadratic equation $ax^2 + bx + c = 0$ is $x = (-b \pm \sqrt{b^2 - 4ac})/2a$, we have

$$\psi^1 = \left(-i\alpha \pm \sqrt{(i\alpha)^2 + 4}\right)/2 = \left(-i\alpha \pm \sqrt{4 - \alpha^2}\right)/2.$$

Rewriting ψ^1 in terms of its real and imaginary components yields

$$\left.\begin{array}{l} \lambda \cos \omega_r \Delta t = \pm\sqrt{4 - \alpha^2}/2 \\ \lambda \sin \omega_r \Delta t = -\alpha/2 \end{array}\right\} \quad \text{if } \alpha^2 \le 4$$

and

$$\left.\begin{array}{l} \lambda \cos \omega_r \Delta t = 0 \\ \lambda \sin \omega_r \Delta t = \left(-\alpha \pm \sqrt{\alpha^2 - 4}\right)/2 \end{array}\right\} \quad \text{if } \alpha^2 > 4.$$

When $\alpha^2 \le 4$, squaring the real and imaginary components gives

$$\lambda^2 = \frac{1}{4}\alpha^2 + 1 - \frac{1}{4}\alpha^2 = 1, \text{ or } \lambda = \pm 1,$$

so that the *amplitude is preserved for all wavelengths* and the scheme is said to be *neutrally stable*.

When $\alpha^2 > 4$, $\cos \omega_r \Delta t = 0$, so that the imaginary component can be written as

$$\lambda = -\frac{1}{2}\alpha \pm \frac{1}{2}\sqrt{\alpha^2 - 4}.$$

To ascertain whether this quantity is less than or greater than unity, let

$$\alpha = 2 + \epsilon,$$

where $\epsilon > 0$, so that

$$\lambda = -1 - \frac{1}{2}\epsilon \pm \frac{1}{2}\sqrt{4\epsilon + \epsilon^2}.$$

Since either root is possible,

$$\lambda = -1 - \frac{1}{2}\epsilon - \frac{1}{2}\sqrt{4\epsilon + \epsilon^2} < -1,$$

($|\lambda| > 1$), so that when $\alpha^2 > 4$, the leapfrog scheme is linearly unstable. Since $\alpha^2 = 4C^2 \sin^2 k\Delta x$, stability is retained only when

$$C^2 \sin^2 k\Delta x \leq 1,$$

or since the maximum value of $\sin^2 k\Delta x$ is unity for a $4\Delta x$ wave ($k\Delta x = \pi/2$),

$$|C| \leq 1$$

is a necessary and sufficient condition for the linear stability of the scheme.

The ratio of the predicted phase speed to the advecting velocity for this technique can be obtained by dividing the imaginary component by the real component for $\alpha^2 \leq 4$ and solving for the phase speed. However, since $|\lambda| = 1$, it is also possible to use either the imaginary or the real components separately to obtain the phase speed. Using the imaginary part, therefore, gives the ratio of the calculated to analytic phase speeds as

$$\frac{\tilde{c}_\phi}{U} = \frac{1}{Uk\Delta t} \sin^{-1}\left(\pm \frac{\alpha}{2}\right).$$

Because of the quadratic form of Eq. (10-18), two wave solutions occur. One solution moves downstream ($\tilde{c}_\phi > 0$, when $U > 0$) and is related to the real solution of the advection equation, and the other travels upstream and is called the *computational mode*.[7] The computational mode occurs because the leapfrog is a second-order difference equation. Such separation of solutions by the centered-in-time leapfrog scheme can be controlled by occasionally averaging in time to ensure that the even and odd time steps remain consistent with one another. As long as the time steps are consistent, the amplitude of the computational mode is small.

Values of λ and $\tilde{c}_\phi$ for the physical solution for different values of C and wavelength are displayed in Table 10-1. There is also the computational solution, which is shown for the phase of the leapfrog scheme in the first edition of this book. Although the leapfrog scheme preserves amplitudes exactly as long as $|C| \leq 1$, the accuracy of the phase representation deteriorates markedly for the shorter wavelengths. Because the numerical representation of these waves travels more slowly than the true solution, the scheme is said to be *dispersive*, since when waves of different wavelengths are linearly superimposed, they travel with different speeds relative to one another even if the advecting velocity is a constant. Retention of these dispersive shorter waves in the solution can cause computational problems through nonlinear instability, as discussed in Section 10.5.[8] The important conclusion obtained from the analysis of the leapfrog scheme is that *the exact representation of the amplitude does not by itself guarantee successful simulations, since the fictitious dispersion of waves of different lengths can generate errors*. Baer and Simons (1970), for example, have reported that in approximating nonlinear advection terms, individual energy components may have large errors when the total energy has essentially none. They further conclude that neither conservation of integral properties nor satisfactory prediction of amplitude is sufficient to justify confidence in the results—one must also assure the accurate calculation of phase speed.

Smolarkiewicz and Margolin (1998) summarize how the error characteristics of a finite difference scheme can be used to improve the accuracy of the solution. They show, for example, how using the successive iterative application of the positive definite[9] properties of the upstream difference scheme can compensate for the residual truncation error. More iteration results in smaller truncation errors. This numerical technique is also discussed in Wortmann-Vierthaler and Moussiopoulos (1995).

10.1.1.3   *Adams–Bashford Differencing Scheme*

A fourth representation of advection is the Adams–Bashford algorithm (Durran 1991) as used in, for example, the Song and Haidvogel (1994) ocean model. The analysis of this scheme was completed by Alex Costa and Sue van den Heever as part of a class at Colorado State University on mesoscale modeling. The scheme can be written as

$$\frac{\phi^{\tau+1} - \phi^\tau}{\Delta t} = \frac{1}{12}[23F(\phi^\tau) - 16F(\phi^{\tau-1}) + 5F(\phi^{\tau-2})], \qquad (10\text{-}19)$$

where in one dimension,

$$F(\phi^\tau) = -U\frac{\partial \phi}{\partial x} = -U\frac{\phi^\tau_{i+1} - \phi^\tau_{i-1}}{2\Delta x} \qquad (10\text{-}20)$$

is used.

Substituting Eq. (10-20) into Eq. (10-19) yields

$$\phi_i^{\tau+1} = \phi_i^\tau - U \frac{\Delta t}{\Delta x} \frac{1}{24} \big[23\big(\phi_{i+1}^\tau - \phi_{i-1}^\tau\big) - 16\big(\phi_{i+1}^{\tau-1} - \phi_{i-1}^{\tau-1}\big)$$
$$+ 5\big(\phi_{i+1}^{\tau-2} - \phi_{i-1}^{\tau-2}\big)\big]. \tag{10-21}$$

Substituting ψ^1, ψ^0, ψ^{-1}, and ψ^{-2} into Eq. (10-21) yields

$$\psi^3 - \left(1 - \frac{23}{12}i\alpha\right)\psi^2 - \frac{4}{3}i\alpha\psi^1 + \frac{5}{12}i\alpha = 0, \tag{10-22}$$

where $\alpha = U \frac{\Delta t}{\Delta x} \sin k\Delta x$.

The amplitude and phase for the physical solution of ψ^1, as computed by Alex Costa and Sue van den Heever, are given in Table 10-1. The solutions for the two computational amplitudes and phases can be obtained from the solution of Eq. (10-22). A surprising result of the analysis for the computational modes is that for one of the modes, the computational values of λ are greater than unity for values of C larger than about 0.72 (for a $4\Delta x$ wavelength). For this reason, all values of the physical solution are left out of Table 10-1 for these values of C, even though the physical solution itself is not linearly unstable. As soon as a computational mode develops, if $C > 0.72$ and $4\Delta x$ waves occur, then the computational mode will quickly swamp the solution of the advection equation.

In both the forward-upstream and leapfrog schemes that we have examined, the time step must be less than or equal to the time that it takes for changes at one grid point to be translated by advection to the next grid point downstream. With the Adams–Bashford scheme, the time step must be even smaller. When we generalize this result to all types of wave propagation, the need to filter rapidly moving waves, which are not considered important on the mesoscale, is apparent. This is the reason that scale analysis is used to derive simplified conservation relations [e.g., the anelastic conservation-of-mass equation (3-11) in Chapter 3], so that sound waves can be eliminated as a possible solution, as discussed in Section 5.2.2.

10.1.1.4   Flux Correction[10]

Using the characteristic of the numerical solution to improve the accuracy of the representation of advection has been proposed. This technique, called "flux correction," is described in this section. However, although this technique improves the accuracy of the results, it cannot be analyzed using the linear stability analysis discussed in the previous section, since the flux correction scheme has a nonlinear formulation (Smolarkiewicz 1989).

The original form of the flux correction technique was introduced by Bott (1989). In that paper, the numerical representations of the advective fluxes

reported in Tremback *et al.* (1987) are normalized to reduce phase speed errors. Negative values are redistributed across wavelengths, so that the result of the advection is positive definite. Bott's solution procedure is discussed and improved on in Easter (1993) and Costa and Sampaio (1997).

The simplicity and acceptable computational cost of most flux-limitation procedures makes this technique attractive because of its physical basis. Most of the flux-corrected advection schemes maintain, by construction, the positive definiteness (e.g., Smolarkiewicz 1983; Bott 1989) or the monotonicity (e.g., Grabowski and Smolarkiewicz 1990; Bott 1992) of the advected variable. However, not only positive definiteness is required for accurate solutions, but also the conservation-of-mass and higher-order moments of the advected distribution function are needed to achieve an accurate solution. Therefore, it is useful to examine potential errors from flux correction.

In this section, Bott's positive definite scheme is used in simple numerical experiments to investigate the errors associated with flux correction. The analyses show that, although case dependent, errors related to energy partitioning among individual waves might indeed be significant.

The scheme discussed here is the third-order version of Bott's positive definite scheme described by Easter (1993). As pointed out by Costa and Sampaio (1997), depending on the case, the modified third-order and the fifth-order schemes exhibit the most appropriate balance between accuracy and computational cost. The third-order algorithm was chosen for simplicity.

The amplitude and phase errors for the modified third-order Bott's scheme, assuming constant grid spacing and not applying flux constraints, are given in Tables 10-2 and 10-3. Note that the scheme exhibits small damping, especially for $8\Delta x$ and broader modes. For $2\Delta x$ wavelengths (and, since the damping is cumulative, also for $4\Delta x$ waves), numerical diffusion is often significant. Except for the $2\Delta x$ mode, the phase errors are small.

As flux correction is introduced, one should expect changes in the propagation of the individual modes. Flux correction is based on the calculation of coefficients that physically limit the value of the fluxes, to avoid the appearance of spurious negative values of the advected variable. Since such a calculation involves the actual value of the advected function, which includes all of the distinctive waves, the propagation of an individual mode becomes dependent on the other modes. (A detailed description of the flux-limiting procedures for positive definiteness can be found in Bott 1989 and Chlond 1994.) One might expect such a mode interaction to lead to amplitude (and also phase) errors that are distinct from those related to the noncorrected scheme. This is verified for two particular cases.

Two numerical experiments were performed to assess the errors associated with the flux-limiting procedures. In both cases, one-dimensional advection by a

TABLE 10-2

Amplitude Errors as a Function of the Wavelength and Courant Number for the
Third-Order Bott's Scheme Without Flux Correction

Courant number	Wavelength				
	$2\Delta x$	$4\Delta x$	$6\Delta x$	$8\Delta x$	$10\Delta x$
0.01	0.986468	0.998338	0.999793	0.999959	0.999989
0.1	0.848000	0.983972	0.998091	0.999622	0.999896
0.2	0.664000	0.970045	0.996568	0.999330	0.999817
0.3	0.456000	0.959285	0.995465	0.999123	0.999761
0.4	0.232000	0.952495	0.994799	0.999000	0.999728
0.5	0.000000	0.950175	0.994576	0.998959	0.999718
0.6	0.232000	0.952495	0.994799	0.999000	0.999728
0.7	0.456000	0.959285	0.995465	0.999123	0.999761
0.8	0.664000	0.970045	0.996568	0.999330	0.999817
0.9	0.848000	0.983972	0.998091	0.999622	0.999896
1.0	1.000000	1.000000	1.000000	1.000000	1.000000

From Costa et al. 2000.

TABLE 10-3

Phase Errors as a Function of the Wavelength and Courant Number for the
Third-Order Bott's Scheme Without Flux Correction

Courant number	Wavelength				
	$2\Delta x$	$4\Delta x$	$6\Delta x$	$8\Delta x$	$10\Delta x$
0.01	0.000000	0.955992	0.999319	1.001065	1.000714
0.1	0.000000	0.965610	0.999584	1.000851	1.000559
0.2	0.000000	0.976014	0.999780	1.000604	1.000391
0.3	0.000000	0.985548	0.999898	1.000368	1.000235
0.4	0.000000	0.993684	0.999963	1.000162	1.000103
0.5	0.000000	1.000000	1.000000	1.000000	1.000000
0.6	0.000000	1.004211	1.000024	0.999892	0.999931
0.7	0.000000	1.006194	1.000044	0.999842	0.999899
0.8	0.000000	1.005996	1.000055	0.999849	0.999902
0.9	0.000000	1.003821	1.000046	0.999905	0.999938
1.0	0.000000	1.000000	1.000000	1.000000	1.000000

From Costa et al. 2000.

uniform flow is considered. The Courant number in both numerical experiments
is 0.8.

Experiment 1: Superposition of Short Waves.   In this experiment, the advec-
tion of superposed waves ranging from $2\Delta x$ to $8\Delta x$ is evaluated in an integration
domain of 32 grid points with periodic boundary conditions. The analytical form

of the advected function is given by

$$\phi = a + b\cos(\pi x) + c\cos\left(\frac{\pi x}{2}\right) + d\cos\left(\frac{\pi x}{4}\right), \tag{10-23}$$

where $a = 1$, $b = -(2 - \sqrt{2})/(2 + \sqrt{2})$, $c = 2\sqrt{2}/(2 + \sqrt{2})$, and $d = 4/(1 + \sqrt{2})$. ϕ is depicted in Figure 10-3. The choice of this set of coefficients makes ϕ a positive definite function, with major contributions from the $4\Delta x$ and $8\Delta x$ components.

The results obtained with the noncorrected and the corrected schemes after displacement of $80\Delta x$, which corresponds to 100 time iterations, are shown in Figures 10-4 and 10-5, respectively. The exact solution is obviously identical to the initial condition, depicted in Figure 10-3. The existence of negative values in Figure 10-4 is obvious, but these are completely suppressed in Figure 10-5.

Of course, the corrected solution is globally superior. Not only is it physically consistent, while the noncorrected solution is not, but also the root mean square error is smaller for the corrected solution (0.453) and larger for the solution without correction (0.505).

In both solutions mass is conserved, which is valid in general for flux-form advective schemes by construction. However, higher-order moments, such as the "energy" (second-order moment of the distribution), are not conserved. The "energy ratio," defined as $(\sum \phi^2|_{\text{numerical}})/(\sum \phi^2|_{\text{exact}})$ for the two numerical solutions, is 0.813 (noncorrected) and 0.666 (corrected).

Since the corrected solution is "less energetic," more dissipation might be occurring at certain modes. To require positive definiteness, flux correction forces (in at least some degree) maintenance of the smaller-scale structure; the extra damping apparently occurs at the coarser modes.
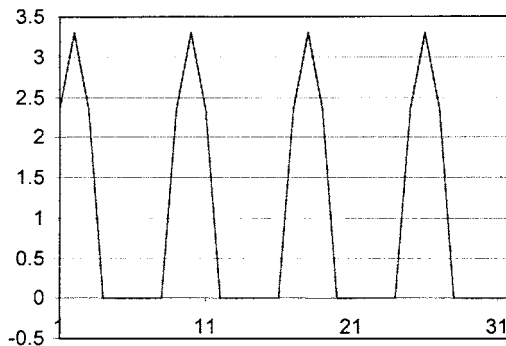
Fig. 10-3. Initial condition and exact solution for Experiment 1. (From Costa *et al.* 2000.)
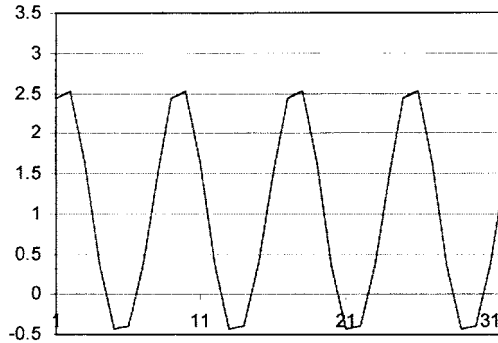
Fig. 10-4. Numerical solution without flux correction for Experiment 1. (From Costa *et al.* 2000.)

Such a hypothesis can be verified by evaluating the Fourier spectrum of the numerical solutions. Figure 10-6 shows the amplitude of the individual Fourier model for the exact solution and the two numerical solutions. The noncorrected solution essentially preserves the amplitude of the $8\Delta x$ mode, while the $4\Delta x$ mode is drastically damped. On the other hand, the $4\Delta x$ component has an amplitude about four times larger in the corrected solution, while the $8\Delta x$ wave is damped by a factor of 14%. These results suggest not only that the energy of the $4\Delta x$ mode is maintained at the expense of the $8\Delta x$ mode, but also that part of the energy that downscales is actually dissipated.

Experiment 2: Exponential Function.   To evaluate how the redistribution of energy operates in a more complex case, one must use a more complex function, for which a wide range of scales must be superposed. Since the exponential function has a very simple Fourier transform, the distribution used in this test
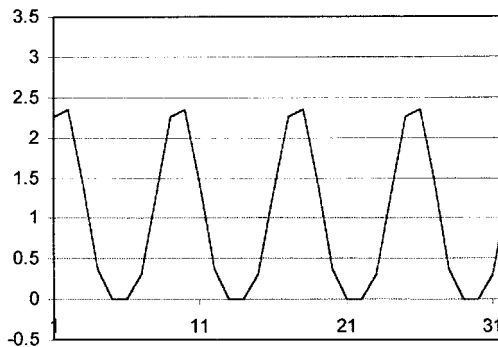
Fig. 10-5. Numerical solution with flux correction for Experiment 1. (From Costa *et al.* 2000.)
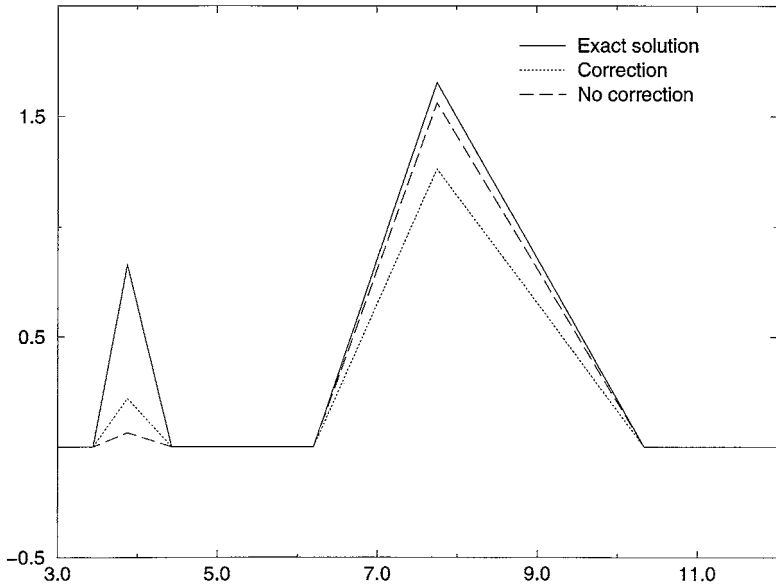
Fig. 10-6. Coefficients of the Fourier transform for the exact and numerical solutions as a function of wavelength for Experiment 1. (From Costa *et al.* 2000.)

follows the relation

$$\phi = \begin{cases} e^{-(L/2-x)} & \text{if } x < L/2 \\ e^{-x} & \text{if } x > L/2, \end{cases} \qquad (10\text{-}24)$$

where L is the length (number of grid points) of the integration domain, which was set to 128 in this experiment. The coefficients of the Fourier modes for the exact solution are proportional to $(n\Delta x)^2/[(n\Delta x)^2 + 1]$, where $n\Delta x$ is the wavelength.

As in the previous experiment, periodic boundary conditions were used. Advection was evaluated for one full revolution (160 time steps for a Courant number of 0.8). Figure 10-7 shows the exact and numerical solutions for this case. The most obvious deficiency of both numerical solutions is the attenuation of the prominent peak in the initial condition, which suggests significant dissipation at the smallest scales.

The coefficients of the Fourier transform for the numerical solutions are depicted in Figure 10-8. Both the corrected and noncorrected solutions damp out most of the very short waves ($\leq 4\Delta x$). Nonetheless, the same feature as observed in the previous experiment occurred. The corrected solution contains more energy at the shortwave range, while the coarse modes present a smaller
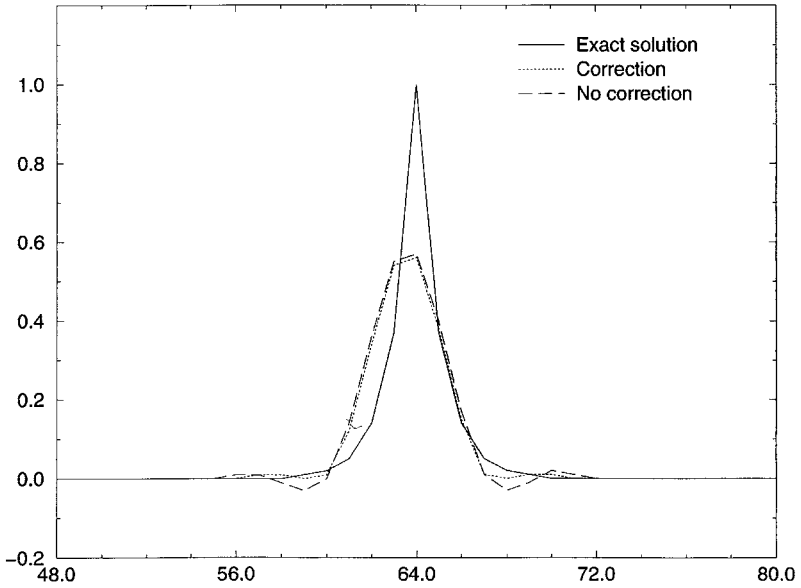
Fig. 10-7.   Initial conditions, exact solutions, and numerical solutions for Experiment 2 (with only the portion of the domain $48 \leq x \leq 80$ shown.) (From Costa *et al.* 2000.)
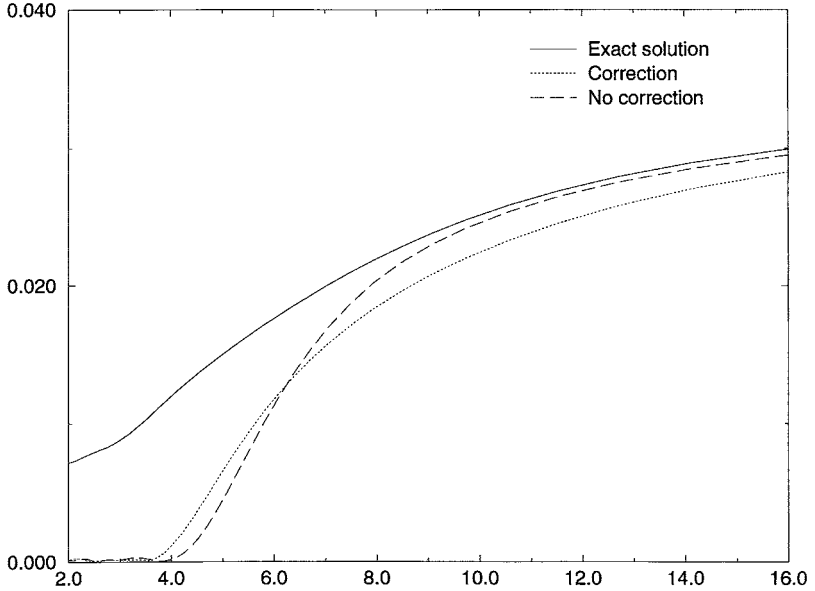
Fig. 10-8.   Coefficients of the Fourier transform for the exact and numerical solutions as a function of wavelength for Experiment 2. (From Costa *et al.* 2000.)

amplitude than in the noncorrected case. Again, the results suggest that flux correction tries to preserve the shortwave components by consuming energy from coarser scales and that extra dissipation occurs as the scheme redistributes the energy among the modes.

The results of simple numerical experiments lead to significant conclusions on how flux-corrected advective techniques operate in terms of modifying the propagation of individual waves. Flux-corrected numerical solutions represent a valuable numerical solution technique. Nonetheless, flux correction can introduce errors, as shown in the two experiments.

In general, flux-corrected solutions contain less energy, which implies that extra dissipation is introduced in association with the flux-limiting procedure. To maintain positive definiteness (in the case of a positive definite scheme), energy must be supplied to the smaller scales, which is done at the expense of the larger scales. In fact, in such a process, energy not only is redistributed toward the shortwave range, but is also dissipated. This process is shown in Figure 10-9.

Without flux correction, the advection scheme is linear, and the individual modes are independent from one another. Dissipation occurs mostly at the smaller scales, while the coarse modes do not exhibit significant damping. When flux correction is introduced, the individual waves start to interact, and energy is supplied to the small scales from the large scales. Such a transfer of energy is accompanied by dissipation. As a consequence, the global energy content of the numerical solution, as well as the energy content of the large scales, are reduced when flux correction is applied.
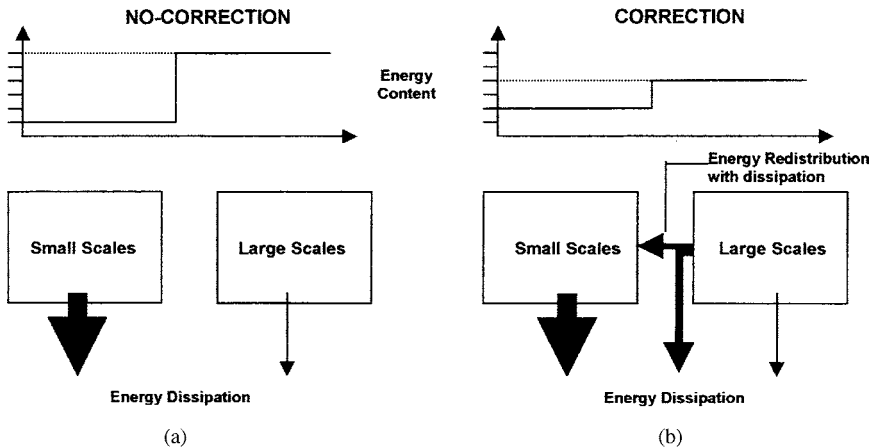
Fig. 10-9. "Energy diagrams" for the numerical schemes (a) without correction and (b) with correction. See text for comments. (From Costa *et al.* 2000.)

Other investigators have also suggested improved techniques to conserve mass. These include Galperin and Kastrel (1998), Walcek and Aleksic (1998), and Walcek (1999a, b). The latter papers provided their Fortran code, a publication procedure that should be encouraged.

10.1.2 Subgrid-Scale Flux

As shown by Eq. (7-7), the subgrid-scale correlation terms can be represented as the product of an exchange coefficient and the gradient of the appropriate dependent variable. This relation can be written as, for example,

$$\frac{\partial \bar{\phi}}{\partial t} = \frac{\partial}{\partial z} K \frac{\partial \bar{\phi}}{\partial z} \simeq \frac{\phi_i^{\tau+1} - \phi_i^{\tau}}{\Delta t}$$

$$= K_{i+\frac{1}{2}} \frac{\phi_{i+1}^{\tau} - \phi_i^{\tau}}{(\Delta z)^2} - K_{i-\frac{1}{2}} \frac{\phi_i^{\tau} - \phi_i^{\tau} - 1}{(\Delta z)^2}, \qquad (10\text{-}25)$$

where $\Delta z = z(i+1) - z(i) = z(i) - z(i-1)$ and ϕ represents any one of the dependent variables. This equation is often referred to as the *diffusion equation*. To study the linear stability of this scheme, the exchange coefficient is assumed to be a constant ($K_{i+1/2} = K_{i-1/2} = K$) and Eq. (10-25) is written as

$$\phi_i^{\tau+1} = \phi_i^{\tau} + K \frac{\Delta t}{(\Delta z)^2} \left(\phi_{i+1}^{\tau} - 2\phi_i^{\tau} + \phi_{i-1}^{\tau} \right). \qquad (10\text{-}26)$$

The exact solution to the diffusion equation [the left side of Eq. (10-25) with K equal to a constant, i.e., $\partial \bar{\phi}/\partial t = K \, \partial^2 \bar{\phi}/\partial z^2$] can be determined by assuming

$$\bar{\phi} = \phi_0 e^{i(kz+\omega t)} = \phi_0 e^{-\omega_i t} e^{i(k_r z + \omega_r t)},$$

where damping in the z direction is not permitted (i.e., $k_i \equiv 0$). Substituting this expression into the linearized diffusion equation and simplifying yields

$$i\omega_r - \omega_i = -Kk^2,$$

where the subscript "r" on k has been eliminated to simplify the notation. Equating real and imaginary components shows that $\omega_r \equiv 0$, so the exact solution can be written as

$$\bar{\phi} = \phi_0 e^{-Kk^2 t} e^{ikz}.$$

Expressing the dependent variables as a function of frequency and wavenumber, Eq. (10-26) can be rewritten as

$$\psi^1 = 1 + \gamma(\psi_1 - 2 + \psi_{-1}) = 1 + 2\gamma(\cos k\Delta z - 1),$$

where $\gamma = K\Delta t/(\Delta z)^2$ and $\psi_1 + \psi_{-1} = 2\cos k\,\Delta z$. The nondimensional parameter γ is called the *Fourier number*. Equating real and imaginary components yields

$$\lambda\cos\omega_r\Delta t = 1 + 2\gamma(\cos k\Delta z - 1)$$

$$\lambda\sin\omega_r\Delta t = 0.$$

Since $\sin\omega_r\Delta t$ must be identically equal to 0, $\omega_r\Delta t$ and thus the phase speed are also equal to 0. Thus the solution to Eq. (10-26) does not propagate as a wave, but rather amplifies or decays in place. Since $\cos\omega_r\Delta t = 1$, the real part can be divided by the analytic solution,[11] $\lambda_a = e^{-Kk^2\Delta t} = e^{-\gamma(2\pi)^2/n^2}$, and rewritten as

$$\frac{\lambda}{\lambda_a} = \frac{1 + 2\gamma(\cos k\Delta z - 1)}{e^{-\gamma(2\pi)^2/n^2}}$$

where n is the number of grid points per wavelength. For very long waves $(n \to \infty)$, $\lambda_a = 1$ and $\lambda = 1$, since $\cos k\Delta z = \cos(2\pi/L)\Delta z = 1$, and thus no damping or amplification occurs. For the shortest waves that can be resolved $(L = 2\Delta z; n = 2)$,

$$\lambda = 1 - 4\gamma.$$

To ensure that the magnitude of λ is less than unity and thus computationally stable, 4γ must be less than or equal to 2, or

$$\gamma \le \frac{1}{2}.$$

The condition $\gamma = \frac{1}{2}$, however, causes γ to switch between $+1$ and -1 with each application of Eq. (10-26), but the analytic solution is $\lambda_a = e^{-4.95} = 0.00719$. This unrealistic response of $2\Delta z$ wavelength features can cause computational problems in a nonlinear model, as discussed in Section 10.5. To eliminate $2\Delta z$ waves at each application of Eq. (10-26), λ can be set to 0 for a $2\Delta z$ wave, resulting in $\gamma = \frac{1}{4}$. Thus the standard requirement specified in using this scheme is that

$$\gamma = K\Delta t/(\Delta z)^2 \le \frac{1}{4},$$

with the expectation that γ is close to $\frac{1}{4}$ so that the presence of $2\Delta z$ waves is minimized.

Up to this point, the approximations to the advective and subgrid-scale flux terms have always been defined at the current time step (i.e., ϕ_i^τ). The predicted dependent variable $\phi_i^{\tau+1}$ enters only through the time tendency term. Such schemes are referred to as *explicit* and can be written in general as

$$\phi^{\tau+1} = f(\phi^\tau),$$

where the function f can include spatial derivatives of ϕ^τ as well as the variable itself.

In contrast, an *implicit* scheme uses information from the future time step, as well as present values. For this case,

$$\phi^{\tau+1} = f(\phi^{\tau+1}, \phi^\tau).$$

In general, the use of an implicit representation permits longer time steps than the explicit form without causing linear instability. An implicit form of the left side of Eq. (10-25) for variable Δz (e.g., Paegle *et al.* 1976) can be written as

$$\frac{\phi^{\tau+1} - \phi^\tau}{\Delta t} = \frac{1}{\Delta z_j} \left[K_{j+\frac{1}{2}} \frac{\beta_\tau (\phi_{j+1}^\tau - \phi_j^\tau) + \beta_{\tau+1}(\phi_{j+1}^{\tau+1} - \phi_j^{\tau+1})}{\Delta z_{j+\frac{1}{2}}} \right.$$
$$\left. - K_{j-\frac{1}{2}} \frac{\beta_\tau (\phi_j^\tau - \phi_{j-1}^\tau) + \beta_{\tau+1}(\phi_j^{\tau+1} - \phi_{j-1}^{\tau+1})}{\Delta z_{j-\frac{1}{2}}} \right] \qquad (10\text{-}27)$$

where $\beta_\tau + \beta_{\tau+1} = 1$, $\Delta z_j = z_{j+\frac{1}{2}} - z_{j-\frac{1}{2}}$, $\Delta z_{j+1} = z_{j+1} - z_j$, and $\Delta z_{j-1} = z_j - z_{j-1}$. The use of β_τ and $\beta_{\tau+1}$ weights the current and future contributions to the numerical approximation of the left side of Eq. (10-25). Note that when $\beta_{\tau+1} = 0$ and $\Delta z_j = \Delta z_{j+1} = \Delta z_{j-1} = \Delta z$, the scheme reverts back to the explicit scheme given by the right side of Eq. (10-25). Linearizing Eq. (10-27) by setting $K_{j+\frac{1}{2}}$ and $K_{j-\frac{1}{2}}$ equal to a constant, using a constant grid interval Δz, and representing the dependent variable in terms of wavenumber and frequency results in

$$\psi^1 = 1 + \gamma[\beta_\tau(\psi_1 - 2 + \psi_{-1}) + \beta_{\tau+1}(\psi_1^1 - 2\psi^1 + \psi_{-1}^1)],$$

where, as with the explicit scheme, $\gamma = K\Delta t/(\Delta z)^2$. Since $\psi_1^1 = \psi^1\psi_1$ and $\psi_{-1}^1 = \psi^1\psi_{-1}$,

$$\psi^1 = 1 + \gamma\beta_\tau(\psi_1 - 2 + \psi_{-1}) + \gamma\beta_{\tau+1}\psi^1(\psi_1 - 2 + \psi_{-1}),$$

or

$$\psi^1 = \frac{[1 + \gamma\beta_\tau(\psi_1 + \psi_{-1} - 2)]}{[1 - \gamma\beta_{\tau+1}(\psi_1 + \psi_{-1} - 2)]} = \frac{1 + 2\gamma\beta_\tau(\cos k\Delta z - 1)}{1 - 2\gamma\beta_{\tau+1}(\cos k\Delta z - 1)} = \lambda,$$

where, as with the analysis of the explicit representation, the imaginary part is 0, so that $\gamma = \psi^1$.

Values of the ratio of the computational approximation of the damping to the analytic damping λ/λ_a are presented in Table 10-4 as a function of wavelength and β_τ. For a given value of γ, the $2\Delta z$ wave is the most poorly represented. In addition, the $2\Delta z$ wave is always insufficiently damped, and the value of λ is often negative, yielding a wave whose amplitude reverses (flip-flops) at each time step. The solutions become more accurate as γ becomes smaller, and the

TABLE 10-4

Values of the Ratio of the Computational to Analytic Damping as a Function of Wavelength for Different Forms of the Forward-in-Time, Centered-in-Space Approximation to the Linearized Diffusion Equation ($\partial\phi/\partial t = K = \partial^2\phi/\partial z^2$)

Scheme	Wavelength	γ									
		0.1	0.2	0.3	0.4	0.5	0.6	0.7	0.8	0.9	1.0
Forward-in-time, centered-in-space diffusion											
Explicit	$2\Delta x$	1.610	1.440	−3.863	−31.094	< − 100					
	$4\Delta x$	1.024	0.983	0.839	0.537	0.0					
$\beta_\tau = 1$	$10\Delta x$	1.001	0.999	0.997	0.992	0.986		$\lambda > 1$ for a $2\Delta z$ wave			
	$20\Delta x$	1.000	1.000	1.000	1.000	0.999					
Implicit	$2\Delta x$	1.725	2.554	2.272	−4.202	−34.761	< − 100	< − 100	< − 100	< − 100	< − 100
	$4\Delta x$	1.038	1.053	1.030	0.952	0.792	0.517	0.079	0.584	−1.555	−2.948
$\beta_\tau = 0.7$	$10\Delta x$	1.001	1.001	1.001	1.000	0.998	0.996	0.992	0.988	0.982	0.975
	$20\Delta x$	1.000	1.000	1.000	1.000	1.000	1.000	1.000	0.999	0.999	0.999
	$2\Delta x$	1.789	3.085	4.829	5.758	0.00	−33.91	< − 100	< − 100	< − 100	< − 100
	$4\Delta x$	1.047	1.092	1.129	1.150	1.145	1.099	0.993	0.800	0.485	0.00
$\beta_\tau = 0.5$	$10\Delta x$	1.001	1.003	1.004	1.005	1.006	1.007	1.007	1.008	1.008	1.008
	$20\Delta x$	1.000	1.000	1.000	1.000	1.000	1.000	1.000	1.001	1.001	1.001
	$2\Delta x$	1.845	3.507	6.718	12.711	23.17	38.97	54.11	33.16	< − 100	< − 100
	$4\Delta x$	1.055	1.126	1.211	1.307	1.414	1.529	1.648	1.766	1.875	1.965
$\beta_\tau = 0.3$	$10\Delta x$	1.002	1.004	1.006	1.009	1.013	1.017	1.021	1.026	1.031	1.037
	$20\Delta x$	1.000	1.000	1.000	1.001	1.001	1.001	1.001	1.002	1.002	1.003
	$2\Delta x$	1.916	3.999	8.779	19.93	46.35	>100	>100	>100	>100	>100
	$4\Delta x$	1.067	1.170	1.310	1.491	1.717	1.998	2.344	2.769	3.290	3.931
$\beta_\tau = 0.1$	$10\Delta x$	1.002	1.005	1.010	1.016	1.023	1.031	1.040	1.050	1.062	1.074
	$20\Delta x$	1.000	1.000	1.001	1.001	1.002	1.002	1.003	1.004	1.004	1.005

Computed by C. Martin.

implicit representation gives reasonable results for large wavelengths even when the explicit form is linearly unstable for all spatial scales.

Equation (10-27) can be written in the following form:

$$
-\frac{\Delta t K_{j-\frac{1}{2}}\beta_{\tau+1}}{\Delta z_j \Delta z_{j-\frac{1}{2}}}\phi_{j-1}^{\tau+1} + \left[1 + \frac{\Delta t K_{j+\frac{1}{2}}\beta_{\tau+1}}{\Delta z_j \Delta z_{j+\frac{1}{2}}} + \frac{\Delta t K_{j-\frac{1}{2}}\beta_{\tau+1}}{\Delta z_j \Delta z_{j-\frac{1}{2}}}\right]\phi_j^{\tau+1}
$$

$$
-\frac{\Delta t K_{j+\frac{1}{2}}\beta_{\tau+1}}{\Delta z_j \Delta z_{j+\frac{1}{2}}}\phi_{j+1}^{\tau+1}
$$

$$
= \phi_j^{\tau} + \frac{\Delta t}{\Delta z_j}\left[\frac{K_{j+\frac{1}{2}}\beta_{\tau}\left(\phi_{j+1}^{\tau} - \phi_j^{\tau}\right)}{\Delta z_{j+\frac{1}{2}}} - \frac{K_{j-\frac{1}{2}}\beta_{\tau}\left(\phi_j^{\tau} - \phi_{j-1}^{\tau}\right)}{\Delta z_{j-\frac{1}{2}}}\right] \qquad (10\text{-}28)
$$

and solved for nonperiodic boundary conditions using a procedure described in Section 10.2. Its solution for periodic boundary conditions is given in Appendix A.

When $\beta_{\tau} = \beta_{\tau+1}$, this representation is called the Crank–Nicholson scheme. Paegle *et al.* (1976) have presented results showing that $\beta_{\tau+1} = 0.75$ provides a representation as accurate as the explicit scheme but with a much longer permissible time step. Figure 10-10, reproduced from Mahrer and Pielke (1978a), illustrates predictions of the growth of a heated boundary layer using both the explicit representation of diffusion given by Eq. (10-25) and the implicit form [Eq. (10-27)] with $\beta_{\tau+1} = 0.75$. As reported in that paper, use of the implicit
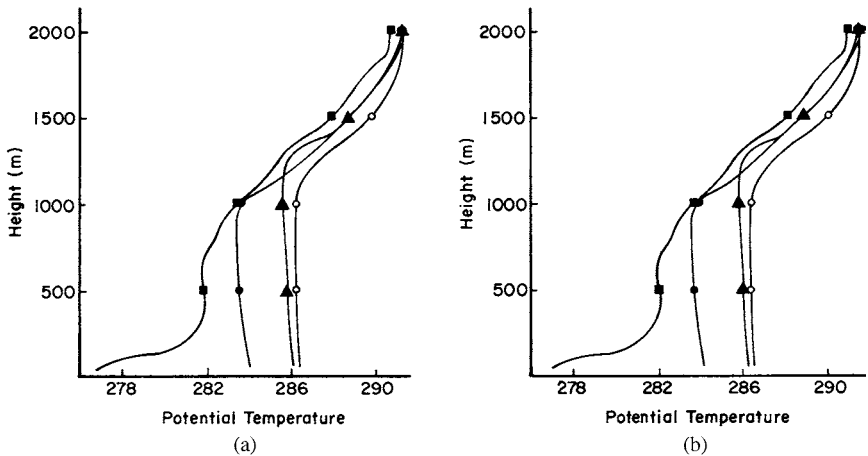
Fig. 10-10. Vertical profiles of the potential temperature for Wangara Day 33 with (a) the implicit scheme ($\beta_{\tau+1} = 0.75$) and (b) the explicit scheme ($\beta_{\tau+1} = 0$), where the darkened squares are at 0900, the darkened circles at 1200, the darkened triangles at 1500, and the open circles at 1700. (From Mahrer and Pielke 1978a.)

form permitted a much longer time step, so the calculation ran 17 times faster than when the explicit form was used.

10.1.3   Coriolis Terms

The implicit scheme can also be shown to be a necessity for the Coriolis terms. The terms dealing with the earth's rotation [see Eq. (4-21)] are already in linear form and with $L_z \ll L_x$ can be written as

$$\partial \bar{u}/\partial t = f\bar{v} \qquad \text{and} \qquad \partial \bar{v}/\partial t = -f\bar{u}. \qquad (10\text{-}29)$$

If these relations are approximated using an explicit representation, they are written as

$$(u_i^{\tau+1} - u_i^{\tau})/\Delta t = fv_i^{\tau} \qquad \text{and} \qquad (v_i^{\tau+1} - v_i^{\tau})/\Delta t = fu_i^{\tau}. \qquad (10\text{-}30)$$

Rewriting the dependent variables in terms of frequency and wavenumber, and rearranging yields

$$\hat{u}(\psi^1 - 1) - \hat{v}\Delta t f = 0$$

and

$$\hat{u}f\Delta t + \hat{v}(\psi^1 - 1) = 0,$$

where $\hat{u}$ and $\hat{v}$ are functions of ω and k. In matrix form, these equations can be written as

$$\begin{bmatrix} \psi^1 - 1 & -\Delta t f \\ \Delta t f & \psi^1 - 1 \end{bmatrix} \begin{bmatrix} \hat{u} \\ \hat{v} \end{bmatrix} = \begin{bmatrix} 0 \\ 0 \end{bmatrix}.$$

As shown preceding Eq. (5-31), this homogeneous set of algebraic equations has a solution only if the determinant of the coefficients is equal to 0, thus

$$(\psi^1 - 1)^2 + (\Delta t)^2 f^2 = \psi^2 - 2\psi^1 + 1 + (\Delta t)^2 f^2 = 0.$$

Using the formula for the solution of a quadratic equation,

$$\psi^1 = \left[2 \pm \sqrt{4 - 4(1 + (\Delta t)^2 f^2)}\right]/2 = 1 \pm i\Delta t f.$$

Equating real and imaginary components,

$$\lambda \cos \omega_r \Delta t = 1$$

$$\lambda \sin \omega_r \Delta t = \pm \Delta t f,$$

and then summing and squaring yields

$$\lambda^2 = 1 + (\Delta t)^2 f^2, \quad \text{so } \lambda = \sqrt{1 + (\Delta t)^2 f^2} \geq 1.$$

Thus except when $\Delta t = 0$ or $f = 0$ (at the equator) the explicit representation of the Coriolis terms given by Eq. (10-30) is *linearly unstable.*[12] The analytic solution of course requires that $\lambda = 1$.

A second representation of Eq. (10-29) is to use an implicit form given by

$$(u_i^{\tau+1} - u_i^{\tau})/\Delta t = fv_i^{\tau} \quad \text{and} \quad (v_i^{\tau+1} - v_i^{\tau})/\Delta t = -fu_i^{\tau+1}, \quad (10\text{-}31)$$

so that the updated value of u is used in the v equation. Rewriting Eq. (10-31) in terms of frequency and wavenumber, rearranging, and writing in matrix form results in

$$\begin{bmatrix} \psi^1 - 1 & -\Delta t f \\ \psi^1 f \, \Delta t & \psi^1 - 1 \end{bmatrix} \begin{bmatrix} \hat{u} \\ \hat{v} \end{bmatrix} = \begin{bmatrix} 0 \\ 0 \end{bmatrix}.$$

Setting the determinant of the matrix of coefficients to 0 gives the equation

$$\psi^2 + \psi^1[(\Delta t)^2 f^2 - 2] + 1 = 0,$$

which, using the quadratic formula and rearranging, has the solution

$$\psi^1 = 1 - \frac{(\Delta t)^2 f^2}{2} \pm \frac{(\Delta t) f \sqrt{(\Delta t)^2 f^2 - 4}}{2}. \quad (10\text{-}32)$$

Two forms of this relation need to be examined. If $(\Delta t)^2 f^2 > 4$, then the entire expression is real and $\omega_r \Delta t = 0$. Thus if $(\Delta t)^2 f^2 = 4 + \epsilon^2$, where $\epsilon > 0$ but $\epsilon^2 \ll 4$, then

$$\psi^1 = \lambda \simeq 1 - \frac{4 + \epsilon^2}{2} \pm \epsilon = 1 - 2 - \frac{\epsilon^2}{2} \pm \epsilon.$$

Since both roots are possible,

$$\lambda \simeq -1 - \frac{\epsilon^2}{2} - \epsilon < -1 \text{ (i.e., } |\lambda| > 1),$$

so that when $(\Delta t)^2 f^2 > 4$, the representation is linearly unstable.

If $(\Delta t)^2 f^2 \leq 4$, then Eq. (10-32) can be rewritten as

$$\psi^1 = 1 - \frac{(\Delta t)^2 f^2}{2} \pm \frac{i(\Delta t) f \sqrt{4 - (\Delta t)^2 f^2}}{2}.$$

Equating real and imaginary parts yields

$$\lambda \cos \omega_r \Delta t = 1 - [(\Delta t)^2 f^2/2]$$

$$\lambda \sin \omega_r \Delta t = \left[\pm \Delta t f \sqrt{4 - (\Delta t)^2 f^2}\right]/2.$$

Squaring the two expressions and adding results in

$$\lambda^2 = 1 - (\Delta t)^2 f^2 + \frac{1}{4}\left[(\Delta t)^2 f^2\right]^2 + (\Delta t)^2 f^2 - \frac{1}{4}\left[(\Delta t)^2 f^2\right]^2 = 1.$$

The scheme is, therefore, neutrally stable as long as $(\Delta t)^2 f^2 \leq 4$. Since the maximum value of f on the earth is $1.45 \times 10^{-4}\,\mathrm{s}^{-1}$, time steps shorter than 13,793 seconds ensure linear stability of this term.

10.1.4 Pressure Gradient and Velocity Divergence

To investigate different approximations to the pressure gradient force and velocity divergence terms, it is useful to use the linear form of the one-fluid tank model introduced in Chapter 5, Section 5.2.1.1. The linear equations (5-22) and (5-23) developed in that chapter are given by

$$\frac{\partial u'}{\partial t} = -g\,\frac{\partial h}{\partial x} \qquad \text{and} \qquad \frac{\partial h}{\partial t} = -h_0\,\frac{\partial u'}{\partial x}. \tag{10-33}$$

As expressed by Eq. (5-32), the analytic solution to Eq. (10-33) corresponds to a wave traveling with a speed of $\sqrt{gh_0}$. Since the amplitude of this wave is unchanging, a computationally accurate scheme will have $\lambda = 1$ in the stability analysis.

In a forward-in-time, centered-in-space explicit representation, these equations can be approximated by

$$\frac{u_i^{\tau+1} - u_i^{\tau}}{\Delta t} = -g\,\frac{h_{i+1}^{\tau} - h_{i-1}^{\tau}}{2\Delta x}$$

$$\frac{h_i^{\tau+1} - h_i^{\tau}}{\Delta t} = -h_0\,\frac{u_{i+1}^{\tau} - u_{i-1}^{\tau}}{2\Delta x}.$$

Representing these two finite difference equations in wavenumber and frequency space yields the algebraic equations

$$(\psi^1 - 1)\hat{u} + \frac{g\Delta t}{2\Delta x}(\psi_1 - \psi_{-1})\hat{h} = 0$$

$$(\psi^1 - 1)\hat{h} + \frac{h_0\Delta t}{2\Delta x}(\psi_1 - \psi_{-1})\hat{u} = 0,$$

which, after substituting for $\psi_1 - \psi_{-1}$ and rearranging, can be written in matrix form as

$$\begin{bmatrix} (\psi^1 - 1) & \frac{g\Delta t}{\Delta x}i\sin k\Delta x \\ h_0\frac{\Delta t}{\Delta x}i\sin k\,\Delta x & (\psi^1 - 1) \end{bmatrix} \begin{bmatrix} \hat{u} \\ \hat{h} \end{bmatrix} = \begin{bmatrix} 0 \\ 0 \end{bmatrix}.$$

For a nontrivial solution, the determinant of the coefficients must be 0, so that

$$\psi^2 - 2\psi^1 + 1 + gh_0\left(\frac{\Delta t}{\Delta x}\right)^2 \sin^2 k\Delta x = 0,$$

and, using the quadratic formula,

$$\psi^1 = \frac{2 \pm \sqrt{4 - 4\big(1 + gh_0(\Delta t/\Delta x)^2 \sin^2 k\Delta x\big)}}{2}$$

or

$$\psi^1 = 1 \pm \sqrt{-gh_0(\Delta t/\Delta x)^2 \sin^2 k\Delta x} = 1 \pm i\sqrt{gh_0}(\Delta t/\Delta x) \sin k\Delta x.$$

The real and imaginary components of this expression are

$$\lambda \cos \omega_r \Delta t = 1$$

$$\lambda \sin \omega_r \Delta t = \pm\sqrt{gh_0}(\Delta t/\Delta x) \sin k\Delta x,$$

Squaring and summing the two equations results in

$$\lambda^2 = 1 + gh_0(\Delta t/\Delta x)^2 \sin^2 k\Delta x,$$

so that $|\lambda| > 1$, and the *explicit representation* is *linearly unstable*.

Since the Coriolis terms are linearly unstable for an explicit scheme, but stable when an implicit representation is used, it seems reasonable to examine a similar form, in which dependent variables are updated to their $\tau + 1$ values in the second equation of the simultaneous set. Equation (10-33) thus can be approximated[13] by

$$\frac{u_i^{\tau+1} - u_i^{\tau}}{\Delta t} + g\frac{h_{i+1}^{\tau} - h_{i-1}^{\tau}}{2\Delta x} = 0$$

$$\frac{h_i^{\tau+1} - h_i^{\tau}}{\Delta t} + h_0\frac{u_{i+1}^{\tau+1} - u_{i-1}^{\tau+1}}{2\Delta x} = 0.$$

(10-34)

When programming this system of equations on a computer, the choice of initial conditions will determine the initial amplitude and phase. Using $u^{\tau=0} = (g/h)^{1/2}h^{\tau=0}$, for example, with $h^{\tau=0} = \cos kj\Delta k$ will result in an amplitude change for the first time step of $\lambda = 1 + [\frac{1}{2}\tan(kj\Delta x) \sin k\Delta x]$ defining $g/h = 1$ for simplicity. The following stability analysis is valid only after this time.

Rewriting this expression in terms of frequency and wavenumber yields

$$(\psi^1 - 1)\hat{u} + \frac{g\,\Delta t}{2\,\Delta x}(\psi_1 - \psi_{-1})\hat{h} = 0$$

$$(\psi^1 - 1)\hat{h} + \frac{h_0\,\Delta t}{2\,\Delta x}(\psi_1^1 - \psi_{-1}^1)\hat{u} = 0$$

or, in the equivalent matrix form, substituting for $\psi_i - \psi_{-1}$, $(\psi_1^1 - \psi_{-1}^1 = \psi^1(\psi_1 - \psi_{-1}))$,

$$\begin{bmatrix} (\psi^1 - 1) & \frac{g\,\Delta t}{\Delta x} i \sin k\Delta x \\ \frac{h_0\,\Delta t}{\Delta x} i \sin k\Delta x & (\psi^1 - 1) \end{bmatrix} \begin{bmatrix} \hat{u} \\ \hat{h} \end{bmatrix} = \begin{bmatrix} 0 \\ 0 \end{bmatrix}.$$

The determinant of the coefficients must equal 0 for this system of equations to have a nontrivial solution, so that

$$\psi^2 + \psi^1(\gamma^2 - 2) + 1 = 0,$$

where $\gamma^2 = gh_0(\Delta t/\Delta x)^2 \sin^2 k\Delta x$ is the resultant quadratic equation. Solving for ψ^1 gives

$$\psi^1 = \left[(2 - \gamma^2) \pm \gamma\sqrt{\gamma^2 - 4}\right]/2. \qquad (10\text{-}35)$$

Two possible situations arise: $\gamma^2 \leq 4$ and $\gamma^2 > 4$. For the first situation, ψ^1 can be rewritten as $\psi^1 = \left[(2 - \gamma^2) \pm i\gamma\sqrt{4 - \gamma^2}\right]/2$, so that equating real and imaginary components yields

$$\lambda \cos \omega_r \Delta t = (2 - \gamma^2)/2$$
$$\lambda \sin \omega_r \Delta t = \left(\pm\gamma\sqrt{4 - \gamma^2}\right)/2.$$

Squaring and summing these two expressions results in

$$\lambda^2 = \frac{1}{4}\left(4 - 4\gamma^2 + \gamma^4 + 4\gamma^2 - \gamma^4\right) = 1.$$

Since $|\lambda| = 1$, the scheme is neutrally stable, and the phase speed as a function of wavelength c can be obtained from either the imaginary or real components. Using the imaginary component, the ratio of the calculated to analytic phase speeds is

$$\frac{c}{c_a} = \frac{c}{\pm\sqrt{gh_0}} = \frac{1}{\pm k\Delta t\sqrt{gh_0}} \sin^{-1}\left(\frac{\gamma\sqrt{4 - \gamma^2}}{2}\right).$$

From this expression, if $\gamma^2 = 4$, then the calculated phase speed c is 0, which is undesirable, of course, because the analytic solution is $\sqrt{gh_0}$. Table 10-5 gives values of c/c_a for selected values of k and γ.

When $\gamma^2 > 4$, the real and imaginary components of Eq. (10-35) are given by

$$\lambda \cos \omega_r \Delta t = \frac{1}{2}\left[2 - \gamma^2 \pm \gamma\sqrt{\gamma^2 - 4}\right]$$
$$\lambda \sin \omega_r \Delta t = 0.$$

Since there is no nonzero imaginary contribution, $\cos \omega_r \Delta t = 1$ ($\omega_r = 0$, so the wave has no phase speed) and

$$\lambda = 1 - \frac{1}{2}\left[\gamma^2 \pm \gamma\sqrt{\gamma^2 - 4}\right].$$

TABLE 10-5

Values of the Amplitude and Phase Error per Time Step as a Function of Wavelength and $\sqrt{gh_0}\Delta t/\Delta x$ for the Centered-in-Space, Implicit, Forward-in-Time Approximation to the Linearized Tank Model Equations

								$\sqrt{gh_0}\Delta t/\Delta x$							
	Wavelength	0.001	0.01	0.1	0.2	0.3	0.4	0.5	0.6	0.7	0.8	0.9	1.0	1.5	2.0
λ	$2\Delta x$	1.0	1.0	1.0	1.0	1.0	1.0	1.0	1.0	1.0	1.0	1.0	1.0	1.0	1.0
	$4\Delta x$	1.0	1.0	1.0	1.0	1.0	1.0	1.0	1.0	1.0	1.0	1.0	1.0	1.0	1.0
	$10\Delta x$	1.0	1.0	1.0	1.0	1.0	1.0	1.0	1.0	1.0	1.0	1.0	1.0	1.0	1.0
	$20\Delta x$	1.0	1.0	1.0	1.0	1.0	1.0	1.0	1.0	1.0	1.0	1.0	1.0	1.0	1.0
c/c_a	$2\Delta x$	0.0	0.0	0.0	0.0	0.0	0.0	0.0	0.0	0.0	0.0	0.0	0.0	0.0	0.0
	$4\Delta x$	0.637	0.637	0.637	0.638	0.639	0.641	0.643	0.647	0.650	0.655	0.660	0.667	0.613	0.0
	$10\Delta x$	0.935	0.935	0.936	0.936	0.937	0.938	0.939	0.940	0.942	0.944	0.947	0.950	0.969	1.0
	$20\Delta x$	0.984	0.984	0.984	0.984	0.984	0.984	0.985	0.985	0.986	0.986	0.987	0.988	0.993	1.0

Calculations performed by S. Weidman.

If $\gamma^2 = 4 + \epsilon^2$, where $\epsilon > 0$, then with $\gamma > 0$,

$$\lambda = -1 - \frac{1}{2}\epsilon^2 - \epsilon < -1,$$

so the scheme is linearly unstable.

Thus, obtaining stable results with the implicit finite difference representation to the tank model equations requires that

$$\gamma^2 = gh_0(\Delta t/\Delta x)^2 \sin^2 k\Delta x < 4.$$

Since $\sin^2 k\Delta x = 1$ when the wavelength is $4\Delta x(k = 2\pi/4\Delta x)$, the stability condition is

$$\left|\pm\sqrt{gh_0}\Delta t/\Delta x\right| < 2.$$

Sun (1980) has investigated the linear stability of finite difference approximations to equations of the form given by Eqs. (5-37) and (5-39)–(5-41) with $f = 0$, $\rho'/\rho_0 = \theta'/\theta_0$, and $\lambda_2 = 0$. As shown in Section 5.2.2, this system of equations has internal gravity waves as the solution. Using approximate solution techniques, Sun showed that when the hydrostatic assumption is used ($\lambda_1 = 0$), the dependent variables are staggered in space, updated velocities are used in the potential temperature equation, and the pressure gradient is approximated by a centered-in-space scheme, a computationally stable solution results. This sequence of calculations discussed by Sun is called the forward-backward time-integration scheme and has been adopted in a number of mesoscale models (e.g., Bhumralkar 1972, 1973; Jones 1973; Pielke 1974a, b). Bhumralkar (1972) similarly found that unless updated values of velocity were used in the computation of potential temperature, the results would be linearly unstable. Also, as he and others have concluded, the time step must be less than or equal to the time that it takes a disturbance to propagate between grid points, or else the solutions will be unstable.

It is also interesting to note that the approximation to the pressure gradient force [e.g., $g\partial h/\partial x$ in Eq. (10-33)] uses what closely corresponds to a first-order Taylor series approximation to this gradient. As shown by Eq. (2-31) in Chapter 2, however, such a representation to the pressure gradient force is only valid in the limit as the spatial distance over which this force is evaluated approaches 0. Since this distance is not 0 in a numerical model, it should be investigated as to whether the inclusion of higher-order terms in the series expansion [i.e., Eq. (2-31)] and their representation by approximate solution techniques would produce improved representations of phase speed.

Finally, other finite difference representations for these and other terms can be examined in the same fashion as presented in this section. At this point, however, we investigate other forms of representation for these terms.

10.2   Upstream Interpolation Schemes—An Introduction

A second category of approximation schemes is the interpolation technique.[14] With this method, dependent variables at grid points are used to derive interpolation formulae for the spaces between as well as at the grid points. Such schemes have been used in mesoscale models to represent advection. The finite difference method is one form of interpolation, of course, since upstream differencing, for example, assumes a piecewise continuous function, as sketched in Figure 10-11(a), that is linear between grid points.

In the general category of interpolation schemes, however, all of the grid points in the domain, or at least all of the grid points in one coordinate direction, are used to approximate the dependent variables. Figures 10-11(b) and (c) illustrate two such functions, where one requires that the function equal the dependent variables at the grid point [Figure 10-11(b)] and the other to minimize overshoot does not make such a requirement. Texts such as Nielsen (1964) discuss the various types of interpolation formulas, and Goodin *et al.* (1981) provide an effective, concise discussion of the use of weighted interpolation. When using these formulae to represent advection, the change in a dependent variable at time $\tau + 1$ caused by advection is determined by going upstream for a distance $u_i^\tau \Delta t$ and using the resultant interpolated value at that point to represent the change.

In this section, we examine one particular interpolation function (reported by Ahlberg et al. 1967) that has been used effectively in mesoscale models. The technique outlined can be used for any desired interpolation scheme. Rüshøjgaard *et al.* (1998), for example, describe a different procedure to represent the second derivation of the interpolation scheme.

Let $S(x)$ be the interpolation function and require the following:

- $S(x)$, $S'(x)$, and $S''(x)$ are continuous.
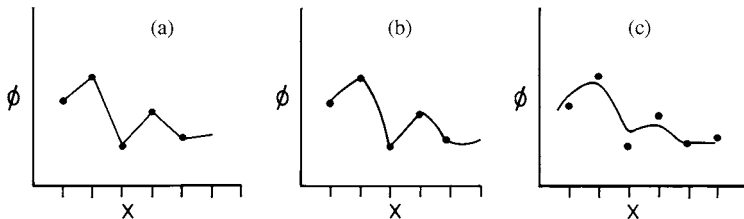
Fig. 10-11.   Schematic examples of interpolation formula that can be used to represent dependent variables on a one-dimensional grid: (a) a piecewise, continuous, linear fit; (b) a polynomial fit with grid point values defined exactly by the interpolation formula; and (c) a polynomial fit that limits the curvature of the interpolation formula.

- $S(x)$ is a cubic polynomial over the interval $x_{i-1} \leq x \leq x_i$ [i.e., $S(x) = ax^3 + bx^2 + cx + d$; $S''(x) = 6ax + 2b$].
- $S(x_i) = \phi_i$.

Here ϕ_i is the value of the dependent variable ϕ at the grid point x_i. If we define

$$M_{i-1} = S''(x_{i-1}) \quad \text{and} \quad M_i = S''(x_i),$$

then

$$S''(x) = M_{i-1}\frac{x_i - x}{h_i} + M_i\frac{x - x_{i-1}}{h_i}, \tag{10-36}$$

where $h_i = x_i - x_{i-1}$ [Eq. (10-36) is of the form $S''(x) = 6ax + 2b$, where $6a = (M_i - M_{i-1})/h_i$ and $2b = (M_{i-1}x_i - M_i x_{i-1})/h_i).$]
    Integrating Eq. (10-36) with respect to x gives

$$S'(x) = -M_{i-1}\frac{(x_i - x)^2}{2h_i} + \frac{M_i(x - x_{i-1})^2}{2h_i} + E,$$

and integrating again yields

$$S(x) = M_{i-1}\frac{(x_i - x)^3}{6h_i} + \frac{M_i(x - x_{i-1})^3}{6h_i} + Ex + F. \tag{10-37}$$

Since $S(x_{i-1}) = \phi_{i-1}$ and $S(x_i) = \phi_i$, we have

$$S(x_{i-1}) = M_{i-1}\frac{(x_i - x_{i-1})^2}{6} + Ex_{i-1} + F = \phi_{i-1} \tag{10-38}$$

and

$$S(x_i) = M_i\frac{(x_i - x_{i-1})^2}{6} + Ex_i + F = \phi_i. \tag{10-39}$$

Subtracting Eq. (10-38) from Eq. (10-39) gives

$$\phi_i - \phi_{i-1} = M_i\frac{h_i^2}{6} - M_{i-1}\frac{h_i^2}{6} + E(x_i - x_{i-1}),$$

so that

$$E = \frac{\phi_i - \phi_{i-1}}{h_i} - \frac{h_i}{6}(M_i - M_{i-1}).$$

To obtain the constant F, multiply Eq. (10-38) by x_i and Eq. (10-39) by x_{i-1} and subtract Eq. (10-39) from Eq. (10-38), resulting in

$$\frac{\phi_{i-1}x_i - \phi_i x_{i-1}}{h_i} = \frac{M_{i-1}x_i h_i}{6} - \frac{M_i x_{i-1}h_i}{6} + F,$$

so that

$$F = \frac{\phi_{i-1}x_i - \phi_i x_{i-1}}{h_i} + \frac{h_i}{6}(M_i x_{i-1} - M_{i-1}x_i).$$

Equation (10-37), after rearranging, can thus be written as

$$S(x) = M_{i-1}\frac{(x_i - x)^3}{6h_i} + M_i\frac{(x - x_{i-1})^3}{6h_i} + \left(\phi_{i-1} - \frac{h_i^2}{6}M_{i-1}\right)\frac{(x_i - x)}{h_i}$$
$$+ \left(\phi_i - \frac{h_i^2}{6}M_i\right)\frac{(x - x_{i-1})}{h_i},$$

with the first derivative given by

$$S'(x) = -M_{i-1}\frac{(x_i - x)^2}{2h_i} + \frac{M_i(x - x_{i-1})^2}{2h_i}$$
$$+ \frac{\phi_i - \phi_{i-1}}{h_i} - \frac{M_i - M_{i-1}}{6}h_i. \tag{10-40}$$

In using the spline to approximate advective terms, use is made of the slope $S'(x)$ rather than the second derivative term $S''(x)$. To do this, let

$$N_i = S'(x_i) = \frac{M_i h_i}{2} + \frac{\phi_i - \phi_{i-1}}{h_i} - \frac{M_i - M_{i-1}}{6}h_i \tag{10-41}$$

and

$$N_{i-1} = S'(x_{i-1}) = -M_{i-1}\frac{h_i}{2} + \frac{\phi_i - \phi_{i-1}}{h_i} - \frac{M_i - M_{i-1}}{6}h_i. \tag{10-42}$$

Adding the equations for N_i and N_{i-1} and rearranging yields

$$\frac{M_i - M_{i-1}}{6}h_i = N_i + N_{i-1} - \frac{2(\phi_i - \phi_{i-1})}{h_i},$$

so that Eqs. (10-41) and (10-42) can be rewritten as

$$N_i = \frac{M_i h_i}{2} + \frac{3(\phi_i - \phi_{i-1})}{h_i} - N_i - N_{i-1}$$

$$N_{i-1} = -\frac{M_{i-1}h_i}{2} + \frac{3(\phi_i - \phi_{i-1})}{h_i} - N_i - N_{i-1}.$$

Solving these equations for M_i and M_{i-1},

$$M_i = \frac{1}{h_i}\left[4N_i + 2N_{i-1} - \frac{6(\phi_i - \phi_{i-1})}{h_i}\right]$$

$$M_{i-1} = \frac{1}{h_i}\left[-4N_{i-1} - 2N_i + \frac{6(\phi_i - \phi_{i-1})}{h_i}\right],$$

gives the relation between the first and second derivatives at the grid points.

Substituting these expressions for M_i and M_{i-1} back into Eq. (10-40) and prodigious rearranging yields

$$S'(x) = \frac{N_i}{h_i^2}(x_{i-1} - x)(2x_i + x_{i-1} - 3x) + \frac{N_{i-1}}{h_i^2}(x_i - x)(2x_{i-1} + x_i - 3x)$$
$$+ \frac{6(\phi_i - \phi_{i-1})}{h_i^3}(x_i - x)(x - x_{i-1}). \tag{10-43}$$

Integration of $S'(x)$ yields $S(x)$ in terms of the first derivatives,

$$S(x) = -\frac{N_i}{h_i^2}(x - x_{i-1})^2(x_i - x) + \frac{N_{i-1}}{h_i^2}(x_i - x)^2(x - x_{i-1})$$
$$+ \frac{\phi_{i-1}}{h_i^3}(x_i - x)^2[2(x - x_{i-1}) + h_i]$$
$$+ \frac{\phi_i}{h_i^3}(x - x_{i-1})^2[2(x_i - x) + h_i], \tag{10-44}$$

and differentiating Eq. (10-43) and rearranging yields

$$S''(x) = -\frac{2N_i}{h_i^2}(x_i + 2x_{i-1} - 3x) - \frac{2N_{i-1}}{h_i^2}(x_{i-1} + 2x_i - 3x)$$
$$+ \frac{6(\phi_i - \phi_{i-1})}{h_i^3}(x_i + x_{i-1} - 2x). \tag{10-45}$$

This last equation for $S''(x)$ is used to obtain the values of N_i and N_{i-1} required in the spline interpolation, Eq. (10-44).

Since the second derivatives' spline interpolations must be continuous at grid points, the value of $S''(x)$ approaching x_i from the $x \geq x_i$ side [denoted by $S''(x_i^+)$] must equal $S''(x)$ approaching x_i from the $x \leq x_i$ side [denoted by $S''(x_i^-)$]. From Eq. (10-45), after setting $x = x_i$ and rearranging,

$$S''(x_i^-) = \frac{4N_i}{h_i} + \frac{2N_{i-1}}{h_i} - \frac{6(\phi_i - \phi_{i-1})}{h_i^2}.$$

By replacing $i - 1$ with i and i with $i + 1$, $S''(x_i^+)$ can be obtained from Eq. (10-45), giving, after rearranging,

$$S''(x_i^+) = -\frac{2N_{i+1}}{h_{i+1}} - \frac{4N_i}{h_{i+1}} + \frac{6(\phi_{i+1} - \phi_i)}{h_{i+1}^2},$$

where $h_{i+1} = x_{i+1} - x_i$.

Since continuity is required,

$$S''(x_i^+) = S''(x_i^-),$$

so that

$$\frac{3(\phi_{i+1} - \phi_i)}{h_{i+1}^2} + \frac{3(\phi_i - \phi_{i-1})}{h_i^2} = \frac{N_{i-1}}{h_i} + \frac{2N_i}{h_i} + \frac{2N_i}{h_{i+1}} + \frac{N_{i+1}}{h_{i+1}}. \qquad (10\text{-}46)$$

Put in a simpler form, let

$$\alpha_i = h_{i+1}/(h_i + h_{i+1}) \qquad \text{and} \qquad \mu_i = 1 - \alpha_i = h_i/(h_{i+1} + h_i).$$

Using these definitions and multiplying Eq. (10-46) by $h_i h_{i+1}/(h_i + h_{i+1})$ yields

$$\frac{3\mu_i}{h_{i+1}}(\phi_{i+1} - \phi_i) + \frac{3\alpha_i}{h_i}(\phi_i - \phi_{i-1}) = \alpha_i N_{i-1} + 2N_i + \mu_i N_{i+1}. \qquad (10\text{-}47)$$

In matrix form, for nonperiodic boundary conditions, this equation can be written as

$$\begin{bmatrix} b_1 & b_2 & 0 & 0 & 0 & \cdots & 0 & 0 & 0 \\ \alpha_2 & 2 & \mu_2 & 0 & 0 & \cdots & 0 & 0 & 0 \\ 0 & \alpha_3 & 2 & \mu_3 & 0 & \cdots & 0 & 0 & 0 \\ 0 & 0 & \alpha_4 & 2 & \mu_4 & \cdots & 0 & 0 & 0 \\ \vdots & \vdots & \vdots & \vdots & \vdots & \cdots & \vdots & \vdots & \vdots \\ 0 & 0 & 0 & 0 & 0 & \cdots & \alpha_{D-1} & 2 & \mu_{D-1} \\ 0 & 0 & 0 & 0 & 0 & \cdots & 0 & b_{D-1} & b_D \end{bmatrix} \begin{bmatrix} N_1 \\ N_2 \\ N_3 \\ N_4 \\ \vdots \\ N_{D-1} \\ N_D \end{bmatrix} = \begin{bmatrix} d_1 \\ d_2 \\ d_3 \\ d_4 \\ \vdots \\ d_{D-1} \\ d_D \end{bmatrix},$$

$$(10\text{-}48)$$

where D is the number of grid points in the x direction. For i not equal to 1 or D,

$$d_i = \frac{3\mu_i}{h_{i+1}}(\phi_{i+1} - \phi_i) + \frac{3\alpha_i}{h_i}(\phi_i - \phi_{i-1}), \quad \text{for } i = 2, 3, \dots, D - 2, D - 1.$$

The matrix of coefficients in this system of equations is called *tridiagonal*, because only elements along the three central diagonals are nonzero.

The values of b_1, b_2, b_{D-1}, and b_D are determined from the form of the assumed boundary conditions.[15] One type of boundary condition is obtained from $S''(x_1^+)$ and $S''(x_D^-)$, so that

$$\phi_1'' = S''(x_1^+) = -\frac{2N_2}{h_2} - \frac{4N_1}{h_2} + \frac{6(\phi_2 - \phi_1)}{h_2^2}$$

and

$$\phi_D'' = S''(x_D^-) = \frac{4N_D}{h_D} + \frac{2N_{D-1}}{h_D} - \frac{6(\phi_D - \phi_{D-1})}{h_D^2}.$$

If ϕ_1'', ϕ_D'', ϕ_1, and ϕ_D are specified, then

$$2N_1 + N_2 = \frac{3(\phi_2 - \phi_1)}{h_2} - \frac{\phi_1''}{2}h_2$$

and

$$N_{D-1} + 2N_D = \frac{3(\phi_D - \phi_{D-1})}{h_D} - \frac{\phi_D'' h_D}{2},$$

so that in the matrix equation,

$$d_1 = \frac{3(\phi_2 - \phi_1)}{h_2} - \frac{\phi_1''}{2} h_2 \qquad \text{and} \qquad d_D = \frac{3(\phi_D - \phi_{D-1})}{h_D} - \frac{\phi_D'' h_D}{2}$$

and

$$b_1 = 2, \qquad b_2 = 1, \qquad b_{D-1} = 1, \qquad \text{and} \qquad b_D = 2.$$

In specifying ϕ'' and ϕ at the boundaries, larger-scale information (if available) could be used, or data from one or more grid points inside the grid domain could be interpolated to the boundaries. Boundary conditions are discussed in more detail in Chapter 11.

The determination of the first derivatives from the matrix equation (10-48) is performed by the *method of Gaussian elimination* (see, e.g., Hadley 1962:51).[16] With this technique, the first row is multiplied by α_2/b_1 and subtracted from the second row, giving the values of

$$(0, 2 - (b_2\alpha_2/b_1), \mu_2, 0, 0, \ldots, 0) = (0, P_2, \mu_2, 0, 0, \ldots, 0)$$

on the left side and

$$d_2 - (d_1\alpha_2/b_1) = G_2$$

on the right side. This row of coefficients is used to replace the second row of Eq. (10-48).

Next, this new second row is multiplied by α_3/P_2 and subtracted from the third row, yielding

$$(0, 0, 2 - (\mu_2\alpha_3/P_2), \mu_3, 0, 0, \ldots, 0) = (0, 0, P_3, \mu_3, 0, \ldots, 0)$$

on the left side and

$$d_3 - (G_2\alpha_3/P_2) = G_3$$

on the right side. This row of coefficients is then used to replace the third row of Eq. (10-48). This same type of operation continues for the rest of the rows.

The object of these algebraic operations on the matrix equation is to create all 0's on the left side of the diagonal of the matrix. As will be seen shortly, rewriting the matrix equation in this form creates an efficient algorithm for solving for the first derivative of the spline.

With these operations of the matrix equation and using $b_2 = b_{D-1} = 1$ and $b_1 = b_D = 2$, Eq. (10-48) can be rewritten as

$$
\begin{bmatrix}
2 & 1 & 0 & & \cdots & & 0 \\
0 & P_2 & \mu_2 & 0 & \cdots & & 0 \\
0 & 0 & P_3 & \mu_3 & 0 & \cdots & 0 \\
0 & 0 & 0 & P_4 & \mu_4 & \cdots & 0 \\
\vdots & \vdots & \vdots & \vdots & \vdots & \cdots & \vdots \\
& & & & & P_{D-1} & \mu_{D-1} \\
0 & 0 & 0 & 0 & 0 & \cdots & 0 & P_D
\end{bmatrix}
\begin{bmatrix}
N_1 \\ N_2 \\ N_3 \\ N_4 \\ \vdots \\ N_{D-1} \\ N_D
\end{bmatrix}
=
\begin{bmatrix}
d_1 \\ G_2 \\ G_3 \\ G_4 \\ \vdots \\ G_{D-1} \\ G_D
\end{bmatrix},
$$

where

$$P_i = 2 - [\mu_{i-1}\alpha_i/P_{i-1}]$$

$$G_i = d_i - [G_{i-1}\alpha_i/P_{i-1}],$$

with $i = (2, \ldots D)$, $G_{i-1} = \mu_{i-1} = 0$, and $P_{i-1} \neq 0$ for $i = 1$. In the method of Gaussian elimination, the algebraic operations required to create 0's to the left of the diagonal is called the *forward sweep*.

With the matrix in this form, the slopes of the spline at the grid points are determined by a *backward sweep* starting with N_D and continuing until N is determined. Expressed algebraically,

$$N_D = G_D/P_D \quad (i = D),$$

$$N_i = (G_i - \mu_i N_{i+1})/P_i \quad (i = 1, 2, \ldots, D-1).$$

To eliminate the need to compute G_i, these expressions are often written in an equivalent fashion as

$$N_D = R_D \quad (i = D),$$

$$N_i = R_i - (\mu_i N_{i+1}/P_i) \quad (i = 1, 2, \ldots, D-1),$$

(10-49)

where

$$R_i = (d_i - R_{i-1}\alpha_i)/P_i \text{ (with } R_{i-1} = 0 \text{ for } i = 1).$$

With these expressions for N_i, it is possible to compute $S(x)$ from Eq. (10-44) for any point in the domain. In the interpolation scheme, estimating changes caused by advection at time level $\tau + 1$ are performed by evaluating the value of the spline (or other approximation formula) a distance of $|u_i^\tau|\Delta t$ *upstream* from the grid point of interest. The assumption is that the value of the dependent variable at $|u_i^\tau|\Delta t$ upstream of grid point i at time level τ is equal to its value at $\tau + 1$ at the grid point. This distance can also be written as $|u_i^\tau|\Delta t = Ch_i$, where C is the Courant number defined using the absolute value of the velocity at a grid point ($C = |u_i^\tau|\Delta t/h_i$).

One could also be tempted to use the values of N_i directly in the conservation relations to approximate the spatial derivatives. Experience has shown (e.g., Price and MacPherson 1973), however, that this method can cause undesirable growth of short wavelength noise for a nonlinear problem if used without smoothing.

To determine the value of the spline at $x_i - Ch_i$ for the case of $u_i^\tau \geq 0$, the value of x in Eq. (10-44) is replaced with $x_i - Ch_i$, yielding

$$
\begin{aligned}
S(x_i - Ch_i) = \; & N_{i-1}(x_i - x_i + Ch_i)^2(x_i - Ch_i - x_{i-1})/h_i^2 \\
& - N_i(x_i - CH_i - x_{i-1})^2(x_i - x_i + Ch_i)/h_i^2 \\
& + \phi_{-i-1}(x_i - x_i - Ch_i)^2[2(x_i - Ch_i - x_{i-1}) + h_i]/h_i^3 \\
& + \phi_i(x_i - Ch_i - x_{i-1})^2[2(x_i - x_i + Ch_i) + h_i]/h_i^3.
\end{aligned}
$$

Expanding this relation and rearranging yields

$$
\begin{aligned}
S(x_i - Ch_i) = \; & \phi_i^\tau - CN_ih_i + C^2[N_{i-1}h_i + 2N_ih_i + 3(\phi_{i-1}^\tau - \phi_i^\tau)] \\
& - C^3[h_iN_{i-1} + h_iN_i + 2(\phi_{i-1}^\tau - \phi_i^\tau)] \; (u_i^\tau \geq 0). \qquad (10\text{-}50)
\end{aligned}
$$

For the case where $u_i^\tau < 0$, the spline must be evaluated between grid points x_i and x_{i+1}. An expression for the spline, analogous to Eq. (10-44) [Eq. (10-44) is for application between grid points x_{i-1} and x_i], is obtained by replacing $i-1$ by i and i by $i+1$ in Eq. (10-44), yielding

$$
\begin{aligned}
S(x) = \; & -\frac{N_{i+1}}{h_{i+1}^2}(x - x_i)^2(x_{i+1} - x) + \frac{N_i}{h_{i+1}^2}(x_{i+1} - x)^2(x - x_i) \\
& + \frac{\phi_i}{h_{i+1}^3}(x_{i+1} - x)^2[2(x - x_i) + h_{i+1}] \\
& + \frac{\phi_{i+1}}{h_{i+1}^3}(x - x_i)^2[2(x_{i+1} - x) + h_{i+1}].
\end{aligned}
$$

Substituting $x_i + Ch_{i+1}$ for x in this expression and rearranging gives

$$
\begin{aligned}
S(x_i + Ch_{i+1}) = \; & \phi_i^\tau + CN_ih_{i+1} - C^2[N_{i+1}h_{i+1} + 2N_ih_{i+1} + 3(\phi_i^\tau - \phi_{i+1}^\tau)] \\
& + C^3[h_{i+1}N_i + h_{i+1}N_{i+1} + 2(\phi_i^\tau - \phi_{i+1}^\tau)] \quad (u_i^\tau < 0). \qquad (10\text{-}51)
\end{aligned}
$$

Equations (10-50) and (10-51) are thus used to determine the changes in the dependent variable due to advection from

$$\phi_i^{\tau+1}\big|\text{ advective changes} = S(x_i - Ch_i) \quad (u_i^\tau \geq 0) \qquad (10\text{-}52)$$

$$\phi_i^{\tau+1}\big|\text{ advective changes} = S(x_i + Ch_{i+1}) \quad (u_i^\tau < 0). \qquad (10\text{-}53)$$

To determine the linear computational characteristics of this scheme, let $u_i^\tau = U \geq 0$ and $h_i = h_{i+1} = \Delta x$, so that $\alpha_i = \mu_i = 1/2$. The equation for the slope of the spline [Eq. (10-47)] interior to the boundaries for this situation is given by

$$(3/\Delta x)\left(\phi_{i+1}^\tau - \phi_{i-1}^\tau\right) = N_{i-1} + 4N_i + N_{i+1}.$$

Expressing the values of ϕ and N in terms of frequency and wavenumber yields

$$(3\hat{\phi}/\Delta x)(\psi_1 - \psi_{-1}) = \widehat{N}(\psi_{-1} + 4 + \psi_1).$$

Solving for $\widehat{N}$ in terms of $\hat{\phi}$ gives

$$\widehat{N} = \frac{3\hat{\phi}(\psi_1 - \psi_{-1})}{\Delta x(\psi_{-1} + 4 + \psi_1)} = \frac{3i\hat{\phi}}{\Delta x}\frac{\sin k\Delta x}{(\cos k\Delta x + 2)} = \frac{Gi\hat{\phi}}{\Delta x}. \tag{10-54}$$

For notational convenience, G is defined to be equal to $3\sin k\Delta x/(\cos k\Delta x + 2)$.

Equation (10-52), where the right side is determined from Eq. (10-50), can be similarly rewritten in terms of frequency and wavenumber as

$$\hat{\phi}\psi^1 = \hat{\phi} - C\Delta x\widehat{N} + C^2\left[\Delta x\psi_{-1}\widehat{N} + 2\widehat{N}\,\Delta x + 3\hat{\phi}(\psi_{-1} - 1)\right]$$

$$- C^3\left[\Delta x\widehat{N}\psi_{-1} + \Delta x\widehat{N} + 2\hat{\phi}(\psi_{-1} - 1)\right].$$

Substituting for $\widehat{N}$ from Eq. (10-54) and rearranging results in

$$\psi^1 = 1 + C^2(G\sin k\Delta x + 3\cos k\Delta x - 3) + C^3(2 - G\sin k\Delta x - 2\cos k\Delta x)$$

$$+ i[-GC + C^2(2G + G\cos k\Delta x - 3\sin k\Delta x)$$

$$+ C^3(2\sin k\Delta x - G\cos k\Delta x - G)]. \tag{10-55}$$

Clearly, when the Courant number goes to 0, $\psi^1 = 1$, so that the spline upstream interpolation scheme is a consistent representation of the advective equation.

However, the evaluation of amplitude and phase characteristics from Eq. (10-55) when $C \neq 0$ is not as straightforwardly performed as was possible with the finite difference representations. Equating real and imaginary components of Eq. (10-55),

$$\lambda \cos \omega_r \Delta t = 1 + C^2(G\sin k\Delta x + 3\cos k\Delta x - 3)$$

$$+ C^3(2 - G\sin k\Delta x - 2\cos k\Delta x)$$

and

$$\lambda \sin \omega_r \Delta t = -GC + C^2(2G + G\cos k\Delta x - 3\sin k\Delta x)$$

$$+ C^3(2\sin k\Delta x - G\cos k\Delta x - G).$$

To compute λ and $\tilde{c}_\phi/U(\tilde{c}_\phi = -\omega_r/k; k$ is real) from these equations, it is most convenient to substitute particular values of C and k into these relations and solve for λ and ω_r on the computer. This is done either by using complex

arithmetic, which is routinely available on most computers, or by simply per-
forming the squaring, summing, and division of the imaginary component by
the real component numerically.

Table 10-1 presents values of λ and $\tilde{c}_\phi/U$ for this scheme. In contrast to the
leapfrog technique, the amplitude is not preserved for all wavelengths, and $2\Delta x$
waves are eliminated completely when $C = 0.5$. The phase for the $2\Delta x$ wave is
also incorrectly represented, because it remains stationary. This latter problem
with $2\Delta x$ waves is not particularly severe, however, especially with values of C
between 0.2 and 0.8, because features with this wavelength are rapidly damped
with time (e.g., at $C = 0.2$, the amplitude is reduced by 90% after 10 time steps;
$\lambda^{10} = 0.097$). At $4\Delta x$, the spline provides a much more accurate representation
of the advection. At $C = 0.5$, for example, which is the worst case[17] in terms
of amplitude, $\lambda = 0.972$ and $\tilde{c}_\phi = U$. The leapfrog scheme, in contrast, has a
value of $\lambda = 1.0$ at $C = 0.5$ for a $4\Delta x$ wave, but $\tilde{c}_\phi/U = 0.67$, or a 33% error
in phase.

Thus, although the leapfrog preserves amplitude exactly, it does a poor job of
representing the phase characteristics of the shorter waves. Thus the amplitude
conservation of leapfrog becomes a liability since the presence of $2\Delta x$ waves
in the wrong location can create erroneous results through nonlinear interac-
tions when physical forcings (e.g., condensation) occur. The spline technique, in
contrast, has the desirable feature of damping wavelengths in which the phase
characteristics are poorly represented. Therefore, in choosing a computational
scheme, it appears desirable to select one in which the accuracy of λ and $\tilde{c}_\phi/U$
are closely correlated (i.e., $|\lambda|$ much less than unity when the numerical phase
accuracy is poor).

The most substantial problem with the spline is its tendency to overshoot. If,
for example, a field has a string of 0's followed by nonzero values, then the
spline can create small values less than 0 near the interface with the 0's because
of its cubic form. Although not a serious source of error, it is nonphysical to
have negative values in such fields as specific humidity. Requiring values to
exceed or equal 0 is one correction for this inconsistency.

In using schemes such as the spline in numerical models, the interpolation
formula could be derived in terms of more than one spatial direction (e.g., as a
two-dimensional spline in x and y). Krishnamurti et al. (1973) used a bilinear
interpolation scheme (Krishnamurti 1962; Mathur 1970) defined in two space
dimensions in his synoptic tropical prediction model.

Unfortunately, however, most interpolation schemes become very complicated
and expensive if more than one spatial coordinate is used. An alternate approach
is to use the spline separately in each spatial direction. This approach of eval-
uating each coordinate direction separately is called *splitting*[18] (e.g., Long and
Hicks 1975; Mesinger and Arakawa 1976) and is used to represent the spline in
the mesoscale model reported by Mahrer and Pielke (1978a). Using this tech-

nique with the spline in a two-dimensional model, for instance, where i and k are the grid points in x and z and $u_i^\tau \geq 0$ and $w_k^\tau \geq 0$,

$$\phi_{i,k}^{\tau+1^*}| \text{ changes caused by advection in } x = S_u(x_i - C_u h_i), \qquad (10\text{-}56)$$

where $C_u = |u_i^\tau|\Delta t/h_i$, with values of ϕ at time τ used in S_u, is determined for all i; then

$$\phi_{i,k}^{\tau+1}| \text{ changes caused by advection in } z = S_w(z_k - C_w h_k), \qquad (10\text{-}57)$$

where $C_w = |w_i^\tau|\Delta t/h_k$, with values of ϕ at $\tau + 1^*$ determined from Eq. (10-56) used in S_w, is calculated for all k. Pepper *et al.* (1979) have shown that splitting does not degrade the accuracy of the solutions.

Other interpolation schemes besides the spline could also be used to represent advection. The methodology would be developed in an analogous fashion to that of the spline. Bates and McDonald (1982) provide a useful study of the application of such upstream interpolation techniques to atmospheric models. Smolarkiewicz and Margolin (1997) contrast the use of interpolation and centered-in-time and space-finite difference schemes. Benoit *et al.* (1997a) describe the use of an interpolation scheme in the Canadian MC2 model. Other examples of the use of interpolation schemes to represent advection include Janjić (1995), Pinty *et al.* (1995), Böttcher (1996), Héreil and Laprise (1996), Li and Bates (1996), Makar and Karpik (1996), Ritchie and Tanguay (1996), Sun *et al.* (1996), Lin and Rood (1997), Sun and Yeh (1997), Caya *et al.* (1998), Finkele (1998), Qian et al. (1998), McDonald (1999), and Xiao (2000). Laprise and Plante (1995) discuss the use of the interpolation solution technique both upstream and downstream.

Tremback *et al.* (1987) provides a detailed analysis of the extension of the forward-in-time upstream advection approach to a higher-order accuracy. A sixth-order scheme was found to have the best balance between efficiency and accuracy. Finkele (1998) describes the accuracy of a third-order interpolation advection scheme for use in her simulation of sea breezes. Another paper that discusses this solution technique is Pellerin *et al.* (1995).

10.3   Diagnostic Equations

Up to this point, only the solution of prognostic conservation equations have been considered. However, as discussed in Section 3.1 in Chapter 3, scale analysis arguments allow removal of the explicit derivative of time from the conservation-of-mass relation when density fluctuations are much less than the mean value of density. Thus a diagnostic equation for mass conservation [e.g.,

Eq. (3-11)] results. In addition, pressure must be evaluated from a diagnostic relation [e.g., as given by Eq. (4-35)] if the prognostic equation for density has been removed. A diagnostic equation for pressure can be of the form given by Eq. (4-33) when the hydrostatic approximation is valid or by Eq. (4-35) when it is not.

When a diagnostic relation does not involve derivatives, all of the dependent variables are defined at the same grid point, and it is straightforward to solve by algebraic rearrangement. One example is the approximate form of the gas law given by Eq. (4-19). If derivatives are involved, however, it is necessary to integrate the diagnostic relation. For example, with the hydrostatic equation and the anelastic conservation-of-mass relation [e.g., Eqs. (4-33) and (4-23)], pressure and vertical velocity are obtained by vertical integration,

$$p'_z = p'_{z+\delta z} + g \int_z^{z+\delta z} \frac{\alpha'_{[z+(\delta z/2)]}}{\alpha^2_{0[z+(\delta z/2)]}} \, dz$$

$$\bar{w}_z = \bar{w}_{z-\delta z} - \int_{z-\delta z}^z \left(\frac{\partial \bar{u}}{\partial x} + \frac{\partial \bar{v}}{\partial y} \right) dz.$$

One form of the numerical approximation to these terms is given by

$$p'_{i,j,k} = p'_{i,j,k+1} + g \frac{\alpha'_{i,j,k+\frac{1}{2}}}{\alpha^2_{0_{i,j,k+\frac{1}{2}}}} \Delta z$$

$$\bar{w}_{i,j,k} = \bar{w}_{i,j,k-1} - \left(\frac{\bar{u}_{i+\frac{1}{2},j,k-\frac{1}{2}} - \bar{u}_{i-\frac{1}{2},j,k-\frac{1}{2}}}{\Delta x} + \frac{\bar{v}_{i,j+\frac{1}{2},k-\frac{1}{2}} + \bar{v}_{i,j-\frac{1}{2},k-\frac{1}{2}}}{\Delta y} \right) \Delta z,$$

where a centered-in-space representation is used and the subscripts i, j, and k refer to the grid points in the x, y, and z coordinate directions, respectively. To solve these two relations, the pressure at the top (i.e., $p_{i,j,K}$) and vertical velocity at the bottom (i.e., $w_{i,j,0}$) must be specified as the constants of integration, as discussed in Sections 11.3.2 and 11.3.3 in Chapter 11.

However, when a diagnostic equation for pressure, such as Eq. (4-35) (or other equation of this form, such as vorticity) is used, the integration must be in more than one coordinate direction. As an example, Eq. (4-35) can be written for a shallow atmospheric circulation ($\alpha'/\alpha_0 \simeq \theta'/\theta_0$) in a two-dimensional model in finite difference form for a constant grid as

$$\frac{p'_{i+1,j} - 2p'_{i,j} + p'_{i-1,j}}{(\Delta x)^2} + \frac{p'_{i,j-1} - 2p'_{i,j} + p'_{i,j+1}}{(\Delta z)^2} = F, \tag{10-58}$$

where F refers to the finite difference approximation to the right-side terms in Eq. (4-35); F includes approximations to derivatives and is a function of grid

location. To make a consistent set of the approximate representations to the conservation relations, the formulation of derivative terms in F must be defined consistently with the numerical approximation form of the conservation-of-motion equations from which it was derived. In other words, the divergence of Eq. (4-21), used to obtain Eq. (4-35), must be performed on the finite difference (or other approximate) form of that equation, so that two different approximate representations of the same terms do not occur.

Several solution techniques exist to evaluate Eq. (10-58), and only the most straightforward procedure is introduced here.[19] This diagnostic equation for pressure can be rearranged to give

$$P_{i,j} - p'_{i,j} - H = \epsilon, \tag{10-59}$$

where

$$
\begin{aligned}
P_{i,j} &= \frac{(p'_{i+1} + p'_{i-1})(\Delta z)^2 + (p'_{j+1} + p'_{j-1})(\Delta x)^2}{2[(\Delta z)^2 + (\Delta x)^2]} \\
H &= \frac{F(\Delta x)^2(\Delta z)^2}{2[(\Delta z)^2 + (\Delta x)^2]},
\end{aligned}
\tag{10-60}
$$

with $\epsilon = 0$ if the finite difference is an exact representation of the differential equation. [In Eq. (10-59), ϵ is referred to as the *residual*.] In general, $\epsilon \neq 0$ at most or all of the grid points in a domain. To require that $\epsilon = 0$ at one grid point, subtract ϵ from both sides of Eq. (10-59) and define

$$P^*_{i,j} = P_{i,j} - \epsilon. \tag{10-61}$$

If the domain had only one interior grid point, then only one iteration would be necessary. However, with more interior grid points, the change of $P_{i,j}$ by a residual at a grid point affects Eq. (10-59) at surrounding grid points. Subsequently, the iteration must be repeated at all interior grid points until the values of ϵ at each grid point are arbitrarily small. The pressure at each location is updated according to Eq. (10-61), where, for example, for the second guess, $P^{**}_{i,j} = P^*_{i,j} - \epsilon$. This repeated substitution for $P_{i,j}$ is called *relaxation*.

In practice, convergence to a solution (which is defined when all the residuals are less than an arbitrary value) is found to be more rapid when

$$P^*_{i,j} = P_{i,j} - \alpha\epsilon, \tag{10-62}$$

where α is a constant. When $\alpha > 1$, Eq. (10-62) is referred to as *overrelaxation*, with $\alpha\epsilon$ used in lieu of ϵ alone in Eq. (10-59). Convergence to a solution is also enhanced when guess values computed by Eq. (10-62) are inserted

in Eq. (10-59) as soon as they become available. This operation is referred to as *sequential relaxation*. Convergence to a solution is usually very rapid as long as grid point values at and next to the grid point of interest are the only ones involved in the diagnostic equation. (For a more detailed discussion of relaxation, see Thompson 1961.) Clark (1977) presents what he calls a double-iteration scheme to solve a more general form of the diagnostic pressure equation. A solution approach suggested by Brandt (1977), in which sequential relaxation is evaluated on widely different but interactive mesh sizes, is a versatile calculation tool with which to solve general forms of the diagnostic pressure equation. Smolarkiewicz *et al.* (1997) discuss when convergence of the anelastic pressure equation is adequate.

10.4 Time Splitting

In Chapter 5, Section 5.2.2, it was shown that the neglect of local variations in density in the conservation-of-mass relation eliminates rapidly propagating sound waves as a possible solution. Therefore, use of the resultant anelastic (soundproof) conservation-of-mass equation in atmospheric flows, limits the fastest wave speeds to gravity waves. As implied from the results presented in this chapter, time steps must be selected such that the distance traveled by a wave in one time step is less than or equal to the appropriate grid spacing; that is, $c\Delta t \leq \Delta$, where c is the propagation speed of the fastest traveling wave where, for instance, $c = U$ and $\Delta = \Delta x$ in the advection equation, $c = \sqrt{gh_0}$ and $\Delta = 2\Delta x$ in the tank model, and, by analogy, $c = \sqrt{RT_0(c_p/c_v)}$ and $\Delta = 2\Delta x$ when sound waves are present. If these criteria are not attained, then either the approximate solutions are linearly unstable or the representation is very inaccurate.

If, however, the anelastic equation is used to represent mass conservation, and thus to eliminate sound waves, then the solution of a complex elliptic partial differential equation for pressure [e.g., Eq. (4-35)] is required. To eliminate the need to compute pressure from such an equation, but still retain stable and accurate solutions in a nonhydrostatic model, one can compute the time tendency of the terms that generate the sound waves separately from the remainder of the dynamic equations. Thus a very short time step is used for the relatively few terms that generate sound, and a much more economical time interval can be selected for the features considered more important on the mesoscale. Klemp and Wilhelmson (1978a, b), and Tripoli and Cotton (1982) used this approach in three-dimensional cloud models, and Tapp and White (1976) used it in their mesoscale model. Daley (1980) discussed the splitting of fast gravity wave computations from slower gravity and Rossby waves using a procedure called model normal mode expansion for the fast waves.

Using the analysis of the forms of wave motion discussed in Section 5.2.2, the equations and terms that give rise to sound waves can be written in the form

$$\frac{\partial \bar{u}_i}{\partial t} + \frac{1}{\bar{\rho}}\frac{\partial \bar{p}}{\partial x_i} = f_{u_i}, \quad \frac{\partial \bar{\rho}}{\partial t} + \frac{\partial}{\partial x_j}\bar{\rho}\bar{u}_j = f_\rho, \quad \frac{\partial \bar{\theta}}{\partial t} = f_\theta,$$

(10-63)

$$\bar{p} \text{ (in mb)} = C_p^{C_p/C_v} R_d^{C_p/C_v} \text{ (1000 mb)}^{-R_d/C_v} (\bar{\rho}\bar{\theta})^{C_p/C_v} = f_p,$$

where f_{u_i}, f_ρ, f_θ, and f_p contain the terms in these conservation relations that are not written explicitly here. These six equations in the six unknowns u_i, $\bar{\rho}$, $\bar{p}$, and $\bar{\theta}$ can then be written in an appropriate numerical approximation form and evaluated quickly and efficiently for short time steps where f_{u_i}, f_ρ, f_θ, and f_p are kept fixed for a specified time period (e.g., equal to 10 times the time step used to represent the sound waves). With this approach, sound waves are simulated in an accurate fashion, and a longer time step can be used to update values of f_{u_i}, f_ρ, f_θ, and f_p. Alternatively, the sound waves can be evaluated using an implicit differencing scheme such that longer time steps are used although the accuracy of the representation of the sound waves themselves are degraded by the implicit scheme. Recent discussions of the time-splitting schemes are reported in Saito (1997) and Wicker and Skamarock (1998). The first reference to this very effective time-splitting approach appeared in Derickson (1974).

10.5   Nonlinear Effects

10.5.1   Aliasing

There has been little discussion in this text on the influence of products of dependent variables on the approximated solutions of the conservation relations. This neglect, of course, results from the inability of existing mathematical techniques to provide analytic solutions to nonlinear differential equations, except for idealized specific cases. Thus, even though the conservation relations are nonlinear, most of Chapter 5, for example, concentrated on solutions to linear equations, with previous sections of this chapter emphasizing linear analysis tools in the investigation of solution techniques to be used in nonlinear models. In this section, the actual and computational results of nonlinear interactions are discussed.

In the atmosphere on the mesoscale there are spatial scales in which kinetic energy is being produced (e.g., the scale of the horizontal temperature gradient associated with a seacoast, such as illustrated in Figure 13-3 in Chapter 13) and scales in which this kinetic energy is being dissipated into heat by molecular interactions. In the first case, scales of motion are on the order of 100 m to 100 km, for example, whereas the sizes of motion significantly affected by

molecular interactions are 1 cm or smaller. Somewhere in between exist scales of motion that are not directly influenced by either molecular dissipation or the forces generating the kinetic energy in the first place.

Thus it is expected that in this region, the kinetic energy per unit wavenumber per unit mass as a function of wavenumber $E(k)$ is proportional to only the spatial scale of the motion (as specified by its wavenumber) and by the rate at which energy is being removed at the much smaller scales. Moreover, since kinetic energy does not accumulate once the larger-scale forcing is terminated, the energy must be transformed with time into smaller and smaller sizes until they are 1 cm or smaller and can be removed by molecular interactions. From dimensional arguments, if $E(k)$ is dependent only on wavenumber and dissipation rate, then

$$E(k) = a\epsilon^{2/3}k^{-5/3}, \tag{10-64}$$

where a is a proportionality constant and ϵ has units of energy per unit time per unit mass. This region, in which kinetic energy is independent of the original forcings of the motion and of its dissipation by molecular viscosity, is called the *inertial subrange*. This name arises because the advective terms (in this context these terms are also called the inertial terms) transfer kinetic energy among the three components of velocity, and also generate smaller and smaller sizes of circulations. Lumley and Panofsky (1964) have provided a detailed discussion of the transfer of kinetic energy by turbulence. Tennekes (1978), Gage (1979), Lilly (1983), and Moran (1992) discussed the observed occurrence of such a $k^{-5/3}$ relation in mesoscale and larger atmospheric features.

In contrast, in a numerical mesoscale model this cascade of energy to smaller scales cannot occur, because the smallest feature that can be resolved has a wavelength of two times the grid spacing.[20] If, for example,

$$\phi_1 = \phi_0 \cos k_1 \Delta x \qquad \text{and} \qquad \phi_2 = \phi_0 \cos k_2 \Delta x$$

represent two waves in a model with equal amplitudes ϕ_0, then a nonlinear interaction between the two can be represented by

$$\phi_1 \phi_2 = \phi_0^2 \cos k_1 \Delta x \cos k_2 \Delta x$$

or, using trigonometric identities,

$$\phi_1 \phi_2 = \frac{1}{2}\phi_0^2[\cos(k_1 + k_2)\Delta x + \cos(k_1 - k_2)\Delta x]. \tag{10-65}$$

Thus two waves result from this interaction with wavenumbers $k_1 + k_2$ and $k_1 - k_2$.

As an example, suppose that a $2\Delta x$ and a $4\Delta x$ wave interact ($k_1 = 2\pi/2\Delta x$, $k_2 = 2\pi/4\Delta x$), the resultant waves are given by

$$\phi_1 \phi_2 = \frac{1}{2}\phi_0^2 \left(\cos 2\pi \left(\frac{6}{8} \right) \Delta x + \cos 2\pi \left(\frac{1}{4} \right) \Delta x \right),$$

which corresponds to a $1.33\Delta x$ and a $4\Delta x$ wave. Of course, the latter size wave can be resolved, but the $1.33\Delta x$ wave cannot! Instead, it will be fictitiously seen as a $4\Delta x$, since that size is the first integer multiple of $\frac{4}{3}\Delta x$ equal to $n\Delta x$, where n is also an integer and $n \geq 2$. Waves that appear erroneously in this fashion are said to have *aliased* or *folded* to longer wavelengths. As seen from Eq. (10-65), to have aliasing, one of the waves must be less than $4\Delta x$ in length to generate physical solutions less than $2\Delta x$.

Table 10-6 lists examples of wave–wave interactions that will produce aliased waves. Figure 10-12 illustrates how a $1.33\Delta x$ wave would be misinterpreted as a $4\Delta x$ wave on a computational grid. Even if no $2\Delta x$ waves were initially present, they would be created, since the interaction of two $4\Delta x$ waves generates a $2\Delta x$ wave, whereas longer wave–wave interactions produce $4\Delta x$ waves. Two interactive waves each with a $2\Delta x$ wavelength will not produce a wave of $1\Delta x$, because identical values will result at each grid point. In this case, the energy in the $1\Delta x$ wave will be seen fictitiously as the addition of a constant value of energy to the model.

Thus when wave interactions occur in the real world, smaller and larger wavelengths result. Eventually the smaller waves attain a size in which molecular dissipation can eliminate motion. In a numerical model, however, which has a discrete grid, waves smaller than $2\Delta x$ are erroneously seen as larger-scale waves. These erroneous larger-scale waves interact and again transfer their energy to larger and smaller scales. Because the proper cascade of energy to smaller and smaller scales is interrupted, a fictitious energy buildup occurs as energy is added to the model through the forcing terms, but with its dissipation improperly represented.

TABLE 10-6

Examples of Wave–Wave Interactions That
Will Produce Aliased Waves

Interactive wavelengths	Should produce	Will produce due to aliasing
$2\Delta x$ and $2\Delta x$	$1\Delta x$	*Add a constant to the entire model*
$2\Delta x$ and $4\Delta x$	$1.33\Delta x$	$4\Delta x$
$2\Delta x$ and $6\Delta x$	$1.5\Delta x$	$3\Delta x$
$2\Delta x$ and $8\Delta x$	$1.6\Delta x$	$8\Delta x$
$2\Delta x$ and $10\Delta x$	$1.67\Delta x$	$5\Delta x$
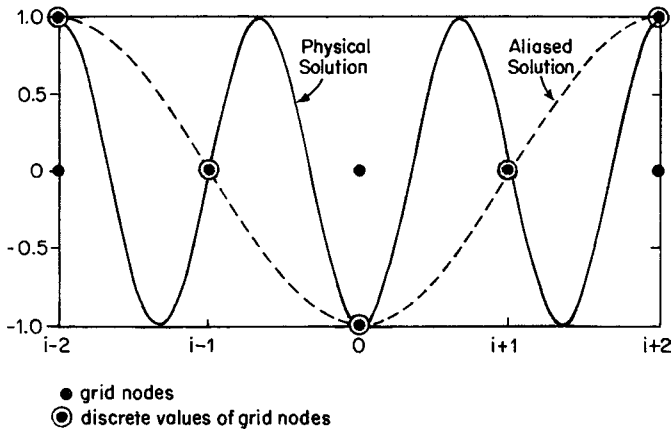
Fig. 10-12. Schematic illustration of how a physical solution with a wavelength of $1.33\Delta x$, caused by the nonlinear interaction of waves of $2\Delta x$ and $4\Delta x$ in length, is seen as a computational $4\Delta x$ wave in the computational grid.

Therefore, even if a computational solution technique is linearly stable, the results can degrade into physically meaningless computational noise. Indeed, with many computational solution schemes, this erroneous accumulation of energy can cause the model-dependent variables to increase in magnitude without bound—an error referred to as *nonlinear instability*.[21]

Wavelengths smaller than $4\Delta x$ are required for aliasing to occur. As shown previously in this chapter, such short waves are inadequately resolved on a computational grid and even in the linearized equations are poorly represented in terms of amplitude and/or phase. For these reasons, and because they are expected to cascade to even smaller scales anyway, it is desirable to remove these waves.

Two methods can be used to accomplish this task:

- proper parameterization of the subgrid-scale correlation terms (i.e., $\overline{u_i'' u_j''}$, $\overline{\theta'' u_j''}$, etc.), so that energy is extracted from the averaged equations in a manner consistent with reality
- the use of a spatial smoother (also referred to as a filter), which removes the shortest waves but leaves the longer ones relatively unaffected.

The first method is the most attractive, of course, because it is based on fundamental physical concepts. Unfortunately, however, as shown in Chapter 7, only the vertical subgrid-scale correlation terms are reasonably well known and can be parameterized accurately in terms of the dependent variables. In contrast, horizontal subgrid mixing in mesoscale models can be estimated only crudely, since the horizontal averaging scale in such models is typically larger than the

vertical scale [i.e., $\Delta x \simeq \Delta y \gg \Delta z$ in Eq. (4-6)]. Moreover, few theoretical or observational studies have been conducted on the structure of horizontal mixing over heterogenous ground surfaces.

Therefore, the forms used in the representation of the horizontal subgrid correlation terms, have been chosen to *control nonlinear aliasing, not to represent actual physical processes accurately.* One form of horizontal mixing used (which has the appearance of a physical parameterization but in a mesoscale model is not) is

$$-\overline{u_i'' u_j''} = K_H \partial \bar{u}_i / \partial x_j \quad (i = 1, 2), \tag{10-66}$$

where

$$K_H = \alpha(\Delta x)^2 \left[\frac{1}{2} \left(\frac{\partial \bar{v}}{\partial x} + \frac{\partial \bar{u}}{\partial y} \right)^2 + \left(\frac{\partial \bar{u}}{\partial x} \right)^2 + \left(\frac{\partial \bar{v}}{\partial y} \right)^2 \right]^{1/2},$$

with the coefficient α arbitrarily adjusted until $2\Delta x$ wavelengths do not appear to degrade the solutions significantly. This procedure, which is completely ad hoc, permits solutions to be changed in magnitude simply by changing the value of α. Tag *et al.* (1979) provided a useful discussion of several forms of these variable-eddy coefficient formulations. Laprise *et al.* (1998) gave a very useful analysis of different forms of K_H.

The alternative to an explicit diffusion equation is to formally apply a filter, such as discussed by Shapiro (1970). Cullen (1976) compared solutions in a simplified synoptic-scale model using several types of filters and explicit diffusion representations and showed that selective filters can be used more effectively in finite element representations than with finite difference techniques because of the greater accuracy of the first method. The use of optimal filters is also discussed by von Storch (1978). Jones (1977a) outlines a smoothing technique to control computational noise as information is transferred between coarse and fine grids in a hurricane model.

When a terrain-following coordinate system is used (see, e.g., Figure 6-3 and associated text in Chapter 6), a modeler must ensure that the explicit horizontal diffusion or the smoother is applied on the $x - y$ plane, since $\tilde{x}^1$ and $\tilde{x}^2$ are not in general horizontal. If an intended horizontal filter is mistakenly applied to the $\tilde{x}^1 - \tilde{x}^2$ surface, then diffusion will be inadvertently input into the z direction. This smoothing is not desirable if a physically realistic representation of vertical diffusion is included in the model and if the vertical component of the computational diffusion, erroneously evaluated on the $\tilde{x}^1 - \tilde{x}^2$ surface, is of the same order as the physical vertical mixing.

Smoothers can be explicit or implicit. With implicit smoothing, computational techniques that involve inherent damping, such as upstream differencing or the cubic spline interpolation, are chosen (see, e.g., the values for λ in

Table 10-1). Explicit smoothers, in contrast, require the addition of an operation to the prognostic equations to generate smoothed dependent variables from the original predicted dependent variables. The ideal smoother is one that eliminates wavelengths smaller than $4\Delta x$ at each time step but leaves the larger sizes unaffected. Such smoothers are called *low-pass filters* and are said to be *selective*.

Pepper *et al.* (1979) reported on a highly selective filter of the form

$$(1 - \delta)\phi_{i+1}^* + 2(1 + \delta)\phi_i^* + (1 - \delta)\phi_{i-1}^* = \phi_{i+1} + 2\phi_i + \phi_{i-1}, \quad (10\text{-}67)$$

where ϕ and ϕ^* are the dependent variables to be smoothed and the smoothed value and δ is an arbitrarily chosen weighting parameter for the smoothed values. As shown later, this filter eliminates $2\Delta x$ waves at each application, and its smoothing of longer waves is dependent on the value of δ.

Let

$$\phi_{i+1}^* = \psi_1^1 \phi, \qquad \phi_i^* = \psi^1 \phi, \qquad \text{and} \qquad \phi_{i-1}^* = \psi_{-1}^1 \phi, \quad (10\text{-}68)$$

which is similar to the form used in the section on linear stability analysis except here,

$$\psi^1 = \lambda$$

corresponds to the change in magnitude of the solution per application of the filter. One application of the filter, performed at each time step, can also be written as

$$\lambda = e^{-Kk^2\Delta t} = e^{-\gamma(2\pi)^2/n^2},$$

where $\gamma = K \Delta t (\Delta x)^2$. Thus when λ is known, it is possible to compute a value of K that will give the same smoothing when the linear diffusion equation[22] is used as when Eq. (10-67) is applied.

Using the decomposition of the dependent variable given by Eq. (10-68), Eq. (10-67) can be rewritten as

$$(1 - \delta)\psi_1^1 + 2(1 + \delta)\psi^1 + (1 - \delta)\psi_{-1}^1 = \psi_1 + 2 + \psi_{-1}.$$

Solving for $\psi^1 = \lambda$ gives

$$\lambda = \frac{\cos k\Delta x + 1}{(1 - \delta)\cos k\Delta x + 1 + \delta}, \quad (10\text{-}69)$$

and the equivalent value of K (Long 1979, personal communication) can be determined from

$$K(k, \delta) = -(1/k^2\Delta t)\ln \lambda. \quad (10\text{-}70)$$

As is evident from these expressions, $\lambda = 0$ ($K = \infty$) for a $2\Delta x$ wave $[\cos(2\pi/2\Delta x)\Delta x = \cos \pi = -1]$. For a very long wave, $\cos k\Delta x$ approaches

1 and $\lambda \simeq 1$ $(K \simeq 0)$, as it should. For wavelengths between these two values, the amount of damping is dependent on the value of δ. Table 10-7 illustrates the damping by Eq. (10-67) for several selected values of wavelength and δ. As is evident from this table, for small values of δ, the formulation given by Eq. (10-67) is highly selective, and its influence on longer wavelengths is very small. It should be noted, however, that in separately applying the filter to more than one spatial direction (i.e., splitting), application of this filter to the second direction can reintroduce $2\Delta x$ wavelengths into the first direction of application. This can be controlled to some extent (as suggested by Xubin Zeng, personal communication) by alternating the order of the direction of smoothing between time steps (i.e., at the n time, filter x then y; at the $n + 1$ time, filter y then x).

All mesoscale models use some sort of horizontal filtering to control nonlinear aliasing. Either explicit smoothers, such as Eq. (10-67), are used, or implicit computational diffusion inherent to the numerical approximation, such as with upstream differencing or the cubic spline, provide the necessary removal of the shortest wavelengths.

The use of a smoother can also prevent linear instability as long as the magnitude of λ for the smoother times λ of the linearly unstable numerical scheme is less than or equal to unity. For example, if

$$\left| \left(\frac{\cos k\Delta x + 1}{(1 - \delta)\cos k\Delta x + 1 + \delta} \right) \left(\sqrt{1 + C^2 \sin^2 k\Delta x} \right) \right| \le 1,$$

where Eq. (10-69) gives λ for the smoother and the positive root of Eq. (10-12) is used for λ resulting from the forward-in-time, centered-in-space representation to the advection equation, then the solutions can be made stable. Unfortunately, however, in a mesoscale model, without performing a Fourier decomposition it is impossible to determine the wavelengths of all the features at each time step to select the proper value of the smoother to counteract the

TABLE 10-7

Values of λ per Application of Eq. (10-67) as a Function of Wavelength and δ.

	δ			
Wavelength	0.001	0.005	0.10	0.50
$2\Delta x$	0	0	0	0
$4\Delta x$	0.999	0.995	0.090	0.667
$6\Delta x$	1.000	0.998	0.968	0.857
$8\Delta x$	1.000	0.999	0.988	0.945
$10\Delta x$	1.000	0.999	0.990	0.950
$12\Delta x$	1.000	1.000	0.993	0.966
$14\Delta x$	1.000	1.000	0.995	0.974

linear instability of the difference scheme. Thus, in general, using Eq. (10-67) to control the linear instability of a scheme will create a damped system, and, even more importantly, the phase characteristics of such a scheme will be poor. Thus this approach should not be used in numerical models.

10.5.2   A More Accurate Method for the Numerical Solution of Nonlinear Partial Differential Equations

In this section, originally reported in Weidman and Pielke (1983), a general two-step method is introduced that reduces the computational error by partially solving the equations analytically rather than totally numerically. LeVeque (1982) and LeVeque and Oliger (1981) discuss in detail the additive splitting of hyperbolic partial differential equations to solve such equations. This technique is applied to a simple model to illustrate the value of solving at each time step part of the system analytically and then using this result in the numerical computation needed to complete the time step.

As a concrete example of the method, the tank model equations

$$
\begin{aligned}
\frac{\partial u}{\partial t} &= -u\frac{\partial u}{\partial x} - g\frac{\partial h}{\partial x} \\
\frac{\partial h}{\partial t} &= -u\frac{\partial h}{\partial x} - h\frac{\partial u}{\partial x},
\end{aligned}
\tag{10-71}
$$

as derived in Section 5.2.1.1, are used. The linearized version of Eq. (10-71) is

$$
\begin{aligned}
\frac{\partial u'}{\partial t} &= -g\frac{\partial h}{\partial x}, \\
\frac{\partial h'}{\partial t} &= -h_0\frac{\partial u'}{\partial x}
\end{aligned}
\tag{10-72}
$$

[Eqs. (5-22) and (5-23)].

The initial conditions are

$$
h'(x, 0) = \cos(kx) \quad \text{and} \quad u'(x, 0) = (g/h_0)^{1/2} h'(x, 0)
\tag{10-73}
$$

with periodic boundary conditions (i.e., no reflection). The linear solution can be written as

$$
h'(x, t) = \cos(kx - \omega t) \quad \text{and} \quad u'(x, t) = (g/h_0)^{1/2} h'(x, t).
\tag{10-74}
$$

Here $k = 2\pi/(n\Delta x)$ is the wave number (where $n\Delta x$ is the wavelength) and $\omega = 2\pi/P$, where the period P is the time required for a wave to traverse the distance $n\Delta x$.

The finite difference version of Eq. (10-72) is analyzed in Section 10.1.4. The finite difference approximation does not introduce any amplification factor, but

does exhibit a pronounced phase error. As shown in Section 10.1.4, phase error is expressed as the ratio of calculated (c) to exact (c_a) wave speeds,

$$c/c_a = \left(\pm k \Delta t (gh_0)^{1/2}\right)^{-1} \sin^{-1}\left(\gamma(4 - \gamma^2)^{1/2}/2\right),$$

where $\gamma^2 = gh_0(\Delta t/\Delta x)^2 \sin^2 k\Delta x$. This error can be appreciable, as shown in Table 10-5. For the parameters used in the following numerical experiments, this ratio is 0.901.

As a numerical experiment, the initial conditions given by Eq. (10-72) are used with $g = 1$ and $h_0 = 1.6$, a $\Delta t/\Delta x$ ratio of 0.125 $(gh_0)^{-1/2}$ unless otherwise stated, and a wavelength of $8 \Delta x$. For notational convenience, the primes are dropped from u' and h'.

To evaluate the accuracy of separately solving the linear and nonlinear components of Eq. (10-72) vis-a-vis a totally numerical technique, the exact solution is needed. This is calculated as closely as possible using a spectral method.

To perform this evaluation, u and h are expressed in terms of truncated Fourier series. The periodicity of $8\Delta x$ dictates the form

$$u = \sum_{n=1}^{3}(a_n \cos nx + b_n \sin nx) + a_4 \cos 4x + b_4 \cos 8x, \qquad (10\text{-}75)$$

where a number of the trigonometric terms are skipped because they add no new information on the eight grid points; h is expressed analogously.

For use in the spectral scheme, Eq. (10-71) becomes

$$u^{\tau+1} = u^\tau - \Delta t\left(u^\tau \frac{\partial u^\tau}{\partial x} - g\frac{\partial h^\tau}{\partial x}\right) \qquad (10\text{-}76)$$

$$h^{\tau+1} = h^\tau - \Delta t\left(u^{\tau+1}\frac{\partial h^\tau}{\partial x} - h^\tau \frac{\partial u^{\tau+1}}{\partial x}\right). \qquad (10\text{-}77)$$

At each time step, we calculate $u^{\tau+1}$ and $h^{\tau+1}$ for the eight grid points, then fit these new values to a series of the form given by Eq. (10-75) to obtain new coefficients, thus always working with an eight-term series at each step.

For increased accuracy, the time step is reduced by a factor of five compared to what is used in the finite difference solution method. These exacts results are graphed in Figure 10-13.

The finite difference approximation to Eq. (10-71) is given by the following equations:

$$u_i^{\tau+1} = \frac{\Delta t}{\Delta x}\left[-u_i^\tau\left(u_i^\tau - u_{i-1}^\tau\right) - \frac{g}{2}\left(h_{i+1}^\tau - h_{i-1}^\tau\right)\right] + u_i^\tau, \text{ if } u_i^\tau > 0$$

$$= \frac{\Delta t}{\Delta x}\left[-u_i^\tau\left(u_{i+1}^\tau - u_i^\tau\right) - \frac{g}{2}\left(h_{i+1}^\tau - h_{i-1}^\tau\right)\right] + u_i^\tau, \text{ if } u_i^\tau \le 0 \quad (10\text{-}78)$$

Wave Amplitude h;   after 20 Δt

(a)

Wave   Amplitude   h;   after 40 Δt
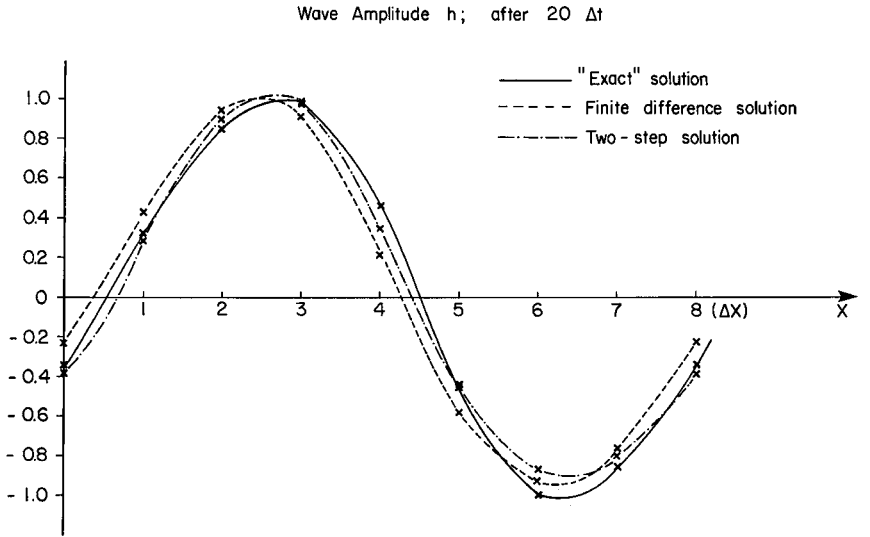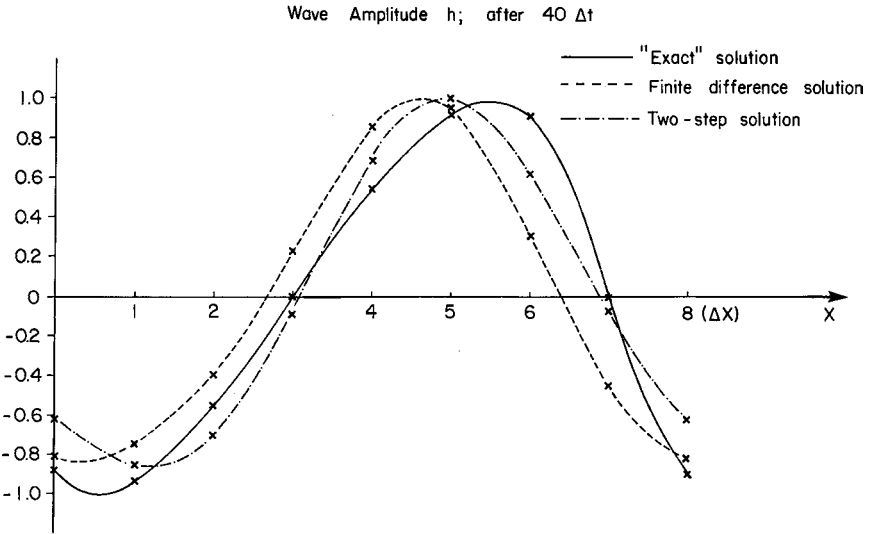
(b)

Fig. 10-13.   Wave amplitude h as computed by the compared methods (wave speed u behaves similarly) after (a) 20 times steps and (b) 40 time steps. (From Weidman and Pielke 1983.)

and

$$h_i^{\tau+1} = \frac{\Delta t}{\Delta x}\left[-u_i^{\tau+1}\left(h_i^{\tau}-h_{i-1}^{\tau}\right) - \frac{h_i^{\tau}}{2}\left(u_{i+1}^{\tau+1}-u_{i-1}^{\tau+1}\right)\right] + h_i^{\tau}, \text{ if } u_i^{\tau+1} > 0$$

$$= \frac{\Delta t}{\Delta x}\left[-u_i^{\tau+1}\left(h_{i+1}^{\tau}-h_i^{\tau}\right) - \frac{h_i^{\tau}}{2}\left(u_{i+1}^{\tau+1}-u_{i-1}^{\tau+1}\right)\right] + h_i^{\tau}, \text{ if } u_i^{\tau+1} \le 0. \quad (10\text{-}79)$$

The solution as computed by Eqs. (10-78) and (10-79) is also plotted in Figure 10-13.

In the two-step method of solution, first, the linear system is solved analytically. The result is Eq. (10-74), which is propagated by one time step, giving the intermediate solution values denoted by h^* and u^*,

$$h^* = \cos(kx - \omega\Delta t) \qquad \text{and} \qquad u^* = (g/h_0)^{1/2}h^*. \quad (10\text{-}80)$$

At the second step, the intermediate solution is used in the numerical computation necessary to complete the time step. Analogous to Eqs. (10-78) and (10-79),

$$u_i^{\tau+1} = \frac{\Delta t}{\Delta x}\left[-u_i^{\tau}\left(u_i^{\tau}-u_{i-1}^{\tau}\right)\right] + u^*, \text{ if } u_i^{\tau} > 0$$

$$= \frac{\Delta t}{\Delta x}\left[-u_i^{\tau}\left(u_{i+1}^{\tau}-u_i^{\tau}\right)\right] + u^*, \text{ if } u_i^{\tau} \le 0 \quad (10\text{-}81)$$

and

$$h_i^{\tau+1} = \frac{\Delta t}{\Delta x}\left[-u_i^{\tau+1}\left(h_i^{\tau}-h_{i-1}^{\tau}\right) - \frac{h_i^{\tau}}{2}\left(u_{i+1}^{\tau+1}-u_{i-1}^{\tau+1}\right)\right] + h^*, \text{ if } u_i^{\tau+1} > 0$$

$$= \frac{\Delta t}{\Delta x}\left[-u_i^{\tau+1}\left(h_{i+1}^{\tau}-h_i^{\tau}\right) - \frac{h_i^{\tau}}{2}\left(u_{i+1}^{\tau+1}-u_{i-1}^{\tau+1}\right)\right] + h^*, \text{ if } u_i^{\tau+1} \le 0. \quad (10\text{-}82)$$

Note that except for u^* and h^*, all of the terms on the right sides of Eqs. (10-81) and (10-82) are nonlinear.

The solution as computed with Eqs. (10-80)–(10-82) is also displayed in Figure 10-13. It is apparent that the two-step solution eliminates much of the phase error found in the straight finite difference solution. Both the finite difference and two-step solutions show an asymmetry (overshoot of positive peak and spreading in the trough) that is not true to the exact solution. The two-step method is also competitive with the straight numerical computation in terms of computer time, as discussed in Weidman and Pielke (1983).

The two-step procedure outlined previously is valid for a large class of problems. Suppose that a system of the form

$$\frac{\partial \vec{y}(x_1\ldots,x_n, t)}{\partial t} = A\vec{y}(x_1\ldots,x_n, t) \quad (10\text{-}83)$$

exists where A is some operator on a $(n + 1)$-dimensional complex-valued vector space and $\vec{y}(x_1, \ldots, x_n, t)$ is an $n + 1$ vector. Split A into the sum of operators L and N, where L is such that

$$\partial \vec{y}/\partial t = L\vec{y}, \tag{10-84}$$

which with chosen initial and boundary conditions can be solved analytically. Interpret $L\vec{y}$ as being the linear terms from $A\vec{y}$, while $N\vec{y}$ consists of the nonlinear terms. Thus Eq. (10-83) becomes

$$\partial \vec{y}/\partial t = L\vec{y} + N\vec{y}. \tag{10-85}$$

This type of equation can be studied with functional analysis techniques (see, e.g., Schechter 1977). Equation (10-85) can be formally solved with a variation of parameters argument.

First, solve homogeneous equation (10-84) with the given initial and boundary conditions. In the two-step method, deliberately choose L such that Eq. (10-84) has an analytic solution, which may be denoted by $\vec{y}_a(t)$. Equation (10-80) then corresponds to $\vec{y}_a(t + \Delta t)$, which is defined as $\vec{y}^*$.

Also, solving Eq. (10-84) formally,

$$\vec{y}_a = e^{(t - t_0)L}\vec{y}_0, \tag{10-86}$$

where t_0 is some initial time and $\vec{y}_0$ is the solution at t_0.

Following the lead of the classic variation of parameters derivation, replace $\vec{y}_0$ with $\vec{y}_0(t)$ and use Eq. (10-86) in Eq. (10-85). The resulting expression for the particular solution is

$$\vec{y}_p = \int_{t_0}^{t} e^{(t - \tau)L} N(\vec{y}(\tau)) dt. \tag{10-87}$$

This is well defined whenever $N\vec{y}$ is an integrable function. Thus the total solution to Eq. (10-85) may be written as

$$\vec{y}(t) = \vec{y}_a(t) + \int_{t_0}^{t} e^{(t - \tau)L} N(\vec{y}(\tau)) d\tau. \tag{10-88}$$

In a given time step, compute $\vec{y}(t_0 + \Delta t)$ as

$$\vec{y}(t_0 + \Delta t) = \vec{y}^* + \int_{t_0}^{t_0 + \Delta t} e^{(t_0 + \Delta t - \tau)L} N(\vec{y}(\tau)) d\tau. \tag{10-89}$$

The two-step scheme is, therefore, approximating the foregoing integral by $(\Delta t)N(\vec{y}(t_0))$, then computing the term numerically; compare Eqs. (10-81) and (10-82). Of course, this is just the simplest such approximation of the integral in Eq. (10-89); one could, for example, evaluate $N\vec{y}$ at some midpoint rather than at t_0, or approximate the integral with three points.

This two-step scheme improves accuracy in the numerical solution of nonlinear partial differential equations. In a simple experimental case, this method

reduced the error of a basic numerical scheme with no appreciable increase in computing time. As a next step, it would be very illuminating to try an experiment, such as performed here, on a solvable nonlinear partial differential equation (such as the Long model derived in Chapter 5, Section 5.3); that is, one for which the exact solution is known in closed form. In that case, we would be able to see very clearly how well the two-step version works compared to a straight numerical scheme for a variety of such equations. Work is also needed to ascertain what difficulties occur in implementing a two-step scheme with more involved nonlinear equations.

Mathematically much analysis remains to be done, complicated by the fact that most of it is nonlinear analysis. The sources and magnitudes of errors with the two-step scheme must be known and optimum approximations for the integral in Eq. (10-89) applied to minimize errors. There are also questions of convergence of the method. It may be that with certain approximations to the integral in Eq. (10-89), the size of the time steps can be significantly increased.

The method proposed here may have utility for a wide range of geophysical problems, including numerical weather prediction. *By computing a linear solution at each time step and evaluating only the nonlinear components numerically, a major source of computational error may be avoided.*

10.6   Summary

This chapter has introduced the concepts of linear and nonlinear stability and presented examples of specific computational solution techniques. The conclusions of relevance to mesoscale modeling that are implied from the chapter include the following:

1.   When advection is considered an important component of the mesoscale circulation, the advection terms should be approximated with formulations that provide accurate predictions of phase *and* amplitude for wavelengths of $4\Delta x$ and longer. The interpolated schemes are examples of solution techniques that have this attribute.

2.   When vertical turbulent diffusion is considered an important component of a mesoscale circulation, it is desirable to use a scheme that provides accurate solutions yet is economical to apply, such as the implicit formation.

3.   When the pressure gradient force is an important component of a mesoscale circulation, a forward-in-time, centered-in-space representation is an accurate representation. This result is implied from the linear tank model solutions. The gradient terms that appear in the conservation-of-mass equation similarly can be accurately represented by a centered-in-space approximation.

To obtain these accurate solutions, however, an implicit formulation between the pressure gradient and conservation-of-mass relation must be used.

4. In a nonlinear representation, aliasing causes the fictitious accumulation of energy on wavelengths shorter than $4\Delta x$. To eliminate this problem, horizontal diffusion must be applied either through an explicit representation, such as a smoother, or implicitly as part of the computation scheme.

5. The approximation of advection, pressure gradient force, and subgrid-scale diffusion can only be reasonably well represented for spatial scales of at least four grid increments in each spatial direction. The term *model resolution*, therefore, should be used only for spatial scales that are four grid increments or larger (Pielke 1991; Grasso 2000). This conclusion also applies to spectral models (Laprise 1992b).

6. The separation of a nonlinear model into its linear and nonlinear components may provide improved solution accuracy. The linear portion could be computed analytically. Only the remaining nonlinear portion would need to be solved numerically.

7. Parameterizations (from Chapters 7–9, for example) should be inserted appropriately in a model so that their spatial scale is at least four grid increments in each direction. Otherwise, the approximate forms of the advection, subgrid-scale mixing, and pressure gradient force will produce significant errors in the computational solution.

Notes to Chapter 10

1. Finite difference schemes can be written in what is called a *finite volume* form, where fluxes across the grid volume interface are calculated (Derickson 1992). The mathematical formulation of finite volume techniques, however, can be described in terms of a Taylor series expansion.

2. If Δx approaches 0 in the limit then $k\Delta x$ also approaches 0, so that Eq. (10-3) is a *consistent* representation of the derivative quantity. If $\Delta x \neq 0$, however, then it is clear that the accuracy of the approximation is a function of wavenumber.

3. This technique is often referred to as the *Von Neumann method*. A second method, called the *matrix method of stability*, includes boundary conditions in the analysis. This latter methodology, however, is more difficult to apply. It is generally preferable to show the stability, or lack of it, of a numerical scheme using the Von Neumann method, and this approach is adopted in this chapter.

4. The real and imaginary parts of a complex number can be considered a vector with two perpendicular components. In an equation, the real and imaginary components must separately be equal.

5. A similar analysis can be performed for $U < 0$, and the result will be of the same form.

6. To obtain this result, simply replace $\bar{\phi}$ with $\bar{\phi} = \hat{\phi} + e^{i(kx+\omega t)}$ in the differential equation and solve for ω/k.

7. To determine the quadrant of the $\sin^{-1}(\pm\frac{\alpha}{2})$ requires assessing which solution propagates in the same direction as the physical solution. For the leapfrog scheme, the physical mode is quadrant 1 of the sine function, while the computational mode is in quadrant 3 (π to $3\pi/2$).

8. The retention of $2\Delta x$ features in a model is undesirable since they are poorly resolved and can create nonlinear instability. The challenge is to eliminate this wavelength but leave the longer waves relatively unaffected.

9. "Positive definite" means that the finite difference solution never produces negative values.

10. This section is adapted from Costa *et al.* (2000).

11. The exact damping per time step is λ_a.

12. From a practical viewpoint, however, $\lambda \simeq 1$ since $(\Delta t)^2 f^2$ is very small for commonly found values of Δt and f in a mesoscale model (e.g., for $\Delta t = 100$ s and $f = 10^{-4}\,\text{s}^{-1}$, $\lambda = \sqrt{1 + 10^{-6}}$).

13. Note that since the second difference equation requires $u_{i+1}^{\tau+1}$ and $u_{i-1}^{\tau+1}$, it is necessary to compute all of the values of $u^{\tau+1}$ before beginning the computations for $h^{\tau+1}$.

14. The term "semi-Lagrangian scheme" is also used for this technique.

15. The solution of Eq. (10-47) with periodic boundary conditions is described in Appendix A.

16. Modern computers also have standard algorithms for efficiently solving such tridiagonal matrix equations (e.g., Adams *et al.* 1975).

17. The spline has its worst representation of phase speed in Table 10-1 for a $4\Delta x$ wave ($\tilde{c}_\phi/U = 0.955$) at $C = 0.001$.

18. Splitting is also referred to as the *Marchuk method* (Mesinger and Arakawa 1976).

19. Haltiner and Williams (1980) discuss in detail the solution of diagnostic equations of the form given by Eq. 10-58 using direct, as well as iterative methods such as described in the remainder of this section.

20. As discussed in Section 4.1, because of computer resource limitations, the grid intervals in meteorological models cannot be made small enough to represent molecular processes and yet still simulate mesoscale atmospheric phenomena.

21. Unbounded growth of nonlinear instability can be controlled by requiring conservation of energy in the selected differencing scheme. However, even with these schemes, the solution can degrade into small-scale noise. Initial conditions that contain considerable shortwave features can cause more rapid development of nonlinear instability.

22. $\partial\bar{\phi}/\partial t = K\partial^2\bar{\phi}/\partial x^2$.

Additional Readings

Derickson, R. 1992. Finite difference methods in geophysical flow simulations. Ph.D. dissertation, Dept. of Civil Engineering, Colorado State University.

> This Ph.D. dissertation provides a thorough detailed analysis of the minimum resolution possible as a function of the number of grid points. Derickson uses the computational error characteristics of the solution techniques to produce more accurate solutions.

Foufoula-Georgiou, E., and P. Kumar (Eds.). 1994. "Wavelets in Geophysics." Academic Press, New York.

> This book discusses a procedure called "wavelet analysis" that uses a localized transform in space and time with which to analyze geophysical signals, including atmospheric features.

Haltiner, G. J., and R. T. Williams. 1980. "Numerical Prediction and Dynamic Meteorology," 2nd ed. John Wiley & Sons, New York.

> Although this text is oriented toward synoptic-scale numerical weather prediction, the discussion in Chapters 5 and 6 on numerical solution technique complements the material discussed in this chapter.

Jacobson, M. Z. 1999. "Fundamentals of Atmospheric Modeling," Cambridge University Press, Cambridge, England, 656 pp.

> This recent book describes meteorological modeling including an emphasis on air pollution modeling.

Krishnamurti, T. N., and L. Bounoua. 1995. "An Introduction to Numerical Weather Prediction Techniques." CRC Press, Washington DC.

This book provides an introduction to finite difference techniques as well as information on parameterizations in larger-scale models.

Larson, V. E., R. Wood, P. R. Field, J.-C. Golaz, T. H. Vonder Haar, and W. R. Cotton. 2001. Systematic biases in the microphysics and thermodynamics of numerical models that ignore subgrid-scale variability, *J. Atmos. Sci.*, **58**, 1117–1128.

This paper discusses errors that result when subgrid-scale variability is ignored.

Mesinger, F. 1997. Dynamics of limited-area models: Formulation and numerical methods. *Meteor. Atmos. Phys.* **63**, 3–14.

This paper provides a valuable perspective on regional and mesoscale modeling. Mesinger is one of the pioneers in this field and an innovator in the use of these models in operational weather forecasting, so this is a must read.

Mesinger, F., and A. Arakawa. 1976. Numerical methods used in atmospheric models. *GARP Publ. Ser.* **17**, 1–64.

This publication provides a useful discussion of finite difference techniques. Volume 2 of this GARP series (published in 1979) presents summaries of the spectral, pseudospectral, and finite element techniques.

Moran, M. D. 2000. Basic aspects of mesoscale atmospheric dispersion. Chapter 2 in: *Mesoscale Atmospheric Dispersion*, Z. Boybeyi, Ed., WIT Press, London, Great Britain, 27–120.

This book chapter presents observational data on the magnitude of real-world horizontal dispersion.

Pielke, R. A., and R. W. Arritt. 1984. A proposal to standardize models. *Bull. Amer. Meteor. Soc.* **65**, 1082.

A recommendation to develop plug-compatible components of models is proposed.

Pielke, R. A., L. R. Bernardet, P. J. Fitzpatrick, S. C. Gillies, R. F. Hertenstein, A. S. Jones, X. Lin, J. E. Nachamkin, U. S. Nair, J. M. Papineau, G. S. Poulos, M. H. Savoie, and P. L. Vidale. 1995b. Standardized test to evaluate numerical weather prediction algorithms. *Bull. Amer. Meteor. Soc.* **76**, 46–48.

Students who completed a mesoscale modeling class using the first edition of this book summarize recommended procedures to evaluate modeling algorithms.

Richtmyer, R. D., and K. W. Morton. 1967. "Difference Methods for Initial-Value Problems." Interscience Publishers, New York.

Although somewhat dated, this text provides a valuable fundamental discussion of numerical solution techniques.

Sun, W.-Y. 1993b. Numerical experiments for advection equation. *J. Comput. Phys.* **108**, 264–271. This article provides a concise, effective summary of two additional computational representations of advection.

Problems

For problems 1–4, calculate the analytic solution using the solution techniques for difference equations given in Section 10.1. Since the exact solution of the advection equation ($\partial \phi / \partial t = U \phi / \partial \phi / \partial x$) is $\lambda_{act} = 1$ and $c_\phi = U$, tabulate the ratios of the analytic to exact solutions for Courant numbers of 0.001, 0.01, 0.1, 0.2, 0.3, 0.4, 0.5, 0.6, 0.7, 0.8, 0.9, 1.0, 1.5, and for wavelengths of $2\Delta x$, $4\Delta x$, $10\Delta x$, and $20\Delta x$ for the following finite difference equations.

1.

$$\frac{\phi_i^{\tau+1} - \phi_i^{\tau}}{\Delta t} = -\frac{U}{6\Delta x}[\phi_{i+2}^{\tau} - 2\phi_{i+1}^{\tau} + 9\phi_i^{\tau} - 10\phi_{i-1}^{\tau} + 2\phi_{i-2}^{\tau}], \ U > 0$$

(Reference: Kawamura, T., H. Takami, and K. Kuwahara. 1986. Computation of high Reynolds number around a circular cylinder with surface roughness. *Fluid Dyn. Res.* **1**, 145–162.)

   2.

$$\frac{\phi_i^{\tau+1} - \phi_i^{\tau}}{\Delta t} = -\frac{U}{6\Delta x}[2\phi_{i+1}^{\tau} + 3\phi_i^{\tau} - 6\phi_{i-1}^{\tau} + \phi_{i-2}^{\tau}], \ U > 0$$

(Reference: Agarwal, R. K. 1981. A third-order–accurate upwind scheme for Navier–Stokes solutions at high Reynolds numbers. Paper No. AIAA-81-0112, AIAA 19th Aerospace Sciences Meeting, January 12–15 1981, St. Louis, MO.)

   3.

$$\frac{\phi_i^{\tau+1} - \phi_i^{\tau}}{\Delta t} = -\frac{U}{\Delta x}[b_1(\phi_{i+1}^{\tau} - \phi_{i-1}^{\tau}) + b_2(\phi_{i+2}^{\tau} - \phi_{i-2}^{\tau})], \ U > 0$$

$$b_1 = 0.785398 \quad b_2 = -0.155076$$

(Reference: Derickson, R. 1992. Finite difference methods in geophysical flow simulations. Ph.D. dissertation, Department of Civil Engineering, Colorado State University.)

   4.

$$\frac{\phi_i^{\tau+1} - \phi_i^{\tau-1}}{\Delta t} = -\frac{U}{\Delta x}\left[\frac{4}{3}(\phi_{j+1}^{\tau} - \phi_{j-1}^{\tau}) - \frac{1}{6}(\phi_{j+2}^{\tau} - \phi_{j-2}^{\tau})\right]$$

which is a fourth order in space, leapfrog differencing scheme.

   5.   Program the difference equation (10-7) using cyclic boundary conditions. Compare your amplifying solution with that of Eq. (10-10). Why do the results differ after only a few time steps?

   6.   Program the difference equation (10-13) for $U > 0$. Using the cyclic boundary conditions, integrate the model forward for 100 time steps. Evaluate the change of amplitude with time and the phase speed of your results for the values of Courant number and wavelength given in Table 10-1. Compare the numerically computed values with the analytic results. They should be identical.

   7.   Perform problem 6 but with Eq. (10-16). Note that leapfrog has two solutions, only one of which is physical.

   8.   Program Eq. (10-27) with cyclic boundary conditions and constant K, and calculate the change of amplitude after integrating for 100 time steps with $\beta_{\tau} = 1$ and $\beta_{\tau} = 0.5$. Refer to Appendix A with respect to how to solve an implicit equation. Use the same values of γ and wavelength as in Table 10-2, and compare your numerical results with the solutions tabulated in Table 10-2.

   9.   Program Eq. (10-34) with cyclic boundary conditions and calculate the change of amplitude and phase after 100 time steps. Use the same values of $\sqrt{gh_0}\Delta t/\Delta x$ and wavelength as shown in Table 10-3. Compare your numerical results with the analytic results.

   10.   From problem 4 in Chapter 6, write the approximate form for each term (for flat terrain). Describe the phase and amplitude change per time step for the linear form of each term.

   11.   Obtain the text by Porte-Agel *et al.* (2000; their Appendix) and confirm the error that is introduced when a finite difference algorithm is used to compute the vertical gradient of the horizontal velocity. Then assess the error when a nonneutral surface layer is presented (using the theory for the surface layer developed in Section 7.2).

Chapter 11

Boundary and Initial Conditions

Chapter 10 provided an introduction to methodologies for obtaining solutions to the conservation relations. In that discussion it was shown that, for example, certain approximate representations of the differential equations produce more accurate solutions than others. Linear forms of the conservation equations (e.g., one-dimensional advection, one-dimensional diffusion, Coriolis terms) were examined independently of one another with the assumption that a *necessary requirement for satisfactory solutions to the nonlinear partial differential equations is an accurate approximation for the linearized version*. Moreover, these components of the conservation equations were studied independently from one another, even in the linear version, with the presumption that each portion of the relations must separately be accurate.

Once optimal approximate forms of the equations are selected, however, it is still necessary to define the domain and grid structure over which the equations will be evaluated. In addition, boundary and initial conditions are required to provide unique solutions for any set of differential equations. The modeler has to also ask whether the boundary is independent of what occurs in the atmosphere or is interactive with the atmosphere. When the latter condition occurs, the boundary is more appropriately called a *flux interface*.

11.1 Grid and Domain Structure

The selection of the domain size and grid increments in a mesoscale model are dictated by the following constraints:

- What is the dimensionality of the forcing?
- What are the spatial scales of the physical response to this forcing?
- What are the available computer resources?

Mesoscale models can have either two or three independent spatial coordinates. In addition, models have been developed in which either the dependent variables are evaluated at specific grid points or averages of the resolvable dependent variables are obtained over a layer. With the second methodology, the averaging operation can be defined as

$$\langle \phi \rangle = \int_{z}^{z+\delta h} \bar{\phi} d\hat{z} / \delta h,$$

where $\bar{\phi}$ is defined by Eq. (4-6) and δh is the depth of the layer average.

The following are examples of mesoscale models and their spatial representation.

- *x-y layered representation* (e.g., Lavoie 1972, 1974; Lee 1973). In these formulations, the dependent variables are averaged over discrete layers, such as the planetary boundary layer, so that the explicit vertical dependency in the conservation relation is removed. Such a layered representation is also often used in oceanographic models (e.g., O'Brien and Hurlburt 1972).
- *x-σ representation*[1] (e.g., Estoque 1961, 1962). This formulation has been used to provide horizontal and vertical resolution of mesoscale structure, but without the added cost of a second horizontal coordinate. The *x-σ* coordinate form is appropriate only for those mesoscale features that are predominantly forced by two-dimensional features (e.g., a uniform mountain ridge) and for the theoretical analysis of the conservation relations. In addition, an axisymmetric formulation in which radius *r* replaces *x* as the horizontal coordinate has also been used to better simulate circular atmosphere features. Examples of such axisymmetric models include hurricane models (e.g., Rosenthal 1970), circular lake and island circulations (e.g., Neumann and Mahrer 1974, 1975), and cumulus clouds (Murray 1970).
- *x-y-σ representation* (e.g., McPherson 1970; Pielke 1974a). This is the most general form of spatial coordinates and should provide the best representation of actual mesoscale features.

The spatial scales of the forcings and of the resultant perturbation fields determine the necessary domain size of the model as well as its grid spacing. To represent mesoscale systems properly, (1) the meteorologically significant variations in the dependent variables caused by the mesoscale forcing must be contained within the model, and (2) the averaging volume used to define the model grid spacings must be sufficiently small so that the mesoscale forcings and responses are accurately represented.
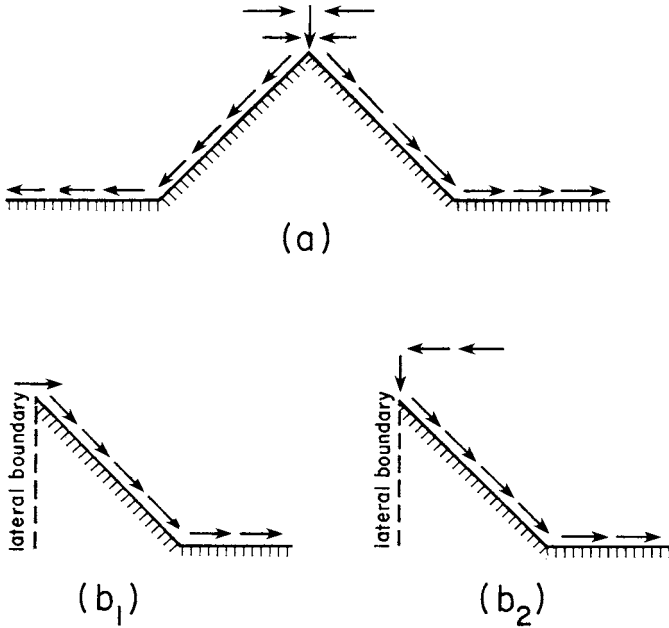
Fig. 11-1.   (a) Schematic of a nocturnal drainage flow in the absence of synoptic winds where the replacement air at a ridge crest comes both from aloft and from the same level. (b_1) A simulation with an open lateral boundary at a ridge top, and (b_2) a simulation with a closed lateral boundary at a ridge top; $\partial\theta_0/\partial z > 0$ is assumed.

Figure 11-1 schematically illustrates one problem that can arise from inappropriate domain selection. In this example, the actual drainage flow on a clear night with synoptic winds is expected to originate along both slopes of a mountain ridge, as discussed in more detail in Chapter 13, Section 13.1.3. However, to save money, a modeler elects to truncate the domain at the ridge crest, so that only one slope is represented. Because of this constraint, downslope air to the east of the ridge line in a model with $\partial\theta_0/\partial z > 0$ will be predominantly replaced by air from the left lateral boundary (if it is an open boundary[2]) or from aloft (if it is a closed boundary). In other words, *the lateral boundary will determine the solutions.* In the real atmosphere, in contrast, downslope winds can develop on both eastern and western slopes, so that the origin of the replacement air needed to preserve mass will depend only on such physical factors as the magnitude of the overlying thermodynamic stability. To represent this fundamental physical interaction correctly, it is thus necessary to include the complete mesoscale variations within the model.

11.1.1   Horizontal Grid

11.1.1.1   Grid Size

   The grid size used in a numerical model depends on the anticipated or, if available, observed spatial sizes of the mesoscale feature of interest. If surface topography is considered to be the dominant forcing, then the ragged landscape of Grand Teton National Park obviously will require a smaller grid interval than the undulating Flint Hill region of central Kansas, for example.

   The representation of surface topography as a function of wavelength can be used to determine the characteristic scales of the terrain. Figure 11-2 illustrates the contribution of topographic features of different horizontal scales to the total
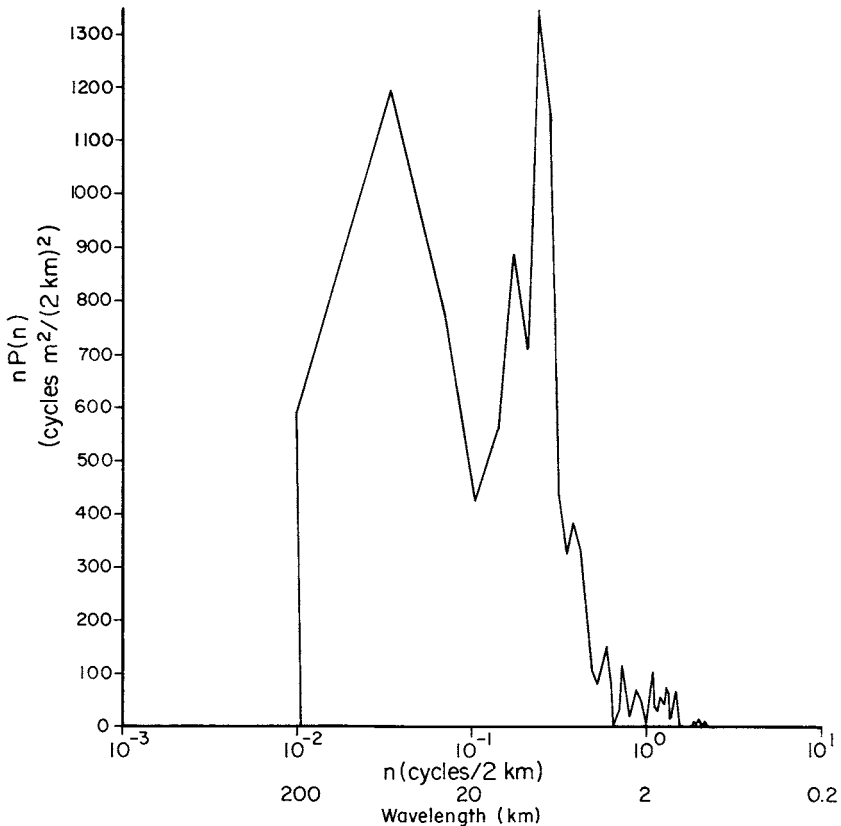
Fig. 11-2.   The variance of topography plotted as a function of horizontal wavelength for a cross-section across a portion of the Blue Ridge Mountains in central Virginia. (From Pielke and Kennedy 1980.)

variations in ground surface elevation for a northwest–southeast cross-section of the Blue Ridge Mountains of central Virginia. A one-dimensional Fourier transformation, as shown by Panofsky and Brier (1968) and given by

$$z_G(x_j) = \bar{z}_G + \sum_{n=1}^{I_x/2} [a_n \sin(2\pi nj\Delta x/D_x) + b_n \cos(2\pi nj\Delta x/D_x)]$$

$$(j = 1, 2, \ldots, I_x),$$

was used, where

$$a_n = \frac{2}{I_x} \sum_{n=1}^{(I_x/2)-1} z_G'(x_j) \sin(2\pi nj\Delta x/D_x), \quad a_{I_x/2} = 0$$

$$b_n = \frac{2}{I_x} \sum_{n=1}^{(I_x/2)-1} z_G'(x_j) \cos(2\pi nj\Delta x/D_x), \quad b_{I_x/2} = -z_G'(x_j)/I_x.$$

In this expression, I_x is an even integer number of grid points of separation, Δx, used to represent the terrain height within the interval, D_x. The variable n is referred to as the number of the harmonic. The quantity $(a_n^2 + b_n^2)^{1/2}$ represents the contribution of each wavelength of size $2\Delta x, 3\Delta x, 4\Delta x, \ldots$, up to $I_x\Delta x/2$ to the function $z_G'(x_j)$. The domain-averaged terrain height is given by $\bar{z}_G$, with z_G' denoting the variations from this value.

Ideally, one would prefer to use a two-dimensional Fourier transformation, but such programs are not routinely available for large amounts of data. The two-dimensional terrain data from which the information used to compute Figure 11-2 was derived had 61-m intervals over a 200- by 200-km area. Using this number of grid points (about 10 million) in a two-dimensional transform is expensive to process. If only one-dimensional transforms are calculated, then it is necessary to perform a series of cross-sections through the regions of most rapidly varying terrain.

The cross-section shown in Figure 11-2 demonstrates that most of the terrain features vary significantly over scales substantially larger than 2 km. The predominant horizontal scales for this cross-section are at 40 and 10 km, with 95% of the variance[3] of topography having horizontal wavelengths greater than 6 km. Therefore, for this example, a horizontal grid increment of 1.5 km or smaller is a necessary condition to resolve 95% of the terrain irregularities with a resolution of $4\Delta x$ or larger. Pielke and Kennedy (1980), Young and Pielke (1983), Young *et al.* (1984), Steyn and Ayotte (1985), and Salvador *et al.* (1999) have discussed the spatial analysis of terrain scales in more detail. McQueen *et al.* (1995) investigated the influence of grid increment size with respect to the resolution of terrain in an operational mesoscale model. Gollvik (1999) explored the capabilities of different horizontal grid increments (22 km, 11 km, and 5.5 km) and resolution of topography in model simulations of precipitation

in a regional model. Salvador *et al.* (1999) used two-dimensional spectral analysis to determine the needed spatial resolution of mesoscale model simulations for a portion of the east coast of Spain.

Salmon *et al.* (1981) have discussed the implications of high-wavenumber terrain features in a model and concluded that such features cause noisy solutions that tend to overemphasize the real impact of these small-scale terrain variations. Unfortunately, since the horizontal gradient of a pressure perturbation is proportional to horizontal wavenumber [see, e.g., following Eq. (5-43), where $\partial p'/\partial x = ik_x \tilde{p}$ after the Fourier transform] as well as the spatial scale of terrain variations [see, e.g., Eq. (6-57), where the pressure gradient force contains a term with $\partial z_G/\partial x$); the relative contribution of short wavelength terrain features to velocity accelerations would be expected to be larger than that implied from a decomposition of terrain variations alone (Walmsley *et al.* 1982).

Observational studies, including Lenschow *et al.* (1979) and Mahrt and Heald (1981), show that terrain slope and small-scale three-dimensional features exert substantial influence on surface temperature distribution and boundary layer structure over even mildly irregular terrain. From observations of drainage wind fluctuations in the Geysers area of California, Porch (1982) found that a correspondence may exist between prominent spectral peaks of wind velocity and characteristic variations in complex terrain, as represented by a two-dimensional Fourier transform of the terrain relief. Thus the approach of analyzing surface inhomogeneities (whether they are terrain features, land-water contrasts, or whatever) is a necessary (although not a sufficient) tool in establishing the horizontal grid size required in a mesoscale model.

If the conservation relations were linear, the spatial scale of the forcing would equal the spatial scale of the resultant atmospheric circulation, as illustrated for sea and land breezes in Section 5.2.3.1, and the use of Fourier transforms of terrain by itself could yield the minimum spatial grid resolution required. As shown in Figure 11-3, however, for two separate nonlinear sea-breeze simulations (with maximum surface temperature amplitudes, $T_{G_{max}}$, of 1°C and 10°C, respectively), when the terrain forcing becomes sufficiently strong (i.e., for $T_{G_{max}} = 10°C$), the nonlinearity of the conservation relations acts to decrease the horizontal spatial scale of the circulation L_x from that of the forcing. In practice, the only way to ensure that the correct spatial scales are simulated in a nonlinear model is to perform integrations with progressively finer resolution. When the results do not significantly change for a given scale of forcing with further reduction of the grid mesh, the model has achieved sufficient spatial resolution.

11.1.1.2   Grid Mesh

When setting up a horizontal grid, one can keep grid increments constant or allow them to stretch. The advantages of a constant grid include the relative
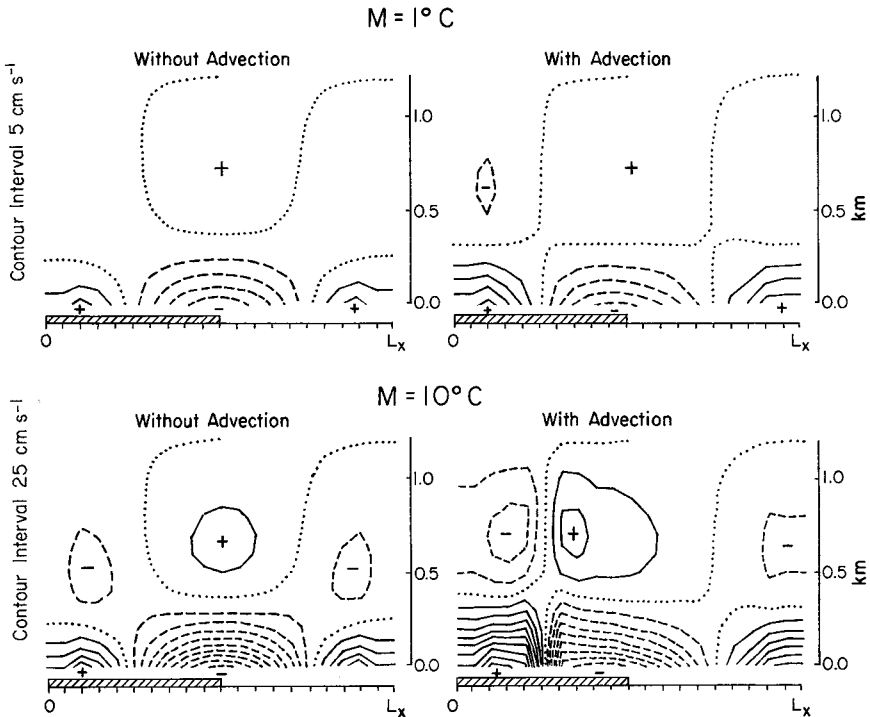
Fig. 11-3. The horizontal velocity field 6 hours after sunrise (at the time of maximum heating), calculated with the nonlinear analog to Defant's sea-breeze model introduced in Section 5.2.3.1. The large-scale vertical gradient of potential temperature was 1 K km^{-1}, and the horizontal scale of heating was $L_x = 100$ km with a maximum surface temperature perturbation M of (a) 1°C and (b) 10°C. Defant's analytic results, discussed in Section 5.2.3.1, were used to initialize the model runs. (From Martin 1981.)

ease of coding such a framework onto the computer, as well as the comparative simplicity of inputing geographic features into the model. Disadvantages arise in using an economically feasible number of grid points, however, including the close proximity of the sides of the model to the region of interest as well as the difficulty of properly incorporating large- and small-scale features within the same model domain.

Two different horizontal grid representations have been developed that are designed to reduce the problems associated with the constant grid. These are the *stretched grid* and the technique of *grid meshing*.

With a stretched grid, one can remove the boundaries of the model as far from the area of interest as one would like, so a much larger domain can be simulated than with the constant grid with the same number of grid points. In practice, either stretched grids are simply specified by assigning values to the

grid locations (e.g., $x_1 = 0$, $x_2 = 50$ km, $x_3 = x_2 + 40$ km, $x_4 = x_3 + 30$ km, $x_5 = x_4 + 20$ km, $\ldots$, $x_{I_x-1} = x_{I_x-2} + 40$ km, $x_{I_x} = x_{I_x-1} + 50$ km) or the independent spatial coordinates are transformed by a mathematical relation.

Lee (1973), for example, in his simulation of the airflow over the island of Barbados, uses a normalized transformation[4] adapted from Schulman (1970), given by

$$s(x) = c\{ax + \tanh[(x - x_0)/\eta] + b\};$$

$$b = \tanh x_0/\sigma, \quad x_0 = 0.5, \quad a = 0.5, \quad \eta = 0.044;$$

$$c = [a + b + \tanh(1 - x_0)/\eta]^{-1}$$

and Anthes (1970) offers an example of a stretched horizontal grid in two dimensions (Figure 11-4). Fox-Rabinovitz *et al.* (1997) discuss the stretched grid approach, including the problems that it introduces, and recommend solutions including the introduction of diffusion-type filters and uniformly-stretched grids. Applications of their stretched grid formulation are reported in Fox-Rabinovitz (2000) and Fox-Rabinovitz et al. (2001).

In Lee's formulation, η is a stretching scale factor, and $s(x = 0) = 0$ and $s(x = 1) = 1$. With this type of representation, the chain rule of calculus is used to replace the spatial derivatives in the conservation relations with terms such as

$$\frac{ds}{dx}\frac{\partial}{\partial s} = \frac{\partial}{\partial x} \quad \text{and} \quad \left(\frac{ds}{dx}\right)^2\frac{\partial^2}{\partial s^2} + \frac{d^2s}{dx^2}\frac{\partial}{\partial s} = \frac{\partial^2}{\partial x^2}. \quad (11\text{-}1)$$

In the stretched horizontal coordinate system, $\Delta s = s_{i+1} - s_i$ is a constant. However, this constant grid interval is not found to be superior to simply specifying the stretched grid in terms of the original independent variable x, since *the advantage of a constant grid Δs is nullified by the need to compute extra terms*, as given in Eq. (11-1). The term ds/dx, for example, must be computed as the average value over the particular interval Δx to which Δs corresponds. Since ds/dx itself is a function of x and thus varies over Δs, no advantage is gained by using this mathematical transformation. Simply specifying the grid locations of x_i is adequate.

In addition, the number of grid points between an interior location and the boundary is of equal importance to the size of the grid spacing. *Irrespective of the size of Δs (or Δx), for example, a location one grid length inside a boundary will be influenced by the boundary after only one time step.*

Using a fine-mesh grid inserted inside of a coarse grid is an alternative to the stretched grid approach.[5] In this case, a constant grid representation with grid increments Δ is surrounded by a grid with separation $n\Delta = \delta$, where $n > 1$. In contrast to the stretched grid, where changes in grid size are defined by a continuous function, the meshed grid approach requires a discontinuity
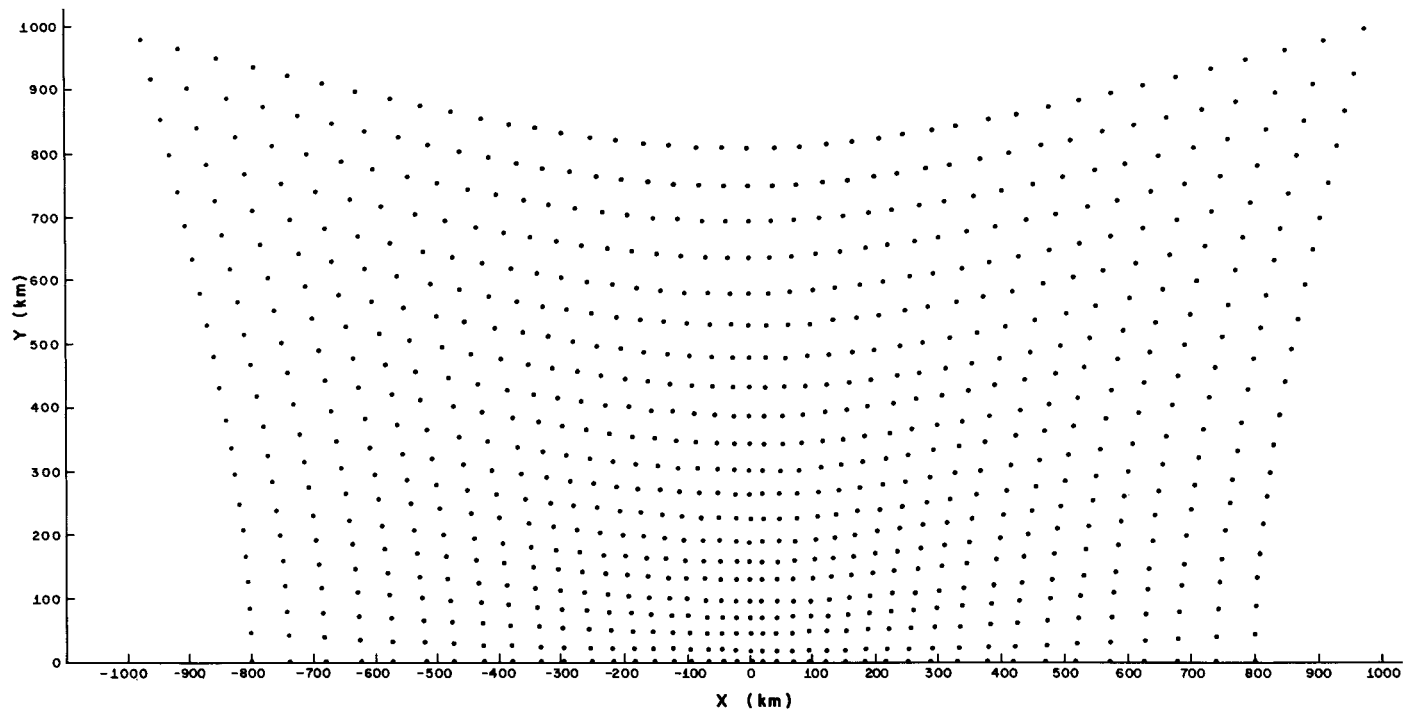
Fig. 11-4. The northern half of a two-dimensional variable horizontal stretched grid with a minimum grid separation of 20 km. (From Anthes 1970.)
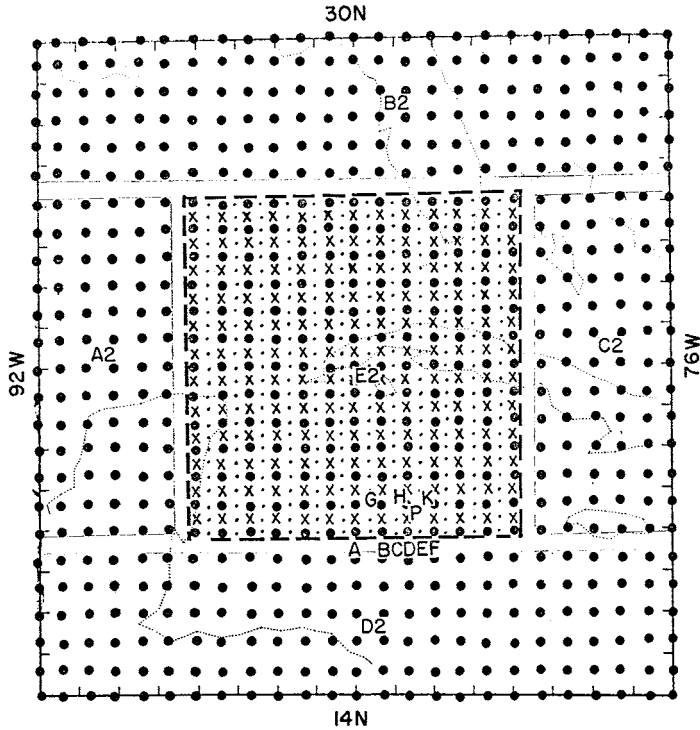
Fig. 11-5. A fine mesh with a grid increment of approximately 37 km, inserted inside of a coarse mesh with grid lengths of approximately 74 km. Variables within the fine mesh are defined as the small dots and x's, as well as the darkened circles. (From Mathur 1974.)

between the fine and coarse grids. Figure 11-5, reproduced from Mathur (1974), illustrates such a grid mesh representation in a hurricane model. Using this approach, Mathur was able to accurately simulate the fine structure of the hurricane near the eye wall as well as the larger-scale environment influencing the storm intensity and movement. More recent applications of the nested grid representation are described in Clark and Farley (1984), Pielke *et al.* (1992), and Walko *et al.* (1995b).

The meshed grids (as well as the stretched and constant horizontal grids) can also be defined to move relative to the earth's surface. Schlesinger (1973) has used a *movable grid* to prevent a simulated thunderstorm from exiting his domain, and Jones (1977b) used three meshed grids of lengths 10, 30, and 90 km to simulate the dynamics of a moving hurricane, with the smaller two grids moving with the storm.

Problems arise in using stretched or grid mesh representations, however. As shown in Chapter 10 (e.g., Table 10-1), waves with lengths that are short rela-

tive to the model grid size propagate erroneously relative to the exact analytic solution. Thus a wave in a fine mesh with a wavelength of 8Δ would have a representation of 2δ in the coarser grid if the grid separation were four times larger in the coarse grid ($\delta = 4\Delta$). Thus the wave would be poorly represented in the coarse grid. Moreover, as this wave travels from one grid region to another, the change in grid resolution can cause reflection and refraction of the wave (Morse 1973) in much the same fashion as occurs when electromagnetic waves travel from one physical medium to another (e.g., as light travels from air into water).

Thus, although stretched and nested grids increase the domain size, another source of computational error is introduced. For meshed grids, minimization of these errors is best accomplished by judicious use of filtering near the boundary between the coarse mesh and the fine mesh; see Perkey and Kreitzberg (1976) and Jones (1977a) for specifics concerning their schemes. Another discussion of procedures for nested grids is provided in Panin *et al.* (1999).

In applying boundary conditions between coarse and fine meshes, modelers can choose to permit perturbations to enter and leave the fine mesh (i.e., *two-way interaction*) or to prevent waves in the fine-grid mesh from exiting the fine mesh, but permitting coarse waves to enter (i.e., *parasitic grid representation*) (Perkey and Kreitzberg 1976; Baumhefner and Perkey 1982). The use of nested grids to obtain higher spatial resolution in a region is referred to as *downscaling*. Cionco (1994) was among the first to introduce this concept.

11.1.2   Vertical Grid

As for the horizontal grid, the vertical grid of a mesoscale model is selected to have the most resolution in and near the region of interest. Uniform grid spacing at all levels generally is not feasible, because of limitations of computer storage and of cost. The concept of a representative vertical scale length of the circulation can be used to estimate the required resolution, since, as discussed in Chapter 10, as many as 10 or more grid increments may be needed to resolve the atmospheric system adequately (see, e.g., Tables 10-1 and 10-4).

If vertical turbulent mixing is an important component of the circulation, then its characteristic length scale provides a measure of the needed grid resolution. As discussed in Chapter 7, Section 7.3, for example, the turbulent length scale when the surface layer is stable is a function of height above the ground near the surface and a prescribed length scale, or function of local shear and temperature gradients above that level. The definition of l_θ by Eq. (7-64) gives one form of this length scale. In contrast, when the surface layer is neutral or unstable, the representation for the length scale remains a function of distance above the ground even well removed from the surface, as implied by the form of the exchange coefficient indicated by Figure 7.8. For this reason, mesoscale models

in general have the smallest grid increments near the ground, with the grid mesh expanding upward.

Modelers who use such an expanding grid generally attempt to make the transition from fine to coarse resolution as smooth as possible. Levels of the vertical grid are either arbitrarily selected or output from a functional form. Orlanski *et al.* (1974), for example, tested two forms,

$$s = \ln\left(\frac{z + 30.5}{30.5}\right)\bigg/ \ln\left(\frac{S + 30.5}{30.5}\right) \qquad \text{and} \qquad s = \frac{z}{1600} + \frac{1}{17.9}\ln\frac{z + 15}{15},$$

for representing his vertical grid. In the first formulation, S is the top of the model (they used $S = 20$ km). With the left-side expression for s, using 70 levels, the grid resolution was 3 m near the ground and 1700 m near the top, whereas using 80 levels, the right-side form varied more slowly from 3.7 m near the surface to an approximately constant grid of 175 m from 4000 m to the top (which was set at 10.16 km in that representation). Orlanski *et al.* (1974) rejected the left-side form for s because the extremely coarse resolution in the upper levels produced a significant distortion of gravity waves, which propagated upward from the active lower layers. This problem was much less apparent when the second coordinate stretching was used, despite the lower top.

Orlanski *et al.* (1974) used a large number of levels in their two-dimensional model simulation. In a three-dimensional simulation, the use of 70 or 80 vertical levels is computationally expensive. Pielke (1974b) examined the amount of vertical resolution needed in a two-dimensional model to properly resolve a sea-breeze circulation. Such an evaluation appears to be necessary if the investigator is to establish whether the numerical grid separation rather than the physics determines the form of the solution.

In the study reported in Pielke (1974b), a sea-breeze simulation was performed as a control. Two separate experiments were performed, one in which the depth of the model was doubled but the same resolution below 4.22 km was retained, and another in which the vertical grid spacings were halved but the initial model depth was the same as the control experiment. The predicted sea-breeze patterns 8 hours after simulated sunrise, shown in Figure 11-6, illustrate that for this particular situation, the results were not forced by the grid spacing. In those experiments, the sea-breeze convergence zones remained below 3 km with about the same vertical length scale, regardless of the grid resolution. Sensitivity experiments such as this are required to establish the needed vertical resolution.

Two examples of observationally determined vertical and horizontal scales of mesoscale motion are shown in Figures 11-7 and 11-8. In Figure 11-7, the sea and land breezes were observed to have relatively shallow vertical depth (consistent with the results given in Figure 11-6). Forced airflow over rough terrain creates a deep tropospheric perturbation, as illustrated in Figure 11-8.
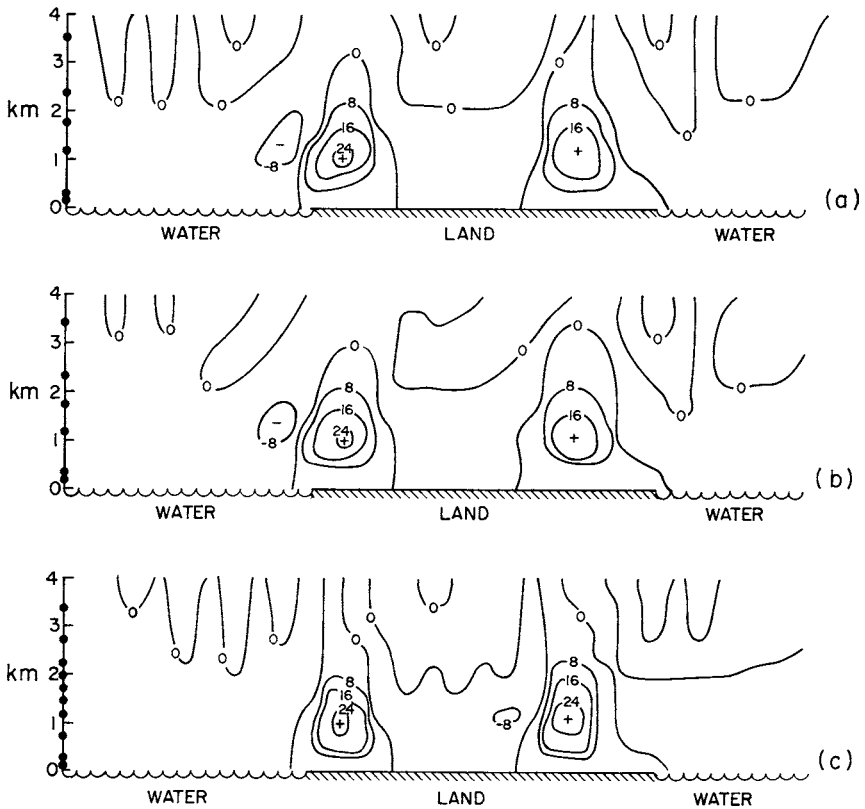
Fig. 11-6. (a) The vertical motion field in a two-dimensional sea-breeze model with 7 vertical levels and an initial top of 4.22 km, (b) with 13 vertical levels and an initial top of 12.02 km, and (c) with 13 vertical levels and an initial top of 4.22 km. Grid point levels 4 km and below are indicated by darkened circles. (From Pielke 1974b.)

11.1.3   Definition of Grid Points

In setting up the model grid, the locations at which the dependent variables are defined must be specified. In the differential representation no such problem arises, of course, since all variables are defined at every point. Although the dependent variables could be defined at the same grid point, in general the variables are *staggered* with respect to one another. Lilly (1961), for example, presented a staggered grid representation that helps preserve such properties as total kinetic energy[6] within a model domain. Batteen and Han (1981) examine the use of different spatial distributions of dependent variables on a rectangular grid in ocean models.
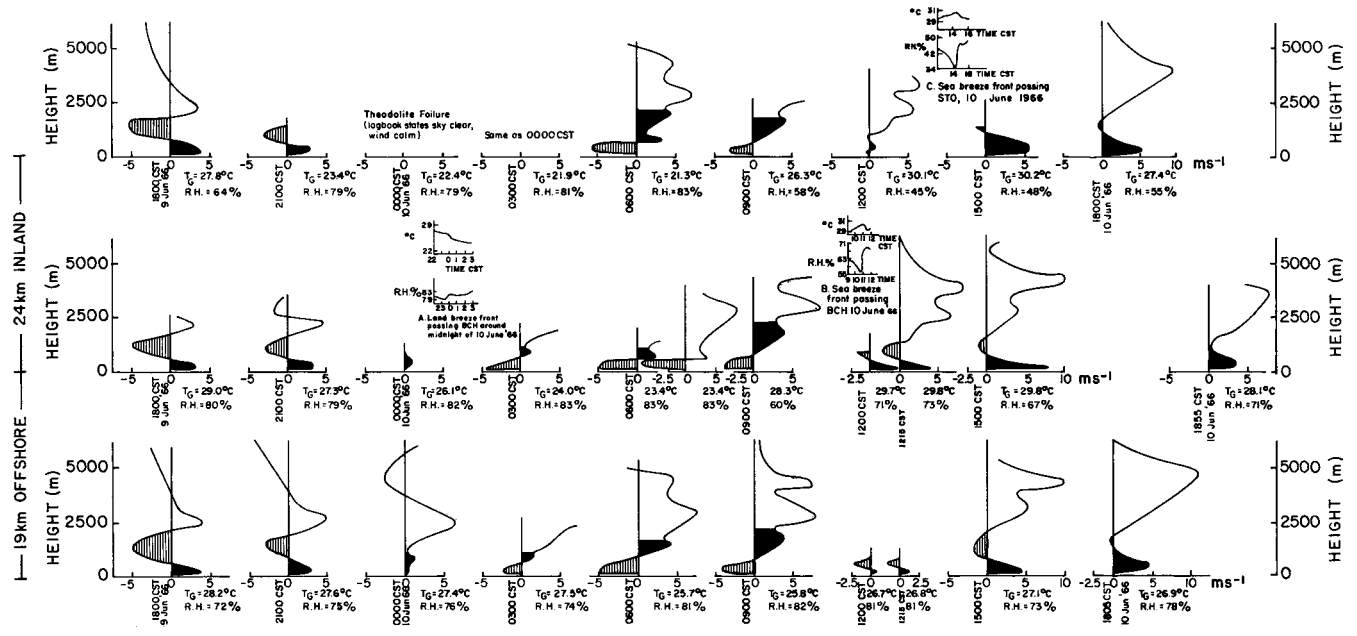
Fig. 11-7. The z–t variations of land and sea breezes normal to the coast from 1800 CST on June 9 to 1855 CST on June 10, 1966, at three stations perpendicular to the Texas coast. The average top of the sea breeze during the day was 570 m, and the average height of the return flow was 1800 m. (From Hsu 1970.)
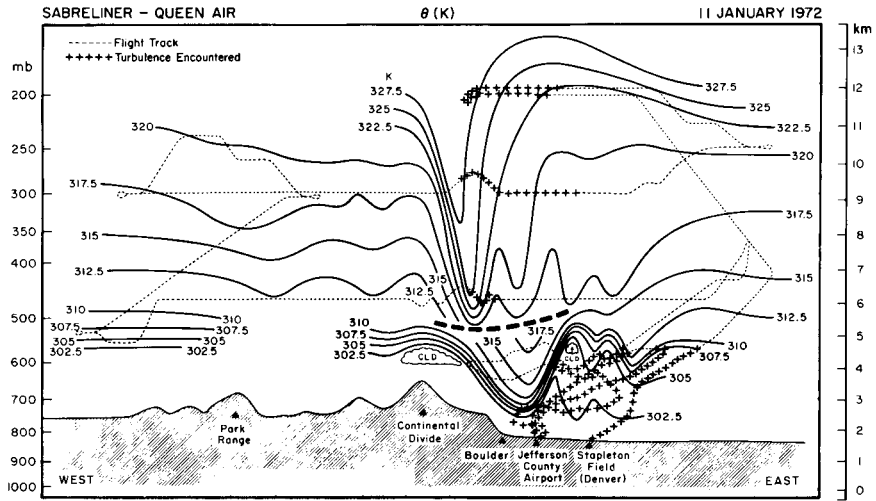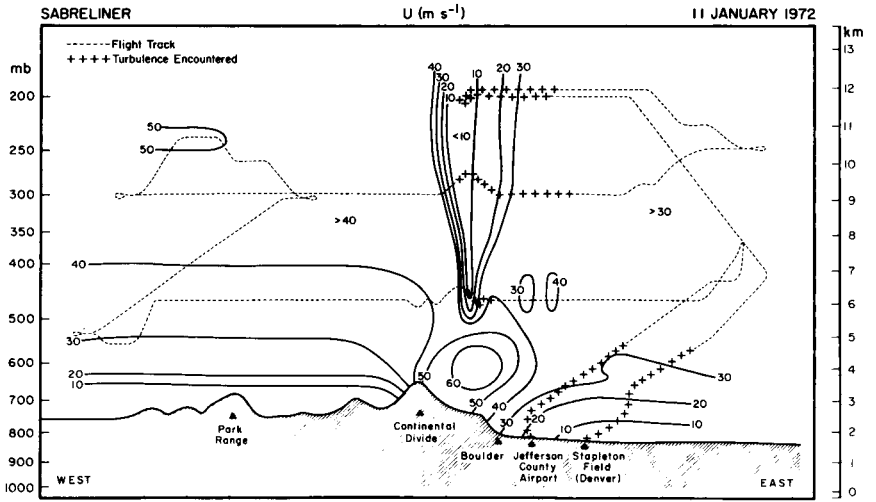
Fig. 11-8. The x–z structure of (a) isentropes and (b) winds observed across a portion of central Colorado during a downslope wind storm. (From Lilly and Zipser 1972.)
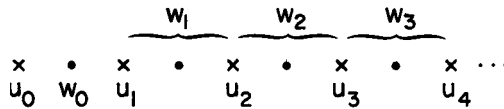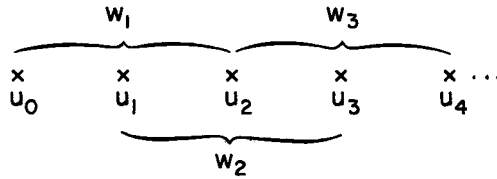
Fig. 11-9. A schematic of (a) a staggered grid and (b) a nonstaggered grid for the computation of $\bar{u}$ and $\bar{w}$. The symbols u_0 and w_0 represent the boundary values. The braces indicate which values are used in the computation of w from the continuity equation, (11-2) for (a) and (11-3) for (b). In (a), the horizontal velocity is defined at the $\times$ points and the vertical velocity at points with blackened circles, whereas in (b) both velocities are defined at the $\times$ points.

The need for a staggered grid is motivated by the differential nature of the conservation relations. In the two-dimensional form of the incompressible continuity equation [e.g., Eq (4-23) with $\partial \bar{v}/\partial y = 0$], for example, it is convenient to stagger the vertical and horizontal velocities $\bar{w}$ and $\bar{u}$. The numerical finite difference approximation for a constant horizontal and vertical grid can then be written as

$$\bar{w}_{i,k} = \bar{w}_{i,k-1} - \frac{\bar{u}_{i+\frac{1}{2},k-\frac{1}{2}} - \bar{u}_{i-\frac{1}{2},k-\frac{1}{2}}}{\Delta x}\Delta z, \qquad (11\text{-}2)$$

where $\bar{u}$ is defined to be located halfway between the grid points at which $\bar{w}$ is defined, instead of a form such as

$$\bar{w}_{i,k} = \bar{w}_{i,k-1} - \frac{\hat{u}_{i+\frac{1}{2},k-\frac{1}{2}} - \hat{u}_{i-\frac{1}{2},k-\frac{1}{2}}}{\Delta x}\Delta z, \qquad (11\text{-}3)$$

where

$$\hat{u}_{i+\frac{1}{2},k-\frac{1}{2}} = \left(\bar{u}_{i+1,k} + \bar{u}_{i,k} + \bar{u}_{i+1,k-1} + \bar{u}_{i,k-1}\right)/4$$

and

$$\hat{u}_{i-\frac{1}{2},k-\frac{1}{2}} = \left(\bar{u}_{i,k} + \bar{u}_{i-1,k} + \bar{u}_{i,k-1} + \bar{u}_{i-1,k-1}\right)/4.$$

It is found that staggering the dependent variables as given by Eq. (11-2) increases the effective resolution by a factor of two, since derivatives are defined over an increment Δx, for instance, rather than $2\Delta x$, yet without requiring

averaging as in Eq. (11-3). The horizontal and vertical pressure gradient term [e.g., in Eq. (4-21)], is also effectively represented by such staggering.

Anthes (1971, personal communication) has also reported that staggering the horizontal and vertical velocities in the mass-continuity equation, such as done in Eq. (11-2), can minimize the direct influence of the lateral boundaries on the computation of vertical velocity. As illustrated in Figure 11-9, for example,
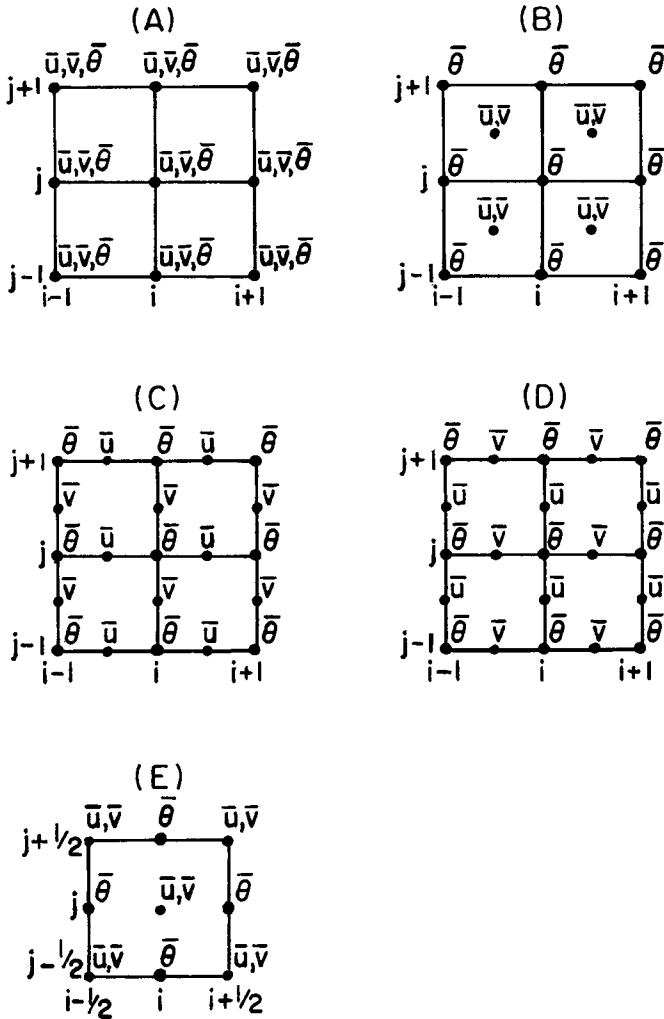
Fig. 11-10. Illustration of the Arakawa and Lamb grid stagger for a two-dimensional grid for the variables $\bar{u}$, $\bar{v}$, and $\bar{\theta}$ for a two-dimensional grid. (Adapted from Arakawa and Lamb 1977.)

using Eq. (11-2), $\bar{w}$ must be computed using only interior values of $\bar{u}$. As suggested by Anthes and replicated by others (e.g., Pielke 1974a), elimination of the lateral boundary values of $\bar{u}$ (and $\bar{v}$) from the computation of vertical velocity in the continuity equation generally provides much better-behaved solutions.

Winninghoff (1968) and Arakawa and Lamb (1977) introduced classes of grid staggering that are referred to extensively today (Figure 11-10). The mesoscale models presented in Appendix B usually refer to the types of grid stagger that are presented in Figure 11-10.

Once the domain size, vertical and horizontal grid increments, and locations at which the variables are defined are established, the temporal and spatial boundary conditions for the conservation relations must be specified. Temporal boundary values are required because the differential conservation equations represent an *initial value* problem, and spatial boundary information is needed because the domain size is finite, yielding a *boundary value* problem. The procedure for determining the values of the dependent variables required to commence the integration of the model equations is called *initialization*, and the values assigned to the perimeter of the model domain are termed *boundary conditions*.[7]

11.2   Initialization

The dependent variables that appear in a model representation require initial values before integration of the equations can begin. For instance, values of $\bar{u}, \bar{v}, \bar{w}, \bar{\pi}, \bar{\theta}, \bar{q}_n$ and $\bar{\chi}_m$ are required at the start up of the simulation.[8]

In terms of initialization of the wind and temperature fields, mesoscale and synoptic models are very different. Recall from Chapter 3, Section 3.3.2, that for the synoptic and larger scales, the Rossby number R_0 is much less than unity. Hence the wind is seldom far from gradient wind balance, indicating that the mass field dominates the response of the wind field. Thus for these scales, it is more important to measure the temperature distribution horizontally and with height than to measure the wind field. The temperature field is used to obtain the mass field through the hydrostatic equation, with the distribution of mass represented by the pressure field (i.e., $\partial \bar{p} / \partial z = -\bar{\rho} g$, so that $\partial \ln \bar{p} / \partial z = -g/R\overline{T}$). A useful approximation to the winds can then be diagnosed from the mass field.

As the horizontal scales of the circulation are reduced, however, the relation between the wind and temperature (i.e., mass) fields becomes more complex. The ratio of the advective to the horizontal pressure gradient terms, given in Table 3-1 in Chapter 3, can be used to estimate whether the velocity or the mass field dominates the structure of the mesoscale circulation.

Using the scale analysis for the advection and horizontal pressure gradient force presented in Table 3-1, their ratio can be defined as

$$I_0 = U^2 \big/ R\, \delta T. \qquad (11\text{-}4)$$

Thus when $I_0 \gg 1$, the velocity field is expected to be dominant, whereas the temperature distribution should be more important for $I_0 \ll 1$. When $I_0 \simeq 1$, both fields are equally significant in determining the form of the mesoscale system.

Over heated land under light synoptic flow, for example, I_0 would be much less than unity, and the temperature distribution will dominate the development and evolution of the sea breeze. The model simulation depicted in Figure 11-3 illustrates such a circulation, where the sea-breeze pattern was determined predominantly by the horizontal temperature gradient, even though advection was important in determining its detailed structure. Further demonstration of the importance of a proper temperature initialization, as opposed to an accurate wind initialization, in a mesoscale sea-breeze model is given by Carpenter and Lowther (1982). Wind speeds are lower for atmospheric systems near the ground than aloft because of ground friction (see, e.g., Chapter 7, Section 7.2), so that the mass field would be expected to exert a substantial control on the wind field at low levels (D. Keyser 1980, personal communication). Conversely, if the winds are strong, I_0 can be much larger than unity, and the wind field will dominate the temperature pattern.

Hoke and Anthes (1976) performed experiments to evaluate the relative need to determine the winds as opposed to the temperatures in a two-dimensional simulation of a jet stream with a north–south extent of approximately 700 km [Figure 11-11(a)]. The first experiment attempted to generate the jet using the observed winds, but ignored the observed temperatures and instead linearly interpolated the temperatures inside the domain from values on the side boundary. This assumed temperature distribution gave a horizontally uniform geostrophic speed with a maximum value of 34 m s^{-1}. Figure 11-11(b) presents the errors produced for the two fields. A second experiment was then performed in which the temperature field was forced to agree with the observations at each stage of the initialization process,[9] but the first guess of the wind field used the geostrophic wind at each grid point. The error field for this experiment is given in Figure 11-11(c).

Comparing Figures 11-11(b) and (c) shows that the wind velocity errors are smaller and thus the jet core is better represented when the wind field is known. That is, the maximum error in the wind field exceeds 10 m s^{-1} in Figure 11-11(c) but is substantially less in Figure 11-11(b).

Calculation of the *root mean square error* (RMSE) is a convenient tool for quantitatively comparing these two results. RMSE is calculated for the velocity
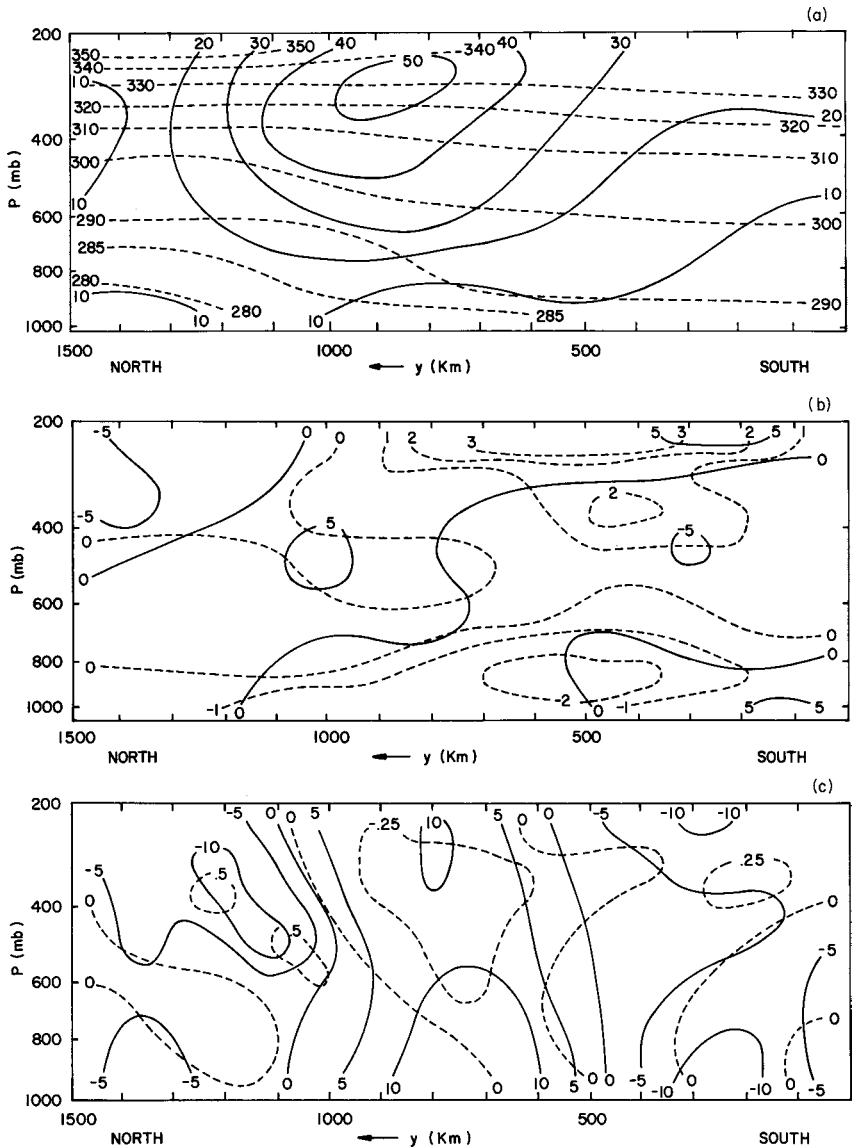
Fig. 11-11. (a) North–south cross-section through Manawski, Ontario of the observed winds (solid lines, m s^{-1}) and geostrophically balanced potential temperature field (dashed line, K) for 0700 EST, October 16, 1973. (b) The same as (a) except for the difference field between actual and computed winds and temperature where assumed fields had perfect initial winds [i.e., as given in (a), but with erroneous initial temperatures]. (c) The same as (b) except with perfect initial temperature [i.e., from (a)] but erroneous initial winds. (From Hoke and Anthes 1976.)

and temperature from

$$\text{RMSE}_u = \sum_{i=1}^{I_x} \sum_{k=1}^{K_z} \left(u_{\text{obs}} - u_{\text{pred}} \right)^2 / I_x K_z$$

$$\text{RMSE}_T = \sum_{i=1}^{I_x} \sum_{k=1}^{K_z} \left(T_{\text{obs}} - T_{\text{pred}} \right)^2 / I_x K_z,$$

(11-5)

where I_x and K_z are the number of grid points in the horizontal and vertical directions, respectively, and the subscripts "obs" and "pred" refer to the observed and predicted values of east–west velocity and temperature. For the experiment in which the observed winds were used [Figure 11-11(b)], $\text{RMSE}_u =$ 2.8 m s^{-1} and $\text{RMSE}_T = 1.1$ K, and when the observed temperatures were used alone [Figure 11-11(c)][10] $\text{RMSE}_u = 6.9$ m s^{-1} and $\text{RMSE}_T = 0.2$ K. Thus in mesoscale circulations where $I_0 \gg 1$, it appears to be much more important to measure winds than temperature when initializing a model simulation. In contrast, the initialization of the other dependent variables in a mesoscale model is similar to that for a synoptic model.

11.2.1 Initialization Procedures

The methodology for initializing a mesoscale model can be grouped into four categories:

- objective analysis
- dynamic initialization
- normal mode initialization
- the adjoint method.

Initialization of the model involves dependent variables in the atmosphere and at the surface interface (Liston *et al.* 1999; Pielke *et al.* 1999a). Model solutions are often very sensitive to initial conditions. Park and Droegemeier (2000), for example, illustrated the sensitivity of the simulation of deep cumulus convection to errors in the water vapor field.

With *objective analysis*, available observational data are extrapolated to grid points by using either simple weighting functions, in which the initial dependent variables are a function of the distance from the observation, or by applying a *variational analysis* routine (O'Brien 1970a; Sasaki 1970a, b, c; Sasaki and Lewis 1970; Sinha *et al.* 1998), in which one or more conservation relations are applied to minimize the variance of the difference between the observations and the analyzed fields. This technique uses concepts of variational calculus, in which the fundamental equations along with specified constraints as to the amount of agreement between the observations and analysis are given (e.g., the

local time derivative must be very small to remove high-frequency motions). An explanation of this approach is beyond the scope of the text, and the reader is referred to Sasaki (1970a) for a detailed discussion of the technique.

The *dynamic initialization* technique offers an alternative to objective analysis. With this approach, the model equations are integrated over a period of time, so that values in the observed fields that are not representative of mesoscale resolution data are minimized.[11] By using the model equations, an approximate dynamic balance among the dependent variables is achieved, since computational features generated by data inconsistency will be removed through damping or outward propagation through the side boundaries of the model as it adjusts toward equilibrium. As shown by Hoke and Anthes (1976), this propagation will appear as gravity, inertial, or inertial-gravitational waves but will have no physical significance. If large inconsistencies in the measurements occur, however, then large computational adjustments will result in completely erroneous solutions.

One form of dynamic initialization suggested by Hoke and Anthes (1976) involves performing an *initialization integration*, in which terms are added to the conservation relations to nudge the solutions toward the observed conditions. For example, the conservation-of-motion equation in the x direction can be rewritten to include this term as

$$\frac{\partial \bar{u}}{\partial t} = -\bar{u}_j \frac{\partial \bar{u}}{\partial x_j} - \frac{1}{\rho_0} \frac{\partial}{\partial x_j} \rho_0 \overline{u_j'' u''} - \theta_0 \frac{\partial \bar{\pi}}{\partial x} + fv + \hat{f}\bar{w} + G_u \left(u_{\text{obs}} - \bar{u} \right),$$

where G_u is called the *nudging coefficient*. The other prognostic equations can be written in a similar fashion. By integrating the model equations for a period of time (say 12 hours), where the geostrophic wind may be the first guess, the imbalances in the solutions are reduced and large unrealistic accelerations will not occur when the simulation experiment actually commences.

Nudging coefficients added to each prognostic equation can be assumed to be a function of observation accuracy, of the distance between an observation and the grid point, of the variable nudged, and of the typical magnitudes of the other terms in the prognostic equations. By using dynamic initialization, the conservation relations themselves are used to distribute initial values of the dependent variables throughout the model in a physically consistent fashion. The major disadvantage of this approach is the cost in computer resources of an extended initialization integration, which could be 12 hours or so in a mesoscale model simulation, whereas the model experiment may be only 24 hours long. Examples of dynamic initialization include those of Temperton (1973), Anthes (1974a), Hoke and Anthes (1977), Kurihara and Tuleya (1978), Kurihara and Bender (1979), and Kuo and Guo (1989). Douville *et al.* (1999) discuss the use of nudging and an optimal interpolation scheme to insert soil moisture into models. Liston *et al.* (1999) describes a procedure to more effectively insert snow cover into regional and mesoscale models.

Nonlinear normal mode initialization provides a useful and efficient alternative to dynamic initialization. As summarized by Daley (1981), this approach eliminates the integration time period needed by the dynamic initialization method to remove inconsistencies in the input data. This approach, which is discussed in Daley's review paper, has been adopted by the Canadian government weather service and by the European Centre for Medium Range Forecasts for use in their synoptic models.

The nonlinear normal mode initialization scheme involves segregating high-frequency and low-frequency components of the initial input data using horizontal and vertical structure functions[12] for the initial atmosphere. By removing the high frequencies, which are assumed to have no meteorological significance, only relevant low-frequency information is assumed to remain. This scheme offers promise as an effective initialization scheme provided that sufficient observation data are available. Kasahara (1982) has presented a methodology in which the normal mode initialization procedure can be used in limited area numerical weather prediction models. Figure 11-12, reproduced from Daley (1981), illustrates the reduced period of initialization required using the normal mode method as contrasted with the dynamic initialization scheme.

Intensive interest in the normal mode initialization technique continues. Brutsaert (1982), for example, presented a scheme that uses concepts in normal model initialization (but without explicitly calculating the modes) as part of a type of dynamic initialization procedure. Wergen (1981) discusses nonlinear normal model initialization in the presence of a 2000-m mountain with a hori-
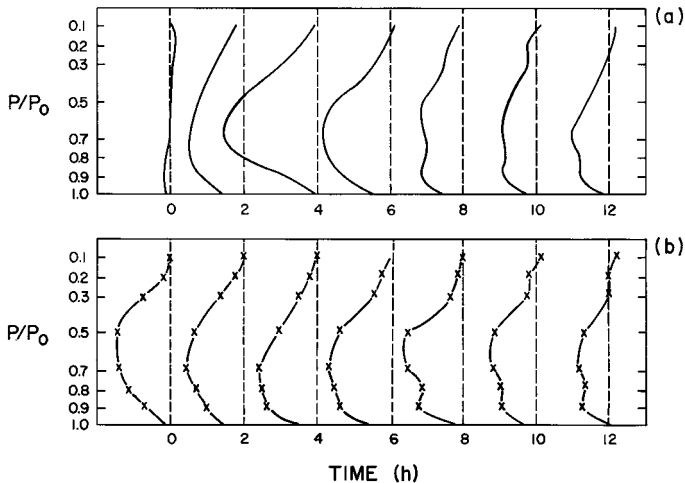
Fig. 11-12.   The variation of vertical motion with time near Labrador, Canada for a synoptic model prediction (a) without and (b) with nonlinear normal mode initialization. (From Daley 1979.)

zontal grid interval of 63.5 km and a slope of up to 1 to 63. Lipton and Pielke (1986) evaluated the vertical normal modes for the type of terrain-following coordinate system discussed in Section 6.3.

The *adjoint method* is overviewed in the following discussion, provided by Vukićević and Hess (2000) and Vukićević *et al.* (2001). The time rate of change (i.e., the evolution) of mesoscale flow can be represented by the following general governing equation:

$$\frac{\partial \vec{X}}{\partial t} = M\vec{X} + \vec{F}(t), \tag{11-6}$$

where $\vec{X}$ is a vector of the physical quantities studied (e.g., surface temperature, wind, and CO_2 flux as a function of time and space in general), t is time, M is a physical/dynamic model, and $\vec{F}(t)$ is time-dependent forcing (e.g., precipitation and radiation for the land-surface processes). The solution of Eq. (11-6) depends on the initial condition vector ($\vec{X}_0$), the boundary condition vector ($\vec{X}_b$), and a set of free physical parameters denoted by $\vec{\alpha}$.

We are interested in the system's response measured by the change of a diagnostic function, defined in general form as

$$J(x) = \int_0^T \int_\Omega g(\vec{X}) d\omega dt, \tag{11-7}$$

where $[0, T]$ is time interval, Ω is the spatial domain, and $g(\vec{X})$ is a diagnostic operator [e.g., $g(\vec{X}) = \vec{X}$ or $g(\vec{X})$ = flux of moisture]. It is obvious that the change of J can occur when either the control parameters or the forcing are varied. The dependence of the change of J on the control parameters is expressed as

$$\Delta J = \frac{\partial J}{\partial \vec{Y}} \delta \vec{Y} + O(\delta \vec{Y}^2), \tag{11-8}$$

where, for brevity, $\vec{Y}$ is defined as a vector of variations of the control parameters, $\delta \vec{Y} = (\delta \vec{X}_0, \delta \vec{X}_b, \delta \alpha)$.

Assuming that second- and higher-order terms are small,

$$O(\delta \vec{Y}^2) \ll O(\delta \vec{Y}), \tag{11-9}$$

and using the theory of variations, Eq. (11-8) becomes

$$\Delta J = \int_0^T \int_\Omega \Lambda(t, \omega) M_{\vec{\alpha}} \delta \vec{\alpha} d\omega dt - \int_\Omega [\Lambda(t, \omega) \delta \vec{X}]_0^T$$
$$- \int_0^T [\Lambda(t, \omega) \delta \vec{X}]_{O(\Omega)}, \tag{11-10}$$

where Λ is the solution of an adjoint system associated with the system [Eq. (11-6)] and $M_{\tilde{\alpha}}$ is a portion of the model in Eq. (11-6) that depends on the parameters only.

Also, from Green's function theory of solutions for partial differential equations (e.g., Roach 1970), the solution of the system [Eq. (11-6)] for the given (i.e., fixed) set of control parameters can be expressed as a function of the adjoint solution and the forcing $\vec{F}$,

$$x(t) = \int_0^t \int_\Omega \Lambda(t, \tau) \vec{F}(\tau) \, d\tau d\omega. \tag{11-11}$$

Substitution of Eq. (11-11) in Eq. (11-7) gives the relationship between J and the adjoint solution and forcing.

Because the adjoint solution multiplies variations of the control parameters and the forcing function in Eqs. (11-10) and (11-11), respectively, these expressions show that to know the sensitivity of the diagnostic function J to the variation of control parameters or the forcing, one can compute the solution of the adjoint system (Λ). The adjoint system is readily derived from the homogeneous part of the original system [Eq. (11-6)] (e.g., Roach 1970). The adjoint solution is a function of time and space and represents a map in phase space of the influences of the controlling factors on the system studied. From this map, we can learn, for example, about the physical mechanisms of interactions between different components of the mesoscale system.

The adjoint sensitivity analysis is exact for the linear systems [i.e., when M in Eq. (11-6) is linear, implying that $O(\delta \vec{Y}^2) = 0$.] For the nonlinear systems (i.e., M is nonlinear), this analysis is exact under the assumption that variations of the controlling factors are small. In the nonlinear case, therefore, the adjoint analysis produces a first-order sensitivity. Consequently, the adjoint analysis of a mesoscale system examines the first-order interactions between the components of the system. Understanding the first-order interactions is beneficial, as shown in the studies where the adjoint analysis has been used to examine nonlinear systems (e.g., Zou *et al.* 1993; Vukićević 1998).

The system's sensitivity to control parameters can also be studied by perturbation sensitivity experiments whereby the value of a parameter within one of the model's parameterizations is changed by a small amount and the new model solution is computed. However this method is inefficient for systems where the number of parameters is large. Moreover, this method can be very inefficient in computing the influence functions associated with the forcing (i.e., Green's functions). In contrast, only one adjoint model solution is required to evaluate the sensitivity of the given J to all controlling factors.

Detailed examples of the use of the adjoint method can be found in Rabier *et al.* (1992), Robertson (1992), Marchuk (1995), Vukićević and Raeder (1995),

Kaminski *et al.* (1997), Vukićević (1998), and Vukićević and Hess (2000). The adjoint method is also applied by Uliasz *et al.* (1996).

11.2.2 Initialization With Sparse Data

   The objective analysis, dynamic, adjoint, and nonlinear normal model initialization routines are effective when observational data are available (see, e.g., Seaman *et al.* 1995; Jones *et al.* 1998a, b; Michelson and Seaman 1999). On the smaller spatial scales, however, extensive measurements, particularly of vertical structure, are the exception, and usually only one or two radiosonde sites with soundings made twice a day are present in a domain region. Barnes and Lilly (1975), for example, suggest that sufficient variance exists on the mesoscale such that upper air stations must be spaced about 100 km apart to detect important severe thunderstorm-triggering mechanisms. Moreover, the initialization problem is complicated even further if terrain is present, since one ascent is even less likely to be representative of the initial conditions over the entire domain area. Satellite sounding data at high spatial and temporal resolution continues to offer promise for improving mesoscale model initialization data, but the satellite resolution still suffers from either high spatial but low temporal resolution coverage (i.e., lower earth-orbiting satellites, such as polar orbiters) or high temporal but low spatial coverage (i.e., geostationary satellites) of the needed dependent variables (e.g., $\bar{u}_i$, $\bar{\theta}$, $\bar{q}_n$).
   When observations are this sparse over level ground, the advantages of a dynamic or normal mode initialization scheme are likely to be negligible when compared with an objective analysis routine, since small-scale data inconsistencies will not be introduced by widely spaced measurements. For this situation, an objective initialization, such as that suggested by Segal and Pielke (1981), is useful. With this approach, when two radiosonde sites are available, values of the dependent variables at each grid point can be determined from[13]

$$\phi_p = \left(\phi_1 \frac{1}{r_{1p}^2} + \phi_2 \frac{1}{r_{2p}^2} \right) \left(\frac{1}{r_{1p}^2} + \frac{1}{r_{2p}^2} \right)^{-1}, \qquad (11\text{-}12)$$

where ϕ_1 and ϕ_2 are the observed values from the two radiosonde ascends at a distance of r_{1p} and r_{2p} from the grid point being determined. After this objective analysis is applied, the model can be integrated for a short time. Segal and Pielke (1981) used 3 hours to generate a consistent set of the dependent variables (i.e., a simplified form of dynamic initialization). Since only long-wavelength phenomena will be introduced into the model using Eq. (11-12), this short period of dynamic initialization does not excite large-amplitude, high-frequency gravity or inertial gravity waves such as those reported by Hoke and Anthes (1976), where much higher spatial resolution initial data were provided.

One drawback of using Eq. (11-12), however, is that there is no coupling in the vertical, which is the reason for the 3-hour initialization period.

Figure 11-13 illustrates the use of Eq. (11-12) to obtain the wind fields over the Chesapeake Bay region at 0700 LST on July 21, 1978 using the Dulles and Wallops Island standard radiosonde soundings. If only the Dulles sounding were
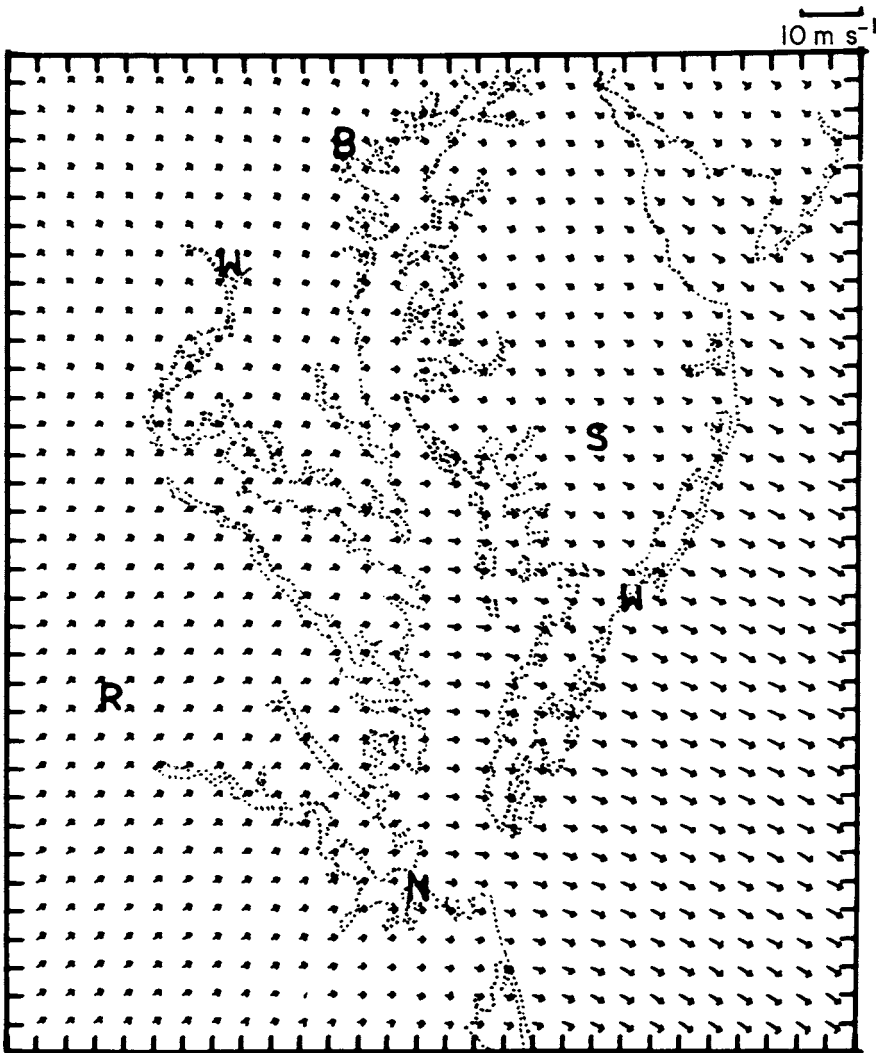
Fig. 11-13. An initial wind field at 5 m obtained using Eq. (11-12) with the morning Dulles and Wallops radiosonde soundings. (From Segal and Pielke 1981.)

used, then southwesterly winds would be analyzed over the entire region at the
initial time, whereas with the Wallops Island sounding included, northwesterly
winds result over the eastern portion of the domain. The integration of the model
for this day, reported in Segal and Pielke (1981) produced a superior forecast
when both soundings were included.

In applying this type of objective analysis scheme to radiosonde data, how-
ever, it is not always certain that the measured values are representative of
the atmosphere near the ground throughout the domain. For example, if the
radiosonde ascents are made during the early morning from an island, then radi-
ational cooling over land will result in a sounding near the ground, which is not
representative of the ocean areas. For this type of situation, an alternative pro-
cedure for estimating the low-level winds is available using a one-dimensional
boundary layer model. Such an approach is a form of one-dimensional dynamic
initialization. This method is used at the radiosonde observing sites, and the
results are extrapolated to the remaining grid points by Eq. (11-12), as per-
formed by Segal and Pielke (1981).

The equations for computing the wind profile in the planetary boundary layer
can be calculated from

$$
\begin{aligned}
\frac{\partial u_R}{\partial t} &= \frac{\partial}{\partial z}\overline{u''w''^*} + f\left(v_R - v_{gR}\right) \\
\frac{\partial v_R}{\partial t} &= \frac{\partial}{\partial z}\overline{v''w''^*} + f\left(u_R - u_{gR}\right).
\end{aligned}
\tag{11-13}
$$

where u_R, v_R and u_{gR}, v_{gR} are the components of velocity and of geostrophic
wind, respectively, at the radiosonde site. The overbar with an asterisk over the
subgrid-scale term indicates that the term is defined for a grid-sized volume
centered at the radiosonde site. The subgrid-scale flux terms, for example, can
be evaluated using one of the methods given in Section 7.3. These equations
are integrated until the changes in u_R and v_R (i.e., $\partial u_R/\partial t$ and $\partial v_R/\partial t$) become
arbitrarily small (about six inertial periods are sufficient, as reported by Mahrer
and Pielke 1976, where one inertial period equals $2\pi/f$). Figure 11-14 illus-
trates the convergence of Eq. (11-13) to an equilibrium solution for a latitude
of $\phi = 38°N$ and a first-guess profile of $\bar{u} = u_g = 5\ \mathrm{m\,s}^{-1}$ and $\bar{v} = v_g = 0$.
The subgrid-scale fluxes are estimated for a neutrally stratified surface layer
using Eq. (7-7), a profile form of the vertical exchange coefficient above the
surface layer suggested by O'Brien (1970b), and $z_i = 0.33u_*/f$. The surface
layer fluxes are evaluated using the Businger (1973) parameterization.

Over rough terrain, determination of the initial fields of the dependent vari-
ables is not so straightforward, because one or two vertical soundings is sel-
dom, if ever, representative of conditions over a mesoscale-sized area. Three
procedures have been developed to accomplish the initialization over irregu-
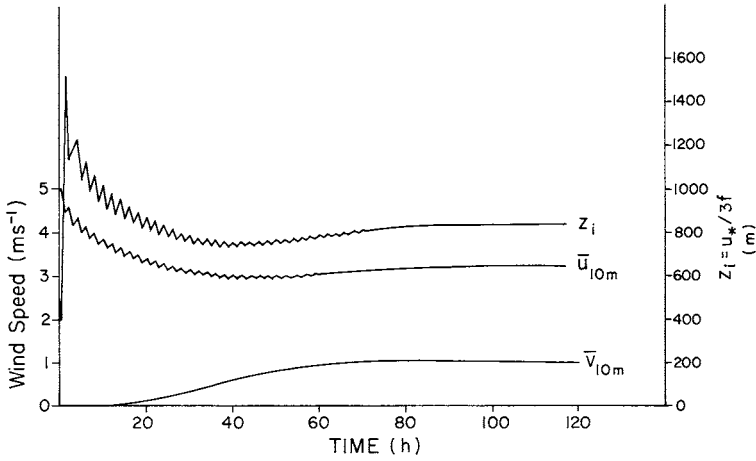
Fig. 11-14. The convergence of Eq. (11-13) to a steady solution with $u_g = 5\ \mathrm{m\,s^{-1}}$ and $v_g = 0$ for a latitude of 38°N. A neutrally stratified planetary boundary layer is assumed (i.e., $\partial\theta_0/\partial z = 0$), so z_i is computed from $z_i = u_*/3f$. (Calculations performed by R. Kessler, 1982.)

lar terrain. With the first procedure, the terrain is assumed to be initially flat, and either an objective analysis routine, dynamic initialization, nonlinear normal mode, or adjoint initialization can be used to generate analyzed fields of the dependent variables. Using a terrain-following coordinate system such as that discussed in Chapter 6, topography is then permitted to grow to its assigned height in a specified period. The model equations are integrated forward in time as the terrain grows, with the requirement that no time-dependent forcing terms other than the growing terrain are permitted to occur. This procedure, called *diastrophism*,[14] and is a form of dynamic initialization. Mahrer and Pielke (1975, 1977b), Deaven (1976), and Klemp and Lilly (1978) used this technique in their simulation of airflow over an isolated mountain ridge. The mountain was permitted to grow to its maximum height over a period of a few hours.

Unfortunately, using this approach, it is not possible to assign a particular lapse rate of temperature along a mountain slope such as might be available from surface observations. Moreover, the diastrophism tends to create a potential temperature distribution that parallels the ground surface at low levels, such as illustrated in Figure 11-15(a). To circumvent this problem, Mahrer and Pielke (1977b) reported an initialization methodology for inputting irregular terrain at its full height without resorting to diastrophism. With this procedure, the horizontal distribution of potential temperature at the initial time is assumed to be flat [as illustrated schematically in Figure 11-15(b)]. The grid-volume–averaged form of the hydrostatic equation (6-62) is used to evaluate the vertical

(a)

(b)
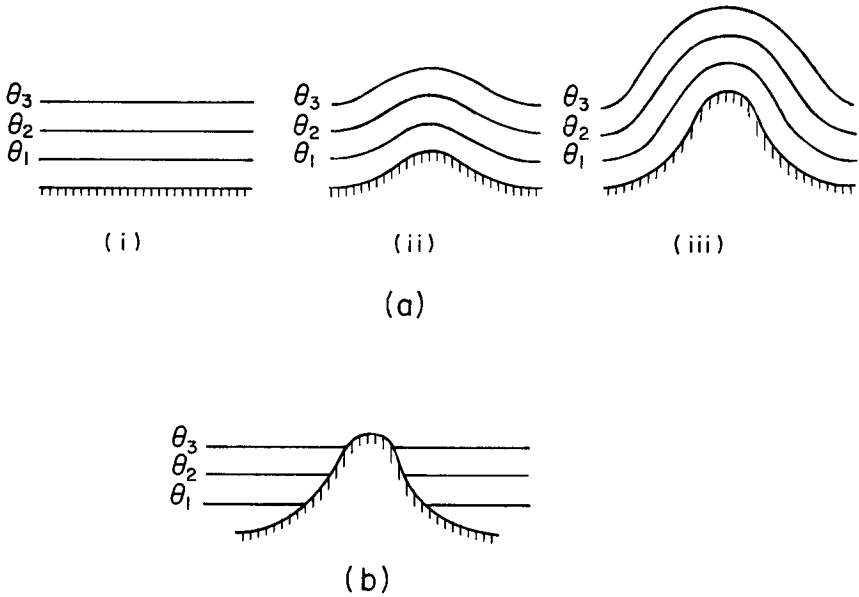
Fig. 11-15. (a) A schematic of the evolution of isentropes over growing terrain in a mesoscale model where the bottom surface is a θ level. Note that the perturbation of the θ contours from their initial horizontal orientation will cause a horizontal pressure gradient and resultant circulation owing to this forced uplift. In (b), the mountain is present initially, and hence the θ surfaces remain horizontal as long as the horizontal and vertical pressure gradient relations given by Eqs. (11-14) and (11-15) are consistent.

pressure distribution from

$$\bar{\pi}_{i,j} = \bar{\pi}_{i,j+1} + \frac{s - z_{G_i}}{s}\left[\frac{g}{\bar{\theta}_{i,j+\frac{3}{4}}}(z^*_{j+1} - z^*_{j+\frac{1}{2}}) + \frac{g}{\bar{\theta}_{i,j+\frac{1}{4}}}(z^*_{j+\frac{1}{2}} - z^*_j)\right], \quad (11\text{-}14)$$

where to reduce notation y variations have been ignored, $\tilde{x}^3$ has been written as z^*, and the subscripts i and j denote grid location. To remain consistent with this approximated form of the hydrostatic equation, the pressure gradient term in Eq. (6-57) is written as

$$-\bar{\theta}\frac{\partial\bar{\pi}}{\partial\tilde{x}^1} + \frac{g}{s}(z^* - s)\frac{\partial z_G}{\partial x} \simeq -\langle\bar{\theta}\rangle_i\frac{\bar{\pi}_{i+1,j} - \bar{\pi}_{i-1,j}}{2\Delta x}$$
$$+ \frac{\langle\bar{\theta}\rangle_i(z^*_j - s)(z_{G_{i+1}} - z_{G_{i-1}})g}{[s(\langle\bar{\theta}\rangle_{i+1} + \langle\bar{\theta}\rangle_{i-1})/2]2\Delta x}, \quad (11\text{-}15)$$

where

$$\langle\theta\rangle_i = [\bar{\theta}_{i,j+\frac{1}{2}}(z_j + z_{j-\frac{1}{2}}) + \bar{\theta}_{i,j-\frac{1}{2}}(z_{j+\frac{1}{2}} + z_j)]/(z_{j+\frac{1}{2}} + z_{j-\frac{1}{2}}).$$

This particular form is used to account for uneven vertical grid staggering when $\bar{\theta}$ is defined at intermediate vertical grid levels to $\bar{\bar{\pi}}$. For a case of zero large-scale flow, Mahrer and Pielke (1977b) found erroneous accelerations resulting from the imbalance between the approximate forms of $-\bar{\theta}\partial\bar{\bar{\pi}}/\partial\tilde{x}^1$ and $(g/s)(z^* - s)\ \partial z_G/\partial x$ to be only 5 cm s^{-1} h^{-1} for a 1-km bell-shaped mountain with a half-width of 15 km.

As discussed by Janjić (1977), Mahrer and Pielke (1977b), Sundqvist (1979), Mihailović (1981), Tomine and Abe (1982), Johnson and Uccellini (1983), and others, it is essential to make the approximate form of the hydrostatic equation consistent with the representation of the horizontal pressure gradient terms; otherwise, large fictitious accelerations will result. The sensitivity of a model to the horizontal pressure gradient force in irregular terrain results from the need to accurately compute the difference between two large terms [e.g., $\bar{\theta}\partial\bar{\bar{\pi}}/\partial\tilde{x}^1$ and $(g/s)(z^* - s)\ \partial z_G/\partial x$]. Unfortunately, the establishment of a velocity field over this terrain at the initial time still generates large imbalances in the system of conservation equations. This imbalance occurs because the wind field is significantly out of balance with the temperature field at the start of the integration. As the velocity increases [so that I_0 from Eq. (11-4) becomes larger], the need to properly initialize the wind field becomes more critical.

A third alternative for initializing a mountain in a mesoscale model is to include the topographic relief initially, but input the horizontal velocity linearly with time, starting with $\bar{u} = \bar{v} = 0$, everywhere. With this approach, the imbalance between the velocity and temperature fields during the initialization should be minimized. Also, the use of an exact solution (see, e.g., Section 5.3) for a particular terrain configuration may be a useful form of initialization.

In using initialization procedures, the question arises as to whether the dependent variables are in equilibrium. Usually, modelers are satisfied if a quasi-equilibrium exists in which dependent variables are changing only slowly with time.[15] The length of time required to attain this quasi-equilibrium is dependent on such features as the complexity of the first-guess fields, the terrain characteristics, and latitude. In the real world, such quasi-equilibrium may occur only infrequently, because the larger-scale environment is seldom static for long periods, particularly when strong synoptic winds occur. Thus in the application of mesoscale models to practical situations, it may be more appropriate to analyze the fields of dependent variables objectively using the data generally available and integrate forward in time, including all time-dependent forcing terms, without requiring that a quasi-equilibrium occur first. For example, strong wind flow that develops over mountainous terrain after a synoptic cold front passage often develops abruptly and probably would not be well represented by a quasi-equilibrium initial condition in a model.

A complete equilibrium where the local changes of the dependent variables are identically 0 is even less likely on the mesoscale. If, for instance, the

winds above the planetary boundary layer are perturbed from gradient balance, then inertial oscillations in the wind speed are established. Before the balanced conditions can be reestablished [which required six inertial periods near the ground when substantial vertical mixing was present, as discussed following Eq. (11-7); more time is required if the subgrid-scale mixing is less], the air would exit the mesoscale model domain.[16]

Using synthetic data to initialize a model has also been proposed. With this approach, an atmospheric circulation that closely corresponds to the available observational data is inserted into the model. This circulation can be made so that it is dynamically consistent in the three spatial dimensions and in time. For example, Davidson and Weber (2000) used this approach to insert a tropical cyclone into the Australian Bureau of Meteorology's Tropical Cyclone Limited Area Prediction System.

From the discussion in this section, the most effective initialization procedure in mesoscale models appears to be the following:

1.   Where initial data are sparse, objectively analyze the available observational data to generate values of the dependent variables at grid points. Synthetic data can be applied to provide a dynamically consistent initial meteorological field.

2.   If extensive observational data are available, then a nonlinear normal mode initialization or adjoint procedure should be used. Greater weight should be placed on the horizontal wind field than on the temperature field if $I_0 \gg 1$, whereas the converse should be applied if $I_0 \ll 1$. If $I_0 \simeq 1$, then both fields should have equal weight. The nonlinear normal mode procedure could be used to eliminate small-scale data inconsistencies and should be performed with terrain features present (Lipton and Pielke 1986).

3.   A quasi-equilibrium initialization is desirable only if the large-scale conditions have been persistent for about the same time as is required to achieve such an equilibrium in the model simulation.

4.   As satellite observations of the temperature field (and, therefore, the pressure field) achieve better resolution, it may become possible to obtain high-resolution initial velocity fields on the mesoscale if the time evolution of the pressure field is known. Unfortunately, as inferred from Table 11-1 and discussed further in Section 11.3.1, as the resolution of the pressure field increases, the required measurement accuracy must also improve significantly. On a relatively large scale (i.e., $\Delta x = 67$ km), Mills and Hayden (1983) have used high-resolution satellite imagery to initialize a numerical prediction model. Rogers and Gentry (1983) have used rapid-scan geostationary satellite imagery to obtain high spatial resolution ($\Delta x = \Delta y \simeq 44$ km) wind fields. However, mesoscale model initializations require horizontal grid increment data of 10 km or smaller.

11.3   Spatial Boundary Conditions

Since the mesoscale model domain is artificially enclosed with sides, it is necessary to specify the values of the dependent variables at this perimeter surface of the model. Such values, called *boundary conditions*, are required to integrate in time the approximate forms of the conservation relations.

In discussing boundary conditions in mesoscale models, it is convenient to discuss the top, lateral, and bottom sides separately. Because of the finite domain of these models, the top and lateral perimeters are incorporated only because of computational necessity and have no physical meaning. The bottom, however, is a real boundary, and the transfer of such physical properties as heat and moisture across this interface plays a fundamental role in most mesoscale meteorological circulations.

The number of boundary conditions that can be applied in a model depends on the form of the differential equations used. Model equations that have the correct number are said to be *well posed*; those that use more than are required are said to be *overspecified*. As maintained by Oliger and Sundström (1976), discussing in detail the mathematical properties of boundary conditions of initial-spatial boundary value problems, conservation relations that are represented by nondissipative approximate solutions (e.g., leapfrog) and are overspecified generate physically erroneous shortwave features that travel across the model grid at the fastest wave speed permitted in the model. Such waves are generated at the boundary. Oliger and Sundström have argued that models that are hydrostatic are ill-posed for any choice of local[17] boundary conditions (except for the unlikely case where the exact solution is known on the boundary without error), and thus erroneous wave motions are expected to be created at the boundaries in such a model. Chen (1973) also reports that overspecification of boundary conditions can excite computational modes, but that smoothing at points next to the boundaries suppresses these erroneous perturbations. Oliger and Sundström (1976) contend that the anelastic nonhydrostatic form of the conservation relations can be written in a well-posed form.

In their three-dimensional nonhydrostatic cloud model, which uses the compressible form of the conservation equations, Klemp and Wilhelmson (1978a, b) suggested, based on the work of Oliger and Sundström (1976), that all prognostic variables but one should be specified on the inflow boundary of the model, whereas only one such boundary conditions should be applied at the outflow boundary. Such boundary conditions, they maintain, are required to retain a well-posed set of differential equations.

As a practical problem, erroneous solutions generated at the boundaries are only serious when they propagate from the boundary into the region of significant mesoscale perturbation of the flow from the larger-scale environment. Since these are shortwave features, they can be effectively removed by a selective

low-pass filter such as Eq. (10-67). Larger-scale trends in the model variables caused by the boundaries can also introduce very serious errors, as discussed in Section 11.3.1.

A serious problem also arises when modelers differentiate the conservation relations so as to permit additional boundary conditions (Neumann and Mahrer 1971). For example, the incompressible conservation-of-mass relation [Eq. (4-23)] can be written as

$$\frac{\partial \bar{w}}{\partial z} = -\left(\frac{\partial \bar{u}}{\partial x} + \frac{\partial \bar{v}}{\partial y}\right).$$
(11-16)

Integrating Eq. (11-16) with respect to z permits one boundary condition from this relation. To add an additional boundary condition, some investigators (e.g., Estoque 1961; Vukovich *et al.* 1976) have differentiated Eq. (11-16) with respect to z, yielding

$$\frac{\partial^2 \bar{w}}{\partial z^2} = -\frac{\partial}{\partial z}\left(\frac{\partial \bar{u}}{\partial x} + \frac{\partial \bar{v}}{\partial y}\right).$$
(11-17)

With this form, two boundary conditions are required. Such an equation has been used to specify a rigid boundary at the bottom and top of a model. As shown by Neumann and Mahrer (1971), however, integrating Eq. (11-17) with respect to z yields

$$\int \frac{\partial^2 \bar{w}}{\partial z^2}\, dz = \frac{\partial \bar{w}}{\partial z} + F(x, y, t),$$
(11-18)

where $F(x, y, t)$ is the constant of integration. Unless the limits of the integral on the left side are properly specified, so that $F(x, y.t)$ is identically 0, mass is *not* conserved. Thus Eq. (11-17) generally is not a proper form of the conservation-of-mass relation and should not be used. A similar criticism, of course, can be applied to any differential operation on the original conservation relations if the proper integration constants are not applied.

11.3.1   Lateral Boundary Conditions

As already mentioned, the lateral boundaries of a mesoscale model are required only because the simulated domain must be limited in horizontal extent because of constraints in computer resources. However, because it is impossible to specify values on this boundary properly, at least in a hydrostatic model (and even in compressible models, physically accurate values generally are difficult to find), it is desirable to remove this boundary as far from the region of interest as possible. Expanding the grid horizontally is one available mechanism to minimize the effect of the lateral boundary, as discussed in Section 11.1.1.2.

Anthes and Warner (1978) have demonstrated the serious errors in mesoscale model results that can occur if the lateral boundary conditions are incorrectly specified. Following the procedure introduced by Anthes and Warner, the sensitivity of a mesoscale model to erroneous values on the boundaries can be illustrated using the east–west component of Eq. (4-21), written as

$$\frac{\partial \bar{u}}{\partial t} = -\frac{\partial}{\partial x}\left(\frac{\bar{u}^2}{2}\right) - \alpha_0 \frac{\partial p'}{\partial x} + R, \qquad (11\text{-}19)$$

where R represents the remaining terms. Integrating Eq. (11-19) using the domain-volume average given by Eq. (4-12), where D_x and D_y correspond exactly to the domain size of the model, and assuming symmetry in the y direction to simplify the analysis, yields

$$\frac{\partial u_0}{\partial t} = \frac{\bar{u}_W^2 - \bar{u}_E^2}{2D_x} - \alpha_0 \frac{p'_E - p'_W}{D_x} + \int_x^{x+D_x} \int_y^{y+D_y} R dx dy / D_x D_y. \qquad (11\text{-}20)$$

The quantity $\partial u_0/\partial t$ represents the average acceleration of the entire model domain at level z, and the subscripts "E" and "W" refer to the model's east and west boundaries.

From Eq. (11-20), it is evident that an error in the specification of the values of $\bar{u}$ and p' at either boundary will introduce a fictitious acceleration of the entire model domain at that level. The error is inversely proportional to the size of the domain D_x. Table 11-1 illustrates values of velocity and pressure difference across a model domain that will generate a domain acceleration of 1 m s^{-1} h^{-1} for three values of D_x. In Table 11-1, the eastern velocity component $\bar{u}_E$ is written in terms of the western component $\bar{u}_W$ as $\bar{u}_E = \bar{u}_W + \Delta u$, so that

$$\left(\bar{u}_E^2 - \bar{u}_W^2\right)/2 = (\Delta u \bar{u}_W) + \left[(\Delta u)^2/\right]. \qquad (11\text{-}21)$$

TABLE 11-1

The Values Needed in Eq. (11-20) to Generate a Domain-Averaged Acceleration at Level z of 1 m s^{-1} h^{-1}. The Velocity Difference Δu Can be Determined from Eq. (11-21) Using the Quadratic Equation (i.e., $\Delta \bar{u} = -\bar{u}_W \pm \sqrt{\bar{u}_W^2 + 2F}$, where $F = \bar{u}_E^2 - \bar{u}_W^2/2$). The Value $\alpha_0 = 1$ m^3 kg^{-1} was Used in Computing the Pressure Gradient Force

D_x (km)	$(\bar{u}_E^2 - \bar{u}_W^2)/2$ (m^2 s^{-2})	$\alpha_0(p'_E - p'_W)$ (m^2 s^{-2})	Δu in m s^{-1} for $\bar{u}_W$ in m s^{-1} of			$p'_E - p'_w$ (mb)
			0	10	20	
1000	278.0	278.0	23.6	15.6	10.9	2.78
100	28.0	28.0	7.5	2.5	1.4	0.28
10	2.8	2.8	2.4	0.3	0.1	0.03

Adapted from Anthes and Warner 1978.

The analysis of Eq. (11-20), as tabulated in Table 11-1, shows that for small domain sizes, small errors in the prescription of wind speed at the lateral boundaries can cause a significant acceleration within the model domain. This effect becomes more serious for higher wind speeds because of the quadratic form of the advective term in Eq. (11-20). The model results are even more sensitive to specification of the mesoscale pressure perturbation on the lateral boundaries. Even a fraction of a millibar of error in pressure on one of the boundaries can generate substantial accelerations throughout the smaller domain sizes. Pielke *et al.* (1989) discuss the significance of those errors in the context of mesoscale observational networks.

Unfortunately, there has been little quantitative discussion in the literature of techniques to control such erroneous acceleration. Most recent work has concentrated on minimization of the backward reflection into the model domain of outward-propagating advective and gravity waves.

11.3.1.1   Types of Lateral Boundary Conditions

Lateral boundary conditions can be *open* (i.e., mesoscale perturbations can pass into and out of the model domain) or *closed* (i.e., such perturbations are not permitted to exit or enter).[18] There are several types of these lateral boundary conditions, some of which are designed to minimize the reflection of erroneous information back into the model domain, yet still permit input of larger-scale flow into the region. Types of boundary conditions include the following.

Constant Inflow, Gradient Outflow Conditions. With this procedure, air entering the model is assumed to be unaffected by the downstream mesoscale perturbation to the flow, so that the dependent variables remain unchanged at inflow boundaries (i.e., a closed boundary). Air exiting the model, however, is assumed to instantaneously have the same value as is found one grid point upstream (hence the term gradient boundary condition, since, for example, $\partial \phi / \partial x \simeq \phi(N-1) - \phi(N) = 0$, where ϕ is any one of the dependent variables and N is the outflow boundary). Inflow and outflow are defined in terms of the wind direction at the boundaries. Unfortunately, this procedure cannot properly handle disturbances that propagate upstream (e.g., internal gravity waves) and simultaneously correctly handle changes to the downstream boundary as advection and wave propagation move information at a finite speed from the last interior grid point to the boundary.

Mason and Sykes (1979) use a modification to this scheme applied to the velocity components as $u_N^{\tau+1} = 1.5\,u_{N-1}^{\tau} - 0.5\,u_{N-3}^{\tau}$. This condition is applied at outflow points. They concluded that this representation, although resulting in some reflection at boundaries, is not only extremely simple, but also stable and effective. (In testing this outflow boundary condition, u_{N-2}^{τ} produced improved results compared to the use of u_{N-3}^{τ}.)

Radiative Boundary Conditions. With this procedure, the variables at the lateral boundaries are changed in value so as to minimize reflection of outward-propagating perturbations to the flow, back into the model domain. Several procedures have been introduced to implement radiative boundary conditions using, for the east–west boundary, an equation of the form

$$\partial \bar{u}/\partial t = -c \partial \bar{u}/\partial x.$$

The other prognostic conservation equations can be similarly evaluated at the boundary from $\partial \bar{\phi}/\partial t = -c \, \partial \bar{\phi}/\partial x$, where $\bar{\phi}$ is any one of the prognostic dependent variables. These methods include those of Orlanski (1976), Klemp and Lilly (1978) and Klemp and Wihelmson (1978a), and Hack and Schubert (1981).

In Orlanski (1976),

$$c = \frac{-\partial u}{\partial t} \bigg/ \frac{\partial u}{\partial x}$$

is evaluated at the last grid point immediately in from the boundary with the requirement that $0 \leq c \leq \Delta x/\Delta t$. Miller and Thorpe (1981) proposed improvements to Orlanski's method, including the use of an upstream formulation rather than a leapfrog scheme. Carpenter (1982a) describes how the Miller and Thorpe scheme can be generalized to include changes introduced at the boundary from a larger-scale model.

In the method of Klemp and Lilly (1978) and Klemp and Wilhelmson (1978a), c is a constant, equal to the model domain height times the Brunt–Väisälä frequency[19] divided by π, chosen to represent the dominant phase velocity of an internal gravity wave.

With the technique of Hack and Schubert (1981), c is evaluated separately for individual phase speeds for all of the internal gravity wave modes near the model boundary. The resultant change of the dependent variable at the boundary is evaluated by the summation of the changes resulting from each wave. The advantage of the method of Hack and Schubert over that of Orlanski is that the evaluated wave speeds are determined from atmospheric structure through the depth of the model, whereas Orlanski's condition is determined separately at each vertical level. Hack and Schubert reported on a comparison of results for a hurricane model using these and other more reflective lateral boundary conditions. Using their results as a control, Orlanski's condition was nevertheless found to be very effective, even though it used information at one level.

Lilly (1981) has sought to explain the importance of lateral radiative conditions using an idealized linear model of convection. In the context of a convective storm simulation, he concluded that the effect of this boundary condition on the mass flow into or out of the model produced by the convection is more important than the avoidance of wave reflection at the boundary. However, he

found that a boundary condition designed to minimize reflection is also nearly optimal to control the mass flow. Tripoli and Cotton (1982) offered an approach in which both backward reflection and domain-averaged acceleration are controlled using a larger-scale compensation region external to the primary model domain.

Sponge Boundary Conditions.   Enhanced filtering near the lateral boundaries can be used to damp advective and wave disturbances as they move toward the periphery of the model domain. These filters are added either by increasing the value of a horizontal exchange coefficient in an explicit diffusion formulation[20] near the boundary (e.g., Deaven 1974) or by applying larger smoothers[21] in that region (e.g., Perkey and Kreitzberg 1976; Jones 1977a). Alternatively, the prognostic equations can be written in the form

$$\frac{\partial \bar{\phi}}{\partial t} = -\bar{u} \frac{\partial \bar{\phi}}{\partial x} - r(\bar{\phi} - \phi_0),$$

where r is called a *relaxation coefficient* (Davis 1983) and ϕ_0 is the desired value of $\bar{\phi}$ at the boundary. The relaxation coefficient is defined to become nonzero within some distance of the boundary, reaching a maximum at the boundary. Durran (1981) used such a formulation to represent an absorbing layer[22] at the top of his model flow simulation.

As implied by the results of Morse (1973), the increased filtering cannot be applied abruptly at some selected distance from the lateral boundary because erroneous reflection back into the center of the model domain will result. As stated in Section 11.1.1.2, such reflections are analogous to those found in the study of optics, when electromagnetic radiation travels from a material of one index of refraction to another.

The sponge boundary condition is a form of radiative boundary condition in which increasingly greater explicit viscosity is applied close to the lateral sides of a model. In contrast to the types of radiative boundary conditions discussed previously, however, the sponge condition requires a number of grid points near the boundary to permit the smoothing to increase gradually. These added grid points contribute to the computational cost of a model simulation.

Sponge boundary conditions are frequently used in meshed models, such as those discussed in Section 11.1.1.2. In the parasitic form of grid meshing reported by Perkey and Kreitzberg (1976), for example, a sponge boundary condition is applied near the exterior of the fine mesh to prevent disturbances generated within that region from propagating to the coarse grid. Since the sponge is a low-pass filter, longer wave features are permitted to move from the coarse grid into the interior of the fine mesh.

Periodic Boundary Conditions.   The values of the dependent variables at one boundary of the model domain are assumed identically equal to the values at the

other end [e.g., $\phi(x_\mathrm{D}) = \phi(x_0)$]. Although of considerable value in comparing a numerical model with an exact analytic solution, realistic mesoscale simulations generally do not permit the reintroduction of perturbations to the flow into the inflow region of the model after they have exited the boundary. The application of periodic boundary conditions to selected approximations to the advection equation and to the diffusion equation is given in Appendix A.

Larger-Scale Model or Analyzed Boundary Conditions.   Davis (1983) has provided a more complete summary of lateral boundary conditions including an analysis of their advantages and disadvantages. Among his results, he concluded that Oliger and Sundström's (1976) analysis regarding the ill-posed characteristic of any local boundary condition in a hydrostatic model does not result in serious errors in such models when the relaxation form of lateral boundary condition is used. Anthes (1983) also presented an overview of lateral boundary conditions, including a discussion of the use of nested models for regional-scale forecasting. The use of analyzed large-scale fields by the National Center for Environmental Prediction (NCEP), as reported in Kalnay *et al.* (1996), has been found to be very useful in providing initial and lateral boundary conditions to regional and mesoscale models (see, e.g., Liston and Pielke 2000).

11.3.1.2   *Summary of Lateral Boundary Conditions*

A necessary test to apply to any selected lateral boundary condition is to enlarge the model domain progressively (i.e., by adding grid points) until successive enlargements have no appreciable changes on the solutions within the region of interest. Smaller domain sizes would result in mesoscale circulations that are significantly altered as the lateral boundaries are moved.

In summary, the main recommendations concerning lateral boundary conditions are as follows:

1.   Remove the lateral boundaries far enough from the region of interest so that a subsequent further enlargement has no appreciable change to the solutions within the interior. Enlarging the model requires that the number of grid points as well as the grid spacing be increased in the vicinity of the lateral boundary.

2.   The radiative lateral boundary condition appears to be the form that permits the least expansion of the model domain. Several forms of the radiative boundary condition exist, and each modeler will probably need to test them individually for their particular applications. Orlanski's (1976) form has been reported by several investigators (e.g., Clark 1979; Hack and Schubert 1981) to perhaps have a general utility.

3.   The sensitivity of the mesoscale model domain to grid-volume–averaged accelerations also indicates that the model domain must have as large a horizontal scale as possible. Although changes in the large-scale field can be input

through these boundaries, the sensitivity of the results for mesoscale domain sizes to even small variations in pressure and velocity (see Table 11-1) makes the acquisition of observational input with suitable accuracy difficult to obtain (Anthes and Warner 1978).

An early example of a successful incorporation of larger-scale information into a mesoscale model is that of Carpenter (1979), who has succeeded in changing boundary conditions to represent a varying synoptic regime in his simulation of the sea breezes over England for a case study day. He found that his simulated sea-breeze fronts were very sensitive to the position of synoptic-scale features. Ballentine (1980) has been equally successful in applying synoptic tendencies to a simulation of New England coastal frontogenesis. In both of these studies, however, the mesoscale systems were forced primarily by the underlying terrain, rather than by input through the side walls of the models (i.e., terrain-induced mesoscale systems, as discussed in Section 13.1).

In more recent work, Seth and Giorgi (1998) discuss the role of lateral domain size with respect to accurate regional atmospheric model simulations. A summary on issues associated with lateral boundary conditions is given in Warner *et al.* (1997). Another paper that discusses the role of lateral boundary conditions is Fukutome *et al.* (1999).

11.3.2   Top Boundary Conditions

The top of the mesoscale model, as with the lateral boundaries, should be removed as far as possible from the region of significant mesoscale disturbance. Ideally, this would place the top at $\bar{p} = 0$, so that the density of air is 0.

It is not necessary to go this high in mesoscale models, however, because of the deep layer of stable thermodynamic stratification, which always exists throughout the stratosphere and in much of the upper troposphere. Such layers, almost always stable even to the lifting of saturated air, inhibit vertical advection and tend to generate circulations that have larger horizontal than vertical scales. As shown by, for example, Pielke (1972), increased stratification causes shallower circulations to develop and makes the hydrostatic assumption more applicable, since the characteristic horizontal length scale, L_x, becomes larger and the vertical length scale, L_z, becomes smaller. Only through vertical propagation by wave motion can information from near the surface be propagated upward through this stable region.

Using this characteristic of the earth's atmosphere, modelers have placed the tops of their domains (1) deep within the stratosphere (e.g., Klemp and Lilly 1978; Peltier and Clark 1979), (2) at the tropopause (e.g., Mahrer and Pielke 1975), or (3) within the stable layer of the troposphere (e.g., Estoque 1961; Pielke 1974a). Selection of these levels is based on numerical experimentation

with different depths for a model, as well as from linear models, suggesting the depth in the atmosphere to which the mesoscale circulation will extend. In sea-breeze models over flat terrain, for example (see Figure 11-6), the simulation results are essentially unaffected by increasing the depth of the model from 4.2 km to 12 km. With strong airflow over rough terrain, however, Peltier and Clark (1979) maintain that the lower stratosphere must be resolved to represent turbulence at those levels properly. They concluded that the turbulence can reflect upward-propagating internal gravity waves, thereby causing large amplifications in the flow over the mountain near the ground.

The form of the top is also important. Modelers have used rigid tops (e.g., Estoque 1961, 1962), impervious material surfaces (e.g., Pielke 1974a), porous lids (e.g., Lavoie 1972), and absorbing layers (e.g., Anthes and Warner 1978; Klemp and Lilly 1978; Mahrer and Pielke 1978b). In the past, rigid tops were used since they purportedly eliminated rapidly moving external gravity waves from the solutions, thereby permitting longer time steps in the explicit finite difference schemes that were used.

With a rigid top, the vertical velocity is set to 0 and pressure is adjusted to account for mesoscale perturbations at that level. As can be expected, however, unless the solutions would naturally approach 0 at that level, the solutions are arbitrarily constrained. Estoque (1973) performed a set of equivalent experiments using a sea-breeze model with and without a rigid lid. When the rigid lid was used, pressure was changed on the top boundary to compensate for the restrictive requirement on vertical velocity, whereas in the second experiment, pressure was set equal to a constant at that level and vertical velocity changes were permitted. Solutions from these two experiments, given in Figure 11-16, are significantly different. It is not certain, of course, whether either solution is realistic, yet it is clear that if a rigid lid is to be imposed, it must be located well above the region of significant mesoscale disturbance.

The impervious material surface lid was introduced to remedy some of the criticisms of the rigid top assumption. The form of this lid used by Pielke (1974a) illustrates this approach. Assuming that the incompressible form of the conservation-of-mass relation is valid [i.e., Eq. (4-23)], that expression is integrated between the highest fixed grid level in the model z_t and a material surface s_θ, yielding

$$\bar{w}_s = \bar{w}_{z_t} - \int_{z_t}^{s_\theta} \left(\frac{\partial \bar{u}}{\partial x} + \frac{\partial \bar{v}}{\partial y} \right) dz,$$

where $\bar{w}_{z_t}$ and $\bar{w}_s$ are the vertical velocities at z_t and of the material surface. In the absence of diabatic effects at these levels, the material surface corresponds to a surface of constant potential temperature—hence the use of the subscript "θ" on s.

Distance in x direction (m)
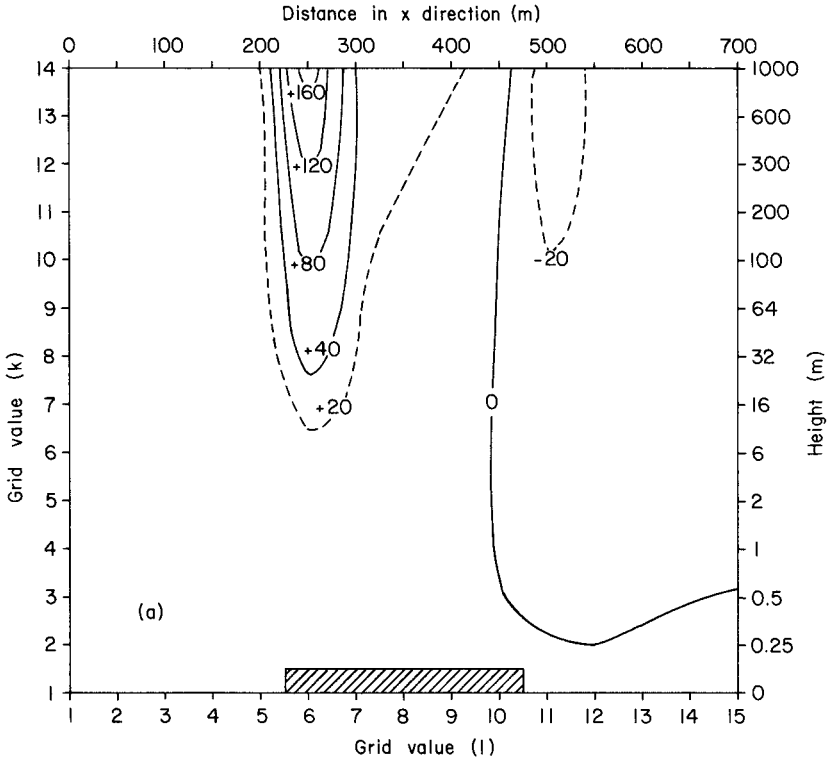
Fig. 11-16a. The vertical motion (in centimeters per second) owing to airflow over an island having a roughness length of 100 cm (between grid points 6 and 10, inclusive), and initial wind speed of 10 m s⁻¹; θ at the surface and at 1 km is 303 and 309 K, respectively. The horizontal grid spacing is 50 m. In run (a), the pressure of the top is kept fixed at 900 mb while vertical motion at that level varies. In run (b), the top is made rigid and pressure varies. (From Estoque 1973.)

Defining $\bar{w}_s = ds_\theta/dt$ and using the chain rule of calculus with $s_\theta = s_\theta(t, x(t), y(t))$, we have

$$\frac{\partial s_\theta}{\partial t} = -\bar{u}\frac{\partial s_\theta}{\partial x} - \bar{v}\frac{\partial s_\theta}{\partial y} + \bar{w}_{z_t} - \int_{z_t}^{s_\theta}\left(\frac{\partial \bar{u}}{\partial x} + \frac{\partial \bar{v}}{\partial y}\right)dz. \tag{11-22}$$

In contrast to the rigid top, the material surface moves in response to divergence below and is considered a more realistic representation of conditions at the top of the model. This material surface is usually defined coincident with a surface of constant potential temperature and is placed at the tropopause level. If diabatic changes and vertical subgrid-scale mixing at this level are small relative to changes at a location because of advection, such a representation should closely correspond to the movement of the tropopause.
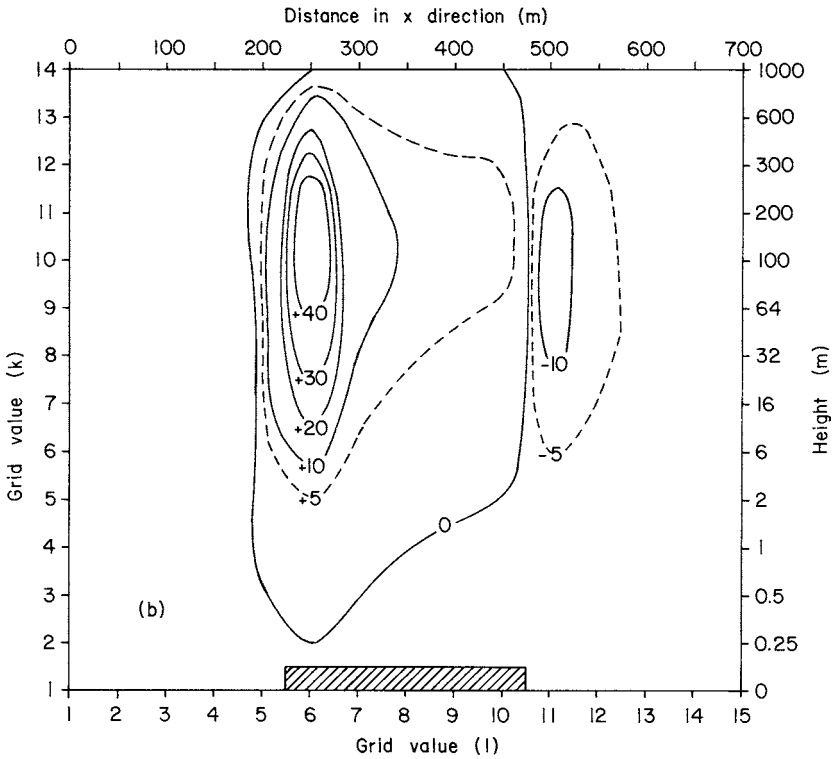
Fig. 11-16b

    With the assumption that s_θ is a potential temperature surface, $\bar{\theta}$ is kept con-
stant on it. The remaining dependent variables must be estimated, however. One
procedure is to use the initial values of these variables at whatever height is
predicted for s_θ. But this method assumes that changes below s_θ have no influ-
ence on the variables, other than $\bar{\theta}$, at s_θ and above. Another possibility, as yet
untested, is to insert several additional potential temperature layers above s_θ and
to integrate an adiabatic form of the conservation relations at those levels in an
isentropic coordinate representation to permit dynamic adjustment of the depen-
dent variables on s_θ. Another alternative is to treat s_θ as an interface between
fluids of two different densities and thereby include a pressure gradient force
on s_θ analogous to that derived for the two-layer tank model in Section 5.2.1.2,
where h corresponds to s_θ.
    The use of a porous model top differs from the impervious lid in that mass
transport is permitted across s_θ. Lavoie (1972) used such an approach, since the
lid of his model was the top of the planetary boundary layer, and he needed
to entrain mass into it as it grew. Deardorff's (1974a) prognostic equation for

the depth of the planetary boundary layer [i.e., Eq. (7-50)] is of the same form. Other than using such a level as a cap on the boundary layer, such an approach has not been used in mesoscale models.

The use of an *absorbing layer* with multiple levels to represent the top of the model was introduced by Klemp and Lilly (1978) in their simulation of airflow over rough terrain. As they maintained in that paper, and based in part on results that they reported in earlier (1975) linear model results, vertically propagating internal gravity wave energy can be erroneously reflected downward by a single level top. From Klemp and Lilly's linear theory, some downward reflection is expected when discontinuities of temperature and wind occur, but the bulk of the energy is usually expected to propagate into the stratosphere and there to be dissipated by small-scale turbulence. In a linear model, incorporation of a radiation boundary condition that permits this wave energy to leave is straightforward, but in a nonlinear model, Klemp and Lilly (1978) argued that local boundary conditions were unable to handle this effect properly.

Klemp and Lilly stated than an absorbing layer must be placed above the main portion of the model domain. In this region, horizontal filtering is increased from the base of the absorbing layer to the top of the model to prevent energy from being erroneously reflected downward. To prevent reflections caused by the smoothing, the filter must be increased gradually. This approach is analogous to the sponge method used to minimize lateral boundary effects, as discussed in Section 11.3.1.1.

Figure 11-17, reproduced from Klemp and Lilly (1978), shows the depth of absorbing layer required as a function of the vertical wavelength of the mesoscale disturbance in the lower portion of the model domain, using a particular form of viscosity in the absorbing layer, as given in the figure caption. As Klemp and Lilly discussed in their paper, large reflection at low viscosity results from reflection off of the upper boundary because of insufficient damping; excessive damping in the absorbing layer also causes reflection. In addition, an absorbing layer with a depth greater than the vertical wavelength of the mesoscale disturbance is required.

Bougeault (1983) and Klemp and Durran (1983) have suggested a local upper boundary condition (called a *radiative boundary condition*) that eliminates the need for a computationally expensive absorbing layer. In their formulation, if the mesoscale pressure perturbation (expressed in terms of $\hat{\pi}'$) is computed from

$$\hat{\pi}' = \hat{w}' \frac{1}{k_{\mathrm{H}}\theta_0^{3/2}} \left(g \frac{\partial \bar{\theta}}{\partial z} \right)^{1/2}, \tag{11-23}$$

where $\hat{\pi}'$ and $\hat{w}'$ are expressed as functions of horizontal wavenumber k_{H}, then downward reflection into the computational domain from the top is minimized when π' is determined by summing over all horizontal wavenumbers in the model. Klemp and Durran showed that although derived from a linear model
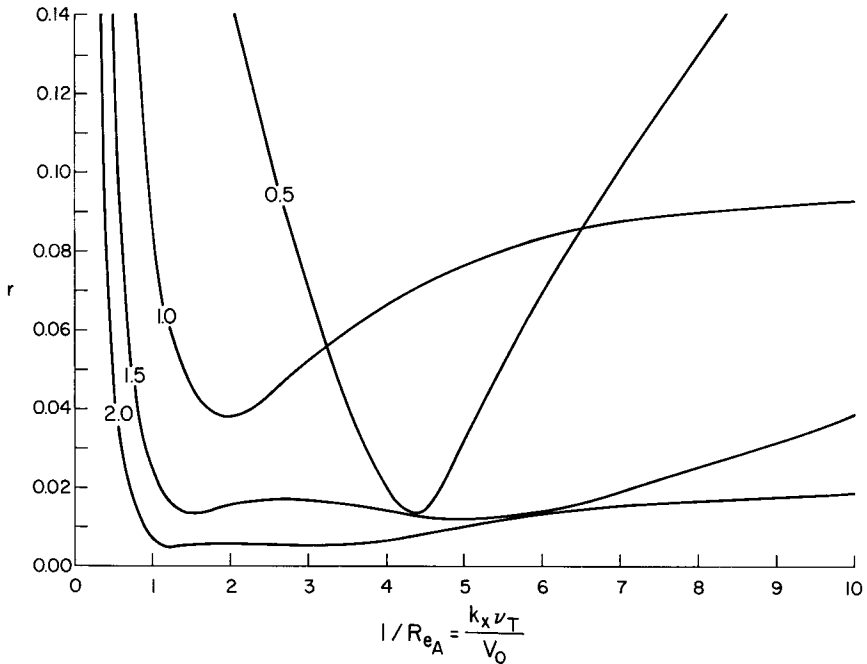
Fig. 11-17. Reflectivity, from the absorbing layer as a function of a nondimensional inverse Reynolds number, $1/R_{e_A}$, for several nondimensional viscous layer depths ($D_v = 0.5$, 1.0, 1.5, and 2.0). A value of $r = 1.0$ corresponds to complete reflection. The nondimensional numbers are defined as $R_{e_A} = V_0/k_x v_T$ and $D_v = \Delta z_a/l_z$, where k_x is the horizontal wavenumber of the atmospheric disturbance, V_0 is the large-scale horizontal wind speed assumed to be constant with height in the absorbing layer, Δz_a is the depth of the absorbing layer, and l_z is the vertical wavelength of the mesoscale disturbance. The vertical wavelength is defined as $l_z = 2\pi V_0/[(g/\theta_0)\partial\theta_0/\partial z]^{1/2}$, where the denominator is the Brunt–Väisälä frequency. The viscosity in the absorbing layer is defined by $v = v_T \sin^2[\pi \ln(\bar{\theta}/\theta_1)/2\ln(\theta_T/\theta_1)]$, where θ_1 and θ_T are the values of potential temperature at the bottom and the top of the absorbing layer, respectively. (From Klemp and Lilly 1978.)

in the absence of Coriolis effects, this economical top boundary condition to also be effective for nonlinear problems when Coriolis effects are included. Appendix A of their paper provides a procedure to implement this boundary condition in a numerical model.

Based on the studies of top boundary conditions, the following conclusions are made:

1.   If the vertical propagation of internal gravity wave energy is equal to or more important than advective properties in a mesoscale model, then an absorbing layer [or a boundary condition such as Eq. (11-23)] is required.

2.   Otherwise, a material surface top placed along an isentropic surface well removed from the region where advective changes are significant is sufficient.

3.   Use of a rigid top in a mesoscale model is inappropriate unless advective effects are dominant and the depth of the model is much greater than the region of mesoscale disturbance. In this case, the precise form of the top (e.g., material surface, rigid top, absorbing layer) is unimportant, since perturbations that reach that level will be inconsequential for any of the dependent variables.

11.3.3   Bottom Boundary Condition

In a mesoscale atmospheric model, the bottom is the only boundary that has physical significance. Moreover, it is the differential gradient of the dependent variables along this surface that generates many mesoscale circulations (i.e., surface boundary-forced mesoscale systems, see Chapter 13, Section 13.1) and that has a pronounced influence on the remaining mesoscale flows (i.e., initial value/lateral boundary-forced mesoscale systems, see Section 13.2). Changes in this lower boundary over time (from, e.g., anthropogenic activity or overgrazing by animals) can cause substantial climatic changes such as desertification (Otterman 1975; Idso 1981). Because of this boundary's crucial importance in mesoscale atmospheric systems, it must be represented as accurately as possible.

In discussing this component of mesoscale models, it is convenient to consider the land and water surfaces separately. This is done because water is translucent to solar radiation and overturns much more easily than land.

11.3.3.1   Water Bodies

To represent the surface of water bodies such as lakes, bays, and oceans properly in a mesoscale atmospheric model, dynamic and thermodynamic interactions between the air and the water must be permitted (Pielke 1981). Such a connection can involve small-scale boundary layer interactions, such as gaseous interchanges between the water–air interface, or larger-scale transports of heat by wind-driven currents. Since these interactions generally involve complex non-linear processes, it is necessary to use an oceanographic model to simulate these interactions properly and to provide appropriate bottom boundary conditions over water for the meteorological model.

Clancy *et al.* (1979) have attempted some simulations using a coupled sea-breeze and upwelling oceanographic model to study the interactions between these two geophysical phenomena. In their model, the sea-surface temperature generated by upwelling was used as a bottom condition in the sea-breeze part of the model, and the wind shearing stress at the sea surface was used to influence the intensity of upwelling. Mizzi (1982), and Mizzi and Pielke (1984) continued this work, using a more complete atmospheric model. Both studies determined

that the interaction between upwelling and sea-breeze intensity was weak for this particular region of the Oregon coast. The direction of the *synoptic* flow is important, however. Hawkins and Stuart (1980), for example, reported that northerly flow along the Oregon coast is associated with upwelling and strong sea breezes, whereas southerly synoptic flow results in a cessation of upwelling and weak sea breezes.

Avissar and Pan (2000) used the Regional Atmospheric Modeling System (RAMS) to simulate summer hydrometeorological processes of Lake Kinneret (Sea of Galilee) in Israel as a first step in developing a coupled atmosphere–lake modeling system. Costa *et al.* (2001) has coupled RAMS to the Princeton Ocean Model to investigate deep cumulus cloud–ocean interactions in the western tropical Pacific Ocean. Xue *et al.* (2000a) describe results from a coupled mesoscale atmospheric–water body modeling system.

Over the Gulf Stream, Sweet *et al.* (1981) have shown that the large horizontal sea-surface temperature gradient on the north side of that well-defined current generates lines of low-level cloud paralleling the edge of the Gulf Stream. In addition, the sea state is significantly affected by the difference in stability across the Gulf Stream boundary with rougher seas and stronger low-level winds on the warm side of the boundary and calmer, more humid conditions north of the current. In the area off the west coast of Africa, Brown *et al.* (1982a, b) have used an air–sea interaction model to show the close coupling between the depth of convective mixing in the ocean and in the atmosphere. Jacobs and Brown (1974) performed preliminary three-dimensional simulations of the air–lake interactions over Lake Ontario. Zeng *et al.* (1999a) uses observed data to describe the relation between sea-surface skin temperature and wind speed and a sea-surface bucket temperature.

Other past work has documented a number of effects of wind on ocean dynamics, including the following:

1.   An increase in wind speed produces a deepening of the ocean-mixed layer (Marchuk *et al.* 1977; Chang and Anthes 1978; Elsberry and Randy 1978; Kondo *et al.* 1979).

2.   An increase in wind speed produces small-scale wave breaking. This change over from an aerodynamically smooth to a rough water surface occurs over a rather narrow velocity range ($u_* \simeq 23$ cm s^{-1}) (Melville 1977).

3.   Spatial and temporal variations in wind velocity cause currents in coastal waters (Emery and Csanady 1973; Blackford 1978; Sheng *et al.* 1978; Svendsen and Thompson 1978).

4.   Changes in wind speed and direction along a coastline alter the upwelling–downwelling pattern (Csanady 1975; Knowles and Singer 1977; Hamilton and Rattray 1978; Allender 1979).

5. Changes in wind speed alter the circulation in estuaries and harbors through mixing and the resultant creation of horizontal gradients of temperature and salinity in the water (Hachey 1934; Weisberg 1976; Long 1977; Wang 1979).

6. Wind energy absorbed by coastal waters is a function of the wind's spectral energy (Lazier and Sandstrom 1978).

7. Wind velocity affects the drift of coastal pack ice (McPhee 1979).

8. The wind velocity field influences the movement of pollutants in the water (Pickett and Dossett 1979).

9. The wind causes the formation of helical circulation patterns in the water, with the resultant accumulation of surface debris in lines parallel to the surface wind direction (Gross 1977).

10. The orientation of the coastline and ocean bathymetry influence wind-induced upwelling (Hua and Thomasset 1983).

11. The wind profile near the ocean surface is significantly influenced by blowing sea spray and rain during strong winds (Pielke and Lee 1991).

12. Diurnal variations of the sea-surface temperature can result in significant variations of surface turbulent fluxes (Zeng and Dickinson 1998).

The effects of mesoscale circulations on the coastal waters, therefore, often include diurnal changes in the vertical gradients of temperature, of salinity, and of other gaseous and aerosol materials in the upper levels of the water caused by changes in the temporal and spatial fields of the atmospheric-dependent variables over the water surface. Pielke (1991) suggested that mesoscale resolution of ocean upwelling is needed to properly simulate the ocean uptake of carbon dioxide. The advection of aerosol may also affect the temperature of the coastal waters (through changes in the turbidity of the water) and hence feedback to the intensity of mesoscale circulations, as well as to local baroclinic circulations in the water. In general, however, the most significant influence of mesoscale atmospheric circulations on ocean dynamics is a result of the low-level wind that, through surface shearing stresses, influences currents and vertical turbulent mixing in the water. The water body, in contrast, primarily influences atmospheric mesoscale circulations through its surface temperature, including its time and space variability. Pielke (1981) discussed the interactions between coastal waters and the atmosphere in more detail. A relatively recent overview of air–sea interactions is given in Rogers (1995).

11.3.3.2   Land Surfaces

The representation of land surfaces as a bottom boundary requires different types of models than those required to properly represent the water interface. In contrast to water, the ground is opaque and does not readily overturn. To

represent land as a bottom surface, it is convenient to consider bare soil separately from vegetated ground. The former characterization is much easier to simulate, and mesoscale models have become increasingly more sophisticated in its representation. Vegetation effects, in contrast, are very complex. A variety of field campaigns have been performed to develop improved understanding of land–atmosphere interactions (Rango *et al.* 1998; Hall 1999 and references therein; LeMone *et al.* 2000). An overview of land–atmosphere interactions is given in Avissar (1995), Bales and Harrington (1995), Dickinson (1995), and Entekhabi (1995).

Bare Soil   As discussed in Chapter 7 [see after Eq. (7-19)], the mesoscale horizontal velocity is 0 at a roughness height z_0. Micrometeorological observations have shown the value of z_0 generally to be very small over bare soil, because rocks, stones, and grains of soil are usually small and offer relatively little resistance to the wind. A tabulation of representative values of z_0 was given in Chapter 7, Table 7-2, for bare soils as well as for various vegetative surfaces. The mesoscale vertical velocity perpendicular to the ground surface is also equal to 0, so that the velocity and vertical subgrid momentum flux at the ground surface can be approximated by[23]

$$u(z_0) = v(z_0) = w(z_0) = 0, \qquad \overline{u''w''} = -u_*^2 \cos\mu,$$
$$\overline{v''w''} = -u_*^2 \sin\mu. \tag{11-24}$$

The specification of potential temperature, $\bar{\theta}$, water substance, $\bar{q}_n$, other gaseous and aerosol atmospheric materials, $\bar{\chi}_m$, and pressure, $\bar{\pi}$, at the land surface are not as simple to estimate as are $\bar{u}$, $\bar{v}$, and $\bar{w}$. The variables $\bar{\theta}$, $\bar{q}_n$, and $\bar{\chi}_m$ generally depend on fluxes of these quantities into and out of the ground. For example, Walko *et al.* (2000a), based on the work of Garratt (1992), show that $T(z_0) = T_G + 2\theta_*/k$ over bare soil.

The pressure at level z_0 can be diagnosed from Eq. (4-32) or (4-41) if the hydrostatic representation is used and if the pressure at some arbitrary level above z_0 is known. Equations (4-32) and (4-41) can then be integrated downward from that level. In an anelastic or a compressible model, local hydrostatic equilibrium between the first grid point above the ground and the surface has often been assumed to diagnose pressure at the surface.

The need to introduce a boundary condition on Eq. (4-41) [or (4-32)] introduces a problem in the integration of these relations, however. If the top of the model s_θ [defined by Eq. (11-22)] is the level where the pressure boundary condition is needed, then a method to estimate pressure at that level must be devised. Defining it as a constant is not satisfactory, since net warming in a column must *initially* result in its expansion so that the pressure at s_θ will rise while remaining a constant at z_0 (Nicholls and Pielke 1994a).

To illustrate the problem, Eqs. (4-32) and (4-41) can be differentiated with time and integrated between z_0 and s_θ, yielding[24]

$$\left.\frac{\partial \bar{\pi}}{\partial t}\right|_{s_\theta} - \left.\frac{\partial \bar{\pi}}{\partial t}\right|_{z_0} = g \int_{z_0}^{s_\theta} \frac{1}{\bar{\theta}^2} \frac{\partial \bar{\theta}}{\partial t} \, dz, \tag{11-25}$$

$$\left.\frac{\partial \bar{p}}{\partial t}\right|_{s_\theta} - \left.\frac{\partial \bar{p}}{\partial t}\right|_{z_0} = -g \int_{z_0}^{s_\theta} \frac{\partial \bar{p}}{\partial t} \, dz. \tag{11-26}$$

Using the definition of $\bar{\pi}$ [after Eq. (4-36)] of potential temperature [Eq. (2-48)] and the ideal gas law [Eq. (2-49)], Eqs. (11-25) and (11-26) are related by

$$\frac{\partial \bar{\pi}}{\partial t} = \frac{1}{\bar{\rho}\bar{\theta}} \frac{\partial \bar{p}}{\partial t},$$

so that Eq. (11-25) can be rewritten as

$$\left.\frac{\partial \bar{\pi}}{\partial t}\right|_{s_\theta} - \left.\frac{\partial \bar{\pi}}{\partial t}\right|_{z_0} = g \int_{z_0}^{s_\theta} \frac{1}{\bar{\theta}^2} \frac{\partial \bar{\theta}}{\partial t} \, dz = \frac{-g}{\bar{\rho}\bar{\theta}} \int_{z_0}^{s_\theta} \frac{\partial \bar{p}}{\partial t} \, dz. \tag{11-27}$$

As evident in Eq. (11-27), for a fixed s_θ, a change in the heat content of a column is equivalent to a change of the mass in that column for a hydrostatic atmosphere. Such changes in heat could occur from physical mechanisms such as radiative flux divergence [i.e., see Eq. (8-1)]. With fixed pressure on s_θ (i.e., $\partial \bar{\pi}/\partial t|_{s_\theta} \equiv 0$), the result of heating, as represented by the middle term in Eq. (11-27), would be a drop in surface pressure.

In contrast, in the real atmosphere, net heating in a column would result in a thickness adjustment such that in the absence of advection or wave propagation in the horizontal,

$$-g \int_{z_0}^{s_\theta} \frac{1}{\bar{\theta}} \, dz = C, \tag{11-28}$$

where C is a negative constant (since $\bar{\pi}_{s_\theta} < \bar{\pi}_{z_0}$). In the atmosphere, such a thickness adjustment can be performed by compressibility (Nicholls and Pielke 1994a), which is not permitted in the model if either of the conservation-of-mass relations given by Eq. (4-23) are used. Equation (11-28) is obtained by integrating Eq. (4-41) between z_0 and s_θ. Differentiating Eq. (11-28) with respect to time and using Leibnitz's rule (see, e.g., Hildebrand 1962:360) yields

$$\int_{z_0}^{s_\theta} \frac{1}{\bar{\theta}^2} \frac{\partial \bar{\theta}}{\partial t} \, dz - \frac{1}{\bar{\theta}_{s_\theta}} \frac{\partial s_\theta}{\partial t} = 0,$$

where $\bar{\theta}_{s_\theta}$ is the value of potential temperature on s_θ. Solving for $\partial s_\theta/\partial t$ gives

$$\frac{\partial s_\theta}{\partial t} = \bar{\theta}_{s_\theta} \int_{z_0}^{s_\theta} \frac{1}{\bar{\theta}^2} \frac{\partial \bar{\theta}}{\partial t} \, dz, \tag{11-29}$$

so that net heating increases the thickness of the layer (i.e., $\partial s_\theta / \partial t > 0$), whereas cooling generates a decrease in the thickness. Feliks and Huss (1982) discussed the need to include this effect in mesoscale models. The change in thickness caused by expansion or contraction in Eq. (11-29) should be added to the expression for s_θ in Eq. (11-22) [i.e., $\partial s_\theta / \partial t = \partial s_\theta / \partial t|$ from Eq. (11-22) $+ \partial s_\theta / \partial t|$ from Eq. (11-29)].

Surface Temperature. At the surface, early mesoscale models prescribed potential temperature as a periodic heating function and permitted no feedback between the mesoscale circulation and the ground surface temperature. Pielke (1974a) used such a representation, given as

$$\bar{\theta}(z_0) = \bar{\theta}_0(z_0) + \Delta \bar{\theta}_{max} \sin \frac{2\pi t}{\text{day}}, \tag{11-30}$$

where day was equal to twice the length of daylight, t is the time after sunrise, $\bar{\theta}_0(z_0)$ the potential temperature at z_0 at sunrise, and $\Delta \bar{\theta}_{max}$ the maximum temperature attained during the day. Downward-looking radiometer measurements from aircraft were used to estimate $\Delta \bar{\theta}_{max}$.

A more general periodic form was used by Neumann and Mahrer (1971) and Mahrer and Pielke (1976), in which observed temperature data were fitted to a series of periodic functions of the form suggested by Kuo (1968). Such a periodic form can be written following Panofsky and Brier (1968) as

$$\bar{\theta}(z_0) = \bar{\theta}_T(z_0) + \sum_{n=1}^{N/2} \left(a_n \sin \frac{2\pi nt}{T} + b_n \cos \frac{2\pi nt}{T} \right), \tag{11-31}$$

where

$$a_n = \frac{2}{N} \sum_{n=1}^{(N/2)-1} \bar{\theta}^+(z_0) \sin \frac{2\pi nt}{T}, \qquad a_{N/2} = 0$$

$$b_n = \frac{2}{N} \sum_{n=1}^{(N/2)-1} \bar{\theta}^+(z_0) \cos \frac{2\pi nt}{T}, \qquad b_{N/2} = -\frac{\bar{\theta}^+(z_0)}{N}, \tag{11-32}$$

with T usually chosen as 1 day (i.e., to correspond to the diurnal cycle), with $t = 0$ corresponding to midnight and N an even integer number of observations. The value of $\bar{\theta}_T(z_0)$ corresponds to the average temperature over T and is assumed to be constant within T. The quantity $\bar{\theta}^+(z_0)$ is the deviation of potential temperature at time t from $\bar{\theta}_T(z_0)$. In practice, a different temperature than $\bar{\theta}^+(z_0)$ is often used to obtain a_n and b_n. Neumann and Mahrer (1971), for example, used a series expansion equivalent to Eq. (11-31) with $N = 4$ and values of temperature from Kuo (1968, Figure 6) at a soil depth of 0.5 cm. Mahrer

and Pielke (1976) applied an expansion with $N = 8$ for use in Eq. (11-31) using radiometer data collected over Barbados in 1969 and analyzed for the diurnal temperature wave by Holley (1972). Estoque *et al.* (1976) used a representation of the form given by Eq. (11-31), with t defined in terms of hours after 0700 LST using infrared measurements of surface temperature from aircraft flights over Lake Ontario.

Although simple to apply, such formulations imply an infinite reservoir of heat and permit no feedbacks between the ground and the atmosphere.

Surface Heat Energy Budget.   Physick (1976) developed the first mesoscale model that permitted feedbacks between the temperature of the ground surface and the atmosphere. He used a heat budget technique in which the ground surface was assumed to have zero heat storage. Similar approaches were subsequently adopted by Mahrer and Pielke (1977a, b), Estoque and Gross (1981), and others.

With the heat budget method, the conductive Q_G, convective Q_C, and radiative Q_R contributions of heat to the ground surface are balanced, resulting in an equilibrium surface temperature. Written more formally,

$$-Q_G + Q_C + Q_R = 0.$$

In the soil, in general,

$$|Q_G| \gg |Q_C| \qquad \text{and} \qquad |Q_G| \gg |Q_R|,$$

so that only ground conduction is retained as the principal contribution to the heat balance. (When rain falls or snow melts and percolates into the soil, substantial heat can be transferred, so these inequalities may not be satisfied.)

In the atmosphere, the inequalities are reversed, that is,

$$|Q_C| \gg |Q_G| \qquad \text{and} \qquad |Q_R| \gg |Q_G|,$$

since molecular transfers of heat in turbulent air are ineffective compared to radiation and convection [as discussed in Section 5.1 for convection; i.e., $e_{u_i}^2/S^2 \gg v/LS$ in Eq. (5-2)].

Retaining the symbol Q_G to refer to ground heat conduction, the convective and radiative heat transfers in the atmosphere can be written as

$$Q_C = -\bar{\rho} C_p \overline{w''\theta''} - \bar{\rho} L_v \overline{w''q_3''}$$

and

$$Q_R = Q_N = (1 - A)(\bar{R}\downarrow_{sw_G} + \bar{R}^D_{sw_G}) + \bar{R}\downarrow_{LW_G} - \bar{R}\uparrow_{LW_G},$$

where the formulations for the turbulent sensible and latent heat fluxes Q_C are obtained using expressions such as Eq. (7-29) and Q_R is composed of direct and diffuse shortwave radiation [such as from Eq. (8-63)] and of upward and

downward longwave radiation [such as from Eq. (8-39) evaluated at the ground level]. The quantity Q_N is called the *net radiation*. An example of this balance of heat fluxes,

$$+ Q_G + \bar{\rho} C_p \overline{w'' \theta''} + \bar{\rho} L_v \overline{w'' q_3''} - (1 - A)(\bar{R} \!\downarrow_{\text{sw}_G} + \bar{R}^D_{\text{sw}_G})$$

$$- \bar{R} \!\downarrow_{\text{lw}_G} + \bar{R} \!\uparrow_{\text{lw}_G} = 0, \tag{11-33}$$

is illustrated in Figure 11-18 for a location in Saudi Arabia. The length of the arrows plotted in the figure represent examples of the relative magnitudes of these fluxes, where the vector sum is 0 since the interface is assumed to be infinitesimally thin and to have no heat storage.

An additional term can be added to Eq. (11-33) if anthropogenic or natural sources and sinks of heat exist (Grimmond and Oke 1999; Masson 2000). When
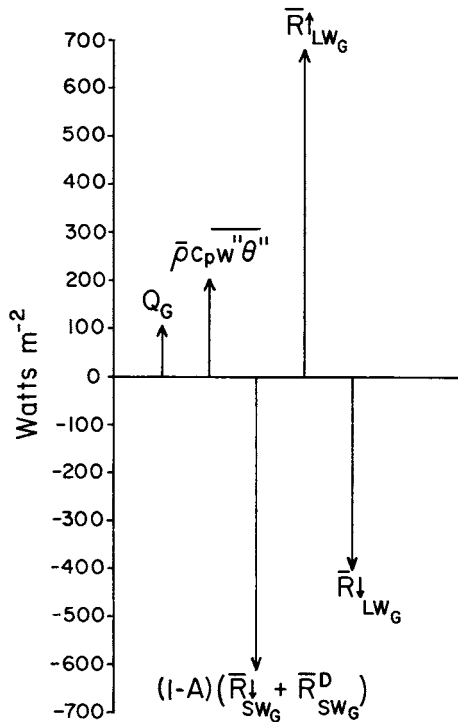
Fig. 11-18.   Average heat fluxes at 1300 LST observed over the Empty Quarter of Saudi Arabia. A positive value represents a loss to the surface and a negative value is a gain. The sum of the fluxes equals 0. Over the Empty Quarter, the latent heat flux is essentially 0. (From Eric Smith, CSU 1982, personal communication.)

this is important, the heat budget should be written as

$$+ Q_G + \bar{\rho}C_p\overline{w''\theta''} + \bar{\rho}L_v\overline{w''q_3''} - (1-A)(\bar{R}\downarrow_{sw_G} + \bar{R}^D_{sw_G})$$
$$- \bar{R}\downarrow_{lw_G} + \bar{R}\uparrow_{lw_G} + Q_m = 0, \qquad (11\text{-}34)$$

where $Q_m > 0$ could refer to waste heat from heating or air conditioning in a city, heat from a forest fire or volcano, etc. Ichinose *et al.* (1999), for example, found that Q_m in central Tokyo, Japan exceeded 400 W m^{-2} in the daytime in the winter, with a maximum value of 1590 W m^{-2}.

Since at the ground, $u = 0$, in the expression for the grid-volume average for $R\uparrow_{lw}$ in Eq. (8-39), $\bar{R}\uparrow_{lw_G} = \sigma\overline{T}_G^4$ if a ground emissivity of $\epsilon_G = 1$ is assumed. The temperature of the ground surface, $\overline{T}_G$, is called the *equilibrium surface temperature*. If $\epsilon_G < 1$, then the upward longwave flux from the ground should be written as

$$\bar{R}\uparrow_{lw_G} = \epsilon_G\sigma\overline{T}_G^4 + (1-\epsilon_G)\bar{R}\downarrow_{lw_G} . \qquad (11\text{-}35)$$

The second term on the right side of Eq. (11-35) is the reflection of downward longwave radiation when $\epsilon_G \neq 1$. In this situation, the ground does not radiate as a blackbody [the definition of which is given after Eq. (8-6)]. Most ground surfaces, however, radiate close to a blackbody, as shown in Table 11-2. As discussed by Lee (1978:71), values of $\epsilon_G = 0.95$ and $\overline{T}_G = 25°C$ and an effective radiating temperature of the air above the surface[25] of 20°C results in a relative error of -1% when Eq. (11-35) is used with $\epsilon_G = 1$.

Some modelers (e.g., Estoque and Gross 1981) have used an empirical relation to estimate the net longwave radiation reaching the ground. However, such formulas use only data that can be derived from the surface and neglect the overlying moisture stratification. Kondratyev (1969) cautions against using such formulas for time periods shorter than monthly averages.

One formulation (given by Idso and Jackson 1969 and Lee 1978) used to estimate monthly averaged net longwave radiation at the ground is

$$\bar{R}\downarrow_{lw_G} - \bar{R}\uparrow_{lw_G} = \sigma\big[\{E_a(1-c) + c\}\overline{T}_a^4 - \overline{T}_G^4\big],$$

where

$$E_a = 1 - 0.261\exp\big(-7.77 \times 10^{-4}(273 - \overline{T}_a)^2\big).$$

The constants in this expression are empirically derived and are needed to account for the absorption of radiation by CO_2 and O_3 at the measurement sites used to derive this expression. The temperature $\overline{T}_a$ is determined at Stevensen screen height ($\sim$1.5 m), and c is the fraction of the sky covered by clouds.

TABLE 11-2

Emissivities of Longwave Radiation for Representative
Types of Ground Covers

Ground cover	ϵ
Fresh snow	0.99[a]
Old snow	0.82[a]
Dry sand	0.95[b], 0.914[c]
Wet sand	0.98[b], 0.936[c]
Dry peat	0.97[b]
Wet peat	0.98[b]
Soils	0.90–0.98[a]
Asphalt	0.95[a], 0.956[c]
Concrete	0.71–0.90[a], 0.966[c]
Tar and gravel	0.92[a]
Limestone gravel	0.92[b]
Light sandstone rock	0.98[b]
Desert	0.84–0.91[a]
Grass lawn	0.97[b]
Grass	0.90–0.95[a]
Deciduous forests	0.97–0.98[a], 0.95[b]
Coniferous forests	0.97–0.98[a], 0.97[b]
Range over an urban area	0.85–0.95[a]
Pure water	0.993[c]
Water plus thin film of petroleum oil	0.972[c]

[a] From Oke (1973:15, 247).
[b] From Lee (1978:69).
[c] From Paltridge and Platt (1976:135).

Soil Heat Flux.   The rate of conduction of heat within the soil, $Q_G = v\,\partial T/\partial z|_G$, can be evaluated from a one-dimensional diffusion equation[26] within the soil,

$$\frac{\partial T}{\partial t} = \frac{\partial}{\partial z}\frac{v}{\rho c}\frac{\partial T}{\partial z}, \tag{11-36}$$

where v, c, and ρ are the thermal conductivity, specific heat capacity, and soil density, respectively. The $v/\rho c = k_s$ is called the *thermal diffusivity*.[27] The quantity k_s determines the speed of penetration of a temperature wave into the soil, and v indicates the rate of heat transport. The temperature gradient at ground level is $\partial T/\partial z|_G$. Examples of values of these parameters for different types of soils are given in Table 11-3.

   Soil conductivity depends on a number of factors, including the conductivity of the individual soil particles, their sizes, the compaction of the soil as measured by porosity, and the soil moisture. Soil particle size, for example, can vary widely from on the order of 1 μm for clay to 100 μm for sand. In addition,

TABLE 11-3

Representative Values of Thermal Conductivity v, Specific Heat Capacity, c, Density, ρ, and Thermal Diffusivity, k_s, for Various Types of Surfaces

Concrete	4.60^a	879^a	$2.3^a \times 10^3$	$2.3^a \times 10^{-6}$
Rock	2.93^a	753^a	$2.7^a \times 10^3$	$1.4^a \times 10^{-6}$
Ice	2.51^a	2093^a	$0.9^a \times 10^3$	$1.3^a \times 10^{-6}$
		2100^b	$0.92^b \times 10^3$	$1.16^b \times 10^{-6}$
Snow				
New	0.14^a	2093^a	$0.2^a \times 10^3$	0.3×10^{-6}
	0.08^b	2090^b	$0.10^b \times 10^3$	$0.1^b \times 10^{-6}$
Old	1.67^a	2093^a	$0.8^a \times 10^3$	$1.0^a \times 10^{-6}$
	0.42^b	2090^b	$0.48^b \times 10^3$	$0.4^b \times 10^{-6}$
Nonturbulent air	$0.03^a, 0.02^c,$	1005	$0.0012^a \times 10^3$	$21^a \times 10^{-6}$
	0.025^b			
Clay soil (40% pore space)				
Dry	0.25^b	890^b	$1.6^b \times 10^3$	$0.18^b \times 10^{-6}$
10% liquid water	0.63^a	1005^a	$1.7^a \times 10^3$	$0.37^a \times 10^{-6}$
20% liquid water	1.12^a	1172^a	$1.8^a \times 10^3$	$0.53^a \times 10^{-6}$
30% liquid water	1.33^a	1340^a	$1.9^b \times 10^3$	$0.52^b \times 10^{-6}$
40% liquid water	1.58^b	1550^b	$2.0^b \times 10^3$	$0.51^b \times 10^{-6}$
Sand soil (40% pore space)				
Dry	0.30^b	800^b	$1.6^b \times 10^3$	$0.24^b \times 10^{-6}$
10% liquid water	1.05^a	1088^a	$1.7^a \times 10^3$	$0.57^a \times 10^{-6}$
20% liquid water	1.95^a	1256^a	$1.8^a \times 10^3$	$0.85^a \times 10^{-6}$
30% liquid water	2.16^a	1423^a	$1.9^a \times 10^3$	$0.80^a \times 10^{-6}$
40% liquid water	2.20^b	1480^b	$2.0^b \times 10^3$	$0.74^b \times 10^{-6}$
Peat soil (80% pore space)				
Dry	0.06^b	1920^b	$0.3^b \times 10^3$	$0.10^b \times 10^{-6}$
10% liquid water	0.10^a	2302^a	$0.4^a \times 10^3$	$0.12^a \times 10^{-6}$
40% liquid water	0.29^a	3098^a	$0.7^a \times 10^3$	$0.13^a \times 10^{-6}$
70% liquid water	0.43^a	3433^a	$1.0^a \times 10^3$	$0.13^a \times 10^{-6}$
80% liquid water	0.50^b	3650^b	$1.1^a \times 10^3$	$0.12^b \times 10^{-6}$
Light soil with roots	0.11^c	1256^c	$0.3^c \times 10^3$	$0.30^c \times 10^{-6}$
Liquid water	$0.63^a, 0.57^b$	4186^a	$1.0^a \times 10^3$	0.15×10^{-6}

[a] From Lee (1978:87).
[b] From Oke (1973:38).
[c] From Rosenberg (1974:66).

although it is not considered here, heat can be transferred by the percolation of water and change of phase of water. The freezing and thawing of soils, for example, contributes significantly to the heat budget within the soil (see, e.g., Viterbo *et al.* 1999).

When water is present in the soil, its heat capacity, density, and thermal conductivity vary depending on the amount of water present. As reported in

McCumber (1980),

$$\rho c = (1 - \eta_s)\rho_i c_i + \eta\rho_w c_w, \tag{11-37}$$

where η_s is the saturation moisture content (its porosity), η is the volumetric moisture content (cm^3 cm^{-3}), and $\rho_i c_i$ is the product of the density and heat capacity of the dry soil type i (η and η_s are discussed in more detail shortly). The density and specific heat capacity of water $\rho_w c_w$ are given in Table 11-3. Equation (11-37) is simply a weighting of the contributions to the volumetric heat capacity of the dry soil and of the liquid water that is present. The heat capacity of air has been omitted, since it is negligibly small compared to the other two terms.

The thermal conductivity varies over several orders of magnitude as soil dries out. McCumber (1980), referring to empirical date of Al Nakshabandi and Kohnkes (1965), expresses v in units of J/(m s °C) as

$$v = \begin{cases} 419\exp -[(P_f + 2.7)], & P_f \le 5.1 \\ 0.172, & P_f > 5.1, \end{cases}$$

where P_f is the base-10 logarithm of the magnitude of the moisture potential Ψ. [Moisture potential is defined after Eq. (11-46).] Figure 11-19 illustrates the strong dependence of heat diffusivity on moisture potential. As shown by Al Nakshabandi and Kohnke (1965), moisture potential is virtually independent of the soil type, so that it is convenient to express v in this form.

Equation (11-36) is of the same form as discussed in Chapter 10, Section 10.1.2 and can be solved on a vertical grid lattice by the implicit finite difference solution technique given by Eq. (10-27). Since the largest gradients in the diurnal variation of temperature are observed within 50 cm or so of soil surfaces (see, e.g., Figure 11-20), very fine resolution is required in such representations. McCumber (1980) and McCumber and Pielke (1981) used vertical grids of 0, 0.5, 1.5, 3, 5, 8, 12, 18, 26, 36, 48, 62, 79, and 100 cm in simulations of heat and moisture fluxes within various types of soils.

If the thermal diffusivity is a constant, then an analytic solution to Eq. (11-36) is possible. Rewriting Eq. (11-36) as

$$\frac{\partial T}{\partial t} = k_s \frac{\partial^2 T}{\partial z^2}, \tag{11-38}$$

let the temperature at the surface at time t be given by $T(0, t) = T_0 \cos \omega t$, where ω is the frequency of the heating. Also require that the temperature always be finite. Similar to the substitution used in the solution of the sea-breeze model given in Chapter 5, Section 5.2.3.1, let

$$T(z, t) = \widehat{T}(z)e^{i\omega t},$$
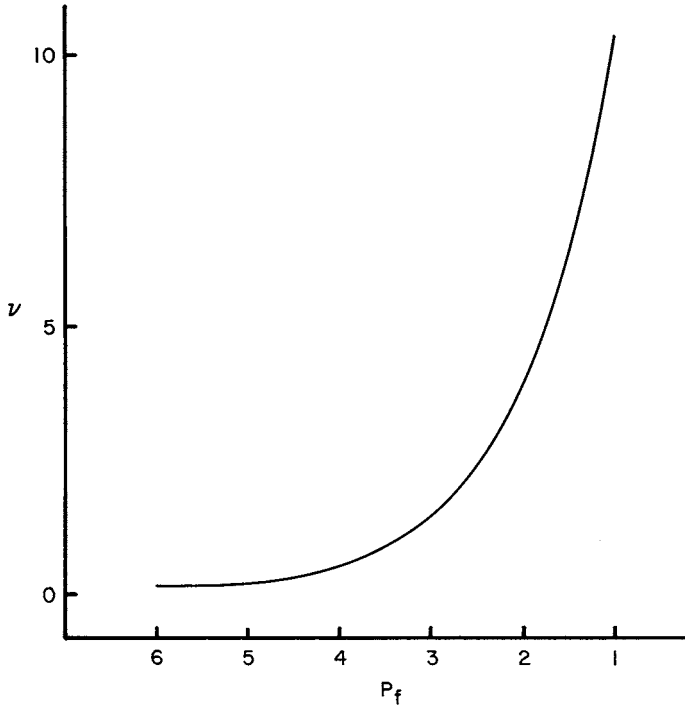
Fig. 11-19.   Dependence of soil thermal conductivity on moisture potential. The magnitude of the base-10 logarithm of the moisture potential in centimeters is P_f [i.e., $P_f = \log_{10} \Psi$ (cm)]. The thermal conductivity v is plotted in units of J/(m s °C). This diagram corresponds to Figure 4 in Al Nakshabandi and Kohnke (1965). (From McCumber 1980, Figure 2.)

so that a periodic solution is assumed in time but not with depth. Substituting this relation for $T(z, t)$ into Eq. (11-38) yields the ordinary differential equation

$$\frac{d^2\widehat{T}(z)}{dz^2} - \frac{i\omega}{k_s}\widehat{T}(z) = 0.$$

As can be shown by substitution, this differential equation has a solution of the form

$$\widehat{T}(z) = a_1 \exp\left(-\sqrt{(i\omega/k_s)}z\right) + a_2 \exp\left(\sqrt{(i\omega/k_s)}z\right),$$

where a_1 and a_2 are constants of integration. Since $\sqrt{i} = (i + 1)/\sqrt{2}$,[28] this expression can also be written as

$$\widehat{T}(z) = a_1 \exp\left[-(i + 1)\sqrt{(\omega/2k_s)}z\right] + a_2 \exp\left[(i + 1)\sqrt{(\omega/2k_s)}z\right].$$
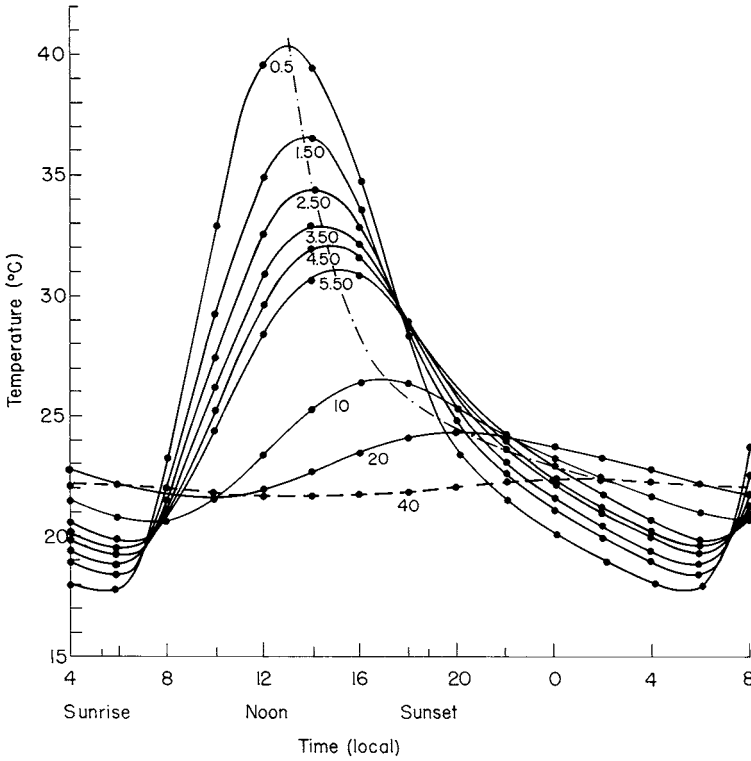
Fig. 11-20. Average diurnal temperature variations at various depths (in centimeters) in the ground, based on the University of Texas observations from 0.5 to 5.5 cm and the Johns Hopkins University observations below 10 cm taken at O'Neill, Nebraska in the summer of 1953. The dash–dot curve represents the locus of the temperature maxima. (From Kuo 1968.)

From the requirement that $T(z, t)$ be finite, a_2 is identically equal to 0. Thus the temperature as a function of depth is given by

$$T(z, t) = a_1 \exp\left(-\sqrt{(\omega/2k_s)}z\right) \exp i\left[(\omega t - \sqrt{(\omega/2k_s)}z)\right].$$

Since only the real portion of this solution has physical significance, the desired solution is

$$T(z, t) = a_1 \exp\left[-\sqrt{(\omega/2k_s)}z\right] \cos\left(\omega t - \sqrt{(\omega/2k_s)}z\right), \qquad (11\text{-}39)$$

where the identity $e^{i\theta} = \cos\theta + i\sin\theta$ has been used. Using the boundary condition at $z = 0$,

$$T(0, t) = a_1 \cos \omega t = T_0 \cos \omega t,$$

so that $a_1 = T_0$. The final desired solution is thus

$$T(z, t) = T_0 \exp\left[-\sqrt{(\omega/2k_s)}z\right] \cos\left(\omega t - \sqrt{(\omega/2k_s)}z\right).$$

The properties of this solution are that (1) the temperature within the soil varies in time with the same frequency as at the surface, (2) the amplitude is a maximum at the surface and decreases exponentially downward, and (3) there is a phase shift in the solution with depth. These aspects of the solution are illustrated in Figure 11-20. In addition, (1) the greater the frequency of heating and cooling at the surface, the more rapidly the temperature perturbation diminishes with depth (i.e., diurnal heating dampens more rapidly with depth than seasonal temperature changes), and (2) the larger the diffusivity, k_s, the more slowly the temperature perturbation diminishes with depth.

Soils generally are not homogeneous with depth. Nonetheless, this simple model provides a useful theoretical framework for understanding the rate of transfer of heat into the ground, as illustrated in Figure 11-20.

An integrated form of Eq. (11-36) can also be used to compute the soil heat flux Q_G. Assuming that ρ and c are constant with depth, Eq. (11-36) can be rewritten as

$$c\rho \frac{\partial T}{\partial t} = \frac{\partial}{\partial z} v \frac{\partial T}{\partial z} = \frac{\partial}{\partial z} Q_s, \qquad (11\text{-}40)$$

where Q_s is the heat flux within the soil. Integrating Eq. (11-40) between the surface and a depth δ_z sufficiently deep so that $Q_s \equiv 0$ yields

$$Q_G = \rho c \int_{-\delta_z}^{0} \frac{\partial T}{\partial t} \, dz. \qquad (11\text{-}41)$$

Integrating the temporal temperature changes within the soil using this expression could provide a more accurate estimate of the soil heat flux at ground level than computing Q_G from $Q_G = v\partial T/\partial z|_G$. The quantity Q_G is also called the *heat storage* term.

Albedo.   The amount of solar radiation impinging on a horizontal surface is a function of such factors as latitude, cloud cover, and time of year and of day (see Section 8.4). In this discussion, the only additional information required is the effect of terrain slope $\partial z_G/\partial x$ and $\partial z_G/\partial y$, albedo A, and ground wetness. This latter input is needed, for example, to estimate the relative partitioning between latent and sensible turbulent heat fluxes in Eqs. (11-33) and (11-34).

The albedo of a surface is the fractional reflectance of radiation that reaches it. Although albedo is a function of wavelength, in mesoscale meteorology it usually refers to the reflectance of solar radiation, both direct and diffuse. Exam-

ples of representative albedos for a range of characteristic soils and other bare surfaces are given in Table 11-4, which shows that, for instance, fresh snow can reflect up to 95% of the solar radiation that reaches it, whereas dark soil (e.g., wet peat) reflects only 5%.

The albedo is not a constant at a given location, even with a uniform surface, but rather varies as a function of sun zenith angle as well as soil wetness (e.g., McCumber 1980). As reported in McCumber (1980), the variability of albedo with zenith angle, Z, has been estimated empirically, based on the work of Idso *et al.* (1975a), and the influence of wetness has been given by Idso *et al.* (1975a) and Gannon (1978). The effect of zenith angle and wetness on albedo can be represented mathematically as

$$A = A_Z + A_s, \tag{11-42}$$

where

$$A_Z = \left[\exp \left(0.003286 Z^{1.5} \right) - 1 \right]/100$$

and A_s is a function of the ratio of the volumetric moisture content η, and porosity η_s, of the soil. Figure 11-21 plots the functional form of A_Z. The functional form of A_s is not available for all soil types; Idso *et al.* (1975a) gives its value for Avondale loam soil as

$$A_s = \begin{cases} 0.31 - 0.34\Delta, & \Delta \le 0.5 \\ 0.14, & \Delta > 0.5, \end{cases}$$

with $\Delta = \eta/\eta_s$. For Florida peat, Gannon gives

$$A_s = \begin{cases} 0.14(1 - \Delta), & \Delta \le 0.5 \\ 0.07, & \Delta > 0.5. \end{cases} \tag{11-43}$$

Using these expressions for A_Z and A_s in Eq. (11-42), it is evident that albedos are larger when the sun is lower in the sky and for drier soils. For example, as given by A_s for Avondale loam, the albedo is 0.31 for dry soil (i.e., $\Delta = 0$) but decreases by more than 50%, to 0.14, for wet soils (i.e., $\Delta > 0.5$). Idso *et al.* (1975b) have provided additional details on the influence of soil moisture on albedo and other components of the surface energy budget. Otterman (1974), Berkofsky (1977), and others have argued that changes in albedo can have a profound influence on average vertical motion, with increased albedo (caused by overgrazing, for example) causing subsidence and a tendency toward *desertification* in arid areas. Viterbo and Betts (1999) demonstrated the improvement in synoptic weather prediction accuracy when a more accurate representation of the albedo of snow in the boreal forest is included.

TABLE 11-4

Albedo of Shortwave Radiation for Assorted Types of Ground Covers

Ground cover	A
Fresh snow	0.75–0.95[b], 0.70–0.95[c], 0.80–0.95[d], 0.95[e]
Fresh snow (low density)	0.85[f]
Fresh snow (high density)	0.65[f]
Fresh dry snow	0.80–0.95[g]
Pure white snow	0.60–0.70[g]
Polluted snow	0.40–0.50[g]
Snow, several days old	0.40–0.70[b], 0.70[c], 0.42–0.70[d], 0.40[e]
Clean old snow	0.55[f]
Dirty old snow	0.45[f]
Clean glacier ice	0.35[f]
Dirty glacier ice	0.25[f]
Glacier	0.20–0.40[e]
Dark soil	0.05–0.15[b], 0.05–0.15[g]
Dry clay or gray soil	0.20–0.35[b], 0.20–0.35[g]
Dark organic soils	0.10[f]
Clay	0.20[f]
Moist gray soils	0.10–0.20[g]
Dry clay soils	0.20–0.35[d]
Dry light sand	0.25–0.45[b]
Dry light sandy soils	0.25–0.45[g]
Dry sandy soils	0.25–0.45[d]
Light sandy soils	0.35[f]
Dry sand dune	0.35–0.45[b], 0.37[c]
Wet sand dune	0.20–0.30[b], 0.24[c]
Dry light sand, high sun	0.35[f]
Dry light sand, low sun	0.60[f]
Wet gray sand	0.10[f]
Dry gray sand	0.20[f]
Wet white sand	0.25[f]
Dry white sand	0.35[f]
Peat soils	0.05–0.15[d]
Dry black coal spoil, high sun	0.05[f]
Dry concrete	0.17–0.27[b], 0.10–0.35[e]
Road, blacktop	0.05–0.10[b]
Asphalt	0.05–0.20[e]
Tar and gravel	0.08–0.18[e]
Long grass (1.0 m)	0.16[e]
Short grass (2 cm)	0.26[e]
Wet dead grass	0.20[f]
Dry dead grass	0.30[f]
Typical fields	0.20[f]
Dry steppe	0.25[f], 0.20–0.30[g]

<div align="center">

TABLE 11-4

Continued

</div>

Ground cover	A
Tundra and heather	0.15[f]
Tundra	0.18–0.25[e], 0.15–0.20[g]
Meadows	0.15–0.25[g]
Cereal and tobacco crops	0.25[f]
Cotton, potato, and tomato crops	0.20[f]
Sugar cane	0.15[f]
Agricultural crops	0.18–0.25[e], 0.20–0.30[d]
Rye and wheat fields	0.10–0.25[g]
Potato plantations	0.15–0.25[g]
Cotton plantations	0.20–0.25[g]
Orchards	0.15–0.20[e]
Deciduous forests, bare of leaves	0.15[e]
Deciduous forests, leaved	0.20[e]
Deciduous forests	0.15–0.20[g]
Deciduous forests, bare with snow on the ground	0.20[d]
Mixed hardwoods in leaf	0.18[f]
Rain forest	0.15[f]
Eucalyptus	0.20[f]
Forest	
Pine, fir, oak	0.10–0.18[c]
Coniferous forests	0.10–0.15[g], 0.10–0.15[d]
Red pine forests	0.10[f]
Urban area	0.10–0.27, with an average of 0.15[e]
Water	$-0.0139 + 0.0467 \tan Z$ $1 \geq A \geq 0.03$[h]

[a]The smaller number is for high solar zenith angles, while the larger albedo is more representative for low sun angles.

[b]From Sellers (1965:21).

[c]From Munn (1966:15).

[d]From Rosenberg (1974:27).

[e]From Oke (1973:15, 247).

[f]From Lee (1978:58–59).

[g]From de Jong (1973).

[h]From Atwater and Ball (1981:879).

Soil Moisture Flux Representation.   Determination of η and η_s requires a model of the flux of moisture into and out of the soil. Detailed relationships for computing the temporal fluctuations in soil moisture content are available (e.g., Philip 1957) and have been used in atmospheric models such as those of Sasamori (1970) and Garrett (1978). Beljaars *et al.* (1996) and Viterbo and Betts (1999) demonstrated the importance of accurate soil moisture values in the context of numerical weather prediction. In this section, we explore the approach used by McCumber. Other useful discussion of the parameterization
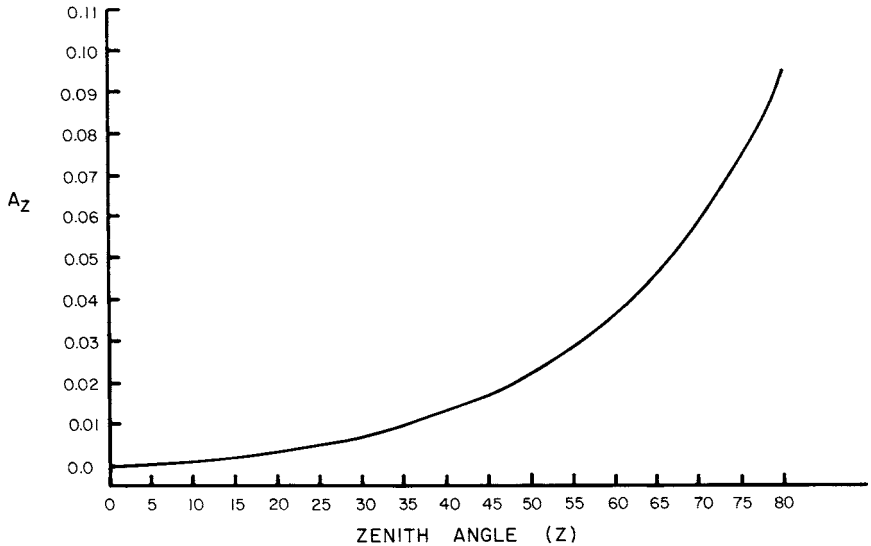
Fig. 11-21. Albedo as a function of zenith angle Z. The enhancement to the surface albedo is expressed as a fractional increase relative to its value when the sun is directly overhead. (From McCumber 1980.)

of heat and moisture flows in and at the surface of soils are given in Camillo and Schmugge (1981), Sievers *et al.* (1983), Lee and Pielke (1992), and Mihailovic *et al.* (1993, 1995, 1999a). Shao and Irannejad (1999) compare the impact of four soil hydraulic models on land-surface processes.

The derivation of equations for soil moisture flux is presented in most courses in hydrology. For use in mesoscale meteorological models in which the determination of the soil moisture at the surface W_G is required, the following form (McCumber 1980) can be used.

In Chapter 2, the conservation-of-motion relation for the atmosphere was derived. A similar expression can be derived for the conservation of motion of water within the soil. For short-term (~24 hours) mesoscale atmospheric applications, the vertical transport of water in the soil is usually much more significant than horizontal transport, so that only the vertical equation-of-water movement need be considered. The neglect of horizontal advection within the ground on these time periods arises because the movement of water through soil is usually relatively slow relative to atmospheric transports, and the horizontal gradients of water are generally assumed to be much less than vertical gradients. For longer time periods, however, as shown by Walko *et al.* (2000a), surface and subsurface flow over water can significantly alter the amount of water available for evaporation and transpiration into the atmosphere. In this section, however, we retain the short-term mesoscale focus of this book.

Therefore, using only the vertical equation of motion and assuming horizontal homogeneity,

$$\frac{\partial w}{\partial t} + w\frac{\partial w}{\partial z} = -\frac{1}{\rho_w}\frac{\partial p}{\partial z} - g + F_w,$$

where F_w is the dissipation of water motion by viscous forces. In the atmosphere, as discussed after Eq. (3-29), scale arguments were used to show that, away from the ground, molecular dissipation of air motion was much smaller than the advective transport of air. This is not generally the case in soil.

If it is further assumed that local changes in vertical velocity are small relative to the other terms, the Reynolds number is much less than unity, and F_w can be parameterized[29] by

$$F_W = \frac{\mu_w}{\rho_w}\nabla^2 w,$$

(where ρ_w and μ_w are the density and the dynamic viscosity of water, respectively), then the vertical equation-of-water movement is given by

$$0 = -\frac{1}{\rho_w}\frac{\partial p}{\partial z} - g + \frac{\mu_w}{\rho_w}\nabla^2 w. \tag{11-44}$$

As with the atmospheric equations (as discussed in Chapter 4), this differential equation is averaged over a grid volume. The need for averaging in the soil, however, is different than the reason for performing this operation in the atmosphere. In a mesoscale atmospheric model, averaging is required because sufficient computer resources are unavailable to solve the conservation relations at intervals of 1 cm or so. In the soil, however, averaging is needed because otherwise, the conservation relation for vertical water movement would have to be evaluated separately for each grain of soil and interconnecting air space.

The averaging volume is defined as

$$\Delta V = \int_{\Delta v} dv = \int_{\eta_s \Delta V} dv + \int_{(1-\eta_s)\Delta V} dv, \tag{11-45}$$

where $\Delta V = \Delta x \Delta y \Delta z$ and η_s (the *porosity*) is the fraction of the soil volume containing air space (also called void space). Because the transfer of water is much more rapid through the air spaces between soil grains than through the soil material itself, Eq. (11-44) is averaged using the first integral on the right side of Eq. (11-45).

The first term on the right side of Eq. (11-44), after averaging, becomes

$$\int_{\eta_s \Delta V} \frac{1}{\rho_w}\frac{\partial p}{\partial z} dv = \frac{1}{\rho_w}\frac{\overline{\partial p}}{\partial z}\eta_s \Delta V = \frac{1}{\rho_w}\frac{\partial \bar{p}}{\partial z}\eta_s \Delta V,$$

where $\overline{\partial p/\partial z} = \partial \bar{p}/\partial z$ because the averaging volume is not a function of depth. The gravitational acceleration term is straightforward and becomes

$$\int_{\eta_s \Delta V} g \, dv = g \eta_s \Delta V.$$

The third term on the right side of Eq. (11-44) is rewritten as

$$\frac{\mu_w}{\rho_w} \nabla^2 w = \alpha \frac{\mu_w}{\rho_w} \frac{u_d}{d^2}, \tag{11-46}$$

where d is a length scale, u_d is a velocity scale (called the Darcian velocity) representing the mean velocity of water flow through the soil, and α is a proportionality factor. This formulation is based on the dimensions of the component terms in $\nabla^2 w$. Assuming that each term in Eq. (11-46) except α is constant in the averaging volume, the integrated form of this expression is given as

$$\int_{\eta_s \Delta V} \frac{\mu_w}{\rho_w} \alpha \frac{u_d}{d^2} \, dV = \frac{\mu_w}{\rho_w} \bar{\alpha} \frac{u_d}{d^2} \eta_s \Delta V.$$

Equation (11-44) can now be written as

$$0 = -\frac{1}{\rho_w} \frac{\partial \bar{p}}{\partial z} \eta_s \Delta V - g \eta_s \Delta V + \frac{\mu_w}{\rho_w} \bar{\alpha} \frac{u_d}{d^2} \eta_s \Delta V$$

or, after rearranging,

$$g + \frac{1}{\rho_w} \frac{\partial \bar{p}}{\partial z} = \frac{\mu_w}{\rho_w} \bar{\alpha} \frac{u_d}{d^2}.$$

Solving for u_d yields

$$u_d = g \frac{\rho_w d^2}{\mu_w \bar{\alpha}} \frac{\partial}{\partial z} \left(z + \frac{\bar{p}}{g \rho_w} \right)$$

or

$$u_d = K_\eta \frac{\partial}{\partial z} (z + \Psi),$$

where $K_\eta = (g d^2/\mu_w \bar{\alpha}) \rho_w$ is called the *hydraulic conductivity* and $\Psi = -\bar{p}/g \rho_w$ is called the *moisture potential*. The exchange coefficient K_η accounts for the influence of gravity drainage in the viscous soil, and Ψ represents the potential energy needed to extract water against capillary and adhesive forces in the soil.

The soil moisture flux is thus given as

$$W_s = \rho_w u_d = \rho_w K_\eta \frac{\partial}{\partial z} (z + \Psi). \tag{11-47}$$

With the specification of the soil moisture flux, the local time rate of change of the volumetric moisture content η is given by

$$\frac{\partial \eta}{\partial t} = \frac{1}{\rho_w} \frac{\partial W_s}{\partial z}, \tag{11-48}$$

where, consistent with the derivation of Eq. (11-44), advection of water is neglected. In addition, sources and sinks of water, such as from rainfall, are neglected.

Equation (11-47) can also be written as

$$W_s = D_\eta \rho_w \frac{\partial \eta}{\partial z} + K_\eta \rho_w, \tag{11-49}$$

where the chain rule of calculus has been used to write $D_\eta = K_\eta \partial \Psi / \partial \eta$.

The parameters of K_η, D_η, and Ψ are related to η using a set of empirical relations reported in Clapp and Hornberger (1978) and given as

$$\Psi = \Psi_s \left(\frac{\eta_s}{\eta} \right)^b, \quad K_\eta = K_{\eta_s} \left(\frac{\eta}{\eta_s} \right)^{2b+3}, \quad \text{and} \quad D_\eta = -\frac{b K_{\eta_s} \Psi_s}{\eta} \left(\frac{\eta}{\eta_s} \right)^{b+3},$$

where Ψ_s and K_{η_s} refer to the saturated soil values. McCumber (1980) listed a table of these parameters (reproduced here as Table 11-5) as a function of 11 U.S. Department of Agriculture (1951) soil textural classes plus peat.

Another option uses the work of van Genuchten (1980). In his work, as reported in Walko *et al.* (1998, 2000a),

$$K_\eta = K_{\eta_s} \eta_e^{0.5} [1 - (1 - \eta^{1/m})^m]^2$$

$$\Psi = \frac{1}{a_1} [(\eta_e)^{-1/m} - 1]^{1/n}$$

with

$$\eta_e = \frac{\eta - \eta_r}{\eta_s - \eta_n}.$$

The variable η_n is the minimum possible value of η, and a, m, and n are empirical parameters given by Carsel and Parrish (1988).

In these formulations, K_{η_s} can be assumed to decrease exponentially, based on the work of Beven (1982, 1984),

$$K_{\eta_s}(z) = K_0 e^{f\hat{z}},$$

where f^{-1} is the *e*-folding depth of K_{η_s}. The height $\hat{z}$ is the distance below the ground surface. The use of these formulations is discussed further in Walko *et al.* (2000a).

Solving Eq. (11-48) at the surface permits the determination of A_s for use in Eq. (11-42), which is needed in the surface heat budget calculation. In addition,

TABLE 11-5

Soil Parameters as a Function of 11 U. S. Department of Agriculture
(USDA 1951) Textural Classes Plus Peat

Soil type	η_s	Ψ_s	K_{η_s}	b	η_{wilt}	$\rho_i c_i$
Sand	.395	−12.1	.01760	4.05	.0677	1.47
Loamy sand	.410	−9.0	.01563	4.38	.0750	1.41
Sandy loam	.435	−21.8	.00341	4.90	.1142	1.34
Silt loam	.485	−78.6	.00072	5.30	.1794	1.27
Loam	.451	−47.8	.00070	5.39	.1547	1.21
Sandy clay loam	.420	−29.9	.00063	7.12	.1749	1.18
Silty clay loam	.477	−35.6	.00017	7.75	.2181	1.32
Clay loam	.476	−63.0	.00025	8.52	.2498	1.23
Sandy clay	.426	−15.3	.00022	10.40	.2193	1.18
Silty clay	.492	−49.0	.00010	10.40	.2832	1.15
Clay	.482	−40.5	.00013	11.40	.2864	1.09
Peat	.863	−35.6	.00080	7.75	.3947	0.84

Units for soil porosity (η_s) are centimeters per centimeters cubed, saturated moisture potential (Ψ_s) is in centimeters, and saturated hydraulic conductivity (K_{η_s}) is expressed in centimeters per second. The exponent b is dimensionless. Permanent wilting moisture content (η_{wilt}) is in centimeters cubed per centimeters cubed, and it corresponds to 153 m (15 b) suction. Dry volumetric heat capacity ($\rho_i c_i$) is in joules per centimeter cubed per degree Celsius. The first four variables for the USDA textures are reproduced from Clapp and Hornberger (1978). Table adapted from McCumber (1980). Recent values for the saturated hydraulic conductivity for peat range from 1×10^{-5} centimeters per second for deeply humidified sapric peat to 2.8×10^{-2} centimeters per second in relatively undecomposed fibric peat. Average soil porosity ranges from 0.83 to 0.93 (Letts *et al.* 2000).

as shown after Eq. (11-52), η is needed in the determination of the equilibrium moisture value at the ground surface.

Figures 11-22, 11-23, 11-24, and 11-25,[30] reproduced from McCumber (1980), illustrate the influence of different types of bare soil on diurnal variations of surface temperature, specific humidity, sensible heat flux, and latent heat flux. As shown in Figure 11-22, for example, a sand surface has a much larger variation in temperature than the other soils (as evident by anyone who has walked on a beach in the summer), whereas peat and marsh have the largest excursions in surface moisture (Figure 11-23). McCumber concluded that the large excursions in the sand temperature were a result of its inability to hold water effectively and to transfer it up from below, whereas peat and marsh, even with their much lower albedos than sand, had less variability because of the efficiency with which incoming radiation was used to cause evaporation as opposed to an elevation in surface temperature.

From his results, McCumber (1980) concluded that soil moisture and albedo were the two most important controls for regulating feedback to the atmosphere from bare soils. The amount of soil moisture determined the fractional partitioning of sensible and latent subgrid-scale fluxes, and the albedo was a crucial parameter in determining the available radiation reaching the surface. Physick
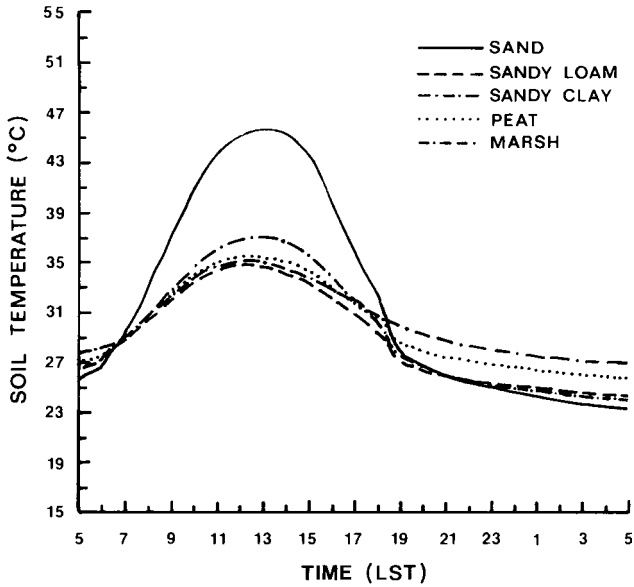
Fig. 11-22.   Predicted soil surface temperature (degrees Celsius) as a function of soil type for a July summer day in south Florida. (From McCumber 1980.)
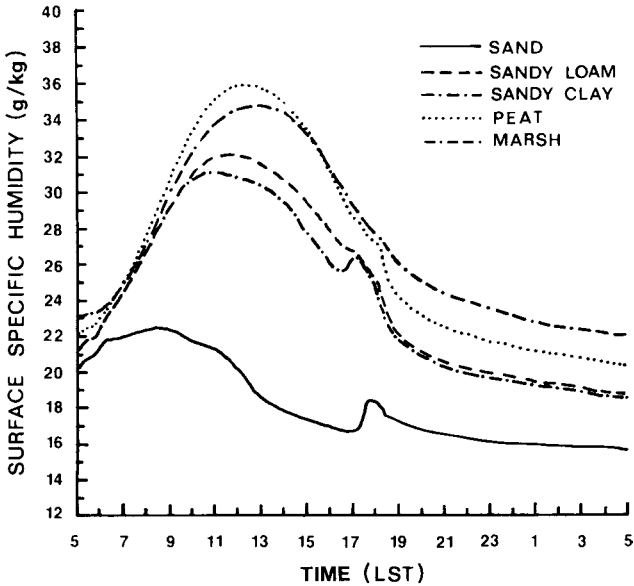
Fig. 11-23.   Same as Figure 11-22 except for soil surface specific humidity. (From McCumber 1980.)
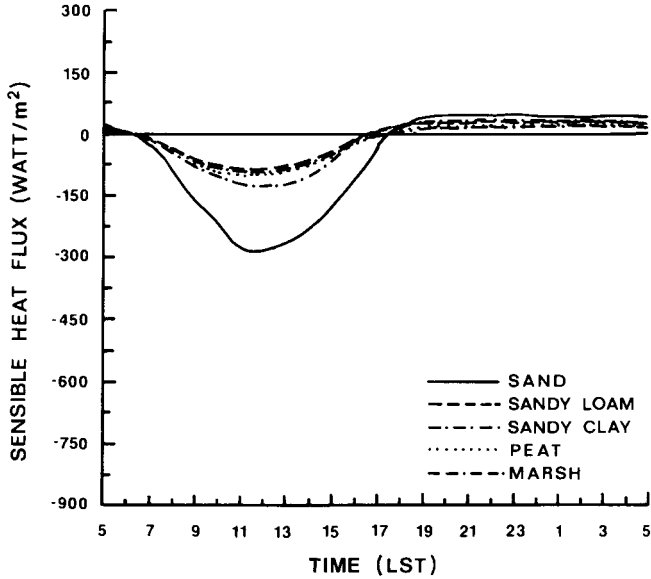
Fig. 11-24.   Same as Figure 11-22 except for surface layer turbulent sensible heat flux. (From McCumber 1980.)
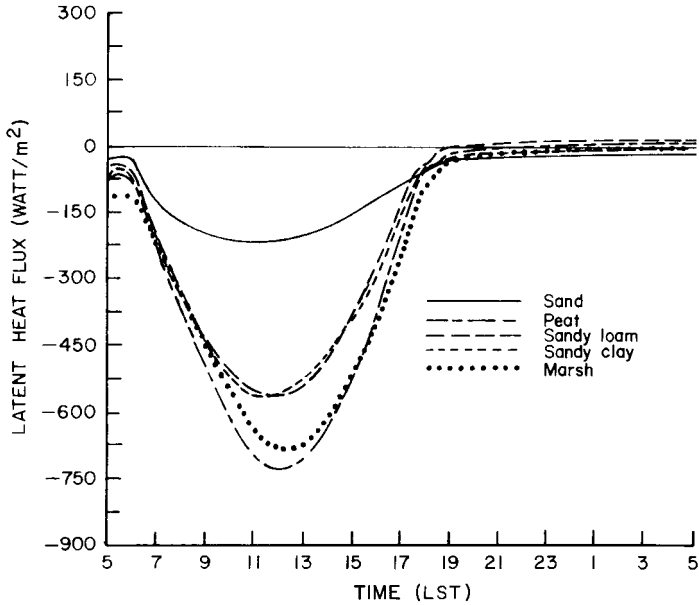
Fig. 11-25.   Same as Figure 11-22 except for surface layer turbulent latent heat flux. (From McCumber 1980).

(1980) showed that the relative contributions of the sensible and latent heat fluxes determined the inland penetration rate of sea breezes. Larger values of sensible heat provide more direct heating of the atmosphere, thereby producing a larger horizontal pressure gradient and more rapid inland propagation of the sea breeze. Idso *et al.* (1975b, c) documented observationally major changes in evaporation that can occur from the wetting of a dry soil surface. Wetzel (1978) used a one-dimensional boundary layer model to show that even the irrigation (i.e., wetting) of a relatively small percentage of land ($\sim$20%) can have a large effect on an unstably stratified boundary layer even well downstream from the irrigated region. Using a one-dimensional model, Zhang and Anthes (1982) illustrated the strong sensitivity of the planetary boundary layer to moisture availability.

Anthropogenic Sources of Surface Heating.   The contributions to the surface heat budget by anthropogenic and natural sources, Q_m, have been estimated based on such factors as population density, heat content of a forest fire, etc. Such studies include those of Orville *et al.* (1981), who examined the influence of cooling towers on cumulus convection using a two-dimensional cloud model.

Hanna and Swisher (1971), Hanna and Gifford (1975), and Pielke (1976) have reported estimates of heat released from some of these activities. Using their values, along with other estimates, the power per unit area and the area of input that would be included in Q_m are given in Table 11-6. Harrison and McGoldrick (1981) have provided levels of current artificial heat input on a 10×10 km grid over Great Britain. Over this size area, they calculated that in February, values of Q_m are nearly 30 W m^{-2} in the London and Bir-

TABLE 11-6

Representative Values of Heat Input from Anthropogenic and Natural Sources

Feature	Heat (W m^{-2})	Area (km^2)	Observational effect
Suburban area	4	10	Negligible
Urban area	100	1,000	Effects on local climate, local convergence due to a city results in enhanced precipitation downwind
Tropical island	400	600	Influence on rainfall pattern downwind due to enhanced convergence
Australian bushfire	2,000	50	Cumulonimbus cloud generation
Surtsey volcano	100,000	1	Deep cumulus cloud, water spouts
Saturn V booster rocket tests	4,900,000	0.0003	Cumulus cloud

mingham areas, whereas over 1-km^2 areas in Teeside, England, Q_m exceeds 600 W m^{-2}.

Based on previous mesoscale model calculations, Pielke (1976) estimated that heat releases on the mesoscale (e.g., 10^3 km^2) of 10 W m^{-2} would have no detectable effect on local weather, whereas 100 W m^{-2} input uniformly over the same area would cause influences on weather that could be detected statistically. If 1000 W m^{-2} were input, however, the response of the mesoscale system would be significant and immediate. By inputting various values of Q_m into a mesoscale model for different situations, useful information can be obtained regarding inadvertent weather modification effects.

Table 11-6 also shows the influence of area on the observed meteorological response. Even an immense input of heat, such as from a Saturn rocket booster, had only a very localized effect if the area of input is small. Hence substantially smaller rates of heating over a mesoscale area have a much more pronounced effect on the mesoscale meteorological response, a conclusion that is substantiated using the linear model results reported in Dalu and Pielke (1993) and Dalu *et al.* (1996).

Solution Technique for the Equilibrium Surface Temperature. With the evaluation of the individual heat fluxes in Eq. (11-33) [or Eq. (11-34)], their sum should equal 0. In general, however, they do not because several of the terms are dependent on one another through the surface temperature T_G. This temperature, also called the *skin temperature*, is the value that properly partitions the various heat fluxes so that their sum is 0.

The terms that have the most direct relation to surface temperature are:

- $\bar{\rho} C_p \overline{w'' \theta''}$, since the value of T_G strongly influences the magnitude of $\overline{w'' \theta''}$ [see, e.g., Eqs. (7-29), (7-39), and (7-40) where $T_G = \bar{\theta}_G$ (P (in mb)/1000 mb)$^{R_d/C_p}$]
- $\bar{\rho} L_v \overline{w'' q_3''}$, since the value of T_G strongly influences the value of $\overline{w'' q''}$ [see, e.g., Eqs. (7-29), (7-39), and (7-40)], the definition of L given after Eq. (7-24), and the definition of $W_s|_G$ given after Eq. (11-53)
- Q_G, since the ground heat conduction is proportional to the vertical temperature gradient at the surface [i.e., $Q_G = v \partial T / \partial z|_G$; see Eq. (11-36)]
- $\bar{R} \uparrow_{lw_G}$, since the longwave radiation from the ground is a function of T_G^4 [see, e.g., Eq. (11-35)].

The rest of the fluxes have a less direct impact on T_G. The solar radiation reaching the ground, for instance, might be affected by changes in atmospheric turbidity as T_G varies, but this effect is not expected to be immediate.

To evaluate the equilibrium skin temperature, it is convenient to write Eq. (11-33) [or Eq. (11-34)] as

$$+ Q_G + \bar{\rho} C_p \overline{w'' \theta''} + \bar{\rho} L_v \overline{w'' q_3''} - (1 - A)\left(\bar{R} \downarrow_{sw_G} + \bar{R} \downarrow^D_{sw_G}\right)$$
$$- \bar{R} \downarrow_{lw_G} + \bar{R} \uparrow_{lw_G} + Q_M = F(T_G), \tag{11-50}$$

where $F(T_G) = 0$ if the fluxes are in exact balance. In general, $F(T_G) \neq 0$, however, and a truncated Taylor series expansion given by

$$F(T_G + \delta T_G) = F(T_G) + \frac{\partial F}{\partial T_G}(T_G)\delta T_G = F(T_G) + F'(T_G)\delta T_G$$

is used to obtain a better estimate. Requiring $F(T_G + \delta T_G)$ to be 0 (as it should if the fluxes are in balance) with $\delta T_G = T_G^{n+1} - T_G^n$ (where the superscripts n and $n + 1$ refer to the original and new estimates, respectively) and rearranging yields

$$T_G^{n+1} = T_G^n - F(T_G)/F'(T_G). \tag{11-51}$$

The derivative of F with respect to T_G, $F'(T_G)$, is obtained from Eq. (11-50), yielding

$$F'(T_G) = 4\sigma T_G^3 + \frac{\partial}{\partial T_G}(\bar{\rho} C_p \overline{w'' \theta''}) + \frac{\partial}{\partial T_G}(\bar{\rho} L_v \overline{w'' q_3''}) + v \frac{\partial}{\partial z} \frac{\partial T}{\partial T_G},$$

where it is assumed that $\epsilon_G = 1$ and v is not a function of depth or temperature. An equilibrium temperature is said to be attained when $|\delta T_G| < \epsilon$, where ϵ is some arbitrarily small number. Mahrer and Pielke (1977b) used $\epsilon = 10^{-5}$. If $|\delta T_G| \not< \epsilon$, T_G^n is replaced with T_G^{n+1}, then the heat fluxes are recomputed and Eq. (11-51) is reevaluated. This procedure is called the *Newton–Raphson iteration* process.

To simplify the computation of Eqs. (11-50) and (11-51), Mahrer and Pielke (1977b) applied this scheme by assuming that $\bar{\rho}$, u_*, q_*, ψ_m, and ψ_H are not functions of T_G and used the formulations for surface layer fluxes given by Eq. (7-29), so that

$$\frac{\partial}{\partial T_G}(\bar{\rho} C_p \overline{w'' \theta''}) \simeq -\bar{\rho} C_p u_* \frac{\partial \theta_*}{\partial T_G}.$$

Rather than differentiate θ_* directly, however, Mahrer and Pielke evaluated Eq. (11-51) assuming that θ_* is constant. Then, after an equilibrium temperature is obtained, θ_* is recomputed with the new value of T_G. If the absolute change in θ_* is greater than 0.01 K, then new values of θ_*, u_*, q_*, ψ_M, and ψ_H are computed from surface layer equations similar to those given in Eqs. (7-40) and (7-41) and a new estimate of T_G is obtained from Eq. (11-51). This double-iteration procedure continues until both δT_G and changes in θ_* are arbitrarily small. In using the surface profile equations such as Eq. (7-40), to compute θ_*

in this iteration, Eq. (7-39) and the definition of potential temperature are used to relate the skin temperature T_G to the potential temperature at z_0.

Mahrer and Pielke (1977b) also simplified the derivative of the ground heat flux term by approximating $\partial T / \partial z$ with a finite difference form and assuming that $\partial T / \partial T_G$ at $z = -\Delta z$ corresponds to 0. Expressed formally,

$$\frac{\partial Q_G}{\partial T_G} = \frac{\partial}{\partial T_G} v \frac{\partial T}{\partial z} \simeq v \frac{\partial}{\partial T_G} \left[\frac{T_G - T(-\Delta z)}{\Delta z} \right] = \frac{v}{\Delta z}.$$

Figure 11-26 illustrates the surface temperature predicted using a surface energy budget in a sea-breeze calculation. As the sea-breeze front moves inland, the marine air cools the surface resulting in reduced maxima. In a model with a prescribed surface temperature distribution that is only a function of time, such as given by Eq. (11-30), the curve as given for 73.75 km inland would apply at all locations over land.

If the surface is assumed to have a finite heat storage, then the right side of Eqs. (11-33) and (11-34) can be replaced by $\rho c \Delta z \frac{\partial T_G}{\partial t}$ (Tremback and Kessler 1985). This new form of the surface heat budget can then be integrated forward in time (solving for $\frac{\partial T_G}{\partial t}$) and removing the need to solve an iterative equation such as (11-51). Blackadar (1976) introduced a "force–restore" method to solve for the surface temperature where a deep soil reservoir of heat is available to constrain the heating at the surface. Mihailović *et al.* (1999a) reviews and evaluates the force-restore equation.

Ground Wetness.   McCumber (1980) has improved the heat budget to include a more realistic representation of the turbulent latent heat flux term through a better representation of the value of specific humidity at the ground surface q_G [q_G is related to $\bar{q}_{z_0}$ by Eq. (7-39)].

McCumber computes the equilibrium surface-specific humidity from

$$q_G = h q_s(T_G),$$

where

$$q_s(T_G) = 0.622 \left[\frac{e_s(T_G)}{P \text{ (in mb)} - 0.378 e_s(T_G)} \right] \tag{11-52}$$

(from the definition of specific humidity),

$$e_s(T_G) = 6.1078 \exp \left[\left(\frac{T_G - 273.16}{T_G - 35.86} \right) 17.269 \right]$$

[from Teten's formula (see e.g., Murray 1970), with T_G in degrees Kelvin], and

$$h = \exp \left(\frac{+g \Psi_G}{R_v T_G} \right).$$
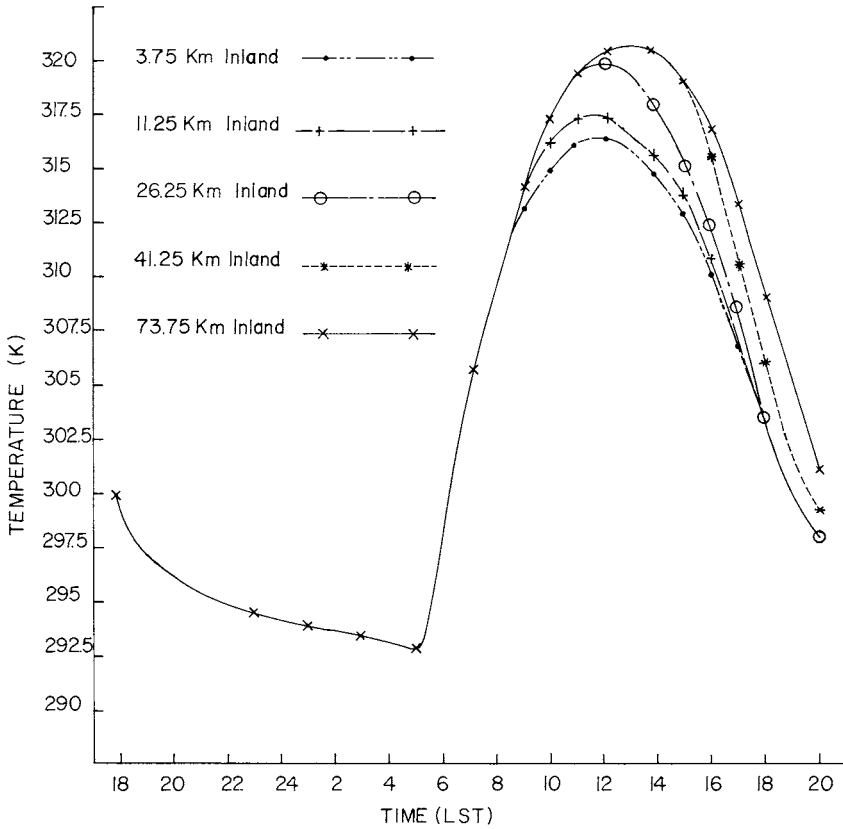
Fig. 11-26.   The predicted surface temperature as a function of time and inland distance from the coast for a sea-breeze simulation, using a surface energy budget of the form given by Eq. (11-50). (From Mahrer and Pielke 1977b.)

The variable Ψ_G is the moisture potential (expressed as a head of water) at the ground surface, and R_v is the gas constant for water vapor ($R_v = 461$ J K^{-1} kg^{-1}). The soil moisture potential at the ground surface is obtained by McCumber (1980) from a finite difference analog to Eq. (11-47) and is given by

$$\Psi_G = \Psi_{G-\Delta z} + \left[\frac{W_s|_G}{\rho_w K_\eta|_G} - 1 \right] \Delta z, \qquad (11\text{-}53)$$

where $W_s|_G$ is the soil moisture flux at the surface. Continuity of moisture flux is required at $z = 0$, so that

$$W_s|_G - \bar{\rho}\overline{w''q''} \simeq W_s|_G + \bar{\rho}u_* q_* \simeq 0$$

must be obtained. Garrett (1978) defines this to occur when

$$\left| \frac{\bar{\rho} u_* q_* - W_s|_G}{\bar{\rho} u_* q_*} \right| < 0.001. \tag{11-54}$$

In determining Ψ_G, at each time step at each grid point, $W_s|_G$ is initially determined using values of Ψ_G and $\Psi_{G-\Delta_z}$ from the last time step. Subsequently,

$$W_s|_G^{n+1} = \delta W_s|_G^n + (1 - \delta)\bar{\rho} u_* q_*,$$

where δ is a weighting factor ($0 \le \delta \le 1$) used to promote a convergent solution [as defined by Eq. (11-54)] and the superscript $n + 1$ refers to the next guess in the iteration. The value of $W_s|_G^{n+1}$ is used to recompute a value of Ψ_G from Eq. (11-53), which then provides updated values of η, and then K_η and D_η, at the surface. McCumber found the fastest convergence to a solution when $\delta > 0.5$, with dry soils (e.g., $h < 0.70$) requiring values closer to unity. Once the surface moisture characteristics are computed, Eq. (11-49) can be used to calculate moisture fluxes within the soil.

Influence of Terrain Slope.   Up to now in our discussion, the influence of sloping terrain on the amount of shortwave radiation that reaches the ground has not been considered in the surface heat budget. In Chapter 8, Section 8.4, it was shown that in a horizontal layer of the atmosphere the amount of solar radiation on a unit cross-sectional area is dependent on such factors as the time of the year, opacity of the atmosphere, latitude, and time of day. For irregular terrain, the orientation of the ground surface with respect to the sun must also be considered.

Kondratyev (1969) presented a formula that accounts for the influence of sloping terrain on the direct solar radiation per unit area, and his analysis was used by Mahrer and Pielke (1977b) to investigate the effect of irregular terrain heating on mesoscale circulations. Figure 11-27, adapted from Kondratyev (1969), illustrates the angle, i, at which direct solar radiation impinges on sloping terrain, where $S_H = \bar{R}\downarrow_{sw_G} / \cos Z$ is the value of direct solar radiation at the ground on a unit cross-sectional area perpendicular to the sun's rays. The value of $\bar{R}\downarrow_{sw_G}$ can be obtained for clear skies from the integrated form of the Eq. (8-62) evaluated at the ground.

Expressed mathematically,

$$\bar{R}\downarrow_{sw_G}^{sl} = S_H \cos i, \tag{11-55}$$

where

$$\cos i = \cos \alpha \cos Z + \sin \alpha \sin Z \cos(\beta - \gamma).$$
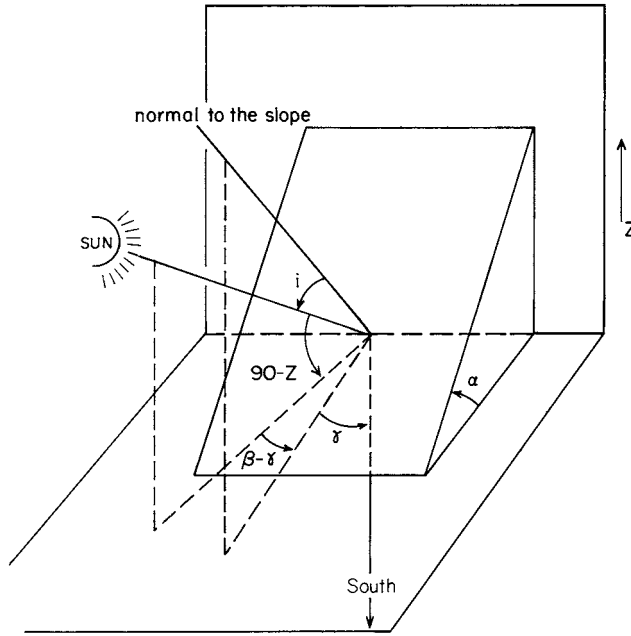
Fig. 11-27. An illustration of the angles used in the definition of Eq. (11-55). (Adapted from Kondratyev 1969, Figure 5-38.)

The zenith angle Z was defined by Eq. (8-61), and α, the slope of the terrain, is given by

$$\alpha = \tan^{-1}\left[\left(\frac{\partial z_G}{\partial x}\right)^2 + \left(\frac{\partial z_G}{\partial y}\right)^2\right]^{1/2},$$

where z_G is terrain height. The quantity $\beta - \gamma$ is the orientation of the sun's azimuth, β, with respect to the azimuth of the terrain slope, γ. The slope azimuth is expressed by

$$\gamma = \frac{\pi}{2} - \tan^{-1}\left(\frac{\partial z_G}{\partial y} \bigg/ \frac{\partial z_G}{\partial x}\right)$$

(so that south has zero azimuth), and the azimuth of the sun is obtained by projecting the location of the sun onto a horizontal surface and also requiring that south have zero azimuth. The expression for β is given by

$$\beta = \sin^{-1}\left(\frac{\cos \delta_{sun} \sin h_r}{\sin Z}\right),$$

where, as in Section 8.4, δ_{sun} is the declination of the sun and h_r is the hour angle. Spherical trigonometric identities such as given in, for example, Selby (1967:161–164), are used to derive γ and β.

The following example is presented to illustrate the dependence of direct solar heating on terrain slope and azimuth. Assuming $\phi = 40°N$, clear sky, local noon, $\gamma = 0°$ (i.e., south-facing slope), June 21 ($\delta_{sun} = 23.5°$), $r = 1.015a$, $S_0 = 1380$ W m^{-2}, $A = 0.2$, $\alpha = 10°$, and $R\downarrow_{sw_0}$ in Eq. (8-58) is attenuated by 40% between the top of the atmosphere and the ground, Eq. (11-55) yields $\bar{R}\downarrow_{sw_G}^{sl} = 625$ W m^{-2}. Table 11-7 gives the same calculation except $\gamma = \pi/2$, π, and $3\pi/2$ corresponding to east-, north-, and west-facing slopes, respectively. Table 11-7 also presents calculations for the same situation except for December 21 ($\delta_{sun} = -23.5°$) with $r = 0.985a$.

These and even smaller slopes can have a substantial influence on mesoscale circulations. Mahrer and Pielke (1977b, Figure 4) found the eastern slope of a 1-km mountain (with a slope of about 2°) to be about 1° to 2°C warmer in the morning and cooler by the same amount in the afternoon than the same location on the western slope. Observed solar radiation on four different slopes in Kansas is discussed in Nie *et al.* (1992).

The influence of slope on the diffuse shortwave radiation, $\bar{R}_{sw_G}^D$, is considered negligible for slopes of less than about 20°, however, as explained by Lee (1978:61–62). Although the diffuse radiation is reduced in magnitude because only a portion of the sky is visible, if the diffuse radiation is isotropic (see Note 5 in Chapter 8), then $\bar{R}_{sw_G}^D$ received on a flat, open surface is only modified by

$$\bar{R}_{sw_G}^{D_{sl}} = \bar{R}_{sw_G}^D \cos^2(\alpha/2).$$

As given by Lee, for $\alpha = 16.7°$ (a slope of 0.3), the difference between $\bar{R}_{sw_G}^D$ and $\bar{R}_{sw_G}^{D_{sl}}$ is only 2%. Lee also showed that the contribution to the total solar radiation by the reflection of total solar radiation from surrounding terrain is only about 3% or less of $\bar{R}_{sw_G}^{sl}$ for slopes of less than 20° ($\bar{R}_{sw_G}^{sl} = \bar{R}\downarrow_{sw_G}^{sl} + \bar{R}_{sw_G}^D$). Ignoring attenuation in the intervening atmosphere of the reflected light from

TABLE 11-7

Solar Radiation at Noon on a Slope of 10° Oriented in Four Different Directions on June 21 and December 21 Using the Values Given in the Text

Variable	Date	Solar radiation (Wm^{-2})			
		South	East	North	West
$\bar{R}_{sw_G}^{sl}\downarrow$	21 June	625	594	563	594
$\bar{R}_{sw_G}^{sl}\downarrow$	21 December	215	159	103	159

the surrounding terrain, the increased solar absorption on the slope for a uniform albedo is

$$\Delta R \downarrow_{sw_G} = (1 - A)A(\bar{R} \downarrow_{sw_G} + \bar{R}^{D}_{sw_G}) \sin^2(\alpha/2).$$

There is also a small effect on albedo, since the effective zenith angle in Eq. (11-42) is the angle between the solar beam and the angle normal to the slope. As seen in Figure 11-21, for slopes less than 20°, the effect of terrain slope on albedo is relatively small even for large zenith angles. With $\alpha = 0.3$ sloping toward the north, for example, a value of Z of 50° at noon would provide an effective zenith angle along the slope of 66.7°, resulting in a change of albedo of about 2.5%.

The influence of slight slopes on the longwave radiation balance is also small, as discussed by Lee (1978:71) using the same type of geometric argument as applied to derive $\bar{R}^{D_{sl}}_{sw_G}$ and $\Delta R \downarrow_{sw_G}$; that is, for an equilateral triangular valley, $\bar{R} \downarrow^{sl}_{lw} = \bar{R} \downarrow \cos^2(\alpha/2) + \bar{R}_{lw} \sin^2(\alpha/2)$, where $\bar{R}_{lw}$ is the longwave radiation reaching one side of the valley from the other and $\bar{R} \downarrow$ comes from the atmosphere above the slope [using, e.g., Eq. (8-39)].

Zdunkowski *et al.* (1980) and Welch and Zdunkowski (1981b) have provided a discussion of the influence of slope on the amount of direct and diffuse solar radiation incident on sloped surfaces as a function of optical depth and solar zenith angle. They report, for example, that at 40° of latitude during the equinox, a north-facing slope receives more integrated daily shortwave radiation on a cloudy day than on a clear day.

A consequence of this analysis is that the direct shortwave radiation term $\bar{R} \downarrow_{sw_G}$ in Eqs. (11-33) and (11-34) must be replaced with $\bar{R} \downarrow^{sl}_{sw_G}$ [Eq. (11-55)] over sloping terrain.

Snow.   Sturm *et al.* (1995) and Sturm and Holmgren (1998) describe snow on the ground in six separate classes where the typical seasonal range of bulk density in g cm^{-3} is: tundra (0.38), taiga (0.10–0.25), alpine (0.20–0.35), maritime (0.15–0.40), ephemeral (variable), and prairie (est. 0.30). Snow can be represented similar to soil with the important additional characteristic that snow can change its phase (melt, refreeze, sublimate). Snow can also saltate (i.e., bounce along the surface), and blow through the air. Liston and Sturm (1998) developed a model to simulate this drifting of snow. Greene *et al.* (1999) applied this model to a portion of the Continental Divide in Colorado, where it was found that as much as 30% of the snow can sublimate into the air. Although this has not yet been done, this drifting/blowing snow model could also be used to simulate the movement of sand and dust by the wind.

Liston (1999) also developed a snow melt model that uses solar input and wind speed, along with the terrain slope and azimuth, to represent this phase

change. Liston illustrates the close interrelationships among the spatial snow distribution, snow melt, and snow cover depletion.

Other examples of model representations of snow processes include Marshall and Oglesby (1994), Marshall *et al.* (1994), Horne and Kavvas (1997), and Walko *et al.* (2000a). For example, over snow cover during the day and with a calm wind, Halberstam and Schieldge (1981) demonstrated the importance of radiative flux divergence and moisture flux from the surface in determining temperature and wind profiles. Because of the high albedo of the snow and the creation of a moist layer of air immediately above the surface, both downward- and upward-reflected solar radiation are absorbed just above the surface, thereby creating a local region of enhanced warming within the surface layer.

Vegetation.   When vegetation is introduced at the ground, the proper representation of the bottom boundary conditions becomes more difficult than for bare soil, since the observational and theoretical information concerning the fluxes of heat, moisture, momentum, and other gaseous and aerosol materials into and out of the vegetation remains limited. Since much of the world is vegetated and the vegetation dynamically changes over time (Eidenshink and Haas 1992), however, it would be inappropriate to neglect this important component of the ground characteristics in a mesoscale model. Even for arid regions with sparse vegetation, Otterman (1981a, b) has illustrated the importance of protruding plant material on the flux of heat.

This section describes one type of parameterization for the influence vegetation on the boundary layer, that of McCumber (1980). McCumber's soil-vegetation-atmosphere transfer (SVAT) scheme was among the earliest developed. Other early formulations are described for drainage flow simulations by Garrett (1983a) and for boundary-layer structure over flat terrain by Yamada (1982). Terjung and O'Rourke (1981) examined the influence of vegetation on the magnitude of the terms in the surface energy budget in an urban area. Although the accuracy of physically elaborate parameterizations of vegetation, such as that of Deardorff (1978), have been questioned (e.g., Monteith 1981), realistic representations of this ground–air interaction must be included in mesoscale models.

There are three temporal scales of interaction between vegetation and the atmosphere: *biophysical, biogeochemical,* and *biogeographic* (Pielke 1998). Biophysical influences include controls on the transpiration of water vapor through the stoma of plants. Biogeochemical effects include above- and below-ground vegetation growth, such as that represented by the CENTURY model (Lu *et al.* 2001). Biogeographic models include changes in the mixture of vegetation species and the spatial movement of biomes. Models that represent both biophysics and biogeochemistry include Chen and Coughenour (1994), Eastman *et al.* (2001a, b), and Tsvetsinskaya *et al.* (2001a, b). Benoit *et al.* (2000)

discuss the use of coupled atmospheric-hydrologic modeling. In this chapter, since the focus is on the use of mesoscale models in weather forecasting, only biophysics models are discussed.

Deardorff (1978) introduced a bulk type of parameterization for vegetation in which he assumed that a single-level canopy had the characteristics of a large leaf. Garrett (1982) applied Deardorff's parameterization to simulate convection over the southeastern United States. McCumber (1980) introduced this type of representation into a mesoscale model in which an energy balance analogous to Eq. (11-33) is applied to the vegetation canopy. McCumber's discussion of the vegetation parameterization differs in interpretation from that of Deardorff. As described by McCumber (1982, personal communication), Deardorff's technique parameterizes a canopy of a given density throughout a grid area, whereas McCumber's formulation assumes a dense canopy that occurs over a fraction of a grid area with entirely bare soil in the remainder.

Assuming that the storage of heat in vegetation is negligible (Monteith 1975a; Deardorff 1978), an equilibrium temperature, T_f, is determined from the heat energy gains and loss at the top of the vegetation and at the ground surface. The net flux within the vegetation can be expressed as[31]

$$(\bar{R}\downarrow_{sw_c} - \bar{R}\uparrow_{sw_c}) + (\bar{R}\downarrow_{lw_c} - \bar{R}\uparrow_{lw_c}) - (\bar{R}\downarrow_{sw_G} - \bar{R}\uparrow_{sw_G})$$
$$- (\bar{R}\downarrow_{lw_G} - \bar{R}\uparrow_{lw_G}) + (H + LE)_c - (H + LE)_G = 0, \quad (11\text{-}56)$$

where the subscripts "c" and "G" refer to the vegetation canopy and the ground surface. The individual terms in this heat budget can be written as

$$\bar{R}_{sw_c}\downarrow = (\bar{R}\downarrow_{sw} + \bar{R}_{sw}^{D}) \text{ at the canopy level,} \qquad (11\text{-}57)$$

$$\bar{R}_{sw_c}\uparrow = [(1 - \sigma_f)(A_Z + A_s) + \sigma_f(A_f + A_Z)]\bar{R}\downarrow_{sw_c}, \qquad (11\text{-}58)$$

$$\bar{R}_{sw_G}\downarrow = (1 - \sigma_f)\bar{R}\downarrow_{sw_c}, \qquad (11\text{-}59)$$

$$\bar{R}_{sw_G}\uparrow = (A_Z + A_s)(1 - \sigma_f)\bar{R}\downarrow_{sw_c}, \qquad (11\text{-}60)$$

where σ_f is called the *shielding factor* and represents the fractional coverage of a grid area by a dense vegetation canopy. The albedo A_f is that of the canopy. In this particular formulation, the shortwave radiation flux below the canopy top is ignored. For dense forests in full foliage, this assumption is reasonable with the net shortwave radiation reaching the ground on the order of 6–8% of the net shortwave radiation at the top of the canopy (see, e.g., Table 11-8).

The individual longwave radiation terms are given as[32]

$$\bar{R}\downarrow_{lw_c} = \bar{R}\downarrow_{lw} \text{ at the canopy level,} \qquad (11\text{-}61)$$

$$\bar{R}\uparrow_{lw_c} = (1 - \sigma_f)[\epsilon_G \sigma T_G^4 + (1 - \epsilon_G)\bar{R}\downarrow_{lw_c}]$$
$$+ \sigma_f[\epsilon_f \sigma T_f^4 + (1 - \epsilon_f)\bar{R}\downarrow_{lw_c}], \qquad (11\text{-}62)$$

TABLE 11-8

Representative Values of Leaf Area Index L_A, Transmissivity, Absorption, and Albedo
for Shortwave Radiation $\bar{\tau}$, $\bar{a}$, and A_f, and Emissivity for Longwave Radiation ϵ_f
for Various Types of Vegetation

	L_A	$\bar{\tau}$	$\bar{a}$	A_f	ϵ_f
Maize, rice					
June 1	0	~0.90	~0.0	~0.10	0.95
Mid-July	1.8	~0.55	~0.30	~0.15	0.95
September 1	4	~0.15	~0.65	~0.20	0.95
Mid-October	6	~0.10	~0.70	~.0.20	0.95
Cotton	2	~0.23	~0.57	~0.20	0.95
Wheat, barley	4	~0.25	~0.55	~0.20	0.95
Prairie grasslands					
Green	~1				0.96
Dead	~4				0.96
Meadow	2		~0.48		0.96
	4		~0.72		0.96
	6		~0.82		0.96
Coniferous forest	2	~0.20	~0.70	~0.10	0.97
	4	~0.08	~0.82	~0.10	0.97
Deciduous forest					
Aspen (in foliage)	2	~0.45	~0.35	~0.20	0.95[a]
	4	~0.23	~0.65	~0.12	0.95[a]
	6	~0.06	~0.82	~ 0.12	0.95[a]
Oak					
30-year-old stand					
No foliage		~0.63	~0.25	0.12	0.95[a]
Full foliage		~0.12	~0.72	0.16	0.95[a]
160-year-old stand					
No foliage		~0.30	~0.58	0.12	0.95[a]
Full foliage		~0.25	~0.59	0.16	0.95[a]

[a]These values of ϵ_f were obtained from Lee (1978:69).
Values were estimated from data given in papers published in Monteith (1975b). Additional values of A_f are given
in Table 11-4. Similarly, additional values of ϵ_f are listed in Table 11-2.

$$\bar{R}\downarrow_{lw_G} = (1 - \sigma_f)\bar{R}\downarrow_{lw_c} + \sigma_f\bar{R}^v\downarrow_{lw_G}, \tag{11-63}$$

$$\bar{R}\uparrow_{lw_G} = (1 - \sigma_f)[\epsilon_G\sigma T_G^4 + (1 - \epsilon_G)\bar{R}\downarrow_{lw_G}] + \sigma_f\bar{R}^v_{lw_G}\uparrow, \tag{11-64}$$

where ϵ_G and ϵ_f are the emissivities of the ground and the foliage, respectively.
Representative values of ϵ_f are given in Table 11-8.[33] The downward and upward
longwave radiation fluxes are $\bar{R}^v_{lw_G}\downarrow$ and $\bar{R}^v_{lw_G}\uparrow$ beneath the vegetation and are
defined as

$$\bar{R}^v_{lw_G}\uparrow = \epsilon_G\sigma T_G^4 + (1 - \epsilon_G)\bar{R}^v_{lw_G}\downarrow \tag{11-65}$$

$$\bar{R}^v_{lw_G}\downarrow = \epsilon_f\sigma T_f^4 + (1 - \epsilon_f)\bar{R}^v_{lw_G}\uparrow. \tag{11-66}$$

Substituting $\bar{R}^{v}_{lw_G} \downarrow$ into Eq. (11-65) and $\bar{R}^{v}_{lw_G} \uparrow$ into Eq. (11-66) yields

$$\bar{R}^{v}_{lw_G} \uparrow = \epsilon_G \sigma T_G^4 + (1 - \epsilon_G)\epsilon_f \sigma T_f^4 + (1 - \epsilon_f)(1 - \epsilon_G)\bar{R}^{v}_{lw_G} \uparrow$$

and

$$\bar{R}^{v}_{lw_G} \downarrow = \epsilon_f \sigma T_f^4 + (1 - \epsilon_f)\epsilon_G \sigma T_G^4 + (1 - \epsilon_G)(1 - \epsilon_f)\bar{R}^{v}_{lw_G} \downarrow .$$

Rearranging and solving for $\bar{R}^{v}_{lw_G} \uparrow$ and $\bar{R}^{v}_{lw_G} \downarrow$ gives

$$\bar{R}^{v}_{lw_G} \uparrow = [\epsilon_G \sigma T_G^4 + (1 - \epsilon_G)\epsilon_f \sigma T_f^4]/(\epsilon_f + \epsilon_G - \epsilon_f \epsilon_G) \qquad (11\text{-}67)$$

$$\bar{R}^{v}_{lw_G} \downarrow = [\epsilon_f \sigma T_f^4 + (1 - \epsilon_f)\epsilon_G \sigma T_G^4]/(\epsilon_f + \epsilon_G - \epsilon_f \epsilon_G) \qquad (11\text{-}68)$$

(see also Lee 1978:179). These two expressions can then be substituted into Eqs. (11-63) and (11-64).

The sensible and latent heat flux terms in the heat budget can be written as

$$(H + LE)_c = \sigma_f \left[\bar{\rho} C_p \overline{w''\theta''}^f + \bar{\rho} L_v \overline{w''q_3''}^f \right] + (1 - \sigma_f)\left[\bar{\rho} C_p \overline{w''\theta''}^G + \bar{\rho} L_v \overline{w''q_3''}^G \right]$$

and

$$(H + LE)_G = (1 - \sigma_f)\left[\bar{\rho} C_p \overline{w''\theta''}^G + \bar{\rho} L_v \overline{w''q_3''}^G \right],$$

where the subgrid-scale terms with the subscripts "f" and "G" correspond to fluxes from the foliage and the ground surface. The difference between these two terms required in Eq. (11-56) is then

$$(H + LE)_c - (H + LE)_G = \sigma_f \left[\bar{\rho} C_p \overline{w''\theta''}^f + \bar{\rho} L_v \overline{w''q_3''}^f \right].$$

The sensible and latent heat fluxes from the foliage are estimated (Deardorff 1978) as

$$\bar{\rho} C_p \overline{w''\theta''}^f = 1.1 L_A \bar{\rho} C_p c_f u_{af} \left(\frac{1000 \text{ mb}}{p(\text{in mb})} \right)^{0.286} (T_{af} - T_f) \qquad (11\text{-}69)$$

and

$$\bar{\rho} L_v \overline{w''q_3''}^f = L_A \bar{\rho} L_v f' c_f u_{af}(q_{af} - q_s(T_f)), \qquad (11\text{-}70)$$

where L_A is the *leaf area index*, defined as the total one-sided leaf area of the foliage relative to the same size ground area (i.e., meters squared of foliage area per meters squared of ground area). The equation for L_A is given by Eq. (7-38). The leaf area index, L_A, can be a function of height within the vegetation. Representative values of L_A are given in Table 11-8 for various types of vegetation. Deardorff assumed a relation between leaf area index and fractional coverage of ground by foliage of $L_A = 7\sigma_f$.

The variables u_{af}, T_{af}, and q_{af} are representative values of wind speed, temperature, and specific humidity, respectively, between the top of the vegetation

and the ground, and c_f is a nondimensional transfer coefficient [equivalent to a drag coefficient, as discussed after Eq. (7-55)]. The coefficient 1.1 was included by Deardorff (1978) to account roughly for stems, branches, and trunks of vegetation, which were assumed to not be included in L_A. The transfer coefficient is estimated by

$$c_f = 0.01\left(1 + \frac{0.3}{u_{af}}\right), \qquad \text{with } u_{af} \text{ in meters per second} \qquad (11\text{-}71)$$

based on the work of Kumar and Barthakur (1971) and Allen and Lemon (1972) as reported by Deardorff. The value of 0.01 was derived for forced convection over several different types of plants, and the second term within the parentheses was added to account for transfers of heat, moisture, and momentum during free convection.[34]

The wind speed, u_{af}, is estimated by

$$u_{af} = 0.83 c_d^{1/2} u_a, \qquad (11\text{-}72)$$

where u_a is the wind speed just above the vegetation (e.g., at the first grid level in a mesoscale model above the plants) and c_d can be estimated as

$$c_d = \left[\frac{k}{\ln[(z - D)/z_0] - \psi_M[(z - D)/L]}\right]^2. \qquad (11\text{-}73)$$

In Eq. (11-73), D is the zero displacement height defined by Eq. (7-34).

As reported in Deardorff (1978), the coefficient 0.83 is based on the investigations of Geiger (1965), Thom (1971), Legg and Long (1975), and Webb (1975), with the assumption that in a relatively dense vegetation canopy,

$$u_{af} \simeq 0.3 u_a, \qquad D \simeq 3/4 h, \qquad \text{and} \qquad z_0 \simeq 1/3(h - D),$$

where h is the height of the top of the vegetation. The quantity $c_d^{1/2} u_a$ roughly corresponds to a friction velocity similar to u_*, which was defined in Section 7.2.

The values of T_{af} and q_{af} are assumed to be

$$T_{af} = 0.3 T_a + 0.6 T_f + 0.1 T_G \qquad (11\text{-}74)$$

$$q_{af} = 0.3 a_a + 0.6 q_f + 0.1 q_G. \qquad (11\text{-}75)$$

This form was chosen by Deardorff using a heuristic argument that the greatest influence on temperature within vegetation is caused by the foliage (when the vegetation is comparatively dense, $L_A \gtrsim 2$). Deardorff experimented with coefficients of 0.45, 0.45, and 0.1 in these two expressions (i.e., replacing coefficients 0.3, 0.6, and 0.1) and found little change in the final heat budget solutions.

The specific humidity of the foliage stoma is obtained from

$$q_f = f' q_s(T_f) + (1 - f') q_{af},$$

with the restriction that $q_f \leq q_s(T_f)$. The parameter f' is the fraction of potential evaporation/transpiration available from the vegetation and is given by

$$f' = 1 - \frac{\delta_w r_s}{r_s + r_a}\left[1 - \left(\frac{W_L}{W_I}\right)^{0.67}\right] \tag{11-76}$$

where $\delta_w = 0$ if condensation is occurring and $\delta_w = 1$ otherwise, W_L is the liquid water per unit surface leaf area, and W_I is the maximum *interception* storage (in units of depth per unit surface leaf area) and refers to the amount of water that can remain on vegetation before it falls to the ground of its own weight[35] ($W_L \leq W_I$). Hicks (1981) reported values of W_L of about 0.2 mm from dew formation at night under cloudless skies in the arid summer climate in Wangara, Australia. The maximum interception storage, W_I, is a function of plant type and depends on rainfall rate (Clark 1940; Ovington 1954; Burgy and Pomeroy 1958; Helvey and Patric 1965; Sim 1972). According to Monteith (1975a:118), values of W_I range from about 0.4 mm to 2.0 mm, with little distinction between forest and herbaceous communities. Details of individual plant geometry apparently determine the precise value of W_I. McCumber used values of $W_I = 0.6$ mm for grass and 1.6 mm for trees. The exponent 0.67 in the equation for f', as discussed by Deardorff (1978), is intended to approximate the agglomeration of an evaporating film of water into discrete droplets, thereby covering less leaf surface and accelerating water evaporation.

The parameters r_a and r_s, coefficients of air resistance and of bulk stomatal resistance, respectively, as adapted from Deardorff (1978) and McCumber (1980), are represented by

$$r_a = \left(\frac{1}{c_f u_{af}}\right) \tag{11-77}$$

and

$$r_s = r_c\left[\frac{\bar{R}_{sw_c}\downarrow^{max}}{0.03 R_{sw_c}\downarrow^{max} + \bar{R}\downarrow_{sw_c}} + P + \left\{\frac{\eta_{wilt}}{\eta_{root}}\right\}^2\right], \tag{11-78}$$

where $R_{sw_c}\downarrow^{max}$ is the noon incoming solar radiation under a cloudless, clear sky; P is a function of the time of year ($P = 0$ during the growing season and $P \gg 0$ at other times); η_{wilt} is the level of soil moisture below which permanent wilting of the plant occurs (see, e.g., Table 11-5), and η_{root} is the minimum value of soil moisture occurring in the root zone of the plant. The coefficient r_c is a function of plant type and measures the surface (biological) resistance of a canopy to losses of water; representative values of r_c are given in Table 11-9. McCumber used $r_c = 400$ s m^{-1} for grasslands and 600 s m^{-1} for trees. Segal (1987, personal communication) suggests that for both types of vegetation, r_c should remain at or below 200 s m^{-1} to prevent the canopy temperature from becoming unrealistically high.

TABLE 11-9

Characteristic Values of Surface Biological
Resistance of a Canopy to Loss of Water

Type of vegetation	r_c (s m^{-1})
Cotton field	
0600 LST	~130
Noon	~17
1800 LST	~330
Sunflower field	
$L_A = 1.8$	110
$L_A = 3.6$	80
Coniferous forest	
0600 LST	
Spruce	~20
Hemlock	~240
Pine	~50
Noon	
Spruce	~100
Hemlock	~150
Pine	~130
1800 LST	
Spruce	~120
Hemlock	~200
Pine	~310
Prairie grasslands	
0800 LST	
Late July	~100
Mid-September	~150
1200 LST	
Late July	~100
Mid-September	~500
1800 LST	
Late July	~150
Mid-September	~550

Values are estimated from published values given in papers presented in Monteith (1975b).

The value of liquid water on the leaves, W_L, required in Eq. (11-76) can be obtained from the conservation relation

$$\frac{\partial W_L}{\partial t} = \begin{cases} \sigma_f P_r + \bar{\rho}\left(\overline{w''q_3''}^f - \overline{w''q_3''}^{tr}\right), & 0 \leq W_L < W_I \\ 0, & W_L = W_I, \end{cases}$$

where P_r is the precipitation rate.[36] The transpiration rate is given by

$$\bar{\rho}\overline{w''q_3''}^{tr} = \frac{L_A \bar{\rho} c_f u_{af} r_s}{r_s + r_a}\left[1 - \left(\frac{W_L}{W_I}\right)^{0.67}\right](q_{af} - q_s(T_f)). \qquad (11\text{-}79)$$

This transpiration term represents the water extracted from the root zone of the plant. Therefore, in addition to considering this term in the heat budget of the vegetation, Eq. (11-48) for volumetric moisture content must be rewritten as

$$\frac{\partial \eta}{\partial t} = \frac{1}{\rho_w} \frac{\partial W_s}{\partial z} + A(z), \tag{11-80}$$

where $A(z)$ is called a *root extraction term*. In general, this term is dependent on such factors as root distribution and density, soil moisture content, and soil type. McCumber (1980) uses a form of this function, adopted by Molz and Remson (1970), given by

$$A(z) = \bar{\rho}\overline{w''q_3''}^{\,\mathrm{tr}} \left[\frac{R(z)D_\eta}{\int_{z_{G-\Delta R}}^{z_G} R(z)D_\eta dz} \right],$$

where $R(z)$ is the vertical distribution of roots and ΔR is the depth in the soil of the roots. According to McCumber, Molz and Remson obtained good results using this formulation and concluded that such a macroscopic approach can reasonably approximate the integrated microscopic flow of soil moisture into the roots and up to the foliage level of the plants.

With the specification of the individual components of the heat budget, the representative temperature of the foliage, T_f, can be determined from Eq. (11-56) using Eqs. (11-57)–(11-62) and (11-67)–(11-70). Substituting these expressions into Eq. (11-56) and rearranging yields the budget equation

$$\sigma_f \Bigg[(1 - A_f - A_s)\bar{R}\!\downarrow_{sw_c} + \epsilon_f \bar{R}\!\downarrow_{lw_c} + \frac{\epsilon_f \epsilon_G}{\epsilon_f + \epsilon_G - \epsilon_f \epsilon_G} \sigma T_G^4$$

$$- \frac{\epsilon_f + 2\epsilon_G - \epsilon_f \epsilon_G}{\epsilon_f + \epsilon_G - \epsilon_f \epsilon_G} \epsilon_f \sigma T_f^4 + L_A \bar{\rho} c_f u_{af} \Bigg[1.1 C_p \left(\frac{1000 \text{ mb}}{p(\text{mb})} \right)^{0.286}$$

$$\times (T_{af} - T_f) + L_v f'(q_{af} - q_s(T_f)) \Bigg] = 0. \tag{11-81}$$

Since L_A is assumed to be proportional to the fractional coverage of ground by foliage, σ_f, as applied by McCumber (e.g., Deardorff used $L_A = 7\sigma_f$), σ_f can be removed from this balance equation. The solution of Eq. (11-81) for T_f was performed by McCumber using the Newton–Raphson method, as discussed previously in this chapter [Eq. (11-51) and following]. In obtaining $F'(T_f)$, which is required to use the Newton–Raphson method, McCumber differentiated the two terms in Eq. (11-81) containing σT_f^4 and $(T_{af} - T_f)$ with respect to T_f, and iterating for the correct value of $q_s(T_f)$ and T_{af} in a fashion similar to that used to obtain an accurate value of θ_* for use in Eq. (11-51).

The ground surface heat budget, of course, is also modified by the presence of vegetation from that given by Eq. (11-33). Still using McCumber's formulation,

the budget equation for ground surface temperature T_G is then given by[37]

$$-(\bar{R}\downarrow_{\mathrm{sw_G}} - \bar{R}\uparrow_{\mathrm{sw_G}}) - (\bar{R}\downarrow_{\mathrm{lw_G}} - \bar{R}\uparrow_{\mathrm{lw_G}}) + \bar{\rho}C_p\overline{w''\theta''} + \bar{\rho}L_v\overline{w''q''} + Q_G = 0,$$

where

$$\bar{\rho}C_p\overline{w''\theta''} = -(1 - \sigma_f)\bar{\rho}C_p u_* \theta_* - \sigma_f\left(\bar{\rho}C_p\overline{w''\theta''}^G + \bar{\rho}C_p\overline{w''\theta''}^f\right)$$

$$\bar{\rho}L_v\overline{w''q''} = -(1 - \sigma_f)\bar{\rho}L_v u_* q_* - \sigma_f\left(\bar{\rho}L_v\overline{w''q''}^G + \bar{\rho}L_v\overline{w''q''}^f\right).$$

Q_G could be obtained using Eq. (11-41), and the four radiative flux terms are given by Eqs. (11-59), (11-60), (11-67), and (11-68). The subgrid-scale flux terms have been represented as (e.g., Deardorff 1978; McCumber 1980)

$$\bar{\rho}C_p\overline{w''\theta''}^G = \bar{\rho}C_p c_d u_{af}(T_{af} - T_G)\left(\frac{1000\,\mathrm{mb}}{p(\mathrm{mb})}\right)^{0.286} \tag{11-82}$$

and

$$\bar{\rho}L_v\overline{w''q''}^G = \bar{\rho}L_v c_d u_{af}(q_{af} - \bar{q}_s(T_G)), \tag{11-83}$$

where a drag coefficient formulation [see Eq. (11-73)] has been used. These fluxes are evaluated at the ground surface beneath the vegetation. The sums of Eqs. (11-82) and (11-69) and of (11-83) and (11-70) give the subgrid-scale contribution of heat and moisture flux to the atmosphere from the ground and foliage. These fluxes are used as the lower boundary condition for the subgrid-scale correlation terms in the conservation-of-heat and water vapor equations (i.e., $\overline{w''\theta''}$ and $\overline{w''q_3''}$) over vegetation. The vertical subgrid-flux terms over a grid area at the top of the vegetation in the horizontal equations-of-motion (i.e., $\overline{w''u''}$ and $\overline{w''v''}$) similarly can be given by

$$-\overline{w''u''} = \left[(1 - \sigma_f)u_*^2 + \sigma_f c_d u_a^2\right]\cos\mu$$

$$-\overline{w''v''} = \left[(1 - \sigma_f)u_*^2 + \sigma_f c_d u_a^2\right]\sin\mu,$$

with μ defined by Eq. (7-16).

Within the vegetation (indicated by the subscript "v"), the momentum flux can be represented by

$$-\overline{w''u''}\big|_v = \sigma_f L_A c_d u_a^2 \cos\mu \qquad \text{and} \qquad -\overline{w''v''}\big|_v = \sigma_f L_A c_d u_a^2 \sin\mu$$

[see also Eq. (7-37) and the subsequent discussion].

McCumber used the following iterative procedure to compute these subgrid-scale fluxes when vegetation is present:

1. Calculate the shortwave and longwave radiation terms in Eq. (11-56) that are not directly dependent on T_f; these include Eqs. (11-57)–(11-61).

2. Compute c_f, u_{af}, r_a, and r_s from Eqs. (11-71), (11-72), (11-77), and (11-78).

   3.   Compute T_{af}, q_s, and f' from Eqs. (11-74), (11-52), and (11-76). [Equation (11-52) is used to compute $q_s(T_f)$, where T_f is inserted in the right side in place of T_G.]

   4.   Calculate q_{af} from Eq. (11-75).

   5.   Compute $\bar{\rho}C_p\overline{w''\theta''}^f$, $\bar{\rho}L_v\overline{w''q''}^f$, and $\bar{\rho}L_v\overline{w''q''}^{tr}$ from Eqs. (11-69), (11-70), and (11-79).

   6.   Use the Newton–Raphson method to compute T_f from the budget equation (11.81).

   7.   If the iteration has converged, then compute $\bar{\rho}C_p\overline{w''\theta''}^G$ and $\bar{\rho}L_v\overline{w''q''}^G$ using Eqs. (11-82) and (11-83).

   8.   Solve for the temperature and moisture in the soil using Eqs. (11-36) and (11-80).

Incorporating vegetation into a mesoscale model can be very important. For example, Figure 11-28 (reproduced from McCumber 1980), using input synoptic meteorological data for July 17, 1973 applicable to south Florida, shows substantially different profiles of potential temperature in the afternoon and morning over a forested area (with $\sigma_f = 0.90$) for a sandy loam soil and over a bare soil of the same soil type ($\sigma_f = 0.0$). The differences in temperature are as large as 3°C, with the depth of the mixed layer during the day differing by more than 300 meters. Figure 11-29, also adopted from McCumber (1980), illustrates large variations of foliage, canopy, and ground temperatures over four different types of vegetation soil combinations. Because the surface temperature dominates the forcing for many types of mesoscale systems, different vegetation and soils, therefore, are expected to play an important role in such atmospheric phenomena and must be included in model simulations.
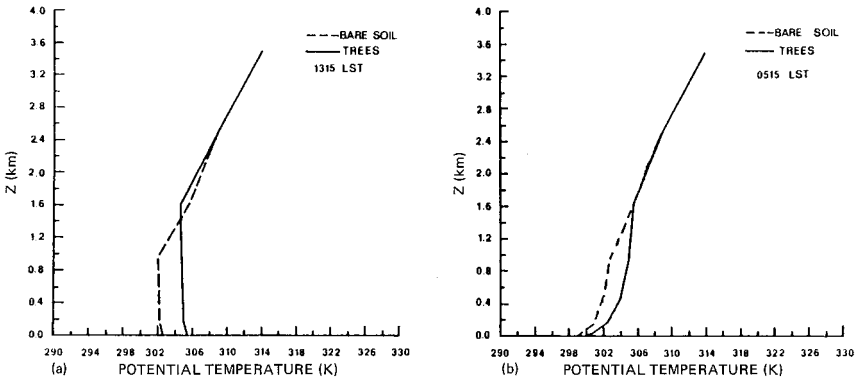
Fig. 11-28. Vertical profile of (a) potential temperature for early afternoon and (b) at sunrise the following day for bare sandy loam ($\sigma = 0.0$) soil and for a forested area, where $\sigma_f = 0.90$. Initial synoptic data were for July 17, 1973 over south Florida. (From McCumber 1980.)
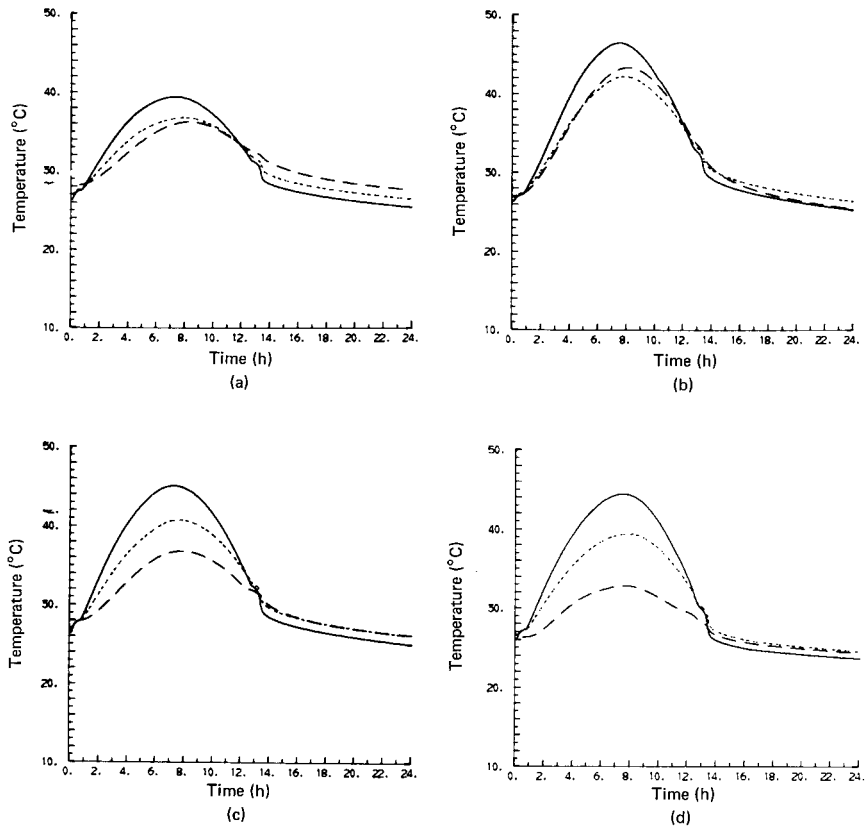
Fig. 11-29. Diurnal variation of predicted foliage temperature T_f (solid line), canopy air temperature T_{af} (short dashed line) and ground temperature T_G (long dashed line) for (a) grass on top of peat soil ($\sigma_f = 0.85$), (b) grass on top of sandy soil ($\sigma_f = 0.75$), (c) trees on top of sandy clay ($\sigma_f = 0.90$), and (d) trees on top of sandy loam ($\sigma_f = 0.90$). The abscissa is time in hours after sunrise. The simulation is for July 17, 1973 conditions over south Florida. (From McCumber 1980.)

More recent evaluations using later forms of this SVAT model, now referred to as the Land Atmosphere Ecosystem Feedback (LEAF) model, are referred to in Lee *et al.* (1995), and Shaw *et al.* (1997). The latest (1999) version, called LEAF-2, is described in Walko *et al.* (2000a) and has been used by Pielke *et al.* (1999b). Runoff is also represented in LEAF-2 and is an important loss of immediate return of water vapor to the atmosphere. Famiglietti and Wood (1991) discuss the role of runoff.

Figure 11-30 illustrates how SVATs represents atmosphere–surface interactions for three different models (BATS, LAPS, and LEAF). A figure of this type for three other SVATs was given by Schultz *et al.* (1998, Figure 1). As evident
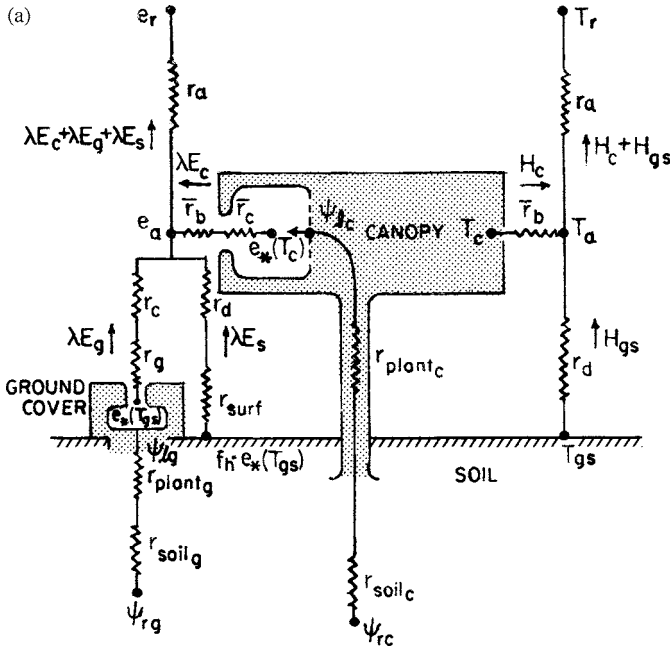
Fig. 11-30. (a) Framework of the simple biosphere (SiB) model. The transfer pathways for latent and sensible heat flux are shown on the left and right sides of the diagram, respectively. (From Sellers *et al.* 1986.) Symbols are described in the text. (b) Same as (a) except for the biosphere-atmosphere transfer scheme (BATS). (c) Same as (a) except for the land ecosystem atmosphere feedback (LEAF) model. (From Lee *et al.* 1993. Used by permission of Oxford University Press, Inc.)

in Figure 11-30, the transfer of moisture and heat between different components of the vegetation and soil system are represented by the electrical analog of a resistor.

Basic equations used in three SVATS are presented in Appendix D. The original sources for these models include Mihailovic and Ruml (1996), Mihailovic and Kallos (1997), Mihailovic *et al.* (1993, 1998, 1999a), and Walko *et al.* (2000a). Mihailovic *et al.* (1999b) discuss how to represent deep soil in such models. Vegetation datasets have been described in Zeng *et al.* (2000a). A summary of land-surface datasets is given in Hof (1999). For a summary of datasets, see Appendix E. Reviews of land–atmosphere interactions are given in Monteith (1981), Avissar (1995), Betts *et al.* (1996), Chen *et al.* (2001), and Pielke (2001). The Project for Intercomparison of Land-Surface Parameterization Schemes (PILPS) was introduced to assess the ability of the SVATS to represent actual observed surface data (Henderson-Sellers *et al.* 1993, 1995; Shao and Henderson-Sellers 1996).[38]
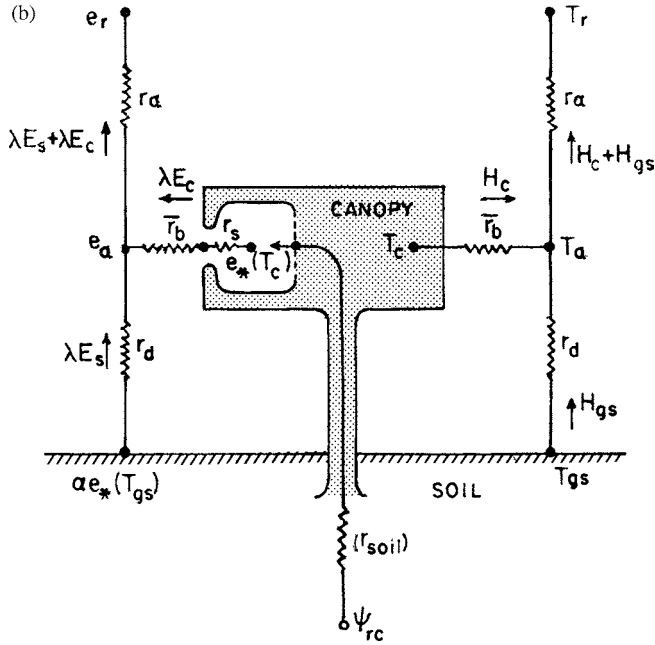
Fig. 11-30b

Notes to Chapter 11

1. Here σ is used to indicate the generalized vertical coordinate discussed in Chapter 6. In many model applications, the rectangular vertical coordinate z is used.

2. Open and closed boundaries are defined in Section 11.3.1.1.

3. The integral over a given set of wavelengths in Figure 11-2 is equal to the variance of the topography over this interval. Integrating over all wavelengths yields the total variance of the terrain, assuming that significant terrain variations do not occur on scales less than twice the minimum resolution in the topographic data.

4. $x = 0$ and $x = 1$ correspond to the model domain sides, so that $0 \leq x \leq 1$.

5. The use of two or more distinct grid meshes is referred to as a *nested grid*. Elsberry (1978) provides a short review of nested grid procedures.

6. See Chapter 12, Section 12.5.2, for a discussion of kinetic energy conservation.

7. The prognostic form of the conservation equations, called hyperbolic differential equations, require both initial and spatial boundary conditions for their solution. Certain subsets of these conservation equations [e.g., Eq. (4-35)], however, are elliptic differential equations and require only spatial boundary conditions. Most texts on partial differential equations discuss the determination of the particular types of partial differential equations in more detail. Haltiner and Williams (1980) gave a brief summary of types of partial differential equations.

8. Guiraud and Zeytounian (1982) briefly discussed the influence on initialization of the reduced number of initial conditions needed when a model is made hydrostatic.

9. This initialization process, called dynamic initialization, is defined in Section 11.2.1.
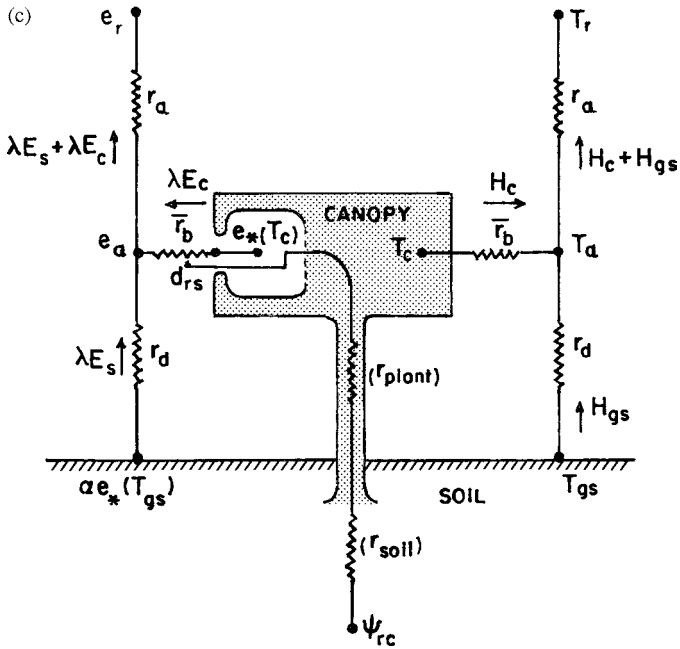
Fig. 11-30c

10. The small value of $RMSE_T$ from Figure 11-11(c) resulted because temperature was continually forced back to the observed value during the initialization. No such adjustment, however, was used on the wind field in obtaining Figure 11-11(b).

11. The mesoscale model requires values of the dependent variables averaged over a grid volume as defined in Chapter 4 (e.g., $\bar{u}$, $\bar{\theta}$, etc.), and the observations provide values over the sampling volume of the instrumentation. This difference gives rise to observational data that are not consistent with the mesoscale-averaged variables needed for input to a model.

12. Structure functions arise when a dependent variable is decomposed into products of dependent variables that individually are functions of only a subset of the entire range of independent variables. Each separate function represents a different subset of the independent variables. A vertical structure function, for example, can be written as $\phi(x, y, z, t) = \Phi(z)\psi(x, y, t)$. Baer and Katz (1980) and Daley (1981) described the advantages of such a decomposition of the dependent variables.

13. If only one observation site is used, then the field is assumed to be horizontally homogeneous over the entire region.

14. In geological time periods, the development of mountains is referred to as diastrophism; this term has been adopted in mesoscale meteorology to describe the construction of terrain in a model.

15. The definition of slowness is arbitrarily, of course, but if the wind field changes by only 10% in 12 hours, for example, and the forcing is constant, then it is reasonable to conclude that a quasi-steady solution has been achieved.

16. At a latitude of 48°, six inertial periods equal about 4 days. With a wind velocity of 20 m s^{-1}, the advective transit time from one side of the model to the other for a 200-km long domain is less than 3 hours.

17. A local boundary condition is one that is generated at the boundary and is not a function of interior grid points.

18. Closed boundaries could also be defined where no flow occurs at that perimeter of a model. This definition seems too limited, however, so that in this text a closed boundary means that $u', v', w' \equiv 0$ at the boundary, rather than $\bar{u}, \bar{v}, \bar{w} \equiv 0$. Such a boundary is closed to mesoscale flow but not to larger-scale motions.

19. The Brunt–Väisälä frequency is defined by Note 5 in Chapter 5.

20. See, for example, Eq. (10-66), where α would increase near the lateral boundaries.

21. See, for example, Eq. (10-67), where δ would increase near the lateral boundaries.

22. See Section 11.3.2 for a discussion of the absorbing layer.

23. If a terrain-following coordinate system is used (see Chapter 6), then the boundary conditions given by Eq. (11-24) must be transformed properly to the new coordinate system.

24. Note that even when the incompressible continuity Eq. (4-23) is used, $\partial\bar{\rho}/\partial t \neq 0$. As shown in Section 3.1, the use of the incompressible and anelastic forms of the conservation of mass are permitted when temporal changes of density are small relative to the other terms in Eq. (2-38), but not necessarily equal to 0.

25. The effective radiating temperature, T_*, is defined from $R\downarrow_{lwG} = \sigma T_*^4$.

26. On the mesoscale, the horizontal conduction of heat in the soil is neglected, since the horizontal grid is much larger than the vertical grid in the soil.

27. The thermal diffusivity, k_s, is also referred to as *heat conductivity* and *thermometric conductivity* (Huschke 1959).

28. This identity can be shown by squaring both sides; $i = (i+1)^2/2 = (i^2 + 2i + 1)/2 = i$.

29. The equivalent atmospheric term is given by Eq. (3-29) in Chapter 3.

30. The procedure for calculating the equilibrium moisture value discussed after Eq. (11-46) was used to make these calculations.

31. Note that upward (downward) arrows are used to indicate that the direct plus diffuse solar radiation has an upward (downward) direction of propagation. This notation is, therefore, somewhat different from that used in Chapter 8, where an arrow was used with shortwave radiation only when referring to direct radiation.

32. Fleagle and Businger (1980:233,234) provide a discussion of longwave radiative exchange between two parallel surfaces (such as a canopy and the ground) where there is negligible absorption in the intervening space.

33. For a more detailed discussion of emissivities and other aspects of the micrometeorology of vegetation stands, Monteith (1975b) offers a useful survey.

34. Forced and free convection are defined after Eq. (7-8).

35. Lockwood and Sellers (1982) is an example of a paper that compares the amount of interception by different types of vegetation canopies.

36. P_r for rain and snow could be estimated from Eq. (9-6) for $\bar{q}_2^R$ and $\bar{q}_1^S$ evaluated at the vegetation level.

37. The form of the sensible and latent heat fluxes used here is somewhat different from those applied by McCumber in that the fluxes are weighted by σ_f, whereas McCumber weighted u_*, θ_*, and q_* separately to compute a grid-volume–averaged flux. Weighting the fluxes, however, is the procedure used in more recent SVATs, as reported in Walko *et al.* (2000a).

38. Other papers that discuss SVATS and their use include Dickinson (1984), Sellers *et al.* (1986), Noilhan and Planton (1989), Pinty *et al.* (1989), Avissar and Pielke (1991), Ye and Pielke (1993), Lakhtakia and Warner (1994), Lee *et al.* (1995), Pleim and Xiu (1995), Viterbo and Beljaars (1995), Chen *et al.* (1996, 1997), Gao *et al.* (1996), DeRidder and Schayes (1997), Dai and Zeng (1997), Mölders and Raabe (1997), Niyogi and SethuRaman (1997), Betts *et al.* (1998), Bosilovich and Sun (1998), Dai *et al.* (1998), Qu *et al.* (1998), Qingcun *et al.* (1998), Schultz *et al.* (1998), Yang *et al.* (1998, 1999a, b), Yongjiu *et al.* (1998), Ashby (1999), Bastidas *et al.* (1999), Bonan

et al. (1999), Boone *et al.* (1999), Chang *et al.* (1999), Chapin *et al.* (1999), Entin *et al.* (1999), Gupta *et al.* (1999), Liu *et al.* (1999), Lynch *et al.* (1999a), Oki *et al.* (1999), Pauwels and Wood (1999), Zeng *et al.* (1999b), Xu *et al.* (1999), Boone *et al.* (2000), Ding *et al.* (2000), Dirmeyer *et al.* (2000), Marshall *et al.* (2000), Mihailovic *et al.* (2000), Mohr *et al.* (2000), Schlosser *et al.* (2000), Sen *et al.* (2000), van den Hurk *et al.* (2000), Verseghy (2000), Walko *et al.* (2000a), Wu *et al.* (2000a), Zeller and Nikolov (2000), and Zeng *et al.* (2000b). As evident from this extensive list of citations, SVAT research has become an active area of research.

Additional Readings

Recent books and review papers that explore the subjects in this chapter in greater depth include the following.

Brutsaert, W. 1982a. "Evaporation into the Atmosphere: Theory, History and Applications," D. Reidel, Norwell, MA.

Halldin, S., and S.-E. Gryning. 1999. Boreal forests and climate. *Agric. Forest Meteor.* **98-99**, 1–4.

Hayden, B.P. 1998. Ecosystem feedbacks on climate at the landscape scale. *Phil. Trans. R. Soc. Lond. Ser. B.* **353**, 5–18.

Parlange, M. B., A. T. Cahill, D. R. Nielsen, J. W. Hopmans, and O. Wendroth. 1998. Review of heat and water movement in field soils. *Soil and Tillage Research.* **47**, 5–10.

Tenhunen, J. D., and P. Kabat, (Eds.). 1999. Integrating hydrology, ecosystem dynamics, and biogeochemistry in complex landscapes. Report of the Dahlem Workshop on Integrating Hydrology, Ecosystem Dynamics, and Biogeochemistry in Complex Landscapes, January 18–23, 1998. Wiley, New York.

Special journal issues of land-surface field campaigns include (listed by editors) Murphy (1992), Sellers *et al.* (1997), Avissar and Lawford (1999), and Hall (1999). Recent reviews of field campaigns are presented in Kabat (1999) and LeMone *et al.* (2000).

Problems

1. Using Eq. (11-55), compute the lowest latitude at which the sun does not set on June 21. Then compute the latitudes at which the sun does not rise on December 21. (Hint: You are computing the latitude of the Arctic Circle.)

2. Using the simple energy budget $\sigma T^4 = S(1 - A)/4$, where S is the solar constant, A is the albedo, σ is the Stefan–Boltzmann constant, and T is the temperature, derive the quantity $\partial T/\partial A$. Calculate the change of albedo required to obtain a 1°C change in temperature.

3. Program the tank model in Section 10.1.4. Run with cyclic boundary conditions to show that the values in Table 10-3 can be reproduced. Then run the tank model with (a) constant inflow–gradient outflow and (b) constant inflow–radiative outflow (see Section 11.3.1.1). Discuss the resultant solutions and how they differ from the results with cyclic boundary conditions.

4. Select a SVAT (such as LEAF, LEAF-2, or LAPS in Appendix D), and determine the dependent variables, tunable coefficients, and universal constants (if any).

Chapter 12

Model Evaluation

12.1   Evaluation Criteria

Six basic requirements must be met before the credibility of simulations performed with that a mesoscale numerical model can be established by the scientific community. In reading papers in the published literature, one must consider the same criteria when evaluating the results and conclusions of those papers. These requirements are as follows.

1. The model must be compared with known analytic solutions. To perform these experiments, the mesoscale model is forced by very small perturbations, so that essentially linearized results are produced, or the initial and boundary conditions are idealized, so that exact solutions to the nonlinear equations are possible.

2. Nonlinear simulations with the model must be compared with the results from other models that have been developed independently.

3. The mass, moisture, and energy budgets of the model must be computed to determine the conservation of these important physical quantities.

4. The model predictions must be quantitatively compared with observations.

5. The computer logic of the model must be available on request, so that the flow structure of the code can be examined.

6. The published version of the model must have been subjected to peer review. For this reason, model results presented in recognized professional journals (e.g., *Monthly Weather Review, The Journal of Atmospheric Science, The Quarterly Journal of the Royal Meteorological Society, Tellus, The Journal of the Meteorological Society of Japan, The Chinese Journal of Atmospheric Sciences, Atmosfera, Atmosphere-Ocean, Boundary-Layer Meteorology, The Journal of Geophysical Research, Meteorology and Atmospheric Physics, Russian Meteorology and Hydrology*) should carry more weight than those distributed in report formats.

Hanna (1994) provides a similar list of evaluation criteria. In this chapter, several of these criteria are examined in more detail.

12.2   Comparison with Analytic Theory

To compare a numerical model with its analytic analog, the equations in the computational model must be used in the same form as used to develop the solution for the analytic version. Except for special cases, the development of an analogous system of equations in a numerical model usually requires that the equations be linearized. In addition, to minimize computational errors, the grid resolution of the model must be sufficiently small such that the spatial scale of the forcing (e.g., L_x and L_z) are adequately resolved, as summarized in Chapter 10, Section 10.6.

Figure 12-1, reproduced from Martin (1981), illustrates a numerical simulation performed to validate the model against Defant's (1950) exact linear
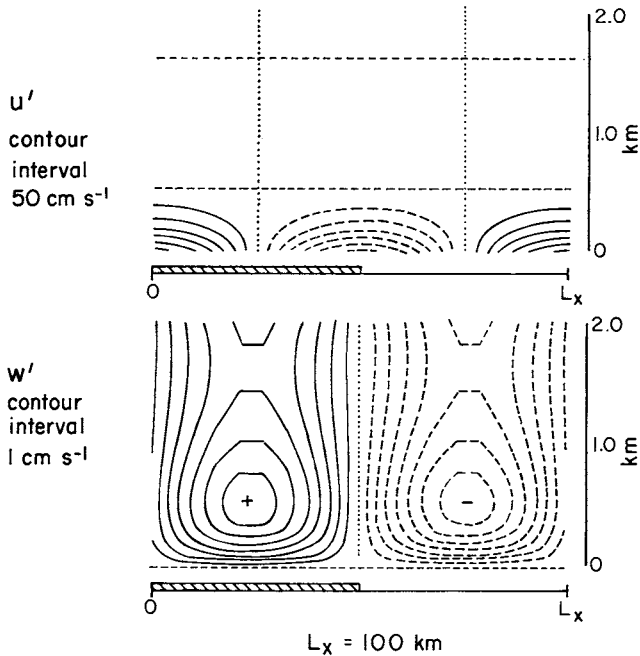
Fig. 12-1. The horizontal and vertical velocity fields 6 hours after sunrise predicted by a numerical model analog to Defant's (1950) analytic model. The input parameters are given by Eq. (5-99), the results correspond to the exact solution given in Figure 5-4. (From Martin 1981.)

solution. Defant's analytic model was derived in Chapter 5, Section 5.2.3.1. Although there are minor differences between the fields in Figure 12-1 and those evaluated from Defant's solution (e.g., Figure 5-4), the solutions are almost identical.

   Klemp and Lilly (1978) have performed similar comparisons between analytic and numerical solutions for airflow over rough terrain. One example is reproduced in Figure 12-2. In addition to validations against linear theory, Klemp and Lilly (1978) and Lilly and Klemp (1979) also performed comparisons against analytic solutions of a subset set of the nonlinear conservation equations developed by Long (1953, 1955); see Section 5.3 for a derivation of the Long model. Although Long's solutions are valid only for the special case when the flow is steady state and the density multiplied by the domain-averaged horizontal velocity squared is independent of height, such comparisons offer some evidence of the accuracy of the numerical computations. The limitations of Long's solution to actual stratified flows over an obstacle are discussed by Baines (1977). Durran (1981) has referenced studies by other investigators who obtained exact solutions for specialized sets of the nonlinear conservation equations.
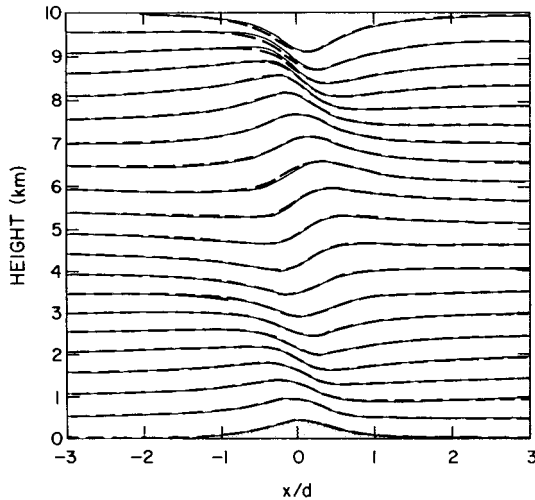
Fig. 12-2. Comparison of predicted contours of potential temperature $\bar{\theta}$ for an analytic solution (dashed line) and the equivalent numerical solution (solid line) for a bell-shaped mountain of 10 m. Results have been amplified by 50 for illustration purposes. The normalizing factor d is the characteristic half-width of the mountain. The atmosphere in this simulation was prescribed as isothermal initially with a large-scale wind flow of 20 m s^{-1}, constant with height. (From Klemp and Lilly 1978.)

12.3   Comparison with Other Numerical Models

In evaluating a numerical model, it is useful to compare its results for a particular simulation with those of a model from a different set of investigators, such as reported by Cox *et al.* (1998). Although all models start with the conservation equations discussed in Chapter 2, such model facets as the computational schemes, parameterizations, and particular simplified form of the conservation equations result in different model formulations. Although similar model results do not necessarily indicate a realistic reproduction of the actual atmospheric system, they are useful experiments to ascertain whether independent researchers using different model structures can replicate each others' results.

Mahrer and Pielke (1977b) performed a qualitative evaluation of their three-dimensional simulation of the airflow over the White Sands Missile Range in New Mexico against that of Anthes and Warner (1974), but used no quantitative measures of degree of agreement. Tapp and White (1976), Hsu (1979), and MacDonald *et al.* (2000) performed a similar qualitative comparison of their results against the sea-breeze simulation reported in Pielke (1974a). An example of an intercomparison between the results of Tapp and White (1976) and of Pielke (1974a) are illustrated in Figure 12-3. Carpenter and Lowther (1981) have shown that these Florida sea-breeze results are relatively insensitive to changes

(a)   (b)
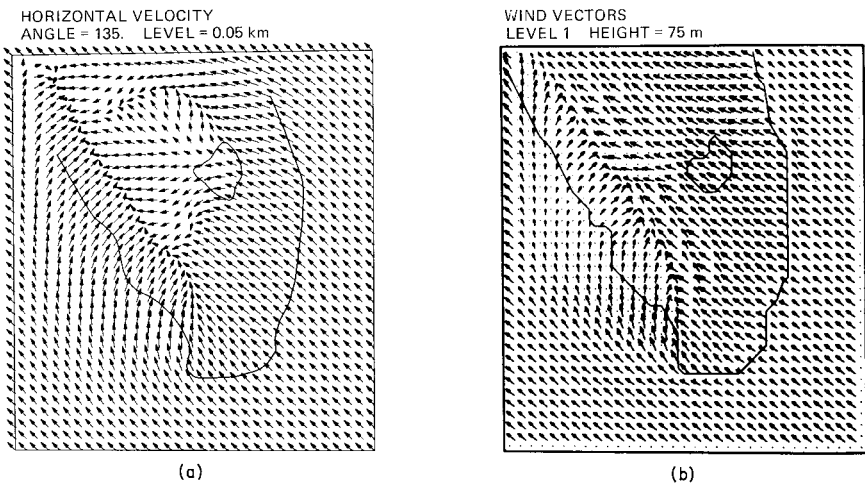
Fig. 12-3. The predicted horizontal winds (a) at 50 m, 10 hours after sunrise (Pielke 1974a) and (b) at 75 m, 12 hours after sunrise (Tapp and White 1976). The synoptic geostrophic wind for both simulations was from the southeast to 6 m s^{-1}, and the maximum land-surface temperature during the day was 10°C warmer than the surrounding ocean temperature. The distance between one grid point (indicated by the origin of the arrows) corresponds to 6 m s^{-1}.

in the vertical grid mesh used. This result is consistent with the two-dimensional vertical grid resolution sensitivity test illustrated in Chapter 11, Figure 11-6.

Using two-dimensional models, Kessler and Pielke (1982), Mahrer and Pielke (1978b), and Peltier and Clark (1979) have simulated the airflow over rough terrain for the Colorado Front Range windstorm of January 11, 1972 (described by Lilly and Zipser 1972), and compared their results to those of Klemp and Lilly (1978). A more recent model intercomparison of the simulations of this wind storm, using 11 different models, is reported in Doyle et al. (2000).

12.4   Comparison Against Different Model Formulations

Rather than comparing results from models of different investigators, one can examine alternative forms of the same model. In one form of *sensitivity* study,[1] changes to the model can include different computational schemes, other approximations to the conservation equations, and so on. Tapp and White (1976), for example, contrasted the use of forward-in-time, upstream differencing (Scheme I in Table 10-1) of the advective terms in their sea-breeze model with the use of a second-order leapfrog representation (Scheme II in Table 10-1). Although the results were similar, the use of upstream differencing produced smoother vertical and horizontal velocity fields. The noisier fields resulting from the leapfrog representation may have occurred due to the poor handling of phase speed with that scheme. Mahrer and Pielke (1978b) performed a test of the upstream spline interpolation (Scheme III in Table 10-1) and the upstream differencing in a two-dimensional sea-breeze simulation and found no significant differences in the results. (In the same paper, however, Mahrer and Pielke found that the upstream differencing scheme produced mountain wave solutions with excessive damping, as contrasted with the more realistic appearing solutions obtained with the spline. Sea-breeze simulations can produce reasonable solutions with upstream differencing because such a mesoscale feature is strongly controlled by vertical subgrid-scale mixing, whereas simulations of forced airflow over rough terrain require a much more accurate representation of advection and gravity wave propagation.)

The evaluation of nonlinear model results with and without the hydrostatic assumption is of particular interest. For the sea-breeze circulation, Pielke (1972), Martin (1981), and Martin and Pielke (1983) examined the relative magnitude of the nonhydrostatic pressure in a nonlinear model in considerable depth. One procedure used to evaluate this pressure is to derive a Poisson equation for the hydrostatic component of the pressure, $\bar{p}_H = p'_H + p_0$, as was performed for the Defant sea-breeze model in Section 5.2.3.2. The difference between the total

and hydrostatic pressure, defined here as R', represents a grid-volume–averaged nonhydrostatic pressure residual. In an anelastic formulation, since $\partial p_0/\partial x_i$ is already required to be in hydrostatic balance, the ratio given by

$$\left|\frac{\partial p'_H}{\partial x_i} + \frac{\partial R'}{\partial x_i}\right| \Big/ \left|\frac{\partial p'_H}{\partial x_i}\right|, \qquad i = 1, 2, \tag{12-1}$$

indicates the significance of the nonhydrostatic effect.

To illustrate the derivation of R' for a nonlinear model, assume that the depth of the atmospheric circulation of interest is much smaller than the density scale depth of the atmosphere (i.e., $L_z \ll H_\alpha$) so that the shallow continuity equation in (4-23) can be used, the second term on the left of Eq. (4-35) can be ignored, and α'/α_0 can be approximated by θ'/θ_0. In addition, to simplify the analysis (without losing the generality of the result since p_0 is assumed hydrostatically determined) assume $(\partial/\partial x_i)p_0 = 0\,(i = 1, 2)$. For this situation, differentiating Eq. (4-34) with respect to z and Eq. (4-14) with respect to x and y (i.e., $\partial/\partial x_i$ with $i = 1, 2$), where $\bar{p}$ is replaced with $\bar{p}_H$, and adding the two equations yields

$$\left(\frac{\partial^2}{\partial x^2} + \frac{\partial^2}{\partial y^2} + \frac{\partial^2}{\partial z^2}\right)p'_H = \nabla^2 p'_H = \frac{\partial^2}{\partial x_i \partial x_j}\rho_0 \bar{u}_i \bar{u}_j$$

$$- \frac{\partial^2}{\partial x_i \partial x_j}\rho_0 \overline{u''_j u''_i} - 2\rho_0 \epsilon_{ijk}\Omega_j \frac{\partial}{\partial x_i}\bar{u}_k$$

$$- \frac{\partial}{\partial x_i}\rho_0 \frac{\partial \bar{u}^*_i}{\partial t} + g\frac{\partial}{\partial z}\rho_0 \frac{\theta'}{\theta_0}\,(i = 1, 2), \tag{12-2}$$

where $\partial \bar{u}^*_i/\partial t$ is evaluated from Eq. (4-14) using $\bar{p}_H$ in place of the total pressure $\bar{p}$. Subtracting Eq. (12-2) from the form of Eq. (4-35) for a shallow atmospheric system and with $\partial p_0/\partial x_i\,(i = 1, 2) = 0$, and assuming that the velocities occurring in Eq. (12-2) that do not involve a time tendency term are the same as the equivalent velocities in Eq. (4-35), results in the equation[2]

$$\frac{\partial^2 R'}{\partial x_i^2} = -\frac{\partial^2}{\partial z\partial x_j}\rho_0 \bar{u}_j \bar{w} - \frac{\partial^2}{\partial z\partial x_j}\rho_0 \overline{u''_j w''} + \frac{\partial}{\partial x}\rho_0 \frac{\partial \bar{u}^*}{\partial t} + \frac{\partial}{\partial y}\rho_0 \frac{\partial \bar{v}^*}{\partial t}, \tag{12-3}$$

where $R' = \bar{p} - \bar{p}_H = p' - p'_H$. Since the magnitude of $\partial/\partial x_i$ in Eq. (12-1) is over the same distance for each term, examination of

$$\epsilon = |R'/p'_H|$$

at each grid point over a model simulation is an adequate test of the adequacy of the hydrostatic assumption.

Pielke (1972) found for sea-breeze simulations that for the same scale of horizontal heating, ϵ became larger as the heating was increased and as the thermodynamic stratification was made less stable. This result agrees with that found by Martin for the linear model results discussed in Section 5.2.3 and

illustrated in Figures 5-5 and 5-6. The variation of the maximum nonhydrostatic pressure residual as a function of heat input and overlying stratification from Pielke's (1972) results are illustrated in Figure 12-4 as a function of the horizontal grid scale used. For each experiment, heat was input within the lowest 300 m over a horizontal distance of $9\Delta x$ and over a time scale such that the maximum heating was reached at the time indicated at the top of the figure. Even for relatively small scales of horizontal heating over short time periods (e.g., with $L_x = 9$ km, the time to maximum heating was 30 min), the hydrostatic relation appears to be a valid assumption for the pressure distribution.

Figures 12-5 and 12-6 illustrate results from Pielke (1972) for a hydrostatic model run, where p'_H is used to represent the horizontal pressure gradient, and for a nonhydrostatic simulation, where $p' = p'_H + R'$ is used for that horizontal gradient. The scales of horizontal heating in the calculation are 2.7 and 9 km, with a maximum temperature amplitude, $\Delta\bar{\theta}_{max}$, in Eq. (11-30) of 5°, and a potential temperature gradient in the lowest 2.7 km of the model of 1°C/300 m. In Figures 12-5 and 12-6, day in Eq. (11-30) was defined as 2160 s and
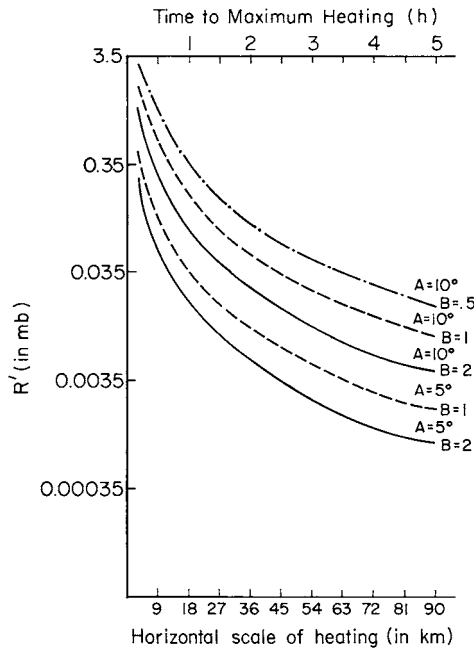
Fig. 12-4. The maximum absolute value of the nonhydrostatic pressure residual, R', as a function of horizontal scale of heating and time to maximum heating (Pielke 1972). To determine R' from Pielke (1972:26), a large-scale pressure of 1000 mb was used. The magnitude of maximum heating is A [i.e., using $A = \Delta\bar{\theta}_{max}$ in Eq. (11-30)] and B is the value of $\partial\theta_0/\partial z$ in the middle and lower levels of the model in terms of $B°C/300$ m.

NONHYDROSTATIC   (a)   Time = 578.12 s

HYDROSTATIC   (b)   Time = 577.15 s
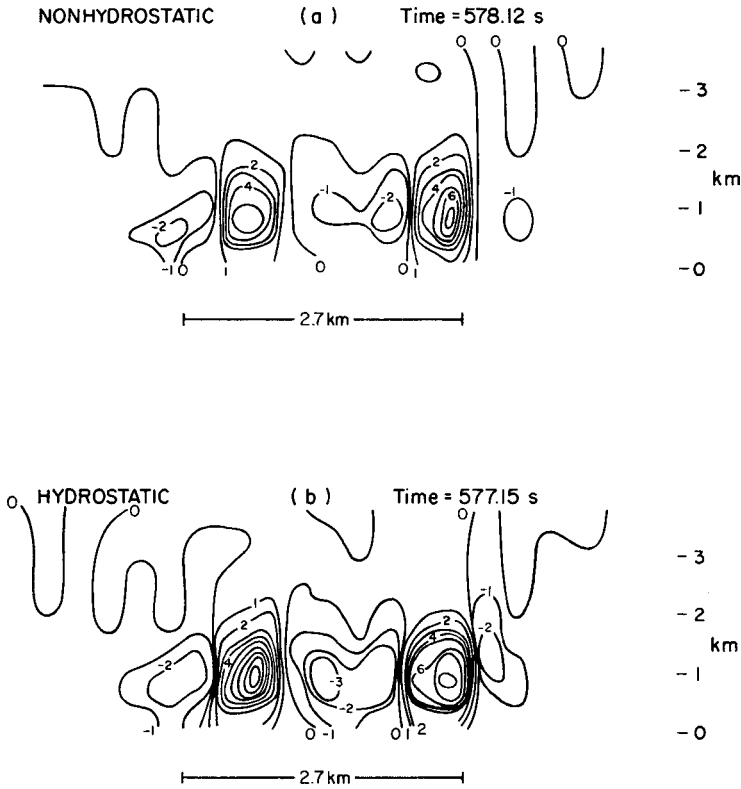
Fig. 12-5.   The vertical velocity in centimeters per second in (a) an anelastic, nonhydrostatic model and (b) a hydrostatic model, where L_x = 2.7 km, $\Delta x = 0.3$ km, $\Delta \bar{\theta}_{max}$ and day in Eq. (11-30) of 5°C and 2160 s, and $\partial \theta_0 / \partial z = 1$°C/300 m in the lowest 2.7 km. The horizontal scale of heating is indicated at the bottom. (From Pielke 1972.)

7200 s, respectively. Despite the short time period of heat input, however, the differences between the hydrostatic and nonhydrostatic simulations for $L_x = 9$ km were small. With $L_x = 2.7$ km, the hydrostatic solution had substantially larger amplitude, although the locations of the convergence zones were similar. Figure 12-7 illustrates the contribution of the nonhydrostatic pressure residual, R', to the total pressure for Pielke's (1972) sea-breeze calculations. In a nonhydrostatic model, the vertical accelerations act to diminish the magnitude of the hydrostatic horizontal pressure gradients.

Martin's (1981) study substantiated Pielke's (1972) investigation of the relative influence of the nonhydrostatic pressure residual. In Martin's thesis, the nonlinear advection terms are added to Defant's (1950) analytic equations given

NONHYDROSTATIC   (a)   Time = 1924.22 s

HYDROSTATIC   (b)   Time=1923.24 s
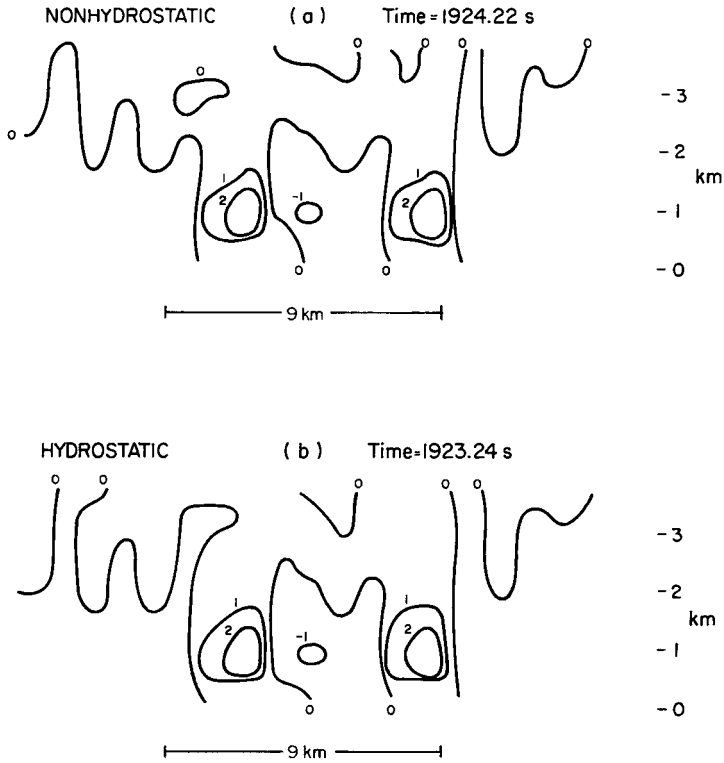
Fig. 12-6. Same as Figure 12-5 except $L_x = 9$ km and day = 7200 s. (From Pielke 1972.)

by Eqs. (5-66)–(5-70); that is, $u' \partial u'/\partial x$ and $w' \partial u'/\partial z$ to Eq. (5-66), $u' \partial v'/\partial x$ and $w' \partial v'/\partial z$ to Eq. (5-67), $u' \partial w'/\partial x$ and $w' \partial w'/\partial z$ to Eq. (5-68), and $u' \partial \theta'/\partial x$ and $w' \partial \theta'/\partial z$ to Eq. (5-70). A hydrostatic model is formed from these equations using $\partial p_H'/\partial z = \rho_0 \theta'/\theta_0$ in place of Eq. (5-68) (i.e., $\lambda_1 = 0$), and a nonhydrostatic version is derived of the form given by Eq. (12-3) where $p' = p_H' + R'$ is used in Eqs. (5-66) and (5-68) with $\lambda_1 = 1$. Figure 12-8 illustrates predicted results for horizontal velocity at the time of maximum heating, where $L_x = 6.25$ km and the largest temperature perturbation is 2.5°C. As in Pielke's (1972) earlier study, the nonhydrostatic and hydrostatic results are similar even for this relatively small spatial scale of heating.

Tag and Rosmond (1980) extended the hydrostatic–nonhydrostatic comparison to a three-dimensional cloud simulation. Among their findings was that moist processes magnified the nonhydrostatic effect, although increasing the stability from 1 to 2°C km^{-1} almost eliminated the differences caused by the nonhydrostatic effect.
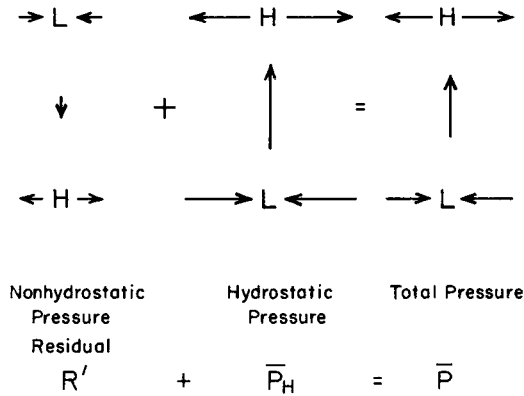
Fig. 12-7. A schematic of the relative contributions of the nonhydrostatic pressure residual and the hydrostatic pressure to the total pressure at a location over land in the center of the lowest pressure in the sea-breeze convergence zone. The arrows illustrate the instantaneous horizontal winds that would be expected from these pressure distributions. (Adapted from Pielke 1972.)

One of the advantages of using Eq. (12-3) to compute the nonhydrostatic pressure residual is that it must be computed only in a region where significant vertical accelerations exist. As illustrated in Figure 12-9, the boundary condition for R on the subdomain is straightforward to apply, since $R = 0$ where the motions are hydrostatic.

The importance of the nonhydrostatic residual has also been examined, to some extent, for forced air over rough terrain. Figure 12-10, reproduced from Durran (1981), shows potential temperature surfaces from one of Klemp and
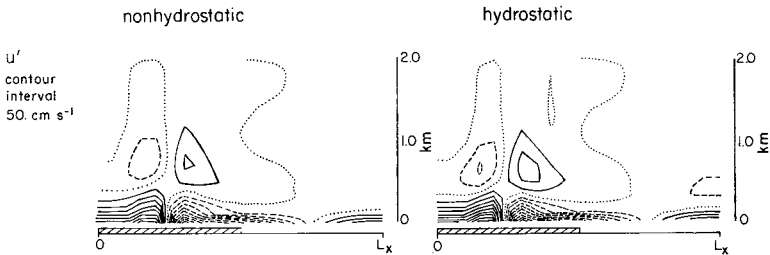
Fig. 12-8. Nonhydrostatic and hydrostatic simulations for $L_x = 6.25$ km after 2700 s with a surface heating function of $\bar{\theta} = \theta_0(t = 0) + |\Delta\theta|_{max} \sin(2\pi x/L_x) \sin(\pi t/T)$, where $|\Delta\theta|_{max} = 2.5°C$ and $T = 3$ h. The horizontal and vertical grid spacings were $\Delta x = 0.306$ km and $\Delta z = 100$ m. Periodic lateral boundary conditions were used. Other prescribed values include $\partial\theta_0/\partial x = 10°C$ km^{-1}, $K_\theta = 10$ m^2 s^{-1}, $f = 1.301 \times 10^{-4}$ s^{-1}, and σ_H and $\sigma_v = 10^{-3}$ s^{-1}. (These symbols are explained in Section 5.2.3.1.) Positive values are given by the solid line and negative values are represented by dashed lines, with 0 indicated by the dotted line. (From Martin 1981.)

Computation   of   a   Local   Nonhydrostatic   Effect   in
Numerical   Model
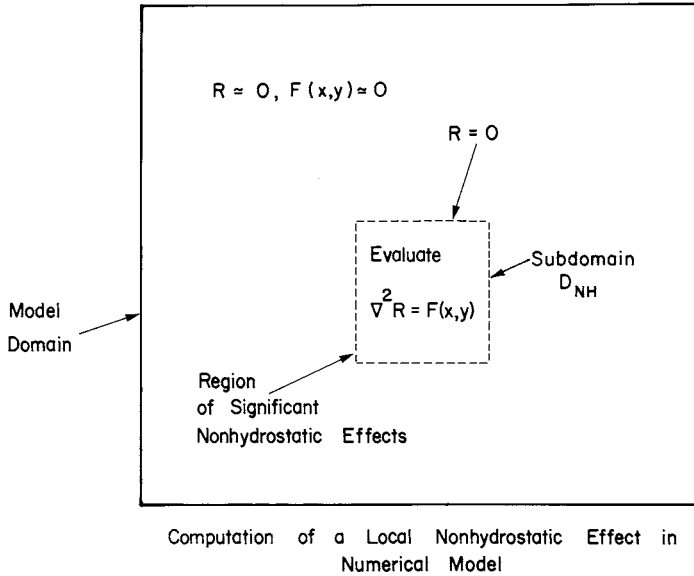
Fig. 12-9. The definition of a subdomain, D_{NH}, in a model where nonhydrostatic effects are significant. Such a domain is defined to enclose those regions where $F(x, y)$ is significantly different from 0.

Lilly's (1978, Figure 10) hydrostatic simulations and an equivalent result performed by Durran for a nonhydrostatic simulation. In both model runs the upstream wind was 20 m s^{-1}, constant with height, the mountain height reached 1 km, $\partial\theta_0/\partial z = 4°C$ km^{-1} within the lowest 10 km, and an isothermal absorbing layer (see Section 11.3.2 and Figure 11-18) was prescribed between 10 and 20 km in height. The half-width of the mountain was 20 km, where the terrain was defined as

$$z_{\mathrm{G}} = b^2 z_{\mathrm{G_{max}}}/(x^2 + b^2), \tag{12-4}$$

where b is the half-width and $z_{\mathrm{G_{max}}}$ is the maximum height of the terrain. Although the nonhydrostatic simulation produced a slightly steeper wave in the upper stratosphere, the hydrostatic and nonhydrostatic results are almost identical. Klemp and Lilly (1980) concluded that for realistic atmospheres with simple, uniform structure (i.e., constant large-scale velocity and static stability with height), ratios of $(b/|u_0|)[(g/\theta_0)(\partial\theta_0/\partial z)]^{1/2} \geq 10$ or so yield nearly identical hydrostatic and nonhydrostatic results. For example, with $\partial\theta_0/\partial z = 1$ K 100 m^{-1}, $\theta_0 = 300$ K, and $u_0 = 20$ m s^{-1}, $b \geq 10$ km or so satisfies this requirement. For a more general atmospheric structure, however, it is desirable to check the hydrostatic assumption for each situation.
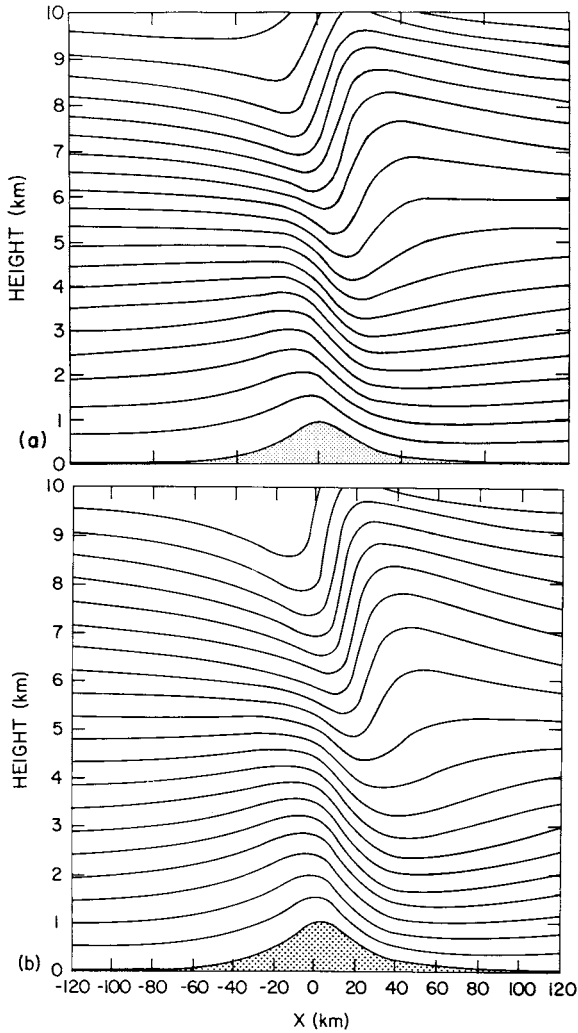
Fig. 12-10. Contours of potential temperature from (a) a nonlinear hydrostatic simulation by Klemp and Lilly (1978), and (b) a nonlinear nonhydrostatic simulation by Durran (1981). The upstream winds were 20 m s^{-1}, and the upstream stratification within the lowest 10 km was 4°C km^{-1}. Note that because of scale differences the height scale in (b) is about 8% larger than that in (a). To more quantitatively compare the two results, measure the trough-to-crest difference for equivalent initial inflow potential temperature heights.

12.5   Calculation of Model Budgets

Evaluation of the budgets of such physical quantities as kinetic energy and mass is useful not only to improve our understanding of mesoscale physical processes, but also, as a diagnostic tool to examine the fidelity of the computer program logic. Before discussing such budgets of mesoscale models, it is useful to examine this approach with the single fluid tank model introduced in Section 5.2.1.1.

12.5.1   Mass and Energy Equations for the Homogeneous Tank Model

The mass budget for this simplified model given by Eqs. (5-17) and (5-20) is particularly easy to compute, since the fluid is assumed to be homogeneous. Using the product rule of differentiation and integrating Eq. (5-20) over the tank model domain, D_x, yields

$$\int_0^{D_x} \frac{\partial h}{\partial t}\, dx + \int_0^{D_x} \frac{\partial}{\partial x} u'h\, dx = \int_0^{D_x} \frac{\partial h}{\partial t}\, dx + u'h\Big|_0^{D_x} = 0.$$

If the sides of the tank $(x = 0, D_x)$ are rigid (i.e., $u'_0 = u'_{D_x} = 0$),[3] or if periodic boundary conditions for h and u' are used (i.e., $u'h$ at $x = 0$ is equal to $u'h$ at $x = D_x$), then

$$\int_0^{D_x} \frac{\partial h}{\partial t}\, dx = \frac{\partial}{\partial t}\int_0^{D_x} h\, dx = \frac{\partial \bar{h}}{\partial t} = 0,$$

so that the average height of the fluid must be constant in time. In a numerical model, the conservation of mass, as represented by the depth of the fluid, can be checked at each time step by

$$\bar{h} = \frac{1}{I_D} \sum_{i=1}^{I_D} h_i,$$

where I_D is the number of grid points. If $\Delta\bar{h}/\Delta t \neq 0$, then mass is not conserved.

The kinetic energy of the tank model can be computed by multiplying Eq. (5-17) by hu' and Eq. (5-20) by $u'^2/2$, yielding the two simultaneous partial differential equations

$$hu'\frac{\partial u'}{\partial t} + hu'^2\frac{\partial u'}{\partial x} + ghu'\frac{\partial h'}{\partial x} = h\frac{\partial u'^2/2}{\partial t} + hu'\frac{\partial}{\partial x}\left(\frac{u'^2}{2}\right) + ghu'\frac{\partial h}{\partial x} = 0$$

$$\frac{u'^2}{2}\frac{\partial h}{\partial t} + \frac{u'^2}{2}u'\frac{\partial h}{\partial x} + \frac{u'^2}{2}h\frac{\partial u'}{\partial x} = \frac{u'^2}{2}\frac{\partial h}{\partial t} + \frac{u'^2}{2}\frac{\partial}{\partial x}(hu') = 0.$$

Adding these two equations using the product rule of differentiation and multiplying through by the constant density ρ_0 yields

$$\frac{\partial}{\partial t}\left(\rho_0 \frac{u'^2}{2} h\right) + \frac{\partial}{\partial x}\left(\rho_0 \frac{u'^2}{2} hu'\right) + \rho_0 g hu' \frac{\partial h}{\partial x} = 0, \qquad (12\text{-}5)$$

where $\rho_0(u'^2/2h)$ as units of kinetic energy per unit area.

The potential energy equation is obtained by multiplying Eq. (5-20) by $\rho_0 gh$, resulting in

$$\rho_0 gh \frac{\partial h}{\partial t} + \rho_0 gh \frac{\partial}{\partial x} hu' = \rho_0 g \frac{\partial h^2/2}{\partial t} + \rho_0 gh \frac{\partial u' h}{\partial x} = 0, \qquad (12\text{-}6)$$

where $\rho_0 gh^2/2$ has units of potential energy per unit area.

To obtain the total energy, add Eqs. (12-5) and (12-6) and rearrange, giving

$$\frac{\partial}{\partial t}\left[\rho_0 \frac{u'^2}{2} h + \rho_0 g \frac{h^2}{2}\right] + \frac{\partial}{\partial x}\left[hu'\left(\rho_0 \frac{u'^2}{2} + \rho_0 gh\right)\right] = 0. \qquad (12\text{-}7)$$

The first term on the left is the local change of total energy per unit area E, and the second term is proportional to the horizontal flux divergence of this energy per unit area.

Integrating this expression over the model domain (i.e., the size of the tank) gives

$$\int_0^{D_x} \frac{\partial E}{\partial t}\, dx = -hu'\left(\rho_0 \frac{u'^2}{2} + \rho_0 gh\right)\Bigg|_0^{D_x} = \frac{\partial}{\partial t}\int_0^{D_x} E\, dx = \frac{\partial E_0}{\partial t},$$

which is equal to 0 if the walls are rigid or if cyclic boundary conditions are applied. If $\partial E_0/\partial t = 0$, then total energy is conserved in the tank model. Thus numerical approximations of the tank model equations should also conserve total energy; that is, evaluating the approximate form for the first bracketed term on the left of Eq. (12-7) at each grid point and summing across the domain should yield a number that is identical at each time step. Thus simulations that differ significantly from such mass- and energy-conservation criteria are suspect, and results from them should be used cautiously, if at all.

12.5.2   Mass and Energy Equations for a Mesoscale Model

In mesoscale models, much more involved conservation relations are used; however, it is similarly desirable to conserve mass and energy. To illustrate the procedure, the hydrostatic, anelastic form of the equations given by Eqs. (6-87)–(6-90) and (6.93) with σ defined by Eq. (6-48) are used to derive the kinetic energy and mass-conservation relations.

The shallow-slope, hydrostatic form of Eq. (6-90) [Eq. (6-62)] can be differentiated with time and the order of operation reversed to yield

$$\frac{\partial}{\partial \tilde{x}^3} \frac{\partial \bar{\pi}}{\partial t} = \frac{g}{\bar{\theta}^2} \frac{s - z_G}{s} \frac{\partial \bar{\theta}}{\partial t}.$$

Integrating between $\tilde{x}^3 = 0$ and s_θ and rearranging yields[4]

$$\left. \frac{\partial \bar{\pi}}{\partial t} \right|_{z_G} = \left. \frac{\partial \bar{\pi}}{\partial t} \right|_{s_\theta} - g \frac{s - z_G}{s} \int_0^{s_\theta} \frac{1}{\bar{\theta}^2} \frac{\partial \bar{\theta}}{\partial t} d\tilde{x}^3, \tag{12-8}$$

which is the same form as Eq. (11-25) except $z_G \neq 0$ in Eq. (12-8). The pressure tendency $\partial \bar{\pi} / \partial t |_{s_\theta}$ must be specified as a boundary condition [i.e., see after Eq. (11-22)], and the integrated term in Eq. (12-8) is evaluated using Eq. (6-90). Integrating the right side of Eq. (12-8) over the model domain gives[5]

$$\frac{1}{D_{\tilde{x}^1} D_{\tilde{x}^2}} \int_0^{D_{\tilde{x}^1}} \int_0^{D_{\tilde{x}^2}} \left. \frac{\partial \bar{\pi}}{\partial t} \right|_{z_G} \left(\frac{s - z_G}{s} \right) \left(\frac{s}{s - z_G} \right) d\tilde{x}^2 d\tilde{x}^1$$

$$= \frac{1}{D_{\tilde{x}^1} D_{\tilde{x}^2}} \frac{\partial}{\partial t} \int_0^{D_{\tilde{x}^1}} \int_0^{D_{\tilde{x}^2}} \bar{\pi}_* d\tilde{x}^2 d\tilde{x}^1 = \frac{\partial \Pi_*}{\partial t}. \tag{12-9}$$

Values of $\partial \bar{\theta} / \partial t$ needed at $\tilde{x}^1 = 0, D_{\tilde{x}^1}$ and at $\tilde{x}^2 = 0, D_{\tilde{x}^2}$ are obtained from the assumed lateral boundary condition on $\bar{\theta}$ (see Section 11.3.1).

Since from Eq. (11-27) a change of π at the surface is equivalent to a change of mass above that level, Π_* in Eq. (12-9) provides the value of the average mass change per unit area over the model domain. This value of Π_* can be compared against the integrated value of $\overline{\Pi}_{z_G}$ computed directly from Eq. (6-62); that is,

$$\frac{\overline{\Pi}_{z_G}}{\partial t} = \frac{1}{D_{\tilde{x}^1} D_{\tilde{x}^2}} \frac{\partial}{\partial t} \int_0^{D_{\tilde{x}^1}} \int_0^{D_{\tilde{x}^2}} \bar{\pi}_{z_G} d\tilde{x}^2 d\tilde{x}^1,$$

where

$$\bar{\pi}_{z_G} = +g \frac{s - z_G}{s} \int_0^{s_\theta} \frac{d\tilde{x}^3}{\bar{\theta}} + \overline{\Pi}|_{s_\theta}.$$

The difference $(\partial / \partial t)(\Pi_{z_G} - \Pi_*)$ is proportional to the mass loss.

A kinetic energy equation for the flow parallel to the terrain can also be derived from the set of equations. Since $\tilde{u}^1 = u$ and $\tilde{u}^2 = v$ from Eq. (6-34), multiplying Eq. (6-57) by $\rho_0 \bar{\tilde{u}}^1 (s - z_G)/s$ and Eq. (6-58) by $\rho_0 \bar{\tilde{u}}^2 (s - z_G)/s$, adding the two equations, and using the anelastic conservation-of-mass equation,

after multiplying by $\bar{k} = \frac{1}{2}(\bar{\tilde{u}}^1\bar{\tilde{u}}^1 + \bar{\tilde{u}}^2\bar{\tilde{u}}^2)$, results in the terrain-following kinetic energy equation

$$\rho_0 \frac{s - z_G}{s} \frac{\partial \bar{k}}{\partial t} = -\frac{\partial}{\partial \tilde{x}^j} \rho_0 \frac{s - z_G}{s} \bar{\tilde{u}}^j \bar{k} - \bar{\tilde{u}}^1 \rho_0 \frac{s - z_G}{s} \overline{\tilde{u}^{j''} \frac{\partial \tilde{u}^{1''}}{\partial \tilde{x}^j}}$$

$$- \bar{\tilde{u}}^2 \rho_0 \frac{s - z_G}{s} \overline{\tilde{u}^{j''} \frac{\partial \tilde{u}^{2''}}{\partial \tilde{x}^j}} - \bar{\tilde{u}}^1 \rho_0 \frac{s - z_G}{s}$$

$$\times \left\{ \theta \frac{\partial \bar{\pi}}{\partial \tilde{x}^1} - g \frac{\sigma - s}{s} \frac{\partial z_G}{\partial x} \right\} - \bar{\tilde{u}}^2 \rho_0 \frac{s - z_G}{s}$$

$$\times \left\{ \theta \frac{\partial \bar{\pi}}{\partial \tilde{x}^2} - g \frac{\sigma - s}{s} \frac{\partial z_G}{\partial y} \right\} - \bar{\tilde{u}}^1 \rho_0 \frac{s - z_G}{s} f \hat{\bar{\tilde{u}}}^3. \quad (12\text{-}10)$$

Equation (12.10) can be integrated over the model domain, yielding

$$\frac{\partial K_*}{\partial t} = -\int_0^{s_\theta} \left\{ \int_0^{D_{\tilde{x}^2}} \rho_0 \frac{s - z_G}{s} \bar{\tilde{u}}^1 \bar{k} \Big|_0^{D_{\tilde{x}^1}} d\tilde{x}^2 + \int_0^{D_{\tilde{x}^1}} \rho_0 \frac{s - z_G}{s} \bar{\tilde{u}}^2 \bar{k} \Big|_0^{D_{\tilde{x}^2}} d\tilde{x}^1 \right.$$

$$+ \int_0^{D_{\tilde{x}^2}} \int_0^{D_{\tilde{x}^1}} \rho_0 \frac{s - z_G}{s} \left[\bar{\tilde{u}}^1 \overline{\tilde{u}^{j''} \frac{\partial \tilde{u}^{1''}}{\partial \tilde{x}^j}} + \bar{\tilde{u}}^2 \overline{\tilde{u}^{j''} \frac{\partial \tilde{u}^{2''}}{\partial \tilde{x}^j}} \right] d\tilde{x}^1 d\tilde{x}^2$$

$$+ \int_0^{D_{\tilde{x}^2}} \int_0^{D_{\tilde{x}^1}} \rho_0 \frac{s - z_G}{s} \left[\bar{\tilde{u}}^1 \bar{\theta} \frac{\partial \bar{\pi}}{\partial \tilde{x}^1} + \bar{\tilde{u}}^2 \bar{\theta} \frac{\partial \bar{\pi}}{\partial \tilde{x}^2} \right] d\tilde{x}^1 d\tilde{x}^2$$

$$- \int_0^{D_{\tilde{x}^2}} \int_0^{D_{\tilde{x}^1}} \rho_0 \frac{s - z_G}{s} \left[\bar{\tilde{u}}^1 g \frac{\sigma - s}{s} \frac{\partial z_G}{\partial x} + \bar{\tilde{u}}^2 g \frac{\sigma - s}{s} \frac{\partial z_G}{\partial y} \right] d\tilde{x}^1 d\tilde{x}^2$$

$$- \int_0^{D_{\tilde{x}^2}} \int_0^{D_{\tilde{x}^1}} \rho_0 \frac{s - z_G}{s} \bar{\tilde{u}}^1 f \hat{\bar{\tilde{u}}}^3 d\tilde{x}^1 d\tilde{x}^2 \bigg\} d\tilde{x}^3$$

$$+ \int_0^{D_{\tilde{x}^2}} \int_0^{D_{\tilde{x}^1}} \rho_0 \frac{s - z_G}{s} \bar{k}_{s_\theta} \frac{\partial s_\theta}{\partial t} d\tilde{x}^1 d\tilde{x}^2, \quad (12\text{-}11)$$

where

$$K_* = \int_0^{s_\theta} \int_0^{D_{\tilde{x}^1}} \int_0^{D_{\tilde{x}^2}} \left(\rho_0 \frac{s - z_G}{s} \bar{k} \right) d\tilde{x}^2 d\tilde{x}^1 d\tilde{x}^3.$$

In deriving Eq. (12-11), the condition that $\bar{\tilde{u}}^3 = 0$ at z_G and s_θ has been used. The last term in Eq. (12-11) arises from Leibnitz's rule,[6] since s_θ is a function of time. Each of the variables in the last term is evaluated at s_θ.

  The first two terms on the right side of Eq. (12-11) are proportional to the net flow of terrain-following kinetic energy through the sides of the model domain, and the next term represents the change in kinetic energy from subgrid-scale effects. The terms involving $\partial \bar{\pi}/\partial \tilde{x}^1$ and $\partial \bar{\pi}/\partial \tilde{x}^2$ are proportional to the conversion of potential to kinetic energy by cross-isobaric flow, and the expressions containing the gradients of terrain represent the conversion of potential

to kinetic energy through upslope and downslope flow. The next to last term in Eq. (12-11) (with $\hat{f}$) would not appear in a three-dimensional kinetic energy equation using the complete conservation-of-motion equation (i.e., without the hydrostatic assumption), since the Coriolis force arises solely because of a coordinate transformation (see Section 2.3) and thus cannot do work. Therefore, to have a physically consistent terrain-following energy equation, it is necessary to remove this term in Eq. (12-11) and in Eq. (6-87).

In using Eq. (12-11) to determine the total terrain-following kinetic energy changes, it is imperative that the approximation technique used to evaluate the individual terms in that expression be the same as that used in the original approximate form of the conservation relation [i.e., the approximated forms of Eqs. (6-60) and (6-61)] from which Eq. (12-11) was derived.

The time rate of change of terrain-following kinetic energy can also be evaluated directly at each individual grid point and then summed; that is,

$$
\begin{aligned}
\frac{\partial K}{\partial t} &= \int_0^{s_\theta} \int_0^{D_{\tilde{x}^2}} \int_0^{D_{\tilde{x}^2}} \rho_0 \frac{s - z_{\mathrm{G}}}{s} \frac{\partial \bar{k}}{\partial t}\, d\tilde{x}^2 d\tilde{x}^1 d\tilde{x}^3 \\
&+ \int_0^{D_{\tilde{x}^2}} \int_0^{D_{\tilde{x}^1}} \rho_0 \frac{s - z_{\mathrm{G}}}{s} \bar{k}_{s_\theta} \frac{\partial s_\theta}{\partial t}\, d\tilde{x}^1 d\tilde{x}^2
\end{aligned}
\tag{12-12}
$$

is used instead of Eq. (12-11) to obtain an estimate of the total terrain-following kinetic energy change. If the kinetic energy changes computed by the numerical approximation to this expression and the approximated form of Eq. (12-11) closely agree, then the modeler can be certain that mistakes, such as coding errors, are not causing significant sources of unexplained changes of kinetic energy. Note that since the last term is the same in Eqs. (12-11) and (12-12), there is no need to compute it for a comparison of K and K_*.

Anthes and Warner (1978) discuss the use of kinetic energy budgets in mesoscale models as a tool to check the model code, as well as to seek additional insight into the energetics of mesoscale systems. Among their results, they showed that the flux of kinetic energy through the side walls of a mesoscale model crucially affects the solutions in the interior. They conclude that because of the extreme sensitivity of mesoscale model results to domain size and the form of lateral boundary conditions, studies of the energetics of real-world mesoscale systems will be very difficult to perform and very sensitive to errors and small-scale variations of wind, potential temperature, and pressure at the model boundaries. Figure 12-11 illustrates the magnitude of individual terms as a function of time in a two-dimensional analog of Eq. (12-11), computed by Anthes and Warner for strong airflow over rough terrain. Of particular importance is the large magnitude of the boundary fluxes of kinetic energy through the west and east boundaries. Even small percentage errors in these terms can cause serious errors in the results, a conclusion illustrated in Table 11-1. In a
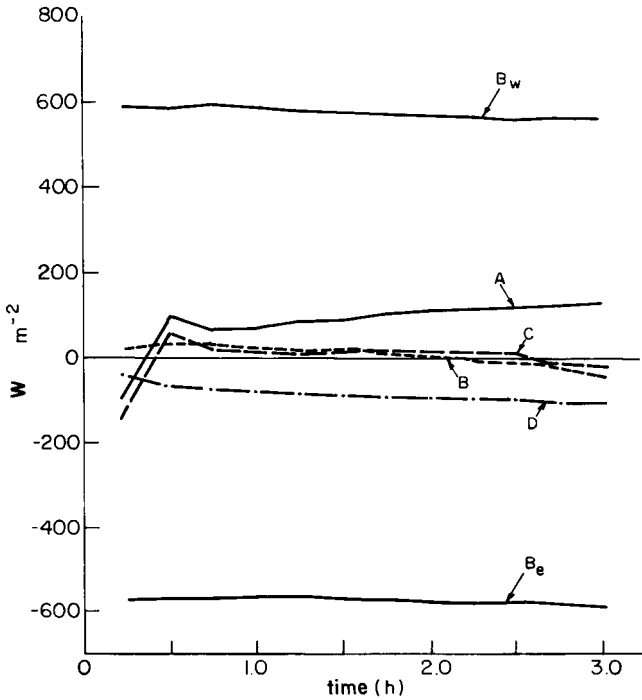
Fig. 12-11.   Individual components of a two-dimensional form of the domain-averaged kinetic energy equation, which is equivalent to Eq. (12-11). (A) Generation of kinetic energy by cross-isobaric flow, from the terms with $\bar{\bar{u}}^1[\bar{\theta}(\partial\bar{\pi}/\partial\tilde{x}^1) - g\{(\sigma - s)/s\}(\partial z_G/\partial x)]$; B_w and B_e are the flux of kinetic energy across the west and east boundaries from the two terms evaluated from $\bar{\bar{u}}^1\bar{k}|_0^{D\tilde{x}^1}$). (B) Net flux across the west and east boundaries (from $B_e - B_w$). (C) The domain-averaged change of kinetic energy. (D) The dissipation of kinetic energy by horizontal diffusion (from the term with $\bar{\bar{u}}^1\overline{\tilde{u}^{1''}\partial\tilde{u}^{1''}/\partial\tilde{x}^1}$.). Analogs to the last two terms in Eq. (12-11) were not evaluated. (Reproduced from Anthes and Warner 1978.)

different study, Tag and Rosmond (1980) discuss energy conservation in a three-dimensional small-scale (nonhydrostatic) model in considerable detail. Pearson (1975), Dalu and Green (1980), and Green and Dalu (1980), provide additional studies of the energetics of mesoscale systems. Avissar and Chen (1993) use a mesoscale kinetic energy equation similar to Eq. (12-11) to develop a parameterization of mesoscale fluxes for use in larger-scale models.

12.5.3   Momentum Flux

Another useful diagnostic tool for model evaluation involves calculation of the momentum flux. Used most often in the study of the dynamics of forced air over rough terrain (e.g., Klemp and Lilly 1978), this is straightforward to calculate.

   To illustrate its evaluation, in the absence of the Coriolis term for two-dimensional flow, Eq. (4-14) for $i = 1$ can be written as

$$\frac{\partial \rho_0 \bar{u}}{\partial t} = -\frac{\partial}{\partial x}\rho_0 \bar{u}^2 - \frac{\partial}{\partial z}\rho_0 \bar{w}\bar{u} - \frac{\partial}{\partial x}\rho_0 \overline{u''^2} - \frac{\partial}{\partial z}\rho_0 \overline{u''w''} - \frac{\partial \bar{p}}{\partial x}, \qquad (12\text{-}13)$$

where the conservation-of-mass equation (4.23) has been used. Assuming a steady state and that $\bar{u}$, $\bar{p}$, and $\overline{u''^2}$, far enough upstream and downstream of a two-dimensional barrier to the flow, are constant, Eq. (12-13) can be integrated to yield

$$-\frac{\partial}{\partial z}\int_{-\infty}^{\infty}\left(\rho_0 \bar{w}\bar{u} + \rho_0 \overline{w''u''}\right)dx = 0$$

or

$$\int_{-\infty}^{\infty}\rho_0\left(\bar{w}\bar{u} + \overline{w''u''}\right)dx = m_1, \qquad (12\text{-}14)$$

where m_1 is a constant with dimensions of kilogram per seconds squared. Equation (12.14) can be written as

$$\int_{-\infty}^{\infty}\rho_0\left[w_0 u_0 + w'u_0 + w_0 u' + w'u' + \overline{w''u''}\right]dx = m_1 \qquad (12\text{-}15)$$

using the definition of a mesoscale perturbation from the domain-averaged (i.e., synoptic) value given by Eq. (4-11). For the case where $w_0 = 0$ and u_0 is equal to a positive constant, Eq. (12-15) reduces to

$$\int_{-\infty}^{\infty}\rho_0[w'u' + \overline{w''u''}]dx = m_2,$$

since $(\partial/\partial z)\rho_0\bar{w}\bar{u}$ can be written as $(\partial/\partial z)\rho_0 w'u'$ in Eq. (12-13). Assuming nonturbulent flow, the equation can be further reduced to

$$\int_{-\infty}^{\infty}\rho_0 w'u'\,dx = m_3. \qquad (12\text{-}16)$$

The constant m_3 is less than 0 if the source of the mesoscale motion is the ground surface and there is no downward reflection or generation of perturbed flow above the ground. In this situation, the movement of a parcel upward (i.e., $w' > 0$) toward a level of higher potential energy results in a reduction of kinetic energy (i.e., $u' < 0$). The converse is true for the downward movement of a parcel. Hence $w'u' < 0$ is required to satisfy the conservation of total energy.

   Equation (12.16) is of the form most commonly applied in the diagnosis of a mesoscale simulation of airflow over rough terrain. In a numerical model, u_0 is equal to a constant, $w_0 = 0$, nonturbulent flow can be assumed for an atmosphere of constant large-scale velocity and static stability, and $w'u'$ can be calculated to ascertain whether it satisfies Eq. (12-16). To prevent aliasing problems (described in Section 10.5.1), however, long-term inviscid calculations (i.e., with no explicit or computational smoothing) can be performed only for

small mountain perturbations where the nonlinear effects are minimal. Klemp and Lilly (1978) show that for inviscid, isothermal analytic solutions over a bell-shaped mountain given by Eq. (12-4) with u_0 equal to a constant and $w_0 = 0$, the momentum flux is of the form

$$m_{3a} \simeq \frac{-\pi}{4} \rho_0 u_0 z_{G_{max}}^2 \left(\frac{g}{\theta_0} \frac{\partial \theta_0}{\partial z} \right)^{1/2} \simeq -\frac{\pi}{4} \rho_0 z_{G_{max}}^2 \sigma u_0^2. \qquad (12\text{-}17)$$

Here the definition of σ is from Eq. (5-129) and the relation between density and potential temperature vertical gradients is given by Eqs. (5-135) and (5-136). Figure 12-12, reproduced from Klemp and Lilly, illustrates a comparison of a numerically computed, horizontally integrated momentum flux [from Eq. (12-16)] for a simulation of airflow with $u_0 = 20$ m s^{-1} over a mountain of the form given by Eq. (12-4), along with the analytic result given by Eq. (12-17). The numerical model was integrated with $z_{G_{max}} = 10$ m, and m_3 was multiplied by 10^2 for comparison against the linear solution m_{3_a}. The results are almost coincident up to 10 km, thereby providing proof of the fidelity of the numerical model. Above 10 km, the numerical model uses an absorbing layer (see Section 11.3.2) to mimic the radiation boundary condition of the analytic model.

Another useful parameter that can be calculated from a model of forced air over rough terrain is the surface drag. This drag occurs because the sloping
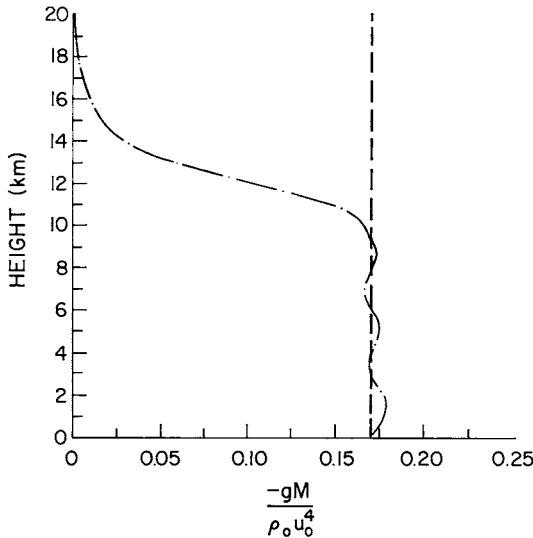
Fig. 12-12. A plot of m_3 calculated from Eq. (12-16) from a numerical model result for a bell-shaped mountain (dashed-dotted line) and m_{3_a} evaluated using Eq. (12-17) for the same mountain shape (dashed line), as a function of height for $u_0 = 20$ m s^{-1}, $z_{G_{max}}$ equivalent to 100 m, and $\rho_0 = 1$ kg m^{-3}. The atmosphere is isothermal, and M corresponds to m_3 and m_{3_a}. (Adapted from Klemp and Lilly 1978.)

terrain is a partial barrier and impedes the large-scale wind flow. The wave drag for a two-dimensional mountain can be written as

$$D = \int_{-\infty}^{\infty} \bar{p}(z_{\mathrm{G}}) \frac{\partial z_{\mathrm{G}}}{\partial x}\, dx, \qquad (12\text{-}18)$$

where $\bar{p}$ is evaluated on z_{G}. The momentum flux [Eq. (12-16)] evaluated at z_{G} is identical to the surface drag given by Eq. (12-18). The integrand of Eq. (12-18) arises from the force per unit area exerted on a two-dimensional mountain in the x direction.[7] For a mountain that is symmetric around its crest, for example, an asymmetric pressure field will result in a value of D that is not equal to 0. Moreover, since total energy must be conserved, the generation of internal gravity waves by a mountain must result in the extraction of energy from the ground.

From the Lilly and Klemp (1979) solution to Long's model presented in Section 5.3,

$$D_{\mathrm{LK}} = -\rho_0 u_0^2 \int_{-\infty}^{\infty} \sigma \left(z_{\mathrm{G}_i} - \left(\frac{\sigma z_{\mathrm{G}_i}^2}{2} \right) \right) \frac{\partial z_{\mathrm{G}}}{\partial x}\, dx, \qquad (12\text{-}19)$$

where the subscript "LK" indicates that it is from the Lilly–Klemp solution to the Long model. Lilly and Klemp (1979) contrast the drag [Eq. (12-19)] from their solution to Long's equation for an isothermal atmosphere with constant velocity using a nonlinear bottom boundary condition, with the drag [Eq. (12-17)] computed for a linear lower boundary condition. Among their results, they found that the drag was enhanced compared to linear theory for mountains with a gentle upslope and steep downslope terrain.

12.6   Comparison with Observations

The validation of a model using observations can be cataloged into two general classes: (1) subjective validation and (2) point and pattern quantitative validation. In subjective validation, one or more of the predicted fields are qualitatively compared against observations of a related phenomena. Pielke (1974a), for example, compared the simulated vertical motion at an elevation of 1.22 km over south Florida with the observed locations of rain showers as seen via a 10-cm radar located in Miami. The justification for the comparison is that the primary control for rain shower development over south Florida during a synoptically undisturbed summer day is the location and intensity of the low-level convergence (Pielke *et al.* 1991). Since 1.22 km is approximately at the top of the planetary boundary layer, the predicted vertical velocity at that level yields an appropriate estimate for low-level convergence. Figure 12-13 illustrates one such comparison for June 29, 1971, 9-1/2 hours after sunrise. As evident in the
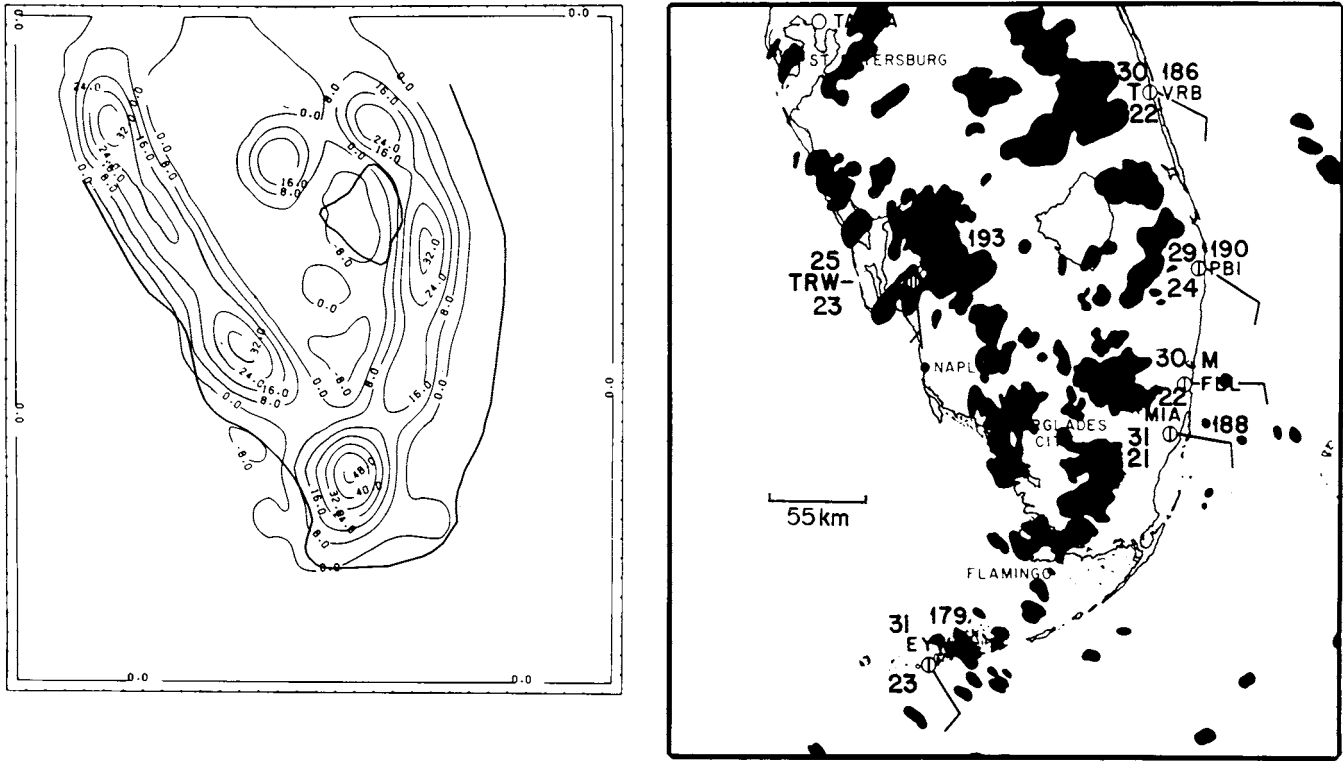
Fig. 12-13. A model-predicted vertical motion field at 1.22 km and the radar echo map at about 9.5 hours after sunrise for June 29, 1971. The large-scale horizontal velocity used in the model simulation above the initial height of the planetary boundary layer was 2.5 m s^{-1} from the east-southeast. The model used in this simulation is reported in Pielke (1974a).

figure, the wishbone pattern of the rain showers is closely correlated with the distribution of vertical motion at 1.22 km.

Point-to-point correspondence between model prediction and observation of the same meteorological parameter provides a quantitative test of model skill. Keyser and Anthes (1977) use a technique in which if ϕ_i and $\phi_{i_{obs}}$ are individual predictions and observations at the same grid point, ϕ_0 and $\phi_{0_{obs}}$ are the average values of ϕ_i and $\phi_{i_{obs}}$ at a level, and $\#N$ is the number of observations, then

$$E = \left\{ \sum_{i=1}^{\#N} (\phi_i - \phi_{i_{obs}})^2 / \#N \right\}^{1/2},$$

$$E_{UB} = \left\{ \sum_{i=1}^{\#N} [(\phi_i - \phi_0) - (\phi_{i_{obs}} - \phi_{0_{obs}})]^2 / \#N \right\}^{1/2}, \qquad (12\text{-}20)$$

$$\sigma_{obs} = \left\{ \sum_{i=1}^{\#N} (\phi_{i_{obs}} - \phi_{0_{obs}})^2 / \#N \right\}^{1/2},$$

and

$$\sigma = \left\{ \sum_{i=1}^{\#N} (\phi_i - \phi_0)^2 / \#N \right\}^{1/2}$$

can be used to determine the skill of the model results. The parameter E is the *root mean square error* (RMSE), E_{UB} is the RMSE after a constant bias is removed, and σ and σ_{obs} are the standard deviations of the predictions and the observations, respectively.[8] Keyser and Anthes found that the RMSE can be significantly reduced when a constant bias is removed. Such a bias, they suggested, could result from incorrect specification of the initial and/or bottom and lateral boundary conditions.

Skill is demonstrated when (1) $\sigma \simeq \sigma_{obs}$, (2) $E < \sigma_{obs}$, and (3) $E_{UB} < \sigma_{obs}$. Pielke and Mahrer (1978) applied these criteria to their simulation of the sea breezes over south Florida to show that the model could accurately predict wind velocity and temperature at 3 m. Temperature predictions over the entire daylight period, as given in Table 12-1, for example, had a ratio of $E_{UB}/\sigma_{obs} = 0.6$. Segal and Pielke (1981) have applied this analysis tool over the Chesapeake Bay region to evaluate the accuracy of a mesoscale model prediction of biometeorological heat load during the daylight hours. For temperature, for example, Segal and Pielke found that $E/\sigma_{obs} = 0.53$ with $\sigma_{obs} = 2.12°C$ and $\sigma = 2.24°C$. This evaluation technique has also been applied by Shaw *et al.* (1997) in the modeling of a Great Plains dryline.

One problem with point-to-point validation, however, is that spatial and temporal displacement of the predicted from the observed fields could yield a poor verification according to Eq. (12-20), even though the shape and magnitude of the simulated pattern could be almost exact. Although not yet attempted in a

TABLE 12-1

Error Analysis of Model-Predicted Winds and Temperature Using Eq. (12-20) for an
East–West Cross-Section From Naples to Just North of Fort Lauderdale, Florida
(See Figure 12-13 for the Location)

Variable	E	E_{UB}	σ	σ_{obs}	E_{UB}/E	E_{UB}/σ_{obs}
$\bar{u}$ (m s^{-1})	3.1	3.1	1.2	2.2	1.0	1.4
$\bar{v}$ (m s^{-1})	2.2	1.2	0.8	1.2	0.5	1.0
$\overline{T}$ (°C)	5.1	2.8	3.9	4.6	0.5	0.6

From Pielke and Mahrer 1978.

mesoscale model, rigid translation of the predicted results on the model grid
(e.g., in one–grid-interval increments) relative to the observations, and recom-
putation of E and E_{UB} in Eq. (12-20), offers one possibility for considering the
effect of displacement on the accuracy of the results.

A quantitative measure of a model's ability to predict observed meteorological
fields, such as displayed in Figure 12-13, is also possible using concepts of set
theory. Pielke and Mahrer (1978) applied this technique to determine the degree
of correspondence between predicted low-level convergence zones (as estimated
by the vertical velocity, $\bar{w}$, at 1.22 km) and the locations of radar echos over
south Florida. Two major questions were answered using this technique:

1.   What fraction of the predicted convergence zones are covered by
showers?
2.   What fraction of the showers that occur lie inside of the predicted con-
vergence zones?

To illustrate the procedure of analysis, let $D_x D_y$ be the model domain area, let
C be the area of the model domain covered by predicted convergence of a given
magnitude or larger, and let R be the area of the model domain covered by radar
echoes of a specified intensity and greater. With these definitions, the following
apply:

1. $F_E = (C \cap R)/R$ is the fraction of echoes in convergence zones with
values equal to or greater than a certain value of convergence (where the symbol
$\cap$ is an intersection in set theory symbolism).
2. $F_m = C/D_x D_y$ is the fraction of the model domain covered by a specified
value of convergence and larger.
3. $F_c = (C \cap R)/C$ is a measure of the fraction of convergence zones, of a
given magnitude and larger. covered by echoes.

Capability is demonstrated if $F_E/F_m > 1$, since the ratio would be expected
to be unity by random chance. A necessary condition for perfect skill is

$F_c = 1$, since in that case the entire convergence zone would be covered with echoes.[9]

This methodology is illustrated schematically in Figure 12-14 for an idealized distribution of radar echoes and convergence. Results for an actual model simulation of a sea breeze over south Florida (for July 1, 1973) from Pielke and Mahrer (1978) are given in Table 12-2, where the ratio of F_E/F_m was greater than unity in 26 out of 30 categories. The ratio was larger than 2.0 in 20 of the categories. In contrast, F_c was much less than unity, indicating that most of the convergence zones were not covered by rain showers—a result indicating that sea-breeze convergence alone does not completely explain the spatial variability of radar echoes over south Florida in the summer.

The application of this analysis procedure to other meteorological variables, such as cloud cover and rainfall, is straightforward. Simpson *et al.* (1980), for example, quantitatively examined the skill of the mesoscale model predictions over south Florida on several days during the summer to predict locations of shower mergers as seen by radar. This technique can, of course, be applied to other geographic areas and to different mesoscale systems.

Anthes (1983) provides an effective summary of additional evaluations of model capability. These include

$$TS = \frac{CFA}{FA + OA - CFA},$$

where TS is called the "threat score," CFA is the correctly forecast area, FA is the forecast area, and OA is the observed area. These quantities are equivalent to $CFA = C \cap R$, $FA = C$, and $OA = R$ used to obtain Table 12.2.
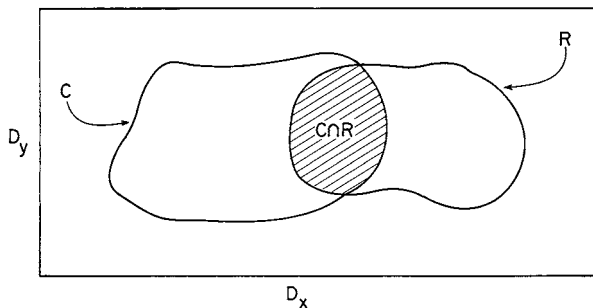
Fig. 12-14. A schematic illustration of the juxtaposition of a field of radar echoes R and low-level convergence of a given magnitude and larger C. The two fields are coincident at $C \cap R$. The quantity $F_c = (C \cap R)/C$ indicates the fraction of a convergence zone covered by radar echoes, and $F_E/F_m = [(C \cap R)/R]/(C/D_x D_y)$ measures the ratio of echoes within the convergence zone to the fraction of the model domain covered by that magnitude of convergence and larger.

TABLE 12-2

The Fraction of Convergence Zones F_c of a Given Magnitude and Larger, Covered by Radar Echoes, and the Ratio of the Fraction of Echoes in Convergence Zones of a Given Magnitude and Larger to the Fraction of the Model Domain Covered by that Magnitude of Convergence and Larger; This Ratio is Given by F_E/F_m.

Time	F_c					F_E/F_m				
(EST)	(i)	(ii)	(iii)	(iv)	(v)	(i)	(ii)	(iii)	(iv)	(v)
1200	0.0049	0.0118	0.0	0.0	0.0	1.31	2.67	0.0	–	–
1300	0.0571	0.1237	0.0072	0.0	0.0	2.16	3.17	0.20	–	–
1400	0.0945	0.1770	0.3111	0.0	0.0	1.98	2.78	3.50	0.0	–
1500	0.1396	0.1337	0.1942	0.3040	0.0	2.25	2.56	3.29	6.00	–
1600	0.0889	0.1765	0.1156	0.00	0.0	2.44	2.95	2.00	0.0	–
1700	0.1609	0.2829	0.2950	0.2379	0.0	2.49	3.16	3.00	2.33	–
1800	0.1451	0.1976	0.3403	0.3866	0.0909	2.19	3.07	3.75	3.75	0.10
1900	0.0759	0.1205	0.1313	0.0211	0.0	1.06	1.43	1.67	1.67	–

Convergence is defined by vertical velocity $\bar{w}$ at 1.22 km. For 1200–1800 EST, (i) $\bar{w} > 0$ cm s^{-1}, (ii) $\bar{w} > 8$ cm s^{-1}, (iii) $\bar{w} > 16$ cm s^{-1}, (iv) $\bar{w} > 24$ cm s^{-1}, (v) $\bar{w} > 32$ cm s^{-1}. For 1900 EST (i) $\bar{w} > 0$ cm s^{-1}, (ii) $\bar{w} > 8$ cm s^{-1}, (iii) $\bar{w} > 24$ cm s^{-1}, (iv) $\bar{w} > 40$ cm s^{-1}, (v) $\bar{w} > 56$ cm s^{-1}. (From Pielke and Mahrer 1978.)

The threat score can also be defined as

$$TS = C/(F + O - C),$$

where C is the number of locations in which a forecast is defined to be correct, F is the number of locations for which a forecast is made, and O is the number of locations that observed the forecast quantity.

A bias score, B, can be defined as

$$B = FA/OA$$

and by

$$B = F/O.$$

Colle *et al.* (1999) discuss the changes in bias scores as the spatial grid increment in the MM5 model is made smaller.

To assess model skill, Mielke (1984, 1991) introduced a new statistical evaluation scheme called the Multivariate Randomized Block Permutation (MRBP) procedure. His approach has the advantage in that regression relations and comparisons between model and observed data is based on the absolute value of the differences, rather than on the square of the distances.

A summary of the MRBP technique is provided in Lee *et al.* (1995) and is reproduced here. As described by Sheynin (1973), the initial known use of regression by Bernoulli (circa 1734) for astronomical problems involved the

least sum of absolute deviations (LADs) regression. The distance function asso-
ciated with LAD regression is the common Euclidean distance between observed
and predicted response values. Further work in developing LAD regression was
accomplished by Boscovich (circa 1755), Laplace (circa 1789), and Gauss (circa
1809). Sheynin (1973) points out that Gauss developed linear programming
for the sole purpose of estimating the parameters associated with LAD regres-
sion. Gauss consequently had to introduce the least sum of squared deviations
(LSD) regression (also termed least squares regression), simply because calcu-
lus provided an efficient way to estimate the parameters associated with LSD
regression. Thus LSD regression is a default procedure that was introduced only
because Gauss lacked appropriate computational equipment for solving linear
programming problems. The American mathematician and astronomer Bowditch
(circa 1809) immediately attacked LSD regression because squared deviations
unduly overemphasize questionable observations in comparison to the absolute
deviations associated with LAD regression (Sheynin 1973).

The MRBP procedure developed by Mielke (1984, 1991) is based on the
LAD regression. Specifically, MRBP randomly permutes the observed vector
of values $(\vec{X})$ relative to the model-predicted vector of values $(\widetilde{\vec{X}})$ with the
agreement measure, ρ, defined by

$$\rho = \frac{\mu_\delta - \delta}{\mu_\delta}, \tag{12-21}$$

where $\delta = (1/n) \sum_{i=1}^{n} |\vec{X}_i - \widetilde{\vec{X}}_i|$ is the average distance between n-observed and
model-predicted data pairs and μ_δ is the average value of δ over all $n!$ permu-
tations. Note that the Euclidean distance between vector value pairs is used to
evaluate the agreement measure, and that good predictions are associated with
relatively small values of δ. The LAD regression used here is both multivari-
ate (i.e., n vectors of two or more dependent variables may be involved) and
nonlinear. The remaining problem is to determine whether a realized value of δ
for observed and model-predicted values is due merely to chance. The standard
measurement for this purpose is the P value; that is, the probability of obtaining
a value of δ that is not larger than a realized value of δ given that each of the
$n!$ values of δ occurs with equal probability. Although the exact calculation of
all $n!$ values of δ is seldom computationally feasible, an approximate P value
is based on the standardized test statistic given by

$$T = (\delta - \mu_\delta)/\sigma_\delta, \tag{12-22}$$

where σ_δ is the exact standard deviation of δ and T is approximately distributed
as a Pearson type III distribution (Mielke 1984, 1991). Examples of the use of
the MRBP evaluation technique in mesoscale modeling are reported in Cotton
et al. (1994), Lee *et al.* (1995), and Mielke and Berry (2000).

12.7 Model Sensitivity Analyses

Stein and Alpert (1993) and Alpert *et al.* (1995) have introduced a very effective analysis procedure for assessing model sensitivity to the alteration of model formulations. These alterations, for example, could include integrating a model with surface latent turbulent heat fluxes excluded, as contrasted with a control run in which these fluxes are included.

When one alteration is contrasted with the control run, simply subtracting the two model runs at equivalent times of integrations is the obvious procedure for assessing the model's sensitivity to the alteration. However, when two alterations are evaluated (e.g., surface turbulent sensible heat fluxes are also excluded), the interaction between the two alterations must be assessed. Only if the alterations are not interactive (i.e., "orthogonal") to each other would running the two alteration experiments and then adding them together provide the model's sensitivity to the combined effect of both alterations.

The Stein–Alpert analysis procedure includes the effect of the interactions. Following this analysis procedure, if f_0 is the control and f_1, f_2, and f_3 represent three alteration experiments, then

$$\hat{f}_1 = f_1 - f_0,$$
$$\hat{f}_2 = f_2 - f_0,$$
$$\hat{f}_3 = f_3 - f_0,$$

where $\hat{f}_1$, $\hat{f}_2$, and $\hat{f}_3$ represent the individual effects of making just one alteration to the control. In the past, this is where most sensitivity experiments ended. However, as shown by Stein and Alpert,

$$\hat{f}_{12} = f_{12} - (f_1 + f_2) + f_0,$$
$$\hat{f}_{13} = f_{13} - (f_1 + f_3) + f_0,$$
$$\hat{f}_{23} = f_{23} - (f_2 + f_3) + f_0$$

represent the interaction between each pair of alterations when two alterations from the control are made in the same experiment. When these alterations are made in the same experiment, the three-way interaction effect is

$$\hat{f}_{123} = f_{123} - (f_{12} + f_{13} + f_{23}) + (f_1 + f_2 + f_3) - f_0.$$

Examples of uses of the Stein–Alpert sensitivity analysis procedure are reported in Alpert *et al.* (1995, 1996a, 1999), DeRidder and Gallee (1998), Romero *et al.* (1998, 2000), Eastman (1999), Grossi *et al.* (2000), and Eastman *et al.* (2001).

Notes to Chapter 12

1. The other type of sensitivity study involves changes in the physical parameters within the model (e.g., initial wind speed, Coriolis value, ground roughness).

2. The solution to this diagnostic differential equation can be obtained using the procedure of sequential relaxation discussed in Section 10.3. Haltiner and Williams (1980, Chap. 5) also present procedures to solve Eq. (12-3) using direct matrix procedures. Mason and Sykes (1978) discuss the use of a direct method to solve for pressure in a Cartesian coordinate framework even when topography exists in the model domain.

Also, in deriving Eq. (12-2), the velocities on the right of Eq. (4-14), were assumed to be the velocities obtained when the complete nonhydrostatic pressure, $\bar{p}_{\mathrm{H}} + R'$, was used (e.g., as available at the beginning of a time step). This assumption does not have to be made, however (it simply results in more terms in Eq. (12-3) if it is not made). As long as changes of R' at a grid point between time steps are small relative to the magnitude of R', it is a reasonable assumption.

3. If $u' \equiv 0$ at the boundaries, then $\partial u'/\partial x$ and $\partial u'/\partial t$ must also be identically 0 at these locations. Therefore, from Eq. (5-17), $g\partial h/\partial x = 0$ at the boundaries, so that no slope to the fluid is permitted at the walls. Numerical approximations to the tank model equations with rigid walls must use this boundary condition on h, recognizing that $\partial h/\partial x = 0$ at the boundary does not mean that $\Delta h/\Delta x = 0$ between the boundary and one grid point inside when Δx is finite.

4. As used here and in Section 6.3, s is a constant, usually defined to correspond to the initial value of s_θ as defined by Eqs. (11-13) and (11-19) and following material. The variable s_θ corresponds to a movable potential temperature surface.

5. As shown by Dutton (1976:144), differential area on a constant $\tilde{x}^3$ surface can be written as $dS = |\tilde{\mathrm{n}}^3| \sqrt{\widetilde{G}} d\tilde{x}^2 d\tilde{x}^1$. For the terrain-following coordinate system defined by Eq. (6-48), $\sqrt{\widetilde{G}} = (s - z_{\mathrm{G}})/s$ [from Eqs. (6-32) and (6-51)] and for small slopes $|\tilde{\mathrm{n}}^3| \simeq s/(s - z_{\mathrm{G}})$ [from Eqs. (6-33) and (6-51)].

6. Leibnitz's rule is given in such sources as Hildebrand (1962:360) and Dutton (1976:115).

7. The change in force per unit area in the x direction can be written as $\bar{p}(z_{\mathrm{G}}) \cos \alpha \Delta n/\Delta x$, where α is the terrain slope and Δn is distance along the slope. Since $\Delta n \cos \alpha = \Delta z$, at $z = z_{\mathrm{G}}$, the change in force per unit area in the x direction becomes $\bar{p}(z_{\mathrm{G}})\Delta z_{\mathrm{G}}/\Delta x$. In the limit as Δz_{G} and Δx approach 0, and integrating from $+$ to $-\infty$ yields Eq. (12-18).

8. The use of RMSE analysis to examine the skill of model results for different sets of initial conditions was also discussed in Section 11.2 associated with Eq. (11-5).

9. Since R can be larger than C, $F_{\mathrm{c}} = 1$ is not a sufficient measure of perfect skill.

Additional Readings

Several studies provide additional examples of model evaluations.

Cox, R., B. L. Bauer, and T. Smith. 1998. A mesoscale model intercomparison. *Bull. Amer. Meteor. Soc.* **79**, 265–283.

Hanna, S. R., and R. Yang. 2001. Evaluations of mesoscale models' simulations of near-surface winds, temperature gradients, and mixing depths. *J. Appl. Meteor.*, **40**, 1095–1104.

Snook, J. S., P. A. Stamus, J. Edwards, Z. Christidis, and J. A. McGinley. 1998. Local-domain mesoscale analysis and forecast model support for the 1996 Centennial Olympic Games. *Wea. Forecasting* **13**, 138–150.

Problems

1. Using the one-layer tank model programmed in problem 9 in Chapter 10, use the equations in Section 12.5.1 to compute the time rate of change of the mass and energy budget of the model by summing over the grid points of the model and then compare to what they should be from the requirement that h is a constant and Eqs. (12-5) and (12-7). Use cyclic lateral boundary conditions.

2. Repeat problem 1 with constant inflow and gradient outflow lateral boundary conditions.

3. Repeat problem 1 with constant inflow and radiative outflow lateral boundary conditions.

4. Select a mesoscale model and describe which of the model evaluations reported in this chapter have been used.

Chapter 13

Examples of Mesoscale Models

Mesoscale atmospheric systems can be divided into two groups: (1) those forced primarily by surface inhomogeneities (terrain- and physiographic-induced mesoscale systems), and (2) those forced primarily by instabilities in traveling larger-scale disturbances (synoptically induced mesoscale systems). The first group includes such features as sea and land breezes, mountain valley winds, urban circulations, and forced airflow over rough terrain; the second group includes squall lines, hurricanes, and traveling mesoscale cloud clusters. The first group is the least difficult to simulate, because the sources of these mesoscale circulations are geographically fixed with time scales of 12 hours or so, and they recur frequently. These mesoscale systems do not generally move far from their point of origin, and in general do not require a detailed spatial representation of the initial and the lateral and top boundary conditions for the dependent variables. These types of weather systems are readily forecast in general, although weather services have not yet taken full advantage of the repetitive nature of terrain-induced mesoscale circulations (Pielke 1982). These mesoscale systems can be considered a boundary value problem.

Mesoscale disturbances initiated by some type of atmospheric instability [e.g., conditional instability of the second kind (CISK); see Holton 1972; Wallace and Hobbs 1977:442; Mak 1981; Ooyama 1982) usually occur less frequently at a given location, however. Moreover, because they are not forced by well-defined geographic features, the data requirements needed to initialize mesoscale simulations of these phenomena are more formidable. A large percentage of the rainfall over the earth results from the tendency for synoptically driven weather disturbances to organize into such synoptically induced mesoscale-sized precipitating cloud systems (Houze and Hobbs 1982). These mesoscale systems can be considered to be an initial and lateral boundary value problem. Browning (1980) provides a similar categorization of mesoscale systems as described in this chapter.

13.1   Terrain-Induced Mesoscale Systems

13.1.1   Sea- and Land-Breezes Over Flat Terrain

Of all the mesoscale phenomena, sea and land breezes over flat terrain appear to have been the most studied, both observationally and theoretically. This is undoubtedly a result of the geographically fixed nature of the phenomenon (the location of land–water boundaries), as well as the repetitive nature of the event. The sea breeze is defined to occur when the wind is onshore, whereas the land breeze is when the opposite flow exists.

In the case of nonexistent large-scale winds, it is comparatively easy to describe the diurnal variations of the coastal wind circulations. Defant (1951) presented an excellent qualitative description for this condition, which is illustrated in Figure 13-1. For this case, the idealized sequence of events is as follows:

1.   At some time in the early morning, the pressure surfaces become flat and no winds occur (e.g., at 0800 LST—perhaps an hour after sunrise).

2.   Later in the morning, mass is mixed upward over land by turbulent mixing in the unstably stratified boundary layer, creating an offshore pressure gradient at some distance above the ground.[1] Over water, its translucent character and ability to mix prevent significant heating of the surface (e.g., at 1100 LST).
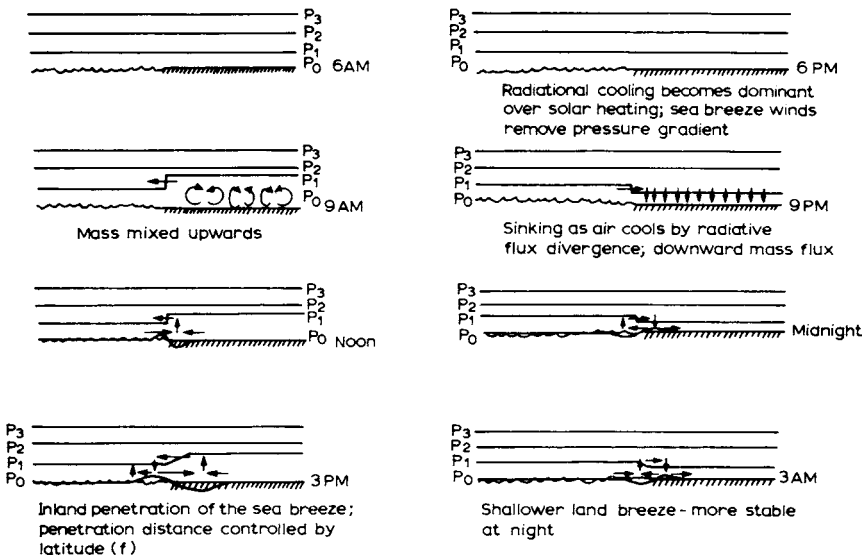
Fig. 13-1.   Schematic of the diurnal evolution of the sea and land breeze in the absence of synoptic flow. (From Pielke 1981.)

3.   The resultant offshore flow of air above the ground near the coast creates a low-pressure region at the ground, and onshore winds (the *sea breeze*) develop (e.g., at 1300 LST).

4.   The onshore winds transport cooler marine air over the land, thereby advecting the horizontal temperature gradient and, hence, the sea breeze inland. The distance that the sea breeze travels inland depends most directly on the intensity of the total heat input to the air (Pearson 1973) and the latitude (e.g., at 1600 LST).

5.   As the sun sets, longwave radiational cooling becomes dominant over solar heating, and the local wind field removes the horizontal temperature gradient. The pressure surfaces again become horizontal (e.g., at 1900 LST).

6.   As longwave cooling continues, the air near the ground becomes more dense and sinks. The resultant lowering of the pressure surfaces a short distance above the ground creates an onshore wind at that level (e.g., at 2200 LST).

7.   In response to the loss of mass above the surface over the water, a pressure minimum develops at the ocean interface immediately off the coast. The offshore wind that then develops near the surface is called the *land breeze* (e.g., at 0100 LST).

8.   The distance of offshore penetration of the land breeze depends on the amount of cooling over the land. Because the planetary boundary layer over land is stably stratified at night and thus vertical mixing is weaker and closer to the ground, the land breeze is a shallower and weaker phenomenon than the daytime sea breeze.

When the coastline is irregular, local regions of enhanced or weakened low-level convergence develop, as illustrated for the daytime portion of the cycle in Figure 13-2. (Such zones of preferential convergence help explain the preference for showers in certain locations in south Florida during the summer, as seen in, e.g., Figure 12-13.) This preference for showers results from the enhancement of convective potential energy associated with the horizontal convergence of water vapor (Pielke *et al.* 1991) and the moistening of the deeper troposphere as repeated cumulus convection in this region detrains water vapor into the same atmospheric column.

The evolution of the sea breeze is somewhat more complicated when a weak or moderate (i.e., $\lesssim 6$ m s^{-1}) prevailing synoptic flow is included. For the two distinct situations of comparatively cold water and comparatively warm water relative to land, a synoptic wind direction from the colder to the warmer surface weakens the intensity of the local wind by diminishing the horizontal temperature gradient. In contrast, when a prevailing larger-scale flow of the same strength is from the warmer to the colder surface, the temperature gradient is strengthened and the subsequent local wind flow is stronger.
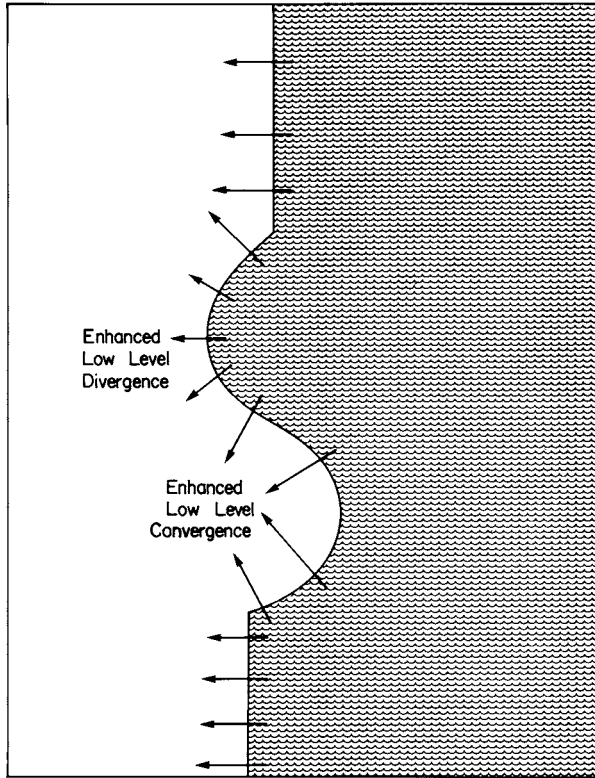
Fig. 13-2. Schematic of the influence of coastline configuration on the sea breeze in the absence of large-scale flow.

Examples of water that is warm relative to the land include the eastern sides of continents in the tropics and midlatitudes at night and over coastal water during a polar outbreak. Situations with water that is cold relative to the adjacent land include the eastern sides of continents in tropical and midlatitudes during sunny days, along the west side of continents in which upwelling is occurring, and along polar coastal areas in the summer.

Fog and low stratus often form over the relatively cold water in polar and upwelling ocean areas (e.g., Noonkester 1979; Pilié *et al.* 1979). Noonkester discussed fog formation caused by the offshore movement of warm, dry air along the coast of southern California and its subsequent movement back toward and over land in the sea breeze. Estoque (1962) performed numerical experiments showing the influence of the prevailing synoptic flow on sea-breeze convergence, and Yoshikado (1981) used observations to illustrate the influence of the geostrophic wind direction on the sea-breeze pattern.

Figure 13-3 illustrates predicted sea-breeze results for weak and moderate onshore synoptic flow. With the weaker winds, the large horizontal gradient of potential temperature (and, therefore, large horizontal gradient of pressure) results in a tight, well-defined sea-breeze circulation as it moves inland. However, when the prevailing onshore flow is stronger, such a large pressure gradient cannot develop, because of the rapid inland movement and greater warming of the marine air. In this and subsequent figures, the ends of the dumbbells are spaced 100 km apart to illustrate the approximate horizontal grid spacing of a large-scale model, as contrasted with mesoscale grid resolution.

The magnitude of the effect of a particular horizontal temperature gradient can be estimated from existing observational and numerical studies (e.g., Hanna and Swisher 1971, Hanna and Gifford 1975). These and other related works show that in the tropics and midlatitudes, a horizontal gradient of less than about 10 W m^{-2}/30 km has only a minor influence on local wind patterns. But with a gradient of 100 W m^{-2}/30 km, significant effects are discernible from the statistical evaluation of observational data, whereas at 1000 W m^{-2}/30 km the influence on local wind patterns is very pronounced in case-by-case studies.

Observational studies of significance to this phenomenon are numerous; a sampling includes those of Byers and Rodebush (1948), Day (1953), Carson (1954), Gentry and Moore (1954), Randerson and Thompson (1964), Plank (1966), Frank *et al.* (1967), Pielke and Cotton (1977), Burpee (1979), Schwartz and Bosart (1979), Cunning *et al.* (1982), and Blanchard (1983) for Florida; Kozo (1982a) for part of the Alaskan coast; Lyons (1975), Keen and Lyons (1978), and Ryznar and Touma (1981) for Lake Michigan; Hsu (1969) for the Texas coast; Neumann (1951), Doran (1979), Skibin and Hod (1979), and Bitan (1981) for Israel; Druilhet *et al.* (1982) for the southern coast of France; Johnson and O'Brien (1973) along the coast of Oregon; Simpson (1996) for southern England; Skinner and Tapper (1994) for islands along the coast of northern Australia; and Lalas *et al.* (1983) for Athens, Greece.

Using observational data, Biggs and Graves (1962) and Lyons (1972) have developed indices to estimate whether a sea breeze will occur. Lyons, for example, has shown that when $V_g^2/\Delta T$ is greater than 10 (where V_g is the 0600 CST surface geostrophic wind speed in meters per second and ΔT is the maximum temperature difference between the inland air temperature and the mean lake surface temperature in degrees Celsius), a sea breeze will not occur at the Chicago shoreline. A sea breeze does not develop when this ratio is large, because the horizontal pressure gradient generated by the differential heating between the land and the lake is insufficient to overcome the kinetic energy of the large-scale flow.

These studies have demonstrated that land and sea breezes (and other similar mesoscale circulations) are poorly resolved in conventional weather-observing
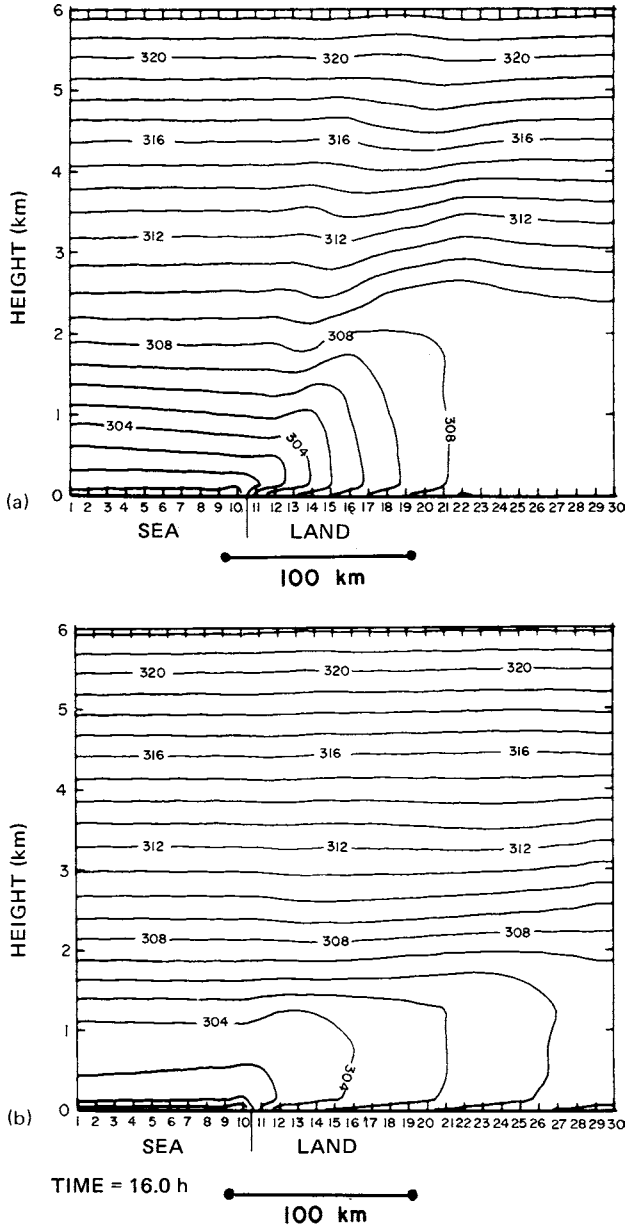
Fig. 13-3.   The vertical cross-section of potential temperature along a coastline at 1600 LST for (a) a 1-m s^{-1} onshore synoptic wind and (b) a 6-m s^{-1} onshore synoptic wind. Initial input was for a typical summer day over south Florida. (From Mahrer and Pielke 1978b.)

network systems. Such a lack of resolution creates serious problems in developing routine operational forecasts of these phenomena.

Lyons and Keen (1976) also concluded that studies of transport and diffusion over land are generally invalid when applied to the coastal environment. Lyons and Cole (1976) and Eastman *et al.* (1995), for example, have discussed the accumulation of pollutants that results from the recirculation associated with the Lake Michigan sea breeze—an effect not considered in commonly used dispersion models. Keen *et al.* (1979) also concluded that size sorting of aerosols occurs within this lake breeze system. In a different geographic area, Carroll and Baskett (1979) concluded that the most serious degradation of air quality in Yosemite National Park occurs because of the transport of material from several hundred kilometers away by the sea breeze from the Pacific coast, as well as by the mountain-valley circulation generated by the Sierras.

In southern California, Sackinger *et al.* (1982) used a tracer study to document that essentially all of the released material transported to sea during a land breeze was advected back across the shore during the subsequent sea breeze. McRae *et al.* (1982b) found similarly that in this situation, material emitted into an elevated stable layer at night is transported offshore, fumigated to the surface, and returned onshore during the daytime. Fumigation occurred over the ocean, because the ocean was warmer than the overlying air. Blumenthal *et al.* (1978) documented the relation between sea breeze and smog in the Los Angeles Basin, and Lalas *et al.* (1982) discussed sulfur dioxide concentrations in Athens, Greece and the need to determine the local sea-breeze, heat island, and terrain circulations.

Examples of early analytic studies of direct relevance to the sea-breeze phenomenon include those of Haurwitz (1947), Schmidt (1947), Defant (1950), Malkus and Stern (1953), Stern and Malkus (1953), and Smith (1955, 1957). More recent studies of this sort include those of Geisler and Bretherton (1969), Walsh (1974), Neumann (1977), Kimura and Eguchi (1978), Dalu and Green (1980), Sun and Orlanski (1981a), Rotunno (1983), Uedo (1983), Dalu and Pielke (1989), and Dalu *et al.* (1996, 2000). The first nonlinear numerical modeling study of this phenomenon, performed using two-dimensional models, was that of Estoque (1961, 1962); this was followed by Fisher (1961), Moroz (1967), Neumann and Mahrer (1971), and others. More recent two-dimensional simulations, such as those of Pielke (1974b), Neumann and Mahrer (1974, 1975), Estoque *et al.* (1976, 1994), Physick (1976, 1980), Patrinos and Kistler (1977), Dalu (1978), Gannon (1978), Sahashi (1981), Sun and Orlanski (1981b), Kozo (1982b), Okeyo (1982), Maddukuri (1982), Alpert and Neumann (1983), Segal *et al.* (1983a), Xian and Pielke (1991), Nicholls *et al.* (1991), Tijm *et al.* (1999a, b), and Baker *et al.* (2001), have continued to use such models to improve our understanding of the physical processes associated with the sea breeze.

Anthes (1978), for instance, using a two-dimensional model, has shown that with a zero large-scale prevailing flow, the return flow of the sea breeze occurs entirely above the boundary layer, whereas the onshore winds are confined below that level. Abe and Yoshida (1982) examined the influence of peninsula width on the intensity of the sea breeze and found that a width of 30–50 km produces the strongest upward vertical velocities. Ozoe *et al.* (1983) used a two-dimensional model to investigate the local pollution patterns and average parcel trajectories in the presence of land and sea breezes. Satomura (2000) used a two-dimensional model to study the diurnal variation of precipitation over the Indo-China region.

Since the early 1970s, computer capability has improved sufficiently to permit three-dimensional simulations. McPherson (1970) was the first to report such calculations of the sea breeze and was followed, for instance, by studies such as those of Pielke (1974a), Mahrer and Pielke (1976, 1978b), Warner *et al.* (1978), Carpenter (1979), Hsu (1979), Kikuchi *et al.* (1981), Xu *et al.* (1996), Kotroni *et al.* (1997), Pielke *et al.* (1999b), Cai and Steyn (2000), Sheng *et al.* (2000), Yimin and Lyons (2000), and Baker *et al.* (2001). These studies provided valuable insight into the sea breeze, including the conclusion that along coastlines, under undisturbed synoptic conditions during the summer in the tropics and subtropics, the sea breeze exerts a dominant influence on the sites of formation and the movement of thunderstorm complexes (Pielke 1974a). A sea breeze (or lake breeze) also significantly influences the transport and dispersion of pollution (Eastman *et al.* 1995; Kassomenos *et al.* 1995; Lyons *et al.* 1992, 1995; Kotroni *et al.* 1999a).

Figure 13-4 presents a sea-breeze model calculation during an afternoon over the Chesapeake Bay that illustrates the need for three-dimensional simulations. A quantitative numerical study of the sea breeze in this region is presented in Segal and Pielke (1981) and Segal *et al.* (1982a). Figure 13-5 (reproduced from Carpenter 1979) illustrates a similar complex wind field for a sea breeze over England, and Figure 13-6(a) contrasts simulated daytime and nighttime lake–land breeze wind fields over Lake Michigan. Sarvijarvi and Jarvenoja (2000) modeled the mesoscale atmospheric conditions over Lake Tanganyika in Africa.

The sea breeze may also be involved in the generation of severe local weather. Clarke *et al.* (1981), for example, reported on the generation of wind squalls accompanied with spectacular roll clouds, which move onshore in northern Australia, whose origin often appears to be related to the interaction of a sea-breeze front and a developing nocturnal inversion.

The establishment of a mesoscale horizontal temperature gradient along a coastline can cause or enhance low-level jets as a mesoscale-generated wind seeks to adjust to gradient wind balance. This mechanism has been used to explain observed wind maxima along the coasts of south Texas (McNider *et al.* 1982) and Oregon (Mizzi and Pielke 1984).
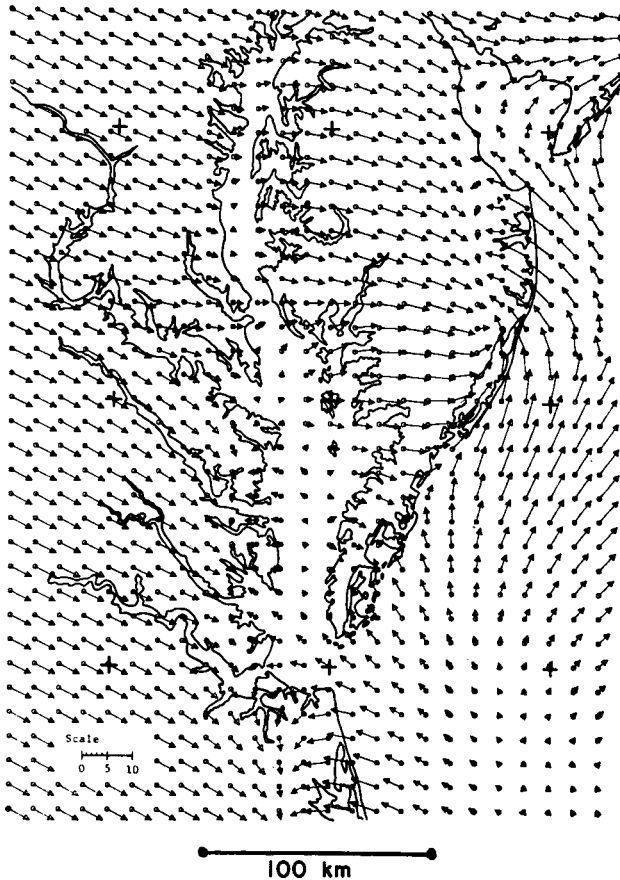
Fig. 13-4. Predicted winds at 4 m at about 1500 LST over the Chesapeake Bay for August 9, 1975. Scale bar in meters per second. (Model simulations were performed by W. Snow at the University of Virginia.)

Other mesoscale modeling studies of the low-level jet include that of Zhong *et al.* (1996). A review of coastal meteorology is given in Rogers (1995).

13.1.2 Vegetation and Snow Breezes

Since horizontal variations of vegetation coverage and type, and of snow can result in differences in surface sensible heat fluxes as large as those between the land and adjacent sea, it should be expected that landscape heterogeneities will also generate mesoscale flows (Cotton and Pielke 1995; Pielke 2001).

Fig. 13-5. The 50-m wind and sea-level pressure forecast for 1800 LST on June 14, 1973. The experiment includes orographic effects, the movement of a synoptic-scale anticyclone, and differential heating between land and water. The isopleth interval is 0.5 mb. One grid interval corresponds to 10 m s^{-1}. (From Carpenter 1979.)

Figure 13-7(a)., for example, illustrates the role of different shapes of deforestation in a tropical region, on the generation of mesoscale circulations.

Modeling and observational studies of flows resulting from vegetation and soil moisture variations and change include those of Lanicci *et al.* (1987), Segal *et al.* (1988, 1989a, b), Pielke and Zeng (1989), Bryant *et al.* (1990), Pielke and Avissar (1990), Chang and Wetzel (1991), Kimura and Takahashi (1991), Pielke *et al.* (1991), Avissar (1992), Entekhabi *et al.* (1992), Chen and Avissar (1994), Dirmeyer (1994), Clark and Arritt (1995), Cotton and Pielke (1995), Cutrim (1995), Hong *et al.* (1995), Klink (1995), Crook (1996), Eltahir (1996), Lyons *et al.* (1996), Nadezhina and Shklyarevich (1996), Schrieber *et al.* (1996), Taylor *et al.* (1997), Vidale *et al.* (1997), Eastman *et al.* (1998),
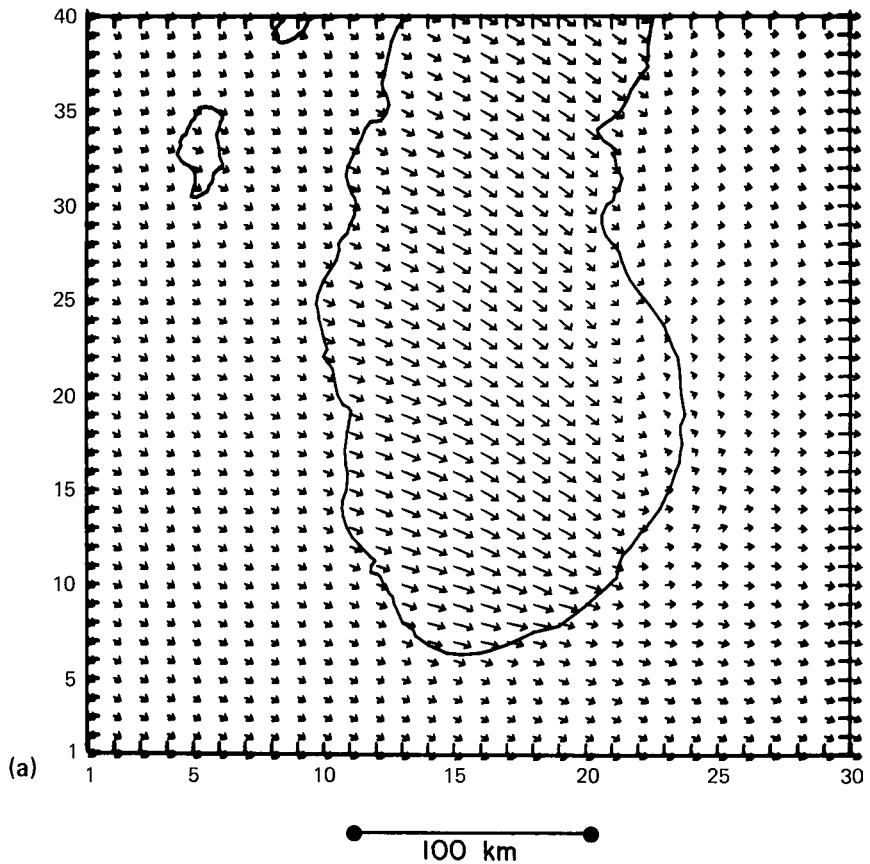
Fig. 13-6(a). The mesoscale model–predicted wind field at 10 m at 0800 LST over the southern and central Lake Michigan area with a synoptic geostrophic wind within the planetary boundary layer of 2.8 m s^{-1} from 310°. A wind vector of one grid length corresponds to 6 m s^{-1}. (Calculations performed by Mike McCumber and reported in Lyons and Schuh 1979.)

Emori (1998), Stohlgren *et al.* (1998), Chase *et al.* (1999), Kalthoff *et al.* (1999), Mölders (1999a), Zeng and Neelin (1999), Friedrich *et al.* (2000), Chen *et al.* (2001), Eastman *et al.* (2001b), Freedman *et al.* (2001), Kanae *et al.* (2001), Lu *et al.* (2001), Lynn and Tao (2001), Lynn *et al.* (2001) and Weaver and Avissar (2001). Mölders (1999b) discusses how floods can alter the local mesoscale system. Nykanen *et al.* (2001) discuss how small-scale precipitation variability influences the larger-scale organization of land-atmosphere fluxes. Sud *et al.* (1993, 1995) discuss the dependence of rainfall on vegetation.

Fires also can generate mesoscale atmospheric circulations. The influence of fire on the surface energy budget is discussed in, for example, Amiro
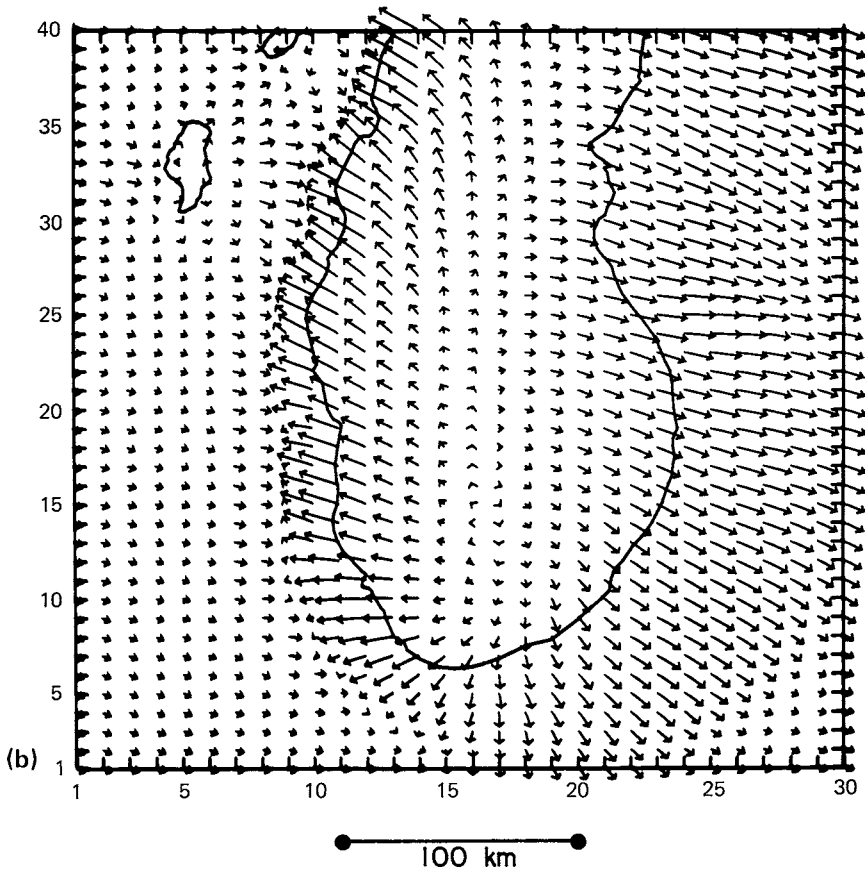
Fig. 13-6(b). The mesoscale model–predicted wind field at 10 m at 1600 LST over the southern and central Lake Michigan area with a synoptic geostrophic wind within the planetary boundary layer of 2.8 m s^{-1} from 310°. A wind vector of one grid length corresponds to 6 m s^{-1}. (Calculations performed by Mike McCumber and reported in Lyons and Schuh 1979.)

et al. (1999) and Bremer and Ham (1999). The influence of the fire's heat on the physical and chemical of properties of soil are described in Giovanninni *et al.* (1988).

Variations of snow cover also generate mesoscale flows, as simulated by Taylor *et al.* (1998) and Segal *et al.* (1991a, b, c). However, Liston (1995) illustrates, that when the snow patches are small enough, mesoscale effects can be ignored and the individual surface fluxes simply added using the mosaic approach discussed by Avissar and Pielke (1989). Liston and Sturm (1998) present a model that shows how winds can create snow patches of varying
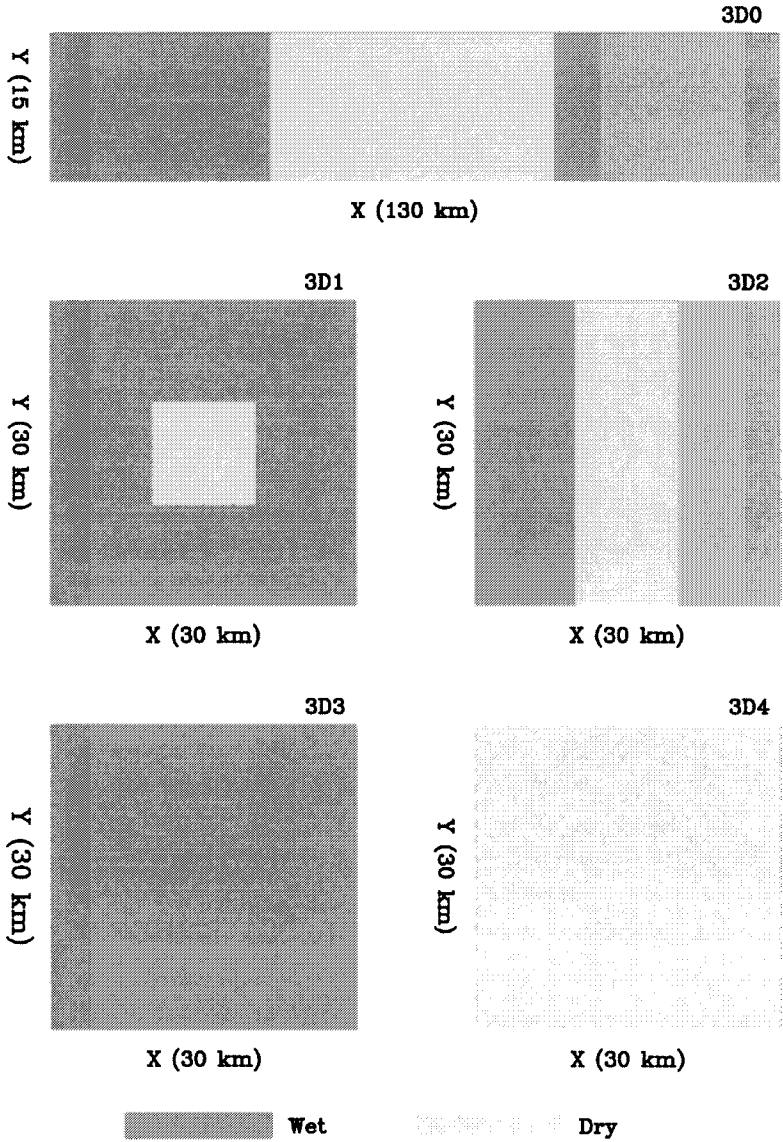
Fig. 13-7(a). Representation of the simulated horizontal domains. (From Avissar and Liu 1996.)
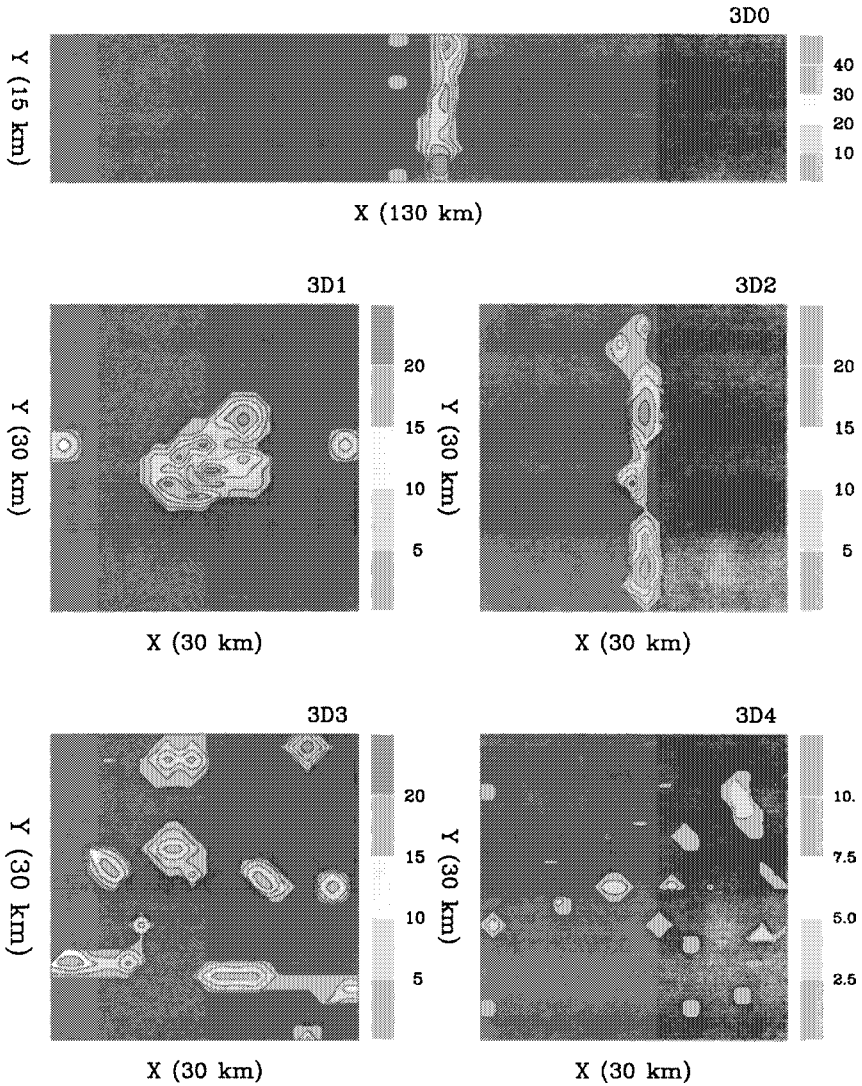
Fig. 13-7(b). Accumulated precipitation (millimeters) at 1800 LST in domain 3D0, 3D1, 3D2, 3D3, and 3D4. Contour intervals are 2 mm in 3D0; 1 mm in 3D1, 3D2, and 3D3; and 0.05 mm in 3D4. (From Avissar and Liu 1996.)

depth as a result of drifting and blowing of the snow. Hartman *et al.* (1999) show that wind-driven sublimation of snow must be known to properly predict moisture fluxes. Liston (1999) discusses this approach further. Green *et al.* (1999) assesses how landscape influences snow-cover depletion and regional weather.

Procedures to parameterize land-surface heterogeneity for use in larger-scale models are discussed in Zeng and Pielke (1993, 1995a, b), Avissar and Chen (1995), Lynn *et al.* (1995a, b), Arola (1999), and Liu *et al.* (1999a). Overviews of the role of the land surface in weather include Avissar (1995), Pitman *et al.* (1999) and Claussen (2002).

13.1.3 Mountain-Valley Winds

In a region with irregular terrain, local wind patterns can develop because of the differential heating between the ground surface and the free atmosphere at the same elevation some distance away. A larger diurnal temperature variation usually occurs at the ground, so that during the day the higher terrain becomes an *elevated heat source*, whereas at night it is an *elevated heat sink*.

Two categories of mountain–valley winds are generally recognized: (1) *slope flow* and (2) *valley winds*. These types are easiest to recognize when the prevailing large-scale flow is light. Slope flow refers to cool, dense air flowing down elevated terrain at night and warm, less dense air moving toward higher elevations during the day. Such air movement is often referred to as *nocturnal drainage flow* and the *daytime upslope*. The nocturnal drainage flow is also called a *katabatic wind* (e.g., Manins and Sawford 1979a, b).[2] Manins and Sawford (1979b), for example, found that such drainage winds are three-dimensional phenomena and that a critical gradient Richardson number of about 0.25 is required to maintain mixing between the katabatic and ambient winds. Other studies of drainage flows include those of Andersen (1981), Egger (1981), Horst and Doran (1981), Mahrt (1982), Mahrt and Larsen (1982), McNider (1982), Clements and Nappo (1983), Doran and Horst (1983), Arritt and Pielke (1986), Ye *et al.* (1989, 1990), Banta and Gannon (1995), and Winstead and Young (2000). Upslope winds have been studied by Ye *et al.* (1987, 1990). The Atmospheric Studies in Complex Terrain (ASCOT) program[3] (e.g., Dickerson and Gudiksen 1980, 1981) studied this type of wind field in detail in the Geysers area of California. Yamada (1981) performed a three-dimensional numerical simulation of the drainage winds in the ASCOT study area, and Lange (1981) reports on the use of a diagnostic[4] wind field model (that of Sherman 1978) to model the movement of tracers in the drainage flow of this valley.

Valley winds, the second category of mountain-valley flow, are up- and down-valley circulations that develop from along-valley horizontal pressure gradients in one segment of a valley, which occur because of the input into that part of a

valley by the slope flow of air of a different temperature structure than occurs adjacent to that segment. Since both slope flows and these horizontal pressure gradients along the valley floor must be resolved, three-dimensional models are required to simulate valley winds (see, e.g., McNider 1981, who models a valley flow that develops at the exit of a valley). Slope flows generally occur when topographic gradients along the slope are steeper than those found along the valley bottom; hence slope winds tend to develop more quickly than valley flow.

When slope flows occur but valley winds cannot develop as a result of blocking by the terrain configuration, the valley can be called a *trapping valley*, as suggested by T. McKee of Colorado State University. In contrast, McKee refers to valleys with a substantial valley flow as *flushing valleys*. Magono *et al.* (1982) concluded that extremely low temperatures can develop in snow-covered trapped valleys.

During sunny days, slope winds tend to be deeper than at night, as with the sea breeze, because the heating of the ground by the sun is mixed upward effectively by turbulent heat fluxes. At night, radiational cooling predominates if the winds are light and the resultant perturbation flow field is more shallow. Figure 13-8 (reproduced from Mahrer and Pielke 1977b) illustrates the differences in depth and strength of upslope and downslope winds in a two-dimensional simulation in the absence of a prevailing synoptic flow. These figures also illustrate that the airflow tends to form a closed circulation, so that if pollutants were continuously released in one segment of the flow, they would tend to accumulate in a region. Such *recirculation* is ignored in the Gaussian plume models commonly used to estimate concentrations of pollutants in irregular terrain. Using tracer data, Kossmann *et al.* (1999) has shown that discontinuities in the boundary-layer height associated with mountainous terrain and its associated mesoscale flow can enhance the transfer of boundary-layer air into the free atmosphere.

The diurnal evolution of the planetary boundary layer in mountainous topography is more complicated than that observed over flat terrain, however. Whiteman (1982) and Whiteman and McKee (1978, 1982), for example, discussed the breakup of temperature inversions within deep valleys because of upward heat flux after sunrise and the sinking of the inversion layer over the valley center as upslope flows develop along the valley walls. When the inversion height becomes sufficiently low, turbulent mixing resulting from the heating of the ground eliminates the inversion, and a relatively deep boundary layer is produced. [Over Colorado in the summer, McKee (1982, personal communication) reported observed mixed layers as high as 5 km or so above the surface]. Before the inversion is eliminated, however, enhanced air pollution can occur since the vertical depth of mixing of an effluent becomes more limited.

When a large-scale flow (often including a vertical shear of the horizontal wind), variable surface characteristics, and/or three-dimensional topographic
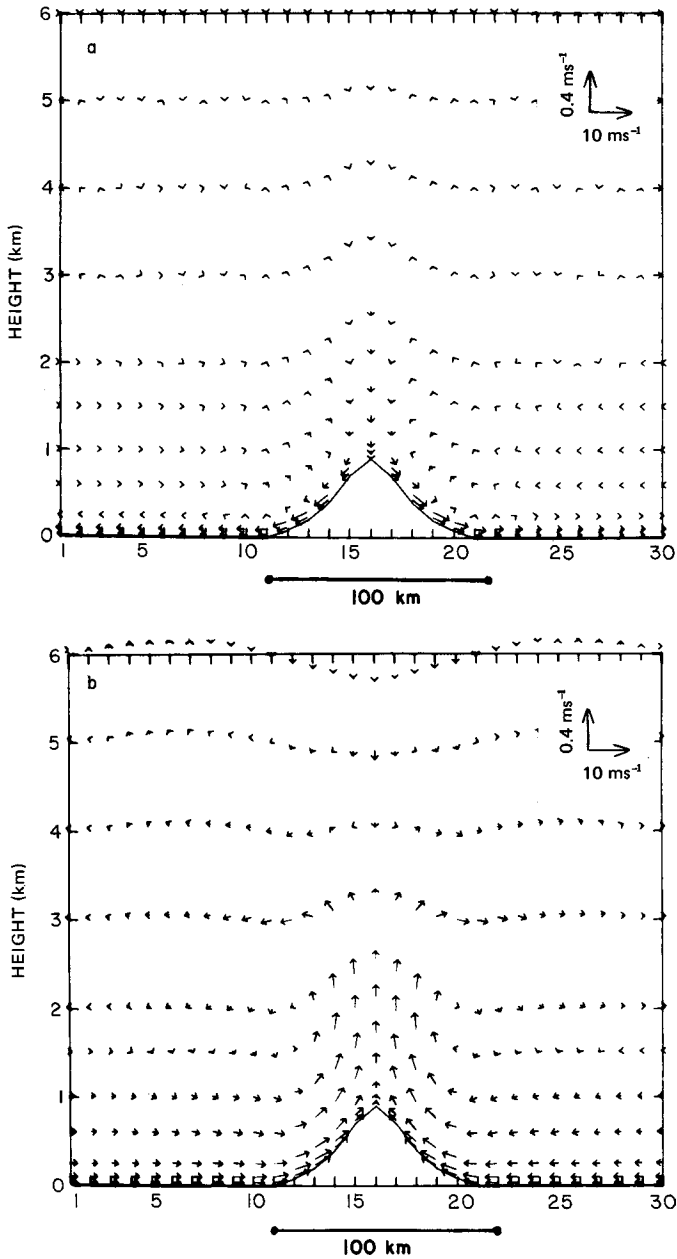
Fig. 13-8. Two-dimensional simulation of (a) nocturnal drainage flow and (b) upslope flow with no prevailing synoptic flow. Input condition typical of summer in midlatitudes. (From Mahrer and Pielke 1977b.)

features are present, the resultant mesoscale flow field can become even more complex. Without extensive observations or an accurate three-dimensional mesoscale model, it is generally impossible to anticipate the details of the diurnal variations in the wind field. Figure 13-9 (reproduced from Mahrer and Pielke 1977b) illustrates the complicated wind field predicted over the Sacramento and San Andreas Mountains of New Mexico at about 1300 LST during a summer afternoon with a prevailing westerly wind of 5 m s^{-1}. Another study of three-dimensional mountain–valley type flow patterns is that of Hughes (1978).

Wipperman and Gross (1981) have used a two-dimensional mesoscale model to construct a wind rose in irregular terrain for stable atmospheric stratification at Mannheim, West Germany, using 12 computations with different geostrophic wind directions and speeds. The large-scale winds were taken from averaged synoptic values over a 5-year period. In their study, they concluded that a non-hydrostatic version provided a somewhat better replication of the wind rose than the hydrostatic version, where their horizontal grid spacing was 2 km. However, Wipperman and Gross did not explain the reason for the difference between
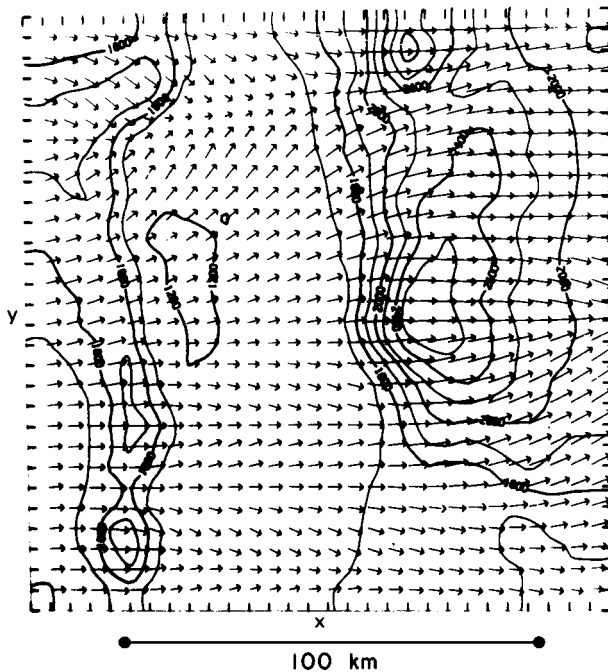
Fig. 13-9. The predicted surface winds at 3 m at 1300 LST over the White Sands Missile Range for an average June day. One grid interval corresponds to 6 m s^{-1}. Terrain is contoured at intervals of 200 m. (From Mahrer and Pielke 1977b.)

the two models in which the assumed stable stratification in the lowest 1800 m ($\partial\bar{\theta}/\partial z = 0.6°C/100$ m) would be expected to minimize vertical accelerations (see, e.g., Figure 5-5).

Modeling simulations of mountain–valley winds include those of McNider (1981), Mannouji (1982), Kimura and Kuwagata (1995), Kuwagata and Kimura (1997), and Chase *et al.* (1999), and observational studies of this atmospheric feature are represented by MacHattie (1968), Wooldridge and Orgill (1978), George (1979), Banta and Cotton (1981), Broder *et al.* (1981), Ohata *et al.* (1981), Banta (1982, 1984), Hootman and Blumen (1983), and DeWekker *et al.* (1998). Whiteman (1980), Bader (1981), and Whiteman *et al.* (1999) have studied the breakup of temperature inversions in Colorado mountain valleys after sunrise. Also in Colorado, the South Park Area Cumulus Experiment (SPACE) (Danielson and Cotton 1977; Cotton *et al.* 1982a; Knupp and Cotton 1982a, b) was an investigation of the influence of mountain winds on cumulus cloud development. Nair *et al.* (1997) simulated the development of cumulus cloud convection over the Black Hills of South Dakota. Poulos and Bossart (1995) modeled dispersion within complex terrain. Doran and Zhong (2000) investigated thermally driven gap winds in the Mexico City area.

As an example of results from these studies, MacHattie found that the synoptic wind was most strongly coupled to the flow in the direction of the main valley. Thus the diurnal perturbation was reduced more in that direction than it was normal to the valley axis. Also, the diurnal variation of the wind was observed to be less well defined on days with intense solar radiation, because the strong heating was effective in developing a deep planetary boundary layer, which enhanced mixing of the gradient wind down to the ground.

Whiteman and Doran (1993) explore the influence of terrain and the horizontal pressure gradient force orientation on the diurnal variation of the wind in complex terrain. They illustrate very effectively, as shown in Figure 13-10, the differences in the diurnal variation of the valley wind direction as a function of the wind direction above the valley for four distinct mechanisms that can control the wind direction. *Thermally driven winds* are independent of the above-valley winds and are solely controlled by locally developed along-valley pressure gradients. *Downward momentum transport* of the above-valley winds (such as associated with a deep convective boundary layer) would produce similar wind directions at all levels. *Forced channeling* occurs when the valley flow aligns itself as to whether the above-valley flow has a net flow down- or up-valley. A sharp transition occurs within the valley when this net flow changes from a down- or up-valley direction. *Pressure-driven channeling* (which is 90° out of phase with the forced channeling) occurs when the winds in the valley respond only to the large-scale horizontal pressure, and not to winds that occur above the valley. The valley winds blow directly toward low pressure synoptic systems in this case. Pressure-driven channeling should be important when there
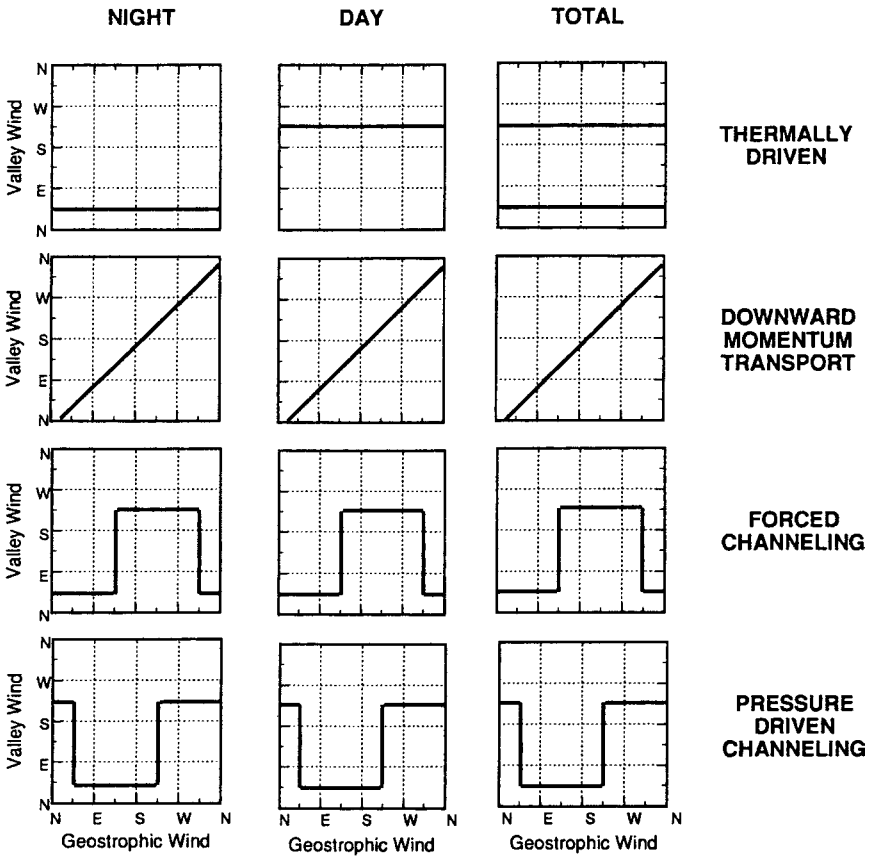
Fig. 13-10. Relationships between above-valley (geostrophic) and valley wind directions for four possible forcing mechanisms: thermal forcing, downward momentum transport, forced channeling, and pressure-driven channeling. The valley is assumed to run from northeast to southwest. (From Whiteman and Doran 1993.)

is a lack of downward momentum transport (such as when the valley is stably stratified) and thermal mesoscale wind effects are weak.

A stable surface layer that persists throughout the day can produce a less well-defined mesoscale system. Ohata *et al.* (1981), for instance, documented the major influence of snow cover in minimizing the strength of the local mountain–valley wind circulation in Nepal.

Weaver and Kelly (1982) documented that mountain ranges in Colorado are preferred locations for thunderstorm development during the summer, and Johnson and Toth (1982a, b), and Smith and McKee (1983) have shown the influence of topography in northeastern Colorado on controlling the local diurnal

wind field. Johnson and Toth found that near the Front Range of the Rockies, upslope winds tend to dominate during most of the day, with downslope winds later in the afternoon and at night. The downslope winds before sunset apparently result from the entrainment of synoptic westerly winds aloft down to lower levels, as well as from downdrafts initiated by cumulus convection over the higher terrain to the west. This preference for westerly flow of air throughout the troposphere in the late afternoon causes cumulonimbus convection to propagate toward the east at the time of their maximum development.

Holroyd (1982) summarized climatologically the occurrence and movement of mountain-generated cumulonimbus rainfall over the northern Great Plains during the May–July period. In this study, the maximum rainfall from these systems was found about 400 km northeast of the eastern boundary of the Rockies. Cotton *et al.* (1983), Wetzel *et al.* (1983), McAnelly and Cotton (1986), Tripoli (1989a, b), Tremback (1990), Nachamkin and Cotton (2000), and Nachamkin *et al.* (2000) have investigated these mountain-generated thunderstorm complexes. The observed monthly mean temperature distribution in areas of complex topography is also strongly dependent on terrain, as illustrated in Figure 13-11 for central Virginia.

Sea- and land-breeze circulations interacting with mountain-valley systems have also been studied (e.g., Doran and Neumann 1977; Mahrer and Pielke 1977a, b; Ookouchi *et al.* 1978; Garrett 1980; Alpert *et al.* 1982; Segal *et al.* 1982b). Such interactions can be very complex and, as shown by Segal *et al.* (1983b), are not simply a superposition of the two different phenomena. Rather, mountains along coastal regions, acting as elevated heat sources, create subsidence over and just inland from the coastal waters, thereby influencing the intensity and distribution of the sea breeze. Mass (1982) illustrated how such a terrain configuration can influence the diurnal pattern of rainfall in the Puget Sound region of Washington State.

Other related studies include that of Asai and Mitsumoto (1978), who investigated the influence of slope on sea and land breezes with a linear and nonlinear representation, and of Kikuchi *et al.* (1981), who used a three-dimensional model to examine the importance of elevated terrain along the coast of Japan around Tokyo in the evolution of the sea breeze. Sahashi (1981) reported on the use of a two-dimensional nonhydrostatic model to study sea breezes over irregular terrain. Figure 13-12 gives a schematic of the onshore-offshore diurnal wind pattern over the island of Hawaii, reproduced from Garrett (1980). In Greenland, Gryning and Lyck (1983) discuss the possible interplay of a drainage wind and a sea breeze along the coast in influencing the transport and diffusion of tracer material. Regional-scale mountain wind circulations are reported by Bossert and Cotton (1994a, b).
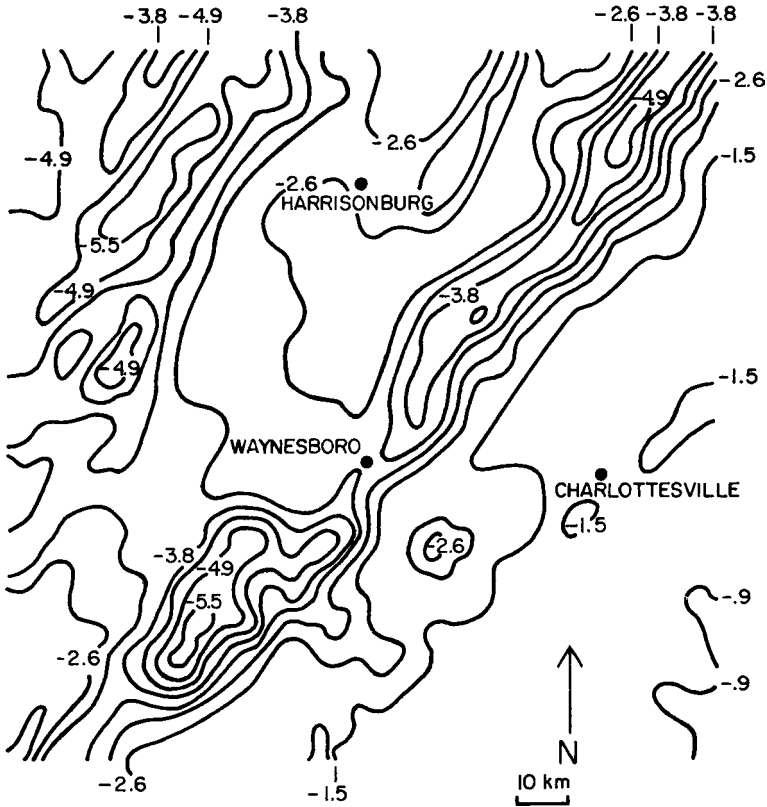
Fig. 13-11.   The estimated mean temperatures in degrees Celsius at Stevensen screen height (∼2 m) over central Virginia in January 1961. (From Pielke and Mehring 1977.)

13.1.4   Forced Airflow Over and Around Rough Terrain

When air flows over terrain features that have horizontal scales of 25–100 km or so, another type of mesoscale system develops. This atmospheric feature is different from the sea and land breezes, and mountain-valley winds because forced ascent of air in a prevailing stably stratified air mass, rather than differential heating of the ground by the sun, generates the mesoscale perturbation. The intensity of this mesoscale system is directly proportional to the pressure gradient generated by this forced movement of air.

Since the pressure gradient force [of the form

$$-\bar{\theta}\,\partial\bar{\tilde{\pi}}/\partial\tilde{x}^1 + g\big((\sigma - s)/s\big)\partial z_{\mathrm{G}}/\partial x + f\bar{\tilde{u}}^2,$$

for example, as obtained from Eq. (6-87)] is of such importance in the evolution of this type of flow, and because it is approximately a linear term, exact analytic
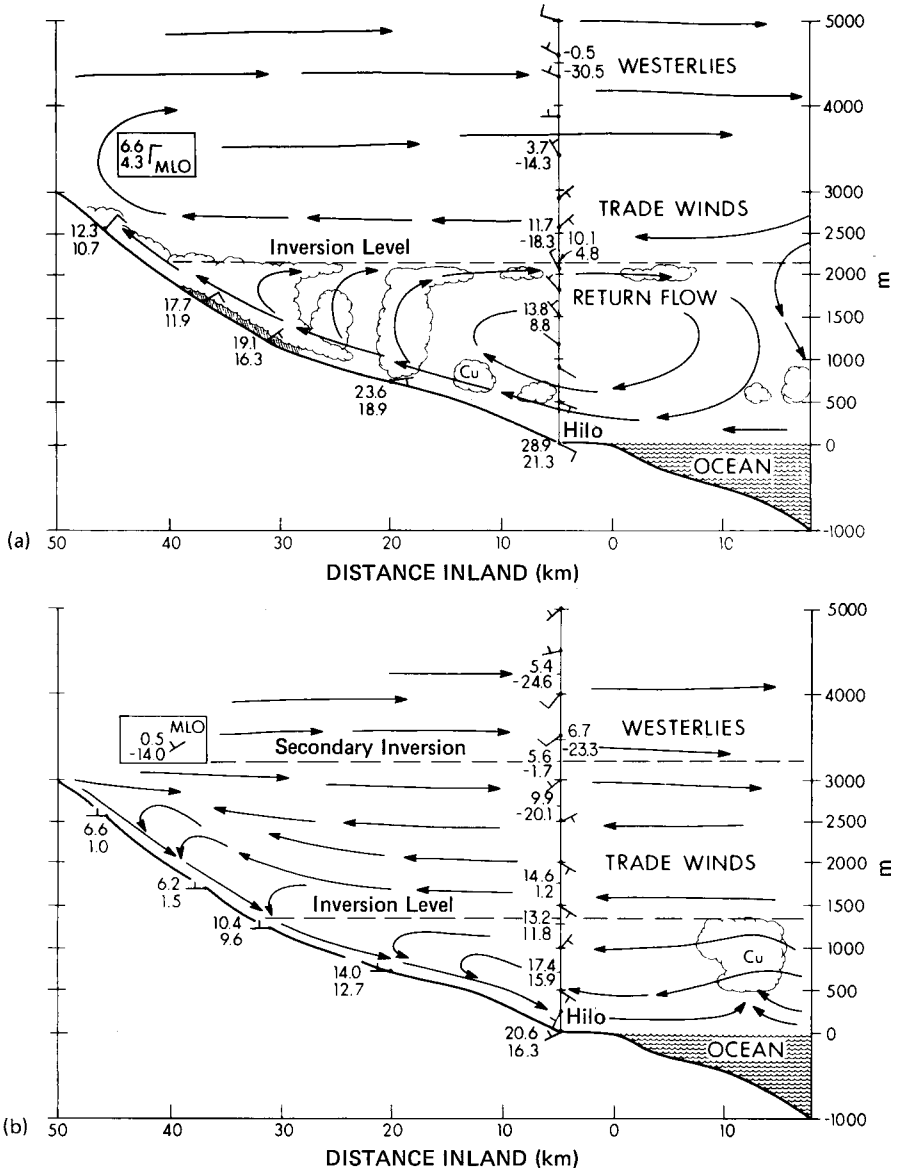
Fig. 13-12. An east–west cross-section of the onshore–offshore flow pattern over the island of Hawaii (a) during midafternoon and (b) in the early morning. Temperature (°C), dewpoint temperature (°C), and wind velocity (using wind barbs) are from observations plotted together with the schematic flow field. (From Garrett 1980.)

wave solutions have been applied with considerable success. Early investigators who used exact solutions include Queney (1947, 1948), Scorer (1949), Eliassen and Palm (1960), Covez (1971), and Vergeiner (1971). Eliassen and Palm (1960) found that, depending on wavelength, 65–100% of the wave energy generated as airflow is forced over mountains could be reflected downward from layers of strong wind in the upper troposphere. A recent analytic study is that of Kumar *et al.* (1998).

Klemp and Lilly (1975) have had some success at applying a linear model to estimate the occurrence or nonoccurrence of extreme downslope winds in the lee of the Colorado Rockies, and Sangster (1977) tested a statistical procedure to forecast these winds using observed synoptic information and parameters derived from linear theory. Klemp and Lilly found that the maximum downslope winds occur when an inversion is present near mountaintop level upstream, and if the temperature and wind profiles are such that the wave induced by the terrain approximately reverses phase between the surface and the tropopause. Sangster determined that temperature differences in the vertical and strong westerly winds at 700 mb were important parameters in causing strong downslope winds, although in contrast with Klemp and Lilly's result, such information as the vertical wavelength, Scorer parameter (defined subsequently), and the presence of an inversion were not. Extending Klemp and Lilly's work, Hyun and Kim (1979) gave another example of a linear two-dimensional model of this type of mesoscale system.

Three-dimensional linear models (e.g., Blumen and McGregor 1976; Somieski 1981) provide guidance as to what fraction of the airstream goes around topographic barriers and how much advects over it as a function of factors such as the thermodynamic stability. When air can neither go over nor go around because it is too stable and the terrain feature is too elongated, the influence of the mountain propagates rapidly upwind—a process called *blocking*. Baker (1971) and Richwien (1978, 1980) gave examples of such blocking by segments of the Appalachian Mountains in the eastern United States, and Schwerdtfeger (1974) and Kozo (1982c) described the effect of blocking by the Brooks Range in Alaska on the local wind field along the Beaufort sea coast. Schwerdtfeger (1975) discussed the influence of blocking due to a peninsula in Antarctica, while Wesley and Pielke (1990) described how blocking east of the Front Range of the Colorado Rockies can produce convergence zones that locally enhance precipitation. Reason *et al.* (1999) studied and simulated with a mesoscale model the development of propagating mesoscale systems along the coast of southeast Australia that are associated to some extent with topography.

Smith (1982a) suggested that this blocking causes a deformation of the potential temperature surfaces such as to create an unstable layer upstream of the mountain. Parrish (1982), using observational and modeling results concluded that low-level, mountain-parallel jets can form during the winter in the Sierra

Nevadas of California as a result of blocking. Harada (1981) suggested that over the Kanto plains of Japan, mountains to the west may play a role in the generation of low-level jets.

Manins and Sawford (1982), using observational data from a small valley in southeast Australia, found that blocking occurred when $F_r \overset{\sim}{\leq} 1.6$, where F_r is called the *Froude number* and is defined by

$$F_r = \overline{V}_g \left(z_{G_{max}}^2 g \frac{\partial \theta_0}{\partial z} \Big/ \theta_0 \right)^{-1/2};$$

$\overline{V}_g$ is the ridge-perpendicular, large-scale wind speed above the maximum terrain $z_{G_{max}}$; and θ_0 is the large-scale potential temperature. Manins and Sawford found that when F_r was greater than about 1.6, the air within the valley became coupled with the large-scale flow and was flushed out. It would be expected that this critical value of F_r would vary for different terrain configurations. The critical Froude number, as discussed by Manins and Sawford, represents the relative magnitudes of kinetic energy of the large-scale wind to the potential energy change needed to move an air parcel near the surface over a terrain barrier. Lyons and Steedman (1981) found a critical value of $F_r = 1.5$ for a shallow valley in western Australia.

Linear theory predicts that the vertical wavelength of lee waves induced by a single ridge is given by

$$L_z = 2\pi/S_0^{1/2} = 2\pi \, \overline{V}_g \big/ \left[(g/\theta_0)(\partial \theta_0/\partial z) \right]^{1/2},$$

where S_0 is called the *Scorer parameter* (e.g., Alaka 1960; Anthes and Warner 1978). According to linear theory, for well-developed waves to develop (as listed by Anthes and Warner), the Scorer parameter must be less in the upper troposphere than at lower levels. This requires that if $\partial \theta_0/\partial z$ is constant, then $\overline{V}_g$ must increase with height, whereas if $\overline{V}_g$ is a constant, then $\partial \theta_0/\partial z$ must be less stable in the higher levels. According to linear theory, in the absence of the Coriolis effect, two types of wave motions are induced as air flows over rough terrain; the *forced wave*, which is collocated with the underlying topography, and the *lee wave*, which propagates downstream. Trapped lee waves (which propagate indefinitely downstream in the absence of friction but which decay in amplitude rapidly with height) are a common type of air motion to the lee of mountain barriers when S_0 decreases rapidly with height. Only the forced wave is realistically simulated in a hydrostatic model, as is evident from the reviews of Smith (1979) and Klemp and Lilly (1980).

The use of nonlinear models to simulate the airflow over mountains originated with Hovermale (1965), who felt that the large perturbation velocities observed in actual mountain flows violated the requirements of linear theory in which the products of perturbations must be small. Nonlinear studies have continued with the work of such investigators as Furukawa (1973), Anthes and

Warner (1974), Gal-Chen and Somerville (1975b), Deaven (1976), Clark (1977), Clark and Peltier (1977), Klemp and Lilly (1978), Mahrer and Pielke (1978b), Peltier and Clark (1979, 1983), Seaman and Anthes (1981), Seaman (1982), Arritt *et al.* (1987), Poulos and Pielke (1994), Sun and Chern (1994), Pinty *et al.* (1995), Snook and Pielke (1995), Kang *et al.* (1998), and Mayr and Gohm (2000). Peltier and Clark (1979, 1983), for example, disagree with Klemp and Lilly's (1975) explanation for strong downslope wind events and suggest that downward reflection of energy from breaking waves in the stratosphere is the primary mechanism. Poulos *et al.* (2001) investigated the interaction between large-scale airflow over the Front Range mountains of Colorado and nocturnal drainage flow. Figure 13-13 illustrates a simulation by Klemp and Lilly (1978) for a particular windstorm in Colorado on January 11, 1972, a day also studied by Mahrer and Pielke (1978b) and Peltier and Clark (1979).

Other geographic areas have also been studied. Clark and Gall (1982) provided observational comparison of several model-predicted and observed parameters at different levels over the Elk Mountain region of Wyoming. Seaman (1982) also performed a model prediction of the airflow over this terrain feature.

Peltier and Clark imply that a nonhydrostatic model is necessary to simulate the windstorm properly on this day, whereas Klemp and Lilly and Mahrer and Pielke claim that a hydrostatic representation is adequate. The scale analysis introduced previously in this book [e.g., Eq. (5-59) and after] indicates that the hydrostatic formulation is adequate for representing this windstorm; however, additional quantitative experiments are needed to settle the issue conclusively. An exchange of correspondence on the different mechanisms for the generation of downslope wind storms is given by Lilly and Klemp (1980) and Peltier and Clark (1980). Durran (1986) concludes that these wind storms behave as a generalized hydraulic jump, which is apparently the reason that Mahrer and Pielke (1978b) were successful in producing a simulated wind storm even though the diffusive forward upstream differencing scheme was used to represent advection.

When the Coriolis effect and boundary-layer dynamics are included, the response of the atmosphere to terrain is more complex. As shown by Kessler and Pielke (1982), air that becomes ageostrophic after passing over one ridge does not adjust again to equilibrium for a long distance downstream. Therefore, if a second ridge were situated a short distance downstream, then its upstream wind profile would be markedly different from that obtained if the Coriolis effect were not included. Smith's (1982b) results support this conclusion. Using a linear model, he demonstrated that although the pressure and vertical motion fields over mesoscale-sized mountains are unaffected by the Coriolis force, the horizontal trajectories are altered, with a significant ageostrophic component produced.

Kessler and Pielke also suggested that net boundary-layer warming could occur downwind of a second ridge relative to the first, even in the absence of
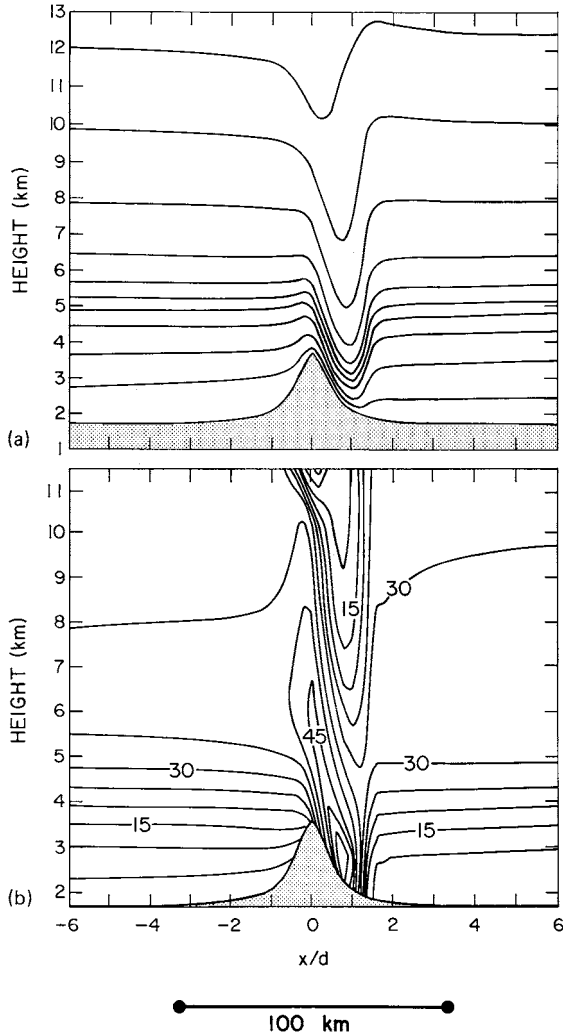
Fig. 13-13. (a) The predicted potential temperature cross-section and (b) horizontal wind field in m s^{-1} for a simulation of the January 11, 1972 windstorm along the east slopes of the Colorado Rockies. (From Klemp and Lilly 1978.)

the Coriolis effect, because of the enhanced mixing of potentially warmer air downward as it accelerates over the upstream ridge. This net warming can occur in the absence of precipitation on the upwind side of the mountain barrier.

Lee *et al.* (1989) discussed how a cold pool of air downstream from a mountain barrier inhibits strong downslope wind flow. They found that the development of a large-amplitude mountain wave is inhibited. Based on observations

and modeling results, they concluded that in the absence of significant surface heating, a large-scale horizontal surface pressure gradient directed away from the mountain must be present to remove the cold pool before the downslope winds can reach the surface.

Observational studies of strong airflow over rough terrain include those of Lilly and Zipser (1972), Lilly and Kennedy (1973), Brinkmann (1974), Hoinka (1980), Lilly *et al.* (1982), and Zipser and Bedard (1982). Lilly and Zipser, for example, observed wind gusts of 166–200 km h^{-1} associated with a chinook immediately downwind of the Rockies. Reed (1981) described a case study of downslope winds with gusts to around 100 km h^{-1} downwind from low sections of the Cascade Mountains in Washington. Under lighter winds in this geographic area, Mass (1981) reported on a zone of preferential convergence and precipitation in the Puget Sound area associated with the wind flow around the Olympic Mountains. Walter and Overland (1982) discussed theoretically and observationally several different synoptic flows over and around the Olympic Peninsula, including the damaging winds associated with the Hood Canal Bridge disaster. The ALPEX (Kuettner 1986; Pichler *et al.* 1995; Alpert *et al.* 1996b) and PYREX (Bougeault *et al.* 1990, 1997) field campaigns were designed to study airflow associated with mountain barriers in Europe.

In Europe, Pettré (1982) reported on violent winds associated with forced airflow down the Rhône Valley in France. At the top of Sierra Grande Mountain in New Mexico, Barnett and Reynolds (1981) measured winds for a 6-month period to assess the potential for wind energy electric-conversion systems. A report by the Centre for Advanced Studies in Atmospheric and Fluids Science (1983) summarized studies of the influence of strong wind flows over the Himalayas on the local wind fields in India, and Arakawa *et al.* (1982) reported on an observational study of forced airflow over rough terrain in Japan. In this latter study, the wind to the lee of the terrain barrier is found to be strongest during the night and morning, at which time the synoptic flow, land breeze, and nocturnal downslope winds are superimposed.

Over many mountainous and hilly regions of the world, this forced lifting on the upwind slopes causes condensation and/or sublimation and precipitation (e.g., Marwitz 1983; Passarelli and Boehme 1983) and is an important factor in the local water budget. Blocking and the resultant deformation of the upstream isentropes could also create regions of convective instability even if no such instability were present in the upwind synoptic flow, thereby enhancing precipitation immediately upwind of the mountains (Smith 1982a) and increasing the spatial irregularity of the precipitation (Gocho 1982). The merger of cumulus clouds in the blocked flow may also increase precipitation amounts, as suggested by the work of Sakakibara (1981). For instance, huge snow packs of more than 800 cm occur in the San Juan Mountains of southwestern Colorado in large part because of this effect.

Because of the increase in potential temperature that results from the release of latent heat (and entrainment of potentially warmer air from above the planetary boundary layer), comparatively dry and even arid regions often occur in the lee of mountains, particularly when the prevailing flow is persistently from one direction.[5] As suggested by Smith and Lin (1982) from a linearized model result, this latent heat release also alters the structure of wave motions as air is forced over rough terrain.

Figure 13-14 illustrates the annual rainfall pattern in Washington, which is controlled in large measure by the distribution of terrain relative to the prevailing, generally southwest synoptic flow during the wet season. Figure 9-2 in Chapter 9 (from the two-dimensional results of Colton 1976) illustrates an example of the predicted and observed orographic rainfall pattern over the Sierra Nevadas of California, with precipitation confined to the windward slope. Over south Wales in Great Britain, Hill *et al.* (1981) documented observationally the average enhancement by a factor of three of frontal rainfall during southwest wind flow by even hills of modest height (maximum elevations of 600 m).

Simulations of clouds or precipitation, or both, over rough terrain using three-dimensional models include those of Chappell *et al.* (1978) for the San Juan Mountains, Nickerson and Magaziner (1976) and Nickerson (1979) for the
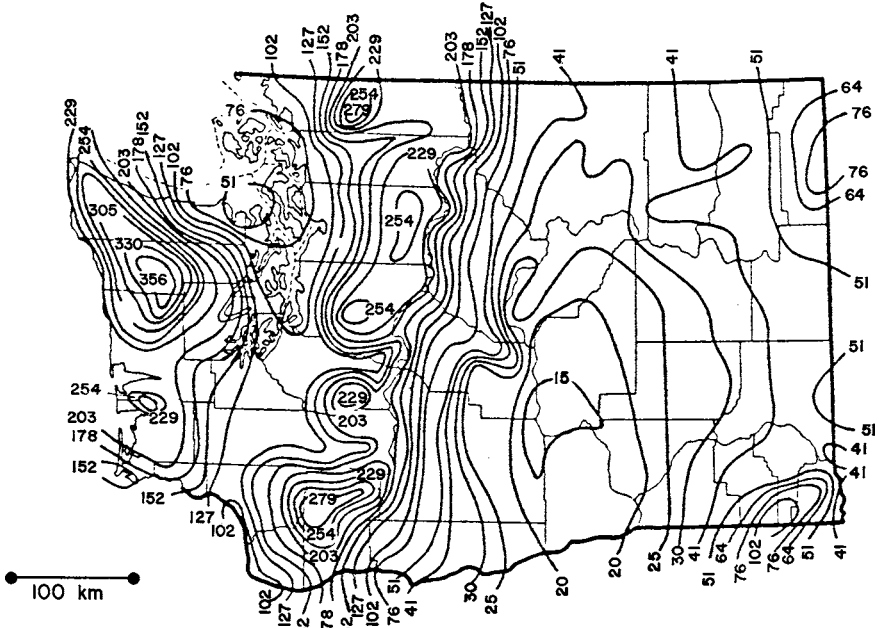
Fig. 13-14.   Annual rainfall (in centimeters) over Washington State. (From Climate and Man 1941.)

island of Hawaii, and Abbs and Pielke (1987) and Snook and Pielke (1995) for Colorado. Lavoie (1974) presented a one-layer simulation of Oahu in Hawaii, and Chang (1970) applied Lavoie's model to the Black Hills of South Dakota. Raddatz and Khandekar (1979) also successfully applied Lavoie's model to the western plains of Canada using a 47.6-km horizontal grid. Hutchison (1995, 1998a, b) discussed the coherence of weather that occurs as a result of the presence of topographic features, which permits an interpolation of weather information to smaller scales than the model-simulated resolution.

When the atmosphere is particularly moist and potential instability is released, the resultant rains over rough terrain can be heavy and can cause disastrous flash floods, such as occurred in Fort Collins, Colorado in July 1998 (Petersen *et al.* 1999) over the Black Hills of South Dakota in 1972, and in the Big Thompson watershed in Colorado in 1976 (e.g., Caracena *et al.* 1979). Mesoscale models may provide an effective tool for explaining these extreme events.

Accurate simulations of airflow over rough terrain when precipitation and cloudiness occur must not only properly represent the complex terrain but also the dynamic and thermodynamic changes caused by the phase transformations of water. For example, Hill (1978) found that circulation cells are formed over mountain areas by the precipitation itself, and Reid *et al.* (1976) determined that cloud shadowing over irregular terrain also affects the intensity of the airflow over mountains. Fraser *et al.* (1973) and Hobbs *et al.* (1973) described a diagnostic two-dimensional simulation of the airflow over the Cascade Mountains in Washington in which a detailed description of the cloud and precipitation microphysics is included. Gocho (1978) used a two-dimensional linear steadystate model to investigate the influence of microphysical processes on rainfall over the Suzuka Mountains in Japan. Cotton *et al.* (1982b) and Meyers and Cotton (1992) applied an ice-phase parameterization to a two-dimensional model simulation of stable wintertime orographic flow.

Durran (1981), Durran and Klemp (1982b), and Kessler and Pielke (1983), in a confirmation of the conclusions of Smith and Lin (1982), have shown that latent heat release can substantially alter the structure of internal waves over mountainous terrain. Kessler and Pielke found that the release of heat of condensation over a ridgetop results in a more symmetric wind field over the mountain than is produced when no phase change of water occurs.

Simulations of wind flow over rough terrain using a form of dynamic initialization or objective analysis include those reported in Collier (1975, 1977), Fosberg *et al.* (1976), Danard (1977), Rhea (1977), Bell (1978), Dickerson (1978), Sherman (1978), and Patnack *et al.* (1983). Ludwig and Byrd (1980) outlined what they claim to be a particularly efficient procedure to compute mass consistent flow fields from wind observations in rough terrain. Such models are called *diagnostic*, even if the conservation relations are used, because they are
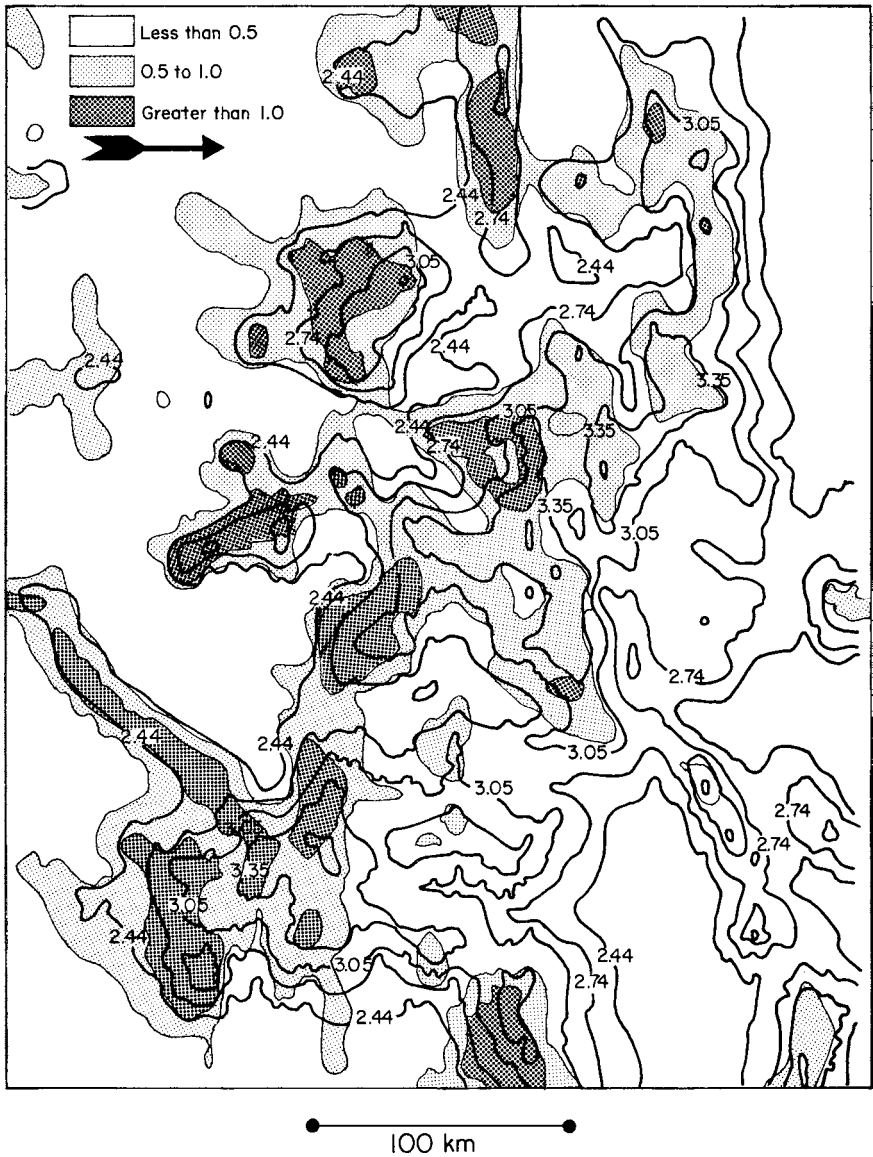
Fig. 13-15.   The predicted precipitation pattern over Colorado with a westerly synoptic wind. The darkest shading indicates the heaviest precipitation. Terrain is contoured in units of kilometers above sea level, whereas precipitation is given in relative units (i.e., for this flow a contour location with a value of 1.0 receives twice as much precipitation as a contour value of 0.5; based on work in Rhea 1977).
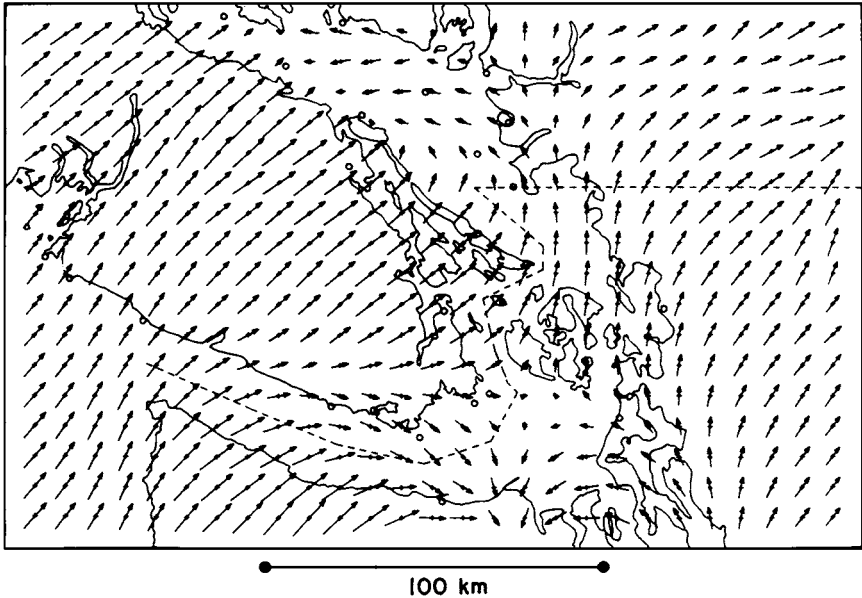
Fig. 13-16. The simulated winds over the region around the southern end of Vancouver Island, British Columbia. One grid distance represents 10 m s^{-1}. (From Danard 1977.)

not used to forecast forward in time through the integration of the conservation relations. Figures 13-15 and 13-16 show examples of results from two of these models.

Diagnostic models are very economical and appear to be effective mesoscale analysis tools when (1) the dominant forcing is the terrain; (2) below the highest terrain heights a strong, well-defined inversion exists at the top of the planetary boundary layer; and (3) sufficient observational data are available to input to the analysis.

13.1.5   Urban Circulations

Urban circulations are similar to sea and land breezes and mountain-valley winds in that it is the differential heating and cooling between the rural and urban areas that generates and sustains the wind system. Over cities and suburban areas, such alterations as asphalting, buildings, and the removal of vegetation have markedly altered the surface heat budget and thus the intensity of heat flux to the air.

The influence of these urban areas on the local weather pattern has received increased attention as the areal extent of such regions expands and as we realize

the major influence of industrial and populated areas on climate and on human health and well being. It is in the study of urban circulations that Eq. (4-26) becomes an important component in the conservation laws relevant to mesoscale atmospheric flows. As reported by Pielke (1978), an estimated 15,000 deaths per year in the United States are due to air pollution. This number exceeds the annual average number of fatalities of all other weather-related hazards combined.

Health effects from poor air quality occur throughout the world. In Italy during July 1976, for example, the accidental venting of the highly toxic organic compound dioxin (2, 3, 7, 8-tetrachlorodibenzo-p-dioxin) from a factory and its transport and dispersal by the local flow field caused death to farm animals and sickness to people and forced the permanent evacuation of individuals from their homes (*Science News* 1976; Fuller 1978). Seinfeld (1975) summarized the effects of air pollution on human health as known up to that time.

In the eastern United States, the emission of sulfates from coal-burning power plants and nitrates from automobile exhausts and power plants has greatly increased the acidity of precipitation (Likens and Bormann 1974). J. Galloway of the University of Virginia (1978, personal communication) has sampled precipitation in Virginia and found that on occasion, it has an acidity over 250 times the naturally expected value (pH as low as 3.2). Figure 13-17 illustrates an example of the enhanced levels of sulfur over an urban area, with its peak concentration elevated somewhat above the ground. Such high concentrations of sulfur, along with its possible long residence time over a city during stagnate synoptic conditions, result in mesoscale-enhanced levels of acid deposition. For such a situation, dry deposition would occur throughout the stagnate period, and wet deposition would happen when precipitation finally does fall.

The impact of anthropogenic gases and aerosol contaminants in the atmosphere demands greater complexity in mesoscale models, since the number of interactions is greater. In addition, Gaussian plume simulations, as originally proposed by Pasquill (1961) and used by the U.S. Environmental Protection Agency (e.g., Turner 1969), are inaccurate representations of pollutant distributions when phenomena such as the recirculation of the urban air occur. Calder (1977), for example, in a serious oversimplification of urban meteorology, assumed that a single wind speed and direction are representative of an entire city area for 1-hour periods in his multiple-source plume model formulation. However, van Egmond and Onderdelinden (1981) found that even with 108 stations monitoring SO_2 over a 15×220 km^2 area in Holland, relative errors of 20% occurred in the analyzed fields. These errors are due to measurement errors and small-scale influences of local sources (including the local wind and turbulence fields).

Urban models have tended to evolve separately in the areas of air chemistry and meteorology. In the former case, models have treated detailed chemical
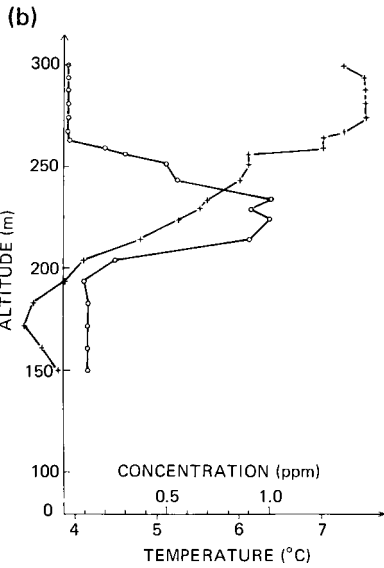
Fig. 13-17.   (a) A photograph taken from the Eiffel tower of a layer of pollution over Paris, France (b) measurements of sulfur (o) and temperature (+) at various heights from the tower at 1140 LST on December 12, 1977. The top of the pollution is distinctly evident as the approximately horizontal discontinuity in grey shading in the upper middle of the photograph. The photograph and figure were supplied by Pierre Huguet (1982, personal communication). This information is also reported in Huguet *et al.* (1978) and Fage and Moussafir (1980).

interactions (e.g., Peterson 1970; Appel *et al.* 1978; Kowalczyk *et al.* 1978; Brewer *et al.* 1981; Seigneur 1994) but have not adequately handled the mesoscale dynamics. Such models are often called *Box models* (e.g., Schere and Demerjian 1978). Surveys of the knowledge of atmospheric chemistry are given by Hales (1975), McEwan and Phillips (1975), and Heicklen (1976). EPA (1980) provides a summary of selected photochemical grid models for use over urban areas.

Mesoscale meteorological models have been used to estimate the transport and dispersion of pollutants. McNider (1981), for example, simulated the movement of effluent under drainage wind flow. McRae *et al.* (1982a) used the advection-diffusion equation of the form given by Eq. (4-26), including surface removal processes and parameterized photochemistry, to estimate urban air pollution. Other work in formulating transport and dispersion representations of pollutants for use in three-dimensional models includes that of Yamada (1977) and Uliasz *et al.* (1996). Sheih (1977) and others have considered the influence of thermal coagulation and gravitation on pollution concentrations. Hane (1978) simulated the wet deposition of pollutants over St. Louis using a two-dimensional squall line model.

In general, however, the meteorological observations and simulations have concentrated on the effects of an urban area on the wind, temperature, and moisture fields rather than on chemical interactions. Loose and Bornstein (1977), for instance, investigated the influence of New York City on the synoptic flow and observed that when a heat island was well developed, synoptic fronts decelerated over the upwind half of the city and accelerated over its downwind half in response to the higher surface roughness of the urban area. Bornstein directed a study of the influence of New York City on the sea breeze (Anderson 1979; Fontana 1979; Thompson 1979) and further illustrated the large drag effect of the buildings in this urban area. Bornstein and Thompson (1981) described the influence of this wind retardation on sulfur dioxide concentrations in New York City. Among their results, they found decreased concentrations near the coast, but larger concentrations on the downwind side of the city, associated with the inland passage of the sea breeze. Such an observation is explained as the contamination of relatively clean, onshore flow as it traverses the city.

The St. Louis area has been studied extensively as part of the METROMEX program (see Project METROMEX 1976 for a summary and the May 1978 issue of the *Journal of Applied Meteorology* for a series of articles with results from this program). Vukovich *et al.* (1976), for example, found from a mesoscale model that the urban effect of St. Louis depends on wind direction when the synoptic wind is above a certain threshold. From the observational data, Oochs and Johnson (1980) concluded that both radar echo tops and bases over St. Louis were lower than their rural counterparts. They attributed this difference to weaker updrafts in urban clouds. Changnon (1982) reported on the substantial

reduction in visibility over this city from locally generated pollutants. Shreffler (1982) discussed the variability of winds over the St. Louis area and its influence on short-term air quality predictions, while Ching *et al.* (1983) described the relative importance of vertical heat flux and horizontal advection over this city. Other mesoscale-modeling studies of this urban area include those of Vukovich *et al.* (1979), Vukovich and King (1980), and Hjelmfelt (1980, 1982). An example of Hjelmfelt's (1980) simulation of the wind flow over St. Louis is given in Figure 13-18.

Changnon (1980) found results over Chicago to be similar to those observed over St. Louis, although the rainfall increase due to the urban area was less, a
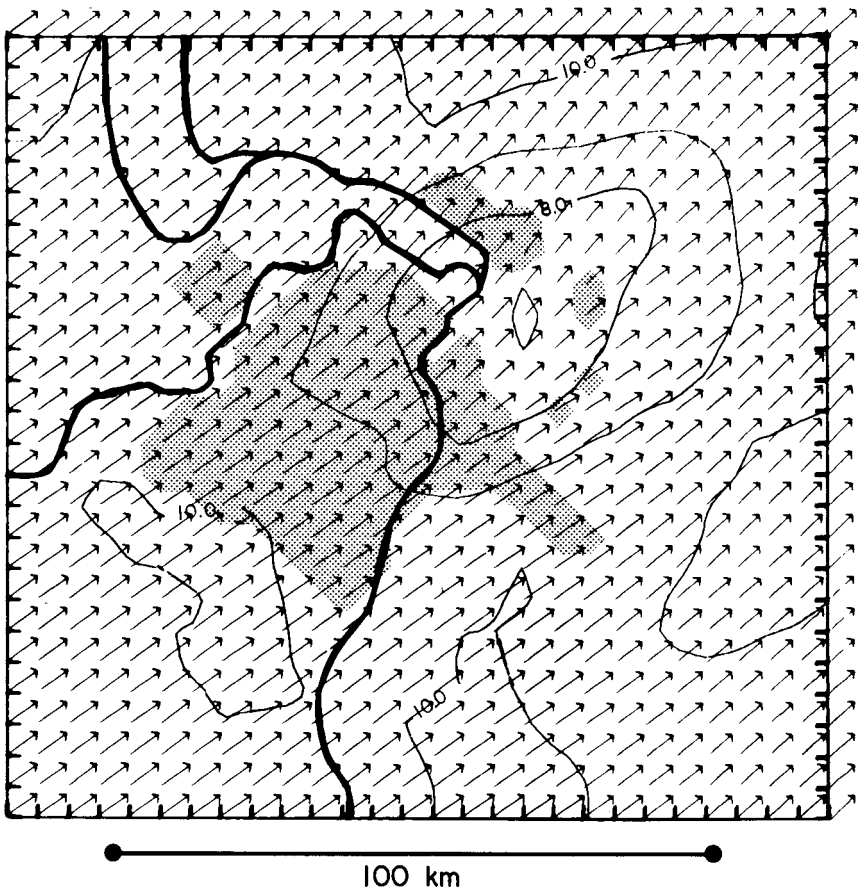
Fig. 13-18.   The predicted winds at 1 km at 1100 LST on July 18, 1975 over St. Louis, Missouri. The urban land-use areas are located within the stippled area. The wind arrows are drawn to a scale of 8 m s^{-1} per grid interval, and the isotachs are contoured at 1-m s^{-1} intervals. (From Hjelmfelt 1980.)

result that he attributed to the proximity of Lake Michigan. He observed a 15%
increase of rainfall over central Chicago compared with the surrounding rural
areas. Fujita and Wakimoto (1982) showed a reduction of mean wind speeds
over Chicago by more than one-half as compared with the open terrain to the
west of the city.

Additional observational and theoretical urban studies include those of
Anderson (1971), Olfe and Lee (1971), Oke and Fuggle (1972), Lee and Olfe
(1974), Taylor (1974), Yap and Oke (1974), Fuggle and Oke (1976), Nunez and
Oke (1976), Oke (1976), Loose and Bornstein (1977), Sawai (1978), Sisterson
and Dirks (1978), Shreffler (1979), Goodin *et al.* (1980), Goldreich *et al.* (1981),
Leduc *et al.* (1981), Tapper *et al.* (1981), Sorbjan and Uliasz (1982), Yonetani
(1983), Ulrickson and Mass (1990), Kallos *et al.* (1993), Pilinis *et al.* (1993),
Sailor (1995), Tso (1995), Banta *et al.* (1998), Kitada *et al.* (1998), Grimmond
and Oke (1999), Hafner and Kidder (1999), Ichinose *et al.* (1999), Kallo and
Owen (1999), Philandras *et al.* (1999), Bornstein and Lin (2000), Jazcilevich
et al. (2000), Sharan *et al.* (2000) and Kanda *et al.* (2001). Air pollution studies
in India are reported by the Centre for Advanced Studies in Atmospheric and
Fluids Science (1983), and Kotroni *et al.* (1999a) simulate an air pollution
episode in Athens, Greece. Air pollution studies using mesoscale models also
include Kallos *et al.* (1998), Cautenet *et al.* (1999), Varinou *et al.* (1999),
Yamada (1999), Bornstein and Lin (2001), Seaman and Michelson (2000),
and Warner and Sheu (2000). Arritt *et al.* (1988) used a mesoscale model to
investigate the spatial variations of the deposition velocity of sulphur dioxide
resulting from mesoscale flow. Taha (1999) and Taha *et al.* (1999) discuss
the importance of urban heat storage on mesoscale weather. A summary of
mesoscale air quality modeling issues is given by Dabberdt (2001).

Among the results of these types of studies, Oke (1973) determined from
an observational study that the heat island effect of a city on its surroundings
under cloudless skies is inversely proportional to the large-scale wind speed
and directly related to the logarithm of the population. The heat island effect
is also apparently dependent on the culture and age of settlement. Oke (1982,
Figure 3), for instance, found less heat island intensity in Europe than in North
America for the same population size. Over Australia, Manton and Ayers (1982)
reported that aerosol production is proportional to the town population and has
a rate of input of 8×10^{13} s^{-1} per person.

Nkemdirim (1980) found that for Calgary, Canada, the urban heat island
intensity is directly proportional to the magnitude of the stable lapse rate and
inversely proportional to the wind speed at the upwind edge of the city. Large-
scale wind speeds greater than 15 m s^{-1} or so essentially eliminated the heat
island effect, as did near neutral lapse rates. Palumbo and Mazzarella (1980)
ascertained that urbanization of Naples, Italy has resulted in a local increase of
rainfall. Yonetani (1982) reported on an increase of precipitation in the urban-

ized area of Tokyo as compared to its suburbs. Harada (1980) suggested the possibility that the increase between 1927 and 1976 of rainfall and thunder occurrences during the warm season at the town of Muroran, Japan was from increased industrial activity associated with the making of steel.

Schultz and Warner (1982), using a two-dimensional numerical model, investigated the importance of the sea-breeze, mountain-valley, and urban circulations in the Los Angeles Basin and concluded that the urban heat island effect was negligible in their simulation. Van der Hoven (1967) reported on an early transport and diffusion study in the same geographic area. Goodin *et al.* (1980), used a diagnostic model (see Section 13.1.4) to construct a three-dimensional mass-conservative wind field over the Los Angeles Basin. McRae and Seinfeld (1983) reported on an evaluation of an urban photochemical air pollution model that contains chemical reactivity for the Los Angeles Basin, although measured surface wind fields rather than a mesoscale model simulation were used to estimate air parcel trajectories. As shown by Reible *et al.* (1983), the behavior of plumes cannot be determined from surface winds alone but will also depend on the wind directional shear with height.

Studies of islands have also been performed to estimate the influence of urban areas on climate and weather (as well as to study the effects of the islands themselves, of course). Such investigations are particularly useful because pollution is not generally significant over an island, whereas it may be significant in the city environment. Mahrer and Pielke (1976) performed such a study using the island of Barbados in the West Indies, and found a downwind pressure minimum created by the advection offshore of the heat generated by the island. Figure 13-19 illustrates the resultant low-level convergent zone produced downwind of the island. Scofield and Weiss (1977) and the principal investigators of Project METROMEX (1976) reported on preferred regions of thunderstorm development downwind of urban areas, apparently at least partially because of this type of convergent wind field. Figure 13-20 (reproduced from Scofield and Weiss 1977) illustrates the strong heating of a metropolitan area (in this case Washington, D.C. and Baltimore) relative to the rural area.

Matson *et al.* (1978) used satellite imagery to illustrate maximum urban-rural differences ranging from 2.6 to 6.5°C in the midwestern and northeastern United States on a particular summer day. Price (1979), using high-resolution satellite imagery, found peak rural–urban temperature differences as large as 17°C over New York City, a result that is substantially larger than surface-based observed temperatures. He suggests that this difference could be from satellite sensing of industrial areas and rooftops, as well as the trapping of energy within urban canyons (Nunez and Oke 1977) which are not sensed by the surface observations. Thus actual heat fluxes into the atmosphere must be proportionally larger than if only surface-based observed data are used to estimate fluxes in mesoscale models of the urban circulation. The cover of the March 1980 issue
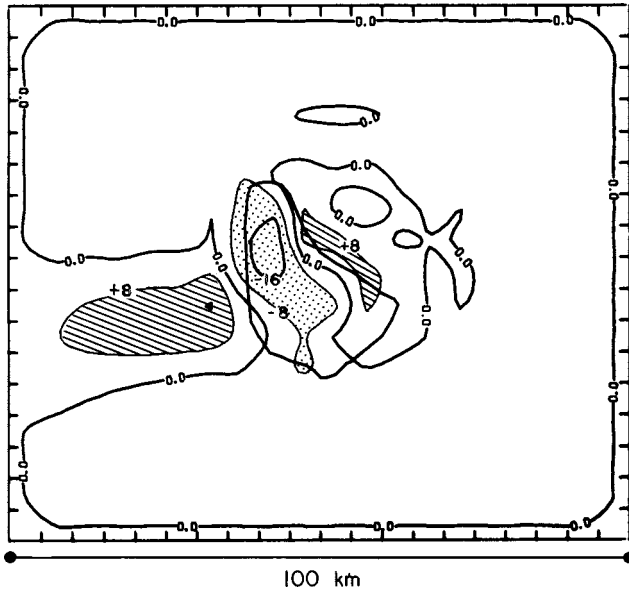
Fig. 13-19. The vertical velocity field at 1 km above the water and land surface at 1300 LST in the vicinity of Barbados during a typical summer afternoon. The contour interval is 8 cm s^{-1}. The synoptic geostrophic wind was 10 m s^{-1} from the east. (From Mahrer and Pielke 1976.)

of the *Bulletin of the American Meteorological Society* (Matson and Legeckis 1980) illustrates another satellite image of urban heat islands (this example is for eastern New England), and Carlson and Augustine (1978) presented an image for the Los Angeles area. Using surface station data, Winkler *et al.* (1981) showed that the difference in the January and July mean temperatures between downtown Minneapolis–St. Paul and the surrounding countryside is about 2°C and 3°C, respectively.

Other studies of heated islands include those of Estoque and Bhumralkar (1969), Delage and Taylor (1970), Bhumralkar (1972), Lee (1973), Lal (1979), and Carbone *et al.* (2000). Chopra (1973) summarized these and other aspects of the influence of islands on atmospheric flow patterns. Melgarejo (1980) used a two-dimensional boundary-layer model to help assess wind energy over the island of Gotland, Sweden. Garstang *et al.* (1975) presented a summary of heat island studies.

On a somewhat larger scale, Keyser and Anthes (1977) reported on predictions of planetary boundary-layer depths over the mid–Atlantic states using a mesoscale model. The concentration of pollution is, of course, closely related to the boundary-layer depth. Sheih (1978), Hanna (1979), and McNider
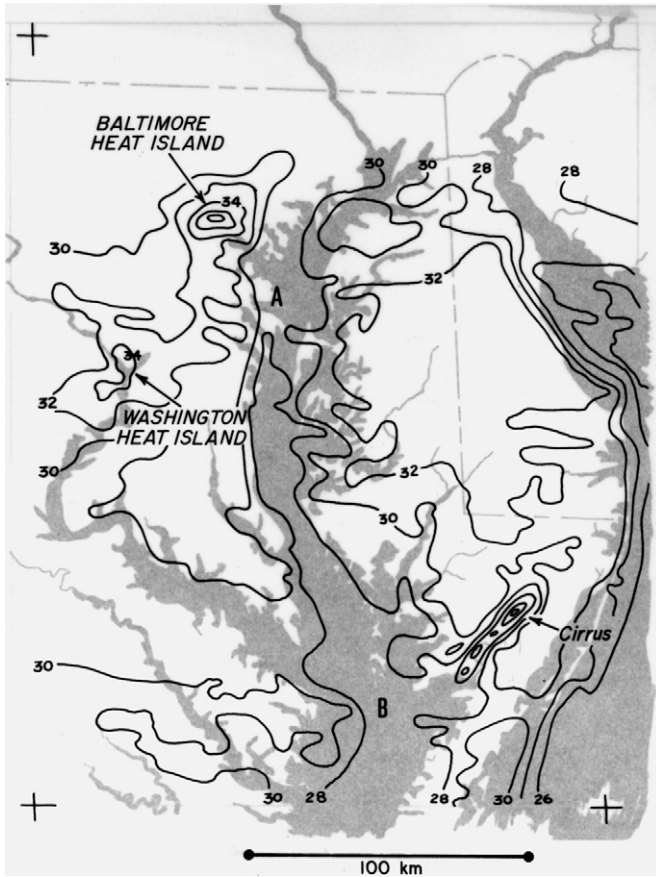
Fig. 13-20.   The observed surface temperature (in degrees Celsius) over the Chesa-peake Bay Region (as seen via the NOAA-4 satellite) at 0848 LST on June 26, 1976. (From Scofield and Weiss 1977.)

et al. (1980), provided more accurate representations of pollution dispersion for use in urban and other types of mesoscale models. de Wispelaere (1981) and Zannetti (1990) provided summaries of a number of techniques for estimating pollution concentration over mesoscale-sized areas. Moran (1992) and Moran and Pielke (1996a, b) compared mesoscale and regional model simulations of dispersion with tracer data.

Efforts to couple air chemistry and meteorology continue (e.g., Swan and Lee 1980); however, comprehensive coupled three-dimensional mesoscale sim-ulations of this interaction (including radiative interactions; see Sections 8.3.3 and 8.4.3) need to be performed. Swan and Lee (1980), for example, have

reported that because of the highly nonlinear interactions between chemical reactions in the atmosphere and the meteorology, both chemistry and meteorology must be considered simultaneously to accurately assess the effects of individual sources on air quality.

Gas and aerosol pollutants are known to have large temporal fluctuations and large spatial mesoscale variations. Health standards for such pollutants as carbon monoxide, ozone, nitrogen oxide, sulfur dioxide, lead, and fine aerosol particles have been developed. Many urban areas do not satisfy air quality standards and are said to be in *nonattainment*. Although these air quality standards were chosen primarily for health reasons (and, more recently, to monitor visibility), the effect on local weather could also be substantially influenced by lesser concentrations than are mandated as upper air quality limits. Viskanta and Weirich (1978) used a two-dimensional mesoscale model in which initial pollutant concentrations at the surface in a rural and an urban area were 20 and 100 $\mu g\ m^{-3}$, respectively, for gases and aerosols. They showed that in midlatitudes, surface temperatures were reduced about 0.3°C during midday downwind of an urban area in both winter and summer, whereas around sunrise it was 0.8°C warmer in winter and 0.5°C warmer in summer. Even upwind of the city, changes in surface temperature were predicted from the influence of changes in radiative flux divergence on the urban circulation. These pollutants also affect visibility (e.g., Mumpower *et al.* 1981).

Other studies of the effect of pollution on urban weather include those of Atwater (1971a, b; 1974; 1977), Bergstrom and Viskanta (1973a, b), Pandolfo *et al.* (1976), Zdunkowski *et al.* (1976), Viskanta *et al.* (1977b), Welch *et al.* (1978), and Viskanta and Daniel (1980). This last article reported on a two-dimensional simulation of St. Louis during the summer and found a maximum heat island effect of +3°C. Viskanta *et al.* found that the interaction of radiation with air pollution acts to decrease stability near the ground at night and to increase it during the day. Welch *et al.* (1978) found significant changes in the modeled planetary boundary-layer structure over and downwind from a city because of changes in atmospheric turbidity, roughness, heating, and soil types over the urban area. Atwater (1977) investigated urban effects in desert, tropical, midlatitude, and tundra locations and concluded that the largest thermal effects were in the tundra and the smallest were in the tropics and deserts. In contrast to Viskanta and Daniel (1980) and others, however, he concluded that except in the tundra, pollutants are only minor factors in the formation of heat islands. Pandolfo *et al.* (1976) also suggested that NO_2 and the particulate aerosols are the only commonly found anthropogenic pollutant constituents with significant radiative effects, and that their concentrations can be represented as a fixed fraction of carbon monoxide, which is the only pollutant they predicted explicitly.

Robinson (1977), Bornstein and Oke (1980), Landsberg (1981), and Bennett and Saab (1982) reviewed the influence of pollution and urbanization on urban climate. The 1983 AMS/EPA Specialty Conference on Air Quality Modeling of the Nonhomogeneous, Nonstationary Urban Boundary Layer reviewed our current understanding of urban meteorology with papers on such topics as ground-air exchange (Garrett 1983b), parameterization of subgrid-scale fluxes (Lewellen 1983), pollution removal mechanisms (Hales 1983), parameterization of radiation (Kerschgens 1983), modeling techniques (Warner 1983), transport and diffusion (McNider 1983), and synoptic influences in urban circulations (McKee 1983). Seaman (2000) provides a recent review of the use of meteorological models for air quality assessments. Accurate modeling simulations of urban areas requires that both air chemistry and the meteorology must interact. The primary interactions are as follows:

1.   The rates of input, transport, diffusion, and fallout of pollutants, as well as the types and rates of chemical reactions, depend on the mesoscale meteorological dynamics and thermodynamics.

2.   Mesoscale circulations are influenced by alterations in radiative characteristics due to changes in the clarity of the atmosphere because of pollutant gases and aerosols.

13.1.6   Lake Effect

When cold air advects over warmer ocean or lake water, the sensible and latent heat fluxes to the atmosphere can be very large, deepening the planetary boundary layer as the air continues its traverse over water. Over the East China Sea during arctic outbreaks, total heat fluxes of more than 450 W m^{-2} are supplied from the sea surface (Nitta 1976), and average heat fluxes of 600 W m^{-2} occur in cold arctic air in the advance of an extratropical cyclone (Bosart 1981). This latter heating was apparently critical in the subsequent explosive deepening of the cyclone. Chou and Atlas (1981, 1982) and Stage (1983) have shown how to estimate these ocean-air heat fluxes during cold air outbreaks using satellite imagery. In a related study, Atlas and Chou (1982) and Atlas *et al.* (1983) calculated that the top of the boundary layer rose from about 1–1.4 km over a distance of about 250 km as polar air advected south-southeast from the New York City area over relatively warm ocean water on February 17, 1979. Garstang *et al.* (1980), using both mesoscale observations and model simulations, documented, that arctic air initially accelerates substantially as it advects offshore of the Delmarva peninsula during cold outbreaks.

When the body of water is sufficiently broad, marked changes in local weather occur along the windward shore relative to conditions found on the lee coast as a result of these large heat fluxes. The shorelines of the Great Lakes (see,

e.g., Hill 1971; Jiusto and Kaplan 1972; Strommen and Harman 1978) and the Sea of Japan (see, e.g., Takeda *et al.* 1982), for example, suffer from major localized snowstorms because of the over-water advection of arctic and polar air during the winter. Lavoie (1972) and Estoque and Ninomiya (1976) successfully represented this phenomena using a one-layer mesoscale model, and Hjelmfelt and Braham (1983) used a three-dimensional numerical model. The Hjelmfelt–Braham study found that horizontal grid lengths of 24 and 40 km were unable to adequately simulate lake-effect snow on the windward shore of Lake Michigan. Only with a horizontal grid interval of 8 km could an accurate simulation be achieved.

Boudra (1977), with a 50-km, and Boudra (1981), with a 40 to 45-km, grid interval reported on somewhat larger domain simulations of the influence of all of the Great Lakes on the flow field. Ellenton and Danard (1979) applied a model with a 48-km grid interval to Lake Huron and vicinity. Recent studies of lake effect snowstorms include those of Schultz (1999) and Sousounis *et al.* (1999).

Figure 13-21 illustrates an example from Lavoie's (1972) work showing the predicted and observed precipitation resulting from cold air advection across Lake Erie. Lavoie also found that upslope winds over low topographic relief enhance precipitation. This type of phenomenon, highly localized in space, occurs over many midlatitude windward coastal regions of the world during cold air outbreaks. For example, the weather over the entire Great Lakes region is substantially influenced by this juxtaposition of land and water (see, e.g., Figure 13-22). Figure 13-23 (reproduced from Jiusto *et al.* 1970) gives the observed snowfall downwind of Lake Ontario and Lake Erie after several days of arctic airflow over the area. The large spatial variability, evident in both of these figures, illustrates the strong influence of lake effect snowstorms on local weather. Indeed, the effect of the lakes extend far inland. Leffler and Foster (1974), for instance, reported on probable annual snowfall in excess of 5 m at elevations above 1.3 km in West Virginia. Such large precipitation amounts result primarily from orographic lifting of lake-moistened air during northwesterly, cold, low-level synoptic flow.

13.2   Synoptically-Induced Mesoscale Systems

13.2.1   Convective Bands Embedded in Stratiform Cloud Systems

In extratropical cyclones and along synoptic-scale fronts, precipitation often is not uniformly distributed but rather occurs in well-organized mesoscale-sized bands of heavier snow or rain (e.g., Akiyama 1978). These smaller-scale systems are generally a part of the synoptic system but usually are not resolvable with

(a)

├────────────┤
100 km

(b)
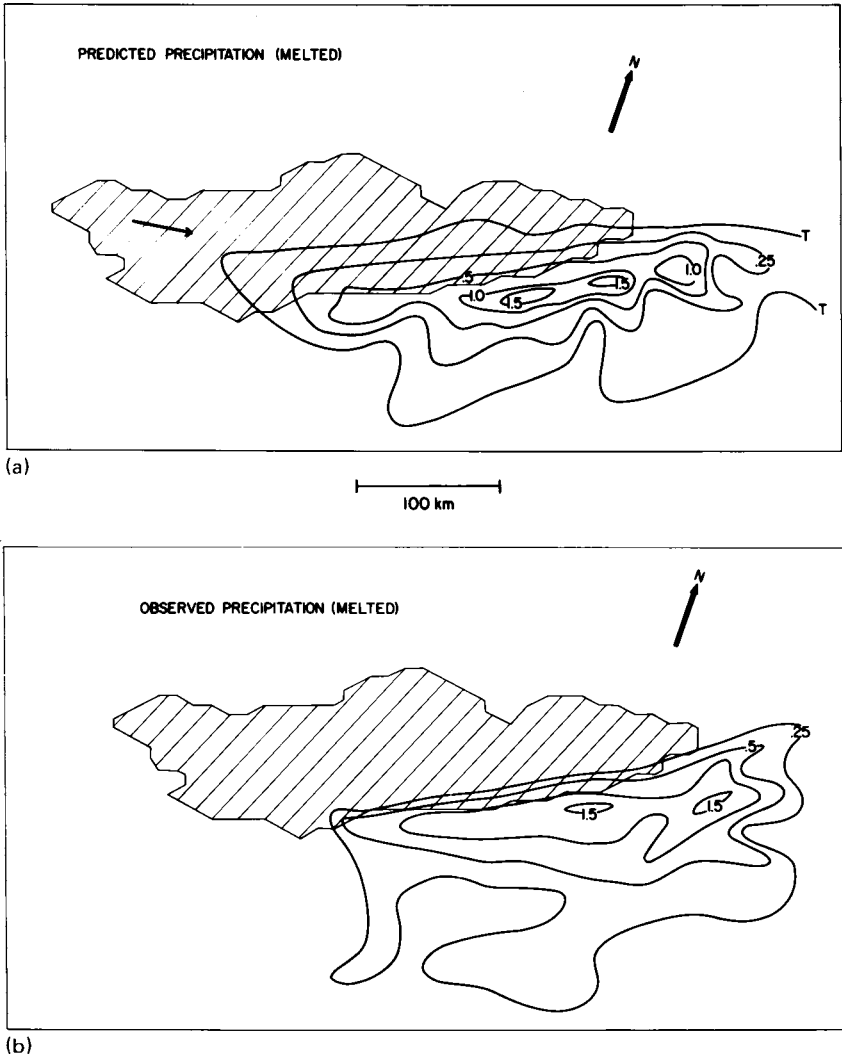
Fig. 13-21. (a) The predicted and (b) observed melted precipitation in centimeters for the 30-hour lake-effect snowstorm of December 1–2, 1966. (From Lavoie 1972.)

conventional meteorological observations, except by satellite and radar. They occur when organized local regions of the atmosphere are convectively unstable, whereas the mean atmosphere is stable to moist adiabatic displacements in the vertical. Such bands can be reinforced by terrain inhomogeneities, such as the development of small-scale baroclinic zones (small-scale fronts) along the coast associated with the passage of extratropical storms, as reported by Bosart
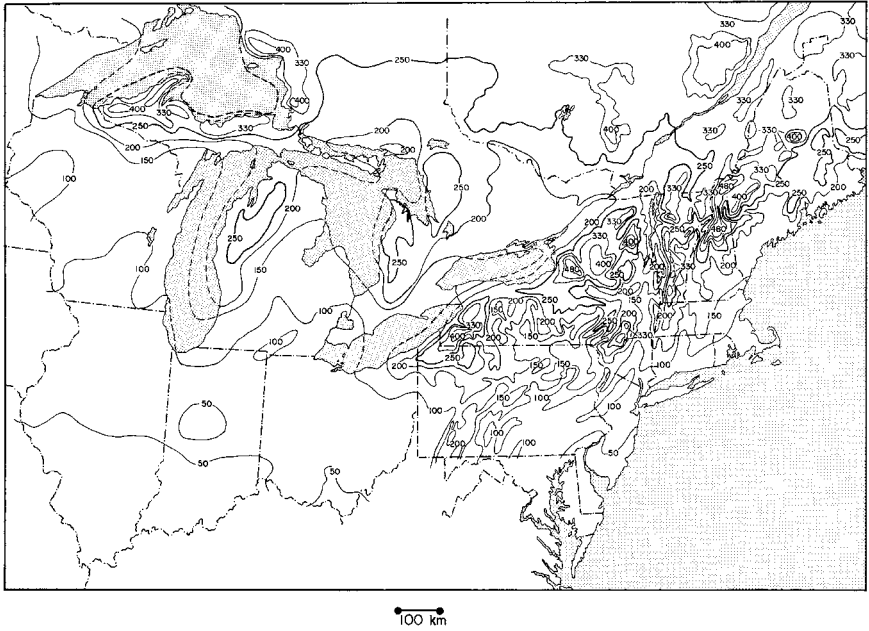
Fig. 13-22.   The mean winter snowfall in centimeters over a portion of eastern North America. U.S. data 1951–1960; Canadian data 1931–1960. (From Muller 1966.)
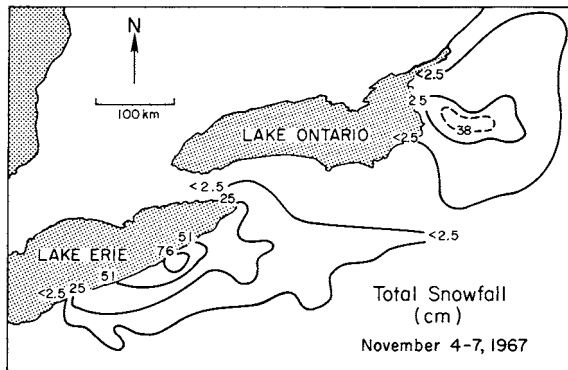
Fig. 13-23.   The observed snowfall resulting from a severe lake-effect storm. All of the precipitation was attributed to this terrain-induced mesoscale phenomena. (Adapted from Jiusto *et al.* 1970 and Jiusto and Kaplan 1972.)

et al. (1972), Bosart (1975, 1981), and Marks and Austin (1979), or they can be disrupted or destroyed as they descend larger terrain barriers, as reported by Hobbs (1978). Over the open ocean, they are well defined in satellite imagery and clearly an important component of the extratropical storm system.

In the vicinity of northwest Europe, distinct subsynoptic-scale disturbances of this type, called *polar lows* (Rasmussen 2000), apparently driven to some extent by latent heat release (e.g., Oerlemans 1980; Rasmussen 1979, 1981, 1982) are relatively common features in polar outbreaks, associated with extratropical storms. Similar-appearing features also occur in the winter over the north Pacific (e.g., Mullen 1979; Reed 1979). Locatelli *et al.* (1982), in a case study of several such mesoscale disturbances over and off of the northwest coast of Washington and Oregon, concluded that the systems that they investigated were deep baroclinic disturbances that extended as high as the 400-mb level. In general, however, the relative contributions of latent heat release from cumulus activity and of horizontal thickness gradients to the generation and evolution of these synoptically-induced mesoscale systems is not completely understood. In a study contrasting polar lows in the Pacific Ocean and Atlantic Ocean, Sardie and Warner (1983) concluded that moist cumulus convection plays a major role in their evolution in the Atlantic, whereas such a mechanism is not necessary in the north Pacific region. Winter mesoscale cyclogenesis to the east of Korea is modeled by Lee *et al.* (1998).

The interactions between the mesoscale and synoptic scales for this type of mesoscale system are complex. Ballentine's (1980) work represents an early numerical study of the quasi-stationary coastal fronts reported by Bosart, and the Cyclonic Extratropical Storms Project (CYCLES) (e.g., Herzegh and Hobbs 1980, 1981, Hobbs *et al.* 1980, Matejka *et al.* 1980, Parsons and Hobbs 1983; Rutledge and Hobbs 1983; Wang *et al.* 1983) represents an extensive observational program aimed at understanding these systems along the northwest Washington coast. In the CYCLES study, for example, Houze *et al.* (1981b) found that the presence of low-level mesoscale ascent was crucial in generating significant cloud condensate at the lower levels. The accretion of this condensate by hydrometeors falling from higher levels resulted in substantially larger precipitation rates in the warm frontal region of extratropical cyclones than would have occurred otherwise. From the CYCLES project, mesoscale rainbands were catalogued into the five basic types (Hobbs 1978): warm-frontal, warm-sector, cold-frontal (wide and narrow), prefrontal cold-surge (wide and wavelike), and postfrontal bands. Recent mesoscale model simulations of embedded convective systems include those of Nicosia and Grumm (1999).

13.2.2 Squall Lines

Along with the convective bands embedded in stratiform clouds, the squall line is among the most difficult of mesoscale phenomena to simulate. Although the squall line is undoubtedly influenced (and often generated) by fixed geographic features such as terrain, it is highly variable in space and transient in time, making accurate lateral boundary and initial conditions, essential to satisfactory predictions, difficult and expensive to obtain. Uccellini (1980), for instance, documented the strong synoptic forcing of upper- and lower-level tropospheric jets, which are frequently associated with squall line formation. Therefore, although it may be possible to build a climatology of mesoscale model forecasts for representative conditions for terrain-induced mesoscale systems, it is necessary to perform squall line predictions for each event, which is one of the main goals in the development of the Center for Analysis and Prediction of Storms (CAPS) at the University of Okalahoma. The explosive growth of a squall line over Virginia is illustrated in Figure 13-24.
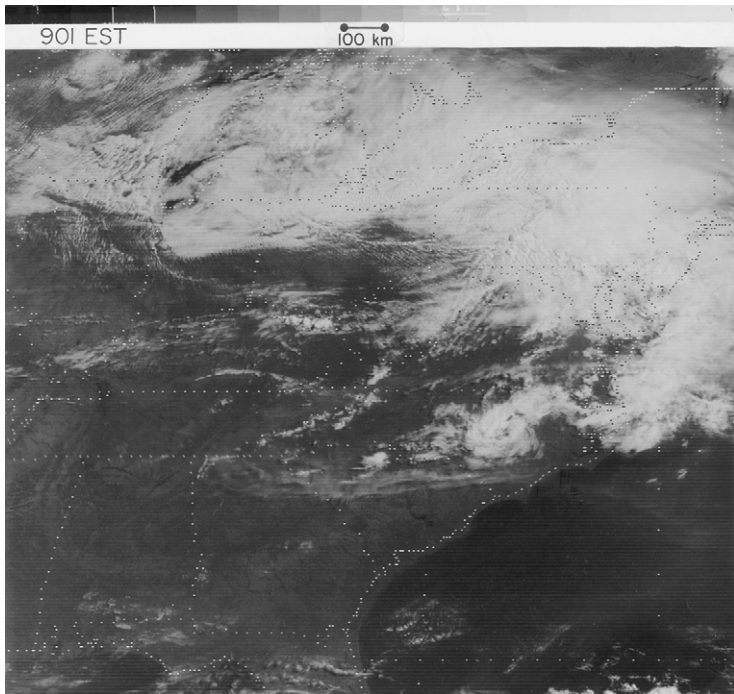
Fig. 13-24. The development of a squall line over the middle Atlantic states on June 6, 1977 as observed at 2-hour intervals by geostationary satellite imagery. The times of observation are given in Eastern Standard Time (EST) in the upper left.
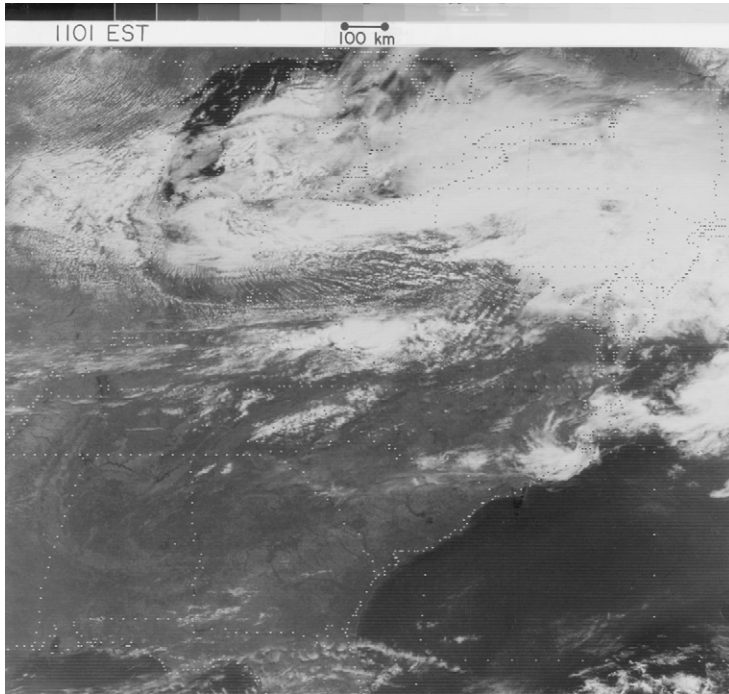
Fig. 13-24(b)

Squall lines often form in association with synoptic weather features such as cold and warm fronts, dry lines (e.g., Schaeffer 1974; Ogura and Liou 1980; Koch and McCarthy 1982; McCarthy and Koch 1982; Shapiro 1982; Homan and Vincent 1983), and tropical waves (e.g., Fortune 1980), although they typically travel at a greater speed than these larger-scale weather phenomena. Squall lines develop in air masses that are convectively unstable and, as shown by Weiss and Purdom (1974), their appearance is strongly influenced by factors such as the occurrence of early morning cloudiness.

Negri and Vonder Haar (1980) have used 5-min–interval satellite imagery to determine the magnitude of moisture convergence in the presquall line environment. They found maximum values of this convergence to be 2.2 $\times$ 10^{-3} g kg^{-1} s^{-1} for a severe storm outbreak in the midwest in April 1975. Purdom and Marcus (1982) provided evidence that the merger and intersection of thunderstorm-produced outflow boundaries are the major source of low-level convergence for subsequent deep cumulus convection over the southeastern United States during the summer, particularly in the mid- and late afternoons. Holle and Maier (1980) documented the formation of a tornado caused by the intersection of thunderstorm outflows over south Florida.
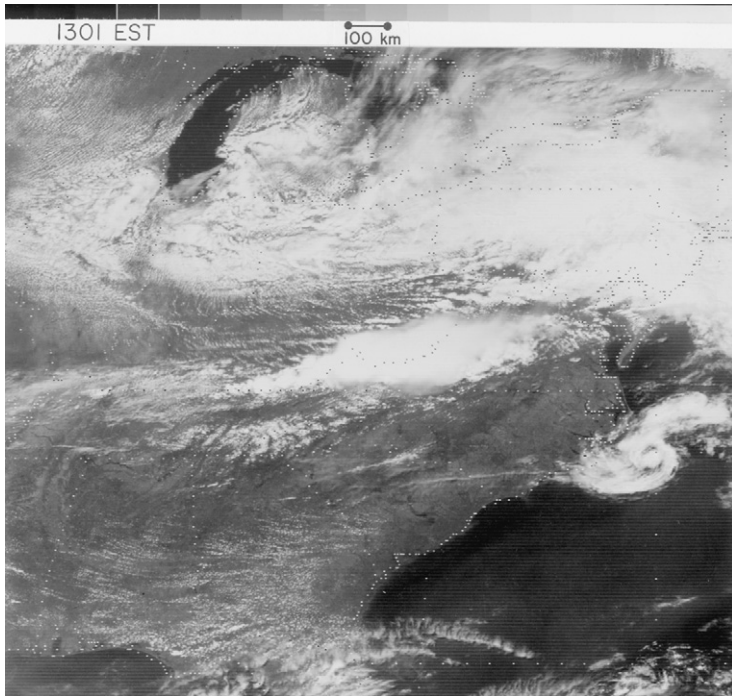
Fig. 13-24(c)

Using linearized forms of the conservation relations, studies (e.g., Raymond 1975) indicate that squall lines apparently propagate as waves with particularly intense convective activity occurring where two or more of these waves constructively reinforce one another and where the atmosphere is convectively unstable. Ley and Peltier (1981) provided a detailed analysis of a propagating wave-cloud formation with a horizontal wavelength of 10 km whose origin was assumed to be from the transient latent heat released by a severe storm some distance away. Silva Dias (1979) performed a linear analysis of tropical squall lines. Also using a linear model, Raymond (1983) examined the influence of cumulonimbus-induced downdrafts on subsequent convection.

Sun and Ogura (1979) suggested that squall lines may also be initiated through differential temperature gradients in the boundary layer interacting with the synoptic flow in an analogous manner to that causing sea and land breezes. From a case study for June 8, 1966 over Oklahoma, Sun and Ogura observed a well-defined band of horizontal convergence at low levels prior to the appearance of the first radar echoes in a region of large horizontal temperature contrast. Colby (1980) showed that large convective instability was also a necessary prerequisite for the squall line development on this day, which explained why the
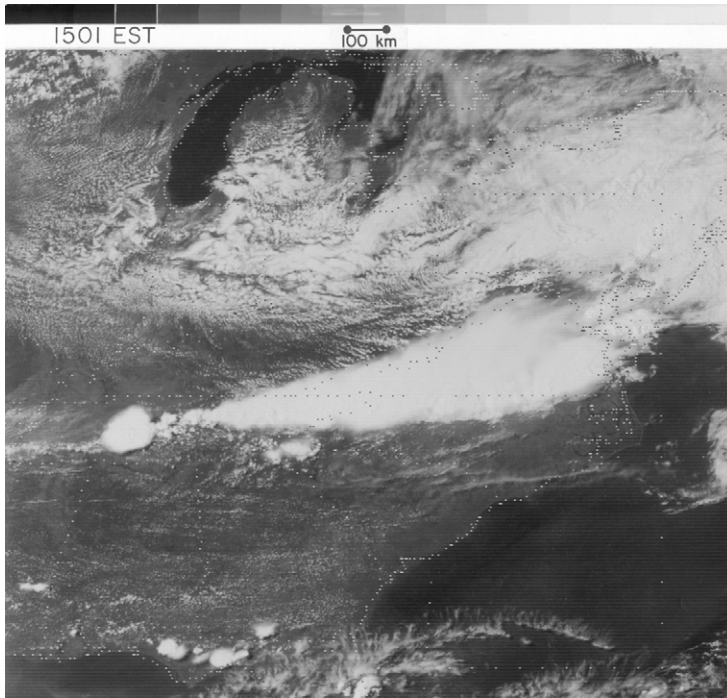
Fig. 13-24(d)

convection formed in the eastern portion of the region of upward vertical motion. Uccellini and Johnson (1979) examined the role of tropospheric jet streaks in squall line development. Emanuel (1982b) discussed the possibility that squall lines are self-exciting and involve a CISK-like cooperative interaction between the cumulus and mesoscale.

Hane (1973), Schaeffer (1974), Perkey (1976), Ross and Orlanski (1978), Chang *et al.* (1981), Kondo (1981), Kaplen *et al.* (1982), Thorpe *et al.* (1982), Wong *et al.* (1983b), Cram *et al.* (1992a, b), and Finley *et al.* (2001a, b), provide examples of nonlinear mesoscale simulations of features related to squall lines, and a review of the understanding of squall line dynamics is presented by Lilly (1979). Brown (1979) has modeled mesoscale unsaturated downdrafts driven by rainfall evaporation from precipitating cloud features, such as anvils created by squall lines. Bradberry (1981) suggested from an observational study of a squall line over Oklahoma on April 26, 1969 that mesoscale ascent associated with condensational heating about 5 km behind the leading edge of radar echoes, and descent due to evaporative cooling from cumulus cloud tops and from the dissipation of a middle cloud layer 10 km ahead of the echoes may be typical of large, mature convective storm systems.
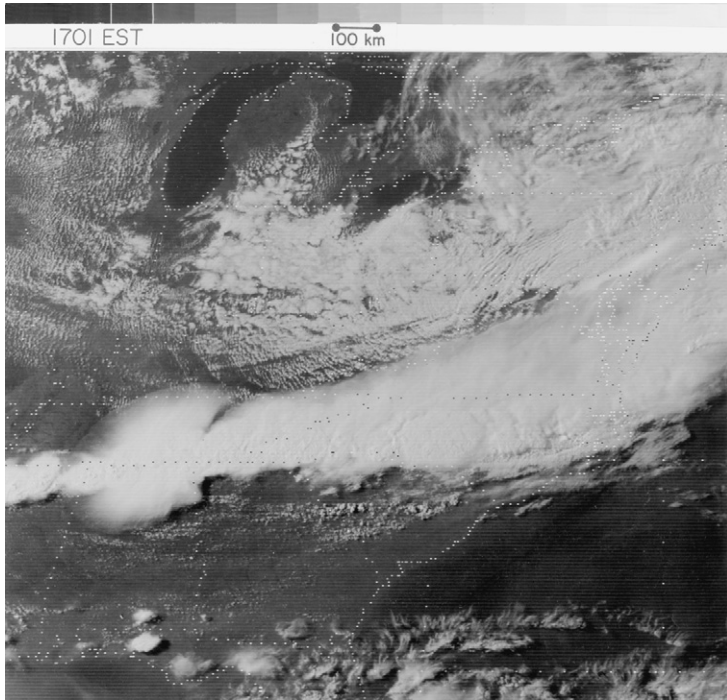
Fig. 13-24(e)

Squall lines that become stagnant over one geographic location [e.g., Johnstown, Pennsylvania in July 1977 (Hoxit *et al.* 1978); London, England in August 1975 (Bailey *et al.* 1981)] can produce devastating floods. Squall lines also often produce devastating tornado outbreaks (see, e.g., Fritsch 1975; Hoxit and Chappell 1975a, b). The Severe Environmental Storms and Mesoscale Experiment (SESAME) (e.g., Lilly 1975; Alberty and Barnes 1979; Alberty *et al.* 1979) was a mesoscale observational program designed to improve our understanding of the influence of the local environment on the generation of these intense cumulus convective systems over the Great Plains of the United States. The GARP Atlantic Tropical Experiment (GATE) (e.g., Frank 1978, 1980; Zipser and Gautier 1978; Warner *et al.* 1979; Houze and Betts 1981), the Venezuelan International Meteorological and Hydrological Experiment (VIMHEX) (e.g., Betts *et al.* 1976), and the winter monsoon experiment (MONEX) (e.g., Warner 1982) represent similar observational programs in the tropical eastern Atlantic, over land in tropical South America, and over water southeast of Vietnam.

Examples of studies of squall lines observed in the tropics include those of Fernandez (1982), Gamache and Houze (1982), and Ishihara and Yanagisawa

(1982). Zipser *et al.* (1981) documented a weaker mesoscale convective system off the coast of west Africa. Johnson and Nicholls (1983) analyzed boundary-layer structure associated with tropical squall lines over the eastern Atlantic. Additional discussions of squall lines and their dynamics have been given by for example, Dudhia and Moncrieff (1989) and Houze (1989).

13.2.3   Mesoscale Convective Clusters

Since geostationary satellite imagery over the United States became routinely available, the frequent occurrence of persistent mesoscale areas of cumulus convection, such as illustrated in Figure 13-25, has been noted, as first suggested by W. R. Cotton (1977, personal communication). Defined as *mesoscale convective*
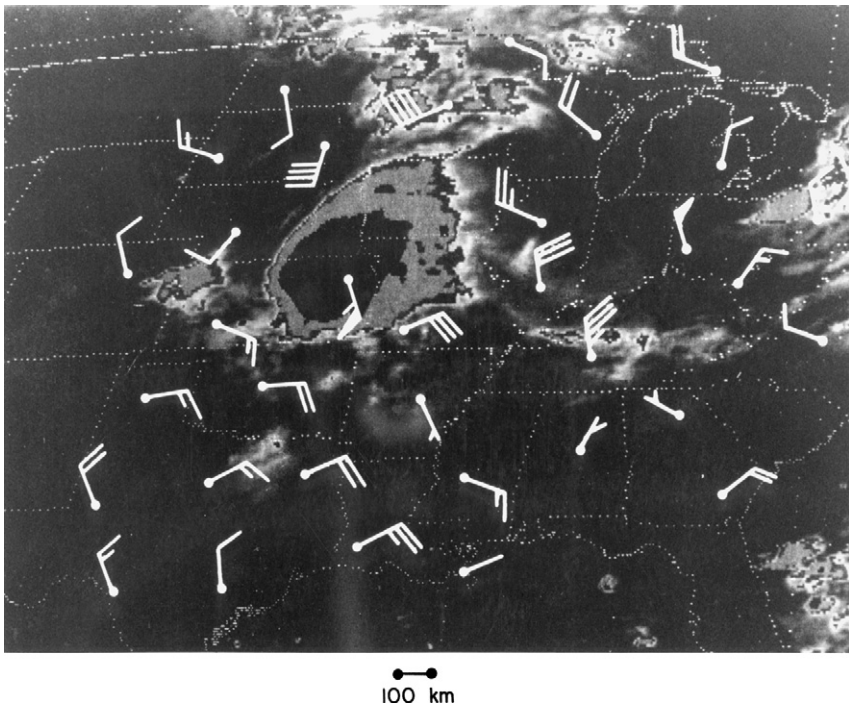
Fig. 13-25.   A mesoscale convective cluster (MCC) on June 28, 1979 at 0600 Central Standard Time as seen via infrared geostationary satellite imagery. Wind barbs are vector errors of the 12 h National Weather Service limited fine mesh (LFM) model-predicted 200 mb wind field. A full barb represents 5 m s^{-1}; a flag represents 25 m s^{-1}. Note that the largest errors usually occur in the vicinity of the MCC. (Figure provided by J. M. Fritsch, 1982.)

clusters (MCCs) by Maddox (1980a, c), these systems appear to originate over and downstream of the Rocky Mountains and to propagate from west to east (Nachamkin and Cotton 2000; Nachamkin *et al.* 2000).[6] As warm core systems, they have been shown (Fritsch and Maddox 1980, 1981a; Maddox 1980b; Maddox *et al.* 1981, Keyser and Johnson 1982) to cause major alterations in the synoptic flow field. Fritsch *et al.* (1980) presented a scheme to initialize model simulations of these mesoscale convective clusters, and Fritsch and Maddox (1981b) performed a model simulation of an MCC using a 20-km horizontal grid mesh. Electrification in mesoscale convective systems is discussed in Schuur and Rutledge (2000a, b).

Cotton *et al.* (1983) and Wetzel *et al.* (1983) document the initiation of an MCC over the Rockies and its eventual passage into the western Atlantic 2 days later. Park and Sikdar (1982) documented an MCC over Oklahoma and illustrated its complex interaction with the synoptic scale. Ninomiya *et al.* (1981) illustrated what is apparently a small MCC moving over and off of the coast of China toward Japan at about 32°N. Its origin was just east of the Tibetan Plateau. Other studies of mesoscale convective systems include those of Chen *et al.* (1999b), Tucker and Zentmire (1999), Bernardet *et al.* (2000), Stensrud *et al.* (2000), and Xu *et al.* (2001a, b). Table 13-1, adapted from Maddox (1980c) gives his definition of an MCC.

Bosart and Sanders (1981) concluded from an observational analysis of the data for the July 1977 flood in Johnstown, Pennsylvania, that an MCC, rather than a stagnant squall line, was responsible for the excessive rainfall. MCCs also are a major component of the tropical atmosphere and are also referred to as *cloud clusters*. Observational studies of these tropical systems include those of Houze and Cheng (1981), Zipser *et al.* (1981), and Houze (1982). Houze *et al.* (1981a), Johnson (1982), and Johnson and Kriete (1982) documented a diurnally-varying mesoscale precipitating cloud system over the ocean in the Asian tropics that is related to the winter monsoon flow pattern and the daily

TABLE 13-1

The Definition of a Mesoscale Convective Cluster (MCC)

Size	Contiguous cloud shield with temperatures less than or equal to −32°C covering an area of more than 100,000 km^2 and an interior cloud region with temperatures less than or equal to −52°C covering an area of more than 50,000 km^2.
Duration	The above two conditions must last for at least 6 hours. The MCC is then defined as an entity until the two conditions listed above no longer apply.
Shape	The eccentricity (i.e., ratio of minor to major axis) must be greater or equal to 0.7 at the time of its maximum extent.

From Maddox 1980c.

heating cycle of the adjacent land. Potty and Sethu Raman (2000) simulated the structure and track of monsoon depressions over India. Zipser (1982) briefly summarized our understanding of MCCs. A recent review of mesoscale convective systems is given in Smull (1995).

13.2.4 Tropical Cyclones

Tropical cyclones, which are generally smaller than the extratropical cyclones that form along the polar front, represent one of the larger mesoscale phenomena. Their location of formation and subsequent movement are strongly influenced by the synoptic scale. Ooyama (1982), for instance, defined the tropical cyclone as "a mesoscale power plant with a synoptic-scale supportive system."

Tropical storms form when the heating from cumulonimbus activity positively reinforces the low-level convergent wind flow such that an increasingly more intense mesoscale vortex develops. Simulations of this phenomenon include two-dimensional studies such as those of Rosenthal (1970, 1971) and Kurihara (1975). Anthes *et al.* (1971), Anthes (1972), Kurihara and Tuleya (1974), and Jones (1980), and others have performed idealized three-dimensional calculations. Kurihara and Bender (1982) and Bender and Kurihara (1983) performed a three-dimensional hurricane simulation with 5-km horizontal grid increments in the finest grid of their quadruply nested model. Anthes *et al.* (1971) contrasted solutions using two- and three-dimensional simulations.

Ceselski (1974) and Mathur (1974, 1975) have given examples of simulations for actual observed tropical storms; an example of the wind field predicted by Mathur 1974 for a Caribbean hurricane is given in Figure 13-26. Eastman (1995), Eastman *et al.* (1996), Lui *et al.* (1997, 1999b), and Zhang *et al.* (2000) simulated Hurricane Andrew (1992) as it approached and made landfall in south Florida. Lagouvardos *et al.* (1999) modeled a system in the Mediterranean Sea that had characteristics of a tropical cyclone.

The effect of landfall on tropical cyclone structure has been studied by Moss and Jones (1978), Tuleya and Kurihara (1978), Tuleya *et al.* (1984), and Powell *et al.* (1996). Wind flow in mountainous terrain caused by such storms has been investigated by a diagnostic model and a physical model (Brand *et al.* 1979) and by numerical models (Chang 1982; Lin *et al.* 1999). Chang's model simulation demonstrated that the original low-level center of a tropical storm is blocked by the mountainous terrain of a large island, with a secondary low-level circulation forming in the lee of the island as the upper-level center propagates over the region immediately downwind of the island.

Using observations of damage, Fujita (1980) estimated the wind field pattern of landfalling hurricanes, and Powell (1980) examined the use of several boundary-layer models in estimating wind speed near the surface in hurricanes. Surface observations associated with hurricanes were reported in Cione *et al.* (2000).
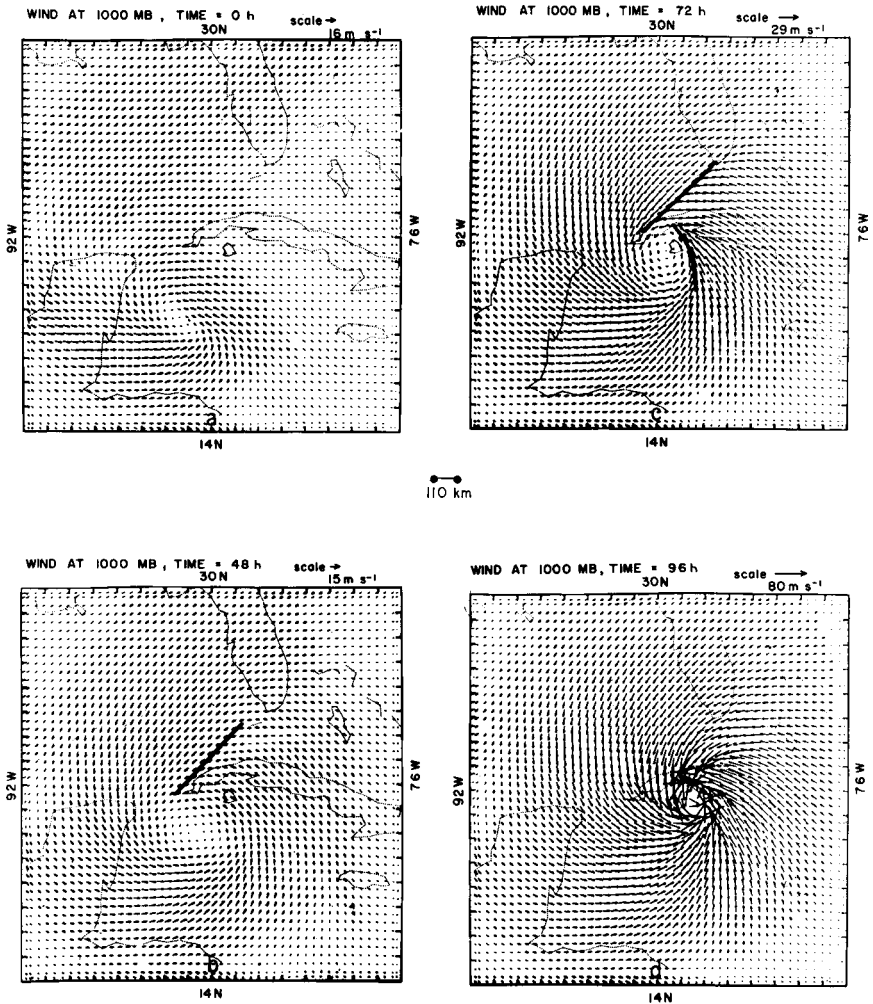
Fig. 13-26. Three-dimensional model prediction of the winds at 1000 mb associated with the development of Hurricane Isbell in 1964. (From Mathur 1974.)

An overview of tropical storm modeling was given by Simpson and Pielke (1976), and more extensive reviews were presented by Anthes (1974b, 1982a), Pielke (1990), and Pielke and Pielke (1997). Krishnamurti and Kanamitsu (1973) simulated the more common tropical disturbance referred to as the nondeveloping tropical wave. The latter model was described in Krishnamurti *et al.* (1973). Another example of a mesoscale tropical cyclone simulation is that of Mathur (1997).
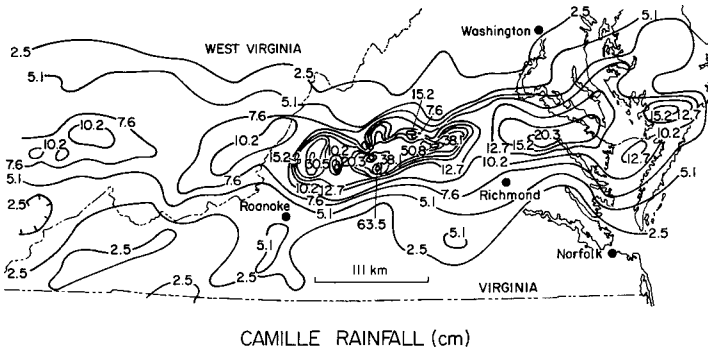
Fig. 13-27. The observed precipitation (in centimeters) from the remnants of Hurricane Camille from noon August 19 to midnight August 20, 1969. (From the December 1969 issue of the *Virginia Climatological Summary*, NOAA, Asheville, NC.)

Figure 13-27 (reproduced from the December 1969 issue of the *Virginia Climatological Summary*) illustrates the complex precipitation patterns that can occur over land from the overland track of a tropical storm interacting with a cold front (in this case Hurricane Camille). Zhou (1980) presented a similar study over central China. The ability of nonlinear numerical models to reproduce such complicated precipitation patterns has not yet been achieved, and given the severe lateral and initial boundary constraints required for actual mesoscale situations (e.g., Anthes and Warner 1978), it may never be attained. Discussions are presented on the societal impacts of hurricanes in Pielke and Pielke (1997).

13.2.5 Frontal Circulations

Synoptic-scale fronts are directly related to a horizontal temperature gradient averaged over a depth in the atmosphere (e.g., between 1000–850 mb or 1000–500 mb). Such a mean temperature gradient is referred to as a *thickness gradient*, as described in detail in most texts on basic meteorology (e.g., Wallace and Hobbs 1977; Pielke 1995). This relation between the mean temperature between two pressure surfaces and the thickness results directly from the hydrostatic assumption. Synoptic-scale cold, warm, and stationary fronts are found on the leading warm edge of these baroclinic zones, and occluded fronts lie in the middle of a polarward extension of warm thickness. An early discussion of fronts and their relation to extratropical cyclones was given by Bjerknes and Solberg (1921). Synoptic fronts are associated with the genesis of extratropical low pressure systems. Gyakum *et al.* (1996) summarized the ability of regional models to simulated explosive ocean extratropical low development. Kuo *et al.* (1992) simulated the dynamics of an occluded marine cyclone.

When the horizontal thickness gradient associated with a front has been steady for a long period, the wind field closely approximates gradient wind balance. Using the definition of mesoscale presented in Chapter 1, these fronts are not mesoscale features. When the thickness distribution changes rapidly, however, significant nongradient winds are generated as the adjustment toward a new balanced state begins. Williams (1967), for example, suggested that cold frontogenesis is created from the large-scale baroclinic field by the divergent component of the wind. Such frontal circulations are mesoscale and are an integral component in frontogenesis and cyclogenesis.

Studies of frontal circulations include those of Palmén and Newton (1969), Browning and Harrold (1970), Rao (1971), Hoskins and Bretherton (1972), Shapiro (1981), Bennetts and Sharp (1982), Lagouvardos *et al.* (1996), and Kotroni *et al.* (1999b, c). Uccellini *et al.* (1981) examined the importance of circulations associated with jet streaks in frontal zones during intense cyclogenesis along the east coast of the United States, and Uccellini (1980) discussed the role of jet streaks in the formation of low-level jets over the Great Plains. Carbone (1982) documented intense rainfall associated with a cold front in central California, and Hobbs and Persson (1982) reported on precipitation associated with a cold front moving onshore along the Washington coast. As suggested at the end of Section 13.2.1, these mesoscale frontal circulations are closely related to the convective bands embedded in stratiform cloud systems.

Ross and Orlanski (1982) used a three-dimensional numerical model to simulate the 48-hour evolution of a cold front in early May 1967 over the southeastern United States, while Sergeev (1983) used a parameterization of precipitation forming processes to examine the influence of precipitation on frontal dynamics. Dickison *et al.* (1983) documented that flying insects can accumulate in the convergence zones associated with cold fronts. Lagouvardos *et al.* (1998) simulated an extreme cold frontal surge over Greece that produced the worst snowfall in 100 years. A cold outbreak in Kenya was discussed by Okoola (2000).

In eastern Asia, a frontal circulation that extends southwest to northeast for several thousand km is established each year associated with the Asian summer monsoon. Mesoscale model simulations of this feature (called the "Baiu front" or the "Mei-Yu front") have been performed by Sun (1984b) and Hsu and Sun (1994). Observational studies of this front have been reported by, for example, Ninomiya (1992, 2000), Yamazaki and Chen (1993), and Takahashi *et al.* (1996).

Williams (1972) contrasted the creation of fronts by a nondivergent horizontal wind field that contains stretching deformation with the generation of fronts by the divergent component of the wind. He concluded that the first mechanism requires too much time to cause frontogenesis. Apparently, the low-level convergence of the thickness gradient by nonlinear horizontal advection (such as

discussed for the sea breeze in Section 11.1.1.1 and shown in Figure 11-3) is required to create fronts in the observed time period.

Shaw *et al.* (1997), Ziegler *et al.* (1995, 1997), Ziegler and Rasmussen (1998), and Grasso (2000) discussed the inititation of deep cumulus convection along another type of frontal zone called the *dryline*. The dryline is an interface between shallow moist and deep dry boundary layers. This feature is frequently found in the western high plains of the United States in the summer, for example. Other mesoscale model simulations of the dryline include those of Sun (1987) and Sun and Wu (1992).

Notes to Chapter 13

1. Nicholls and Pielke (1994a, b) demonstrate that the expansion of the volume, as required by the ideal gas law, also elevates the pressure surface over land.

2. Some authors distinguish between a drainage flow caused by a source of cool air high on a slope and a katabatic flow that is continuously cooled from below as the air sinks. For analytic solutions of downhill flows, such a division is useful; however, in the real atmosphere, this categorization is generally not distinct. A general discussion of gravitationally-forced flows for a number of geophysical phenomena is given in Simpson (1982).

3. The ASCOT program was designed to develop the technology needed to assess atmospheric properties and the impact of new energy sources on air quality in areas of complex terrain, as described by M.H. Dickerson in the Foreword of Orgill (1981), and by Knox *et al.* (1983:15–19). The report by Orgill presents a review of past meteorological and diffusion work in complex terrain.

4. Diagnostic models are discussed briefly in Section 13.1.4.

5. The warm wind that occurs to the lee of mountains as a result of such forced ascent and descent is called, for example, a *chinook* in North American and a *föhn* in Germany. When cold advection is occurring, a strong downslope wind is called a *bora*.

6. To include mesoscale convective cloud features that do not fit into the MCC classification given in Table 13-1, the more inclusive term *mesoscale convective system* (MCS) is used.

Additional Readings

Books and articles that provide in-depth discussions of the different types of mesoscale systems include the following.

Anthes, R. A. 1982. "Tropical Cyclones, Their Evolution, Structure and Effect." American Meteorological Society, Monograph, Boston.

Atkinson, B. W. 1981. "Mesoscale Atmospheric Circulations." Academic Press, New York.

Baines, P. G. 1995. "Topographic Effects in Stratified Flows." Cambridge University Press, New York.

Banta, R., and W. Blumen. 1990. "Atmospheric Processes Over Complex Terrain." Meteor. Monographs, 45, W. Blumen, Ed., American Meteorological Society, Boston.

Browning, K. A. (Ed.). 1982. "Nowcasting." Academic Press, New York.

Browning, K. A. 1986. Conceptual models of precipitation systems. *Wea. Forecasting* **1**, 23–41.

Cotton, W. R., and R. A. Pielke. 1995. "Human Impacts on Weather and Climate." Cambridge University Press, New York.

Pielke, R. A. 1990. "The Hurricane." Routledge Press, London.

Pielke, R. A., and R. P. Pearce. (Eds.). 1994. "Mesoscale Modeling of the Atmosphere." American Meteorological Society, Monographs, 25, Boston, MA.

Pielke, R. A., Jr., and R. A. Pielke, Sr. 1997. "Hurricanes. Their Nature and Impacts on Society." John Wiley and Sons, Chichester, U.K.

Pielke, R. A. Jr., and R. A. Pielke, Sr. (Eds.). 2000. "Storms." Vols. I and II. Routledge Press, London.

Rotunno, R., J. A. Curry, C. W. Fairall, C. A. Friehe, W. A. Lyons, J. E. Overland, R. A. Pielke, D. P. Rogers, S. A. Stage, G. L. Geernaert, J. W. Nielsen, and W. A. Sprigg. 1992. "Coastal Meteorology—A Review of the State of the Science." Panel on Coastal Meteorology, Committee on Meteorological Analysis, Prediction, and Research, Board on Atmospheric Sciences and Climate, Commission on Geosciences, Environment, and Resources, National Research Council. National Academy Press, Washington, D.C.

Smith, R. B. 1979. Influence of mountains on the atmosphere. *Adv. Geophys.* **21**, 217–230.

Whiteman, C. D. 2000. "Mountain Meteorology: Fundamentals and Applications." Oxford University Press, London.

Yih, C.-S. 1980. "Stratified flows." Academic Press, New York.

Zannetti, P. 1990. "Air Pollution Modeling: Theories, Computational Methods, and Available Software." Computational Mechanics Publications, Boston, MA.

The value of predictive models, which includes mesoscale models, is discussed in the following.

Droegemeier, K. K., J. D. Smith, S. Businger, C. Doswell III, J. Doyle, C. Duffy, E. Foufoula-Georgiou, V. Krajewski, M. Lemone, C. Mass, R. Pielke Sr., P. Ray, S. Rutledge, and E. Zipser. 2000. Hydrological aspects of weather prediction and flood warnings: Report of the Ninth Prospectus Development Team of the U.S. Weather Research Program, *Bull. Amer. Meteorol. Soc.,* **81**, 2665–2680.

Mass, C. F., and Y.-H. Kuo. 1998. Regional real-time numerical weather prediction: Current status and future potential. *Bull. Amer. Meteor. Soc.* **79**, 253–263.

Pielke, R. A. 1994. The status of mesoscale meteorological models. In *"Planning and Managing Regional Air Quality: Modeling and Measurement Studies"*, P. A. Solomon and T. A. Silver, Eds., 435–458. Lewis Publishers, Chelsea, MI.

Pielke, R. A. Jr., D. Sarewitz, R. Byerly Jr., and D. Jamieson. 1999. Prediction in the Earth sciences and environmental policy making. *Eos, Trans. Amer. Geophys. Union,* **80**, 312–313.

Sarewitz, D., R. A. Pielke Jr., and R. Byerly, editors. 2000. *"Prediction: Science Decision Making and the Future of Nature."* Island Press, Covelo. CA.

Appendix A

The Solution of Eqs. (10-28) and (10-47) with Periodic Boundary Conditions

From Ahlberg *et al.* (1967:15), the equations of the form (10-28) and (10-47) for a periodic condition can be written as

$$b_1 x_1 + c_1 x_2 + a_1 x_D = d_1$$
$$a_2 x_1 + b_2 x_2 + c_2 x_3 = d_2$$
$$\vdots$$
$$a_i x_{i-1} + b_i x_i + c_i x_{i+a} = d_i \qquad \text{(A-1)}$$
$$\vdots$$
$$a_{D-1} x_{D-2} + b_{D-1} x_{D-1} + c_{D-1} x_D = d_{D-1}$$
$$c_D x_1 + a_D x_{D-1} + b_D x_D = d_D$$

for $i = 1$ to D.

For Eq. (10-28), $x_i = \phi_j^{\tau+1}$,

$$a_i = \frac{-\Delta t}{\Delta z_j} \frac{K_{j-\frac{1}{2}}}{\Delta z_{j-\frac{1}{2}}} \beta_{\tau+1}, \qquad c_i = \frac{-\Delta t}{\Delta z_j} \frac{K_{j+\frac{1}{2}}}{\Delta z_{j+\frac{1}{2}}} \beta_{\tau+1},$$

$$b_i = \left[1 + \frac{\Delta t}{\Delta z_j} \frac{K_{j+\frac{1}{2}}}{\Delta z_{j+\frac{1}{2}}} \beta_{\tau+1} + \frac{\Delta t}{\Delta z_j} \frac{K_{j-\frac{1}{2}}}{\Delta z_{j-\frac{1}{2}}} \beta_{\tau+1} \right],$$

$$d_i = \phi_j^\tau + \frac{\Delta t}{\Delta z_j} \left\{ \frac{K_{j+\frac{1}{2}} \beta_\tau (\phi_{j+1}^\tau - \phi_j^\tau)}{\Delta z_{j+\frac{1}{2}}} - \frac{K_{j-\frac{1}{2}}}{\Delta z_{j-\frac{1}{2}}} \beta_\tau (\phi_j^\tau - \phi_{j-1}^\tau) \right\};$$

for $i = 2$ to $D - 1$.

$$a_1 = \frac{-\Delta t}{\Delta z_1} \frac{K_{\frac{1}{2}}}{\Delta z_{\frac{1}{2}}} \beta_{\tau+1}, \qquad c_1 = \frac{-\Delta t}{\Delta z_1} \frac{K_{1\frac{1}{2}}}{\Delta z_{1\frac{1}{2}}} \beta_{\tau+1},$$

$$b_1 = \left[1 + \frac{\Delta t}{\Delta z_1} \frac{K_{1\frac{1}{2}}}{\Delta z_{1\frac{1}{2}}} \beta_{\tau+1} + \frac{\Delta t}{\Delta z_1} \frac{K_{\frac{1}{2}}}{\Delta z_{\frac{1}{2}}} \beta_{\tau+1} \right],$$

531

$$d_1 = \phi_1^\tau + \frac{\Delta t}{\Delta z_1}\left\{\frac{K_{1\frac{1}{2}}\beta_\tau}{\Delta z_{1\frac{1}{2}}}(\phi_2^\tau - \phi_1^\tau) - \frac{K_{\frac{1}{2}}\beta_\tau}{\Delta z_{\frac{1}{2}}}(\phi_1^\tau - \phi_D^\tau)\right\},$$

and

$$a_D = \frac{-\Delta t}{\Delta z_D}\frac{K_{D-\frac{1}{2}}}{\Delta z_{D-\frac{1}{2}}}\beta_{\tau+1}, \qquad c_D = \frac{-\Delta t}{\Delta z_D}\frac{K_{D+\frac{1}{2}}}{\Delta z_{D+\frac{1}{2}}}\beta_{\tau+1},$$

$$b_D = \left[1 + \frac{\Delta t}{\Delta z_D}\frac{K_{\frac{1}{2}}}{\Delta z_{\frac{1}{2}}}\beta_{\tau+1} + \frac{\Delta t}{\Delta z_D}\frac{K_{D-\frac{1}{2}}}{\Delta z_{D-\frac{1}{2}}}\beta_{\tau+1}\right],$$

$$d_D = \phi_D^\tau + \frac{\Delta t}{\Delta z_D}\left\{\frac{K_{\frac{1}{2}}}{\Delta z_{\frac{1}{2}}}\beta_\tau(\phi_1^\tau - \phi_D^\tau) - \frac{K_{D-\frac{1}{2}}}{\Delta z_{D-\frac{1}{2}}}\beta_\tau(\phi_D^\tau - \phi_{D-1}^\tau)\right\},$$

where $\Delta z_{1/2} = \Delta z_D = \Delta z_{D+1/2} = \Delta z_1$ should be assumed.

For Eq. (10-47), $x_i = N_i$,

$$\left.\begin{array}{l} a_i = \alpha_i,\ b_i = 2,\ c_i = \mu_i \\[2mm] d_i = 3\dfrac{\mu_i}{h_{i+1}}(\phi_{i+1} - \phi_i) + 3\dfrac{\alpha_i}{h_i}(\phi_i - \phi_{i-1}) \end{array}\right\} \quad \text{for } i = 2 \text{ to } D - 1;$$

$$a_1 = \alpha_1,\ b_1 = 2,\ c_1 = \mu_1;$$

$$d_1 = 3\frac{\mu_1}{h_2}(\phi_2 - \phi_1) + 3\frac{\alpha_1}{h_1}(\phi_1 - \phi_D);$$

$$a_D = h_1/(h_D + h_1),\ b_D = 2,\ c_D = 1 - \alpha_D;$$

$$d_D = 3\frac{\mu_D}{h_1}(\phi_1 - \phi_D) + 3\frac{\alpha_D}{h_D}(\phi_D - \phi_{D-1}),$$

where $h_1 = h_D$ should be assumed.

The procedure for solving (A-1) involves letting the right side of the top and second from the bottom equations in (A-1) be written as $d_1 - a_1 x_D$ and $d_{D-1} - c_{D-1} x_D$, then solving the first $D - 1$ equations, as performed in Section 10.2. The result is a solution in terms of x_D, whose value is determined algebraically from the last equation in (A-1).

The algorithm for solving (A-1) is similar in form to that given by Eq. (10-49) and, following Ahlberg *et al.* (1967), can be written in general form in terms of the coefficients of (A-1) as

$$x_i = u_i + q_i x_{i+1} + s_i x_D, \quad i = 1, \ldots, D - 1, \tag{A-2}$$

where

$$s_i = -a_i s_{i-1}/p_i, \quad s_0 = 1,$$

$$p_i = b_i + a_i q_{i-1}, \quad q_0 = 0,$$

$$q_i = -c_i/p_i,$$

$$u_i = (d_i - a_i u_{i-1})/p_i, \quad u_o = 0.$$

If the equation

$$x_i = t_i x_D + v_i, \quad i = 1, \ldots, D - 1 \tag{A-3}$$

is defined, then substituting into (A-2) for x_{i+1} yields

$$x_i = u_i + q_i v_{i+1} + (q_i t_{i+1} + s_i) x_D, \quad i = 1, \ldots, D - 1. \tag{A-4}$$

Equating like terms between (A-3) and (A-4) produces

$$
\begin{aligned}
t_i &= q_i t_{i+1} + s_i, \quad i = 1, \ldots, D - 1 \\
v_i &= u_i + q_i v_{i+1},
\end{aligned}
\tag{A-5}
$$

where $v_D = 0$ and $t_D = 1$, as required by (A-2) for $i = D - 1$.

After values of t_i and v_i are obtained from (A-5), x_D is obtained algebraically from the equation

$$c_d(t_1 x_D + v_1) + a_D(t_{D-1} x_D + v_{D-1}) + b_D x_D = d_D,$$

where (A-3) is used to substitute into the last line of (A-1). The remaining values of x_i are then determined from (A-3).

Appensix B

Model Summaries

As in the first edition of this text, summaries of several mesoscale models are included as an Appendix. Most of these models were discussed as part of an American Meteorological Society Short Course on "Mesoscale Atmospheric Modeling by Original Model Developers" held on January 9, 2000 in Long Beach, California. This short course was organized by the Yamada Science and Art Corporation of Santa Fe, New Mexico.

These models are by no means the only state-of-the-art codes. They are presented to demonstrate how models can be decomposed into their component parts, following the individual chapters of this text. To avoid misrepresentation, the text provided by each modeling group was retained verbatim as much as possible, with only minor editorial revisions to conform more with the notation in the text. Each modeling group reviewed the description of its model during the preparation of this Appendix.

Other valuable state-of-the-art mesoscale and regional models not described here include the Clark model (Farley *et al.* 2000); the Australian Air Quality Forecasting System (AAQFS) (Cope *et al.* 1999; Hess *et al.* 2000), which includes the BMRC Limited Area Prediction System (Puri *et al.* 1998), the Deutschland model (Gross and Hense 1999), the UK Mesoscale model (Met. Office 1999/2000), the North Carolina State University (NCSU) mesoscale model (Wu and Raman 1997), the MRI nonhydrostatic model (Fujibe *et al.* 1999; Saito 1997), Gesthacht's Simulation Model of the Atmosphere (GESIMA) (Mölders 2000), the Regional Spectral model (RSM) (Juang *et al.* 1994) a nonhydrostatic version of which is described in Juang (2000); HIRLAM (Savijärvi and Jarvenoja 2000), the Quasi-Nonhydrostatic (QNH) mesoscale model (MacDonald *et al.* 1999, 2000), which uses the bounded derivative initialization technique introduced by Browning and Kreiss (1986) and discussed by Lee and MacDonald (2000); the Central University Mesoscale model (CUMM) (Huang 2000); the Collaborative Model for Multiscale Atmospheric Simulation (Peckham and Wicker 2000); and the Meso-NH model (Giordani and Planton 2000; Lafore *et al.* 1998). Schlunzen (1994) overviewed German nonhydrostatic models. Clearly, the suite of mesoscale models has expanded since the first edition of this book appeared!

The value of community mesoscale models with which individuals other than model developers can use codes is discussed in Anthes (2000). Additional datasets for validating mesoscale models have been developed over the last decade or so. These include the First International Satellite Land Surface Climatology Project (ISLSCP) Field Experiment (FIFE) (Sellers *et al.* 1992), the Global Energy and Water Cycle Experiment (GEWEX)

Continental Scale International Project (GCIP) (Coughlan and Avissar 1996), the Boreal Ecosystem-Atmosphere Study (BOREAS) (Sellers *et al.* 1995), the Hydrologic and Atmospheric Pilot Experiment (HAPEX) (André *et al.* 1998; Goutorbe *et al.* 1994), the European Field Experiment in a Desertification-Threatened Area (EFEDA) (Bolle *et al.* 1993), the Wind in Non-uniform Domains program (WIND) (Cionco 1994), the Fronts and Atlantic Storm Track Experiment (FASTEX) (Williams 2000), and the Meteorology And Diffusion Over Non-uniform Areas program (MADONA) (Cionco *et al.* 1999).

New initiatives for comparing mesoscale models (or components of these models) to observations include GLASS FLUXNET (Valentini *et al.* 1999), and the *L*arge-Scale *B*iosphere-Atmospheric Experiment in *A*mazonia (LBA) (Dolman *et al.* 1999; Kabat *et al.* 1998).

Overviews of land surface experiments have been provided by Gash and Kabat (1999). New initiatives to create mesoscale models include the Weather and Research Forecasting Model (WRFM) (Rasmussen 1999; Fullerton 2000).

Model: The Operational Multiscale Environment Model with Grid Adaptivity (OMEGA)

Name(s): Dr. David Bacon
Organization: Science Applications International Corporation
Address: 1710 SAIC Dr., McLean, VA 22102
Telephone: (703) 676-4594
Fax: (703) 676-5509
E-mail: bacon@apo.saic.com

   A.   Group: Science Applications International Corporation.
   B.   Equations: Fully compressible, nonhydrostatic, primitive equations.
   C.   Dimensionality: 3-D prognostic.
   D.   Grid: Variable resolution unstructured and adaptive grid.
   E.   Minimum horizontal resolution: Usually 1 km.
   F.   Vertical resolution: Variable; $\sim$10 m–1 km stretched grid.
   G.   Model domain: User selectable via an easy-to-use graphical user interface.
   H.   Initialization: Gridded initial conditions from coarser resolution models (such as NOGAPS, MRF, NGM, or ETA) with analysis of rawinsonde and surface observations in many different formats.
   I.   Solution technique: The numerical scheme uses a finite-volume technique with a Smolarkiewicz-type advection scheme modified for use in unstructured triangular grids.
   J.   Coordinate system: Rotating Cartesian system with origin at the center of the earth.
   K.   Lateral boundary condition: Open boundaries with a radiational scheme.
   L.   Top boundary condition: Rigid lid, free slip.
   M.   Surface boundary: No slip, with thermal, momentum, and vapor fluxes determined via air–surface interaction routines.
   N.   Parameterization of subgrid mixing: Two-and-a-half level closure k-ϵ model.

O.   Cumulus parameterization: Modified Kuo scheme.

P.   Radiation parameterization: Sasamori scheme.

Q.   Stable precipitation parameterization: Bulk water parameterization from Lin *et al.* (1983).

R.   Other:

S.   Phenomena studied: Dispersion over complex terrain, reconstruction of Desert Storm weather, hurricane simulations, validation simulation using weather conditions from different parts of the world and different seasonal regimes, etc.

T.   Computer used; example of time of integration for a specific problem: A 25 degree × 25 degree domain gridded down to 20-km resolution can produce a 24-hour forecast in about 90 minutes on 8 processors of an Origin 2000 (230 MHz).

An example of an application of this model is given in Bacon *et al.* (2000).

Model: MC2

Name(s): Robert Benoit
Organization: Recherche en Prevision Numerique, Environment Canada
Address: 2121 TransCanada, Suite 564, Dorval, Quebec, Canada H9P 1J3
Telephone: (514) 421-4762
Fax: (514) 421-2106
E-mail: Robert.Benoit@ec.gc.ca

A.   Group: Limited Area Model.

B.   Equations: Nonhydrostatic Euler equations.

C.   Dimensionality: 3-D.

D.   Grid: Arakawa-C; staggered. Range of problems solved: Workstation (UNIX or Linux) $100 \times 100 \times 25$; supercomputers: $800 \times 800 \times 25$; largest problem (production type for MAP 1999): $350 \times 300 \times 50$ at 3 km mesh/27 h duration; case study type: $1500 \times 1300 \times 30$ grid, 1-day forecast at 2 km (60 gb memory, 13 hours wall clock on 10 NEC SX5 PEs).

E.   Minimum horizontal resolution: Tested down to $\sim$500 m.

F.   Vertical resolution: Up to several hundreds of levels tested; usually for full atmospheric column.

G.   Model domain: Limited area.

H.   Initialization: Not sophisticated; dynamical (forth and back steps.)

I.   Solution technique: Semi-implicit, semi-Lagrangian. Nonseparable 3-D Helmholtz pressure (or W) problem. Domain decomposition. FGMRES solver with multiple preconditioners (ADI, etc.).

J.   Coordinate system: Conformal projections (polar stereographic, mercator), Gal-Chen vertical coordinate; option of Gal-Chen/geometrical height hybrid coordinate.

K.   Lateral boundary condition: With truly open boundary conditions; Staniforth's acid test passed.

L.   Top boundary condition: Rigid lid or diffusive (del2) sponge layer.

M.   Surface boundary: Force-restore/ISBA/CLASS land-surface scheme.

N.   Parameterization of subgrid mixing: (optionally advective) TKE (with 1.5 order closure). Del4 diffusion in fluid interior.

O.   Cumulus parameterization: None at high resolution; explicit convection dynamics. At lower resolution, options of Kuo, Fritsch–Chappell, Kain–Fritsch, and reduced Arakawa–Schubert types.

P.   Radiation parameterization: Solar (Fouquart and Bonnel 1980) and infrared radiation.

Q.   Stable precipitation parameterization: Kong and Yau 2-ice microphysics, Tremblay mixed-phase scheme (inclusive of freezing rain).

R.   Other:

S.   Phenomena studied: Chinook, foehn, heavy orographic precipitation, flash floods, breaking gravity waves.

T.   Computer used: Workstations: SGI, HP; Supercomputers: NEC SX4, SX5, Cray T3E, Linux with Pentium Intel chips.

Publications include Tanguay *et al.* (1990), Gyakum *et al.* (1995, 1996), Pinty *et al.* (1995), Tremblay *et al.* (1996), Benoit *et al.* (1997a, b), Kong and Yau (1997), Laprise *et al.* (1997), Ruel *et al.* (1997), Thomas *et al.* (1997), Yu *et al.* (1997, 1998), Desjardins *et al.* (1998), Lackmann *et al.* (1998), Mailhot *et al.* (1998), Gong *et al.* (1999), and Ruel and Benoit (1999).

Model: Boundary-Layer Mesoscale Forecast Model (BLFMESO), Version 3.0

Name(s): S. M. Daggupaty
Organization: Meteorological Service of Canada (formerly Atmospheric Environment Service) Air Quality Research Branch
Address: 4905 Dufferin St., Downsview, Ontario, Canada M3H 5T4
Telephone: (416) 739-4451
Fax: (416) 739-5708
E-mail: sam.daggupaty@ec.gc.ca

A.   Group: Meteorological Service of Canada, Air Quality Research Branch.

B.   Equations: Hydrostatic, primitive equations.

C.   Dimensionality: 3-D.

D.   Grid: Flexible limited area with uniform grid in x and y; nonuniform in the vertical; $36 \times 36 \times 10$ (Daggupaty *et al.* 1994); at present, 81×81 grid points in the horizontal and 10 vertical levels (Daggupaty 2001).

E.   Minimum horizontal resolution: $\Delta x = \Delta y = 5$ km.

F.   Vertical resolution: Nonuniform, with high resolution closer to the surface; first level at 1.5 m above surface, top level at 3000 m above terrain height.

G.   Model domain: Flexible limited area; typically 400 km $\times$ 400 km in the horizontal and 3 km in the vertical.

H.   Initialization: Objectively analyzed data of the regional Canadian weather forecast model is interpolated to the model grid, followed by 1-D dynamic initialization (Pielke 1984).

I.   Solution technique: Model equations are solved with implicit finite difference methods. Upstream space difference is used for horizontal advection terms, and the

implicit centered-space difference method is applied for horizontal diffusion terms. A semi-implicit method (Mahrer and Pielke 1978a) is adopted for the vertical advection and diffusion terms.

J. Coordinate system: UTM coordinate projection in x, y, and terrain-following relative Z vertical coordinate. $Z = z - h(x, y)$; h is terrain height above sea level.

K. Lateral boundary condition: Time-dependent lateral boundary conditions (Davies 1976) are used. This involves the relaxation of the interior flow in the vicinity of the boundary to the external fully prescribed flow with 4-D data from the Canadian regional forecast model.

L. Top boundary condition: Dependent variables specified at $t = 0$, as a function of horizontal space and kept invariant with time.

M. Surface boundary: No-slip for wind at z_0. $W = 0$. Surface energy budget and ground temperature prediction following the force-restore method (Deardorff 1978). Surface fluxes of momentum, heat, and surface layer parameters are computed through surface similarity theory (Byun 1990) and allowing different roughness lengths z_{0h} and z_{0m} (Lo 1996). Surface grid cells are subdivided into 1-km-square subgrid cells to account for multiple land-use characteristics of the underlying surface. A subgrid-scale parameterization scheme with the formulation of "effective" roughness length and other "effective" surface parameters and fluxes is used (Ma and Daggupaty 1998).

N. Parameterization of subgrid mixing: Surface similarity theory in the surface layer, as specified in M; exchange coefficient following O'Brien (1970) profile in the PBL (Daggupaty *et al.* 1994). In the current version, a nonlocal diffusion scheme (Holtslag *et al.* 1995) for momentum and heat transfer is used.

O. Cumulus parameterization: None.

P. Radiation parameterization: None.

Q. Stable precipitation parameterization: None.

R. Other: Evolution of boundary-layer height (Vogelezang and Holtslag 1996).

S. Phenomena studied: Meso-β scale phenomena, boundary-layer flow over complex terrain, lake/sea and land breezes, upslope and downslope flows (Daggupaty 2001, Daggupaty and Ma 1999); air quality applications, including subgrid-scale surface effects on deposition of gases and particles (Ma and Daggupaty 1999), impact of lead emissions to Lake Ontario and vicinity (Daggupaty 1998).

T. Computer used: The CPU time for a 24-hour forecast with BLFMESO (Version 3.0) for a domain of $81 \times 81 \times 10$ is about 35 minutes on a 200-MHz personal computer.

Model: FITNAH

Name(s): Dr. Günter Gross
Organization: Department of Meteorology, University Hannover, Germany
Address: Herrenhäuser Str. 2, 30419 Hannover, Germany
Telephone: (+49) 511-762-5408
Fax: (+49) 511-762-4418
E-mail: gross@muk.uni-hannover.de

A. Group: Güter Gross.

B. Equations: Navier-Stokes, nonhydrostatic, Boussinesq-approximation (Gross 1992).

C. Dimensionality: 3-D (Gross 1992).

D. Grid: Staggered grid, Arakawa-C type (Gross 1992).

E. Minimum horizontal resolution: 1–100 m.

F. Vertical resolution: surface, 1–10 m; upper layers, $\sim$1000 m.

G. Model domain: 1 km $\times$ 1 km–50 km $\times$ 50 km.

H. Initialization: Diastrophy, variational technique.

I. Solution technique: Time: forward, leapfrog, space: centered, advection, upstream-upstream spline (Gross 1995).

J. Coordinate system: Terrain-following (Gross 1987a).

K. Lateral boundary condition: Fixed (time-dependent), derivatives specified, radiation condition.

L. Top boundary condition: Damping layer.

M. Surface boundary: Surface energy budget for temperature (Gross 1986).

N. Parameterization of subgrid mixing: First-order closure, K from turbulent kinetic energy (Gross 1986).

O. Cumulus parameterization: (Gross 1986).

P. Radiation parameterization: Two-stream approximation (Gross 1986).

Q. Stable precipitation parameterization: (Gross 1986).

R. Other: Kessler scheme for precipitation (Gross 1986).

S. Phenomena studied: Airflow in complex terrain, land-sea breeze, slope winds, air flow in urban canopies and in forest canopies, dispersion of air pollutants, of odours and of sound (see Wipperman and Gross 1986; Gross 1987b, 1996, 1997, 1998; Gross and Wipperman 1987; Gross *et al.* 1987; Alpers *et al.* 1998, Heimann and Gross 1999).

T. Computer used: Example of time of integration for a specific problem. Workstation; supercomputer.

Model: COAMPS

Name(s): Dr. Richard M. Hodur
Organization: Naval Research Laboratory
Address: 7 Grace Hopper Ave., Monterey, CA 93943-5502
Telephone: (831) 656-4788
Fax: (831) 656-4769
E-mail: hodur@nrlmry.navy.mil

A. Group: Naval Research Laboratory, Marine Meteorology Division; R. Hodur, S. Chen, J. Doyle, T. Holt, J. Schmidt.

B. Equations: Nonhydrostatic compressible equations (Klemp and Wilhelmson 1978a, b).

C. Dimensionality: 3-D (Hodur 1997).

D. Grid: Arakawa-C grid, supports any number of nests, with multiple nests of one resolution allowed (Hodur 1997).

E. Minimum horizontal resolution: Flexible: Using real data, typical resolutions range from 1–81 km, with resolutions as low as 333 m used. In LES mode, resolutions as low as 1 m have been used (Hodur 1997).

F.   Vertical resolution: Flexible, stretched sigma coordinate. For real data forecasts, typical resolutions range from 20 m at the lowest level to several thousand meters at the model top, typically near 10 mb. The typical number of levels used is 30, with as many as 120 used in some experiments (Hodur 1997).

G.   Model domain: Flexible, user specifies latitude and longitude of any position on the earth (Hodur 1997).

H.   Initialization: 3-D multivariate optimum interpolation analysis of winds and heights (Goerss and Phoebus 1992); Cressman analysis of temperature and moisture; 2-D optimum interpolation analysis of SST using ship and mcsst observations; digital filter and/or variational balancing of temperature and pressure analysis increments (Hodur 1997).

I.   Solution technique: Time-splitting; explicit formulation for advective modes; semi-implicit solution for treatment of vertically propagating sound waves and Brunt–Väisälä frequency. Fourth-order differencing is used for diffusion, and second-order differencing is used for all other terms (Hodur 1997).

J.   Coordinate system: $x, y, \sigma = H(z - z_{sfc})/(H - z_{sfc})$. The horizontal grid is globally relocatable and can use either the polar stereographic, Lambert conformal, mercator, spherical, or Cartesian grid coordinates (Hodur 1997).

K.   Lateral boundary condition: Davies (1976) or Perkey-Krietzberg (1976) for real-data runs; periodic, radiation, fixed, or no-slip for idealized runs (Hodur 1997).

L.   Top boundary condition: Sponge or $w = 0$ (Hodur 1997).

M.   Surface boundary: Force-restore slab soil model, surface fluxes (Louis 1979), specification of land parameters (surface roughness, albedo, coastline, terrain height).

N.   Parameterization of subgrid mixing: Level-2.5 Mellor–Yamada (Mellor and Yamada 1982).

O.   Cumulus parameterization: Kain–Fritsch (1990) or Kuo (1974).

P.   Radiation parameterization: Harshvardhan (1987).

Q.   Stable precipitation parameterization: Rutledge-Hobbs (1983).

R.   Other:

S.   Phenomena studied: Coastal jets and rainbands (Doyle 1997), barrier jets (Xu *et al.* 2000), air–sea interaction and coupling (Doyle 1995; Hodur 1997; Hodur and Doyle 1998; Marshall *et al.* 1998), aerosols (Westphal *et al.* 1999), tropical cyclones (Hodur 1997), coastally trapped wind reversals (Thompson *et al.* 1997; Nuss *et al.* 2000), landfalling cyclones (Bond *et al.* 1997; Doyle and Bond 2001), sea-surface temperature fronts (Glendening and Doyle 1995), extratropical cyclones (Hirschberg and Doyle 1995; Shapiro *et al.* 1999), breaking gravity waves (Doyle *et al.* 2000), downslope windstorms (Doyle and Shapiro 2000), topographic jets (Doyle and Shapiro 1999), undular bores (Burk and Haack 2000), and supercritical, subcritical and transcritical flows (Burk *et al.* 1999; Dorman *et al.* 1999; Haack *et al.* 2001).

T.   Computer used: Example of time of integration for a specific problem: Double-nested grids using 81 and 27 km resolution with 87×51 and 190×91 grids, respectively, and 30 vertical levels uses approximately 2.3 CPU hours on a Cray C90 for a 24-hour forecast using a time step of 240 s on the 81-km grids. Multitasking across 6 processors reduces the wall time to approximately 30 minutes. The model code has been successfully ported to massively parallel computer architectures including SGI O2000 and O3000 using MPI.

Model: MM5

Name(s): Ying-Hwa Kuo and Jimy Dudhia
Organization: NCAR/MMM Division
Address: P.O. Box 3000, Boulder CO 80307
Telephone: (303) 497-8910; (303) 497-8950
Fax: (303) 497-8171
E-mail: kuo@ucar.edu; dudhia@ucar.edu
Website: http://www.mmm.ucar.edu/mm5/mm5-home.html

   A.   Group: NCAR/MMM Division.
   B.   Equations: Primitive nonhydrostatic (Dudhia 1993) or hydrostatic equations.
   C.   Dimensionality: 3-D.
   D.   Grid: Arakawa B-grid.
   E.   Minimum horizontal resolution: 500 m–1 km.
   F.   Vertical resolution: Variable, stretched.
   G.   Model domain: Globally relocatable, multiple-level nests.
   H.   Initialization: Integrated divergence removal.
   I.   Solution technique: Leapfrog in time with time-splitting, second order in space.
   J.   Coordinate system: Sigma.
   K.   Lateral boundary condition: Relaxation.
   L.   Top boundary condition: Rigid or radiative.
   M.   Surface boundary: Friction, fluxes using similarity theory, land-use categories.
   N.   Parameterization of subgrid mixing: Bulk, Blackadar (Zhang and Anthes 1982), Mellor–Yamada (Burk and Thompson 1989; Ballard *et al.* 1991; Janjić 1994), MRF (Hong and Pan 1996).
   O.   Cumulus parameterization: Anthes–Kuo (Anthes 1977), Grell (Grell *et al.* 1994), Kain–Fritsch (Kain and Fritsch 1993), Fritsch and Chappell (Fritsch and Chappell 1980a), Arakawa–Schubert (Grell *et al.* 1991), Betts–Miller (Betts 1986; Betts and Miller 1986; Janjić 1994).
   P.   Radiation parameterization: Broadband (Dudhia 1989) or CCM2 (Hack *et al.* 1993).
   Q.   Stable precipitation parameterization: Supersaturation removal, warm rain (Hsie and Anthes 1984), ice physics (Dudhia 1993), ice number concentration and graupel (Tao and Simpson 1993; Schultz 1995; Reisner *et al.* 1998).
   R.   Other: Land surface module (Pan and Mahrt 1987; Chen and Dudhia 2000), 4-D data assimilation (Stauffer and Seaman 1990).
   S.   Phenomena studied: Cyclones, fronts, MCS, severe weather, mountain waves.
   T.   Computer used; example of time of integration for a specific problem: Computer used: SGI, Sun, DEC, IBM, HP, Cray, Linux-PC, and a number of distributed memory machines from IBM, DEC, Cray, Fujitsu, and network of PCs. Example of CPU times: For a 2-grid simulation of Hurricane Opal on 45-km and 15-km grids, $121 \times 131 \times 31$ grid points on 45-km grid, and $151 \times 151 \times 31$ grid points on 15-km grid, it takes 115,000 s on single Cray J90 processor for a 24-hour integration. The wall clock time on a 16-processor J90 would be about 9,600 s.

Examples of other studies using this model include Zängl (1999), Bao *et al.* (2000), Colle and Mass (2000), Mass and Steenburgh (2000), Ritchie and Elsberry (2000), Stensrud *et al.* (2000), Wang *et al.* (2000), and Xiao *et al.* (2000). Derivatives of earlier versions of this model are reported in Giorgi *et al.* (1993a, b) and Liu *et al.* (1996) for RegCM2, and Lynch *et al.* (1999a, b), and Lynch and Wu (2000) for ARCSyM.

Model: Eta Model

Name(s): Fedor Mesinger
Organization: NCEP Environmental Modeling Center
Address: 5200 Auth Rd., Room 207, Camp Springs, MD 20746-4304
Telephone: (301) 763-8000, ext. 7249
Fax: (301) 763-8545
E-mail: fedor.mesinger@noaa.gov

A.   Group: NOAA/NCEP Environmental Modeling Center; numerous other weather services and/or centers. The current NCEP operational version is described in the sequel, unless specifically mentioned otherwise.

B.   Equations: Primitive hydrostatic equations. Nonhydrostatic version available (Janjić *et al.* 2001).

C.   Dimensionality: 3-D.

D.   Grid: Arakawa E-grid in horizontal, Lorenz grid in vertical.

E.   Minimum horizontal resolution: Minimum resolution extensively used 10 km (e.g., Black *et al.* 1998). The lowest resolution on which the model was run was 4 km.

F.   Vertical resolution: 50 layers, more for horizontal resolutions higher than the operational 22 km.

G.   Model domain: 106 × 80 degrees of rotated longitude × latitude.

H.   Initialization: 3-D fully cycled variational data assimilation (EDAS) (e.g., http://www.nws.noaa.gov/om/tpeta.htm). Digital filtering for 10-km runs with no EDAS.

I.   Solution technique: Time; split-explicit time differencing; forward-backward adjustment terms, with trapezoidal-implicit Coriolis terms, and adjustment time step of 60 s; forward-then-off-centered horizontal advection of momentum and temperature; "forward-in-time" horizontal advection of moisture variables; Matsuno vertical advection of momentum and temperature. Space: Arakawa-type, Janjić (1984) horizontal advection of momentum and temperature; conserving, among other quantities, energy and C-grid defined enstrophy; conserving momentum apart from the effect of mountains; Smolarkiewicz-type, Janjić (1997) horizontal moisture advection; Arakawa vertical advection of momentum and temperature, conserving momentum and energy; piecewise-linear (Mesinger and Jovic 2001) vertical moisture advection; energy conservation in transformations between the kinetic and potential energy in space differencing (Mesinger 1984, Mesinger *et al.* 1988); gravity-wave coupling scheme (Mesinger 1973, 1974; Janjić 1979) preventing separation of gravity waves on two C-subgrids of the E-grid.

J.   Coordinate system: Rotated spherical coordinates in horizontal; eta (step-mountain) coordinate in vertical.

K.   Lateral boundary condition: Prescribed/extrapolated along a single outer boundary line, followed by a buffer line of four-point averaging of the boundary and the third line variables (Mesinger 1977). Integration starting in the third line, with no relaxation or enhanced diffusion.

L.   Top boundary condition: Eta vertical velocity set to 0 at the model top at 25 mb.

M.   Surface boundary: Topography. Silhouette-mean step topography (Mesinger 1996). Mason–type parameterization of orographic roughness; surface fluxes over land. Monin–Obukhov, Paulson similarity functions. Zilitinkevich parameterization of viscous sublayer; land surface schemes. Multilayer (currently four layers) soil/vegetation/snowpack land surface model ("NOAH" LSM) (Chen *et al.* 1996, 1997; Chen and Mitchell 1999; Mitchell *et al.* 1999, 2000). Provides, or provides input to, soil moisture/temperature, skin temperature, and surface fluxes of heat, moisture, and upward radiation (longwave, shortwave). Uses as input spatial databases of 12 vegetation types, 9 soil types, seasonal albedo, and a NESDIS satellite-based NDVI-derived seasonal cycle of vegetation greenness, as well as a daily updated, 23-km, Northern Hemisphere, operational snow cover analysis produced by NESDIS. The LSM land state variables cycle continuously in the Eta EDAS and are driven by EDAS precipitation, surface radiation, etc. Surface fluxes over water. Monin-Obukhov, Lobocki (1993) Mellor-Yamada level-2 derived similarity functions. Viscous sublayer (Janjić 1994), linear approximation of Liu *et al.* (1979), with parameters according to Mangarella *et al.* (1973) and Brutsaert (1982b).

N.   Parameterization of subgrid mixing: Vertical: Mellor-Yamada level-2.5 turbulence closure (Mellor and Yamada 1982), with improved treatment of the master length scale/realizability problems (Mesinger 1993a, b; Janjić 1996); Horizontal: Second-order, Smagorinsky-like, aimed to parameterize the impact of advection by subgrid-scale motions.

O.   Cumulus parameterization: Betts–Miller–Janjić scheme for deep and shallow convection (Betts 1986; Betts and Miller 1986; Janjić 1994).

P.   Radiation parameterization: GFDL radiation scheme (Lacis and Hansen 1974; Fels and Schwarzkopf 1975).

Q.   Stable precipitation parameterization: Explicit prediction of grid-scale cloud water/ice mixing ratio (Zhao and Carr 1997; Zhao *et al.* 1997), with predicted clouds used by the radiation scheme.

R.   Other: Divergence damping (optional/not required for stability).

S.   Phenomena studied: QPF performance, depending on systems, regions, and/or model features; moisture transport impacts and basin/subbasin budgets, return flow; land surface phenomena, in particular vegetation and soil moisture/water transport impacts; effects of topography, depending on the choice of the vertical coordinate; tropical cyclones; slantwise instability; other.

T.   Computer used; example of time of integration for a specific problem: On an Origin 2000, the Eta 32-km (about 2.2×10^7 atmospheric prognostic variables) in a dedicated run (32 processors) takes about 30 minutes for a 48-hour forecast; in a nondedicated run (25 processors), it takes about 43 minutes. On the IBM SP, in a dedicated run (160 nodes and threading) 48-hour forecast takes about 11 minutes (times as of October 1999, from T. Black and E. Rogers). The code is regularly run on numerous other computers workstations and on upper-end PCs.

Other authors who have discussed and used the Eta model include Janjić (1994), Mesinger and Treadon (1995), Mesinger *et al.* (1997), Gallus (1999), Mathur *et al.* (1999), and Mesinger (2000). Cacciamani *et al.* (2000) introduced the LAMBO model, which is a derivative of a 1989 version of Eta.

Model: The Regional Atmospheric Modeling System (RAMS)

Name(s): Roger A. Pielke, Sr., W. R. Cotton, C. Tremback, and R. L. Walko Organization: Colorado State University and ASTeR Division of Mission Research Corporation
Address: Department of Atmospheric Science, Fort Collins, CO 80523 or P.O. Box 466, Fort Collins, CO 80522
Telephone: (970) 491-8293 or (970) 282-4400
Fax: (970) 491-8293
E-mail: pielke@atmos.colostate.edu and tremback@aster.com
Website: http://blue.atmos.colostate.edu/

A. Group: Department of Atmospheric Science,/ASTeR Division, Mission Research Corporation.

B. Equations: Basic dynamical system uses Navier Stokes, compressible, nonhydrostatic equations.

C. Dimensionality: 2-D or 3-D.

D. Grid: Staggered Arakawa-C grid. Vertical grid spacing can be stretched. Two-way interactive grid nesting allows any number of nested grids. Vertical grid nest ratio is allowed to vary with height.

E. Minimum horizontal resolution: No minimum horizontal resolution (model has been used at 2 cm).

F. Vertical resolution: No limit on vertical resolution.

G. Model domain: No lower size limit on limited-area model domain. Model may be run on global domain.

H. Initialization: Method 1: Horizontally homogeneous interpolation from single sounding; Method 2: Barnes objective analysis of gridded pressure level data, rawinsonde data, and surface observations.

I. Solution technique: Initial value solution technique. Velocity components and Exner function marched forward with leapfrog time differencing. All scalar quantities other than the Exner function use forward time differencing. Acoustic terms are stepped forward on smaller time step using time-splitting technique.

J. Coordinate system: Polar stereographic or Cartesian coordinates in horizontal, terrain-following sigma-z coordinates in vertical.

K. Lateral boundary condition: Klemp–Wilhelmson, Klemp–Lilly, Orlanski, and cyclic options are available for lateral boundary condition on normal velocity component. Zero gradient, zero divergence of gradient, and cyclic options are available for lateral boundary conditions on all other variables. When model is initialized from an objectively analyzed 3-D dataset, lateral boundaries are also nudged in time toward analyzed observed field values.

L. Top boundary condition: Wall on top ($w = 0$); Newtonian relaxation toward sounding or observed fields can be used in upper layers to absorb gravity waves.

M. Surface boundary: Vertical velocity at surface is the scalar product of horizontal velocity and terrain height gradient. Surface fluxes of momentum, heat, and water vapor are computed from surface similarity theory using the Louis (1979) method. Characterization of land surface includes prognosis of energy and moisture in multiple soil layers, snowcover, vegetation, and canopy air. Surface grid cells are subdivided into multiple landuse areas, each of which may have a different vegetation, soil type, or water surface.

N. Parameterization of subgrid mixing: Options are Smagorinsky–Lilly, Mellor–Yamada, and Deardorff; the latter two prognose and use a turbulent kinetic energy field.

O. Cumulus parameterization: Modified Kuo cumulus parameterization.

P. Radiation parameterization: Options are (1) a new two-stream model developed by Harrington that accounts for specific optical properties of cloud droplets, rain, and different types of ice hydrometeors; (2) a scheme by Chen and Cotton that considers attenuation by clouds; and (3) a scheme by Mahrer and Pielke that does not account for condensation of any type.

Q. Stable precipitation parameterization: Detailed bulk microphysical model prognoses cloud water, rain, small and larger categories of ice crystals, aggregates, graupel, and hail for both stable and, where grid resolution permits, convective regimes. Physical processes represented in bulk model include nucleation of cloud droplets, nucleation of ice crystals by Brownian motion, thermophoresis, diffusiophoresis, contact freezing, deposition freezing, homogeneous nucleation of cloud droplets and haze, collisions between all pairs of hydrometeor species including self-collection, evaporation, condensation, sublimation, deposition, freezing, melting, shedding of water by hail, heat exchange in hydrometeor collisions, sedimentation, and secondary ice production. Both mixing ratio and number concentration are predicted for hydrometeors.

R. Other: Parallel processing using MPI has been implemented in RAMS in a very efficient manner. A simulation on a 16-processor SP-2 has run 14 times faster than on a single processor. RAMS has a surface and subsoil hydrology model that transports water downslope. An arbitrary number of additional prognostic scalar quantities may be easily added for studying transport and dispersion. RAMS has been coupled with a bin microphysics model and two dynamic vegetation models (CENTURY and GEMTM). Nested grids may move in time to follow a moving system, such as a convective storm or tropical cyclone. Vegetation biophysical parameters and other environmental quantities undergo automatic annual variation to enable long (e.g., year-long) model integrations.

S. Phenomena studied: Winter storms, supercell storms and tornadoes, mesoscale convective systems, sea breezes, drylines, small cumulus convection, turbulent flow around buildings, flow in wind tunnels, flow in laboratory tornado simulator, quantitative precipitation forecasting, severe downslope winds, operational forecasting, transport and dispersion of pollutants, effect of land-use change on weather and climate, propagation of acoustic waves, tropical cyclones, large-eddy simulation of the convective boundary layer.

T. Computer used: Historically, several mainframe computers, including Cray and CYBER machines were used. More recently, RAMS is usually used on workstation and PC computers. A single PC processor (500 MHz) will advance approximately 50,000

grid cells one step forward in time per CPU or wall clock second. How long a simulation actually takes to run depends to a huge extent on the number of grid cells and nested grids used, the simulation time, and the grid resolution. The duration of the simulation also depends on the complexity of the physics options chosen. A simulation can run more than 100 times slower than real time or more than 100 times faster than real time. The 50,000 grid cell updates per second figure is a quantity that is most useful in evaluating model speed (without the use of bulk microphysics).

Publications include Tripoli and Cotton (1982); Tremback *et al.* (1987, 1994); Meyers *et al.* (1992, 1997); Pielke *et al.* (1992); Nicholls *et al.* (1993, 1995); Lyons *et al.* (1994); Harrington *et al.* (1995); Walko *et al.* (1995a, b, 2000a, b); Pielke and Nicholls (1997); and Olsson (2000). Examples of RAMS applications include Abbs (1999).

Model: The Topographic Vorticity Model (TVM)

Name(s): (1) P. Thunis, (2) G. Schayes, (3) R. Bornstein
Organizations: (1) Joint Research Centre (JRC), (2) Universite Catholique Louvain, (3) San Jose State University
Address (1): JRC, Environment Institute, TP280, Ispra, 21020, Italy
Telephone: 39-0332-785.670
Fax: 39-0332-785.022
E-mail: philippe.thunis@jrc.it
Website: http://rtmod.ei.jrc.it/thunis/TVM/tvm.html

A.   Group: Joint Research Centre
B.   Equations: Basic dynamical system uses Navier Stokes, anelastic, nonhydrostatic equations written in vorticity mode. TVM is advanced version of previous hydrostatic-vorticity URB-MET model.
C.   Dimensionality: One, two, or three dimensions.
D.   Grid: Staggered Arakawa-C grid. Vertical and horizontal grid spacings can be stretched.
E.   Minimum horizontal resolution: Model has been used up to 500 m resolution but no limitation exists when used in large-eddy simulations.
F.   Vertical resolution: No limit on vertical resolution.
G.   Model domain: No lower size limit on limited-area model domain. Model currently designed for mesoscale areas only (up to a few hundreds of kilometers).
H.   Initialization: Horizontally homogeneous interpolation from single sounding.
I.   Solution technique: Advection terms approximated by the 3rd order Parabolic Piecewise Method (PPM) (Collela and Woodward 1984). Diffusion, vorticity tilting, and buoyancy terms approximated by classical FTCS differencing. Elliptic stream function equations are solved through iterative variant of bi-conjugate gradient method (van de Vorst 1992).
J.   Coordinate system: Terrain-influenced sigma-z coordinates.
K.   Lateral boundary conditions: For advection, only inflow boundary conditions are specified (value or zero-gradient). Zero gradient for lateral boundary conditions on all other processes.

L. Top boundary condition: Zero vorticity, and horizontal wind set to geostrophic value. Damping layer can be used in the upper layers to absorb gravity waves.

M. Surface boundary: Wind components set to zero. Surface fluxes of momentum, heat, and water vapor computed using one of the following methods: a. modified force-restore model of Deardorff (Schayes *et al.* 1996) and surface similarity theory. IAGL land-surface model (De Ridder and Schayes 1997), including vegetation parameterization and various transfer resistances.

N. Parameterization of subgrid mixing: Prognostic turbulent kinetic energy field and one of the following methods: a. 1.5 order closure from Therry and Lacarrere (1983) b. E-ϵ parameterization of Duynkerke (1988) c. in LES mode, with subgrid turbulent energy and adequate 3-D parameterization.

O. Cumulus parameterization: None

P. Radiation parameterization: Shortwave: Lacis and Hansen (1974) or Stephens (1978) Longwave: Sasamori (1968) or Stephens (1978)

Q. Stable precipitation parameterization: Kessler-type microphysics parameterization with 5 species (water, rain, ice crystal, snow, and graupel) used in convective precipitation with horizontal grid size less than 2 km.

R. Other: None

S. Phenomena studied: Sea breezes (Grossi *et al.* 2000), slope winds (Schayes *et al.* 1996, Bornstein *et al.* 1996), urban circulations (Bornstein *et al.* 1994), mountain waves (Thunis and Clappier 2000), transport and diffusion of pollutants (Sistla *et al.* 1996), Thunis and Cuvelier 1999, Clappier *et al.* 2000), residual layers (Freedman and Bornstein 1998), and large-eddy simulation of convective boundary layers.

T. Computer used: PC to supercomputers.

Model: ARPS

Name(s): Ming Xue and Kelvin Droegemeier
Organization: University of Oklahoma (School of Meteorology and Center for Analysis and Prediction of Storms)
Address: 100 East Boyd, Suite 1110; Norman, OK 73019
Telephone: (405) 325-0453
Fax: (405) 325-7614
E-mail: mxue@ou.edu/kkd@ou.edu
Website: http://www.caps.ou.edu/ARPS

A. Group: Nonhydrostatic storm- and mesoscale model (Xue *et al.* 1995; Xue *et al.* 2000b, 2001).

B. Equations: Nonhydrostatic, fully compressible.

C. Dimensionality: 1-D, 2-D, 3-D.

D. Grid: Arakawa C-grid.

E. Minimum horizontal resolution: No lower limit; typically run at 1–2 km.

F. Vertical resolution: At user's choice; typically stretches from 5–500 m.

G. Model domain: Fully variable; can be applied to hemispheric domain down to domains a few km across or even smaller.

H. Initialization: Single-sounding or 3-D real data analysis.

I.   Solution technique: Split-explicit time integration (Klemp and Wilhelmson 1978a) with high-order monotonic advection (FCT), (Zalesak 1979) options for scalars.

J.   Coordinate system: Height-based generalized terrain-following coordinate in map projection space.

K.   Lateral boundary condition: Several options, including zero-gradient, periodic, open, and externally-forced condition.

L.   Top boundary condition: Rigid, sponge, or wave-radiating.

M.   Surface boundary: Semi-slip lower boundary.

N.   Parameterization of subgrid mixing: Smagorinsky–Lilly (Lilly 1962; Smagorinsky 1963), 1.5-order TKE (Deardorff 1980; Moeng 1984), Germano dynamic closure (Germano *et al.* 1991; Wong and Lilly 1994), and their variations.

O.   Cumulus parameterization: Kain–Fritsch, Kuo.

P.   Radiation parameterization: Based on NASA/GSFC radiation package (Chou 1990, 1992; Chou and Suarez 1994; Tao *et al.* 1996).

Q.   Stable precipitation parameterization: Handled by grid-scale saturation adjustment and microphysics parameterization. The latter includes Kessler-type warm rain, Lin–Tao (Lin *et al.* 1983; Tao and Simpson 1991) six-category ice, and Schultz (1995) simple ice schemes.

R.   Other: Additional physics, including stability-dependent surface flux parameterizations (Monin and Obukhov 1954; Deardorff 1972; Byun 1990), 1.5-order TKE-based nonlocal vertical mixing inside PBL (Sun and Chang 1986: Xue *et al.* 1996), and two-layer soil–vegetation model (Noilhan and Planton 1989; Jacquemin and Noilhan 1990; Pleim and Xiu 1995; Boone *et al.* 1999). A data analysis and assimilation system including single-Doppler velocity retrieval, satellite, and other conventional data types (Brewster 1996; Shapiro *et al.* 1996).

S.   Phenomena studied: All-season weather from synoptic to storm scales, orographic flows, idealized simulations of thunderstorms, squall lines, fronts, etc.

T.   Computer used; example of time of integration for a specific problem: Origin 2000 (256 processors), Cray T3E (512 processors) (Droegemeier *et al.* 1995; Sathye *et al.* 1997), all other computers (Cray J90, C90, T90, IBM SP-2, Unix workstations, Linux and Windows PCs, NT and Linux PC clusters, etc.). A 6-hour forecast at 3-km resolution in a domain covering the southern Great Plains takes about 1 hour on a 256-node Origin 2000 (full physics).

Model: HOTMAC

Name(s): Dr. Ted Yamada
Organization: Yamada Science and Art Corporation
Address: Rt. 4 Box 81-A, Santa Fe, NM 87501
Telephone: (505) 989-7351
Fax: (505) 989-7965
E-mail: ysa@ysasoft.com
Website: www.ysasoft.com/ysa

A.   Group: Yamada Science and Art Corporation (YSA).

B.   Primitive Equations: Hydrostatic, incompressible (Mellor and Yamada 1974; Yamada 1978b, 1981) and nonhydrostatic (Yamada 2000a).

C.   Dimensionality: 1-D (Yamada and Mellor 1975; Yamada and Mellor 1979; Yamada 1982), 2-D (Yamada 1983), or 3-D (Yamada and Bunker 1988, 1989; Yamada 2000b).

D.   Grid: 1-D, 80 (Yamada and Mellor 1975); 2-D, 29×40 (Yamada 1983); 3-D, $93 \times 64 \times 26$ (Yamada 2000b).

E.   Minimum horizontal resolution: 2-D, 200 m (Yamada 1983); 3-D, 380 m (Yamada 1981), 4 km (Yamada 2000b), 4 m (Yamada 2000a).

F.   Vertical resolution: 1-D, $\sim$0.1 m (Yamada and Mellor 1975); 2-D, $\sim$2 (Yamada 1983); 3-D, $\sim$4 m (Yamada 2000b), 1 m (Yamada 2000a), expanded with height.

G.   Model domain:

	x	y	z	
1-D			1~10 km	(Yamada and Mellor 1975, 1979)
2-D	~6 km		~1 km	(Yamada 1983)
3-D	200 m	200 m	500 m	(Yamada 2000a)
	10 km 368 km		7 km 252 km	1.3 km 8.4 km
	(Yamada 1981)	(Yamada 2000b)		

H.   Initialization: Homogeneous or four-dimensional data assimilation (4DDA) (Yamada 2000b).

I.   Solution technique: 2-D and 3-D, alternating direction implicit (ADI) Yamada and Bunker 1988; 1-D, Laasonen (Yamada and Mellor 1975).

J.   Coordinate system: Terrain-following (Yamada and Bunker 1988).

K.   Lateral boundary condition: Solutions of 1-D (vertical) equations; smoothing using interior values (Yamada and Bunker 1988).

L.   Top boundary condition: Rigid (Yamada 1981, 1983).

M.   Surface boundary: Surface energy budget (Yamada 1981), soil layer, tall tree canopy (Yamada 1982).

N.   Parameterization of subgrid mixing: Based on second-moment turbulence closure equations (Mellor and Yamada 1974, 1982).

O.   Cumulus parameterization: Second-moment closure equations coupled with Gaussian cloud model (Mellor 1977; Yamada and Mellor 1979).

P.   Radiation parameterization: Sasomori's scheme (Sasamori 1968).

Q.   Stable precipitation parameterization: Nickerson *et al.* (1986); equations for the mixing ratios of water vapor and rain, and the raindrop number concentration.

R.   Other: User-friendly graphical interface, 3-D graphics for animation, pre- and post-processors, well-written, illustrated manuals.

S.   Phenomena studied: Diurnal variations of PBL (Yamada and Mellor 1975), nocturnal drainage flow over complex terrain (Yamada 1981, 1983; Yamada and Bunker 1988, 1989), turbulence in clouds in marine boundary layer (Yamada and Mellor 1979), long-range plume transport (Yamada 2000b), tall tree canopy flows (Yamada 1982), urban canopy flows (Yamada 2000a).

T.   Computer used: Runs on low-end workstations and PCS. An hour of a sample simulation on a PC with a 200-MHz processor took 30 min of CPU time, where a total of $78 \times 55 \times 30$ (vertical) grid points were used and the horizontal grid spacing was 2 km.

Appendix C

Summary of Several Cumulus Cloud Parameterization Schemes

The information included herein was provided courtesy of Nelson Seaman (2000, personal communication).

The Anthes–Kuo Parameterization

Key References: Kuo (1965, 1974); Anthes (1977)

Key Assumptions:

1.   Closure is based on the assumption that the intensity of subgrid deep convection is proportional to the vertically integrated convergence of water-mass in a grid column (the net resolved-scale moisture convergence, M_t, (including surface evaporation) must exceed a critical threshold value, M_c).
2.   For the moisture convergence to trigger convection, both the cloud depth and the available buoyant energy (ABE) in the column must exceed minimum threshold values.
3.   The moisture-convergence closure assumes that the area of a grid box is large (by $\gg 10^2$) compared to the area of convective updrafts.
4.   The water convergence can be used to produce rain or to moisten the column. The fraction rained out, b, is a function of mean relative humidity of the column.

Strong Points:

1.   The moisture-convergence closure is well designed for tropics and coarse-grid applications.
2.   Tends to be robust for a wide variety of coarse-grid applications (e.g., NCEP's NGM and many global models).
3.   Anthes added an easily scaled, empirically based profile for net heating and moistening from convection that allows efficient calculation of feedbacks to the environment.

Weak Points:

1.   At mesh sizes of 30 km or less, can produce extreme rainfall similar to Molinar and Dudek's (1992) "grid-point storms" for explicit-microphysics-only applications.

2. Does not include convective downdrafts, so is not well suited for simulating mesoscale convective systems influenced strongly by outflow boundaries.

The Arakawa–Schubert Parameterization

Key References: Arakawa and Schubert (1974)

Key Assumptions:

1. A cloud field exists as an ensemble of many smaller clouds with decreasing numbers of successively larger clouds.

2. The closure is based on the assumption that convection intensity is controlled by a cloudwork function, a measure of the generation of integrated buoyancy force in the environment, which then is related to kinetic energy generation inside the cloud. Thus the convection is closely tied to the rate of buoyancy production at the grid scale.

3. The cloud model includes the effects of entrainment, but detrains only at the cloud top (detrainment has been added by some investigators), and defines a steady-state plume.

4. The rain rate is a fraction of the liquid water in the updraft, which may depend on cloud size and wind shear.

Strong Points:

1. Inclusion of an ensemble of clouds is physically more reasonable than other parameterizations that assume all clouds in a grid box are identical.

2. The scheme is well designed for convection over tropical oceans where the rate of buoyancy generation is gradual.

Weak Points:

1. The cloud-work function closure is not well related to non–steady-state situations, such as explosive convection over midlatitude continents.

2. Can be comparatively expensive due to calculations for cloud-size ensembles.

3. Does not include treatment of convective-scale downdrafts (although Grell 1993 added a downdraft scheme).

The Fritsch–Chappell Parameterization

Key References: Fritsch and Chappell (1980a); Fritsch and Kain (1993)

Key Assumptions:

1. Designed for grid lengths between 10–30 km.

2. The amount of convective activity originates with the concept of potential buoyant energy (PBE), or positive area on a thermodynamic diagram between the level of free convection (LFC) and the equilibrium level. This energy becomes "available" if the negative area below the LFC can be overcome, so that a subcloud parcel reaches its LFC with positive vertical motion. Thus the convective available potential energy (CAPE) is the PBE—the negative area below the LFC.

3. The time scale of the convection t_c, is defined as the advective time, which is the grid length divided by the horizontal wind speed ($DX/|\vec{V}|$).

4. Closure is based on the assumption that convective tendencies are such that all CAPE in the column is removed within one convective time period, t_c.

5. Separate updrafts and downdrafts are calculated. The cloud model allows for parcel entrainment into the updrafts (an entraining plume cloud model). Clouds detrain only at their top through the anvil, or at their base because of downdrafts.

6. The area of the updraft initially is assumed to be 1%, and the submodel iterates until the calculated updraft/downdraft removes all CAPE during t_c.

7. The trigger mechanism is based on whether a parcel with T_v and q_v (average values for a subcloud mixed layer), and with a perturbation temperature, DT, can reach the LFC with positive buoyancy. The perturbation $DT = C_1 w^{1/3}$, where C_1 is a constant and w is the resolved-scale vertical velocity at the LFC.

Strong Points:

1. Recognized CAPE is a suitable closure for Great Plains storms.

2. Possibly the first convective parameterization specifically designed for meso-β–scale applications.

Weak Points:

1. Does not conserve water and air mass.

The Betts–Miller Parameterization

Key References: Betts (1986); Betts and Miller (1986)

Key Assumptions:

1. There is a quasi-equilibrium thermodynamic structure toward which the environment is moved because of convection. This structure can be defined in terms of a "mixing line" determined from observational data.

2. For the purpose of representing convection in global models, it is unnecessary to explicitly represent heating and moistening because of the subgrid processes of updrafts, downdrafts, entrainment, and detrainment. On the assumption that simplicity of design is more efficient and less prone to errors, all of these are treated implicitly.

3. The closure assumes that the rate at which convective instability is generated in the environment determines how rapidly the environment profile is changed toward the mixing line. The relaxation time scale for the convective is roughly 2 hours.

Strong Points:

1. Mixing-line closure is well designed for tropical oceans, coarse grids, and cases in which the response of the environment evolves slowly.

2. Quite robust for a wide variety of applications and can be adapted for the mesoscale by adjustment of several parameters. It is used operationally in NCEP's Eta model.

Weak Points:

1.   Does not include a convective-scale downdraft parameterization (although later versions by some investigators have attempted to add their effects).

2.   The mixing-line closure appears to be less appropriate in cases of explosive deep convection and does not directly generate meso-β–scale highs and lows.

The Grell Parameterization

Key References: Grell et al. (1991); Grell (1993)

Key Assumptions:

1.   Assumes that deep convective clouds are all of one size.

2.   The original Grell scheme used the Arakawa–Schubert cloud-work function for its closure, but this was later changed to use a CAPE closure, as in Kain–Fritsch.

3.   No direct mixing laterally with the environment (no entrainment or detrainment), except at the levels of origin or termination of updrafts and downdrafts. Thus mass flux is constant with height.

4.   Since there is no lateral mixing (Reynolds averaging), it is not necessary to assume that the fractional area coverage of updrafts and downdrafts in the grid column is small. This allows the scheme to operate easily at finer scales, although some degree of scale separation is still important.

Strong Points:

1.   Very robust scheme, which has been modified to look more like Kain–Fritsch.
2.   Includes effects of downdrafts.
3.   Well adapted for grids as fine as 10–12 km.

Weak Points:

1.   Original Arakawa–Schubert characteristics of the closure have been mostly replaced (but this has also improved performance for explosive convection).

2.   Ignores entrainment-detrainment effects.

The Kain–Fritsch Parameterization

Key References: Kain and Fritsch (1990, 1993)

Key Assumptions:

1.   Most of the assumptions of the Fritsch–Chappell parameterization are retained, including the critical CAPE-removal closure assumption.

2.   The cloud model is reformulated into an entraining-detraining model, with parcel buoyancy calculated as a function of parcels mixed laterally between the environment and the updrafts.

3.   The differencing is reformulated to conserve mass, thermal energy, mass, and momentum.

4.   Designed for grid sizes of ∼20–25 km.

Strong Points:

1.   Contains the most complete treatment of in-cloud physical processes of currently available convective parameterizations.

2.   Downdraft parameterization allows better simulation of mesoscale responses than is possible with most schemes.

Weak Points:

1.   CAPE closure is not well suited to tropical environments and can result in overly vigorous convection.

The PENN State Shallow Convection Parameterization

Key References: Seaman et al. (1996); Deng (1999); Deng et al. (1999, 2000)

Key Assumptions:

1.   Closure is based on the assumption that convective intensity, in terms of cloud-base mass flux, is controlled by a hybrid of the boundary-layer turbulent kinetic energy (TKE) and the CAPE in the column.

2.   The cloud radius is a function of planetary boundary-layer (PBL) depth and cloud depth.

3.   Cloud top height grows at a fraction of the maximum updraft speed because of resistance in the environment above the cloud.

4.   Cloud mass detrained from the shallow convective updrafts is not mixed immediately with the environment, but rather becomes part of a nearly-neutrally buoyant cloud (NBC) at its level of detrainment.

5.   The area and liquid water content of NBCs are predicted based on source terms from the cumulus updrafts, advection of cloud properties, and dissipation from mixing, settling, instability, and precipitation processes.

6.   Updraft-initiating parcels are released at the top of the PBL, they have thermal and moisture characteristics defined from the air in the lowest 20% of the PBL and a vertical velocity based on the maximum TKE in the PBL.

7.   Radiative effects of shallow clouds include effects of partial vertical randomness of NBCs.

Strong Points:

1.   The hybrid mass-flux closure is consistent with size-dependent cumulus forcing in the atmosphere.

2.   The inclusion of an NBC class provides flexibility between stratocumulus and cumulus environments.

3.   Smoothly transitions from shallow convection to deep convection (Kain and Fritsch 1990) to solid stratiform cloud (Dudhia 1989).

4. Suitable for marine and land environments and for use in mesoscale models.

Weak Points:

1. A number of parameters and subgrid processes need to be studied further and modeled based on LES and additional observations.

2. As a new scheme, this parameterization needs further testing and evaluation in a variety of 3-D environments.

Appendix D

BATS, LAPS, and LEAF Comparison Tables

Canopy Air, Vegetation, Temporary Surface Water, Ground Surface, and Deep Soil Temperature[a]

	LAPS	LEAF	LEAF-2[b]
Vegetation	$C_{veg}\dfrac{\partial T_v}{\partial t} = R_{vnet} - H_{vc} - \lambda E_{vc}$	$C_{veg}\dfrac{\partial T_v}{\partial t} = R_{vnet} - H_{vc} - \lambda E_{vc} + H_{pv}$	$C_{veg}\dfrac{\partial T_v}{\partial t} = R_{vnet} - H_{vc} - \lambda E_{vc} + H_{pv}$
Canopy air	$H_{ca}(T_c) = H_{vc}(T_c) + H_{gc}(T_c)$	$C_c\dfrac{\partial T_c}{\partial t} = H_{vc} - H_{ca} + H_{gc}$	$C_c\dfrac{\partial T_c}{\partial t} = H_{vc} - H_{ca} + H_{gc} + H_{sc}$
Temporary surface water (snow)[c]	Not used	Not used	$T_{si} = \dfrac{Q_{si} - f_l\lambda_f}{f_i c_i + f_l c_l}$
Soil surface[c]	$C_g\dfrac{\partial T_{gt}}{\partial t} = R_{gnet} - H_{gc} - \lambda E_{gc}$ $-C_v\left(\dfrac{K_t\omega}{2}\right)^{1/2}(T_{gt} - T_d)$ $\omega = \dfrac{2\pi}{\tau_d}$	$C_g\dfrac{\partial T_{gt}}{\partial t} = R_{gnet} - H_{gc} - \lambda E_{gc} + H_{t-1,t}$	$T_{gt} = \dfrac{Q_{gt} - W_{gt}f_l\lambda_f}{W_{gt}f_i c_i + W_{gt}f_l c_l + c_g m_g}$
Deep soil[c]	$C_g\dfrac{\partial T_d}{\partial t} = \dfrac{2(R_{gnet} - H_{gc} - \lambda E_{gc})}{(365\pi)^{1/2}}$ $C_g = 0.95\left[\lambda_H C_v/(2\omega)\right]^{1/2}$	$\lambda_H = 418.62 \exp\left(-(P_f + 2.7)\right)\quad P_f \le 5.1$ $\lambda_H = 418.62 \; x \; 0.00041 \; P_f > 5.1$ $C_v\dfrac{\partial T_{gt}}{\partial t} = \dfrac{\partial}{\partial_z}\left(\lambda_H\dfrac{\partial T_{gi}}{\partial_z}\right) C_v = C_i + C_w w_i$	$T_{gi} = \dfrac{Q_{gi} - W_{gi}f_l\lambda_f}{W_{gi}f_i c_i + W_{gi}f_l c_l + c_g m_g}$

[a]The tables in this appendix were compiled by Pier Luigi Vidale, Robert Walko, Guta Mihailovic, and John Strack.

[b]LEAF-2 does not prognose soil and temporary surface water temperatures, but instead diagnoses them from the internal energy.

[c]In LEAF and LEAF-2, multiple soil layers are allowed. The layers are numbered increasing upward from the deepest layer. In LEAF-2, multiple temporary surface water layers may exist when it is in the form of snow. These layers are numbered increasing upward from the surface.

Internal Energy of Temporary Surface Water (Snow) and Soil Layers

LEAF-2

Top snow layer	$\dfrac{\partial}{\partial t}(W_{st}Q_{st}) = R_{snwt} + H_{t-1,\,t} - H_{sc} - \lambda E_{sc} + H_{ps} - H_{w(t,\,t-1)}$
Intermediate snow layers	$\dfrac{\partial}{\partial t}(W_{si}Q_{si}) = R_{snwi} + H_{i-1,\,i} - H_{i,\,i+1} + H_{w(i+1,\,i)} - H_{w(i,\,i-1)}$
Bottom snow layer	$\dfrac{\partial}{\partial t}(W_{sb}Q_{sb}) = R_{snwb} + H_{gs} - H_{b,\,b+1} + H_{w(b+1,\,b)} - H_{wsg}$
Soil surface	$D_t\dfrac{\partial Q_{gt}}{\partial t} = R_{gnet} + H_{t-1,\,t} - H_{gc} - H_{gs} - \lambda E_{gc} + H_{wsg} - H_{w(t,\,t-1)}$
Deep soil layers	$D_i\dfrac{\partial Q_{gi}}{\partial t} = D_i\dfrac{\partial}{\partial z}\left(\lambda_H\dfrac{\partial T_{gi}}{\partial z}\right) + H_{w(i+1,\,i)} - H_{w(i,\,i-1)}$
	$\lambda_H = -2.70\left(\dfrac{w_i}{w_s}\right)^2 + 4.80\left(\dfrac{w_i}{w_s}\right) + 0.30 \quad \text{Sand}$
	$\lambda_H = -0.96\left(\dfrac{w_i}{w_s}\right)^2 + 2.40\left(\dfrac{w_i}{w_s}\right) + 0.25 \quad \text{Clay}$
	$\lambda_H = 0.46\left(\dfrac{w_i}{w_s}\right) + 0.06 \quad \text{Peat}$

Interception Stores

	LAPS	LEAF	LEAF-2
Vegetation	$\dfrac{\partial W_f}{\partial t} = P_{veg} - E_{wf}$	$\dfrac{\partial W_f}{\partial t} = P_{veg} - E_{wf} - R_{veg}$	$\dfrac{\partial W_f}{\partial t} = P_{veg} - E_{wf} - R_{veg}$

Temporary Surface Water (Snow) Stores

LEAF-2

Top layer	$\dfrac{\partial W_{st}}{\partial t} = P_g + R_{veg} - E_{sc} - F_{w(t,\,t-1)}$, when multiple layers are allowed
	$\dfrac{\partial W_{st}}{\partial t} = P_g + R_{veg} - E_{sc} - I$, when only one layer is present
Intermediate layers	$\dfrac{\partial W_{si}}{\partial t} = F_{w(i+1,\,i)} - F_{w(i,\,i-1)}$
Bottom layer	$\dfrac{\partial W_{sb}}{\partial t} = F_{w(b+1,\,b)} - I$

Soil Moisture Stores

	LAPS	LEAF	LEAF-2
Surface layer	$\dfrac{\partial W_{g3}}{\partial t} = \dfrac{1}{D_3}[P_g - Q_{3,2} - E_{gc} - E_{t3} - R_s - R_3]$	$\dfrac{\partial W_{gt}}{\partial t} = \dfrac{1}{D_t}[P_g - Q_{t,t-1} - E_{gc} - E_{tt} - R_s]$	$\dfrac{\partial W_{gt}}{\partial t} = \dfrac{1}{D_t}[P_g - Q_{t,t-1} - E_{gc} - E_{tt} - R_s - R_t]$
Intermediate layers	$\dfrac{\partial W_{g2}}{\partial t} = \dfrac{1}{D_2}[Q_{3,2} - Q_{2,1} - E_{t2} - R_2]$	$\dfrac{\partial W_{gi}}{\partial t} = \dfrac{1}{D_i}[Q_{i+1,i} - Q_{i,i-1} - E_{ti}]$	$\dfrac{\partial W_{gi}}{\partial t} = \dfrac{1}{D_i}[Q_{i+1,i} - Q_{i,i-1} - E_{ti} - R_i]$
Deep layer	$\dfrac{\partial W_{g1}}{\partial t} = \dfrac{1}{D_1}[Q_{2,1} - R_g - R_l]$	$\dfrac{\partial W_{gd}}{\partial t} = \dfrac{1}{D_d}(Q_{d+1,d} - E_{td})$	$\dfrac{\partial W_{gd}}{\partial t} = \dfrac{1}{D_d}(Q_{d+1,d} - E_{td} - R_d)$

Fluxes from Vegetation to Canopy Air Space

	LAPS	LEAF	LEAF-2
Evaporation from interception stores	$E_{wf} = \dfrac{\rho C_p}{\Upsilon \lambda} \dfrac{e_{vs} - e_c}{r_b} \bullet \left(\dfrac{W_f}{W_m}\right)^{2/3}$	$E_{wf} = \rho \dfrac{q_{vs} - q_c}{r_b} \bullet \left(\dfrac{W_f}{W_m}\right)^{2/3}$	$E_{wf} = \rho \dfrac{q_{vs} - q_c}{r_b} \bullet \left(\dfrac{W_f}{W_m}\right)^{2/3}$
Transpiration rates	$E_t = \dfrac{\rho C_p}{\Upsilon \lambda} \dfrac{e_{vs} - e_c}{r_b + r_c} \bullet \left[\left(1 - \dfrac{W_f}{W_m}\right)^{2/3}\right]$	$E_t = \rho \dfrac{q_{vs} - q_c}{r_b + r_c} \bullet \left[\left(1 - \dfrac{W_f}{W_m}\right)^{2/3}\right]$	$E_t = \rho \dfrac{q_{vs} - q_c}{r_b + r_c} \bullet \left[\left(1 - \dfrac{W_f}{W_m}\right)^{2/3}\right]$
Evapotranspiration rate	$E_{vc} = \dfrac{\rho C_p}{\Upsilon \lambda}(e_{vs} - e_c)$ $\bullet \left[\dfrac{\left(\dfrac{W_f}{W_m}\right)^{2/3}}{r_b} + \dfrac{1 - \left(\dfrac{W_f}{W_m}\right)^{2/3}}{r_b + r_c}\right]$	$E_{vc} = \rho(q_{vs} - q_c)$ $\bullet \left[\dfrac{\left(\dfrac{W_f}{W_m}\right)^{2/3}}{r_b} + \dfrac{1 - \left(\dfrac{W_f}{W_m}\right)^{2/3}}{r_b + r_c}\right]$	$E_{vc} = \rho(q_{vs} - q_c)$ $\bullet \left[\dfrac{\left(\dfrac{W_f}{W_m}\right)^{2/3}}{r_b} + \dfrac{1 - \left(\dfrac{W_f}{W_m}\right)^{2/3}}{r_b + r_c}\right]$
Sensible heat flux	$H_{vc} = 2\rho C_p \dfrac{T_V - T_c}{r_b}$	$H_{vc} = \rho C_p \dfrac{T_v - T_c}{r_b}$	$H_{vc} = \rho C_p \dfrac{T_v - T_c}{r_b}$

Fluxes from Canopy Air Space to the Atmosphere

	LAPS	LEAF	LEAF-2
Evaporation rate	$E_{ca} = \dfrac{\rho C_p}{\Upsilon \lambda} \dfrac{e_c - e_r}{r_a}$	$E_{ca} = \rho \dfrac{q_c - q_r}{r_a}$	$E_{ca} = \rho \dfrac{q_c - q_r}{r_a}$
Sensible heat flux	$H_{ca} = \rho C_p \dfrac{T_c - T_r}{r_a}$	$H_{ca} = \rho C_p \dfrac{T_c - T_r}{r_a}$	$H_{ca} = \rho C_p \dfrac{T_c - T_r}{r_a}$

Vertical Movement of Water Through Soil and Snow

	LAPS	LEAF	LEAF-2
Vertical water flux through soil	$Q_{i,i-1} = \rho_w \dfrac{D_i K_i + D_{i+1} K_{i+1}}{D_i + D_{i+1}} \bullet \left[\dfrac{2(\psi_i - \psi_{i+1})}{D_i + D_{i+1}} + 1 \right]$	$Q_{i,i-1} = -\rho_w K_i \dfrac{d}{dz}(\psi_i + z)$	$Q_{i,i-1} = -\rho_w K_i \dfrac{d}{dz}(\psi_i + z)$
Vertical water flux through snow	Not used	Not used	$F_{w(i,i-1)} = \dfrac{\max[0, W_{si}(1.1 f_l - 0.1)]}{\Delta t}$
Hydraulic conductivity	$K_i = K_s \left(\dfrac{w_i}{w_s} \right)^{2B+3}$	$K_i = K_s \left(\dfrac{w_i}{w_s} \right)^{2B+3}$	$K_i = K_s \left(\dfrac{w_i}{w_s} \right)^{2B+3}$
Soil water potential	$\psi_i = \psi_s \left(\dfrac{w_i}{w_s} \right)^{-B}$	$\psi_i = \psi_s \left(\dfrac{w_i}{w_s} \right)^{-B}$	$\psi_i = \psi_s \left(\dfrac{w_i}{w_s} \right)^{-B}$
Gravitational drainage[a]	$R_g = \rho_w K_s \left(\dfrac{w_l}{w_s} \right)^{2B+3} \sin x$	$\dfrac{\partial}{\partial t}(w_d) = 0$	None

[a] In LEAF the gravitational drainage is equal to that required to maintain a constant w_d.

Horizontal Movement of Water in Soil

	LAPS	LEAF	LEAF-2
Surface runoff	$R_s = P_g - \min(P_g, \rho_w K_s)$	$R_s = 0 \quad \dfrac{w_i}{w_s} < 1$	Predicted by TOPMODEL (see Beven and Kirkby 1979; Walko *et al.* 2000a).
		$R_s = P_g - \rho_w K_s \dfrac{w_i}{w_s} = 1$	
Subsurface runoff	$R_i = Q_{i, i-1} - \min(Q_{i, i-1}, \rho_w K_S)$	Not used in version 1	Predicted by TOPMODEL (see Beven and Kirkby 1979; Walko *et al.* 2000a).

Fluxes from Ground Surface to Canopy Air Space

	LAPS	LEAF	LEAF-2
Evaporation rate	$E_{gc} = \dfrac{\rho C_p}{\Upsilon \lambda} \dfrac{\alpha_m e_{gs} - e_c}{r_l + r_d}$	$E_{gc} = \rho \dfrac{q_g - q_c}{r_d}$	$E_{gc} = \rho \dfrac{q_g - q_c}{r_d}$
Sensible heat flux	$H_{gc} = \rho C_p \dfrac{T_{gt} - T_c}{r_d}$	$H_{gc} = \rho C_p \dfrac{T_{gt} - T_c}{r_d}$	$H_{gc} = \rho C_p \dfrac{T_{gt} - T_c}{r_d}$

Fluxes from Temporary Surface Water (Snow) to Canopy Air Space

	LEAF-2
Evaporation rate	$E_{sc} = \rho \dfrac{q_{snw} - q_c}{r_d}$
Sensible heat flux	$H_{sc} = \rho C_p \dfrac{T_{st} - T_c}{r_d}$

Surface Resistance

LAPS	LEAF	LEAF-2
$r_l = p_1 + p_2 \left(\dfrac{w_3}{w_s} \right)^{p_3}$	not used	not used

Soil Surface Resistance

LAPS	LEAF	LEAF-2
$r_d = \dfrac{1}{k^2 u_H} \left[\dfrac{\sinh(\beta)}{\sinh(\alpha_g \beta)} \right]^{[1/2]} \bullet \left[\ln \left(\dfrac{z}{z_0} \right) \right]^2$	$r_d = r_{bare} \max \left[\left(1 - \dfrac{LSAI}{\sigma} \right), 0 \right] + r_{close} \min \left[\dfrac{LSAI}{\sigma}, 1 \right]$	$r_d = r_{bare} \max \left[\left(1 - \dfrac{LSAI}{\sigma} \right), 0 \right] + r_{close} \min \left[\dfrac{LSAI}{\sigma}, 1 \right]$

Bulk Leaf Boundary-Layer Resistance

LAPS	LEAF	LEAF-2
$r_b = \dfrac{P_s}{C_t} \dfrac{(\sinh \beta)^{1/4}}{(u_H)^{1/2} L_d H} \bullet \int_{\alpha_g \beta}^{\beta} \left[\sinh \left(\dfrac{\beta_z}{H} \right) \right] d\left(\beta \dfrac{z}{H} \right)$	$r_b = \dfrac{P_s}{C_f LSAI} \left(\dfrac{l}{U_f} \right)^{1/2}$ $P_s = 1 + 0.5 LSAI$	$r_b = \dfrac{P_s}{C_f LSAI} \left(\dfrac{l}{U_f} \right)^{1/2}$ $P_s = 1 + 0.5 LSAI$

Canopy Resistance

LAPS	LEAF	LEAF-2
$r_c = \dfrac{r_{\mathrm{smin}}}{LAI} f_R [f_v f_T f_w]^{-1}$	$r_c = \dfrac{1}{LAI} [d_{\mathrm{smin}} f_R f_{Tc} f_{Th} f_v f_\psi]^{-1}$	$r_c = \dfrac{1}{LAI} [d_{\mathrm{smin}} f_R f_{Tc} f_{Th} f_v f_\psi]^{-1}$

Aerodynamic Resistance

LAPS	LEAF	LEAF-2
$r_a = \dfrac{1}{ku} \ln \dfrac{z_r - d}{H - d}$	$r_a = \dfrac{1}{k^2 U_r} \left[\ln \dfrac{z_r - d}{z_0} + \psi_M \right]$ $\bullet \left[\ln \dfrac{z_r - d}{z_0} + \psi_H \right]$	$r_a = \dfrac{1}{k^2 U_r} \left[\ln \dfrac{z_r - d}{z_0} + \psi_M \right]$ $\bullet \left[\ln \dfrac{z_r - d}{z_0} + \psi_H \right]$

Adjustment Factors

$$f_R = \left[1 + \frac{1.1 S/S_g}{LAI} \right] \left[\frac{1.1 S/S_g}{LAI} + \frac{r_{\mathrm{smin}}}{r_{\mathrm{smax}}} \right]^{-1}$$

$$f_T = 1 - 0.0016 (298.0 - T_c)^2$$

$f_s = $ (see Dickinson et al. 1986: 48–51)

$$f_v = 1 - 0.0025 \ \mathrm{h\,Pa^{-1}} [e_{vs} - e_c]$$

$$f_w = \begin{cases} 1 & w_a > w_{fc} \\ 1 - \left[\dfrac{w_{wil}}{w} \right]^{1.5} & w_{wil} \le w_a \le w_{fc} \\ 0 & w_a < w_{wil} \end{cases}$$

$f_{Tc}, f_{Th}, f_\psi = $ (see Lee *et al.* 1993; Avissar and Pielke 1991)

B	=	Clapp–Hornberger constant
c_g	=	specific heat of dry soil (J kg^{-1} K^{-1})
c_i	=	specific heat of ice (J kg^{-1} K^{-1})
c_l	=	specific heat of liquid water (J kg^{-1} K^{-1})
C_p	=	specific heat of air at constant pressure (J kg^{-1} K^{-1})
C_c	=	effective heat capacity of canopy air (J m^{-2} K^{-1})
C_D	=	drag coefficient
C_f	=	0.01 m s$^{-1/2}$
C_g	=	effective heat capacity of soil (J m^{-2} K^{-1})
C_i	=	volumetric heat capacity of dry soil (J m^{-3} K^{-1})
C_t	=	transfer coefficient (m$^{1/2}$ s$^{-1/2}$)
C_v	=	volumetric soil heat capacity (J m^{-3} K^{-1})
C_{veg}	=	effective heat capacity of vegetation (J m^{-2} K^{-1})
C_w	=	volumetric heat capacity of water (J m^{-3} K^{-1})
d	=	zero plane displacement (m)
$d_{s\,max}$	=	maximum stomatal conductance (m s^{-1})
$d_{s\,min}$	=	minimum stomatal conductance (m s^{-1})
D_d	=	thickness of the deepest soil layer (m)
D_i	=	thickness of the ith soil layer (m)
D_t	=	thickness of the topmost soil layer (m)
e_c	=	vapor pressure of canopy air (mb)
e_{gs}	=	saturated vapor pressure at ground surface temperature (mb)
e_r	=	vapor pressure at reference height (mb)
e_{vs}	=	saturated vapor pressure at vegetation temperature (mb)
E_{ca}	=	evaporation from canopy air to atmosphere (kg m^{-2} s-1)
E_{gc}	=	evaporation from soil to canopy air (kg m^{-2} s^{-1})
E_{sc}	=	evaporation from snowcover to canopy air (kg m^{-2} s^{-1})
E_t	=	transpiration rate from the dry fraction of the leaves (kg m^{-2} s-1)
E_{td}	=	water extracted from the deepest soil layer by transpiration (kg m^{-2} s^{-1})
E_{ti}	=	water extracted from the ith soil layer by transpiration (kg m^{-2} s^{-1})
E_{tt}	=	water extracted from the topmost soil layer by transpiration (kg m^{-2} s^{-1})
E_{vc}	=	evaporation and transpiration from vegetation to canopy air (kg m^{-2} s^{-1})
E_{wf}	=	evaporation from interception stores (kg m^{-2} s^{-1})
f_i	=	ice fraction of temporary surface water
f_l	=	liquid water fraction of temporary surface water
f_R	=	adjustment factor for total solar radiation
f_s	=	adjustment factor for soil moisture
f_T	=	adjustment factor for seasonal air temperature changes
f_{Tc}	=	adjustment factor for leaf temperature at cold range
f_{Th}	=	adjustment factor for leaf temperature at hot range
f_v	=	adjustment factor for water vapor pressure deficit
f_w	=	adjustment factor for soil moisture
f_ψ	=	adjustment factor for soil water potential
$F_{w(b+1,\,b)}$	=	flux of water between the bottommost snow layer and the next snow layer above, positive downward (kg m^{-2} s^{-1})

$F_{w(i, i-l)}$	= flux of water between snow layer $i + 1$ and snow layer i, positive downward (kg m^{-2}s^{-1})
$F_{w(t, t-1)}$	= flux of water between the top snow layer and below, positive downward (kg m^{-2}s^{-1})
H	= canopy height (m)
$H_{b, b+1}$	= sensible heat flux between bottom snow layer and next snow layer above, positive upward (W m^{-2})
H_{ca}	= sensible heat flux from canopy air to atmosphere (W m^{-2})
H_{gc}	= sensible heat flux from soil to canopy air (W m^{-2})
H_{gs}	= sensible heat flux from soil to snow cover (W m^{-2})
$H_{i-1, i}$	= sensible heat flux between soil/snow layer $i - 1$ and soil/snow layer i, positive upward (W m^{-2})
H_{ps}	= sensible heat flux from precipitation to snow (W m^{-2})
H_{pv}	= sensible heat flux from intercepted precipitation to vegetation (W m^{-2})
H_{sc}	= sensible heat flux from snow cover to canopy air (W m^{-2})
$H_{t-1, t}$	= sensible heat flux top soil/snow layer and the next soil/snow layer below, positive upward (W m^{-2})
H_{vc}	= sensible heat flux from vegetation to canopy air (W m^{-2})
H_{wsg}	= internal energy carried by water between snow cover and topsoil layer, positive downward (W m^{-2})
$H_{w(b+1,b)}$	= internal energy carried by water between bottom snow layer and next snow layer above, positive downward (W m^{-2})
$H_{w(i, i-1)}$	= internal energy carried by water between soil/snow layer i and the next soil/snow layer $i - 1$, positive downward (W m^{-2})
$H_{w(t, t-1)}$	= internal energy carried by water between top soil/snow layer and the next soil/snow layer below, positive downward (W m^{-2})
I	= infiltration of precipitation into the upper soil moisture store, positive downward (kg m^{-2} s^{-1})
k	= von Karman constant
K_i	= hydraulic conductivity of ith layer (m s^{-1})
K_s	= saturated hydraulic conductivity (m s^{-1})
K_t	= thermal diffusivity (m^2 s^{-1})
l	= topical dimension of leaves or the stems along the wind directions (m)
L_d	= stem and leaf density (m^{-2} m^3)
LAI	= leaf area index
$LSAI$	= leaf and stem area index
m_g	= mass of dry soil per cubic meter of total volume (water, soil, and air) (kg m^{-3})
p_1, p_2, p_3	= 30 s m^{-1}, 3.5, 2.3 empirical constants, respectively (see Mihailovic and Ruml 1996)
P_g	= precipitation reaching the ground (kg m^{-2} s^{-1})
P_f	= base-10 logarithm of moisture potential, ψ (cm)
P_s	= shelter factor
P_{veg}	= precipitation intercepted by vegetation (kg m^{-2} s^{-1})
q_c	= specific humidity of the canopy air (kg kg^{-1})
q_g	= effective specific humidity at the surface (see Lee and

Pielke 1992) (kg kg^{-1})

q_r = specific humidity at reference height (kg kg^{-1})

q_{snw} = specific humidity at top snow surface (kg kg^{-1})

q_{vs} = saturated specific humidity at vegetation temperature (kg kg^{-1})

$Q_{d+1,d}$ = flux of water between the deepest soil layer and the next layer above (kg m^{-2} s^{-1})

Q_{gi} = internal energy of the ith soil layer (J m^{-3})

Q_{gt} = internal energy of top soil layer (J m^{-3})

$Q_{i,i-1}$ = flux of water between the ith and $i+1$ soil layers, positive downward (kg m^{-2} s^{-1})

Q_{sb} = internal energy of the bottommost snow layer (J kg^{-1})

Q_{si} = internal energy of the ith snow layer (J kg^{-1})

Q_{st} = internal energy of the topmost snow layer (J kg^{-1})

$Q_{t,t-1}$ = flux of water between the topmost soil layer and the next layer below, positive downward (kg m^{-2} s^{-1})

r_a = aerodynamic resistance (s m^{-1})

r_b = bulk leaf boundary-layer resistance (s m^{-1})

r_{bare} = resistance when the surface is bare (see Lee et al. 1992 for LEAF, and $r_{bare} = 5/u_*$ in LEAF-2) (s m^{-1})

r_c = canopy resistance (s m^{-1})

r_{close} = resistance when the surface is covered by a closed canopy (s m^{-1})

r_d = soil surface aerodynamic resistance (s m^{-1})

r_l = surface resistance (s m^{-1})

r_{smax} = maximum stomatal resistance (s m^{-1})

r_{smin} = minimum stomatal resistance (s m^{-1})

R_d = subsurface runoff in the deepest soil layer (kg m^{-2} s^{-1})

R_g = gravitational drainage (kg m^{-2} s^{-1})

R_{gnet} = net radiation absorbed by the soil (W m^{-2})

R_i = subsurface runoff in ith soil layer (kg m^{-2} s^{-1})

R_{iB} = surface bulk Richardson number

R_s = surface runoff (kg m^{-2} s^{-1})

R_{snwb} = net radiation absorbed by the bottommost snow layer (W m^{-2})

R_{snwi} = net radiation absorbed by the ith snow layer (W m^{-2})

R_{snwt} = net radiation absorbed by the topmost snow layer (W m^{-2})

R_t = subsurface runoff in the top soil layer (kg m^{-2} s^{-1})

R_{veg} = runoff from vegetation (kg m^{-2} s^{-1})

R_{vnet} = net radiation absorbed by the vegetation (W m^{-2})

S = incoming shortwave radiation (W m^{-2})

S_g = the limit value of 30 W m^{-2} for a forest and 100 W m^{-2} for crops

SAI = stem area index

T_c, T_d, T_{gt}, T_v = temperature of canopy air, deep soil, soil surface, and vegetation, respectively (K)

T_{gi} = temperature of the ith soil layer (K)

T_r = air temperature at reference height (K)

T_{si} = temperature of the ith snow layer (K)

T_{st}	=	temperature of the topmost snow layer (K)
u_H	=	wind speed at canopy top height (m s^{-1})
u_*	=	friction velocity (m s^{-1})
U_f	=	magnitude of wind within the canopy (m s^{-1})
U_r	=	wind speed at reference level (m s^{-1})
$w_3, w_2, w_1,$	=	volumetric soil moisture content in the upper soil layer, root zone, and deep soil, respectively (m^3 m^{-3})
w_a	=	mean volumetric soil moisture content in first and second layer (m^3 m^{-3})
w_d	=	volumetric soil moisture content of the deep layer (m^3 m^{-3})
w_{fc}	=	volumetric soil moisture content at field capacity (m^3 m^{-3})
w_i	=	volumetric soil moisture content of the ith layer (m^3 m^{-3})
w_s	=	saturated volumetric soil moisture content (m^3 m^{-3})
w_{wil}	=	volumetric soil moisture content at the wilting point (m^3 m^{-3})
$W_3, W_2, W_1,$	=	soil moisture content in the upper soil layer, root zone, and deep soil, respectively (kg m^{-3})
W_f	=	water stored on vegetation (kg m^{-2})
W_{gd}	=	soil water content of the deepest soil layer (kg m^{-3})
W_{gi}	=	soil water content of the ith soil layer (kg m^{-3})
W_{gt}	=	soil water content of the topmost soil layer (kg m^{-3})
W_m	=	maximum water reservoir capacity (kg m^{-2})
W_{sb}	=	water content of bottommost snow layer (kg m^{-2})
W_{si}	=	water content of ith snow layer (kg m^{-2})
W_{st}	=	water content of topmost snow layer (kg m^{-2})
x	=	mean slope angle (°)
z	=	vertical coordinate (m)
z_r	=	reference height (m)
z_0	=	roughness length of bare soil (m)
α_g	=	ratio of canopy bottom height and canopy top height
α_m	=	wetness factor (see Mihailovic et al. 1993)
β	=	extinction factor (see Mihailovic et al. 1993)
Δt	=	time step (s)
γ	=	psychometric constant (mb K^{-1})
λ	=	latent heat of vaporization of water (J kg^{-1})
λ_f	=	latent heat of fusion of water (J kg^{-1})
λ_H	=	thermal conductivity (J s^{-1} m^{-1} K^{-1})
ρ	=	air density (kg m^{-3})
ρ_w	=	density of water (kg m^{-3})
σ	=	critical value of LSAI for closed canopy (m^2 m^{-2})
τ_d	=	day length (s)
ψ_H	=	stability function for moisture transfer
ψ_i	=	soil water potential (m)
ψ_M	=	stability function for momentum transfer
ψ_s	=	saturated soil water potential (m)

Appendix E

Summary of Datasets (2000)

This access to data on the Web will undoubtedly change with time, but these topic areas provide the reader with topics (and sites) to start with.

Atmospheric data: http://dss.ucar.edu/pub/reanalysis

Soils

Soil wetness (Dirmeyer et al. 1999)
Soils (Miller and White 1998): http://EarthInteractions.org
Soil water holding capacity (Kern 1995a, b).
Active layer in permafrost regions [Circumpolar Active-Layer Monitoring Network (CALM)]: http://www.geography.uc.edu/~kenhinke/ CALM
Land use history: http://biology.usgs.gov/luhna/index.html

Snow and sea ice

National Snow and Ice Data Center: http://nsidc.org
Byrd Polar Research Center: http://www-bprc.mps.ohio-state.edu
National Ice Center: http://www.natice.noaa.gov
National Operational Hydrologic Remote Sensing Center: http://www. nohrsc.nws.gov

Vegetation data

Ramanukutty and Foley historical crop data: http://cpep.meteor.wisc.edu/pages/ available.html
NOAA/NASA Land Data Assimilation System (LDAS): http://ldas. gsfc.nasa.gov
Land cover: http://www.usgs.gov (link to the EROS Data Center in Sioux Falls, South Dakota)
Soils and roots (Feddes *et al.* 2001)

Ocean data

Sea surface temperatures
Climate Diagnostics Center: ftp.cdc.noaa.gov

Surface Radiative Fluxes–Rachel Pinker (personal communication, 1999) http: //www.meto.umd.edu/~srb/gcip

References

Abbs, D. J. 1999. A numerical modeling study to investigate the assumptions used in the calculation of probable maximum precipitation. *Water Resour. Res.* **35**, 785–796.

Abbs, D. J., and R. A. Pielke. 1987. Numerical simulations of orographic effects on NE Colorado snowstorms. *Meteor. Atmos. Phys.* **37**, 1–10.

Abdella, K., and N. McFarlane. 1997. A new second-order turbulence closure scheme for the planetary boundary layer. *J. Atmos. Sci.* **54**, 1850–1867.

Abdella, K., and N. McFarlane. 1999. Reply to comments on "A new second-order turbulence closure scheme for the planetary boundary layer." *J. Atmos. Sci.* **56**, 3482–3483.

Abe, S., and T. Yoshida. 1982. The effect of the width of a peninsula to the sea breeze. *J. Meteor. Soc. Japan* **60**, 1074–1084.

Abele, J., and D. Clement. 1980. Chebyshev approach to fit atmospheric aerosol size distributions. *Contrib. Atmos. Phys.* **53**, 469–485.

Achtemeier, G. L. 1983. The relationship between the surface wind field and convective precipitation over the St. Louis area. *J. Climate Appl. Meteor.* **22**, 982–999.

Ackerman, S. A., and S. K. Cox. 1982. The Saudi Arabian heat low: Aerosol distributions and thermodynamic structure. *J. Geophys. Res.* **87**, 8991–9002.

Ackerman, T. P., K.-N. Lion, and C. B. Levoy. 1976. Infrared radiative transfer in polluted atmospheres. *J. Appl. Meteor.* **15**, 28–35.

Adams, J. C., A. K. Cline, M. A. Drake, and R. A. Sweet. 1975. NCAR Software Support Library, Volume I. Technical Note/1A-105. NCAR, Boulder, CO.

Adcroft, A., C. Hill, and J. Marshall. 1997. Representation of topography by shaved cells in a height coordinate ocean model. *Mon. Wea. Rev.* **25**, 2293–2315.

Ahlberg, J. H., E. N. Nilson, and J. L. Walsh. 1967. *Theory of Splines and Their Applications.* Academic Press, New York.

Akiyama, T. 1978. Mesoscale pulsation of convective rain in medium-scale disturbances developed in Bain front. *J. Meteor. Soc. Japan* **56**, 267–283.

Alaka, M. A. 1960. The airflow over mountains. Technical Report 34, WMO, Geneva.

Alapaty, K., and R. Mathur. 1998. Effects of atmospheric boundary layer mixing representations on vertical distribution of passive and reactive tracers. *Meteor. Atmos. Phys.* **69**, 101–118.

Alberty, R. L., and S. L. Barnes. 1979. *SESAME 1979 Plans for Operations and Data Archival.* NOAA/ERL, Boulder, CO.

Alberty, R. L., D. W. Burgess, C. E. Hand, and J. F. Weaver. 1979. *SESAME 1979 Operations Summary.* NOAA/ERL, Boulder, CO.

Allen, L. H. Jr., and E. R. Lemon. 1972. Net radiation frequency distribution in a corn crop. *Bound.-Layer Meteor.* **3**, 246–254.

Allender, J. H. 1979. Model and observed circulation throughout the annual temperature cycle of Lake Michigan. *J. Phys. Oceanogr.* **9**, 573–579.

Al Nakshabandi, G., and H. Kohnke. 1965. Thermal conductivity and diffusivity of soils as related to moisture tension and other physical properties. *Agric. Meteor.* **2**, 271–279.

Alpers, W., U. Pahl, and G. Gross. 1998. Katabatic wind fields in coastal areas studied by ERS-1 synthetic aperture radar imagery and numerical modeling. *J. Geophys. Res.* **103**, 7875–7886.

Alpert, P., and J. Neumann. 1983. A simulation of a Lake Michigan winter land breeze on the 7th of November 1978. *Mon. Wea. Rev.* **111**, 1873–1881.

Alpert, P., A. Cohen, E. Doron, and J. Neumann. 1982. A model simulation of the summer circulation from the eastern Mediterranean past Lake Kinneret in the Jordan Valley. *Mon. Wea. Rev.* **110**, 994–1006.

Alpert, P., M. Tsidulko, and U. Stein. 1995. Can sensitivity studies yield absolute comparisons for the effects of several processes? *J. Atmos. Sci.* **52**, 597–601.

Alpert, P., S. O. Krichak, T. N. Krishnamurti, U. Stein, and M. Tsidulko. 1996a. The relative roles of lateral boundaries, initial conditions, and topography in mesoscale simulations of lee cyclogenesis. *J. Atmos. Sci.* **35**, 1091–1099.

Alpert, P., M. Tsidulko, S. Krichak, and U. Stein. 1996b. A multi-stage evolution of an ALPEX cyclone. *Tellus* **48A**, 209–220.

Alpert, P., Y. J. Kaufman, Y. Shay-El, D. Tanre, A. da Silva, S. Schubert, and J. H. Joseph. 1998. Quantification of dust-forced heating of the lower troposphere. *Nature* **395**, 367–370.

Alpert, P., M. Tsidulko, and D. Izigsohn. 1999. A shallow short-lived meso-beta cyclone over the gulf of Antalya, eastern Mediterranean. *Tellus* **51A**, 249–262.

Amiro, B. D., J. I. MacPherson, and R. L. Desjardins. 1999. BOREAS flight measurements of forest-fire effects on carbon dioxide and energy fluxes. *Agric. Forest Meteor.* **96**, 199–208.

AMS. 1978. Accuracy of dispersion models. A position paper of the AMS 1977 Committee on Atmospheric Turbulence and Diffusion. *Bull. Amer. Meteor. Soc.* **59**, 1025–1026.

Andersen, O. J. 1981. The katabatic wind field and nocturnal inversions in valleys: A 2-dimensional model. Report No. 1, Dept. Meteorology, University of Bergen, Norway.

Anderson, G. E. 1971. Mesoscale influences on wind fields. *J. Appl. Meteor.* **10**, 377–386.

Anderson, S. F. 1979. Effects of New York City on the horizontal and vertical structure of sea breeze fronts. Vol. II, Observations of sea breeze frontal slopes and vertical velocities over an urban area. Report, Dept. of Meteorology, San Jose State University, San Jose, CA.

André, J. C., and L. Mahrt. 1982. The nocturnal surface inversion and influence of clean-air radiative cooling. *J. Atmos. Sci.* **39**, 864–878.

André, J. C., G. DeMoor, P. Lacarrere, G. Therry, and R. du Vachat. 1978. Modeling the 24-hour evolution of the mean and turbulent structures of the planetary boundary layer. *J. Atmos. Sci.* **35**, 1862–1883.

André, J. C., J.-P. Goutorbe, A. Perrier, F. Becker, P. Besslemoulin, P. Bougeault, Y. Brunet, W. Brutsaert, T. Carlson, R. Cuenca, J. Gash, J. Gelpe, P. Hildebrand, P. Lagouarde, C. Lloyd, L. Mahrt, P. Mascart, C. Mazaudier, J. Noilhan, C. Ottle, M. Payen, T. Phulpin, R. Stull, J. Shuttleworth, T. Schmugge, O. Taconet, C. Tarrieu, R.-M. Thepenier, C. Valencogne, D. Vidal-Madjar, and A. Weill. 1998. HAPEX-MOBILHY. First results from the special observing period. *Ann. Geophys.* **6**, 477–492.

Andreas, E. L. and G. Treviño. 2000. Comment on "A physical interpretation of von Karman's constant based on asymptotic considerations—A new value." *J. Atmos. Sci.* **57**, 1189–1192.

Andreyev, S. D., and L. S. Ivlev. 1980. Infrared radiation absorption by various atmospheric aerosol fractions. *Izv. Atmos. Oceanic Phys.* **16**, 663–669.

Anthes, R. A. 1970. Numerical experiments with a two-dimensional horizontal variable grid. *Mon. Wea. Rev.* **98**, 810–822.

Anthes, R. A. 1972. The development of asymmetries in a three-dimensional numerical model of the tropical cyclone. *Mon. Wea. Rev.* **100**, 461–476.

Anthes, R. A. 1974a. Data assimilation and initialization of hurricane prediction models. *J. Atmos. Sci.* **31**, 702–719.

Anthes, R. A. 1974b. The dynamics and energetics of mature tropical cyclones. *Rev. Geophys. Space Phys.* **12**, 495–522.

Anthes, R. A. 1977. A cumulus parameterization scheme utilizing a one-dimensional cloud model. *Mon. Wea. Rev.* **105**, 270–286.

Anthes, R. A. 1978. The height of the planetary boundary layer and the production of circulation in a sea breeze model. *J. Atmos. Sci.* **35**, 1231–1239.

Anthes, R. A. 1982. *Tropical Cyclones, Their Evolution, Structure and Effect*. American Meteorological Society Monograph, Boston.

Anthes, R. A. 1983. A review of regional models of the atmosphere in middle latitudes. *Mon. Wea. Rev.* **111**, 1306–1335.

Anthes, R. A. 2000. Community models and collaboration. *UCAR Quarterly*, Presidents Corner, Summer 2000, National Center for Atmospheric Research.

Anthes, R. A., and T. T. Warner. 1974. Prediction of mesoscale flows over complex terrain. U.S. Army Research Development Technical Report ECOM-5532. U.S. Army Electronics Command, White Sands Missile Range, New Mexico.

Anthes, R. A., and T. T. Warner. 1978. Development of hydrodynamic models suitable for air pollution and other mesometeorological studies. *Mon. Wea. Rev.* **106**, 1045–1078.

Anthes, R. A., J. W. Trout, and S. L. Rosenthal. 1971. Comparisons of tropical cyclone simulations with and without the assumption of circular symmetry. *Mon. Wea. Rev.* **99**, 759–766.

Anthes, R. A., N. L. Seaman, and T. T. Warner. 1980. Comparisons of numerical simulations of the planetary boundary layer by a mixed-layer and multi-level model. *Mon. Wea. Rev.* **108**, 365–376.

Appel, B. R., E. L. Kothny, E. M. Hoffer, G. M. Hidy, and J. J. Wesolowski. 1978. Sulfate and nitrate data from the California aerosol characterization experiment (ACHEX). *Environ. Sci. Tech.* **12**, 418–425.

Arakawa, A., and V. R. Lamb. 1977. Computational design of the basic dynamical processes of the UCLA general circulation model. *Meth. Comput. Phys.* **17**, 173–265.

Arakawa, A., and W. H. Schubert. 1974. Interaction of a cumulus cloud ensemble with the large-scale environment. Part I. *J. Atmos. Sci.* **31**, 674–701.

Arakawa, S., K. Yamada, and T. Toya. 1982. A study of foehn in the Hokuriku district using the AMe DAS data. *Pap. Meteor. Geophys.* **33**, 149–163.

Arola, A. 1999. Parameterization of turbulent and mesoscale fluxes for heterogeneous surfaces. *J. Atmos. Sci.* **56**, 584–598.

Arritt, R. W. 1985. Numerical studies of thermally and mechanically forced circulations over complex terrain. Ph.D. dissertation, Dept. of Atmospheric Science, Colorado State University, Fort Collins, CO.

Arritt, R. W., and R. A. Pielke. 1986. Interactions of nocturnal slope flows with ambient winds. *Bound.-Layer Meteor.* **37**, 183–195.

Arritt, R. W., R. T. McNider, and R. A. Pielke. 1987. Numerical model evaluation of the extension of the critical dividing streamline hypothesis to mesoscale two-dimensional terrain. *Atmos. Environ.* **21**, 1905–1913.

Arritt, R. W., R. A. Pielke, and M. Segal. 1988. Variations of sulfur dioxide deposition velocity resulting from terrain-forced mesoscale circulations. *Atmos. Environ.* **22**, 715–723.

Arya, S. P. 1981. Parameterizing the height of the stable atmospheric boundary layer. *J. Appl. Meteor.* **20**, 1192–1202.

Arya, S. P. 1988. *Introduction to Micrometeorology*. Academic Press, San Diego, CA.

Asai, T. 1965. A numerical study of the air-mass transformation over the Japan Sea in winter. *J. Meteor. Soc. Japan* **43**, 1–15.

Asai, T., and S. Mitsumoto. 1978. Effects of an inclined land surface on the land and sea breeze circulation: A numerical experiment. *J. Meteor. Soc. Japan* **56**, 559–570.

Ashby, M. 1999. Modelling the water and energy balances of Amazonian rainforest and pasture using Anglo-Brazilian Amazonian climate observation study data. *Agric. Forest Meteor.* **94**, 79–101.

Atkinson, B. W. 1981. *Mesoscale Atmospheric Circulations*. Academic Press, New York.

Atlas, D., and S.-H. Chou. 1982. Coast-ocean–atmosphere-ocean mesoscale interaction. Technical Memorandum 83903, NASA.

Atlas, D., S.-H. Chou, and W. P. Byerly. 1983. The influence of coastal shape on winter mesoscale air-sea interaction. *Mon. Wea. Rev.* **111**, 245–252.

Atwater, M. A. 1971a. The radiation budget for polluted layers of the urban environment. *J. Appl. Meteor.* **10**, 205–214.

Atwater, M. A. 1971b. Radiation effects of pollutants in the atmospheric boundary layer. *J. Atmos. Sci.* **28**, 1367–1373.

Atwater, M. A. 1974. The radiation model. Sec. 4, Vol. I, CEM Report No. 4131-4099. A description of a general three-dimensional numerical simulation model of a coupled air-water and/or air-land boundary layer. Center for the Environment and Man, Hartford, CT.

Atwater, M. A. 1977. Urbanization and pollutant effects on the thermal structure in four climatic regions. *J. Appl. Meteor.* **16**, 888–895.

Atwater, M. A., and J. T. Ball. 1981. A surface solar radiation model for cloudy atmospheres. *Mon. Wea. Rev.* **109**, 878–895.

Atwater, M. A., and P. Brown Jr. 1974. Numerical calculation of the latitudinal variation of solar radiation for an atmosphere of varying opacity. *J. Appl. Meteor.* **13**, 289–297.

Auer, A. H., and J. D. Marwitz. 1968. Estimates of air and moisture flux into hailstorms on the high plains. *J. Appl. Meteor.* **7**, 196–198.

Augstein, E., and M. Wendel. 1980. Modeling of the time-dependent atmospheric tradewind boundary layer with non-precipitating cumulus clouds. *Contrib. Atmos. Phys.* **53**, 509–538.

Avissar, R. 1991. A statistical-dynamical approach to parameterize subgrid-scale land-surface heterogeneity in climate models. *Surv. Geophys.* **12**, 155–178.

Avissar, R. 1992. Conceptual aspects of a statistical-dynamical approach to represent landscape subgrid-scale heterogeneities in atmospheric models. *J. Geophys. Res.* **97**, 2729–2742.

Avissar, R. 1995. Recent advances in the representation of land-atmosphere interactions in general circulation models. *Rev. Geophys.* **33** (Supp.), 1005–1010.

Avissar, R., and F. Chen. 1993. Development and analysis of prognostic equations for mesoscale kinetic energy and mesoscale (subgrid scale) fluxes for large-scale atmospheric models. *J. Atmos. Sci.* **50**, 3751–3774.

Avissar, R., and F. Chen. 1995. An approach to represent mesoscale (subgrid-scale) fluxes on GCMs demonstrated with simulations of local deforestation in Amazonia. In *Space and Time Scale Variability and Interdependencies in Hydrological Processes*, R. A. Feddes, Ed., Press Syndicate of the University of Cambridge, Cambridge, U.K., 89–109.

Avissar, R., and R. D. Lawford (Eds.). 1999. GCIP-GEWEX Continental-Scale International Project Part II. *J. Geophys. Res.* **104, D16**, 19,275–19,757.

Avissar, R., and Y. Liu. 1996. Three-dimensional numerical study of shallow convective clouds and precipitation induced by land surface forcing. *J. Geophys. Res.* **101**, 7499–7518.

Avissar, R., and H. Pan. 2000. Simulations of the summer hydrometeorological processes of Lake Kinneret. *J. Hydrometeor.* **1**, 95–109.

Avissar, R., and R. A. Pielke. 1989. A parameterization of heterogeneous land surfaces for atmospheric numerical models and its impact on regional meteorology. *Mon. Wea. Rev.* **117**, 2113–2136.

Avissar, R., and R. A. Pielke. 1991. The impact of plant stomatal control on mesoscale atmospheric circulations. *Agric. Forest Meteor.* **54**, 353–372.

Avissar, R., and T. Schmidt. 1998. An evaluation of the scale at which ground-surface heat flux patchiness affects the convective boundary layer using large-eddy simulations. *J. Atmos. Sci.* **55**, 2666–2689.

Avissar, R., M. D. Moran, R. A. Pielke, G. Wu, and R. N. Meroney. 1990. Operating ranges of mesoscale numerical models and meteorological wind tunnels for the simulation of sea and land breezes. *Bound.-Layer Meteor.* Special Anniversary Issue, Golden Jubilee, **50**, 227–275.

Avissar, R., E. W. Eloranta, K. Gurer, and G. J. Tripoli. 1998. An evaluation of the large-eddy simulation option of the regional atmospheric modeling system in simulating a convective boundary layer: A FIFE case study. *J. Atmos. Sci.* **55**, 1109–1130.

Bacon, D. P., N. N. Ahmad, Z. Boybeyi, T. J. Dunn, M. S. Hall, P. C. S. Lee, R. A. Sarma, M. D. Turner, K. T. Waight III, S. H. Young, and J. W. Zack. 2000. A dynamically adapting weather and dispersion model: The Operational Multiscale Environment model with Grid Adaptivity (OMEGA). *Mon. Wea. Rev.* **128**, 2044–2076.

Bader, D. C. 1981. Simulation of the daytime boundary layer evolution in deep mountain valleys. M.S. thesis, Dept. of Atmospheric Science, Colorado State University, Fort Collins, CO.

Bader, D. C., and T. B. McKee. 1983. Dynamical model simulation of the morning boundary layer development in deep mountain valleys. *J. Climate Appl. Meteor.* **22**, 341–351.

Baer, F., and B. Katz. 1980. Normal mode analysis. In *Multidisciplinary Research Program in Atmospheric Science—A Quasi-Biennial Report*, O. E. Thompson, Ed., Dept. of Meteorology, University of Maryland, College Park, MD, 45–62.

Baer, F., and T. J. Simons. 1970. Computational stability and time truncation of coupled on linear equations with exact solutions. *Mon. Wea. Rev.* **98**, 665–679.

Bagnold, R. A. 1973. *The Physics of Blown Sand and Desert Dunes*. Chapman and Hall, London.

Bailey, M. J., K. M. Carpenter, L. R. Lowther, and C. W. Passant. 1981. A mesoscale forecast for 14 August 1975—the Hampstead storm. *Meteor. Mag.* **110**, 147–161.

Baines, P. G. 1977. Upstream influence and Long's model in stratified flows. *J. Fluid Mech.* **82**, 147–159.

Baines, P. G. 1979. Observations of stratified flows over two-dimensional obstacles in fluid of finite depth. *Tellus* **31**, 351–371.

Baines, P. G. 1995. *Topographic Effects in Stratified Flows*. Cambridge University Press, New York.

Baines, P. G., and P. A. Davies. 1980. Laboratory studies of topographic effects in rotating and/or stratified fluids. GARP Series No. 23, WMO, Geneva.

Baker, D. G. 1971. A study of high pressure ridges to the east of the Appalachian mountains. Ph.D. dissertation, Massachusetts Institute of Technology, Cambridge, MA.

Baker, R. D., B. H. Lynn, A. Boone, W.-K. Tao, and J. Simpson. 2001. The influence of soil moisture, coastline curvature, and land-breeze circulations on sea-breeze initiated precipitation. *J. Hydrometeor.* **2**, 193–211.

Ball, F. K. 1960. Control of inversion height by surface heating. *Quart. J. Roy. Meteor. Soc.* **86**, 483–494.

Ballard, S. P., B. W. Golding, and R. N. Smith. 1991. Mesoscale model experimental forecasts of the Haar of northeast Scotland. *Mon. Wea. Rev.* **119**, 2107–2123.

Ballentine, R. J. 1980. A numerical investigation of New England coastal frontogenesis. *Mon. Wea. Rev.* **108**, 1479–1497.

Bankes, S. 1993. Exploratory modeling for policy analysis. *Oper. Res.* **41**, 435–449.

Bannon, P. R. 1995. Hydrostatic adjustment: Lamb's problem. *J. Atmos. Sci.* **52**, 1743–1752.

Bannon, P. R., C. H. Bishop, and J. B. Kerr. 1997. Does the surface pressure equal the weight per unit area of a hydrostatic atmosphere? *Bull. Amer. Meteor. Soc.* **78**, 2637–2642.

Banta, R. M. 1982. An observational and numerical study of mountain boundary layer flow. Dept. of Atmospheric Science Paper No. 350, Colorado State University, Fort Collins, CO.

Banta, R. M. 1984. Daytime boundary-layer evolution over mountainous terrain, Pt. 1, Observations of the dry circulations. *Mon. Wea. Rev.* **112**, 340–356.

Banta, R. M., and W. Blumen. 1990. *Atmospheric Processes Over Complex Terrain*. Meteor. Monogr., 45, American Meteorological Society, Boston, MA.

Banta, R. M., and W. R. Cotton. 1981. An analysis of the structure of local wind systems in a broad mountain basin. *J. Appl. Meteor.* **20**, 1255–1266.

Banta, R. M., and P. T. Gannon Sr. 1995. Influence of soil moisture on simulations of katabatic flow. *Theor. Appl. Climatol.* **52**, 85–94.

Banta, R. M., C. J. Senff, A. B. White, M. Trainer, R. T. McNider, R. J. Valente, S. D. Mayor, R. J. Alvarez, R. M. Hardesty, D. Parrish, and F. C. Fehsenfeld. 1998. Daytime buildup and nighttime transport of urban ozone in the boundary layer during a stagnation episode. *J. Geophys. Res.* **103**, 22,519–22,544.

Bao, J.-W., J. M. Wilczak, J.-K. Choi, and L. H. Kantha. 2000. Numerical simulations of air-sea interaction under high wind conditions using a coupled model: A study of hurricane development. *Mon. Wea. Rev.* **128**, 2190–2210.

Barnes, S. L., and D. K. Lilly. 1975. Covariance analysis of severe storm environments. Preprint, AMS 9th Conference on Severe Local Storms, 301–306.

Barnett, K. M., and R. D. Reynolds. 1981. Assessing the local wind field at Sierra Grande Mountains in New Mexico with instrumentation. Report PNL-3623, Battelle Pacific Northwest Laboratory.

Bastidas, L. A., H. V. Gupta, S. Sorooshian, W. J. Shuttleworth, and Z. L. Yang. 1999. Sensitivity analysis of a land surface scheme using multicriteria methods. *J. Geophys. Res.* **104**, 19,481–19,490.

Batchvarova, E., X. M. Cai, S. E. Gryning, and D. Steyn. 1999. Modelling internal boundary-layer development in a region with a complex coastline. *Bound.-Layer Meteor.* **90**, 1–20.

Bates, J. R., and A. McDonald. 1982. Multiply-upstream, semi-Lagrangian advection schemes: Analysis and application to a multi-level primitive equation model. *Mon. Wea. Rev.* **110**, 1831–1842.

Batteen, M. L., and Y.-J. Han. 1981. On the computational noise of finite difference schemes used in ocean models. *Tellus* **33**, 387–396.

Baumhefner, D. P., and D. J. Perkey. 1982. Evaluation of lateral boundary errors in a limited-domain model. *Tellus* **34**, 409–428.

Beard, K. V., and H. R. Pruppacher. 1971. A wind tunnel investigation of the rate of evaporation of small water droplets falling at terminal velocity in air. *J. Atmos. Sci.* **28**, 1455–1464.

Bélair, S., J. Mailhot, J. W. Strapp, and J. I. MacPherson. 1999. An examination of local versus nonlocal aspects of a TKE-based boundary layer scheme in clear convective conditions. *J. Appl. Meteor.* **38**, 1499–1518.

Bélair, S., A. Methot, J. Mailhot, B. Bilodeau, A. Patoine, G. Pellerin, and J. Cote. 2000. Operational implementation of the Fritsch-Chappell convective scheme in the 24-km Canadian regional model. *Wea. Forecasting* **15**, 257–274.

Beljaars, A. C. M., and P. Viterbo. 1998. Role of the boundary layer in a numerical weather prediction model. In *Clear and Cloudy Boundary Layers*, A. M. Holstlag and P. G. Duynkerke, Eds., Royal Netherlands Academy of Arts and Sciences, Amsterdam, 287–304.

Beljaars, A. C. M., P. Viterbo, M. J. Miller, and A. K. Betts. 1996. The anomalous rainfall over the United States during July 1993: Sensitivity to land surface parameterization and soil moisture anomalies. *Mon. Wea. Rev.* **124**, 362–383.

Bell, R. S. 1978. The forecasting of orographically enhanced rainfall accumulations using 10-level model data. *Meteor. Mag.* **107**, 113–124.

Bender, M. A., and Y. Kurihara. 1983. The energy budgets for the eye and eyewall of a numerically simulated tropical cyclone. *J. Meteor. Soc. Japan* **61**, 239–243.

Beniston, M. G., and G. Sommeria. 1981. Use of a detailed planetary boundary model for parameterization purposes. *J. Atmos. Sci.* **38**, 780–797.

Bennett, M., and A. E. Saab. 1982. Modelling of the urban heat island and of its interaction with pollutant dispersion. *Atmos. Environ.* **16**, 1797–1822.

Bennetts, D. A., and J. C. Sharp. 1982. The relevance of conditional symmetric instability to the prediction of mesoscale frontal rainbands. *Quart. J. Roy. Meteor. Soc.* **108**, 595–602.

Benoit, R., M. Desgagné, P. Pellerin, S. Pellerin, Y. Chartier, and S. Desjardins. 1997a. The Canadian MC2: A semi-Lagrangian, semi-implicit wideband atmospheric model suited for finescale process studies and simulation. *Mon. Wea. Rev.* **125**, 2382–2415.

Benoit, R., S. Pellerin, and W. Yu. 1997b. MC2 model performance during the Beaufort and Arctic storm experiment. In *Numerical Methods in Atmospheric and Oceanic Modelling, The Andre J. Robert Memorial Volume*, C. A. Lin, R. Laprise, and H. Ritchie, Eds., NRC Research Press, Ottawa, Ontario, Canada, 221–244.

Benoit, R., P. Pellerin, N. Kouwen, H. Ritchie, N. Donaldson, P. Joe, and E. D. Soulis. 2000. Toward the use of coupled atmospheric and hydrologic models at regional scale. *Mon. Wea. Rev.* **128**, 1681–1706.

Bergmann, J. C. 1998. A physical interpretation of von Karman's constant based on asymptotic considerations—A new value. *J. Atmos. Sci.* **55**, 3403–3405.

Bergmann, J. C. 2000. Reply. *J. Atmos. Sci.* **57**, 1193–1195.

Bergstrom, R. W. 1972. Predictions of the spectral absorption and extinction coefficients of an urban air pollution aerosol model. *Atmos. Environ.* **6**, 247–258.

Bergstrom, R. W., and R. Viskanta. 1973a. Prediction of the solar radiant flux and heating rates in a polluted atmosphere. *Tellus* **25**, 486–498.

Bergstrom, R. W., and R. Viskanta. 1973b. Modeling of the effects of gaseous and particulate pollutants in the urban atmosphere. Part II. Pollutant dispersion. *J. Appl. Meteor.* **12**, 913–318.

Berkofsky, L. 1977. The relation between surface albedo and vertical velocity in a desert. *Contrib. Atmos. Phys.* **50**, 312–320.

Berkofsky, L. 1993. Comments on "Derivation of slope flow equations using two different coordinate representations." *J. Atmos. Sci.* **50**, 1444–1445.

Bernardet, L. R., L. D. Grasso, J. E. Nachamkin, C. A. Finley, and W. R. Cotton. 2000. Simulating convective events using a high-resolution mesoscale model. *J. Geophys. Res.* **105**, 14,963–14,982.

Berry, E. X. 1967. Cloud droplet growth by collection. *J. Atmos. Sci.* **24**, 688–701.

Betts, A. K. 1974. Thermodynamic classification of tropical convective soundings. *Mon. Wea. Rev.* **102**, 760–764.

Betts, A. K. 1975. Parametric interpretation of trade-wind cumulus budget studies. *J. Atmos. Sci.* **32**, 1934–1945.

Betts, A. K. 1976. Modelling subcloud layer structure and interaction with a shallow cumulus layer. *J. Atmos. Sci.* **33**, 2363–2382.

Betts, A. K. 1982. Saturation point analysis of moist convective overturning. *J. Atmos. Sci.* **39**, 1484–1505.

Betts, A. K. 1986. A new convective adjustment scheme. Part I: Observational and theoretical basis. *Quart. J. Roy. Meteor. Soc.* **112**, 677–692.

Betts, A. K., and M. J. Miller. 1986. A new convective adjustment scheme. Part II: Single column tests using GATE wave, BOMEX, ATEX, and Arctic air-mass data sets. *Quart. J. Roy. Meteor. Soc.* **112**, 693–709.

Betts, A. K., R. W. Grover, and M. W. Moncrieff. 1976. Structure and motion of tropical squall lines over Venezuela. *Quart. J. Roy. Meteor. Soc.* **102**, 395–404.

Betts, A. K., R. L. Desjardins, and J. I MacPherson. 1992. Budget analysis of the boundary layer grid flights during FIFE 1987. *J. Geophys. Res.* **97**, 18,533–18,546.

Betts, A. K., J. H. Ball, A. C. M. Beljaars, M. J. Miller, and P. Viterbo. 1996. The land-surface-atmosphere interaction: A review based on observational and global modelling perspectives. *J. Geophys. Res.* **101**, 7209–7225.

Betts, A. K., P. Viterbo, and A. C. M. Beljaars. 1998. Comparison of the land-surface interaction in the ECMWF reanalysis model with the 1987 FIFE Data. *Mon. Wea. Rev.* **126**, 186–198.

Beven, K. J. 1982. On subsurface stormflow, an analysis of response times. *Hydrol. Sci. J.* **27**, 505–521.

Beven, K. J. 1984. Infiltration into a class of vertically non-uniform soils. *Hydrol. Sci. J.* **29**, 424–434.

Bhumralkar, C. M. 1972. An observational and theoretical study of atmospheric flow over a heated island. National Science Foundation Final Report, Grant No. GA-14156. Rosenstiel School of Marine and Atmospheric Science, University of Miami, Coral Gables, FL.

Bhumralkar, C. M. 1973. An observational and theoretical study of atmospheric flow over a heated island. Parts I and II. *Mon. Wea. Rev.* **101**, 719–745.

Biggs, W. G., and M. E. Graves. 1962. A lake breeze index. *J. Appl. Meteor.* **1**, 474–480.

Bitan, A. 1981. Lake Kinneret (Sea of Galilee) and its exceptional wind system. *Bound.-Layer Meteor.* **21**, 477–487.

Bjerknes, J., and H. Solberg. 1921. *Meteorological Conditions for the Formation of Rain.* Geofysiske Publikationer, Vol. 2, No. 3, Oslo, Norway, I Kommission hos Cammermeyers Boghandel.

Black, P. G., and G. J. Holland. 1995. The boundary layer of Tropical Cyclone Kerry (1979). *Mon. Wea. Rev.* **123**, 2007–2008.

Black, T. J. 1994. The new NMC mesoscale Eta model: Description and forecast examples. *Wea. Forecasting* **9**, 265–278.

Black, T., M. Baldwin, G. DiMego, and E. Rogers. 1998. Results from daily forecasts of the NCEP Eta-10 model over the western United States. 12th AMS Conference on Numerical Weather Prediction, Phoenix, AZ, 246–247.

Blackadar, A. K. 1957. Boundary layer wind maxima and their significance for the growth of nocturnal inversions. *Bull. Amer. Meteor. Soc.* **38**, 283–290.

Blackadar, A. K. 1976. Modeling the nocturnal boundary layer. Preprint, AMS 3rd Symposium on Atmospheric Turbulence, Diffusion, and Air Quality, 46–49.

Blackadar, A. K. 1979. High-resolution models of the planetary boundary layer. In *Advances in Environmental Science and Engineering*, Vol. 1, J. R. Pfafflin and E. N. Ziegler, Eds., Gordon and Breach Science Publishers, New York, 50–85.

Blackadar, A. K., and H. Tennekes. 1968. Asymptotic similarity in neutral barotropic planetary boundary layers. *J. Atmos. Sci.* **25**, 1015–1020.

Blackford, B. L. 1978. Wind-driven inertial currents in the Magdalen Shallows, Gulf of St. Lawrence. *J. Phys. Oceanogr.* **8**, 655–665.

Blanchard, D. O. 1983. Variability of the convective field pattern in south Florida and its relationship to the synoptic flow. M.S. thesis, Dept. of Atmospheric Science, Colorado State University, Fort Collins, CO.

Bleck, R. 1978. On the use of hybrid vertical coordinates in numerical weather prediction models. *Mon. Wea. Rev.* **106**, 1233–1244.

Bleck, R., and D. B. Boudra. 1981. Initial testing of a numerical ocean circulation model using a hybrid (quasi-isopycnin) vertical coordinate. *J. Phys. Oceanogr.* **11**, 755–770.

Blodin, C. 1978. Un modele de meso-echelle-conception-utilisation-developement. Note Technique de L'Etablissement d'Etudes et de Recherches Météorologiques, Direction de la Météorologie, Ministére des Transports, Paris. (In French)

Blondin, C., and G. Therry. 1981. Analysis of particle trajectories during a land-sea breeze cycle using two-dimensional numerical mesoscale models. Proceedings, 12th NATO Committee on the Challenge of Modern Society, International Technical Symposium.

Bluestein, H. 1992. *Synoptic-Dynamic Meteorology in Midlatitudes. Volume I: Principles of Kinematics and Dynamics.* Oxford University Press, New York.

Bluestein, H. 1993. *Synoptic-Dynamic Meteorology in Midlatitudes. Volume II: Observations and Theory of Weather Systems.* Oxford University Press, New York.

Blumen, W., and C. D. McGregor. 1976. Wave drag by three-dimensional mountain lee-waves in nonplanar shear flow. *Tellus* **28**, 287–298.

Blumenthal, D. L., W. H. White, and T. B. Smith. 1978. Anatomy of a Los Angeles smog episode: Pollutant transport in the daytime sea breeze regime. *Atmos. Environ.* **15**, 893–907.

Bohren, C. F., and B. A. Albrecht. 1998. *Atmospheric Thermodynamics*. Oxford University Press, New York.

Bolle, H. J., J.-C. André Jr., J. L. Arrue, H. K. Barth, P. Bessemoulin, A. Brasa, H. A. R. de Bruin, J. Cruces, G. Dugdale, E. T. Engman, D. L. Evans, R. Fantechi, F. Fiedler, A. van de Griend, A. C. Imeson, A. Jochum, P. Kabat, T. Kratzsch, J. P. Lagouarde, I. Langer, R. Llamas, E. Lopez-Baeza, J. Melia Miralles, L. S. Muniosguren, F. Nerry, J. Noilhan, H. R. Oliver, R. Roth, S. S. Saatchi, J. Sanchez Dias, M. de Santa Olalla, W. J. Shuttleworth, H. Soegaard, J. Stricker, J. Thomes, M. Vauclin, and D. Wickland. 1993. EFEDA: European field experiment in a desertification threatened area. *Annales Geophysicae* **11**, 173–189.

Bolton, D. 1980. The computation of equivalent potential temperature. *Mon. Wea. Rev.* **108**, 1046–1053.

Bonan, G. B., F. S. Chapin III, and W. Wu. 1999. The impact of tundra ecosystems on the surface energy budget and climate of Alaska. *J. Geophys. Res.* **104**, 6647–6660.

Bond, N., C. Mass, B. Smull, R. Houze, M. Yang, B. Colle, S. Braun, M. Shapiro, B. Colman, P. Nieman, J. Overland, W. Neff, and J. Doyle. 1997. The coastal observation and simulation with topography (COAST) experiment. *Bull. Amer. Meteor. Soc.* **78**, 1941–1955.

Boone, A., J. C. Calvet, and J. Noilhan. 1999. Inclusion of a third soil layer in a land surface scheme using the force-restore method. *J. Appl. Meteor.* **38**, 1611–1630.

Boone, A., V. Masson, T. Meyers, and J. Noilhan. 2000. The influence of the inclusion of soil freezing on simulations by a soil-vegetation-atmosphere transfer scheme. *J. Appl. Meteor.* **39**, 1544–1569.

Bornstein, R., and Q. Lin. 2000. Urban heat islands and summertime convective thunderstorms in Atlanta: Three case studies. *Atmos. Environ.* **34**, 507–516.

Bornstein, R. D., and T. Oke. 1980. Influence of pollution and urbanization on urban climates. *Adv. Environ. Sci. Eng.* **3**, 171–202.

Bornstein, R. D., and A. Robock. 1976. Effects of unequal and variable advective and diffusive time steps in variable grid models. *Mon. Wea. Rev.* **104**, 260–267.

Bornstein, R. D., and W. T. Thompson. 1981. Effects of frictionally retarded sea breeze and synoptic frontal passages on sulfur dioxide concentrations in New York City. *J. Appl. Meteor.* **20**, 843–858.

Bornstein, R. D., P. Thunis, P. Grossi, and G. Schayes. 1996. Development of the topographic vorticity-mode mesoscale-beta (TVM) model. Part II: Evaluation. *J. Appl. Meteor.* **35**, 1824–1834.

Bornstein, R., P. Thunis, and G. Schayes. 1994. Observation and simulation of urban-topography barrier effects on boundary layer structure using the three dimensional TVM/URBMET model. In *Air Pollution and its Application*, Vol. X, Plenum Press, NY, 101–108.

Bosart, L. F. 1975. New England coastal frontogenesis. *Quart. J. Roy. Meteor. Soc.* **101**, 957–978.

Bosart, L. F. 1981. The President's Day snowstorm of 18–19 February 1979: A subsynoptic-scale event. *Mon. Wea. Rev.* **109**, 1542–1566.

Bosart, L. F. and F. Sanders. 1981. The Johnstown flood of July 1977: A long-lived convective system. *J. Atmos. Sci.* **38**, 1616–1642.

Bosart, L. F., C. J. Vaudo, and J. H. Helsdon Jr. 1972. Coastal frontogenesis. *J. Appl. Meteor.* **11**, 1236–1258.

Bosilovich, M. G., and W.-Y. Sun. 1998. Monthly simulation of surface layer fluxes and soil properties during FIFE. *J. Atmos. Sci.* **55**, 1170–1183.

Bossert, J. E., and W. R. Cotton. 1994a. Regional-scale flows in mountainous terrain. Part I: A numerical and observational comparison. *Mon. Wea. Rev.* **122**, 1449–1471.

Bossert, J. E., and W. R. Cotton. 1994b. Regional-scale flows in mountainous terrain. Part II: Simplified numerical experiments. *Mon. Wea. Rev.* **122**, 1472–1489.

Bosveld, F. C., A. A. M. Holtslag, and B. J. J. M. van den Hurk. 1999. Interpretation of crown radiation temperatures of a dense Douglas fir forest with similarity theory. *Bound.-Layer Meteor.* **92**, 429–451.

Bott, A. 1989. A positive definite advection scheme obtained by nonlinear renormalization of the advective fluxes. *Mon. Wea. Rev.* **117**, 1006–1015.

Bott, A. 1992. Monotone flux limitation in the area-preserving flux-form advection algorithm. *Mon. Wea. Rev.* **120**, 2592–2602.

Böttcher, M. 1996. A semi-Lagrangian advection scheme with modified exponential splines. *Mon. Wea. Rev.* **124**, 716–729.

Boudra, D. B. 1977. A numerical study describing regional modification of the atmosphere by the Great Lakes. Ph.D. dissertation, University of Michigan, Ann Arbor, MI.

Boudra, D. B. 1981. A study of the early winter effects of the Great Lakes. I: Comparison of very fine scale numerical simulations with observed data. *Mon. Wea. Rev.* **109**, 2507–2526.

Bougeault, P. 1983. A non-reflective upper boundary condition for limited-height hydrostatic models. *Mon. Wea. Rev.* **111**, 420–429.

Bougeault, P., A. Jansa Clar, B. Benech, B. Carissimo, J. Pelon, and E. Richard. 1990. Momentum budget over the Pyrenees: The PYREX experiment. *Bull. Amer. Meteor. Soc.* **71**, 806–818.

Bougeault, P., B. Benech, P. Bessemoulin, B. Carissimo, A. Jansa Clar, J. Pelon, M. Petitdidier, and E. Richard. 1997. PYREX: A summary of findings. *Bull. Amer. Meteor. Soc.* **78**, 637–650.

Bradberry, J. S. 1981. Mesoscale structure of an Oklahoma squall line. *Mon. Wea. Rev.* **109**, 1110–1117.

Brand, S., R. P. Chambers, W. J. Woo, J. C. Cermak, J. E. Lou, and M. Denard. 1979. A preliminary analysis of mesoscale effects of topography on tropical cyclone-associated surface winds. NAVENVPREDRESCHFAC Technical Report TR79-04, Naval Environmental Prediction Research Facility, Monterey, CA.

Brandt, A. 1977. Multi-level adaptive solutions to boundary value problems. *Math. Comput.* **31**, 333–390.

Branković, C. 1981. A transformed isentropic coordinate and its use in an atmospheric model. *Mon. Wea. Rev.* **109**, 2029–2039.

Bremer, D. J., and J. M. Ham. 1999. Effect of spring burning on the surface energy balance in a tallgrass prairie. *Agric. Forest Meteor.* **97**, 43–54.

Brewer, D. A., E. E. Remsberg, and G. E. Woodbury. 1981. A diagnostic model for studying daytime urban air-quality trends. Technical Paper 1843, NASA.

Brewster, K. 1996. Application of a Bratseth analysis scheme including Doppler radar data. Preprint, 15th AMS Conference on Weather Analysis and Forecasting, Norfolk, VA, 92–95.

Brinkmann, W. A. R. 1974. Strong downslope winds at Boulder, CO. *Mon. Wea. Rev.* **102**, 592–602.

Britter, R. E., J. C. R. Hunt, and K. J. Richards. 1981. Air flow over a two-dimensional hill: Studies of velocity speed-up, roughness effects and turbulence. *Quart. J. Roy. Meteor. Soc.* **107**, 91–110.

Broder, B., H. U. Dütsch, and W. Graber. 1981. Ozone fluxes in the nocturnal planetary boundary layer over hilly terrain. *Atmos. Environ.* **15**, 1195–1199.

Brook, J. R., L. Zhang, F. DiGiovanni, and J. Padro. 1999. Description and evaluation of a model of deposition velocities for routine estimates of air pollutant dry deposition over North America. Part I: Model development. *Atmos. Environ.* **33**, 5037–5051.

Brost, R. A., and J. C. Wyngaard. 1978. A model study of the stably stratified planetary boundary layer. *J. Atmos. Sci.* **35**, 1427–1440.

Brost, R. A., D. H. Lenschow, and J. C. Wyngaard. 1982a. Marine stratocumulus layers. Part I: Mean conditions. *J. Atmos. Sci.* **39**, 800–817.

Brost, R. A., D. H. Lenschow, and J. C. Wyngaard. 1982b. Marine stratocumulus layers. Part II: Turbulence budgets. *J. Atmos. Sci.* **39**, 818–836.

Brown, J. M. 1979. Mesoscale unsaturated downdrafts driven by rainfall evaporation: A numerical study. *J. Atmos. Sci.* **36**, 313–338.

Brown, P. S. Jr., and J. P. Pandolfo. 1980. A gravity-wave problem with the upstream difference method. *J. Comput. Phys.* **37**, 141–150.

Browning, K. A. 1980. Local weather forecasting. *Proc. Roy. Soc. London A* **371**, 179–211.

Browning, K. A. (Ed.). 1982. *Nowcasting*. Academic Press, London.

Browning, K. A. 1986. Conceptual models of precipitation systems. *Wea. Forecasting* **1**, 23–41.

Browning, K. A., and T. W. Harrold. 1970. Air motion and precipitation growth at a cold front. *Quart. J. Roy. Meteor. Soc.* **96**, 369–389.

Browning, K. A., and H. O. Kreiss. 1986. Scaling and computation of smooth atmospheric motions. *Tellus* **38**, 295–313.

Brutsaert, W. H. 1982a. *Evaporation into the Atmosphere: Theory, History and Applications*, D. Reidel, Norwell, MA.

Brutsaert, W. H. 1982b. Exchange processes at the earth-atmosphere interface. In *Engineering Meteorology*, E. Plate, Ed., Elsevier, New York, 319–369.

Brutsaert, W. H. 1998. Land-surface water vapor and sensible heat flux: Spatial variability, homogeneity, and measurement scales. *Water Resour. Res.* **34**, 2433–2442.

Brutsaert, W. H. 1999. Aspects of bulk atmospheric boundary layer similarity under free-convective conditions. *Rev. Geophys.* **37**, 439–451.

Bryant, N. A., L. F. Johnson, A. J. Brazel, R. C. Balling, C. F. Hutchinson, and L. R. Beck. 1990. Measuring the effect of overgrazing in the Sonoran desert. *Climatic Change* **17**, 243–264.

Buckingham, E. 1914. On physically similar systems; illustrations of the use of dimensional equations. *Phys. Rev. IV* **4**, 345.

Burba, G. G., S. B. Verma, and J. Kim. 1999. Energy fluxes of an open water area in a midlatitude prairie wetland. *Bound.-Layer Meteor.* **91**, 495–504.

Burgy, R., and C. Pomeroy. 1958. Interception losses in grassy vegetation *Trans. Am. Geophys. Union* **39**, 1095–1100.

Burk, S. D. 1977. The moist boundary layer with a higher order turbulence closure model. *J. Atmos. Sci.* **34**, 629–638.

Burk, S. D. 1981. Comparison of structure parameter scaling expression with turbulence closure model predictions. *J. Atmos. Sci.* **38**, 751–761.

Burk, S. D., and T. Haack. 2000. The dynamics of wave clouds upwind of coastal orography. *Mon. Wea. Rev.* **128**, 1438–1455.

Burk, S. D., and W. T. Thompson. 1989. A vertically nested regional numerical prediction model with second-order closure physics. *Mon. Wea. Rev.* **117**, 2305–2324.

Burk, S. D., T. Haack, and R. M. Samelson. 1999. Mesoscale simulation of supercritical, subcritical, and transcritical flow along coastal topography. *J. Atmos. Sci.* **56**, 2780–2795.

Burpee, R. W. 1979. Peninsula-scale convergence in the south Florida sea breeze. *Mon. Wea. Rev.* **107**, 852–860.

Busch, N., U. Ebel, H. Kraus, and E. Schaller. 1982. The structure of the subpolar inversion-capped ABL. *Arch. Meteor. Geophys. Bioklimatol. Ser. A*, 1–18.

Businger, J. A. 1973. Turbulent transfer in the atmospheric surface layer. In *Workshop on Micrometeorology*, D. A. Haugen, Ed., Chap. 2. American Meteorological Society, Boston, 67–100.

Businger, J. A., J. C. Wyngaard, Y. Izumi, and E. F. Bradley. 1971. Flux-profile relationships in the atmospheric surface layer. *J. Atmos. Sci.* **28**, 181–189.

Byers, H. R. 1959. *General Meteorology*. McGraw-Hill, New York.

Byers, H. R. 1965. *Elements of Cloud Physics*. The University of Chicago Press, Chicago.

Byers, H. R., and H. R. Rodebush. 1948. Causes of thunderstorms of the Florida peninsula. *J. Meteor.* **5**, 275–280.

Byun, D. W. 1990. On the analytical solutions of flux-profile relationships for the atmospheric surface layer. *J. Appl. Meteor.* **29**, 652–657.

Byun, D. W. 1999a. Dynamically consistent formulations in meteorological and air quality models for multiscale atmospheric studies. Part I: Governing equations in a generalized coordinate system. *J. Atmos. Sci.* **56**, 3789–3807.

Byun, D. W. 1999b. Dynamically consistent formulations in meteorological and air quality models for multiscale atmospheric studies. Part II: Mass conservation issues. *J. Atmos. Sci.* **56**, 3808–3820.

Cacciamani, C., D. Cesari, G. Grazzini, T. Paccagnella, and M. Pantone. 2000. Numerical simulation of intense precipitation events south of the Alps: Sensitivity to initial conditions and horizontal resolution. *Meteor. Atmos. Phys.* **72**, 147–159.

Cai, X.-M. 1999. Large-eddy simulation of the convective boundary layer over an idealized patchy urban surface. *Quart. J. Roy. Meteor. Soc.* **125**, 1427–1444.

Cai, X.-M., and D. G. Steyn. 2000. Modelling study of sea breezes in a complex coastal environment. *Atmos. Environ.* **34**, 2873–2885.

Calder, K. L. 1977. Multiple-source plume models of urban air pollution—Their general structure. *Atmos. Environ.* **11**, 403–414.

Camillo, P., and T. J. Schmugge. 1981. A computer program for the simulation of heat and moisture flow in soils. NASA Technical Memo 82121, NAS 5-24350. Available from NTIS.

Camuffo, D. 1982. The nocturnal IBL over a hilly island with reference to the diffusion of radioactive nuclei. *Bound.-Layer Meteor.* **22**, 233–240.

Caracena, F., R. A. Maddox, L. R. Hoxit, and C. F. Chappell. 1979. Mesoanalysis of the Big Thompson storm. *Mon. Wea. Rev.* **107**, 1–17.

Carbone, R. E. 1982. A severe frontal rainband. Part I: Stormwide hydrodynamics structure. *J. Atmos. Sci.* **39**, 258–279.

Carbone, R. E., J. W. Wilson, T. D. Keenan, and J. M. Hacker. 2000. Tropical island convection in the absence of significant topography. Part I: Lifecycle of diurnally forced convection. *Mon. Wea. Rev.* **128**, 3459–3480.

Carl, D. M., T. C. Tarbell, and H. A. Panofsky. 1973. Profiles of wind and temperature from towers over homogeneous terrain. *J. Atmos. Sci.* **30**, 788–794.

Carlson, T. N. 1991. *Mid-Latitude Weather Systems*. Harper Collins Academics, London.

Carlson, T. N., and J. A. Augustine. 1978. Temperature mapping of land use in urban areas using satellite data. *Earth Mineral Sci.* **47**, 41–45.

Carlson, T. N., and S. G. Benjamin. 1980. Radiative heating rates for Saharan dust. *J. Atmos. Sci.* **37**, 193–213.

Carpenter, K. M. 1979. An experimental forecast using a nonhydrostatic mesoscale model. *Quart. J. Roy. Meteor. Soc.* **105**, 629–655.

Carpenter, K. M. 1982a. Radiation conditions for the lateral boundaries of limited-area numerical models. *Quart. J. Roy. Meteor. Soc.* **108**, 717–719.

Carpenter, K. M. 1982b. Model forecasts for locally forced mesoscale systems. In *Nowcasting*, K. Browning, Ed. Academic Press, London.

Carpenter, K. M., and L. R. Lowther. 1981. Effect of varying the levels used in Florida sea-breeze simulation. Technical Note 150, British Meteorological Office.

Carpenter, K. M., and L. R. Lowther. 1982. An experiment on the initial conditions for a mesoscale forecast. *Quart. J. Roy. Meteor. Soc.* **108**, 643–660.

Carrier, G. F., M. Krook, and C. E. Pearson. 1966. *Functions of a Complex Variable, Theory and Technique*. McGraw-Hill, New York.

Carroll, J. J., and R. L. Baskett. 1979. Dependence of air quality in a remote location on local and mesoscale transports: A case study. *J. Appl. Meteor.* **18**, 474–486.

Carruthers, D. J., and T. W. Choularton. 1982. Airflow over hills of moderate slope. *Quart. J. Roy. Meteor. Soc.* **108**, 603–624.

Carsel, R. F., and R. S. Parrish. 1988. Developing joint probability distributions of soil water retention characteristics. *Water Resour. Res.* **24**, 755–769.

Carson, R. B. 1954. Some objective quantitative criteria for summer showers at Miami, Florida. *Mon. Wea. Rev.* **82**, 9–28.

Cassano, J. J., and T. R. Parish. 2000. An analysis of the nonhydrostatic dynamics in numerically simulated Antarctic katabatic flows. *J. Atmos. Sci.* **57**, 891–898.

Caughey, S. J., B. A. Crease, and W. T. Roach. 1982. A field study of nocturnal stratocumulus—II, turbulence structure and entrainment. *Quart. J. Roy. Meteor. Soc.* **108**, 125–144.

Cautenet, G., F. Guillard, B. Marticorena, G. Bergametti, F. Dulac, and J. Eds. 2000. Modeling of a Saharan dust event. *Meteor. Z.* **9**, 221–230.

Caya, A., R. Laprise, and P. Zwack. 1998. Consequences of using the splitting method for implementing physical forcings in a semi-implicit semi-Lagrangian model. *Mon. Wea. Rev.* **126**, 1707–1713.

Centre for Advanced Studies in Atmospheric and Fluids Science. 1983. A brief review of research and developments in atmospheric sciences. Report, Indian Institute of Technology, New Delhi, India.

Cermak, J. E. 1970. Air motion in and near cities—Determination by laboratory simulation. Report, Fluid Dynamics and Diffusion Laboratory, Colorado State University, Fort Collins, CO.

Cermak, J. E. 1971. Laboratory simulation of the atmospheric boundary layer. *AIAAJ* **9**, 1746–1754.

Cermak, J. E. 1975. Applications of fluid mechanics to wind engineering—A Freeman Scholar lecture. *J. Fluids Eng.* **97**, 9–38.

Cermak, J. E. 1996. Thermal effects on flow and dispersion over urban areas: Capabilities for prediction by physical modeling. *Atmos. Environ.* **30**, 393–401.

Cerni, T. A. 1982. Comments on the ratio of diffuse to direct solar irradiance (perpendicular to the sun's rays) with clear skies—A conserved quantity throughout the day. *J. Appl. Meteor.* **21**, 886–887.

Ceselski, B. F. 1974. Cumulus convection in weak and strong tropical disturbance. *J. Appl. Sci.* **31**, 1241–1255.

Chamberlain, A. C. 1983. Roughness length of sea, sand and snow. *Bound.-Layer Meteor.* **25**, 405–409.

Chang, C. 1970. A mesoscale numerical model of airflow over the Black Hills. M.S. thesis, Dept. of Meteorology, South Dakota School of Mines and Technology, Rapid City, SD.

Chang, C. B., D. J. Perkey, and C. W. Kreitzberg. 1981. A numerical case study of the squall line of 6 May 1975. *J. Atmos. Sci.* **38**, 1601–1615.

Chang, C. H. 1977. Ice generation in clouds. M.S. thesis, Dept. of Meteorology, South Dakota School of Mines and Technology, Rapid City, SD.

Chang, J. T., and P. J. Wetzel. 1991. Effects of spatial variations of soil moisture and vegetation on the evolution of a prestorm environments: A numerical case study. *Mon. Wea. Rev.* **119**, 1368–1390.

Chang, S. W. 1979. An efficient parameterization of convective and nonconvective planetary boundary layers for use in numerical models. *J. Appl. Meteor.* **18**, 1205–1215.

Chang, S. W. 1982. *The Orographic Effects Induced by an Island Mountain Range on Propagating Tropical Cyclones*. Science Applications, McLean, VA.

Chang, S. W., and R. A. Anthes. 1978. Numerical simulations of the ocean's nonlinear, baroclinic response to translating hurricanes. *J. Phys. Oceanogr.* **8**, 468–480.

Chang, S. W., and H. D. Orville. 1973. Large-scale convergence in a numerical cloud model. *J. Atmos. Sci.* **30**, 947–950.

Chang, S., D. Hahn, C.-H. Yang, and D. Norquist. 1999. Validation study of the CAPS model land surface scheme using the 1987 Cabauw/PILPS dataset. *J. Appl. Meteor.* **38**, 405–422.

Changnon, S. A. Jr. 1980. Evidence of urban and lake differences on precipitation in the Chicago area. *J. Appl. Meteor.* **19**, 1137–1159.

Changnon, S. A. Jr. 1982. Visibility changes caused by St. Louis. *Atmos. Environ.* **16**, 595–598.

Chapin, F. S. III, L. D. Hinzman, W. Wu, E. Lilly, G. Vourlitis, and E. Kim. 1999. Surface energy balance on the Arctic tundra: Measurements and models. *J. Climate* **12**, 2583–2604.

Chappell, C. F., D. R. Smith, and E. C. Nickerson. 1978. Numerical simulation of clouds and snowfall over mountainous terrain. *Preprints, Conferences on Cloud Physics, Atmos. Electr.*, American Meteorological Society, Boston, 259–265.

Charlock, T. P. 1982. Cloud optical feedback and climate stability in a radiative-convective model. *Tellus* **34**, 245–254.

Chase, T. N., R. A. Pielke, Sr., T. G. F. Kittel, J. S. Baron, and T. J. Stohlgren. 1999. Potential impacts on Colorado Rocky Mountain weather due to land use changes on the adjacent Great Plains. *J. Geophys. Res.* **104**, 16,673–16,690.

Chaudhry, F. H., and J. E. Cermak. 1971. Wind-tunnel modeling of flow and diffusion over an urban complex. Project Themis Technical Report No. 17, Fluid Dynamics and Diffusion Laboratory, Colorado State University, Fort Collins, CO.

Chen, C., and W. R. Cotton. 1983a. Numerical experiments with a one-dimensional higher turbulence model simulation of the Wangara Day 33 case. *Bound.-Layer Meteor.* **25**, 375–404.

Chen, C., and W. R. Cotton. 1983b. A one-dimensional simulation of the stratocumulus-capped mixed layer. *Bound.-Layer Meteor.* **25**, 289–321.

Chen, C., and H. D. Orville. 1980. Effects of mesoscale convergence on cloud convection. *J. Appl. Meteor.* **19**, 256–274.

Chen, D.-X., and M. B. Coughenour. 1994. GEMTM: A general model for energy and mass transfer of land surfaces and its application at the FIFE sites. *Agric. Forest Meteor.* **68**, 145–171.

Chen, F., and R. Avissar. 1994. Impact of land-surface moisture variability on local shallow convective cumulus and precipitation in large-scale models. *J. Appl. Meteor.* **33**, 1382–1401.

Chen, F., Z. Janjić, and K. Mitchell. 1997. Impact of atmospheric surface layer parameterization in the new land-surface scheme of the NCEP mesoscale Eta numerical model. *Bound.-Layer Meteor.* **85**, 391–421.

Chen, F., and K. Mitchell. 1999. Using the GEWEX/ISLSCP forcing data to simulate global soil moisture fileds and hydrological cycle for 1987–1988. *J. Meteor. Soc. Japan* **77**, 167–182.

Chen, F., K, Mitchell, J. Schaake, Y. Xue, H. L. Pan, V. Koren, Q. Y. Duan, K. Ek, and A. Betts. 1996. Modeling of land-surface evaporation by four schemes and comparison with FIFE observations. *J. Geophys. Res.* **101**, 7251–7268.

Chen, F., R. Pielke, Sr., and K. Mitchell. 2001. Development and application of land-surface models for mesoscale atmospheric models: Problems and Promises. In *Observation and Modeling of the Land Surface Hydrological Process*, V. Lakshmi, J. Alberston, and J. Schaake, Eds., American Geophysical Union, **3**, 107–135.

Chen, J. H. 1973. Numerical boundary conditions and computational modes. *J. Comput. Phys.* **13**, 522–535.

Chen, R.-R., N. S. Berman, D. L. Boyer, and H. J. S. Fernando. 1999a. Physical model of nocturnal drainage flow in complex terrain. *Contrib. Atmos. Phys.* **72**, 219–242.

Chen, S.-J., D.-K. Lee, Z.-Y. Tao, and Y.-H. Kuo. 1999b. Mesoscale convective system over the Yellow Sea—A numerical case study. *Meteor. Atmos. Phys.* **70**, 185–199.

Ching, J. K. S., J. F. Clarke, and J. M. Godowitch. 1983. Modulation of heat flux by different scales of advection in an urban environment. *Bound.-Layer Meteor.* **25**, 171–191.

Chisholm, A. J. 1970. Alberta hailstorms: A radar study and model. Ph.D. Thesis, McGill University, Montreal, Canada.

Chlond, A. 1994. Locally modified version of Bott's advection scheme. *Mon. Wea. Rev.* **122**, 111–125.

Chopra, K. P. 1973. Atmospheric and oceanic flow problems introduced by islands. *Adv. Geophys.* **16**, 297–421.

Chou, M.-D. 1990. Parameterization for the absorption of solar radiation by O_2 and CO_2 with application to climate studies. *J. Climate* **3**, 209–217.

Chou, M.-D. 1992. A solar radiation model for climate studies. *J. Atmos. Sci.* **49**, 762–772.

Chou, M.-D., and M. J. Suarez. 1994. An efficient thermal infrared radiation parameterization for use in general circulation models. Technical Memo 104606, Linthicum NASA Center for Aerospace Information, Linthicum Heights, MD.

Chou, S.-H., and D. Atlas. 1981. Estimating ocean-air heat fluxes during cold air outbreaks by satellite. Technical Memo 83854, NASA, Goddard Space Flight Center, Greenbelt, MD.

Chou, S.-H., and D. Atlas. 1982. Satellite estimates of ocean-air heat fluxes during cold air outbreaks. *Mon. Wea. Rev.* **110**, 1434–1450.

Christensen, O., and L. P. Prahm. 1976. A pseudospectral model for dispersion of atmospheric pollutants. *J. Appl. Meteor.* **15**, 1284–1294.

Churchill, R. V. 1963. *Fourier Series and Boundary Value Problems.* McGraw-Hill, New York.

Chýlek, P., and V. Ramaswamy. 1982. Simple approximation for infrared emissivity of water clouds. *J. Atmos. Sci.* **39**, 171–177.

Cionco, R. M. 1994. Overview of the project WIND data. In *Mesoscale Modeling of the Atmosphere*, R. A. Pielke and R. P. Pearce, Eds., American Meteorological Society, Boston, 63–71.

Cionco, R. M., W. aufm Kampe, C. Biltoft, J. H. Byers, C. G. Collins, T. J. Higgs, A. R. T. Hin, P.-E. Johansson, C. D. Jones, H. E. Jorgensen, J. F. Kimber, T. Mikkelsen, K. Nyren, D. J. Ride, R. Robson, J. M. Santabarbara, J. Streicher, S. Thykier-Nielsen, H. van Raden, and H. Weber. 1999. An overview of MADONA: A multinational field study of high-resolution meteorology and diffusion over complex terrain. *Bull. Amer. Meteor. Soc.* **80**, 5–19.

Cione, J. J., P. G. Black, and S. H. Houston. 2000. Surface observations in the hurricane environment. *Mon. Wea. Rev.* **128**, 1550–1561.

Clancy, R. M., J. D. Thompson, J. D. Lee, and H. E. Hurlburt. 1979. A model of mesoscale air-sea interaction in a sea breeze-coastal upwelling regime. *Mon. Wea. Rev.* **107**, 1476–1505.

Clapp, R., and G. Hornberger. 1978. Empirical equations for some soil hydraulic properties. *Water Resour. Res.* **14**, 601–604.

Clappier, A., A. Martilli, P. Grossi, P. Thunis, F. Pasi, B. C. Krueger, B. Calpini, G. Graziani, and H. Van Den Bergh. 2000. Effect of sea breeze on air pollution in the greater Athens area. Part I: Numerical simulations and field observations. *J. Appl. Meteor.* **39**, 546–562.

Clark, C. A., and R. W. Arritt. 1995. Numerical simulations of the effect of soil moisture and vegetation cover on the development of deep convection. *J. Appl. Meteor.* **34**, 2029–2045.

Clark, O. 1940. Interception of rainfall by prairie grasses, weeds, and certain crop plants. *Ecol. Monographs* **10**, 244–277.

Clark, T. L. 1973. Numerical modeling of the dynamics and microphysics of warm cumulus convection. *J. Atmos. Sci.* **30**, 857–878.

Clark, T. L. 1977. A small-scale dynamic model using a terrain-following coordinate transformation. *J. Comput. Phys.* **24**, 186–215.

Clark, T. L. 1979. Numerical simulations with a three-dimensional cloud model. Lateral boundary condition experiments and multicellular severe storm simulations. *J. Atmos. Sci.* **36**, 2191–2215.

Clark, T. L., and R. D. Farley. 1984. Severe downslope windstorm calculations in two and three spatial dimensions using anelastic interactive grid nesting: A possible mechanism for gustiness. *J. Atmos. Sci.* **41**, 329–350.

Clark, T. L., and R. Gall. 1982. Three-dimensional numerical model simulations of airflow over mountainous terrain: A comparison with observations. *Mon. Wea. Rev.* **110**, 766–791.

Clark, T. L., and W. R. Peltier. 1977. On the evolution and stability of finite-amplitude mountain waves. *J. Atmos. Sci.* **34**, 1714–1730.

Clarke, R. H., A. J. Dyer, P. R. Brook, D. G. Reid, and A. J. Troup. 1971. The Wangara Experiment—Boundary layer data. Paper 19, Division of Meteorological Physics, CSIRO, Australia.

Clarke, R. H., R. K. Smith, and D. G. Reid. 1981. The morning glory of the Gulf of Carpentaria: An atmospheric undular bore. *Mon. Wea. Rev.* **109**, 1726–1750.

Claussen, M. (Ed.). 2002. Does landsurface matter in climate and weather? In *Biospheric Feedbacks in the Climate System and the Hydrological Cycle*, Part A. In: Vegetation, Water, Humans and the Climate: A New Perspective on an Interactive System, A Synthesis of the IGBP Core Project, Biosphere Aspects of the Hydrological Cycle, in preparation.

Clements, W. E., and C. J. Nappo. 1983. Observation of a drainage flow event on a high-altitude simple slope. *J. Climate Appl. Meteor.* **22**, 331–335.

Climate and Man. 1941. U.S. Dept. of Agriculture Handbook, US Govt. Printing Office, Washington, 1248 pp.

Colby, F. P. Jr. 1980. The role of convective instability in an Oklahoma squall line. *J. Atmos. Sci.* **37**, 2113–2119.

Colle, B. A., and C. F. Mass. 2000. High-resolution observations and numerical simulations of easterly gap flow through the Strait of Juan de Fuca on 9–10 December 1995. *Mon. Wea. Rev.* **128**, 2398–2422.

Colle, B. A., K. J. Westrick, and C. F. Mass. 1999. Evaluation of MM5 and Eta-10 precipitation forecasts over the Pacific Northwest during the cool season. *Wea. Forecasting* **14**, 137–154.

Collela, P., and P. Woodward. 1984. The piece-wise parabolic method (PPM) for gas dynamical simulations. *J. Comp. Phys.* **54**, 174–201.

Collier, C. G. 1975. A representation of the effects of topography on surface rainfall within moving baroclinic disturbances. *Quart. J. Roy. Meteor. Soc.* **101**, 407–422.

Collier, C. G. 1977. The effect of model grid length and orographic rainfall efficient on computed surface rainfall. *Quart. J. Roy. Meteor. Soc.* **103**, 247–253.

Colton, D. E. 1976. Numerical simulation of the orographically induced precipitation distribution for use in hydrologic analysis. *J. Appl. Meteor.* **15**, 1241–1251.

Cooper, H. J., M. Garstang, and J. Simpson. 1982. The diurnal interaction between convection and peninsular-scale forcing over south Florida. *Mon. Wea. Rev.* **110**, 486–503.

Cope, M., D. Hess, S. Lee, M. Azzi, J. Carras, N. Wong, and M. Young. 1999. Development of the Australian air quality forecasting system. Current status. Proceedings of the International Conference on Urban Climatology, Sydney, Australia, November 8–12, 1999.

Costa, A. A., and A. J. C. Sampaio. 1997. Bott's area-preserving flux form advection algorithm: Extension to higher orders and additional tests. *Mon. Wea. Rev.* **125**, 1983–1989.

Costa, A. A., R. A. Pielke Sr., and G. Dalu. 2000. Errors due to non-linear wave interactions in flux-corrected schemes. Unpublished manuscript.

Costa, A. A., W. R. Cotton, R. L. Walko, and R. A. Pielke Sr. 2001. Coupled ocean-cloud-resolving simulations of the air-sea interaction over the equatorial western Pacific. *J. Atmos. Sci.*, in press.

Cotton, W. R. 1975. Theoretical cumulus dynamics. *Rev. Geophys. Space Phys.* **13**, 419–448.

Cotton, W. R., and R. A. Anthes. 1989. *Storm and Cloud Dynamics*. Academic Press, San Diego.

Cotton, W. R., and R. A. Pielke. 1995. *Human Impacts on Weather and Climate*. Cambridge University Press, New York.

Cotton, W. R., and G. J. Tripoli. 1978. Cumulus convection in shear flow three-dimensional numerical experiments. *J. Atmos. Sci.* **35**, 1503–1521.

Cotton, W. R., R. A. Pielke, and P. T. Gannon. 1976. Numerical experiments on the influence of the mesoscale circulation on the cumulus scale. *J. Atmos. Sci.* **33**, 252–261.

Cotton, W. R., R. L. George, and K. R. Knupp. 1982a. An intense, quasi-steady thunderstorm over mountainous terrain. Part I: Evolution of the storm-initiating mesoscale circulation. *J. Atmos. Sci.* **39**, 328–342.

Cotton, W. R., M. A. Stephens, T. Nehrkorn, and G. J. Tripoli. 1982b. The Colorado State University three-dimensional cloud/mesoscale model—1981. Part II: An ice phase parameterization. *J. Rech. Atmos.* **16**, 295–320.

Cotton, W. R., R. L. George, P. J. Wetzel, and R. L. McAnelly. 1983. A long-lived mesoscale convective complex. Part I—The mountain generated component. *Mon. Wea. Rev.* **111**, 1893–1918.

Cotton, W. R., G. Thompson, and P. W. Mielke. 1994. Realtime mesoscale prediction on workstations. *Bull. Amer. Meteor. Soc.* **75**, 349–362.

Coulson, K. L. 1975. *Solar and Terrestrial Radiation*. Academic Press, New York.

Coughlan, M., and R. Avissar. 1996. The Global Energy and Water Cycle Experiment (GEWEX) Continental-Scale International Project (GCIP): An overview. *J. Geophys. Res.* **101**, 7139–7147.

Covez, L. 1971. Mountain waves in a turbulent atmosphere. *Tellus* **23**, 104–109.

Cox, R., B. L. Bauer, and T. Smith. 1998. A mesoscale model intercomparison. *Bull. Amer. Meteor. Soc.* **79**, 265–283.

Cram, J. M., and R. A. Pielke. 1989. Further comparison of two synoptic surface wind and pressure analysis methods. *Mon. Wea. Rev.* **117**, 696–706.

Cram, J. M., R. A. Pielke Sr., and W. R. Cotton. 1992a. Numerical simulation and analysis of a prefrontal squall line. Part I: Observations and basic simulation results. *J. Atmos. Sci.* **49**, 189–208.

Cram, J. M., R. A. Pielke Sr., and W. R. Cotton. 1992b. Numerical simulation and analysis of a prefrontal squall line. Part II: Propagation of the squall line as an internal gravity wave. *J. Atmos. Sci.* **49**, 209–225.

Crook, N. A. 1996. Sensitivity of moist convection forced by boundary layer processes to low-level thermodynamic fields. *Mon. Wea. Rev.* **124**, 1767–1785.

Crook, N. A., and J. B. Klemp. 2000. Lifting by convergence lines. *J. Atmos. Sci.* **57**, 873–890.

Csanady, G. T. 1975. Lateral momentum flux in boundary currents. *J. Phys. Oceanogr.* **5**, 705–717.

Cuijpers, J. W. M., and A. A. M. Holtslag. 1998. Impact of skewness and nonlocal effects on scalar and buoyancy fluxes in convective boundary layers. *J. Atmos. Sci.* **55**, 151–162.

Cullen, M. J. P. 1976. On the use of artificial smoothing in Galerkin and finite difference solutions of the primitive equations. *Quart. J. Roy. Meteor. Soc.* **102**, 77–93.

Cunning, J. B., R. L. Holle, P. T. Gannon, and A. I. Watson. 1982. Convective evolution and merger in the FACE experimental area: Mesoscale convergence and boundary layer interactions. *J. Appl. Meteor.* **21**, 953–977.

Cutrim, E., D. W. Martin, and R. Rabin. 1995. Enhancement of cumulus clouds over deforested lands in Amazonia. *Bull. Amer. Meteor. Soc.* **76**, 1801–1805.

Dabberdt, W. F. 2001. On the confluence of mesoscale meteorological research and urban air pollution applications. In preparation.

Daggupaty, S. M. 1997. A case study of the simultaneous development of three lake breeze fronts with a boundary layer forecast model. Preprint, AMS 1st Symposium on Integrated Observing Systems, Long Beach, CA, 150–154.

Daggupaty, S. M. 1998. Numerical modelling of the impact of lead emissions to Lake Ontario and vicinity from Ontario industrial point sources. Abstract, IAGLR'98 Conference, Hamilton, Ontario, May 18–22, p. 100.

Daggupaty, S. M. 2001. A case study of the simultaneous development of multiple lake-breeze fronts with a boundary layer forecast model. *J. Appl. Meteor.* **40**, 239–311.

Daggupaty, S. M., and J. Ma. 1999. Parameterization of sub-grid scale surface fluxes by stability dependence height scales and effective roughness length in a mesoscale model. Preprint, AMS 13th Symposium on Boundary Layers and Turbulence, Dallas, TX, 464–467.

Daggupaty, S. M., R. S. Tangirala, and H. Sahota. 1994. BLFMESO—A 3-dimensional mesoscale meteorological model for microcomputers. *Bound.-Layer Meteor.* **71**, 81–107.

Dai, Y. J., and Q. Zeng. 1997. A land surface model (IAP94) for climate studies, Part I: Formulation and validation in off-line experiments. *Adv. Atmos. Sci.* **14**, 433–459.

Dai, Y. J., F. Xue, and Q. Zeng. 1998. A land surface model (IAP94) for climate studies, Part II: implementation and preliminary results of coupled model with IAP GCM. *Adv. Atmos. Sci.* **15**, 47–62.

Daley, R. 1979. The application of non-linear normal mode initialization to an operational forecast model. *Atmos. Ocean* **17**, 97–124.

Daley, R. 1980. The development of efficient time integration schemes using model normal modes. *Mon. Wea. Rev.* **108**, 100–110.

Daley, R. 1981. Normal mode initialization. *Rev. Geophys. Space Phys.* **19**, 450–468.

Dalu, G. A. 1978. A parameterization of heat convection for a numerical sea breeze model. *Quart. J. Roy. Meteor. Soc.* **104**, 797–807.

Dalu, G. N. and J. S. A. Green. 1980. Energetics of diabatic mesoscale circulation: A numerical study. *Quart. J. Roy. Meteor. Soc.* **106**, 727–734.

Dalu, G. A. and R. A. Pielke. 1989. An analytical study of the sea breeze. *J. Atmos. Sci.* **46**, 1815–1825.

Dalu, G. A., and R. A. Pielke. 1993. Vertical heat fluxes generated by mesoscale atmospheric flow induced by thermal inhomogeneities in the PBL. *J. Atmos. Sci.* **50**, 919–926.

Dalu, G. A., R. A. Pielke, R. Avissar, G. Kallos, M. Baldi, and A. Guerrini. 1991. Linear impact of thermal inhomogeneities on mesoscale atmospheric flow with zero synoptic wind. *Ann. Geophys.* **9**, 641–647.

Dalu, G. A., R. A. Pielke, M. Baldi, and X. Zeng. 1996. Heat and momentum fluxes induced by thermal inhomogeneities with and without large-scale flow. *J. Atmos. Sci.* **53**, 3286–3302.

Dalu, G. A., R. A. Pielke, P. L. Vidale, and M. Baldi. 2000. Heat transport and weakening of the atmospheric stability induced by mesoscale flows. *J. Geophys. Res.* **105**, 9349–9363.

Danard, M. 1977. A simple model for mesoscale effects of topography on surface winds. *Mon. Wea. Rev.* **105**, 572–581.

Danielson, K. S., and W. R. Cotton (Eds.). 1977. Space log 1977. Dept. of Atmospheric Science, Colorado State University, Fort Collins, CO.

Das, S., D. Johnson, and W.-K. Tao. 1999. Single-column and cloud ensemble model simulations of TOGA-COARE convective systems. *J. Meteor. Soc. Japan* **77**, 803–826.

Davenport, A. G., C. S. B. Grimmond, T. R. Oke, and J. Wieringa, 2000. Estimating the rough-
ness of cities and sheltered country. Preprint, 12th AMS Conference on Applied Climatology,
Asheville, NC, 1–4.

Davidson, N. E., and H. C. Weber. 2000. The BMRC high-resolution tropical cyclone prediction
system: TC-LAPS. *Mon. Wea. Rev.* **128**, 1245–1265.

Davies, H. C. 1976. A lateral boundary formulation for multi-level prediction models. *Quart. J.
Roy. Meteor. Soc.* **102**, 405–418.

Davis, H. C. 1983. Limitations of some common lateral boundary schemes used in regional NWP
models. *Mon. Wea. Rev.* **111**, 1002–1012.

Day, S. 1953. Horizontal convergence and the occurrence of summer precipitation at Miami, Florida.
Mon. Wea. Rev. **81**, 155–161.

Dayan, U., and J. Rodnizki. 1999. The temporal behavior of the atmospheric boundary layer in
Israel. *J. Appl. Meteor.* **38**, 830–836.

DeBruin, H. A. R. 1999. A note on Businger's derivation of nondimensional wind and temperature
profiles under unstable conditions. *J. Appl. Meteor.* **38**, 626–628.

de Jong, B. 1973. *Net Radiation Received by a Horizontal Surface at the Earth*. Delft University
Press, Nijgh-Wolters-Noordhoff University Publishers, Rotterdam, The Netherlands.

DeRidder, K., and H. Gallee. 1998. Land surface-induced regional climate change in southern Israel.
J. Appl. Meteor. **37**, 1470–1485.

DeRidder, K., and G. Schayes. 1997. The IAGL land surface model. *J. Appl. Meteor.* **36**, 167–182.

DeWekker, S. F. J., S. Zhong, J. D. Fast, and C. D. Whiteman. 1998. A numerical study of the
thermally driven plain-to-basin wind over idealized basin topographies. *J. Appl. Meteor.* **37**,
606–622.

de Wispelaere, C. (Ed.). 1981. *Air Pollution Modeling and Its Application*. Plenum Press, New York.

Deardorff, J. W. 1966. The contragradient heat flux in the lower atmosphere and in the laboratory.
J. Atmos. Sci. **23**, 503–506.

Deardorff, J. W. 1972. Parameterization of the planetary boundary layer for use in general circulation
models. *Mon. Wea. Rev.* **100**, 93–106.

Deardorff, J. W. 1973. Three-dimensional modeling of the planetary boundary layer. In *Workshop
on Micrometeorology*, Chap. 7, D. A. Haugen, Ed. American Meteorological Society, Boston,
271–311.

Deardorff, J. W. 1974a. Three-dimensional numerical study of the height and mean structure of a
heated planetary boundary layer. *Bound.-Layer Meteor.* **7**, 81–106.

Deardorff, J. W. 1974b. A three-dimensional numerical study of turbulence in an entraining mixed
layer. *Bound.-Layer Meteor.* **7**, 199–226.

Deardorff, J. W. 1978. Efficient prediction of ground surface temperature and moisture, with inclu-
sion of a layer of vegetation. *J. Geophys. Res.* **83**, 1889–1903.

Deardorff, J. W. 1980. Stratocumulus-capped mixed layers derived from a three-dimensional model.
Bound.-Layer Meteor. **18**, 495–527.

Deardorff, J. W. 1981. On the distribution of mean radiative cooling at the top of a stratocumulus-
capped mixed layer. *Quart. J. Roy. Meteor. Soc.* **107**, 191–202.

Deaven, D. G. 1974. A solution for boundary problems in isentropic coordinate models. Ph.D.
dissertation, Pennsylvania State University, University Park, PA.

Deaven, D. G. 1976. Solution for boundary problems in isentropic coordinate models. *J. Atmos. Sci.*
33, 1702–1713.

Defant, F. 1950. Theorie der land- und seewind. *Arch. Meteor. Geophys. Bioklimatol., Ser. A* **2**,
404–425. (In German)

Defant, F. 1951. Local winds. In *Compendium of Meteorology*, T. F. Maloney, Ed., American Mete-
orological Society, Boston, 655–672.

Delage, Y., and P. A. Taylor. 1970. A numerical study of heat island circulations. *Bound.-Layer Meteor.* **1**, 201–226.

Deng, A. 1999. A shallow convection parameterization scheme for mesoscale models. Ph.D. thesis, Dept. of Meteorology, Pennsylvania State University, University Park, PA.

Deng, A., N. L. Seaman, and J. S. Kain. 1999. Evaluation of the Penn State shallow convection scheme in the marine atmosphere using the ASTEX first Lagrangian experiment. Preprint, 9th PSU/NCAR MM5 Users' Workshop, June 23–24, Boulder, CO.

Deng, A., N. L. Seaman, and A. M. Lario-Gibbs. 2000. A shallow convection scheme of 3-D regional scale air quality applications. 11th AMS Conference on Applications of Air Pollution Meteorology with A&WMA, Long Beach, CA, January 9–14, pp. 102–106.

Derickson, R. G. 1974. Three dimensional modeling of cold orographic cloud systems. Preprint, AMS Conference on Cloud Physics, Tucson, AZ, October 21–24, pp. 227–232.

Derickson, R. G. 1992. Finite difference methods in geophysical flow simulations. Ph.D. dissertation, Dept. of Civil Engineering, Colorado State University, Fort Collins, CO.

Derickson, R. G., and R. A. Pielke. 2000. A preliminary study of Burger's Equation with symbolic computation. *J. Comput. Phys.* **162**, 219–244.

Desjardins, S., R. Benoit, and V. Swail. 1998. The influence of mesoscale features of the sea surface temperature distribution on marine boundary layer winds off the Scotian Shelf during the superstorm of March 1993. *Mon. Wea. Rev.* **126**, 2793–2808.

Dickerson, M. H. 1978. MASCON—A mass-consistent atmospheric flux model for regions with complex terrain. *J. Appl. Meteor.* **17**, 241–253.

Dickerson, M. H., and P. H. Gudiksen. 1980. ASCOT-FY-1979 progress report. Lawrence Livermore National Laboratory Report, UCRL-42899, ASCOT-1, Livermore, CA.

Dickerson, M. H., and P. H. Gudiksen. 1981. ASCOT-FY-1981 progress report. Lawrence Livermore National Laboratory Report UCID-18878-81, ASCOT-2, Livermore, CA.

Dickinson, R. E. 1984. Modeling evapotranspiration for three-dimensional global climate models. *AGU Geophysical Monograph, Maurice Ewing, Vol. 5* **29**, 58–72.

Dickinson, R. E., A. Henderson-Sellers, P. J. Kennedy, and M. F. Wilson. 1986. Biosphere-Atmosphere Transfer Scheme (BATS) for the NCAR Community Climate Model. Technical Report NCAR/TN-275+STR, National Center for Atmospheric Research, Boulder, CO.

Dickison, R. B. B., M. J. Haggis, and R. C. Rainey. 1983. Spruce budworm moth flight and storms: Case study of a cold front system. *J. Climate Appl. Meteor.* **22**, 278–286.

Ding, Y., J. Zhang, and Z. Zhao. 2000. An improved land-surface process model and its simulation experiment—Part II: coupling simulation experiment of land-surface process model with regional climate model. *Acta Meteorologica Sinica* **14**, 30–45.

Dirmeyer, P. A. 1994. Vegetation stress as a feedback mechanism in midlatitude drought. *J. Climate* **7**, 1463–1483.

Dirmeyer, P. A., A. J. Dolman, and N. Sato. 1999. The pilot phase of the Global Soil Wetness Project. *Bull. Amer. Meteor. Soc.* **80**, 1–27.

Dirmeyer, P. A., F. J. Zeng, A. Ducharne, J. C. Morrill, and R. D. Koster. 2000. The sensitivity of surface fluxes to soil water content in three land surface schemes. *J. Hydrometeorol.* **1**, 121–134.

Dobosy, R. 1979. Dispersion of atmospheric pollutants in flow over the shoreline of a large body of water. *J. Appl. Meteor.* **18**, 117–132.

Dolman, A. J., M. A. Silva Dias, J.-C. Calvet, M. Ashby, A. S. Tahara, C. Delire, P. Kabat, G. A. Fisch, and C. A. Nobre. 1999. Mesoscale effects of tropical deforestation in Amazonia: Preparatory LBA modelling studies. *Agric. Meteor.* **17**, 1095–1110.

Donaldson, C. du P. 1973. Construction of a dynamic model of the production of atmospheric turbulence and dispersion of atmospheric pollutants. In *Workshop Micrometeorology*, Chap. 8, D. A. Haugen, Ed. American Meteorological Society, Boston, 313–392.

Donelan, M. A., W. M. Drennan, and K. B. Katsaros. 1997. The air-sea momentum flux in conditions of wind, sea, and swell. *J. Phys. Oceanogr.* **27**, 2087–2099.

Doneaud, A. A., J. R. Miller Jr., D. L. Priegnitz, and L. Viswanath. 1983. Surface mesoscale features as potential storm predictors in the northern Great Plains—Two case studies. *Mon. Wea. Rev.* **111**, 273–293.

Doran, E. 1979. Objective analysis of mesoscale flow fields in Israel and trajectory calculations. *Israel J. Earth Sci.* **28**, 33–41.

Doran, E. and J. Neumann. 1977. Land and mountain breezes with special attention to Israel's Mediterranean coastal plain. G. Steinitz Memorial Volume, *Israel Meteorol. Res. Papers* **1** 109–122.

Doran, J. C., and T. W. Horst. 1983. Observations and models of simple nocturnal slope flows. *J. Atmos. Sci.* **40**, 708–717.

Doran, J. C., and S. Zhong. 2000. Thermally driven gap winds into the Mexico City Basin. *J. Appl. Meteor.* **39**, 1330–1340.

Dorman, C. E., D. P. Rogers, W. A. Nuss, and W. T. Thompson. 1999. Adjustment of the summer marine boundary layer around Pt. Sur, California. *Mon. Wea. Rev.* **127**, 2143–2159.

Douville, H., P. Viterbo, J.-F. Mahfouf, and A. C. M. Beljaars. 1999. Evaluation of the optimum interpolation and nudging techniques for soil moisture analysis using FIFE data. *Mon. Wea. Rev.* **128**, 1733–1756.

Doyle, J. D. 1995. Coupled ocean wave/atmosphere mesoscale model simulations of cyclogenesis. *Tellus* **47A**, 766–788.

Doyle, J. D. 1997. The influence of mesoscale orography on a coastal jet and rainband. *Mon. Wea. Rev.* **125**, 1465–1488.

Doyle, J. D. and N. A. Bond. 2001. Research aircraft observations and numerical simulations of a warm front approaching Vancouver Island. *Mon. Wea. Rev.* **129**, 978–998.

Doyle, J. D. and M. A. Shapiro. 1999. Flow response to large-scale topography: The Greenland tip jet. *Tellus* **51A**, 728–748.

Doyle, J. D. and M. A. Shapiro. 2000. A multi-scale simulation of an extreme downslope windstorm over Norway. *Meteorol. Atmos. Phys.* **74**, 83–101.

Doyle, J. D., D. R. Durran, C. Chen, B. A. Colle, M. Georgelin, V. Grubisic, W. R. Hsu, C. Y. Huang, D. Landau, Y. L. Lin, G. S. Poulos, W. Y. Sun, D. B. Weber, M. G. Wurtele, and M. Xue. 2000. An intercomparison of model-predicted wave breaking for the 11 January 1972 Boulder windstorm. *Mon. Wea. Rev.* **128**, 901–914.

Driedonks, A. G. M. 1982a. Models and observations of the growth of the atmospheric boundary layer. *Bound.-Layer Meteor.* **23**, 283–306.

Driedonks, A. G. M. 1982b. Sensitivity analysis of the equations for a convective mixed layer. *Bound.-Layer Meteor.* **22**, 475–480.

Driese, K. L., and W. A. Reiners. 1997. Aerodynamic roughness parameters for semi-arid natural shrub communities of Wyoming, USA. *Agric. Forest Meteor.* **88**, 1–14.

Droegemeier, K. K. 1997. The numerical prediction of thunderstorms: Challenges, potential benefits, and results from realtime operational tests. *WMO Bull.* **46**, 324–336.

Droegemeier, K. K., J. D. Smith, S. Businger, C. Doswell III, J. Doyle, C. Duffy, E. Foufoula-Georgiou, V. Krajewski, M. Lemone, C. Mass, R. Pielke Sr., P. Ray, S. Rutledge, and E. Zipser. 2000. Hydrological aspects of weather prediction and flood warnings: Report of the Ninth Prospectus Development Team of the U.S. Weather Research Program, *Bull. Amer. Meteor. Sci.* **81**, 2665–2680.

Droegemeier, K. K., M. Xue, K. Johnson, M. O'Keefe, A. Sawdey, G. Sabot, S. Wholey, N. T. Lin, and K. Mills. 1995. Weather prediction: A scalable storm-sale model. In *High Performance Computing*, G. Sabot, Ed., Addison-Wesley, Reading, MA, 45–92.

Druilhet, A., A. Herrada, J.-P. Pages, J. Saissai, C. Allet, and M. Ravaut. 1982. Etude expérimentale de la couche lmite interne associée à la brise de mer. *Bound.-Layer Meteor.* **22**, 511–524.

Dudhia, J. 1984. A numerical study of tropical band convection. Ph.D. thesis, Imperial College, University of London.

Dudhia, J. 1989. Numerical study of convection observed during the Winter Monsoon Experiment using a mesoscale two-dimensional model. *J. Atmos. Sci.* **46**, 3077–3107.

Dudhia, J. 1993. A nonhydrostatic version of the Penn State/NCAR mesoscale model: Validation tests and simulations of an Atlantic cyclone and cold front. *Mon. Wea. Rev.* **121**, 1493–1513.

Dudhia, J., and M. W. Moncrieff. 1989. A three-dimensional numerical study of an Oklahoma squall line containing right-flank supercells. *J. Atmos. Sci.* **46**, 3363–3391.

Durran, D. R. 1981. The effects of moisture on mountain lee waves. Massachusetts Institute of Technology, Cambridge, MA.

Durran, D. R. 1986. Another look at downslope wind storms, Pt. 1: Development of analogs to super-critical flow in an infinitely deep continuously stratified fluid. *J. Atmos. Sci.* **43**, 2527–2543.

Durran, D. R. 1991. The third-order Adams–Bashford method. An attractive alternative to leapfrog time differencing. *Mon. Wea. Rev.* **119**, 702–720.

Durran, D. R., and J. B. Klemp. 1982a. On the effects of moisture on the Brunt–Väisälä frequency. *J. Atmos. Sci.* **39**, 2152–2158.

Durran, D. R., and J. B. Klemp. 1982b. The effects of moisture on trapped mountain lee waves. *J. Atmos. Sci.* **26**, 241–254.

Dutton, J. A. 1976. *The Ceaseless Wind. An Introduction to the Theory of Atmospheric Motion.* McGraw-Hill, New York.

Dutton, J. A., and G. H. Fichtl. 1969. Approximate equations of motion for gases and liquids. *J. Atmos. Sci.* **26**, 241–254.

Dyer, A. J. 1974. A review of flux-profile relationships. *Bound.-Layer Meteor.* **42**, 9–17.

Dyer, A. J., and E. F. Bradley. 1982. An alternative analysis of flux-gradient relationships at the 1976 ITCE. *Bound.-Layer Meteor.* **22**, 3–19.

Easter, R. C. 1993. Two modified versions of Bott's positive definite numerical advection scheme. *Mon. Wea. Rev.* **121**, 297–304.

Eastman, J. L. 1995. Numerical simulation of Hurricane Andrew—Rapid intensification. 21st AMS Conference on Hurricanes and Tropical Meteorology, April 24–28, 1995, Miami, 111–113.

Eastman, J. L. 1999. Analysis of the effects of CO_2 and landscape change using a coupled plant and meteorological model. Ph.D. dissertation, Dept. of Atmospheric Science Paper No. 686, Colorado State University, Fort Collins, CO.

Eastman, J. L., R. A. Pielke, and W. A. Lyons. 1995. Comparison of lake-breeze model simulations with tracer data. *J. Appl. Meteor.* **34**, 1398–1418.

Eastman, J. L., M. E. Nicholls, and R. A. Pielke. 1996. A numerical simulation of Hurricane Andrew. Second International Symposium on Computational Wind Engineering, August 4–8, 1996, Fort Collins, CO.

Eastman, J. L., R. A. Pielke, and D. J. McDonald. 1998. Calibration of soil moisture for large eddy simulations over the FIFE area. *J. Atmos. Sci.* **55**, 1131–1140.

Eastman, J. L., M. B. Coughenour, and R. A. Pielke. 2001a. The effects of CO_2 and landscape change using a coupled plant and meteorological model. *Global Change Biology*, in press.

Eastman, J. L., M. B. Coughenour, and R. A. Pielke. 2001b. Does grazing affect regional climate. *J. Hydrometeor.* **2**, 243–253.

Egan, B. A. 1975. Turbulent diffusion in complex terrain. In *Lectures on Air Pollution and Environmental Impact Analysis*, D. Haugen, Ed., American Meteorological Society, Boston, 112–135.

Egger, J. 1981. On the linear two-dimensional theory of thermally induced slope winds. *Contrib. Atmos. Phys.* **54**, 465–481.

Egger, J. 1999. Inertial oscillations revisited. *J. Atmos. Sci.* **56**, 2951–2954.

Eidenshink, J. C., and R. H. Haas. 1992. Analyzing vegetation dynamics of land systems with satellite data. *Geocarto Intl.* **1**, 53–61.

Eliassen, A. 1980. A review of long-range transport modeling. *J. Appl. Meteor.* **19**, 231–240.

Eliassen, A., and E. Palm. 1960. On the transfer of energy in stationary mountain waves. *Geophys. Norv.* **22**, 1–23.

Ellenton, G. E., and M. B. Danard. 1979. Inclusion of sensible heating in convective a parameterization applied to lake-effect snow. *Mon. Wea. Rev.* **107**, 551–565.

Elsberry, R. L. 1978. Prediction of atmospheric flows on nested grids. In *Computational Techniques for Interface Problems*, K. C. Park and D. K. Gartling, Eds., American Society of Mechanical Engineering, New York, 67–85.

Eltahir, E. A. B. 1996. Role of vegetation in sustaining large-scale atmospheric circulations in the tropics. *J. Geophys. Res.* **101**, 4255–4268.

Emanuel, K. A. 1982a. Forced and free mesoscale motions in the atmosphere. Proceedings of the CIMMS Symposium, Norman, OK, May 12–16, 1980.

Emanuel, K. A. 1982b. Inertial instability and mesoscale convective systems. Part II: Symmetric CISK in a baroclinic flow. *J. Atmos. Sci.* **39**, 1080–1097.

Emery, K. O., and G. T. Csanady. 1973. Surface circulation of lakes and nearly land-locked seas. *Proc. Natl. Acad. Sci.* **70**, 93–97.

Emori, S. 1998. The interaction of cumulus convection with soil moisture distribution: An idealized simulation. *J. Geophys. Res.* **103**, 8873–8884.

Entekhabi, D. 1995. Recent advances in land-atmosphere interaction research 1995. *Rev. Geophys.* **33** (suppl.), 995–1003.

Entekhabi, D., I. Rodriguez-Iturbe, and R. L. Bras. 1992. Variability in large-scale water balance with land surface-atmosphere interaction. *J. Climate* **5**, 798–813.

Entin, J. K., A. Robock, K. Y. Vinnikov, V. Zabelin, S. Liu, A. Namkhai, and T. Adyasuren. 1999. Evaluation of Global Soil Wetness Project soil moisture simulations. *J. Meteor. Soc. Japan* **77**, 183–198.

EPA. 1980. Guideline for applying the Airshed Model to urban areas. EPA Report 450/4-80-020.

Erdélyi, A., W. Magnus, F. Oberhettinger, and F. G. Tricomi. 1954. *Tables of Integral Transforms*, Vol. II. McGraw-Hill, New York.

Estoque, M. A. 1961. A theoretical investigation of the sea breeze. *Quart. J. Roy. Meteor. Soc.* **87**, 136–146.

Estoque, M. A. 1962. The sea breeze as a function of prevailing synoptic situation. *J. Atmos. Sci.* **19**, 244–250.

Estoque, M. A. 1973. Numerical modeling of the planetary boundary layer. In *Workshop on Micrometeorology*, D. A. Haugen, Ed. Chap. 6. American Meteorological Society, Boston, 217–270.

Estoque, M. A., and C. M. Bhumralkar. 1969. Flow over a localized heat source. *Mon. Wea. Rev.* **97**, 850–859.

Estoque, M. A., and J. M. Gross. 1981. Further studies of a lake breeze, Part II: Theoretical study. *Mon. Wea. Rev.* **109**, 619–634.

Estoque, M. A., and K. Ninomiya. 1976. Numerical simulation of Japan Sea effect snowfall. *Tellus* **28**, 243–253.

Estoque, M. A., J. Gross, and H. W. Lai. 1976. A lake breeze over southern Lake Ontario. *Mon. Wea. Rev.* **104**, 386–396.

Estoque, M. A., S. V. Almazan, and J. C. Mondares. 1994. A sea breeze rainfall model. *Atmósfera* **7**, 221–240.

Eugster, W., W. R. Rouse, R. A. Pielke Sr., J. P. McFadden, D. D. Baldocchi, T. G. F. Kittel, F. S. Chapin III., G. E. Liston, P. L. Vidale, E. Vaganov, and S. Chambers. 2000. Land-atmosphere

energy exchange in Arctic tundra and boreal forest: Available data and feedbacks to climate. *Global Change Biology* **6**, 84–115.

Everett, R. G., B. B. Hicks, W. W. Berg, and J. W. Winchester. 1979. An analysis of particulate sulfur and lead gradient data collected at Argonne National Laboratory. *Atmos. Environ.* **13**, 931–934.

Fage, J. M., and J. Moussafir. 1980. Forecasting of pollution episodes under stagnation conditions. Colloque Meteorologie et Environment, October 6–7, 1980, Ministere de L'Environement Neuilly/Seine, France.

Famiglietti, J. S., and E. F. Wood. 1991. Evapotranspiration and runoff from large land areas: Land surface hydrology for atmospheric general circulation models. *Surv. Geophys.* **12**, 179–204.

Fankhauser, J. C. 1971. Thunderstorm-environment interactions determined from the aircraft and radar observations. *Mon. Wea. Rev.* **99**, 171–192.

Farley, R. D., D. L. Hjermstad, and H. D. Orville. 2000. Numerical simulation of a 4-day early spring storm period in the Black Hills. *J. Appl. Meteor.* **39**, 1299–1317.

Feddes, R. A., H. Hoff, M. Bruen, T. E. Dawson, P. de Rosnay, P. Dirmeyer, R. B. Jackson, P. Kabat, A. Kleidon, A. Lilly, and A. J. Pitman. 2001. Modelling root water uptake in hydrological and climate models. *Bull. Amer. Meteor. Soc.*, in press.

Feingold, G., and S. M. Kreidenweis. 2000. Does heterogeneous processing of aerosol increase the number of cloud droplets? *J. Geophys. Res.* **105**, 24,351–24,361.

Feliks, Y., and A. Huss. 1982. Spurious mass loss in some mesometeorological models. *Bound.-Layer Meteor.* **24**, 387–391.

Fels, S. B., and M. D. Schwarzkopf. 1975. The simplified exchange approximation: A new method for radiative transfer calculation. *J. Atmos. Sci.* **32**, 1475–1488.

Fernandez, W. 1982. Environmental conditions and structure of the west African and eastern tropical Atlantic squall lines. *Arch. Meteor. Geophys. Bioklimatol., Ser. A* **31**, 71–89.

Ferretti, R., T. Paolucci, W. Zheng, G. Visconti, and P. Bonelli. 2000. Analyses of the precipitation pattern on the alpine region using different cumulus convection parameterizations. *J. Appl. Meteor.* **39**, 182–200.

Finkele, K. 1998. Inland and offshore propagation speeds of a sea breeze from simulations and measurements. *Bound.-Layer Meteor.* **87**, 307–329.

Finley, C. A., W. R. Cotton, and R. A. Pielke. 2001a. Numerical simulation of tornadogenesis in a high-precipitation supercell: Part I: Storm evolution and transition into a bow echo. *J. Atmos. Sci.* **58**, 1597–1629.

Finley, C. A., W. R. Cotton, and R. A. Pielke. 2001b. Numerical simulation of tornadogenesis in a high-precipitation supercell: Part II: Tornado evolution and tornadogenesis. *J. Atmos. Sci.* in press.

Finnigan, F., and J. J. Finnigan. 1981. The interaction between an internal gravity wave and the planetary boundary layer. Part II: Effect of the wave on the turbulence structure. *Quart. J. Roy. Meteor. Soc.* **107**, 807–832.

Fisher, E. L. 1961. A theoretical study of the sea breeze. *J. Meteor.* **18**, 215–233.

Fleagle, R. G., and J. A. Businger. 1980. *An Introduction to Atmospheric Physics*, 2nd Ed. Academic Press, New York.

Foken, T., and G. Skeib. 1983. Profile measurement in the atmospheric near-surface layer and the use of suitable universal functions for the determination of the turbulent energy exchange. *Bound.-Layer Meteor.* **25**, 55–62.

Fontana, P. H. 1979. Effects of New York City on the horizontal and vertical structure of sea breeze fronts. Volume 1: Observations of frictional retardation of sea breeze fronts. Report, Dept. of Meteorology, San Jose State University, San Jose, CA.

Foote, G. B., and Fankhauser, J. C. 1973. Airflow and moisture budge beneath a northeast Colorado hailstorm. *J. Appl. Meteor.* **12**, 1330–1353.

Fouquart, Y., and B. Bonnel. 1980. Computations of solar heating of the Earth's atmosphere: A new parameterization. *Contrib. Atmos. Phys.* **53**, 35–62.

Fortunato, A. B., and A. M. Baptista. 1996. Evaluation of horizontal gradients in sigma coordinate shallow water models. *Atmos. Ocean* **34**, 489–514.

Fortune, M. 1980. Properties of African squall lines inferred from time-lapse satellite imagery. *Mon. Wea. Rev.* **108**, 153–168.

Fosberg, M. A., W. E. Marlatt, and L. Krupnak. 1976. Estimating air-flow patterns over complex terrain. Research Paper RM-162, U.S. Forest Service, Rocky Mountain Forest Range Experiment Station.

Foufoula-Georgiou, E., and P. Kumar (Eds.). 1994. *Wavelets in Geophysics*. Academic Press, New York.

Foufoula-Georgiou, E., and W. Krajewski. 1995. Recent advances in rainfall modeling estimation, and forecasting. U.S. National Report to the IUGG 1991–1994. *Revs. Geophys.* (Supp.), **33**, 1125–1137.

Fox, D. G., and J. W. Deardorff. 1972. Computer methods for simulation of multidimensional, nonlinear, subsonic, incompressible flow. *J. Heat Transfer, Ser. C* **94**, 337–346.

Fox, D. G., and S. A. Orszag. 1973. Pseudospectral approximation to two-dimensional turbulence. *J. Comp. Physiol.* **11**, 612–619.

Fox-Rabinovitz, M. S. 2000. Simulation of anomalous regional climate events with a variable-resolution stretched-grid GCM. *J. Geophys. Res.* **105**, 29,635–29,645.

Fox-Rabinovitz, M. S., G. L. Stenchikov, M. J. Suarez, and L. L. Takas. 1997. A finite-difference GCM dynamical core with a variation-resolution stretched grid. *Mon. Wea. Rev.* **125**, 2943–2968.

Fox-Rabinovitz, M. S., L. L. Takacs, R. C. Govindaraju, and M. J. Suarez. 2001. A variable-resolution stretched-grid general circulation model: Regional climate simulation. *Mon. Wea. Rev.* **129**, 453–469.

Fraedrich, K. 1976. A mass budget of an ensemble of transient cumulus clouds determined from direct cloud observations. *J. Atmos. Sci.* **33**, 262–268.

Frank, N. L., P. L. Moore, and G. E. Fisher. 1967. Summer shower distribution over the Florida Peninsula as deduced from digitized radar data. *J. Appl. Meteor.* **6**, 309–316.

Frank, W. M. 1978. The life cycles of GATE convective systems. *J. Atmos. Sci.* **35**, 1256–1264.

Frank, W. M. 1980. Modulations of the net tropospheric temperature during GATE. *J. Atmos. Sci.* **37**, 1056–1064.

Frank, W. M. 1983. The cumulus parameterization problem. *Mon. Wea. Rev.* **111**, 1859–1871.

Fraser, A. B., R. C. Easter, and P. V. Hobbs. 1973. A theoretical study of the flow of air and fallout of solid precipitation over mountainous terrain. Part I. Airflow model. *J. Atmos. Sci.* **30**, 801–812.

Freedman, J. M., D. R. Fitzjarrald, K. E. Moore, and R. K. Sakai. 2001. Boundary layer clouds and vegetation-atmosphere feedbacks. *J. Climate* **14**, 180–197.

French, J. R., G. Vali, and R. D. Kelly. 1999. Evolution of small cumulus clouds in Florida: Observations of pulsating growth. *Atmos. Res.* **52**, 143–165.

Friedrich, K., N. Mölders, and G. Tetzlaff. 2000. On the influence of surface heterogeneity on the Bowen ratio: A theoretical case study. *Theor. Appl. Climatol.* **65**, 181–196.

Friend, A. L., D. Djurié, and K. C. Brundidge. 1977. A combination of isentropic and sigma coordinates in numerical weather prediction. *Contrib. Atmos. Phys.* **50**, 290–295.

Fritsch, J. M. 1975. Synoptic-mesoscale budget relationships for a tornado producing squall line. Proceedings of the 9th AMS Conference on Severe Local Storms, October 21–23, 1975, Norman OK, 165–172.

Fritsch, J. M., and C. F. Chappell. 1980a. Numerical prediction of convectively driven mesoscale pressure systems. Part I: Convective parameterization. *J. Atmos. Sci.* **37**, 1722–1733.

Fritsch, J. M., and C. F. Chappell. 1980b. Numerical prediction of convectively driven mesoscale pressure systems. Part II: Mesoscale model. *J. Atmos. Sci.* **37**, 1734–1762.

Fritsch, J. M., and J. S. Kain. 1993. Convective parameterization for mesoscale models: The Fritsch–Chappell Scheme. In *The Representation of Cumulus Convection in Numerical Models*, K. A. Emanuel and D. J. Raymond, Eds., American Meteorological Society, Boston, 159–164.

Fritsch, J. M., and R. A. Maddox. 1980. Analyses of upper tropospheric wind perturbations associated with midlatitude mesoscale convective complexes. Preprint, AMS Conference on Weather Forecasting and Analysis, 339–345.

Fritsch, J. M., and R. A. Maddox. 1981a. Convectively driven mesoscale systems aloft. Part I: Observations. *J. Appl. Meteor.* **20**, 9–19.

Fritsch, J. M., C. F. Chappell, and L. K. Hoxit. 1976. The use of large-scale budgets for convective parameterizations. *Mon. Wea. Rev.* **104**, 1408–1418.

Fritsch, J. M., and R. A. Maddox. 1981b. Convectively driven mesoscale systems aloft. Part II: Numerical simulation. *J. Appl. Meteor.* **20**, 20–26.

Fritsch, J. M., E. L. Magaziner, and C. F. Chappell. 1980. Analytical initialization for three-dimensional numerical models. *J. Appl. Meteor.* **19**, 809–818.

Fuggle, R. F., and T. R. Oke. 1976. Long-wave radiative flux divergence and nocturnal cooling of the urban atmosphere. I: Above roof-level. *Bound.-Layer Meteor.* **10**, 113–120.

Fujibe, F., K. Saito, D. S. Wratt, and S. G. Bradley. 1999. A numerical study on the diurnal variation of low-level wind in the lee of a two-dimensional mountain. *J. Meteor. Soc. Japan* **77**, 827–843.

Fujita, T. T. 1980. In search of mesoscale wind fields in landfalling hurricanes. 13th AMS Conference on Hurricanes and Tropical Meteorology, Miami Beach, FL, December 1–5.

Fujita, T. T., and R. M. Wakimoto. 1982. Effects of miso- and mesoscale observations on PAM winds obtained during project NIMROD. *J. Appl. Meteor.* **21**, 840–858.

Fujitani, T. 1981. Direct measurement of turbulent fluxes over the sea during AMTEX. *Pap. Meteor. Geophys.* **32**, 119–134.

Fukutome, S., C. Frei, D. Luthi, and C. Schar. 1999. The interannual variability as a test ground for regional climate simulations over Japan. *J. Meteor. Soc. Japan* **77**, 649–672.

Fuller, J. G. 1978. *The Poison that Fell from the Sky*, Random House, New York.

Fullerton, N. (Ed.). 2000. FSL in review. Forecast Systems Laboratory, U.S. Dept. of Commerce, NOAA, Office of Atmospheric Research, Boulder, CO.

Furukawa, T. 1973. numerical experiments of the airflow over mountains. I. Uniform current with constant static stability. *J. Meteor. Soc. Japan* **51**, 400–419.

Gage, K. S. 1979. Evidence of a $k^{-5/3}$ low inertial range in mesoscale two-dimensional turbulence. *J. Atmos. Sci.* **36**, 1950–1954.

Gal-Chen, T., and R. C. J. Somerville. 1975a. On the use of a coordinate transformation for the solution of the Navier–Stokes equations. *J. Comput. Phys.* **17**, 209–228.

Gal-Chen, T., and R. C. J. Somerville. 1975b. Numerical solution of the Navier–Stokes equations with topography. *J. Comput. Phys.* **17**, 276–309.

Galloway, J. N., S. J. Eisenreich, and B. C. Scott (Eds.). 1980. Toxic substances in atmospheric deposition: A review and assessment. Report on a Workshop at Jekyll Island, Georgia, November 1979, prepared for the EPA Office of Pesticides and Toxic Substances, Washington, D.C.

Gallus, W. A. Jr. 1999. Eta simulations of three extreme precipitation events: Sensitivity to resolution and convective parameterization. *Wea. Forecasting* **14**, 405–426.

Gallus, W. A. Jr., and J. B. Klemp. 2000. Behavior of flow over step orography. *Mon. Wea. Rev.* **128**, 1153–1164.

Galmarini, S., and P. Thunis. 1999. On the validity of Reynolds assumptions for running-mean filters in the absence of a spectral gap. *J. Atmos. Sci.* **56**, 1785–1796.

Galmarini, S., F. Michelutti, and P. Thunis. 2000. Estimating the contribution of Leonard and cross terms to the subfilter scale from atmospheric measurements. *J. Atmos. Sci.* **57**, 2968–2976.

Galperin, M. V., and A. D. Kastrel. 1998. The development and comparative study of some numerical advection schemes. *Russ. Meteorol. Hydrol.* **7**, 32–38.

Gamache, J. F., and R. A. Houze Jr. 1982. Mesoscale air motions associated with a tropical squall line. *Mon. Wea. Rev.* **110**, 118–135.

Gambo, K. 1978. Notes on the turbulence closure model for atmospheric boundary layers. *J. Meteor. Soc. Japan* **56**, 466–480.

Gamo, M., S. Yamamoto, and O. Yokoyama. 1982. Airborne measurements of the free convective internal boundary layer during the sea breeze. *J. Meteor. Soc. Japan* **60**, 1284–1298.

Gamo, M., S. Yamamoto, O. Yokoyama, and H. Yoshikado. 1983. Structure of the free convective internal boundary layer above the coastal area. *J. Meteor. Soc. Japan* **61**, 110–124.

Gannon, P. T. Sr. 1978. Influence of earth surface and cloud properties on the south Florida sea breeze. NOAA Technical Report ERL 402-NHEML-2.

Gao, X., S. Sorooshian, and H. V. Gupta. 1996. Sensitivity analysis of the biosphere–atmosphere transfer scheme. *J. Geophys. Res.* **101**, 7279–7289.

Garratt, J. R. 1992. *The Atmospheric Boundary Layer*, Cambridge University Press, Cambridge, U.K.

Garratt, J. R., and R. A. Brost. 1981. Radiative cooling within and above the nocturnal boundary layer. *J. Atmos. Sci.* **38**, 2730–2746.

Garratt, J. R., and G. D. Hess. 2001. The idealized neutrally stratified planetary boundary layer. In *Encyclopedia of Atmospheric Sciences*, J. Holton and P. Taylor, Eds. Academic Press, London, in press.

Garratt, J. R., and R. A. Pielke. 1989. On the sensitivity of mesoscale models to surface-layer parameterization constants. *Bound.-Layer Meteor.* **48**, 377–387.

Garratt, J. R., R. A. Pielke, W. Miller, and T. J. Lee. 1990. Mesoscale model response to random, surface-based perturbations—A sea-breeze experiment. *Bound.-Layer Meteor.* **52**, 313–334.

Garrett, A. J. 1978. Numerical simulations of atmospheric convection over the southeastern U.S. in undisturbed conditions. Report No. 47, Atmospheric Science Group, College of Engineering, University of Texas, Austin, TX.

Garrett, A. J. 1980. Orographic cloud over the eastern slopes of Mauna Loa Volcano, Hawaii, related to insolation and wind. *Mon. Wea. Rev.* **108**, 931–941.

Garrett, A. J. 1982. A parameter study of interactions between convective clouds, the convective boundary layer, and a forested surface. *Mon. Wea. Rev.* **110**, 1041–1059.

Garrett, A. J. 1983a. Drainage flow prediction with a one-dimensional model including canopy, soil and radiation parameterization. *J. Appl. Meteor.* **22**, 79–91.

Garrett, A. J. 1983b. Treatment of ground-air and water-air exchange. AMS/EPA Specialty Conference on Air Quality Modeling of the Nonstationary, Nonhomogeneous Urban Boundary Layers, October 31–November 4, Baltimore, MD.

Garstang, M., and D. Fitzjarrald. 1999. *Observations of Surface to Atmospheric Interactions in the Tropics*. Oxford University Press, New York.

Garstang, M., P. D. Tyson, and G. D. Emmitt. 1975. The structure of heat islands. *Rev. Geophys. Space Phys.* **13**, 139–165.

Garstang, M., R. A. Pielke, and W. J. Snow. 1980. A comparison of model predicted to observed winds in the coastal zone. Final report on Contract B-93492-A-Q for the period 3/80–10/80. For Pacific Northwest Laboratory, Richland, WA.

Gash, J., and P. Kabat. 1999. Land-surface experiments: 1. *IGBP Global Change Newsletter* **39**, 12–13.

Gedzelman, S. D., and W. L. Donn. 1979. Atmospheric gravity waves and coastal cyclones. *Mon. Wea. Rev.* **107**, 667–681.

Geiger, R. 1965. *The Climate Near the Ground*. Harvard University Press, Cambridge, MA.

Geisler, J. E., and F. P. Bretherton. 1969. The sea-breeze forerunner. *J. Atmos. Sci.* **26**, 82–95.

Gentry, R. C., and P. L. Moore. 1954. Relation of local and general wind interaction near the sea coast to time and location of air-mass showers. *J. Meteor.* **11**, 507–511.

George, R. L. 1979. Evolution of mesoscale convective systems over mountainous terrain. Paper No. 318, Dept. of Atmospheric Science, Colorado State University, Fort Collins, CO.

Germano, M., U. Piomelli, P. Moin, and W. H. Cabot. 1991. A dynamic subgrid-scale eddy viscosity model. *Phys. Fluids* **A3**, 1760–1765.

Gibson, C. H. 1999. Fossil turbulence revisited. *J. Mar. Syst.* **21**, 147–167.

Giordani, H., and S. Planton. 2000. Modeling and analysis of ageostrophic circulation over the Azores Oceanic Front during the SEMAPHORE experiment. *Mon. Wea. Rev.* **128**, 2270–2287.

Giorgi, F., M. R. Marinucci, and G. T. Bates. 1993a. Development of a second-generation regional climate model (RegCM2). Part I: Boundary-layer and radiative transfer processes. *Mon. Wea. Rev.* **121**, 2794–2813.

Giorgi, F., M. R. Marinucci, and G. T. Bates. 1993b. Development of a second-generation regional climate model (RegCM2). Part II: Convective processes and assimilation of lateral boundary conditions. *Mon. Wea. Rev.* **121**, 2814–2832.

Giovannini, G., S. Lucchesi, and M. Giachetti. 1988. Effect of heating on some physical and chemical parameters related to soil aggregation and erodibility. *Soil Sci.* **146**, 255–261.

Glendening, J. W. 2000. Budgets of linear and nonlinear turbulent kinetic energy under strong shear conditions. *J. Atmos. Sci.* **57**, 2297–2318.

Glendening, J. W., and J. D. Doyle. 1995. Mesoscale response to a meandering surface temperature interface. *J. Atmos. Sci.* **52**, 505–518.

Gocho, Y. 1978. Numerical experiment of orographic heavy rainfall due to a stratiform cloud. *J. Meteor. Soc. Japan* **56**, 405–423.

Gocho, Y. 1982. Statistical study on the relations among characteristics of rainfall around the Suzuka Mountains and meteorological conditions during warm season. *J. Meteor. Soc. Japan* **60**, 739–757.

Goerss, J. S., and P. A. Phoebus. 1992. The Navy's operational atmospheric analysis. *Wea. Forecasting* **7**, 232–249.

Golden, J. H., and J. D. Sartor. 1978. AMS Workshop on mesoscale interactions with cloud processes, October 24–25, 1977, Boulder, CO. *Bull. Amer. Meteor. Soc.* **59**, 720–730.

Goldreich, Y., P. D. Tyson, R. G. Van Gogh, and G. P. N. Venter. 1981. Enhancement and suppression of urban heat plumes over Johannesburg. *Bound.-Layer Meteor.* **21**, 115–126.

Gollvik, S. 1999. On the effects of horizontal diffusion, resolution and orography on precipitation forecasting in a limited area model. *Meteorol. Appl.* **6**, 49–58.

Gong, W., X. Lin, S. Ménard, P. Pellerin, and R. Benoit. 1999. Modelling the Canadian southern Atlantic region oxidants—A study of a Canadian EMEFS-1 hyper-intensive period. *J. Geophys. Res.* **104**, 18,599–18,617.

Goode, K., and S. E. Belcher. 1999. On the parameterisation of the effective roughness length for momentum transfer over heterogeneous terrain. *Bound.-Layer Meteor.* **93**, 133–154.

Goodin, W. R., G. J. McRae, and J. H. Seinfeld. 1980. An objective analysis technique for constructing three-dimensional urban scale wind fields. *J. Appl. Meteor.* **19**, 98–108.

Goodin, W. R., G. J. McRae, and J. H. Seinfeld. 1981. Reply. *J. Appl. Meteor.* **20**, 92–94.

Gopalakrishnan, S. G. 1996. Mesoscale dispersion modelling in a weak wind stable boundary layer with a special reference to the Bhopal gas episode. Ph.D. dissertation, Centre for Atmospheric Sciences, Indian Institute of Technology, Delhi, India.

Gopalakrishnan, S. G., and R. Avissar. 2000. An LES study of the impacts of land surface heterogeneity on dispersion in the convective boundary layer. *J. Atmos. Sci.* **57**, 352–371.

Gopalakrishnan, S. G., M. Sharan, R. T. McNider, and M. P. Singh. 1998. Study of radiative and turbulent processes in the stable boundary layer under weak wind conditions. *J. Atmos. Sci.* **55**, 954–960.

Gopalakrishnan, S. G., S. B. Roy, and R. Avissar. 2000. An evaluation of the scale at which topographical features affect the convective boundary layer using large eddy simulations. *J. Atmos. Sci.* **57**, 334–351.

Gossard, E. E. 1978. The height distribution of refractive index structure parameter in an atmosphere being modified by spatial transition at its lower boundary. *Radio Sci.* **13**, 489–500.

Goutorbe, J. P., T. Lebel, A. Tinga, P. Bessemoulin, J. Brouwer, A. J. Dolman, E. T. Engman, J. H. C. Gash, M. Hoeppfner, P. Kabat, Y. Kerr, B. Monteny, S. Prince, F. Said, P. Sellers, and J. S. Wallace. 1994. HAPEX-Sahel: A large-scale study of land-atmosphere interactions in the semi-arid tropics. *Ann. Geophys.* **12**, 53–64.

Grabowski, W. W. 1998. Toward cloud resolving modeling of large-scale tropical circulations: A simple cloud microphysics parameterization. *J. Atmos. Sci.* **21**, 3283–3298.

Grabowski, W. W. 2000. Cloud microphysics and the tropical climate: Cloud-resolving model perspective. *J. Climate* **13**, 2306–2322.

Grabowski, W. W., and P. K. Smolarkiewicz. 1990. Monotone finite-difference approximations to the advection-condensation problem. *Mon. Wea. Rev.* **118**, 2082–2097.

Grams, G. W., I. H. Blifford Jr., B. G. Schuster, and J. J. DeLuisi. 1972. Complex index of refraction of airborne fly ash determined by lasar radar and collection of particles at 13 km. *J. Atmos. Sci.* **29**, 900–905.

Grasso, L. D. 2000. A numerical simulation of dryline sensitivity to soil moisture. *Mon. Wea. Rev.* **128**, 2816–2834.

Green, J. S. A., and G. A. Dalu. 1980. Mesoscale energy-generated in the boundary layer. *Quart. J. Roy Meteor. Soc.* **106**, 721–726.

Green, S. (Ed.). 1994. *Fluid Vortices*. Kluwer Academic Publishers, Amsterdam.

Greene, E. M., G. E. Liston, and R. A. Pielke. 1999. Simulation of above treeline snowdrift formation using a numerical snow-transport model. *Cold Reg. Sci. Tech.* **30**, 135–144.

Grell, G. A. 1993. Prognostic evaluation of assumptions used by cumulus parameterization. *Mon. Wea. Rev.* **121**, 764–787.

Grell, G. A., Y.-H. Kuo, and R. Pasch. 1991. Semi-prognostic test of cumulus parameterization schemes in the middle latitudes. *Mon. Wea. Rev.* **119**, 5–31.

Grell, G. A., J. Dudhia, and D. R. Stauffer. 1994. A description of the fifth-generation Penn State/NCAR mesoscale modeling system (MM5). Technical Note NCAR/TN-397+STR, NCAR.

Griffies, S. M., R. C. Pacanowski, and R. W. Hallberg. 2000. Spurious diapycnal mixing associated with advection in a z-coordinate ocean model. *Mon. Wea. Rev.* **128**, 538–564.

Griffith, K. T., S. K. Cox, and R. G. Knollenberg. 1980. Infrared radiative properties of tropical cirrus clouds inferred from aircraft measurements. *J. Atmos. Sci.* **37**, 1077–1087.

Grimmond, C. S. B., and T. R. Oke. 1999. Heat storage in urban areas: Local-scale observations and evaluation of a simple model. *J. Appl. Meteor.* **38**, 922–940.

Gross, G. 1986. A numerical study of the land and sea breeze including cloud formation. *Beitr. Phys. Atmos.* **59**, 97–114.

Gross, G. 1987a. Some effects of deforestation on nocturnal drainage flow and local climate—A numerical study. *Bound.-Layer Meteor.* **38**, 315–337.

Gross, G. 1987b. A numerical study of the air flow within and around a single tree. *Bound.-Layer Meteor.* **40**, 311–327.

Gross, G. 1992. Results of supercomputer simulations of meteorological mesoscale phenomena. *Fluid Dyn. Res.* **10**, 483–490.

Gross, G. 1995. Optimum time step and remerging Feigenbaum trees in a one-dimensional boundary-layer model. *Beit. Phys. Atmos.* **68**, 271–273.

Gross, G. 1996. On the applicability of numerical mass-consistent wind field models. *Bound.-Layer Meteor.* **77**, 379–394.

Gross, G. 1997. ASMUS—Ein numerisches modell zur Berechnung der Strömung und der Schadstoffverteilung im Bereich einzelner Gebäude. (A numerical model for air-flow and dispersion around individual buildings). *Meteor. Z.* **6**, 130–136. (In German)

Gross, G. 1998. Berechnung der ausbreitung von organischen partikeln aus tierställen und vergleichbaren anlagen. (Dispersion modeling of organic particles emitted from stables). *Dtsch. Tierärztl. Wschr.* **105**, 209–252. (In German)

Gross, G., and F. Wipperman. 1987. Channeling and countercurrent in the Upper-Rhine valley: numerical simulations. *J. Climate Appl. Meteor.* **26**, 1293–1304.

Gross, G., H. Vogel, and F. Wippermann. 1987. Dispersion over and around a steep obstacle for varying thermal stratification—Numerical simulations. *Atmos. Environ.* **21**, 483–490.

Gross, M. G. 1977. *Oceanography: A View of the Earth*. 2nd ed. Prentice-Hall, Englewood Cliffs, NJ.

Gross, P., and A. Hense. 1999. Effects of a total solar eclipse on the mesoscale atmospheric circulation over Europe-A model experiment. *Meteor. Atmos. Phys.* **71**, 229–242.

Grossi, P., P. Thunis, A. Martilli, and A. Clappier. 2000. Effect of sea-breeze on air pollution in the Greater Athens Area. Part II: Analysis of different emission scenarios. *J. Appl. Meteor.* **39**, 563–575.

Gryning, S.-E., and S. E. Larsen. 1981. Relation between dispersion characteristics over surfaces with dissimilar roughness and atmospheric stability, under conditions of equal geostrophic winds. *Atmos. Environ.* **15**, 983–987.

Gryning, S.-E., and E. Lyck. 1983. A tracer investigation of the atmospheric dispersion in the Dyrnaes Valley, Greenland. Report Risø R–481, Risø National Laboratory, Denmark.

Gu, L., J. D. Fuentes, M. Garstang, J. Tota da Silva, R. Heitz, J. Sigler, and H. H. Shugart. 2001. Cloud modulation of surface solar irradiance at a pasture site in southern Brazil. *Agric. Forest Meteor.* **106**, 117–129.

Gube, M., J. Schmetz, and E. Raschke. 1980. Solar radiative transfer in a cloud field. *Contrib. Atmos. Phys.* **53**, 24–34.

Guiraud, J. P., and R. K. H. Zeytounian. 1982. A note on the adjustment to hydrostatic balance. *Tellus* **34**, 50–54.

Gunn, R., and J. S. Marshall. 1958. The distribution with size and aggregate snowflakes. *J. Meteor.* **15**, 452–461.

Gupta, H. V., L. A. Bastidas, S. Sorooshian, W. J. Shuttleworth, and Z. L. Yang. 1999. Parameter estimation of a land surface scheme using multicriteria methods. *J. Geophys. Res.* **104**, 19,491–19,503.

Gutman, L. N. 1972. *Introduction to the Nonlinear Theory of Mesoscale Meteorological Processes*. Keter Press, Jerusalem, Israel.

Gutman, L. N., and J. W. Melgarejo. 1981. On the laws of geostrophic drag and heat transfer over a slightly inclined terrain. *J. Atmos. Sci.* **38**, 1714–1724.

Gutman, D. P., K. E. Torrance, and M. A. Estoque. 1973. Use of the numerical method of Estoque and Bhumralkar for the planetary boundary layer. *Bound.-Layer Meteor.* **5**, 341–346.

Gyakum, J. R., C. Chouinard, A. Staniforth, M. Éland, R. Benoit, R. de Elia, F. Drummond, Y.-H. Kuo, F. Lalaurette, R. Laprise, L. Leslie, H. Lin, J. Mailhot, P. E. Merilees, R. Tyler, and W. Wintels. 1995. First COMPARE Workshop Summary. *Bull. Amer. Meteor. Soc.* **76**, 1209–1218.

Gyakum, J. R., M. Carrera, D.-L. Zhang, S. Miller, J. Caveen, R. Benoit, T. Black, A. Buzzi, C. Chouinard, M. Fantini, C. Folloni, J. J. Katzfey, Y.-H. Kuo, F. Lalaurette, S. Low-Nam, J. Mailhot, P. Malguzzi, J. L. McGregor, M. Nakamura, G. Tripoli, and C. Wilson. 1996. A regional model intercomparison using a case of explosive oceanic cyclogenesis. *Wea. Forecasting* **11**, 521–543.

Haack, T., S. D. Burk, C. Dorman, and D. Rogers. 2001. Supercritical flow interaction within the Cape Blanco-Cape Mendocino orographic complex. *Mon. Wea. Rev.* **129**, 688–708.

Hachey, H. B. 1934. Movements resulting from mixing of stratified waters. *J. Biol. Board Canada* **1**, 133–143.

Hack, J. J., and W. H. Schubert. 1981. Lateral boundary conditions for tropical cyclone models. *Mon. Wea. Rev.* **109**, 1404–1420.

Hack, J. J., B. A. Boville, B. P. Briegleb, J. T. Kiehl, P. J. Rasch, and D. L. Williamson. 1993. Description of the NCAR Community Climate Model (CCM2). Technical Note, NCAR/TN-382+STR, NCAR.

Hadfield, M. G., W. R. Cotton, and R. A. Pielke. 1991. Large-eddy simulations of thermally-forced circulations in the convective boundary layer. Part I: A small-scale circulation with zero wind. *Bound.-Layer Meteor.* **57**, 79–114.

Hadfield, M. G., W. R. Cotton, and R. A. Pielke. 1992. Large-eddy simulations of thermally forced circulations in the convective boundary-layer. Part II: The effect of changes in wavelength and wind-speed. *Bound.-Layer Meteor.* **58**, 307–327.

Hadley, G. 1962. *Linear Programming*. Addison-Wesley, Reading, MA.

Hafner, J., and S. Q. Kidder. 1999. Urban heat island modeling in conjunction with satellite-derived surface/soil parameters. *J. Appl. Meteor.* **38**, 448–465.

Hägeli, P., D. G. Steyn, and K. B. Strawbridge. 2000. Spatial and temporal variability of mixed-layer depth and entrainment zone thickness. *Bound.-Layer Meteor.* **97**, 47–71.

Halberstam, I., and J. P. Schieldge. 1981. Anomalous behavior of the atmospheric surface layer over a melting snowpack. *J. Appl. Meteor.* **20**, 255–265.

Hales, J. M. 1975. Atmospheric transformations of pollutants. In *Lectures on Air Pollution and Environmental Impact Analysis*, D. Haugen, Ed. American Meteorological Society, Boston.

Hales, J. M. 1983. Parameterization of removal mechanism. AMS/EPA Specialty Conference on Air Quality Modeling of the Nonstationary, Nonhomogeneous Urban Boundary Layer, October 31–November 4, Baltimore, MD.

Hall, F. G. (Ed.). 1999. BOREAS in 1999: Experiment in science overview. *J. Geophys. Res.* **104, D22**, 27,627–27,971.

Halldin, S., and S.-E. Gryning. 1999. Boreal forests and climate. *Agric. Forest Meteor.* **98–99**, 1–4.

Haltiner, G. J. 1971. *Numerical Weather Prediction*. John Wiley & Sons, New York.

Haltiner, G. J., and F. L. Martin. 1957. *Dynamical and Physical Meteorology*. McGraw-Hill, New York.

Haltiner, G. J., and R. T. Williams. 1980. *Numerical Prediction and Dynamic Meteorology*, 2nd ed. John Wiley & Sons, New York.

Hamilton, P., and M. Rattray Jr. 1978. A numerical model of the depth-dependent, wind-driven upwelling circulation on a continental shelf. *J. Phys. Oceanogr.* **8**, 437–457.

Hane, C. E. 1973. The squall line thunderstorm: Numerical experimentation. *J. Atmos. Sci.* **30**, 1672–1690.

Hane, C. E. 1978. Scavenging of urban pollutants by thunderstorm rainfall: Numerical experimentation. *J. Appl. Meteor.* **17**, 699–710.

Hänel, G. 1971. New results concerning the dependence of visibility on relative humidity and their significance in a model for visibility forecast. *Contrib. Atmos. Phys.* **44**, 137–167.

Hänel, G., R. Busen, C. Hillenbrand, and R. Schloss. 1982. Light absorption measurements: New techniques. *Appl. Opt.* **21**, 382–386.

Hanna, S. R. 1979. Some statistics of Lagrangian and Eulerian wind fluctuation. *J. Appl. Meteor.* **18**, 518–531.

Hanna, S. R. 1994. Mesoscale meteorological model evaluation techniques with emphasis on needs of air quality models. In *Mesoscale Modeling of the Atmosphere*, R. A. Pielke, Sr. and R. P. Pearce, Eds., American Meteorological Society, Boston, 47–58.

Hanna, S. R., and F. A. Gifford. 1975. Meteorological effects of energy dissipation at large power parks. *Bull. Amer. Meteor. Soc.* **56**, 1069–1077.

Hanna, S. R., and S. D. Swisher. 1971. Meteorological effects of the heat and moisture produced by man. *Nuclear Safety* **12**, 114–122.

Hanna, S. R., and R. Yang. 2001. Evaluations of mesoscale models' simulations of near-surface winds, temperature gradients, and mixing depths. *J. Appl. Meteor.* **40**, 1095–1104.

Harada, A. 1981. Urban and industrial effects on precipitation and thunder days in Hokkaido, Japan. *Pap. Meteor. Geophys.* **32**, 233–245.

Harrington, J. Y., G. Feingold, and W. R. Cotton. 2000. Radiative impacts on the growth of a population of drops within simulated summertime Arctic stratus. *J. Atmos. Sci.* **57**, 766–785.

Harrington, J. Y., M. P. Meyers, R. L. Walko, and W. R. Cotton. 1995. Parameterization of ice crystal conversion processes due to vapor deposition for mesoscale models using double-moment basis functions. Part I: Basic formulation and parcel model results. *J. Atmos. Sci.* **52**, 4344–4366.

Harrison, R., and B. McGoldrick. 1981. Mapping artificial heat release in Great Britain. *Atmos. Environ.* **15**, 667–674.

Harshvardhan, 1987. Fast radiation parameterization for atmospheric circulation models. *J. Geophys. Res.* **92**, 1009–1016.

Hartman, M. D., J. S. Baron, R. B. Lammers, D. W. Cline, L. E. Band, G. E. Liston, and C. Tague. 1999. Simulations of snow distribution and hydrology in a mountain basin. *Water Resour. Res.* **35**, 1587–1603.

Hartsell, C. 1970. Case study of a traveling hailstorm. Report No. 70-1. Institute of Atmospheric Science, South Dakota School of Mines and Technology, Rapid City, SD.

Hasager, C. B., and N. O. Jensen. 1999. Surface-flux aggregation in heterogeneous terrain. *Quart. J. Roy. Meteor. Soc.* **125**, 2017–2101.

Haurwitz, B. 1947. Comments on the sea breeze circulation. *J. Meteor.* **4**, 1–8.

Hawkins, J. D., and D. W. Stuart. 1980. Low-level atmospheric changes over Oregon's coastal upwelling region. *Mon. Wea. Rev.* **108**, 1029–1040.

Hayden, B. P. 1998. Ecosystem feedbacks on climate at the landscape scale. *Phil. Trans. Roy. Soc. London, Ser. B* **353**, 5–18.

Hearn, A. C. 1973. Reduce 2 user manual. Report prepared in part from support by the National Science Foundation under Grant No. GJ-32181 and the Advanced Research Projects Agency of the Office of the Department of Defense under Contract No. DAHC 15-73-C-0363.

Heicklen, J. 1976. *Atmospheric Chemistry*. Academic Press, New York.

Heimann, D., and G. Gross. 1999. Coupled simulation of meteorological parameters and sound level in a narrow valley. *Appl. Acoustics* **56**, 73–100.

Helvey, J., and J. Patric. 1965. Canopy and litter interception of rainfall by hardwoods of eastern United States. *Water Resour. Res.* **1**, 193–206.

Henderson-Sellers, A., Z.-L. Yang, and R. E. Dickinson. 1993. The project for intercomparison of land-surface parameterization schemes. *Bull. Amer. Meteor. Soc.* **74**, 1335–1349.

Henderson-Sellers, A., A. J. Pitman, P. K. Love, P. Irannejad, and T. H. Chen. 1995. The project for intercomparison of land-surface parameterization schemes (PILPS): Phases 2 and 3. *Bull. Amer. Meteor. Soc.* **76**, 489–503.

Héreil, P., and R. Laprise. 1996. Sensitivity of internal gravity waves solutions to the time step of a semi-implicit semi-Lagrangian nonhydrostatic model. *Mon. Wea. Rev.* **124**, 972–999.

Herzegh, P. H., and P. V. Hobbs. 1980. The mesoscale and microscale structure and organization of clouds and precipitation in midlatitude cyclones. II: Warm-frontal clouds. *J. Atmos. Sci.* **37**, 597–611.

Herzegh, P. H., and P. V. Hobbs. 1981. The mesoscale and microscale structure and organization of clouds and precipitation in midlatitude cyclones. IV. Vertical air motions and microphysical structures of prefrontal surge clouds and cold-frontal clouds. *J. Atmos. Sci.* **38**, 1771–1784.

Hess, G. D., M. E. Cope, S. Lee, P. C. Manins, G. A. Mills, K. Puri, and K. Tory. 2000. The development of the Australian Air Quality Forecasting System: Current status. In *Air Pollution Modeling and Its Application,* Vol. XIV, S.-E. Gryning and F. A. Schiermeier, Eds. Kluwer Academic/Plenum Publishers, London.

Hickey, J. R., L. L. Stowe, H. Jocobowitz, P. Pellegrino, R. H. Maschkoff, F. House, and T. H. Vonder Haar. 1980. Initial solar irradiance determinations form Nimbus 7 cavity radiometer measurements. *Science* **208**, 281–283.

Hicks, B. B. 1978. Comments on the characteristics of turbulent velocity components in the surface layer under convective conditions. *Bound.-Layer Meteor.* **15**, 255–258.

Hicks, B. B. 1981. An analysis of Wangara micrometeorology: Surface stress, sensible heat, evaporation, and dewfall. Technical Memorandum ERL ARL-104, NOAA Boulder, CO.

Hicks, B. B., and R. G. Everett. 1979. Comment on "Turbulent exchange coefficients for sensible heat and water vapor under advective conditions." *J. Appl. Meteor.* **18**, 381–382.

Hildebrand, F. B. 1962. *Advanced Calculus for Applications.* Prentice-Hall, Englewood Cliffs, NJ.

Hill, F. F., K. A. Browning, and M. J. Bader. 1981. Radar and rain-gauge observations of orographic rain over south Wales. *Quart. J. Roy. Meteor. Soc.* **107**, 643–670.

Hill, G. E. 1974. Factors controlling the size and spacing of cumulus clouds as revealed by numerical experiments. *J. Atmos. Sci.* **31**, 646–673.

Hill, G. E. 1978. Observations of precipitation-forced circulations in winter orographic storms. *J. Atmos. Sci.* **35**, 1463–1472.

Hill, J. D. 1971. Snow squalls in the lee of Lake Erie and Lake Ontario. Technical Memorandum NWS ER-43, NOAA, Boulder, CO.

Hirschberg, P. A., and J. D. Doyle. 1995. An examination of pressure tendency mechanisms in an idealized simulation of extratropical cyclogenesis. *Tellus* **47A**, 747–758.

Hjelmfelt, M. R. 1980. Numerical simulation of the effects of St. Louis on boundary layer airflow and convection. Ph.D. dissertation, University of Chicago.

Hjelmfelt, M. R. 1982. Numerical simulation of the effects of St. Louis on mesoscale boundary layer airflow and vertical air motion: Simulations of urban vs. non-urban effects. *J. Appl. Meteor.* **21**, 1239–1257.

Hjelmfelt, M. R., and R. R. Braham Jr. 1983. Numerical simulation of the airflow over Lake Michigan for a major lake-effect snow event. *Mon. Wea. Rev.* **111**, 205–219.

Hobbs, P. V. 1978. Organization and structure of clouds and precipitation on the mesoscale and microscale in cyclonic storms. *Rev. Geophys. Space Phys.* **16**, 741–755.

Hobbs, P. V., and P. O. G. Persson. 1982. The mesoscale and microscale structure and organization of clouds and precipitation in mid-latitude cyclones. 5. The substructure of narrow cold-frontal rainbands. *J. Atmos. Sci.* **39**, 280–295.

Hobbs, P. V., R. C. Eastern, and A. B. Fraser. 1973. A theoretical study of the flow of air and fallout of solid precipitation over mountainous terrain. Part II. Microphysics. *J. Atmos. Sci.* **30**, 813–823.

Hobbs, P. V., T. J. Matejka, P. H. Herzegh, J. D. Locatelli, and R. A. Houze Jr. 1980. The mesoscale and microscale structure and organization of clouds and precipitation in midlatitude cyclone. I. A case study of a cold front. *J. Atmos. Sci.* **37**, 568–596.

Hodur, R. M. 1997. The Naval Research Laboratory's Coupled Ocean/Atmosphere Mesoscale Prediction System (COAMPS). *Mon. Wea. Rev.* **125**, 1414–1430.

Hodur, R. M., and J. D. Doyle. 1998. The coupled ocean/atmosphere mesoscale model prediction system (COAMPS). *Coastal Ocean Predict. Coastal and Estuarine Stud.* **56**, 125–155.

Hof, H. 1999. Land surface data sets. *IGBP Global Change Newsletter* **39**, 18–19.

Hogstrom, U. 1988. Non-dimensional wind and temperature profiles in the atmospheric surface layer: A re-evaluation. *Bound.-Layer Meteor.* **42**, 55–78.

Hogstrom, U. 1996. Review of some basic characteristics of the atmospheric surface layer. *Bound.-Layer Meteor.* **78**, 215–246.

Hoinka, K. P. 1980. Synoptic-scale atmospheric features and foehn. *Contrib. Atmos. Phys.* **53**, 486–508.

Højstrup, J. 1981. A simple model for the adjustment of velocity spectra in unstable conditions downstream of an abrupt change in roughness and heat flux. *Bound.-Layer Meteor.* **21**, 341–356.

Hoke, J. E., and R. A. Anthes. 1976. The initialization of numerical models by a dynamic-initialization technique. *Mon. Wea. Rev.* **104**, 1551–1556.

Hoke, J. E., and R. A. Anthes. 1977. Dynamic initialization of a three-dimensional primitive-equation model of Hurricane Alma of 1962. *Mon. Wea. Rev.* **111**, 1046–1051.

Holle, R. L., and M. W. Maier. 1980. Tornado formation from downdraft interaction in the FACE mesonetwork. *Mon. Wea. Rev.* **108**, 1010–1028.

Holle, R. L., and A. I. Watson. 1983. Duration of convective events related to visible cloud, convergence, radar, and rain gauge parameters over south Florida. *Mon. Wea. Rev.* **111**, 1046–1051.

Holley, R. M. 1972. Surface temperature of a tropical island and surrounding ocean measured with an airborne infrared radiometer. M.S. thesis, Florida State University.

Holroyd, E. W. 1982. Some observations on mountain-generated cumulonimbus rainfall on the northern Great Plains. *J. Appl. Meteor.* **21**, 560–565.

Holton, J. R. 1972. *An Introduction to Dynamic Meteorology*. Academic Press, New York.

Holtslag, A. A. M. 1998. Fluxes and gradients in atmospheric boundary layers. In *Clear and Cloudy Boundary Layers*, A. A. M. Holtslag and P. G. Duynkerke, Eds. Royal Netherlands Academy of Arts and Sciences, Amsterdam.

Holtslag, A. A. M., and B. A. Boville. 1993. Local versus nonlocal boundary-layer diffusion in a global climate model. *J. Climate* **6**, 1825–1842.

Holtslag, A. A. M., and P. G. Duynkerke. 1998. *Clear and Cloudy Boundary Layers*. Royal Netherlands Academy of Arts and Sciences, Amsterdam.

Holtslag, A. A. M., E. Van Meijgaard, and W. C. De Roody. 1995. A comparison of boundary layer diffusion schemes in unstable conditions over land. *Bound.-Layer Meteor.* **76**, 69–95.

Homan, J. H., and D. G. Vincent. 1983. Mesoscale analysis of surface variables during the severe storm outbreak of April 10–11, 1979. *Mon. Wea. Rev.* **111**, 1122–1130.

Hong, S.-H., and H.-L. Pan. 1996. Nonlocal boundary layer vertical diffusion in a medium-range forecast model. *Mon. Wea. Rev.* **124**, 2322–2339.

Hong, S.-Y., and H.-L. Pan. 1998. Convective trigger function for a mass-flux cumulus parameterization scheme. *Mon. Wea. Rev.* **126**, 2599–2620.

Hong, X., M. J. Leach, and S. Raman. 1995. A sensitivity study of convective cloud formation by vegetation forcing with different atmospheric conditions. *J. Appl. Meteor.* **34**, 2008–2028.

Hootman, B. W., and W. Blumen. 1983. Analysis of nighttime drainage winds in Boulder, Colorado during 1980. *Mon. Wea. Rev.* **111**, 1052–1061.

Horne, F. E., and M. L. Kavvas. 1997. Physics of the spatially averaged snowmelt process. *J. Hydrol.* **191**, 179–207.

Horst, T. W., and J. C. Doran. 1981. Observations of the structure and development of nocturnal slope winds. Preprint, 2nd AMS Conference on Mountain Meteorology, November 10–13, 1981, Steamboat Springs, CO.

Hoskins, B. J., and F. P. Bretherton. 1972. Atmospheric frontogenesis models: Mathematical formulation and solution. *J. Atmos. Sci.* **29**, 11–37.

Houze, R. A. Jr. 1981. Structures of atmospheric precipitation systems: A global survey. *Radio Sci.* **16**, 671–689.

Houze, R. A. Jr. 1982. Cloud clusters and large-scale vertical motions in the tropics. *J. Meteor. Soc. Japan* **60**, 396–410.

Houze, R. A. Jr. 1989. Observed structure of mesoscale convective systems and implications for large-scale heating. *Quart. J. Roy. Meteor. Soc.* **115**, 425–461.

Houze, R. A. Jr., and A. K. Betts. 1981. Convection in GATE. *Rev. Geophys. Space Phys.* **19**, 541–576.

Houze, R. A. Jr., and C.-P. Cheng. 1981. Inclusion of mesoscale updrafts and downdrafts in computations of vertical fluxes by ensembles of tropical clouds. *J. Atmos. Sci.* **38**, 1751–1770.

Houze, R. A. Jr., and P. V. Hobbs. 1982. Organization and structure of precipitation cloud systems. *Adv. Geophys.* **24**, 225–315.

Houze, R. A. Jr., P. V. Hobbs, P. H. Herzegh, and D. B. Parsons. 1979. Size distributions of precipitation particles in frontal clouds. *J. Atmos. Sci.* **36**, 156–162.

Houze, R. A. Jr., S. G. Geotis, F. D. Marks Jr., and A. K. West. 1981a. Winter monsoon convection in the vicinity of north Borneo, Part I: Structure and time variation of the clouds and precipitation. *Mon. Wea. Rev.* **109**, 1595–1614.

Houze, R. A. Jr., S. A. Rutledge, T. J. Matejka, and P. V. Hobbs. 1981b. The mesoscale and microscale structure and organization of clouds and precipitation in midlatitude cyclones. III: Air motions and precipitation growth in a warm-frontal rainband. *J. Atmos. Sci.* **38**, 639–649.

Hovermale, J. B. 1965. A non-linear treatment of the problem of airflow over mountains. Ph.D. thesis, Pennsylvania State University, University Park, PA.

Hoxit, L. R. 1975. Diurnal variations in planetary boundary layer winds over land. *Bound.-Layer Meteor.* **8**, 21–38.

Hoxit, L. R., and C. F. Chappell. 1975a. Tornado outbreak of April 3–4, 1974. Synoptic analysis. Technical Report NOAA TR ERL 338-APCL 37, NOAA, Boulder, CO.

Hoxit, L. R., and C. F. Chappell. 1975b. An analysis of the mesoscale circulations which produced the April 3, 1974 tornadoes in northern Indiana. Proceedings of the 9th AMS Conference on Severe Local Storms, October 21–23, Norman, OK, 256–263.

Hoxit, L. R., R. A. Maddox, C. F. Chappell, F. L. Zurkerberg, H. M. Mogil, I. Jones, D. R. Greene, R. E. Saffle, and R. A. Scofield. 1978. Meteorological aspects of the Johnstown, PA flash flood 19–20 July 1977. Technical Report ERL 401-APCL 43, NOAA, Boulder, CO.

Hsie, E.-Y., and R. A. Anthes. 1984. Simulations of frontogenesis in a moist atmosphere using alternative parameterizations of condensation and precipitation. *J. Atmos. Sci.* **41**, 2701–2716.

Hsu, H.-M. 1979. Numerical simulations of mesoscale precipitation systems. Ph.D. dissertation, Dept. of Atmospheric and Oceanic Science, University of Michigan, Ann Arbor, MI.

Hsu, S. 1969. Mesoscale structure of the Texas coast sea breeze. Report No. 16, Atmospheric Science Group, College of Engineering, University of Texas, Austin, TX.

Hsu, S. 1970. Coastal air circulation system. Observations and empirical model. *Mon. Wea. Rev.* **98**, 487–509.

Hsu, S. 1973. Dynamics of the sea breeze in the atmospheric boundary layer: A case study of the free convection region. *Mon. Wea. Rev.* **101**, 187–194.

Hsu, S., B. W. Blanchard, and Z. Yan. 1999. A simplified equation for Paulson's $\sigma_m(Z/L)$ formulation for overwater applications. *J. Appl. Meteor.* **38**, 623–625.

Hsu, W.-R., and W.-Y. Sun. 1994. A numerical study of a low-level jet and its accompanying secondary circulation in a Mei-Yu system. *Mon. Wea. Rev.* **122**, 324–340.

Hu, Q., E. R. Reiter, and R. A. Pielke. 1988. Analytic solutions to Long's model: A comparison of nonhydrostatic and hydrostatic cases. *Meteor. Atmos. Phys.* **39**, 184–196.

Hu, Z., S. Islam, and L. Jiang. 1999. Approaches for aggregating heterogeneous surface parameters and fluxes for mesoscale and climate models. *Bound.-Layer Meteor.* **93**, 313–336.

Hua, B.-L., and F. Thomasset. 1983. A numerical study of the effects of coastline geometry on wind-induced upwelling in the Gulf of Lions. *J. Phys. Oceanogr.* **13**, 678–694.

Huang, C.-Y. 2000. A forward-in-time anelastic nonhydrostatic model in a terrain-following coordinate. *Mon. Wea. Rev.* **128**, 2108–2134.

Hughes, R. L. 1978. A numerical simulation of mesoscale flow over mountains terrain. Paper No. 303, US ISSN 0067-0340, Dept. of Atmospheric Science, Colorado State University, Fort Collins, CO.

Huguet, P., J. Moussafir, and R. Poisson. 1978. Eiffel Tower and radio tower field study, 1977–1978. Bertin Technical Report to Ministere de L'Environment, France.

Hunt, J. C. R., and J. E. Simpson. 1982. Atmospheric boundary layers over non-homogeneous terrain. In *Engineering Meteorology*, E. Plate, Ed., Elsevier, New York, 269–318.

Hunt, J. C. R., W. H. Snyder, and R. E. Lawson Jr. 1978. Flow structure and turbulent diffusion around a three-dimensional hill. Part I. Flow structure. Report EPA-600/4-78-041, U.S. Environmental Protection Agency, Office of Research and Development, pp. 1–83.

Huschke, R. E. 1959. *Glossary of Meteorology*. American Meteorological Society, Boston.

Hutchinson, M. F. 1995. Stochastic space-time weather models from ground-based date. *Agric. Forest Meteor.* **73**, 237–264.

Hutchinson, M. F. 1998a. Interpolation of rainfall data with thin plate smoothing splines: I. Two-dimensional smoothing of data with short range correlation. *J. Geogr. Info. Dec. Anal.* **2**, 152–167.

Hutchinson, M. F. 1998b. Interpolation of rainfall data with thin plate smoothing splines: II. Analysis of topographic dependence. *J. Geogr. Info. Dec. Anal.* **2**, 168–185.

Hyun, J. M., and M. Kim. 1979. The effect of nonuniform wind shear on the intensification and reflection of mountain waves. *J. Atmos. Sci.* **36**, 2379–2384.

Ichinose, T., K. Shimodozono, and K. Hanaki. 1999. Impact of anthropogenic heat on urban climate in Tokyo. *Atmos. Environ.* **33**, 3897–3909.

Idso, S. B. 1981. Surface energy balance and the genesis of deserts. *Arch. Meteor. Geophys. Bioklimatol.* **30**, 253–260.

Idso, S. B., and R. D. Jackson. 1969. Thermal radiation from the atmosphere. *J. Geophys. Res.* **74**, 5397–5403.

Idso, S. B., R. D. Jackson, B. Kimball, and F. Nakayama. 1975a. The dependence of bare soil albedo on soil water content. *J. Appl. Meteor.* **14**, 109–113.

Idso, S. B., R. D. Jackson, and R. J. Reginato. 1975b. Detection of soil moisture by remote surveillance. *Amer. Sci.* **63**, 549–557.

Idso, S., J. A. Aase, and R. D. Jackson. 1975c. Net radiation-soil heat flux relations as influenced by soil water content variations. *Bound.-Layer Meteor.* **9**, 113–122.

Iribarne, J. V., and W. L. Godson. 1973. *Atmospheric Thermodynamics*. D. Reidel, Boston.

Ishihara, M., and Z. Yanagisawa. 1982. Structure of a tropical squall line observed in the western tropical Pacific during MONEX. *Pap. Meteor. Geophys.* **33**, 117–135.

Jackson, P. S., and J. C. R. Hunt. 1975. Turbulent wind flow over a low hill. *Quart. J. Roy. Meteor. Soc.* **101**, 929–955.

Jackson, S. T., and M. E. Lyford. 1999. Pollen dispersal models in quaternary plant ecology: Assumptions, parameters, and prescriptions. *Bot. Rev.* **65**, 39–75.

Jacobs, C. A., and P. S. Brown Jr. 1974. IFYCL Final Report, Vol. IV. Three-dimensional results. CEM Report No. 4131–509d. The Center for the Environment and Man, Hartford, CT.

Jacobson, M. Z. 1999. Fundamentals of atmospheric modeling. Cambridge University Press, Cambrigde, England, 656 pp.

Jacquemin, B., and J. Noilhan. 1990. Sensitivity study and validation of a land surface parameterization using the HAPEX-MOBILHY data set. *Bound.-Layer Meteor.* **52**, 93–134.

Janjić, Z. I. 1979. Forward-backward scheme modified to prevent two-grid-interval noise and its application in sigma coordinate models. *Contrib. Atmos. Phys.* **52**, 69–84.

Janjić, Z. I. 1990. A step-mountain coordinate: physical package. *Mon. Wea. Rev.* **118**, 1429–1443.

Janjić, Z. I. 1994. The step-mountain Eta coordinate model: Further developments of the convection, viscous sublayer, and turbulence closure schemes. *Mon. Wea. Rev.* **122**, 927–945.

Janjić, Z. I. 1995. A note on the performance of the multiply-upstream semi-Lagrangian advection schemes for one-dimensional nonlinear momentum conservation equation. *Meteor. Atmos. Phys.* **55**, 1–16.

Janjić, Z. I. 1996. The Mellor-Yamada level-2.5 scheme in the NCEP Eta model. Preprint, 11th AMS Conference on Numerical Weather Prediction, Norfolk VA, 333–334.

Janjić, Z. I. 1997. Advection scheme for passive substances in the NCEP Eta model. Research Activities in Atmospheric Oceanic Modelling, Report 25, WMO, Geneva.

Janjić, Z. I., S. Nickovic, D. Gavrilov, and D. G. Deaven. 1988. The step mountain coordinate: Model description and performance for cases of alpine cyclogenesis and for a case of an Appalachian redevelopment. *Mon. Wea. Rev.* **116**, 1493–1518.

Janjić, Z. I., J. P. Gerrity, and S. Nickovic. 2001. An alternative approach to nonhydrostatic modeling. *Mon. Wea. Rev.* **129**, 1164–1518.

Jazcilevich, A., V. Fuentes, E. Jauregui, and E. Luna. 2000. Simulated urban climate response to historical land use modification in the basin of Mexico. *Climate Change* **44**, 515–536.

Jegede, O. O., and T. Foken. 1999. A study of the internal boundary layer due to a roughness change in neutral conditions observe during the LINEX field campaigns. *Theor. Appl. Climatol.* **62**, 31–41.

Jensen, N. O., and N. E. Busch. 1982. Atmospheric turbulence. In *Engineering Meteorology*, E. Plate, Ed., Elsevier, New York, 179–231.

Jiang, H., W. R. Cotton, J. O. Pinto, J. A. Curry, and M. J. Weissbluth. 2000. Cloud-resolving simulations of mixed-phase arctic stratus observed during BASE: Sensitivity to concentration of ice crystals and large-scale heat and moisture advection. *J. Atmos. Sci.* **57**, 2105–2117.

Jiusto, J. E., and G. Bosworth. 1971. Fall velocity of snowflakes. *J. Appl. Meteor.* **10**, 1352–1354.

Jiusto, J. E., and M. L. Kaplan. 1972. Snowfall from lake-effect storms. *Mon. Wea. Rev.* **100**, 62–66.

Jiusto, J. E., D. A. Paine, and M. L. Kaplan. 1970. Great Lakes snowstorms, Part 2: Synoptic and climatological aspects. ESSA Grant Report E22-13-69(G), U.S. Department of Commerce.

Johnson, A. Jr., and J. J. O'Brien. 1973. A study of an Oregon sea breeze event. *J. Appl. Meteor.* **12**, 1267–1283.

Johnson, D. R., and L. W. Uccellini. 1983. A comparison of methods for computing the sigma-coordinate pressure gradient force for flow over sloped terrain in a hybrid theta-sigma model. *Mon. Wea. Rev.* **111**, 870–886.

Johnson, R. H. 1977. Effects of cumulus convection on the structure and growth of the mixed layer over south Florida. *Mon. Wea. Rev.* **105**, 713–724.

Johnson, R. H. 1982. Vertical motion in near-equatorial winter monsoon convection. *J. Meteor. Soc. Japan* **60**, 682–690.

Johnson, R. H., and D. C. Kriete. 1982. Thermodynamics and circulation characteristic of winter monsoon tropical mesoscale convection. *Mon. Wea. Rev.* **110**, 1898–1911.

Johnson, R. H., and M. E. Nicholls. 1983. A composite analysis of the boundary layer accompanying a tropical squall line. *Mon. Wea. Rev.* **111**, 308–319.

Johnson, R. H., and J. J. Toth. 1982a. Topographic effects and weather forecasting in the Colorado PROFS mesonetwork area. Preprint, AMS Conference on Weather Forecasting and Analysis, Seattle, WA.

Johnson, R. H., and J. J. Toth. 1982b. A climatology of the July 1981 surface flow over northeast Colorado. Paper No. 342, Dept. of Atmospheric Science, Colorado State University, Fort Collins, CO.

Johnson, R. H., T. M. Rickenbach, S. A. Rutledge, P. E. Ciesielski, and W. H. Schubert. 1999. Trimodal characteristics of tropical convection. *J. Climate* **12**, 2397–2418.

Jones, A. S., I. C. Guch, and T. H. Vonder Haar. 1998a. Data assimilation of satellite-derived heating rates as proxy surface wetness data into regional atmospheric mesoscale model. Part I: Methodology. *Mon. Wea. Rev.* **126**, 634–645.

Jones, A. S., I. C. Guch, and T. H. Vonder Haar. 1998b. Data assimilation of satellite-derived heating rates as proxy surface wetness data into a regional atmospheric mesoscale model. Part II: A case study. *Mon. Wea. Rev.* **126**, 646–667.

Jones, R. W. 1973. A numerical experiment on the prediction of the northeast (winter) monsoon in southwest Asia. Technical Report ERL 272-WMPO-3, NOAA, 1–56.

Jones, R. W. 1977a. Noise control for a nested grid tropical cyclone model. *Contrib. Atmos. Phys.* **50**, 393–402.

Jones, R. W. 1977b. A nested grid for a three-dimensional model. *J. Atmos. Sci.* **34**, 1528–1553.

Jones, R. W. 1980. A three-dimensional tropical cyclone model with release of latent heat by the resolvable scales. *J. Atmos. Sci.* **37**, 930–938.

Juang, H.-M. H. 2000. The NCEP mesoscale spectral model: A revised version of the nonhydrostatic regional spectral model. *Mon. Wea. Rev.* **128**, 2329–2362.

Juang, H.-M. H., and M. Kanamitsu. 1994. The NMC nested regional spectral model. *Mon. Wea. Rev.* **122**, 3–26.

Junfang, R., B. Su, and M. Zhao. 1999. The influence of scalar roughness on land surface–atmosphere transfer. *Chinese. J. Atmos. Sci.* **23**, 179–188.

Junge, C. E. 1963. *Air Chemistry and Radioactivity*. Academic Press, New York.

Kabat, P. (Ed.). 1999. Global Change Newsletter—The IGBP-BAHC Special Issue, **39**, September.

Kabat, P., C. A. Nobre, A. C. Janetos, and R. W. A. Hutjes (Eds.). 1998. LBA is moving forward. *IGBP Global Change Newsletter,* **33**, 1–9.

Kader, B. A., and A. M. Yaglom. 1990. Mean fields and fluctuation moments in unstably stratified turbulent boundary layers. *J. Fluid Mech.* **212**, 637–661.

Kahl, J. D., and P. J. Samson. 1988. Shear effects on wind interpolation accuracy. *J. Appl. Meteor.* **27**, 1299–1301.

Kain, J. S., and J. M. Fritsch. 1990. A one-dimensional entraining/detraining plume model and its application in convective parameterization. *J. Atmos. Sci.* **47**, 2784–2802.

Kain, J. S., and J. M. Fritsch. 1993. Convective parameterization for mesoscale models: The Kain-Fritsch Scheme. In *The Representation of Cumulus Convection in Numerical Models,* Meteor. Monogr. K. A. Emanuel and D. J. Raymond, Eds. No. 46, American Meteorological Society, Boston, 165–170.

Kallo, K. P., and T. W. Owen. 1999. Satellite-based adjustments for urban heat island bias. *J. Appl. Meteor.* **38**, 806–813.

Kallos, G., P. Kassomenos, and R. A. Pielke. 1993. Synoptic and mesoscale weather conditions during air pollution episodes in Athens, Greece. *Bound.-Layer Meteor.* **62**, 163–184.

Kallos, G., V. Kotroni, K. Lagouvardos, and A. Papadopoulos. 1998. On the long-range transport of air pollutants from Europe to Africa. *Geophys. Res. Lett.* **25**, 619–622.

Kalthoff, N., F. Fiedler, M. Kohler, O. Kolle, H. Mayer, and A. Wenzel. 1999. Analysis of energy balance components as a function of orography and land use and comparison of results with the distribution of variables influencing local climate. *Theor. Appl. Climatol.* **62**, 65–84.

Kaminski, T., R. Giering, and M. Heimann. 1997. Sensitivity of the seasonal cycle of CO_2 at remote monitoring stations with respect to seasonal surface exchange fluxes determined with the adjoint of an atmospheric transport model. *Phys. Chem. Earth*, **22**, 457–463.

Kanae, S., T. Oki, and K. Musiake. 2001. Impact of deforestation on regional precipitation over the Indochina Peninsula. *J. Hydrometeor.* **2**, 51–70.

Kanda, M., Y. Inoue, and I. Uno. 2001. Numerical study on cloud lines over an urban street in Tokyo. *Bound.-Layer Meteor.* **98**, 251–273.

Kang, S.-D., F. Kimura, and S. Takahashi. 1998. A numerical study on the Karman vortex generated by divergence of momentum flux in flow past an isolated mountain. *J. Meteor. Soc. Japan* **76**, 925–935.

Kaplan, W. 1952. *Advanced Calculus*. Addison-Wesley, Reading, MA.

Kaplen, M. L., J. W. Zack, V. C. Wong, and J. J. Tuccillo. 1982. Initial results from a mesoscale atmospheric simulation system and comparisons with the AVE-SESAME I data set. *Mon. Wea. Rev.* **110**, 1564–1590.

Kasahara, A. 1974. Various vertical coordinate systems used for numerical weather prediction. *Mon. Wea. Rev.* **102**, 509–522.

Kasahara, A. 1982. Nonlinear normal mode initialization and the bounded derivative method. *Rev. Geophys. Space Phys.* **20**, 385–397.

Kassomenos, P., V. Kotroni, and G. Kallos. 1995. Analysis of climatological and air quality observations from greater Athens area. *Atmos. Environ.* **29**, 3671–3688.

Kasten, F. 1969. Visibility forecast in the phase of precondensation. *Tellus* **21**, 631–635.

Keen, C. S., and W. A. Lyons. 1978. Lake/land breeze circulations on the western shore of Lake Michigan. *J. Appl. Meteor.* **17**, 1843–1855.

Keen, C. S., W. A. Lyons, and J. A. Schuh. 1979. Air pollution transport studies in a coastal zone using kinematic diagnostic analysis. *J. Appl. Meteor.* **18**, 606–615.

Kerman, B. R. 1982. A similarity model of shoreline fumigation. *Atmos. Environ.* **16**, 467–477.

Kerman, B. R., R. E. Mickle, R. V. Portelli, N. B. Trivett, and P. K. Misra. 1982. The Nanticoke shoreline diffusion experiment—II. Internal boundary layer structure. *Atmos. Environ.* **16**, 423–437.

Kern, J. S. 1995a. Evaluation of soil water retention models based on basic soil physical properties. *Soil Sci. Soc. Am. J.* **59**, 1134–1141.

Kern, J. S. 1995b. Geographic patterns of soil water-holding capacity in the contiguous United States. *Soil Sci. Soc. Am. J.* **59**, 1126–1133.

Kerschgens, M. 1983. Parameterization of radiation for the modeling of the urban-boundary layer. AMS/EPA Specialty Conference on Air Quality Modeling of the Nonstationary, Nonhomogeneous Urban Boundary Layer, October 31–November 4, Baltimore, MD.

Kessler, E. 1969. On the distribution and continuity of water substance in atmospheric circulations. *Meteor. Mag.* **32**, 1–84.

Kessler, R. C., and R. A. Pielke. 1982. A numerical study of airflow over adjacent ridges. Unpublished manuscript.

Kessler, R. C., and R. A. Pielke. 1983. A numerical study of the effect of latent heat release on the airflow over a mountain. Unpublished manuscript.

Keyser, D., and R. A. Anthes. 1977. The applicability of a mixed-layer model of the planetary boundary layer to real-data forecasting. *Mon. Wea. Rev.* **105**, 1351–1371.

Keyser, D., and D. R. Johnson. 1982. Effects of diabatic heating on the ageostrophic circulation of an upper tropospheric jet streak. NASA Contractor Report 3497, NASA Marshall Space Flight Center.

Kikuchi, Y., S. Arakawa, F. Kimura, K. Shirasaki, and Y. Nagano. 1981. Numerical study on the effects of mountains on the land and sea breeze circulation in the Kanto district. *J. Meteor. Soc. Japan* **59**, 67–85.

Kimura, F., and T. Kuwagata. 1995. Horizontal heat fluxes over complex terrain computed using a simple mixed-layer model and a numerical model. *J. Appl. Meteor.* **34**, 549–558.

Kimura, F., and S. Takahashi. 1991. The effects of land-use and anthropogenic heating on the surface temperature in the Tokyo metropolitan area: a numerical experiment. *Atmos. Environ.* **25B**, 155–164.

Kimura, R., and T. Eguchi. 1978. On dynamical processes of sea and land breeze circulations. *J. Meteor. Soc. Japan* **59**, 67–85.

Klemp, J. B., and D. R. Durran. 1983. An upper boundary condition permitting internal gravity wave radiation in numerical mesoscale models. *Mon. Wea. Rev.* **111**, 430–444.

Klemp, J. B., and D. K. Lilly. 1975. The dynamics of wave-induced downslope winds. *J. Atmos. Sci.* **32**, 320–339.

Klemp, J. B., and D. K. Lilly. 1978. Numerical simulation of hydrostatic mountain waves. *J. Atmos. Sci.* **35**, 78–107.

Klemp, J. B., and D. K. Lilly. 1980. Mountain waves and momentum flux. GARP Series No. 23, June 1980, WMO, Geneva, 116–141.

Klemp, J. B., and R. B. Wilhelmson. 1978a. The simulation of three-dimensional convective storm dynamics. *J. Atmos. Sci.* **35**, 1070–1096.

Klemp, J. B., and R. B. Wilhelmson. 1978b. Simulations of right- and left-moving storms produced through storm splitting. *J. Atmos. Sci.* **35**, 1097–1110.

Klink, K. 1995. Temporal sensitivity of regional climate to land-surface heterogeneity. *Phys. Geogr.* **16**, 289–314.

Klöppel, M., G. Stilke, and C. Wamser. 1978. Experimental investigations into variations of ground-based inversions and comparisons with results of simple boundary-layer models. *Bound.-Layer Meteor.* **15**, 135–145.

Knowles, C. E., and J. J. Singer. 1977. Exchange through a barrier island inlet: Additional evidence of upwelling off the northeast coast of North Carolina. *J. Phys. Oceanogr.* **7**, 146–152.

Knox, J. B., M. C. MacCracken, M. H. Dickerson, P. M. Gresho, F. M. Luther, and R. C. Orphan. 1983. Program report for FY 1982. Report UCRL-51444-82, Atmospheric and Geophysical Sciences Division, Physics Dept., Lawrence Livermore Laboratory.

Knupp, K. R. 1987. Downdrafts within High Plains cumulonimbi, Part. 1: General kinematic structure. *J. Atmos. Sci.* **44**, 987–1008.

Knupp, K. R., and W. R. Cotton. 1982a. An intense, quasi-steady thunderstorm over mountainous terrain. Part II: Doppler radar observations of the storm morphological structure. *J. Atmos. Sci.* **39**, 343–358.

Knupp, K. R., and W. R. Cotton. 1982b. An intense quasi-steady thunderstorm over mountainous terrain. Part III: Doppler radar observations of the turbulent structure. *J. Atmos. Sci.* **39**, 359–368.

Koch, S. E., and J. McCarthy. 1982. The evolution of an Oklahoma dryline, Part II: Boundary-layer forcing of mesoconvective systems. *J. Atmos. Sci.* **39**, 237–257.

Kondo, H. 1981. A numerical simulation of the influence of the large scale field on a mesoscale disturbance. *J. Meteor. Soc. Japan* **59**, 123–132.

Kondo, J., Y. Sasano, and T. Ishii. 1979. On wind-driven current and temperature profiles with diurnal period in the oceanic planetary boundary layer. *J. Phys. Oceanogr.* **9**, 360–372.

Kondratyev, J. 1969. *Radiation in the Atmosphere*. Academic Press, New York.

Kong, F. Y., and M. K. Yau. 1997. An explicit approach to microphysics in MC2. *Atmos. Ocean* **35**, 257–291.

Korb, G. J., R. M. Welch, and W. G. Zdunkowski. 1975. An approximate method for the determination of infrared fluxes in scattering and absorbing media. *Contrib. Atmos. Phys.* **48**, 84–95.

Kossmann, M., U. Corsmeier, S. F. J. DeWekker, F. Fielder, R. Vogtlin, N. Kalthoff, H. Gusten, and B. Neininger. 1999. Observations of handover processes between the atmospheric boundary layer and the free troposphere over mountainous terrain. *Contrib. Atmos. Phys.* **72**, 329–350.

Kotroni, V., G. Kallos, and K. Lagouvardos. 1997. Convergence zones over the Greek peninsula and associated thunderstorm activity. *Quart. J. Roy. Meteor. Soc.* **123**, 1961–1984.

Kotroni, V., G. Kallos, K. Lagouvardos, M. Varinou, and R. Walko. 1999a. Numerical simulations of the meteorological and dispersion conditions during an air pollution episode over Athens, Greece. *J. Appl. Meteor.* **38**, 432–447.

Kotroni, V., K. Lagouvardos, and G. Kallos. 1999b. Model investigation of a cloudband associated with a cold front over Eastern Mediterranean. *Phys. Chem. Earth* **24**, 633–636.

Kotroni, V., K. Lagouvardos, G. Kallos, and D. Ziakopoulos. 1999c. Severe flooding over central and southern Greece associated with pre-cold frontal orographic lifting. *Quart. J. Roy. Meteor. Soc.* **125**, 967–991.

Kowalczyk, G. S., C. E. Choquette, and G. E. Gordon. 1978. Chemical element balances and identification of air pollution sources in Washington, D.C. *Atmos. Environ.* **12**, 1143–1153.

Kozo, T. L. 1982a. An observational study of sea breezes along the Alaskan Beaufort sea coast: Part I. *J. Appl. Meteor.* **21**, 891–905.

Kozo, T. L. 1982b. An mathematical model of sea breezes along the Alaskan Beaufort sea coast: Part II. *J. Appl. Meteor.* **21**, 906–924.

Kozo, T. L. 1982c. Mesoscale wind phenomena along the Alaskan Beaufort sea coast. In *The Alaskan Beaufort Sea*, E. Reimnitz, Ed. Pacific Arctic Branch of Marine Geology, U.S. Department of the Interior.

Kreitzberg, C. W. 1976. Interactive applications of satellite observations and mesoscale numerical models. *Bull. Amer. Meteor. Soc.* **57**, 679–685.

Kreitzberg, C. W., and D. J. Perkey. 1976. Release of potential instability. Part I: A sequential plume model within a hydrostatic primitive equation model. *J. Atmos. Sci.* **33**, 40–63.

Kreitzberg, C. W., and D. J. Perkey. 1977. Release of potential instability. Part II. The mechanism of convective/mesoscale interaction. *J. Atmos. Sci.* **34**, 1579–1595.

Krishnamurti, T. N. 1962. Numerical integration of primitive equations by a quasi-Lagrangian advective scheme. *J. Appl. Meteor.* **1**, 508–521.

Krishnamurti, T. N., and L. Bounoua. 1995. *An Introduction to Numerical Weather Prediction Techniques*. CRC Press, Washington D.C.

Krishnamurti, T. N., and M. Kanamitsu. 1973. A study of a coasting easterly wave. *Tellus* **25**, 568–585.

Krishnamurti, T. N., and W. J. Moxim. 1971. On parameterization of convective and nonconvective latent heat releases. *J. Appl. Meteor.* **10**, 3–13.

Krishnamurti, T. N., M. Kanamitsu, B. Ceselski, and M. B. Mathur. 1973. Florida State University's Tropical Prediction Model. *Tellus* **25**, 523–535.

Krishnamurti, T. N., Y. Ramanathan, H.-L. Pan, R. J. Rasch, and J. Molinari. 1980. Cumulus parameterization and rainfall rates. *Mon. Wea. Rev.* **108**, 465–472.

Krishnamurti, T. N., V. Wong, H.-L. Pan, R. Pasch, J. Molinari, and P. Ardanuy. 1983. A three-dimensional planetary boundary layer model for the Somali jet. *J. Atmos. Sci.* **40**, 894–908.

Kuettner, J. P. 1986. Aim and conduct of ALPEX. In *Global Atmospheric Research Programme*, GARP Publications Series No. 27, WMO/TD-No. 108, WMO, Geneva, 3–13.

Kuhn, P. 1963. Radiometeorsonde observations of infrared flux emissivity of water vapor. *J. Appl. Meteor.* **2**, 368–378.

Kumar, A., and N. Barthakur. 1971. Convective heat transfer measurements of plants in a wind tunnel. *Bound.-Layer Meteor.* **2**, 218–227.

Kumar, P., M. P. Singh, and A. N. Natarajan. 1998. An analytical model for mountain wave in stratified atmosphere. *MAUSAM* **49**, 433–438.

Kuo, H. L. 1965. On the formation and intensification of tropical cyclones through latent heat release by cumulus convection. *J. Atmos. Sci.* **22**, 40–63.

Kuo, H. L. 1968. The thermal interaction between the atmosphere and the earth and propagation of diurnal temperature waves. *J. Atmos. Sci.* **25**, 682–706.

Kuo, H. L. 1974. Further studies of the parameterization of the influence of cumulus convection on large-scale flow. *J. Atmos. Sci.* **31**, 1232–1240.

Kuo, H. L. 1979. Infrared cooling rate in a standard atmosphere. *Contrib. Atmos. Phys.* **52**, 85–94.

Kuo, H. L., and W. H. Raymond. 1980. A quasi–one-dimensional cumulus cloud model and parameterization of cumulus heating and mixing effects. *Mon. Wea. Rev.* **108**, 991–1009.

Kuo, Y.-H., and Y.-R. Guo. 1989. Dynamic initialization using observations from a network of profilers and its impact on short-range numerical weather prediction. *Mon. Wea. Rev.* **117**, 1975–1998.

Kuo, Y.-H., and S. Low-Nam. 1990. Thermal structure and airflow in a model simulation of an occluded marine cyclone. *Mon. Wea. Rev.* **120**, 2280–2297.

Kuo, Y.-H., R. J. Reed, and S. Low-Nam. 1992. Thermal structure and airflow in a model simulation of an occluded marine cyclone. *Mon. Wea. Rev.* **120**, 2280–2297.

Kurihara, Y. 1973. A scheme for moist convective adjustment. *Mon. Wea. Rev.* **101**, 547–553.

Kurihara, Y. 1975. Budget analysis of a tropical cyclone simulated in an axisymmetric numerical model. *J. Atmos. Sci.* **32**, 25–59.

Kurihara, Y. 1976. On the development of spiral bands in a tropical cyclone. *J. Atmos. Sci.* **33**, 940–958.

Kurihara, Y., and M. A. Bender. 1979. Supplementary note on a scheme of dynamic initialization of the boundary layer in a primitive equation model. *Mon. Wea. Rev.* **107**, 1219–1221.

Kurihara, Y., and M. A. Bender. 1982. Structure and analysis of the eye of a numerically simulated tropical cyclone. *J. Meteor. Soc. Japan* **60**, 381–395.

Kurihara, Y., and R. E. Tuleya. 1974. Structure of a tropical cyclone developed in a three-dimensional numerical simulation model. *J. Atmos. Sci.* **31**, 893–919.

Kurihara, Y., and R. E. Tuleya. 1978. A scheme for dynamic initialization of the boundary layer in a primitive equation model. *Mon. Wea. Rev.* **106**, 113–123.

Kuwagata, T., and F. Kimura. 1997. Daytime boundary layer evolution in a deep valley. Part II: Numerical simulation of the cross-valley circulation. *J. Appl. Meteor.* **36**, 883–895.

Lacis, A. A., and J. E. Hansen. 1974. A parameterization for the absorption of solar radiation in the earth's atmosphere. *J. Atmos. Sci.* **31**, 118–133.

Lackmann, G. M., J. R. Gyakum, and R. Benoit. 1998. Moisture transport diagnosis of a wintertime precipitation event in the Mackenzie River basin. *Mon. Wea. Rev.* **126**, 668–691.

Lafore, J. P., J. Stein, N. Asencio, P. Bougeault, V. Ducrocq, J. Duron, C. Fischer, P. Hereil, P. Mascart, V. Masson, J. P. Pinty, J. L. Redelsperger, E. Richard, and J. Vila-Guerau de Arellano. 1998. The Meso-NH Atmospheric Simulation System. Part I: Adiabatic formulation and control simulations. *Ann. Geophys.* **16**, 90–109.

Lagouvardos, K., V. Kotroni, S. Dobricic, S. Nickovic, and G. Kallos. 1996. The storm of October 21–22, 1994, over Greece: Observations and model results. *J. Geophys. Res.* **101**, 26,217–26,226.

Lagouvardos, K., V. Kotroni, and G. Kallos. 1998. An extreme cold surge over the Greek peninsula. *Quart. J. Roy. Meteor. Soc.* **124**, 2299–2327.

Lagouvardos, K., V. Kotroni, S. Nickovic, D. Jovic, and G. Kallos. 1999. Observations and model simulations of a winter sub-synoptic vortex over the central Mediterranean. *Meteor. Appl.* **6**, 371–383.

Lakhtakia, M. N., and T. T. Warner. 1994. A comparison of simple and complex treatments of surface hydrology and thermodynamics suitable for mesoscale atmospheric models. *Mon. Wea. Rev.* **122**, 880–896.

Lal, M. 1979. Application of Pielke model to air quality studies. *MAUSAM* **30**, 69–78.

Lalas, D. P., V. R. Veirs, G. Karras, and G. Kallos. 1982. An analysis of the SO_2 concentration levels in Athens, Greece. *Atmos. Environ.* **16**, 531–544.

Lalas, D. P., D. N. Asimakopoulos, D. G. Deligiorgi, and C. G. Helmis. 1983. Sea breeze circulation and photochemical pollution in Athens, Greece. *Atmos. Environ.* **17**, 1621–1632.

Landsea, C., and J. Knaff. 2000. How much skill was there in forecasting the very strong 1997–98 El Niño? *Bull. Amer. Meteor. Soc.* **81**, 2107–2119.

Landsberg, H. E. 1981. *The Urban Climate*. Academic Press, New York.

Lang, A. R. G., K. G. McNauton, C. Fazu, E. F. Bradley, and E. Ohtaki. 1983. Inequality of eddy transfer coefficients for vertical transport of sensible and latent heats during advective inversions. *Bound.-Layer Meteor.* **25**, 25–41.

Lange, R. 1981. Modeling a multiple tracer release experiment during nocturnal drainage flow in complex terrain. Preprint, 2nd AMS Conference on Mountain Meteorology, Steamboat Springs, CO, November 10–13.

Lanicci, J. M., T. N. Carlson, and T. T. Warner. 1987. Sensitivity of the Great Plains severe-storm environment to soil-moisture distribution. *Mon. Wea. Rev.* **115**, 2660–2673.

Lapidus, A. 1967. A detached shock calculation by second-order finite differences. *J. Comput. Phys.* **2**, 154–177.

Laprise, J. P. R., and A. Plante. 1995. A class of Semi-Lagrangian Integrated-Mass (SLIM) numerical transport algorithms. *Mon. Wea. Rev.* **123**, 553–565.

Laprise, R. 1992a. The Euler equations of motion with hydrostatic pressure as an independent variable. *Mon. Wea. Rev.* **120**, 197–207.

Laprise, R. 1992b. The resolution of global spectral models. *Bull. Amer. Meteor. Soc.* **73**, 1453–1454.

Laprise, R., and W. R. Peltier. 1989a. The linear stability of nonlinear mountain waves: Implications for the understanding of the severe downslope windstorms. *J. Atmos. Sci.* **46**, 545–564.

Laprise, R., and W. R. Peltier. 1989b. The structure and energetics of transient eddies in numerical simulation of breaking mountain waves. *J. Atmos. Sci.* **46**, 565–585.

Laprise, R., D. Caya, G. Bergeson, and M. Giguére. 1997. The formulation of the André Robert MC2 (mesoscale compressible community) model. *Atmos. Ocean* **35**, 195–220.

Laprise, R., D. Caya, M. Giguére, G. Bergeron, H. Côté, J.-P. Blanchet, G. J. Boer, and N. A. McFarlane. 1998. Climate and climate change in western Canada as simulated by the Canadian Regional Climate Model. *Atmos. Ocean* **26**, 119–167.

Larson, V. E., R. Wood, P. R. Field, J.-C. Golaz, T. H. Vonder Haar, and W. R. Cotton. 2001. Systematic biases i the microphysics and thermodynamics of numerical models that ignore subgrid-scale variability. *J. Atmos. Sci.* **58**, 1117–1128.

Laubach, J., and U. Teichmann. 1999. Surface energy budget variability: A case study over grass with special regard to minor inhomogeneities in the source area. *Theor. Appl. Climatol.* **62**, 9–24.

Lavoie, R. L. 1972. A mesoscale numerical model of lake-effect storms. *J. Atmos. Sci.* **29**, 1025–1040.

Lavoie, R. L. 1974. A numerical model of trade wind weather over Oahu. *Mon. Wea. Rev.* **102**, 630–637.

Lazier, J., and H. Sandstrom. 1978. Migrating thermal structure in a freshwater thermocline. *J. Phys. Oceanogr.* **8**, 1070–1079.

Leduc, R., G. Jacques, M. Ferland, and C. Lelièvre. 1981. Ilot de Chaleur a Quebec: Cas d'hiver. *Bound.-Layer Meteor.* **21**, 315–324.

Lee, H. N. 1981. An alternate pseudospectral model for pollutant transport, diffusion and deposition in the atmosphere. *Atmos. Environ.* **15**, 1017–1024.

Lee, H. N., and S. K. Kao. 1979. Finite element numerical modeling of atmospheric turbulent boundary layer. *J. Appl. Meteor.* **18**, 1287–1295.

Lee, J. D. 1973. Numerical simulation of the planetary boundary layer over Barbados, W.I. Ph.D. thesis, Florida State University, Tallahassee, FL.

Lee, J. L., and A. E. MacDonald. 2000. QNH: Mesoscale-bounded derivative initialization and winter storm test over complex terrain. *Mon. Wea. Rev.* **128**, 1016–1036.

Lee, J. T., S. Barr, W. H. Snyder, and R. E. Lawson Jr. 1981. Wind tunnel studies of flow channeling in valleys. Preprint, 2nd AMS Conference on Mountain Meteorology, Steamboat Springs, CO, November 9–12, 331–338.

Lee, R. 1978. *Forest Micrometeorology*. Columbia University Press, New York.

Lee, R. L., and D. B. Olfe. 1974. Numerical calculations of temperature profiles over an urban heat island. *Bound.-Layer Meteor.* **7**, 39–52.

Lee, T. J., and R. A. Pielke. 1992. Estimating the soil surface specific humidity. *J. Appl. Meteor.* **31**, 480–484.

Lee, T. J., R. A. Pielke, R. C. Kessler, and J. Weaver. 1989. Influence of cold pools downstream of mountain barriers on downslope winds and flushing. *Mon. Wea. Rev.* **117**, 2041–2058.

Lee, T. J., R. A. Pielke, T. G. F. Kittel, and J. F. Weaver. 1993. Atmospheric modeling and its spatial representation of land surface characteristics. *Environmental Modeling with GIS*, M. Goodchild, B. Parks, and L. T. Steyaert, Eds. Oxford University Press, London, 108–122.

Lee, T. J., R. A. Pielke, and P. W. Mielke Jr. 1995. Modeling the clear-sky surface energy budget during FIFE87. *J. Geophys. Res.* **100**, 25,585–25,593.

Lee, T.-Y., Y.-Y. Park, and Y.-L. Lin. 1998. A numerical modeling study of mesoscale cyclogenesis to the east of the Korean Peninsula. *Mon. Wea. Rev.* **126**, 2305–2329.

Leffler, R. L., and J. L. Foster. 1974. Snowfall on the Allegheny plateau of Maryland and West Virginia. *Weatherwise* **27**, 199–201.

Legg, B. J., and I. F. Long. 1975. Turbulent diffusion within a wheat canopy. II Results and interpretation. *Quart. J. Roy. Meteor. Soc.* **101**, 611–628.

LeMone, M. A., R. L. Grossman, R. L. Coulter, M. L. Wesley, G. E. Klazura, G. S. Poulos, W. Blumen, J. K. Lundquist, R. H. Cuenca, S. F. Kelly, E. A. Brandes, S. P. Oncley, R. T. McMillen, and B. B. Hicks. 2000. Land atmosphere interaction research, early results, and opportunities in the walnut river watershed in southeast Kansas: CASES and ABLE. *Bull. Amer. Meteor. Soc.* **81**, 757–779.

Lenschow, D. H., B. B. Stankov, and L. Mahrt. 1979. The rapid morning boundary-layer transition. *J. Atmos. Sci.* **36**, 2108–2124.

Lenschow, D. H., R. Pearson Jr., and B. B. Stankov. 1981. Estimating the ozone budget in the boundary layer by use of aircraft measurements of ozone eddy flux and mean concentrations. *J. Geophys. Res.* **86**, 7291–7297.

Letts, M. G., N. T. Roulet, N. T. Comer, M. R. Skarupa, and D. L. Vereghy. 2000. Parameterization of peatland hydraulic properties for the Canadian Land Surface Scheme. *Atmos. Ocean* **38**, 141–160.

LeVeque, K. L. 1982. Time split methods for partial differential equations. Ph.D. dissertation, Computer Science Dept., Stanford University, Stanford, CA.

LeVeque, R. J., and J. Oliger. 1981. Numerical methods based on additive splittings for hyperbolic partial differential equations. Numerical Analysis Project Manuscript NA-81-16, Computer Science Dept., Stanford University, Stanford, CA.

Lewellen, W. S. 1981. Modeling the lowest 1 km of the atmosphere. Advisory Group for Aerospace Research and Development Publication (AGARD-AG-276). NTIS.

Lewellen, W. S. 1983. Parameterization of subgrid-scale fluxes and estimation of dispersion. AMS/EPA Specialty Conference on Air Quality Modeling of the Nonstationary, Nonhomogeneous Urban Boundary Layer, October 31–November 4, Baltimore, MD.

Lewellen, W. S., R. I. Sykes, and D. A. Oliver. 1983. Further developments of the A.R.A.P. model for the atmosphere marine environment. Naval Environmental Prediction Facility Contract Report No. N00228-81-C-H459, Aeronautical Research Associates of Princeton, Inc., PO Box 2229, Princeton, NJ 08450.

Ley, B. E., and W. R. Peltier. 1981. Propagating mesoscale cloud bands. *J. Atmos. Sci.* **38**, 1206–1219.

Li, Y., and J. R. Bates. 1996. A study of the behaviour of semi-Lagrangian models in the presence of orography. *Quart. J. Roy. Meteor. Soc.* **122**, 1675–1700.

Libersky, L. D. 1980. Turbulence in cumulus clouds. *J. Atmos. Sci.* **37**, 2332–2346.

Likens, G. E., and F. H. Bormann. 1974. Acid rain: A serious regional environmental problem. *Science* **184**, 1176–1179.

Lilly, D. K. 1961. A proposed staggered-grid system for numerical integration of dynamic equations. *Mon. Wea. Rev.* **89**, 59–65.

Lilly, D. K. 1962. On numerical simulation of buoyant convection. *Tellus* **14**, 148–172.

Lilly, D. K. 1968. Models of cloud-topped mixed layers under a strong inversion. *Quart. J. Roy. Meteor. Soc.* **94**, 292–309.

Lilly, D. K. (Ed.). 1975. Open SESAME. *Proceedings of SESAME Open Meeting, September 4–6, 1974*. Prepared by NOAA, ERL, Boulder, CO.

Lilly, D. K. 1979. The dynamical structure and evolution of thunderstorms and squall lines. *Ann. Rev. Earth Planet. Sci.* **7**, 117–161.

Lilly, D. K. 1981. Wave-permeable lateral boundary conditions for convective cloud and storm simulations. *J. Atmos. Sci.* **38**, 1313–1316.

Lilly, D. K. 1982. Gravity waves and mountain waves. Lecture notes, NATO Advanced Study Institute on Mesoscale Meteorology–Theory, Observations, and Models, July 13–31, Gascogne, France.

Lilly, D. K. 1983. Stratified turbulence and the mesoscale variability of the atmosphere. *J. Atmos. Sci.* **40**, 749–761.

Lilly, D. K. 1996. A comparison of incompressible, anelastic and Boussinesq dynamics. *Atmos. Res.* **40**, 143–151.

Lilly, D. K. and P. J. Kennedy. 1973. Observations of a stationary mountain wave and its associated momentum flux and energy dissipation. *J. Atmos. Sci.* **30**, 1135–1152.

Lilly, D. K., and J. B. Klemp. 1979. The effects of terrain shape on nonlinear hydrostatic mountain waves. *J. Fluid Mech.* **95**, 241–261.

Lilly, D. K., and J. B. Klemp. 1980. Comments on the evolution and stability of finite-amplitude mountain waves. Part II: Surface wave drag and severe downslope windstorms. *J. Atmos. Sci.* **37**, 2119–2121.

Lilly, D. K., and E. J. Zipser. 1972. The Front Range windstorm of 11 January 1972. *Weatherwise* **25**, 56–63.

Lilly, D. K., J. M. Nickolls, R. M. Chervin, P. J. Kennedy, and J. B. Klemp. 1982. Aircraft measurements of wave momentum flux over the Colorado Rocky Mountains. *Quart. J. Roy. Meteor. Soc.* **108**, 625–642.

Lin, S.-J., and R. B. Rood. 1997. An explicit flux-form semi-Lagrangian shallow-water model on the sphere. *Quart. J. Roy. Meteor. Soc.* **123**, 2477–2498.

Lin, Y.-L., R. D. Farley, and H. D. Orville. 1983. Bulk parameterization of the snow field in a cloud model. *J. Climate Appl. Meteor.* **22**, 1065–1092.

Lin, Y.-L., J. Han, D. W. Hamilton, and C.-Y. Huang. 1999. Orographic influence on a drifting cyclone. *J. Atmos. Sci.* **56**, 534–562.

Liou, K.-N. 1980. *An Introduction to Atmospheric Radiation*. Academic Press, New York.

Liou, K.-N., and S. C. S. Ou. 1981. Parameterization of infrared radiative transfer in cloudy atmospheres. *J. Atmos. Sci.* **38**, 2707–2716.

Liou, K.-N., and G. D. Wittman. 1979. Parameterization of the radiation balance of clouds. *J. Atmos. Sci.* **38**, 2707–2716.

Lipps, F. B., and R. S. Hemler. 1982. A scale analysis of deep moist convection and some related numerical calculations. *J. Atmos. Sci.* **39**, 2192–2210.

Lipton, A. E., and R. A. Pielke. 1986. Vertical normal modes of a mesoscale model using a scaled height coordinate. *J. Atmos. Sci.* **43**, 1650–1655.

List, R. J. 1971. *Smithsonian Meteorological Tables*, 6th rev. ed. Smithsonian Institution Press, Washington, D.C.

Liston, G. E. 1995. Local advection of momentum, heat, and moisture during the melt of patchy snow covers. *J. Appl. Meteor.* **34**, 1705–1715.

Liston, G. E. 1999. Interrelationships among snow distribution, snowmelt, and snow cover depletion: Implications for atmospheric, hydrologic, and ecologic modeling. *J. Appl. Meteor.* **38**, 1474–1487.

Liston, G. E., and R. A. Pielke. 2000. A climate version of the Regional Atmospheric Modeling System. *Theor. Appl. Climatol.* **66**, 29–47.

Liston, G. E., and M. Sturm. 1998. A snow-transport model for complex terrain. *J. Glaciol.* **44**, 498–516.

Liston, G. E., R. A. Pielke, and E. M. Greene. 1999. Improving first-order snow-related deficiencies in a regional climate model. *J. Geophys. Res.* **104**, 19,559–19,567.

Liu, H., S. Liu, and J. Sang. 1999. A modified SiB to simulate momentum, heat and water transfer over various underlying surfaces. *Chinese J. Atmos. Sci.* **23**, 189–201.

Liu, W. T., K. B. Katsaros, and J. B. Businger. 1979. Bulk parameterization of air-sea exchanges of heat and water vapor including the molecular constraints at the interface. *J. Atmos. Sci.* **36**, 1722–1735.

Liu, Y., R. Avissar, and F. Giorgi. 1996. Simulation with the regional climate model RegCM2 of extremely anomalous precipitation during the 1991 east Asian flood: An evaluation study. *J. Geophys. Res.* **101**, 26,199–26,215.

Liu, Y., D.-L. Zhang, and M. K. Yau. 1997. A multiscale numerical study of Hurricane Andrew (1992). Part I: Explicit simulation and verification. *Mon. Wea. Rev.* **125**, 3073–3093.

Liu, Y., C. P. Weaver, and R. Avissar. 1999a. Toward a parameterization of mesoscale fluxes and moist convection induced by landscape heterogeneity. *J. Geophys. Res.* **104**, 19,515–19,533.

Liu, Y., D.-L. Zhang, and M. K. Yau. 1999b. A multiscale numerical study of Hurricane Andrew (1992). Part III: Dynamically-induced vertical motion. *Mon. Wea. Rev.* **127**, 2597–2616.

Lo, A. K. 1996. On the role of roughness lengths in flux parameterizations of boundary-layer models. *Bound.-Layer Meteor.* **80**, 403–413.

Lobocki, L. 1993. A procedure for the derivation of surface- layer bulk relationships from simplified second-order closure models. *J. Appl. Meteor.* **32**, 126–138.

Locatelli, J. D., P. V. Hobbs, and J. A. Werth. 1982. Mesoscale structures of vortices in polar air streams. *Mon. Wea. Rev.* **110**, 1417–1433.

Lockwood, J. G., and P. J. Sellers. 1982. Comparisons of interception loss from tropical and temperature vegetation canopies. *J. Appl. Meteor.* **21**, 1405–1412.

Long, R. R. 1953. Some aspects of the flow of stratified fluids. I. A theoretical investigation. *Tellus* **5**, 42–58.

Long, R. R. 1955. Some aspects of the flow of stratified fluids. II. Continuous density gradients. *Tellus* **7**, 341–357.

Long, R. L. 1977. Three layer circulations in estuaries and harbors. *J. Phys. Oceanogr.* **7**, 415–421.

Long, P. E. Jr., and F. J. Hicks. 1975. Simple properties of Chapeau functions and their application to the solution of the advection equation. NOAA NWS TDL Office Note 75-8, NOAA Techniques Development Lab, Silver Spring, MD.

Loose, T., and R. D. Bornstein. 1977. Observations of mesoscale effects on frontal movement through an urban area. *Mon. Wea. Rev.* **105**, 562–571.

Lord, N. W., J. P. Pandolfo, and M. A. Atwater. 1972. Simulations of meteorological variations over arctic coastal tundra under various physical interface conditions. *Arctic Alpine Res.* **4**, 189–209.

Louis, J.-F. 1979. Parametric model of vertical eddy fluxes in the atmosphere. *Bound.-Layer Meteor.* **17**, 187–202.

Lu, L., R. A. Pielke, G. E. Liston, W. J. Parton, D. Ojima, and M. Hartman. 2001. Implementation of a two-way interactive atmospheric and ecological model and its application to the central United States. *J. Climate* **14**, 900–919.

Ludlam, F. H. 1980. *Clouds and Storms*. Pennsylvania State University Press, University Park, PA.

Ludwig, F. L., and G. Byrd. 1980. An efficient method for deriving mass-consistent flow fields from wind observations in rough terrain. *Atmos. Environ.* **14**, 585–587.

Lumley, J. L., and B. Khajeh-Nouri. 1974. Computational modeling of turbulent transport. *Adv. Geophys.* **18A**, 169–192.

Lumley, J. L., and H. A. Panofsky. 1964. *The Structure of Atmospheric Turbulence*. Interscience, Monogr., 12, New York.

Lynch, A. H., and W. Wu. 2000. Impacts of fire and warming on ecosystem uptake in the Boreal Forest. *J. Climate* **13**, 2334–2338.

Lynch, A. H., F. S. Chapin III, L. D. Hinzman, W. Wu, E. Lilly, G. Vourlitis, and E. Kim. 1999a. Surface energy balance on the Arctic tundra: Measurements and models. *J. Climate* **12**, 2585–2606.

Lynch, A. H., G. B. Bonan, F. S. Chapin III, and W. Wu. 1999b. The impact of tundra ecosystems on the surface energy budget and climate of Alaska. *J. Geophys. Res.* **104**, 6647–6660.

Lynn, B. H., and W.-K. Tao. 2001. A parameterization for the triggering of landscape-generated moist convection. Part II: Zero-order and first-order closure. *J. Atmos. Sci.* **58**, 593–607.

Lynn, B. H., F. Abramopoulos, and R. Avissar. 1995a. Using similarity theory to parameterize mesoscale heat fluxes generated by subgrid-scale landscape discontinuities in GCMs. *J. Climate* **8**, 932–951.

Lynn, B. H., D. Rind, and R. Avissar. 1995b. The importance of mesoscale circulations generated by subgrid-scale landscape-heterogeneities in general circulation models. *J. Climate* **8**, 191–205.

Lynn, B. H., W.-K. Tao, and F. Abramopoulos. 2001. A parameterization for the triggering of landscape-generated moist convection. Part I: Analysis of high-resolution model results. *J. Atmos. Sci.* **58**, 575–592.

Lyons, T. J., and R. K. Steedman. 1981. Stagnation and nocturnal temperature jumps in a desert region of low relief. *Bound.-Layer Meteor.* **21**, 369–387.

Lyons, T. J., R. C. G. Smith, and H. Xinmei. 1996. The impact of clearing for agriculture on the surface energy budget. *Int. J. Climate* **16**, 551–558.

Lyons, W. A. 1972. The climatology and prediction of the Chicago lake breeze. *J. Appl. Meteor.* **11**, 1259–1270.

Lyons, W. A. 1975. *Lectures on Air Pollution and Environmental Impact Analysis*. D. Haugen, Ed., American Meteorological Society, Boston, 136–208.

Lyons, W. A., and H. S. Cole. 1976. Photochemical oxidant transport: Mesoscale lake breeze and synoptic-scale aspects. *J. Appl. Meteor.* **15**, 733–743.

Lyons, W. A., and C. S. Keen. 1976. Particulate transport in a Great Lakes coastal environment. Proceedings of the Second Federal Conference of the Great Lakes, 222–237.

Lyons, W. A., and J. A. Schuh. 1979. Comparison of observed mesoscale lake breeze wind fields to computations using the University of Virginia Mesoscale Model. Preprint, 4th AMS Symposium on Turbulence, Diffusion and Air Pollution, Reno, NV, 572–575.

Lyons, W. A., R. A. Pielke, W. R. Cotton, C. S. Keen, D. A. Moon, and N. R. Lincoln. 1992. Some considerations of the role of the land/lake breeze in causing elevated ozone levels in the southern Lake Michigan region. In *Environmental Modeling*, P. Melli and P. Zannetti, Eds. Computational Mechanics Publications, Southampton, U.K., 151–171.

Lyons, W. A., R. A. Pielke, W. R. Cotton, C. J. Tremback, R. L. Walko, M. Uliasz, and J. I. Ibarra. 1994. Recent applications of the RAMS meteorological and the HYPACT dispersion models. In *Air Pollution Modeling and Its Application, X*, S.-V. Gryning and M. M. Millán, Eds. Plenum Press, New York, 19–26.

Lyons, W. A., C. J. Tremback, and R. A. Pielke. 1995. Applications of the Regional Atmospheric Modeling System (RAMS) to provide input to photochemical grid models for the Lake Michigan Ozone Study (LMOS). *J. Appl. Meteor.* **34**, 1762–1786.

Ma, J., and S. M. Daggupaty. 1998. Stability dependence of height scales and effective roughness lengths of momentum and heat transfer over roughness changes. *Bound.-Layer Meteor.* **88**, 145–160.

Ma, J., and S. M. Daggupaty. 1999. Effective dry deposition velocity of ozone over Great Lakes area. Preprint, AMS Symposium on Interdisciplinary Issues in Atmospheric Chemistry, Dallas, TX, 62–65.

Ma, J., and S. M. Daggupaty. 2000. Effective dry deposition velocities for gases and particles over heterogeneous terrain. *J. Appl. Meteor.* **39**, 1379–1390.

MacDonald, A. E., J. L. Lee, and S. Sun. 1999. QNH: Design and test of a quasi-nonhydrostatic model for mesoscale weather prediction. *Mon. Wea. Rev.* **128**, 1016–1036.

MacDonald, A. E., J. L. Lee, and Y. Xie. 2000. The use of quasi-nonhydrostatic models for mesoscale weather prediction. *J. Atmos. Sci.* **57**, 2493–2517.

MacHattie, L. B. 1968. Kananaskis Valley winds in summer. *J. Appl. Meteor.* **7**, 348–352.

Machenhauer, B. 1979. The spectral model: Numerical methods used in atmospheric models. GARP Report 17, Vol. II, 121–275. WMO Secretariat, Geneva.

Maddox, R. A. 1980a. Mesoscale convective clusters. *Bull. Amer. Meteor. Soc.* **61**, 1374–1387.

Maddox, R. A. 1980b. An objective technique for separating macroscale and mesoscale features in meteorological data. *Mon. Wea. Rev.* **108**, 1108–1121.

Maddox, R. A. 1980c. A satellite based study of midlatitude, mesoscale convective complexes. Preprint, 8th AMS Conference on Weather Forecasting and Analysis, Denver, CO, June 10–13, 329–338.

Maddox, R. A., D. J. Perkey, and J. M. Fritsch. 1981. Evolution of upper tropospheric features during the development of a mesoscale convective complex. *J. Atmos. Sci.* **38**, 1664–1674.

Maddukuri, C. S. 1982. A numerical simulation of an observed lake breeze over southern Lake Ontario. *Bound.-Layer Meteor.* **23**, 369–387.

Magono, C., C. Nakamura, and Y. Yoshida. 1982. Nocturnal cooling of the Moshiri Basin, Hokkaido in midwinter. *J. Meteor Soc. Japan* **60**, 1106–1116.

Mahrer, Y. 1984. An improved numerical approximation of the horizontal gradient in a terrain-following coordinate system. *Mon. Wea. Rev.* **112**, 918–922.

Mahrer, Y., and R. A. Pielke. 1975. The numerical study of the air flow over mountains using the University of Virginia mesoscale model. *J. Atmos. Sci.* **32**, 2144–2155.

Mahrer, Y., and R. A. Pielke. 1976. The numerical simulation of the airflow over Barbados. *Mon. Wea. Rev.* **104**, 1392–1402.

Mahrer, Y., and R. A. Pielke. 1977a. The effects of topography on sea and land breezes in a two-dimensional numerical model. *Mon. Wea. Rev.* **105**, 1151–1162.

Mahrer, Y., and R. A. Pielke. 1977b. A numerical study of the airflow over irregular terrain. *Beit. Phys. Atmos.* **50**, 98–113.

Mahrer, Y., and R. A. Pielke. 1978a. A test of an upstream spline interpolation technique for the advective terms in a numerical mesoscale model. *Mon. Wea. Rev.* **106**, 818–830.

Mahrer, Y., and R. A. Pielke. 1978b. The meteorological effect of the changes in surface albedo and moisture. *Israel Meteor. Res. Papers (IMS)* **2**, 55–70.

Mahrt, L. J. 1972. Some basic theoretical concepts of boundary layer flow at low latitudes. In *Dynamics of the Tropical Atmosphere: Notes from a Colloquium, Summer 1972*, NCAR, Boulder, CO, 411–420.

Mahrt, L. J. 1974. Time-dependent integrated planetary boundary layer flow. *J. Atmos. Sci.* **31**, 457–464.

Mahrt, L. J. 1976. Mixed layer moisture structure. *Mon. Wea. Rev.* **104**, 1403–1407.

Mahrt, L. J. 1981a. Modeling the depth of the stable boundary layer. *Bound.-Layer Meteor.* **21**, 3–19.

Mahrt, L. J. 1981b. The early evening boundary layer transition. *Quart. J. Roy. Meteor. Soc.* **107**, 329–343.

Mahrt, L. 1982. Momentum balance of gravity flows. *J. Atmos. Sci.* **39**, 2701–2711.

Mahrt, L. J. 1983. Atmospheric boundary layers. *Rev. Geophys. Space Phys.* **21**, 1042–1048.

Mahrt, L. 1996. The bulk aerodynamic formulation over heterogeneous surfaces. *Bound.-Layer Meteor.* **78**, 87–119.

Mahrt, L. 2000. Surface heterogeneity and vertical structure of the boundary layer. *Bound.-Layer Meteor.* **96**, 33–62.

Mahrt, L. J., and R. C. Heald. 1981. Nocturnal surface temperatures over undulating terrain. Preprint, 15th AMS Conference on Agriculture and Forest Meteorology and 5th AMS Conference on Biometeorology, Anaheim, CA, April 1–3, 197–199.

Mahrt, L. J., and S. Larsen. 1982. Small scale drainage front. *Tellus* **34**, 579–587.

Mailhot, J., and R. Benoit. 1982. A finite element model of the atmospheric boundary layer suitable for use with numerical weather prediction models. *J. Atmos. Sci.* **39**, 2249–2266.

Mailhot, J., J. W. Strapp, J. I. MacPherson, R. Benoit, S. Bélair, N. R. Donaldson, F. Froude, M. Benjamin, I. Zawadzki, and R. R. Rodgers. 1998. The Montreal-96 Experiment on Regional Mixing and Ozone (MERMOZ): An overview and some preliminary results. *Bull. Amer. Meteor. Soc.* **79**, 433–442.

Mak, M. 1981. An inquiry on the nature of CISK. Part 1. *Tellus* **33**, 531–537.

Makar, P. A., and S. R. Karpik. 1996. Basis-spline interpolation on the sphere: Applications to semi-Lagrangian advection. *Mon. Wea. Rev.* **124**, 182–199.

Malkus, J. S., and M. E. Stern. 1953. The flow of a stable atmosphere over a heated island. Part I. *J. Meteor.* **10**, 30–41.

Mangarella, P. A., A. J. Chambers, R. L. Street, and E. Y. Hsu. 1973. Laboratory studies of evaporation and energy transfer through a wavy air-water interface. *J. Phys. Oceanogr.* **3**, 93–101.

Manins, P. C., and B. L. Sawford. 1979a. A model of katabatic winds. *J. Atmos. Sci.* **36**, 619–630.

Manins, P. C., and B. L. Sawford. 1979b. Katabatic winds: A field case study. *Quart. J. Roy. Meteor. Soc.* **105**, 1105–1025.

Manins, P. C., and B. L. Sawford. 1982. Mesoscale observations of upstream blocking. *Quart. J. Roy. Meteor. Soc.* **108**, 427–434.

Mannouji, N. 1982. A numerical experiment on the mountain and valley winds. *J. Meteor. Soc. Japan* **60**, 1085–1105.

Manton, M. J., and G. P. Ayers. 1982. On the number concentration of aerosols in towns. *Bound.-Layer Meteor.* **22**, 171–181.

Marchuk, G. I. 1995. *Adjoint Equations and Analysis of Complex Systems.* Kluwer Academic Publishers, Dordrecht, The Netherlands.

Marchuk, G. I., V. P. Kochergin, V. I. Klimok, and V. A. Sukhorukov. 1977. On the dynamics of the ocean surface mixed layer. *J. Phys. Oceanogr.* **7**, 865–875.

Marks, F. D. Jr., and P. M. Austin. 1979. Effects of the New England coastal front on the distribution of precipitation. *Mon. Wea. Rev.* **107**, 53–67.

Marshall, C. H., K. C. Crawford, K. E. Mitchell, and D. J. Stensrud. 2001. Evaluation of the land-surface and planetary boundary layer schemes in the operational NCEP Eta model using Oklahoma mesonet data. *J. Hydrometeor.*, accepted.

Marshall, J., A. Adcroft, C. Hill, L. Perelman, and C. Heisey. 1997. A finite-volume, incompressible Navier Stokes model for studies of the ocean on parallel computers. *J. Geophys. Res.* **102**, 5753–5766.

Marshall, J., F. Dobson, K. Moore, P. Rhines, M. Visbeckm, E. d'Asaro, K. Bumke, S. Chang, R. Davis, K. Fischer, R. Garwood, P. Guest, R. Harcourt, C. Herbaut, T. Holt, J. Lazier, S.

Legg, J. McWilliams, R. Pickart, M. Prater, I. Renfrew, U. Send, and W. Smethie. 1998. The Labrador Sea Deep Convection Experiment. *Bull. Amer. Meteor. Soc.* **79**, 2033–2058.

Marshall, J. S., and W. M. K. Palmer. 1948. The distribution of raindrops with size. *J. Meteor.* **5**, 165–166.

Marshall, S., and R. J. Oglesby. 1994. An improved snow hydrology for GCMs. Part 1: Snow cover fraction, albedo, grain size, and age. *Climate Dyn.* **10**, 21–37.

Marshall, S., J. O. Roads, and G. Glatzmaier. 1994. Snow hydrology in a general circulation model. *J. Climate* **7**, 1251–1269.

Martin, C. 1981. Numerical accuracy in a mesoscale meteorological model. M.S. thesis, Dept. of Environmental Science, University of Virginia, Charlottesville, VA.

Martin, C. L., and R. A. Pielke. 1983. The adequacy of the hydrostatic assumption in sea breeze modeling over flat terrain. *J. Atmos. Sci.* **40**, 1472–1481.

Marwitz, J. D. 1972. Precipitation efficiency of thunderstorms on the High Plains. *J. Rech. Atmos.* **6**, 367–370.

Marwitz, J. D. 1983. The kinematics of orographic airflow during Sierra storms. *J. Atmos. Sci.* **40**, 1218–1227.

Mason, B. J. 1956. On the melting of hailstones. *Quart. J. Roy. Meteor. Soc.* **82**, 209–216.

Mason, P. J., and A. R. Brown. 1999. On subgrid models and filter operations in large eddy simulations. *J. Atmos. Sci.* **56**, 2101–2114.

Mason, P. J., and R. I. Sykes. 1978. A simple Cartesian model of boundary layer flow over topography. *J. Comput. Phys.* **28**, 198–210.

Mason, P. J., and R. I. Sykes. 1979. Three-dimensional numerical integrations of the Navier–Stokes equations for flow over surface-mounted obstacles. *J. Fluid Mech.* **91**, 433–450.

Mason, P. J., and R. I. Sykes. 1980. A two-dimensional numerical study of horizontal roll vortices in the neutral atmospheric boundary layer. *Quart. J. Roy. Meteor. Soc.* **106**, 351–366.

Mason, P. J., and R. I. Sykes. 1982. A two-dimensional numerical study of horizontal roll vortices in an inversion capped planetary boundary layer. *Quart. J. Roy. Meteor. Soc.* **108**, 801–823.

Mass, C. 1981. Topographically forced convergence in western Washington State. *Mon. Wea. Rev.* **109**, 1335–1347.

Mass, C. 1982. The topographically forced diurnal circulations of western Washington State and their influence on precipitation. *Mon. Wea. Rev.* **110**, 170–183.

Mass, C. F., and Y.-H. Kuo. 1998. Regional real-time numerical weather prediction: Current status and future potential. *Bull. Amer. Meteor. Soc.* **79**, 253–263.

Mass, C. F., and W. J. Steenburgh. 2000. An observational and numerical study of an orographically trapped wind reversal along the west coast of the United States. *Mon. Wea. Rev.* **128**, 2363–2396.

Masson, V. 2000. A physically-based scheme for the urban energy budget in atmospheric models. *Bound.-Layer Meteor.* **94**, 357–397.

Matejka, T. J., R. A. Houze Jr., and P. V. Hobbs. 1980. Microphysics and dynamics of clouds associated with mesoscale rainbands in extratropical cyclones. *Quart. J. Roy. Meteor. Soc.* **106**, 29–56.

Mathur, M. B. 1970. A note on an improved quasi-Lagrangian advection scheme for primitive equations. *Mon. Wea. Rev.* **98**, 214–219.

Mathur, M. B. 1974. A multiple grid primitive equation model to simulate the development of an asymmetric hurricane (Isbell 1964). *J. Atmos. Sci.* **31**, 371–393.

Mathur, M. B. 1975. Development of banded structure in a numerically simulated hurricane. *J. Atmos. Sci.* **32**, 512–522.

Mathur, M. B. 1997. Development of an eye-wall like structure in a tropical cyclone model simulation. *Dyn. Atmos. Oceans* **27**, 527–547.

Mathur, M. B., K. F. Brill, and C. J. Seman. 1999. Evolution of slantwise vertical motions in NCEP's mesoscale Eta model. *Mon. Wea. Rev.* **127**, 5–25.

Matson, M., and R. V. Legeckis. 1980. Urban heat islands detected by satellite. *Bull. Amer. Meteor. Soc.* **61**, 212.

Matson, M., E. P. McClain, D. F. McGinnis Jr., and J. A. Pritchard. 1978. Satellite detection of urban heat islands. *Mon. Wea. Rev.* **106**, 1725–1734.

Mayr, G. J., and A. Gohm. 2000. 2D airflow over a double bell-shaped mountain. *Meteor. Atmos. Phys.* **72**, 13–27.

McAnelly, R. L., and W. R. Cotton. 1986. Meso-beta-scale characteristics of an episode of meso-alpha-scale convective complexes. *Mon. Wea. Rev.* **114**, 1740–1770.

McCarthy, J., and S. E. Koch. 1982. The evolution of an Oklahoma dryline. Part I: A meso- and subsynoptic-scale analysis. *J. Atmos. Sci.* **39**, 225–236.

McClatckey, R. A., and J. E. A. Selby. 1972. Atmospheric transmittance, 7–30 μm: Attenuation of CO_2 laser radiation. Environmental Research Paper No. 419, AFCRL-72-0611.

McCumber, M. D. 1980. A numerical simulation of the influence of heat and moisture fluxes upon mesoscale circulation. Ph.D. dissertation, Dept. of Environmental Science, University of Virginia, Charlottesville, VA.

McCumber, M. D., and R. A. Pielke. 1981. Simulation of the effects of surface fluxes of heat and moisture in a mesoscale numerical model. Part I: Soil layer. *J. Geophys. Res.* **86**, 9929–9938.

McDonald, A. 1999. An examination of alternative extrapolations to find the departure point position in a "two-time-level" semi-Lagrangian integration. *Mon. Wea. Rev.* **127**, 1985–1993.

McDonald, J. 1960. Direct absorption of solar radiation by atmospheric water vapor. *J. Meteor.* **17**, 319–328.

McEwan, M. J., and L. F. Phillips. 1975. *Chemistry of the Atmosphere*. John Wiley & Sons, New York.

McFarlane, N. A. 1987. The effect of orographically excited gravity-wave drag on the general-circulation of the lower stratosphere and troposphere. *J. Atmos. Sci.* **44**, 1775–1800.

McKee, T. B., D. C. Bader, and K. Hansen. 1983. Synoptic influence of urban circulation. AMS/EPA Specialty Conference on Air Quality Modeling of the Nonstationary, Nonhomogeneous Urban Boundary Layer, October 31–November 4, Baltimore, MD.

McNider, R. T. 1981. Investigation of the impact of topographic circulations on the transport and dispersion of air pollutants. Ph.D. dissertation, Dept. of Environmental Sciences, University of Virginia, Charlottesville, VA.

McNider, R. T. 1982. A note on velocity fluctuations in drainage flows. *J. Atmos. Sci.* **39**, 1658–1660.

McNider, R. T. 1983. Transport and diffusion models for the urban boundary layer. AMS/EPA Specialty Conference on Air Quality Modeling of the Nonstationary, Nonhomogeneous Urban Boundary Layer, October 31–November 4, Baltimore, MD.

McNider, R. T., and F. J. Kopp. 1990. Specification of the scale and magnitude of thermals used to initiate convection in cloud models. *J. Appl. Meteor.* **29**, 99–104.

McNider, R. T., and R. A. Pielke. 1981. Diurnal boundary layer development over sloping terrain. *J. Atmos. Sci.* **38**, 2198–2212.

McNider, R. T., S. R. Hanna, and R. A. Pielke. 1980. Sub-grid scale plume dispersion in coarse resolution mesoscale models. Proceedings of the Second AMS Joint Conference on Applications of Air Pollution Meteorology, New Orleans, LA, 424–429.

McNider, R. T., A. P. Mizzi, and R. A. Pielke. 1982. Numerical investigation of low-level jets in coastal zones. Proceedings of the First International Conference on Meteorology and Air/Sea Interactions of the Coastal Zone, May 10–14, The Hague, Netherlands, 190–195.

McPhee, M. G. 1979. The effect of the oceanic boundary layer on the mean drift of pack ice: Application of a simple mode. *J. Phys. Oceanogr.* **9**, 388–400.

McPherson, R. D. 1970. A numerical study of the effect of a coastal irregularity on the sea breeze. *J. Appl. Meteor.* **9**, 767–777.

McQueen, J. T., R. R. Draxler, and G. D. Rolph. 1995. Influence of grid size and terrain resolution on wind-field predictions from an operational mesoscale model. *J. Appl. Meteor.* **34**, 2166–2181.

McRae, G. J., and J. H. Seinfeld. 1983. Development of a second-generation mathematical model for urban air pollution—II: Evaluation of model performance. *Atmos. Environ.* **17**, 491–499.

McRae, G. J., W. R. Goodin, and J. H. Seinfeld. 1982a. Development of a second-generation mathematical model for urban air pollution—I. Model formulation. *Atmos. Environ.* **16**, 679–696.

McRae, G. J., F. H. Shair, and J. H. Seinfeld. 1982b. Convective downmixing of plumes in a coastal environment. *J. Appl. Meteor.* **20**, 1312–1324.

Melgarejo, J. 1980. A numerical simulation of wind over Gotland with a two-dimensional mesometeorological boundary layer model. Report No. 11, Swedish Meteorological and Hydrological Institute.

Mellor, G. L. 1977. The Gaussian cloud model relations. *J. Atmos. Sci.* **34**, 356–358.

Mellor, G. L., and T. Yamada. 1974. A hierarchy of turbulence closure models for the planetary boundary Lares. *J. Atmos. Sci.* **31**, 1791–1806.

Mellor, G. L., and T. Yamada. 1982. Development of a turbulence closure model for geophysical fluid problems. *Rev. Geophys. Space Phys.* **20**, 851–875.

Melville, W. K. 1977. Wind stress and roughness length over breaking waves. *J. Phys. Oceanogr.* **7**, 702–710.

Merceret, F. J. 1975. Relating rainfall rate to the slope of raindrop size spectra. *J. Appl. Meteor.* **14**, 259–260.

Merilees, P. E., and S. A. Orszag. 1979. The pseudospectral method. In: Global Atmosphere Research Programme. GARP Report 17, WMO Secretariat, Geneva, 276–299.

Meroney, R. N. 1998. Spurious or virtual correlation errors commonly encountered in reduction of scientific data. *J. Wind Eng.* **77–78**, 543–553.

Meroney, R. N., A. J. Bowen, B. Lindley, and J. R. Pearse. 1978. Wind characteristics over complex terrain: Laboratory simulation and field measurements at Rakaia Gorge, New Zealand. Final report: Part II. Fluid Mechanics and Wind Engineering Program, Colorado State University, Fort Collins, CO.

Mesinger, F. 1973. A method for construction of second-order accuracy difference schemes permitting no false two-grid-interval wave in the height field. *Tellus* **5**, 444–458.

Mesinger, F. 1974. An economical explicit scheme which inherently prevents the false two-grid interval wave in the forecast fields. Proceedings of the Symposium on Difference and Spectral Methods for Atmosphere and Ocean Dynamics Problems, Novosibirsk 1973, Part 11, 18–34.

Mesinger, F. 1984. A blocking technique for representation of mountains in atmospheric models. *Riv. Meteor. Aeronautica* **44**, 195–202.

Mesinger, F. 1993a. Forecasting upper tropospheric turbulence within the framework of the Mellor–Yamada 2.5 closure. *Res. Activ. Atmos. Oceanic Mod.*, CAS/JSC WGNE Rep. 18, 4.28–4.29, WMO, Geneva.

Mesinger, F. 1993b. Sensitivity of the definition of a cold front to the parameterization of turbulent fluxes in the NMC's Eta model. *Res. Activ. Atmos. Oceanic Mod.*, CAS/JSC WGNE Rep. 18, 4.36–4.38, WMO, Geneva.

Mesinger, F. 1996. Improvements in quantitative precipitation forecasts with the Eta Regional Model at the National Centers for Environmental Prediction: The 48-km upgrade. *Bull. Amer. Meteor. Soc.* **77**, 2637–2649; Corr. **78**, 506.

Mesinger, F. 1997. Dynamics of limited-area models: Formulation and numerical methods. *Meteor. Atmos. Phys.* **63**, 3–14.

Mesinger, F. 1998. Comparison of quantitative precipitation forecasts by the 48- and the 29-km Eta models: An update and possible implications. Preprints, *12th Conf. on Numerical Weather Prediction,* American Meteorological Society, Phoenix, AZ, J22–J23.

Mesinger, F. 2000. Numerical methods: The Arakawa approach, horizontal grid, global and limited-area modeling. In *General Circulation Model Development: Past, Present and Future,* D. Randall, Ed., Academic Press, San Diego, 373–419.

Mesinger, F., and A. Arakawa. 1976. Numerical methods used in atmospheric models. *GARP Publ. Ser.* **17**, 1–64.

Mesinger, F., and T. L. Black. 1992. On the impact on forecast accuracy of the step-mountain (Eta) vs. sigma coordinate. *Meteor. Atmos. Phys.* **50**, 47–60.

Mesinger, F., and D. Jovic. 2001. The Eta slope adjustment: Contender for an optimal steepening in a piecewise-linear advection scheme? Comparison tests. *Quart. J. Roy. Meteor. Soc.*, submitted.

Mesinger, F., and R. E. Treadon. 1995. "Horizontal" reduction of pressure to sea level: Comparison against the NMC's Shuell method. *Mon. Wea. Rev.* **123**, 59–68.

Mesinger, F., Z. I. Janjić, S. Nickovic, D. Gavrilov, and D. G. Deaven. 1988. The step-mountain coordinate: Model description, and performance for cases of Alpine lee cyclogenesis and for a case of an Appalachian redevelopment. *Mon. Wea. Rev.* **116**, 1493–1518.

Mesinger, F., T. L. Black, and M. E. Baldwin. 1997. Impact of resolution and of the Eta coordinate on skill of the Eta model precipitation forecasts. In *Numerical Methods in Atmospheric and Oceanic Modelling*, C. Lin, R. Laprise, and H. Ritchie, Eds. Soc./NRC Research-Press, Ottawa, Ontario, Canada, 399–423.

Met. Office. 1999/2000. Scientific and technical review. An Executive Agency of The Ministry of Defence, Bracknell, Berkshire, UK.

Method, T. J., and T. N. Carlson. 1982. Radiative heating rates and some optical properties of the St. Louis aerosol, as inferred from aircraft measurements. *Atmos. Environ.* **16**, 53–66.

Meyers, M. P., and W. R. Cotton. 1992. Evaluation of the potential for wintertime quantitative precipitation forecasting over mountainous terrain with an explicit cloud model. Part I: Two-dimensional sensitivity experiments. *J. Appl. Meteor.* **31**, 26–50.

Meyers, M. P., P. J. DeMott, and W. R. Cotton. 1992: New primary ice nucleation parameterizations in an explicit cloud model. *J. Appl. Meteor.* **31**, 708–721.

Meyers, M. P., R. L. Walko, J. Y. Harrington, and W. R. Cotton. 1997. New RAMS cloud microphysics parameterization. Part II: The two-moment scheme. *Atmos. Res.* **45**, 3–39.

Michelson, S. A., and N. L. Seaman. 1999. Assimilation of NEXRAD-VAD winds in summertime meteorological simulations over the Northeastern United States. *J. Appl. Meteor.* **39**, 92–108.

Mielke, P. W. 1984. Meteorological applications of permutation techniques based on distance functions. In *Handbook of Statistics*, Vol. 4, P. R. Krishnaiah and P. K. Sen, Eds. 813–830. North-Holland, New York.

Mielke, P. W. 1991. The application of multivariate permutation methods based on distance functions in the earth sciences. *Earth Sci. Rev.* **31**, 55–71.

Mielke, P. W., and K. J. Berry. 2000. Euclidean distance based permutation methods in atmospheric science. *Data Mining and Knowl. Disc.* **7**, 7–27.

Mihailovic, D. T., and G. Kallos. 1997. A sensitivity study of a coupled soil-vegetation boundary-layer scheme for use in atmospheric modeling. *Bound.-Layer Meteor.* **82**, 283–315.

Mihailovic, D. T., and M. Ruml. 1996. Design of land-air parameterization scheme (LAPS) for modeling boundary layer surface processes. *Meteor. Atmos. Phys.* **6**, 65–81.

Mihailovic, D. T., R. A. Pielke, B. Rajkovic, T. J. Lee, and M. Jeftic. 1993. A resistance representation of schemes for evaporation from bare and partly plant-covered surfaces for use in atmospheric models. *J. Appl. Meteor.* **32**, 1038–1054.

Mihailovic, D. T., B. Rajkovic, L. Dekic, R. A. Pielke, T. J. Lee, and Z. Ye. 1995. The validation of various schemes for parameterizing evaporation from bare soil for use in meteorological models: A numerical study using in situ data. *Bound.-Layer Meteor.* **76**, 259–289.

Mihailovic, D. T., B. Rajkovic, B. Lalic, D. Jovic, and L. Dekic. 1998. Partitioning the land surface water simulated by a land-air surface scheme. *J. Hydrol.* **211**, 17–33.

Mihailovic, D. T., G. Kallos, I. D. Arsenic, B. Lalic, B. Rajkovic, and A. Papadopoulos. 1999a. Sensitivity of soil surface temperature in a force-restore equation to heat fluxes and deep soil temperature. *Int. J. Climatol.* **19**, 1617–1632.

Mihailovic, D. T., G. Kallos, B. Lalic, A. Papadopoulos, and I. Arsenic. 1999b. Parameterization of hydrological processes for application to regional and mesoscale modeling. *Global Atmos. Ocean Sys.* **7**, 73–89.

Mihailovic, D. T., T. J. Lee, R. A. Pielke Sr., B. Lalic, I. Arsenic, B. Rajkovic, and P. L. Vidale. 2000. Comparison of different boundary layer schemes using single point micrometeorological field data. *Theor. Appl. Climatol.* **67**, 135–151.

Miller, D. A., and R. A. White. 1998. A conterminous United States multi-layer soil characteristics data set for regional climate and hydrology modeling. *Earth Interac.* **2**, 12–539.

Miller, M. J., and R. P. Pearce. 1974. A three-dimensional primitive equation model of cumulonimbus convection. *Quart. J. Roy. Meteor. Soc.* **100**, 133–154.

Miller, M. J., and A. J. Thorpe. 1981. Radiation conditions for the lateral boundaries of limited-area numerical models. *Quart. J. Roy. Meteor. Soc.* **107**, 615–628.

Mills, G. A., and C. M. Hayden. 1983. The use of high resolution satellite temperature and moisture profiles to initialize a mesoscale numerical weather prediction model—a severe weather event case study. *J. Climate Appl. Meteor.* **22**, 649–663.

Mironov, D. V., V. M. Gryanik, V. N. Lykossov, and S. S. Zilitinkevich. 1999. Comments on "A new second-order turbulence closure scheme for the planetary boundary layer." *J. Atmos. Sci.* **56**, 3478–3481.

Mitchell, K., J. Schaake, D. Tarpley, F. Chen, Y. Lin, M. Baldwin, E. Rogers, G. Manikin, A. Betts, Z. Janjić, Q. Duan, and V. Koren. 1999. Recent GCIP advancements in coupled land-surface modeling and data assimilation in the NCEP mesoscale Eta model. Proceedings of the 14th AMS Conference on Hydrology, Dallas, TX, 261–264.

Mitchell, K., C. Marshall, D. Lohmann, M. Ek, Y. Lin, P. Grunmann, P. Houser, E. Wood, J. Schaake, D. Lettenmaier, D. Tarpley, W. Higgins, R. Pinker, A. Robock, B. Cosgrove, J. Entin, and Q. Duan. 2000. The collaborative GCIP Land Data Assimilation (LDAS) Project and supportive NCEP uncoupled land-surface modeling initiatives. Proceedings of the 15th AMS Conference on Hydrology, January 9–14, Long Beach, CA, 1–4.

Mitsumoto, S., H. Ueda, and H. Ozoe. 1983. A laboratory experiment on the dynamics of the land and sea breeze. *J. Atmos. Sci.* **40**, 1228–1240.

Mizzi, A. P. 1982. A numerical investigation of the mesoscale atmospheric circulation in the Oregon coastal zone with a coupled atmosphere-ocean model. M.S. thesis, University of Virginia, Charlottesville, VA.

Mizzi, A. P., and R. A. Pielke. 1984. A numerical study of the mesoscale atmospheric circulation observed during a coastal upwelling event on August 23, 1972. Part I: Sensitivity studies. *Mon. Wea. Rev.* **112**, 76–90.

Mocko, D. M., and W. R. Cotton. 1995. Evaluation of fractional cloudiness parameterizations for use in a mesoscale model. *J. Atmos. Sci.* **52**, 2884–2901.

Moeng, C.-H. 1984. A large-eddy-simulation model for the study of planetary boundary layer turbulence. *J. Atmos. Sci.* **41**, 2052–2062.

Mohr, P. J., and B. N. Taylor. 2000. The fundamental physical constants: A recent least-squares adjustment has produced a new set of recommended values of the basic constants and conversion factors of physics and chemistry. *Phys. Today* **53** BG6–BG13.

Mohr, K. I., J. S. Famiglietti, A. Boone, and P. J. Starks. 2000. Modeling soil moisture and surface flux variability with an untuned land surface scheme: A case study from the Southern Great Plains 1997 hydrology experiment. *J. Hydrometeor.* **1**, 154–169.

Mölders, N. 1999a. On the atmospheric response to urbanization and open-pit mining under various geostrophic wind conditions. *Meteor. Atmos. Phys.* **71**, 205–228.

Mölders, N. 1999b. On the effects of different flooding stages of the Oder and different land-use types on the distributions of evapotranspiration, cloudiness and rainfall in the Brandenburg-Polish border area. *Contrib. Atmos. Phys.* **72**, 1–25.

Mölders, N. 2000. Application of the principle of superposition to detect nonlinearity in the short-term atmospheric response to concurrent land-use changes associated with future landscapes. *Meteor. Atmos. Phys.* **72**, 47–68.

Mölders, N., and A. Raabe. 1997. Testing the effect of a two-way-coupling of a meteorological and a hydrologic model on the predicted local weather. *Atmos. Res.* **45**, 81–107.

Molinari, J. 1982. A method for calculating the effects of deep cumulus convection in numerical models. *Mon. Wea. Rev.* **110**, 1527–1534.

Molinari, J. 1985. A general form of Kuo's cumulus parameterization. *Mon. Wea. Rev.* **113**, 1411–1416.

Molinari, J., and T. Corsetti. 1985. Incorporation of cloud-scale and mesoscale down-drafts into a cumulus parameterization: Results of one- and three-dimensional integrations. *Mon. Wea. Rev.* **113**, 485–501.

Molinari, J., and M. Dudek. 1992. Parameterization of convective precipitation in mesoscale numerical models: A critical review. *Mon. Wea. Rev.* **120**, 326–344.

Molz, E., and I. Remson. 1970. Extraction of term models of soil moisture use by transpiring plants. *Water Resour. Res.* **6**, 1346–1356.

Monin, A. S., and A. M. Obukhov. 1954. Basic laws of mixing in the ground layer of the atmosphere. *Tr. Geofiz, Inst. Akad. Nauk SSSR* **151**, 163–187.

Monteith, J. L. (Ed.). 1975a. *Vegetation and the Atmosphere. Vol. 1, Principles*. Academic Press, New York.

Monteith, J. L. (Ed.). 1975b. *Vegetation and the Atmosphere. Vol. 2, Case Studies*. Academic Press, New York.

Monteith, J. L. 1981. Evaporation and surface temperature. *Quart. J. Roy. Meteor. Soc.* **107**, 1–27.

Moores, W. H. 1982. Direct measurements of radiative and turbulence flux convergencies in the lowest 1000 m of the convective boundary layer. *Bound.-Layer Meteor.* **22**, 283–294.

Moran, M. D. 1992. Numerical modelling of mesoscale atmospheric dispersion. Ph.D. dissertation, Dept. of Atmospheric Science, Colorado State University, Fort Collins, CO.

Moran, M. D. 2000. Basic aspects of mesoscale atmospheric dispersion. Chapter 2 in: *Mesoscale Atmospheric Dispersion*, Z. Boybeyi, Ed., WIT Press, London, Great Britain, 27–120.

Moran, M. D. 2001: Basic aspects of mesoscale atmospheric dispersion. In: Mesoscale Atmospheric Dispersion, Z. Boybeyi, Ed. Vol. 9, Advances in Air Pollution Series. Wit Press, Ashurst, Southampton, United Kingdom.

Moran, M. D., and R. A. Pielke. 1996a. Evaluation of a mesoscale atmospheric dispersion modeling system with observations from the 1980 Great Plains mesoscale tracer field experiment. Part I: Data sets and meteorological simulations. *J. Appl. Meteor.* **35**, 281–307.

Moran, M. D., and R. A. Pielke. 1996b. Evaluation of a mesoscale atmospheric dispersion modeling system with observations from the 1980 Great Plains mesoscale tracer field experiment. Part II: Dispersion simulations. *J. Appl. Meteor.* **35**, 308–329.

Moroz, W. J. 1967. A lake breeze on the eastern shore of Lake Michigan: Observations and model. *J. Atmos. Sci.* **24**, 337–355.

Morse, B. J. 1973. An analytical study of mesh refinement applied to the wave equation. Technical Memorandum WMPO-5, NOAA, Boulder, CO.

Moss, M. S. 1978. Low-layer features of two limited area hurricane regions. Technical Report ERL 394-NHEML 1, NOAA, Boulder, CO.

Moss, M. S., and R. W. Jones. 1978. A numerical simulation of hurricane landfall. Technical Memo ERL-NHEML-3, NOAA, Boulder, CO.

Mulhearn, P. J. 1981. On the formation of a stably stratified internal boundary-layer by advection of warm air over a cooler sea. *Bound.-Layer Meteor.* **21**, 247–254.

Mullen, S. L. 1979. An investigation of small synoptic-scale cyclones in polar air stream. *Mon. Wea. Rev.* **107**, 1636–1647.

Muller, R. A. 1966. Snowbelts of the Great Lakes. *Weatherwise* **19**, 248–255.

Mumpower, J., P. Middleton, R. L. Dennis, T. R. Stewart, and V. Viers. 1981. Visual air quality assessment: Denver case study. *Atmos. Environ.* **15**, 2433–2441.

Munn, R. E. 1966. *Descriptive Micrometeorology*. Academic Press, New York.

Murdoch, D. C. 1957. *Linear Algebra for Undergraduates*. John Wiley & Sons, New York.

Murphy, R. E. (Ed.). 1992. FIFE Special Issue, *J. Geophys. Res.* **97**, 18,343–19,109.

Murray, F. W. 1967. On the computation of saturation vapor pressure. *J. Appl. Meteor.* **6**, 203–204.

Murray, F. W. 1970. Numerical models of a tropical cumulus cloud with bilateral and axial symmetry. *Mon. Wea. Rev.* **98**, 14–28.

Nachamkin, J. E., and W. R. Cotton. 2000. Interactions between a developing mesoscale convective system and its environment. Part II: Numerical simulation. *Mon. Wea. Rev.* **128**, 1225–1244.

Nachamkin, J., R. L. McAnelly, and W. R. Cotton. 2000. Interactions between a developing mesoscale convective system and its environment. Part I. Observational analysis. *Mon. Wea. Rev.* **128**, 1205–1224.

Nadezhina, E. D., and O. B. Shklyarevich. 1996. A numerical simulation of the atmospheric boundary layer in a coastal area with allowance for vegetation. *Russ. Meteor. Hydrol.* **11**, 21–28.

Nair, U. S., M. R. Hjelmfelt, and R. A. Pielke. 1997. Numerical simulation of the June 9–10, 1972 Black Hills storm using CSU RAMS. *Mon. Wea. Rev.* **125**, 1753–1766.

Nair, U. S., R. C. Weger, K. S. Kuo, and R. M. Welch. 1998. Clustering, randomness, and regularity in cloud fields 5. The nature of regular cumulus cloud fields. *J. Geophys. Res.* **103**, 11,363–11,380.

NBS. 1974. *Fundamental Physical Constants.* National Bureau of Standards Special Publication 398, U.S. Government Printing Office, Washington, D.C.

Neal, D., D. C. Stevenson, and D. Lindley. 1982. A wind tunnel boundary-layer simulation of wind flow over complex terrain: Effect of terrain and model construction. *Bound.-Layer Meteor.* **21**, 271–293.

Negri, A. J., and T. H. Vonder Haar. 1980. Moisture convergence using satellite-derived wind fields: A severe local storm case study. *Mon. Wea. Rev.* **108**, 1170–1182.

Neumann, J. 1951. Land breezes and nocturnal thunderstorms. *J. Meteor.* **8**, 60–67.

Neumann, J. 1977. On the rotation rate of the direction of sea and land breezes. *J. Atmos. Sci.* **34**, 1913–1917.

Neumann, J., and Y. Mahrer. 1971. A theoretical study of the land and sea breeze circulations. *J. Atmos. Sci.* **28**, 532–542.

Neumann, J., and Y. Mahrer. 1974. A theoretical study of the sea and land breezes of circular islands. *J. Atmos. Sci.* **31**, 2027–2039.

Neumann, J., and Y. Mahrer. 1975. A theoretical study of the lake and land breezes of circular lakes. *Mon. Wea. Rev.* **103**, 474–485.

Newiger, M., and K. Bähnke. 1981. Influence of cloud composition and cloud geometry on the absorption of solar radiation. *Contrib. Atmos. Phys.* **54**, 370–382.

Newton, C. W. 1966. Circulations in large sheared cumulonimbus. *Tellus* **18**, 699–712.

Nicholls, M. E., and R. A. Pielke. 1994a. Thermal compression waves. I: Total energy transfer. *Quart. J. Roy. Meteor. Soc.* **120**, 305–332.

Nicholls, M. E., and R. A. Pielke. 1994b. Thermal compression waves. II: Mass adjustment and vertical transfer of total energy. *Quart. J. Roy. Meteor. Soc.* **120**, 333–359.

Nicholls, M. E., and R. A. Pielke Sr. 2000. Thermally induced compression waves and gravity waves generated by convective storms. *J. Atmos. Sci.* **57**, 3251–3271.

Nicholls, M. E., R. A. Pielke, and W. R. Cotton. 1991. A two-dimensional numerical investigation of the interaction between sea-breezes and deep convection over the Florida peninsula. *Mon. Wea. Rev.* **119**, 298–323.

Nicholls, M. E., R. A. Pielke, and R. Meroney. 1993. Large eddy simulation of microburst winds flowing around a building. *J. Wind Eng. Indus. Aerodyn.* **46–47**, 229–237.

Nicholls, M. E., R. A. Pielke, J. L. Eastman, C. A. Finley, W. A. Lyons, C. J. Tremback, R. L. Walko, and W. R. Cotton. 1995. Applications of the RAMS numerical model to dispersion over urban areas. In *Wind Climate in Cities*, J. E. Cermak, Ed., Kluwer Academic Publishers, Amsterdam, 703–732.

Nickerson, E. C. 1979. On the numerical simulation of airflow and clouds over mountainous terrain. *Contrib. Atmos. Phys.* **52**, 161–177.

Nickerson, E. C., and E. L. Magaziner. 1976. A three-dimensional simulation of winds and non-precipitating orographic clouds over Hawaii. Technical Report ERL 377-APCL 39, NOAA, Boulder, CO.

Nickerson, E. C., E. Richard, R. Rosset, and D. R. Smith. 1986. The numerical simulation of clouds, rain, and airflow over the Vosges and Black Forest Mountains: A meso-model with parameterized microphysics. *Mon. Wea. Rev.* **114**, 398–414.

Nicosia, D. J., and R. H. Grumm. 1999. Mesoscale band formation in three major northeastern United States snowstorms. *Wea. Forecasting* **14**, 346–368.

Nie, D., T. Demetriades-Shah, and E. T. Kanemasu. 1992. Surface energy fluxes on four slope sites during FIFE 1988. *J. Geophys. Res.* **97**, 18,641–18,649.

Nielsen, K. L. 1964. *Methods in Numerical Analysis*, 2nd ed. MacMillan, New York.

Nieuwstadt, F. T. M., and R. A. Brost. 1986. Decay of convective turbulence. *J. Atmos. Sci.* **43**, 532–546.

Nieuwstadt, F. T. M., and A. G. M. Driedonks. 1979. The nocturnal boundary layer: A case study compared with model calculations. *J. Appl. Meteor.* **18**, 1397–1405.

Nieuwstadt, F. T. M., and H. Tennekes. 1981. A rate equation for the nocturnal boundary-layer height. *J. Atmos. Sci.* **38**, 1418–1428.

Nikuradse, J. 1933. Strömungsgesetze in rauhen Rohren. *Forschungsheft*, No. 361.

Nilsson, B. 1979. Meteorological influence on aerosol extinction in the 0.2–40 μm wavelength range. *Appl. Opt.* **18**, 3457–3473.

Ninomiya, K. 1992. Multi-scale features of Baiu, the summer monsoon over Japan and the East Asia. *J. Meteor. Soc. Japan* **70**, 467–495.

Ninomiya, K. 2000. Large- and meso-alpha-scale characteristics of Meiyu/Baiu front associated with intense rainfalls in 1–10 July 1991. *J. Meteor. Soc. Japan* **78**, 141–157.

Ninomiya, K., M. Ikawa, and T. Akiyama. 1981. Long-level medium-scale cumulonimbus cluster in Asian subtropical humid region. *J. Meteor. Soc. Japan* **59**, 564–577.

Nitta, T. 1976. Large-scale heat and moisture budgets during the air mass transformation experiment. *J. Meteor. Soc. Japan* **54**, 1–14.

Niyogi, D. S., and S. SethuRaman. 1997. Comparison of four different stomatal resistance schemes using FIFE observations. *J. Appl. Meteor.* **36**, 903–917.

Niyogi, D. S., S. SethuRaman, and K. Alapaty. 1999. Uncertainty in the specification of surface characteristics, Part II: Hierarchy of interaction—Explicit statistical analysis. *Bound.-Layer Meteor.* **91**, 341–366.

Nkemdirim, L. C. 1980. A test of a lapse rate/wind speed model for estimating heat island magnitude in an urban airshed. *J. Appl. Meteor.* **19**, 749–756.

Noilhan, J., and S. Planton. 1989. A simple parameterization of land surface processes for meteo-rological models. *Mon. Wea. Rev.* **117**, 536–549.

Noonkester, V. R. 1979. Coastal marine fog in southern California. *Mon. Wea. Rev.* **107**, 830–851.

Noto, K. 1996. Dependence of heat island phenomena on stable stratification and heat quantity in a calm environment. *Atmos. Environ.* **30**, 475–485.

Nunez, M., and T. R. Oke. 1976. Long-wave radiative flux divergence and nocturnal cooling of the urban atmosphere. II. Within an urban canyon. *Bound.-Layer Meteor.* **10**, 121–135.

Nunez, M., and T. R. Oke. 1977. The energy balance of an urban canyon. *J. Appl. Meteor.* **16**, 11–19.

Nuss, W. A., J. Bane, W. T. Thompson, T. Holt, C. Dorman, M. Ralph, R. Rotunno, J. Klemp, W. Skamrock, R. Samelson, A. Rogerson, C. Reason, and P. Jackson. 2000. Coastally trapped wind reversals: A new level of understanding. *Bull. Amer. Meteor. Soc.* **81**, 719–744.

Nykanen, D. K., E. Foufoula-Georgiou, and W. M. Lapenta. 2001. Impact of small-scale rainfall variability on larger-scale spatial organization of land-atmosphere fluxes. *J. Hydrometeor.* **2**, 105–121.

O'Brien, J. J. 1970a. Alternative solutions to the classical vertical velocity problem. *J. Appl. Meteor.* **9**, 197–203.

O'Brien, J. J. 1970b. A note on the vertical structure of the eddy exchange coefficient in the planetary boundary layer. *J. Atmos. Sci.* **27**, 1213–1215.

O'Brien, J. J., and H. E. Hurlburt. 1972. A numerical model of coastal upwelling. *J. Phys. Oceanogr.* **2**, 14–26.

O'Hirok, W., and C. Gautier. 1998. A three-dimensional radiative transfer model to investigate the solar radiation within a cloudy atmosphere. Part I: Spatial effects. *J. Atmos. Sci.* **55**, 2162–2179.

O'Hirok, W., and C. Gautier. 1998. A three-dimensional radiative transfer model to investigate the solar radiation within a cloudy atmosphere. Part II: Spectral effects. *J. Atmos. Sci.* **55**, 3065–3076.

Oerlemans, J. 1980. A case study of a subsynoptic disturbance in a polar outbreak. *Quart. J. Roy. Meteor. Soc.* **106**, 313–325.

Ogura, Y. 1972. *Clouds and Convection*. GARP Publication Series No. 8, WMO, Geneva, 20–29.

Ogura, Y., and J. G. Charney. 1961. A numerical model of thermal convection in the atmosphere. Proceedings of the International Symposium on Numerical Weather Prediction, 431–450.

Ogura, Y., and M.-T. Liou. 1980. The structure of a midlatitude squall line: A case study. *J. Atmos. Sci.* **37**, 553–567.

Ogura, Y., and N. A. Phillips. 1962. Scale analysis of deep and shallow convection in the atmo-sphere. *J. Atmos. Sci.* **19**, 173–179.

Ogura, Y., and T. Takahashi. 1971. Numerical simulation of the life cycle of a thunderstorm cell. *Mon. Wea. Rev.* **99**, 895–911.

Ogura, Y., and T. Takahashi. 1973. The development of warm rain in a cumulus model. *J. Atmos. Sci.* **30**, 262–277.

Ogura, Y., Y.-L. Chen, J. Russell, and S.-T. Soong. 1979. On the formation of organized convective systems observed over the eastern Atlantic. *Mon. Wea. Rev.* **107**, 426–441.

Ohata, T., K. Higuchi, and K. Ikegami. 1981. Mountain-valley wind system in the Khumbu Himal, East Nepal. *J. Meteor. Soc. Japan* **59**, 753–762.

Oke, T. R. 1973. City size and the urban heat island. *Atmos. Environ.* **7**, 769–779.

Oke, T. R. 1976. The distinction between canopy and boundary-layer urban heat islands. *Atmósfera* **14**, 268–277.

Oke, T. R. 1978. *Boundary Layer Climates*. Methuen, London.

Oke, T. R. 1982. The energetic basis of the urban heat island. *Quart. J. Roy. Meteor. Soc.* **108**, 1–24.

Oke, T. R., and R. F. Fuggle. 1972. Comparison of urban/rural counter and net radiation at night. *Bound.-Layer Meteor.* **2**, 290–308.

Okeyo, A. E. 1982. A two-dimensional numerical model of the lake-land and sea-land breezes over Kenya. M.S. thesis, Dept. of Meteorology, University of Nairobi, Kenya.

Oki, T., T. Nishimura, and P. Dirmeyer. 1999. Assessment of annual runoff from land surface models using Total Runoff Integrating Pathways (TRIP). *J. Meteor. Soc. Japan* **77**, 235–255.

Okoola, R. E. 2000. The characteristics of cold air outbreaks over the eastern highlands of Kenya. *Meteor. Atmos. Phys.* **73**, 177–187.

Olfe, D. B., and R. L. Lee. 1971. Linearized calculations of urban heat island convection effects. *J. Atmos. Sci.* **28**, 1374–1388.

Oliger, J., and A. Sundstroöm. 1976. Theoretical and practical aspects of some initial-boundary value problems in fluid dynamics. Report STAN-CS-76-578, Computer Science Dept. Stanford University, Stanford, CA.

Olsson, P. Q., and J. Y. Harrington. 2000. Dynamics and energetics of the cloudy boundary layer in simulations of off-ice flow in the marginal ice zone. *J. Geophys. Res.* **105**, 11,889–11,899.

Onishi, G. 1968. Numerical study on atmospheric boundary layer flow over inhomogeneous terrain. *J. Meteor. Soc. Japan* **46**, 280–286.

Oochs, H. J. III, and D. B. Johnson. 1980. Urban effects on the properties of first echoes. *J. Appl. Meteor.* **19**, 1160–1166.

Ookouchi, Y., M. Uryu, and R. Sawada. 1978. A numerical study of the effects of a mountain on the land and sea breezes. *J. Meteor. Sco. Japan* **56**, 368–385.

Ooyama, K. V. 1971. A theory of parameterization of cumulus convection. *J. Meteor. Soc. Japan* **49**, 744–756.

Ooyama, K. V. 1982. Conceptual evolution of the theory and modeling of the tropical cyclone. *J. Meteor. Soc. Japan* **60**, 369–380.

Orgill, M. M. 1981. A planning guide for future studies. Report No. PNL-3656, ASCOT/80/4, DOE Contract Report prepared by Battelle Pacific Northwest Laboratory.

Orlanski, I. 1975. A rational subdivision of scales for atmospheric process. *Bull. Amer. Meteor. Soc.* **56**, 527–530.

Orlanski, I. 1976. A simple boundary condition for unbounded hyperbolic flows. *J. Comput. Phys.* **21**, 251–269.

Orlanski, I. 1981. The quasi-hydrostatic approximation. *J. Atmos. Sci.* **38**, 572–582.

Orlanski, I., B. Ross, and L. Polinsky. 1974. Diurnal variation of the planetary boundary layer in a mesoscale model. *J. Atmos. Sci.* **31**, 965–989.

Orszag, S. A. 1971. Numerical simulation of incompressible flows within simple boundaries: Accuracy. *J. Fluid Mech.* **49**, 76–112.

Orville, H. D. 1965. A numerical study of the initiation of cumulus clouds over mountainous terrain. *J. Atmos. Sci.* **22**, 684–699.

Orville, H. D. 1968. Ambient wind effects on the initiation and development of cumulus clouds over mountains. *J. Atmos. Sci.* **25**, 385–403.

Orville, H. D. 1980. Numerical modeling of clouds. Lecture notes, IFAORS Short Course 450 on Clouds: Their Formation, Properties, and Effects, Williamsburg, VA, December 1980. Held at the Institute for Atmospheric Optics and Remote Sensing, Hampton, VA, 1–5.

Orville, H. D., P. A. Eckhoff, J. E. Peak, J. H. Hirsch, and F. J. Kopp. 1981. Numerical simulation of the effects of cooling tower complexes on clouds and severe weather. *Atmos. Environ.* **15**, 823–836.

Orville, H. D., and L. J. Sloan. 1970. A numerical simulation of the life history of a rainstorm. *J. Atmos. Sci.* **27**, 1148–1159.

Otterman, J. 1974. Baring high albedo soils by desertification—A hypothesized desertification mechanism. *Science* **184**, 531–533.

Otterman, J. 1975. Possible rainfall reduction through reduced surface temperature due to overgrazing. Report, Technical Information Division, Code 250, NASA Goddard Space Flight Center, Greenbelt, MD.

Otterman, J. 1981a. Plane with protrusions as an atmospheric boundary. *J. Geophys. Res.* **86**, 6627–6630.

Otterman, J. 1981b. Satellite and field studies of man's impact on the surface in arid regions. *Tellus* **33**, 68–77.

Ovington, J. 1954. A comparison of rainfall in different woodlands. *Forestry* **27**, 41–53.

Ozoe, H., T. Shibata, H. Sayama, and H. Ueda. 1983. Characteristics of air pollution in the presence of land and sea breeze—A numerical simulation. *Atmos. Environ.* **17**, 35–42.

Paegle, J., W. G. Zdunkowski, and R. M. Welch. 1976. Implicit differencing of predictive equations of the boundary layer. *Mon. Wea. Rev.* **104**, 1321–1324.

Palmén, E., and C. W. Newton. 1969. *Atmospheric Circulation Systems*. Academic Press, New York.

Palmer, T. N., G. J. Shutts, and R. Swinbank. 1986. Alleviation of a systematic westerly bias in general circulation and numerical weather prediction models through an orographic-wave parameterization. *Quart. J. Roy. Meteor. Soc.* **112**, 947–975.

Paltridge, G. W., and C. M. R. Platt. 1976. *Radiative Processes in Meteorology and Climatology*. Elsevier, New York.

Paltridge, G. W., and C. M. R. Platt. 1981. Aircraft measurements of solar and infrared radiation and the microphysics of cirrus clouds. *Quart. J. Roy. Meteor. Soc.* **107**, 367–380.

Palumbo, A., and A. Mazzarella. 1980. Rainfall statistical properties in Naples. *Mon. Wea. Rev.* **108**, 1041–1045.

Pan, H.-L., and L. Mahrt. 1987. Interaction between soil hydrology and boundary-layer development. *Bound.-Layer Meteor.* **38**, 185–202.

Pandolfo, J. P. 1966. Wind and temperature profiles for constant-flux boundary layers in lapse conditions with a variable eddy conductivity to eddy viscosity ratio. *J. Atmos. Sci.* **23**, 495–502.

Pandolfo, J. P., C. A. Jacobs, R. J. Ball, M. A. Atwater, and J. A. Sekorski. 1976. Refinement and validation of an urban meteorological-pollutant model. Report EPA-600/4-76-037, U.S. Environmental Protection Agency, Office of Research Development.

Panin, B. D., R. P. Repinskaya, K. Buzian, and W. Feng-Lei. 1999. A diabatic regional model with a nested grid. *Russ. Meteor. Hydrol.* **3**, 25–33.

Panin, G. N., and G. Tetzlaff. 1999. A measure of inhomogeneity of the land surface and parameterization of turbulent fluxes under natural conditions. *Theor. Appl. Climatol.* **62**, 3–8.

Panofsky, H. A., and G. W. Brier. 1968. *Some Applications of Statistics to Meteorology*. Pennsylvania State University, 224 pp.

Panofsky, H. A., A. K. Blackadar, and G. E. McVehil. 1960. The diabatic wind profile. *Quart. J. Roy. Meteor. Soc.* **86**, 390–398.

Panofsky, H. A., D. Larko, R. Lipschutz, and G. Stone. 1981. Spectra over complex terrain. Preprint, 4th U.S. National Conference on Wind Engineering Research, Seattle, WA, July 26–29.

Panofsky, H. A., D. Larko, R. Lipschutz, G. Stone, E. F. Bradley, A. J. Bowen, and J. Højstrup. 1982. Spectra of velocity components over complex terrain. *Quart. J. Roy. Meteor. Soc.* **108**, 214–230.

Park, S. K., and K. K. Droegemeier. 1999. Sensitivity analysis of a moist 1D Eulerian cloud model using automatic differentiation. *Mon. Wea. Rev.* **127**, 2180–2196.

Park, S. K., and K. K. Droegemeier. 2000. Sensitivity analysis of a 3D convective storm: Implications for variational data assimilation and forecast error. *Mon. Wea. Rev.* **128**, 140–159.

Park, S.-U., and D. N. Sikdar. 1982. Evolution of the dynamics and thermodynamics of a mesoscale convective system: A case study. *Mon. Wea. Rev.* **110**, 1024–1040.

Parlange, M. B., A. T. Cahill, D. R. Nielsen, J. W. Hopmans, and O. Wendroth. 1998. Review of heat and water movement in field soils. *Soil Tillage Res.* **47**, 5–10.

Parrish, T. R. 1982. Barrier winds along the Sierra Nevada Mountains. *J. Appl. Meteor.* **21**, 925–930.

Parsons, D. B., and P. V. Hobbs. 1983. The mesoscale and microscale structure and organization of clouds and precipitation in midlatitude cyclones VII: Formation, development, interaction and dissipation of rainbands. *J. Atmos. Sci.* **40**, 559–579.

Pasquill, F. 1961. The estimation of the dispersion of windborne material. *Meterorol. Mag.* **90**, 33–49.

Passarelli, R. E. Jr., and H. Boehme. 1983. The orographic modulation of pre-warm-front precipitation in southern New England. *Mon. Wea. Rev.* **111**, 1062–1070.

Pastushkov, R. S. 1975. The effects of vertical wind shear on the evolution of convective clouds. *Quart. J. Roy. Meteor. Soc.* **101**, 281–291.

Patnack, P. C., B. E. Freeman, R. M. Traci, and G. T. Phillips. 1983. Improved simulations of mesoscale meteorology. Report NM ASL CR-83-0127-1, Atmospheric Science Laboratory, White Sands Missile Range.

Patrinos, A. N. A., and A. L. Kistler. 1977. A numerical study of the Chicago lake breeze. *Bound.-Layer Meteor.* **12**, 93–123.

Patrinos, A. N. A., and M. J. Leach. 1982. On the use of the pseudo-spectral technique in air-pollution modelling. Preprint, 3rd AMS Joint Conference on Applications of Air Pollution Meteorology, San Antonio, TX, January 11–15.

Pauwels, V. R. N., and E. F. Wood. 1999. A soil-vegetation-atmosphere transfer scheme for the modeling of water and energy balance processes in high latitudes. 2. Application and validation. *J. Geophys. Res.* **104**, 27,823–27,839.

Pearse, J. R., D. Lindley, and D. C. Stevenson. 1981. Wind flow over ridges in simulated atmospheric boundary layers. *Bound.-Layer Meteor.* **21**, 77–92.

Pearson, R. A. 1973. Properties of the sea breeze front as shown by a numerical model. *J. Atmos. Sci.* **30**, 1050–1060.

Pearson, R. A. 1975. On the asymmetry of the land-breeze sea breeze circulation. *Quart. J. Roy. Meteor. Soc.* **101**, 529–536.

Peckham, S. E., and L. J. Wicker. 2000. The influence of topography and lower-tropospheric winds on dryline morphology. *Mon. Wea. Rev.* **128**, 2165–2189.

Pellerin, P., R. Laprise, and I. Zawadzki. 1995. The performance of a semi-Lagrangian transport scheme for the advection-condensation problem. *Mon. Wea. Rev.* **123**, 3318–3330.

Peltier, W. R., and T. L. Clark. 1979. The evolution and stability of finite-amplitude mountain waves. Part II. Surface wave drag and severe downslope windstorms. *J. Atmos. Sci.* **36**, 1498–1529.

Peltier, W. R., and T. L. Clark. 1980. Reply. *J. Atmos. Sci.* **37**, 2122–2125.

Peltier, W. R., and T. L. Clark. 1983. Nonlinear mountain waves in two and three spatial dimensions. *Quart. J. Roy. Meteor. Soc.* **109**, 527–548.

Pepper, D. W., C. D. Keen, and P. E. Long Jr. 1979. Modeling the dispersion of atmospheric pollution using cubic splines and Chapeau functions. *Atmos. Environ.* **13**, 223–237.

Perkey, D. J. 1976. A description and preliminary results from a fine-mesh model for forecasting quantitative precipitation. *Mon. Wea. Rev.* **104**, 1513–1526.

Perkey, D. J., and C. W. Kreitzberg. 1976. A time-dependent lateral boundary scheme for limited-area primitive equation models. *Mon. Wea. Rev.* **104**, 744–755.

Petersen, A. C., and A. A. M. Holtslag. 1999. A first-order closure for covariances and fluxes of reactive species in the convective boundary layer. *J. Appl. Meteor.* **38**, 1758–1776.

Petersen, W. A., L. D. Carey, S. A. Rutledge, J. C. Knievel, N. J. Doesken, R. H. Johnson, T. B. McKee, T. Vonder Haar, and J. F. Weaver. 1999. Mesoscale and radar observations of the Fort Collins flash flood of 28 July 1997. *Bull. Amer. Meteor. Soc.* **80**, 191–216.

Peterson, E. Q. 1969. Distribution of sulfur dioxide over metropolitan St. Louis, as described by empirical eigenvectors, and its relation to meteorological parameters. *Atmos. Environ.* **4**, 501–518.

Peterson, J. T. 1970. Distribution of sulfur dioxide over metropolitan St. Louis, as described by empirical eigen vectors, and its relation to meteorological parameters. *Atmos. Environ.* **4**, 501–518.

Pettré, P. 1982. On the problem of violent valley winds. *J. Atmos. Sci.* **39**, 542–554.

Philandras, C. M., D. A. Metaxas, and P. T. Nastos. 1999. Climate variability and urbanization in Athens. *Theor. Appl. Climatol.* **63**, 65–72.

Philip, J. 1957. Evaporation and moisture and heat fields in the soil. *J. Meteor.* **14**, 354–366.

Phillips, N. A. 1957. A coordinate system having some special advantages for numerical forecasting. *J. Meteor.* **14**, 184–185.

Physick, W. 1976. A numerical model of the sea-breeze phenomenon over a lake or gulf. *J. Atmos. Sci.* **33**, 2107–2135.

Physick, W. L. 1980. Numerical experiments on the inland penetration of the sea breeze. *Quart. J. Roy. Meteor. Soc.* **106**, 735–746.

Physick, W. L. 1986. Application of a mesoscale flow model in the irregular terrain of the Grand Canyon National Park. Contract NA-85-RAH05045, Amendment 17, Item 15, National Park Service, Department of the Interior, Denver, CO.

Physick, W. L., D. J. Abbs, and R. A. Pielke. 1989. Formulation of the thermal internal boundary layer in a mesoscale model. *Bound.-Layer Meteor.* **49**, 99–111.

Pichler, H., R. Steinacker, E. Hagenauer, and A. Jager. 1995. ALPEX-simulation. *Meteor. Atmos. Phys.* **56**, 197–208.

Pielke, R. A. Jr., and R. A. Pielke Sr. 1997. *Hurricanes: Their Nature and Impacts on Society.* John Wiley and Sons, Chichester, U.K.

Pielke, R. A. Jr., and R. A. Pielke Sr. (Eds.). 2000. *Storms.* Vols. I and II. Routledge Press, London.

Pielke, R. A. 1972. Comparison of a hydrostatic and anelastic dry shallow primitive equation model. Technical Memo ERL OD-13, NOAA, Boulder, CO.

Pielke, R. A. 1974a. A three-dimensional numerical model of the sea breezes over south Florida. *Mon. Wea. Rev.* **102**, 115–139.

Pielke, R. A. 1974b. A comparison of three-dimensional and two-dimensional numerical predictions of sea breezes. *J. Atmos. Sci.* **31**, 1577–1585.

Pielke, R. A. 1976. Inadvertent weather modification potentials due to microwave transmissions and the thermal heating at SPS rectenna sites. Report prepared in consultation with M. Garstang, J. Simpson, and R. H. Simpson for Lockheed Electronics Company, Inc.

Pielke, R. A. 1978. The role of man and machine in the weather service of the future. Preprint, AMS Conference on Weather Forecasting and Analysis and Aviation Meteorology, October 16–19, Silver Spring, MD, 271–272.

Pielke, R. A. 1981. An overview of our current understanding of the physical interactions between the sea- and land-breeze and the coastal waters. *Ocean Manage.* **6**, 87–100.

Pielke, R. A. 1982. The role of mesoscale numerical models in very short-range forecasting. In *Nowcasting*, K. Browning, Ed., Academic Press, New York, 207–221.

Pielke, R. A. 1984. *Mesoscale Meteorological Modeling.* Academic Press, New York.

Pielke, R. A. 1990. *The Hurricane.* Routledge Press, London.

Pielke, R. A. 1991. Overlooked scientific issues in assessing hypothesized greenhouse gas warming. *Environ. Software* **6**, 100–107.

Pielke, R. A. 1994. The status of mesoscale meteorological models. In *Planning and Managing Regional Air Quality: Modeling and Measurement Studies,* P. A. Solomon and T. A. Silver, Eds., Lewis Publishers, Chelsea, MI, 435–458.

Pielke, R. A. 1995. Synoptic Weather Lab notes. Dept. of Atmospheric Science Class Report No. 1, Colorado State University, Fort Collins, CO.

Pielke, R. A. 1998. Climate prediction as an initial value problem. *Bull. Amer. Meteor. Soc.* **79**, 2743–2746.

Pielke, R. A. 2001. Influence of the spatial distribution of vegetation and soils on the prediction of cumulus convective rainfall. *Rev. Geophys.* **39**, 151–177.

Pielke, R. A., L. R. Bernardet, P. J. Fitzpatrick, S. C. Gillies, R. F. Hertenstein, A. S. Jones, X. Lin, J. E. Nachamkin, U. S. Nair, J. M. Papineau, G. S. Poulos, M. H. Savoie, and P. L. Vidale. 1995b. Standardized test to evaluate numerical weather prediction algorithms. *Bull. Amer. Meteor. Soc.* **76**, 46–48.

Pielke, R. A., and R. W. Arritt. 1984. A proposal to standardize models. *Bull. Amer. Meteor. Soc.* **65**, 1082.

Pielke, R. A., and R. Avissar. 1990. Influence of landscape structure on local and regional climate. *Landscape Ecol.* **4**, 133–155.

Pielke, R. A., and W. R. Cotton. 1977. A mesoscale analysis over south Florida for a high rainfall event. *Mon. Wea. Rev.* **105**, 343–362.

Pielke, R. A., and J. M. Cram. 1987. An alternate procedure for analyzing surface geostrophic winds and pressure over elevated terrain. *Wea. Forecasting* **2**, 229–236.

Pielke, R. A., and J. M. Cram. 1989. A terrain-following coordinate system—Derivation of diagnostic relationships. *Meteor. Atmos. Phys.* **40**, 189–193.

Pielke, R. A., and E. Kennedy. 1980. Mesoscale terrain features, January 1980. Report UVA-ENV SCI-MESO-1980-1, University of Virginia, Dept. of Environmental Science, Charlottesville, VA.

Pielke, R. A., and Y. Mahrer. 1975. Representation of the heated-planetary boundary layer in mesoscale models with coarse vertical resolution. *J. Atmos. Sci.* **32**, 2288–2308.

Pielke, R. A., and Y. Mahrer. 1978. Verification analysis of the University of Virginia three-dimensional mesoscale model prediction over south Florida for July 1, 1973. *Mon. Wea. Rev.* **106**, 1568–1589.

Pielke, R. A., and P. Mehring. 1977. Mesoscale climatology in mountainous terrain—Mean monthly temperatures. *Mon. Wea. Rev.* **105**, 108–112.

Pielke, R. A., and M. E. Nicholls. 1997. Use of meteorological models in computational wind engineering. *J. Wind Eng. Indus. Aerodyn.* **67–68**, 363–372.

Pielke, R. A., and R. P. Pearce. (Eds.). 1994. *Mesoscale Modeling of the Atmosphere*. American Meteorological Society, Boston.

Pielke, R. A., and X. Zeng. 1989. Influence on severe storm development of irrigated land. *Natl. Wea. Dig.* **14**, 16–17.

Pielke, R. A., R. T. McNider, M. Segal, and Y. Mahrer. 1983. The use of a mesoscale numerical model for evaluations of pollutant transport and diffusion in coastal regions and over irregular terrain. *Bull. Amer. Meteor. Soc.* **64**, 243–249.

Pielke, R. A., M. Segal, R. T. McNider, and Y. Mahrer. 1985. Derivation of slope flow equations using two different coordinate representations. *J. Atmos. Sci.* **42**, 1102–1106.

Pielke, R. A., G. Kallos, and M. Segal. 1989. Horizontal resolution needs for adequate lower tropospheric profiling involved with thermally-forced atmospheric systems. *J. Atmos. Oceanic Tech.* **6**, 741–758.

Pielke, R. A., A. Song, P. J. Michaels, W. A. Lyons, and R. W. Arritt. 1991. The predictability of sea-breeze–generated thunderstorms. *Atmósfera* **4**, 65–78.

Pielke, R. A., W. R. Cotton, R. L. Walko, C. J. Tremback, W. A. Lyons, L. D. Grasso, M. E. Nicholls, M. D. Moran, D. A. Wesley, T. J. Lee, and J. H. Copeland. 1992. A comprehensive meteorological modeling system—RAMS. *Meteor. Atmos. Phys.* **49**, 69–91.

Pielke, R. A., M. E. Nicholls, and A. J. Bedard. 1993. Using thermal compression waves to assess latent heating from clouds. *EOS* **74**, 493.

Pielke, R. A., J. Eastman, L. D. Grasso, J. Knowles, M. Nicholls, R. L. Walko, and X. Zeng. 1995a. Atmospheric vortices. In *Fluid Vortices*, S. Green, Ed. Kluwer Academic Publishers, Dordrecht, The Netherlands, 617–650.

Pielke, R. A., G. E. Liston, J. L. Eastman, L. Lu, and M. Coughenour. 1999a. Seasonal weather prediction as an initial value problem. *J. Geophys. Res.* **104**, 19,463–19,479.

Pielke, R. A., R. L. Walko, L. T. Steyaert, P. L. Vidale, G. E. Liston, W. A. Lyons, and T. N. Chase. 1999b. The influence of anthropogenic landscape changes on weather in south Florida. *Mon. Wea. Rev.* **127**, 1663–1673.

Pilié, R. J., E. J. Mark, C. W. Rogers, U. Katz, and W. C. Kocmond. 1979. The formation of marine fog and the development of fog-stratus systems along the California coast. *J. Appl. Meteor.* **18**, 1275–1286.

Pilinis, C., P. Kassomenos, and G. Kallos. 1993. Modeling of photochemical pollution in Athens, Greece. Application of the RAMS-CALGRID modeling system. *Atmos. Environ.* **27B**, 353–370.

Pinker, R. T., and J. F. Moses. 1982. On the canopy flow index of a tropical forest. *Bound.-Layer Meteor.* **22**, 313–324.

Pinty, J.-P., R. Benoit, E. Richard, and R. Laprise. 1995. Simple tests of a semi-implicit semi-Lagrangian model on 2D mountain wave problems. *Mon. Wea. Rev.* **123**, 3042–3058.

Pinty, J. P., P. Mascart, E. Richard, and R. Rosset. 1989. An investigation of mesoscale flows included by vegetation inhomogeneities using an evapotranspiration model calibrated against HAPEX-MOBILHY data. *J. Appl. Meteor.* **9**, 976–992.

Pitman, A. J., M. Zhao, and C. E. Desborough. 1999. Investigating the sensitivity of a land surface scheme to spatial and temporal leaf area index variability within the Global Soil Wetness Project. *J. Meteor. Soc. Japan* **77**, 281–290.

Plank, V. G. 1966. Wind conditions in situations of pattern form and non-pattern form cumulus convection. *Tellus* **18**, 1–12.

Platt, C. M. R. 1981. The effect of cirrus of varying optical depth on the extraterrestrial net radiative flux. *Quart. J. Roy. Meteor. Soc.* **107**, 671–678.

Pleim, J. E., and A. Xiu. 1995. Development and testing of a surface flux and planetary boundary layer model for application in mesoscale models. *J. Appl. Meteor.* **34**, 16–32.

Porch, W. M. 1982. Implication of spatial averaging in complex-terrain wind studies. *J. Appl. Meteor.* **21**, 1258–1265.

Porch, W. M., and M. C. MacCracken. 1982. Parametric study of the effects of arctic soot on solar radiation. *Atmos. Environ.* **16**, 1365–1371.

Poreh, M. 1996. Investigation of heat islands using small scale models. *Atmos. Environ.* **30**, 467–474.

Porte-Agel, F., C. Meneveau, and M. B. Parlange. 2000. A scale-dependent dynamic model for large-eddy simulation: Application to a neutral atmospheric boundary layer. *J. Fluid Mech.* **415**, 261–284.

Potty, K. V. J., and S. SethuRaman. 2000. Numerical simulation of monsoon depressions over India with a high-resolution nested regional model. *Meteor. Appl.* **7**, 45–60.

Poulos, G. S., and J. E. Bossert. 1995. An observational and prognostic numerical investigation of complex terrain dispersion. *J. Appl. Meteor.* **34**, 650–660.

Poulos, G. S., and R. A. Pielke. 1994. A numerical analysis of Los Angeles Basin pollution transport to the Grand Canyon under stably stratified, southwest flow conditions. *Atmos. Environ.* **28**, 3329–3357.

Poulos, G. S., W. Blumen, D. C. Fritts, J. K. Lundquist, J. Sun, S. P. Burns, C. Nappo, R. Banta, R. Newsome, J. Cuxart, E. Terradellas, B. Balsley, and M. Jensen. 2001. CASES-99: A comprehensive investigation of the stable nocturnal boundary layer. *Bull. Amer. Meteor. Soc.*, submitted.

Powell, M. D. 1980. Evaluations of diagnostic marine boundary-layer models applied to hurricanes. *Mon. Wea. Rev.* **108**, 757–766.

Powell, M. D. 1982. The transition of the Hurricane Frederic boundary-layer wind field from the open Gulf of Mexico to landfall. *Mon. Wea. Rev.* **110**, 1912–1932.

Powell, M. D., S. H. Houston, and T. A. Reinhold. 1996. Hurricane Andrew's landfall in south Florida. Part I: Standardizing measurements for documentation of surface wind fields. *Wea. Forecasting* **11**, 304–328.

Powers, J. G., and M. T. Stoelinga. 2000. A coupled air-sea mesoscale model: Experiments in atmospheric sensitivity to marine roughness. *Mon. Wea. Rev.* **128**, 208–228.

Price, J. C. 1979. Assessment of the urban heat island effect through the use of satellite data. *Mon. Wea. Rev.* **107**, 1554–1557.

Price, G. V., and A. K. MacPherson. 1973. A numerical weather forecasting method using cubic splines on a variable mesh. *J. Appl. Meteor.* **12**, 1102–1113.

Priestly, C. H. B. 1959. *Turbulent Transfer in the Lower Atmosphere*. The University of Chicago Press, Chicago.

Project METROMEX. 1976. METROMEX update. *Bull. Amer. Meteor. Soc.* **57**, 304–308.

Pruppacher, H. R. 1982. Cloud and precipitation physics and the water budget of the atmosphere. In *Engineering Meteorology*, E. Plate, Ed., Elsevier, New York, 71–124.

Pruppacher, H. R., and J. D. Klett. 1978. *Microphysics of Clouds and Precipitation*. D. Reidel, Dordrecht, The Netherlands.

Purdom, J. F. W., and K. Marcus. 1982. Thunderstorm trigger mechanisms over the southeast United States. Preprint, 12th AMS Conference on Severe Local Storms, January 11–15, San Antonio, TX, 487–488.

Puri, K., G. Dietachmayer, G. A. Mills, N. E. Davidson, R. A. Bowen, and L. W. Logan. 1998. The new BMRC Limited Area Prediction System, LAPS. *Aust. Meteor. Mag.* **47**, 203–233.

Qian, J. H., F. H. M. Semazzi, and J. S. Scroogs. 1998. A global nonhydrostatic semi-Lagrangian atmospheric model with orography. *Mon. Wea. Rev.* **126**, 747–771.

Qingcun, Z., Y. J. Dai, and F. Xue. 1998. Simulation of the Asian monsoon by IAP AGCM coupled with an advanced land surface model (IAP94). *Adv. Atmos. Sci.* **15**, 1–16.

Qu, W., A. Henderson-Sellers, A. J. Pitman, T. H. Chen, F. Abramopoulos, A. Boone, S. Chang, F. Chen, Y. Dai, R. E. Dickinson, L. Dumenil, M. Ek, N. Gedney, Y. M. Gusev, J. Kim, R. Koster, E. A. Kowalczyk, J. Lean, D. Lettenmaier, X. Liang, J.-F. Mahfouf, H.-T. Mengelkamp, K. Mitchell, O. N. Nasonova, J. Noilhan, A. Robock, C. Rosenzweig, J. Schaake, C. A. Schlosser, J.-P. Schultz, A. B. Shmakin, D. L. Verseghy, P. Wetzel, E. F. Wood, Z.-L. Yang, and Q. Zeng. 1998. Sensitivity of latent heat flux from PILPS land-surface schemes to perturbations of surface air temperature. *J. Atmos. Sci.* **55**, 1909–1927.

Queney, P. 1947. Theory of perturbations in stratified currents with applications to air flow over mountain barriers. Misc. Report No. 23, Dept. of Meteorology, University of Chicago.

Queney, P. 1948. The problem of air flow over mountains: A summary of theoretical studies. *Bull. Amer. Meteor. Soc.* **29**, 16–26.

Rabier, F., P. Courtier, and O. Talagrand. 1992. An application of adjoint models to sensitivity analysis. *Contrib. Atmos. Phys.* **65**, 177–192.

Rabier, F., P. Courtier, J. Pailleux, O. Talagrand, and D. Vasiljevic. 1993. A comparison between four-dimensional variational assimilation and simplified sequential assimilation relying on three-dimensional variational analysis. *Quart. J. Roy. Meteor. Soc.* **119**, 845–880.

Raddatz, R. L., and M. L. Khandekar. 1979. Upslope enhanced extreme rainfall events over the Canadian western plains: A mesoscale numerical simulation. *Mon. Wea. Rev.* **107**, 650–661.

Randerson, D., and A. H. Thompson. 1964. Investigation of a Tiros III photograph of the Florida peninsula taken on 14 July 1961. Science Report No. 6, Air Force Cambridge Research Labs, Office of Aerospace Research, Bedford, MA.

Rao, G. V. 1971. A numerical study of the frontal circulation in the atmospheric boundary layer. *J. Appl. Meteor.* **10**, 26–35.

Rasmussen, C. 1999. Weather research and forecasting model. *UCAR Quarterly* **24**, 10–11.

Rasmussen, E. 1979. The polar low as an extratropical CISK disturbance. *Quart. J. Roy. Meteor. Soc.* **105**, 531–549.

Rasmussen, E. 1981. An investigation of a polar low with a spiral cloud structure. *J. Atmos. Sci.* **38**, 1785–1792.

Rasmussen, E. 1982. A review of mesoscale disturbances in cold air masses. NATO Advanced Study Institute on Mesoscale Meteorology—Theory, Observations, and Models, July 13–31, Gascogne, France.

Rasmussen, E. A. 2000. Polar lows for storms. In *Storms, Vol. II*, R. A. Pielke Jr. and R. A. Pielke Sr., Eds., Routledge Press, London, 255–269.

Raupach, M. R., and R. H. Shaw. 1982. Averaging procedures for flow within vegetation canopies. *Bound.-Layer Meteor.* **22**, 79–90.

Raymond, D. J. 1972. Calculation of airflow over an arbitrary ridge including diabatic heating and cooling. *J. Atmos. Sci.* **29**, 837–843.

Raymond, D. J. 1975. A model for predicting the movement of continuously propagating convective storms. *J. Atmos. Sci.* **32**, 1308–1317.

Raymond, D. J. 1983. Wave-CISK in mass flux form. *J. Atmos. Sci.* **40**, 2561–2572.

Raynor, G. S., P. Michael, R. M. Brown, and S. SethuRaman. 1974. A research program on atmospheric diffusion from an oceanic site. Preprint, Symposium on Atmospheric Diffusion and Air Pollution, Santa Barbara, CA, 289–295.

Reason, C. J. C., K. J. Tory, and P. L. Jackson. 1999. Evolution of a southeast Australian coastally trapped disturbance. *Meteor. Atmos. Phys.* **70**, 141–165.

Reck, R. A., and J. R. Hummel. 1981. Influence of aerosol optical properties on surface temperatures computed with a radiative-convective model. *Atmos. Environ.* **15**, 1727–1731.

Reed, R. J. 1979. Cyclogenesis in polar air streams. *Mon. Wea. Rev.* **107**, 38–52.

Reed, R. J. 1981. A case study of a bora-like windstorm in western Washington. *Mon. Wea. Rev.* **109**, 2382–2393.

Reible, D. D., F. H. Shair, and R. Aris. 1983. A two-layer model of the atmosphere indicating the effects of mixing between the surface layer and the air aloft. *Atmos. Environ.* **17**, 25–33.

Reid, J. D., L. O. Grant, R. A. Pielke, and Y. Mahrer. 1976. Observations and numerical modeling of seeding agent delivery from ground based generations to orographic cloud base. Proceedings of the International Weather Modification Conference, August 26, Boulder, CO, 521–527.

Reisner, J., R. J. Rasmussen, and R. T. Bruintjes. 1998. Explicit forecasting of supercooled liquid water in winter storms using the MM5 mesoscale model. *Quart. J. Roy. Meteor. Soc.* **124B**, 1071–1107.

Ren, J., B. Su, and M. Zhao. 1999. The influence of scalar roughness on land surface-atmosphere transfer. *Chinese J. Atmos. Sci.* **23**, 179–188.

Rhea, O. J. 1977. Orographic precipitation model for hydrometeorological use. Ph.D. dissertation, Dept. of Atmospheric Science, Colorado State University, Fort Collins, CO.

Richtmyer, R. D., and K. W. Morton. 1967. *Difference Methods for Initial-Value Problems*. Interscience, New York.

Richwien, B. A. 1978. The damming effect of the southern Appalachians. Proceedings of the AMS Conference on Weather Forecasting Analysis and Aviation Meteorology, 94–101.

Richwien, B. A. 1980. The damming effect of the southern Appalachians. *Natl. Wea. Dig.* **5**, 2–12.

Rieck, R. W. (Ed.). 1979. *Facsimile Products.* NWS Forecasting Handbook No. 1, NOAA, Boulder, CO.

Ritchie, E. A., and R. L. Elsberry. 2000. Simulated impacts of a mesoscale convective system on the track of Typhoon Robyn during TCM-93. *Mon. Wea. Rev.* **128**, 2232–2251.

Ritchie, H., and M. Tanguay. 1996. A comparison of spatially averaged Eulerian and semi-Lagrangian treatment of mountains. *Mon. Wea. Rev.* **124**, 167–181.

Roach, G. F. 1970. *Green's Functions: Introductory Theory With Applications.* Van Nostrand, London.

Roach, W. T., and A. Slingo. 1979. A high-resolution infrared radiative transfer scheme to study the interaction of radiation with cloud. *Quart. J. Roy. Meteor. Soc.* **105**, 603–614.

Robinson, G. D. (Ed.). 1977. Inadvertent weather modification workshop. Final report to the National Science Foundation under Grant No. ENV-77-10186. Center for the Environment and Man, Hartford, CT.

Rockel, B., and E. Raschke. 1994. Inclusion of radiation in mesoscale models. In *Mesoscale Modeling of the Atmosphere*, R. A. Pielke Sr. and R. P. Pearce, Eds. American Meteorological Society, Boston, 39–45.

Rodriguez-Camino, E., and R. Avissar. 1999. Effective parameters for surface heat fluxes in heterogeneous terrain. *Tellus* **51A**, 387–399.

Rogers, D. P. 1995. Air–sea interaction: Connecting the ocean and atmosphere. *Rev. Geophys.* **33** (Supp.), 1377–1383.

Romero, R., C. Ramis, S. Alonso, C. A. Doswell III, and D. J. Stensrud. 1998. Mesoscale model simulations of three heavy precipitation events in the western Mediterranean region. *Mon. Wea. Rev.* **126**, 1859–1881.

Romero, R., C. A. Doswell III, and C. Ramis. 2000. Mèsoscale numerical study of two cases of long-lived quasi-stationary convective systems over eastern Spain. *Mon. Wea. Rev.* **128**, 3731–3751.

Ronda, R. J., and H. A. R. DeBruin. 1999. A note on the concept of 'effective' bulk exchange coefficients for determination of surface flux densities. *Bound.-Layer Meteor.* **93**, 155–162.

Rõõm, R., and A. Männik. 1999. Responses of different nonhydrostatic, pressure-coordinate models to orographic forcing. *J. Atmos. Sci.* **56**, 2553–2570.

Rosenberg, N. 1974. *Microclimate: The Biological Environment.* John Wiley & Sons, New York.

Rosenthal, S. L. 1970. A circularly symmetric primitive equation model of tropical cyclone development containing an explicit water vapor cycle. *Mon. Wea. Rev.* **98**, 643–663.

Rosenthal, S. L. 1971. The response of a tropical cyclone model to variations in boundary layer parameters, initial conditions, lateral boundary conditions and domain size. *Mon. Wea. Rev.* **99**, 767–777.

Rosenthal, S. L. 1978. Numerical simulation of tropical cyclone development with latent heat release by the resolvable scales. I. Model description and preliminary results. *J. Atmos. Sci.* **35**, 258–271.

Rosenthal, S. L. 1979a. Cumulus effects in hurricane models—To parameterize or not to parameterize. Proceedings of the Seminar on the Impact of GATE on Large-Scale Numerical Modeling of the Atmosphere and Ocean, Woods Hole, MA, August 20–29, U.S. GARP Program, 242–248.

Rosenthal, S. L. 1979b. The sensitivity of simulated hurricane development to cumulus parameterization details. *Mon. Wea. Rev.* **107**, 193–197.

Rosenthal, S. L. 1980. Numerical simulation of tropical cyclone development with latent heat release by the resolvable scales, II: Propagating small-scale features observed in the pre-hurricane phase. Technical Report ERL413-AOML29, NOAA, Boulder, CO.

Ross, B. B., and I. Orlanski. 1978. The circulation associated with a cold front. Part II. Moist case. *J. Atmos. Sci.* **35**, 445–465.

Ross, B. B., and I. Orlanski. 1982. The evolution of an observed cold front. Part I: Numerical simulation. *J. Atmos. Sci.* **39**, 296–327.

Roth, M. 2000. Review of atmospheric turbulence over cities. *Quart. J. Roy. Meteor. Soc.* **126**, 941–990.

Rotstayn, L. D. 1999. Climate sensitivity of the CSIRO GCM: Effect of cloud modeling assumptions. *J. Climate* **12**, 334–356.

Rotstayn, L. D., B. F. Ryan, and J. J. Katzfey. 2000. A scheme for calculation of the liquid fraction in mixed-phase stratiform clouds in large-scale models. *Mon. Wea. Rev.* **128**, 1070–1088.

Rotunno, R. 1983. On the linear theory of the land- and sea-breeze. *J. Atmos. Sci.* **40**, 1999–2005.

Rotunno, R., J. A. Curry, C. W. Fairall, C. A. Friehe, W. A. Lyons, J. E. Overland, R. A. Pielke, D. P. Rogers, S. A. Stage, G. L. Geernaert, J. W. Nielsen, and W. A. Sprigg. 1992. *Coastal Meteorology—A Review of the State of the Science.* Panel on Coastal Meteorology, Committee on Meteorological Analysis, Prediction, and Research, Board on Atmospheric Sciences and Climate, Commission on Geosciences, Environment, and Resources, National Research Council. National Academy Press, Washington, D.C.

Ruel, J. C., and R. Benoit. 1999. Analysis of the November 7, 1994, windthrow in the regions of Charlevoix and Gaspesie (Quebec, Canada). *Forestry Chron.* **75**, 293–301. (In French)

Ruel, J. C., D. Pin, L. Spacek, K. Cooper, and R. Benoit. 1997. The estimation of wind exposure for windthrow hazard rating: Comparison between Strongblow, MC2, Topex and a wind tunnel study. *Forestry* **70**, 253–266.

Rüshøjgaard, L. P., S. E. Cohn, Y. Li, and R. Ménard. 1998. The use of spline interpolation in semi-Lagrangian transport models. *Mon. Wea. Rev.* **126**, 2008–2016.

Rutledge, S. A., and P. V. Hobbs. 1983. The mesoscale and microscale structure and organization of clouds and precipitation in midlatitude cyclones, VIII: A model for the "seeder-feeder" process in warm-frontal rainbands. *J. Atmos. Sci.* **40**, 1185–1206.

Rutledge, S. A., and P. V. Hobbs. 1984. The mesoscale and microscale structure and organization of clouds and precipitation in midlatitude cyclones. 12. A diagnostic modeling study of precipitation development in narrow cold-frontal rainbands. *J. Atmos. Sci.* **41**, 2949–2972.

Ryznar, E., and J. S Touma. 1981. Characteristics of true lake breezes along the eastern shore of Lake Michigan. *Atmos. Environ.* **15**, 1201–1205.

Sackinger, P. A., D. D. Reible, and F. H. Shair. 1982. Uncertainties associated with the estimation of mass balances and Gaussian parameters from atmospheric tracer studies. *J. Air Pollut. Control Assoc.* **32**, 720–724.

Sahashi, K. 1981. Numerical experiment of land and sea breeze circulation with undulating orography. Part I: Model. *J. Meteor. Soc. Japan* **59**, 254–261.

Sailor, D. J. 1995. Simulated urban climate response to modifications in surface albedo and vegetative cover. *J. Appl. Meteor.* **34**, 1694–1704.

Saito, T. 1981. The relationship between the increased rate of downward long-wave radiation by atmospheric pollution and the visibility. *J. Meteor. Soc. Japan* **59**, 254–261.

Saito, K. 1997. Semi-implicit fully compressible version of the MRI Mesoscale Nonhydrostatic Model—Forecast experiment of the 6 August 1993 Kagashima torrential rain. *Geophys. Mag.* **2**, Ser. 2, 109–137.

Sakakibara, H. 1981. Heavy rainfall from very shallow convective clouds. *J. Meteor. Soc. Japan* **59**, 387–394.

Salmon, J. R., J. L. Walmsley, and P. A. Taylor. 1981. Development of a model of neutrally stratified boundary layer flow over real terrain. Internal report, Boundary Layer Division, Atmospheric Environment Service, Downsview, Ontario, Canada.

Salvador, R., J. Calbo, and M. M. Millan. 1999. Horizontal grid size selection and its influence on mesoscale model simulations. *J. Appl. Meteor.* **38**, 1311–1329.

Sangster, W. E. 1960. A method of representing the horizontal pressure force without reduction of station pressures to sea level. *J. Meteor.* **17**, 166–176.

Sangster, W. E. 1977. An updated objective forecast technique for Colorado downslope winds. Technical Memo NWS CR-61, NOAA, Boulder, CO.

Sangster, W. E. 1987. An improved technique for computing the horizontal pressure-gradient force at the earth's surface. *Mon. Wea. Rev.* **115**, 1358–1368.

Sardie, J. M., and T. T. Warner. 1983. On the mechanism for the development of polar lows. *J. Atmos. Sci.* **40**, 869–881.

Sarewitz, D., R. A. Pielke Jr., and R. Byerly (Eds.). 2000. *Prediction: Science Decision Making and the Future of Nature.* Island Press, Covelo, CA.

Sasaki, Y. 1970a. Some basic formalisms in numerical variational analysis. *Mon. Wea. Rev.* **98**, 875–883.

Sasaki, Y. 1970b. Numerical variational analysis formulated under the constraints as determined by longwave equations and low-pass filter. *Mon. Wea. Rev.* **98**, 884–898.

Sasaki, Y. 1970c. Numerical variational analysis with weak constraint and application to surface analysis of a severe gust front. *Mon. Wea. Rev.* **98**, 899–910.

Sasaki, Y., and J. M. Lewis. 1970. Numerical variational objective analysis of the planetary boundary layer in conjunction with squall line formation. *J. Meteor. Soc. Japan* **48**, 381–393.

Sasamori, T. 1968. Radiative cooling calculation for application to general circulation experiments. *J. Appl. Meteor.* **7**, 721–729.

Sasamori, T. 1970. A numerical study of atmospheric and soil boundary layers. *J. Atmos. Sci.* **27**, 1122–1137.

Sasamori, T. 1972. A linear harmonic analysis of atmospheric motion with radiative dissipation. *J. Meteor. Soc. Japan* **50**, 505–517.

Sathye, A., M. Xue, G. Bassett, and K. Droegemeier. 1997. Parallel weather modeling with the Advanced Regional Prediction System. *Parallel Comput.* **23**, 2243–2256.

Satomura, T. 2000. Diurnal variation of precipitation over the Indo-China peninsula: Two-dimensional numerical simulation. *J. Meteor. Soc. Japan* **78**, 461–474.

Savijarvi, H., and S. Jarvenoja. 2000. Aspects of the fine-scale climatology over Lake Tanganyika as resolved by a mesoscale model. *Meteor. Atmos. Phys.* **73**, 77–88.

Sawai, T. 1978. Formation of the urban air mass and the associated local circulations. *J. Meteor. Soc. Japan* **56**, 159–173.

Schaeffer, J. T. 1974. A simulative model of dryline motion. *J. Atmos. Sci.* **31**, 956–964.

Schayes, G., P. Thunis, and R. Bornstein. 1996. Topographic vorticity-mode mesoscale (TVM) model: Part I: Formulation. *J. Appl. Meteor.* **35**, 1815–1823.

Schechter, M. 1977. *Modern Methods in Partial Differential Equations*. McGraw-Hill, New York.

Schere, K. L., and K. L. Demerjian. 1978. A photochemical box model for urban air quality simulation. 4th Joint Conference on Sens. Environmental Pollution, 427–433.

Schlesinger, R. E. 1973. A numerical model of deep moist convection. I. Comparative experiments for variable ambient moisture and wind shear. *J. Atmos. Sci.* **30**, 835–856.

Schlesinger, R. E. 1980. A three-dimensional numerical model of an isolated thunderstorm. II. Dynamics of updraft splitting and mesovortex couplet evolution. *J. Atmos. Sci.* **37**, 395–420.

Schlesinger, R. E. 1982a. Three-dimensional numerical modeling of convective storms. A review of milestones and challenges. 12th AMS Conference on Severe Local Storms, San Antonio, TX, January 11–15, 506–515.

Schlesinger, R. E. 1982b. Effects of mesoscale lifting, precipitation and boundary layer shear on severe storm dynamics in a three-dimensional numerical modeling study. 12th AMS Conference on Severe Local Storms, San Antonio, TX, January 11–15, 536–541.

Schlosser, C. A., A. G. Slater, A. Robock, A. J. Pitman, K. Y. Vinnikov, A. Henderson-Sellers, N. A. Speranskaya, K, Mitchell, and the PILPS 2(D) Contributors. 2000. Simulations of a Boreal grassland hydrology at Valdi, Russia. PILPS Phase 2(D). *Mon. Wea. Rev.* **128**, 301–321.

Schlunzen, K. H. 1994. Mesoscale modelling in complex terrain—An overview on the German nonhydrostatic models. *Beitr. Phys. Atmos.* **67**, 243–253.

Schmidt, F. H. 1947. An elementary theory of the land- and sea-breeze circulation. *J. Meteor.* **4**, 9–15.

Schmidt, R., and K. Housen. 1995. Problem solving with dimensional analysis. *Indust. Phys.* **1**, 21–24.

Schrieber, K., R. Stull, and Q. Zhang. 1996. Distributions of surface-layer buoyancy versus lifting condensation level over a heterogeneous land surface. *J. Atmos. Sci.* **53**, 1086–1107.

Schulman, E. E. 1970. The Antarctic circumpolar current. Proceedings of the 1970 Summer Computer Simulation Conference, Denver, CO, 955–961.

Schultz, D. M. 1999. Lake-effect snowstorms in northern Utah and western New York with and without lightning. *Wea. Forecasting* **14**, 1023–1031.

Schultz, J.-P., L. Dumenil, J. Polcher, C. A. Schlosser, and Y. Xue. 1998. Land surface energy and moisture fluxes: Comparing three models. *J. Appl. Meteor.* **37**, 288–307.

Schultz, P. 1995. An explicit cloud physics parameterization for operational numerical weather prediction. *Mon. Wea. Rev.* **123**, 3331–3343.

Schultz, P., and T. T. Warner. 1982. Characteristics of summer-time circulations and pollutant ventilation in the Los Angeles Basin. *J. Appl. Meteor.* **21**, 672–682.

Schuur, T. J., and S. A. Rutledge. 2000a. Electrification of stratiform regions in mesoscale convective systems. Part I: An observational comparison of symmetric and asymmetric MCSs. *J. Atmos. Sci.* **57**, 1961–1982.

Schuur, T. J., and S. A. Rutledge. 2000b. Electrification of stratiform regions in mesoscale convective systems. Part II: Two-dimensional numerical model simulations of a symmetric MCS. *J. Atmos. Sci.* **57**, 1983–2006.

Schwartz, B. E., and L. F. Bosart. 1979. The diurnal variability of Florida rainfall. *Mon. Wea. Rev.* **107**, 1535–1545.

Schwerdtfeger, W. 1974. Mountain barrier effect on the flow of stable air north of the Brooks Range. Proceedings of the 24th Alaskan Science Conference, Geophysical Institute University of Alaska, Fairbanks, 204–208.

Schwerdtfeger, W. 1975. The effect of the Antarctic peninsula on the temperature regime of the Weddell Sea. *Mon. Wea. Rev.* **103**, 45–51.

Science News. 1976. Dioxin toxicity data sent to aid Italy. **110**, 359.

Scofield, R. A., and C. E. Weiss. 1977. A report on the Chesapeake Bay Region Nowcasting Experiment. Technical Memo NESS 94, NOAA, Boulder, CO.

Scorer, R. S. 1949. Theory of waves in the lee of mountains. *Quart. J. Roy. Meteor. Soc.* **75**, 41–56.

Scott, B. C. 1982. Theoretical estimates of the scavenging coefficient for soluble aerosol particles as a function of precipitation type, rate and altitude. *Atmos. Environ.* **16**, 1753–1762.

Seaman, N. L. 1982. A numerical simulation of three-dimensional mesoscale flows over mountainous terrain. Report No. AS 135, Dept. of Atmospheric Science, University of Wyoming.

Seaman, N. L. 1999. Cumulus parameterizations. Invited lecture, COMET Faculty Course on Numerical Weather Prediction, Boulder, CO.

Seaman, N. L. 2000. Meteorological modeling for air-quality assessments. *Atmos. Environ.* **34**, 2231–2259.

Seaman, N. L., and R. A. Anthes. 1981. A mesoscale semi-implicit numerical model. *Quart. J. Roy. Meteor. Soc.* **107**, 167–190.

Seaman, N. L., and S. A. Michelson. 2000. Mesoscale meteorological structure of a high-ozone episode during the 1995 NARSTO-Northeast study. *J. Appl. Meteor.* **39**, 109–123.

Seaman, N. L., D. R. Stauffer, and A. M. Lario-Gibbs. 1995. A multiscale four-dimensional data assimilation system applied in the San Joaquin Valley during SARMAP. Part I: Modeling design and basic performance characteristics. *J. Appl. Meteor.* **34**, 1739–1761.

Seaman, N. L., J. S. Kain, and A. Deng. 1996. Development of a shallow convection parameterization for mesoscale models. Preprint, 11th AMS Conference on Numerical Weather Prediction, Aug. 19–23, Norfolk, VA, 340–342.

Segal, M., and R. A. Pielke. 1981. Numerical model simulation of human biometeorological heat load conditions—Summer day case study for the Chesapeake Bay area. *J. Appl. Meteor.* **20**, 735–749.

Segal, M., R. T. McNider, R. A. Pielke, and D. S. McDougal. 1982a. A numerical model simulation of the regional air pollution meteorology of the greater Chesapeake Bay area—Summer day case study. *Atmos. Environ.* **16**, 1381–1397.

Segal, M., Y. Mahrer, and R. A. Pielke. 1982b. Application of a numerical mesoscale model for the evaluation of seasonal persistent regional climatological patterns. *J. Appl. Meteor.* **21**, 1754–1762.

Segal, M., R. A. Pielke, and Y. Mahrer. 1983a. On climatic changes due to a deliberate flooding of the Qattara depression (Egypt). *Climatic Change* **5**, 73–83.

Segal, M., Y. Mahrer, and R. A. Pielke. 1983b. A study of meteorological patterns associated with a lake confined by mountains—The Dead Sea case. *Quart. J. Roy. Meteor. Soc.* **109**, 549–564.

Segal, M., R. Avissar, M. C. McCumber, and R. A. Pielke, 1988. Evaluation of vegetation effects on the generation and modification of mesoscale circulations. *J. Atmos. Sci.* **45**, 2268–2292.

Segal, M., J. R. Garratt, G. Kallos, and R. A. Pielke. 1989a. The impact of wet soil and canopy temperatures on daytime boundary-layer growth. *J. Atmos. Sci.* **46**, 3673–3684.

Segal, M., W. Schreiber, G. Kallos, R. A. Pielke, J. R. Garratt, J. Weaver, A. Rodi, and J. Wilson. 1989b. The impact of crop areas in northeast Colorado on midsummer mesoscale thermal circulations. *Mon. Wea. Rev.* **117**, 809–825.

Segal, M., J. R. Garratt, R. A. Pielke, and Z. Ye. 1991a. Scaling and numerical model evaluation of snow-cover effects on the generation and modification of daytime mesoscale circulations. *J. Atmos. Sci.* **48**, 1024–1042.

Segal, M., J. H. Cramer, R. A. Pielke, J. R. Garratt, and P. Hildebrand. 1991b. Observational evaluation of the snow-breeze. *Mon. Wea. Rev.* **119**, 412–424.

Segal, M., J. R. Garratt, R. A. Pielke, P. Hildebrand, F. A. Rogers, and J. Cramer. 1991c. On the impact of snow cover on daytime pollution dispersion. *Atmos. Environ.* **25B**, 177–192.

Seigneur, C. 1994. The status of mesoscale air quality models. In *Planning and Managing Regional Air Quality Modeling and Measurement Studies. Part III: Studies Supporting Project Planning*, P. A. Solomon, Ed. CRC Press, Boca Raton, FL, 403–434.

Seinfeld, J. H. 1975. *Air Pollution. Physical and Chemical Fundamentals.* McGraw-Hill, New York.

Seinfeld, J. H., and S. Pandis. 1997. *Atmospheric Chemistry and Physics. Air Pollution to Climate*. John Wiley & Sons, New York.

Selby, S. M. (Ed.). 1967. *CRC Standard Mathematical Tables*, 15th ed. The Chemical Rubber Co., Cleveland, OH.

Sellers, P. J., Y. Mintz, Y. C. Sud, and A. Dalcher. 1986. A simple biosphere model (SiB) for use within general circulation models. *J. Atmos. Sci.* **43**, 505–531.

Sellers, P. J., F. G. Hall, G. Asrar, D. E. Strebel, and R. E. Murphy. 1992. An overview of the First International Satellite Land Surface Climatology Project (ISLSCP) Field Experiment (FIFE). *J. Geophys, Res.* **97D17**, 18,345–18,371.

Sellers, P. J., F. G. Hall, H. Margolis, B. Kelly, D. Baldocchi, G. den Hartog, J. Cihlar, M. G. Ryan, B. Goodison, P. Crill, K. J. Ranson, D. Lettenmaier, and D. Wickland. 1995. The Boreal Ecosystem-Atmosphere Study (BOREAS): An overview and early results from the 1994 field year. *Bull. Amer. Meteor. Soc.* **76**, 1549–1577.

Sellers, P. J., F. G. Hall, R. D. Kelly, A. Black, D. Baldocchi, J. Berry, M. Ryan, K. J. Ranson, P. M. Crill, D. P. Lettenmaier, H. Margolis, J. Cihlar, J. Newcomer, D. Fitzjarrald, P. G. Jarvis, S. T. Gower, D. Halliwell, D. Williams, B. Goodison, D. W. Wickland, and F. E. Guertin, (Eds.). 1997. BOREAS special issue. *J. Geophys, Res.* **102, D24**, 28,731–29,475.

Sellers, W. D. 1965. *Physical Climatology*. University of Chicago Press, Chicago.

Sen, O. L., W. J. Shuttleworth, and Z.-L. Yang. 2000. Comparative evaluation of BATS2, BATS, and SiB2 with Amazon data. *J. Hydrometeor.* **1**, 135–153.

Sergeev, B. N. 1983. Numerical simulation of an atmospheric front with a closed system and precipitation. *Sov. Meteor. Hydro.* **4**, 16–23.

Serreze, M. C., J. A. Maslanik, M. C. Rehder, and R. C. Schnell. 1992. Theoretical heights of buoyant convection above open leads in the winter Arctic pack ice cover. *J. Geophys. Res.* **97**, 9411–9422.

SethuRaman, S., and J. E. Cermak. 1973. Stratified shear flows over a simulated three-dimensional urban heat island. Project Themis Technical Report No. 23, Fluid Dynamics and Diffusion Laboratory, Colorado State University, Fort Collins, CO.

Shafran, P. C., N. L. Seaman, and G. A. Gayno. 2000. Evaluation of numerical predictions of boundary layer structure during the Lake Michigan ozone study. *J. Appl. Meteor.* **39**, 55–69.

Shao, Y., and A. Henderson-Sellers. 1996. Modeling soil moisture: A project for intercomparison of land surface parameterization schemes Phase 2(b). *J. Geophys. Res.* **101**, 7227–7250.

Shao, Y., and P. Irannejad. 1999. On the choice of soil hydraulic models in land-surface schemes. *Bound.-Layer Meteor.* **90**, 83–115.

Shapiro, A., L. Zhao, S. Weygandt, K. Brewster, S. Lazarus, and K. K. Droegemeier. 1996. Initial forecast fields from single-Doppler wind retrieval, thermodynamic retrieval and ADAS. Preprint, 11th AMS Conference on Numerical Weather Prediction, Norfolk, VA, 119–121.

Shapiro, M. A. 1981. Frontogenesis and geostrophically forced secondary circulations in the vicinity of jet stream-frontal zone systems. *J. Atmos. Sci.* **38**, 954–973.

Shapiro, M. A. 1982. Mesoscale weather systems of the Central United States. Report, CIRES and NOAA, Boulder, CO.

Shapiro, M. A., H. Wernli, J.-W. Bao, J. Methven, X. Zou, P. Neiman, E. Donall-Grell, J. D. Doyle, and T. Holt. 1999. A planetary-scale to mesoscale perspective of the life cycles of extratropical cyclones: The bridge between theory and observations. In *The Life Cycles of Extratropical Cyclones*, M. A. Shapiro and S. Gronas, Eds. American Meteorological Society, Boston, 139–185.

Shapiro, R. 1970. Smoothing, filtering and boundary effects. *Rev. Geophys. Space Phys.* **8**, 359–387.

Sharan, M., and S. G. Golpalakrishnan. 1997. Comparative evaluation of eddy exchange coefficients for strong and weak wind stable boundary layer. *J. Appl. Meteor.* **36**, 545–559.

Sharan, M., S. G. Golpalakrishnan, and R. T. McNider. 1999. A local parameterization scheme for σ_w under stable conditions. *J. Appl. Meteor.* **38**, 617–622.

Sharan, M., S. G. Golpalakrishnan, R. T. McNider, and M. P. Singh. 2000. A numerical investigation of urban influences on local meteorological conditions during the Bhopal gas accident. *Atmos. Environ.* **34**, 539–552.

Shaw, B. L., R. A. Pielke, and C. L. Ziegler. 1997. A three-dimensional numerical simulation of a Great Plains dryline. *Mon. Wea. Rev.* **125**, 1489–1506.

Sheih, C. M. 1977. Mathematical modeling of particulate thermal coagulation and transport downstream of an urban source. *Atmos. Environ.* **11**, 1185–1190.

Sheih, C. M. 1978. A puff-on-cell model for computing pollutant transport and diffusion. *J. Appl. Meteor.* **17**, 140–147.

Sheih, C. M., M. L. Wesely, and B. B. Hicks. 1979. Estimated dry deposition velocities of sulfur over the eastern United States and surrounding regions. *Atmos. Environ.* **13**, 1361–1368.

Sheng, L., K. H. Schlunzen, and Z. Wu. 2000. Three-dimensional numerical simulation of the mesoscale wind structure over Shandong Peninsula. *Acta Meteor. Sinica* **14**, 96–107.

Sheng, P. Y., W. Lick, R. T. Gedney, and F. B. Molls. 1978. Numerical computations of three-dimensional circulations in Lake Erie: A comparison of a free-surface model and a rigid-lid model. *J. Phys. Oceanogr.* **8**, 713–727.

Sherman, C. E. 1978. A mass-consistent model for wind fields over complex terrain. *J. Appl. Meteor.* **17**, 312–319.

Sheynin, O. B. 1973. R. J. Boscovich's work on probability. *Arch. Hist. Exact Sci.* **9**, 306–324.

Shi, Y., X. S. Feng, F. S. Wei, and W. Jiang. 2000. Three-dimensional nonhydrostatic numerical simulation for the PBL of an open-pit mine. *Bound.-Layer Meteor.* **94**, 197–224.

Shimanuki, A. 1969. Formulation of a vertical distributions of wind velocity and eddy diffusivity near the ground. *J. Meteor. Soc. Japan* **47**, 292–298.

Shir, C. C., and R. D. Bornstein. 1977. Eddy coefficients in the numerical modeling of the planetary boundary layer: Problems and a new approach. *Bound.-Layer Meteor.* **11**, 171–185.

Shreffler, J. H. 1979. Heat island convergence in St. Louis during calm periods. *J. Appl. Meteor.* **18**, 1512–1520.

Shreffler, J. H. 1982. Intercomparisons of upper air and surface winds in an urban region. *Bound.-Layer Meteor.* **22**, 345–356.

Sievers, V., R. Forkel, and W. Zdunkowski. 1983. Transport equations for heat and moisture in the soil and their application to boundary layer problems. *Contrib. Atmos. Phys.* **56**, 58–83.

Silva Dias, M. R. 1979. Linear spectral model of tropical mesoscale systems. Ph.D. dissertation, Atmospheric Science Paper No. 311, Colorado State University, Fort Collins, CO.

Sim, L. 1972. Interception loss in the humid forested areas (with special reference to Sungai Lui Catchment, West Malaysia). *Malay. Nat.* **25**, 104–111.

Simpson, J. 1976. Precipitation augmentation from cumulus clouds and systems. Scientific and technological foundation, 1975. *Adv. Geophys.* **19**, 1–72.

Simpson, J. E. 1982. Gravity currents in the laboratory, atmosphere and ocean. *Ann. Rev. Fluid Mech.* **14**, 213–234.

Simpson, J. E. 1983. Cumulus clouds: Numerical models, observations and entrainment. In *Mesoscale Meteorology—Theories, Observations and Models.* D. K. Lilly and T. Gal-Chen, Eds. D. Reidel, Dordrecht, Holland, 413–445.

Simpson, J. E. 1996. Diurnal changes in sea-breeze direction. *J. Appl. Meteor.* **35**, 1166–1169.

Simpson, J., G. V. Helvoirt, and M. McCumber. 1982. Three-dimensional simulations of cumulus congestus clouds on GATE Day 261. *J. Atmos. Sci.* **39**, 126–145.

Simpson, J., N. E. Westcott, R. J. Clerman, and R. A. Pielke. 1980. On cumulus mergers. *Arch. Metreorol. Geophys. Bioklimatol.* **29**, 1–40.

Simpson, J., and V. Wiggert. 1969. Models of precipitating cumulus towers. *Mon. Wea. Rev.* **97**, 471–489.

Simpson, R. H. 1978. On the computation of equivalent potential temperature. *Mon. Wea. Rev.* **106**, 124–130.

Simpson, R. H., and R. A. Pielke. 1976. Hurricane development and movement. *Appl. Mech. Rev.* **29**, 601–609.

Sinha, S. K., S. G. Narkhedkar, and S. Rajamani. 1998. Application of Sasaki's numerical variational technique to the analysis of height and wind fields over Indian region. *MAUSAM* **49**, 1–10.

Sisterson, D. L., and R. A. Dirks. 1978. Structure of the daytime urban moisture field. *Atmos. Environ.* **12**, 1943–1949.

Sistla, G., N. Zhou, J. Y. Ku, S. T. Rao, R. D. Bornstein, F. Freedman, and P. Thunis. 1996. Effects of uncertainties in meteorological inputs on UAM predictions and ozone control strategies. *Atmos. Environ.,* **30**, 2011–2025.

Skibin, D., and A. Hod. 1979. Subjective analysis of mesoscale flow patterns in northern Israel. *J. Appl. Meteor.* **18**, 329–337.

Skinner, T., and N. Tapper. 1994. Preliminary sea breeze studies over Bathurst and Melville Islands, Northern Australia, as part of the Island Thunderstorm Experiment (ITEX). *Meteor. Atmos. Phys.* **53**, 77–94.

Slingo, A., R. Brown, and C. L. Wrench. 1982. A field study of nocturnal stratocumulus—III, high resolution radiative and microphysical observations. *Quart. J. Roy. Meteor. Soc.* **108**, 145–165.

Slinn, W. G. N. 1982. Predictions for particle deposition to vegetative canopies. *Atmos. Environ.* **16**, 1785–1794.

Smagorinsky, J. 1963. General circulation experiments with the primitive equations. Part I. The basic experiment. *J. Meteor.* **14**, 184–185.

Smagorinsky, J., S. Manabe, and J. L. Holloway Jr. 1965. Numerical results from a nine-level general circulation model of the atmosphere. *Mon. Wea. Rev.* **93**, 727–798.

Smith, B., and L. Mahrt. 1981. A study of boundary-layer pressure adjustments. *J. Atmos. Sci.* **38**, 334–346.

Smith, J. K., and T. B. McKee. 1983. Undisturbed clear day diurnal wind and temperature pattern in northeastern Colorado. Atmospheric Science Paper No. 365, Colorado State University, Fort Collins, CO.

Smith, R. B. 1979. Influence of mountains on the atmosphere. *Adv. Geophys.* **21**, 217–230.

Smith, R. B. 1982a. A differential advection model of orographic rain. *Mon. Wea. Rev.* **110**, 306–309.

Smith, R. B. 1982b. Synoptic observations and theory of orographically disturbed wind and pressure. *J. Atmos. Sci.* **39**, 60–70.

Smith, R. B., and Y.-L. Lin. 1982. The addition of heat to a stratified airstream with application to the dynamics of orographic rain. *Quart. J. Roy. Meteor. Soc.* **108**, 353–378.

Smith, R. C. 1955. Theory of air flow over a heated land mass. *Quart. J. Roy. Meteor. Soc.* **81**, 382–395.

Smith, R. C. 1957. Air motion over a heated land mass: II. *Quart. J. Roy. Meteor. Soc.* **83**, 248–256.

Smolarkiewicz, P. K. 1983. A simple positive definite advection scheme with small implicit diffusion. *Mon. Wea. Rev.* **111**, 479–486.

Smolarkiewicz, P. K. 1989. Comments on "A positive definite advection scheme obtained by nonlinear renormalization of the advective fluxes." *Mon. Wea. Rev.* **117**, 2626–2632.

Smolarkiewicz, P. K., and L. G. Margolin. 1997. On forward-in-time differencing for fluids: An Eulerian/semi-Lagrangian nonhydrostatic model for stratified flows. *Atmos. Ocean Special* **35**, 127–152.

Smolarkiewicz, P. K., and L. G. Margolin. 1998. MPDATA. A finite-difference solver for geophysical flows. *J. Comput. Phys.* **140**, 459–480.

Smolarkiewicz, P. K., V. Grubisíc, and L. G. Margolin. 1997. On forward-in-time differencing for fluids. Stopping criteria for iterative solutions of anelastic pressure equations. *Mon. Wea. Rev.* **125**, 647–654.

Smull, B. F. 1995. Convectively-induced mesoscale weather systems in the tropical and warm-season midlatitude atmosphere. *Rev. Geophys.* **33** (Supp.), 897–906.

Snook, J. S. and R. A. Pielke. 1995. Diagnosing a Colorado heavy snow event with a nonhydrostatic mesoscale numerical model structured for operational use. *Wea. Forecasting* **10**, 261–285.

Snook, J. S., P. A. Stamus, J. Edwards, Z. Christidis, and J. A. McGinley. 1998. Local-domain mesoscale analysis and forecast model support for the 1996 Centennial Olympic Games. *Wea. Forecasting* **13**, 138–150.

Snow, J. W. 1981. Wind power assessment along the Atlantic and Gulf Coasts of the U.S. Ph.D. dissertation, Dept. of Environmental Sciences, University of Virginia, Charlottesville, VA.

Somieski, F. 1981. Linear theory of three-dimensional flow over mesoscale mountains. *Contrib. Atmos. Phys.* **54**, 315–334.

Sommeria, G. 1976. Three-dimensional simulation of turbulent processes in an undisturbed tradewind boundary layer. *J. Atmos. Sci.* **33**, 216–241.

Sommeria, G., and J. W. Deardorff. 1977. Subgrid-scale condensation in models of nonprecipitating clouds. *J. Atmos. Sci.* **33**, 216–241.

Song, Y., and D. Haidvogel. 1994. A semi-implicit ocean circulation model using a generalized topography-following coordinate system. *J. Comput. Phys.* **115**, 228–244.

Song, J. L., R. A. Pielke, M. Segal, R. W. Arritt, and R. Kessler. 1985. A method to determine non-hydrostatic effects within subdomains in a mesoscale model. *J. Atmos. Sci.* **42**, 2110–2120.

Soong, S.-T., and W.-K. Tao. 1980. Response of deep tropical cumulus clouds to mesoscale processes. *J. Atmos. Sci.* **37**, 2016–2034.

Sorbjan, Z. 1989. *Structure of the Atmospheric Boundary Layer*. Prentice-Hall, Englewood Cliffs, NJ.

Sorbjan, Z., and M. Uliasz. 1982. Some numerical urban boundary-layer studies. *Bound.-Layer Meteor.* **22**, 481–502.

Sousounis, P. J., G. E. Mann, G. S. Young, R. B. Wagenmaker, B. D. Hoggatt, and W. J. Badini. 1999. Forecasting during the Lake-ICE/SNOWBANDS field experiments. *Wea. Forecasting* **14**, 955–975.

Spiegel, M. R. 1967. *Applied Differential Equations*. Prentice-Hall, Englewood Cliffs, NJ.

Srivastava, R. C. 1971. Size distribution of raindrops generated by their breakup and coalescence. *J. Atmos. Sci.* **28**, 410–415.

Stage, S. A. 1983. Boundary layer evolution in the region between shore and cloud edge during cold air outbreaks. *J. Atmos. Sci.* **40**, 1453–1471.

Staley, D. O., and G. M. Jurica. 1970. Flux emissivity tables for water vapor, carbon dioxide and ozone. *J. Appl. Meteor.* **9**, 365–372.

Stauffer, D. R., and N. L. Seaman. 1990. Use of four-dimensional data assimilation in a limited-area mesoscale model. Part I: Experiments with synoptic-scale data. *Mon. Wea. Rev.* **118**, 1250–1277.

Stein, U. and P. Alpert. 1993. Factor separation in numerical simulations. *J. Atmos. Sci.* **50**, 2107–2115.

Stensrud, D. J., J.-W. Bao, and T. T. Warner. 2000. Using initial condition and model physics perturbations in short-range ensemble simulations of mesoscale convective systems. *Mon. Wea. Rev.* **128**, 2077–2107.

Stephens, G. L. 1978a. Radiation profiles in extended water clouds. II: Parameterization schemes. *J. Atmos. Sci.* **35**, 2123–2132.

Stephens, G. L. 1978b. Radiation profiles in extended water clouds. I Theory. *J. Atmos. Sci.* **35**, 2111–2122.

Stephens, G. L. 1984. Parameterization of radiation for numerical weather prediction models. *Mon. Wea. Rev.* **112**, 826–867.

Stephens, G. L. 1994. *Remote Sensing of the Lower Atmosphere. An Introduction*. Oxford University Press, London.

Stephens, G. L., and P. J. Webster. 1981. Clouds and climate: Sensitivity of simple systems. *J. Atmos. Sci.* **38**, 235–247.

Stern, M. E., and J. S. Malkus. 1953. The flow of a stable atmosphere over a heated island. Part II. *J. Meteor.* **10**, 105–120.

Stevens, B., W. R. Cotton, G. Feingold, and C.-H. Moeng. 1998. Large-eddy simulations of strongly precipitating, stratocumulus-topped boundary layers. *J. Atmos. Sci.* **55**, 3616–3638.

Stevens, B., C.-H. Moeng, and P. P. Sullivan. 1999. Large-eddy simulations of radiatively driven convection. Sensitivities to the representation of small scales. *J. Atmos. Sci.* **56**, 3963–3984.

Steyn, D. G., and K. W. Ayotte. 1985. Application of two-dimensional terrain height spectra to mesoscale modeling. *J. Atmos. Sci.* **42**, 2884–2887.

Stohlgren, T. J., T. N. Chase, R. A. Pielke, T. G. F. Kittel, and J. Baron. 1998. Evidence that local land use practices influence regional climate and vegetation patterns in adjacent natural areas. *Global Change Biol.* **4**, 495–504.

Storch, H. V. 1978. Construction of optimal numerical filters fitted for noise damping in numerical simulation models. *Contrib. Atmos. Phys.* **51**, 189–197.

Straka, J. M. 1994. Representing moisture processes in mesoscale numerical models. In *Mesoscale Modeling of the Atmosphere*, R. A. Pielke Sr. and R. P. Pearce, Eds., American Meteorological Society, Boston, 29–38.

Strommen, N. D., and J. R. Harman. 1978. Seasonally changing patterns of lake-effect snowfall in western lower Michigan. *Mon. Wea. Rev.* **106**, 503–509.

Stull, R. B. 1976. The energetics of entrainment across a density interface. *J. Atmos. Sci.* **33**, 1260–1267.

Stull, R. B. 1983. Integral scales for the nocturnal boundary layer. Part I: Empirical depth relationships. *J. Climate Appl. Meteor.* **22**, 673–686.

Stull, R. B. 1988. *An Introduction to Boundary Layer Meteorology*. Kluwer Academic Publishers, Amsterdam.

Stull, R. B. 2000. *Meteorology for Scientists and Engineers*, 2nd ed. Brooks/Cole Thomson Learning, Pacific Grove, CA.

Sturm, M., and J. Holmgren. 1998. Differences in compaction behavior of three climate classes of snow. *Ann. Glaciol.* **26**, 125–130.

Sturm, M., J. Holmgren, and G. E. Liston. 1995. A seasonal snow cover classification system for local to global applications. *J. Climate* **8**, 1261–1283.

Sud, Y. C., and G. K. Walker. 1999a. Microphysics of clouds with the relaxed Arakawa–Schubert Scheme (McRAS). Part I: Design and evaluation with GATE Phase III data. *J. Atmos. Sci.* **56**, 3196–3220.

Sud, Y. C., and G. K. Walker. 1999b. Microphysics of Clouds with the Relaxed Arakawa–Schubert Scheme (McRAS). Part II: Implementation and performance in GEOS II GCM. *J. Atmos. Sci.* **56**, 3221–3240.

Sud, Y. C., W. C. Chao, and G. K. Walker. 1993. Dependence of rainfall on vegetation. Theoretical considerations, simulation experiments, observations, and inferences from simulated atmospheric soundings. *J. Arid Environ.* **25**, 5–18.

Sud, Y. C., K. M. Lau, G. K. Walker, and J. H. Kim. 1995. Understanding biosphere–precipitation relationships: Theory, model simulations and logical inferences. *MAUSAM* **46**, 1–14.

Sun, J. 1999. Diurnal variations of thermal roughness height over a grassland. *Bound.-Layer Meteor.* **92**, 407–427.

Sun, W.-Y. 1980. A forward-backward time integration scheme to treat internal gravity waves. *Mon. Wea. Rev.* **108**, 402–407.

Sun, W.-Y. 1984a. Numerical analysis for hydrostatic and nonhydrostatic equations of inertial internal gravity waves. *Mon. Wea. Rev.* **112**, 259–268.

Sun, W.-Y. 1984b. Rainbands and symmetric instability. *J. Atmos. Sci.* **41**, 3412–3426.

Sun, W.-Y. 1987. Mesoscale convection along the dryline. *J. Atmos. Sci.* **44**, 1394–1403.

Sun, W.-Y. 1993a. Numerical simulation of a planetary boundary layer: Part I. Cloud-free case. *Beitr. Phys. Atmos.* **66**, 3–16.

Sun, W.-Y. 1993b. Numerical experiments for advection equation. *J. Comput. Phys.* **108**, 264–271.

Sun, W.-Y. 1995. Pressure gradient in a sigma coordinate. *Terr. Atmos. Oceanic Sci.* **6**, 579–590.

Sun, W.-Y., and C.-Z. Chang. 1986. Diffusion model for a convective layer. Part I: Numerical simulation of convective boundary layer. *J. Climate Appl. Meteor.* **25**, 1445–1453.

Sun, W.-Y., and J.-D. Chern. 1994. Numerical experiments of vortices in the wakes of large idealized mountains. *J. Atmos. Sci.* **51**, 191–209.

Sun, W.-Y., and P. A. Haines. 1996. Semi-prognostic tests of a new cumulus parameterization scheme for mesoscale modeling. *Tellus* **48A**, 272–289.

Sun, W.-Y., and Y. Ogura. 1979. Boundary-layer forcing as a possible trigger to a squall line formation. *J. Atmos. Sci.* **36**, 235–254.

Sun, W.-Y., and Y. Ogura. 1980. Modeling the evolution of the convection planetary boundary layer. *J. Atmos. Sci.* **37**, 1558–1572.

Sun, W.-Y., and I. Orlanski. 1981a. Large mesoscale convection and sea breeze circulation. Part I: Linear stability analysis. *J. Atmos. Sci.* **38**, 1675–1693.

Sun, W.-Y., and I. Orlanski. 1981b. Large mesoscale convection and sea breeze circulation. Part II: Nonlinear numerical model. *J. Atmos. Sci.* **38**, 1694–1709.

Sun, W.-Y., and C.-C. Wu. 1992. Formation and diurnal variation of the dryline. *J. Atmos. Sci.* **49**, 1606–1619.

Sun, W.-Y., and K.-S. Yeh. 1997. A general semi-Lagrangian advection scheme employing forward trajectories. *Quart. J. Roy. Meteor. Soc.* **123**, 2463–2476.

Sun, W.-Y., K.-S. Yeh, and R.-Y. Sun. 1996. A simple-Lagrangian scheme for advection equations. *Quart. J. Roy. Meteor. Soc.* **122**, 1211–1226.

Sundquist, H. 1979. Vertical coordinates and related discretization. "Numerical Methods Used in Atmospheric Models," GARP Report 17, Volume II, WMO, Geneva, 1–150.

Svendsen, H., and R. Thompson. 1978. Wind-driven circulation in fjords. *J. Phys. Oceanogr.* **8**, 703–712.

Swan, P. R., and I. Y. Lee. 1980. Meteorological and air pollution modeling for an urban airport. *J. Appl. Meteor.* **19**, 534–544.

Sweet, W., R. Fett, J. Kerling, and P. LaViolette. 1981. Air-sea interaction effects in the lower troposphere across the north wall of the Gulf Stream. *Mon. Wea. Rev.* **109**, 1042–4052.

Tag, P. M., and T. E. Rosmond. 1980. Accuracy and energy conservation in a three-dimensional anelastic model. *J. Atmos. Sci.* **37**, 2150–2168.

Tag, P. M., F. W. Murray, and L. R. Kvenig. 1979. A comparison of several forms of eddy viscosity parameterization in a two-dimensional cloud model. *J. Appl. Meteor.* **18**, 1429–1441.

Taha, H. 1999. Modifying a mesoscale meteorological model to better incorporate urban heat storage. A bulk-parameterization approach. *J. Appl. Meteor.* **38**, 466–473.

Taha, H., S. Konopacki, and S. Gabersek. 1999. Impacts of large-scale surface modifications on meteorological conditions and energy use: A 10-region modeling study. *Theor. Appl. Climatol.* **62**, 175–185.

Takahashi, N., H. Uyeda, K. Kikuchi, and K. Iwanami. 1996. Mesoscale and convective scale features of heavy rainfall events in late period of the Baiu season in July 1988, Nagasaki prefecture. *J. Meteor. Soc. Japan* **74**, 539–561.

Takeda, T., K. Isono, M. Wada, Y. Ischizaka, K. Okada, Y. Fujiyoshi, M. Maruyama, Y. Igawa, and K. Nagaya. 1982. Modification of convective snow-clouds in landing the Japan Sea coastal region. *J. Meteor. Soc. Japan* **60**, 967–977.

Tanguay, M., A. Robert, and R. Laprise. 1990. A semi-implicit semi-Lagrangian fully compressible regional forecast model. *Mon. Wea. Rev.* **118**, 1970–1980.

Tao, W.-K., and J. Simpson. 1993. Goddard cumulus ensemble model. Part I: Model description. *Terr. Atmos. Oceanic Sci.* **4**, 35–72.

Tao, W.-K., S. Lang, J. Simpson, C.-H. Sui, B. Ferrier, and M.-D. Chou. 1996. Mechanism of cloud-radiation interaction in the tropics and mid-latitude. *J. Atmos. Sci.* **53**, 2624–2651.

Tao, W.-K., J. Simpson, C.-H. Sui, C.-L. Shie, B. Zhou, K. M. Lau, and M. Moncrieff. 1999. Equilibrium states simulated by cloud-resolving models. *J. Atmos. Sci.* **56**, 3128–3139.

Tao, W.-K., C.-L. Shie, and J. Simpson. 2001. Comments on "The sensitivity study of radiative-convective equilibrium in the tropics with a convective resolving model." *J. Atmos. Sci.,* accepted.

Tapp, M. C., and P. W. White. 1976. A non-hydrostatic mesoscale model. *Quart. J. Roy. Meteor. Soc.* **102**, 277–296.

Tapper, N. J., P. D. Tyson, I. F. Owens, and W. J. Hastie. 1981. Modeling the winter urban heat island over Christchurch, New Zealand. *J. Appl. Meteor.* **20**, 365–376.

Taylor, C. M., F. Said, and T. Lebel. 1997. Interactions between the land surface and mesoscale rainfall variability during HAPEX-Sahel. *Mon. Wea. Rev.* **125**, 2211–2227.

Taylor, C. M., R. J. Harding, R. A. Pielke, Sr., P. L. Vidale, R. L. Walko, and J. W. Pomeroy. 1998. Snow breezes in the boreal forest. *J. Geophys. Res.* **103**, 23,087–23,101.

Taylor, J. P., and A. S. Ackerman. 1999. A case study of pronounced perturbations to cloud properties and boundary-layer dynamics due to aerosol emissions. *Quart. J. Roy. Meteor. Soc.* **125**, 2543–2661.

Taylor, P. A. 1974. Urban meteorological modelling—Some relevant studies. *Adv. Geophys.* **18B**, 173–185.

Taylor, P. A. 1977a. Some numerical studies of surface boundary-layer flow above gentle topography. *Bound.-Layer Meteor.* **11**, 439–465.

Taylor, P. A. 1977b. Numerical studies of neutrally stratified planetary boundary-layer flow above gentle topography. I. Two-dimensional cases. *Bound.-Layer Meteor.* **12**, 37–60.

Taylor, P. A. 1981. Model predictions of neutrally stratified boundary layer flow over ridges. *Quart. J. Roy. Meteor. Soc.* **107**, 111–120.

Taylor, P. A., and P. R. Gent. 1981. Modification of the boundary layer by orography. In *Orographic Effects in Planetary Flows*, R. Hide and P. White, Eds., WMO, Geneva, 143–165.

Temperton, C. 1973. Some experiments in dynamic initialization for a simple primitive equation model. *Quart. J. Roy. Meteor. Soc.* **99**, 303–319.

Tenhunen, J. D., and P. Kabat (Eds.). 1999. Integrating hydrology, ecosystem dynamics, and biogeo-chemistry in complex landscapes. Report of the Dahlem, Germany Workshop on Integrating Hydrology, Ecosystem Dynamics, and Biogeochemistry in Complex Landscapes, January 18–23, 1998,

Tennekes, H. 1973. A model for the dynamics of the inversion above a convective boundary layer. *J. Atmos. Sci.* **30**, 558–567.

Tennekes, H. 1974. The atmospheric boundary layer. *Phys. Today* **27**, 52–63.

Tennekes, H. 1978. Turbulent flow in two and three dimensions. *Bull. Amer. Meteor. Soc.* **59**, 22–28.

Tennekes, H., and J. L. Lumley. 1972. *A First Course in Turbulence*. MIT Press, Cambridge, MA.

Terjung, W. H., and P. A. O'Rourke. 1981. Relative influence of vegetation on urban energy budgets and surface temperatures. *Bound.-Layer Meteor.* **25**, 255–263.

Therry, G., and P. Lacarrere. 1983. Improving the eddy kinetic energy model for planetary boundary layer description. *Bound.-Layer Meteor.* **25**, 63–88.

Thom, A. S. 1971. Momentum absorption by vegetation. *Quart. J. Roy. Meteor. Soc.* **97**, 414–428.

Thomas S. J., C. Girard, R. Benoit, M. Desgagne, and P. Pellerin. 1998. A new adiabatic kernel for the MC2 model. *Atmos. Ocean* **36**, 241–270.

Thomas, S. J., A. V. Malevsky, M. Desgagné, R. Benoit, P. Pellerin, and M. Valin. 1997. Massively parallel implementation of the Mesoscale Compressible Community Model. *Parallel Comput.* **23**, 2143–2160.

Thompson, G. 1993. Prototype real-time mesoscale prediction during 1991–92 winter season and statistical verification of model data. M.S. thesis, Dept. of Atmospheric Science Paper No. 521, Colorado State University, Fort Collins, CO.

Thompson, P. D. 1961. *Numerical Weather Analysis and Prediction.* Macmillan, New York.

Thompson, W. T. 1979. Effects of New York City on the horizontal and vertical structure of sea breeze fronts, Vol. III. Effects of frictionally retarded sea breeze and synoptic frontal passages on sulfur dioxide concentrations. Report, Dept. of Meteorology, San Jose State University, San Jose, CA.

Thompson, W. T., T. Haack, J. D. Doyle, and S. D. Burk. 1997. A nonhydrostatic mesoscale simulation of the 10–11 June 1994 coastally trapped wind reversal. *Mon. Wea. Rev.* **125**, 3211–3230.

Thorpe, A. J., M. J. Miller, and M. W. Moncrieff. 1982. Two-dimensional convection in non-constant shear: A model of mid-latitude squall lines. *Quart. J. Roy Meteor. Soc.* **108**, 739–762.

Thunis, P., and R. Bornstein. 1996. Hierarchy of mesoscale flow assumptions and equations. *J. Atmos. Sci.* **53**, 380–397.

Thunis, P., and A. Clappier. 2000. Formulation and evaluation of a nonhydrostatic Mesoscale Vorticity Model (TVM). *Mon. Wea. Rev.* **128**, 3236–3251.

Thunis, P., and C. Cuvelier. 1999. Impact of biogenic emissions on ozone formation in the Mediterranean area, a BEMA modelling study. *Atmos. Environ.* **34**, 467–481.

Tiedtke, M. 1996. An extension of cloud-radiation parameterization in the ECMWF model: The representation of subgrid-scale variations of optical depth. *Mon. Wea. Rev.* **124**, 745–750.

Tijm, A. B. C., and A. J. Van Delden. 1998. The role of sound waves in sea-breeze initiation. *Quart. J. Roy. Meteor. Soc.* **125**, 1997–2018.

Tijm, A. B. C., A. A. M. Holtslag, and A. J. van Delden. 1999a. Observations and modeling of the sea breeze with the return current. *Mon. Wea. Rev.* **27**, 625–640.

Tijm, A. B. C., A. J. Van Delden, and A. A. M. Holtslag. 1999b. The inland penetration of sea breezes. *Contrib. Atmos. Phys.* **72**, 317–328.

Tomasi, C. 1983. The nocturnal surface inversion height in the Po Valley. *Atmos. Environ.* **17**, 1123–1129.

Tomine, K., and S. Abe. 1982. A trial to reduce truncation errors of the pressure gradient force in the sigma coordinate systems. *J. Meteor. Soc. Japan* **60**, 709–716.

Tompkins, A. M. 2000. The impact of dimensionality on long-term cloud-resolving model simulations. *Mon. Wea. Rev.* **128**, 1521–1535.

Tremback, C. J. 1990. Numerical simulation of a mesoscale convective complex: Model development and numerical results. Ph.D. dissertation, Dept. of Atmospheric Science Paper 465, Colorado State University, Fort Collins, CO.

Tremback, C. J., and R. Kessler. 1985. A surface temperature and moisture parameterization for use in mesoscale numerical models. Preprint, 7th AMS Conference on Numerical Weather Prediction, Montreal, 1–2.

Tremback, C. J., J. Powell, W. R. Cotton, and R. A. Pielke. 1987. The forward-in-time upstream advection scheme-extension to higher orders. *Mon. Wea. Rev.* **115**, 540–555.

Tremback, C. J., R. L. Walko, and W. R. Cotton. 1994. The parallelization of an atmospheric simulation model. Proceedings of the 10th International Conference on Interactive Information and Processing Systems (IPPS) for Meteorology, Oceanography, and Hydrology, January 23–28, 1994, Nashville, TN.

Tremblay, A., A. Glazer, W. Yu, and R. Benoit. 1996. A mixed-phase cloud scheme based on a single prognostic equation. *Tellus* **48A**, 483–500.

Tripoli, G. J. and W. R. Cotton. 1980. A numerical investigation of several factors contributing to the observed variable intensity of deep convection over south Florida. *J. Appl. Meteor.* **19**, 1037–1063.

Tripoli, G. J., and W. R. Cotton. 1981. The use of ice-liquid water potential temperature as a thermodynamic variable in deep atmospheric models. *Mon. Wea. Rev.* **109**, 1094–1102.

Tripoli, G. J., and W. R. Cotton. 1982. The Colorado State University three-dimensional cloud/mesoscale model–1982. Part I: General theoretical framework and sensitivity experiments. *J. Rech. Atmos.* **16**, 185–219.

Tripoli, G., and W. R. Cotton. 1989a. A numerical study of an observed orogenic mesoscale convective system. Part 1. Simulated genesis and comparison with observations. *Mon. Wea. Rev.* **117**, 273–304.

Tripoli, G., and W. R. Cotton. 1989b. A numerical study of an observed orogenic mesoscale convective system. Part 2. Analysis of governing dynamics. *Mon. Wea. Rev.* **117**, 305–328.

Tso, C. P. 1995. A survey of urban heat island studies in two tropical cities. *Atmos. Environ.* **30**, 507–519.

Tsvetsinskaya, E. A., L. O. Mearns, and W. E. Easterling. 2001a. Investigating the effect of seasonal plant growth and development in three-dimensional atmospheric simulations. Part I: Simulation of surface fluxes over the growing season. *J. Climate* **14**, 692–709.

Tsvetsinskaya, E. A., L. O. Mearns, and W. E. Easterling. 2001b. Investigating the effect of seasonal plant growth and development in three-dimensional atmospheric simulations. Part II: Atmospheric response to crop growth and development. *J. Climate* **14**, 711–729.

Tucker, D. F., and K. S. Zentmire. 1999. On the forecasting of orogenic mesoscale convective complexes. *Wea. Forecasting* **14**, 1017–1022.

Tuleya, R. E., and Y. Kurihara. 1978. A numerical simulation of the landfall of tropical cyclones. *J. Atmos. Sci.* **35**, 242–257.

Tuleya, R. E., M. A. Bender, and Y. Kurihara. 1984. A simulation study of the landfall of tropical cyclones using a movable nested-mesh model. *Mon. Wea. Rev.* **12**, 124–136.

Tunick, A. 1999. A review of previous works on observing the atmospheric boundary layer through meteorological measurements. Army Res. Lab., MR-448, 1–41, Adelphi, MD.

Turner, B. D. 1969. Workbook of atmospheric dispersion estimates. Publication 999-AP-26, U.S. Public Health Service.

Twitty, J. T., and J. A. Weinman. 1971. Radiative properties of carbonaceous aerosols. *J. Appl. Meteor.* **10**, 725–731.

Twomey, S. 1978. The influence of aerosols on radiative properties of clouds. In *Climatic Change and Variability: A Southern Perspective*, Pittock *et al.*, Eds. Cambridge University Press, New York.

Uccellini, L. W. 1980. On the role of upper tropospheric jet streaks and leeside cyclogenesis in the development of low-level jets in the Great Plains. *Mon. Wea. Rev.* **108**, 1689–1696.

Uccellini, L. W., and D. R. Johnson. 1979. The coupling of upper and lower tropospheric jet streaks and implications for the development of sever convective storms. *Mon. Wea. Rev.* **107**, 682–703.

Uccellini, L. W., D. R. Johnson, and R. E. Schlesinger. 1979. An isentropic and sigma coordinate hybrid numerical model: Model development and some initial tests. *J. Atmos. Sci.* **36**, 390–414.

Uccellini, L. W., P. J. Korin, and C. H. Wash. 1981. The President's Day cyclone, 17–19 February 1979. An analysis of jet streak interaction prior to cyclogenesis. Technical Memorandum 82077, NASA Goddard Space Flight Center, Greenbelt, MD.

Ueda, H. 1983. Effects of external parameters on the flow field in the coastal region—A linear model. *J. Climate Appl. Meteor.* **22**, 312–321.

Ulanski, S. L., and M. Garstang. 1978. The role of surface divergence and vorticity in the life cycle of convective rainfall. Part I. Observations and analysis. *J. Atmos. Sci.* **35**, 1047–1062.

Uliasz, M. 1994. Subgrid scale parameterizations. In *Mesoscale Modeling of the Atmosphere*, R. Pearce and R. A. Pielke, Eds., American Meteorological Society, Boston, 13–19.

Uliasz, M., R. A. Stocker, and R. A. Pielke. 1996. Regional modeling of air pollution transport in the southwestern United States. In *Environmental Modeling, Vol. III*, P. Zannetti, Ed., Computational Mechanics Publications, Boston, 145–181.

Ulrickson, B. L., and C. F. Mass. 1990. Numerical investigation of mesoscale circulations over the Los Angeles basin. Part 1, A verification study. *Mon. Wea. Rev.* **118**, 2138–2161.

United States Dept. of Agriculture. 1951. *Soil Survey Manual*. Handbook **18**, U.S. Department of Agriculture.

Vaidya, S. S., and S. S. Singh. 2000. Applying the Betts–Miller–Janjić Scheme of convection in prediction of the Indian monsoon. *Wea. Forecasting* **15**, 349–356.

Vali, G., R. D. Kelly, J. French, S. Haimov, D. Leon, R. E. McIntosh, and A. Pazmany. 1998. Finescale structure and microphysics of coastal stratus. *J. Atmos. Sci.* **55**, 3540–3564.

Valentini, R., D. Baldocchi, and R. Olson. 1999. FLUXNET: A challenge that is becoming a reality. *IGBP Global Change Newsletter* **37**, 15–17.

Van Breugel, P. B, W. Klaassen, and E. J. Moors. 1999. The spatial variability of turbulence above a forest. *Theor. Appl. Climatol.* **62**, 43–50.

van den Hurk, B. J. J. M., P. Viterbo, A. C. M. Beljaars, and A. K. Betts. 2000. Offline validation of the ERA40 surface scheme. *Tech. Memor.* **295**, 1–42.

Van der Hoven, I. 1967. Atmospheric transport and diffusion at coastal sites. *Nucl. Safety,* **8**, 490–499.

van der Vorst, H. A. 1992. BI-CGSTAB: A fast and smoothly converging variant of BI-CG for the solution of nonsymmetric linear systems. *J. Sci. Stat. Comput.* **13**, 631–644.

Van Dop, H. 1983. Terrain classification and derived meteorological parameters for interregional transport models. *Atmos. Environ.* **17**, 1099–1105.

van Egmond, N. D., and D. Onderdelinden. 1981. Objective analysis of air pollution monitoring network data; spatial interpolation and network density. *Atmos. Environ.* **15**, 1035–1046.

van Genuchten, M. Th. 1980. A closed-form equation for predicting the hydraulic conductivity of unsaturated soils. *Soil Sci. Soc. Am. J.* **44**, 892–898.

Varinou, M., G. Kallos, G. Tsiligiridis, and G. Sistla. 1999. The role of anthropogenic and biogenic emissions on tropospheric ozone formation over Greece. *Phys. Chem. Earth* **24**, 507–513.

Velho, H. F. C., R. R. Rosa, F. M. Ramos, R. A. Pielke Sr., G. A. Degrazia, C. Rodrigues Neto, and A. Zanandrea, 2001. Multifractal model for eddy diffusivity and counter-gradient term in atmospheric turbulence. *Physica A* **295**, 219–223.

Venkatram, A. 1977. A model of internal boundary-layer development. *Bound.-Layer Meteor.* **11**, 419–437.

Vergeiner, I. 1971. An operational linear lee wave model for arbitrary basic flow and two-dimensional topography. *Quart. J. Roy. Meteor. Soc.* **97**, 30–60.

Vermeulen, J. P. L. 2001. The atmospheric boundary layer over a heterogeneous vegetated landscape. Ph.D. Thesis, Vrije University, Amsterdam, 164 pp.

Verseghy, D. L. 2000. The Canadian Land Surface Scheme (CLASS): Its history and future. *Atmos. Ocean* **38**, 1–13.

Vickers, D., and L. Mahrt. 1999. Observations of non-dimensional wind shear in the coastal zone. *Quart. J. Roy. Meteor. Soc.* **125**, 2685–2702.

Vidale, P. L., R. A. Pielke, A. Barr, L. T. Steyaert. 1997. Case study modeling of turbulent and mesoscale fluxes over the BOREAS region. *J. Geophys. Res.* **102**, 29,167–29,188.

Viskanta, R., and R. A. Daniel. 1980. Radiative effects of elevated pollutant layers on temperature structure and dispersion in an urban atmosphere. *J. Appl. Meteor.* **19**, 53–70.

Viskanta, R., and T. L. Weirich. 1978. Feedback between radiatively interacting pollutants and their dispersion in the urban boundary layer. WMO Symposium on Boundary Layer Physics and Applied Specific Problems of Air Pollution, WMO No. 510, 31–38.

Viskanta, R., R. W. Bergstrom, and R. O. Johnson. 1977a. Effects of air pollution on thermal structure and dispersion in an urban planetary boundary layer. *Contrib. Atmos. Phys.* **50**, 419–440.

Viskanta, R., R. W. Bergstrom, and R. O. Johnson. 1977b. Radiative transfer in a polluted urban planetary boundary layer. *J. Atmos. Sci.* **34**, 1091–1103.

Viswanadham, Y., and M. T. de Lima C. Nogueira. 1982. Diabatic wind profile and its relation to the scale of turbulence. *Arch. Meteor. Geophys. Bioklimatol.* **31**, 103–115.

Viterbo, P., and A. C. M. Beljaars. 1995. An improved surface parameterization scheme in the ECMWF model and its validation. *J. Climate* **8**, 2716–2748.

Viterbo, P., and A. K. Betts. 1999. Impact of ECMWF reanalysis soil water on forecasts of the July 1993 Mississippi flood. *J. Geophys. Res.* **104**, 19,361–19,366.

Viterbo, P., A. Beljaars, J.-F. Mahfouf, and J. Teixeira. 1999. The representation of soil moisture freezing and its impact on the stable boundary layer. *Quart. J. Roy. Meteor. Soc.* **125**, 2401–2426.

Vogel, S. 1998. Exposing life's limits with dimensionless numbers. *Phys. Today* **51**, 22–27.

Vogelezang, D. H. P., and A. A. M. Holtslag. 1996. Evaluation and model impacts of alternative boundary-layer height formulations. *Bound.-Layer Meteor.* **81**, 245–269.

von Storch, H. 1978. Construction of optimal numerical filters fitted for noise damping in numerical simulation models. *Contrib. Atmos. Phys.* **51**, 189–197.

Vugts, H. F. 1980. A study of terrain inhomogeneity. *Bull. Amer. Meteor. Soc.* **61**, 568–569.

Vugts, H. F., and F. Cannemeijer. 1981. Measurements of drag coefficients and roughness length at a sea-beach interface. *J. Appl. Meteor.* **20**, 335–340.

Vukićević, T. 1998. Optimal initial perturbations for two cases of extratropical cyclogenesis. *Tellus* **50**, 143–166.

Vukićević, T., and P. Hess. 2000. Analysis of tropospheric transport in the Pacific basin using the adjoint technique. *J. Geophys. Res.* **105**, 7213–7230.

Vukićević, T., and K. Raeder. 1995. Use of an adjoint model for finding triggers for Alpine lee cyclogenesis. *Mon. Wea. Rev.* **123**, 800–816.

Vukićević, T., B. Braswell, and D. Schimel. 2001. A diagnostic study of temperature controls on global terrestrial carbon exchange. *Tellus B* **53**, 150–170.

Vukovich, F. M., and W. J. King. 1980. A theoretical study of the St. Louis Heat Island: Comparisons between observed data and simulation results on the urban heat island circulation. *J. Appl. Meteor.* **19**, 761–770.

Vukovich, F. M., J. W. Dunn III, and B. W. Crissman. 1976. A theoretical study of the St. Louis heat island: The wind and temperature distribution. *J. Appl. Meteor.* **15**, 417–440.

Vukovich, F. M., W. J. King, J. W. Dunn III, and J. J. B. Worth. 1979. Observations and simulations of the diurnal variation of the urban heat island circulation and associated variations of the ozone distribution. A case study. *J. Appl. Meteor.* **18**, 836–854.

Walcek, C. J. 1999a. A "nearly perfect" numerical advection algorithm for use in meteorology and chemistry models. AMS Symposium on Interdisciplinary Issues in Atmospheric Chemistry, Dallas, TX, 129–130.

Walcek, C. J. 1999b. A highly accurate numerical advection algorithm for calculating transport of atmospheric pollutants. Air Pollution 99 Conference, San Francisco, CA, 1–10.

Walcek, C. J., and N. M. Aleksic. 1998. A simple but accurate mass conservative, peak-preserving, mixing ratio bounded advection algorithm with Fortran code. *Atmos. Environ.* **32**, 3863–3880.

Walko, R. L., W. R. Cotton, and R. A. Pielke. 1992. Large-eddy simulations of the effects of hilly terrain on the convective boundary layer. *Bound.-Layer Meteor.* **58**, 133–150.

Walko, R. L, W. R. Cotton, M. P. Meyers, and J. Y. Harrington. 1995a. New RAMS cloud microphysics parameterization. Part I: The single-moment scheme. *Atmos. Res.* **38**, 29–62.

Walko, R. L., C. J. Tremback, R. A. Pielke, and W. R. Cotton. 1995b. An interactive nesting algorithm for stretched grids and variable nesting ratios. *J. Appl. Meteor.* **34**, 994–999.

Walko, R. L., L. E. Band, J. Baron, T. G. F. Kittel, R. Lammers, T. J. Lee, R. A. Pielke Sr., C. Taylor, C. Tague, C. J. Tremback, and P. L. Vidale. 1998. Coupled atmosphere-terrestrial ecosystem-hydrology models for environmental modeling. Dept. of Atmospheric Science Report No. 9, Colorado State University, Fort Collins, CO.

Walko, R. L., L. E. Band, J. Baron, T. G. F. Kittel, R. Lammers, T. J. Lee, D. S. Ojima, R. A. Pielke, C. Taylor, C. Tague, C. J. Tremback, and P. L. Vidale. 2000a. Coupled atmosphere-biophysics-hydrology models for environmental modeling. *J. Appl. Meteor.* **39**, 931–944.

Walko, R. L., W. R. Cotton, G. Feingold, and B. Stevens. 2000b. Efficient computation of vapor and heat diffusion between hydrometeors in a numerical model. *Atmos. Res.* **53**, 171–183.

Wallace, J. M., and P. V. Hobbs. 1977. *Atmospheric Science: An Introductory Survey.* Academic Press, New York.

Wallace, J. M., S. Tibaldi, and A. J. Simmons. 1983. Reduction of systematic forecast errors in the ECMWF model through the introduction of an envelope orography. *Quart. J. Roy. Meteor. Soc.* **109**, 683–717.

Walmsley, J. L., J. R. Salmon, and P. A. Taylor. 1982. On the application of a model of boundary-layer flow over low hills to real terrain. *Bound.-Layer Meteor.* **23**, 17–46.

Walsh, J. E. 1974. Sea breeze theory and applications. *J. Atmos. Sci.* **31**, 2012–2026.

Walter, B. A., and J. E. Overland. 1982. Response of stratified flow in the lee of the Olympic Mountains. *Mon. Wea. Rev.* **110**, 1458–1473.

Wang, D. P. 1979. Wing-driven circulation in the Chesapeake Bay, Winter 1975. *J. Phys. Oceanogr.* **9**, 564–572.

Wang, P.-Y., D. B. Parsons, and P. V. Hobbs. 1983. The mesoscale and microscale structure and organisation of clouds and precipitation in midlatitude cyclones, VI. Wavelike rainbands associated with a cold-frontal zone. *J. Atmos. Sci.* **40**, 543–558.

Wang, T.-A., and Y.-L. Lin. 1999. Wave ducting in a stratified shear flow over a two-dimensional mountain. Part II: Implications for the development of high-drag states for severe downslope windstorms. *J. Atmos. Sci.* **56**, 437–452.

Wang, W., and N. L. Seaman. 1997. A comparison study of convective parameterization schemes in a mesoscale model. *Mon. Wea. Rev.* **125**, 252–278.

Wang, Y. 1996. On the forward-in-time upstream advection scheme for non-uniform and time-dependent flow. *Meteor. Atmos. Phys.* **61**, 27–38.

Wang, Y., J. Wang, B. Cui, D. Lu, W. Yu, X. Guo, and D. Chen. 2000. The Beijing area mesoscale NWP system and its application. *Acta Meteor. Sinica* **14**, 233–246.

Warhaft, Z. 1976. Heat and moisture flux in the stratified boundary layer. *Quart. J. Roy. Meteor. Soc.* **102**, 703–707.

Warner, C. 1982. Mesoscale features and cloud organization on 10–12 December 1978 over the South China Sea. *J. Atmos. Sci.* **39**, 1619–1641.

Warner, C., J. Simpson, D. W. Martin, D. Suchman, F. R. Mosher, and R. F. Reinking. 1979. Shallow convection on Day 261 of GATE: Mesoscale arcs. *Mon. Wea. Rev.* **107**, 1617–1635.

Warner, T. T. 1983. Fundamental equations and numerical techniques of urban boundary layer modeling. AMS/EPA Specialty Conference on Air Quality Modeling of the Nonstationary, Nonhomogeneous Urban Boundary Layer, October 31–November 4, Baltimore, MD.

Warner, T. T., and H.-M. Hsu. 2000. Nested-model simulation of moist convection: The impact of coarse-grid parameterized convection on fine-grid resolved convection. *Mon. Wea. Rev.* **128**, 2211–2231.

Warner, T. T., and R.-S. Sheu. 2000. Multiscale local forcing of the Arabian Desert daytime boundary layer, and implications for the dispersion of surface-released contaminants. *J. Appl. Meteor.* **39**, 686–707.

Warner, T. T., R. A. Anthes, and A. L. McNab. 1978. Numerical simulations with a three-dimensional mesoscale model. *Mon. Wea. Rev.* **106**, 1079–1099.

Warner, T. T., R. A. Peterson, and R. E. Treadon. 1997. A tutorial on lateral boundary conditions as a basic and potentially serious limitation to regional numerical weather prediction. *Bull. Amer. Meteor. Soc.* **78**, 2599–2617.

Washington, W. M., and D. P. Baumhefner. 1975. A method of removing Lamb waves from initial data for primitive equation models. *J. Appl. Meteor.* **14**, 114–119.

Weaver, C. P., and R. Avissar. 2001. Atmospheric disturbances caused by human modification of the landscape. *Bull. Amer. Meteor. Soc.* **82**, 269–282.

Weaver, J. F., and F. P. Kelly. 1982. A mesoscale, climatologically-based forecast technique for Colorado. *Preprint*, AMS Conference on Weather Forecasting and Analysis, Seattle, WA, June 28–July 1.

Webb, E. K. 1975. Evaporation from catchments. In *Prediction in Catchment Hydrology*, Australian Academy of Science, Canberra, Australia, 203–236.

Webb, E. K. 1982. Profile relationships in the superadiabatic surface layer. *Quart. J. Roy. Meteor. Soc.* **108**, 661–688.

Weber, M. R., and C. B. Baker. 1982. Comments on "The ratio of diffuse to direct solar irradiance (perpendicular to the sun's rays) with clear skies—A conserved quantity throughout the day." *J. Appl. Meteor.* **21**, 883–886.

Weber, R. O. 1999. Remarks on the definition and estimation of friction velocity. *Bound.-Layer Meteor.* **93**, 197–209.

Weidman, S. T., and R. A. Pielke. 1983. A more accurate method for the numerical solution of nonlinear partial differential equations. *J. Comput. Phys.* **49**, 342–348.

Weisberg, R. H. 1976. The nontidal flow in the Providence River of Narragansett Bay: A stochastic approach to estuarine circulation. *J. Phys. Oceanogr.* **6**, 721–734.

Weisman, M. L., J. B. Klemp, and W. C. Skamarock. 1997. The resolution-dependence of explicitly-modeled convective systems. *Mon. Wea. Rev.* **125**, 527–548.

Weiss, C. E., and J. F. W. Purdom. 1974. The effect of early-morning cloudiness on squall-line activity. *Mon. Wea. Rev.* **102**, 400–402.

Weissbluth, M. J., and W. R. Cotton. 1993. The representation of convection in mesoscale models. Part I: Scheme fabrication and calibration. *J. Atmos. Sci.* **50**, 3852–3872.

Welch, R. M., and W. G. Zdunkowski. 1976. A radiation model for the polluted atmospheric boundary layer. *J. Atmos. Sci.* **33**, 2170–2184.

Welch, R. M., and W. G. Zdunkowski. 1981a. The effect of cloud shape on radiative characteristics. *Contrib. Atmos. Phys.* **54**, 482–491.

Welch, R. M., and W. G. Zdunkowski. 1981b. Improved approximation for diffuse solar radiation on oriented sloping terrain. *Contrib. Atmos. Phys.* **54**, 362–369.

Welch, R. M., J. Paegle, and W. G. Zdunkowski. 1978. Two-dimensional numerical simulation of the effects of air pollution upon the urban-rural complex. *Tellus* **30**, 136–150.

Welch, R. M., S. K. Cox, and J. M. Davis. 1980. *Solar Radiation and Clouds*. Meteor. Monographs, 17, American Meteorological Society, Boston.

Wergen, W. 1981. Nonlinear normal model initialization of a multi-level fine-mesh model with steep orography. *Contrib. Atmos. Phys.* **53**, 389–402.

Wesely, M. L., J. A. Eastman, D. R. Cook, and B. B. Hicks. 1978. Daytime variations of ozone eddy fluxes to maize. *Bound.-Layer Meteor.* **15**, 361–373.

Wesely, M. L., and B. B. Hicks. 1977. Some factors that affect the decomposition rates of sulfur dioxide and similar gases on vegetation. *APCAJ* **27**, 1110–1116.

Wesley, D. A., and R. A. Pielke. 1990. Observations of blocking-induced convergence zones and effects on precipitation in complex terrain. *Atmos. Res.* **25**, 235–276.

Westphal, D. L., T. R. Holt, S. W. Chang, N. L. Baker, T. F. Hogan, L. R. Brody, R. A. Godfrey, J. S. Goerss, J. A. Cummings, D. J. Laws, C. W. Hines. 1999. Meteorological re-analysis for the study of Gulf War illness: Khamisiyah case study. *Wea. Forecasting* **14**, 215–241.

Wetzel, P. J. 1978. A detailed parameterization of the atmospheric boundary layer. Ph.D. dissertation, Dept. of Atmospheric Science Paper No. 302, Colorado State University, Fort Collins, CO.

Wetzel, P. J. 1982. Toward parameterization of the stable boundary layer. *J. Appl. Meteor.* **21**, 7–13.

Wetzel, P. J., W. R. Cotton, and R. L. McAnelly. 1983. A long-lived mesoscale convective complex. Part II: Evolution and structure of the mature complex. *Mon. Wea. Rev.* **111**, 1919–1937.

Whiteman, C. D. 1980. Breakup of temperature inversions in Colorado mountain valleys. Dept. of Atmospheric Science Paper No. 328, Colorado State University, Fort Collins, CO.

Whiteman, C. D. 1982. Breakup of temperature inversions in deep mountain valleys: Part I. Observations. *J. Appl. Meteor.* **21**, 270–289.

Whiteman, C. D. 2000. *Mountain Meteorology. Fundamentals and Applications*. Oxford University Press, London.

Whiteman, C. D., and J. C. Doran. 1993. The relationship between overlying synoptic-scale flows and winds within a valley. *J. Appl. Meteor.* **32**, 1669–1682.

Whiteman, C. D., and T. B. McKee. 1978. Air pollution implications of descent in mountain valleys. *Atmos. Environ.* **12**, 2151–2158.

Whiteman, C. D., and T. B. McKee. 1982. Breakup of temperature inversions in deep mountain valleys: Part II. Thermodynamic model. *J. Appl. Meteor.* **21**, 290–302.

Whiteman, C. D., X. Bian, and S. Zhong. 1999. Wintertime evolution of the temperature inversion in the Colorado plateau basin. *J. Appl. Meteor.* **38**, 1103–1117.

Wicker, L. J., and W. C. Skamarock. 1998. A time-splitting scheme for the elastic equations incorporating second-order Runge–Kutter time differencings. *Mon. Wea. Rev.* **126**, 1992–1999.

Williams, K. D. 2000. Mesoscale analysis of a comma cloud observed during FASTEX. *Meteor. Appl.* **7**, 129–134.

Williams, R. T. 1967. Atmospheric frontogenesis: A numerical experiment. *J. Atmos. Sci.* **24**, 627–641.

Williams, R. T. 1972. Quasi-geostrophic versus nongeostrophic frontogenesis. *J. Atmos. Sci.* **29**, 3–10.

Wilson, N. R., and R. H. Shaw. 1977. A higher-order closure model for canopy flow. *J. Appl. Meteor.* **16**, 1197–1205.

Winkler, J. A., R. H. Skaggs, and D. G. Baker. 1981. Effect of temperature adjustments on the Minneapolis-St. Paul urban heat island. *J. Appl. Meteor.* **20**, 1295–1300.

Winninghoff, F. J. 1968. On the adjustment toward a geostrophic balance in a simple primitive equation model with application to the problems of initialization and objective analysis. Ph.D. thesis, University of California, Los Angeles.

Winstead, N. S., and G. S. Young. 2000. An analysis of exit-flow drainage jets over the Chesapeake Bay. *J. Appl. Meteor.* **39**, 1269–1281.

Wipperman, F. 1981. The applicability of several approximations in mesoscale modelling—A linear approach. *Contrib. Atmos. Phys.* **54**, 298–308.

Wipperman, F., and G. Gross. 1981. On the construction of orographically influenced wind roses for given distributions of the large-scale wind. *Beitr. Phys. Atmos.* **54**, 492–501.

Wippermann, F., and G. Gross. 1986. The wind-induced shaping and migration of an isolated dune. A numerical experiment. *Bound.-Layer Meteor.* **36**, 319–334.

Wolfram, S. 1988. *Mathematica: A System for Doing Mathematics by Computer.* Addison-Wesley, Reading, MA.

Wong, V. C., and D. K. Lilly. 1994. A comparison of two dynamic subgrid closure methods for turbulent thermal convection. *Phys. Fluids* **6**, 1016–1023.

Wong, V. C., J. W. Zach, M. L. Kaplan, and S. L. Chuang. 1983a. A numerical investigation of the effects of cloudiness on mesoscale atmosphere circulation. Preprint, 5th AMS Conference on Numerical Weather Atmospheric Radiation, Oct. 31–Nov. 4.

Wong, V. C., J. W. Zach, M. L. Kaplan, and G. D. Coats. 1983b. A nested-grid limited-area model for short term weather forecasting. Preprint, 6th AMS Conference on Numerical Weather Prediction, June 6–9, Omaha, Nebraska, 9–15.

Wooldridge, G. L., and M. M. Orgill. 1978. Airflow, diffusion, and momentum flux patterns in a high mountain valley. *Atmos. Environ.* **12**, 803–808.

Wortman-Vierthaler, M., and N. Moussiopoulos. 1995. Numerical tests of a refined flux corrected transport scheme. *Environ. Software* **10**, 157–175.

Wu, A., T. A. Black, D. L. Verseghy, M. D. Novak, and W. G. Bailey. 2000a. Testing the alpha and beta methods of estimating evaporation from bare and vegetated surfaces in CLASS. *Atmos. Ocean* **38**, 15–35.

Wu, X., M. W. Moncrieff, and K. A. Emanuel. 2000b. Evaluation of large-scale forcing during TOGA COARE for cloud-resolving models and single-column models. *J. Atmos. Sci.* **57**, 2977–2985.

Wu, Y., and S. Raman. 1997. Effect of land-use pattern on the development of low-level jets. *J. Appl. Meteor.* **36**, 573–590.

Wyngaard, J. C. 1982. Boundary layer modeling. In *Atmospheric Turbulence and Air Pollution Modelling*, F. T. M. Nieuwstadt and H. Van Dop, Eds., 69–106. D. Reidel, Dordrecht, The Netherlands.

Wyngaard, J. C. 1983. Lectures on the planetary boundary layer. In *Mesoscale Meteorology—Theories, Observations, and Models*, T. Gal-Chen and D. K. Lilly, D. Reidel, Eds. Dordrecht, The Netherlands.

Wyngaard, J. C., and O. R. Cote. 1974. The evolution of a convective planetary boundary layer—A higher-order-closure model study. *Bound.-Layer Meteor.* **7**, 289–308.

Wyser, K., L. Rontu, and H. Savijarvi. 1999. Introducing the effective radius into a fast radiation scheme of a mesoscale model. *Contrib. Atmos. Phys.* **72**, 205–218.

Xiao, F. 2000. A class of single-cell high-order semi-Lagrangian advection schemes. *Mon. Wea. Rev.* **28**, 1165–1176.

Xiao, Q., X. Zou, and B. Wang. 2000. Initialization and simulation of a landfalling hurricane using a variational bogus data assimilation scheme. *Mon. Wea. Rev.* **128**, 2252–2269.

Xu, L., S. Raman, R. V. Madala, and R. Hodur. 1996. A non-hydrostatic modeling study of surface moisture effects on mesoscale convection induced by sea breeze circulation. *Meteor. Atmos. Phys.* **58**, 103–122.

Xu, M., J.-W. Bao, T. T. Warner, and D. J. Stensrud. 2001a. Effect of time step size in MM5 simulations of a mesoscale convective system. *Mon. Wea. Rev.* **129**, 502–516.

Xu, M., D. J. Stensrud, J.-W. Bao, and T. T. Warner. 2001b. Applications of the adjoint technique to short-range ensemble forecasting of mesoscale convective systems. *Mon. Wea. Rev.* **129**, 1395–1418.

Xu, Q., B. Zhou, S. D. Burk, and E. H. Barker. 1999. An air-soil layer coupled scheme for computing surface heat fluxes. *J. Appl. Meteor.* **38**, 211–223.

Xu, Q., M. Liu, and D. L. Westphal. 2000. A theoretical study of mountain barrier jets over sloping valleys. *J. Atmos. Sci.* **57**, 1393–1405.

Xue, M., K. K. Droegemeier, V. Wong, A. Shapiro, and K. Brewster. 1995. *ARPS Version 4.0 User's Guide*. Center for Analysis and Prediction of Storms, University of Oklahoma, Norman OK.

Xue, M., J. Zong, and K. K. Droegemeier. 1996. Parameterization of PBL turbulence in a multi-scale non-hydrostatic model. Preprint, 11th AMS Conference on Numerical Weather Prediction, Norfolk, VA, 363–365.

Xue, M., Z. Pan, and J. M. Bane Jr. 2000a. A 2D coupled atmosphere-ocean model study of air-sea interactions during a cold air outbreak over the Gulf Stream. *Mon. Wea. Rev.* **128**, 973–996.

Xue, M., K. K. Droegemeier, and V. Wong. 2000b. The Advanced Regional Prediction System (ARPS)—A multi-scale nonhydrostatic atmospheric simulation and prediction model. Part I: Model dynamics and verification. *Meteor. Atmos. Phys.* **75**, 161–193.

Xue, M., K. K. Droegemeier, V. Wong, A Shapiro, K. Brewster, F. Carr, D. Weber, Y. Liu, and D. Wang. 2001. The Advanced Regional Prediction System (ARPS)—A multi-scale nonhydrostatic atmospheric simulation and prediction tool. Part II. Model physics and applications. *Meteor. Atmos. Phys.*, **3/4**, 143–165.

Yamada, T. 1977. A numerical experiment on pollutant dispersion in a horizontally-homogeneous atmospheric boundary layer. *Atmos. Environ.* **11**, 1015–1024.

Yamada, T. 1978a. A three-dimensional numerical study of complex atmospheric circulations produced by terrain. Proceedings of the AMS Conference on Sierra Nevada Meteorology, 61–67, June 19–21, South Lake Tahoe, CA. AMS/USDA Forest Service.

Yamada, T. 1978b. A three-dimensional, second-order closure numerical model of mesoscale circulations in the lower atmosphere: Description of the basic model and application to the simulation of the environment effects of a large cooling pond. Report ANL/RER-78-1, Radiological and Environmental Research Division, Argonne National Laboratory, Argonne, IL.

Yamada, T. 1979a. Predictions of the nocturnal surface inversion height. *J. Appl. Meteor.* **18**, 526–531.

Yamada, T. 1979b. PBL similarity profiles determined from a level-2 turbulence-closure model. *Bound.-Layer Meteor.* **17**, 333–351.

Yamada, T. 1981. A numerical simulation of nocturnal drainage flow. *J. Meteor. Soc. Japan* **59**, 108–122.

Yamada, T. 1982. A numerical model study of turbulent airflow in and above a forest canopy. *J. Meteor. Soc. Japan* **60**, 439–454.

Yamada, T. 1983. Simulations of nocturnal drainage flows by a $q^2 - l$ turbulence closure model. *J. Atmos. Sci.* **40**, 91–106.

Yamada, T. 1999. Numerical simulations of airflows and tracer transport in the southwestern United States. *J. Appl. Meteor.* **39**, 399–411.

Yamada, T. 2000a. Building and terrain effects in a mesoscale model. AMS Annual Meeting, Long Beach, CA, January 10–13.

Yamada, T. 2000b. Numerical simulations of airflows and tracer transport in the southwestern United States. *J. Appl. Meteor.* **39**, 399–411.

Yamada, T., and S. Berman. 1979. A critical evaluation of a simple mixed-layer model with penetrative convection. *J. Appl. Meteor.* **18**, 781–786.

Yamada, T., and S. Bunker. 1988. Development of a nested grid, second-moment turbulence closure model and application to the 1982 ASCOT Brush Creek data simulation. *J. Appl. Meteor.* **27**, 562–578.

Yamada, T., and S. Bunker 1989. A numerical model study of nocturnal drainage flows with strong wind and temperature gradients. *J. Appl. Meteor.* **28**, 545–554.

Yamada, T., and G. Mellor. 1975. A simulation of the Wangara atmospheric boundary layer data. *J. Atmos. Sci.* **32**, 2309–2329.

Yamada, T., and G. L. Mellor. 1979. A numerical simulation of the BOMEX data using a turbulence closure model coupled with ensemble cloud relations. *Quart. J. Roy. Meteor. Soc.* **105**, 915–944.

Yamada, T., and R. N. Meroney. 1971. Numerical and wind tunnel simulation of response of stratified shear layers to nonhomogeneous surface features. Project THEMIS Technical Report No. 9, Fluid Dynamics and Diffusion Laboratory, Colorado State University, Fort Collins, CO.

Yamamoto, G. 1959. Theory of turbulent transfer in non-neutral conditions. *J. Meteor. Soc. Japan* **37**, 60–69.

Yamamoto, G. 1962. Direct absorption of solar radiation by atmospheric water vapor, carbon dioxide and molecular oxygen. *J. Atmos. Sci.* **19**, 182–188.

Yamamoto, G., and A. Shimanuki. 1966. Turbulent transfer in diabatic conditions. *J. Meteor. Soc. Japan* **44**, 301–307.

Yamasaki, M. 1977. A preliminary experiment of the tropical cyclone without parameterizing the effects of cumulus convection. *J. Meteor. Soc. Japan* **55**, 11–31.

Yamazaki, K., and K. Ninomiya. 1981. Response of Arakawa–Schubert cumulus parameterization model to real data in heavy rainfall areas. *J. Meteor. Soc. Japan* **59**, 547–563.

Yamazaki, N., and T.-C. Chen. 1993. Analysis of the East Asian monsoon during early summer of 1979: Structure of the Baiu front and its relationship to large-scale fields. *J. Meteor. Soc. Japan* **71**, 339–355.

Yang, Z.-L., R. E. Dickinson, W. J. Shuttleworth, and M. Shaikh. 1998. Treatment of soil, vegetation and snow in land surface models: A test of the biosphere-atmosphere transfer scheme with the HAPEX-MOBILHY, ABRACOS and Russian data. *J. Hydrometeor.* **212–213**, 109–127.

Yang, Z.-L., Y. Dai, R. E. Dickerson, and W. J. Shuttleworth. 1999a. Sensitivity of ground heat flux to vegetation cover fraction and leaf area index. *J. Geophys. Res.* **104**, 19,505–19,514.

Yang, Z.-L., G.-Y. Niu, and R. E. Dickinson. 1999b. Comparing snow simulations from NCAR LSM and BATS using PILPS 2D data. Preprint, 14th AMS Conference on Hydrology, Dallas, TX, 316–319.

Yap, D., and T. R. Oke. 1974. Sensible heat fluxes over an urban area—Vancouver, B. C. *J. Appl. Meteor.* **13**, 880–890.

Yau, M. K., and R. Michaud. 1982. Numerical simulation of a cumulus ensemble in three dimensions. *J. Atmos. Sci.* **39**, 1062–1079.

Ye, Z., and R. A. Pielke. 1993. Atmospheric parameterization of evaporation from non–plant-covered surfaces. *J. Appl. Meteor.* **32**, 1248–1258.

Ye, Z., M. Segal, and R. A. Pielke. 1987. Effects of atmospheric thermal stability and slope steepness on the development of daytime thermally-induced upslope flow. *J. Atmos. Sci.* **44**, 3341–3354.

Ye, Z., M. Segal, J. R. Garratt, and R. A. Pielke. 1989. On the impact of cloudiness on the characteristics of nocturnal downslope flows. *Bound.-Layer Meteor.* **49**, 23–51.

Ye, Z., J. R. Garratt, M. Segal, and R. A. Pielke. 1990. On the impact of atmospheric thermal stability on the characteristics of nocturnal downslope flows. *Bound.-Layer Meteor.* **51**, 77–97.

Yenai, M. 1975. Tropical meteorology. *Rev. Geophys. Space Phys.* **13**, 685–808.

Yih, C.-S. 1980. *Stratified Flows*. Academic Press, New York.

Yimin, M., and T. J. Lyons. 2000. Numerical simulation of a sea breeze under dominant synoptic conditions at Perth. *Meteor. Atmos. Phys.* **73**, 89–103.

Yonetani, T. 1982. Increase in number of days with heavy precipitation in Tokyo urban area. *J. Appl. Meteor.* **21**, 1466–1471.

Yonetani, T. 1983. Enhancement and initiation of a cumulus by a heat island. *J. Meteor. Soc. Japan* **61**, 244–253.

Yoshikado, H. 1981. Statistical analyses of the sea breeze pattern in relation to general weather patterns. *J. Meteor. Soc. Japan* **59**, 98–107.

Young, G. S., and R. A. Pielke. 1983. Application of terrain height variance spectra to mesoscale modeling. *J. Atmos. Sci.* **40**, 2555–2560.

Young, G. S., R. A. Pielke, and R. C. Kessler. 1984. A comparison of the terrain height variance spectra of the front range with that of a hypothetical mountain. *J. Atmos. Sci.* **41**, 1249–1250.

Young, W. R., P. B. Rhines, and C. J. R. Garrett. 1982. Shear-flow dispersion, internal waves and horizontal mixing in the ocean. *J. Phys. Oceanogr.* **12**, 515–527.

Yu, T. 1977. A comparative study on parameterization of vertical turbulent exchange processes. *Mon. Wea. Rev.* **105**, 57–66.

Yu, T. 1978. Determining height of the nocturnal boundary layer. *J. Appl. Meteor.* **17**, 28–33.

Yu, W., C. A. Lin, and R. Benoit. 1997. High-resolution simulation of the severe precipitation event over the Saguenay, Quebec region in July 1996. *Geophys. Res. Lett.* **24**, 1951–1954.

Yu, W., C. A. Lin, R. Benoit, and I. Zawadzki. 1998. High resolution model simulation of precipitation and evaluation with Doppler radar observations. *Water Sci. Tech.* **37**, 179–186.

Zalesak, S. T. 1979. Fully multidimensional flux-corrected transport algorithms for fluids. *J. Comput. Phys.* **31**, 335–362.

Zangl, G. 1999. Three-dimensional idealized simulations of the Foehn in the region of Innsbruck. *Contrib. Atmos. Phys.* **72**, 243–266.

Zannetti, P. 1990. *Air Pollution Modeling: Theories, Computational Methods, and Available Software*. Computational Mechanics Publications, Boston.

Zdunkowski, W. G., and G. Korb. 1974. An approximate method for the determination of longwave radiation fluxes in scattering and absorbing media. *Beitr. Phys. Atmos.* **47**, 129–144.

Zdunkowski, W. G., and K.-N. Liou. 1976. Humidity effects on the radiative properties of a hazy atmosphere in the visible spectrum. *Tellus* **28**, 31–36.

Zdunkowski, W. G., R. M. Welch, and J. Paegle. 1976. One-dimensional numerical simulation of the effects of air pollution on the planetary boundary layer. *J. Atmos. Sci.* **33**, 2399–2414.

Zdunkowski, W. G., R. M. Welch, and R. C. Hanson. 1980. Direct and diffuse solar radiation on oriented sloping surfaces. *Contrib. Atmos. Phys.* **53**, 449–468.

Zeller, K. F., and N. T. Nikolov. 2000. Quantifying simultaneous fluxes of ozone, carbon dioxide and water vapor above a subalpine forest ecosystem. *Environ. Pollution* **107**, 1–20.

Zeman, O. 1979. Parameterization of the dynamics of stable boundary layers and nocturnal jets. *J. Atmos. Sci.* **36**, 792–804.

Zeman, O. 1981. Progress in the modeling of planetary boundary layers. *Ann. Rev. Fluid Mech.* **13**, 253–272.

Zeng, N., and J. D. Neelin. 1999. A land-atmosphere interaction theory for the tropical deforestation problem. *J. Climate* **12**, 857–872.

Zeng, X., and R. E. Dickinson. 1998. Impact of diurnally-varying skin temperature on surface fluxes over the tropical Pacific. *Geophys. Res. Lett.* **25**, 1411–1414.

Zeng, X., and R. A. Pielke. 1993. Error-growth dynamics and predictability of surface thermally-induced atmospheric flow. *J. Atmos. Sci.* **50**, 2817–2844.

Zeng, X., and R. A. Pielke. 1995a. Further study on the predictability of landscape-induced atmospheric flow. *J. Atmos. Sci.* **52**, 1680–1698.

Zeng, X., and R. A. Pielke. 1995b. Landscape-induced atmospheric flow and its parameterization in large-scale numerical models. *J. Climate* **8**, 1156–1177.

Zeng, X., M. Zhao, and R. E. Dickinson. 1998. Intercomparison of bulk aerodynamic algorithms for the computation of sea surface fluxes using TOGA COARE and TAO data. *J. Climate* **11**, 2628–2644.

Zeng, X., M. Zhao, R. E. Dickinson, and Y. He. 1999a. A multiyear hourly sea surface skin temperature data set derived from the TOGA TAO bulk temperature and wind speed over the tropical Pacific. *J. Geophys. Res.* **104**, 1525–1536.

Zeng, X., M. Xhao, B. Su, and H. Wang. 1999b. Study on a boundary-layer numerical model with inclusion of heterogeneous multi-layer vegetation. *Adv. Atmos. Sci.* **16**, 431–442.

Zeng, X., R. E. Dickinson, A. Walker, M. Shaikh, R. S. DeFries, and J. Qi. 2000a. Derivation and evaluation of global 1-km fractional vegetation cover data for land modeling. *J. Appl. Meteor.* **39**, 826–839.

Zeng, X., M. Zhao, and B. Su. 2000b. A numerical study of land-surface heterogeneity from "combined approach" on atmospheric process, Part I: Principle and method. *Adv. Atmos. Sci.* **17**, 103–120.

Zhang, D.-L., and R. A. Anthes. 1982. A high-resolution model of the planetary boundary layer-sensitivity tests and comparisons with SESAME-79 data. *J. Appl. Meteor.* **21**, 1594–1609.

Zhang, D.-L., Y. Liu, and M. K. Yau. 2000. A multiscale numerical study of Hurricane Andrew (1992). Part III: Dynamically-induced vertical motion. *Mon. Wea. Rev.* **128**, 3772–3788.

Zhao, Q., T. L. Black, and M. E. Baldwin. 1997. Implementation of the cloud prediction scheme in the Eta model at NCEP. *Wea. Forecasting* **12**, 697–712.

Zhao, Q., and F. H. Carr. 1997. A prognostic cloud scheme for operational NWP models. *Mon. Wea. Rev.* **125**, 1931–1953.

Zhong, S., J. D. Fast, and X. Bian. 1996. A case study of the Great Plains low-level jet using wind profiler network data and a high-resolution mesoscale model. *Mon. Wea. Rev.* **124**, 785–806.

Zhou, X. P. 1980. Severe storms research in China. *Bull. Amer. Meteor. Soc.* **61**, 12–21.

Ziegler, C. L., and E. N. Rasmussen. 1998. The initiation of moist convection at the dryline: Forecasting issues from a case study perspective. *Wea. Forecasting* **13**, 1106–1131.

Ziegler, C. L., W. J. Martin, R. A. Pielke, and R. L. Walko. 1995. A modeling study of the dryline. *J. Atmos. Sci.* **52**, 263–285.

Ziegler, C. L., T. J. Lee, and R. A. Pielke. 1997. Convective initiation at the dryline: A modeling study. *Mon. Wea. Rev.* **125**, 1001–1026.

Zilitinkevich, S. S. 1970. *Dynamics of the Atmospheric Boundary Layer.* Hydrometeorol, Leningrad.

Zilitinkevich, S. S., and D. V. Chailikov. 1968. Determining the universal wind-velocity and temperature profiles in the atmospheric boundary layer. *Izvestiya, Atmos. Ocean. Phys.* **4**, 165–170 (English translation).

Zipser, E. J. 1971. Internal structure of cloud clusters. In *GATE Experimental Design Proposal,* Vol. 2, Annex VII. Interim Scientific Management Group, WMO-ICSU, Geneva.

Zipser, E. J. 1977. Mesoscale and convective-scale downdrafts as distinct components of a squall line structure. *Mon. Wea. Rev.* **105**, 1568–1589.

Zipser, E. J. 1982. Use of a conceptual model of the life-cycle of mesoscale convective systems to improve very-short-range forecasts. In *Nowcasting*, K. Browning, Ed., Academic Press, London, 191–204.

Zipser, E. J., and A. J. Bedard Jr. 1982. Front range windstorms revisited. *Weatherwise* **35**, 82–85.

Zipser, E. J., and C. Gautier. 1978. Mesoscale events within a GATE tropical depression. *Mon. Wea. Rev.* **106**, 789–805.

Zipser, E. J., R. J. Meitin, and M. A. LeMone. 1981. Mesoscale motion fields associated with a slowly moving GATE convective band. *J. Atmos. Sci.* **38**, 1725–1750.

Zou, X., A. Barcilon, I. M. Navon, J. Whitaker, and D. G. Caccuci. 1993. An adjoint sensitivity study of blocking in a two-layer isentropic model. *Mon. Wea. Rev.* **121**, 2833–2857.

Index

International Geophysics Series

EDITED BY

RENATA DMOWSKA

Division of Applied Science
Harvard University
Cambridge, Massachusetts

JAMES R. HOLTON

Department of Atmospheric Sciences
University of Washington
Seattle, Washington

H. THOMAS ROSSBY

Graduate School of Oceanography
University of Rhode Island
Narragansett, Rhode Island

*Out of print